XV International Conference on Computational Plasticity. Fundamentals and Applications

COMPLAS 2019

3-5 September, 2019
Barcelona, Spain

E. Oñate, D. R. J. Owen, D. Peric, M. Chiumenti and E. de Souza Neto (Eds.)



XV International Conference on Computational Plasticity. Fundamentals and Applications

COMPLAS 2019

Barcelona, Spain
September 3 - 5, 2019

A publication of:

International Centre for Numerical Methods in Engineering (CIMNE)
Barcelona, Spain

ISBN: 978-84-949194-7-3

Printed by: Artes Gráficas Torres S.L., Huelva 9, 08940 Cornellà de Llobregat, Spain

TABLE OF CONTENTS

Preface 7

Acknowledgements 9

Summary 11

Contents 13

Lectures 19

Authors Index 589

PREFACE

This volume contains the Technical Programme of the papers accepted for presentation at the XV International Conference on Computational Plasticity (COMPLAS 2017), held in Barcelona on 5-7 September 2017. The first fourteen conferences of the series were also held in Barcelona in April 1987, September 1989, April 1992, April 1995, March 1997, September 2000, April 2003 and September 2005, 2007, 2009, 2011, 2013, 2015 and 2017.

COMPLAS 2019 will be a special occasion as we will be celebrating the Jubilee edition of the COMPLAS conference.

The ever increasing rate of development of new engineering materials required to meet advanced technological needs poses fresh challenges in the field of constitutive modelling. The complex behaviour of such materials demands a closer interaction between numerical analysts and material scientists in order to produce thermodynamically consistent models which provide a response, while keeping with fundamental micromechanical principles and experimental observations. This necessity for collaboration is further highlighted by the continuing remarkable developments in computer hardware which makes the numerical simulation of complex deformation responses increasingly possible.

The developments that have taken place in these directions are illustrated by the contents of the papers included in these Proceedings. A stronger interaction between the phenomenological and micromechanical modelling of plasticity behaviour is apparent. The development of efficient and accurate computational methods for plasticity problems continues to be a challenging goal, while it is interesting to note the permanence of element modelling as a research issue. The blending of classical FEM with particle-based and discrete element methods and data mining procedures appears as a prominent area of research. Industrial forming processes, computational material design, geo-mechanics, bio-mechanics, composites, steel, concrete and masonry structures form the core of the applications of the different numerical methods presented.

The organizers would like to thank all authors for submitting their contributions, as well as the supporting organizations for their help in making COMPLAS XV possible.

Eugenio Oñate
Michele Chiumenti
Universitat Politècnica de Catalunya
Barcelona, Spain

Roger Owen
Djordje Peric
Eduardo de Souza Neto
Swansea University
Swansea, Wales, United Kingdom

ACKNOWLEDGEMENTS

The conference organizers acknowledge the support of the following organizations:

International Center for Numerical Methods in Engineering (CIMNE)

Universitat Politècnica de Catalunya (UPC)

Swansea University

European Community on Computational Methods in Applied Sciences (ECCOMAS)

International Association for Computational Mechanics (IACM)

We thank the **Plenary Speakers** and the **Invited Sessions Organizers** for their help in the setting up of a high standard Scientific Programme.

Contents

INVITED SESSIONS

IS-Applications of Computational Methods to Product and Process Design for Industry 21
IS-Computational Modeling of Material Forming Processes 81
IS-Computational Strategies for Metal Cutting & Forming Operations 93
IS-Limit Analysis and Plastic Collapse 100
IS-Model Order Reduction with Emphasis on Non-linear and Multi-scale Problems 145
IS-Multi-physics Simulation of Biomechanical Systems 170
IS-Multi-scale and Computational Scale Bridging 181
IS-Prediction and Utilization Process-induced Residual Stresses 189
IS-Virtual Element and Related Polygonal Methods for Inelastic Structural Applications 235

CONTRIBUTED SESSIONS

Advanced Material Models 249
Advanced Numerical Methods 305
Biomechanics 334
Composites 360
Computational Design of Functional Materials and Structures 395
Contact Problems 402
Damage, Fracture and Fatigue 411
Environment and Geosciences 427
Forming Processes 467
Geomechanics 529
Multi-Fracturing Solids, Multi-Physics Problems 553
Multi-Scale Material Models 577

CONTENTS

INVITED SESSIONS

IS-Applications of Computational Methods to Product and Process Design for Industry

Analysis of Spinner Straightening utilizing the Finite Element Method 21
K. Takashi, K. Keiichiro, K. Shohei, M. Hiromichi, O. Tetsushi and S. Hikaru

FE analysis on the Influence of Width Direction Deformation on Springback control in V-bending by Sheet Forging 31
J. Zhu, W. Liu and T. Iizuka

FE Analysis on Tube Hydroforming of Small Diameter ZM21 Magnesium Alloy Tube 38
H. Yasui, T. Miyagawa, S. Yoshihara, T. Furushima, R. Yamada and Y. Itoh

Finite Element Analysis of Tube Drawing Process with Diameter Expansion 48
S. Kajikawa, H. Kawaguchi, T. Kuboki, I. Akasaka, Y. Terashita and M. Akiyama

Modelling of Width Control for Hot Strip Mill with FEM Analysis 59
M. Sekimoto, M. Sano and K. Ohara

New Ductile Fracture Criterion for Prediction of Internal Fracture in Skew Rolling 69
K. Yamane, K. Shimoda and K. Kuroda

IS-Computational Modeling of Material Forming Processes

Analysis of Damage and Fracture Mechanisms in Ductile Metals under Non-proportional Loading Paths - Keynote Lecture 81
M. Brünig, S. Gerke and M. Zistl

IS-Computational Strategies for Metal Cutting & Forming Operations

Further Studies on Identification of Inelastic Parameters for Damaged Materials 93
M. Vaz jr. and M. Tomiyama

IS-Limit Analysis and Plastic Collapse

A Quasi-Static Nonlinear Analysis for Assessing the Fire Resistance of 3D Frames Exploiting Time-dependent Yield Surfaces 100
D. Magisano, F. Liguori, L. Leonetti, D. de Gregorio, G. Zuccaro and G. Garcea

Application of Numerical Modelling to the Comprehensive Analysis of Slope Stability 112
E. Hrubesova, N. Rapantova and P. Pospisil

High-Performance Interior Point Methods for Three-Dimensional Finite Element Limit Analysis 121
N. Podlich, A. Lyamin and S. Sloan

Limit Analysis and Inf-Sup Conditions on Convex Cones 133
S. Sysala, J. Haslinger and S. Repin

IS-Model Order Reduction with Emphasis on Non-linear and Multi-scale Problems

Identification and Model Reduction of Nonlinear Systems from Measured and Computed Data 145
I. V. Gosea and A. C. Antoulas

Reduced Finite Element square techniques (RFE2): towards industrial multiscale FE software 157
O. Lloberas-Valls, M. Raschi and J. Oliver

IS-Multi-physics Simulation of Biomechanical Systems

Optimization-based Comparison of Different Approaches for the Automatized Calculation of Residual Stresses and Fiber Orientations in Arteries 170
A. Zahn and D. Balzani

IS-Multi-scale and Computational Scale Bridging

FE2 Evaluation of Stress Triaxiality / Lode Angle Dependencies of Void Growing Processes 181
S. Nakamura, S. Suzuki, K. Matsui and T. Yamada

IS-Prediction and Utilization Process-induced Residual Stresses

Calculation of Sub-Surface-Initiated Fatigue Fractures in Gears 189
D. Müller, T. Tobie and K. Stahl

Macro- and micromechanical investigations on residual stresses in extruded components 201
P. Landkammer and P. Steinmann

Macroscopic FE-simulation of residual stresses in thermo-mechanically processed steels considering phase transformation effects 211
B. A. Behrens, A. Chugreev and C. Kock

Numerical thermo-elasto-plastic analysis of residual stresses on different scales during cooling of hot forming parts......223
S. Uebing, L. Scheunemann, D. Brands and J. Schröder

IS-Virtual Element and Related Polygonal Methods for Inelastic Structural Applications

A Virtual Element Approach for Micropolar Continua.....235
M. Pingaro, M. L. De Bellis and P. Trovalusci

CONTRIBUTED SESSIONS

Advanced Material Models

A Finite Strain Thermo-Mechanically Coupled Material Model for Semi-Crystalline Polymers, Incorporating Crystallisation Kinetics.....249
S. Felder, H. Holthusen, S. Hesseler, F. Pohlkemper, J. W. Simon, T. Gries and S. Reese

Crystal Plasticity Finite Element Modelling of Coarse-Grained α-Uranium.....261
N. Grilli, E. Tarleton, J. Askew and A. C. F. Cocks

Extended Concept of Representative Directions to Describe Inelastic Behaviour of Electrospun Polymers.....273
A. V. Shutov

Some Numerical Verification Examples for Plane Stress Elasto-Viscoplasticity.....281
A. Brezolin, T. dos Santos, P. Rosa and R. Rossi

Advanced Numerical Methods

Elastic properties of isotropic discrete systems with skew contact normals.....305
J. Eliáš

On the Accuracy of the Numerical Integrals of Newmark Method for Computing Inelastic Seismic Responses.....314
N. Yoshizaki, K. Ijima, H. Obiya and Z. M. Nizam

The Brezis-Ekeland-Nayroles Minimization Principle with Mixed Finite Element Method for Elastoplastic Dynamic Problems.....322
X. Cao, A. Oueslati, A. D. Nguyen, M. Stoffel, B. Market and G. de Saxcé

Biomechanics

Computational modeling of the behavior of biomarker particles of colorectal cancer in fecal matter.....334
G. Suárez Guerrero, E. Vallejo Morales and L. Hoyos Palacio

Multiscale Modelling of Liver Perfusion 343
E. Rohan, J. Turjanicová and V. Lukeš

Numerical Evaluation of Wearing Pressure and Cloth Stiffness on Vibration of Human Skeletal Muscle during Athletic Movement 354
S. Ueda and A. Sakuma

Composites

Durability Evaluation of Madake bamboo by FE Analysis of Fracture with Consideration of Fibre Direction 360
R. Ramful, A. Sakuma and H. Kimura

Elaboration and characterization of the thermo-mechanical properties of MWCNTs/PP composites by twin-screw mixe 369
S. Mohammed and T. Barriere

FE Analysis on Inhomogeneous Weaving of Metal Mesh by Corner Model of Plain Woven Structure 378
J. Zhang, H. Miyaki and A. Sakuma

Modeling Anisotropic and Rate-Dependent Plasticity in Short-Fiber Reinforced Thermoplastics 385
A. Amiri-Rad, L. V. Pastukhov, L. E. Govaert and J. A. W. van Dommelen

Computational Design of Functional Materials and Structures

Temporal nature of plasticity in the design of materials 395
N. Selyutina and Y. Petrov

Contact Problems

Softness Evaluation of Ultra-thin Elastic Body by Ball Indentation Technique 402
C. Lu and S. Atsushi

Damage, Fracture and Fatigue

A Zero-Thickness Mortar / Interface Formulation with Application to Fracture Mechanics 411
I. Carol and M. de Francisco

New developments in the application of configurational mechanics to crack propagation 420
L. Crusat, I. Carol and D. Garolera

Environment and Geosciences

Computational Analysis of the Behavior of Atmospheric Pollution due to Demographic, Structural Factors, Vehicular Flow, and Commerce Activities 427
G. Suárez Guerrero, J. A. Niño Navia, R. Chakir, J. D. Hoyos Giraldo and B. Streichenberger

Modelling Acid Attack of Oilwell Cement Exposed to Carbonated Brine: Effect of Specimen Geometry on Experimental Results 435
L. Barandiarán, J. Liaudat, C. M. López and I. Carol

Viscoplastic Constitutive Models for Zero-thickness Interface Elements, Formulation and Applications 447
I. Jaqués and I. Carol

Zero-thickness Interface Model with Chemical Degradation by Acid Attack 456
A. Martínez, J. Liaudat, C. M. López and I. Carol

Forming Processes

A Novel indicator for kinematic hardening effect quantification in deep drawing simulation 467
R. Lafarge, N. Küsters and A. Brosius

Finite Element Analysis of Residual Stresses in Large Cold-Rolled Threads 479
J. Unglaub, H. Jahns and K. Thiele

New approach for determination of strain rate sensitivity of mild steel DC01 under stack compression and uniaxial tensile tests.....489
P. Farahnak, M. Urbanek, M. Rund, J. DŽugan, S. Gerke and M. Brunig

Non-linear model-predictive-control for thermomechanical ring rolling....499
A. Brosius, M. Tulke and C. Guilleaume

The breakage prediction for hydro-mechanical deep drawing based on local bifurcation theory.....510
H. Lu, W. Huang, H. B. Yu and S. J. Qin

Thermo-Mechanical Analysis of Additively Manufactured Hybrid Extrusion Dies with Conformal Cooling Channels 519
C. Bertoli, P. Stoll and P. Hora

Geomechanics

Prediction of Unsupported Excavations Behaviour with Machine Learning Techniques 529
S. Commend, S. Wattel, J. Hennebert, P. Kuonen and L. Vulliet

Temporal Characterization of Rock Dynamic Destruction 536
A. N. Martemyanov and Y. Petrov

Thermo-Hydro-Mechanical Simulation of a Full-Scale Steel-Lined Micro-Tunnel Excavated in the Callovo-Oxfordian Argillite 544
S. Tourchi, J. Vaunat, A. Gens, M. N. Vu and F. Bumbieler

Multi-Fracturing Solids, Multi-Physics Problems

Finite Volume Analysis of Reinforced Concrete Structure Cracking Using a Thermoplastic-Damage Model 553
B. Selma, M. Chekired, J. Côté, C. Bessette and L. Jinga

Heat transport with advection in fractured rock 565
A. Pérez, I. Carol and P. Prat

Multi-Scale Material Models

An optimization of the local Hall-Petch relationship using slip trace analysis technique and scale transition rules: Application in an equiaxed Ti-6Al-4V titanium alloy 577
M. Cheikh, F. Benmessaoud, V. Velay, V. Vidal, C. Boher and F. Rezai-Aria

LECTURES

XV International Conference on Computational Plasticity. Fundamentals and Applications
COMPLAS 2019
E. Oñate, D.R.J. Owen, D. Peric, M. Chiumenti & Eduardo de Souza Neto (Eds)

ANALYSIS OF SPINNER STRAIGHTENING UTILIZING THE FINITE ELEMENT METHOD

TAKASHI KUBOKI*, KEIICHIRO KAWASAKI†, SHOHEI KAJIKAWA†, HIROMICHI MATSUMURA††, TETSUSHI ONO†† and HIKARU SEIMIYA††

* Department of Mechanical Engineering & Intelligent Systems
The University of Electro-Communications
1-5-1 Chofu Gaoka, Chofu-shi, Tokyo, 182-8585, Japan
e-mail: kuboki@mce.uec.ac.jp - web page: http://www.mt.mce.uec.ac.jp/

† Department of Mechanical Engineering & Intelligent Systems
The University of Electro-Communications
1-5-1 Chofu Gaoka, Chofu-shi, Tokyo, 182-8585, Japan

†† Shimomura Tokushu Seiko Co.,Ltd.
668-1 Matsuomachi Kashikehongo, Sammu-shi, Chiba, 289-1537, Japan
web page: http://www.sts-shimomura.com/

Key words: Spinner, Straightener, Straightness, Warp, Moment, Curvature

Abstract. This paper presents analysis methods utilizing the Finite Element Method for spinner straightening, and shows a guideline for optimum conditions. Two types of analysis methods were composed. Model [F-Expl], "full actual model with explicit scheme", considers the rotational movement of dies as the actual process using the explicit scheme. Model [BndCr], "a model carrying out fundamental analysis on one cross section based on simple bending in the Finite Element Method (FEM)", uses the FEM only for calculation of simple bending without rotation for obtaining the deformed bar shape. A series of experiments were conducted in an actual production line as well as the analyses by Model [F-Expl] and [BndCr]. The examination mainly focused upon the effect of straightening intensity by changing the die positions. The experimental and analytical results show some mechanism of straightening and a basic guideline for the optimum working condition.

1 INTRODUCTION

Straightening is located at the end of manufacturing process for bars and wire rods, and determines the quality of the final product. The requirement to the dimensional precision of bars and wire rods are getting stricter due to the recent trend of requirements to the final products which use the bars and wire rods, and then the role of straightening

process is getting more important. Figure 1 shows the process line of bars. The initial bar is unwound from the coils on the supply stand, and drawn before the line of straitening processes. The straightening line is composed of a couple of processes, which includes spinner, polishing and two-roll straighteners. These straightening processes would collaboratively determine the quality of the bars, and the spinner is located at the first of the three processes.

There are few research works for spinner, though there are many for the final process, like two-roll straighter. Yanagihashi et al. [1] and Mutrux et al. [2] tried to apply the FEM to solid-bar straightening with deciding the deformed shape in advance. Furugen composed a fundamental analysis for tube straightening considering axial deformation at first, followed by the consideration of cross-sectional deformation [3]. Kuboki et al. composed a FEM model applying the implicit scheme for three-stand tube straightening [4]. Wu et al. carried out theoretical approach for analyzing the mechanism of two-roll straightener [5]. However, all the above works focused upon the final process in the production line without knowing phenomena in the first process, that is spinner straightening. Although Tsurumi et al. conducted a study on a spinner-like machine, the material was a very thin wire and the study is not so general [6].

The present study focuses upon the spinner straightening, which is the first process and may plays an important role in the production line. Analysis methods are composed utilizing the Finite Element Method for proposing a guideline for optimum conditions. Two types of analysis methods are shown. Model 1, "full actual model with explicit scheme [F-Expl]", considers the rotational movement of dies as the actual process using the explicit scheme. Model 2, "a model carrying out fundamental analysis on one cross section based on simple bending in FEM [BndCr]", uses the FEM only for calculation of simple bending without rotation for obtaining the deformed bar shape. A series of experiments were conducted in an actual production line as well as the analyses by Model [F-Expl] and [BndCr]. The examination mainly focused upon the effect of straightening intensity by changing the die positions for showing mechanism in spinner straightening and a guideline for the optimum working condition.

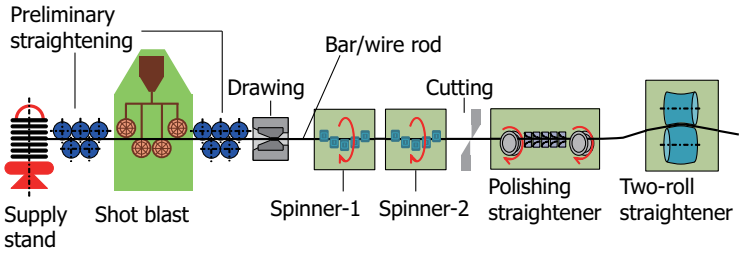


Figure 1: Process line for bars and wire rods

2 CONDITION FOR SPINNER

Figure 2 shows a schematic illustration of spinner. Only the second spinner [Spinner-2] (see Fig. 1) was used in this study. The die positions h_i $(i = 1 \cdots 5)$ was defined so

that the h_i should be zero when the dies contact with a completely straight bar without any load. The sign (positive/negative) of h_i was defined as shown in the figure. The die positions h_i determine the bending intensity during straightening. The detailed condition on the die positions are shown in Table 1. Condition [A] is intuitively expected to have the strongest straightening effect.

Table 2 shows the drawing condition in advance of spinner straightening. Coils of lead-free free-cutting steel was annealed, and drawn. Two-pass drawing was conducted under the condition [a], and the area reduction at the second pass was set to be around 1 % so that the residual stress should be leveled to almost zero as clarified in the literature [7]. Conventioal one-pass drawing was employed for (b) so that the residual stress might generate. The difference between conditions [a] and [b] would show the effect of residual stresses on straightening. Table 3 shows other working conditions.

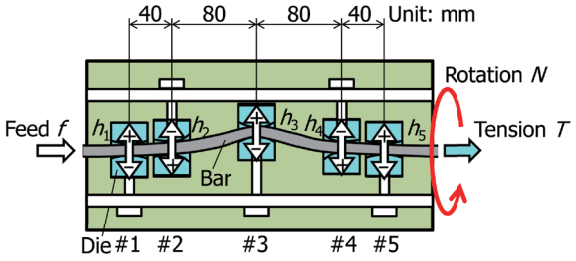


Figure 2: Composition of spinner straightener

Table 1: Die position for spinner straightening

	Position h_i/mm $(i = 1 \cdots 5)$				
[A]	0	-2.25	11.0	-2.25	0
[B]	0	-1.875	10.0	-1.875	0
[C]	0	-1.55	9.0	-1.55	0
[D]	0	-1.3	8.0	-1.3	0
[E]	0	-1.1	7.0	-1.1	0
[F]	0	-0.97	6.0	-0.97	0
[G]	0	-0.92	5.5	-0.92	0

Table 2: Drawing condition before spinner straightening

	Initial		Die inside diameter	
	Diameter d_0/mm	Heat treat	1st d_1/mm	2nd d_b/mm
[a]	7.0	Anneal	6.08	6.05
[b]	7.0	Anneal	-	6.05

Material: Lead-free free-cutting steel
Flow stress (after spinner straightening):
$\sigma = 855(\varepsilon + 0.11)^{0.089}$

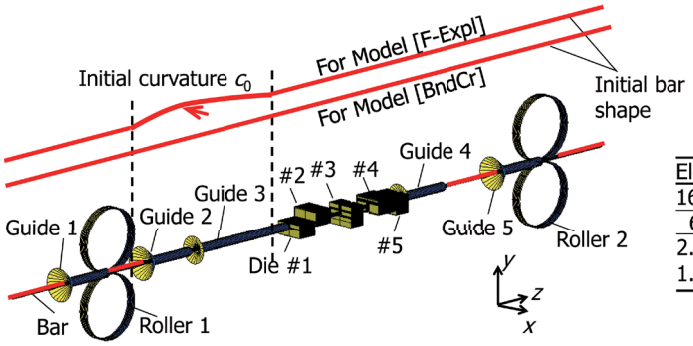
Table 3: Working condition

Feed pitch f/mm · rev^{-1}	9.52
Initial cuvature c_0/mm $^{-1}$	8.8 $\times 10^{-5}$

3 ANALYTICAL MODELS

3.1 Full explicit scheme model [F-Expl]

Two analytical models were composed, and the detailed settings are explained in this section. Figure 3 shows the composition of spinner in the Finite Element Analysis (FEA). Guides and rollers were introduced as well as the bar and the dies. Residual stresses are assumed to be zero in the analyses in this study.



Element size for evaluated portion
16 divisions in hoop
6 divisions in diameter
2.38 mm/division in axis [F-Expl]
1.19 mm/division in axis [BndCr]

Figure 3: Model in FEA

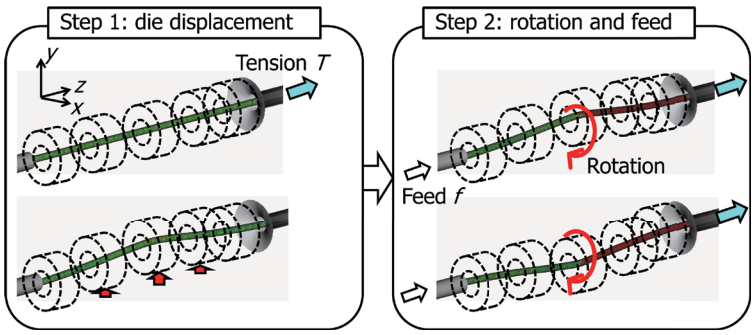


Figure 4: Analysis steps in model [F-Expl]

The first model (F-Expl, full explicit) almost fully reproduced the movement of spinner straightening using the explicit scheme. The analysis was carried out by two steps as shown in Figure 4. The bar was set through Guide 1 to roller 2 via dies #1 – #5, and the front tension T was applied. The dies gradually moved to the target position of $h_i (i = 1, \cdots, 5)$ at Step 1. At Step 2, the rotational movement was given to the dies, while feeding movement was given to the bar end. Although Model [F-Expl] would not be as precise as a model with the implicit scheme, it can consider the centrifugal force and the convergence would be stable. An initial curvature c_0 was given to the bar between the Roller 1 and Die #1, and the curvature was evaluated at the same portion of the bar during and after the spinner straightening.

The FEA was carried out using the commercial code ELFEN, which was developed by Rockfield Software Limited, Swansea. A von Mises' yield criterion was adopted, and

the normality principle was applied to the flow rule. Constraints were dealt with by the penalty function method. 8-node hexahedral elements were employed.

3.2 One cross section analysis following FE bending [BndCr]

The second model (BndCr, bending and cross section) was also composed of two steps as shown in Figure 5. Step 1 is the same to that of Model [F-Expl], and the distribution of axial strains $\varepsilon_u(z)$ on the upper side and $\varepsilon_d(z)$ on the down side were extracted and transferred to Step 2. Step 2 calculated curvature distribution $c(z)$, axial strain distribution $\varepsilon_{ax(x,y,z)}$, axial stress distribution $\sigma_{ax(x,y,z)}$, and Moment distribution $M(z)$ in order. The detailed procedure is shown in Figure 6, and the meanings of the symbols are shown in Table 4. This model assumed that the bar shape should be kept just as the bent shape at Step 1, and calculated the strain and stress history. Kinematic hardening and Bauschinger effect were not taken into account. The curvatures c_{ex} and c_{ey} after spinner straightening were determined so that the moment, which is the integration value of axial stress σ_{ax}, should be zero.

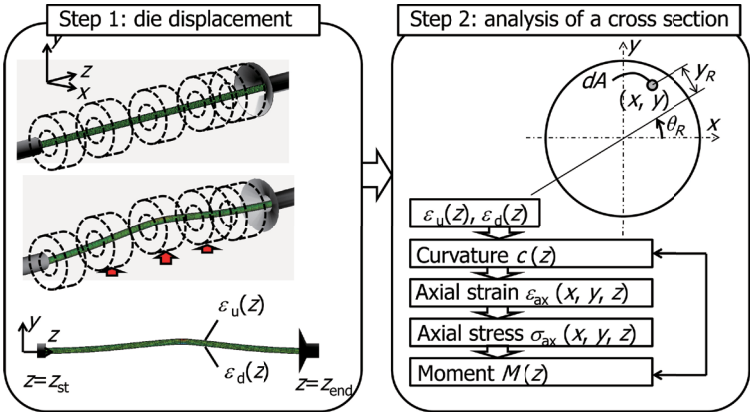


Figure 5: Analysis steps in model [BndCr]

Table 4: Notation

$\phi(k)$	initial curvature direction	z	axial position	z_{st}	start position
z_{end}	end position	c	curvature	ε_{el}	elongation strain
c_x	curvature in x	c_y	curvature in y	ε_{ax}	axial strain
σ_{ax}	axial stress	M_x	moment around x axis	M_y	moment around y axis
c_{ex}	curvature around x axis	c_{ey}	curvature around y axis	c_S	short-span curvature
c_L	long-span curvature	d_b	bar diameter		

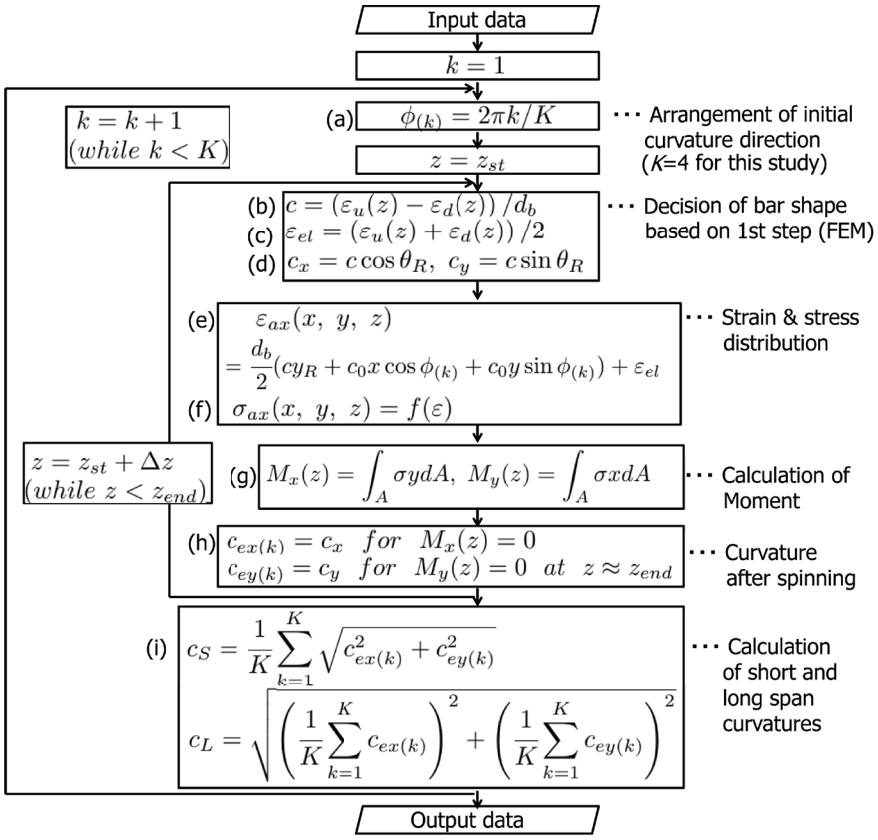


Figure 6: Flow chart for 2nd step in model [BndCr]

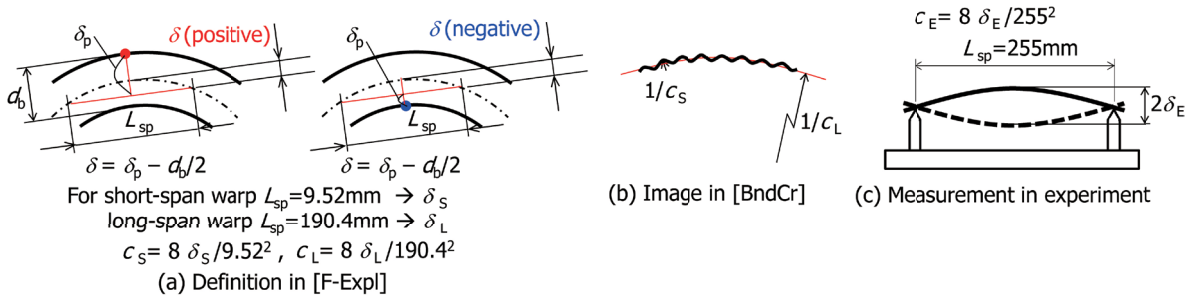


Figure 7: Curvature

3.3 Evaluation of straightness

Curvature was used for the evaluation of straightness, and was defined as shown in Figure 7. Model [F-Expl] can show curvature distribution. The curvature was calculated for each node as shown in Figure 7(a). When the value was positive, the node was placed on the extrados of the bar arc. When it was negative, the node was on the intrados. The chord lengths L_{sp} were set to be 9.52 mm (feed pitch f) and 190.4 mm ($10f$) for evaluation of short-span curvature c_S and long-span curvature c_L. In Model [BndCr], the short-span

curvature c_S and long-span curvature c_L were calculated by equations in Figure 6. The image of c_S and c_L are shown in Figure 7(b). The long span curvature c_E was measured in the experiment as shown in Figure 7(c).

4 ANALYTICAL AND EXPERIMENTAL RESULTS

4.1 Results in full explicit scheme model (F-Expl)

Model [F-Expl] shows the dynamic shape change during spinner straightening. Figure 8 shows the curvature distribution during spinner straightening under the condition of Table 1[B]. "Initially intrados line"in (a) means the intrados line of the curved bar with curvature of c_0 in Figure 3. The bar started to be twisted at Die #3. The short-span curvatures periodically generated at Die #3.

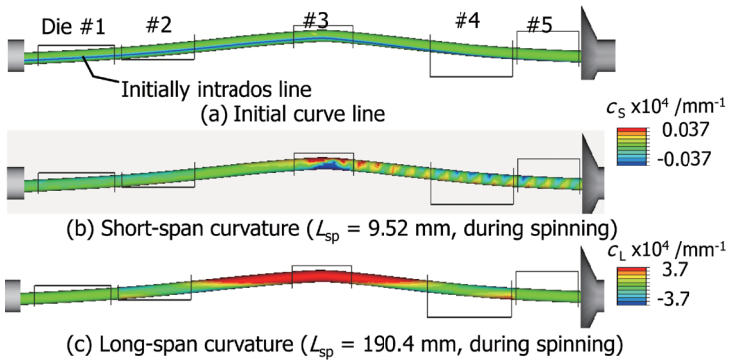


Figure 8: Spiral and warp during spinner straightening under the condition of Table 1[B]

Figure 9 shows the curvature distribution after spinner straightening under the condition of Table 1[B]. It is noteworthy that the extrados (red part) and the intrados (blue part) are found to be inconsistent before and after spinner straightening by comparing (a) and (c). In other words, the initial curvature was eliminated by spinner straightening. On the other hand, short-span curvatures periodically exist as shown in (b). If these curvatures c_S cancel each other, the long-span curvature c_L should be leveled to zero. However, the c_S did not cancel each other, and then c_L appeared.

Figure 10 shows the effect of Die #3 position h_3 on the curvature after spinner straightening. The curvatures c_L and c_E increased with increase of h_3. The model [F-Expl] and experimental results qualitatively show the same results. The spinner conditions in Table 1 might be strong enough for the elimination of the initial curvature, and these conditions would be called as "over straightening". As the result, the large h_3 caused large short-span curvature c_S, resulting in large long-span curvature c_L. The experimental results also showed that the effect of residual stress before spinner straightening on straightening effect was small as the difference between [a] (2-pass drawing: very small residual stresses) and [b] (1-pass drawing) was small. Figure 11 shows the effect of Die #3 position h_3 on twist in spinner straightening. The bars were twisted at Die #3. The spiral angle ϕ

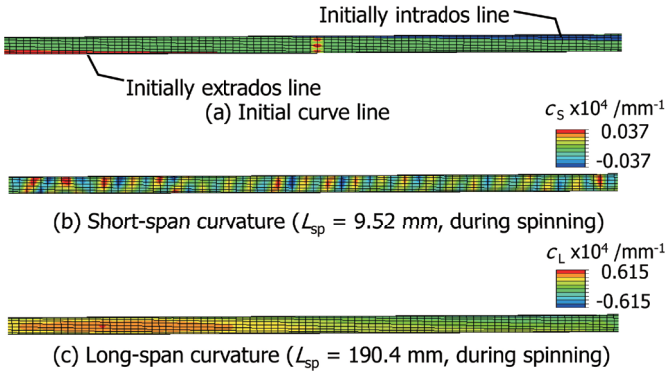


Figure 9: Spiral and warp after spinner straightening under the condition of Table 1[B]

increased with increase of h_3.

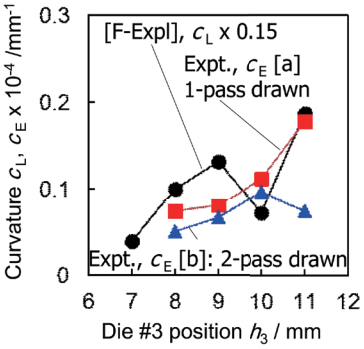


Figure 10: Effecti of die position on curvatures in [F-Expl] and experiment

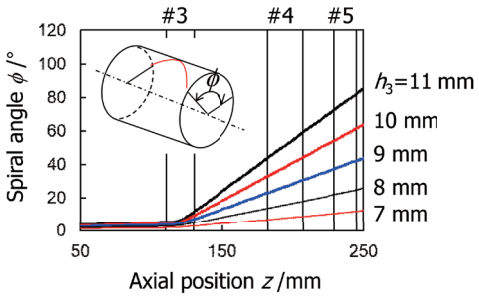


Figure 11: Effect of die position on twist in bar bar obtained by [F-Expl]

4.2 Results in one cross section analysis following FE bending [BndCr]

Model [BndCr] shows the results, which is obtained based on the statically bent bar. Figure 12 shows the effect of Die #3 position h_3 on the curvature after spinner straightening. The analytical long-span curvature c_L decreased with increase of h_3 against the experimental one c_E. On the other hand, the analytical short-span curvature c_S qualitatively show the same tendency to c_E. 0.06 times c_S might be used for the prediction of the experimental long-span curvature c_E. In the static model [BndCr], the local curvatures would cancel each other, and then the long-span curvature c_L decreased with increase of h_3. However, in the experiment, the local curvature do not completely cancel each other, excessive h_3 lead to large curvature c_E.

The mechanism in spinner straightening would be depicted as in Figure 13. When Die #3 position h_3 is small, the initial long-span curvature should exist as (a). When h_3 is appropriate, short-span curvatures or waves periodically appears eliminating the initial long-span curvature as (b). When h_3 is excessively large, the short-span curvatures are

large as (c). If the short-span curvatures cancel each other, the long-span curvature would be kept at the small value as (c1). However, they do not cancel each other in practice, and then the long-span curvature becomes large as (c2).

The residual axial stresses are shown in Figure 14. Under the conditions in this study, the residual stress increased with increase of Die #3 position h_3. In other words, the residual stress increased with increase of long-span curvature c_E in the experiment.

These results show a fundamental guideline for spinner straightening, i.e. it is important to give minimum bare bending intensity to the bent part. Excessive intensity leads to secondary increase of long-span curvature as well as residual stresses.

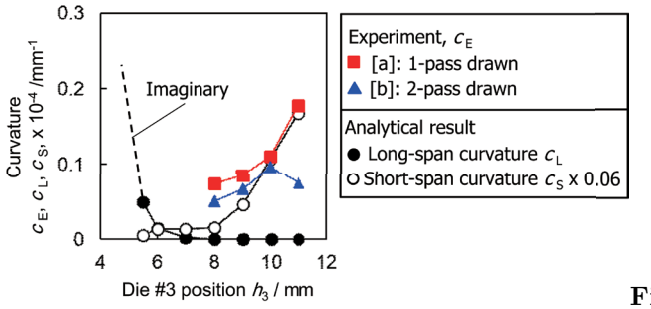


Figure 12: Curvatures in [BndCr] and experiment

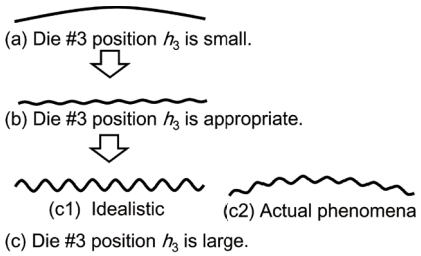


Figure 13: Mechanism for curvature generation

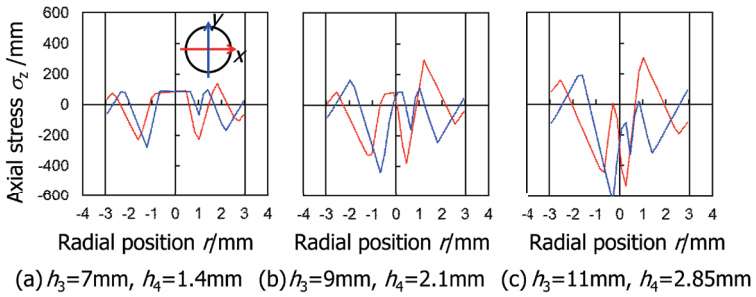


Figure 14: Residual stress after spinner straightening

5 CONCLUSIONS

- This paper presents two analytical models. One is Model [F-Expl] and the other is Model [ExplCr].
- [F-Expl] almost fully reproduced the movement of spinner straightening using the explicit scheme.
- [F-Expl] shows the distribution of both short and long span curvatures in a visual way.

- [F-Expl] showed that long-span curvature increased with increase of Die #3 position, or the increase of the intensity of straightening under the conditions of this study. This analytical tendency is qualitatively the same to that in experiment.
- [ExplCr] analyzed one-cross section based on the simple and static bending of the bar.
- [ExplCr] showed that 0.06 times calculated short-span curvature is the same level of long-span curvature in the experiment. Therefore, the 0.06 times the value might be used for prediction of the experimental curvature for the optimization of straightening condition.
- [ExplCr] showed residual stress might increase with increase of curvature in the experiment.
- Experimental curvature increased with increase of the bending intensity in this study. It would be attributed to the increase of short-span curvatures, which do not cancel each other.
- A fundamental guideline for spinner straightening was obtained, i.e. it is important to give minimum bare bending intensity to the bent part. Excessive intensity leads to secondary increase of long-span curvature as well as residual stresses.

REFERENCES

[1] Yanagihashi, T., Hama, T., Onoda, Y., Asakawa, M. Effect of plastic ratio and repeat bending on straightness in two-roll straightening - higher straightening and lower residual stress technology of bar products 3 -, *J. Jpn. Soc. Technol. Plast.*, (2005), **46**-537:972-976,in Japanese.

[2] Mutrux, A., Berisha, B., Weber, M., Hora, P. Fe simulation of cross roll straightening:, *COMPLAS X*, (2009) Barcelona, 23 in Index.

[3] Furugen, M., Hayashi, C. *Proc. 3rd. Int. Conf. Steel Rolling*, (1985) Tokyo, 497.

[4] Kuboki, T., Huang, H., Murata, M., Yamaguchi, Y., Kuroda, K. Fem analysis of tube straightener adopting implicit scheme, *Steel Research Int.*, (2010) **81**-9:584-587.

[5] Wu, B., Chan, L., Lee, T., Ao, L. A study on the precision modeling of the bars produced in two cross-roll straightening, *J. Mater. Process. Technol.*, (2000) **99**:22-206.

[6] Tsurumi, K., Asakawa, M., Kato, N., Urabe, M., Yoshida, M., Sakumoto, K., Kanno, T. *J. Jpn. Soc. Technol. Plast.*, (2014), **55**-640:435-439,in Japanese.

[7] Kuboki, T., Akiyama, M., Neishi, Y., Kuroda, K. Effect of final drawing with light reduction on the levelling of residual stress distribution in cold bar drawing, *Proc. Instn Mech. Engrs, Part C, J. of Mech. Eng. Sci.*, (2000) **214**-12:1389-1400.

XIV International Conference on Computational Plasticity. Fundamentals and Applications
COMPLAS 2019
E. Oñate, D.R.J. Owen, D. Peric , M. Chiumenti, and Eduardo de Souza Neto (Eds)

FE ANALYSIS ON THE INFLUENCE OF WIDTH DIRECTION DEFORMATION ON SPRINGBACK CONTROL IN V-BENDING BY SHEET FORGING

JUNZE. ZHU[*], WUYANG. LIU[**] AND TAKASHI. IIZUKA[†]

[*] Department of Mechanical Design
Kyoto Institute of Technology
Matsugasaki Goshokaido-cho, Sakyo-ku, Kyoto 606-8585, Japan
e-mail: m8623552@edu.kit.ac.jp

[**] Department of Engineering Design
Kyoto Institute of Technology
Matsugasaki Goshokaido-cho, Sakyo-ku, Kyoto 606-8585, Japan
e-mail: d7821010@edu.kit.ac.jp

[†] Faculty of Mechanical Engineering
Kyoto Institute of Technology
Matsugasaki Goshokaido-cho, Sakyo-ku, Kyoto 606-8585, Japan
e-mail: tiizuka@kit.ac.jp

Key words: FE analysis, Springback, V-bending, Forging, Warp.

Abstract. There have some problems in the press engineering. One of the most representative phenomena is springback. Traditionally, a series of empirical methods were used to obtain target bending angle. However, such methods are relied on the ability and experience of engineer. Therefore, the control of springback is important. According to the viewpoint of plastic processing, it is considered that springback could be controlled by sheet forging method which was added after V-bending process used a punch with a single lump-punch. On the other hand, warp would occur in air bending process when the ratio of width to thickness is relatively small. So, it is considered that width direction deformation would affect springback control to some extent in case of warp is occurred. In this study, V-bending and continuous forging processes were conducted used FE analysis. From the analytical results, occurrence of warp was found. Next, model of these processes in consideration of warp was re-modified. Finally, it was found that the springback was controlled to some extent derived from width direction deformation.

1 INTRODUCTION

In recent decades, lightweighting has become an important subject especially in sheet metal industry for saving resources and reducing the emissions of the carbon dioxide. Therefore, in order to realize lightweighting, many strategies have been proposed [1,2]. At the same time, there are still some problems in press engineering. One of the most representative is large springback in bending process. Traditionally, a series of empirical methods were used to obtain

target bending angle. However, such methods are relied on the ability and experience of engineer. Therefore, controlling springback is necessary. Until now, many studies on the control and prediction method of springback have been reported [3,4].

It is considered that springback could be compensated through varying the mechanical state of bending portion. In our prior study, a sheet forging method was added after V-bending process [5,6]. Both of analytical results and experimental results showed that the spingback amount decreased with increasing forging amount. It is thought that springback could be quantitatively controlled by this continuous sheet forging process.

Actually, warp would be occurred in bending process if the ratio of width to thickness relatively small. However, previous study didn't consider about it. In this study, in order to confirm the effect of width direction deformation on springback control, V-bending and continuous forging processes were conducted used FE analysis. From the analytical results, it was found that warp was occurred. Based on it, the model of these processes in consideration of warp occurrence was re-modified firstly. Then, based on the analytical results, the starting and ending point of warp correction was identified respectively. Finally, it was also found that springback amount was reduced to some extent derived from width direction deformation.

2 MECHANISM OF V-BENDING PROCESS COMPENSATED BY SHEET FORGING

Figure 1 shows the mechanisms of normal bend in loading and unloading. When a sheet metal is subjected to normal bend, as for stress state, the inside surface of bending portion is under compression state and the outside surface is under tension state. Therefore, in case of loading, the inside and the outside of bending portion will be shrunk and stretched respectively. On the other hand, in case of unloading, the inside portion will be stretched, and the outside portion will be shrunk. This difference of deformation mechanism between loading and unloading is considered to be the driving power of springback.

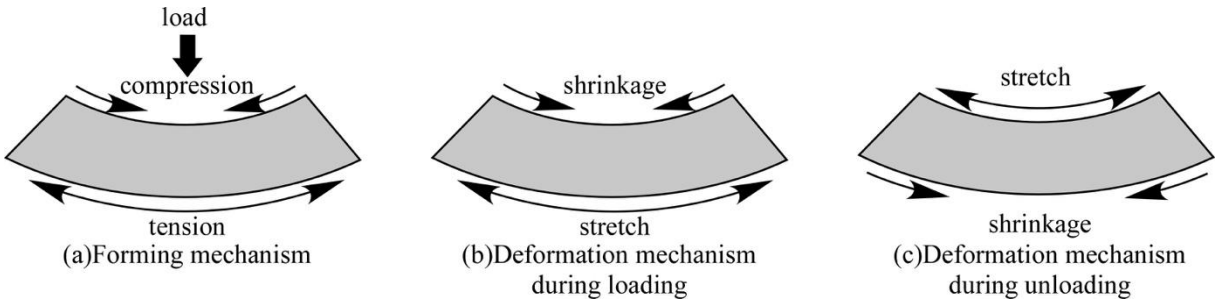


Figure 1: Mechanisms of normal bend in loading and unloading

Figure 2 shows the schematic diagram of mechanism of sheet forging after V-bending process with using lump-punch. Due to the forging process, the inside of bending portion will be stretched locally. In case of loading, both of the inside and the outside of bending portion would be subjected to stretching deformation. When unloading the punch, both of the deformation will be changed to shrinkage. Therefore, it is considered that the springback will be controlled to some extent by this sheet forging method.

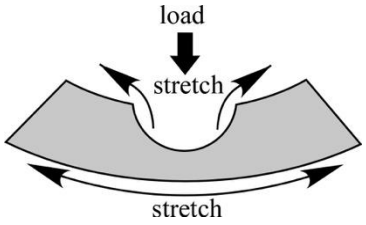


Figure 2: Mechanism of sheet forging after V-bending process with using lump-punch

3 ANALYSIS

3.1 Analytical conditions

In order to investigate the bending and forging deformation behavior of specimen in this test, FE(Finite Element) analysis simulation was conducted. All of the model was referred from the information used in experiment which was in order to reproduce the process conducted in actual experiment. In this study, all FE analysis were carried out utilizing an explicit FE code, SIMUFACT 15.0.

Table 1: Analytical condition

Material	A5052-H
Young modulus / GPa	71
Poisson's ratio	0.33
n-value*	0.13
F-value* / MPa	381
Mesh size / mm	0.3
Punch displacement rate / mm・min^{-1}	5
Friction coefficient between punch (die) and specimen	0.12

*$\sigma = F\varepsilon^{n}$

In this present study, isotropy material model with Mises yield criterion was assumed in order to confirm the effect of width direction deformation on springback control only. **Table 1** lists analytical conditions used in this study. Young's modulus E and Poisson's ratio v were set as 71GPa and 0.33 respectively. Hollomon power law was set as work hardening rule, which follows the relation $\sigma = F\varepsilon^{n}$. Here, F is plastic coefficient and n is work hardening exponent. They were measured from the uniaxial tensile tests used JIS 13B specimen made by Aluminum alloy A5052-H. They were set as 381MPa and 0.13, respectively. As for specimen model, **Figure 3** shows the schematic diagram of specimen. Size of specimen was 70mm×12.5mm with thickness of 3mm. In this study, quarter-size specimen models expressed by solid elements were used in order to reduce computational time. Mesh size was set to 0.3mm. **Figure 4** shows a view of FEA model of die and punch which imitated experimental ones. Radius of the punch and inner diameter of the die is 4mm and 10mm. And the distance between two supporting position is 40mm. The punch was set to run at the constant displacement rate of 1.0mm・min^{-1}. During V-bending and forging process, friction coefficient between punch (or die) and

specimen was set as 0.12.

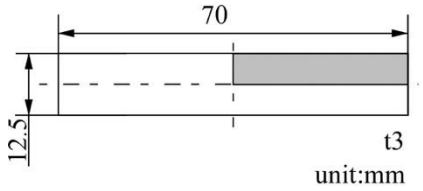


Figure 3: Schematic diagram of specimen

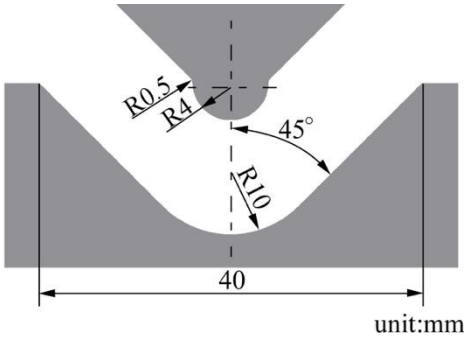


Figure 4: View of die and punch

3.2 Analytical procedure

A series of schematic view of analytical procedure were shown in **Figure 5**. Firstly, the specimen was set and supported by lower die. Then punch started to push down, until the specimen fitted the die, it is thought that specimen was subjected to V-bending deformation. After that, as punch stroke developed, punch would be pushed into specimen. In this stage, specimen was under forging deformation.

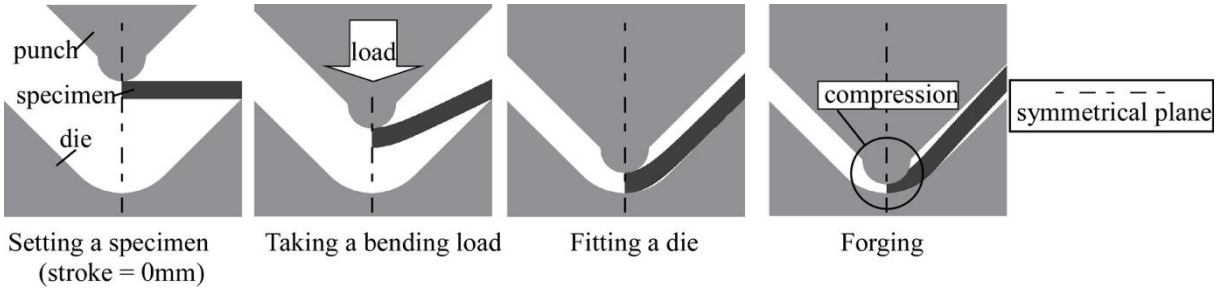


Figure 5: Schematic view of analytical procedure

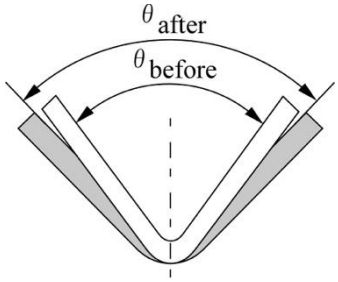


Figure 6: Schematic diagram of springback

Figure 6 shows the schematic diagram of springback. In this study, degree of springback was evaluated by the springback amount $\Delta\theta$, which was calculated by the following equation.

$$\Delta\theta = \theta_{after} - \theta_{before} \quad (1)$$

Where θ_{before} and θ_{after} means the bending angle before and after unloading respectively.

4 ANALYTICAL RESULT

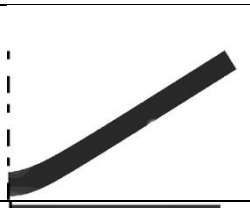
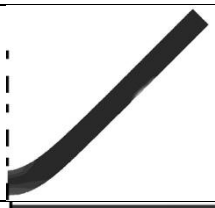
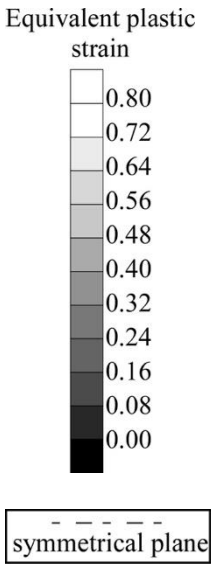
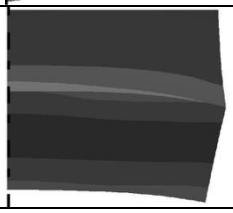
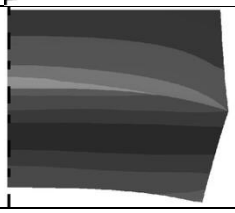
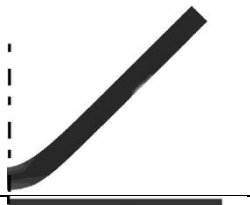
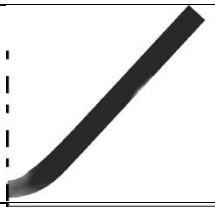
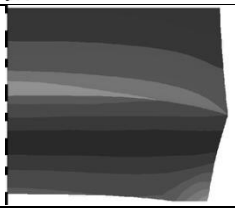
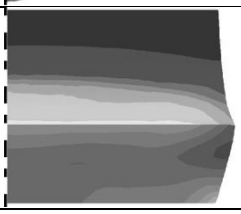
Firstly, we investigated the deformation behavior and the variation of specimen shape with different punch stroke. **Table 2** shows the comparison of equivalent plastic strain distribution of specimen with different punch stroke. The distributions in longitudinal direction and width direction were also compared. From these results, as for specimen start to be subjected to V-bending process, it can be seen that warp was occurred, and the degree of warp shape became more and more obvious with increasing punch stroke. Moreover, it can be also found that, relatively strong plastic deformation had already occurred at inner bending surface of specimen. Next, when stroke was over 15.45mm, it can be seen that, the lowest position at the outermost side in the width direction of specimen contact with the die firstly. After that, as shown in the results of stroke = 15.70mm, it can be found that the warp shape was flattened gradually as punch stroke developed. Here, strong plastic deformation was also occurred at the lowest position of specimen. Finally, with increasing punch stroke, it can be found that the thickness of specimen decreased obviously. And strong plastic deformation was occurred at bending portion totally. It is thought that the forging process has been subjected to specimen.

Therefore, when wrap is occurred in V-bending, it is essential to re-modify the process model which was shown in **Figure 5**. Therefore, the re-modified processes model in consideration of warp should have three stages as following:

(1) V-bending (air bending) stage: In this stage, the specimen is subjected to bending deformation, and the degree of wrap shape become more and more obvious as punch stroke increased.
(2) Warp correction stage: In this stage, the as punch stroke developed, the warp shape would be flattened gradually.
(3) Forging stage: After warp shape being flattened, the bending portion in V-bending stage would be thinner obviously in this stage due to the compression.

Based on this re-modified process model and results shown in **Table 2**, the starting and ending point of warp correction was identified respectively. Here, in this study, the warp starts to be corrected when stroke is 15.45mm. The warp correction stage will last until punch stroke is 15.95mm. Here, the starting point of warp correction stage also means the ending point of V-bending stage. And the ending point of warp correction stage also means the starting point of forging stage.

Table 2: Comparison of equivalent plastic strain distribution of specimen with differnet punch stroke

	Stroke = 10mm	Stroke = 15.45mm	
Longitudinal direction			
Width direction			
	Stroke = 15.70mm	Stroke = 16.50mm	
Longitudinal direction			
Width direction			

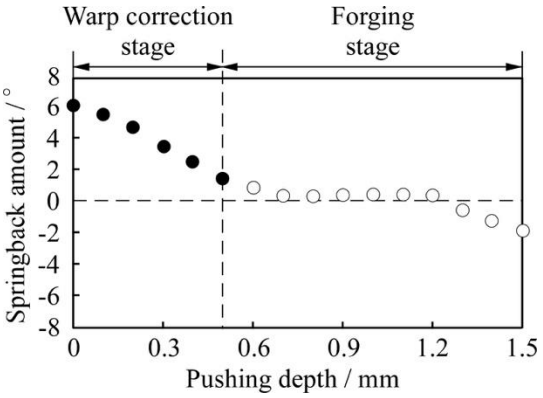


Figure 7: Relationship between pushing depth and springback amount

Based on the results and the consideration of warp occurrence, we defined the moving amount of punch after V-bending stage as pushing depth. **Figure 7** shows the relationship between pushing depth and springback amount. From this result, it was found that the springback amount decreased with increasing pushing depth almost linearly in the range of

pushing depth was 0~0.7mm. After that, the springback amount was almost 0 until pushing depth was 1.2mm, which means that springback has almost been controlled. Then, when pushing depth was over 1.2mm, springback amount would continue to be decreased. Based on the re-modify the process model introduced above, it can be also found that the 78% of the degree of springback was controlled in the warp correction stage. On the other hand, only 22% of springback was controlled in the forging stage. It is considered that, in case of the warp is occurred, the width direction deformation affects the springback control certainly. And the warp correction process contributes a lot more than that of forging process on springback control.

5 CONCLUSION

In this present study, FE analysis was conducted in order to investigate the effect of width direction deformation on springback control. The results obtained from this study are summarized as following:

(1) As for the specimen used in this study, the warp occurrence was confirmed in the V-bending range. The degree of warp shape became more and more obvious with increasing punch stroke.
(2) The processes model which is combined with V-bending and forging was re-modified. In consideration of warp occurrence, the re-modified model was divided into three stages: V-bending stage, Warp correction stage and Forging stage.
(3) After V-bending stage, the springback amount decreased almost linearly as pushing depth increased. Although springback was almost controlled in the forging stage, most of springback was controlled in warp correction stage.

REFERENCES

[1] Kleiner, M., Geiger, M. and Klaus, A. Manufacturing of Lightweight Components by Metal Forming. *Ann. CIRP.* (2003) **52**:521-542.
[2] Tekkaya, A.E., Khalifa, N.B., Grzancic, G. and Holker, R. Forming of Lightweight Metal Components: Need for New Technologies. *Proc. Eng.* (2014) **81**:28-37.
[3] Hino, R., Goto, Y. and Yoshida, F. Springback of Sheet Metal Laminates in Draw-bending. *J. Mater. Process. Tech.* (2003) **139**:341-347.
[4] Zhu, Y.X., Liu, Y.S., Yang, H. and Li, H.P. Development and Application of the Material Constitutive Model in Springback Prediction of Cold-bending. *Mater. Des.* (2012) **42**:245-258.
[5] Aso, T., Iizuka, T. and Ota, T. A New Method of Producing Bend Angle by Applying Sheet Forging to V-Bending Process. *Key Eng. Mater.* (2015) **651-653**:1066-1071.
[6] Aso, T. and Iizuka, T. FEM Analysis of Springback Control with Lump-punch Penetration after V-bending. *J. Phys. Conf. Ser.* (2016) **734(3)**:032068.

XIV International Conference on Computational Plasticity. Fundamentals and Applications
COMPLAS 2019
E. Oñate, D.R.J. Owen, D. Peric , M. Chiumenti, and Eduardo de Souza Neto (Eds)

FE ANALYSIS ON TUBE HYDROFORMING OF SMALL DIAMETR ZM21 MAGNESIUM ALLOY TUBE

H. Yasui*, T. Miyagawa†, S. Yoshihara††, T. Furushima†††, R. Yamada†††† and Y. Ito†††††

*, †Faculty of Engineering, Integrated Graduate School of
Medical, Engineering, and Agricultural Sciences, University of Yamanashi,
4-3-11 Takeda Kofu-shi, Yamanashi, 400-8511, Japan.
*E-mail: g18tma01@yamanashi.ac.jp
†E-mail: g18tm029@yamanashi.ac.jp

††Department of Engineering and Design, Shibaura Institute of Technology,
3-9-14 Minato-ku, Tokyo, 108-8548, Japan.
Email: yoshi@shibaura-it.ac.jp

†††Institute industrial science, The University of Tokyo,
4-6-1 Komaba Megro-ku, Tokyo, 153-8505, Japan.
Email: tsuyoful@iis.u-tokyo.ac.jp

††††, †††††Graduate Faculty of Interdisciplinary Research Faculty of Engineering,
Mechanical Engineering (Mechanical Engineering), University of Yamanashi.
4-3-11 Takeda Kofu-shi, Yamanashi, 400-8511, Japan.
††††Email: ryamada@yamanashi.ac.jp
†††††Email: yasumii@yamanashi.ac.jp

Key words: Tube Hydroforming, Warm forming, Small diameter tube, Magnesium alloy tube.

Abstract. Tube hydroforming (THF) is one of the plasticity processing methods. Tubular parts, for instance automotive components are expanded by forces such as internal pressure and axial compression in order to deform an objective shape. THF has less restriction on shape and size of workpieces owing to adopting the liquid tool. The demand of a small diameter magnesium alloy tubular parts have been increased for applying small medical and electronic devices. In this study, it was investigated that influence of process conditions such as processing temperature, internal pressure and axial feeding amount on formability of small diameter ZM21 magnesium alloy tube with outer diameter of 2.0mm and thickness of 0.20mm. Furthermore, the processing conditions for improving the formability of material in THF were examined. For prior evaluation of deformation characteristics in the warm THF of small diameter ZM21 magnesium alloy tube, a finite element (FE) simulation was conducted. The FE method (FEM) code was used LS-DYNA 3D for analysis of the FE model of the tube and the dies. The material characteristics were obtained by tensile test and fracture test. From FE analysis results, it was elucidated that effect of the processing temperature, the variable internal pressure and the axial feeding amount on deformation behavior. The formability of

ZM21 magnesium alloy tube was improved by processing at 250 ℃. The difference of deformation characteristic between FE results and experimental results was compared. As the results, the processing condition which could improve the formability of ZM21 tube was clarified using this FE model. The effect of adding the straightening stage in the loading path after the preform on formability was investigated. The thinning of the wall thickness of the tube was inhibited by calibration after the axial feeding.

1 INTRODUCTION

Magnesium and its alloys have excellent strength and low density against weight ratio. These materials are widely applied for parts of the automotive, aircraft and telecommunications products. In addition, magnesium is suitable for medical devices because of the essential element for human health [1]. Recent developments in the bioabsorbable implant industry include magnesium alloys [2]. In recent years, the miniaturizations of electronic and medical devices have been required. The demand for manufacturing of small diameter tubular products has been increasing. Tube hydroforming (THF) is a plastic processing method which could expand the tube by loaded the internal pressure and axial compression force during the process. Loaded pressure and axial direction force deform the tubes having complex cross-section shape integrally. This characteristic leads to weight reduction and high strength of the product. THF has less restriction on the shape and size of the workpieces owing to using liquid tools. Therefore, it is expected to manufacture small diameter tube parts made of magnesium alloy by THF [3]. However, it is difficult to deform the magnesium alloy tubes because of low ductility at room temperature (RT). Warm processing is generally applied for improving of formability on magnesium. In previous studies, improvement of formability on AZ31 magnesium alloy tubes with an outer diameter of 22mm was investigated on warm THF. It had succeeded that expanding of the tube with approximately 1.5 times bulge height against the outer diameter of original tube from experiment and FE analysis [4]. The T-shaped AZ31 magnesium alloy tube with an outer diameter of 42.7mm had deformed by FE analysis and experiment at 250℃. The characteristics of fracture and buckling were evaluated by valid FE model [5]. Furthermore, the wall thickness uniforming had studied by setting the temperature distribution in the die cavity [6]. However, applying the process of these studies for small diameter tube less than 10mm of outer diameter is impossible. There are problems such as size effect, accuracy of tool and friction between die and tube materials, these effect the formability of tube. In small diameter tubes, there is a critical problem that is the number of crystal grains relative to the thickness of the material [7]. This problem makes the prediction result of deformation behavior unstable. It is necessary to clarify the formability and deformation characteristics of the small diameter magnesium alloy tube in THF. In this study, the suitable processing conditions and deforming behavior were investigated by FEM for ZM21 magnesium alloy tube with an outer diameter of 2.0mm and a thickness of 0.20mm in order to achieve THF for small diameter tube in warm temperature. The effects of processing temperature, internal pressure and axial feeding amount on the formability and deformation characteristic of tube were investigated. Moreover, the processing conditions which could improve the formability of tube are considered.

2 EXPERIMENTAL SETUP AND FE MODEL

2.1 Material characteristic and results of tensile test and bursting test

Mechanical properties were investigated by tensile test and bursting. The specimens were annealed at 300℃ for 24 hours. ZM21 magnesium alloy bars with an outer diameter of 6.0mm manufactured by hot extrusion and used for tensile tests. **Table1** shows the chemical composition of the rod material. **Table2** shows the tensile test conditions of ZM21. The nominal stress-nominal strain diagram which obtained from the tensile test of the ZM21 rod is shown in **Fig.1**. As the result, it was confirmed that deformation resistance decrease and ductility increase as test temperature increase. It is easy to deform ZM21 at 250℃ because it had excellent ductility. ZM21 magnesium alloy tubes with an outer diameter of 2.0mm and a wall thickness of 0.2mm were tested for tensile test. **Table3** shows the chemical composition of the tube material. The materials were manufactured by drawing process. The tensile speed was set on 0.6mm/min and temperature at RT and 250 ℃. **Fig.2** shows the nominal stress-nominal strain diagram of the ZM21 tube. The comparison of Fig.1 and Fig.2, there is a correlation between ZM21 bar and ZM21 tube for change in the deformation resistance and ductility at warm area. Furthermore, the fracture pressure of tube was measured by bursting test. The internal pressure was loaded as speed of 1.0MPa/s until rupturing. **Fig.3** shows the result of bursting test of ZM21 tube.

Table1 Composition of specimens (ZM21 magnesium alloy rod) for tensile test in mass%

	Al	Zn	Mn	Si	Fe	Cu	Ni	Mg
ZM21	0.004	1.81	0.68	0.01	0.028	0.001	0.001	Bal.

Table2 Test conditions of tensil test (ZM21 magunesium alloy rod)

Material	ZM21
Test pease size [mm]	$\Phi 6 \times L30$
Tensile speed [mm/min]	0.6
Temperature [˚C]	RT, 50, 100, 150, 200, 250, 300

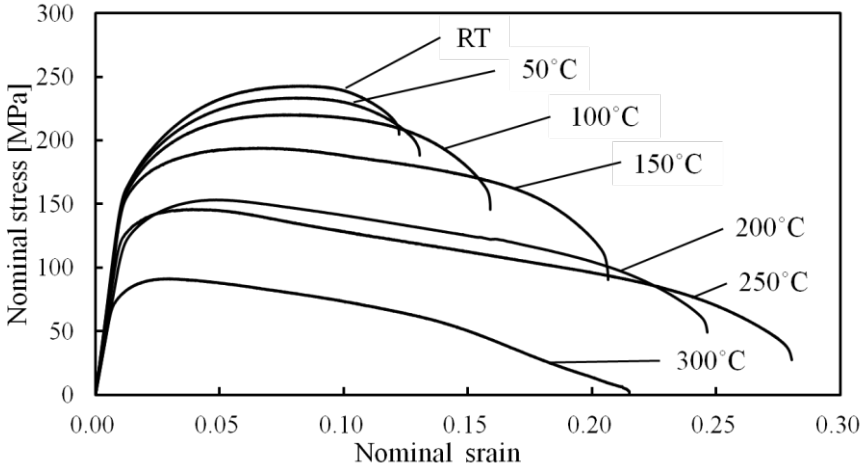


Fig.1 Noninal stress-Nominal strain curve of ZM21rod

Table3 Composition of specimens (ZM21 magnesium alloy tube) for tensile test in mass%

	Al	Zn	Mn	Si	Fe	Cu	Ni	Mg
ZM21	0.0035	1.83	0.7	0.015	0.0026	0.001	0.001	Bal.

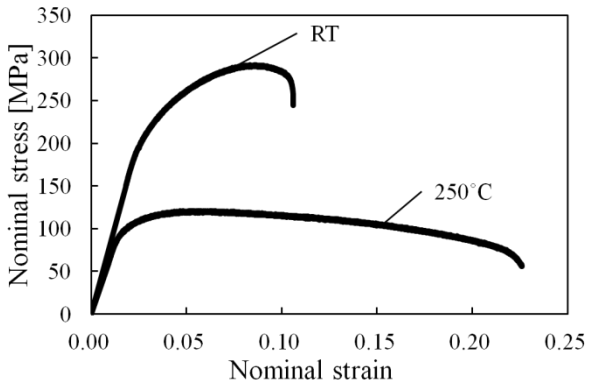


Fig.2 Noninal stress-Nominal strain curve of ZM21tube

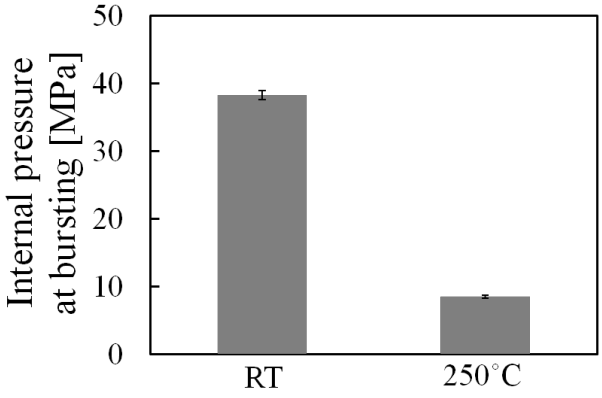


Fig.3 Bursting peressure of ZM21 tube

2.2 FE model

Fig.4 shows FE model for THF which is constructed by dies and tubular blank model. The length of tube is 20mm with an outer diameter of 2.0mm and a wall thickness of 0.2mm. The maximum expansion diameter in the die cavity is 4.0mm. A 1/2 model was selected owing to symmetrical shape. FE analyzes were conducted using the dynamic explicit FEM code LS-DYNA 3D. Material properties are shown in **Table4**. The blank tube is modeled in a solid element with the elastic-plastic material, and the dies are rigid-body models. The model of tube has six elements in the thickness direction. The total number of element is192000 for tube blank, and for the dies, the total number of element is 1350. The dies are defined as a rigid body using surface contact with the tube. The coefficient of friction between the dies and the tube is 0.1. The analysis time is set to 0.01s.

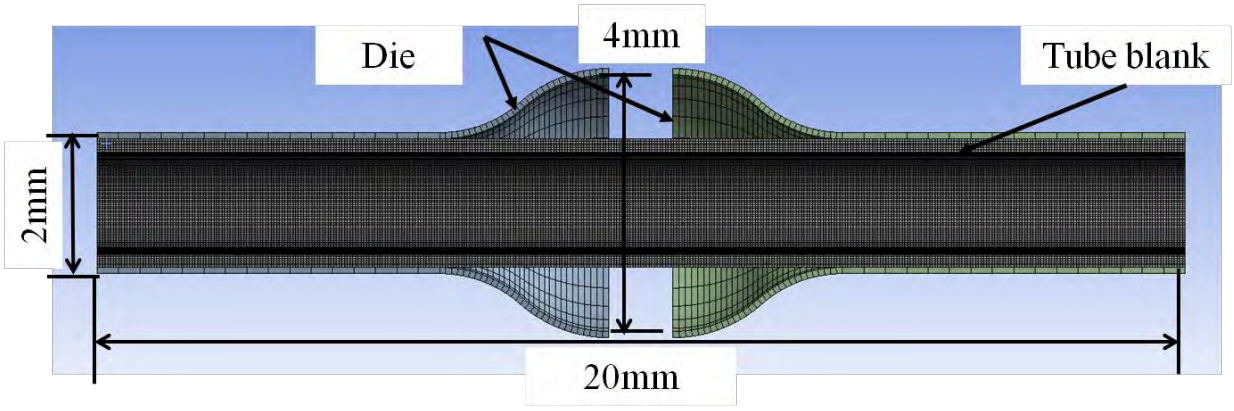


Fig.4 FE model for THF

Table4 Material properties for FE analysis

Body	Blank	Die
Material	ZM21	SKD61
Material model	Multiliner plasticity	Isotropic elastic
Yield stress σ_y [MPa]	90.76	---
Young's modulus E [GPa]	8.2017	200
Density [kg/mm^3]	1800	7850
Poisson coeffcient	0.35	0.3

2.3 FE analysis and experimental conditions

The loading path of the internal pressure and the axial feeding amount is shown at **Fig.5**. Pass (1) in the figure, the pressure was loaded up to the internal pressure p without the applying axial feeding. The internal pressure p was set 80% on against the bursting pressure p_B. In the FE analysis, the pressure was determined by following equation (1). Here, p_B is bursting pressure, σ_B is tensile strength, t is the wall thickness, D_0 is the initial outer diameter of the tube.

$$p_B = 2(t/D_0)\sigma_B \tag{1}$$

The axial feeding was loaded during maintaining the internal pressure constantly. The axial displacement ΔL is 0.5mm. Here, **Fig.6** shows the loading mechanism of the axial feeding and pressure in THF machine. **Fig.7** shows the die cavity. The axial feeding is performed by moving the distance between left and right dies to resolve the problem such as preparation of the high precision punch for the small diameter tube. The die cavity could be corresponding to a spherical expansion which has a cavity of 200% larger than the initial outer diameter of tube.

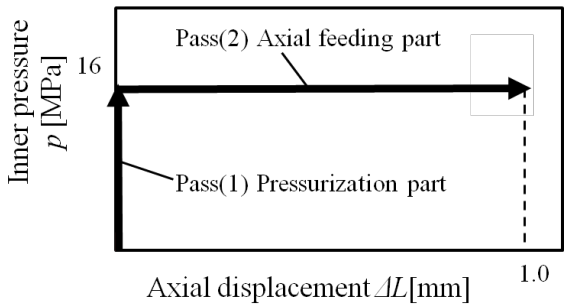


Fig.5 Loading path for THF

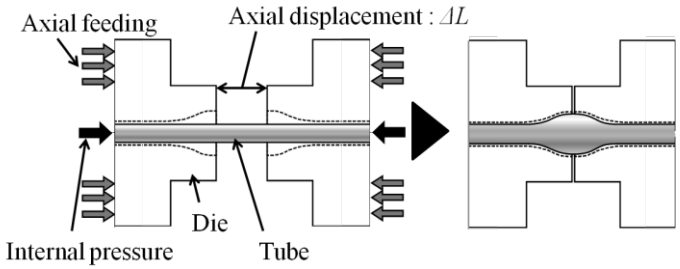


Fig.6 Axial feeding and pressure load system

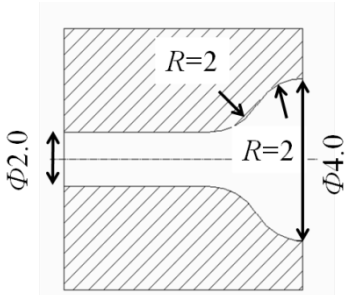


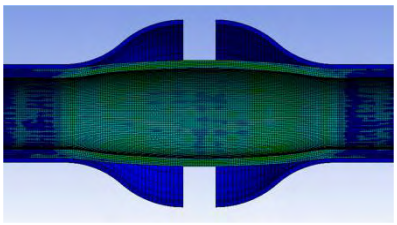
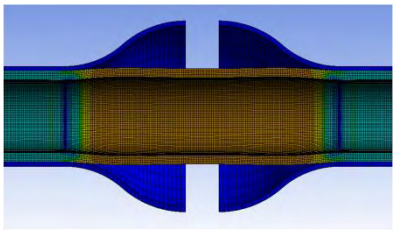
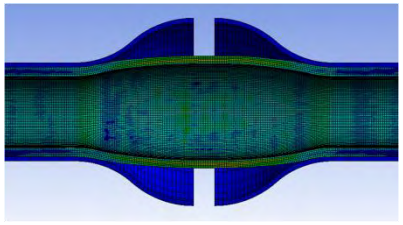
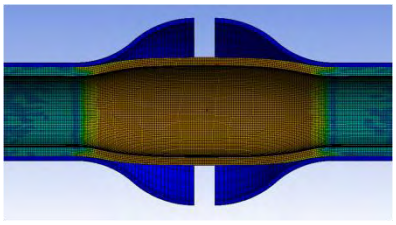
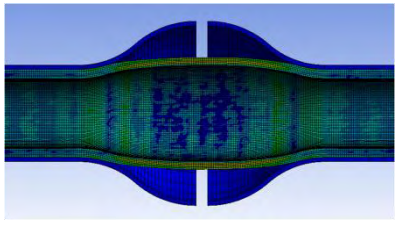
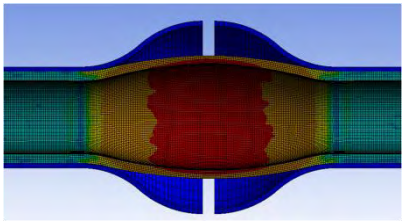
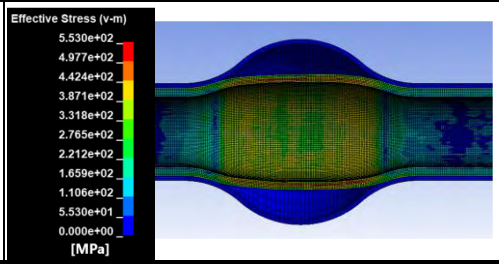
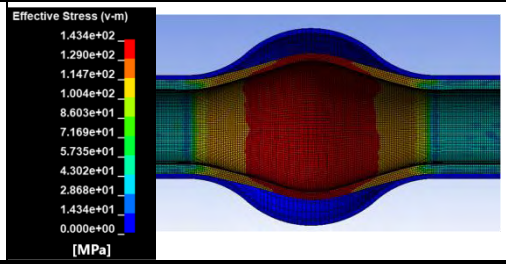
Fig.7 Die cabity

3 RESULTS AND DISCCUSIONS

3.1 Effect of temperature on the formbility

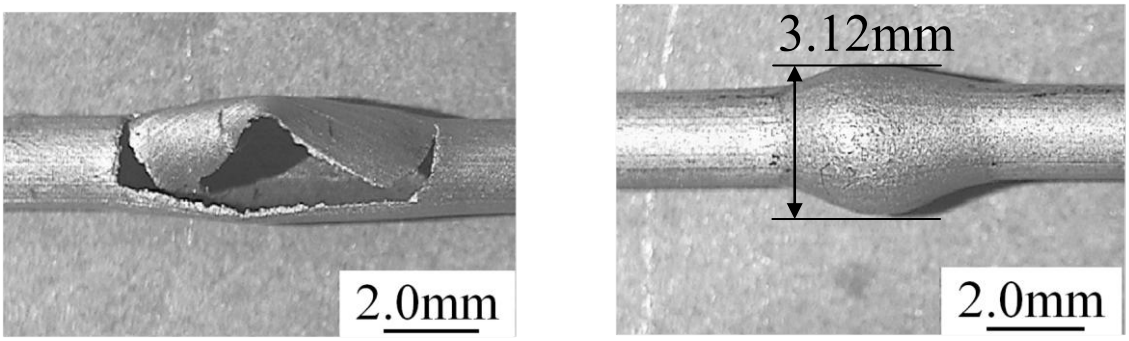
Table5 shows the effect of the temperature on the formability of ZM21 tube. The model was analyzed using material characteristics at RT and 250℃ as shown in Table4. The conditions of processing temperature were named CASE A and CASE B. The internal pressure p was set 80% against the bursting pressure p_B. In FE analysis, the internal pressure is set on p = 35MPa for CASE A and p = 16MPa for CASE B. In Table5, the von Mises stress was shown in FE models. CASE B has large expansion than CASE A because of high ductility in the warm area. The expansions were proceeded by an increase of axial displacement ΔL. The result of effective stress in CASE A means the fracture stress of the tube could be exceeded immediately after the start of axial feeding. A decrease of wall thickness was observed at the center of the expanded section at CASE B.

Table5 Effect of temperature on formability at FEM

	CASE A (RT)	CASE B (250℃)
0.0025s		
0.005s		
0.0075s		
0.01s		

The decrease of the wall thickness during the process is predicted that the thinning leads to failure of tube. It is necessary to avoid the thinning part by examining the internal pressure p in the loading path.

The experiments of warm THF were conducted for comparison with FE analysis results. ZM21 magnesium alloy tubes with an outer diameter of 2.0mm, a wall thickness of 0.2mm and length of 73mm were used for THF. The silicone oil was applied for loading the internal pressure. The surface between the dies and the tube was lubricated by MoS_2 paste. **Fig.8** shows the experiment results of ZM21tube deformed by THF at RT and 250℃. **Fig.8(a)** shows the material bursts immediately after start of the axial feeding at RT. In the experiment, shear mode fracture was observed in spite of no fracture in the FE analysis in Table5. The initiation of this shear type of fracture could not be predicted since the fracture criterion is not considered in the FE simulation [5]. **Fig.8(b)** the experiment result of deformation and expansion of the tube at 250℃. It was possible to deform objective shape with expansion on the loading path in Fig.5 as with FE simulation. The workpiece has not excellent surface quality which is caused by low work hardening in the warm area. In the experiment, the internal pressure p for available deformation of the tube is lower than the FE analysis. The cause of difference could be considered that the anisotropy of the material and the mesh size of FE model influence the internal pressure p for available deformation [3].



(a) Bursting of tube at RT (b) Expansion of tube at 250℃

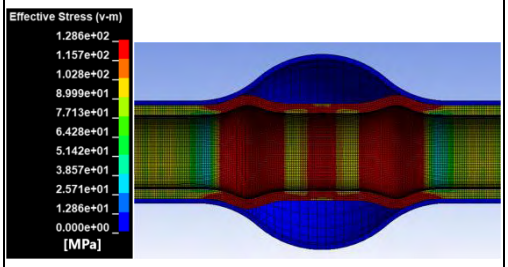
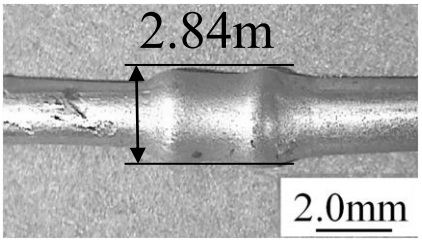
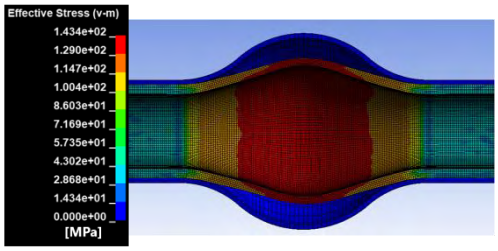
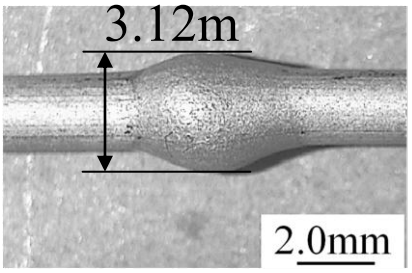
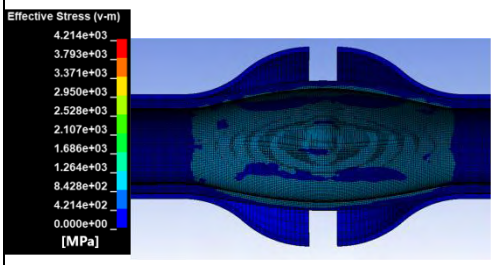
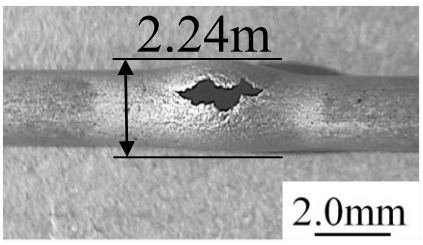
Fig.8 Experimental results of ZM21 tube on warm THF (250˚C)

3.2 Influence of internal pressure on formability

The influence of different internal pressure p on formability was analyzed at 250℃ with the three internal pressure conditions of p = 70%, 80% and 90% against the bursting pressure p_B. Each condition was named CASE 1, CASE 2 and CASE 3. In FE analysis, the internal pressure is set on p = 14MPa for CASE 1, p = 16MPa for CASE 2 and p = 18MPa for CASE 3. **Table6** shows the analysis results and the experimental results of THF. The von Mises stress was shown in FE models. In CASE 1, wrinkles were appeared on the tube owing to not enough internal pressure for expansion of the tube and accumulating of material by axial feeding. The FE analysis was interrupted in CASE 3 because of the negative volume of elements in tube blank. High internal pressure leads to fracture at the thinning section of the wall thickness. As the experimental result of CASE 3, it was tended that tubes burst easily after the start of axial feeding. In experiments, high internal pressure in THF is affected by tube tolerances [8]. It could be difficult to deform stably. If the experiments of THF are

conducted by using the loading path in Fig.5, it is considerate that the internal pressure p setting on 80% against the bursting pressure p_B is suitable for deforming stably.

Table6 Influence of internal pressure on formability at FE analysis and experiment

Condition	FE analysis	Experimental
CASE 1		
CASE 2		
CASE 3		

3.3 Examination for suppress of thinning

It was impossible that the tubes deform larger than ΔL = 1.0mm of axial displacement in the experiment of THF at 250℃. Fracture of material could be affected by the thickness reduction. **Fig.9** shows the measurement results of thickness strain of the tube at the result of FE analysis and experiment of CASE 2. As the result, the decrease of wall thickness was 30% against the original tube was observed at the experiment of THF. In the FE analysis result, the highest thickness strain of thinning was 25%. It is necessary to considerate the suppression of the thinning to expand the tube with high bulge height. Studies have been conducted to expand the tube in THF using a preform with the wrinkles and calibration of the prefom [9], [10]. In this study, the suppression of thinning was investigated with the loading path shown at **Fig.10**. In the loading pass (1) and (2) in Fig.10, the internal pressure p set on 50% against the bursting pressure p_B in order to accumulate the material such as the wrinkles on the tube. The tube is expanded by the straightening in pass (3).

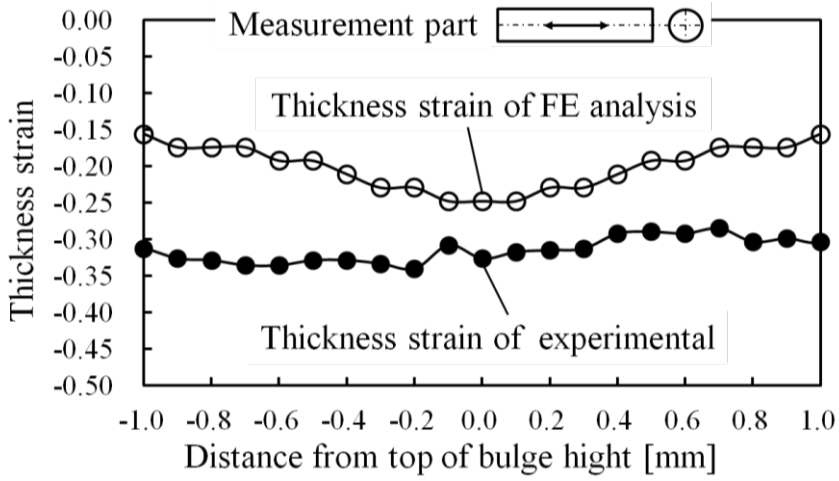


Fig.9 Thickness strain of FE analysis and experimental results with axial feeding amount 1.0mm

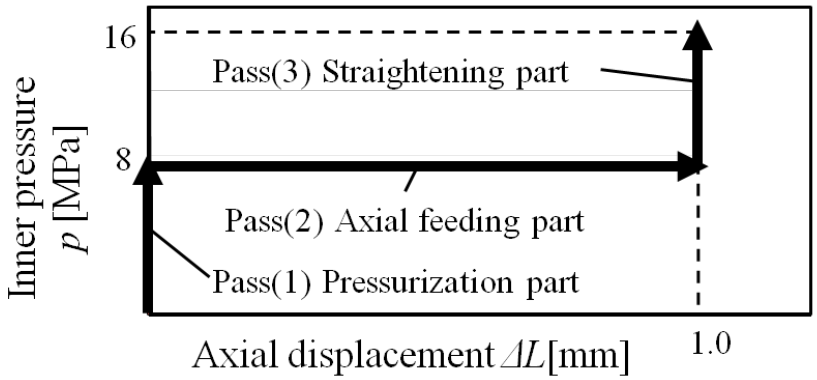
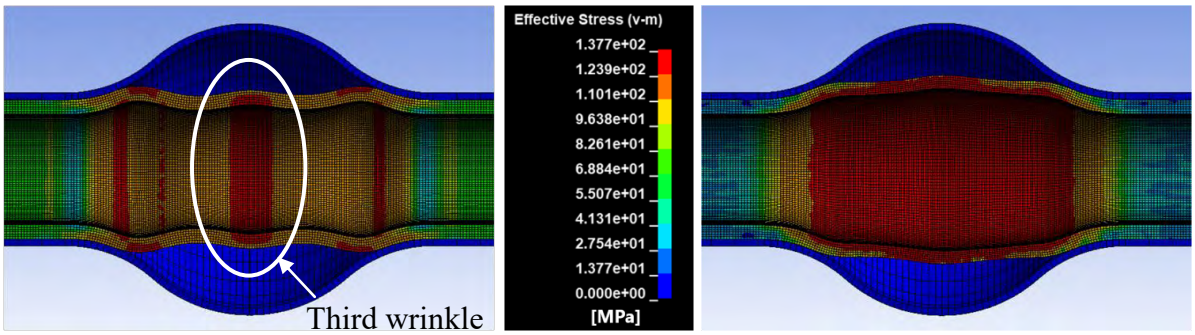


Fig.10 Loading path with straightening part



(a) Before the straightening (b) After the straightening

Fig.11 Wrinkle and straightening in FE analysis

Fig.11 shows the FE analysis result of THF using the straightening in the loading path. FE model of the tube was analyzed at 250℃. The effective stress was shown in FE models. **Fig.11(a)** shows the FE analysis result of the tube after completion of pass(2) at loading path

in Fig.10. A third wrinkle on the tube shown in Fig.11(a) was occurred in the center of the tube blank by lower internal pressure *p* than CASE 1. **Fig.11(b)** shows the FE analysis result the deformation of the tube with the straightening part in loading path. Compared with the FE analysis results of CASE 2 in Table6, the tube at Fig.11(b) has a lower decrease for the wall thickness of the tube. The outer diameter after deformation was 2.80mm, and the highest thickness strain of thinning was 13% against the original tube. As the results, it could be considered that the tube is processed for the die cavity having a maximum expansion ratio of approximately 1.5 times against the original tube with suppressing the thinning of the wall thickness. Also, it was clarified that third wrinkle at center of the tube blank in the FE model was effectiveness preform for suppressing the thinning of wall thickness in THF of small diameter magnesium alloy tube.

4 CONCLUSION

FE analysis and experiment of THF were carried out for small diameter ZM21 magnesium alloy tube to clarify the influence of processing conditions on formability and investigate the deformation behavior of tube. Furthermore, the processing conditions available improve the formability of the tube were investigated. Results obtained in this study are summarized as follows.

(1) The behavior of thinning during the processing is revealed by FE analysis. It is necessary for the suppression of thinning of the wall thickness to avoid the fracture of the tube.
(2) In THF of small diameter magnesium alloy tube, the difference of the formability and the behavior of thinning are clarified by revise the loading path.
(3) The elucidations of influence of anisotropy of material and mesh size on the formability of FE model are required.

REFERENCES

[1] S. Yoshihara and T. Furushima. *J. Jpn. Soc. Technol. Plast*. (2016) **57**-670: 8-13.
[2] R. Yamamoto. *J. Jpn. Inst. Light Met*. (2008) **58**-11: 570-576.
[3] S. Mori, H. Satoh, K. Itai and K. Manabe. *J. Jpn. Soc. Technol. Plast*. (2017) **58**-672: 72-77.
[4] C. L. Cahn. *J. Minerals, Met. Mat. Society*. (2015) **67**-2: 450-458.
[5] K. Manabe, K. Fujita and K. Tada. *J. Chin. Soc. Mech. Eng*. (2010) **31**-4: 284-287.
[6] K. Manabe, T. Morishima, Y. Ogawa, K. Tada, T. Miura and H. Nakagawa. *Mater. Sci. Forum.* (2010) **654**-656: 739-742.
[7] B. J. Macdonald. *J. Jpn. Soc. Technol. Plast*. (2012) **53**-614: 176-179.
[8] A. Shirayori, T. Ando, M. Narazaki and M. Usui. *J. Jpn. Soc. Technol. Plast.* (2013) **54**-634: 42-46.
[9] G. Liu, Z. J. Tang, Z. B. He and S. J. Yuan. *Trans. Nonferrous Met. Soc. China.* (2010) **20**: 2071-2075.
[10] S. Yuan, X. Wang, G. Liu and Z. R. Wang. *J. Mater. Process. Technol.* (2007) **182**: 6-11.

XIV International Conference on Computational Plasticity. Fundamentals and Applications
COMPLAS 2019
E. Oñate, D.R.J. Owen, D. Peric , M. Chiumenti, and Eduardo de Souza Neto (Eds)

FINITE ELEMENT ANALYSIS OF TUBE DRAWING PROCESS WITH DIAMETER EXPANSION

SHOHEI KAJIKAWA[*], HIKARU KAWAGUCHI[*], TAKASHI KUBOKI[*], ISAMU AKASAKA[†], YUZO TERASHITA[†] AND MASAYOSHI AKIYAMA[††]

[*] Department of Mechanical Engineering & Intelligent Systems
The University of Electro-Communications
1-5-1 Chofu Gaoka, Chofu-shi, Tokyo, 182-8585, Japan
e-mail: s.kajikawa@uec.ac.jp, www.uec.ac.jp/eng/

[†] Miyazaki Machinery Systems Co., Ltd.
1 Nii, Kaizuka-shi, Osaka, 597-8588, Japan
www.miyazakijp.com

[††] Akiyama Mechanical Engineering Consulting
2-7-306 Tanaka Sekiden-cho, Sakyo-ku, Kyoto-shi, Kyoto, 606-8203, Japan

Key words: Drawing, Flaring, Tube expansion, Thickness reduction, FEM.

Abstract. This paper presents a tube drawing process with diameter expansion for producing a thin-walled tube effectively. In this proposed process, the tube was flared by a plug pushing into the tube, and then the tube was expanded by drawing the plug in the tube axial direction with chucking the flared tube edge. Optimum plug shape, such as the plug half angle and the corner radius, was investigated by a series of analyses using the finite element method (FEM) for improving the forming limit and the dimension accuracy. At first, a friction coefficient was determined to 0.3 by a comparison of the flaring limit between the analysis and the experiment of the tube flaring. As a result of the analyses in the drawing with the diameter expansion, the forming limit was high when the plug half angle was set to 18~30°. The thickness reduction ratio increased with an increase in the expansion ratio and the plug half angle. In addition, the overshoot, which is a difference between the plug diameter and the tube inner diameter after the drawing, was prevented by using the plug with the corner radius of 20 mm.

1 INTRODUCTION

Drawing process is conventionally applied for manufacturing tubes for reducing thickness and improving dimensional accuracy and strength. The tubes, which is manufactured by the drawing, is used for various machine and construction components, such as plumbing equipment, constructional material and so on. There are many research works for the tube drawing. For example, Kuboki et al. proposed methods for levelling residual stress, and reducing thickness variation in the tube drawing [1, 2].

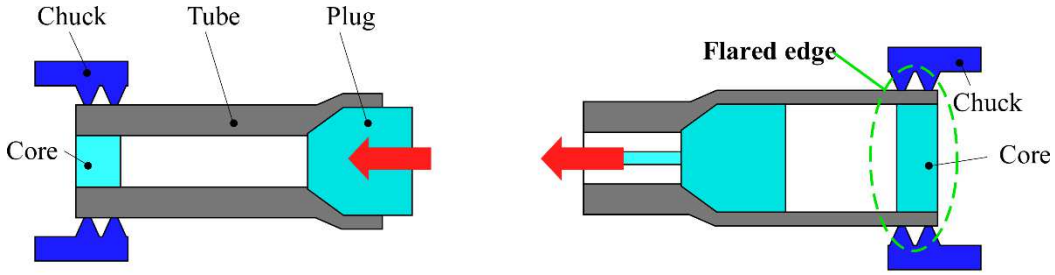
In recent years, thin-walled tubes, which contribute to reduction in size and weight of various machine components, are required for environmental protection. However, typical thickness

reduction is about 20 % in 1 pass drawing [3]. Therefore, many drawing passes are required for manufacturing thin-walled tubes from rather thick-walled raw tubes, and the production cost increases with the increase of the number of the drawing passes. Another method for manufacturing thin-walled tube is pilgering [4]. Area reduction is over 80 %, but productivity and dimensional accuracy is low compared to the drawing, because the pilgering is an incremental processing. Furushima et al. proposed dieless drawing, which contributes to the large area reduction in 1 drawing pass [5]. However, the tubes, which are manufactured by the dieless drawing, are unsuitable for machine component which requires the dimensional accuracy. Therefore, effective processing method should be developed for manufacturing the thin-walled tube.

2 TUBE DRAWING PROCESS WITH DIAMETER EXPANSION

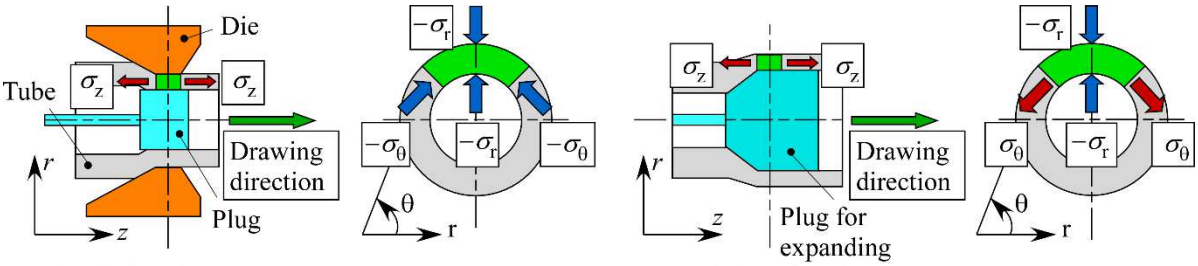
This paper proposed a tube drawing process with a diameter expansion as shown in Figure 1. The proposed method is composed of two steps. In the first step which is tube flaring, the tube edge is expanded by pushing the plug into the tube as shown in Fig. 1 (a). In second step which is the plug drawing, the tube is expanded through the whole tube length by drawing the plug while the flared portion is chucked as shown in Fig. 1 (b).

The advantage of the proposed method is the effective production of the thin-walled tube. Figure 2 shows the comparison of stress state between the conventional and the proposed method. In the case of the proposed method, the tube wall is stretched in both of the axial and the hoop directions, then a negative deviatoric stress is large in the thickness direction, with



(a) Flaring (1st steps) (b) Drawing (2nd step)

Figure 1: Schematic diagram of tube drawing process with diameter expansion



(a) Drawing with shrink（Conventional method） (b) Drawing with expansion（Proposed method）

Figure 2: Comparison of stress state between drawing with shrink and expansion

compared to that of the conventional tube drawing with diameter shrinkage. Thus, the proposed method is considered to be effective for reducing the thickness of the tube.

In this study, optimum plug shape, such as the plug half angle and the corner radius, was investigated for improving the forming limit and the dimension accuracy. At first, the tube flaring, which is 1st step, was carried out in the experiment and the analysis by finite element method (FEM), and the friction coefficient μ was estimated by comparison of the flaring limit between the experiment and the FEM. In drawing process, which is 2nd step, a series of the analyses were carried out for identifying the optimum plug shape.

3 INVESTIGATION IN FLARING PROCESS

3.1 Flaring method and conditions

An elastic-plastic analysis by the FEM was carried out by using the commercial code "ELFEN" which was developed by Rockfield Software Limited, Swansea. Figure 3 shows the schematic diagram of the model for the tube flaring. The model is two dimensional with axisymmetry. The von Mises yield criterion was adopted, and normality principle was applied to the flow rule. The constraints were determined by the penalty function method, and an implicit scheme was adopted. Four-node rectangular elements were adopted. The F-bar method was applied to the element for overcoming volumetric locking [6].

In the analysis of the tube flaring, one tube edge was flared by the plug pushing, while the other edge was fixed in the axial direction and the outer surface was held by the holder. The

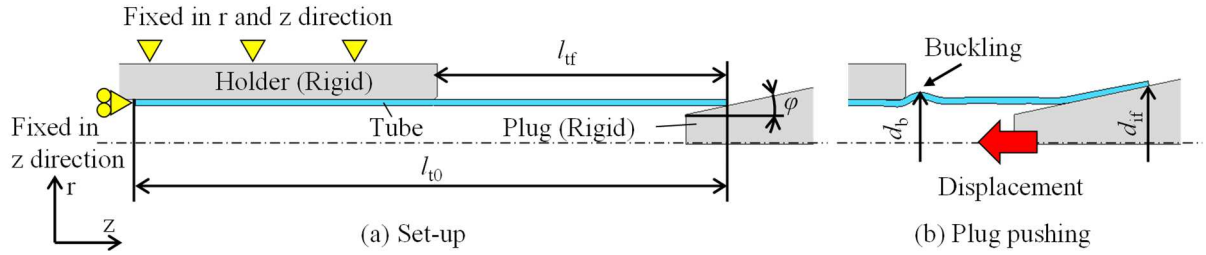


Figure 3: Schematic diagram of FEA model for tube flaring

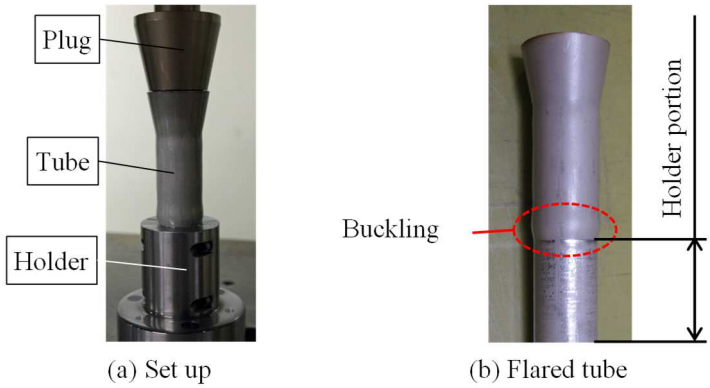


Figure 4: Appearance of experimental set-up and flared tube

Table 1: Working conditions in flaring process

Tube	Tube material	SUS304	
	Swift's equation of SUS304 (FEM)	σ=1275(ε_p+0.01)$^{0.39}$	
	Initial diameter d_0 [mm]	30	
	Initial thickness t_0 [mm]	1, 2, 3, 4	
	Initial length l_{t0} [mm]	200	
	Initial flared length l_{tf} [mm]	100	
	Element size (FEM)	Axial	1 mm/division
		Radial	8 divisions
Plug	Half angle φ [°]	12, 24, 36, 48	
Friction coefficient μ (FEM)		0.1, 0.2, 0.3, 0.4	
Lubrication (Experiment)		With lubricant	

flaring ratio E_f was defined as the following equation.

$$E_f = \frac{d_{if} - d_{i0}}{d_{i0}} \tag{1}$$

where d_{if} is the inner diameter at the flared edge, and d_{i0} is the initial inner diameter. The buckling occurred as a defect by the plug pushing as shown in Fig. 3 (b). The buckling amount B was defined as the following equation.

$$B = \frac{d_b - d_0}{d_0} \tag{2}$$

where d_b was the outer diameter of the buckling portion, and d_0 was the initial outer diameter. Maximum flaring ratio E_{f_max}, which means flaring limit, was defined as the maximum value of E_f before B reaching 0.05. The experiments were carried out in a similar way to FEM as shown in Figure 4. d_{if} and d_b were measured every 2 mm of the plug pushing in the axial direction.

Table 1 shows the working conditions for the tube flaring in the FEM and the experiment. The tube material was SUS304, and thickness t_0 was from 1 to 4 mm. Plugs with various half angle φ, which were from 12 to 48°, were prepared. The experimental results were compared to the FEM results with various friction coefficient μ.

3.2 Maximum flaring ratio

Figure 5 shows the effect of the tube initial thickness t_0 on the maximum flaring ratio E_{f_max} when the plug half angle φ was 12°. E_{f_max} increased with an increase in t_0. In addition, E_{f_max} was higher under the condition of the low friction coefficient μ in FEM results. This is because the axial load, which causes buckling occurrence, decreases with the decrease in the frictional force. The experimental results almost agreed with the FEM result of μ=0.3.

Figure 6 shows the effect of the plug half angle φ on the maximum flaring ratio E_{f_max} when the tube initial thickness t_0 was 2 mm. E_{f_max} was low under the condition of low φ because the frictional force was high due to the large contact area at the plug taper portion. On the other hand, E_{f_max} was also low when φ was too large, because the axial load was high due to the large bending/unbending deformation of the tube wall. Therefore, the optimum φ was ranged from

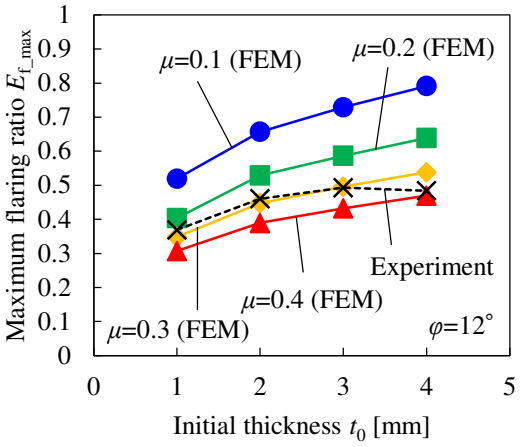


Figure 5: Effect of tube initial thickness t_0 on maximum flaring ratio E_{f_max} (Plug half angle φ=12°)

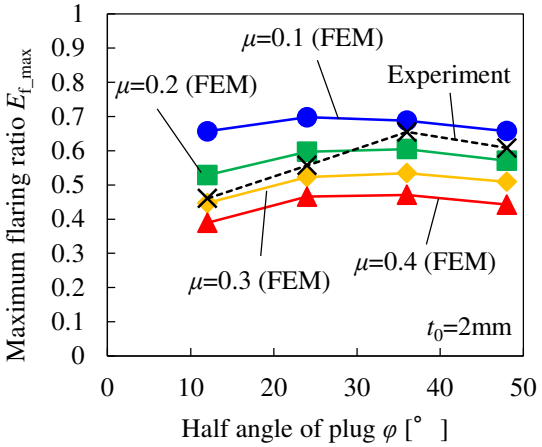


Figure 6: Effect of plug half angle φ on maximum flaring ratio E_{f_max} (Tube initial thickness t_0=2 mm)

24 to 36°.

The experimental results agreed with the FEM result of the friction coefficient μ=0.3 when the plug half angle φ was 12~24°, but the experimental results were ranged from 0.1 to 0.2 of μ in FEM results when φ was 36~48°. It was considered that the lubrication state changed by φ in the experiment. Oil film, which is between the tube wall and the plug, is easy to be lost when the sliding length is long with the low φ in the experiment. In addition, the tube wall waved at the taper portion under the condition of high φ [7]. The waved tube wall did not contact to the plug and held the lubricant in the experiment. Therefore, it was considered that μ which the experimental results agreed with the FEM results decreased with the increase in φ. Base on the results as shown in Fig. 5 and 6, μ was set to 0.3 for the analysis of the drawing process, which is described in the next section, in order to estimate the forming limit in safety.

4 INVESTIGATION IN DRAWING PROCESS

4.1 Drawing method and conditions

Figure 7 shows the schematic diagram of the FEM model for the drawing process. The plug was drawn into the tube, while one tube edge was fixed in the axial direction. Expansion ratio E_d, thickness reduction ratio γ and dimensional accuracy were evaluated. E_d was defined as the following equation.

$$E_d = \frac{d_i - d_{i0}}{d_{i0}} \tag{3}$$

where d_i is the tube inner diameter after the plug drawing, and d_{i0} is the initial tube inner diameter. γ was defined as the following equation.

$$\gamma = \frac{t - t_0}{t_0} \tag{4}$$

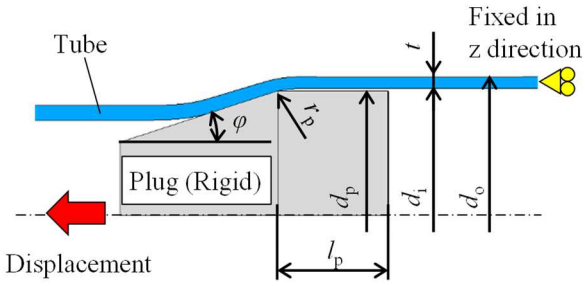


Figure 7: Schematic diagram of FEM model for drawing process

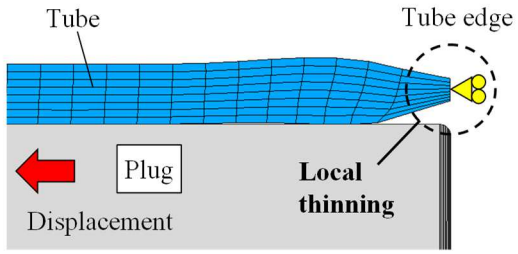


Figure 8: Appearance of local thinning (Tube initial thickness t_0=2 mm, plug half angle φ=18° , Plug diameter d_p=45 mm, plug corner radius r_p=0 mm)

Table 2: Working conditions in drawing process

Tube	Tube material		SUS304
	Swift's equation of SUS304		σ=1275(ε_p+0.01)$^{0.39}$
	Initial diameter d_0 [mm]		30
	Initial thickness t_0 [mm]		1, 2, 3, 4
	Initial length l_{t0} [mm]		200
	Element size	Axial	1 mm/division
		Radial	8 divisions
Plug	Straight length l_p [mm]		15
	Half angle φ [°]		6, 12, 18, 24, 30, 36
	Diameter d_p [mm]		30~47.5
	Corner radius r_p [mm]		0, 10, 20, 30
Friction coefficient μ			0.3

where t is the thickness after the plug drawing, and t_0 is the initial thickness. The dimensional accuracy was evaluated by overshoot δ, which means the difference between d_i and d_p. δ was defined as the following equation.

$$\delta = d_i - d_p \tag{5}$$

Table 2 shows the working conditions in drawing process. The tube initial thickness t_0, the plug diameter d_p, half angle φ and corner radius r_p were changed variously. When d_p was too high in each t_0 and φ, a local thinning occurred at the tube edge, which is fixed in the axial direction, as shown in Figure 8. Maximum expansion ratio E_{d_max} was defined as the maximum value of the expansion ratio E_d when the plug was drawn without the local thinning. E_{d_max} was searched by increasing d_p in the step of 0.5 mm until the local thinning occurred.

4.2 Effect of plug half angle on expansion ratio and thickness reduction

Figure 9 shows the effect of the plug half angle φ and the tube initial thickness t_0 on maximum expansion ratio E_{d_max}. E_{d_max} increased with an increase in φ, and E_{d_max} was higher when φ was 18~30 °. However, E_{d_max} decreased when φ was over 30°. Forming limit was considered to be determined by the drawing load P. Figure 10 shows the effect of φ on the

drawing load P in each d_p. P was higher under the condition that φ was too low or high. In the case that φ was too low, P became high due to the large frictional force, which is derived from the large contact area at the plug taper portion. In the case that φ was too high, P was higher because bending/unbending deformation became large by increasing φ. Optimum φ, which decreases P, increased with the increase in d_p, and the optimum φ was 24° when d_p was 42 mm, which was near the forming limit. This value of φ was same as φ when E_{d_max} was the highest in Fig. 9. This result suggested that P should be decreased by controlling φ appropriately for improving the forming limit.

Figure 11 shows the effect of the plug half angle φ and tube initial thickness t_0 on maximum thickness reduction ratio γ_{max}. γ_{max} is the thickness reduction ratio γ when the expansion ratio E_d was the maximum E_{d_max}. γ_{max} increased drastically with the increase in φ when φ was 6~18°,

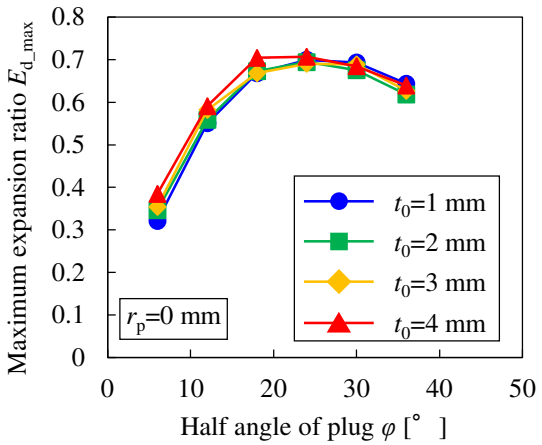


Figure 9: Effect of plug half angle φ and tube initial thickness t_0 on maximum expansion ratio E_{d_max} (Plug corner radius r_p=0 mm)

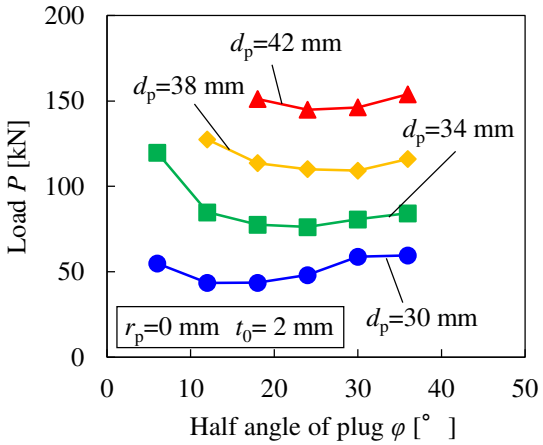


Figure 10: Effect of plug half angle φ and plug diameter d_p on drawing load P (Tube initial thickness t_0=2 mm, plug corner radius r_p=0 mm)

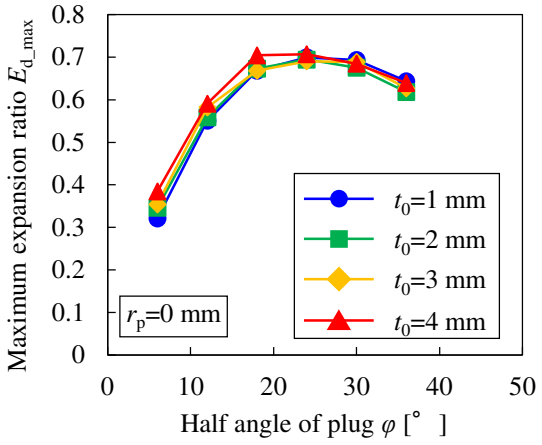


Figure 11: Effect of plug half angle φ and tube initial thickness t_0 on maximum thickness reduction ratio γ_{max} (Plug corner radius r_p=0 mm)

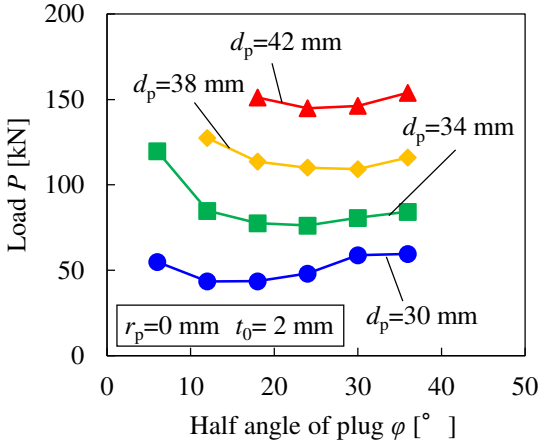


Figure 12: Effect of plug half angle φ and plug diameter d_p on thickness reduction ratio γ (Tube initial thickness t_0=2 mm, plug corner radius r_p=0 mm)

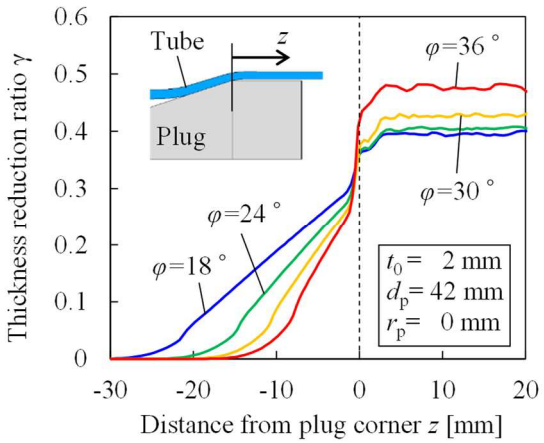


Figure 13: Effect of plug half angle φ on distribution of thickness reduction ratio γ (Tube initial thickness t_0=2 mm, plug diameter d_p=42 mm, plug corner radius r_p=0 mm)

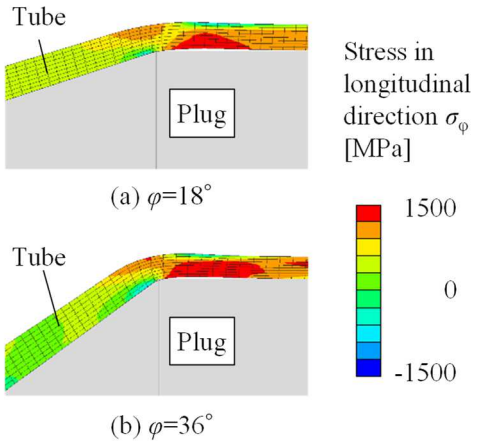


Figure 14: Distribution of stress in logitudinal direction σ_φ (Tube initial thickness t_0=2 mm, plug diameter d_p=42 mm, plug corner radius r_p=0 mm)

and γ_{max} increased gradually with the increase in φ when φ was over 18°, although E_{d_max} decreased with the increase in φ when φ was over 24°. This is because γ increased by increasing φ in each plug diameter d_p, as shown in Figure 12.

Figure 13 shows the effect of the plug half angle φ on the distribution of the thickness reduction ratio γ in the case that the plug diameter d_p was 42 mm. γ increased gradually with the tube expanding at the plug taper portion, and γ increased drastically at the portion near the plug corner. This drastic thickness reduction occurred due to the axial stretching with the bending at the plug corner as shown in Figure 14. The stress in the longitudinal direction σ_φ is large at the plug corner. Therefore, the thickness drastically decreased by stretching the tube wall in the hoop and the axial direction. In addition, γ increased by increasing φ, because σ_φ increased with the increase in φ as shown in Fig. 14 (a) and (b). This result means that the thickness could be controlled by setting φ appropriately.

4.3 Effect of plug corner radius on dimensional accuracy

Figure 15 shows the effect of the plug half angle φ and the expansion ratio E_d on the overshoot δ in the case that the tube initial thickness t_0 was 2 mm, and the plug corner radius r_p was zero. δ decreased with the increase in E_d, but δ increased with the increase in φ. Figure 16 shows the typical appearances of the tube during the plug drawing. When φ and E_d were small, δ was small as shown in Fig. 16 (a). When φ was large with small E_d, δ became large because the bending angle was large as shown in Fig. 16 (b). When φ was large with large E_d, δ became small because the tube wall was stretched strongly in the axial direction due to the large drawing load P, and fit to the plug surface as shown in Fig. 16 (c).

It was considered to be effective to apply the plug with corner radius r_p for improving the dimensional accuracy by preventing the overshoot δ. Figure 17 shows the tube shape during the drawing in the cases that the plug with and without r_p were used. The tube wall was bent with large bending radius, and fit to the plug surface by using the plug with r_p as shown in Fig. 17

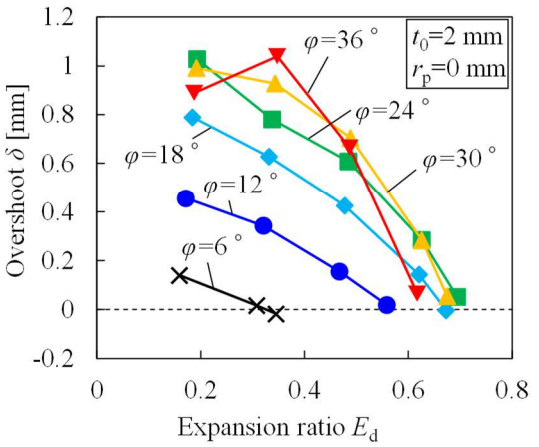


Figure 15: Effect of plug half angle φ and expansion ratio E_d on overshoot δ (Tube initial thickness t_0=2 mm, plug corner radius r_p=0 mm)

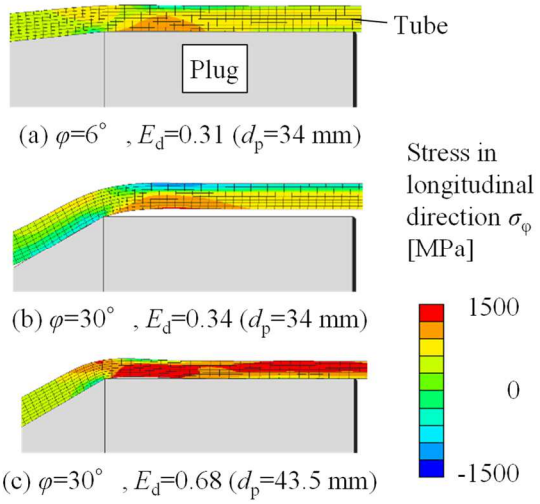


Figure 16: Appearance of tube wall during drawing with diameter expansion (Tube initial thickness t_0=2 mm, plug corner radius r_p=0 mm)

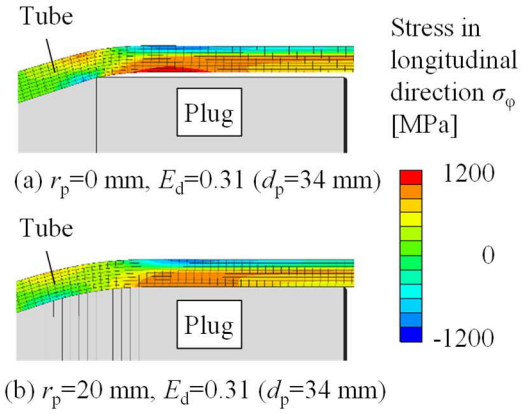


Figure 17: Appearance of tube wall during drawing with diameter expansion (Tube initial thickness t_0=2 mm, plug half angle φ=18°)

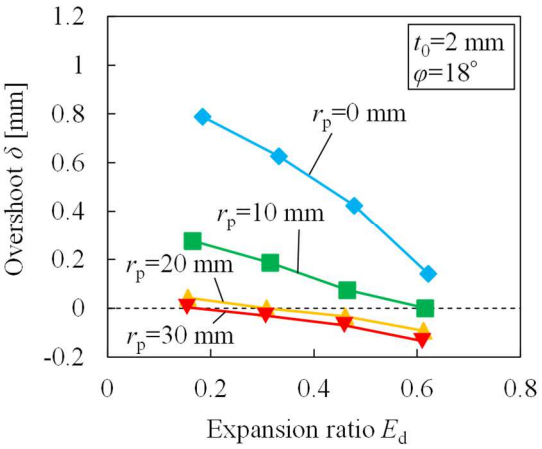


Figure 18: Effect of plug corner radius r_p and expansion ratio E_d on overshoot δ (Tube initial thickness t_0=2 mm, plug half angle φ=18°)

(b). Therefore, δ decreased by applying large r_p to the plug. Figure 18 shows the effect of r_p on δ in the case that the plug half angle φ was 18°. δ decreased with an increase in r_p, and δ was ranged around zero by setting r_p to 20 mm. However, δ was negative value under the condition that E_d was large, such as E_d=0.61. This is because the tube wall shrink in the hoop direction after the plug passing, while the tube wall was stretched strongly in axial direction due to the large drawing load. Figure 19 shows the effect of r_p on δ in the case that φ was 18, 24 and 30°, which was the optimum φ for improving the forming limit as shown in Fig. 9. It was possible to prevent δ by setting r_p to 20 mm regardless of φ.

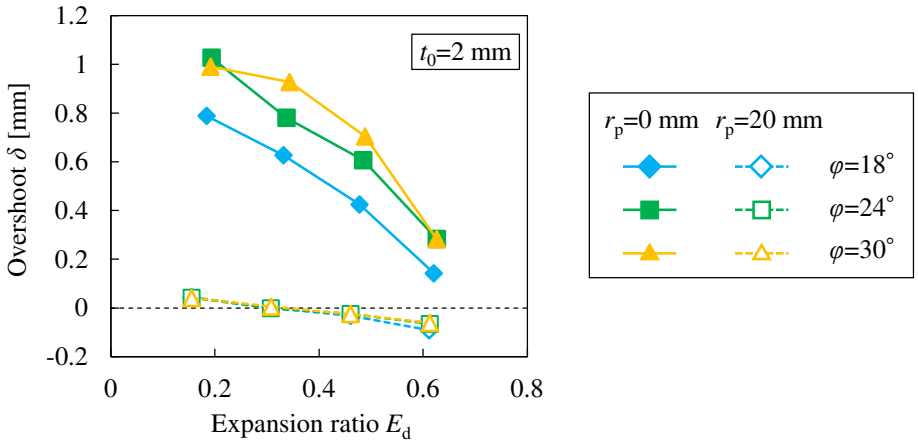


Figure 19: Effect of plug corner radius r_p, plug half angle φ and expansion ratio E_d on overshoot δ (Tube initial thickness t_0=2 mm)

5 CONCLUSIONS

- This paper proposed a tube drawing process with the diameter expansion for producing thin-walled tube effectively, and optimum plug shape, such as the plug half angle φ and the corner radius r_p, was investigated for improving the forming limit and the dimensional accuracy.
- In the tube flaring, the forming limit was higher when the tube initial thickness t_0 was thicker, and the plug half angle φ was 24~36° for improving the flaring limit. The friction coefficient μ was determined to 0.3 by the comparison of the flaring limit between the FEM and the experimental result.
- In the plug drawing, the forming limit was high when the plug half angle φ was set to 18~30°, because the axial load was low during the drawing in this range of φ.
- The thickness reduction ratio γ increased with the increase in the expansion ratio E_d of the tube inner diameter. In the case that E_d was constant, γ became higher by increasing φ.
- The overshoot δ, which is the difference between the plug diameter d_p and the tube inner diameter d_i after the drawing, increased with the increase in the plug half angle φ, and δ changed by the expansion ratio E_d when the plug without the corner radius r_p was used.
- In the case of the plug half angle φ=18~30°, which is the optimum range for improving the forming limit, the overshoot was almost zero regardless of φ and the expansion ratio E_d by using the plug with the corner radius r_p of 20 mm.

REFERENCES

[1] Kuboki, T., Nishida, K., Sakaki and T., Murata, M. Effect of plug on levelling of residual stress in tube drawing. *J. Mater. Process. Technol* (2008) **204**: 162-168.

[2] Kuboki, T., Tasaka and S., Kajikawa, S. Examination of working condition for reducing thickness variation in tube drawing with plug. *Proc. COMPLAS XIV* (2017): 63-71.

[3] The Japan Society for Technology of Plasticity. *Drawing*. Corona Publishing, (2017), in Japanese.
[4] Abe, H., Iwamoto, T., Yamamoto, Y., Nishida and S., Komatsu, R. Dimensional accuracy of tubes in cold pilgering. *J. Mater. Process. Technol.* (2016) **231**: 277-287.
[5] Furushima, T. and Manabe, K., Experimental and numerical study on deformation behavior in dieless drawing process of superplastic microtubes. *J. Mater. Process. Technol.* (2007) 191: 59-63.
[6] de Souza Neto, E.A., Peric, D., Dutko and M., Owen, D.R.J. Design of simple low order finite elements for large strain analysis of nearly incompressible solids. Int. J. Solids Struct. (1996) **33** (20-22): 3277-3296.
[7] Manabe, K. and Nishimura, H. Forming loads in tube-flaring with conical punch – Study on noising and flaring of tube V-. J. Jpn. Soc. Technol. Plast. (1983) **24** (264): 47-52, in Japanese.

XIV International Conference on Computational Plasticity. Fundamentals and Applications
COMPLAS 2019
E. Oñate, D.R.J. Owen, D. Peric , M. Chiumenti, and Eduardo de Souza Neto (Eds)

MODELLING OF WIDTH CONTROL FOR HOT STRIP MILL WITH FEM ANALYSIS

MASAYASU SEKIMOTO[*], MITSUHIKO SANO[†] AND KAZUHIRO OHARA[†]

[*†] Toshiba Mitsubishi-Electric Industrial Systems Corporation (TMEIC)
3-1-1 Kyobashi, Chuo-ku, Tokyo 104-0031, Japan
email: SEKIMOTO.masayasu@tmeic.co.jp, http://www.tmeic.com

Key words: FEM, Simulation, Hot Rolling, Width.

1 INTRODUCTION

In this paper, we discuss the modeling and simulation results of FEM analysis for width rolling for hot strip mill. The number of standard widths that can be produced efficiently in a continuous slab caster feeding a hot strip mill is limited. This has increased the requirement for width reduction in the hot strip mill rolling stands. The width of a slab can be reduced using vertical edger rolling stands in the roughing mill section and by using a slab sizing press. Effective width control using the vertical edgers is important for achieving the accuracy and precision of slab width relative to target values. In addition, effective width control can reduce width fluctuation caused by non-uniform deformation in head and tail part of the slab. The slab sizing press, which is designed to directly press the sides of the slab within molds, can be used to efficiently reduce width over the entire length of the slab. However, due to the physical layout and to construction constraints, the addition of a slab sizing press is not possible in many of the hot strip mills currently in operation. If the installation of a slab sizing press is not possible, the requirement for large width reduction must be accomplished entirely by using the vertical edgers. The width reduction capability of the vertical edgers is often limited since the vertical edgers are normally used only during forward passes in roughing mill. It is possible to increase the width reduction capability by modifying mill operation to use the vertical edgers on both forward and reverse passes. The modified rolling operation is referred to as VVH rolling because of the order of the rolling sequence. First step, vertical edger rolling on a reverse pass (width reduction). Second step, vertical edger rolling on a forward pass (width reduction). Final step, horizontal mill rolling (thickness reduction). However, the behavior of width deformation in VVH rolling is different from standard, forward pass only, edger rolling.

Three-dimensional width deformation of a slab when using VVH rolling was analyzed by FEM (Finite Element Method). The influence of various parameters including slab width, slab thickness, and the distribution pattern of width draft between forward and reverse passes were investigated and their impact on deformation phenomena were studied. Using the results of our analysis, we developed an optimal distribution pattern of width draft between forward and reverse passes for VVH rolling.

2 ROLLING PROCESS IN HOT STRIP MILL AND ROUGHING MILL

An example of conventional hot rolling mill configuration is shown in Figure 1. A slab is heated in the reheating furnace to around 1200 ºC then discharged onto the roughing mill passline and moved to the roughing mill stands using horizontal roller tables. The slab is rolled using several passes in the roughing mill to produce a transfer bar. Vertical edgers, located adjacent to the horizontal rolling stand(s), are used to reduce the slab width to the target value. When the slab has been rolled to the transfer bar target values for width and thickness, the transfer bar is then fed into the finishing mill where the thickness is reduced in each successive rolling stand to produce the target strip thickness. The strip is then cooled as it travels along the run out table to its target coiling temperature.

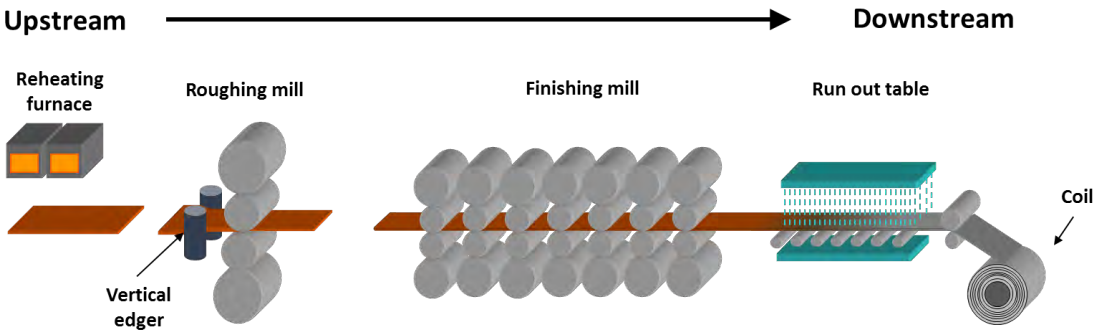


Figure 1: Overview of conventional hot rolling mill

During several passes in the roughing mill, slab width is reduced using the vertical edger and slab thickness is reduced using the horizontal mill. The typical width reduction sequence in the roughing mill is shown in Figure 2. During forward passes, slab moving in the upstream to downstream direction, the slab width is reduced using the vertical edger and thickness is reduced using the horizontal mill. During reverse passes, slab moving in the downstream to upstream direction, only slab thickness is reduced using the horizontal mill.

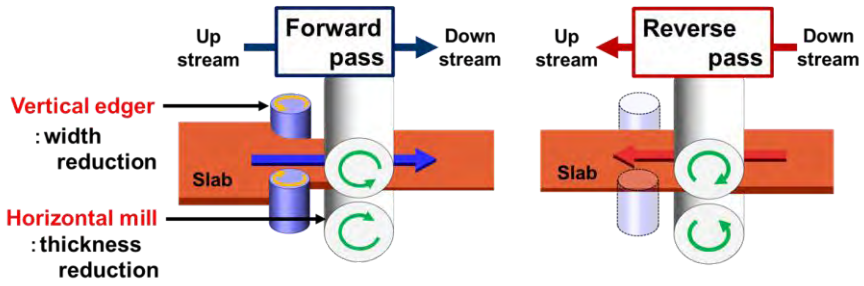


Figure 2: Standard rolling sequence in roughing mill

When using the VVH rolling sequence, slab width is reduced during both forward and reverse passes. A comparison of the standard sequence and the VVH sequence are shown in Figure 3 (Top view).

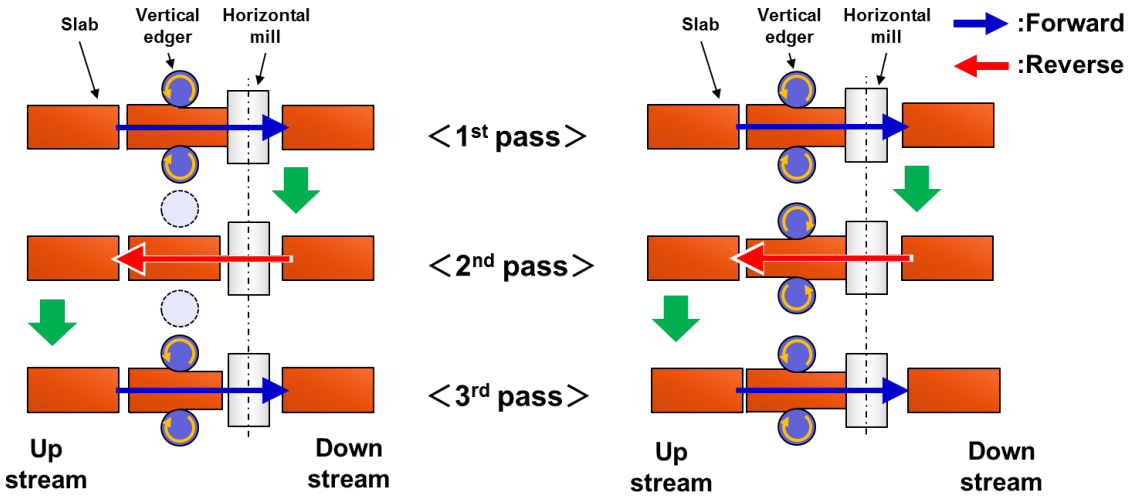


Figure 3: Roughing mill rolling sequence of standard rolling and VVH rolling

3 WIDTH DEFORMATION MECHANISM AT ROUGHING STAND

A considerable number of studies have been constructed on the prediction of width deformation in the roughing mill due to the importance of this process in achieving width accuracy precision. Shibahara et al. [1] had described the width deformation in a roughing mill with standard vertical edger rolling using equation 1:

$$B_x = B_E + \Delta B_D + \Delta B_H \tag{1}$$

where, B_x is delivery width, B_E is width after vertical edger rolling, ΔB_D is width spread due to the reduction of protrusions which appear at both width ends of the slab after vertical edger rolling (the protrusions are often called as "dog-bone" due to the visual appearance of the cross-sectional shape of the slab), and ΔB_H is ordinary width spread caused by horizontal rolling.

In a past, width deformation phenomena using the standard roughing mill sequence had been well studied [2, 3]. However, width deformation phenomena when using the VVH rolling sequence has received little study.

4 ANALYSIS CONDITIONS OF FINITE ELEMENT METHOD

An analysis of VVH rolling was done using finite element methods. The length and thickness of the entry slab were fixed at 4500mm and 200 mm for this analysis. Thickness reduction was 15% of the entry slab thickness. Slab widths and total width draft is shown in Table 1. In this paper, "total width draft" ($\Delta B_{rev} + \Delta B_{fwd}$) is defined as the total width draft achieved using both a forward and a reverse pass. In addition, "reverse pass distribution ratio" (β_{rev}), is calculated using equation 2:

$$\beta_{rev} = \frac{\Delta B_{rev}}{\Delta B_{rev} + \Delta B_{fwd}} \tag{2}$$

Table 1: The conditions of entry slab width, total width draft and reverse pass distribution ratio

Entry slab width [mm]	800, 1400, 2000
Total width draft [mm]	50, 100, 150
Reverse pass distribution ratio [-]	0, 0.1, 0.25, 0.33, 0.5, 0.67, 0.75, 0.9, 1.0

Figure 4 shows the overview of FEM 3-dimensional modeling. Due to the symmetry of thickness and width over the length of the slab, quartered 3-dimensional modeling was utilized in the simulation. To obtain a clear analysis of the effect of total width reduction using two passes, a rectangular slab was fed into vertical edger in the reverse pass direction then turned for a forward pass. During the forward pass, width was reduced using the vertical edger and thickness was reduced using the horizontal with the edger mill and horizontal mill working in tandem.

The work roll diameters of the vertical edger and the horizontal mill were 1200 mm. Both vertical edger rolls and horizontal mill rolls were defined as rigid bodies since roll deformation during rolling is not significant relative to the deformation of the slab. The contact between the surface of the slab and the vertical edger rolls and the contact between the surface of the slab and the horizontal mill rolls were modeled using applied penalty methods.

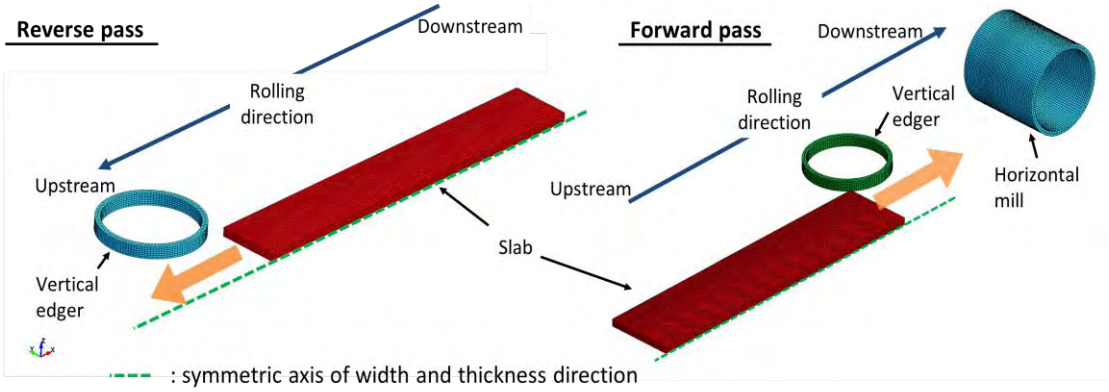


Figure 4: FEM 3-dimensional modeling at a forward pass and at a reverse pass

The mesh size, the number of mesh size, values for the slabs are shown in Table 2. The mesh size and the number of mesh at the edge side of the slab in the width direction, the middle part of the slab in the width direction, and the centerline of the slab, took the values from left to right at the column in 1400mm and 2000mm of the slab width. To simulate detailed behavior at the edge of the slab in the width direction, the mesh size at the edge of the slab was setup to be smaller than at the centerline of the slab.

Table 2: A mesh size and number of mesh for a slab

		Mesh size [mm]	Number of mesh [-]
Entry slab length		30	150
Entry slab thickness		20	5
Entry slab width [mm]	800	25	16
	1400	25, 30, 35	11, 6, 7
	2000	25, 30, 35	14, 10, 10

Material properties of the slab is shown in Table 3. The slab was defined as elastoplastic body. The simulation accuracy might be worse if the stress propagation speed is faster as passing through more than a mesh during a calculation time step. So that, applying properly Young's modulus and density is prefer. However, the stress propagation speed is slower than work speed in this process, so that the value of Young's modulus at room temperature was used. Also, the density was mass-scaled as 1/10. Those allowed to shorten computation time. Strain-hardening exponent and strain rate exponent were defined as the values calculated using Misaka's equation [4].

Table 3: Material properites of the slab

Item	Value	Unit
Density (before mass-scaling)	7850	kg/m^3
Young's modulus	210000	MPa
Poisson's ratio	0.3	-
Deformation resistance (at 1000 ºC)	120	MPa
Strain-hardening exponent	0.21	-
Strain rate exponent	0.13	-
Friction coefficient	0.4	-

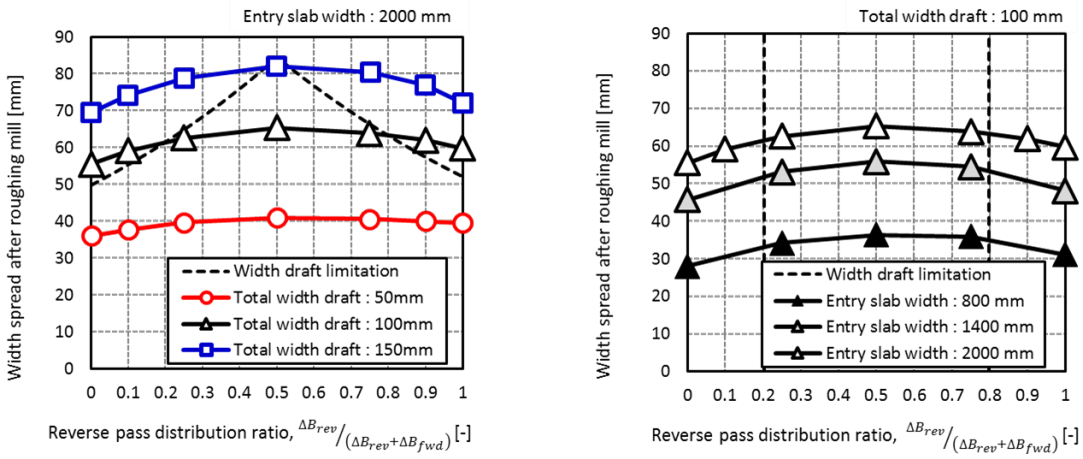
5 ANALYSIS RESULTS

The FEM simulation results were evaluated according to three factors:
(1) The amount of width spread when using VVH rolling ($\Delta B_D + \Delta B_H$)
(2) The dog-bone shape
(3) Width fluctuation at head end and tail end when using VVH rolling

5.1 Width spread after roughing mill

The relationship of the reverse pass distribution ratio and the width spread when using VVH rolling is shown in Figure 5. In Figure 5a, the entry slab width is constant at 2000 mm, and the total width draft changed from 50 mm to 150 mm respectively. In Figure 5b, the total width draft is constant at 100 mm, and the entry slab width changed from 800 mm to 2000 mm respectively. Width draft limits are shown as dotted lines in both Figure 5a and Figure 5b.

Regardless of the entry slab width and the total width draft, width spread is reaches the maximum level when the reverse pass distribution ratio equals 0.5 (forward pass width draft equal to reverse pass width draft). This is affected by the highest dog-bone peak height h_d as shown in Figure 6 of section 5.2. Width spread will be reduced when the target width draft for the forward pass does not equal the target width draft for the reverse pass and the condition where they are equal should be avoided. A reverse pass distribution ratio less than 0.5 will result in lower width spread than a reverse pass distribution ratio greater than 0.5. In addition, width spread will increase when entry slab width increases and when total width draft increases.



5a **5b**

Figure 5: The relationship of the reverse pass distribution ratio and the width spread using VVH rolling (a: entry slab width constant at 2000 mm, b: total width draft constant at 100 mm)

5.2 Dog-bone shape

The dog-bone shape of the slab effects the width spread when using VVH rolling. To evaluate the relationship of the reverse pass distribution ratio and dog-bone shape after forward pass vertical edger rolling, dog-bone shape is defined using a dog-bone peak height ratio and a dog-bone peak position ratio. These parameters are shown in Figure 6 and calculated using equations 3 and 4:

$$\gamma_{height} = \frac{h_D}{h_C} \tag{3}$$

$$\gamma_{position} = \frac{B_D}{B_C} \tag{4}$$

where, h_D is the dog-bone peak height, h_C is the slab thickness at center line of the slab, B_D is the left edge dog-bone peak position to the right edge dog-bone peak distance (measured across the strip width), B_C is the slab width.

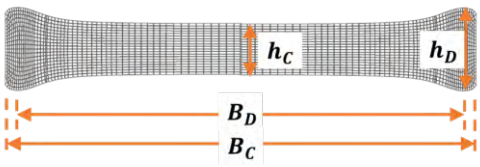
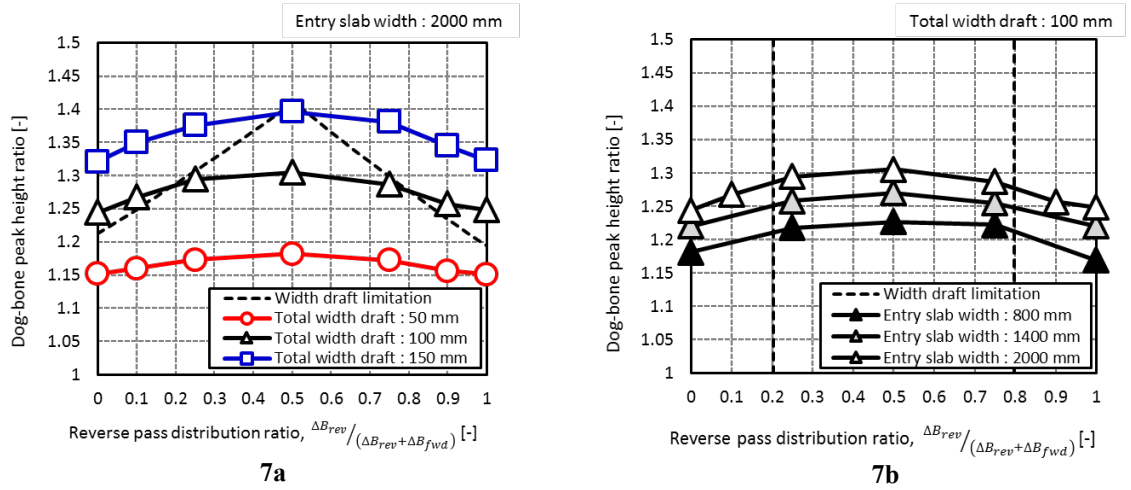


Figure 6: The cross-section shape of dog-bone and definitions of dog-bone peak height raito and dog-bone peak position ratio

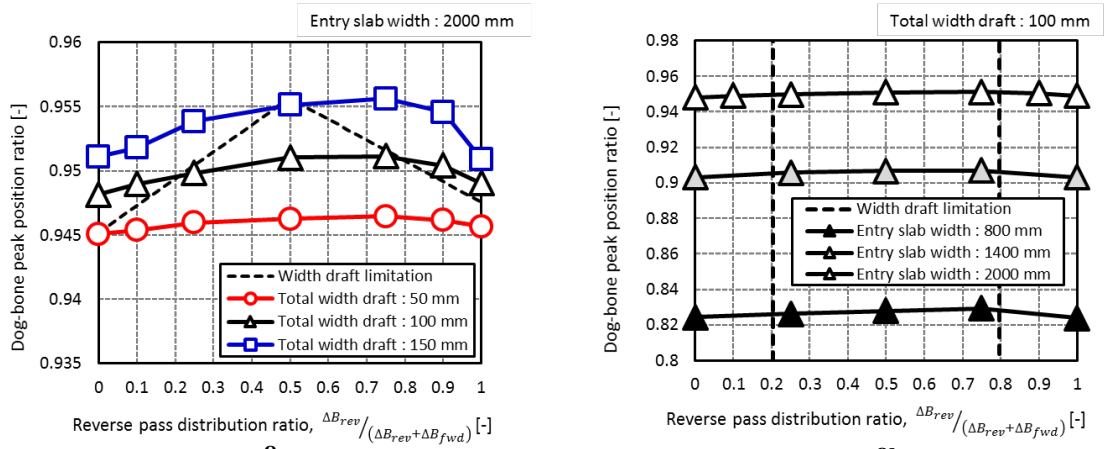
The relationship of the reverse pass distribution ratio and the dog-bone peak height ratio is shown in Figure 7. The relationship of the reverse pass distribution ratio and the dog-bone peak position ratio is shown in Figure 8. In Figure7a and 8a, the entry slab width is constant at 2000 mm. The total width draft is constant at 100 mm in Figure 7b and 8b. The dog-bone peak height

ratio is the greatest when the reverse pass distribution ratio equals 0.5. The highest width spread using VVH rolling when the width draft for the forward pass equals the width draft for the reverse pass is affected by the highest dog-bone peak height as shown in Figure 6.When the reverse pass distribution ratio is greater than 0.5, the dog-bone peak height is less than when the reverse pass ratio is less than 0.5. The greatest dog-bone peak position ratio occurs when the reverse pass distribution ratio equals 0.75. This dog-bone peak position tendency affects the width spread when using VVH rolling to a slightly greater degree when the reverse distribution ratio is more than 0.5.



7a **7b**

Figure 7: The relationship of the reverse pass distribution ratio and the dog-bone peak height ratio (a: entry slab width constant at 2000 mm, b: total width draft constant at 100 mm)



8a **8b**

Figure 8: The relationship of the reverse pass distribution ratio and the dog-bone peak position ratio (a: entry slab width constant at 2000 mm, b: total width draft constant at 100 mm)

5.3 Width at head end and tail end

Unsteady width deformation in head and tail part is also an important factor to consider when evaluating the behavior of VVH rolling. The definitions of width fluctuation at head end and

tail end are shown in Figure 9. The width fluctuations at head and tail end are defined as the amount of width narrowing toward the body portion of the slab. The head end of the slab is the front edge, in the length direction, during forward passes. Figure 10 shows the relationship of the reverse pass distribution ratio and width fluctuation at head and tail end. Figure 10a shows the results for the tail end and Figure 10b shows the results for the head end. For head end, a greater reverse pass distribution ratio results in lower width fluctuation. The highest width fluctuation occurs when the reverse pass distribution ratio is equal to 0.25. For tail end, a greater reverse pass distribution ratio results in higher width fluctuations.

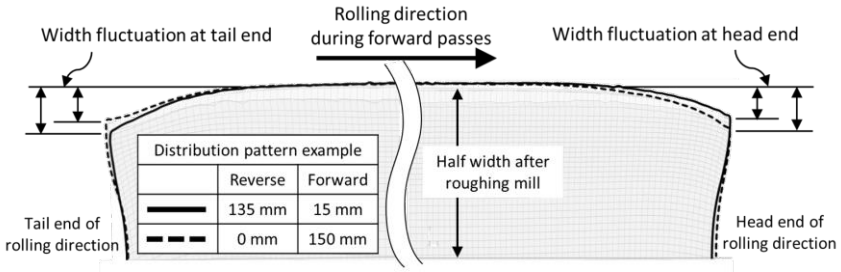
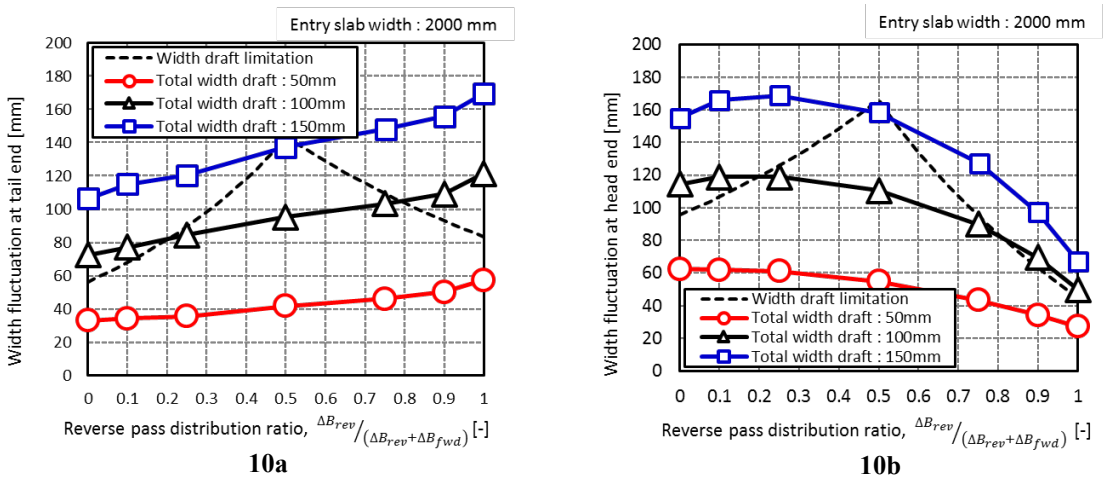


Figure 9: top view of examples when using VVH rolling and definitions of the amount of width fluctuation at head and tail end (deformation 3 times as real)



10a **10b**

Figure 10: The relationship of the reverse pass distribution ratio and width fluctuation at head and tail end (a: tail end, b: head end)

The following table summarizes the analysis of the results:

Table 4: Summary of analysis results

	Reverse pass distribution ratio		
	Low	0.5	High
Width spread when VVH rolling	Small	Big	Small
Dog-bone peak height	Low	High	Low
Dog-bone peak position	Close to center		Close to edge
Width fluctuation at head end	Big		Small
Width fluctuation at tail end	Small		Big

5.4 Evaluation of optimal distribution pattern

Analysis results were used to determine the optimal distribution pattern of width draft between a forward pass and a reverse pass using VVH rolling. The conditions for better width shape were determined from the relationship of reverse pass distribution ratio and width spread when using VVH rolling, dog-bone shape, and width fluctuation at head and tail end. We defined scores $K^n_{\beta_{rev}}$ of width spread when using VVH rolling, dog-bone shape, and width fluctuation at head and tail end with equation 5:

$$K^n_{\beta_{rev}} = \omega_n \cdot \left(\delta^n_{\beta_{rev}} - \delta^n_{\beta_{rev_min}}\right) \tag{5}$$

Where, β_{rev} is the reverse pass distribution ratio, n is each width feature such as width spread when using VVH rolling, dog-bone shape, and width fluctuation at head and tail end, ω_n is weight parameter for each feature, $\delta^n_{\beta_{rev}}$ is feature value at each reverse pass distribution ratio, $\delta^n_{\beta_{rev_min}}$ is the worst value of the feature. A weight parameter for a feature takes the score to be "0" as the worst value in a feature, and to be "0.2" as the best value in a feature.

The relationship of the reverse pass distribution ratio and each score in total width draft 100 mm are shown in Figure 11. The scores can evaluate as below:

- Higher width draft on a forward pass leads to lower width spread and this increases width reduction efficiency.
- Higher width draft on a reverse pass decreases dog-bone peak height ratio. However, this increases dog-bone peak position ratio.
- Higher width draft on a forward pass decreases width fluctuation at the head end. Higher width draft on a reverse pass lowers width fluctuation at the tail end.

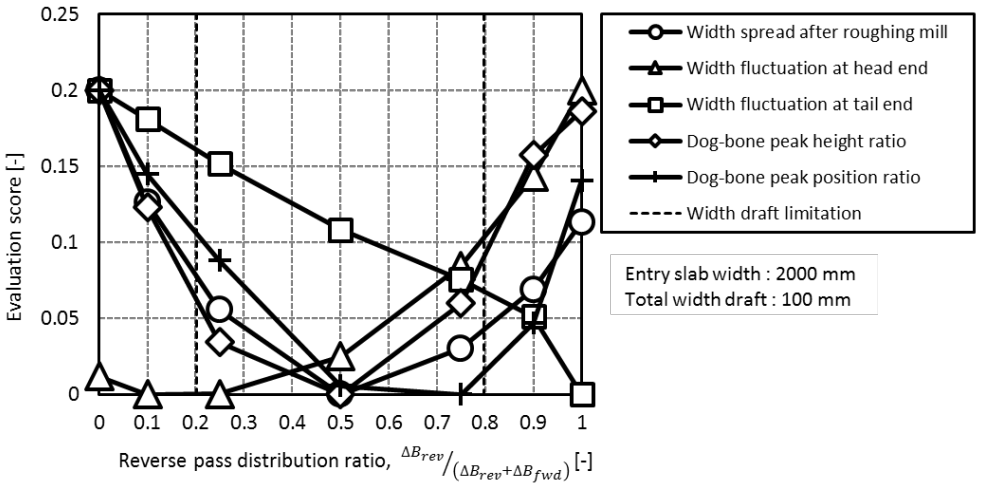


Figure 11: The relationship of reverse pass distribution ratio and evalucation score for each feature (Entry slab width: 2000mm, total width draft: 100mm)

Furthermore, sum of the scores can be used to determine the optimal distribution pattern between a forward pass and a reverse pass based on the combined effect on all the important width measurements. The total score for each reverse pass distribution ratio for entry slab width equals 2000mm is shown in Figure 12. As concern of the width draft limits, the reverse pass

distribution ratio around 0.25 can be identified as the optimal distribution pattern for total width draft equal to 100mm.

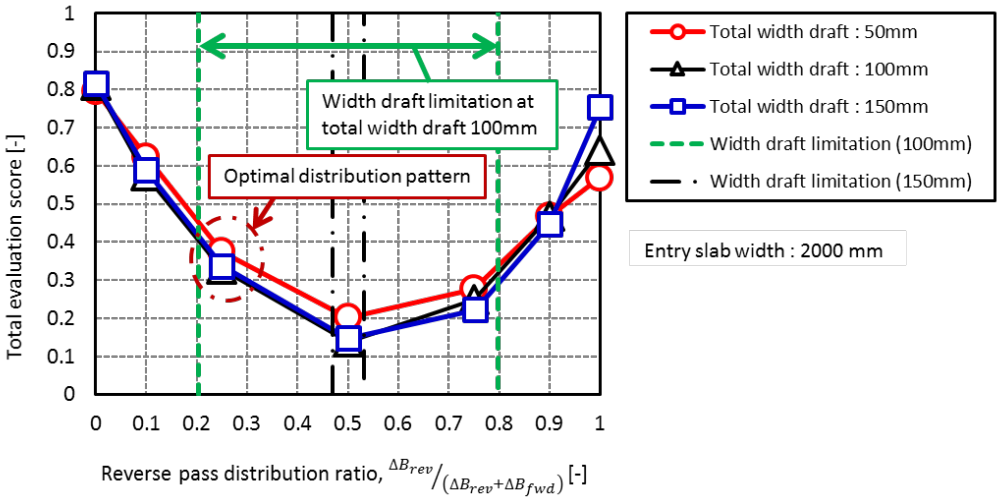


Figure 12: The relationship of reverse pass distribution ratio and total evaluation score (Entry slab width: 2000mm)

6 CONCLUSIONS

The width reduction process in roughing mill stand in a hot strip mill which reduces slab width using both forward and reverse passes was simulated using 3-dimensional FEM. The influence of various conditions and their deformation phenomena were studied. The results allowed the following conclusions:

- The characteristic of width deformation using VVH rolling including width spread, dog-bone peak height and peak position, and width fluctuation at head and tail ends of the slab were analyzed and summarized in Table 4.
- A little higher width draft during forward passes than during reverse passes can be proposed as the optimal distribution pattern based on the evaluation scores.
- FEM analysis concerned with the temperature drop from a pass to next pass will be future work.

REFERENCES

[1] T.Shibahara, R.Takahashi, T.Nunokawa, S.Kubota, “Automatic Width Control System at Roughing Train in Hot Strip Mill”, Advanced Technology of Plasticity, vol. II, 1200-1205, (1986). (in Japanese)

[2] S.Osada, F.Kamiyama, M.Kawaharada, H.Nakajima, S.Yanagimoto, Proceedings of the Japanese Spring Conference for the Technology of Plasticity, 125-128, (1977). (in Japanese)

[3] S.Hamauzu, H.Tokita, K.Ishii, M.Kawaharada, “Experiments by Using Lead on the Control Method of Width Drop at the Top and Tail Ends of Hot Strip”, Journal of the Japan Society for Technology of Plasticity, vol. 25, No. 277, 143-152, (1984). (in Japanese)

[4] Y.Misaka, T.Yoshimoto, Journal of the Japan Society for Technology of Plasticity, 8, 414, (1967). (in Japanese)

XV International Conference on Computational Plasticity. Fundamentals and Applications
COMPLAS 2019
E. Oñate, D.R.J. Owen, D. Peric , M. Chiumenti, and Eduardo de Souza Neto (Eds)

NEW DUCTILE FRACTURE CRITERION FOR PREDICTION OF INTERNAL FRACTURE IN SKEW ROLLING

KOJI YAMANE*, KAZUHIRO SHIMODA* AND KOICHI KURODA*

* Research and Development, Process Research Laboratories
Nippon Steel Corporation
1-8 Fuso-Cho, Amagasaki, Hyogo, 660-0891, Japan
e-mail: yamane.6nq.kohji@jp.nipponsteel.com

Key words: Skew Rolling, Internal fracture, Stress Triaxiality, Ductile Fracture Criterion.

Abstract. Skew rolling is the process of reducing the diameter of a round billet. In this process, internal fracture may occur in the rolled material. This phenomenon is known as the Mannesmann effect. While there has been great discussion about the mechanism of internal fracture, it has yet to be fully clarified. To investigate the internal fracture initiation and propagation, we conducted hot rolling experiments and evaluated the stress and strain of the rolled material by elasto-plastic finite element analysis. The results show that the internal fracture arises on the internal surface in which shear stress acts owing to the combined effect of tensile and shear stress. In this paper, a new ductile fracture criterion is discussed to quantitatively predict the occurrence of internal fracture in skew rolling.

1 INTRODUCTION

The skew rolling process is one method for reducing the diameter of a round billet [1]. In this process, a heated round billet is rotated and advanced by rolls as the roll axes are skewed counterclockwise to the pass line. Depending on the rolling conditions, internal fracture may occur in the rolled material. This phenomenon also occurs in cross rolling to form axially symmetric parts. The mechanism of internal fracture has been researched since the 20th century. On the basis of such studies, many researchers have proposed various theories on its mechanism: shear fracture theory [2–11], ductile fracture theory [12, 13], fatigue fracture theory [14] and so forth. However, since the theories are based on qualitative experimental results that have not been quantitatively evaluated, the mechanism of internal fracture has not been fully clarified. Therefore, this paper discusses the mechanism of internal fracture in three-roll skew rolling which has been little investigated. To investigate the internal fracture initiation and propagation, we conducted hot rolling experiments and quantitatively evaluated the stress and strain history of the rolled material by elasto-plastic finite element analysis. As a result, it was clarified that the internal fracture initiation points in skew rolling lay on a position away from the central axis parts of the rolled material where conventional ductile fracture criteria predicted maximum damage values. Because it is necessary to develop a reasonable model to describe internal fracture, this paper focuses on the validation of a new ductile fracture criterion to quantitatively predict the occurrence of internal fracture in skew rolling.

2 HOT ROLLING EXPERIMENTS

2.1 ROLLING CONDITIONS

In this paper, the actual situations of internal fracture in three-roll skew rolling were investigated. Figure 1 shows a schematic diagram of the three-roll skew rolling mill. This rolling mill is arranged with the rolls placed at circumferential intervals of 120° around the billet, and the roll axes are skewed to the pass line. This angle is referred to as feed angle β. The roll axes being skewed reduce the outer diameter of a material as it performs helix rotation. To investigate the internal fracture behavior in skew rolling, semi-finished products were cut with wire saws into multiple cross sections in the longitudinal direction. The rolling condition is shown in Table 1. The rolls rotate in the same direction with a constant rotational velocity of 100 rpm. The internal fracture was investigated by rolling the material at a feed angle β of 4°, with a billet diameter of 70 mm, a rolled diameter of 42 mm, and a material heating temperature of 1100°C. The chemical composition of the specimens is shown in Table 2. Free-cutting steel SUM24L with low deformability containing inclusions such as MnS and Pb was used for the specimens.

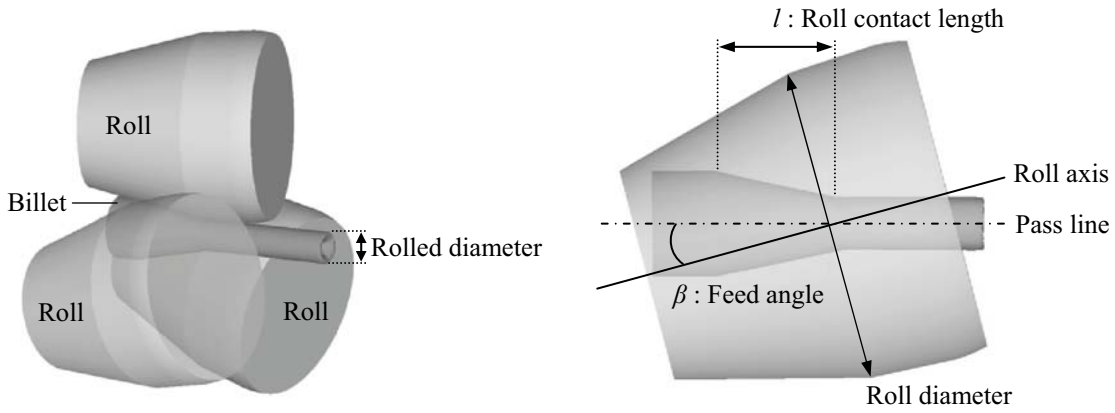


Figure 1: Schematic of skew rolling mill with three rolls

Table 1: Rolling conditions

Roll diameter [mm]	180
Billet diameter [mm]	70
Rolled diameter [mm]	42
Feed angle β [°]	4
Billet heating temperature [°C]	1100

Table 2: Chemical composition of SUM24L [wt.%]

C	Si	Mn	P	S	Pb	Fe
0.07	-	1.04	0.07	0.33	0.17	Bal.

2.2 OBSERVATION OF INTERNAL FRACTURE

A digital microscope VHX-6000 made by KEYENCE was used for the observation of internal fracture in the rolling cross section. The observation procedure is as follows:

(1) Create the entire image of a rolling cross section with high resolution, synthesizing the multiple-shot images of the rolling cross section at each position with magnification of 50, into a sheet of those images.

(2) Count black dots of more than 200 μm^2 (an average diameter of 16 μm) as one void after subjecting those images to binarization processing. Note that the resolution can be considered as adequate because 12 pixels constitute a void of 200 μm^2 as one side of a pixel has a length of 4.15 μm.

(3) Calculate the void density, i.e., the number of voids per unit area, by counting the number of voids at the each ring shaped area with 1 mm band breadth from the central axis of the rolled material as shown in Fig. 2.

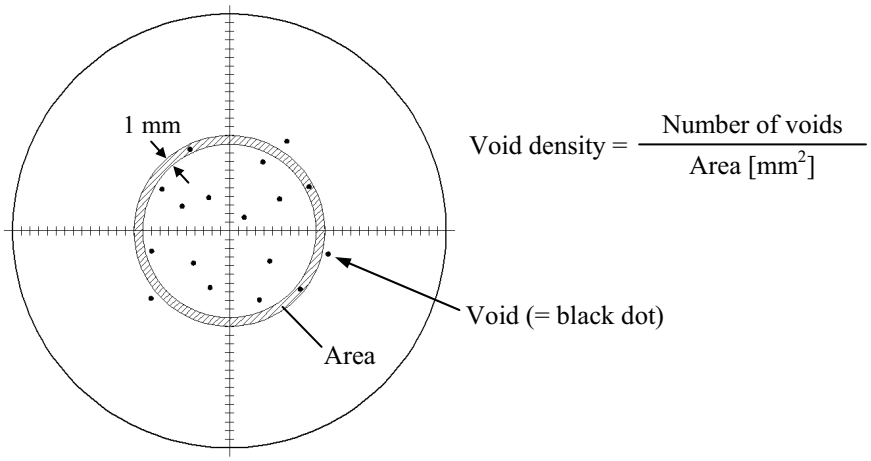


Figure 2: Measurement of void density in rolling cross section

2.3 EXPERIMENTAL RESULTS

Internal fracture was observed in the roll condition of feed angle $\beta = 4°$. Figure 3 shows the measurement position of a semi-finished product. The rolling cross sections each lying at -10 mm and +10 mm distance from termination point O of the outer diameter forming via the tapered roll faces were observed in detail. The macro photographs of the rolling cross section at feed angle $\beta = 4°$ are shown in Fig. 4. It was identified that voids nucleate at the location a couple of millimeters away from the central axis of the rolled materials, grow, and coalesce to each other in the circumferential direction, as the rolled materials advances, and thus, finally occur internal fracture. Figure 5 indicates the distribution of void density in the rolling cross section before the voids coalesce. Most of the voids at the initial stage of internal fracture had a diameter of 30 μm or less. The void density at the central axis of the rolled materials was 0 [/mm^2] in the rolling cross section A, and became high around a radius of 6 mm from the central axis. The fracture initiation points in three-roll skew rolling lay not in the central axis parts of the materials but in their surroundings.

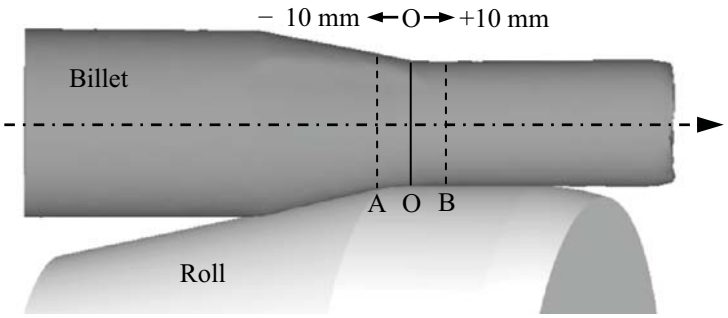


Figure 3: Measurement position of semi-finished product

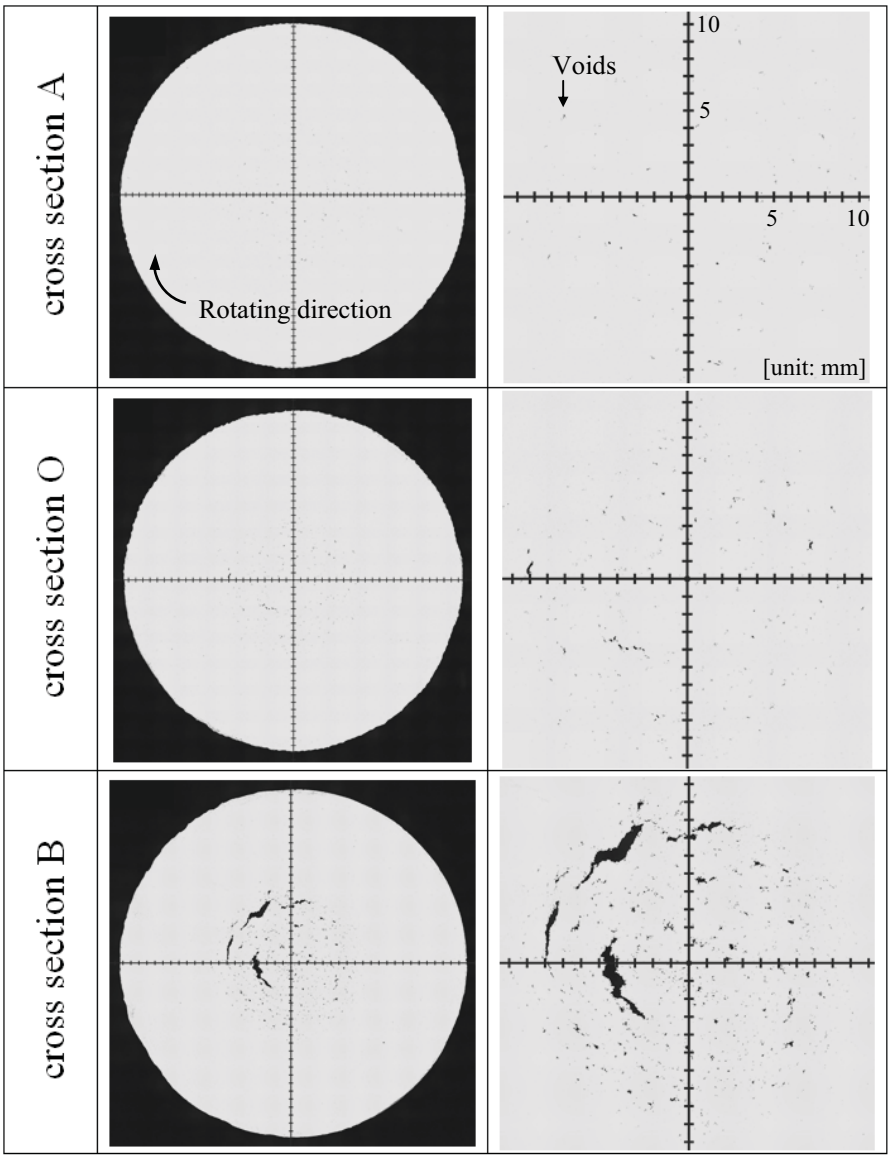
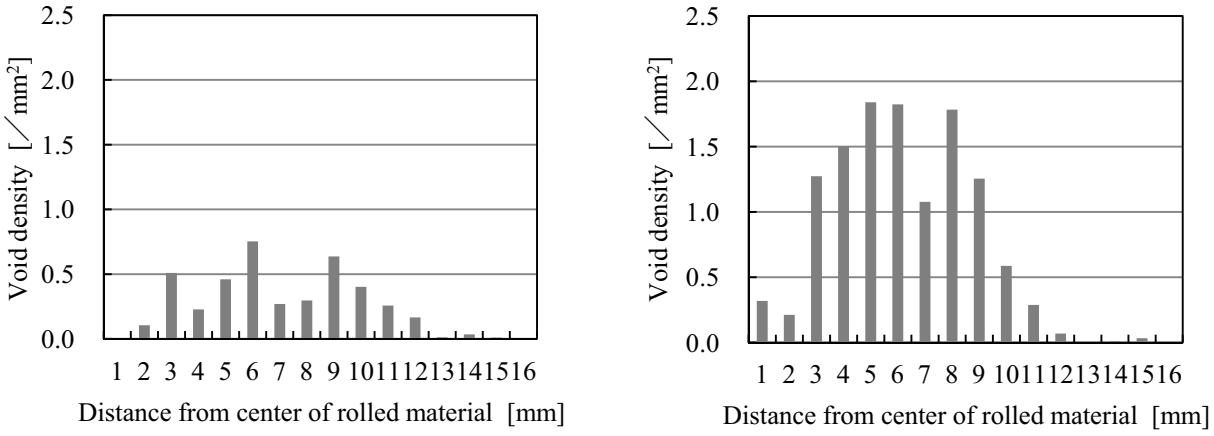


Figure 4: Photographs of voids in rolling cross sections



(a) Cross section A

(b) Cross section O

Figure 5: Distribution of void density in rolling cross sections

3 NUMERICAL ANALYSIS

3.1 NUMERICAL ANALYSIS MODEL

In order to investigate the deformation behavior inside the rolled material in skew rolling, three-dimensional deformation analysis was performed by the elasto-plastic finite element method using FE code Simufact Forming. The numerical analysis model was similar to the skew rolling mill as shown in Fig. 1; the rolls were modeled as rigid bodies, and a rolled material was modeled as hexahedral elements. The Coulomb friction coefficient of the roll was 0.5 because the contact condition between the material and rolls was assumed to be almost sticking. The material temperature, roll temperature, and heat transfer coefficient h between the material and rolls were, respectively, set to be 1100°C, invariable 20°C, and 4000 [W/m^2/K]. For the stress-strain curve of the rolled material, the hot tensile test results of the free-cutting steel SUM24L was selected among the MatILDa functions implemented in Simufact Forming. The selected function is shown in Formula (1). The equivalent stress σ_{eq} in the plastic deformation area is a function of the equivalent strain ε_{eq}, equivalent strain rate $\dot{\varepsilon}_{eq}$, and temperature T. The roll conditions for the numerical analysis were the same as those for the hot rolling experiments as shown in Table 1. The predictability of internal fracture was evaluated by comparing the experimental results with the damage value of ductile fracture criteria calculated by the numerical analyses. The damage accumuration is usually formulated with a function of stress and strain.

$$\sigma_{eq} = 1600 \cdot \exp(-0.00235 \cdot T) \cdot \varepsilon_{eq}^{\left(10^{-4} \cdot T - 0.04488\right)} \cdot \exp\left(\frac{-6.44 \cdot 10^{-6} \cdot T - 0.02466}{\varepsilon_{eq}}\right) \cdot \dot{\varepsilon}_{eq}^{\left(6.0 \cdot 10^{-5} \cdot T + 0.049492\right)} \quad (1)$$

3.2 CONVENTIONAL DUCTILE FRACTURE CRITERIA

Concerning the prediction of fracture in plastic processing, a variety of ductile fracture criteria are proposed by Ayada et al. [15], Oyane [16], Cockcroft & Latham [17], Rice & Tracey [18], McClintock [19], and Brozzo et al. [20]. The damage values in the experiments described in the previous chapter were calculated using the respective criteria; however, no criterion agreed with the distribution of the actual fracture. As an example, the damage values in the criterion by Ayada, which means the integral values of stress triaxiality σ_m/σ_{eq} ($\sigma_m = (\sigma_r+\sigma_\theta+\sigma_z)/3$) and the equivalent strain ε_{eq}, are shown in Fig. 6. The darker the contour, the higher the value, which means that fracture is more likely to occur. In three-roll skew rolling, high tensile stress works along the longitudinal direction in the central axis of the rolled material, and the stress triaxiality indicates the maximum value in the central axis parts. The compressive stresses in the radial direction are high in the vicinity of the portion in contact with the rolls, and the stress triaxiality indicates a negative value with a high absolute value. For the equivalent strain, the maximum is provided on the external surface of the materials due to the shear deformation with the rotation of the material. As a result, for the damage value, the maximum is provided in the central axis where the stress triaxiality always takes a positive value. Ayada's criterion is applied to the prediction of internal fracture during extrusion processing, and its efficacy is recognized; however, it can not be applied to predict internal fracture in skew rolling. This criterion assumes that the direction of the principal stress is constant, which may cause disagreement with the experimental results. The skew rolling mill is characterized by repeated sequential rolling, and the positive and negative values of the stress triaxiality alternate quite often with the rotation of the material so that the damage value fluctuates. Therefore, under the processing involving rotating materials, a new criterion that is represented by stress components coinciding with the fracture growth direction is needed for precise prediction of internal fracture.

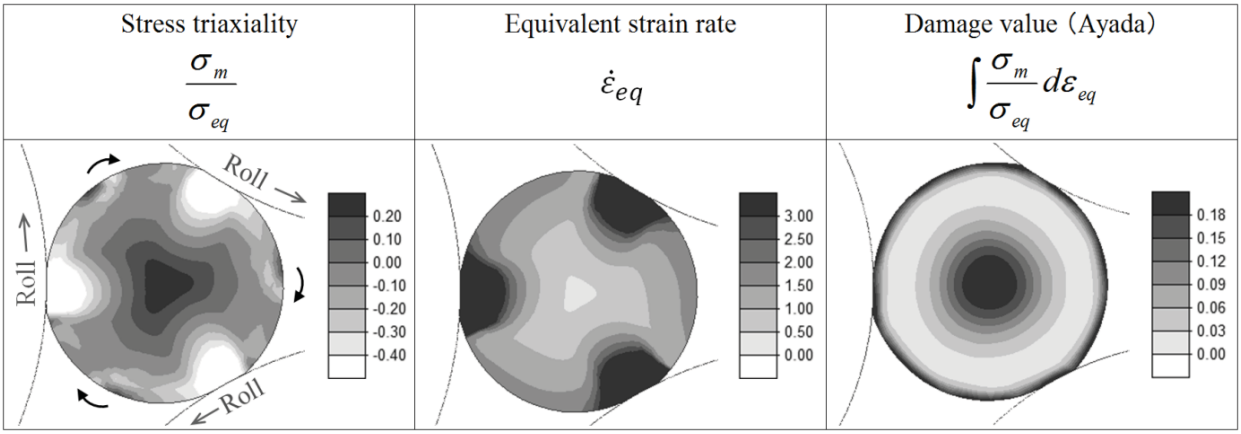


Figure 6: Distribution of damage value in criterion by Ayada

4 RESULTS AND DISCUSSION

4.1 EACH STRESS COMPONENT DURING ROLLING

Stress components inside the materials in three-roll skew rolling were specifically investigated. Figure 7 shows the six components of the stresses during rolling. Stress in the radial direction σ_r takes a compressive value of -80 MPa immediately under the rolls and a tensile value across the roll to roll. Circumferential stresses σ_θ provide a stress distribution opposite to that of σ_r. The materials meet the maximum stress triaxiality in the central axis parts, as stress in the longitudinal direction σ_z assumes significant tension in those parts. Shear stress in the circumferential direction $\sigma_{r\theta}$ works in the same manner as the principal stress. One of the characteristics of skew rolling is that tensile stress and shear stress work simultaneously, because the outer diameter is reduced while allowing the materials to rotate.

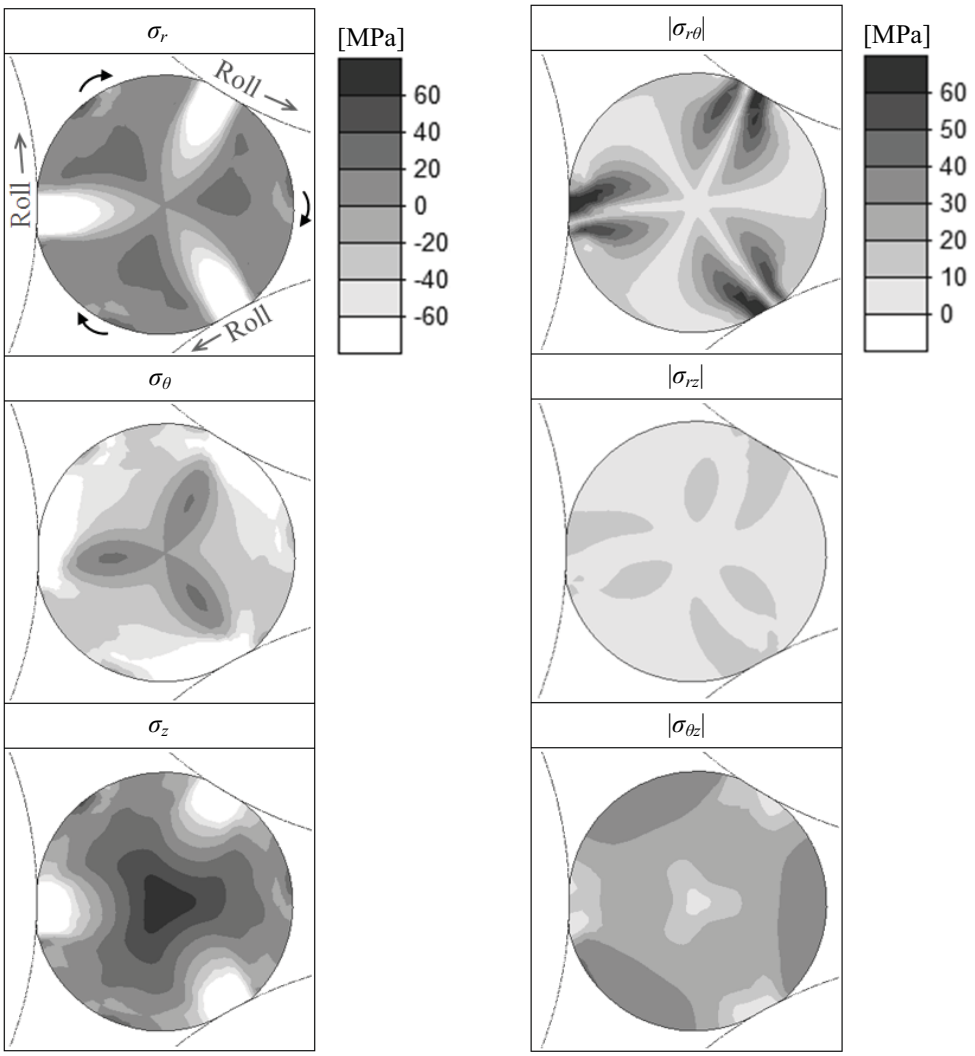


Figure 7: Distribution of stress in rolling cross section A

4.2 PROPOSAL OF NEW DUCTILE FRACTURE CRITERION

The conventional ductile fracture criteria do not agree with the experimental results because the effects of shear stress on void coalescence are not adequately estimated. For example, it is reported by Bao et al. [21–23], Weck et al. [24], Li et al. [25] and Lou et al. [26, 27] that shear stress can contribute to ductile fracture. Bao et al. stated that the value of the equivalent strain to fracture as well as the fracture form depend on the stress state. When the relationship between the stress triaxiality and the equivalent strain to fracture is further clarified, it can be seen that a void can grow and mainly cause ductile fracture if the stress triaxiality takes a positive value, i.e., the stress state is under tension. On the other hand, a void is unlikely to grow and shear fracture can occur if the stress triaxiality takes a negative value, i.e., the stress state is under compression. Furthermore, if the stress triaxiality takes a positive value with a low absolute value, it is proposed that void growth due to tensile stress, mixed with void coalescence due to shear stress, can lead to fracture. Weck et al. revealed the mechanism of void coalescence through performing tensile tests of alminium alloy sheets that have various laser drilled holes. When these specimens are pulled under the condition whereby artificial holes are arrayed, the holes coalesce to each other at 45° with respect to the tensile direction by shear deformation. Li et al. stated that the equivalent strain nucleates fine voids originating from inclusions, tensile stress promotes the growth of these voids, and shear stress allows the voids to coalesce with each other. Lou et al. stated that ductile fracture occurs via the processes of i) void nucleation, ii) void growth, and iii) void coalescence, analyzing the ductile fracture microscopically. They propose such functions as i) equivalent strain ε_{eq}, ii) stress triaxiality σ_m/σ_{eq}, and iii) maximum shear stress τ_{max} are appropriate when those respective phenomena are formulated.

Considering the above mentioned references and our reseach results that the internal fracture initiation shown in Fig. 4 correspond with the positions at which the tensile stress and the shear stress work simultaneously as shown in Fig. 7, we assumed that internal fracture occurs due to the synergistic effects of tensile and shear stress. It is postulated that the void nucleation, void growth, and void coalescence, respectively, are represented by equivalent strain ε_{eq}, tensile stress, and shear stress; these three factors are considered to be requirements for internal fracture. This paper presents a new ductile fracture criterion in which internal fracture is represented by a product of tensile stresses σ_r, σ_θ, and σ_z as well as shear stresses $\sigma_{r\theta}$, σ_{rz}, and $\sigma_{\theta z}$, and the equivalent strain ε_{eq}, concerning the plastic processing by which tensile stress works in phase with shear stress.

Figures 8 and 9, respectively, show a schematic diagram of the stress components, and a combination of normal stress components and shear stress components. The proposed criterion is composed of a combination of stresses that cause a single void to grow in the fracture growth direction observed from the rolling cross section. Therefore, the term of $\sigma_{\theta z}$ is excluded from the proposed criterion, as shear stress $\sigma_{\theta z}$ is assumed to have no impact on initiating internal fracture, because shear stress $\sigma_{\theta z}$ working in the helix direction of the rolled material is orthogonal to the fracture growth direction observed from the rolling cross section. $\sigma_r \cdot \sigma_{rz}$ is excluded from the proposed criterion to avoid duplex addition of the radial direction stress σ_r. Term σ_r has two types, i.e., $\sigma_r \cdot \sigma_{r\theta}$ and $\sigma_r \cdot \sigma_{rz}$, and is the combination of shear stress $\sigma_{r\theta}$ or σ_{rz} caused by the diameter reduction. As shown in Fig. 7, the distribution of stress $\sigma_{r\theta}$ agrees with that of σ_{rz} in the rolled material; $\sigma_{r\theta}$ has evidently large absolute values. That

makes the grown voids to coalesce along the direction in which $\sigma_{r\theta}$ works. The proposed criterion is constituted by such a combination of the three terms $\sigma_r \cdot \sigma_{r\theta}$, $\sigma_\theta \cdot \sigma_{r\theta}$, and $\sigma_z \cdot \sigma_{rz}$, which are assumed to significantly contribute to initiating internal fracture observed from the rolling cross section.

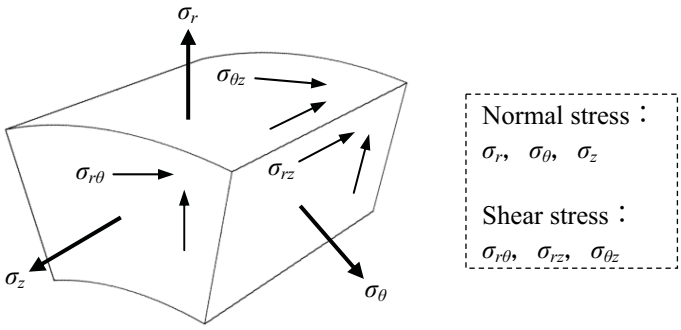


Figure 8: Schematic of each stress component

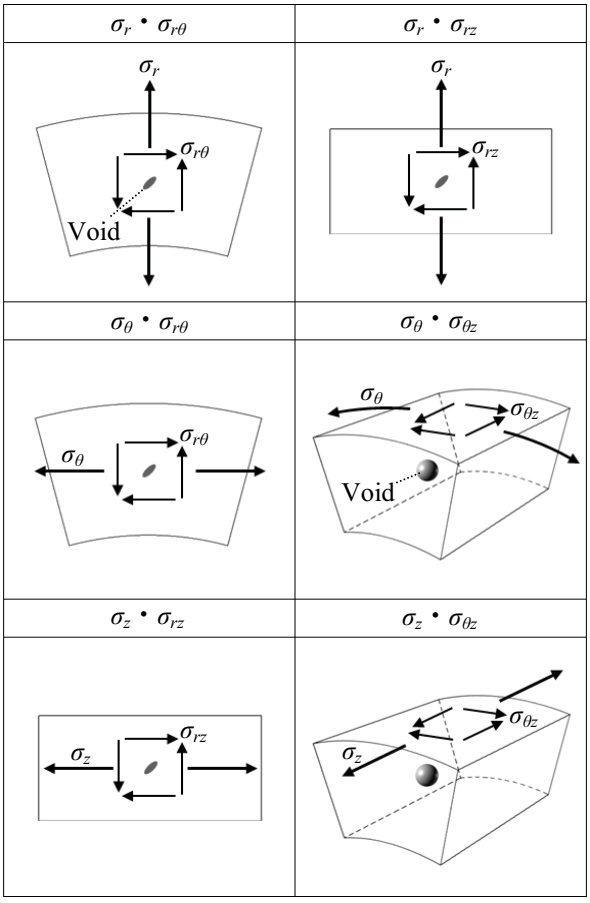


Figure 9: Schematic of combination of normal stress and shear stress

The proposed criterion is shown in Formulas (2) and (3). Shear stresses $\sigma_{r\theta}$ and σ_{rz} can take a negative value within the numerical analysis as their direction is reversed when the material rotates; The shear stress term is defined as an absolute value because shear stress contributes to fracture irrespective of taking a positive or negative value. The incremental value of damage per unit time f is a product of the dimensionless stress term and the equivalent strain rate $\dot{\varepsilon}_{eq}$. The damage value F is the incremental value f integrated with rolling time t, i.e., a product of the dimensionless stress term and the equivalent strain ε_{eq}. When the incremental value f turns positive, f is added as voids can nucleate and grow in a tensile stress field. In contrast, in a compressive stress field in which the increment value f turns negative, $f = 0$ is defined, considering that no voids ever grow, or that any nucleated voids neither shrink nor vanish.

$$f = \left\{ \left(\frac{\sigma_r}{\sigma_{eq}} \right) \left(\frac{|\sigma_{r\theta}|}{\sigma_{eq}} \right) + \left(\frac{\sigma_\theta}{\sigma_{eq}} \right) \left(\frac{|\sigma_{r\theta}|}{\sigma_{eq}} \right) + \left(\frac{\sigma_z}{\sigma_{eq}} \right) \left(\frac{|\sigma_{rz}|}{\sigma_{eq}} \right) \right\} \dot{\varepsilon}_{eq} \tag{2}$$

$$F = \int \langle f \rangle dt \qquad \langle f \rangle = \begin{cases} f & \text{when } f > 0 \\ 0 & \text{when } f \le 0 \end{cases} \tag{3}$$

Figure 10 shows the distribution of the incremental value of damage per unit time f and that of damage value F in the rolling cross section A. Damage value F was calculated from the user subroutines built into the FE code, or calculated by extracting the stress and strain histories from arbitrary integral points. Damage value F takes the maximum value at a position 6 mm away from the central axis parts of the rolled materials. This is because a position away from the central axis parts constitutes a stress field in which tensile stress and shear stress work simultaneously. The increment value f is low, since shear stresses $\sigma_{r\theta}$ and σ_{rz} can hardly work in the central axis parts. Furthermore, the increment value f becomes close to 0, since the rolled materials provide a compressive stress field on the external side. As the materials rotate in such a fluctuating stress field, the region with a high damage value constitutes a ring shaped area.

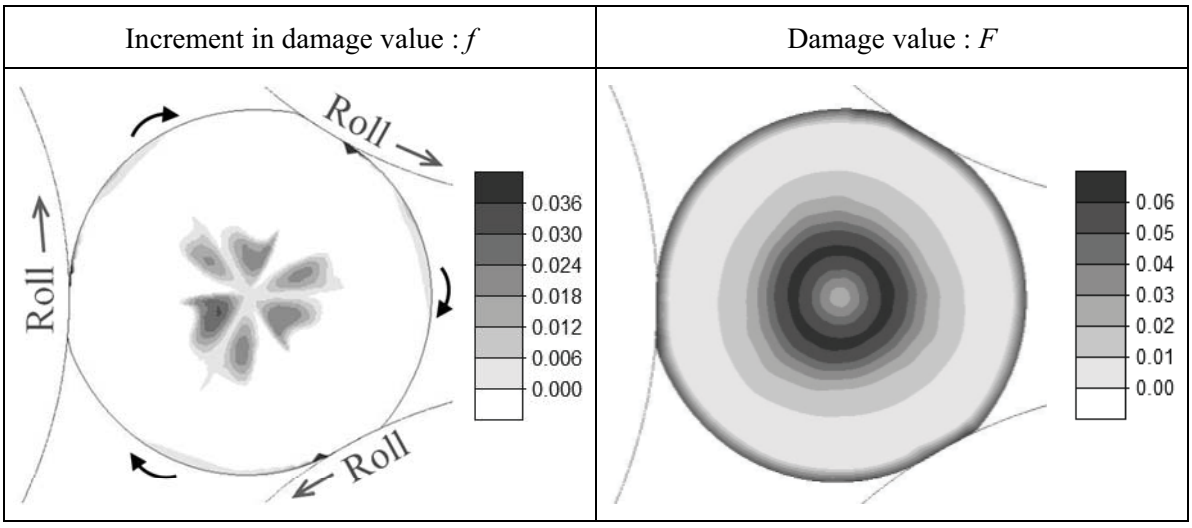
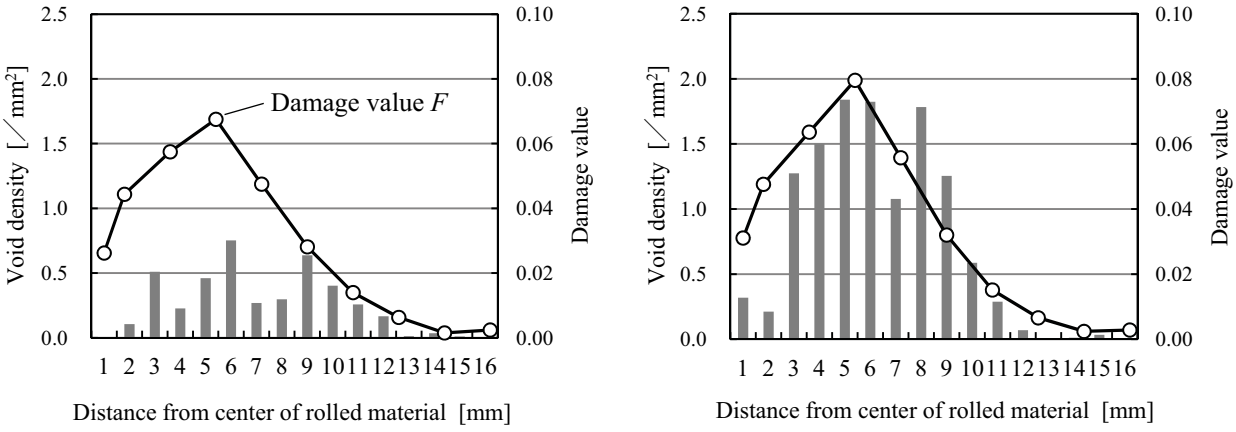


Figure 10: Distribution of damage value using new ductile fracture criterion

Figure 11 shows the contrast between the void density and damage value *F*. The distribution of the void density shown in Fig. 5 qualitatively agrees with that of damage value *F*. In this paper, the number of voids per unit area was measured in such a way as shown in Fig. 2. It is difficult to estimate the void size from the void density since individual voids have their own different volumes. Obtaining quantitative correspondence is a very complicated task; however, we believe that it is necessary to contrast not the void number but the void volume with damage value *F*. It is a future task to clarify the relationship between void growth histories and damage values at arbitrary observation points.



(a) Cross section A (b) Cross section O

Figure 11: Relationship between void density and damage value

5 CONCLUSIONS

- The mechanism of internal fracture in skew rolling has been clarified from hot rolling experiments and numerical analyses. The tensile stress and shear stress that work under plastic deformation induce voids to nucleate, grow and coalesce finally occuring macroscopic internal fracture.
- In three-roll skew rolling, internal fracture occurs around the central axis parts, because a position away from the material's central axis parts constitutes a stress field in which tensile stress and shear stress work simultaneously.
- A new ductile fracture criterion based on tensor quantity, differently from the conventional criteria comprising scalar quantity, has been formulated with tensile stress and shear stress working in the fracture growth direction. This criterion can predict the internal fracture initiation specific to skew rolling. The damage values estimated by this criterion would contribute to the suppression of internal fracture and the optimization of the rolling conditions.
- The proposed ductile fracture criterion is expected to predict internal fracture, regardless of the rolling condition and number of rolls.

REFERENCES

[1] Nakasuji, K., Kuroda, K. & Hayashi, C.: ISIJ Int., **31**-6 (1991), 620-627.
[2] Siebel, E.: Stahl und Eisen, **47** (1927), 1685.
[3] Kocks, F.: Stahl und Eisen, **47** (1927), 433.
[4] New Tube Investments Development: Metallurgia, (1967), 51-56.
[5] Blazynski, T. Z. & Jubb, C.: Journal of the Institute of Metals, **97** (1969), 363-373.
[6] Erman, E.: J. Appl. Metalwork., **4** (1987), 331-341.
[7] Kato, K.: Tetsu-to-Hagané, **56**-7 (1970), 915-929.
[8] Saito, Y., Higashino, T. & Kato, K.: J. Jpn. Soc. Technol. Plast., **17**-191 (1976), 958-965.
[9] Kato, K.: J. Jpn. Inst. Met., **17**-7 (1978), 598-606.
[10] ISIJ: Iron and Steel Handbook 3rd, **2** (1980), 940.
[11] The Japan Society for Technology of Plasticity: Rotary Forming, (1990), 77.
[12] Smirnov, V. S.: Stal', **7** (1947), 511.
[13] Teterin, P. K. & Luzin, Yu. F.: Stal', **10** (1960), 758.
[14] Pater, Zb., Weroñski, W., Kazanecki, J. & Gontarz, A.: J. Mater. Process. Technol., **92-93** (1999), 458-462.
[15] Ayada, M., Higashino, T. & Mori, K.: Adv. Technol. Plast., **1** (1987), 553-558.
[16] Oyane, M.: JSME, **15** (1972), 1507-1513.
[17] Cockcroft, M. G. & Latham, D. J.: Journal of the Institute of Metals, **96** (1968), 33-39.
[18] Rice, J. R. & Tracey, D. M.: J. Mech. Phys. Solids, **17** (1969), 201-217.
[19] McClintock, F. A.: Journal of Applied Mechanics, **35** (1968), 363-371.
[20] Brozzo, P., de Luca, B. & Rendina, R.: International Deep Drawing Research Group, **7** (1972), 3.1-3.5.
[21] Bao, Y. & Wierzbicki, T.: Int. J. Mech. Sci., **46** (2004), 81-98.
[22] Bao, Y. & Wierzbicki, T.: Journal of Engineering Materials and Technology, **126** (2004), 314-324.
[23] Bao, Y. & Wierzbicki, T.: Engineering Fracture Mechanics, **72** (2005), 1049-1069.
[24] Weck, A. & Wilkinson, D.S.: Acta Mater., **56** (2008), 1774-1784.
[25] Li, H., Fu, M. W., Lu, J. & Yang, H.: Int. J. Plast., **27** (2011), 147-180.
[26] Lou, Y., Huh, H., Lim, S. & Pack, K.: Int. J. Solids Struct., **49** (2012), 3605-3615.
[27] Lou, Y. & Huh, H.: Int. J. Solids Struct., **50** (2013), 447-455.

XV International Conference on Computational Plasticity. Fundamentals and Applications
COMPLAS 2019
E. Oñate, D.R.J. Owen, D. Peric, M. Chiumenti & Eduardo de Souza Neto (Eds)

ANALYSIS OF DAMAGE AND FRACTURE MECHANISMS IN DUCTILE METALS UNDER NON-PROPORTIONAL LOADING PATHS

MICHAEL BRÜNIG*, STEFFEN GERKE* AND MORITZ ZISTL*

* Institute for Engineering Mechanics and Structural Analysis
Bundeswehr University Munich
85577 Neubiberg, Germany
e-mail: michael.bruenig@unibw.de, web page: http://www.unibw.de/mechanik-und-statik

Key words: Damage and fracture, ductile metals, non-proportional loading, experiments, numerical simulations

Abstract. The paper discusses biaxial experiments and corresponding numerical simulations to analyze the effect of non-proportional loading paths on damage and fracture behavior of ductile metals. Newly developed specimens are taken from thin metal sheets and are tested under different biaxial loading conditions covering a wide range of stress states. In this context, an anisotropic continuum damage model is presented based on yield and damage conditions as well as on evolution laws for plastic and damage strain rates. Different branches of the damage criteria are taken into account corresponding to various damage and failure processes on the micro-level depending on stress triaxiality and Lode parameter. Experiments with biaxially loaded specimens have been performed. Results for proportional and corresponding non-proportional loading histories are discussed. During the experiments strain fields in critical regions of the specimens are analyzed by digital image correlation (DIC) technique while the fracture surfaces are examined by scanning electron microscopy (SEM). Numerical simulations of the experiments have been performed and numerical results are compared with experimental data. In addition, based on the numerical analyses stress distributions in critical parts of specimens are detected. The results demonstrate the efficiency of the new specimen's geometries covering a wide range of stress states in the shear/tension and shear/compression regime as well as the effect of loading history on damage and fracture behavior in ductile metal sheets.

1 INTRODUCTION

Products of modern metal forming processes have to fulfill requirements of the customers. These are, for example, demands to enforce safety of structural elements or to develop lightweight structures leading to cost reduction or to improvements in energy consumption. These environmental, economic and safety aspects lead to increased inquiries for high quality metals like aluminum alloys or high strength and advanced high

strength steels. On the other hand, numerical studies to optimize metal forming processes have received remarkable attention during the last decades. Thus, highly predictive and practically applicable constitutive models as well as corresponding efficient and accurate numerical algorithms have to be developed to investigate damage and fracture processes on the micro-scale causing macro-defects and fracture in materials and structural elements. Since many industrial processes like forging and rolling undergo non-proportional loading scenarios the analysis of damage and fracture mechanisms caused by non-proportional loading paths is of special interest.

Nowadays it is well known that the stress state acting in a material point affects the damage and failure processes on the micro-scale. For example, formation and growth of nearly spherical micro-voids occur under hydrostatic stress whereas micro-shear-cracks are caused by deviatoric stress states. To examine and to understand these different stress-state-dependent damage and failure mechanisms and their interactions detailed experimental and numerical analyses have to be performed on both the micro- and the macro-scale allowing development of accurate and realistic phenomenological material theories. These constitutive models can be used to quantify damage at different stages of the loading processes as well as to judge the quality of metal forming processes.

In the literature various experiments with different specimens have been proposed to study the effect of stress state on damage and fracture mechanisms as well as their influence on the inelastic deformation and macroscopic failure behavior of ductile metals. For example, in the analysis of sheet metal behavior under positive stress triaxialities enforcement of uniaxial tension tests with unnotched and differently notched flat specimens has been proposed in combination with corresponding numerical simulations [1, 2, 3, 4, 5]. On the other hand, specimens with new geometries have been presented and tested under uniaxial loading conditions to investigate their deformation, damage and fracture behavior under nearly zero stress triaxialities leading to micro-shear-crack processes on the micro-level in their critical parts [1, 2, 4, 5, 6]. In addition, butterfly specimens have been developed to study the effect of different stress states on failure behavior in ductile materials. These specimens are loaded in different directions in a special test equipment leading to combined tensile, shear and compressive stress states [3, 6]. Alternatively, experiments with biaxially loaded flat cruciform specimens have been developed [7]. Further biaxial experiments with newly developed specimens have been presented [8, 9, 10]. Corresponding numerical calculations have been performed to examine the stress states in critical specimens regions to analyze stress-state-dependent damage and fracture processes in thin ductile metal sheets. In addition, first results of experiments with biaxially loaded specimens undergoing non-proportional loading paths have been discussed [11]. They show remarkable influence of the non-proportional loading history on damage and fracture mechanisms.

From theoretical point of view anisotropic continuum damage models seem to be most qualified to predict inelastic deformations as well as stress-state-dependent damage and fracture behavior of ductile sheet metals. On the other hand, their practical use may be limited by large number of constitutive parameters and problems in their identification. Thus, in the present paper an efficient phenomenological anisotropic continuum damage

model is discussed. Results of experiments with biaxially loaded specimens under proportional and corresponding non-proportional loading conditions are shown. Evolution of strain fields are monitored by digital image correlation (DIC) technique and fracture surfaces are visualized by scanning electron microscopy (SEM). Corresponding numerical simulations of the experiments are used to reveal the stress states in critical regions of the specimens allowing explanation of the failure mechanisms shown on the fracture surfaces.

2 CONTINUUM DAMAGE MODEL

The continuum damage model presented in [12, 14] is briefly discussed. With this phenomenological approach inelastic deformations as well as anisotropic evolution of damage in ductile metals are numerically predicted. Stress-state-dependent damage and fracture processes on the micro-scale are accompanied by the formation of macroscopic damage strains. The thermodynamically consistent continuum framework takes into account damaged as well as corresponding fictitious undamaged configurations. The kinematic approach is based on the introduction of elastic, plastic and damage strain rate tensors. Elastic constitutive equations are based on free energy functions formulated in the damaged and undamaged configurations, respectively, and are able to simulate the deteriorating effect of damage on elastic material properties. In addition, considering the undamaged configurations isotropic plastic behavior is governed by a yield criterion and a non-associated flow rule. In a similar way, considering the damaged configurations anisotropic damage behavior is modeled by a damage condition and a damage rule both depending on the stress triaxiality and the Lode parameter to take into account the effect of stress state on damage and fracture behavior.

In particular, isotropic plastic behavior of the investigated aluminum alloy AlSiMgMn (EN AW 6082-T6) is governed by the yield criterion

$$f^{pl} = a\bar{I}_1 + \sqrt{\bar{J}_2} - c = 0 \tag{1}$$

where the first and second invariants, $\bar{I}_1$ and $\bar{J}_2$ of the effective Kirchhoff stress tensor [12] have been used. The plastic hardening behavior of the analyzed aluminum alloy is characterized by the power law

$$c = c_0 \left(\frac{H_0\,\gamma}{n\,c_0} + 1 \right)^n \tag{2}$$

taking into account the initial yield stress $c_0 = 163.5$ MPa, the initial hardening modulus $H_0 = 850$ MPa as well as the hardening exponent $n = 0.182$, and γ represents the equivalent plastic strain measure [12].

In addition, onset and continuation of damage is determined by a damage surface formulated in stress space [12, 13]. In this context, the damage criterion

$$f^{da} = \alpha I_1 + \beta\sqrt{J_2} - \sigma = 0 \tag{3}$$

is expressed in terms of the first and second deviatoric stress invariants I_1 and J_2 of the Kirchhoff stress tensor. In Eq. (3), the equivalent damage stress measure

$$\sigma = \sigma_0 - H_1\,\mu^2 \tag{4}$$

characterizes deterioration of material properties caused by micro-defect propagation [15] with the initial equivalent stress $\sigma_0 = 250$ MPa and the modulus $H_1 = 400$ MPa where μ denotes the equivalent damage strain measure. In Eq. (3) the variables α and β represent damage mode parameters associated with the different stress-state-dependent damage mechanisms acting on the micro-level: void-growth-dominated modes for large positive stress triaxialities, shear modes for negative stress triaxialities and mixed modes (simultaneous growth of voids and formation of micro-shear-cracks) for moderate positive and nearly zero stress triaxialities. In the present continuum damage model, the effect of the Lode parameter is also taken into account because it has been shown that its influence on the formation of the micro-structural processes can be remarkable especially in moderate positive and negative stress triaxiality regions [14]. Hence, the damage mode parameters α and β in the damage criterion (3) depend on the stress intensity $\sigma_{eq} = \sqrt{3J_2}$ (von Mises equivalent stress), the stress triaxiality

$$\eta = \frac{\sigma_m}{\sigma_{eq}} = \frac{I_1}{3\sqrt{3J_2}} \tag{5}$$

defined as the ratio of the mean stress $\sigma_m = I_1/3$ and the von Mises equivalent stress σ_{eq} as well as on the Lode parameter

$$\omega = \frac{2T_2 - T_1 - T_3}{T_1 - T_3} \quad \text{with } T_1 \geq T_2 \geq T_3 \tag{6}$$

expressed in terms of the principal Kirchhoff stress components T_1, T_2 and T_3.

The dependence of α and β on stress state has been studied in detail for aluminum alloys. Numerical analyses on the micro-scale have been performed [14] considering the deformation and failure behavior of void-containing unit cells. Use of simplified functions has been discussed in [9] for practical applications still allowing accurate phenomenological modeling of inelastic deformations as well as of damage and failure behavior in comparison with experiments with biaxially loaded specimens. With these functions the parameters α and β are related to different stress-state-dependent damage and fracture mechanisms acting on the micro-level.

Based on these investigations [9, 14], the parameter α is given by

$$\alpha(\eta) = \begin{cases} 0.0 \;\text{ for }\; \eta \leq 0 \\ 0.33 \;\text{ for }\; \eta > 0 \end{cases} \tag{7}$$

whereas the parameter β is taken to be the non-negative function

$$\beta(\eta, \omega) = -1.28\,\eta + 0.85 - 0.017\,\omega^3 - 0.065\,\omega^2 - 0.078\,\omega \;\geq\; 0\;. \tag{8}$$

Furthermore, the damage strain rate tensor is given by the damage rule

$$\dot{\mathbf{H}}^{da} = \dot{\mu}\left(\bar{\alpha}\,\frac{1}{\sqrt{3}}\,\mathbf{1} + \bar{\beta}\,\mathbf{N}\right) \tag{9}$$

where $\dot{\mu}$ denotes a non-negative scalar-valued factor. In Eq. (9) the stress related deviatoric tensor $\mathbf{N} = \frac{1}{2\sqrt{J_2}}\,\mathrm{dev}\tilde{\mathbf{T}}$ has been used and $\dot{\mu}$ is in the present continuum damage model the equivalent damage strain rate measure quantifying the amount of increase in irreversible damage. The parameters $\bar{\alpha}$ and $\bar{\beta}$ are kinematic variables representing the portion of volumetric and isochoric damage-induced deformations. These parameters also correspond to different damage and fracture mechanisms on the micro-level and, similar to the parameters in the damage criterion (3), they have been identified by numerical analyses with micro-defect-containing representative volume elements undergoing different three-dimensional loading scenarios [14] as well as on comparison of experimental data and results of numerical simulations of experiments with uniaxially and biaxially loaded specimens [9].

In particular, the stress-state-dependence of the parameter $\bar{\alpha}$ related to the amount of volumetric damage strain rates caused by volume changes of micro-defects is written in the form

$$\bar{\alpha}(\eta) = \begin{cases} 0 \;\text{ for }\; \eta \leq 0 \\ 0.5714\,\eta \;\text{ for }\; 0 < \eta \leq 1.75 \\ 1 \;\text{ for }\; \eta > 1.75 \end{cases} . \tag{10}$$

In additon, the stress-state-dependence of the parameter $\bar{\beta}$ modeling the amount of anisotropic isochoric damage strain rates caused by formation of micro-shear-cracks is given by

$$\bar{\beta}(\eta,\, \omega) = \bar{\beta}_0(\eta) + (-0.0252 + 0.0378\,\eta)\; \bar{\beta}_\omega(\omega) \tag{11}$$

with

$$\bar{\beta}_0(\eta) = \begin{cases} 0.87 \;\text{ for }\; \eta \leq \frac{1}{3} \\ 0.979 - 0.326\,\eta \;\text{ for }\; \frac{1}{3} < \eta \leq 3 \\ 0 \;\text{ for }\; \eta > 3 \end{cases} \tag{12}$$

and

$$\bar{\beta}_\omega(\omega) = \begin{cases} 1 - \omega^2 \;\text{ for }\; \eta \leq \frac{2}{3} \\ 0 \;\text{ for }\; \eta > \frac{2}{3} \end{cases} . \tag{13}$$

It can be clearly seen that the macroscopic damage rule (9) takes into account a volumetric part (first term in Eq. (9)) corresponding to isotropic growth of voids on the micro-level as well as a deviatoric part (second term in Eq. (9)) associated with the anisotropic development of micro-shear-cracks, respectively. Therefore, the basic damage mechanisms discussed above (growth of isotropic voids and evolution of micro-shear-cracks) acting on the micro-scale are involved in the macroscopic damage rule (9) of the phenomenological continuum model.

3 EXPERIMENTS AND NUMERICAL SIMULATIONS

An experimental program has been developed to analyze stress-state-dependent behavior in biaxially loaded specimens [10]. The experiments are performed using the biaxial test machine type LFM-BIAX 20 kN. The specimens are biaxially loaded by four electromechanically and individually driven cylinders and are clamped in the four heads of the

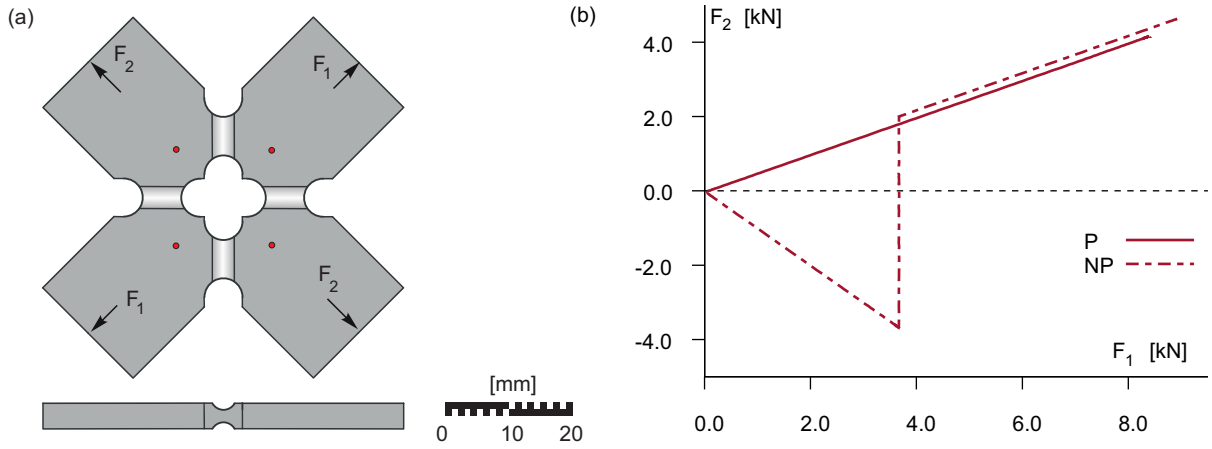


Figure 1: Loading paths

cylinders. Further tests with the X0-specimen to investigate inelastic deformations as well as damage and fracture processes on the micro-level for different proportional and non-proportional loading histories have been performed [11]. The specimens are manufactured from ductile metal sheets with 4 mm thickness and the central part of the geometry of the X0-specimen as well as the acting forces are shown in Fig. 1(a). There are four notched regions with minimum thickness of 2 mm where localization of inelastic strains and damage are expected to occur. In addition to former tests [11] in the present paper the behavior of the X0-specimen for the load ratio $F_1/F_2 = 1/0.5$ is discussed where experimental data are compared with results from corresponding numerical simulations. Proportional (P) and non-proportional (NP) loading paths are taken into account (see Fig. 1(b)) and the influence of the loading history on damage and fracture processes is studied in detail. In the non-proportional case first loading is by the load ratio $F_1/F_2 = 1/-1$ and at the stage $F_1 = -F_2 = 3.8$ kN additional tensile loading by F_2 occurs. When this loading path reaches that one of the proportional case a final proportional part follows until final fracture of the specimen occurs. In these tests with the load ratio $F_1/F_2 = 1/0.5$ the final loads for the non-proportional loading history are about 10% larger than the final loads of the proportional case. Thus, the loading path has an influence on the fracture force.

Corresponding numerical analysis of the specimen's behavior during the biaxial tests are performed to get data of the stress fields acting in the specimens allowing prediction of damage and failure modes. The simulations are carried out using the finite element program ANSYS enhanced by a user-defined material subroutine based on the presented continuum damage model. The X0-specimen is discretized by eight-node-elements of type Solid185.

Figure 2 shows load-displacement curves of experiments and numerical simulations for loads and displacements in axis 1 (a1) and axis 2 (a2) where Δu_{ref} represents the displacements in axis 1 and axis 2, respectively, between the two opposite red points shown in Fig. 1(a). Under the proportional loading case (Fig. 2(a)) the load F_1 in axis 1 (a1) increases and at $F_1 = 6.2$ kN onset of plastic yielding can be seen. Further increase

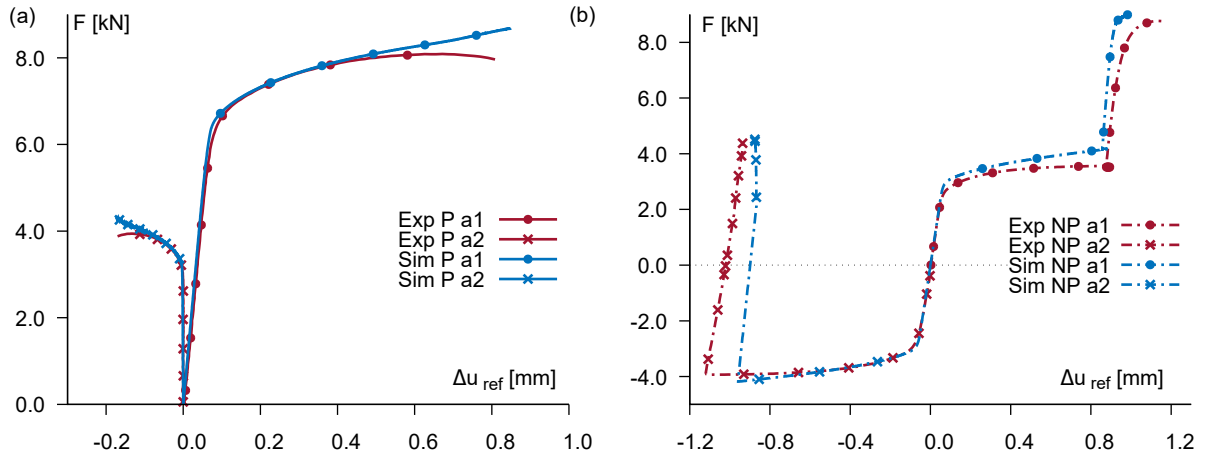


Figure 2: Load-displacement-curves: (a) P, (b) NP

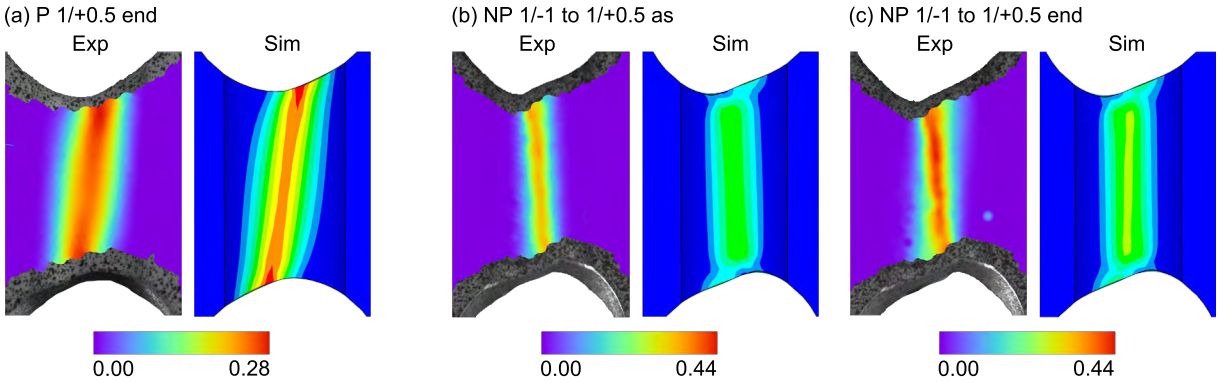


Figure 3: Strain fields (first principal strain) in the notched region

in load is measured and the specimen fails at $\Delta u_{ref1} = 0.8$ mm. In axis 2 (a2) at the load level $F_2 = 3.1$ kN plastic yielding begins and the specimen fails at $\Delta u_{ref2} = -0.2$ mm. The load-displacement curves of the experiments (Exp) and of the numerical simulation (Sim) agree well, only at the end of the test small differences can be seen. In addition, during the non-proportional loading path (Fig. 2(b)) the load in axis 1 (a1) increases up to $F_1 = 2.4$ kN where onset of plastic yielding can be observed. During further increase in load displacements increase up to $\Delta u_{ref1} = 0.9$ mm. Then, load F_2 increases whereas F_1 remains constant and during the final proportional loading step the load F_1 also increases up to final fracture. At this point, the displacement reaches $\Delta u_{ref1} = 1.1$ mm which is remarkably larger compared to the displacement after the proportional loading history. In axis 2 (a2) in the first loading step the displacement reaches $\Delta u_{ref2} = -1.1$ mm and at failure $\Delta u_{ref2} = -0.9$ mm is measured which again is remarkably larger than the final displacement in axis 2 after the proportional loading path. Also in the non-proportional case, the numerical results agree well with the experimental ones.

During the tests with the X0-specimens strain fields are monitored by digital image correlation (DIC) technique. Distributions of the first principal strain in one notched part

of the specimen taken from the experiments (Exp) and based on the numerical simulations (Sim) are shown in Fig. 3. In the tests with proportional loading paths (a) a widespread band of strains with maxima of about 28% and slight right-to-left-orientation can be seen and results of the experiments agree very well with those predicted by the corresponding numerical simulation concerning maxima and orientation of the localized strain field as well as the final shape of the notched region of the X0-specimen. During the tests with the non-proportional loading path after the first load step before axis switch (as) of the loads (Fig. 3(b)) a very small localized band of the first principal strain with maxima of about 35% occurs. Size and orientation of the small band of strains as well as the shape of the notched part of the specimen are well predicted by the numerical simulation whereas the maxima of the first principal strain are only about 23%. In addition, Fig. 3(c) shows the distribution of the first principal strain at the end of the non-proportional test (end). A small localized band of strains with maxima of 44% can be seen with slight left-to-right-orientation. A similar band of localized strains is predicted by the numerical simulation but the maxima are only 26%. The final shape of the notched part of the specimen at the end of the non-proportional test is well predicted. Analysis of the first principal strain fields caused by the proportional and the considered non-proportional loading paths show differences concerning the width and the size as well as the orientation of the localized bands as well as the final shape of the notched region.

Furthermore, distribution of the stress triaxiality η (Eq. (5)) and of the Lode parameter ω (Eq. (6)) predicted by the numerical simulations of the experiments are shown in Fig. 4. In particular, at the end of the proportional loading path (Fig. 4(a)) the distribution of the stress triaxiality in the cross section (C) is nearly homogeneous with maxima $\eta = 0.6$ in the central part. In the longitudinal section (L) of the notched part of the X0-specimen a widespread band of moderate triaxialities $\eta \geq 0.4$ with larger values in butterfly-shaped distribution in the central part with maxima $\eta = 0.6$ occurs. On the surface of the notch (S) the stress triaxialities are smaller with nearly homogeneous distribution. In addition, the Lode parameter shows in the notched region nearly homogeneous distribution with values up to $\omega = -1.0$ which is typical for tension-dominated stress states. On the other hand, after the first step of the non-proportional loading path NP(1) before axis switch (as) of the loads (Fig. 4(b)) the stress triaxiality η in the cross section (C) of the center of the notch is homogeneously distributed with $\eta = 0.0$ and a large region with this value can also be seen in the longitudinal section (L) and the surface of the notch (S). In addition, at this loading stage the corresponding Lode parameter ω is also homogeneously distributed in the cross section (C) with $\omega = 0.0$ and large regions of this value are also visible in the longitudinal section (L) and on the boundary (V), whereas in the center of the boundary slightly higher Lode parameters up to $\omega = 0.3$ can be seen. These stress fields are typical for shear-dominated stress states. Different stress parameters are numerically predicted at the end of the non-proportional loading scenario (NP(12)) shown in Fig. 4(c). Homogeneous field of the stress triaxiality with $\eta = 0.3$ is obtained in the notch and the corresponding Lode parameter is about $\omega = -1.0$. The numerically predicted distributions of the stress triaxiality and of the Lode parameter at the end of the proportional and the non-proportional loading paths are very similar and,

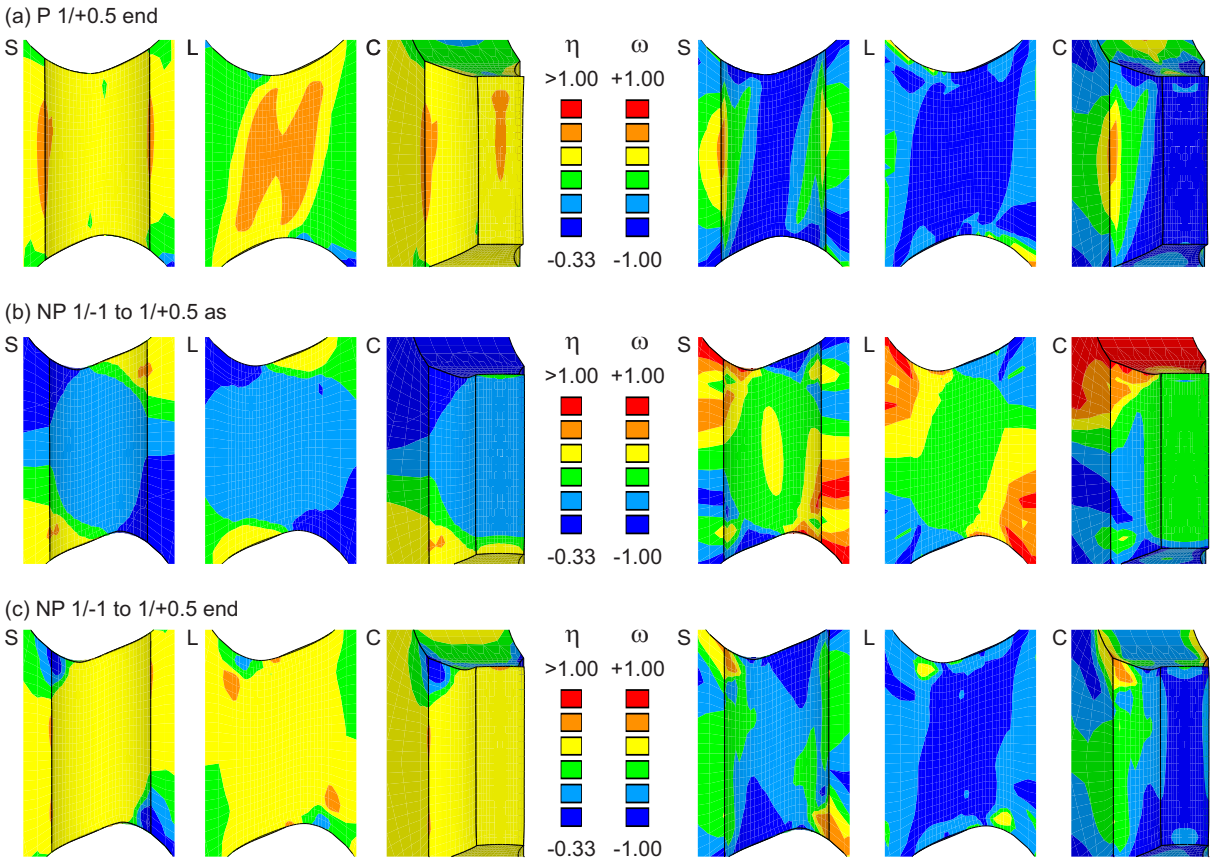


Figure 4: Stress triaxiality η and Lode parameter ω: (a) P, (b) NP (1), (c) NP (12); S = surface, L = longitudinal section, C = cross section

thus, nearly unaffected by the loading history.

Moreover, fracture lines are shown in Fig. 5. After the proportional loading scenario (Fig. 5(a)) nearly straight fracture lines occur with small angle with respect to the vertical line. After non-proportional loading (Fig. 5(b)) S-shaped fracture lines can be seen with vertical orientation. Thus, different fracture lines occur after the two investigated, different loading histories.

In addition, fracture behavior is analyzed in more detail by images of the fracture surfaces taken from scanning electron microscopy (Fig. 6). After the proportional loading path (Fig. 6(a)) remarkable formation of micro-voids can be seen which are slightly sheared. This failure behavior on the micro-level corresponds very well to the stress states shown in Fig. 4(a) with remarkable tensile stresses superimposed by small shear stresses in the notched regions. On the other hand, after the non-proportional loading history micro-shear-cracks with only very small voids are visible. During the first loading step with the load ratio $F_1/F_2 = 1/-1$ (NP(1)) shear behavior is predominant in the notched sections of the X0-specimen leading to formation of micro-shear-cracks. The subsequent increase in load F_2 and the later proportional loading step (NP(12)) lead to additional growth of few very small voids. Thus, different fracture modes are caused by

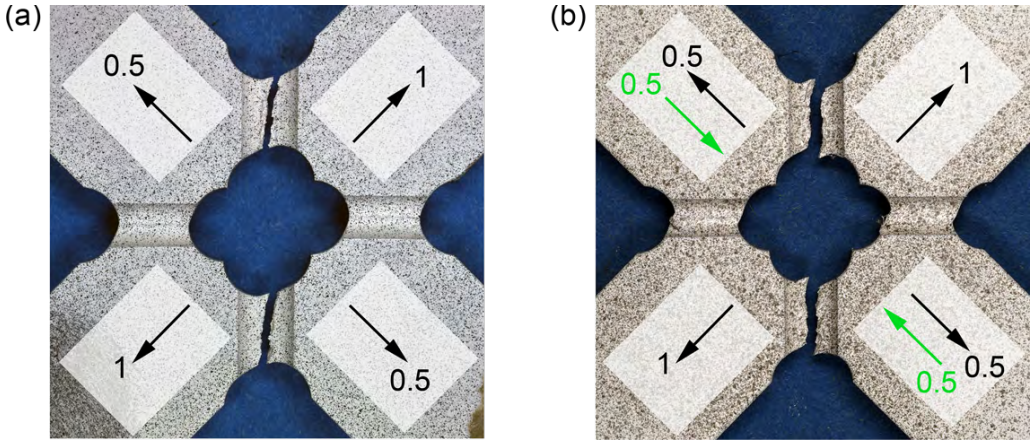


Figure 5: Fracture: (a) P, (b) NP

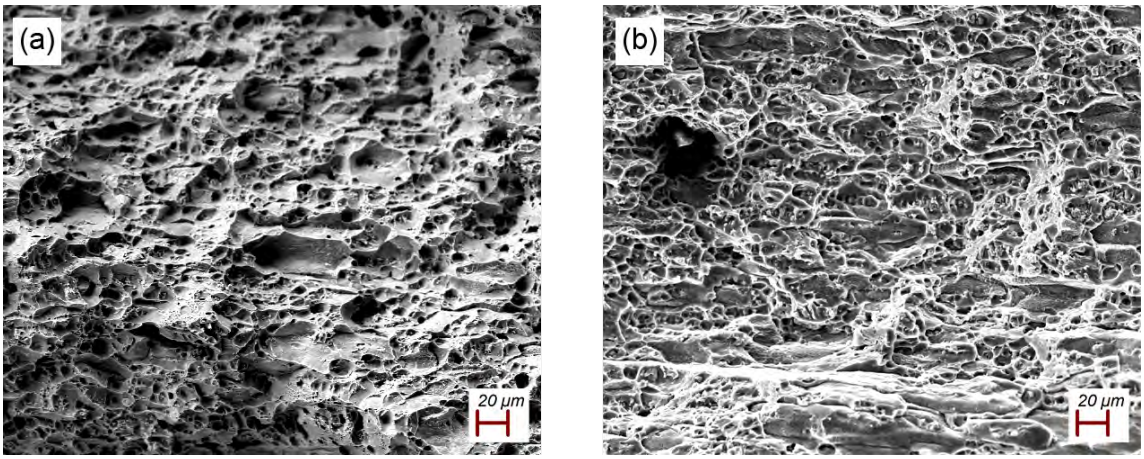


Figure 6: SEM picture of the fracture surface: (a) P, (b) NP

different loading scenarios.

4 CONCLUSIONS

A continuum damage model taking into account stress-state-dependent damage condition and damage rule has been discussed. The phenomenological approach has been validated by biaxial experiments with the X0-specimen with special focus on the effect of proportional and non-proportional loading histories as well as of different stress states on inelastic deformation as well as on damage and fracture behavior of ductile metals. Current strain fields in critical parts of the specimen have been monitored during the experiments by digital image correlation. After the tests fracture surfaces have been analyzed by scanning electron microscopy and showed remarkable differences depending on the loading histories. In addition, numerical simulations of the experiments have been performed. Numerically predicted load-displacement curves and distributions of principal strain fields as well as shapes of the deformed notched parts of the X0-specimen show

good agreement with experimental ones. Examination of numerically obtained stress fields are used to predict evolution of damage and fracture processes on the micro-scale which can be justified by scanning electron microscopy of the fracture surfaces. Therefore, the continuum damage model can be used to analyze and to optimize sheet metal forming processes with complex loading scenarios. Biaxial experiments with the X0-specimen are recommended to investigate stress-state-dependent damage and fracture processes in thin metal sheets.

Acknowledgement
The project has been funded by the Deutsche Forschungsgemeinschaft (DFG, German Research Foundation) – project number 322157331, this financial support is gratefully acknowledged. The SEM images of the fracture surfaces presented in this paper were performed at the Institut für Werkstoffe im Bauwesen, Bundeswehr University Munich and the support of Wolfgang Saur is gratefully acknowledged.

REFERENCES

[1] Bai, Y. and Wierzbicki, T. On the fracture locus in the equivalent strain and stress triaxiality space. *Int. J. Mech. Sci.* (2004) **46**:81-98.

[2] Gao, X., Zhang, G. and Roe, C. A study on the effect of the stress state on ductile fracture. *Int. J. Damage Mech.* (2010) **19**:75-94.

[3] Dunand, M. and Mohr, D. On the predictive capabilities of the shear modified Gurson and the modified Mohr-Coulomb fracture models over a wide range of stress triaxialities and Lode angles. *J.Mech. Phys. Sol.* (2011) **59**:1374-1394

[4] Brünig, M., Chyra, O., Albrecht, D., Driemeier, L. and Alves, M. A ductile damage criterion at various stress triaxilities. *Int. J. Plast.* (2008) **24**:1731-1755.

[5] Driemeier, L., Brünig, M., Micheli, G. and Alves, M. Experiments on stress-triaxiality dependence of material behavior of aluminum alloys. *Mech. Mat.* (2010) **42**:207-217.

[6] Bai, Y. and Wierzbicki, T. A new model of metal plasticity and fracture with pressure and Lode dependence. *Int. J. Plast.* (2008) **24**:1071-1096.

[7] Kuwabara, T. Advances in experiments on metal sheets and tubes in support of constitutive modeling and forming simulations. *Int. J. Plast.* (2007) **23**:385-419.

[8] Brünig, M., Brenner, D. and Gerke, S. Stress state dependence of ductile damage and fracture behavior: Experiments and numerical simulations. *Eng. Fract. Mech.* (2015) **141**:152-169.

[9] Brünig, M., Gerke, S. and Schmidt, M. Biaxial experiments and phenomenological modeling of stress-state-dependent ductile damage and fracture. *Int. J. Fract.* (2016) **200**:63-76.

[10] Gerke, S., Adulyasak, P. and Brünig, M. New biaxially loaded specimens for the analysis of damage and fracture in sheet metals. *Int. J. Solids Struct.* (2017) **110**:209-218.

[11] Gerke, S., Zistl, M., Bhardwaj, A. and Brünig, M. Experiments with the X0-specimen on the effect of non-proportional loading paths on damage and fracture mechanisms in aluminum alloys. *Int. J. Solids Struct.* (2019) **163**:157-169.

[12] Brünig, M. An anisotropic ductile damage model based on irreversible thermodynamics. *Int. J. Plast.* (2003) **19**:1679-1713.

[13] Chow, C. and Wang, J. An anisotropic theory of continuum damage mechanics for ductile fracture. *Eng. Fract. Mech.* (1987) **27**:547-558.

[14] Brünig, M., Gerke, S. and Hagenbrock, V. Micro-mechanical studies on the effect of the stress triaxiality and the Lode parameter on ductile damage. *Int. J. Plast.* (2013) **50**:49-65.

[15] Brünig, M., Gerke, S. Simulation of damage evolution in ductile metals undergoing dynamic loading conditions. *Int. J. Plast.* (2011) **27**:1598-1617.

XV International Conference on Computational Plasticity. Fundamentals and Applications
COMPLAS 2019
E. Oñate, D.R.J. Owen, D. Peric, M. Chiumenti & Eduardo de Souza Neto (Eds)

FURTHER STUDIES ON IDENTIFICATION OF INELASTIC PARAMETERS FOR DAMAGED MATERIALS

M. VAZ JR. AND M. TOMIYAMA

Department of Mechanical Engineering
State University of Santa Catarina (UDESC)
Campus Universitário Prof. Avelino Marcante, 89219-710 Joinville, Brazil
e-mail: miguel.vaz@udesc.br

Key words: Parameter Identification, Lemaitre damage

Abstract. A proper set of material parameters is one of the most important aspects for a successful simulation of metal forming processes. Several issues must be observed when choosing the constitutive relation and corresponding material parameters, amongst which the most important are: (i) the magnitude of the plastic deformation of the target forming operation must be contemplated by the parameters of the constitutive model, (ii) possibility of failure prediction in fracture-free materials, and (iii) accurate prediction of geometrical changes caused by plastic deformation. Within this framework, the present article discusses techniques to obtain constitutive parameters of a Lemaitre-type material model. The strategy requires compliance of multiple tensile tests with specimens prepared according to different technical standards. Parameter identification is regarded as an inverse problem and solved using optimization methods.

1 INTRODUCTION

Since the pioneering works of Tresca, Huber, von Mises and Hencky [1] on modelling inelastic deformation, many researchers have dedicated much effort to design constitutive formulations able to describe several types of materials, such as polymers, metals and composites amongst many others. Notwithstanding, the determination of the corresponding material parameters have constituted a real challenge. Therefore, for many years, identification of material parameters was based only on mechanical tests assuming uniform stress states. Furthermore, complex constitutive models involving large inelastic deformations, non-uniform stress states and material degradation have posed new demands. In recent years, optimization techniques have been proposed to identification problems aiming at circumventing such difficulties. The present work is inserted within this framework in which an optimization method is used to parameter identification of a Lemaitre-type material model based on tensile tests of specimens of different geometry.

2 MATERIAL MODELLING

The literature shows a growing number of material models able to account for mechanical degradation. In general, such models, known as damaged materials, include new internal variables and evolution laws which are fully coupled to the underlying plasticity problem. The great advantage of damaged materials is the possibility to predict failure onset in actual metal forming operations without pre-defined cracks. Availability of damage models in commercial codes has instigated further investigations on robust and efficient parameter identification strategies. The present work addresses a Lemaitre-type material model, as briefly described in the next session.

2.1 Lemaitre-type damage model

A significant number of damage formulations is based upon thermodynamics of irreversible processes and void growth concepts. Kachanov's [2] and Rabotnov's [3] early works, and Lemaitre's [4] equivalence principle laid foundations for further developments, giving rise to material descriptions oftentimes referred as Continuum Damage Mechanics (CDM). The present work uses an extension of Lemaitre's damage model that accounts for void closure and void opening effects. The reader is referred to [5, 6, 7] for further discussions on the damage formulation.

The present constitutive model requires identification of hardening, $\boldsymbol{p}^h$, and damage, $\boldsymbol{p}^l$, parameters. Swift's [8] hardening equation, $\sigma_Y = k(\bar{\varepsilon}_p + \varepsilon_0)^n$ is adopted in this work, where $\bar{\varepsilon}_p$ is the equivalent plastic strain and $\boldsymbol{p}^h = \{k\ ,\ \varepsilon_0\ ,\ n\}$ is the set of hardening parameters. The damage parameters of the model are $\boldsymbol{p}^l = \left\{S\ ,\ h^+\ ,\ h^-\ ,\ \varepsilon_p^D\right\}$. Therefore, the set of design variables for the present formulation can be generally expressed as $\boldsymbol{p} = \boldsymbol{p}^h \cup \boldsymbol{p}^l$.

3 OPTIMIZATION-BASED PARAMETER IDENTIFICATION

Parameter identification is a class of inverse problems which determines material properties from a known response. The present problem is formulated using unconstrained optimization and accounts for experimental data obtained from tensile tests performed with specimens of different geometry. Therefore, the first step of the optimization problem is formulated as

$$\begin{array}{lll} \text{Minimise} & g(\boldsymbol{p}) = \displaystyle\sum_{s=1}^{n_s} \lambda_s g_s(\boldsymbol{p}) & \boldsymbol{p} \in R^{n_d} \\ \text{Such that} & p_i^{\inf} \leq p_i \leq p_i^{\sup} & i = 1, \ldots, n_d \end{array} \quad , \tag{1}$$

where $g(\boldsymbol{p})$ is the global objective function (global fitness), $\boldsymbol{p} = [p_1 \ \ p_2 \ \cdots \ p_i \ \cdots \ p_{n_d}]^T$ is the design vector containing n_d material parameters p_i, and $p_i^{\sup}$ and $p_i^{\inf}$ are lateral constraints. The global fitness, $g(\boldsymbol{p})$, comprises contributions from n_s individual mechanical tests, so that λ_s is the weight function ($\sum_{s=1}^{n_s} \lambda_s = 1$), and $g_s(\boldsymbol{p})$ is the individual fitness and represents a quadratic relative error measure between the experimental, R_s^{Exp}, and

corresponding computed forming load, $R\left(\boldsymbol{p}\right)_s^{Num}$, of a mechanical test "$s$",

$$g_s\left(\boldsymbol{p}\right) = \sqrt{\frac{1}{N_s}\sum_{j=1}^{N_s}\left(\frac{R_{s,j}^{Exp} - R\left(\boldsymbol{p}\right)_{s,j}^{Num}}{R_{s,j}^{Exp}}\right)^2}, \tag{2}$$

in which N_s is the number of experimental points of a mechanical test "s". Particle Swarm Optimization [9, 10] is adopted to solve the optimization problem established in Eqs. (1) and (2) owing to the nature of damage models. Its suitability to this class of problems was extensively discussed in Reference [11].

It is important to note that solution of the optimization problem described in Eqs. (1) and (2) is associated with a given set of weights, λ_s. Inclusion of λ_s as design variable would lead to a set of parameters which provide a minimum for one of the tests only. Therefore, the best set of weights must be determined by an additional optimization problem.

This work proposes a new strategy by comparing the best individual fitness of each test, $g_s^{\min}$, with their counterpart, g_s, calculated evaluated by solution of Eqs. (1) and (2). Therefore, the new optimization problem is solved with weight functions λ_s as design variables, so that

$$\begin{array}{lccl} \text{Minimise} & G(\boldsymbol{\lambda}) & & \boldsymbol{\lambda} \in R^{n_s} \\ \text{Such that} & 0 \leq \lambda_s \leq 1 & & s = 1, \ldots, n_s \\ & \displaystyle\sum_{s=1}^{n_s} \lambda_s = 1 & & \end{array}, \tag{3}$$

in which $G(\boldsymbol{\lambda})$ is the mean global error,

$$G(\boldsymbol{\lambda}) = \sqrt{\frac{1}{n_s}\sum_{s=1}^{n_s}\left[\frac{g_s^{\min} - g_s(\boldsymbol{p})}{g_s^{\min}}\right]^2}, \tag{4}$$

which expresses a quadratic relative error between the best approximation, $g_s^{\min}$, for each mechanical test and individual fitness, $g_s(\boldsymbol{p})$, obtained by solving the optimization problem established in Eq. (1). It is important to mention that there is a unique relation between the individual fitness and weight for each mechanical test, $g_s(\boldsymbol{p}) \Leftrightarrow \lambda_s$.

Numerical experiments show that the proposed optimization scheme represented by Eqs. (3) and (4) is convex, making possible to use the Nelder-Mead optimization algorithm [12]. The optimization scheme establishes a polytope of $n_s + 1$ vertices, upon which expansion/contraction/shrinkage operations are applied. As the optimization process advances, the polytope moves towards the minimum and decreases in size. Therefore, the mean relative distance between the centrepoint and all vertices of the polytope is used as convergence measure,

$$\phi_d^{(k)} = \frac{d(\boldsymbol{\lambda}^{(k)})}{d(\boldsymbol{\lambda}^{(0)})}, \quad \text{where} \quad d(\boldsymbol{\lambda}^{(k)}) = \frac{1}{n_s+1}\sum_{j=1}^{n_s+1}\sqrt{\sum_{s=1}^{n_s}\left(\lambda_{j,s}^{(k)} - \bar{\lambda}_s^{(k)}\right)^2}, \tag{5}$$

in which (k) indicates the iterative step, $\bar{\lambda}_s^{(k)} = 1/(n_s+1)\sum_{i=1}^{n_s+1}\lambda_{s,i}^{(k)}$ is the coordinate of the centrepoint in the direction $s = 1, \cdots, n_s$, and $n_s + 1$ is the number of vertices of the polytope. In this work, convergence is assumed when the initial polytope reduces more than 1,000 times its initial size, i.e. $TOL_d \leqslant 10^{-3}$.

4 NUMERICAL EXAMPLES AND DISCUSSIONS

The identification procedure was performed using tensile tests of cylindrical specimens prepared according to the American ASTM E 8M [13] and Brazilian ABNT NBR ISO 6892 [14] technical standards. Extensometers with initial gauge length $l_0 = 25$ mm or $l_0 = 50$ mm were used according to the specimen with maximum crosshead speed 3 mm/min. The specimens adopted in this work are referred as follows:

- *ASTM #1:* initial gauge length $l_0 = 25$ mm and diameter $d_0 = 6.0$ mm,
- *ASTM #2:* initial gauge length $l_0 = 50$ mm and diameter $d_0 = 12.54$ mm,
- *NBR #3:* initial gauge length $l_0 = 50$ mm and diameter $d_0 = 10.0$ mm,

in which d_0 is the initial diameter.

The geometrical model considers axisymmetry around the rotation axis $Z - Z'$ and symmetry about the $R - R'$ axis, making possible to model only 1/4 of the specimen. It was adopted a structured, eight-noded quadrilateral finite element mesh with 200 elements and 661 nodes with progressive refinement towards the specimen $R-R'$ axis. The meshes used for *ASTM #1* e *NBR #3* specimens were geometrically proportional to *ASTM #2* with identical element topology.

Figure 1(a) shows the evolution of the convergence index, ϕ_d, whereas Figure 1(b) presents the corresponding evolution of the weights, λ_s, of the best vertex of the NM polytope. It was assumed $\lambda_s^{(0)} = 1/3$ as initial values. After some variations in the beginning of the iterative process, the optimization scheme quickly leads the weights to the final values. Little change was observed after fourteen iterations and a convergence criterion $TOL_d \leqslant 10^{-2}$ could have been safely adopted (the maximum difference is 0.48 % for λ_1).

The final material parameters, $\boldsymbol{p}$, weights, $\boldsymbol{\lambda}$, and mean global fitness, $G(\boldsymbol{\lambda})$ are presented in Table 1, whereas Figure 2 illustrates the corresponding load evolution. It is noteworthy that the loading curves represent the best approximation to each individual tensile test with parameters determined simultaneously. The results show that geometry still plays a role in determining of inelastic parameters of phenomenological descriptions of plasticity phenomena. However, from industrial viewpoint, the results constitute a good approximation of complex phenomena as material degradation.

5 FINAL REMARKS

Tensile tests have largely been used to determine inelastic parameters. The classical procedure accounts for plastic deformation up to necking onset in order to ensure uniform stress states. However, such condition is achieved for relatively small plastic strains. On the other hand, metal forming operations oftentimes involve large plastic strains.

(a) Convergence index. (b) Weights, λ_s.

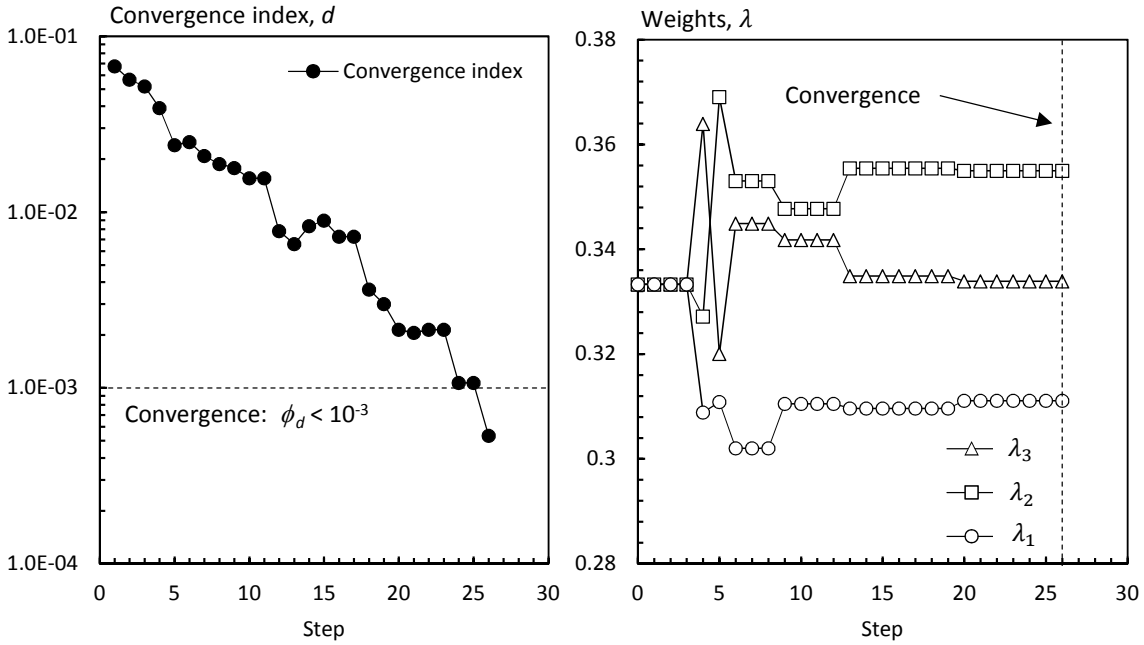


Figure 1: Evolution of the convergence index and weights.

Table 1: Final material parameters, $\boldsymbol{p}$, weights, $\boldsymbol{\lambda}$, and mean global fitness, $G(\boldsymbol{\lambda})$.

	Symbol	**Value**
Hardening	k	1454.42 MPa
Parameters	ε_0	0.0461830
$\boldsymbol{p}^h$	n	0.414118
Damage	S	889.223 MPa
Parameters	h^-	0.00140679
$\boldsymbol{p}^l$	h^+	1.58511
	ε_p^D	0.402607
Weights	$\lambda_1^{\min}$ (ASTM #1)	0.31112
$\boldsymbol{\lambda}$	$\lambda_2^{\min}$ (ASTM #2)	0.35497
	$\lambda_3^{\min}$ (NBR #3)	0.33390
Global error	$G(\boldsymbol{\lambda}^{\min})$	5.15307

Aiming at such applications, this work uses inverse problem techniques to obtain material parameters up to macroscopic failure. A Lemaitre-type damage model was utilised to assess material degradation e failure.

In general, tensile tests of specimens of a single geometry is adopted. However, aiming at better prediction of the inelastic parameters, this work requires simultaneous compliance of tree tensile tests performed with specimens prepared according to two different technical standards. The inverse problem technique used multi-objective optimization

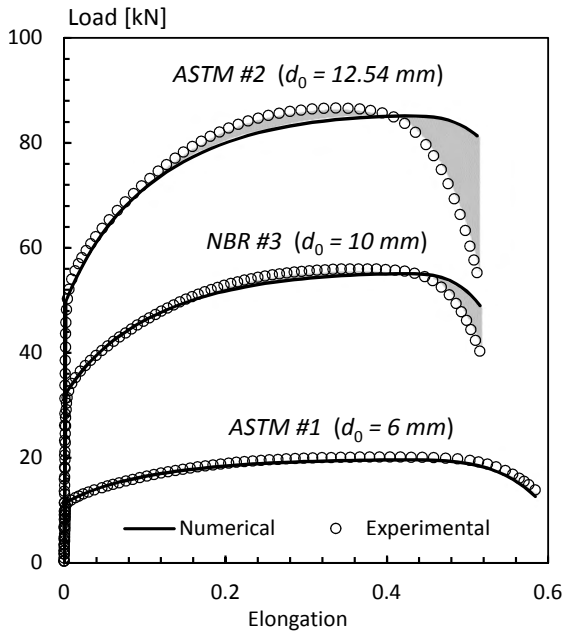


Figure 2: Load evolution for specimens ASTM #1, ASTM #2 and NBR #3.

with the requirement of obtaining the best possible objective function for each individual specimen. Bearing in mind the phenomenological character of the constitutive model, the results indicate a good approximation for all tests. The large discrepancies were found for tensile tests involving the larger tensile loads since the individual objective function has been defined as a relative measure.

Acknowledgements

The author acknowledges the financial support provided by the Brazilian funding agency CNPq - (National Council for Scientific and Technological Development), grant number 303412/2016-0.

REFERENCES

[1] Vaz Jr., M., de Souza Neto, E.A. and Muñoz-Rojas P.A. Materials modelling - challenges and perspectives. In: M. Vaz Jr.; E.A. de Souza Neto; P.A. Muoz-Rojas. (Eds.), *Advanced Computational Materials Modeling: From Classical to Multi-Scale Techniques*. Wiley-VCH, 1–22 (2011).

[2] Kachanov, K.M. Time of the rupture process under creep conditions. *Isv. Akad. Nauk. SSR.* (1958) **8**:21–31.

[3] Rabotnov, Y.N. *Creep Problems in Structural Members*. North-Holland, (1969).

[4] Lemaitre, J. A continuous damage mechanics model for ductile fracture. *J. Eng. Mater. Technol., Trans. ASME* (1985) **107**:83–89.

[5] de Souza Neto, E.A., Peric, D., Owen, D.R.J. *Computational Methods for Plasticity. Theory and Applications*. Wiley, (2008).

[6] Vaz Jr., M., de Santi Jr., N., de Souza Neto, E.A. Numerical prediction of ductile failure onset under tensile and compressive stress states. *Int. J. Damage Mech.* (2010) **19**:175–195.

[7] Vaz Jr., M., Munoz-Rojas, P.A., and Lange, M.R. Damage evolution and thermal coupled effects in inelastic solids. *Int. J. Mech. Sci.* (2011) **53**:387–398.

[8] Swift, H.W. Plastic instability under plane stress. *J. Mech. Physics Solids* (1952) **1**:1–18,

[9] Eberhart, R., Kennedy, J. A new optimizer using particle swarm theory. In: *Proceedings of the 6th International Symposium on Micro Machine and Human Science*. IEEE Press, 39–43 (1995).

[10] Kennedy, J., Eberhart, R. Particle Swarm Optimization. In: *Proceedings of the IEEE International Conference on Neural Networks*. IEEE Press, 1942–1948 (1995).

[11] Vaz Jr., M. Particle swarm optimization and identification of inelastic material parameters. *Eng. Comput.* (2013) **30**:936–960.

[12] Nelder, J.A., Mead, R. A simplex method for function minimization, amage evolution and thermal coupled effects in inelastic solids. *The Comput. Journal* (1965) **7**:308–313.

[13] ASTM - E 8M-86a. Tensile testing of metallic materials. ASTM, (2002).

[14] ABNT NBR ISO 6892. Metallic materials - Tensile testing at ambient temperature (in Portuguese). ABNT, (2002).

XV International Conference on Computational Plasticity. Fundamentals and Applications
COMPLAS 2019
E. Oñate, D.R.J. Owen, D. Peric, M. Chiumenti & Eduardo de Souza Neto (Eds)

A QUASI-STATIC NONLINEAR ANALYSIS FOR ASSESSING THE FIRE RESISTANCE OF 3D FRAMES EXPLOITING TIME-DEPENDENT YIELD SURFACE

D. MAGISANO*, F. LIGUORI*, L. LEONETTI*, D. DE GREGORIO†, G. ZUCCARO† and G. GARCEA*

* Dipartimento di Modellistica per l'Ingegneria
Università della Calabria, 87030 Rende (Cosenza), Italy

† Dipartimento di Strutture per l'Ingegneria e l'Architettura
Università di Napoli Federico II, 801234 Napoli, Italy

Key words: 3D frames, reinforced concrete, yield surface, incremental analysis, fire, fire resistance.

Abstract. In this work an automatic procedure for evaluating the axial force-biaxial bending yield surface of reinforced concrete sections in fire is proposed. It provides an accurate time-dependent expression of the yield condition by a section analysis carried out once and for all, accounting for the strength reduction of the materials, which is a function of the fire duration. The equilibrium state of 3D frames with such yield conditions, once discretized using beam finite elements, is formulated as a nonlinear vectorial equation defining a curve in the hyperspace of the discrete variables and the fire duration. A generalized path-following strategy is proposed for tracing this curve and evaluating, if it exists, the limit fire duration, that is the time of exposure which leads to structural collapse. Compared to the previous proposals on the topic, which are limited to local sectional checks, this work is the first to present a global analysis for assessing the fire resistance of 3D frames, providing a time history of the fire event and taking account of the stress redistribution. Numerical examples are given to illustrate and validate the proposal.

1 Introduction

The evaluation of the carrying capacity of a structure implies not only situations of normal service conditions but also exceptional loadings. An important aspect is to ensure the overall structural integrity during fire events [2]. Usually, frame structures exhibit a relevant overstrength, that is their ultimate capacity can be significantly higher than the elastic limit. For this reason, the material nonlinear analysis is a necessary tool for the structural engineer. A widely employed approach formulates the cross-section yield criterion in terms of generalized stresses, usually axial force and bending moments. For

steel sections, however, the strain limit is sufficiently large to allow the use the classical plasticity theory [19, 11]. A point cloud of generalized yield stresses can be obtained by assigning the corresponding collapse mechanisms, that is the position and orientation of the neutral axis at the collapse states. The Minkowski sum [5] of ellipsoids represents an interesting alternative for the approximation of particular convex shapes known as zonoids, such as the cross-section yield surface [1, 11, 19, 14]. A few ellipsoids can be used to describe the yield surface of homogeneous and composite cross-sections with great accuracy, also in the case of non-smooth shapes. The yield surface at an assigned fire duration can be obtained by simply contracting the ambient temperature yield surface accounting for its strength reduction. The time-dependent yield criteria can be easily used to check the building safety by means of local strength checks of the sections. However, the significant ductility and overstrength of 3D buildings, allow a stress redistribution and can make the sectional check extremely conservative. Although this fact is well known, a global fire analysis accounting for the stress redistribution and the structural overstrength has never been proposed to our knowledge. To deal with the this lack, in this work we propose a quasi-static nonlinear analysis for assessing the global safety of 3D RC frames in conditions of fire. It is a strain-driven incremental strategy which evaluates a sequence of safe states for an increasing fire duration. The time-dependent yield surface together with a finite element beam model allows us to formulate the equilibrium condition of the structure as a nonlinear system of equations defining a curve in the hyperspace of the discrete variables and the fire duration. A generalized path-following strategy is proposed for solving step-by-step the global nonlinear equilibrium equations. The methodology can be seen as an optimisation method [6], which furnishes a sequence of safe states at increasing fire durations according to the lower bound theorem of the limit analysis up to the limit fire duration, that is the time of exposure which leads to the structural collapse. At each step of the analysis the nonlinear internal forces are obtained by an elastic predictor-return mapping process based on the closest point projection (CPP) scheme on the yield surfaces at the current fire duration [16].

2 REINFORCED CONCRETE SECTIONS IN FIRE

In this section, we describe the mechanical model for reinforced concrete sections in fire. In particular, we define the section yield surface in terms of axial force and bending moments corresponding to an assigned fire duration, taking account of the temperature distribution within the section which reduces the strength of the materials.

2.1 Temperature distribution

For a generic solid body with thermal boundary conditions, the heat transfer equations can be solved using the finite element method [10]. For the particular simple case of fire exposed rectangular concrete sections, Wickstrom [21] proposed and validated a set of handy formulas to calculate the 2D temperature distribution. Wickstrom's formulas can be applied for any type of concrete or fire scenario [18]. However, they are particularly easy for ISO 834 standard fire and normal weight concrete.

2.2 Strength reduction for concrete and steel

The concrete compressive strength experiences significant degradation at elevated temperatures. The reduced compressive strength for concretes f_{cT} can be estimated from its ambient value f_c [4] as$f_{cT} = k_c[T]f_c$. Lie et al.'s model [20] is used to predict the reduced yield strength of reinforcing bars f_{yT} from its ambient value f_y as $f_{yT} = k_s[T]f_y$

2.3 Section kinematics and statics

Let us consider a cylinder occupying a reference configuration $\mathcal{B}$ of length ℓ confined by the lateral boundary denoted by $\partial\mathcal{B}$ and two terminal bases Ω_0 and Ω_ℓ. The cylinder is referred to a Cartesian frame $(\mathcal{O}, x_1 \equiv s, x_2, x_3)$ with unit vectors $\{\mathbf{e}_1, \mathbf{e}_2, \mathbf{e}_3\}$ and $\mathbf{e}_1$ aligned with the cylinder axis. In this system, we denote with $\mathbf{X} = s\mathbf{e}_1 + \mathbf{x}$ the position of a point P, where s is an abscissa which identifies the generic cross-section Ω_s of the beam, while $\mathbf{x} = x_2\mathbf{e}_2 + x_3\mathbf{e}_3$ is the position of P inside Ω_s.

The displacement field $\mathbf{u}[\mathbf{X}]$ of the model is expressed, as usual, as a rigid motion of the section

$$\mathbf{u}[\mathbf{X}] = \mathbf{u}_0[s] + \boldsymbol{\varphi}[s] \wedge \mathbf{x} \tag{1}$$

where $\mathbf{u}_0[s]$ and $\boldsymbol{\varphi}[s]$ are the mean translation and rotation of the section and the operator $\wedge$ denotes the cross product. The kinematics assumed in Eq.(1) allows us to evaluate, using a linear Cauchy continuum, the stress-strain work $\mathcal{W}$ in terms of the generalized strains and stresses on the section as

$$\mathcal{W} := \int_\ell (\boldsymbol{\mathcal{N}}[s]^T \boldsymbol{\varepsilon}[s] + \boldsymbol{\mathcal{M}}[s]^T \boldsymbol{\chi}[s]) ds \tag{2}$$

where the generalized strains $\boldsymbol{\varepsilon}$ and $\boldsymbol{\chi}$ are defined as

$$\boldsymbol{\varepsilon}[s] = \mathbf{u}_{0,s}\,[s] + \mathbf{e}_1 \wedge \boldsymbol{\varphi}[s], \quad \boldsymbol{\chi} = \boldsymbol{\varphi}[s]_{,s}\,, \tag{3}$$

a comma stands for derivative and $\boldsymbol{\mathcal{N}}[s] = \{N_1, N_2, N_3\}$ and $\boldsymbol{\mathcal{M}}[s] = \{M_1, M_2, M_3\}$ are the resultant force and moment. Finally, the elastic constitutive law is expressed as

$$\begin{bmatrix} \boldsymbol{\varepsilon} \\ \boldsymbol{\chi} \end{bmatrix} = \mathbf{F} \begin{bmatrix} \boldsymbol{\mathcal{N}} \\ \boldsymbol{\mathcal{M}} \end{bmatrix} \quad , \quad \mathbf{F} = \begin{bmatrix} \mathbf{F}_{NN} & \mathbf{F}_{NM} \\ \mathbf{F}_{NM}^T & \mathbf{F}_{MM} \end{bmatrix} \tag{4}$$

where the coefficients of the cross-section compliance matrix $\mathbf{F}$ can be obtained as in [11, 8].

2.4 The cross-section yield surface

Following [1, 11, 19, 17], we denote with Ω the concrete beam section domain, with A_i the steel rebar area and with (x_{2i}, x_{3i}) its coordinates. The material is assumed to be elastic-perfectly plastic with the plastic admissibility condition expressed in terms of normal stress only as: $-f_{cT} \leq \sigma_{11} \leq 0$ for the concrete and $-f_{yT} \leq \sigma_{11} \leq f_{yT}$ for rebars, where the normal stress is assumed positive in tension. f_{yT} and f_{cT} depend on the value of the temperature T and then from the point coordinates over the section and

fire duration t. Omitting the dependence on s for a clearer exposition, we introduce the plastic mechanism of the cross-section as

$$\mathbf{n} = \{\dot{\epsilon}_1, \dot{\chi}_2, \dot{\chi}_3\} \tag{5}$$

which defines the position and orientation of the neutral axis for the collapse state from the condition

$$\dot{\varepsilon}_{11} \equiv \dot{\epsilon}_1 + x_3\dot{\chi}_2 - x_2\dot{\chi}_3 = 0. \tag{6}$$

The yield stress vector $\boldsymbol{\tau}_y$ collecting the generalized section resultants associated with $\mathbf{n}$ by the Drucker condition, at a given fire duration t, is

$$\boldsymbol{\tau}_y[\mathbf{n}, t] = \begin{bmatrix} N_{y1} \\ M_{y2} \\ M_{y3} \end{bmatrix} \quad \text{with} \quad \begin{cases} N_{y1} = f_y \sum_{i=1}^{N_s} a_i k_s[x_{2i}, x_{3i}, t] A_i - f_c \int_{\Omega_c} k_c[x_2, x_3, t] d\Omega_c \\ M_{y2} = f_y \sum_{i=1}^{N_s} a_i x_{3i} k_s[x_{2i}, x_{3i}, t] A_i - f_c \int_{\Omega_c} x_3 k_c[x_2, x_3, t] d\Omega_c \\ M_{y3} = -f_y \sum_{i=1}^{N_s} a_i x_{2i} k_s[x_{2i}, x_{3i}, t] A_i + f_c \int_{\Omega_c} x_2 k_c[x_2, x_3, t] d\Omega_c \end{cases} \tag{7}$$

where N_s is the number of rebars, Ω_c is the area of the compressed portion of the section according to Eq.(6) and

$$a_i = \text{sign}[\dot{\varepsilon}_{11}[x_{2i}, x_{3i}]]. \tag{8}$$

Equation (7) allows the evaluation, for an assigned fire duration t, of the set of generalized yield stress $\boldsymbol{\tau}_{yk}[t] \equiv \boldsymbol{\tau}_y[\mathbf{n}_k, t]$ associated to the mechanism $\mathbf{n}_k$, simply by assuming uniaxial stress fields reaching their maximum strength capacity in each region, either in tension or in compression.

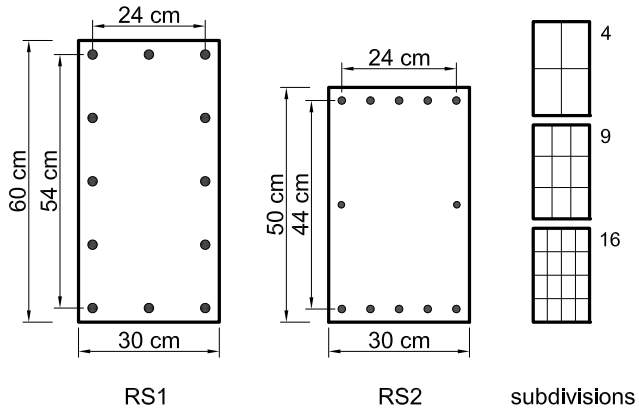
2.5 Construction of yield surface at ambient temperature as a Minkowski sum of ellipsoids

The domain of the composite cross section $\Omega_s = \Omega \cup_i A_i$ is subdivided into a grid of sub-domains $\Omega_s = \cup_I \Omega_I$. Exploiting the properties of the integral in Eq.(7), the true yield stress $\boldsymbol{\tau}_y[\mathbf{n}_k]$ at ambient temperature can be obtained as

$$\boldsymbol{\tau}_y[\mathbf{n}_k] = \sum_I \boldsymbol{\tau}_{yI}[\mathbf{n}_k] \tag{9}$$

where $\boldsymbol{\tau}_{yI}[\mathbf{n}_k]$ is the contribution of the Ith subdomain evaluated for concrete and of the N_{sI} steel reinforcements belonging to the Ith edge of the section. Equation (9) can be interpreted as a Minkowski sum. Following [14] the stress points on the yield surface expressed as a Minkowski sum of ellipsoids can be parametrized in a closed form in terms of the normal vector $\mathbf{n}$ (see [19]), as

$$\boldsymbol{\tau}[\mathbf{n}] = \sum_I \boldsymbol{\tau}_I[\mathbf{n}] \text{ where } \boldsymbol{\tau}_I[\mathbf{n}] = \mathbf{c}_I + \frac{\mathbf{C}_I \mathbf{n}}{\sqrt{\mathbf{n}^T \mathbf{C}_I \mathbf{n}}}.$$



Concrete
$f_{ck} = 20\,MPa$
$\gamma_c = 1.5$
$\sigma_c = f_{ck}/\gamma_c$, $\sigma_t = 0$
Reinforcing bars
$f_{yk} = 450\,MPa$
$\gamma_s = 1.15$
$\sigma_c = \sigma_t = f_{yk}/\gamma_s$
concrete cover $2\,cm$
RS1: $12\phi 20\,mm$
RS2 top and bottom: $10\phi 16\,mm$
RS2 lateral: $2\phi 14\,mm$

Figure 1: Rectangular RC sections: geometry, materials and subdivisions for the geometric Minkowski sum.

2.6 Account of the time-dependent strength reduction

The reduction factors k_c and k_s are functions of the temperature, which depends on the fire duration and on the point (x_2, x_3) within the section, that is we have $k_c[x_2, x_3, t]$ and $k_s[x_2, x_3, t]$. It is possible to evaluate a mean value $\bar{k}_I[t]$ which provides an exact axial force see [16] for details. For the concrete sub-domains, letting $k_I[x_2, x_3, t] = k_c[x_2, x_3, t]$, this means

$$\bar{k}_I[t] = \frac{1}{\Omega_I}\int_{\Omega_I} k_I[x_2, x_3, t]d\Omega_I \;\; \boldsymbol{\tau}[\mathbf{n}, t] = \sum_I \bar{k}_I[t]\boldsymbol{\tau}_I[\mathbf{n}].$$

where the integral can be evaluated analytically as in [3], or numerically using, for instance, the Gauss quadrature.

2.7 Yield surface evaluation of RC sections for beams and columns

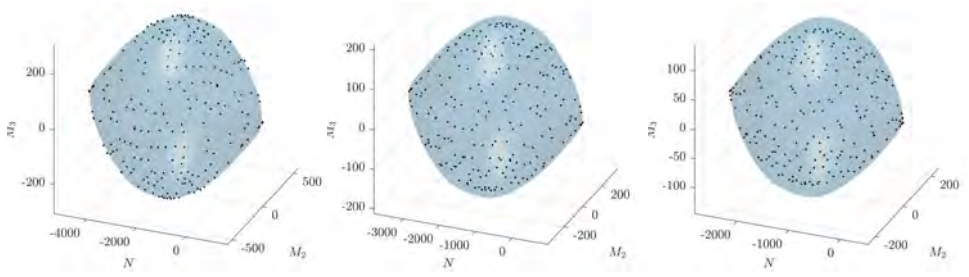
The proposed strategy for the evaluation of the time-dependent yield surface is now tested for two RC cross-sections, called $RS1$ and $RS2$, with steel reinforcements of diameter ϕ typical of columns and beams respectively and reported in Fig.1.

The $RS1$ section is analyzed considering a fire exposure all along its perimeter. Figure 2 shows how the proposed Minkowski approximation fits the yield points of the reference solution for different fire durations.

Finally the $RS2$ section is analyzed considering a fire exposure along three edges: left, bottom and right. In Fig.3 we can observe the quality of the proposed Minkowski approximation in fitting the yield points of the reference solution at various fire durations.

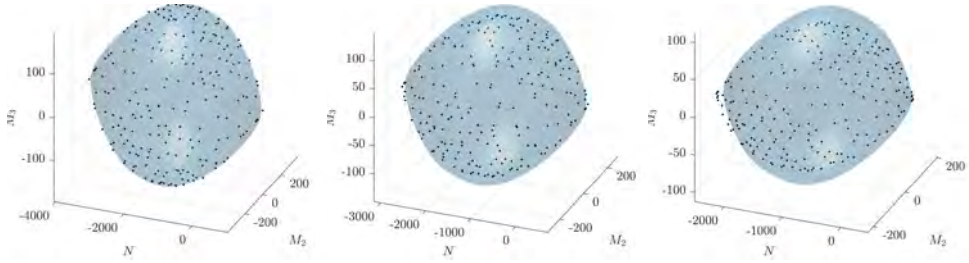
3 THE FINITE ELEMENT QUASI-STATIC ANALYSIS FOR 3D FRAMES SUBJECTED TO FIRE

In the following the finite element beam model for the incremental fire analysis is described.



(a) $t = 0$, 2×2 subdomains(b) $t = 1$h, 2×2 subdomains(c) $t = 2$h, 2×2 subdomains

Figure 2: RS1 section: approximation of the true yield points for different fire durations



(a) $t = 0$, 2×2 subdomains(b) $t = 1$h, 2×2 subdomains(c) $t = 2$h, 2×2 subdomains

Figure 3: RS2 section: approximation of the true yield points for different fire durations

3.1 THE 3D BEAM FINITE ELEMENT

The beam finite element adopted (see [11]) uses an interpolation of the generalized stresses $[\boldsymbol{\mathcal{N}}, \boldsymbol{\mathcal{M}}]^T = \mathbf{D}_t[s]\boldsymbol{\beta}_e$, where the interpolation matrix $\mathbf{D}_t[s]$ is obtained satisfying the equilibrium equations on the element for zero body forces exactly. Body load effects are then included exactly as a "particular solution". This means that $\boldsymbol{\mathcal{N}}$ and the torsional moment component M_1 are constant, while the two flexural components $M_2[s]$ and $M_3[s]$ of $\boldsymbol{\mathcal{M}}[s]$ are linear with s and linked to the shear resultants so that $N_2\ell = -(M_3[\ell]-M_3[0])$ and $N_3\ell = (M_2[\ell] - M_2[0])$. The internal work becomes

$$\mathcal{W} \equiv \boldsymbol{\mathcal{N}}^T (\mathbf{u}_0[\ell] - \mathbf{u}_0[0]) + \boldsymbol{\mathcal{M}}[\ell]^T\boldsymbol{\varphi}[\ell] - \boldsymbol{\mathcal{M}}[0]^T\boldsymbol{\varphi}[0] = \mathbf{d}_e^T\mathbf{Q}_e^T\boldsymbol{\beta}_e \tag{10}$$

allowing us to directly obtain the discrete form of $\mathcal{W}$ without any FEM interpolation for the kinematic variables. The vectors collecting the kinematics $\mathbf{d}_e$ and static $\boldsymbol{\beta}_e$ finite element generalized parameters and the compatibility operator $\mathbf{Q}_e$ are defined as

$$\boldsymbol{\beta}_e = \begin{bmatrix} N \\ M_2[0] \\ M_3[0] \\ M_2[\ell] \\ M_3[\ell] \\ M_1 \end{bmatrix}, \quad \mathbf{d}_e = \begin{bmatrix} \mathbf{u}_0[0] \\ \boldsymbol{\varphi}[0] \\ \mathbf{u}_0[\ell] \\ \boldsymbol{\varphi}[\ell] \end{bmatrix}, \quad \mathbf{Q}_e = \frac{1}{\ell}\begin{bmatrix} -\ell\,\mathbf{e}_1^T & \mathbf{0} & \ell\,\mathbf{e}_1^T & \mathbf{0} \\ \mathbf{e}_3^T & -\ell\,\mathbf{e}_2^T & -\mathbf{e}_3^T & \mathbf{0} \\ -\mathbf{e}_2^T & -\ell\,\mathbf{e}_3 & \mathbf{e}_2^T & \mathbf{0} \\ -\mathbf{e}_3^T & \mathbf{0} & \mathbf{e}_3^T & \ell\,\mathbf{e}_2^T \\ \mathbf{e}_2^T & \mathbf{0} & -\mathbf{e}_2^T & \ell\,\mathbf{e}_3^T \\ \mathbf{0} & -\ell\,\mathbf{e}_1^T & \mathbf{0} & \ell\,\mathbf{e}_1^T \end{bmatrix}. \tag{11}$$

3.2 The linear elastic problem

The linear elastic problem can be formulated as the stationarity of the Hellinger-Reissner functional Π_{HR} that at the element level can be written as

$$\Pi_{HR} = \mathbf{d}_e^T \mathbf{Q}_e^T \boldsymbol{\beta}_e - \frac{1}{2} \boldsymbol{\beta}_e^T \mathbf{F}_e \boldsymbol{\beta}_e - \mathbf{d}_e^T \mathbf{p}_e$$

where $\mathbf{p}_e$ is the element contribution of the external loads and the elastic compliance matrix of the element $\mathbf{F}_e$ is obtained from the equivalence

$$\int_\ell \left(\begin{bmatrix} \boldsymbol{\mathcal{N}} \\ \boldsymbol{\mathcal{M}} \end{bmatrix}^T \begin{bmatrix} \mathbf{F}_{NN} & \mathbf{F}_{NM} \\ \mathbf{F}_{NM}^T & \mathbf{F}_{MM} \end{bmatrix} \begin{bmatrix} \boldsymbol{\mathcal{N}} \\ \boldsymbol{\mathcal{M}} \end{bmatrix} \right) ds = \boldsymbol{\beta}_e^T \mathbf{F}_e \boldsymbol{\beta}_e, \quad \mathbf{F}_e = \int_\ell \mathbf{D}_t[s]^T \mathbf{F} \mathbf{D}_t[s] \, ds. \tag{12}$$

The stationarity of Π_{HR} with respect to the stress variables furnishes the discrete elastic constitutive law

$$\boldsymbol{\beta}_e[\mathbf{d}_e] = \mathbf{E}_e \mathbf{Q}_e \mathbf{d}_e \quad \text{with} \quad \mathbf{E}_e = \mathbf{F}_e^{-1} \tag{13}$$

which allows us to express the elastic problem in terms of displacement variables only. The stationarity condition with respect to $\mathbf{d}_e$ furnishes the equilibrium equations on the element as

$$\mathbf{Q}_e^T \boldsymbol{\beta}_e[\mathbf{d}_e] - \mathbf{p}_e = \mathbf{0} \tag{14}$$

which, in the elastic case, become

$$\mathbf{K}_e \mathbf{d}_e - \mathbf{p}_e = \mathbf{0} \quad \text{with} \quad \mathbf{K}_e = \mathbf{Q}_e^T \mathbf{E}_e \mathbf{Q}_e.$$

3.3 Stress update for time-dependent yield conditions

An elastic behavior with respect to shear effects as well as torsion is assumed. The section yield function $f[s, t, \boldsymbol{\tau}[s]]$ is then defined in a 3D space involving axial force N_1 and bending moments M_2 and M_3 collected in vector $\boldsymbol{\tau}[s] = \{N_1, M_2, M_3\}$. The plastic admissibility condition on the cross-section s then becomes

$$f[s, t, \boldsymbol{\tau}[s]] \leq 0. \tag{15}$$

The update of the stress is obtained, in a strain-driven way, by means of a closest point projection (CPP) which corresponds to a backward Euler scheme for integrating the constitutive law. Starting from a known state $\mathbf{d}_e[t_0], \boldsymbol{\beta}_e[t_0]$ the stress parameters $\boldsymbol{\beta}_e[\boldsymbol{\beta}_e[t_0], t, \Delta\mathbf{d}_e]$ for an assigned displacement increment $\Delta\mathbf{d}_e$ and a given fire duration t are obtained by solving, for each element, the optimization problem

$$\begin{aligned} &\text{minimize} && \frac{1}{2}(\boldsymbol{\beta}_e - \boldsymbol{\beta}_e^*)^T \mathbf{F}_e (\boldsymbol{\beta}_e - \boldsymbol{\beta}_e^*) \\ &\text{subject to} && f[0, t, \boldsymbol{\tau}[0]] \leq 0 \\ & && f[\ell, t, \boldsymbol{\tau}[\ell]] \leq 0 \end{aligned} \tag{16}$$

where $\boldsymbol{\beta}_e^* = \boldsymbol{\beta}_e[t_0] + \mathbf{E}_e \mathbf{Q}_e \Delta\mathbf{d}_e$ is the elastic predictor and, when the admissibility condition is checked on the beam end nodes only, the generalized normal stress vectors of the two end

sections are extracted directly from $\boldsymbol{\beta}_e$ as $\boldsymbol{\tau}[0] = \mathbf{P}_0\boldsymbol{\beta}_e$ and $\boldsymbol{\tau}[\ell] = \mathbf{P}_\ell\boldsymbol{\beta}_e$ by the extraction operators $\mathbf{P}_0$ and $\mathbf{P}_\ell$. Note that since the mixed finite element always satisfies the local equilibrium, the stresses at both end sections are coupled with each other and, then, the CPP has to be performed at the element level. In this case the element equilibrium equations (14) modify as

$$\mathbf{Q}_e^T\boldsymbol{\beta}_e[\boldsymbol{\beta}_e[t_0], t, \Delta\mathbf{d}_e] - \mathbf{p}_e = \mathbf{0}. \tag{17}$$

A specialized stress update strategy for the Minkowski description of the yield condition can be adopted [14]. The main idea is to reformulate the CPP problem using the normal vector as primal unknown. This is convenient since the dimension of the problem is fixed and independent of the number of ellipsoids used in the approximation. An elastic predictor-return mapping scheme is used. Both the admissibility check and the finite element return mapping are formulated as small nonlinear systems of equations of fixed size.

3.4 Incremental nonlinear fire analysis

Once the finite element assemblage has been carried out, the equilibrium condition of a RC building subjected to fire can be written as

$$\mathbf{r}[\mathbf{d}, t] = \mathbf{s}[\mathbf{d}, t] - \mathbf{p} = \mathbf{0} \tag{18}$$

This system of nonlinear equations represents a curve in the hyperspace $\mathbf{d}$-t, which can be traced in a path-following manner.

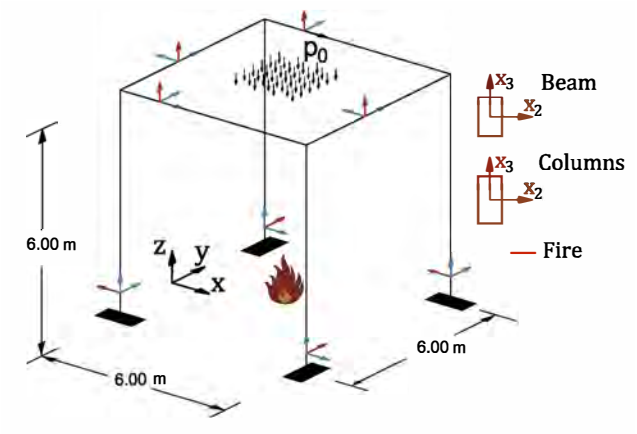
The curve can exhibit a limit fire duration, that is the time of exposure which leads to structural collapse. For this reason it is not convenient to use a time controlled scheme since Eq.(18) could not have a solution, that is no equilibrium state, for a given fire duration. We propose instead the use of a generalized arc-length method. The equilibrium equations are completed with the additional constraint $g[\mathbf{d}, t] - \xi = 0$, which defines a surface in $\mathbb{R}^{N+1}$. Assigning successive values to the control parameter $\xi = \xi_{(k)}$ the solution of the nonlinear system

$$\mathbf{R}[\xi] \equiv \begin{bmatrix} \mathbf{r}[\mathbf{d}, t] \\ g[\mathbf{d}, t] - \xi \end{bmatrix} = \mathbf{0} \tag{19}$$

defines a sequence of points (steps) $\mathbf{z}_{(k)} \equiv \{\mathbf{d}_{(k)},\, t_{(k)}\}$ belonging to the equilibrium path. Starting from a known equilibrium point $\mathbf{z}^0 \equiv \mathbf{z}_{(k)}$, the new one $\mathbf{z}_{(k+1)}$ is evaluated correcting a first *extrapolation* $\mathbf{z}^1 = \{\mathbf{d}^1,\, t^1\}$ by a sequence of estimates $\mathbf{z}^j$ by a Newton–Raphson iteration

$$\begin{cases} \mathbf{J}\Delta\mathbf{z} = -\mathbf{R}^j \\ \mathbf{z}^{j+1} = \mathbf{z}^j + \Delta\mathbf{z} \end{cases} \tag{20}$$

where $\mathbf{R}^j \equiv \mathbf{R}[\mathbf{z}^j]$ and $\mathbf{J}$ is the Jacobian of the non-linear system (19) at $\mathbf{z}^j$ or its suitable estimate. The simplest choice for $g[\mathbf{d}, t]$ is the linear constraint corresponding to the



Loads
vertical $p_0 = 15kN/m^2$
Reinforced concrete
Columns section: RS1
Beams section: RS2

Figure 4: Simple 3D frame: geometry, loads and cross-sections

orthogonal hyperplane

$$\mathbf{n}_d^T(\mathbf{d}-\mathbf{d}^j)+n_t\,(t-t^j)=\Delta\xi \quad \text{where} \quad \begin{cases}\mathbf{n}_d \equiv \mathbf{M}\,(\mathbf{d}^j-\mathbf{d}_{(k)})\\ n_t \equiv \mu\,(t^j-t_{(k)})\end{cases} \tag{21}$$

$\mathbf{M}$ and μ being some suitable metric factors [12, 13], $\Delta\xi$ an assigned increment of ξ and

$$\mathbf{J} \equiv \left[\frac{\partial \mathbf{R}[\mathbf{z}]}{\partial \mathbf{z}}\right]_{\mathbf{z}^j} = \begin{bmatrix}\mathbf{K}_t & \mathbf{s}_t\\ \mathbf{n}_d^T & n_t\end{bmatrix}. \tag{22}$$

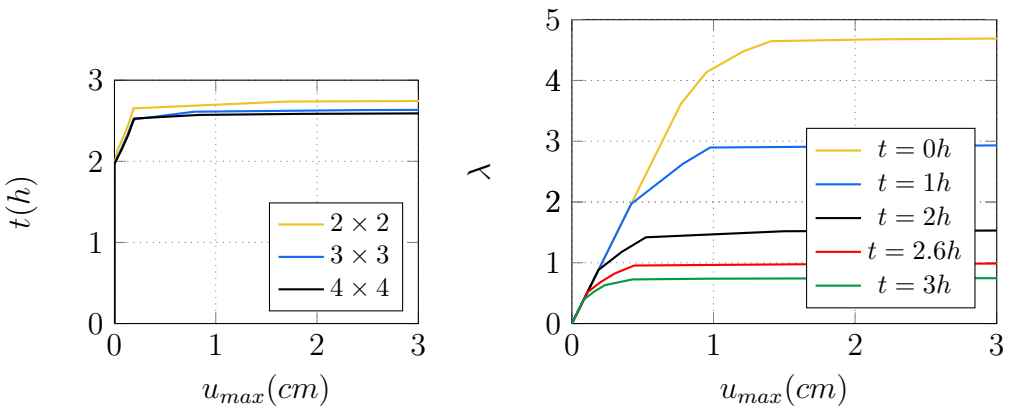
The time-controlled scheme can be recovered assuming $g[\mathbf{d},t]=t$, but it is not convenient as previously discussed. The solution of Eq.(20) is conveniently performed in a partitioned way as follows

$$\begin{cases}\Delta t = \dfrac{\mathbf{n}_d^T\mathbf{K}_t\mathbf{r}^j}{n_t-\mathbf{n}_d^T\mathbf{K}_t\mathbf{s}_t}\\ \mathbf{K}_t\Delta\mathbf{d}=\Delta t\mathbf{s}_t-\mathbf{r}^j\end{cases} \tag{23}$$

in order to exploit the symmetry and the band structure of the tangent stiffness matrix $\mathbf{K}_t$. The points $\mathbf{z}_{(n)}$ evaluated by the scheme are, by definition, equilibrated and plastically admissible at time $t_{(n)}$. In other words, they satisfy the hypotheses of the lower bound theorem of the limit analysis. Furthermore, in [16], it was proven that when $t_{(n+1)}-t_{(n)}=0$ the structure is just at the point of failure because the hypotheses of the upper and lower bound theorems of the limit analysis are satisfied simultaneously.

4 Numerical test on 3D buildings in fire

The second example regards the simple 3D frame reported in Fig.4. The load over the floor is uniformly distributed over the four beams. The fire scenario considered is the columns exposed to fire at each edge while on the beams it is on the three edges excluding the top one.



(a) time history (b) evolution for assigned fire durations

Figure 5: Simple 3D frame: equilibrium paths.

In Fig.5 the fire duration-displacement curve for the assigned distributed load is reported. The curve is characterized by a significant inital portion with zero displacements. This means that the load is largely inside the initial domain at ambient temperature. Two hours are required to observe the first plastic deformations while the limit fire duration is equal to 2.6. The structure is analyzed using the standard incremental elasto-plastic analysis with constant yield surfaces corresponding to different fire durations. The load-displacement paths are reported in Fig.5 for different times of exposure. It is possible to observe how the collapse load factor is equal to one for the yield surface corresponding to the limit fire duration evaluated with the proposed incremental strategy.

5 CONCLUSIONS

In this work, we showed a numerical procedure for constructing the axial force-biaxial bending yield surface of sections in fire in a simple, accurate and efficient way. The strategy is based on a particular Minkowski sum of ellipsoids. The yield conditions depends on the fire durations. We proposed a strain-driven incremental strategy for tracing this curve in a path-following quasi-static manner. This kind of analysis takes account of the stress redistribution and provides the limit duration, that is the time of exposure which leads to the structural collapse. The step-by-step procedure furnishes a sequence of safe states at increasing fire durations according to the lower bound theorem of the limit analysis. When a limit fire duration exists, the approach can be framed as an optimisation problem very similar to the static limit analysis one. The main difference is that the loads are kept constant and the fire duration, which leads to a contraction of the yield surfaces, replaces the load factor as objective function. Future developments will focus on accounting for other significant structural behaviors as the effects of large deformations [9].

REFERENCES

[1] Bleyer, J. and De Buhan, P. Yield surface approximation for lower and upper bound yield design of 3D composite frame structures. *Computers and Structures* (2013) **129**:86-98.

[2] Buchanan, Andrew H. and Abu, Anthony K. *Structural design for fire safety.* Wiley, (2017).

[3] El-Fitiany, S.F. and Youssef, M.A. Interaction diagrams for fire-exposed reinforced concrete sections. *Engineering Structures.* (2014) **70**:246-259.

[4] European Union. *EN 1992 - Eurocode 2: Design of concrete structures.* (1992).

[5] Fogel, E. and Halperin, D., E. Exact and efficient construction of Minkowski sums of convex polyhedra with applications. *CAD Computer Aided Design* (2007) **39**:929-940.

[6] Garcea, G. and Leonetti, L. A unified mathematical programming formulation of strain driven and interior point algorithms for shakedown and limit analysis. *Int. J. Num. Meth. Engng.* (2011) **88**:1085-1111.

[7] Garcea, G. and Gonçalves, R. and Bilotta, A. and Manta, D. and Bebiano, R. and Leonetti, L. and Magisano, D. and Camotim, D. Deformation modes of thin-walled members: A comparison between the method of Generalized Eigenvectors and Generalized Beam Theory *Thin-Walled Structures* (2016) **100**:192-212.

[8] Garcea, G. and Gonçalves, R. and Bilotta, A. and Manta, D. and Bebiano, R. and Leonetti, L. and Magisano, D. and Camotim, D. Deformation modes of thin-walled members: A comparison between the method of Generalized Eigenvectors and Generalized Beam Theory *Thin-Walled Structures* (2016) **100**:192-212.

[9] Garcea, G. and Leonetti, L. and Magisano, D. and Gonçalves, R. and Camotim, D. Deformation modes for the post-critical analysis of thin-walled compressed members by a Koiter semi-analytic approach *International Journal of Solids and Structures* (2017) **110-111**:367-384.

[10] Law, A. and Gillie, M. Interaction diagrams for ambient and heated concrete sections *Engineering Structures* (2010) **110-111**:1641 - 1649.

[11] Leonetti, L. and Casciaro, R. and Garcea, G. Effective treatment of complex statical and dynamical load combinations within shakedown analysis of 3D frames *Computers & Structures* (2015) **158**:124 - 139.

[12] Magisano, D. and Leonetti, L. and Garcea, G. How to improve efficiency and robustness of the Newton method in geometrically non-linear structural problem discretized via displacement-based finite elements *Computer Methods in Applied Mechanics and Engineering* (2017) **313**:986-1005.

[13] Magisano, D. and Leonetti, L. and Garcea, G. Advantages of the mixed format in geometrically nonlinear analysis of beams and shells using solid finite elements *Int. J. Num. Meth. Engng.* (2017) **109**:1237-1262.

[14] Magisano, D. and Liguori, F.S. and Leonetti, L. and Garcea, G. Minkowski plasticity in 3D frames: Decoupled construction of the cross-section yield surface and efficient stress update strategy *Int. J. Num. Meth. Engng.* (2018) **116**:435-464.

[15] Magisano, D. and Liguori,F.S. and Leonetti,L. and de Gregorio, D. and Zuccaro, G. and Garcea, G. Minkowski plasticity in 3D frames: A quasi-static nonlinear analysis for assessing the fire resistance of reinforced concrete 3D frames exploiting time-dependent yield surfaces *Computers & Structures* (2019) **212**:327 - 342.

[16] Magisano, D. and Liguori,F.S. and Leonetti,L. and de Gregorio, D. and Zuccaro, G. and Garcea, G. Minkowski plasticity in 3D frames: A quasi-static nonlinear analysis for assessing the fire resistance of reinforced concrete 3D frames exploiting time-dependent yield surfaces *Computers & Structures* (2019) **212**:327 - 342.

[17] Pham, D.T. and de Buhan, P and Florence, C and Heck, J. and Nguyen, H. H. Interaction diagrams of reinforced concrete sections in fire: A yield design approach *Engineering Structures* (2015) **90**:38 - 47.

[18] Del Prete, I. and Cefarelli, G. and Nigro, E. Application of criteria for selecting fire scenarios for structures within fire safety engineering approach *Journal of Building Engineering* (2016) **8**:208 - 217.

[19] Sessa, S. and Marmo, F. and Rosati, L. and Leonetti, L. and Garcea, G. and Casciaro, R. Evaluation of the capacity surfaces of reinforced concrete sections: Eurocode versus a plasticity-based approach *Meccanica* (2018) **6**:1493–1512.

[20] Lie, T.T. Structural fire protection *ASCE manuals and reports on engineering practice* (1992) **78**:241.

[21] Wickstrom, U. A very simple method for estimating temperature in fire exposed concrete structures *Fire Technology Technical report SP-RAPP* (1986) **46**:186-194.

XIV International Conference on Computational Plasticity. Fundamentals and Applications
COMPLAS 2019
E. Oñate, D.R.J. Owen, D. Peric , M. Chiumenti, and Eduardo de Souza Neto (Eds)

APPLICATION OF NUMERICAL MODELLING TO THE COMPREHENSIVE ANALYSIS OF SLOPE STABILITY

EVA HRUBESOVA*, NADA RAPANTOVA† AND PAVEL POSPISIL†

* VSB-Technical University Ostrava, Faculty of Civil Engineering
17.listopadu 15, 708 00 Ostrava-Poruba
Czech Republic
e-mail: eva.hrubesova@vsb.cz, web page: http://www.fast.vsb.cz

† VSB-Technical University Ostrava, Faculty of Civil Engineering
17.listopadu 15, 708 00 Ostrava-Poruba
Czech Republic
email: nada.rapantova@vsb.cz; pavel.pospisil@vsb.cz

Key words: Slope, landslide, stability, elastic-perfectly plasticity model, numerical modelling

Summary

Paper deals with the comprehensive methodology for the numerical simulation of potentially unstable slopes combining engineering geological, hydrological, hydrogeological and geotechnical computational model for the assessment of slope stability.

Engineering geological model based on available survey data characterizes the rock environment using individual quasi-homogenous units. Model is defined on the basis of documented lithostratigraphic units in exploration probes and field relief documented by advanced methods, including satellite radar interferometry and laser surface scanning.

On the basis of engineering geological model, the hydrological model using MIKE SHE software (Finite Difference Method) was performed. Hydrological model includes simulation of surface runoff, evapotranspiration and flow in unsaturated near-surface zone. The model was calibrated on the basis of available field data. Outputs from this model were used as input initial conditions of the following hydrogeological model.

Software FEFLOW based on the Finite Element Method was subsequently used to the creation of hydrogeological model focused on the water flow and distribution of pore pressures of groundwater in individual quasi-homogeneous units in saturated zone. The infiltration condition determined by the hydrological model is considered and a flow model with variable saturation is applied.

Finally, the geotechnical stability model of slope following the engineering geological, hydrological and hydrogeological models was performed. The occurrence of plastic and failure zones (assuming elastic-perfectly plastic Mohr-Coulomb constitutive model) inside the slope was simulated by using software MIDAS GTS NX based on the Finite Element Method. Stability factor SSRF (Shear Strength Reduction Factor) is evaluated based on the Shear Strength Reduction Method) as the ratio of actual shear strength and minimum shear strength required to maintain stability.

Paper deals also with the comparison of stability factor of natural slope obtained from 3D and 2D numerical model. Generally, in the case of natural slope the condition of plane strain is not

fulfil, 2D model is not realistic and 3D model is needed, especially in case of concave morphology of slope.

1 INTRODUCTION

Slope stability assessment is one of the most important tasks in geotechnical engineering which must consider a comprehensive approach to the modelling and combine the basic principles of soil mechanics, hydraulics and general engineering mechanics. Stability of slopes is influenced by following fundamental factors – geometrical factors (terrain morphology, height, inclination, …), internal factors (geological structure of rock massif, strength and deformational properties of soil, influence of groundwater, filtration and retention properties of soil material, distribution of pore pressures, degree of saturation, …) and external factors (anthropogenic interventions, earthquakes, hydrodynamic effects of water, extreme precipitation, …). The objective implementation of previously mentioned factors into the numerical simulation determines the reliability of modelling results.

Compared to other structural materials (as concrete etc.), the soil mass is more complicated three-phase porous media consisting of solid particles and liquids and gasses in pores. The proportion of water and air in the pores is variable, it depends on many factors including soil character and its texture, weather, surface vegetation etc. The behaviour of soil is essentially dependent on the grain size, the grain shape and its surface character, on the closeness of packing of the grains, water content and corresponding degree of saturation. In unsaturated soils with negative water pore pressure a change in volume, shear strength and hydraulic properties is significant.

Generally, total stresses inside the soil mass can be expressed according Bishop´s theory as the superposition of effective stresses which are transmitted through the particle contact and water- pore pressure u_w and air-pore pressure u_a depending on saturation S:

$$\sigma tot. = \sigma ef. + \chi(S)u_w + (1-\chi(S))u_a \quad (1)$$

$\chi(S)$ – function of saturation S

$\chi(S=1) = 1$: fully saturation

The typical stress - strain behaviour of soil during loading is not elastic for the entire range of loading. In fact, real behaviour of soil is more complicated (Fig. 1), plastic irreversible deformations are manifested, they attain dominating influence near ultimate strength condition especially. No mathematical model cannot completely describe the complex behaviour of real soils. Each constitutive model accepts some idealization and simplification, it captures essential features and disregards some others. Constitutive model of soil can work assuming associated flow rule (plastic potential function characterizing the plastic strain is identical to the yield function) or non-associated flow rule (plastic potential function is different from yield function).

The linear elastic- perfectly plastic constitutive models (no hardering/softening is assumed) are widely used in geotechnical practice due to their simplicity and easily determinable input material parameters. These constitutive models assume the linear elastic behaviour in the elastic range, after the yield values is exceeded, the plastic flow continues under the identical stress. The Mohr-Coulomb (MC) model is the most common linear elastic-perfectly plastic constitutive model which describes a linear relationship between the shear and applied normal

stresses (or maximum and minimum principal stresses) of soil material.

Yield function f for Mohr-Coulomb model in p-q space can be expressed in the following form (p – mean principal stress, q- deviatoric stress):

$$f(p,q,c,\varphi) = q - \left(\frac{(6p+q)}{3}\right) sin\varphi - 2ccos\varphi \tag{2}$$

where c- cohesion, φ–friction angle.

The geometric shape of corresponding yield surface in the principal stress space corresponds to the hexagonal cone shape, on a deviatoric plane is characterized by a hexagon shape with corner points, which implies singularities and difficulties during the numerical calculation.

Drucker and Prager replaced this hexagonal shape of yield surface by a simple cylindrical cone, in the deviatoric plane it corresponds to a circle. Its yield function f can be expressed by the formula:

$$f(p,q,\alpha,\kappa) = \sqrt{\left({}^{q^2}/_{3}\right)} - 3\alpha p - \kappa \tag{3}$$

where

$$\alpha = \frac{2sin\varphi}{\sqrt{3}(3-sin\varphi)} \tag{4}$$

$$\kappa = \frac{6ccos\varphi}{\sqrt{3}(3-sin\varphi)}$$

This Drucker-Prager criterion is quite widely used in geotechnical analysis, but experimental research shows that its circular shape does not agree well with experimental data [1]. The stress-strain response predicted by the Drucker-Prager model corresponds to the experimental results, but the strength value matches better with the Mohr-Coulomb model predictions. Drucker-Prager model predicts greater strength at lower deformation compared to Mohr-Coulomb model (MC model is more conservative) [2].

The Drucker-Prager plasticity model may be useful to model soft clays with low friction angles. However, this model is not generally recommended for application to geologic materials [3].

Because the soil strength is crucial parameter determining slope stability, the Mohr-Coulomb constitutive model is generally more preferred to slope stability analysis than the Drucker-Prager model.

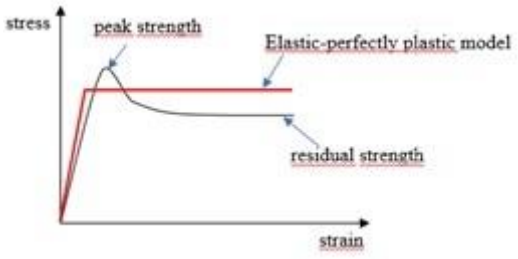


Figure 1: Characteristic stress-strain curve of soil

The numerical approach to the assessment of a slope stability is also significantly affected by the character of slope (natural, anthropogenic slope), Anthropogenic slope (embankment, earthfill dam etc.) has regular geometry usually, the localization of individual material units is usually a-priori known with high reliability, often this slope consists of one or two materials only, the slip zone has simpler shape and finally, the slope is artificial dewatered or the recharge into the slope body is eliminated. On the other hand, the natural slopes represent complex phenomena to model, both in space and time. They are characterized by complicated terrain morphology, which consists of concave and convex parts, by complicated geological structure, including the orientation of geological structures with respect to slip surface, the soil material is significantly non-homogeneous. Previously mentioned factors, together with complicated hydrological and hydrogeological conditions in slope and variable shape of slip zone, affect the computational approaches, dimensionality of simulation and necessity of coupled comprehensive approach to the modelling. The overall concept is presented in the Fig. 2. It provides a systematic methodology for the description and understanding of all geological and geomechanical processes that must be integrated for the successful assessment of potentially unstable slopes.

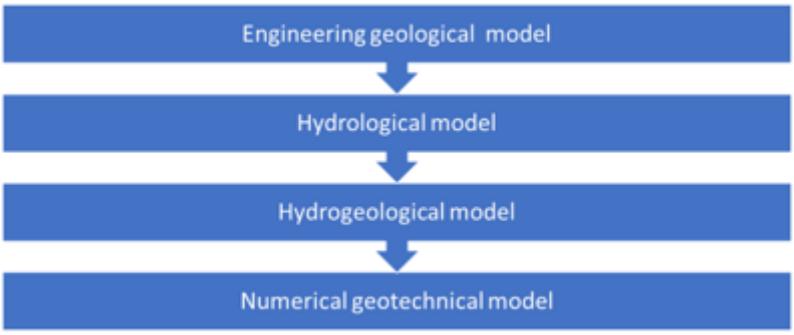


Figure 2: Comprehensive concept of slope stability solution

2 COMPUTATIONAL METHODS FOR SLOPE STABILITY ASSESSMENT

The computational methods used for the slope stability assessment are usually divided into two basic groups. The first group is based on the force, resp. moment equilibrium of the part of slope above the predefined slip surface. This conventional simple limit equilibrium method (slice method) has following limitations and simplifications:

- the predefined slip surface is required
- a rigid-plastic constitutive model with the Mohr-Coulomb limit state surface is commonly
- used in analyses (rigid slice)
- the mobilization of shear strength along the entire slip surface is assumed
- the deformation behaviour of slope is not involved into the calculation
- only quantification of stability can be obtained, no displacements can be evaluated
- stability factor is expressed as ratio of passive (anti-slip forces) and active forces (sliding forces)

Nowadays the numerical methods (including frequently used finite element method) are increasingly used for slope stability assessment due to many particular advantages over the previously mentioned limit equilibrium method. The stability slope factor based on the finite element calculation is very often evaluated by Shear Strength Reduction Method - SSRM using Mohr-Coulomb constitutive model [4]. By this technique, a series of elastic–perfectly plastic problems are analyzed with variably reduced shear strength parameters (cohesion and friction angle) obtained through dividing the actual strength parameters c and φ by a series of factors F, checking the conditions of failure (convergence of solution). The factor F initiating failure is taken as the stability factor of slope.

$$c_r = \frac{c}{F}, (tan\varphi)_r = \frac{tan\varphi}{F} \tag{5}$$

Zheng [5] shows that the stability factor calculated by the finite element-strength reduction technique are slightly greater than those obtained by the limit equilibrium method.

3 PLANAR(2D) VERSUS SPACE(3D) SLOPE STABILITY MODEL

Character of slope determines the numerical modelling approach to the stability analysis. Planar(2D) model of slope is solved under the plane strain condition and, unlike the anthropogenic slope, this condition is not usually filled for natural slopes because of specific factors mentioned in the previous chapter. Spatial(3D) model takes into account the spatial character of stress-strain space inside a natural slope and therefore is more realistic compared to a planar model. Many studies show that evaluated stability factor F(2D) obtained by planar calculation is lower or equal to the stability factor F(3D) based on 3D model. Differences between F(2D) and F(3D) can be more significant for natural slopes (up to 50%). Adriano [6] presented that differences between the F(2D) and F(3D) range between 15%-50% for concave and convex slopes, higher differences are investigated for concave slopes. Fig. 3 presents a comparison between stability factors Fs2D (based on the 2D model) and Fs3D (based on the 3D model) for concave and convex slopes [7].

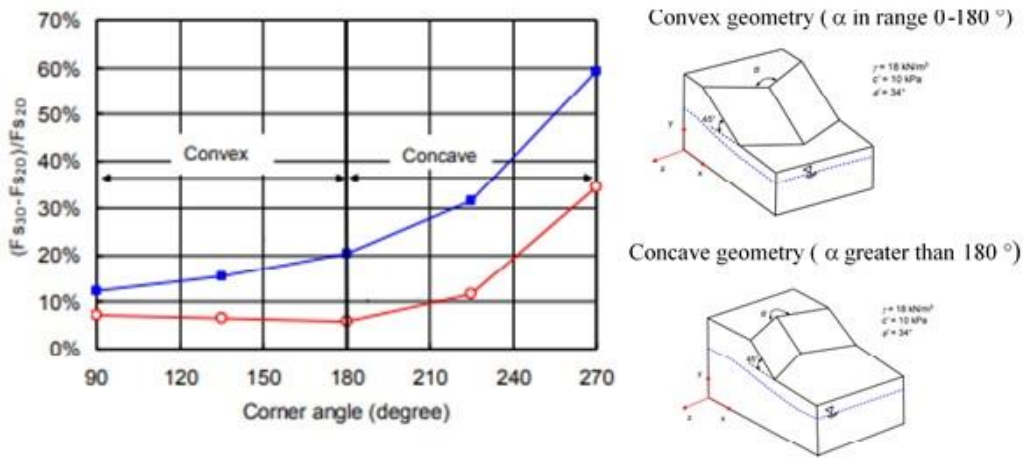


Figure 3: Comparison of Fs2D and Fs3D stability factors for convex and concave slopes [7]

4 APPLICATION OF COMPREHENSIVE APPROACH TO THE NATURAL SLOPE STABILITY ANALYSIS

Brief characterization of the analyzed real natural slope:

- extent of the landslide (approx. 200 m width, 500 m length)
- complicated morphology of natural slope, significant concave shape of slope;
- complicated geological profile – 8 quasi-homogeneous engineering geological units (fractured hard rocks covered by variably grained colluvium);
- the slope is affected by historical landslide activities;
- irregular shape of fully saturated shear zone of fined- grained colluvium;
- complicated hydrogeological conditions, two regional groundwater levels observed (colluvium and hard rock basement), perched aquifers etc.;
- three anthropogenic factors (railway embankment, man-made deposit, road cut) potentially impacted stability of the slope.

Considering the previously mentioned characteristics, the comprehensive 3D numerical modelling approach is needed for the stability analysis (Fig.4). The authors critically assessed the available archive data (exploration boreholes, reports etc.), generated 3D models using various software (RockWorks, GMS), and transferred engineering geological model to hydrogeological model built in FEFLOW and geotechnical simulation software (MIDAS GTS NX).

The engineering geological model characterized the rock environment by defining individual quasi-homogenous lithostratigraphic units and their associated geotechnical parameters. The terrain relief (DRM) was analyzed using advanced geoinformation technologies, including satellite radar interferometry and laser surface scanning. Engineering geological model formed the framework for subsequent set up of hydrogeological and geomechanical processes simulations.

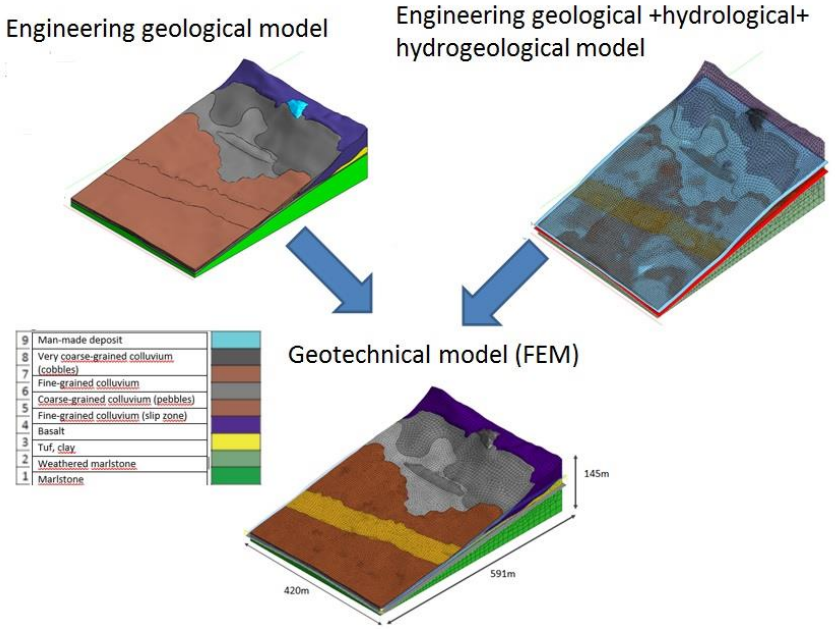


Figure 4: Scheme of comprehensive approach to the stability analysis of real natural slope

3D hydrological model was built in MIKE SHE software (based on Finite Difference Method) by DHI. The surface runoff, evapotranspiration, processes in the unsaturated shallow subsurface zone and in the deeper saturated zone were analyzed using available field data (2009-2013) for the calibration.

The achieved results of the hydrological model were introduced as boundary conditions into the 3D hydrogeological model. The transient variably saturated flow including saturation, moisture content, and distribution of pore pressure in individual quasi-homogeneous units were simulated using FEFLOW software (based on Finite Element Method) – see Fig.5.

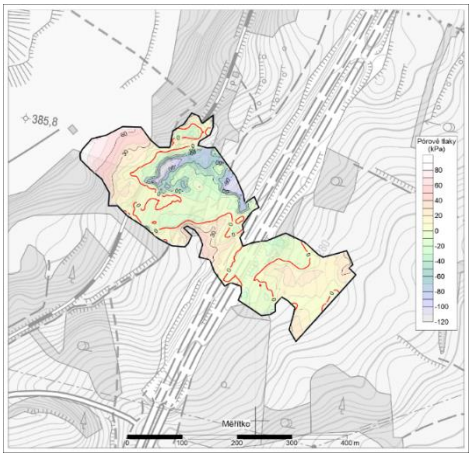


Figure 5: An example of output from variably saturated flow hydrogeological model (pore pressure on shear zone)

Based on the results of hydrogeological model, the 3D geotechnical stability model was performed. The software MIDAS GTS NX (Finite Element Method) was used for the assessment of stress- strain state in the analyzed slope assuming Mohr-Coulomb constitutive model. Due to the documented historical unstable area, the shear strength characteristics in the shear zone were assumed as residual. The stability factor was evaluated using Shear Strength Reduction Method.

The application of presented comprehensive approach enables to determine stability problematic areas, location of shear zones (surfaces), and stability factor of slope stability. The complex analysis of the results allows evaluating the key factors of the landslide activation, interconnection of slip surfaces and the mechanism of landslide formation (Fig.6-7).

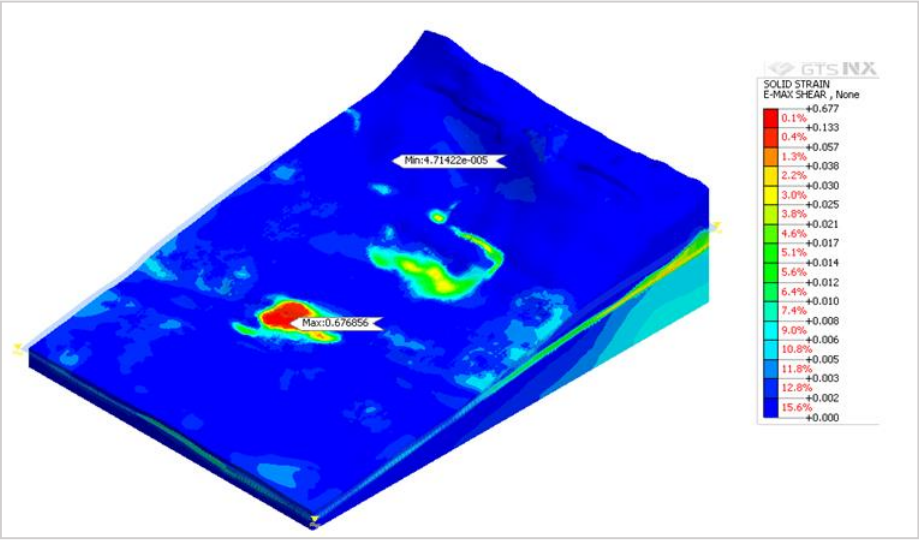


Figure 6: An example of output from geotechnical slope stability model (shear strain)- stability factor F=0.93

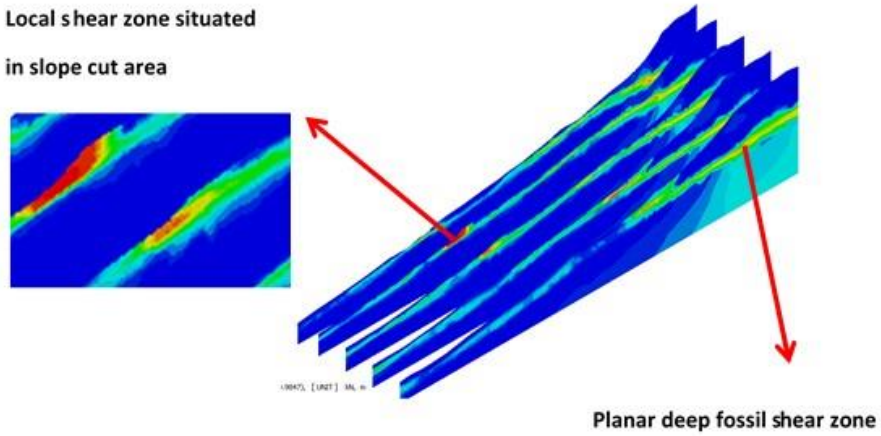


Figure 7: An example of interconnection of global and local shear zones in slope

5 CONCLUSIONS

- The comprehensive approach to stability analyses of slopes increases chances to avoid the misleading conclusions. The realistic behaviour and properties of the rock mass and its potential interaction with the building structure can be assessed and validated using a sequence of specific types of models, simulating processes affecting the rock mass stability.
- Complicated terrain morphology, geological structure including orientation of geological structures relative to slip surface, hydrological and hydrogeological conditions of the site, complex geometry of the slip surface (shear zone) and impact of anthropogenic factors of nonlinear shape requires application of 3D numerical modelling.
- The reliability of the results of numerical models is essentially determined by the

reliability of constitutive material model and the reliability of input data in heterogenous and anisotropic environment.

- The geotechnical risk faced by an engineering project is inversely proportional to the level of details and accuracy of the conceptual model of site developed through ground investigations. The better the model reflects actual conditions, the lower the residual risk.

Acknowledgement: This work was supported by the Czech Science Foundation (GAČR) through project No. 19-11441S.

REFERENCES

[1] Hai-Sui Yu. *Plasticity and Geotechnics*. Springer (2006).
[2] Sandhya Rani.R., Nagendra Prasad.K., Sai Krishna, T. Applicability of Mohr-Coulomb and Drucker-Prager models for assessment of undrained shear behavior of clayey soils. *International Journal of Civil Engineering and Technology* (2014). 5(10): 104-123.
[3] Itasca International Company. ©2019. Retrieved from: https://www.itascacg.com /software/products/flac3d/features/flac3d-constitutive-models.
[4] Zienkiewicz, O. C., C. Humpheson, and R. W. Lewis. Associated and non-associated visco-plasticity and plasticity in soil mechanics. *Geotechnique* (1975). 25(4): 671–689.
[5] Zheng, H., Tham, L.G., Liu, D. On two definitions of the factor safety commonly used in the finite element slope stability analysis. *Computers and Geotechnics* (2006). 33(3): 188-195.
[6] Adriano, P.R.R. et al. Influence of ground surface shape and Poisson's ratio on three-dimensional factor of safety. In *Proceedings of GeoEdmonton '08: 61st Canadian Geotechnical Conference*. Edmonton, Alberta. (2008).
[7] Zhang, L. et al. Comparison of 2-D and 3-D Slope Stability Analysis for Unsaturated Slopes. *67th Canadian Geotechnical Conference*. Regina, Canada. (2014).

XV International Conference on Computational Plasticity. Fundamentals and Applications
COMPLAS 2019
E. Oñate, D.R.J. Owen, D. Peric, M. Chiumenti & Eduardo de Souza Neto (Eds)

HIGH PERFORMANCE INTERIOR POINT METHODS FOR THREE-DIMENSIONAL FINITE ELEMENT LIMIT ANALYSIS

NATHAN C. PODLICH*, ANDREI V. LYAMIN† AND SCOTT W. SLOAN†

*University of Newcastle
Callaghan, NSW 2308, Australia
email nathan.podlich@newcastle.edu.au

† Centre for Geotechnical Science and Engineering
University of Newcastle
Callaghan, NSW 2308, Australia

Key words: finite element limit analysis, interior point methods, Cholesky factorization, parallelization

Abstract. The ability to obtain rigorous upper and lower bounds on collapse loads of various structures makes finite element limit analysis an attractive design tool. The increasingly high cost of computing those bounds, however, has limited its application on problems in three dimensions. This work reports on a high-performance homogeneous self-dual primal-dual interior point method developed for three-dimensional finite element limit analysis. This implementation achieves convergence times over 4.5× faster than the leading commercial solver across a set of three-dimensional finite element limit analysis test problems, making investigation of three dimensional limit loads viable. A comparison between a range of iterative linear solvers and direct methods used to determine the search direction is also provided, demonstrating the superiority of direct methods for this application.

The components of the interior point solver considered include the elimination of and options for handling remaining free variables, multifrontal and supernodal Cholesky comparison for computing the search direction, differences between approximate minimum degree [1] and nested dissection [13] orderings, dealing with dense columns and fixed variables, and accelerating the linear system solver through parallelization. Each of these areas resulted in an improvement on at least one of the problems in the test set, with many achieving gains across the whole set. The serial implementation achieved runtime performance 1.7× faster than the commercial solver `Mosek` [5]. Compared with the parallel version of `Mosek`, the use of parallel BLAS routines in the supernodal solver saw a 1.9× speedup, and with a modified version of the GPU-enabled `CHOLMOD` [11] and a single NVIDIA Tesla K20c this speedup increased to 4.65×.

1 INTRODUCTION

One of the most crucial aspects in the design of ground-based structures is the stability of the supporting material, the soil. The upper and lower bound theorems of limit analysis provide a useful methodology to address the stability of the supporting body [7]. A lower bound on the true collapse load can be identified by finding a stress distribution which satisfies the equilibrium equations and stress boundary conditions, and does not violate the yield criterion at any point (a statically admissible stress field). An upper bound to the true collapse load can be determined by equating the external rate of work to the internal power dissipation through an assumed velocity field, and ensuring that the velocity boundary conditions, and the strain and velocity compatibility conditions are satisfied (a kinematically admissible velocity field). The availability of such a precise measure of the error sets limit analysis apart from many other forms of numerical analysis and makes it a very useful tool in predicting soil stability. Both the lower and upper bound problems can be formulated as a convex optimization problem [14]:

$$\begin{aligned} &\text{maximize } \alpha \\ &\text{subject to } \mathbf{B}^T\sigma = \alpha\mathbf{p} + \mathbf{p_0} \\ &\qquad f\left(\sigma^{(\mathbf{e})}\right) \leq 0 \;\forall\; e = 1, 2, ..., n_e, \end{aligned} \tag{1}$$

where α is the load multiplier, $\mathbf{B}$ is the standard finite element strain-displacement matrix, $\mathbf{p}$ are the optimized loads, $\mathbf{p_0}$ are the prescribed tractions, $\sigma^{(e)}$ are the elemental stresses, f is the convex yield function, and n_e is the number of elements. If the yield function can be cast in terms of a conic constraint then the problem can be solved directly by an interior point method for conic optimization problems. The relevant conic constraints here are the second-order cone and the semidefinite cone which can be used to represent the Drucker-Prager and Mohr-Coulomb yield criteria in three dimensions, respectively. The second-order cone constraint on the n-vector $\mathbf{x}$ restricts the values to those that satisfy $x_0 \geq \sqrt{x_1^2 + x_2^2 + ... + x_3^2}$. The semidefinite constraint on the $n \times n$ symmetric matrix $\mathbf{X}$ requires $\mathbf{z}^T\mathbf{X}\mathbf{z} \geq 0 \;\forall\; \mathbf{z} \in \Re^n$. This paper is restricted to the former case using the Drucker-Prager yield criterion in three dimensions with second-order conic constraints.

The bulk of the computational effort spent by interior point methods lies in determining the search direction at each iteration by solving a set of symmetric indefinite linear equations known as the augmented equations

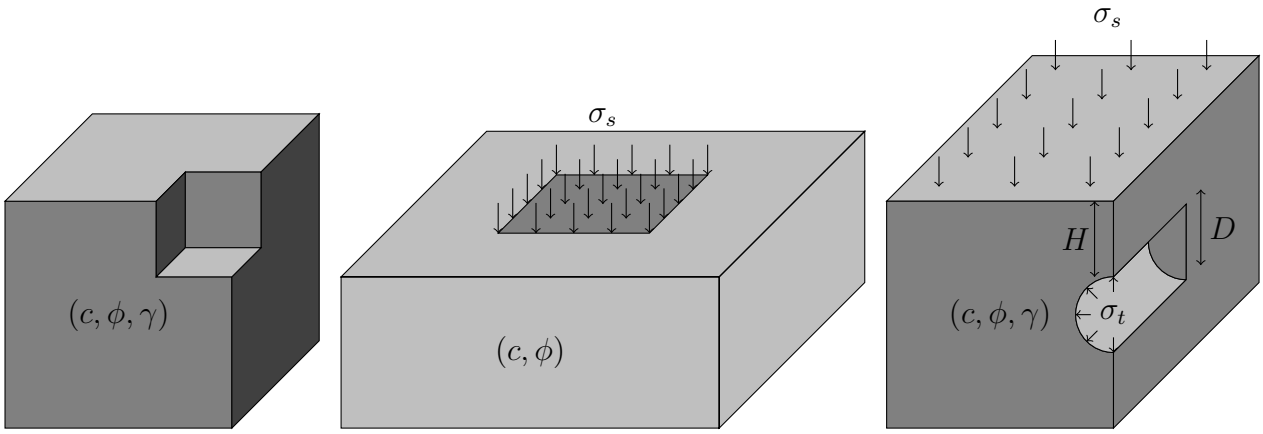
$$\begin{bmatrix} -\mathbf{D} & \mathbf{A}^T \\ \mathbf{A} & \mathbf{0} \end{bmatrix} \begin{Bmatrix} \mathbf{x} \\ \mathbf{y} \end{Bmatrix} = \begin{Bmatrix} \mathbf{p} \\ \mathbf{q} \end{Bmatrix}, \tag{2}$$

(note that $\mathbf{A} = \mathbf{B}^T$) which is often reduced to the symmetric positive definite Schur complement equation

$$\mathbf{A}\mathbf{D}^{-1}\mathbf{A}^T\mathbf{y} = \mathbf{A}\mathbf{D}^{-1}\mathbf{p} + \mathbf{q}. \tag{3}$$

In this case, the coefficient matrix defing the search direction is a very sparse and very large positive definite matrix that is increasingly ill-conditioned as an optimum point is approached. Thus, the majority of the effort in enhancing the performance of the IPM is

Figure 1: Test problems.



(a) Square excavation (b) Square footing (c) Tunnel heading

focussed on Cholesky and Cholesky-like factorization routines. This paper steps through the major choices in developing a state-of-the-art interior point solver for finite element limit analysis using a simplified homogeneous self-dual embedded interior point method [5]. The first section addresses the choice of linear solver, the second compares the two main ordering approaches, the third section looks at improving the linear system defining the search direction, and the fourth section compares the parallel performance against the top commercial solver.

Figure 1 shows the three problems considered in the study. See Table 1 for details. The problems are a square excavation in cohesive-frictional material ($c = 1$, $\phi = 1^\circ$ and $\gamma = 1$), a square footing on weightless cohesive material ($c = 1$), and a tunnel heading in cohesive-frictional material ($c = 1$, $\phi = 10^\circ$, $\gamma = 0.5$, cover of $H = 4$, diameter of $D = 2$ and length $L = 6$). An angle of $\theta = 25^\circ$ is used to determine α and k for the Drucker-Prager criterion from c and ϕ. The UB2 problems use quadratic elements in their formulation.

2 CHOICE OF LINEAR SOLVER

Because of the increasing ill-conditioning of the Schur complement as the IPM converges, the use of a Cholesky solver generally requires some way of dealing with non-positive pivots before taking the square root [18]. This can be achieved by allowing for 2×2 block pivots as in a symmetric indefinite factorization or by using basic pivot modification strategies. For the comparisons here, a left-looking supernodal Cholesky routine based on `CHOLMOD` [11] with a modified BLAS DPOTF2 subroutine that substitutes a large value (10^{32} is used) for any diagonal entry that is less than or equal to zero. `MA57` [9] was used for the multifrontal method and both options used the `MC50` implementation of the approximate minimum degree (AMD) ordering [9]. Free variables were split into the difference of two linear variables. All sequential tests were run on an Apple MacBook Pro with an Intel Core i7-3740QM 2.70GHz CPU with 16GB RAM.

Table 1: Test problem details. The columns from left to right show the number of finite elements, the number of velocity nodes, the number of stress nodes, n_F is the number of free variables, m is the number of equations in $\mathbf{B}^T$, n is the number of columns in $\mathbf{B}^T$, and $nz_{\mathbf{B}}$ is the number of non-zero entries in $\mathbf{B}$.

Problem	**Elements**	**Velocity**	**Stress**	n_F	m	n	$nz_{\mathbf{B}}$
sqexLB	265,632	265,632	155,136	271,488	1,034,703	1,202,304	6,123,526
sqexUB	337,920	196,608	337,920	944,064	1,517,567	2,971,584	9,477,630
sqexUB2	49,152	73,809	196,608	429,158	639,461	1,608,806	22,665,659
sqftLB	357,264	357,264	207,360	208,656	1,227,168	1,452,816	7,493,136
sqftUB	357,264	207,360	357,264	375,408	980,208	2,518,992	8,059,824
sqftUB2	51,840	77,257	207,360	219,750	439,757	1,463,910	22,945,686
tunhLB	561,240	561,240	326,016	335,736	1,998,455	2,291,832	15,051,585
tunhUB	561,240	326,016	561,240	600,984	1,549,007	3,968,424	15,794,780

The multifrontal method required a noticeable amount less storage for the factors than did the supernodal factorization, albeit at a significant time cost. On a smaller set of the same problems used here without the lower bound tunnel heading (which both options failed to solve to the required accuracy), the multifrontal method had an average factor non-zero count of 32 million entries and an average IPM convergence time of 188.7s compared with the supernodal methods 38 million entries and average solution time of 78.8s. The IPM using the supernodal solver was 27s-435s faster with a median improvement of 46s. This is due to the better arrangement of level 3 dense BLAS operations in the supernodal solver. The iteration counts were all the same ± 2 except for the upper bound tunnel heading where the IPM using the multifrontal solver took eight more iterations. Based on these results, the supernodal factorization appears to be superior in terms of computational speed and does not suffer from any severe robustness issues, although multiple problems did encounter numerical indefiniteness (i.e. very small or negative pivots were encountered). For the remainder of the study, the supernodal factorization was used.

2.1 A note on iterative linear solvers

Iterative linear or Krylov-subspace solvers were tested on both the Schur complement and augmented equations with a range of preconditioners [17]. The best approaches tested used a robust incomplete Cholesky factorization preconditioner with the preconditioned conjugate gradients solver. These approaches lacked robustness, failing to solve the lower bound problems in most cases (and some of the upper bound problems) in the small test set. For the problems in which the approaches were successful, the number of non-zero entries in the preconditioner ranged from 44% to 145% (averages of 60% to 75%) of the size of the factor computed in the approach developed below, with a total IPM runtime $8\times$ to $181\times$ slower (with an average around $70\times$ slower). This improved slightly as the problems became larger, although no improvement in the ability to solve the lower bound problems was found [17]. The modest reduction in storage requirements did not overcome the lack of robustness coupled with the significant increase in runtime to warrant further

investigation of this approach.

3 SPARSITY-PRESERVING ORDERINGS

The two resources required by any factorization are storage and time. Both of these are driven by the amount of fill-in in the factor and so good quality orderings that reduce fill-in can yield significant savings. The two main approaches in use for ordering symmetric systems are the approximate minimum degree (AMD) and nested dissection (ND) orderings. These two were compared using the supernodal Cholesky solver and split free variables. The AMD ordering was computed by `MC50` [9] while the ND ordering is computed by `METIS` [13]. The number of IPM iterations, the total IPM solution time and the number of non-zero entries in the Cholesky factor $\mathbf{L}$ are shown in Table 2.

The number of iterations was very similar, being identical for most problems and only showing differences in a small number of problems where convergence had slowed. The computation time of the ND ordering was, in general, longer than that of AMD, but this could be amortized over the duration of the IPM and was more than compensated for in the significant reduction in fill-in. The number of non-zeros in the Cholesky factor ranged from 65% more to 181% more with the AMD ordering. On average, the ND ordering saved 111% over AMD. This led to the IPM with the AMD ordering running 2.4× to 7.7×, with an average of 4.7×, that of the IPM with the ND ordering. The only problems that did not converge to tolerance was the lower bound tunnel headings. From these results it is clear that the nested dissection ordering is superior to AMD for these problems.

Table 2: Performance of solver improvements. *nit* is the number of IPM iterations, t_T is the total IPM solution time, and $nz_{\mathbf{L}}$ is the number of non-zero entries in the Cholesky factor. PREG is the solver with all improvements described.

	AMD			ND			PREG			`Mosek`		
Problem	*nit*	t_T	$nz_{\mathbf{L}}$	*nit*	t_T	$nz_{\mathbf{L}}$	*nit*	t_T	$nz_{\mathbf{L}}$	*nit*	t_T	$nz_{\mathbf{L}}$
sqexLB	24	5,058	835	24	657	297	21	507	267	20	785	237
sqexUB	23	5,350	961	23	1,332	444	18	788	339	17	1,109	293
sqexUB2	55	6,901	556	61	1,942	270	16	248	139	24	523	128
sqftLB	24	7,834	1,079	24	1,636	503	24	1,588	485	20	3,432	564
sqftUB	25	5,947	886	25	1,721	467	21	1,114	383	23	2,031	336
sqftUB2	25	1,436	317	25	599	192	19	379	168	18	556	153
tunhLB	22	12,277	1,670	18	1,618	733	25	2,367	720	22	3,482	660
tunhUB	39	12,999	1,284	35	3,250	673	17	1,350	590	19	2,364	524
Total	469	63,429		492	14,838		328	9,496		329	16,083	

4 EXPLOITING PROBLEM STRUCTURE

4.1 Elimination of free variables

While most authors mention the difficulties posed by free variables in the FELA problem formulation, few provide beneficial methods of dealing with them. Makrodimopoulos and Martin [15] describe how the free variables may be eliminated from a lower bound formulation, but only achieve around 10% improvement in performance. This is likely to be a result of `Mosek` being able to efficiently handle the free variables when not being removed. In the following, an outline is given of the efficient elimination of some (possibly all) free variables from the problem before solving the optimization problem using purely algebraic conditions. Note that a post-solve is also required if free variables are eliminated in order to return a solution suitable for interpretation of the results by the calling program and is included in performance comparisons.

The most general approach seeks to find a full rank row-set of as many free variables as possible on which it is possible to block-pivot without causing too much fill-in and eliminating as many free variables as possible. Because it may not be possible to find a suitable sparsity-preserving and stable block pivot for all free variables, the partitioning leads to

$$\mathbf{B}^T = \begin{bmatrix} \tilde{\mathbf{B}} & \mathbf{E} \\ \mathbf{N} & \bar{\mathbf{A}} \end{bmatrix} \tag{4}$$

where $\tilde{\mathbf{B}}$ is the non-singular block to be pivoted on. The constraint matrix used in the IPM is thus reduced to $\mathbf{A} = \bar{\mathbf{A}} - \mathbf{N}\tilde{\mathbf{B}}^{-1}\mathbf{E}$. This can be achieved by using a truncated LU factorization with the Markowitz criterion (row count less one multiplied by the column count less one) to rank potential pivots [16]. Note that this approach does not consider the actual fill-in, but instead uses an upper bound on the fill-in as a heuristic. An alternative interpretation is that it minimizes the number of updates to the active submatrix when the rank-one outer product update is made to the active submatrix upon eliminating the free variable. The use of doubly linked lists for both rows and columns provides a simple way to find the next pivot of lowest or low Markowitz-count subject to the stability threshold at each step and also allows simple insertion and deletion operations [8]. The process continues until a suitable pivot can no longer be found. The approach considered here uses an approximate minimum local fill-count at each step. A limited number of columns are searched in order of increasing column count [19] for a pivot satisfying the stability threshold for some scalar which produces a minimum fill score upon elimination of this pivot. The fill score is calculated as the amount of fill-in produced by using the pivot less the number of entries that would be eliminated from the active submatrix. An efficient procedure for finding such a pivot checks for stability of the potential pivot, and then computes the amount of fill-in caused by the stable potential pivot.

The elimination of free variables will often lead to a "dense" column in the constraint matrix, which will cause the Schur complement and its factor to contain many more non-zeroes. This can be dealt with as described next.

4.2 Handling dense columns

A column with a large number of non-zeros in the constraint matrix, relative to the other columns, leads to a considerably more dense Schur complement system than would be the case if the column did not contribute to the Schur complement system. For this reason, various approaches for reducing the impact of dense columns have been developed [3, 6]. The approach used here is based on Andersen's [6] modified Schur complement method but differs to allow dense columns associated with free variables to be treated explicitly, without any perturbations or modification to a conic variable. In contrast, Andersen's method will require any dense columns associated with free variables to be to be duplicated, increasing the amount of required work and memory requirements, as well as introducing the numerical difficulties known to be caused by splitting free variables.

From the augmented equations (2), partitioning $\mathbf{A} = [\mathbf{A}_D \mathbf{A}_S]$ along with $\mathbf{x}$ and $\mathbf{D}$ to match, and eliminating $\mathbf{x}_S$ gives

$$\begin{bmatrix} -\mathbf{D}_D & \mathbf{A}_D^T \\ \mathbf{A}_D & \mathbf{A}_S \mathbf{D}_S^{-1} \mathbf{A}_S \end{bmatrix} \begin{Bmatrix} \mathbf{x}_D \\ \mathbf{y} \end{Bmatrix} = \begin{Bmatrix} \mathbf{p}_D \\ \mathbf{q} + \mathbf{A}_S \mathbf{D}_S^{-1} \mathbf{p}_S \end{Bmatrix} \tag{5}$$

To determine $\mathbf{x}$ and $\mathbf{y}$ the process is as follows:

1. compute the Cholesky factorization $\mathbf{L}\mathbf{L}^T = \mathbf{A}_S \mathbf{D}_S^{-1} \mathbf{A}_S$;
2. solve $\mathbf{L}\mathbf{V} = \mathbf{A}_D$ for $\mathbf{V}$;
3. solve $\mathbf{L}\mathbf{r} = (\mathbf{q} + \mathbf{A}_S \mathbf{D}^{-1} \mathbf{p}_S)$ for $\mathbf{r}$;
4. solve $\left(\mathbf{D}_D + \mathbf{V}^T \mathbf{V}\right) \mathbf{x}_D = \mathbf{V}^T \mathbf{r} - \mathbf{q}_D$ for $\mathbf{x}_D$;
5. solve $\mathbf{L}^T \mathbf{y} = (\mathbf{r} - \mathbf{V}\mathbf{x}_D)$ for $\mathbf{y}$; and
6. solve $-\mathbf{D}_S \mathbf{x}_S = \mathbf{q}_S + \mathbf{A}_S^T \mathbf{y}$ for $\mathbf{x}_S$.

From the above it is apparent that an additional solve with the triangular factor plus the solution with the coefficient system is required. Note also that there is no guarantee that the factorization exists, but there is no more than a single dense column as a result of the elimination of free variables for these problems, with no dense columns in the original constraint matrices and no numerical difficulties were encountered in factorizing the matrix without modification.

4.3 Eliminating fixed variables subject to a second-order cone constraint

In some problems, fixed variables subject to second-order cone constraint occur. Obviously, if a fixed variable is free or linear, it may be substituted out of the problem immediately (if they are linear and fixed to be negative, the primal problem is infeasible). If, however, the fixed variable is part of a second-order cone constraint, then they may not be substituted out so easily. If the first variable associated with the kth second-order cone constraint is fixed, i.e. $a_{ij} x_j = b_i$ (that is, the ith row of $\mathbf{A}$ only has an entry in column j) and b_i is non-zero, then the Schur complement may be reduced in size.

Because the values of the unfixed variables associated with the kth second-order cone are not known, the variable may not be removed from the problem. The fixed variables constrained by a second-order cone may still be exploited, however, to reduce the computational effort required to compute the search direction [5]. For each of the fixed variables, they may be easily eliminated from every other constraint. Then symmetrically permuting (2) gives

$$\begin{bmatrix} -\mathbf{D}_{11} & -\mathbf{D}_{12} & \mathbf{0} & \mathbf{I} \\ -\mathbf{D}_{11} & -\mathbf{D}_{22} & \mathbf{A}_{12}^T & \mathbf{0} \\ \mathbf{0} & \mathbf{A}_{12} & \mathbf{0} & \mathbf{0} \\ \mathbf{I} & \mathbf{0} & \mathbf{0} & \mathbf{0} \end{bmatrix} \begin{Bmatrix} \mathbf{x}_1 \\ \mathbf{x}_2 \\ \mathbf{y}_1 \\ \mathbf{y}_2 \end{Bmatrix} = \begin{Bmatrix} \mathbf{p}_1 \\ \mathbf{p}_2 \\ \mathbf{q}_1 \\ \mathbf{q}_2 \end{Bmatrix} \tag{6}$$

where $\mathbf{A}_{12}$ are the constraints with no fixed variables (possibly containing dense columns). From the fourth block equation, it is obvious that $\mathbf{x}_1 = \mathbf{q}_2$. This can be substituted into the second and third block equations, leading to a system very similar to (2) which can then be solved for $\mathbf{x}_2$ and $\mathbf{y}_1$ (there is a well-known explicit inverse for $\mathbf{D}_{22}$ that can be computed just as cheaply as for $\mathbf{D}$ [5]). Finally, $\mathbf{y}_2$ can be found from the first block equation.

4.4 Effect of exploiting problem structure

The performance of the IPM with the free variable elimination, dense column handling and fixed variable routine is shown in Table 2. It should be noted that this option uses regularization instead of splitting free variables (see [17] for details). For comparison, the top commercial solver `Mosek` is included as a benchmark.

The reduction in runtime over all of the problems is 36%. This is, in part, due to the removal of most of the free variables in many of the problems which would otherwise hamper the IPM's performance and exhibited in the reduction in iteration counts on all problems except the larger tunnel heading lower bound problem, where the problem is solved to required tolerances for the first time. The square footing and tunnel heading problems had all but one of the free variables removed, with the one remaining being associated with a dense column in the constraint matrix. The other way in which the solver has benefitted is through a smaller factorization in terms of dimension and non-zero entries. The number of non-zero entries was reduced from 2% to 49% with an average of 16%, and the most benefit occuring on both forms of the upper bound problems. The reduction in dimension resulted from both the free variable elimination and from exploiting the fixed variables. In the square footing problems, a 17% reduction in the dimension of the lower bound problem and reductions of 44% and 50% on the upper bound and quadratic formulation upper bound problems, respectively.

In addition, the solver now compares favourably with `Mosek`. The solver spends, on average, an almost identical number of iterations as the commercial offering and is noticeably quicker in runtime. The number of non-zero entries in the factorization is still considerably better in `Mosek` across the set, suggesting that further improvement in the ordering may be possible, and possibly further free variable eliminations in some of the problems.

5 PARALLELIZATION OF THE LINEAR SOLVER

In the breakdown of the IPM solution time, over 75% of the total time is still spent in the factorization routine. While other areas are able to be parallelized and are likely to yield some improvement [4], the benefit is not expected to be significant for FELA problems. The main hurdle to be overcome for sparse linear equation solvers is ensuring that the dense subproblems are large enough to fully exploit the available performance of the hardware. Fortunately, many of the supernodes, especially as one moves towards the root of the elimination tree, are large enough to expect a major improvement if a machine's parallel computing resources can be exploited. This approach also enables pre-compiled and highly optimized BLAS libraries to be used on single machines. These parallel libraries have been tuned for the hardware and provide a high fraction of peak hardware performance.

The parallel Intel MKL 11.0.5 was used for the dense BLAS operations in the supernodal Cholesky factorization. To exploit the highly parallel capability of recent GPU hardware, a modified version of `CHOLMOD` (version 3.0.3) was used [11]. `CHOLMOD` was modified by discarding the functionality to restart the factorization when a non-positive pivot is encountered and the same modified DPOTF2 routine used above is called in place of the BLAS library routine. To benchmark the improvement in performance, the problem set was solved using `Mosek` with multiple threads. Note that it is not known what specific areas in `Mosek` have been parallelized, while the two parallel options considered are only exploiting parallelism in the factorization of the Schur complement system and subsequent solves, as well as any calls to the BLAS library. The results presented in this chapter summarize simulations performed on an Intel Xeon E5-1620 @ 3.60 GHz with 64GB RAM and an NVIDIA Tesla K20c GPU. The results are shown in Figure 2 and Table 3, while Figure 3 shows the growth in factor size and total solution time with problem dimension for the upper bound tunnel heading problem.

The two options compute the same objective values, with slight differences caused by rounding in the solver with dynamically scheduled accumulation in the GPU solver when computing the contribution from the child supernodes. As expected, the iteration counts are almost identical between the two solvers and `Mosek` computes similar objective values for the problems. The parallel version on a quad-core processor is approximately twice as fast as the sequential version which is consistent with the behaviour of `Mosek` (the parallel test machine yields a 10%-15% edge over the machine used for the sequential tests). The GPU option is more than twice as fast as the parallel CPU-only version, even with the additional time necessary to initialize and finalize the GPU functionality. Both solvers are faster than `Mosek` across the set, with the GPU version achieving 4.65× speedup. As can be seen in Figure 3(b), the GPU version's performance is better as the problems become larger, where the computation is able to better saturate the hardware's capabilities.

6 CONCLUSIONS

The development of a state-of-the-art interior point method has been described, achieving significant gains over the best available solvers. The judicious choice of available linear

Figure 2: Parallel performance.

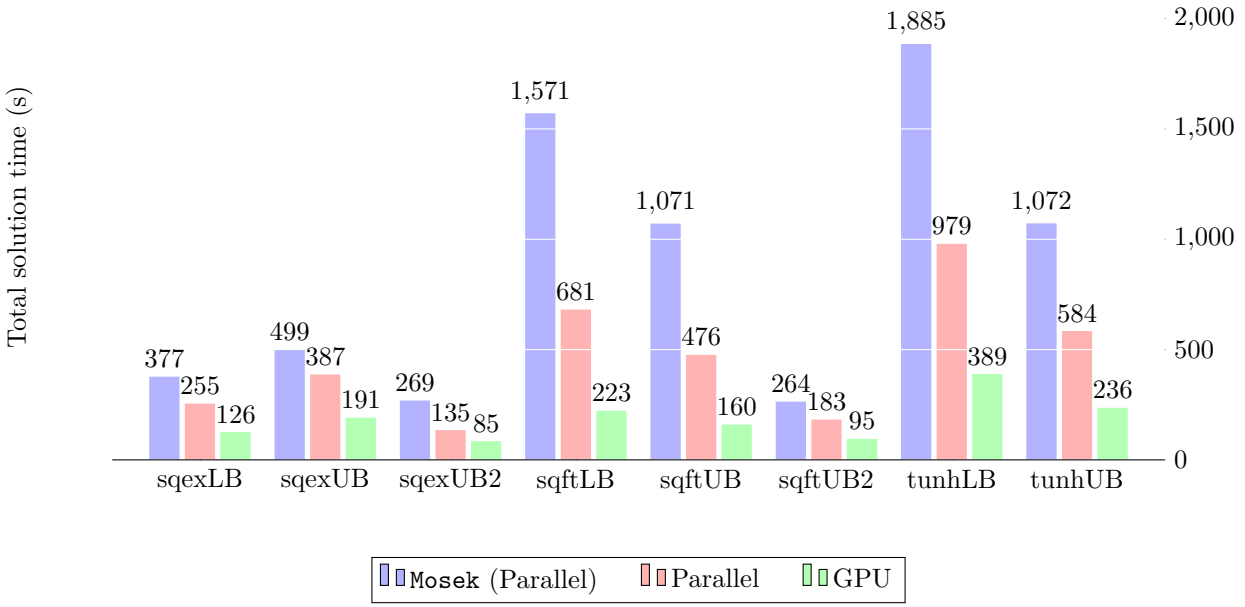
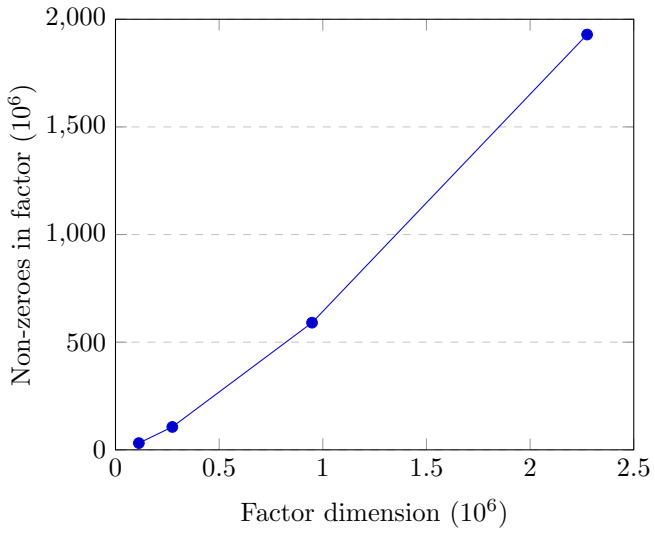
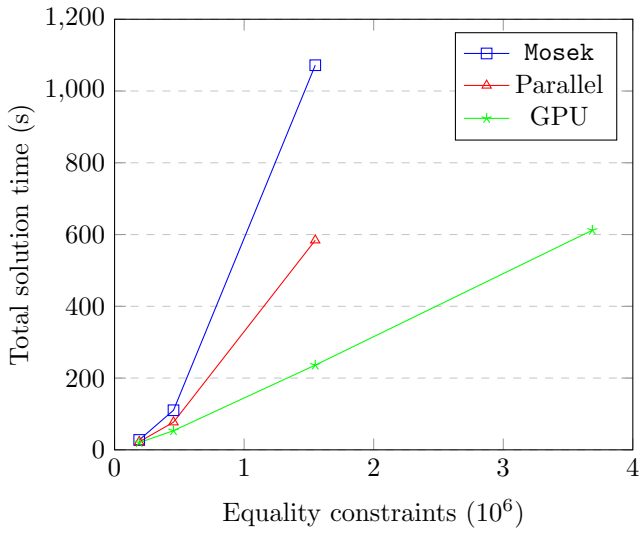


Figure 3: Upper bound tunnel heading problem with varying problem size.



(a) Number of non-zeroes in factorization



(b) Total solution time

Table 3: Performance of parallel solvers. t_P is the initialization, ordering and presolve time spent before the IPM starts.

	`Mosek` (Parallel)			Parallel			GPU		
Problem	*nit*	t_T	t_P	*nit*	t_T	t_P	*nit*	t_T	t_P
sqexLB	20	377	23	21	255	4	21	126	6
sqexUB	17	499	14	18	387	2	18	191	4
sqexUB2	24	269	14	16	135	2	16	85	3
sqftLB	20	1,571	51	24	681	6	24	223	7
sqftUB	23	1,071	27	21	476	4	21	160	6
sqftUB2	18	264	12	19	183	2	19	95	3
tunhLB	22	1,885	56	24	979	9	27	389	11
tunhUB	19	1,072	25	17	584	4	19	236	6
Total	332	8,011	285	327	4,305	44	332	1,914	68

equation solver methods and attention to the nature of finite element limit analysis problems with large numbers of free and fixed variables has led to an improvement in the reliability and efficiency with which these problems can be solved. This progress enables finite element limit analysis to remain a viable and attractive design tool as larger and more sophisticated problems are considered.

To continue improving the applicability of the solver, extending the solver to handle semidefinite cones will enable large three-dimensional Mohr-Coulomb analyses to be conducted. Elastoplastic analysis could also benefit from the development of a solver specifically for the problem formulation while utilizing the developments made here. Use of greater parallelism in the linear equation solver through multiple GPUs and/or clusters should also be considered for extremely large problems.

REFERENCES

[1] Amestoy, P.R., Davis, T.A. and Duff, I.S. An approximate minimum degree ordering algorithm. *SIAM J. Matrix Anal. Appl.* (1996) **17**:886–905.

[2] Andersen, E.D and Andersen, K.D. Presolving in linear programming. *Math. Program.* (1995) **71**:221–245.

[3] Andersen, E.D., Gondzio, J., Meszaros, C. and Xu, X. Implementation of interior point methods for large scale linear programming in Terlaky, T. (Ed.) *Interior Point Methods of Mathematical Programming*. Kluwer Academic Publishers, (1996) 189–252.

[4] Andersen, E.D. and Andersen, K.D. The MOSEK interior point optimizer for linear programming: an implementation of the homogeneous algorithm in Frenk, H., *et al.* (Eds.) *High Performance Optimization*. Springer, (2000) 197–232.

[5] Andersen, E.D., Roos, C. and Terlaky, T. On implementing a primal-dual interior point method for conic quadratic otimization. *Math. Program.* (2003) **95**:249–277.

[6] Andersen, K.D. A modified Schur-complement method for handling dense columns in interior point methods for linear programming. *ACM Trans. Math. Softw.* (1996) **22**:348–356.

[7] Drucker, D.C., Greenberg, H.J. and Prager, W. Extended limit design theorems for continuous media. *Q. Appl. Math.* (1952) **9**:381–389.

[8] Duff, I.S. MA28 - A set of Fortran subroutines for sparse unsymmetric linear equations. Report AERE R8730, HMSO, London.

[9] Duff, I.S. and Rutherford, C. MA57 - A new code for the solution of sparse symmetric definite and indefinite systems. *ACM Trans. Math. Softw.* (2004) **30**:118–144.

[10] Chen, W.F. *Limit Analysis and Soil Plasticity*. Elsevier, (1975).

[11] Chen, Y., Davis, T.A., Hager, W.W. and Rajamanickam, S. Algorithm 887: CHOLMOD, supernodal sparse Cholesky factorization and update/downdate. *ACM Trans. Math. Softw.* (2008) **35**.

[12] Gondzio, J. Presolve analysis of linear programs prior to applying an interior point method. *INFORMS J. Comput.* (1997) **9**:1–110.

[13] Karypis, G. and Kumar, V. A fast and high quality multilevel scheme for partitioning irregular graphs. *SIAM J. Sci. Comput.* (1998) **20**:359–392.

[14] Krabbenhøft, K., Lyamin, A.V. and Sloan, S.W. Formulation and solution of some plasticity problems as conic programs. *Int. J. Solids Struct.* (2007) **44**:1533–1549.

[15] Makrodimopoulos, A. and Martin, C.M. Lower bound limit analysis of cohesive-frictional materials using second-order cone programming. *Int. J. Numer. Anal. Methods Eng.* (2006) **66**:604-634.

[16] Mészáros, C. On free variables in interior point methods. *Optim. Methods Softw.* (1998) **4**:121–139.

[17] Podlich, N.C. *The Development of Efficient Algorithms for Large-Scale Finite Element Limit Analysis*. Ph.D. dissertation. University of Newcastle, (2018)

[18] Wright, S.J. *Primal-Dual Interior Point Methods*. SIAM, (1997).

[19] Zlatev, Z. On some pivotal strategies in Gaussian elimination by sparse technique. *SIAM J. Numer. Anal.* (1980) **17**:18–30.

XV International Conference on Computational Plasticity. Fundamentals and Applications
COMPLAS 2019
E. Oñate, D.R.J. Owen, D. Peric, M. Chiumenti & Eduardo de Souza Neto (Eds)

LIMIT ANALYSIS AND INF-SUP CONDITIONS ON CONVEX CONES

STANISLAV SYSALA*, JAROSLAV HASLINGER*, SERGEY REPIN†,‡

* Institute of Geonics of the Czech Academy of Sciences, (IGN)
Department of Applied Mathematics and Computer Sciences & Department IT4Innovations,
Studentska 1768, 708 00 Ostrava, Czech Republic
e-mails: stanislav.sysala@ugn.cas.cz, hasling@karlin.mff.cuni.cz, web page:
http://www.ugn.cas.cz

† St. Petersburg Department of V.A. Steklov Institute of Mathematics of the Russian
Academy of Sciences,
27 Fontanka, 191023 St.Petersburg, Russia
e-mail: repin@pdmi.ras.ru - web page: http://www.pdmi.ras.ru

‡ University of Jyväskylä,
Mattilanniemi 2, 40100 Jyväskylä, Finland
e-mail: sergey.s.repin@jyu.fi - web page: https://www.jyu.fi

Key words: perfect plasticity, limit analysis, conic optimization, inf-sup condition, finite element method, mesh adaptivity

Abstract. This paper is focused on analysis and reliable computations of limit loads in perfect plasticity. We recapitulate our recent results arising from a continuous setting of the so-called limit analysis problem. This problem is interpreted as a convex optimization subject to conic constraints. A related inf-sup condition on a convex cone is introduced and its importance for theoretical and numerical purposes is explained. Further, we introduce a penalization method for solving the kinematic limit analysis problem. The penalized problem may be solved by standard finite elements due to available convergence analysis using a simple local mesh adaptivity. This solution concept improves the simplest incremental method of limit analysis based on a load parametrization of an elastic-perfectly plastic problem.

1 INTRODUCTION

Stability of a structure is analyzed in many engineering areas. From this analysis, one can get various safety parameters that depend on the applied loads. One can also estimate failure zones describing collapse of the structure. Limit analysis is one of the main methods in stability assessment and is based on a parametrization of the load by a scalar factor. The related safety parameter is defined as a limit (ultimate) value of this factor. Beyond this value, the structure collapses. The limit load factor can be

determined by solving a specific optimization problem, which is called the limit analysis problem. This problem can be formulated either in terms of stresses (the static approach) or in terms of kinematic fields. The static and kinematic approaches are in mutual duality and lead to lower and upper bounds of the limit load factor, respectively. For literature survey, we refer to [6, 15].

Although limit analysis was originally developped as an analytical method [6], now it is widely used in computations. The simplest numerical scheme is based on solution of an elastoplastic problem by standard finite elements and incremental methods. However, such an approach may lead to an overestimation of the limit factor caused by locking effects. More sophisticated numerical schemes take into account two important features of limit analysis problems: possible discontinuities of kinematical fields along surfaces and the presence of conic contraints. The discontinuities influence a choice of finite elements or mixed finite elements. One can also choose one type of finite elements to find upper bounds of the limit factor and another type for lower bounds. Further, it is possible to transform the limit analysis problem to the second order cone programming, semidefinite programming or other conic optimization and to use convenient algorithms for such problems like interior point methods. Finally, mesh adaptivity is used to get the lower and upper bounds close each other or to visualize expected failure zones more accurately. For the numerical treatment, we refer to, e.g., [2, 12, 5, 11, 15].

This contribution arises from the classical theory of limit analysis which is based on perfect plasticity and the associative plastic flow rule. Although mathematical theory for continuous setting of the classical limit analysis problem is known for a long time, see, e.g., [21, 7, 13], some new results have appeared quite recently [8, 9, 14, 10]. We describe two of them and show their importance for numerical analysis and computations.

The first result is inspired by current computational experiences based on conic optimization, see the text above. We introduce a specific inf-sup condition related to the conic optimization, discuss its validity for basic yield criteria and show its consequences. In particular, by using this condition, one can prove the equivalence between the static and kinematic approaches and derive the analytical upper bounds of the limit load using functions which need not belong to the restrictive conic set. These bounds can be computable and used in a posteriori error analysis. The reader will find a systematic exposition in [14, 10].

The second result is inspired by incremental methods and construction of global working diagrams describing the material response during the loading process. To construct the global working diagram for continuous setting of the problem, we penalize the kinematic limit analysis problem (in order to release the conic constraints) and study the relation between the load factor λ and the penalty parameter α. The resulting $\lambda - \alpha$ curve is continuous, nondecreasing and tending to the limit load factor λ^* as $\alpha \to +\infty$. The parameter α may be also interpreted as the work of external forces. In addition, convergence results for standard finite elements and fixed α are available. The penalized problem may be solved by standard elastoplastic solvers and combined with a mesh adaptivity in order to estimate the limit factor λ^* from below within the kinematic approach. For a more detailed discussion and examples we refer to [8, 9].

This paper is organized as follows. Continuous setting the limit analysis problems and their duality relationship are summarized in Section 2. The respective inf-sup conditions on convex cones and their consequences are introduced in Section 3. The penalization of kinematic limit analysis problem is discussed in Section 4. A finite element discretization of the problem and its convergence analysis are presented in Section 5. This section also contains brief notes concerning used mesh adaptivity, solvers and implementation. Illustrative numerical examples to the presented solution concept can be found in recent papers [8, 9, 14, 10, 20, 16].

2 LIMIT ANALYSIS PROBLEM: CONTINUOUS SETTINGS

Let Ω be a bounded domain in $\mathbb{R}^3$ representing the investigated body. Its boundary $\partial\Omega$ is split into two nonempty parts Γ_D, Γ_N where the body is fixed and surface tractions $\boldsymbol{f} : \Gamma_N \to \mathbb{R}^3$ are prescribed, respectively. The volume forces are denoted as $\boldsymbol{F} : \Omega \to \mathbb{R}^3$. Both external forces $\boldsymbol{f}, \boldsymbol{F}$ are multiplied by a positive scalar factor $\lambda \mapsto \lambda\boldsymbol{f}, \lambda\boldsymbol{F}$.

By $\mathbb{M}^{3\times 3}_{sym}$, we denote the space of symmetric 3×3 matrices (second order tensors) equipped with the scalar product $\boldsymbol{\sigma} : \boldsymbol{\varepsilon} = \sum_{i,j} \sigma_{ij}\varepsilon_{ij}$ and the norm $|\boldsymbol{\varepsilon}|^2 = \boldsymbol{\varepsilon} : \boldsymbol{\varepsilon}$. This space will be used for Cauchy stress tensors and infinitesimal small strain tensors, respectively. We assume that the Cauchy stress tensor $\boldsymbol{\sigma}$ belongs to a closed, convex set $B \subset \mathbb{M}^{3\times 3}_{sym}$. This set is usually defined by a yield criterion and we let it independent of the space variable $\boldsymbol{x} \in \Omega$, for the sake of simplicity. Other assumptions on B will be specified in Section 3.

We use notation $\boldsymbol{\sigma}$ also for stress tensor fields, i.e. $\boldsymbol{\sigma} := \boldsymbol{\sigma}(\boldsymbol{x})$, $\boldsymbol{x} \in \Omega$. These fields belong to the space $\mathbb{S} := L^2(\Omega, \mathbb{M}^{3\times 3}_{sym})$ of Lebesgue integrable functions [21]. The set of statically admissible stress fields reads as

$$Q_\lambda = \{\boldsymbol{\sigma} \in \mathbb{S} \,|\, \ -\operatorname{Div}\boldsymbol{\sigma} = \lambda\boldsymbol{F} \ \text{ in } \Omega, \ \ \boldsymbol{\sigma}\boldsymbol{n} = \lambda\boldsymbol{f} \ \text{ on } \Gamma_N\}\,, \quad \lambda \geq 0.$$

where Div denotes the divergence operator, i.e. $(\operatorname{Div}\boldsymbol{\sigma})_i = \sum_j \partial\sigma_{i,j}/\partial x_j$, and $\boldsymbol{n}$ is the unit outward normal vector to Ω. The set of plastically admissible stress fields is defined as follows:

$$P_B = \{\boldsymbol{\sigma} \in \mathbb{S} \,|\, \ \boldsymbol{\sigma}(\boldsymbol{x}) \in B, \ \ \boldsymbol{x} \in \Omega\}\,.$$

The limit load factor λ^* is defined as the supremum over all λ, for which there exists simultaneously a statically and plastically admissible stress field:

$$\lambda^* := \sup\{\lambda \geq 0 \mid \text{ subject to } \exists\boldsymbol{\sigma} \in Q_\lambda \cap P_B\}. \tag{2.1}$$

Problem (2.1) represents the static principle of limit analysis. To derive its dual kinematic form, we introduce the space of kinematically admissible vector fields:

$$\mathbb{V} = \{\boldsymbol{v} \in W^{1,2}(\Omega, \mathbb{R}^3) \mid \ \boldsymbol{v} = \boldsymbol{0} \ \text{ on } \Gamma_D\},$$

where $W^{1,2}$ is standard notation for Sobolev spaces [21]. Within limit analysis, functions $\boldsymbol{v}$ rather represent velocity fields or displacement rates because displacement fields are unbounded as $\lambda \to \lambda^*$. The load functional reads as:

$$L(\boldsymbol{v}) = \int_\Omega \boldsymbol{F} \cdot \boldsymbol{v}\, dV + \int_{\Gamma_N} \boldsymbol{f} \cdot \boldsymbol{v}\, dS, \quad \boldsymbol{v} \in \mathbb{V}.$$

Using Green's theorem, one can rewrite the set Q_λ to a more convenient form [21, 7]:

$$Q_\lambda = \left\{ \boldsymbol{\sigma} \in \mathbb{S} \,|\, \int_\Omega \boldsymbol{\sigma} : \varepsilon(\boldsymbol{v})\, dV = \lambda L(\boldsymbol{v}) \quad \forall \boldsymbol{v} \in \mathbb{V} \right\}, \quad \lambda \geq 0,$$

where $\varepsilon(\boldsymbol{v}) = (\nabla \boldsymbol{v} + (\nabla \boldsymbol{v})^\top)/2$ stands for the linearized strain tensor related to $\boldsymbol{v} \in \mathbb{V}$ and ∇ denotes the gradient operator. Further, it is well-known that

$$\boldsymbol{\sigma} \in Q_\lambda \quad \text{if and only if} \quad \inf_{\substack{\boldsymbol{v} \in \mathbb{V} \\ L(\boldsymbol{v})=1}} \int_\Omega \boldsymbol{\sigma} : \varepsilon(\boldsymbol{v})\, dV = \lambda.$$

Using this equivalence, one can write the static principle as follows:

$$\lambda^* = \sup_{\boldsymbol{\sigma} \in P_B} \inf_{\substack{\boldsymbol{v} \in \mathbb{V} \\ L(\boldsymbol{v})=1}} \int_\Omega \boldsymbol{\sigma} : \varepsilon(\boldsymbol{v})\, dV. \tag{2.2}$$

The dual (kinematic) principle arises from (2.2) by interchanging sup and inf:

$$\zeta^* = \inf_{\substack{\boldsymbol{v} \in \mathbb{V} \\ L(\boldsymbol{v})=1}} J_\infty(\boldsymbol{v}), \quad J_\infty(\boldsymbol{v}) = \sup_{\boldsymbol{\sigma} \in P_B} \int_\Omega \boldsymbol{\sigma} : \varepsilon(\boldsymbol{v})\, dV. \tag{2.3}$$

Here, J_∞ denotes the dissipation potential which need not be finite on $\mathbb{V}$ and thus some additional constraints on $\boldsymbol{v}$ must be taken into account, see Sections 3.1 and 3.2. The value ζ^* is called the kinematic limit factor. Since sup inf $\leq$ inf sup, we have $\lambda^* \leq \zeta^*$, thus ζ^* is only an upper bound of the true limit factor λ^*. Therefore, to use the kinematic principle correctly, it is important to study when $\lambda^* = \zeta^*$. Such a result was proven for specific sets B, but not in general. In particular, $\lambda^* = \zeta^*$ holds for B representing the von Mises and Tresca yield criteria [21, 7] or for bounded B [9]. In [13, 10], this equality was established for the Drucker-Prager yield criterion provided that the slope of the Drucker-Prager cone is sufficiently small. In the next section, we summarize recent results from [10] enabling us to study this equality in a more general way.

It is also worth noticing that the space $\mathbb{V}$ is sufficient for the definition of the kinematic limit value ζ^* but $\mathbb{V}$ may not contain minimizers of (2.3), which in general belong to an extended space $BD(\Omega)$ (BD – bounded deformations) associated with the so–called relaxed variational problem, see [21, 7, 13] and the references therein. The space $BD(\Omega)$ contains vector valued functions, which may have jumps along some surfaces. In limit analysis, these discontinuities are associated with failure zones.

3 INF-SUP CONDITION FOR LIMIT ANALYSIS PROBLEM

From now on, we assume that the set B can be split as follows:

$$B = \mathcal{C} + A = \{\boldsymbol{\sigma} \in \mathbb{M}^{3\times 3}_{sym} \mid \boldsymbol{\sigma} = \boldsymbol{\sigma}_{\mathcal{C}} + \boldsymbol{\sigma}_A,\ \boldsymbol{\sigma}_{\mathcal{C}} \in \mathcal{C},\ \boldsymbol{\sigma}_A \in A\}, \quad A = B \cap \mathcal{C}^-, \tag{3.1}$$

where $\mathcal{C} \subset \mathbb{M}^{3\times 3}_{sym}$ is the largest cone with vertex at zero which is contained in B and A is a bounded subset of the polar cone

$$\mathcal{C}^- = \{\boldsymbol{\eta} \in \mathbb{M}^{3\times 3}_{sym} \mid \boldsymbol{\sigma}_{\mathcal{C}} : \boldsymbol{\eta} \leq 0 \ \ \forall \boldsymbol{\sigma}_{\mathcal{C}} \in \mathcal{C}\}.$$

This split of B is illustrated in Sections 3.1 and 3.2 below for the von Mises and Drucker-Prager yield criteria, respectively. Similarly, one can also split sets B represented by Tresca and Mohr-Coulomb yield criteria.

For B satisfying (3.1), the kinematic limit analysis problem can be written in a more convenient form. First, we have

$$\zeta^* = \inf_{\substack{\boldsymbol{v}\in\mathbb{V}\\ L(\boldsymbol{v})=1}} \int_\Omega j_\infty(\varepsilon(\boldsymbol{v}))\,dV, \quad j_\infty(\boldsymbol{\varepsilon}) = \sup_{\boldsymbol{\sigma}\in B} \boldsymbol{\sigma}:\boldsymbol{\varepsilon}. \tag{3.2}$$

Further, since

$$j_\infty(\boldsymbol{\varepsilon}) = \sup_{\boldsymbol{\tau}\in B} \boldsymbol{\tau}:\boldsymbol{\varepsilon} = \begin{cases} j^A_\infty(\boldsymbol{\varepsilon}), & \boldsymbol{\varepsilon}\in\mathcal{C}^-,\\ \\ +\infty, & \boldsymbol{\varepsilon}\notin\mathcal{C}^-, \end{cases} \qquad j^A_\infty(\boldsymbol{\varepsilon}) := \max_{\boldsymbol{\tau}\in A} \boldsymbol{\tau}:\boldsymbol{\varepsilon}, \quad \forall \boldsymbol{\varepsilon}\in\mathbb{M}^{3\times 3}_{sym}, \tag{3.3}$$

one can specify admissible kinematic fields in (3.2) by

$$\mathcal{K} = \{\boldsymbol{v}\in\mathbb{V} \mid \varepsilon(\boldsymbol{v})\in\mathcal{C}^- \text{ in } \Omega\}, \tag{3.4}$$

and write

$$\zeta^* = \inf_{\substack{\boldsymbol{v}\in\mathcal{K}\\ L(\boldsymbol{v})=1}} J^A_\infty(\boldsymbol{v}), \quad J^A_\infty(\boldsymbol{v}) := \int_\Omega j^A_\infty(\varepsilon(\boldsymbol{v}))\,dV. \tag{3.5}$$

Let us note that the functional J^A_∞ is finite-valued for any $\boldsymbol{v}\in\mathbb{V}$ unlike J_∞. Therefore, the setting (3.5) of the kinematic limit analysis problem is more transparent than the one in (2.3) or (3.2). The contraint set $\mathcal{K}$ has a cone property. It holds that $\boldsymbol{v}\in\mathcal{K}$ if and only if $\int_\Omega \boldsymbol{\sigma}:\varepsilon(\boldsymbol{v})\,dV \le 0$ for any $\boldsymbol{\sigma}\in P_{\mathcal{C}}$, where $P_{\mathcal{C}} := \{\boldsymbol{\sigma}\in\mathbb{S} \mid \boldsymbol{\sigma}(\boldsymbol{x})\in\mathcal{C},\ \ \boldsymbol{x}\in\Omega\}$.

The other and crucial assumption for the limit analysis problem is the satisfaction of the following inf-sup condition:

$$\inf_{\substack{\boldsymbol{\sigma}\in P_{\mathcal{C}}\\ \boldsymbol{\sigma}\neq 0}} \sup_{\substack{\boldsymbol{v}\in\mathbb{V}\\ \boldsymbol{v}\neq 0}} \frac{\int_\Omega \boldsymbol{\sigma}:\varepsilon(\boldsymbol{v})\,dV}{\|\boldsymbol{\sigma}\|_\Omega \|\nabla\boldsymbol{v}\|_\Omega} = c_* > 0, \tag{3.6}$$

where $\|\cdot\|_\Omega$ denotes the standard L^2-norm of scalar, vector or tensor variables. The inf-sup condition (3.6) is non-standard in literature because the infimum is taken over the cone $P_{\mathcal{C}}$ instead of a current linear space. We have the following fundamental result [10].

Theorem 3.1. *Let (3.1) and (3.6) be satisfied. Then $\lambda^* = \zeta^*$.*

It is well-known that inf-sup conditions are also important in numerical analysis, see, e.g., [1]. Here, we use the inf-sup value c_* to find computable majorants of $\lambda^* = \zeta^*$.

From (3.5), it follows that any function $\boldsymbol{v}\in\mathcal{K}$, $L(\boldsymbol{v}) = 1$, defines an upper bound $J^A_\infty(\boldsymbol{v}) \ge \zeta^*$. In general, it is practically impossible to find $\boldsymbol{v}\in\mathcal{K}$ to make this bound sufficiently sharp. Moreover, the constraint set $\mathcal{K}$ has to be approximated within the numerical process. Therefore, we have derived the following upper bound of ζ^*, which uses a larger class of functions than the ones from $\mathcal{K}$, see [14, 10].

Theorem 3.2. *Let (3.1) and (3.6) be satisfied. Then for any* $\boldsymbol{v} \in \mathbb{V}$ *such that* $L(\boldsymbol{v}) > c_*^{-1}\|L\|_*\|\Pi_{\mathcal{C}}\,\varepsilon(\boldsymbol{v})\|_\Omega$, *it holds:*

$$\zeta^* \leq \frac{J_\infty^A(\boldsymbol{v}) + c_*^{-1}\rho_A|\Omega|^{1/2}\|\Pi_{\mathcal{C}}\,\varepsilon(\boldsymbol{v})\|_\Omega}{L(\boldsymbol{v}) - c_*^{-1}\|L\|_*\|\Pi_{\mathcal{C}}\,\varepsilon(\boldsymbol{v})\|_\Omega}, \tag{3.7}$$

where $\|L\|_*$ *is the norm of the load functional,* ρ_A *is the diameter of the bounded set* A *and* Π_C *denotes the projection of* $\mathbb{M}^{3\times 3}_{sym}$ *onto* $\mathcal{C}$.

Let us note that Π_C and ρ_A are known explicitely for classical yield criteria. Computable or analytical bounds of $\|L\|_*$ are standard in literature focused on a posteriori error analysis. Computable majorants of c_*^{-1} have been derived in [14, 10]. Further, for $\boldsymbol{v} \in \mathcal{K}$, $L(\boldsymbol{v}) = 1$, we have $|\Pi_{\mathcal{C}}\,\varepsilon(\boldsymbol{v})| = 0$ and thus the bound on the right of (3.7) coincides with $J_\infty^A(\boldsymbol{v})$ mentioned above. In Section 5, we combine (3.7) with our solution concept in limit analysis.

3.1 Example 1 – von Mises yield criterion

The set B corresponding to the von Mises criterion is defined by

$$B = \left\{\boldsymbol{\sigma} \in \mathbb{M}^{3\times 3}_{sym} \mid \ |\boldsymbol{\sigma}^D| \leq \gamma\right\},$$

where $\gamma > 0$ represents the uniaxial yield stress, $\boldsymbol{\sigma}^D = \boldsymbol{\sigma} - \frac{1}{3}(\operatorname{tr}\boldsymbol{\sigma})\boldsymbol{I}$ stands for the deviatoric part of $\boldsymbol{\sigma}$, $\operatorname{tr}\boldsymbol{\sigma}$ denotes the trace of $\boldsymbol{\sigma}$ and $\boldsymbol{I}$ is the unit 3×3 matrix. This set is an unbounded cylinder aligned with the hydrostatic axis, see Figure 1.

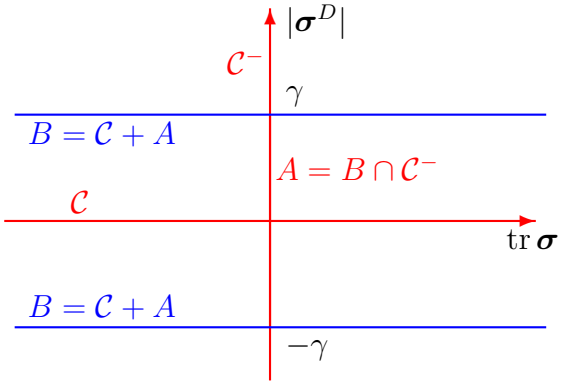


Figure 1: Decomposition of the set B for the von Mises yield criterion.

It is easy to see that B satisfies (3.1) with

$$\mathcal{C} = \{\boldsymbol{\sigma} \in \mathbb{M}^{3\times 3}_{sym} \mid \ \boldsymbol{\sigma} = q\boldsymbol{I},\ \ q \in \mathbb{R}\},\quad A = \{\boldsymbol{\eta} \in \mathcal{C}^- \mid \ |\boldsymbol{\eta}| \leq \gamma\},\quad \mathcal{C}^- = \{\boldsymbol{\eta} \in \mathbb{M}^{3\times 3}_{sym} \mid \ \operatorname{tr}\boldsymbol{\eta} = 0\}.$$

Hence, we arrive at the following kinematic limit analysis problem:

$$\zeta^* = \inf_{\substack{\boldsymbol{v}\in\mathcal{K}\\ L(\boldsymbol{v})=1}} \int_\Omega \gamma|\varepsilon^D(\boldsymbol{v})|\,dV, \quad \mathcal{K} = \{\boldsymbol{v} \in \mathbb{V} \mid \operatorname{div}\boldsymbol{v} = 0 \ \text{ in } \ \Omega\}.$$

Further, (3.6) becomes the well-known inf-sup condition used in incompressible media problems:

$$\inf_{\substack{q\in L^2(\Omega)\\ q\neq 0}} \sup_{\substack{\boldsymbol{v}\in\mathbb{V}\\ \boldsymbol{v}\neq 0}} \frac{\int_\Omega q\,\mathrm{div}\,\boldsymbol{v}\,dV}{\|q\|_\Omega \|\nabla \boldsymbol{v}\|_\Omega} = c_\Omega > 0. \tag{3.8}$$

It is easy to see that $c_\Omega = \sqrt{3}c_*$ for the von Mises yield criterion, where c_* is from (3.6). This inf-sup condition holds if the body is fixed only on a part of the boundary (as assumed in Section 2). Nevertheless, the equality $\lambda^* = \zeta^*$ holds even if $\partial\Omega = \Gamma_D$, see [21, 7, 14]. In [14] and the references therein, there are discussed ways how to get computable majorants of c_Ω^{-1}. Finally, the upper bound (3.7) holds for the von Mises yield criterion with $\rho_A = \gamma$ and $\|\Pi_{\mathcal{C}}\varepsilon(\boldsymbol{v})\|_\Omega = \frac{1}{\sqrt{3}}\|\mathrm{div}\,\boldsymbol{v}\|_\Omega$.

3.2 Example 2 – Drucker-Prager yield criterion

The set B corresponding to the Drucker-Prager yield criterion is defined by

$$B := \left\{\boldsymbol{\sigma}\in\mathbb{M}^{3\times 3}_{sym} \mid\ |\boldsymbol{\sigma}^D| + \frac{a}{3}\mathrm{tr}\,\boldsymbol{\sigma} \le \gamma\right\}, \quad a,\gamma > 0.$$

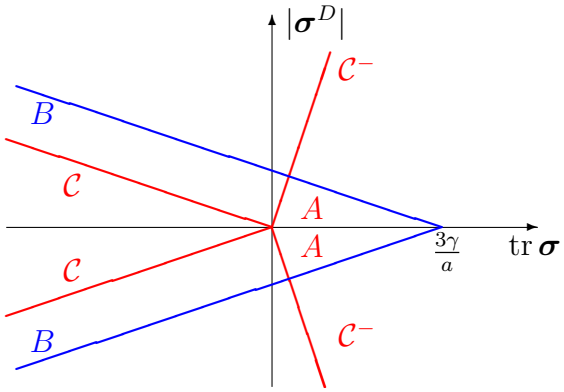


Figure 2: Decomposition of the set B for the Drucker-Prager yield criterion.

It is the cone with vertex at $\frac{\gamma}{a}\boldsymbol{I}$, see Figure 2. Again, B satisfies (3.1) with

$$\mathcal{C} = \{\boldsymbol{\sigma}\in\mathbb{M}^{3\times 3}_{sym} \mid\ |\boldsymbol{\sigma}^D| + \frac{a}{3}\mathrm{tr}\,\boldsymbol{\sigma} \le 0\}, \quad \mathcal{C}^- = \{\boldsymbol{\eta}\in\mathbb{M}^{3\times 3}_{sym} \mid\ \mathrm{tr}\,\boldsymbol{\eta} \ge a|\boldsymbol{\eta}^D|\}, \quad A = B\cap\mathcal{C}^-.$$

Hence, the kinematic limit analysis problem reads as follows:

$$\zeta^* = \inf_{\substack{\boldsymbol{v}\in\mathcal{K}\\ L(\boldsymbol{v})=1}} \int_\Omega \frac{\gamma}{a}\mathrm{div}\,\boldsymbol{v}\,dV, \quad \mathcal{K} = \{\boldsymbol{v}\in\mathbb{V} \mid\ \mathrm{div}\,\boldsymbol{v} \ge a|\varepsilon^D(\boldsymbol{v})| \ \text{ in } \Omega\}.$$

It can be shown that the inf–sup condition (3.6) is valid under the additional assumption on the material parameter a defining the slope of the Drucker-Prager cone [10]:

$$a < (c_\Omega^{-2} - 1/3)^{-1/2},$$

where c_Ω is the inf-sup value from (3.8). Thus (3.6) and $\zeta^* = \lambda^*$ hold for a sufficiently small slope of the Drucker-Prager cone. If the body is fixed on the whole boundary then (3.6) does not hold. In this case, $\mathcal{K} = \{0\}$ and $\lambda^* = \zeta^* = +\infty$ as was shown in [13].

Computable majorants of c_*^{-1} use the bounds of the inf-sup value c_Ω, see [10]. Finally, the upper bound (3.7) for the Drucker-Prager yield criterion holds with $\rho_A = \frac{\gamma}{\alpha}\sqrt{3}$ and

$$\Pi_{\mathcal{C}}\boldsymbol{\varepsilon} = \begin{cases} \boldsymbol{\varepsilon}, & \boldsymbol{\varepsilon} \in \mathcal{C}, \\ 0, & \boldsymbol{\varepsilon} \in \mathcal{C}^-, \\ \frac{a|\boldsymbol{\varepsilon}^D| - \operatorname{tr}\boldsymbol{\varepsilon}}{3+a^2}\left(a\frac{\boldsymbol{\varepsilon}^D}{|\boldsymbol{\varepsilon}^D|} - I\right), & \boldsymbol{\varepsilon} \notin \mathcal{C} \cup \mathcal{C}^-. \end{cases} \tag{3.9}$$

4 PENALIZATION OF KINEMATIC LIMIT ANALYSIS PROBLEM

This section summarizes the results published in [8, 9, 18]. Recall that

$$\zeta^* = \inf_{\substack{\boldsymbol{v}\in\mathbb{V} \\ L(\boldsymbol{v})=1}} \int_\Omega j_\infty(\varepsilon(\boldsymbol{v}))\,dV, \quad j_\infty(\boldsymbol{\varepsilon}) = \sup_{\boldsymbol{\sigma}\in B} \boldsymbol{\sigma} : \boldsymbol{\varepsilon}, \tag{4.1}$$

where j_∞ may be infinite for some $\boldsymbol{v} \in \mathbb{V}$. One can penalize the problem (4.1) as follows:

$$\tilde{\psi}(\alpha) := \inf_{\substack{\boldsymbol{v}\in\mathbb{V} \\ L(\boldsymbol{v})=1}} \int_\Omega j_\alpha(\varepsilon(\boldsymbol{v}))\,dx, \quad j_\alpha(\boldsymbol{\varepsilon}) = \max_{\boldsymbol{\sigma}\in B}\{\boldsymbol{\sigma} : \boldsymbol{\varepsilon} - \frac{1}{2\alpha}\mathbb{C}^{-1}\boldsymbol{\sigma} : \boldsymbol{\sigma}\}, \tag{4.2}$$

where $\alpha > 0$ is the penalization parameter and $\mathbb{C}$ is a fourth order tensor representing the Hooke law (known from elasticity). Let us note that limit analysis and also the results summarized below are independent of elastic material parameters defining $\mathbb{C}$.

It holds that j_α is finite-valued, convex, smooth and $j_\alpha \to j_\infty$ pointwisely in $\mathbb{M}^{3\times3}_{sym}$ as $\alpha \to +\infty$. It is readily seen that $j_\alpha \le j_\infty$ so that $\tilde{\psi}(\alpha) \le \zeta^*$ for any $\alpha > 0$. In addition, the function $\tilde{\psi}$ is continuous, nondecreasing and $\lim_{\alpha\to+\infty} \tilde{\psi}(\alpha) = \lambda^*$. Therefore, the values $\tilde{\psi}(\alpha)$ define lower bounds of the static limit factor λ^* although we used the kinematic principle. For smaller values of α, the function $\tilde{\psi}$ is usually linear and $\lim_{\alpha\to0} \tilde{\psi}(\alpha) = 0$. The properties of $\tilde{\psi}$ are depicted in Figure 3.

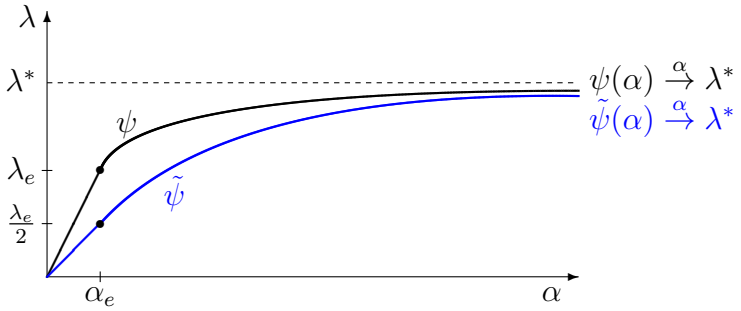


Figure 3: Properties of the functions $\tilde{\psi}$ and ψ. The value α_e is the threshold of purely elastic response.

Let $\boldsymbol{u}_\alpha$ denote a minimizer to the problem (4.2). To simplify the next presentation, we assume that $\boldsymbol{u}_\alpha$ belongs to $\mathbb{V}$ although, in general, $\boldsymbol{u}_\alpha$ belongs to the space $BD(\Omega)$ mentioned above. For a more general treatment, we refer to [8].

Next, we show that the penalized problem (4.2) is closely related to a simplified static version of the elastic-perfectly plastic problem (Hencky's problem) and to incremental limit analysis. To this end, we denote j as the function j_α for $\alpha = 1$. Clearly, $j_\alpha(\boldsymbol{\varepsilon}) = \frac{1}{\alpha} j(\alpha\boldsymbol{\varepsilon})$ for any $\alpha > 0$ and any $\boldsymbol{\varepsilon} \in \mathbb{M}^{3\times 3}_{sym}$. Let $\Pi_B \colon \mathbb{M}^{3\times 3}_{sym} \to \mathbb{M}^{3\times 3}_{sym}$ stand for the (Fréchet) derivative of j. The function Π_B represents the elastic-perfectly plastic constitutive operator, i.e., the projection of the elastic stress tensor $\mathbb{C}\boldsymbol{\varepsilon}$ onto the set B of admissible stress tensors. Notice that the value $\Pi_B(\alpha\boldsymbol{\varepsilon})$ is the derivative of j_α at $\boldsymbol{\varepsilon}$. Then (4.2) can be written as the following saddle-point problem: *given* $\alpha > 0$, *find* $\boldsymbol{u}_\alpha \in \mathbb{V}$ *and* $\lambda_\alpha \in \mathbb{R}$ *such that* $L(\boldsymbol{u}_\alpha) = 1$ *and*

$$\int_\Omega \Pi_B(\alpha\varepsilon(\boldsymbol{u}_\alpha)) : \varepsilon(\boldsymbol{v})\, dV = \lambda_\alpha L(\boldsymbol{v}) \quad \forall \boldsymbol{v} \in \mathbb{V}. \tag{4.3}$$

The above mentioned elastic-perfectly plastic problem reads as: *given* $\lambda > 0$, *find* $\boldsymbol{u}_\lambda \in \mathbb{V}$*:*

$$\int_\Omega \Pi_B(\varepsilon(\boldsymbol{u}_\lambda)) : \varepsilon(\boldsymbol{v})\, dV = \lambda L(\boldsymbol{v}) \quad \forall \boldsymbol{v} \in \mathbb{V}. \tag{4.4}$$

We see that the equations (4.3) and (4.4) are almost identical. In particular, if $\lambda = \lambda_\alpha$ then $\boldsymbol{u}_\lambda = \alpha \boldsymbol{u}_\alpha$. From this, we see that the displacement field $\boldsymbol{u}_\lambda$ is unbounded as $\lambda \to \lambda^*$, i.e. $\alpha \to +\infty$. In [8], it was shown that there exists a unique solution component λ_α in (4.3) and $\lambda_\alpha = \int_\Omega \Pi_B(\alpha\varepsilon(\boldsymbol{u}_\alpha)) : \varepsilon(\boldsymbol{u}_\alpha)\, dV \geq 0$. Therefore, one can introduce the function $\psi : \alpha \mapsto \lambda_\alpha$. It holds that $\psi \geq \tilde{\psi}$. In addition, ψ has analogous properties as $\tilde{\psi}$, i.e. it is a continuous, nondecreasing function satisfying $\psi(0) = 0$ and $\lim_{\alpha\to+\infty} \psi(\alpha) = \lambda^*$, see Figure 3.

Since the function ψ transforms the penalization parameter α into the load factor λ it describes the material response during loading. The inverse mapping $\lambda \mapsto \alpha$ is defined by the relation $\alpha = L(\boldsymbol{u}_\lambda)$. Therefore, the penalty parameter α may be interpreted as the work of external forces. The knowledge of ψ enables us to control the loading process indirectly through α. This idea was originally introduced in [19, 3] for a discrete setting of the problem.

5 DISCRETIZATION AND SOLVERS

The penalized problem (4.2) is solved by standard finite elements which are conforming with respect to $\mathbb{V}$. Let $\mathbb{V}_h$ be the corresponding finite-dimensional subspace of $\mathbb{V}$ and $\boldsymbol{u}_{h,\alpha}$, ψ_h, λ_h^* and ζ_h^* be the discrete counterparts of u_α, ψ, λ^*, and ζ^*, respectively.

We have $\lambda_h^* = \zeta_h^*$. Further, ψ_h is a continuous and nondecreasing function satisfying $\psi_h(0) = 0$ and $\lim_{\alpha\to+\infty} \psi_h(\alpha) = \lambda_h^*$. If we consider a regular system of finite element partitions of Ω then $\psi_h(\alpha) \to \psi(\alpha)$ as $h \to 0_+$ for any $\alpha > 0$. Hence, $\lambda_h^* \geq \lambda^* \geq \psi(\alpha)$ for any $\alpha > 0$ and $h > 0$. These results are depicted in Figure 4 and were proven in [8, 9, 18]. We can see that the standard discretization may lead to reliable results if we fix the parameter α and use a mesh adaptivity. On the other hand, the discrete limit value λ_h^* can significantly overestimate λ^* since convergence $\lambda_h^* \to \lambda^*$ is not guaranteed.

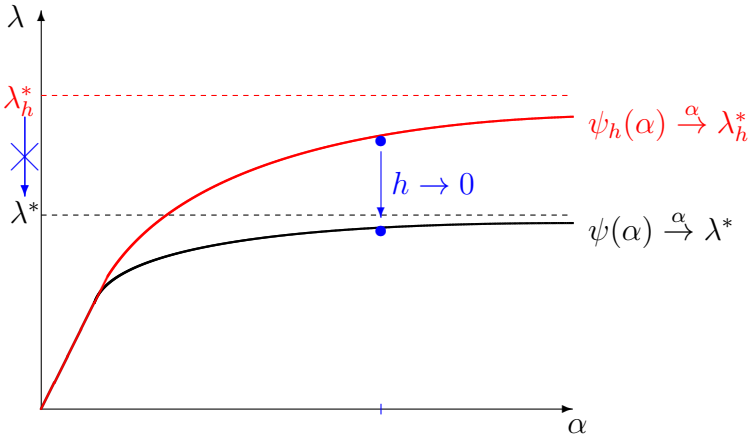


Figure 4: Properties of the functions ψ_h and ψ.

If a positive lower estimate of the inf-sup value c_* is available, one can use the upper bound (3.7) of ζ^* with $\boldsymbol{v} := \boldsymbol{u}_{h,\alpha}$:

$$\lambda^* = \zeta^* \leq \frac{J^A_\infty(\boldsymbol{u}_{h,\alpha}) + c_*^{-1}\rho_A|\Omega|^{1/2}\|\Pi_{\mathcal{C}}\,\varepsilon(\boldsymbol{u}_{h,\alpha})\|_\Omega}{L(\boldsymbol{u}_{h,\alpha}) - c_*^{-1}\|L\|_*\|\Pi_{\mathcal{C}}\,\varepsilon(\boldsymbol{u}_{h,\alpha})\|_\Omega}. \tag{5.1}$$

This bound is well-defined for larger values of α since $\|\Pi_{\mathcal{C}}\,\varepsilon(\boldsymbol{u}_{h,\alpha})\|_\Omega \to 0$ as $\alpha \to +\infty$. In addition, it can be sharp and detect a possible overestimation of λ^*_h as was shown in [14, 10, 20].

In limit analysis, the process of failure is usually localized in a vicinity of a surface discontinuity while rigid deformations appear far from the failure. Therefore, it is quite natural to use mesh adaptive techniques, which can significantly reduce the number of unknowns and improve accuracy of the results. Using a mesh adaptivity, one can also achieve convergence $\psi_h(\alpha) \to \psi(\alpha)$ as $h \to 0_+$ in order to receive a lower bound of λ^*.

We use the following simple strategy of mesh adaptation. First, a sufficiently large value α is found by continuation on the coarsest mesh and then this value is fixed. For the mesh level $k = 0, 1, 2, \ldots$, we find the solution $\boldsymbol{u}_k$. Then $\int_e j^A_\infty(\varepsilon(\boldsymbol{u}_k))\,dV$ is evaluated for any element e and 10% of elements with the highest values is selected. Alternatively, one can also use the criterion based on the values $\int_e j_\alpha(\varepsilon(\boldsymbol{u}_k))\,dV$.

The discrete version of the penalized problem (4.2) is solved by a variant of the semismooth Newton method (SSNM) proposed in [3]. SSNM may be interpreted as a sequential quadratic programming in context of this optimization problem. In order to receive convergence for large α, SSNM is supplied with damping and/or regularized stiffness matrices. Continuation using α also improves convergence. For more details, we refer to [19, 3, 9, 17].

The presented numerical strategy is implemented in Matlab within our codes. Tangential stiffness matrices and load vectors are assembled by vectorized codes described in [4]. These codes are available for P1, P2, Q1 and Q2 elements in 2D and 3D. Illustrative numerical examples for various yield criteria and benchmarks are presented in recent papers [8, 9, 14, 17, 10, 20, 16]. In particular, [16] illustrates that the solution concept

works well even for composite materials with the von Mises yield criterion for one material component and the Drucker-Prager yield criterion for another one.

6 CONCLUSION

Two recent theoretical results in classical limit analysis have been presented: the related inf-sup condition and its importance, and the existence of a continuous loading path in perfect plasticity. Using these results, we have proposed a solution concept based on a penalization of the kinematic limit analysis problem. We have shown that the penalization method may be interpreted as an improved incremental approach and can be solved similarly as standard elastoplastic problems. Therefore, our solution strategy is convenient for scientists familiar with current computational plasticity. This strategy can be realized within commercial softwares which are not specialized in limit analysis.

Acknowledgement: This work was supported by the Czech Science Foundation (GAČR) through project No. 19-11441S.

REFERENCES

[1] Boffi, D., Brezzi, F., and Fortin, M. *Mixed finite element methods and applications.* Springer, Heidelberg (2013).

[2] Borges, L.A., Zouain, N., Costa, C., et al. An adaptive approach to limit analysis. *Int. J. Solids Struct.* (2001) **38**: 1707–1720.

[3] Cermak, M., Haslinger, J., Kozubek, T. and Sysala, S. Discretization and numerical realization of contact problems for elastic-perfectly plastic bodies. PART II – numerical realization. *ZAMM - Z. Angew. Math. Mech.* (2015) **95**: 1348–1371.

[4] Čermák, M., Sysala, S. and Valdman, J. Efficient and flexible MATLAB implementation of 2D and 3D elastoplastic problems. *Applied Mathematics and Computation* (2019) **355**: 595–614.

[5] Ciria, H., Peraire, J. and Bonet, J. Mesh adaptive computation of upper and lower bounds in limit analysis. *Int. J. Numer. Methods Engng* (2008) **75**: 899–944.

[6] Chen, W.F. and Liu, X. *Limit analysis in soil mechanics.* Elsevier, 2012.

[7] Christiansen, E. Limit analysis of colapse states. In: Ciarlet, P.G. and Lions, J.L. (eds), *Handbook of Numer. Anal.*, Vol IV, Part 2, North-Holland (1996), 195–312.

[8] Haslinger, J., Repin, S. and Sysala, S. A reliable incremental method of computing the limit load in deformation plasticity based on compliance: Continuous and discrete setting. *Journal of Computational and Applied Mathematics* (2016) **303**: 156–170.

[9] Haslinger, J., Repin, S. and Sysala, S. Guaranteed and computable bounds of the limit load for variational problems with linear growth energy functionals. *Applications of Mathematics* (2016) **61**: 527–564.

[10] Haslinger, J., Repin, S. and Sysala, S. Inf-sup conditions on convex cones and applications to limit load analysis. *Mathematics and Mechanics of Solids* (2019), on-line available at https://doi.org/10.1177/1081286519843969.

[11] Krabbenhoft, K., Lyamin, A. V. and Sloan, S.W. Three-dimensional Mohr–Coulomb limit analysis using semidefinite programming. *Communications in Numerical Methods in Engineering*, (2008) **24**: 1107–1119.

[12] Makrodimopoulos, A. and Martin, C.M. Upper bound limit analysis using simplex strain elements and second-order cone programming. *Int. J. Numer. Analyt. Methods Geomech.* (2007) **31**: 835–865.

[13] Repin, S. and Seregin, G. Existence of a weak solution of the minimax problem arising in Coulomb-Mohr plasticity. *Nonlinear evolution equations*, 189–220, Amer. Math. Soc. Transl. (2), **164**, Amer. Math. Soc., Providence, RI, (1995).

[14] Repin, S., Sysala, S. and Haslinger, J. Computable majorants of the limit load in Hencky's plasticity problems. *Comp. & Math. with Appl.* (2018) **75**: 199–217.

[15] Sloan, S. Geotechnical stability analysis, *Géotechnique* (2013) **63**, 531–572.

[16] Sysala, S., Blaheta, R., Kolcun, A., Sčučka, J., Souček, K. and Pan, P. Computation of Composite Strengths by Limit Analysis. *Key Engineer. Mat.* (2019). Accepted.

[17] Sysala, S., Čermák, M., and Ligurský, T. Subdifferential-based implicit return-mapping operators in Mohr-Coulomb plasticity. *ZAMM - Z. Angew. Math. Mech.* (2017) **97**: 1502–1523.

[18] Sysala, S. and Haslinger, J. Truncation and Indirect Incremental Methods in Hencky's Perfect Plasticity. In: *Mathematical Modelling in Solid Mechanics*. Springer, Singapore, (2017), 265–284.

[19] Sysala, S., Haslinger, J., Hlaváček, I. and Čermák, M. Discretization and numerical realization of contact problems for elastic-perfectly plastic bodies. PART I – discretization, limit analysis. *ZAMM - Z. Angew. Math. Mech.* (2015) **95**: 333–353.

[20] Sysala, S., Haslinger, J. and Repin, S. Reliable computation and local mesh adaptivity in limit analysis. In *Programs and Algorithms of Numerical Mathematics 19*, Institute of Mathematics of the Czech Academy of Sciences, Prague (2019), 149–158.

[21] Temam, R. *Mathematical Problems in Plasticity*. Gauthier-Villars, Paris, (1985).

XV International Conference on Computational Plasticity. Fundamentals and Applications
COMPLAS 2019
E. Oñate, D.R.J. Owen, D. Peric, M. Chiumenti & Eduardo de Souza Neto (Eds)

A NOTE ON MODELING SOME CLASSES OF NONLINEAR SYSTEMS FROM DATA

ION VICTOR GOSEA[*] AND ATHANASIOS C. ANTOULAS[*,†]

[*] Data-Driven System Reduction and Identification Group
Max Planck Institute for Dynamics of Complex Technical Systems
Sandtorstrasse 1, 39106 Magdeburg, Germany,
e-mail: gosea@mpi-magdeburg.mpg.de, web page: https://www.mpi-magdeburg.mpg.de/dri

[†] Department of Electrical and Computer Engineering
Rice University, 6100 Main St, Houston, Texas, USA, and Baylor College of Medicine
e-mail: aca@rice.edu, web page: https://www.ece.rice.edu

Key words: Nonlinear Systems, Data-driven, Reduced-order Modeling, System Identification

Abstract. We study the modeling of bilinear and quadratic systems from measured data. The measurements are given by samples of higher order frequency response functions. These values can be identified from the corresponding Volterra series of the underlying nonlinear system. We test the method for examples from structural dynamics and chemistry.

1 INTRODUCTION

With the ever-increasing supply of available measurements in the study of physical processes, the need for incorporating data in the modeling process has steadily grown. The main challenge is to use measured data to construct models that can accurately identify the underlying dynamics. Sometimes, the models have large dimensions and are not fitted for fast simulation.

Model reduction is commonly viewed as a methodology used for reducing the computational complexity of large scale complex models in numerical simulations. The goal is to construct a smaller system with the same structure and similar response characteristics as the original. For an overview of model reduction methods, we refer the reader to [1, 5].

The Loewner Framework (LF) is a data-driven identification and reduction technique that uses measured or computed data to construct reliable surrogate models. For a comprehensive tutorial paper on LF for linear systems, we refer the reader to [3]. The framework has been extended and applied to classes of mildly nonlinear systems, such as bilinear systems in [2], and quadratic-bilinear (QB) systems in [7]. These classes are of interest since nonlinear systems can be reformulated, without any approximation, as QB systems (provided that the nonlinearities are analytical).

The Volterra series is a mathematical description of the input/output relationship, valid for a wide class of nonlinear systems. It is based on a functional power series expansion. Applications of this method range in areas such as fluid dynamics, electrical engineering, mechanical engineering or biomedical engineering.

Data-driven modeling of nonlinear systems has been an active field of research over the years. However, there are still many open challenges which can not be addressed by the classical linear

identification theory. One of these issues is choosing a model structure from the many possible classes, without prior knowledge of the system.

In this work, we assume that the unknown nonlinear system to be modeled has bilinear or quadratic nonlinearities. For these classes of mild nonlinear systems, one can directly compute generalized transfer functions in the frequency domain. This is done by means of the harmonic probing method by identifying the leading terms of the Volterra series.

Using the Loewner framework, we first fit a linear model that matches samples of the first (linear) transfer function. Then, from samples of the second transfer function (that includes the nonlinear behavior), we are able to fit appropriate bilinear or quadratic terms. The data required for this procedure can be estimated from direct numerical simulations.

The paper is structured as follows; after the introduction in Section 1, we give a brief overview on the Volterra series in Section 2. Then, Section 3 introduces linear systems and an overview of the Loewner framework. Afterward, Sections 4 and 5 include the derivations of transfer function for bilinear, and respectively, for quadratic systems. The numerical examples are presented Section 6, while Section 7 concludes the paper.

2 VOLTERRA SERIES

The Volterra series theory describes the relationship between the control input and the observed output of a dynamical system whose dynamics is characterized by nonlinear behavior.

It provides an explicit formulation through the so-called higher-order Volterra kernels. In time-domain, the mappings are given vy the higher-order impulse response functions (HOIRFs), while in the frequency domain, we have the higher-order frequency response functions (HOFRFs). The latter quantities can be derived from the HOIRFs by applying a generalized Fourier or Laplace transformation. A method for deriving the analytical expressions of the HOFRFs was proposed in [4]. This has since been referred to as the harmonic (input) probing method for continuous-time nonlinear systems. It is based on the fact that a harmonic input must result in a harmonic output.

Considerable amount of work has been employed into this direction in the 80's. We mention the books [11, 12] which represent exhaustive collections of theoretical results related to the Volterra series. Afterwards, contributions were made on applications in certain fields such as structural dynamics (see [14]), and in signal processing (see [6]).

The input-output relationship for a wide class of nonlinear systems can be expressed as a Volterra series (here $\mathbf{u}(t)$ is the input while $\mathbf{y}(t)$ the output)

$$\mathbf{y}(t) = \sum_{n=1}^{\infty} \mathbf{y}_n(t), \qquad \mathbf{y}_n(t) = \int_{-\infty}^{\infty} \cdots \int_{-\infty}^{\infty} \mathbf{h}_n(\tau_1, \cdots, \tau_n) \prod_{i=1}^{n} \mathbf{u}(t-\tau_i) d\tau_i. \tag{1}$$

In (1), the multivariate function $\mathbf{h}_n(\tau_1, \cdots, \tau_n)$ is the nth-order Volterra kernel or generalized impulse response function of order n. The frequency domain description of this kernel can be found by applying a generalized multidimensional Fourier transform. Hence, one can write

$$\mathbf{H}_n(j\omega_1, \cdots, j\omega_n) = \int_{-\infty}^{\infty} \cdots \int_{-\infty}^{\infty} \mathbf{h}_n(\tau_1, \cdots, \tau_n) e^{-j(\omega_1\tau_1 + \cdots + \omega_n\tau_n)} d\tau_1 \cdots d\tau_n. \tag{2}$$

In (2), the multivariate function $\mathbf{H}_n(j\omega_1, \cdots, j\omega_n)$ is the nth-order generalized transfer function. For example, if $n = 1$, then $\mathbf{H}_1$ is the linear transfer function derived in Section 3.

The harmonic (input) probing method consists in applying periodic functions as input in the following format

$$\mathbf{u}(t) = \sum_{\ell=1}^{p} \alpha_\ell e^{j\omega_\ell}. \tag{3}$$

Then, by replacing this input into (1), one can write the nth element of the output, i.e. $\mathbf{y}_n$ as

$$\mathbf{y}_n(t) = \sum_{\ell_1=1}^{p} \cdots \sum_{\ell_n=1}^{p} \alpha_{\ell_1} \cdots \alpha_{\ell_p} \mathbf{H}_n(j\omega_{\ell_1}, \ldots, j\omega_{\ell_n}) e^{j(\omega_{\ell_1}+\cdots+\omega_{\ell_n})t}. \tag{4}$$

For simplicity, in Sections 4 and 5, we use a single harmonic function ($p = 1$ and $\mathbf{u}(t) = \alpha e^{j\omega t}$) to identify explicit formulas for the generalized transfer functions (in the case of bilinear and quadratic systems). Consequently, the transfer function $\mathbf{H}_n$ will be evaluated at multiple instances of the driving frequency $j\omega$.

3 LINEAR SYSTEMS

A linear system Σ_L is characterized by a set of differential equations, as follows

$$\Sigma_L : \quad \mathbf{E}\dot{\mathbf{x}}(t) = \mathbf{A}\mathbf{x}(t) + \mathbf{B}\mathbf{u}(t), \qquad \mathbf{y}(t) = \mathbf{C}\mathbf{x}(t), \tag{5}$$

where $\mathbf{E}, \mathbf{A} \in \mathbb{R}^{n\times n}$, $\mathbf{B}, \mathbf{C}^T \in \mathbb{R}^n$. The matrix $\mathbf{E}$ is considered to be invertible and hence assimilated into matrices $\mathbf{A}$ and $\mathbf{B}$: $\bar{\mathbf{A}} = \mathbf{E}^{-1}\mathbf{A}, \bar{\mathbf{B}} = \mathbf{E}^{-1}\mathbf{B}$. One can explicitly write the output $\mathbf{y}(t)$ in terms of the input $\mathbf{u}(t)$:

$$\mathbf{y}(t) = \mathbf{C}e^{\bar{\mathbf{A}}t}\mathbf{x}(0) + \int_0^t \mathbf{C}e^{\bar{\mathbf{A}}(t-\tau)}\bar{\mathbf{A}}u(t)d\tau, \ \tau \in [0, t]. \tag{6}$$

The linear time-domain kernel is defined as follows $\mathbf{h}(t) = \mathbf{C}e^{\bar{\mathbf{A}}t}\bar{\mathbf{B}}$ and it is referred to as the impulse response. By considering the Laplace transform of this function, we obtain:

$$\mathbf{H}(s) = \mathcal{L}\{\mathbf{h}(t)\} = \mathbf{C}(s\mathbf{I} - \bar{\mathbf{A}})^{-1}\bar{\mathbf{B}}. \tag{7}$$

Alternatively, simply apply the Laplace transform directly to the differential equation in (5)

$$s\mathbf{E}\mathbf{X}(s) = \mathbf{A}\mathbf{X}(s) + \mathbf{B}\mathbf{U}(s) \Rightarrow \mathbf{X}(s) = (s\mathbf{E} - \mathbf{A})^{-1}\mathbf{B}\mathbf{U}(s) \Rightarrow \mathbf{Y}(s) = \mathbf{C}(s\mathbf{E} - \mathbf{A})^{-1}\mathbf{B}\mathbf{U}(s) \tag{8}$$

Hence, identify the transfer function as the ratio of the transformed output $\mathbf{Y}(s)$ to the transformed input $\mathbf{U}(s)$:

$$\mathbf{H}(s) = \frac{\mathbf{Y}(s)}{\mathbf{U}(s)} = \mathbf{C}(s\mathbf{E} - \mathbf{A})^{-1}\mathbf{B}. \tag{9}$$

3.1 The Loewner framework

The Loewner framework is a data-driven model identification and reduction tool (see [3]). It provides a solution through rational approximation and by means of interpolation. The problem can be formulated as follows; given the following data

$$\text{right data} : (\lambda_i; \mathbf{w}_i), \ i = 1, \cdots, k, \quad \text{and} \quad \text{left data} : (\mu_j; \mathbf{v}_j), \ j = 1, \cdots, q. \tag{10}$$

find the function $\mathbf{H}(s)$, such that the following interpolation conditions are fulfilled:

$$\mathbf{H}(\lambda_i) = \mathbf{w}_i, \quad \mathbf{H}(\mu_j) = \mathbf{v}_j, \tag{11}$$

where $\mathbf{w}_i,\ \mathbf{v}_j \in \mathbb{C}$, could be, for instance, S-parameters, i.e. values that could be measured experimentally. Proceed to arranging the data (10) into matrix format. The Loewner matrix $\mathbb{L} \in \mathbb{C}^{k\times k}$ and the shifted Loewner matrix $\mathbb{L}_s \in \mathbb{C}^{k\times k}$ are defined as follows

$$\mathbb{L} = \begin{bmatrix} \frac{\mathbf{v}_1-\mathbf{w}_1}{\mu_1-\lambda_1} & \dots & \frac{\mathbf{v}_1-\mathbf{w}_k}{\mu_1-\lambda_k} \\ \vdots & \ddots & \vdots \\ \frac{\mathbf{v}_k-\mathbf{w}_1}{\mu_k-\lambda_1} & \dots & \frac{\mathbf{v}_k-\mathbf{w}_k}{\mu_k-\lambda_k} \end{bmatrix}, \quad \mathbb{L}_s = \begin{bmatrix} \frac{\mu_1\mathbf{v}_1-\mathbf{w}_1\lambda_1}{\mu_1-\lambda_1} & \dots & \frac{\mu_1\mathbf{v}_1-\mathbf{w}_k\lambda_k}{\mu_1-\lambda_k} \\ \vdots & \ddots & \vdots \\ \frac{\mu_k\mathbf{v}_k-\mathbf{w}_1\lambda_1}{\mu_k-\lambda_1} & \dots & \frac{\mu_k\mathbf{v}_k-\mathbf{w}_k\lambda_k}{\mu_k-\lambda_k} \end{bmatrix}, \tag{12}$$

while the data vectors $\mathbf{V}, \mathbf{W}^T \in \mathbb{R}^k$ are introduced below

$$\mathbf{V} = \begin{bmatrix} \mathbf{v}_1 \ ; \ \mathbf{v}_2 \ ; \ \dots \ ; \ \mathbf{v}_q \end{bmatrix}, \quad \mathbf{W} = [\mathbf{w}_1 \ \ \mathbf{w}_2 \ \ \cdots \ \ \mathbf{w}_k]. \tag{13}$$

Lemma 1. *If the matrix pencil $(\mathbb{L}_s, \mathbb{L})$ is regular, then one can directly recover the system matrices and the interpolation function. The Loewner model is composed of*

$$\mathbf{E} = -\mathbb{L}, \quad \mathbf{A} = -\mathbb{L}_s, \quad \mathbf{B} = \mathbf{V}, \quad \mathbf{C} = \mathbf{W}, \quad \rightarrow \quad \mathbf{H}(s) = \mathbf{W}(\mathbb{L}_s - s\mathbb{L})^{-1}\mathbf{V}. \tag{14}$$

Introduce $\mathcal{R}$ as the generalized controllability matrix in terms of the right sampling points $\{\lambda_1, \dots, \lambda_k\}$ and matrices $\mathbf{E}, \mathbf{A}, \mathbf{B}$. Additionally, let $\mathcal{O}$ be the generalized observability matrix, written in terms of the left sampling points $\{\mu_1, \dots, \mu_k\}$ and matrices $\mathbf{E}, \mathbf{A}, \mathbf{C}$.

$$\mathcal{O} = \begin{bmatrix} \mathbf{C}(\mu_1\mathbf{E} - \mathbf{A})^{-1} \\ \vdots \\ \mathbf{C}(\mu_k\mathbf{E} - \mathbf{A})^{-1} \end{bmatrix}, \quad \mathcal{R} = \begin{bmatrix} (\lambda_1\mathbf{E} - \mathbf{A})^{-1}\mathbf{B} & \cdots & (\lambda_k\mathbf{E} - \mathbf{A})^{-1}\mathbf{B} \end{bmatrix}. \tag{15}$$

Then, it follows that the data matrices can be factorized as follows

$$\mathbb{L} = -\mathcal{O}\mathbf{E}\mathcal{R}, \quad \mathbb{L}_s = -\mathcal{O}\mathbf{A}\mathcal{R}, \ \mathbf{V} = \mathbf{C}\mathcal{R}, \ \mathbf{W} = \mathcal{O}\mathbf{B}. \tag{16}$$

In practical applications, the pencil $(\mathbb{L}_s, \mathbb{L})$ is often singular. In these cases, perform a rank revealing singular value decomposition (SVD) of the Loewner matrix $\mathbb{L}$. By setting $\operatorname{rank}\mathbb{L} = k$, write (where $\mathbf{X}_r = \mathbf{X}(:, 1:r)$, $\mathbf{Y}_r = \mathbf{Y}(:, 1:r)$, and $\mathbf{S}_r = \mathbf{S}(1:r, 1:r)$)

$$\mathbb{L} = \mathbf{X}\mathbf{S}\mathbf{Y}^* \approx \mathbf{X}_r\mathbf{S}_r\mathbf{Y}_r^*, \quad \text{with} \ \ \mathbf{X}_r, \mathbf{Y}_r \in \mathbb{C}^{k\times r}, \ \mathbf{S}_r \in \mathbb{C}^{r\times r}. \tag{17}$$

Lemma 2. *The system matrices corresponding to a compressed /projected Loewner model for which the transfer function approximately matches the conditions in (11), can be computed as*

$$\hat{\mathbf{E}} = -\mathbf{X}_r^*\mathbb{L}\mathbf{Y}_r, \quad \hat{\mathbf{A}} = -\mathbf{X}_r^*\mathbb{L}_s\mathbf{Y}_r, \quad \hat{\mathbf{B}} = \mathbf{X}_r^*\mathbf{V}, \quad \hat{\mathbf{C}} = \mathbf{W}\mathbf{Y}_r. \tag{18}$$

and the corresponding interpolating function $\hat{\mathbf{H}}(s) = \mathbf{W}\mathbf{Y}_r\Big(\mathbf{X}_r^*(\mathbb{L}_s - s\mathbb{L})\mathbf{Y}_r\Big)^{-1}\mathbf{X}_r^*\mathbf{V}$.

Remark 3.1. *One can incorporate the reduced-order matrix $\hat{\mathbf{E}}$ in (18) into the other system matrices and, in this way, put together a model $(\tilde{\mathbf{A}}, \tilde{\mathbf{B}}, \tilde{\mathbf{C}})$ in standard representation:*

$$\tilde{\mathbf{A}} = \hat{\mathbf{E}}^{-1}\hat{\mathbf{A}} = (\mathbf{X}_r^*\mathbb{L}\mathbf{Y}_r)^{-1}(\mathbf{X}_r^*\mathbb{L}_s\mathbf{Y}_r), \quad \tilde{\mathbf{B}} = \hat{\mathbf{E}}^{-1}\hat{\mathbf{B}} = (\mathbf{X}_r^*\mathbb{L}\mathbf{Y}_r)^{-1}(\mathbf{X}_r^*\mathbf{V}), \ \tilde{\mathbf{C}} = \hat{\mathbf{C}} = \mathbf{W}\mathbf{Y}_r. \tag{19}$$

Definition 3.1. The Kronecker product of two vectors $\mathbf{x} \in \mathbb{C}^m$ and $\mathbf{y} \in \mathbb{C}^m$ is given by the vector $\mathbf{z} \in \mathbb{C}^{mn}$ defined in the following way

$$\mathbf{z} = \mathbf{x} \otimes \mathbf{y} = \begin{bmatrix} x_1y_1, \ x_1y_2, \ \dots \ x_1y_m, \ x_2y_1, \ \dots, \ x_2y_m, \ \dots, \ x_ny_1, \ \dots, \ x_ny_m \end{bmatrix}^T.$$

Note that the product is not commutative. The definition of the product for matrices follows in an analogous way.

4 BILINEAR SYSTEMS

We analyze bilinear systems $\mathbf{\Sigma}_B$ of dimension n described by

$$\mathbf{\Sigma}_B: \quad \dot{\mathbf{x}} = \mathbf{A}\mathbf{x} + \mathbf{N}\mathbf{x}\mathbf{u} + \mathbf{B}\mathbf{u}, \qquad \mathbf{y} = \mathbf{C}\mathbf{u}. \tag{20}$$

where $\mathbf{A}, \mathbf{N} \in \mathbb{R}^{n\times n}$ and $\mathbf{B}, \mathbf{C}^T \in \mathbb{R}^n$. The nonlinearity, although mild, is given by the product of the variable $\mathbf{x}$ with the input $\mathbf{u}$ in (20) (and scaled by matrix $\mathbf{N}$). We introduce a numerical tool that allows approximating nonlinear systems by means of a bilinear system. The technique is commonly known as Carleman linearization (see [11]).

This procedure is a linearization of the initial nonlinear system and it involves approximation techniques (Taylor series expansion and truncation) to yield a bilinear system. We demonstrate the method through an example.

Example 4.1. Consider the following non-linear scalar system characterized by the equations:

$$\mathbf{\Sigma}_{\mathrm{N}}^1: \dot{x}(t) = -2x(t) + \sin\left(x(t)\right) + u(t), \quad y(t) = x(t). \tag{21}$$

Write the Taylor series around 0 for $\sin x$, where $c_{2k+1} = \frac{(-1)^k}{(2k+1)!}$ and $c_{2k} = 0$, as

$$\sin\left(x(t)\right) = \sum_{k=1}^{\infty} c_k x^k(t) = x(t) - \frac{x^3(t)}{3!} + \ldots, \ \Rightarrow \ \dot{x}(t) = -x(t) - \sum_{k=3}^{\infty} c_k x^k(t) + u(t).$$

Truncate at $N = 3$ and assemble the new state vector $\hat{\mathbf{x}} = \begin{bmatrix} x, & x^2, & x^3 \end{bmatrix}^T \in \mathbb{R}^3$. Rewrite the equations in (21) as a bilinear system, exactly as in (20)

$$\dot{\hat{\mathbf{x}}}(t) = \mathbf{A}_1\hat{\mathbf{x}}(t) + \mathbf{N}_1\hat{\mathbf{x}}(t)u(t) + \mathbf{B}_1 u(t), \quad y(t) = \mathbf{C}_1\hat{\mathbf{x}}(t),$$

$$\mathbf{A}_1 = \begin{bmatrix} -1 & 0 & -\frac{1}{3!} \\ 0 & -2 & 0 \\ 0 & 0 & -3 \end{bmatrix}, \ \mathbf{N}_1 = \begin{bmatrix} 0 & 0 & 0 \\ 2 & 0 & 0 \\ 0 & 3 & 0 \end{bmatrix}, \ \mathbf{B}_1 = \begin{bmatrix} 1 \\ 0 \\ 0 \end{bmatrix}, \ \mathbf{C}_1 = \begin{bmatrix} 1 & 0 & 0 \end{bmatrix}.$$

4.1 Deriving transfer functions

We choose the harmonic input signal $\mathbf{u}(t) = \alpha e^{j\omega t}$, $\omega, \alpha > 0$. Next, as in [12], assume that the solution of (20) is written as an infinite power series

$$\mathbf{x}(t) = \sum_{m=1}^{\infty} \mathbf{G}_m(j\omega, \ldots, j\omega)\alpha^m e^{mj\omega t}. \tag{22}$$

Consider the DC term to be 0 ($\mathbf{G}_0 = 0$). By substituting the explicit solution formula (3) into the original differential equation (1), it follows that:

$$\begin{aligned} \sum_{m=1}^{\infty} mj\omega\mathbf{G}_m(j\omega, \ldots, j\omega)\alpha^m e^{mj\omega t} = \mathbf{A}\Big(\sum_{m=1}^{\infty} \mathbf{G}_m(j\omega, \ldots, j\omega)\alpha^m e^{mj\omega t}\Big) + \\ \mathbf{N}\Big(\sum_{m=1}^{\infty} \mathbf{G}_m(j\omega, \ldots, j\omega)\alpha^m e^{mj\omega t}\Big)\alpha e^{j\omega t} + \mathbf{B}\alpha e^{j\omega t}. \end{aligned} \tag{23}$$

In what follows, we refer to $\mathbf{G}_m(j\omega, \ldots, j\omega)$ by using the condensed notation $\mathbf{G}_m(j\omega)$ (similarly, for the transfer function $\mathbf{H}_m(j\omega, \ldots, j\omega)$ use the notation $\mathbf{H}_m(j\omega)$ instead).

Initiate the identification procedure by equating the coefficient of the term $e^{mj\omega t}$, $\forall m \geqslant 1$ from both left and right sides of equation (6).

1). **The case $m = 1 \rightarrow$ coefficients of $e^{j\omega t}$.**

$$j\omega \mathbf{G}_1(j\omega)\alpha = \mathbf{A}\mathbf{G}_1(j\omega)\alpha + \mathbf{B}\alpha \Rightarrow \mathbf{G}_1(j\omega) = (j\omega \mathbf{I} - \mathbf{A})^{-1}\mathbf{B} = \mathbf{\Phi}(j\omega)\mathbf{B}, \tag{24}$$

where $\mathbf{\Phi}(s) = (s\mathbf{I} - \mathbf{A})^{-1}$. Hence, write the first (linear) transfer function as

$$\mathbf{H}_1(j\omega) = \mathbf{C}\mathbf{\Phi}(j\omega)\mathbf{B}. \tag{25}$$

2). **The case $m = 2 \rightarrow$ coefficients of $e^{2j\omega t}$.**

$$2j\omega \mathbf{G}_2(j\omega)\alpha^2 = \mathbf{A}\mathbf{G}_2(j\omega, j\omega)\alpha^2 + \mathbf{N}\mathbf{G}_1(j\omega)\alpha^2 \Rightarrow \mathbf{G}_2(j\omega) = \mathbf{\Phi}(2j\omega)\mathbf{N}\mathbf{\Phi}(j\omega)\mathbf{B}.$$

Hence, write the second transfer function as

$$\mathbf{H}_2(j\omega) = \mathbf{C}\mathbf{\Phi}(2j\omega)\mathbf{N}\mathbf{\Phi}(j\omega)\mathbf{B}. \tag{26}$$

n). **The general case $\rightarrow$ coefficients of $e^{nj\omega t}$.**

$$nj\omega \mathbf{G}_n(j\omega)\alpha^n = \mathbf{A}\mathbf{G}_n(j\omega)\alpha^n + \mathbf{N}\mathbf{G}_{n-1}(j\omega)\alpha^n \Rightarrow (nj\omega \mathbf{I} - \mathbf{A})\mathbf{G}_n(j\omega) = \mathbf{N}\mathbf{G}_{n-1}(j\omega) \tag{27}$$

Hence, one can write $\mathbf{G}_n(j\omega) = \mathbf{\Phi}(nj\omega)\mathbf{N}\mathbf{G}_{n-1}(j\omega)$. In order to derive the nth transfer function $\mathbf{H}_n(j\omega)$, just multiply $\mathbf{G}_n(j\omega)$ to the left with $\mathbf{C}$, i.e.

$$\mathbf{H}_n(j\omega) = \mathbf{C}\mathbf{\Phi}(nj\omega)\mathbf{N}\mathbf{\Phi}((n-1)j\omega)\mathbf{N}\cdots\mathbf{N}\mathbf{\Phi}(j\omega)\mathbf{B}. \tag{28}$$

4.2 Estimating the bilinear term N

As explained in Section 3.1, the first step is to construct a reliable reduced-order linear model $(\mathbf{A}, \mathbf{B}, \mathbf{C})$ of order r as in (19) for the data in (10). This set is composed of samples of the first transfer function $\mathbf{H}_1(j\omega)$ in (25).

The next step is to fit an appropriate matrix $\mathbf{N} \in \mathbb{C}^{r\times r}$ that supplements the linear model as bilinear model. In this direction, it is assumed that information about the second transfer function $\mathbf{H}_2(j\omega)$ in (26) is known at $2k$ points $\{j\omega_1, \ldots, j\omega_{2k}\}$. Introduce the following vectors $\mathbf{r}_\ell \in \mathbb{C}^r$ and $\mathbf{o}_\ell \in \mathbb{C}^{1\times r}$ for $\ell \in \{1, 2, \ldots, 2k\}$:

$$\mathbf{r}_\ell = (j\omega_\ell \mathbf{I} - \mathbf{A})^{-1}\mathbf{B} = \mathbf{\Phi}(j\omega_\ell)\mathbf{B}, \quad \mathbf{o}_\ell = \mathbf{C}(2j\omega_\ell \mathbf{I} - \mathbf{A})^{-1} = \mathbf{C}\mathbf{\Phi}(2j\omega_\ell). \tag{29}$$

Note that one can write the matrices $\mathcal{O}$ and $\mathcal{R}$ in (15) in terms of the new vectors. For the set of points $\{2j\omega_1, \ldots, 2j\omega_{2k}\}$, write the observability matrix as $\mathcal{O} = [\mathbf{o}_1; \mathbf{o}_2; \cdots; \mathbf{o}_{2k}]$. Then write the controllability matrix as $\mathcal{R} = [\mathbf{r}_1\ \mathbf{r}_2\ \cdots\ \mathbf{r}_{2k}]$ for the set of points $\{j\omega_1, \ldots, j\omega_{2k}\}$.

One can write the second transfer function evaluated at $j\omega_\ell$, for $\ell \in \{1, 2, \ldots, 2k\}$, as

$$\mathbf{H}_2(j\omega_\ell) = \mathbf{C}\mathbf{\Phi}(2j\omega)\mathbf{N}\mathbf{\Phi}(j\omega)\mathbf{B} = \mathbf{o}_\ell \mathbf{N}\mathbf{r}_\ell \tag{30}$$

Denote with $\mathbf{v}_\mathbf{N} \in \mathbb{C}^{r^2}$ the vectorization of $\mathbf{N} \in \mathbb{C}^{r\times r}$, i.e. $\mathbf{v}_\mathbf{N} = [\mathbf{N}(:,1)\ ;\ \mathbf{N}(:,2)\ \cdots\ \mathbf{N}(:,r)]$. From (39), we can write that $(\mathbf{r}_\ell^T \otimes \mathbf{o}_\ell)\mathbf{v}_\mathbf{N} = \mathbf{H}_2(j\omega_\ell)$, $\forall 1 \leq \ell \leq 2k$. By collecting this $2k$ equalities into a matrix format, we put together the following linear equation:

$$\mathbf{Z}\mathbf{v}_\mathbf{N} = \mathbf{V}_2, \quad \text{where } \mathbf{Z} \in \mathbb{C}^{2k\times r^2},\ \mathbf{V}_2 \in \mathbb{C}^{2k}, \quad \begin{cases} \mathbf{Z}(\ell,:) = \mathbf{r}_\ell^T \otimes \mathbf{o}_\ell \\ \mathbf{V}_2(\ell) = \mathbf{H}_2(j\omega_\ell) \end{cases}. \tag{31}$$

One can write the solution of (31) by means of the Moore-Penrose pseudo-inverse of the matrix $\mathbf{Z}$ which is denoted with $\mathbf{Z}^\dagger \in \mathbb{C}^{r^2\times 2k}$, as

$$\mathbf{v}_\mathbf{N} = \mathbf{Z}^\dagger \mathbf{V}_2. \tag{32}$$

Finally, simply put together the recovered matrix $\mathbf{N} \in \mathbb{C}^{r\times r^2}$ from $\mathbf{v}_\mathbf{N}$.

5 QUADRATIC SYSTEMS

We analyze quadratic systems $\mathbf{\Sigma}_Q$ of dimension n described by

$$\mathbf{\Sigma}_Q: \quad \dot{\mathbf{x}} = \mathbf{A}\mathbf{x} + \mathbf{Q}(\mathbf{x} \otimes \mathbf{x}) + \mathbf{B}\mathbf{u}, \quad \mathbf{y} = \mathbf{C}\mathbf{u}. \tag{33}$$

where $\mathbf{Q} \in \mathbb{C}^{n \times n^2}$ and $\mathbf{A}, \mathbf{B}$ and $\mathbf{C}$ are as in (5). We introduce a transformation which has been known in the literature as the McCormick relaxation (see [9]). In broad terms, this result states that any nonlinear system characterized by elementary functions can be equivalently recast as a quadratic system (with a possible bilinear term). This result applies, for example, to nonlinearities such as polynomial, rational, exponential, logarithmic, trigonometric, or a composition thereof. We again demonstrate the method through an example.

Example 5.1. Consider the same system as in Example 4.1, but without the control u i.e

$$\mathbf{\Sigma}_{\mathrm{N}}^2 \ : \ \dot{x} = -2x + \sin x, \quad y = x.$$

Introduce two additional variables: $z = \sin x$ and $w = \cos x$, and compute the time derivatives and then substitute the given terms

$$\dot{x} = -2x + z, \quad \dot{z} = \dot{x}\cos x = -2wx + wz, \quad \dot{w} = -\dot{x}\sin x = 2zx - z^2.$$

Let $\tilde{\mathbf{x}} = \begin{bmatrix} x, & z, & w \end{bmatrix}^T$ be the new variable; recast the original system as a quadratic system

$$\dot{\tilde{\mathbf{x}}} = \underbrace{\begin{bmatrix} -2 & 1 & 0 \\ 0 & 0 & 0 \\ 0 & 0 & 0 \end{bmatrix}}_{\mathbf{A}_2} \tilde{\mathbf{x}} + \underbrace{\begin{bmatrix} 0 & 0 & 0 & 0 & 0 & 0 & 0 & 0 & 0 \\ 0 & 0 & -2 & 0 & 0 & 1 & 0 & 0 & 0 \\ 0 & 0 & 2 & 0 & -1 & 0 & 0 & 0 & 0 \end{bmatrix}}_{\mathbf{Q}_2} (\tilde{\mathbf{x}} \otimes \tilde{\mathbf{x}}), \quad y = \underbrace{\begin{bmatrix} 1 & 0 & 0 \end{bmatrix}}_{\mathbf{C}_2} \tilde{\mathbf{x}}.$$

5.1 Deriving transfer functions

Consider the control input signal as for the bilinear case $\mathbf{u}(t) = \alpha e^{j\omega t}$, $\omega, \alpha > 0$ and make the same assumption for the solution of (33), i.e.

$$\mathbf{x}(t) = \sum_{m=1}^{\infty} \mathbf{G}_m(j\omega)\alpha^m e^{mj\omega t}. \tag{34}$$

Substitute the relation (34) into the original differential equation (33), and hence write that:

$$\begin{aligned} \sum_{m=1}^{\infty} mj\omega \mathbf{G}_m(j\omega)\alpha^m e^{mj\omega t} &= \mathbf{A}\sum_{m=1}^{\infty} \mathbf{G}_m(j\omega)\alpha^m e^{mj\omega t} + \\ \mathbf{Q}\Big(\sum_{m=1}^{\infty} \mathbf{G}_m(j\omega)\alpha^m e^{mj\omega t}\Big) \otimes \Big(\sum_{m=1}^{\infty} \mathbf{G}_m(j\omega)\alpha^m e^{mj\omega t}\Big) &+ \mathbf{B}\alpha e^{j\omega t}. \end{aligned} \tag{35}$$

Next, as for the bilinear case, equate the coefficient of the term $e^{mj\omega t}$, $\forall m \geqslant 1$ from both left and right sides of equation (35). The first transfer function is identified as $\mathbf{H}_1(j\omega) = \mathbf{C}\mathbf{\Phi}(j\omega)\mathbf{B}$.

2). **The case $m = 2 \rightarrow$ coefficients of $e^{2j\omega t}$.**

$$\begin{aligned} &2j\omega \mathbf{G}_2(j\omega)\alpha^2 = \mathbf{A}\mathbf{G}_2(j\omega)\alpha^2 + \mathbf{Q}[\mathbf{G}_1(j\omega) \otimes \mathbf{G}_1(j\omega)]\alpha^2, \\ &\Rightarrow \mathbf{G}_2(j\omega) = \mathbf{\Phi}(2j\omega)\mathbf{Q}[\mathbf{\Phi}(j\omega)\mathbf{B} \otimes \mathbf{\Phi}(j\omega)\mathbf{B}]. \end{aligned}$$

Hence, write the second transfer function as

$$\mathbf{H}_2(j\omega) = \mathbf{C}\mathbf{\Phi}(2j\omega)\mathbf{Q}\Big[\mathbf{\Phi}(j\omega)\mathbf{B} \otimes \mathbf{\Phi}(j\omega)\mathbf{B}\Big]. \tag{36}$$

n). **The general case → coefficients of** $e^{nj\omega t}$.

$$\begin{aligned} &nj\omega\mathbf{G}_n(j\omega)\alpha^n = \mathbf{A}\mathbf{G}_n(j\omega)\alpha^n + \mathbf{Q}[\mathbf{G}_{n-1}(j\omega) \otimes \mathbf{G}_1(j\omega) + \ldots + \mathbf{G}_1(j\omega) \otimes \mathbf{G}_{n-1}(j\omega)]\alpha^n. \\ &\Rightarrow (nj\omega\mathbf{I} - \mathbf{A})\mathbf{G}_n(j\omega) = \mathbf{Q}\Big[\sum_{\ell=1}^{n-1} \mathbf{G}_\ell(j\omega) \otimes \mathbf{G}_{n-\ell}(j\omega)\Big]. \end{aligned} \tag{37}$$

Hence identify $\mathbf{G}_n(j\omega)$ and by multiplying it to the left with $\mathbf{C}$, we get

$$\mathbf{H}_n(j\omega) = \mathbf{C}\mathbf{\Phi}(nj\omega)\mathbf{Q}\Big[\sum_{\ell=1}^{n-1} \mathbf{G}_\ell(j\omega) \otimes \mathbf{G}_{n-\ell}(j\omega)\Big],\ \forall n \geqslant 1. \tag{38}$$

5.2 Estimating the quadratic term Q

The next step is to fit an appropriate matrix $\mathbf{Q} \in \mathbb{C}^{r\times r^2}$ for the quadratic model. It is assumed that information about the second transfer function $\mathbf{H}_2(j\omega)$ in (36) is known at $2k$ points $\{j\omega_1, \ldots, j\omega_{2k}\}$.

One can write the second transfer function evaluated at $j\omega_\ell$, $\ell \in \{1, 2, \ldots, 2k\}$, in terms of the vectors $\mathbf{r}, \mathbf{o}^* \in \mathbb{C}^r$ in (29), as follows

$$\mathbf{H}_2(j\omega_\ell) = \mathbf{C}(2j\omega_\ell\mathbf{I} - \mathbf{A})^{-1}\mathbf{Q}\Big[(j\omega_\ell\mathbf{I} - \mathbf{A})^{-1}\mathbf{B} \otimes (j\omega_\ell\mathbf{I} - \mathbf{A})^{-1}\mathbf{B}\Big] = \mathbf{o}_\ell\mathbf{Q}[\mathbf{r}_\ell \otimes \mathbf{r}_\ell] \tag{39}$$

Denote with $\mathbf{v}_\mathbf{Q} \in \mathbb{C}^{r^3}$ the vectorization of $\mathbf{Q} \in \mathbb{C}^{r\times r^2}$, i.e. $\mathbf{v}_\mathbf{Q} = [\mathbf{Q}(:,1)\ ;\ \mathbf{Q}(:,2)\ \cdots\ \mathbf{Q}(:,r^2)]$. From (39), we can write that $(\mathbf{r}_\ell^T \otimes \mathbf{r}_\ell^T \otimes \mathbf{o}_\ell)\mathbf{v}_\mathbf{Q} = \mathbf{H}_2(j\omega_\ell),\ \forall 1 \leq \ell \leq 2k$. By collecting this $2k$ equalities into a matrix format, we put together the following linear equation:

$$\mathbf{T}\mathbf{v}_\mathbf{Q} = \mathbf{V}_2, \quad \text{where } \mathbf{T} \in \mathbb{C}^{2k\times r^3},\ \mathbf{V}_2 \in \mathbb{C}^{2k},\ \begin{cases} \mathbf{T}(\ell,:) = \mathbf{r}_\ell^T \otimes \mathbf{r}_\ell^T \otimes \mathbf{o}_\ell \\ \mathbf{V}_2(\ell) = \mathbf{H}_2(j\omega_\ell) \end{cases}. \tag{40}$$

Finally, one can write the solution of (40) by means of $\mathbf{T}^\dagger \in \mathbb{C}^{r^3\times 2k}$ as in Section 4.2, i.e. $\mathbf{v}_\mathbf{Q} = \mathbf{T}^\dagger\mathbf{V}_2$. Then one can directly put together the recovered matrix $\mathbf{Q} \in \mathbb{C}^{r\times r^2}$.

6 NUMERICAL EXAMPLES

6.1 The Langmuir kinetics model

The first example to be analyzed is given by the Langmuir kinetic equation. We use the same model as in [10]. There, this example is presented as a simple kinetic case for which the adsorption process is governed by the rates of adsorption and desorption of the solute molecules onto and from the surface. The Langmuir kinetic equation is given as follows

$$\dot{Q}(t) = k_a C(t)[Q_0 - Q(t)] - k_d Q(t), \tag{41}$$

where C is the concentration in the gas phase, Q the concentration in the solid phase and Q_0 the concentration in the solid phase corresponding to maximal coverage. Finally, k_a and k_d are the adsorption and, respectively, the desorption rate constant.

Equation (41) can be rewritten as in [10] by using instead variables defined as dimensionless deviations from a stationary state

$$\dot{q}(t) = k'_a c(t)[q_0 - q(t)] - k'_d q(t), \tag{42}$$

where the new quantities can be derived as follows

$$c = \frac{C - C_s}{C_s},\ q = \frac{Q - Q_s}{Q_s},\ q_0 = \frac{Q_0 - Q_s}{Q_s},\ k'_a = k_a C_s,\ k'_d = k_d + k_a C_s. \tag{43}$$

Note that, because of the term $c(t)q(t)$ in (42), the adsorption process is nonlinear. Since $q(t)$ is the variable and $c(t)$ the input, the system is bilinear. In [10], the first three transfer functions are explicitly derived.

By choosing the input of the system to be $c(t) = \alpha e^{j\omega t}$, the functions are identified as follows:

$$\begin{aligned} \mathbf{H}_1(j\omega) = \frac{K q_0}{j\omega\eta + 1}, \quad \mathbf{H}_2(j\omega) = -\frac{1}{q_0}\mathbf{H}_1(2j\omega)\mathbf{H}_1(j\omega), \\ \mathbf{H}_3(j\omega) = \frac{1}{q_0^2}\mathbf{H}_1(3j\omega)\mathbf{H}_1(2j\omega)\mathbf{H}_1(j\omega), \end{aligned} \tag{44}$$

where $K = \frac{k'_a}{k'_d}$ and $\eta = \frac{1}{k'_d}$. Then write $k'_a = \frac{K}{\eta}$.

As in [10], choose $K = 0.1$, $q_0 = 9$ and $\eta = 2$. Hence, by replacing these values into (42), one can find the system scalars as $\mathbf{A} = \frac{1}{\eta} = -\frac{1}{2}$, $\mathbf{B} = q_0 k'_a = \frac{9}{20}$, $\mathbf{N} = -k'_a = -\frac{1}{20}$. Finally, let $\mathbf{C} = 1$ (the observed output coincides with $q(t)$).

Let $\mu_1 = \frac{1}{4}j$ and $\mu_2 = -\frac{1}{4}j$ be the left sampling points. Additionally, let $\lambda_1 = \frac{1}{2}j$ and $\lambda_2 = -\frac{1}{2}j$ be the right sampling points. From (12) and (13), we put together the matrices as

$$\mathbb{L} = \begin{bmatrix} -\frac{9}{25} + \frac{27\mathrm{j}}{25} & -\frac{27}{25} - \frac{9\mathrm{j}}{25} \\ -\frac{27}{25} + \frac{9\mathrm{j}}{25} & -\frac{9}{25} - \frac{27\mathrm{j}}{25} \end{bmatrix}, \mathbb{L}_s = \begin{bmatrix} \frac{9}{50} - \frac{27\mathrm{j}}{50} & \frac{27}{50} + \frac{9\mathrm{j}}{50} \\ \frac{27}{50} - \frac{9\mathrm{j}}{50} & \frac{9}{50} + \frac{27\mathrm{j}}{50} \end{bmatrix}, \mathbf{V} = \begin{bmatrix} \frac{18}{25} - \frac{9\mathrm{j}}{25} \\ \frac{18}{25} + \frac{9\mathrm{j}}{25} \end{bmatrix}, \mathbf{W}^* = \begin{bmatrix} \frac{9}{20} + \frac{9\mathrm{j}}{20} \\ \frac{9}{20} - \frac{9\mathrm{j}}{20} \end{bmatrix}$$

We observe that $\mathrm{rank}(\mathbb{L}) = 1$ and hence the dimension of the underlying system is $r = 1$. We choose projector vectors $\mathbf{x}^* = \mathbf{y} = \begin{bmatrix} \mathrm{j} & -\mathrm{j} \end{bmatrix}$. Then, the recovered values characterizing the dynamics can be found as

$$\hat{\mathbf{A}} = -\frac{1}{2},\ \hat{\mathbf{B}} = \frac{1}{2},\ \hat{\mathbf{C}} = \frac{9}{10}. \tag{45}$$

Then, using only one sample of the second transfer function $\mathbf{H}_2$, for example $\mathbf{H}_2(\frac{1}{2}j) = \hat{\mathbf{C}}\hat{\mathbf{\Phi}}(j)\hat{\mathbf{N}}\hat{\mathbf{\Phi}}(\frac{1}{2}j)\hat{\mathbf{B}}$, one can recover the bilinear term $\hat{\mathbf{N}} = -\frac{1}{20}$. Note that the orginal scalar system is hence recovered ($\hat{\mathbf{A}} = \mathbf{A}$, $\hat{\mathbf{N}} = \mathbf{N}$, and $\hat{\mathbf{B}}\hat{\mathbf{C}} = \mathbf{B}\mathbf{C}$).

6.2 The Duffing oscillator

For the next example, we consider a single degree-of-freedom Duffing oscillator under harmonic input. It is one of the prototype systems of nonlinear dynamics and it became popular for studying anharmonic oscillations and, later, chaotic nonlinear dynamics. It is a non-linear second-order differential equation used to model certain damped and driven oscillators.

In the current example, the nonlinearity is characterized by quadratic and cubic stiffness as follows (see [8]):

$$m\ddot{x}(t) + c\dot{x}(t) + k_1 x(t) + k_2 x^2(t) + k_3 x^3(t) = u(t), \tag{46}$$

where m is the mass coefficient, c is the viscous damping, k_1 is the linear damping, k_2 and k_3 are the quadratic and, respectively, cubic stiffness constants. Traditionally, as noted in [13], the Duffing equation does not have a quadratic term, i.e. $k_2 = 0$ in (46).

Additionally, in (46), the values $\ddot{x}, \dot{x}$ and x represent the acceleration, velocity and displacement, respectively. The input is chosen to be $u(t) = Ae^{j\omega t}$, where A is the forcing level of amplitude and ω the frequency of excitation.

Now, by means of the harmonic probing procedure, one can obtain expressions for the transfer functions. By following the procedure described in [8], the first three transfer functions can be derived as follows (using the control input $u(t) = Ae^{j\omega t}$):

$$\begin{aligned} \mathbf{H}_1(j\omega) &= \frac{1}{-m\omega^2 + cj\omega + k_1}, \quad \mathbf{H}_2(j\omega, j\omega) = -k_2\mathbf{H}_1(j\omega)^2\mathbf{H}_1(2j\omega), \\ \mathbf{H}_3(j\omega, j\omega, j\omega) &= 2k_2^2\mathbf{H}_1^3(j\omega)\mathbf{H}_1(2j\omega)\mathbf{H}_1(3j\omega) - k_3\mathbf{H}_1^3(j\omega)\mathbf{H}_1(3j\omega). \end{aligned} \tag{47}$$

Next, we will introduce additional surrogate state variables in order to rewrite the second-order cubic differential equation in (46) as a first-order quadratic equation.

The case with $k_3 = 0$ In this case, the equation in (46) can be equivalently rewritten as:

$$\ddot{x}(t) = -\frac{c}{m}\dot{x}(t) - \frac{k_1}{m}x(t) - \frac{k_2}{m}x^2(t) + \frac{1}{m}u(t). \tag{48}$$

Introduce the following augmented state variable $\mathbf{z} = [x \ , \ \dot{x}]^T \in \mathbb{R}^2$ by putting together the original variable $x(t)$ and its derivative $\dot{x}(t)$. By doing this, we can rewrite (48) as follows:

$$\underbrace{\begin{bmatrix} \dot{x} \\ \ddot{x} \end{bmatrix}}_{\dot{\mathbf{z}}} = \underbrace{\begin{bmatrix} 0 & 1 \\ -\frac{k_1}{m} & -\frac{c}{m} \end{bmatrix}}_{\mathbf{A}} \underbrace{\begin{bmatrix} x \\ \dot{x} \end{bmatrix}}_{\mathbf{z}} + \underbrace{\begin{bmatrix} 0 & 0 & 0 & 0 \\ -\frac{k_2}{m} & 0 & 0 & 0 \end{bmatrix}}_{\mathbf{Q}} \underbrace{\begin{bmatrix} x \\ \dot{x} \end{bmatrix} \otimes \begin{bmatrix} x \\ \dot{x} \end{bmatrix}}_{\mathbf{z}\otimes\mathbf{z}} + \underbrace{\begin{bmatrix} 0 \\ \frac{1}{m} \end{bmatrix}}_{\mathbf{B}} u, \tag{49}$$

or in short $\dot{\mathbf{z}} = \mathbf{A}\mathbf{z} + \mathbf{Q}(\mathbf{z}\otimes\mathbf{z}) + \mathbf{B}u$, a quadratic system. Choose to observe the original variable x and introduce the observed output $y(t) = x(t)$. Hence write $y = \mathbf{C}\mathbf{z}$, where $\mathbf{C} = \begin{bmatrix} 1 & 0 \end{bmatrix}$.

Choose the following parameters $m = 2$, $c = 10$, $k_1 = 10^2$ and $k_2 = 10^2$.

Let $\mu_1 = j$ and $\mu_2 = -j$ be the left sampling points. Additionally, let $\lambda_1 = 2j$ and $\lambda_2 = -2j$ be the right sampling points. From (12) and (13), we put together the matrices $\mathbb{L}, \mathbb{L}_s$ and vectors $\mathbf{V}, \mathbf{W}$. These matrices have complex entries. By using the matrix $\mathbf{J} = \frac{1}{\sqrt{2}} \begin{bmatrix} 1 & 1 \\ -\mathrm{j} & \mathrm{j} \end{bmatrix}$, we compute a real-valued equivalent realization: $\tilde{\mathbb{L}} = \mathbf{J}\mathbb{L}\mathbf{J}^*$, $\tilde{\mathbb{L}}_s = \mathbf{J}\mathbb{L}_s\mathbf{J}^*, \tilde{\mathbf{V}} = \mathbf{J}\mathbf{V}, \tilde{\mathbf{W}} = \mathbf{W}\mathbf{J}^*$. By incorporating the $\hat{\mathbf{E}}$ matrix into the others, we identify the three matrices of the linear model as

$$\hat{\mathbf{A}} = \begin{bmatrix} -5 & -2 \\ 25 & 0 \end{bmatrix}, \quad \hat{\mathbf{B}} = \begin{bmatrix} 3.5355 \\ -16.2635 \end{bmatrix}, \quad \hat{\mathbf{C}} = \begin{bmatrix} 0.0147 & 0.0032 \end{bmatrix}. \tag{50}$$

Next, in order to recover the quadratic term $\hat{\mathbf{Q}}$, we use the samples of the second transfer function $\mathbf{H}_2(j\omega)$ for $\omega \in \{\pm j, \pm 2j\}$. Then, we explicitly write the vector $\mathbf{V}_2 \in \mathbb{C}^4$ as

$$\mathbf{V}_2 = \begin{bmatrix} \mathbf{H}_2(\mathrm{j}) \ ; \ \mathbf{H}_2(-\mathrm{j}) \ ; \ \mathbf{H}_2(2\mathrm{j}) \ ; \ \mathbf{H}_2(-2\mathrm{j}) \end{bmatrix}. \tag{51}$$

Additionally, we put together the matrix $\mathbf{T} \in \mathbb{C}^{4\times 8}$ based on the recovered matrices in (50) as described in Section 5.2. Finally, the matrix $\mathbf{Q} \in \mathbb{R}^{2\times 4}$

$$\hat{\mathbf{Q}} = \begin{bmatrix} -0.1111 & -0.0526 & -0.0526 & -0.0339 \\ 0.0462 & 0.0549 & 0.0549 & 0.0964 \end{bmatrix}.$$

Note that the lifted quadratic system in (49) is hence perfectly recovered. The system realizations $(\mathbf{A}, \mathbf{B}, \mathbf{C}, \mathbf{Q})$ and $(\hat{\mathbf{A}}, \hat{\mathbf{B}}, \hat{\mathbf{C}}, \hat{\mathbf{Q}})$ are equivalent (they only differ through a similarity transformation).

The case with $k_3 \neq 0$ In this case, the equation in (46) can be equivalently rewritten as:

$$\ddot{x}(t) = -\frac{c}{m}\dot{x}(t) - \frac{k_1}{m}x(t) - \frac{k_2}{m}x^2(t) - \frac{k_3}{m}x^3(t) + \frac{1}{m}u(t). \tag{52}$$

Introduce the new augmented state variable $\mathbf{w} = [x \ , \ \dot{x} \ , \ x^2]^T \in \mathbb{R}^3$ by also including the squared variable x. By doing this, we can rewrite (52) as follows:

$$\underbrace{\begin{bmatrix} \dot{x} \\ \ddot{x} \\ \dot{x^2} \end{bmatrix}}_{\dot{\mathbf{w}}} = \underbrace{\begin{bmatrix} 0 & 1 & 0 \\ -\frac{k_1}{m} & -\frac{c}{m} & -\frac{k_2}{m} \\ 0 & 0 & 0 \end{bmatrix}}_{\mathbf{A}} \underbrace{\begin{bmatrix} x \\ \dot{x} \\ x^2 \end{bmatrix}}_{\mathbf{w}} + \underbrace{\begin{bmatrix} 0 & 0 & 0 & 0 & 0 & 0 & 0 & 0 & 0 \\ 0 & 0 & -\frac{k_3}{m} & 0 & 0 & 0 & 0 & 0 & 0 \\ 0 & 2 & 0 & 0 & 0 & 0 & 0 & 0 & 0 \end{bmatrix}}_{\mathbf{Q}} \underbrace{\begin{bmatrix} x \\ \dot{x} \\ x^2 \end{bmatrix} \otimes \begin{bmatrix} x \\ \dot{x} \\ x^2 \end{bmatrix}}_{\mathbf{w}\otimes\mathbf{w}} + \underbrace{\begin{bmatrix} 0 \\ \frac{1}{m} \\ 0 \end{bmatrix}}_{\mathbf{B}} u,$$

or in short $\dot{\mathbf{w}} = \mathbf{A}\mathbf{w} + \mathbf{Q}(\mathbf{w}\otimes\mathbf{w}) + \mathbf{B}u$. As before, we introduce the observed output $y(t) = x(t)$. Hence write $y = \mathbf{C}\mathbf{w}$, where $\mathbf{C} = \begin{bmatrix} 1 & 0 & 0 \end{bmatrix}$. Next, choose the same parameters as for the previous case and, additionally, take $k_3 = 10^4$.

Let $\mu_1 = 1$, $\mu_2 = j$ and $\mu_3 = -j$ be the left sampling points. Additionally, let $\lambda_1 = 2$, $\lambda_2 = 2j$ and $\lambda_3 = -2j$ be the right sampling points. From (12) and (13), we put together a Loewner model of dimension $k = 3$ (with complex entries). After transforming the matrices into real arithmetics, we note that $\text{rank}(\mathbb{L}) = 2$. Based on the procedure in (18), we compress the dimension of the model to $r = 2$ (by means of left and right singular vector projection matrices). For the new compressed real-valued model, the Loewner pencil is regular. Note that the eigenvalues of this pencil are $-\frac{5}{2} \pm \frac{5}{2}\sqrt{7}$, exactly as the ones of the original matrix $\mathbf{A}$. Moreover, these values are the roots of the denominator of $\mathbf{H}_1(s)$ in (47), i.e. $ms^2 + cs + k_1 = 0$.

We choose the input to be $u(t) = \cos(4t)$ and simulate the original cubic scalar system in (52) for zero initial conditions. Additionally, we also perform a time-domain simulation of the reduced Loewner model. The time horizon is chosen to be $[0, 10]s$. The first order derivative is approximated via a Runge-Kutta 4th/5h order scheme (*ode45* in MATLAB®).

We observe as before the displacement variable, i.e. the output is chosen to be $y = x$. The results are depicted presented in Fig. 1. Note that the Loewner model provides good approximation to the original cubic system.

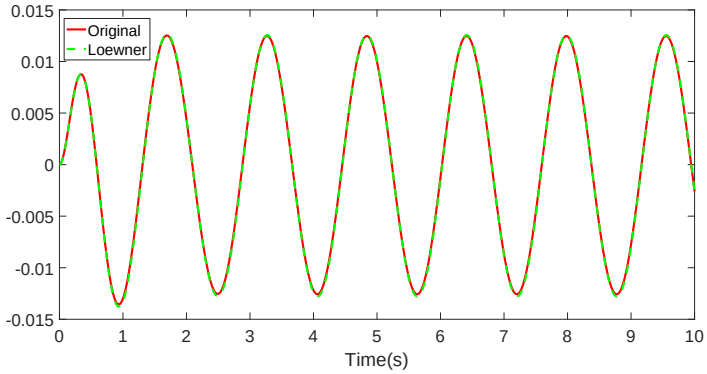


Figure 1: Time-domain simulation of the observed output: the displacement

7 CONCLUSIONS

In this study, we analyze a method that can use experimental data for identifying some classes of nonlinear systems (bilinear and quadratic). A linear model is first fitted from measurements of the first (linear) transfer function. Then, depending on the desired class of nonlinearities, an extra term is added to the differential equation to be modeled. The first numerical example is bilinear while the second has a cubic nonlinearity. For the later, a reformulation as a quadratic system is first enforced. The test cases show promising numerical results. Further research topics include applying this approach to quadratic-bilinear systems and to systems with higher dimension (larger number of degrees of freedom).

REFERENCES

[1] Antoulas, A.C. *Approximation of large-scale dynamical systems*, SIAM, (2005).

[2] Antoulas, A.C., Gosea, I.V. and Ionita, A.C. Model reduction of bilinear systems in the Loewner framework. SIAM J. Sci. Comput. 38(5), B889–B916 (2016).

[3] Antoulas, A.C., Lefteriu, S. and Ionita, A.C. A tutorial introduction to the Loewner framework for model reduction, pp. 335–376. Ch. 8 in [9]. SIAM (2017).

[4] Bedrosian, E. and Rice, S. The output properties of Volterra systems driven by harmonic and Gaussian inputs, Proceedings of the IEEE, 59, 1688–1707, (1971).

[5] Benner, P., Cohen, A., Ohlberger, M. and Willcox, K., (eds.) *Model reduction and approximation*, SIAM (2017).

[6] Billings, S.A. *Nonlinear system identification: NARMAX methods in the time, frequency, and spatio-temporal domains*, John Wiley & Sons, (2013).

[7] Gosea, I.V. and Antoulas, A.C. Data-driven model order reduction of quadratic-bilinear systems. Numer. Linear Algebra Appl. 25(6) (2018).

[8] Kovacic, I. and Brennan, M. J. *The Duffing equation: Nonlinear oscillators and their behaviour*, Wiley, (2011).

[9] McCormick, G.P. Computability of global solutions to factorable nonconvex programs: Part i - convex underestimating problems, Math. Program. 10(1), 147–175 (1976).

[10] Petkovska, M. and Do, D. D. Nonlinear frequency response of adsorption systems: isothermal batch and continuous flow adsorbers, Chemical Engineering Science, 53(17) 3081–3097, (1998).

[11] Rugh, W. J. *Nonlinear system theory - The Volterra/Wiener approach*, University Press, (1981).

[12] Schetzen, M. *The Volterra and Wiener theories of nonlinear systems*, Wiley, (1980).

[13] Tomlinson, G. R., Manson, G. and Lee, G. M. A simple criterion for establishing an upper limit to the harmonic excitation level of the Duffing oscillator using the Volterra series, Journal of Sound and Vibration, 190(5), 751–762, (1995).

[14] Worden, K. and Tomlinson, T. R. *Nonlinearity in structural dynamics: Detection, identification and modelling*, CRC Press, (2000).

XV International Conference on Computational Plasticity. Fundamentals and Applications
COMPLAS 2019
E. Oñate, D.R.J. Owen, D. Peric, M. Chiumenti & Eduardo de Souza Neto (Eds)

REDUCED FINITE ELEMENT SQUARE TECHNIQUES (RFE^2): TOWARDS INDUSTRIAL MULTISCALE FE SOFTWARE

ORIOL LLOBERAS-VALLS[*,†], MARCELO RASCHI[*], ALFREDO E. HUESPE[†,‡] AND JAVIER OLIVER[*,†]

[*] Centre Internacional de Metodes Numerics a l'Enginyeria (CIMNE)
Campus Nord UPC, 08034 Barcelona, Spain
e-mail: olloberas@cimne.upc.edu

[†] Universitat Politècnica de Catalunya (UPC) - BarcelonaTech
Campus Nord UPC, Mòdul C-1 101, c/ Jordi Girona 1-3, 08034 Barcelona, Spain

[‡] CIMEC-UNL-CONICET
Güemes 3450, Santa Fe, Argentina

Key words: FE^2 techniques, reduced order modeling, industrial FE software

Abstract. Reduced order modeling techniques proposed by the authors are assessed for an industrial case study of a 3D reinforced composite laminate. Essentially, the main dominant strain micro-structural modes are obtained through standard reduced order modeling techniques applied over snapshots of a representative training strain space. Additionally, a reduced number of integration points is obtained by exactly integrating the main energy modes resulting from the training energy snapshots. The outcome consists of a number of dominant strain modes integrated over a remarkably reduced number of integration points which provide the support to evaluate the constitutive behavior of the micro-structural phases. Results are discussed in terms of the consistency of the multiscale analysis, tunability of the microscopic material parameters and speed up ratios comparing a high fidelity simulation and the multiscale reduced order model.

1 INTRODUCTION AND SUMMARY OF THE MODEL

In a series of papers ([1], [2]), the authors have presented a reduced order model technique aiming at speeding-up the computational cost of multiscale mechanical problems where materials are intrinsically heterogeneous.

In the same spirit, this work aims at simulating problems where the behavior of the material at the structural scale is complex and can be hardly captured by means of a phenomenological one-scale approach. This typically happens when a strong dependency of the effective material properties with the micro-parameters governing the material deformation phenomena at the lower scales is observed. In this scenario, the use of a FE^2

technique [4], sketched in Figure 1, or a similar procedure, is essential. In this context, the micro-scale analysis, solved in a Representative Volume Element (RVE) Ω_μ, is performed with the present reduced model coined as Reduced Finite Element Square Technique (RFE^2).

This model is based on a Proper Orthogonal Decomposition procedure to build a reduced basis of the primary kinematic variable at the micro-scale problem, and a reduced optimized numerical quadrature rule to account for the constitutive behaviour of the micro-scale formulation.

In the present work, we leave aside the detailed description of the methodology to give particular emphasis to the numerical assessments of the RFE^2 model for solving industrial 3D problems and evaluate the attained speed-ups. In the next sub-Section we summarize the main equations describing the reduced model and the remaining part of the paper deals with the numerical assessment.

1.1 Micro-scale Problem Formulation

Following the formulation presented in [1], here particularized for small deformations, we can formulate the microscale problem in the RVE domain Ω_μ as follows.

Given the macro-scale strain, $\boldsymbol{\varepsilon}^M$, and the spaces of admissible ($\mathcal{U}_\mu^{\mathcal{E}}$) and variational ($\mathcal{V}_\mu^{\mathcal{E}}$) micro-strain fluctuations defined by:

$$\mathcal{U}_\mu^{\mathcal{E}} = \mathcal{V}_\mu^{\mathcal{E}} := \{\tilde{\boldsymbol{\varepsilon}}_\mu \quad | \quad \tilde{\boldsymbol{\varepsilon}}_\mu \in \mathbb{E}_\mu \quad \wedge \quad \int_{\Omega_\mu} \tilde{\boldsymbol{\varepsilon}}_\mu \, d\Omega_\mu = \mathbf{0}\} \,, \tag{1}$$

where $\tilde{\boldsymbol{\varepsilon}}_\mu$ is the micro-strain fluctuations in Ω_μ and $\mathbb{E}_\mu$ is the space of compatible strains; find the micro-strain $\boldsymbol{\varepsilon}_\mu = \boldsymbol{\varepsilon}^M + \tilde{\boldsymbol{\varepsilon}}_\mu$, with $\tilde{\boldsymbol{\varepsilon}}_\mu \in \mathcal{U}_\mu^{\mathcal{E}}$, such that:

$$\int_{\Omega_\mu} \boldsymbol{\sigma}_\mu(\boldsymbol{\varepsilon}_\mu, \alpha_\mu) : \delta\tilde{\boldsymbol{\varepsilon}}_\mu \, d\Omega_\mu = 0 \,; \qquad \forall \delta\tilde{\boldsymbol{\varepsilon}}_\mu \in \mathcal{V}_\mu^{\mathcal{E}} \,, \tag{2}$$

with $\boldsymbol{\sigma}_\mu$ being the micro-stresses expressed as a function of the micro-strain and the set of internal variables α_μ whose temporal evolution has to be specified with the corresponding equations as follows

$$\dot{\alpha}_\mu = g(\boldsymbol{\varepsilon}_\mu, \dot{\boldsymbol{\varepsilon}}_\mu, \alpha_\mu) \,. \tag{3}$$

The macro-stress, computed as the average value of the micro-stress $\boldsymbol{\sigma}_\mu$, is transferred to the coarse scale.

1.1.1 Reduced Finite Element Square Model (RFE^2)

The problem (1)-(3) is solved by introducing a low-dimensional vector space whose elements are the admissible micro-strain fluctuations $\tilde{\boldsymbol{\varepsilon}}_\mu$. Identical approach is taken for the micro-strain variations. Both spaces are spanned by a basis of n_ε vectors $\boldsymbol{\Psi}_j$. This basis is computed with a Proper Orthogonal Decomposition technique from a large set of micro-strain fluctuations that are obtained as solutions of the micro-cell problem during an off-line sampling process. Details of this procedure can be found in [3].

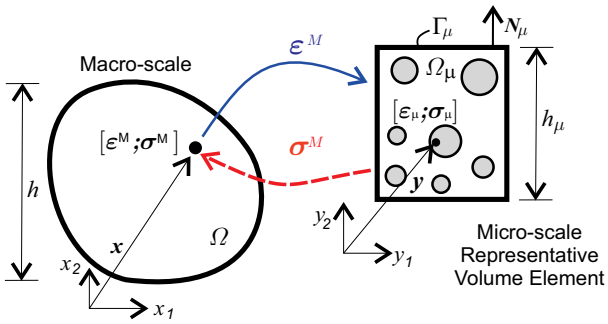


Figure 1: Structural problem involving two well-separated scales of lengths h and h_μ which satisfy $h_\mu \ll h$. Macro-scale domain is Ω and the RVE is Ω_μ. Stress and strains at Ω are denoted $\boldsymbol{\sigma}^M$ and $\boldsymbol{\varepsilon}^M$. Similar objects at the micro-scale are denoted $\boldsymbol{\sigma}_\mu$ and $\boldsymbol{\varepsilon}_\mu$. The stress $\boldsymbol{\sigma}^M$ and strain $\boldsymbol{\varepsilon}^M$ are associated with $\boldsymbol{\sigma}_\mu$ and $\boldsymbol{\varepsilon}_\mu$ through scale transitions equations.

Each element of the spaces is given by the linear combination:

$$\tilde{\boldsymbol{\varepsilon}}_\mu\left(\boldsymbol{y},t\right)=\sum_{j=1}^{n_\varepsilon}\boldsymbol{\Psi}_j\left(\boldsymbol{y}\right)c_j\left(t\right)=\boldsymbol{\Psi}(\boldsymbol{y})\boldsymbol{c}(t)\;, \tag{4}$$

where the coefficients $\boldsymbol{c}$ denote a time-dependent parameter vector. The low dimensional approach of $\tilde{\boldsymbol{\varepsilon}}_\mu$ and the corresponding variation of micro-strain fluctuation are replaced into equation (2). Furthermore, the original Gauss quadrature rule, typically used in the finite element technique to integrate the kernel of equation (2), is replaced by a reduced optimal quadrature rule with N_r reduced quadrature points[1]:

$$\int_{\Omega_\mu}(\bullet)\left(\boldsymbol{y}\right)d\Omega_\mu\approx\int_{\Omega_\mu}^{red}(\bullet)\left(\boldsymbol{y}\right)d\Omega_\mu=\sum_{k=1}^{N_r}(\bullet)\left(\boldsymbol{z}_k\right)\omega_k \tag{5}$$

The weights ω_k and spatial position $\boldsymbol{z}_k$ defining the reduced quadrature rule are defined according to the procedure described in [1].

Thus, the equation (2) can be approached as follows:

$$\int_{\Omega_\mu}\boldsymbol{\sigma}_\mu([\boldsymbol{\Psi c}],\alpha_\mu):[\boldsymbol{\Psi}\delta\boldsymbol{c}]\;d\Omega_\mu\approx\sum_{k=1}^{N_r}\left(\,\boldsymbol{\sigma}_\mu([\boldsymbol{\Psi}(\boldsymbol{z}_k)\boldsymbol{c}],\alpha_\mu(\boldsymbol{z}_k)):[\boldsymbol{\Psi}(\boldsymbol{z}_k)\delta\boldsymbol{c}]\,\right)\,\omega_k(\boldsymbol{z}_k)=\boldsymbol{0}\,;\quad\forall\delta\boldsymbol{c}\in\mathbb{R}^{n_\varepsilon}. \tag{6}$$

This system of n_ε non-linear equations is solved jointly with the evolution equations (3) evaluated in the N_r reduced quadrature points.

[1]The quadrature rule is derived from a low dimensional approach of the internal energy function ψ. A POD technique is used to extract a low dimensional basis for ψ and the reduced quadrature rule has to satisfy the correct integration of every base of ψ. This condition can be satisfied if the number of quadrature points N_r is equal to the number of modes taken for ψ plus 1. Hence, we assume that the number of modes for ψ is equal to the N_r-1.

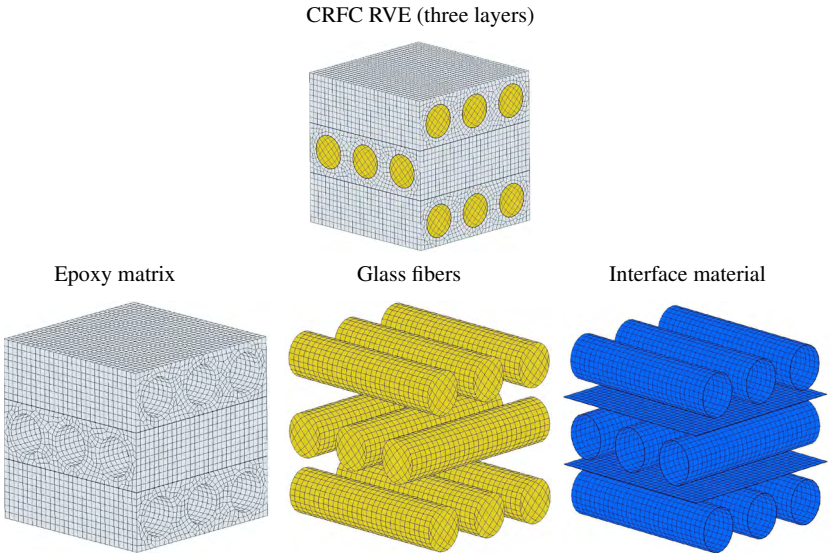


Figure 2: Material phases of the CRFC microstructural RVE.

2 RESULTS

In the following sections a number of results are commented in order to validate and demonstrate the industrial potential of the developed algorithms. The microstructure modelling is introduced and the influence of the number of strain and energy modes in the expected error is justified as well. Moreover, the RFE2 modelling is validated in terms of consistency with respect to the macro-mesh size, the number of strain modes and the corresponding number of energy modes or integration points. Tunability of the material parameters is studied as well and the obtained speed-ups for microstructures with refined discretisations is reported as well.

2.1 Microscopic modelling

The selected material is a fiber reinforced composite laminate with a microscopic representation composed by fibers (glass fiber), an epoxy matrix and an interphase material between matrix layers and fiber and matrix phases responsible for the delamination (between layers) and fiber pull-out (between fiber and matrix) effects. Fibers are assumed to behave elastically and an only-traction-damage model (cf. [5]) with hardening parameter, H, is considered with linear hardening in the matrix and interphase phases. The representation of the material phases and material parameters are given in Figure 2 and Table 1 summarizes the utilized phase parameters.

Minimal kinematic constraints (cf. equation (1)) are considered during the sampling stage of the reduction process allowing precisely to develop the observed delamination, debonding and pull-out effects. Figure 3 shows the deformed configuration and damage distribution of a sampling trajectory that involves the above mentioned physical behaviour.

After the sampling process the strain, energy bases and integration rule are retrieved

Phase	E $[N/mm^2]$	ν	Elastic limit σ_e $[N/mm^2]$	Hardening parameter H
Fiber	72000	0.25	–	–
Matrix	3790	0.37	200	10^{-1}
Interphase	3790	0.37	100	10^{-4}

Table 1: Micro material phase parameters.

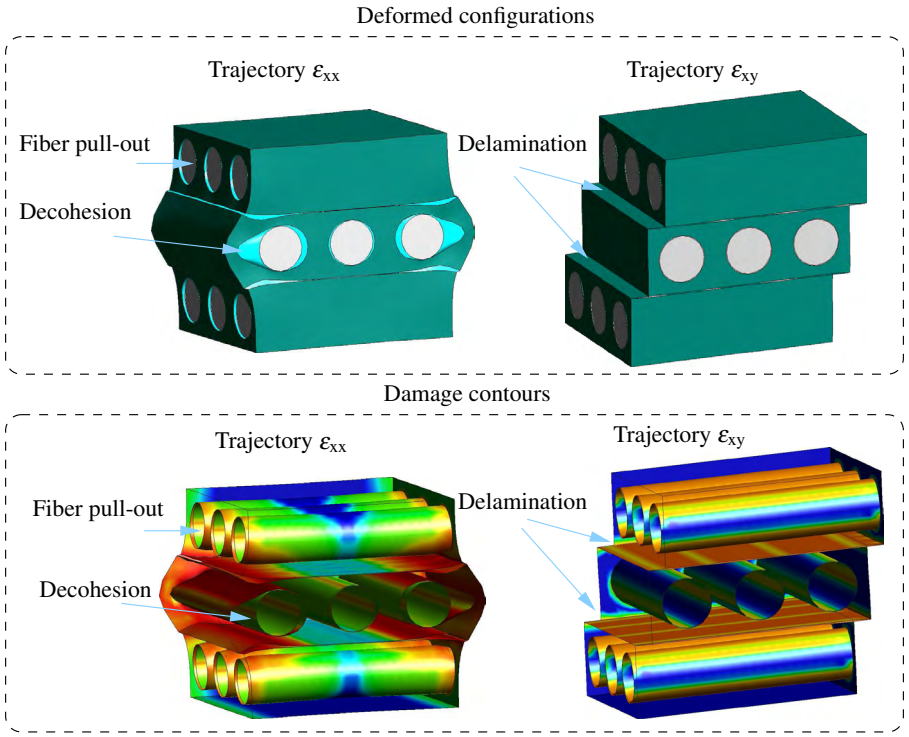


Figure 3: Deformed configuration and damage contours at trajectories ε_{xx} (left) and ε_{xy} (right).

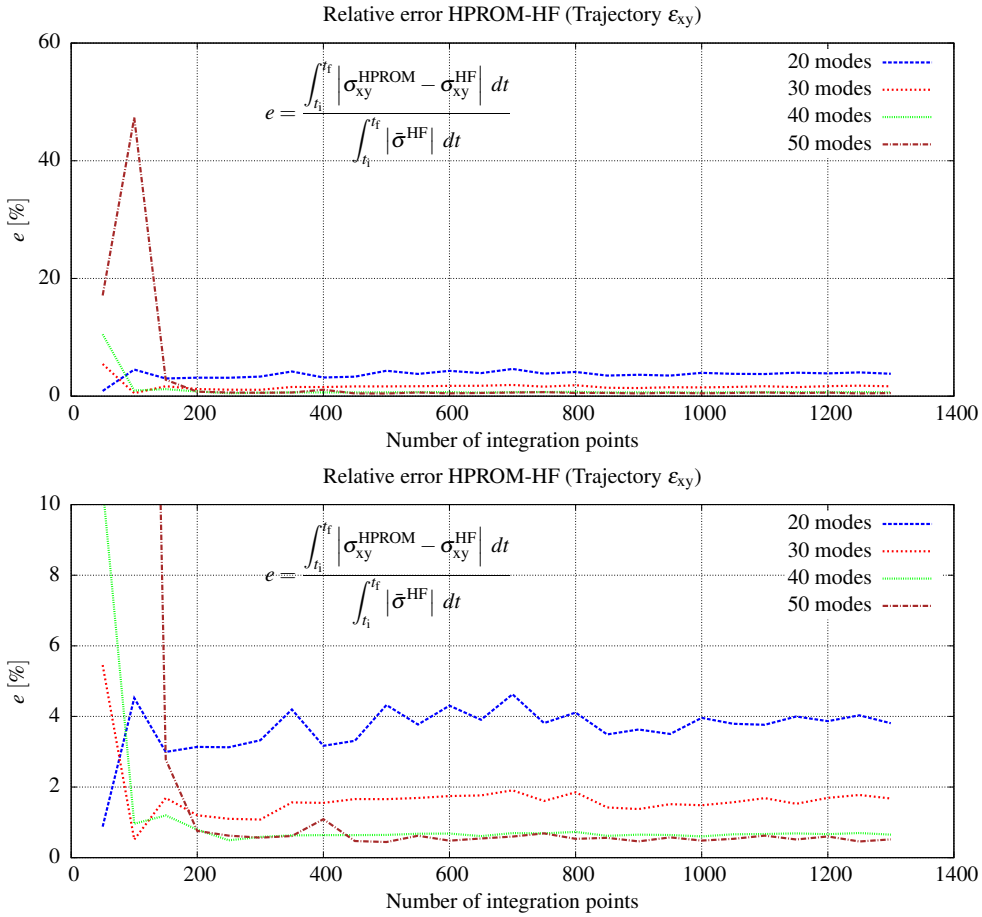


Figure 4: A posteriori error for the ε_{xy} sampling trajectory

which confers the reduced order microstructural model. The accuracy of the solution obtained with the reduced order model is compared with the high fidelity computation for a particular sampling trajectory. The obtained "a posteriori" error is plot for different reduced RVEs considering an increasing number of strain modes and integration points (cf. Figure 4). It is observed that 40 strain modes ($n_\varepsilon = 40$) and 200 integration points ($N_r = 200$) suffice to capture the physics needed to reproduce this trajectory with a relative error lower or equal than one percent.

2.2 Multiscale reduced order modelling

A dogbone specimen as depicted in Figure 5 is considered in which an imposed displacement is applied at the basis around both extremes of the specimen. The objective is to trigger, at the microstructural level, all delamination, fiber pull-out and debonding mechanisms.

A deformed configuration of the dogbone together with a displacement reconstruction

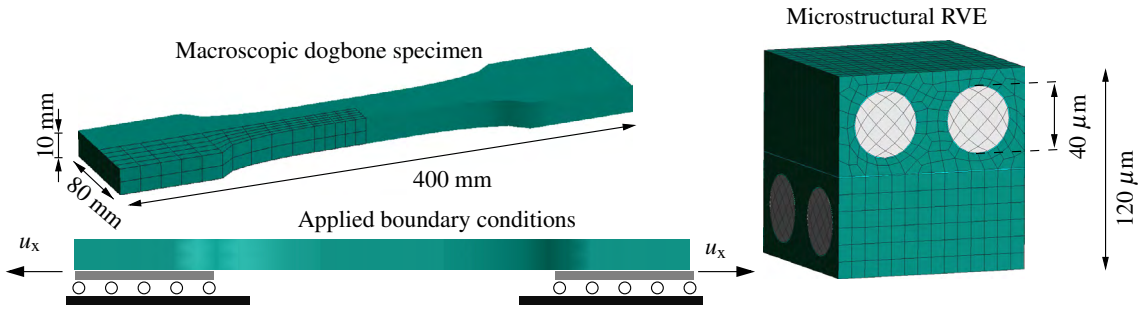


Figure 5: Multiscale analysis of a CRFC dogbone specimen under axial tension with shear: macroscopic geometry and boundary conditions (left) and microstructural RVE (right).

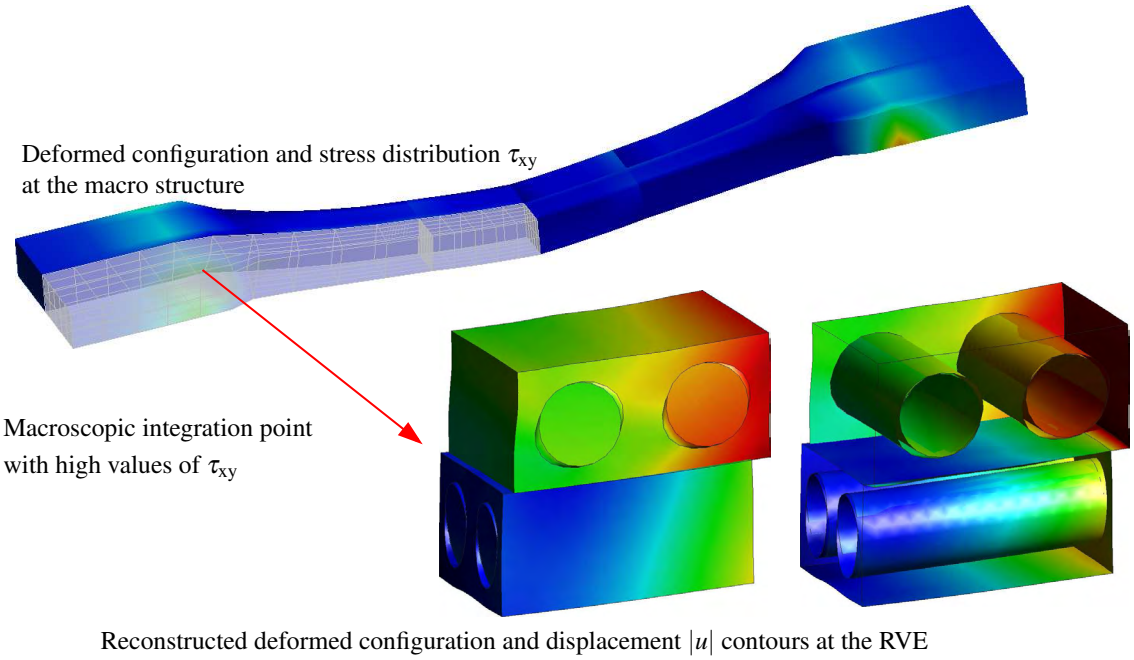


Figure 6: Deformed configuration of the macrostructure (top) and displacement reconstruction of an RVE corresponding to a critical stress point in the macro structure (bottom).

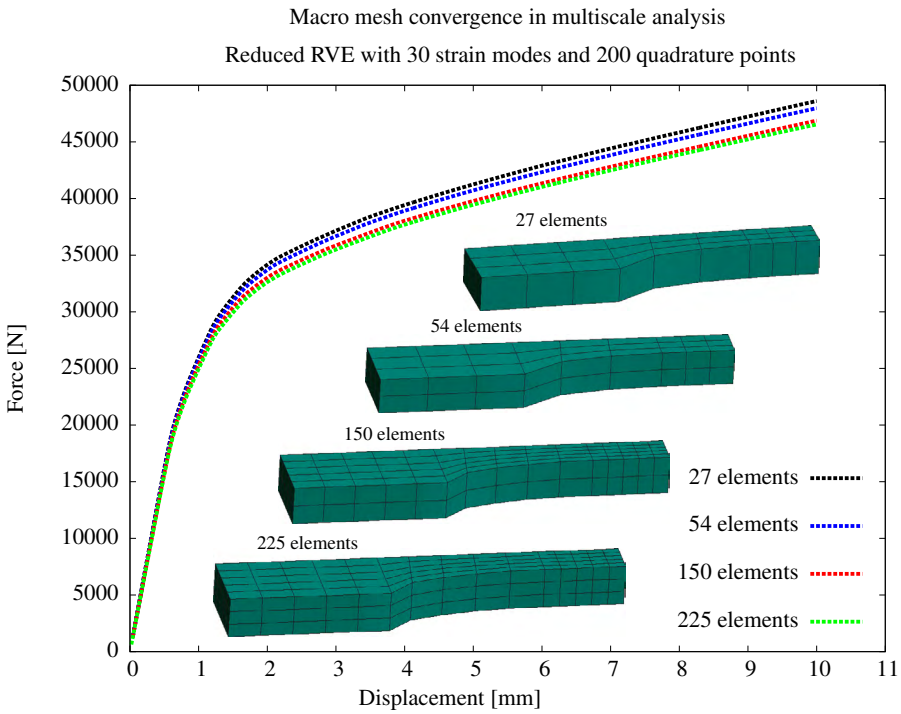


Figure 7: Global mechanical response upon mesh refinement.

of an RVE[2] corresponding to region with high σ_{xy} is given in Figure 6. The RVE reduced model accounts for 30 strain modes and 200 integration points.

2.2.1 Consistency tests

The multiscale analysis depicted in Figure 5 considering the same reduced RVE model is now repeated for a number of macroscale discretizations. The global response in terms of reaction versus applied displacement is shown in Figure 7. It is observed that the global response shows a convergent behaviour upon mesh refinement which verifies the consistency of the multiscale approach. Moreover, a sufficiently accurate response is obtained for a macroscopic discretization of around 150 elements (the total dogbone mesh being 150×4=600 elements).

Another test consists in the impact of the considered number of strain modes in the reduced RVE bases in the global response (cf. Figure 8). It turns out that 30 strain modes suffice to accurately capture the physics stemming out of the proposed multiscale problem. It is unnecessary then to consider more than 30 strain modes although a highly convergent behaviour is observed.

Finally, the number of integration points (linked to the considered energy modes) within the reduced basis is modified to study the global multiscale behaviour. To this end, the reduced RVE with 50 strain modes is considered and the number of integration points is

[2]The reconstruction stage for obtaining the micro-displacement configurations has been detailed in [1].

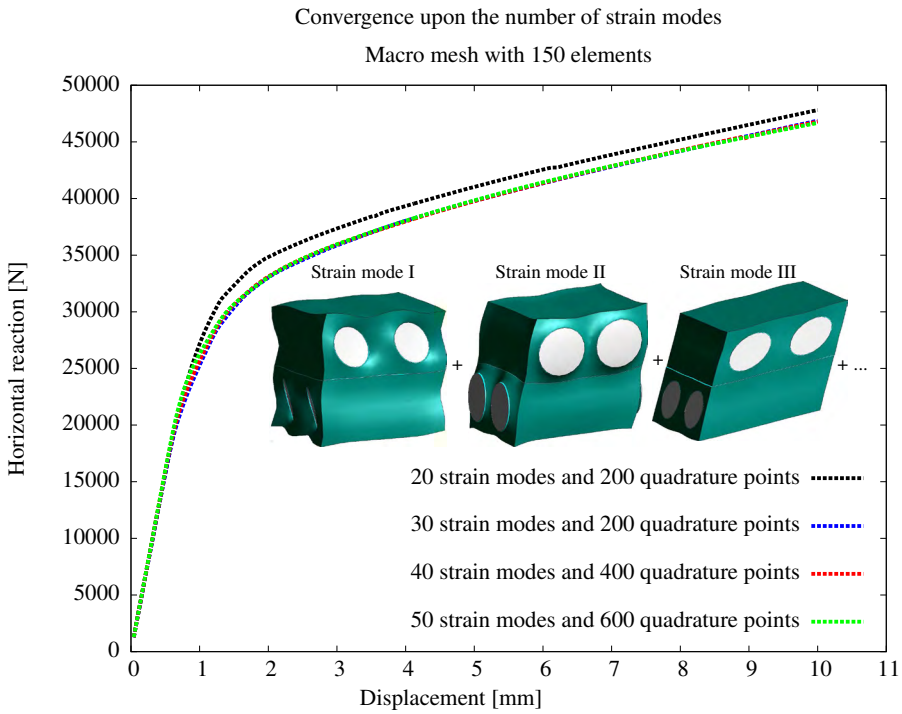


Figure 8: Global mechanical response upon increasing the micro strain modes.

increased from 200 up to 1200. Results are summarized in Figure 9 where a convergent behaviour upon increasing energy modes is observed.

2.2.2 Customization and tunability

The reduced RVE model employed in the previous sections is constructed in the bases of the material phase parameters depicted in Table 1. In order to prove the tunability of the methodology in terms of the micromaterial phase parameters a number of customization tests are outlined. First, the interphase hardening parameter and elastic limit is varied to the new values $H = 0.1$ and $\sigma_e = 175$ MPa. Figure 10 shows the resulting mechanical behaviour of the RVE obtained through a multiscale analysis and with a high fidelity analysis. The multiscale analysis is based on the RVE reduced bases obtained from a sampling procedure based on the properties depicted in Table1. If the material parameters are then modified the result is in good agreement with the response obtained from a direct FE (high fidelity) computation using such user defined parameters. Figure 11 shows a more extreme customization case in which the hardening parameter of the matrix material is set to $H = 0.9$ which is close to an elastic behaviour. It is then observed that 80 strain modes are required for the mutliscale analysis to correctly capture the desired behaviour. It is then concluded that a complete sampling renders a reduced basis capable of reproducing the mechanical behaviour upon changing the material phase parameters if enough strain modes are included in the reduced bases.

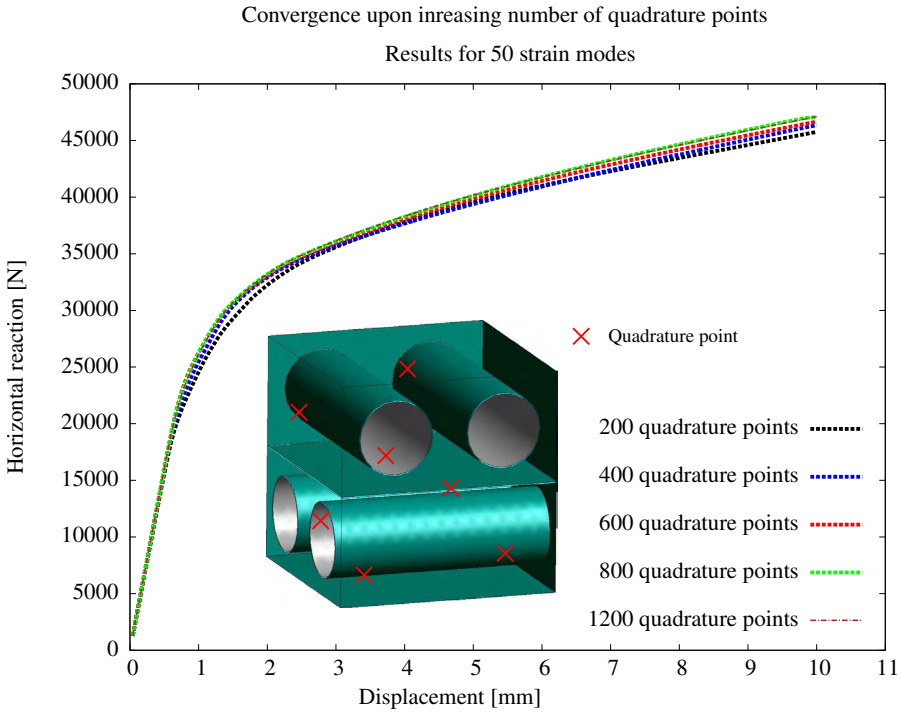


Figure 9: Global mechanical response upon increasing the micro quadrature points.

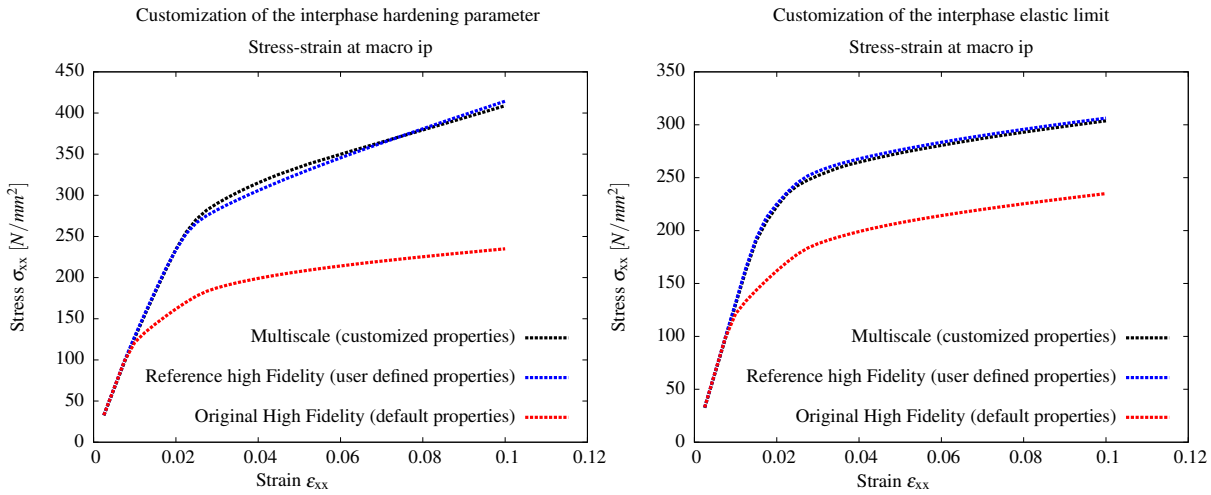


Figure 10: Tuning of the interphase hardening parameter (left) and interphase elastic limit (right). Micro-stress $(\sigma_\mu)xx$ versus micro-strain $(\varepsilon_\mu)xx$.

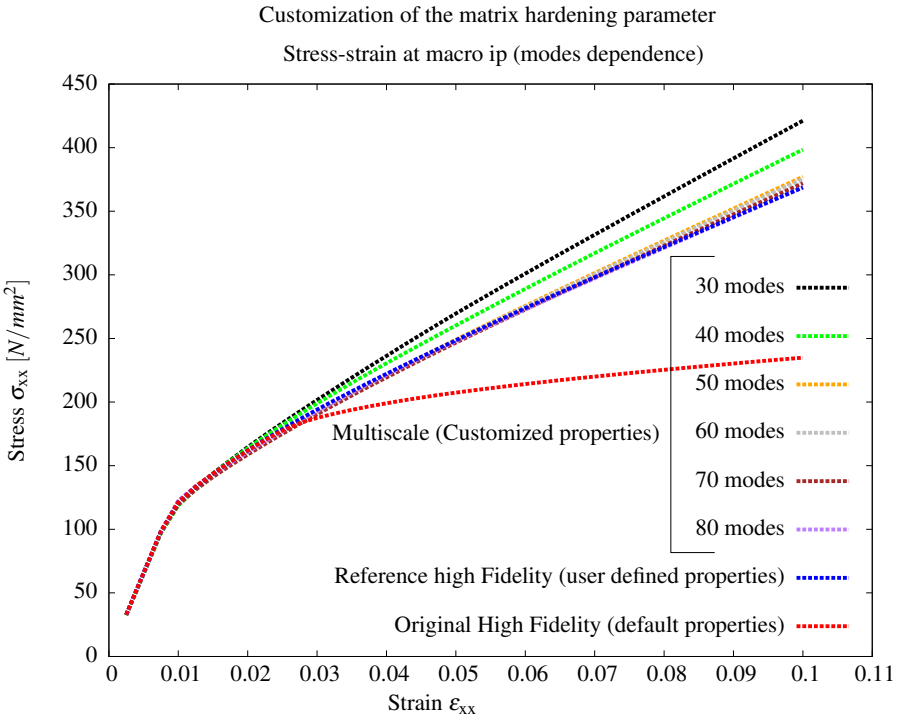


Figure 11: Tuning of the matrix hardening parameter. Micro-stress $(\sigma_\mu)xx$ versus micro-strain $(\varepsilon_\mu)xx$.

2.2.3 Computational and algorithmic Speed-up

The relative computational cost between standard FE^2 and the proposed RFE^2 technology is measured here through the algorithmic and computational speed-up, S_p. The algorithmic speed-up reflects the relative complexity of both techniques in terms of the amount of DOF to solve (DOF speed-up) and amount of quadrature points (IP speed-up). Considering that an RVE basis with 40 strain modes and 200 quadrature points suffice to provide errors below 1% when comparing the reduced order modelling and high fidelity analysis, both DOF and IP speed-ups have been calculated considering 40 DOF and 200 IP in the reduced model. Figure 12 reflects the clearly growing algorithmic speed-ups upon increasing the RVE discretization complexity. Based on the similar CRFC micro-structures with increasing number of layers and fibers one observes that for RVE discretizations with around one million of integration points the relative algorithmic speed-up is around five orders of magnitude, i.e. the reduced RVE model is expected to perform 10^4 times faster than the high fidelity one. Moreover, the reduced basis inherits the type of boundary conditions utilized during the sampling stage and, therefore, avoids any performance overhead due to handling any multi-point constraints and their impact in the bandwidth of the resulting system. Computation times have been compared regarding the high fidelity problem in one selected sampling trajectory and the reduced order model. It is seen that the resulting computational speed-up increases even more upon increasing the RVE discretization and can reach around 30×10^4 for RVEs with around one million of integration points.

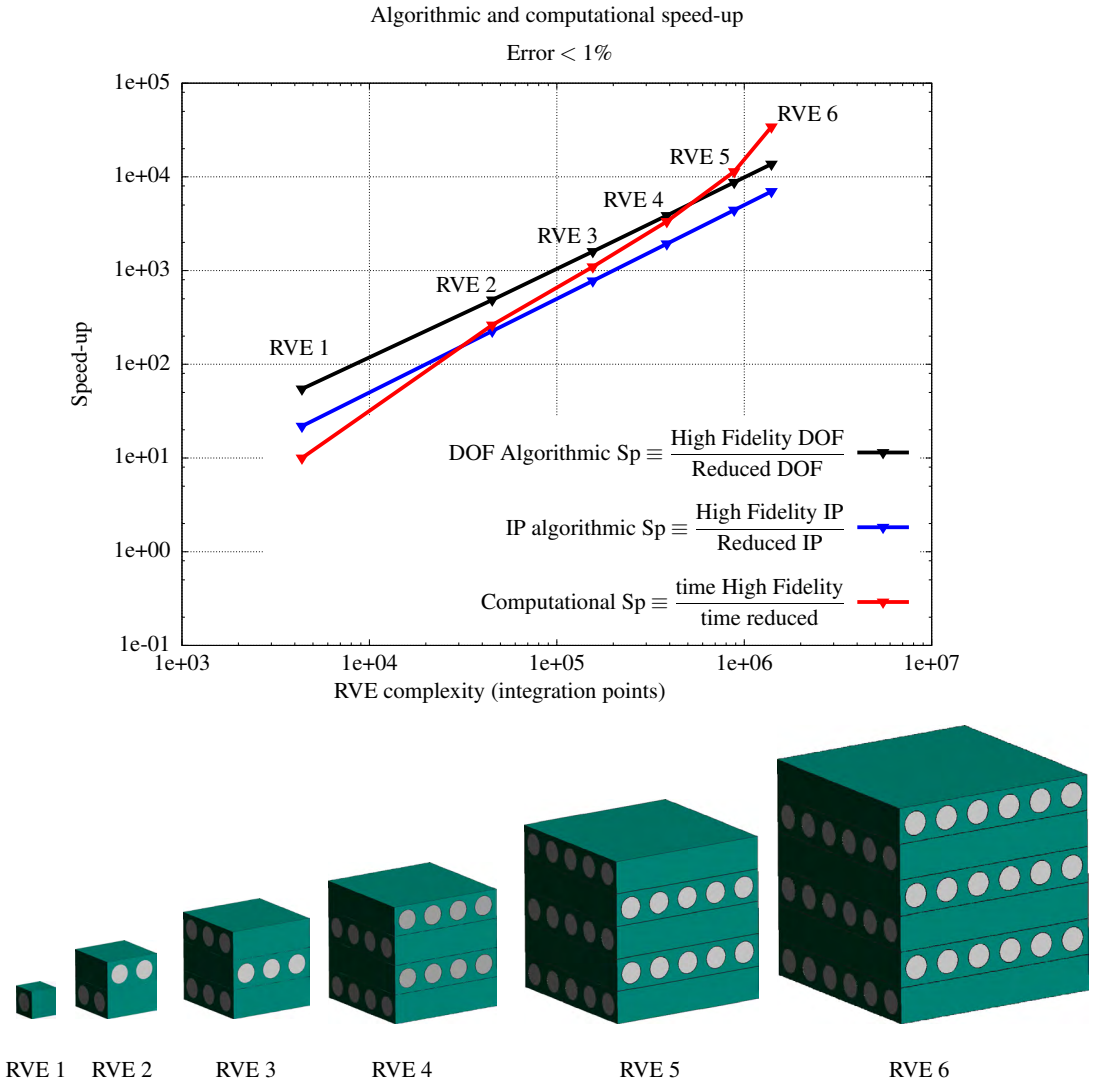


Figure 12: Speed-up values upon increasing material discretization.

3 CONCLUSIONS

The RFE^2 technology is assessed in this contribution for an industrial case study of a 3D reinforced composite laminate. A number of consistency tests have been successfully passed, i.e. convergence upon macroscopic discretization, convergence upon increasing number of reduced strain modes and convergence upon the reduced quadrature for the strain basis. Moreover, the technology proofs to be tunable upon the simulation needs of the user. In other words, different material phase parameters than the ones employed to develop the reduced bases can be adopted during the online multiscale simulation with remarkable accuracy.

The relative performance (speed-up) with respect to standard FE^2 methods increases with increasing the RVE discretization and is found between 10^4 and 10^5 for RVEs with around one million of integration points, e.g. around $100 - 150 \times 10^3$ hexahedral FE, assuming an error below 1% compared to a high fidelity analysis. These qualities are seen ideal to export the RFE^2 technology to the industrial sector.

REFERENCES

[1] Caicedo, M., Mroginski, J.L., Toro, S., Raschi, M., Huespe, A. and Oliver, J. High performance reduced order modeling techniques based on optimal energy quadrature: application to geometrically non-linear multiscale inelastic material modeling. *(2018), pp. 1–22.*

[2] Oliver J., Caicedo M., Huespe A.E., Hernndez J.A., Roubin E. Reduced order modeling strategies for computational multiscale fracture. *Comp. Meth. Appl. Mech. Eng., Vol. 313, (2017), 560–595.*

[3] Hernández J.A., Oliver J., and Huespe A.E., Caicedo, M.A. and Cante, J.C. High-performance model reduction techniques in computational multiscale homogenization. *Comp. Meth. Appl. Mech. Eng., Vol. 276, (2014), 149–189.*

[4] Feyel F. and Chaboche J.L. FE2 multiscale approach for modelling the elastovis-coplastic behaviour of long fibre SiC/Ti composite materials. *Comp. Meth. Appl. Mech. Eng., Vol. 183, (2000), 309–330.*

[5] Faria R., Oliver J. and Cervera M. On Isotropic Scalar Damage Models for the Numerical Analysis of Concrete Structures. *Technical report. Publication CIMNE N-198, (2000).*

XV International Conference on Computational Plasticity. Fundamentals and Applications
COMPLAS 2019
E. Oñate, D.R.J. Owen, D. Peric, M. Chiumenti & Eduardo de Souza Neto (Eds)

OPTIMIZATION-BASED COMPARISON OF DIFFERENT APPROACHES FOR THE AUTOMATIZED CALCULATION OF RESIDUAL STRESSES AND FIBER ORIENTATIONS IN ARTERIES

ANNA ZAHN*† AND DANIEL BALZANI†

†Chair of Continuum Mechanics, Department of Civil and Environmental Engineering,
Ruhr-Universität Bochum, Universitätsstraße 150, 44801 Bochum, Germany
e-mail: anna.zahn@ruhr-uni-bochum.de, daniel.balzani@ruhr-uni-bochum.de

Key words: Arterial Walls, Stress-driven Growth and Fiber Reorientation, Optimization

Abstract. Residual stresses and fiber orientations in arterial walls can be approximated by means of the simulation of growth and remodeling processes. In order to enable a comparison of different approaches of combined growth and remodeling in one framework, a method based on the optimization of model parameters is developed. The minimization of a mechano-biologically motivated objective function permits to evaluate the approaches with respect to their ability of effectively reducing stress peaks and stress inhomogeneities in the arterial wall. This examination is performed for a simplified, one-layered, rotationally symmetric arterial segment in order to enable the analysis of the fundamental mechanisms included in the individual model variants. Once the most probable growth mechanism is identified, multi-layered segments can be analyzed in more detail.

1 INTRODUCTION

The mechanical behavior of arterial tissues is considerably affected by residual stresses, which reduce stress peaks and gradients in the arterial wall [8, 9]. Furthermore, the arrangement of the collagen fibers, whose orientation is graded over the wall thickness, strongly affects the load bearing behavior. Unfortunately, residual stresses or fiber orientations can currently hardly be measured in vivo. However, they have to be known in order to perform reliable patient-specific numerical simulations. Both phenomena can be included by modeling the adaptation of the artery to its mechano-biological environment, which appears as arterial growth and remodeling.

Following Hariton et al. [6], it is assumed that the collagen fibers reorient based on the principal stress state such that they arrange symmetrically with respect to the principal axes. The reorientation towards the target fiber orientations is here described by an evolution equation, which assures that abrupt changes do not occur.

If growth is simulated in tubular structures, residual stresses arise automatically as a consequence of the growth deformation and need not to be taken into account for instance by rather technical approaches as e. g. presented by Balzani et al. [2] or Schröder and von Hoegen [13]. The growth model applied here is based on a multiplicative decomposition of the deformation gradient into an elastic and a growth part as originally proposed by Rodriguez et al. [12] and then pursued amongst others by Kuhl et al. [10] or Göktepe et al. [5]. In order to account for the anisotropy of the growth mechanism, the growth part itself is decomposed here into up to three individual parts, where each part is associated to a principal direction of a stress tensor. By specifying the number and form of the individual growth tensors and by using different growth-driving quantities, a set of different formulations for the automatized calculation of residual stresses and fiber orientations is obtained. A detailed description of the combined growth and remodeling framework has been published in [14].

This contribution aims at developing a method which enables a quantitative comparison of the fundamental mechanisms included in the different formulations. The growth parameters are therefore computed by minimizing a mechano-biologically motivated objective function, which is formulated such that its minimum reflects the most efficient reduction of stress peaks and stress inhomogeneities in the arterial layers. This systematic analysis is conducted for different loading scenarios applied to a simplified one-layered artery which is idealized as a rotationally symmetric tube, enabling an efficient optimization. By comparing the obtained minima of the individual approaches, an assessment regarding the most probable mechano-biological mechanism is enabled.

2 GROWTH AND REMODELING FRAMEWORK

As initially proposed in [12], the growth model is based on the multiplicative decomposition $\boldsymbol{F} = \boldsymbol{F}_\mathrm{e}\boldsymbol{F}_\mathrm{g}$ of the deformation gradient into a pure growth part $\boldsymbol{F}_\mathrm{g}$, which involves a stress-free volume change of factor $J_\mathrm{g} = \det[\boldsymbol{F}_\mathrm{g}]$, and a remaining elastic part $\boldsymbol{F}_\mathrm{e}$, which generates stresses. The 2$^{\mathrm{nd}}$ Piola-Kirchhoff stress tensor is obtained as $\boldsymbol{S} = \boldsymbol{F}_\mathrm{g}^{-1}\boldsymbol{S}_\mathrm{e}\boldsymbol{F}_\mathrm{g}^{-T}$, where $\boldsymbol{S}_\mathrm{e} = 2\,\partial\psi/\partial\boldsymbol{C}_\mathrm{e}$ is the stress in the intermediate configuration, which is defined by an appropriate strain energy function ψ and arises from the deformation tensor $\boldsymbol{C}_\mathrm{e} = \boldsymbol{F}_\mathrm{e}^T\boldsymbol{F}_\mathrm{e} = \boldsymbol{F}_\mathrm{g}^{-T}\boldsymbol{C}\boldsymbol{F}_\mathrm{g}^{-1}$. A polyconvex hyperelastic strain energy function from [1] is used to describe the orthotropic material behavior. It takes two families of fibers into account, whose orientations are given by the vectors $\boldsymbol{A}^{(1)}$ and $\boldsymbol{A}^{(2)}$.

2.1 General framework

Accounting for the orthotropic behavior of soft biological tissues, the growth tensor itself is decomposed into three parts according to

$$\boldsymbol{F}_\mathrm{g} = \boldsymbol{F}_\mathrm{g}^{(3)}\boldsymbol{F}_\mathrm{g}^{(2)}\boldsymbol{F}_\mathrm{g}^{(1)}, \tag{1}$$

where each part is related to one of three perpendicular directions $\boldsymbol{A}_\mathrm{g}^{(a)}$ and an internal variable $\vartheta^{(a)}$, $a = 1, 2, 3$, determining the amount of growth. For the definition of the parts of the growth tensor, it is supposed that growth is a stress-driven process which

aims at reducing high stress values [4]. The directions $\boldsymbol{A}_{\mathrm{g}}^{(a)}$ are therefore not meant to represent coordinate axes or structural directions, but rather refer to the local stress state of the tissue. Assuming that all growth and remodeling processes are driven by the same stress quantity, the elastic part of the Mandel stress tensor, i. e. $\boldsymbol{C}_{\mathrm{e}}\boldsymbol{S}_{\mathrm{e}} =: \boldsymbol{\Sigma}_{\mathrm{e}}$, is chosen as driving quantity as proposed in [7] and the directions $\boldsymbol{A}_{\mathrm{g}}^{(a)}$ are computed as principal directions of this stress tensor. The evolution of the growth factors $\vartheta^{(a)}$ is described by a coupled set of evolution equations

$$\dot{\vartheta}^{(a)} = k_{\vartheta}^{(a)}(\vartheta^{(a)})\, \phi^{(a)}(\boldsymbol{\Sigma}_{\mathrm{e}}), \qquad a = 1, 2, 3, \tag{2}$$

which is also formulated in dependence on the elastic part of the Mandel stress. Besides the growth function $k_{\vartheta}^{(a)}$ from [11] with

$$k_{\vartheta}^{(a)}(\vartheta^{(a)}) = \begin{cases} k_{\vartheta,(a)}^{+} \left[\dfrac{\vartheta_{(a)}^{+} - \vartheta^{(a)}}{\vartheta_{(a)}^{+} - 1} \right]^{m_{\vartheta,(a)}^{+}} & \text{for} \quad \phi^{(a)} > 0 \\ k_{\vartheta,(a)}^{-} \left[\dfrac{\vartheta^{(a)} - \vartheta_{(a)}^{-}}{1 - \vartheta_{(a)}^{-}} \right]^{m_{\vartheta,(a)}^{-}} & \text{for} \quad \phi^{(a)} < 0 \\ 0 & \text{for} \quad \phi^{(a)} = 0, \end{cases} \tag{3}$$

a driving force $\phi^{(a)}$ is involved for each direction a. The algorithmic implementation of the growth model within a finite element framework is explained in detail in [14].

The fiber orientation vectors $\boldsymbol{A}^{(1)}$ and $\boldsymbol{A}^{(2)}$ are considered as variable, adjusting automatically following local demands. Once again, the elastic part of the Mandel stress tensor is used to define this reorientation process. Following the hypothesis in [6], the load-bearing behavior can be improved if the fibers arrange symmetrically with respect to the tensile principal stresses and if their orientation within the plane of the highest tensile principal stresses is governed by the ratio of these stresses. The target fiber orientation vectors are thus defined by

$$\bar{\boldsymbol{A}}_{\mathrm{targ}}^{(1)} = \langle \Sigma_{\mathrm{e}}^{\mathrm{I}} \rangle \boldsymbol{e}_{\mathrm{I}} + \langle \Sigma_{\mathrm{e}}^{\mathrm{II}} \rangle \boldsymbol{e}_{\mathrm{II}} \qquad \text{and} \qquad \bar{\boldsymbol{A}}_{\mathrm{targ}}^{(2)} = \langle \Sigma_{\mathrm{e}}^{\mathrm{I}} \rangle \boldsymbol{e}_{\mathrm{I}} - \langle \Sigma_{\mathrm{e}}^{\mathrm{II}} \rangle \boldsymbol{e}_{\mathrm{II}}, \tag{4}$$

where $\boldsymbol{e}_{\mathrm{I}}$ and $\boldsymbol{e}_{\mathrm{II}}$ are unit vectors in the directions of the principal stresses $\Sigma_{\mathrm{e}}^{\mathrm{I}}$ and $\Sigma_{\mathrm{e}}^{\mathrm{II}}$ of the elastic part of the Mandel stress. Use of the Macaulay brackets, which are defined as $\langle \bullet \rangle = 1/2\,(|\bullet| + \bullet)$, guarantees that only positive principal stresses are included. Since the constitutive equations are formulated in the reference configuration, the target vectors are pulled back and optionally exchanged and/or rotated by 180° to keep the remodeling effort minimal. Finally, the vectors $\boldsymbol{A}_{\mathrm{targ}}^{(1)}$ and $\boldsymbol{A}_{\mathrm{targ}}^{(2)}$ are obtained as target vectors for the fiber orientation vectors $\boldsymbol{A}^{(1)}$ and $\boldsymbol{A}^{(2)}$. The numerical treatment of the reorientation process is handled as described in [14], making use of an evolution equation $\dot{\eta}^{(a)} = k_{\eta}(\eta^{(a)})$ for each fiber family. Herein, the variable $\eta^{(a)}$ represents the angle between $\boldsymbol{A}^{(a)}$ and $\boldsymbol{A}_{\mathrm{targ}}^{(a)}$ and the remodeling function $k_{\eta}(\eta^{(a)}) = -k_{\eta}^{+} \ln(m_{\eta}^{+}|\eta^{(a)}| + 1)$ (with $\eta^{(a)}$ in rad) defines the temporal behavior.

2.2 Variability of model components

So far, the individual parts of the growth tensor in Eq. (1) and the driving forces for the evolution of the growth factors in Eq. (2) have not been specified in detail. Both can be chosen based on hypotheses on the mechanism of growth and stress reduction, but nevertheless, a variety of different approaches is imaginable. The purpose of this contribution is to develop a method which enables an optimization-based comparison of these approaches, such that finally an estimation regarding the most probable mechanism is possible. Thereby, the focus is however rather on the anisotropic character of growth than on bio-chemical aspects.

Concerning the form of the individual parts $\boldsymbol{F}_{\mathrm{g}}^{(a)}$ of the growth tensor, three different approaches, namely

$$\boldsymbol{F}_{\mathrm{g}}^{(a)} = \vartheta^{(a)} \boldsymbol{I}, \tag{5a}$$

$$\boldsymbol{F}_{\mathrm{g}}^{(a)} = \vartheta^{(a)} \boldsymbol{I} + \left(1 - \vartheta^{(a)}\right) \boldsymbol{A}_{\mathrm{g}}^{(a)} \otimes \boldsymbol{A}_{\mathrm{g}}^{(a)}, \tag{5b}$$

$$\boldsymbol{F}_{\mathrm{g}}^{(a)} = \boldsymbol{I} + \left(\vartheta^{(a)} - 1\right) \boldsymbol{A}_{\mathrm{g}}^{(a)} \otimes \boldsymbol{A}_{\mathrm{g}}^{(a)}, \tag{5c}$$

are included to the examination. The first approach in Eq. (5a) describes isotropic growth. Due to the anisotropy of arterial tissues, isotropic growth is expected not to be a realistic model assumption. Therefore, the anisotropic forms in Eqs. (5b) and (5c) are additionally taken into account. They describe growth perpendicular to a direction $\boldsymbol{A}_{\mathrm{g}}^{(a)}$ as well as growth in a direction $\boldsymbol{A}_{\mathrm{g}}^{(a)}$, respectively. Depending on the type of loading, both mechanisms can effectively reduce stresses in the direction of $\boldsymbol{A}_{\mathrm{g}}^{(a)}$, either by an increase of the cross-sectional area or by an elongation in the direction of the load.

For the driving force governing the evolution of the growth factors $\vartheta^{(a)}$, the set of approaches chosen for the examination is given by

$$\phi^{(a)}(\boldsymbol{\Sigma}_{\mathrm{e}}) = \boldsymbol{\Sigma}_{\mathrm{e}} : \boldsymbol{I}, \tag{6a}$$

$$\phi^{(a)}(\boldsymbol{\Sigma}_{\mathrm{e}}) = \boldsymbol{\Sigma}_{\mathrm{e}} : \boldsymbol{M}_{\mathrm{g}}^{(a)}, \tag{6b}$$

$$\phi^{(a)}(\boldsymbol{\Sigma}_{\mathrm{e}}) = \left\langle \boldsymbol{\Sigma}_{\mathrm{e}} : \boldsymbol{M}_{\mathrm{g}}^{(a)} \right\rangle, \tag{6c}$$

$$\phi^{(a)}(\boldsymbol{\Sigma}_{\mathrm{e}}) = \begin{cases} \frac{1}{2}\, \boldsymbol{\Sigma}_{\mathrm{e}} : \left(\boldsymbol{M}_{\mathrm{g}}^{(\mathrm{I})} + \boldsymbol{M}_{\mathrm{g}}^{(\mathrm{II})}\right) & \text{for} \quad \Sigma_{\mathrm{e}}^{\mathrm{I}} > 0, \quad \Sigma_{\mathrm{e}}^{\mathrm{II}} > 0 \\ \boldsymbol{\Sigma}_{\mathrm{e}} : \boldsymbol{M}_{\mathrm{g}}^{(\mathrm{I})} & \text{for} \quad \Sigma_{\mathrm{e}}^{\mathrm{I}} > 0, \quad \Sigma_{\mathrm{e}}^{\mathrm{II}} \leq 0 \end{cases}, \tag{6d}$$

where $\boldsymbol{M}_{\mathrm{g}}^{(\bullet)} = \boldsymbol{A}_{\mathrm{g}}^{(\bullet)} \otimes \boldsymbol{A}_{\mathrm{g}}^{(\bullet)}$. The indices I and II point out that the 1st and 2nd principal directions of $\boldsymbol{\Sigma}_{\mathrm{e}}$ are referred to. Besides the isotropic stress measure in Eq. (6a), a projection of the elastic part of the Mandel stress in the direction of $\boldsymbol{A}_{\mathrm{g}}^{(a)}$ is considered as driving force in Eq. (6b). Furthermore, the case that only positive values of these projected stresses, i. e. tensile stresses, provoke growth, is reflected in Eq. (6b). In addition, Eq. (6d) represents the average stress state within the plane spanned by the fiber families. In the case of only one tensile principal stress, the stress projected in the associated direction is used and both fiber families align in this direction, cf. Eq. (4).

In order to allow for a concise denomination of the different approaches, the numeric identifiers "$\boldsymbol{F}_{\mathrm{g}}$-ID" and "$\phi$-ID" are introduced for the type of growth tensor and the type of driving force, respectively. Their values are summarized in Tables 1 and 2. Note that it is not necessary to include each of the three parts of $\boldsymbol{F}_{\mathrm{g}}$. Purely isotropic growth for instance is already defined by setting $\boldsymbol{F}_{\mathrm{g}} = \boldsymbol{F}_{\mathrm{g}}^{(1)} = \vartheta^{(1)}\boldsymbol{I}$. The number of included directions will be referred to as n_{dir} in the following.

Table 1: Denomination of the different forms of the individual parts of the growth tensor.

$\boldsymbol{F}_{\mathrm{g}}$-ID	type of growth	$\boldsymbol{F}_{\mathrm{g}}^{(a)}$
1	isotropic growth	Eq. (5a)
2	growth perpendicular to $\boldsymbol{A}_{\mathrm{g}}^{(a)}$	Eq. (5b)
4	growth in the direction of $\boldsymbol{A}_{\mathrm{g}}^{(a)}$	Eq. (5c)

Table 2: Denomination of the different driving forces.

ϕ-ID	type of driving force	$\phi^{(a)}$
2	isotropic stress measure	Eq. (6a)
4	stress in the direction of $\boldsymbol{A}_{\mathrm{g}}^{(a)}$	Eq. (6b)
5	stress within the plane of the fibers	Eq. (6d)
6	tensile stress in the direction of $\boldsymbol{A}_{\mathrm{g}}^{(a)}$	Eq. (6c)

3 OPTIMIZATION-BASED COMPARISON OF THE APPROACHES

With the high number of adjustable model components listed above, a multitude of different approaches can be generated. A comparison of these approaches is made even more difficult by the dependence of their behavior on the growth and remodeling parameters. Most of these parameters however mostly affect the velocity of the adaptation processes and not the final result. Provided that a growth equilibrium state is attained, the resulting stress distributions are supposed to mainly depend on the form of the individual parts $\boldsymbol{F}_{\mathrm{g}}^{(a)}$ of the growth tensor, the associated driving forces $\phi^{(a)}$ and the limiting values $\vartheta_{(a)}^{+}$ of the growth factors for positive growth. In order to compare different approaches, these parameters have to be set specifically such that the best possible behavior in a biomechanical sense is achieved. This is done by optimization of a mechano-biologically motivated objective function, which then also serves as comparative value between the approaches.

3.1 Growth equilibrium state

Before evaluating the objective function, it has to be assured that a growth equilibrium state is attained after application of the load. Such a state is indicated by a vanishing

rate of all growth factors and is thus assumed to be attained if the condition

$$\frac{1}{n_{\text{ele}}\, n_{\text{GP}}\, n_{\text{dir}}} \sum_{n_{\text{ele}}} \sum_{n_{\text{GP}}} \sum_{a=1}^{n_{\text{dir}}} \frac{\left|\vartheta_{t+\Delta t}^{(a)} - \vartheta_t^{(a)}\right|}{\vartheta_t^{(a)} \Delta t} < \epsilon \tag{7}$$

is fulfilled. Thereby n_{ele} and n_{GP} are the numbers of elements and Gauß points and ϵ is set to $\epsilon = 10^{-4}/\text{s} = 0.01\,\%/\text{s}$. At growth equilibrium, a final stress state is reached which is used for the evaluation of the objective function.

3.2 Definition of the objective function

For the purpose of evaluating different growth mechanisms with respect to their ability of efficiently improving the load-bearing behavior, an objective function of the structure

$$f_{\text{obj}} = \sum_i \omega_i\, q_i \tag{8}$$

is defined, where q_i are the arguments and ω_i are weighting factors representing the importance of the individual arguments. The arguments q_i denote optimization objectives which are claimed to be minimal at growth equilibrium, for example stress peaks or differences and the volume change due to growth. All these objectives are normalized such that they are unitless and of same order of magnitude, and their optimal value is zero. By minimizing Eq. (8), the specific set of parameters is obtained that leads to the optimal mechano-biological state reachable by the particular model variant. The explicit expressions are

$$\begin{aligned}
q_1 &= \frac{\max\limits_r |\sigma_\varphi|}{\tilde{\sigma}_{\text{peak}}}, & q_4 &= \frac{\max\limits_r |\sigma_\varphi| - \left|\operatorname{mean}\limits_r \sigma_\varphi\right|}{\tilde{\sigma}_{\text{diff}}},\\
q_2 &= \frac{\max\limits_r |\sigma_z|}{\tilde{\sigma}_{\text{peak}}}, & q_5 &= \frac{\max\limits_r |\sigma_z| - \left|\operatorname{mean}\limits_r \sigma_z\right|}{\tilde{\sigma}_{\text{diff}}},\\
q_3 &= \frac{\operatorname{mean}\limits_r |\sigma_\varphi - \sigma_z|}{\left|\operatorname{mean}\limits_r \sigma_\varphi\right|}, & q_6 &= \left|\operatorname{mean}_{\mathcal{B}} J_{\text{g}} - 1\right|,
\end{aligned} \tag{9}$$

where the stresses $\tilde{\sigma}_{\text{peak}}$ and $\tilde{\sigma}_{\text{diff}}$ are introduced as normalizing values for stress peaks and differences. The operator "mean" denotes the volume average of a quantity over the whole domain $\mathcal{B}$ or over the radial direction r, respectively. In a multi-layered model, a layer-wise examination of the means would be more reasonable. Here, the artery is assumed to consist of a single layer in order to keep the numerical effort low, which is justified since the fundamental mechanism is matter of interest. The mechano-biological motivation for the objective definitions above is as follows:

q_1: In a cylindrical tube with internal pressure and moderate axial strain, the highest stress occurs at the internal surface in circumferential direction. A reduction of this stress peak towards a reference level $\tilde{\sigma}_{\text{peak}}$ or less might therefore be desired by the tissue in order to increase its resilience.

q_2: The same might hold for the peak of the axial stress, which however can also become compressive in case of intense axial growth. For this reason, the absolute value is considered.

q_3: Healthy arteries cut from the body contract in axial direction, which means that their natural in vivo state is under axial tension. Zero axial stresses are thus not expected and a layer-wise reduction of the average difference between circumferential and axial stresses is potentially a more realistic goal of arterial adaptation.

q_4/q_5: To obtain stress distributions which are layer-wise constant over the wall thickness as far as possible, the maximal stresses per layer have to approach the mean values. Constant stresses might be desired since the material within a layer is assumed to prefer a uniform exposure that does only marginally vary over the radial position.

q_6: From an energetic point of view, the material is assumed to avoid an unnecessarily high amount of grown material, i. e. to keep the volume change induced by growth, $J_\mathrm{g} - 1$, at the lowest level possible.

In the examination presented here, each of the optimization goals is supposed to be equally important, which means that all weighting factors are set to $\omega_i = 1$. The normalizing stresses are set to

$$\tilde{\sigma}_\mathrm{peak} = 100\,\mathrm{kPa} \qquad \text{and} \qquad \tilde{\sigma}_\mathrm{diff} = 50\,\mathrm{kPa}, \tag{10}$$

since these values are estimated to be in the order of magnitude of average stress peaks and differences between peak and mean values.

4 NUMERICAL EXAMINATION

The boundary value problem considered for the optimization-based comparison of different model approaches is a one-layered arterial segment discretized into seven rotationally symmetric 2D finite elements over the wall thickness, see Fig. 1. Table 3 lists all parameters which are set equally for all simulations. Besides the material parameters, this also applies to the remodeling parameters and to growth parameters with minor impact on the growth equilibrium state. The initial fiber angles are set to $\pm 30°$ with respect to the circumferential direction.

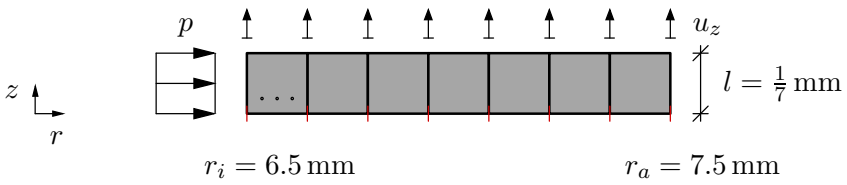


Figure 1: Boundary value problem of a rotationally symmetric arterial segment loaded by an internal pressure p and an axial displacement u_z.

Table 3: Parameters of the material model from [1], adjusted to human media in [3], parameters of the remodeling function k_η and unvaried parameters of the growth function $k_\vartheta^{(a)}$, set equally for all directions.

c_1	ϵ_1	ϵ_2	α_1	α_2	k_η^+	m_η^+	k_ϑ^+	m_ϑ^+	ϑ^-	k_ϑ^-	m_ϑ^-
in kPa	in kPa	in –	in kPa	in –	in s^{-1}	in –	in s^{-1}	in –	in –	in s^{-1}	in –
17.5	499.8	2.4	30 001.9	5.1	0.6	5.0	1.0	3.0	0.95	1.0	3.0

In a first simulation step, an internal pressure of $p = 120\,\text{mmHg}$ and an axial displacement u_z are applied without activating growth and remodeling. After reaching this representative loading, the load is kept constant and growth and remodeling are activated. The computation is then continued until a growth equilibrium state is attained.

To give an example for the values of the objective function in the non-growing reference artery, its stress state for an axial displacement of $u_z = 0.05\,l$ is given in Fig. 2 a and the associated contributions $\omega_i\, q_i$ as well as the summarized value f_{obj} are depicted in the bar plot in Fig. 2 b. Such a plot depicts the reachable performance of an individual model approach and thus, this case with $f_{\text{obj}} = 5.403$ where no growth and remodeling is considered, should indicate a relatively poor performance. However, note that the absolute values of the individual objectives themselves have few meaning and can only be evaluated by comparing them between different model approaches.

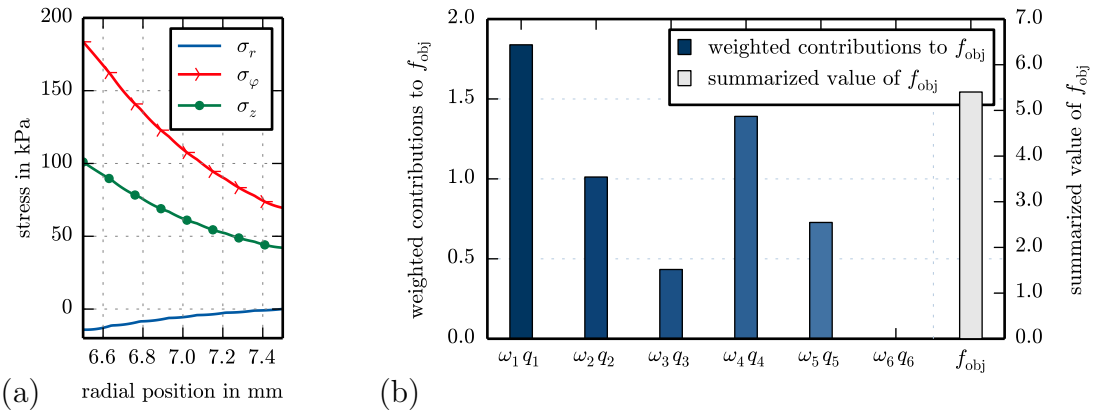


Figure 2: (a) Distribution of the radial, circumferential and axial stresses over the radial position and (b) composition of the value of the objective function in a non-growing pressurized artery with 5 % axial strain.

4.1 Optimization scenarios

For each different combination of $\boldsymbol{F}_{\text{g}}$-ID and ϕ-ID for different numbers of growth directions n_{dir}, the limiting values $\vartheta_{(a)}^+$ of the growth factors are identified by minimizing f_{obj}. In order to also account for different loading scenarios or more specifically, to estimate if a model variant performs insensitive with respect to load changes, the following optimization scenarios are proposed:

1. Optimize $\vartheta^+_{(a)}$ by averaging over different levels of u_z in order to find the best performance over a range of loading situations,

2. Optimize $\vartheta^+_{(a)}$ for a fixed value of u_z in order to find the best performance for a given loading situation,

3. Optimize $\vartheta^+_{(a)}$ and u_z in order to find the best performance of the given growth model over all possible loads.

For the cases where the axial displacement is not an optimization variable, it is chosen among $u_z \in [0.0\,l, 0.1\,l, 0.2\,l]$. For the least sensitive model variant, the value of the objective function obtained in the first case should only minimally differ from the one obtained in the third case. The minimization of the objective function is realized using the "GlobalSearch" algorithm of MATLAB in combination with the solver "fmincon" for constrained nonlinear minimization. Based on preliminary representative numerical calulations, the bounds of the parameters $\vartheta^+_{(a)}$ are chosen as $[1.001, 1.5]$ and the axial displacement is restricted to values within $[0.0\,l, 0.3\,l]$.

4.2 Results and Discussion

Here, the optimization results of some representative model variants are given. Isotropic growth is compared to a series of approaches where three growth directions are included and where the same combination of growth tensor and driving force is considered for each of these directions. An exemplary denomination like "161616" means that $\boldsymbol{F}_{\mathrm{g}}$-ID $= 1$ and ϕ-ID $= 6$ for each of the $n_{\mathrm{dir}} = 3$ parts of the growth tensor. The token "12" denotes isotropic growth, see as well Tables 1 and 2 for explanation of the numbers. For the comparison, a performance measure P is defined as the negative relative deviation of the optimized objective function values with respect to the reference value $f^{\mathrm{ref}}_{\mathrm{obj}} = 5.403$ for the case where no growth and remodeling is included, see Fig. 2 b. Thus, this measure is given by

$$P = -\frac{(f_{\mathrm{obj}} - f^{\mathrm{ref}}_{\mathrm{obj}})}{f^{\mathrm{ref}}_{\mathrm{obj}}}. \tag{11}$$

Higher (positive) values are associated with model variants which indeed lead to stronger improvements in the mechano-biological state. The results for the considered model variants are given in Fig. 3.

For a comprehensive evaluation and discussion, further model variants need to be analyzed and thus, the results given here can only be interpreted as representative examples showing how the proposed methodology for the comparison of different models works. However it can be seen that significantly increased performance measures are observed for anisotropic growth models compared to the purely isotropic formulation. This already indicates that the assumption of isotropic growth may not be realistic as also previously speculated in the literature.

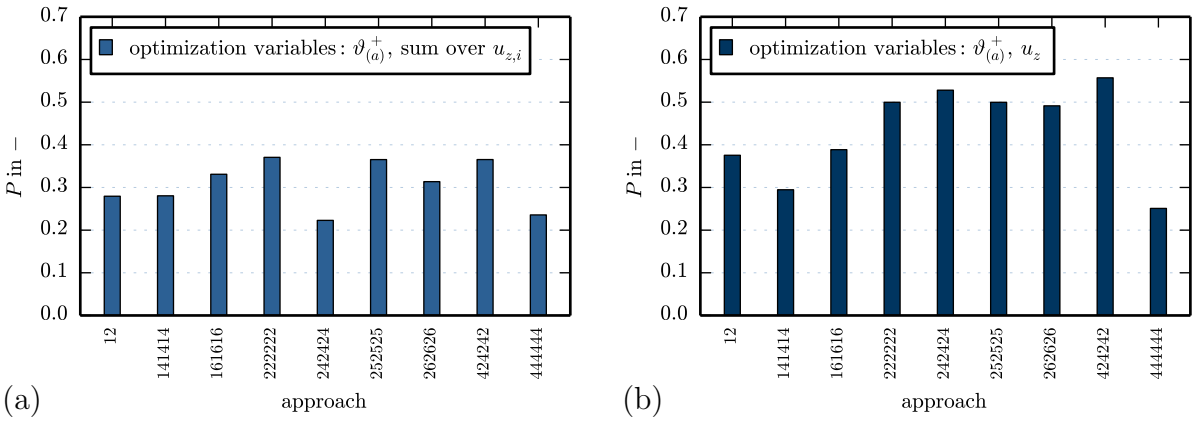


Figure 3: Performance measure P for a subset of different approaches when optimizing (a) the parameters $\vartheta^+_{(a)}$ by averaging over three load levels $u_{z,i}$ or (b) the parameters $\vartheta^+_{(a)}$ and the load level u_z. The tokens on the x-axis are composed of $\boldsymbol{F}_{\mathrm{g}}$-ID and ϕ-ID, consecutively listed for the multiplicative parts of the growth tensor.

5 CONCLUSION

In this contribution, a new method to compare different approaches within an existing framework of combined growth and fiber reorientation in arterial walls was proposed. It relies on the evaluation of a mechano-biologically motivated objective function, which is used to optimize the parameters of different growth models for different loading situations. The objective function is defined at growth equilibrium based on stress peaks, stress inhomogeneities and the volume change due to growth. All these quantities are supposed to be reduced more effectively the better the approach, and hence it might be possible to identify the most realistic growth mechanism. Even though a simplified one-layered model of the artery with a minimized number of optimization variables is used, the results should enable the comparative assessment of the fundamental mechanisms included in the individual model variants. However, only a number of selected variants was analyzed so far and thus, no final conclusion can be drawn with view to which model variant may be most realistic.

6 ACKNOWLEDGEMENT

The authors thank the German Science Foundation (DFG) for financial support in the project BA 2823/13-2.

REFERENCES

[1] Balzani, D.; Neff, P.; Schröder, J. and Holzapfel, G. A. “A polyconvex framework for soft biological tissues. Adjustment to experimental data”, *Int. J. Solids Struct.* (2006) **43**:6052–6070.

[2] Balzani, D.; Schröder, J. and Gross, D. “Simulation of discontinuous damage incorporating residual stresses in circumferentially overstretched atherosclerotic arteries”,

Acta Biomater. (2006) **2**:609–618.

[3] Brands, D.; Klawonn, A.; Rheinbach, O. and Schröder, J. "Modelling and convergence in arterial wall simulations using a parallel FETI solution strategy", *Comput. Methods Biomech. Biomed. Engin.* (2008) **11**:569–583.

[4] Comellas, E.; Carriero, A.; Giorgi, M.; Pereira, A. and Shefelbine, S. J. "Modeling the influence of mechanics on biological growth", in *Numerical Methods and Advanced Simulation in Biomechanics and Biological Processes* (Eds: M. Cerrolaza, S. J. Shefelbine, D. Garzón-Alvarado), chap. 2, pp. 17–35, Elsevier (2018).

[5] Göktepe, S.; Abilez, O. J. and Kuhl, E. "A generic approach towards finite growth with examples of athlete's heart, cardiac dilation, and cardiac wall thickening", *J. Mech. Phys. Solids* (2010) **58**:1661–1680.

[6] Hariton, I.; deBotton, G.; Gasser, T. C. and Holzapfel, G. A. "Stress-driven collagen fiber remodeling in arterial walls", *Biomech. Model. Mechan.* (2007) **6**:163–175.

[7] Himpel, G.; Kuhl, E.; Menzel, A. and Steinmann, P. "Computational modelling of isotropic multiplicative growth", *Comput. Model. Eng. Sci.* (2005) **8**:119–134.

[8] Holzapfel, G. A.; Gasser, T. C. and Ogden, R. W. "A new constitutive framework for arterial wall mechanics and a comparative study of material models", *J. Elasticity* (2000) **61**:1–48.

[9] Humphrey, J. D. "Cardiovascular Solid Mechanics – Cells, Tissues, and Organs" Springer Science + Business Media (2002), New York.

[10] Kuhl, E.; Maas, R.; Himpel, G. and Menzel, A. "Computational modeling of arterial wall growth. Attempts towards patient-specific simulations based on computer tomography", *Biomech. Model. Mechan.* (2007) **6**:321–331.

[11] Lubarda, V. A. and Hoger, A. "On the mechanics of solids with a growing mass", *Int. J. Solids Struct.* (2002) **39**:4627–4664.

[12] Rodriguez, E. K.; Hoger, A. and McCulloch, A. D. "Stress-dependent finite growth in soft elastic tissues", *J. Biomech.* (1994) **27**:455–467.

[13] Schröder, J. and von Hoegen, M. "An engineering tool to estimate eigenstresses in three-dimensional patient-specific arteries", *Comput. Methods Appl. Mech. Engrg.* (2016) **306**:364–381.

[14] Zahn, A. and Balzani, D. "A combined growth and remodeling framework for the approximation of residual stresses in arterial walls", *Z. Angew. Math. Mech.* (2018) **98**:2072–2100.

XV International Conference on Computational Plasticity. Fundamentals and Applications
COMPLAS 2019
E. Oñate, D.R.J. Owen, D. Peric, M. Chiumenti & Eduardo de Souza Neto (Eds)

FE^2 EVALUATION OF STRESS TRIAXIALITY / LODE ANGLE DEPENDENCIES OF VOID GROWING PROCESSES

Shintaro Nakamura*, Sho Suzuki*, Kazumi Matsui*, and Takahiro Yamada*

*Yokohama National University
Tokiwadai 79-7, Hodogaya-Ku, Yokohama 240-8501 JAPAN
e-mail: kzm@ynu.ac.jp - Web page: http://www.cml.ynu.ac.jp

Key words: Damage, Void Growth, Stress triaxiality, Lode angle, Multi-scale simulation

Abstract. This document provides information and instructions for preparing a Full Paper to be included in the Proceedings of *COMPLAS 2019 Conference*.

1 INTRODUCTION

We can find many pieces of research focusing on the behavior of voids at the microscopic structure to predict the ductile failures of metals. It is now recognized that stress triaxiality and Lode parameter strongly affect the damage evolutions, in other words, growing behaviors of micro-voids [1][2][3]. In these researches, experimental material tests have been made to correlate these parameters with the failure processes. However, generally speaking, these stress states quantities are not uniform in the specimen and also in the cross-sections, and are not measurable directly, so they are usually evaluated from deformed shapes or FEM simulations. In addition, it is also difficult to keep the quantities during the loading periods of experiment [2], because these parameters always change depending on the deformations of each material points. It should be also noted that the "damage" quantities, such as damage parameters or void ratio, are difficult to define or evaluate from the experiments [4].

As for the "damage" evolution mechanisms in metals, we can find several investigations, which simulates the micro void's behaviors [5][6]. These reseaches are motivated by the original literatures on damage mechanics, and try to understand the mechanisms of damage occurring inside metals by arranging a void inside the whole strucuture of the specimems and giving many variations of loading conditions. In the research, an arbitrary stress triaxiality and Lode parameter are given to the unit cell, and the relationship between stress state and void damage is investigated [7]. In that, it is common to reproduce an arbitrary stress state by displacement-controlled loading.

In this study, we evaluate the dependencies of void growing processes on the stress state by loading a unit cell model while controlling the stress state using FE^2 simulation . This method can relate the macroscopic behavior of a structure and the corresponding

behavior in the microscopic region, where the material inhomogeneities are defined [8]. We would simulate mechanical behavior of microscopic models with spherical voids against arbitrary stress triaxiality and Lode parameters by changing the macroscopic loading conditions using three-dimensional FE^2 procedure, and evaluate the dependency of voids growth upon the macroscopic stress triaxiality & Lode angle.

2 Multi-scale modeling for Ductile Fracture simulations

In this section, we describe the formulation and modeling method for multi-scale analysis to simulate void growing processes. First, we describe the large deformation / elasto-plastic two-scale boundary value problem based on homogenization methods derived for general composite materials and define the BVP handled in this research [9]. Next, we explain the way of expressing stress states. Finally, Problem settings and the finite element models for Micro and Macro scales are defined to study the dependence on stress states.

2.1 Two-scale boundary value problem

the micro-scale BVP is defined by the representative volume element(RVE) virtual work equation, here stated in its spatial version,

$$\int_{\mathcal{Y}} \boldsymbol{\tau}^0(\boldsymbol{x},\boldsymbol{y}) : \nabla_y \boldsymbol{\eta}^1 \frac{dy}{J_Y} = 0 \quad \forall \boldsymbol{\eta}^1 \in W^{1,p}_{\mathrm{per}}(\mathcal{Y}) \tag{1}$$

along with a selected constitutive equation that relates the microscopic deformation to the microscopic Kirchhoff stress $\boldsymbol{\tau}^0(\boldsymbol{x},\boldsymbol{y})$. Here, dy denotes the differential volume of the current configuration of the RVE, i.e., $dy = J_Y dY$ and $W^{1,p}_{\mathrm{per}}$ is the Sobolev apace of variations of kinematically admissible displacements of the RVE. The functions of $W^{1,p}_{\mathrm{per}}$ are periodic on the boundary of the RVE.

On the other hand, the macro-scale BVP is governed by the following variational equations in spatial description:

$$\int_{\mathcal{B}} \tilde{\boldsymbol{\tau}}(\boldsymbol{x}) : \nabla_x \boldsymbol{\eta}^0 \frac{dx}{\tilde{J}} - g_{\mathrm{ext}}(\boldsymbol{\eta}^0) = 0 \quad \forall \boldsymbol{\eta}^0 \in W_0^{1,p}(\mathcal{B}) \tag{2}$$

$$\tilde{\boldsymbol{\tau}}(\boldsymbol{x}) = \frac{1}{|\mathcal{Y}|} \int_{\mathcal{Y}} \boldsymbol{\tau}^0(\boldsymbol{x},\boldsymbol{y}) \frac{dy}{J_Y} \tag{3}$$

where $|\mathcal{Y}|$ is the volume of the RVE in its current configuration and $W_0^{1,p}(\mathcal{B})$ is the space of kinematically admissible displacement fields over the macroscopic continuum. Here, the microscopic volumetric change is given as $dy = J_Y dY$, whereas for the macroscopic counterpart we have $dx = \tilde{J} dX$.

2.2 Characterization of the stress state

Stress states can be described by three principal stresses. There are some values representing the stress state.

$$p = -\boldsymbol{\sigma}_m = -\frac{1}{3}\mathrm{tr}([\boldsymbol{\sigma}]) = -\frac{1}{3}(\boldsymbol{\sigma}_1 + \boldsymbol{\sigma}_2 + \boldsymbol{\sigma}_3) \tag{4}$$

$$q = \overline{\boldsymbol{\sigma}} = \sqrt{\left(\frac{3}{2}[\boldsymbol{S}] : [\boldsymbol{S}]\right)} = \sqrt{\frac{1}{2}[(\boldsymbol{\sigma}_1 - \boldsymbol{\sigma}_2)^2 + (\boldsymbol{\sigma}_2 - \boldsymbol{\sigma}_3)^2 + (\boldsymbol{\sigma}_3 - \boldsymbol{\sigma}_1)^2]} \tag{5}$$

$$r = \left[\frac{27}{2}\det([\boldsymbol{S}])\right]^{1/3} = \left[\frac{27}{2}(\boldsymbol{\sigma}_1 - \boldsymbol{\sigma}_m)(\boldsymbol{\sigma}_2 - \boldsymbol{\sigma}_m)(\boldsymbol{\sigma}_3 - \boldsymbol{\sigma}_m)\right]^{1/3} \tag{6}$$

Furthermore, stress states can be described by Lode angle θ and stress triaxiality T defined by three stress invariants. The stress triaxiality T can be defined by the following equation as an index for measuring the triaxiality at an arbitrary point of a material.

$$T = \frac{-p}{q} = \frac{\boldsymbol{\sigma}_m}{\overline{\boldsymbol{\sigma}}} \tag{7}$$

$\boldsymbol{\sigma}_m$ and $\overline{\boldsymbol{\sigma}}$ is the average stress and the effective stress. The value of T increases with increasing triaxiality. The Lode angle θ is defined as the angle between the deviatoric stress on the deviatoric stress surface and the adjacent pure shear line. Lode angle is defined by the following equation.

$$\cos(3\theta) = \left(\frac{r}{q}\right)^3 \quad (-30^\circ \leq \theta \leq 30^\circ) \tag{8}$$

Furthermore, Lode angle θ is normalized,

$$\overline{\theta} = 1 - \frac{6\theta}{\pi} \quad (-1 \leq \overline{\theta} \leq 1) \tag{9}$$

Normalized Lode angle $\overline{\theta}$ is called as Lode parameter. From its parameter, it is possible to know whether the current stress state is tension or pure shear or compression. In this paper, the lode angle is defined only in the region where the relationship with $\sigma_1 \geqq \sigma_2 \geqq \sigma_3$ holds.

2.3 Modeling of an initial void

Using models and material properties for multi-scale method are shown in **Fig. 1** and **Table 1**. A micro-scale cell model containing a spherical space is prepared for representing the growth behavior of micro-voids. 3D models is used for controling triaxial stress states. A 3D model was used to control the triaxial stress state. Similar to the assumption in Gurson's damage model , an isotropic spherical initial void was contained in the center of the micro-model. In this paper, the percentage of the void volume to the volume of the whole microstructure model was defined as the void fraction f to quantify the damage level.

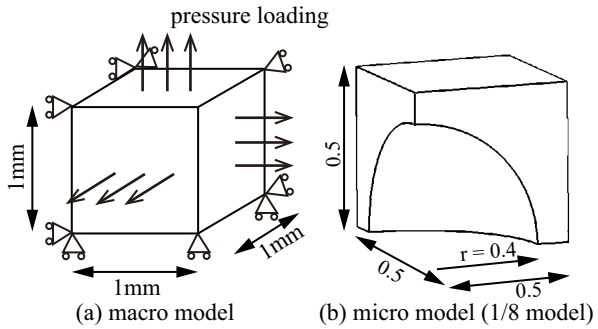


Fig. 1. The chosen model (Macro-model and Micro-model)

Table 1: Macroscopic material parameters

Young's modulus	E [GPa]	200
Poisson's ratio	ν	0.3
Initial yield stress	σ_Y [MPa]	200
Hardening parameter 1	H [MPa]	100
Hardening parameter 2	δ	3
Maximum yield parameter 3	σ_Y^∞ [MPa]	800

3 Results

3.1 simulations of 3-D void growth using Multi-scale simulation

Triaxial stress states is given to the Macro-Micro models shown in **Fig. 1** by Multi-scale methods. **Fig. 2** shows that the relationship between the macroscopic stress and the macroscopic strain, and the void fraction in the micro-structure. Also, the deformation of the microstructure and the corresponding plastic strain distribution at each feature point in **Fig. 2** are shown in **Fig. 3**.

- In the region before the maximum macro-stress, the whole microstructure in a micro-model is deformed as shown in (a) and (b) of **Fig. 3**. Work hardening processes can be also confirmed in the macroscopic stress-strain relationship. In addition, the void fraction in the micro-model increases linearly, which is consistent with the behavior assumed in general damage models.

- In the region after the peak macro-stress, deformation in a micro-model is concentrated in the central part of the void as shown in (c) of **Fig. 3**. This localized deformation in microstructures makes softening behavior in macro stress-strain relationships. In addition, the void fraction increased rapidly compared to before the peak stress, and the rapid damage evolution can be observed as in the damage model.

By modeling the 3-D micro-void in multi-scale simulations, we can describe the drop of macroscopic stress level and the softening behavior of the true stress / true strain

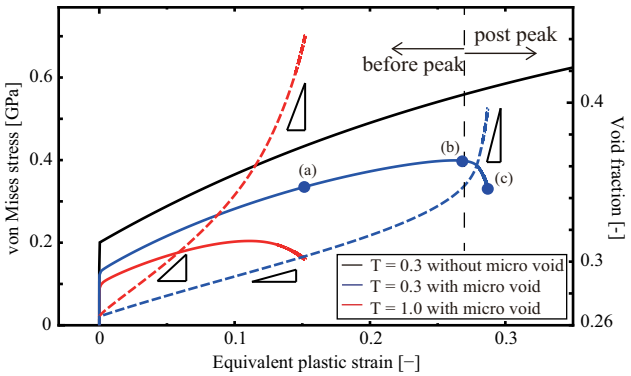


Fig. 2. Macroscopic stress, the void fraction versus Macroscopic strain for $\overline{\theta} = 1,\ T = 0.3, 1.0$

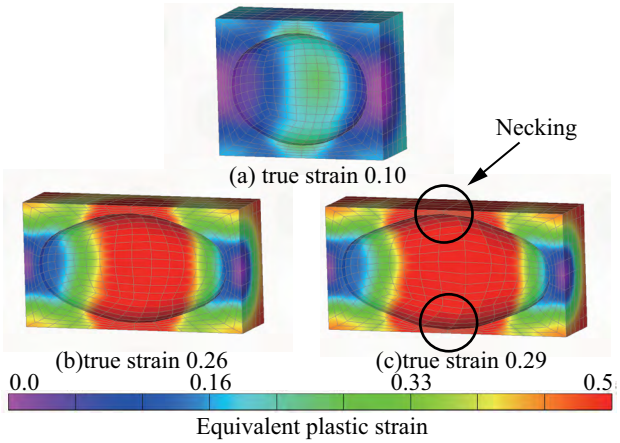


Fig. 3. Contour plots of equivalent plastic strain for void model in micro-structure at each feature points in **Fig. 2**

relationship due to necking, compared with the simulation without a void. By multi-scale analysis assuming void in microstructure, we can obtain qualitatively the similar result as mechanical response assumed by continuum damage mechanics such as void growth in microstructure, stiffness reduction and softening behavior in the macroscopic response.

3.2 Stress triaxiality and Lode angle dependencies of void growing processes

As we mentioned in the previous section, the multi-scale analysis can express void growth behavior. In this section, we would change the stress state and organize the void growth process in each stress state.

Fig. 2 shows the stress-strain relationship in $\overline{\theta} = 1,\ T = 0.3$ and 1.0. From this figure, it can be seen that the maximum stress is reached at low strain levels as the triaxiality increases. It can be considered that this is because the void deforms in three directions when the triaxiality is high, the hole can be expanded more easily as the result. The figure also shows that the void increasing rate before peak stress is larger when the triaxiality

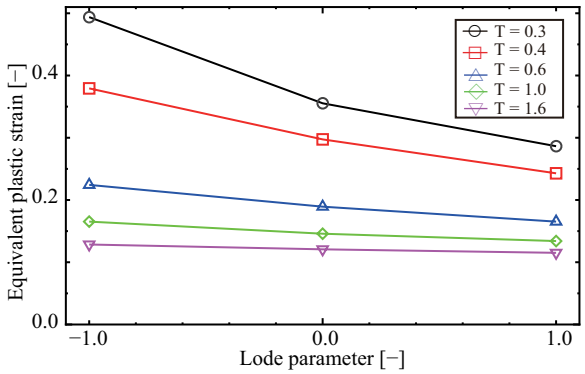


Fig. 4. the evolution of equivalent plastic strain at the same void fraction in different stress triaxiality and Lode angle

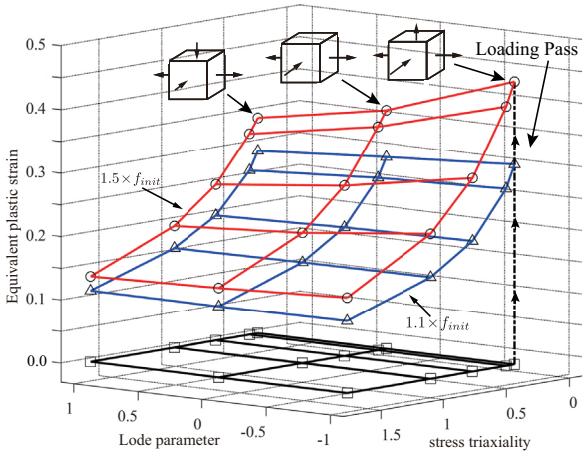


Fig. 5. 3-D damage progress surface in the space of stress triaxiality, the Lode parameter and the equivalent plastic strain of some damage levels

is higher. This result is also reported in the experiment by Yamashita et.al [10], and it can be said that this analysis can properly consider the effect of stress triaxiality.

The equivalent plastic strain when reaching the same void fraction is plotted for each stress state in **Fig. 4**. From this result, it can be confirmed that the equivalent plastic strain required to reach the same void fraction decreases as the stress triaxiality increases. In other words, it can be said that voids are easily to expand in highly stress triaxiality states. As for Lode angle, it can be seen that the void tends to expand as $\theta = 1$, ie, closer to the tensile stress state. Furthermore, it can be read that void growth largely depends on the Lode angle in the low triaxial region of $T = 0.4$ or less. From the above, it can be said that the growing processes of the void depend on the stress triaxiality in the high triaxial region, and conversely, the Lode angle in the low triaxial region.

Furthermore, in order to make it easier to understand visually the dependencies of void growth on the stress state, **Fig. 5** is a replot of **Fig. 4** in three dimensions. This is a damage progress surface formed by connecting the equivalent plastic strains at the same

void fraction. The dotted line is the loading pass. Moreover, the damage surface is made on the basis of the point where the void fraction reached 1.2 and 1.4 times from the initial void fraction. From this figure, it can be seen that the void is most easily to grow in high triaxial and tensile stress conditions, that is, the damage in materials progresses rapidly. This tendency is consistent with the results of the previous research, and in this analysis it can be said that the material behavior under the triaxial stress state can be correctly represented [7].

4 CONCLUSIONS

In this study, dependencies of damage evolution on stress triaxiality and Lode angle is organized using multi-scale analysis. The conclusions can be summarized as follows.

- By using multi-scale analysis with a micro-model containing voids, void damage behaviors can be expressed. Moreover, void growing processes under triaxial stress are expressed using 3D void model.
- The multi-scale simulation is able to express the situation that the void growth and the accompanying damage evolution depend on the stress state. It is confirmed that the damage was most easy to develop at high triaxiality and Lode angles corresponding to tensile stress conditions. It is also confirmed that the influence of the Lode angle is more pronounced in the low triaxiality region.

REFERENCES

[1] Bai, Y., Wierzbicki, T.: A new model of metal plasticity and fracture with pressure and Lode dependence, *International Journal of Plasticity*, Vol.24, 1071-1096, (2007).

[2] Bai, Y., Teng, X., Wierzbicki, T.: On the application of stress triaxiality formula for plane strain fracture testing, *Journal of Engineering Materials and Technology*, Vol.131, 021002-1-021002-10, (2009).

[3] Bao, Y., and Wierzbicki, T.: On fracture locus in the equivalent strain and stress triaxiality space, *International Journal of Mechanical Sciences*, vol.46(1), 81-98, (2004).

[4] Danas, K., Castañeda, P.P.: Influence of the Lode parameter and the stress triaxiality on the failure of elasto-plastic porous materials, *International Journal of Solids and Structures*, Vol.49, 1325-1342, (2012).

[5] Luo, T., Gao, X.: On the prediction of ductile fracture by void coalescence and strain localization, *Journal of the Mechanics and Physics of Solids*, Vol.113, 82-104, (2018).

[6] Barsoum, I. and Jonas F.: Micromechanical analysis on the influence of the Lode parameter on void growth and coalescence, *International Journal of Solids and Structures*, vol.48.6, 925-938 (2011).

[7] Zhang, K.S., Bai, J.B., Francois, D.: Numerical analysis of the influence of the Lode parameter on void growth, *International Journal of Solids and Structures*, Vol.38, 32-33, 5847-5856, (2001).

[8] Geers, M.G.D., Kouznetsova, V.G. and Brekelmans, W.A.M.: Multi-scale computational homogenization: Trends and challenges, *Journal of Computational and Applied Mathematics*, Vol.234, 2175-2182, (2010).

[9] Terada, K., Saiki, I., Matsui, K. and Yamakawa, Y.: Two-scale kinematics and linearization for simultaneous two-scale analysis of periodic heterogeneous solids at finite strain, *Computer Methods in Applied Mechanics and Engineering*, Vol.192, 3531-3563, (2003).

[10] Yamashita, T., Neishi, Y., Shida, A. and Noguchi, Y.: Ductile Fracture Limit at Low Stress Triaxiality, *Journal of the Japan Society of Technology of Plasticity*, Vol.58, 617-623, (2017).

XIV International Conference on Computational Plasticity. Fundamentals and Applications
COMPLAS 2019
E. Oñate, D.R.J. Owen, D. Peric , M. Chiumenti, and Eduardo de Souza Neto (Eds)

CALCULATION OF SUB-SURFACE-INITIATED FATIGUE FRACTURES IN GEARS

DANIEL MÜLLER, THOMAS TOBIE AND KARSTEN STAHL

Gear Research Centre (FZG)
Technical University of Munich (TUM), Germany
email: fzg@fzg.mw.tum.de, website: http://www.fzg.mw.tum.de

Key words: Residual Stresses, Tooth Flank Fracture, Load Carrying Capacity, Gears

Abstract. Power-transmitting gears are typically heat-treated, most often case-hardened, to improve the fatigue strength and therefore to ensure higher fatigue life. The heat treatment causes higher hardness in the surface area as well as compressive residual stresses in the hardened layer. The near-surface compressive residual stresses are compensated by tensile stresses in higher depths of the gear volume.
Pitting and tooth root breakage are the most common failure modes of gears, which are well researched and are also addressed in ISO 6336 [14]. The assessment of these failure modes provides the basis for the dimensioning of gears in the design phase. However, subsurface-initiated failures, like tooth flank fracture (TFF), can also appear at loads below the allowable level of loading for pitting and tooth root bending. TFF is a fatigue damage with crack initiation in the region of the transition between compressive and tensile residual stresses and usually leads to a total loss of drive.

The existing calculation models for fatigue strength of gears with regard to TFF consider residual stresses differently. The base of the investigated calculation models is a local comparison of the occurring stresses and the strength value in the gear volume. The outcome of the calculation model from Oster [26] is highly influenced by the residual stress state. However, the material-physical model by Hertter [10] is more tolerant to slightly varying residual stresses. Further approaches such as Weber [34] and Konowalcyk [18] are based on the ideas of Oster and Hertter.

The verification of the models is complicated due to the lack of residual stress measurements in larger depths under the gear flank surface. For example, residual stress measurement by X-ray diffraction is only possible up to depths of approximately one millimeter. Therefore, tensile residual stresses in the inner tooth volume are considered zero in the common residual stresses calculation of Lang [19] and are not considered in the current calculation approach of ISO/DTS 6336-4 [15].

The paper describes local calculation approaches for the fatigue strength of gears with different consideration of residual stresses. Furthermore, the crack initiation point, which is mandatory for the validation of an approach, is examined. The failure mode TFF is hereby the key.

1 INTRODUCTION

Power-transmitting gears are loaded with a torque that results in contact pressure at the transmitting tooth flanks. These gears are usually heat-treated to achieve higher strength in the surface area. A common heat treatment is case hardening. Case hardening causes higher carbon content in the surface area and a change in the microstructure. The change in the microstructure causes higher hardness and additionally compressive residual stresses in the surface layer, which also support the strength of the gear [9]. The depth of the microstructure change is mostly dependent on the time the gear is heated. For gears, the case hardening process is described with the case hardening depth (CHD), which is the depth of a hardness of 550 HV.

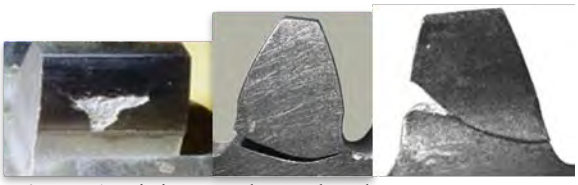


Figure 1: Pitting, tooth root breakage, TFF

To achieve a specified lifetime, different failure modes need to be prevented. The classical failure modes are pitting, tooth root breakage, micropitting, scuffing and wear. The main fatigue failure risks of a gear are currently pitting and tooth root breakage (**Figure 1**). Both failures are initiated by cracks in the near surface area due to cyclic loading. The calculation of the load capacity of these failure modes is well researched and very well manageable with ISO standards (ISO 6336 [14]). In recent years, subsurface-initiated failures have increased due the practice of higher loading and higher material strength at the surface. In addition, the adjustment of the residual stress state in the surface area lead to higher load capacities, which shifted the possible crack initiation in higher depths of the gear. Subsurface-initiated failures are for example tooth flank fracture (TFF).

2 DEFINITION OF TOOTH FLANK FRACTURE (TFF)

Subsurface-initiated failures have the crack initiation point (PR) in higher depths where the material strength of the heat-treated gear declines and significantly lower stresses than at the near surface can lead to crack initiation and growth with every loading cycle. The characteristics of the tooth flank fracture are described in various papers and dissertations [4, 7, 8, 36]. This paper describes tooth flank fracture for case-hardened external spur and helical gears. However, there are TFFs also reported for bevel and hypoid gears but not discussed in this paper [1, 6].

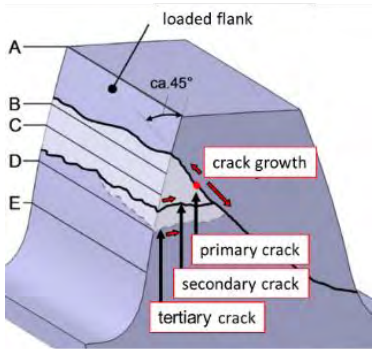


Figure 2: TFF crack growth [4]

TFF is a high cycle fatigue failure. The failure shows S-N curve behavior and therefore the characteristics of a limited lifetime at high loads and an endurance limit at lower loads. The crack growth is slower towards the surface due to the higher material strength. Therefore, the crack is growing internally and is not visible until breakage. The crack initiation is located in the area between the surface and core hardness and mostly where the hardness reaches the core hardness. In addition to the primary crack, secondary and tertiary cracks can occur [36]. The crack growth is internal and slow and under vacuum; therefore, a fisheye around the crack imitation is possible but not mandatory [3]. Due to varying loading, beachmarks indicating the crack growth are possibly visible in the fisheye as shown in

Figure 3. The crack often starts at an inclusion or irregularities in the micro-structure due to a possible local stress increase. [36]

The main influences are the material strength profile , the contact stresses and the residual stresses in higher depths. Additional stresses due to the deformation of the tooth are considered as less significant and depend on the geometry of the tooth [8, 36],30].

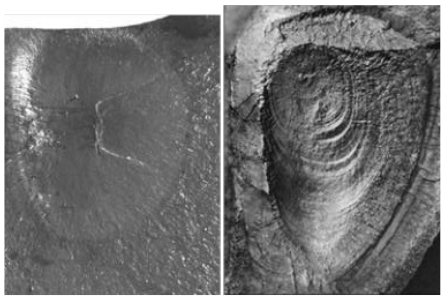


Figure 3: Characteristics of tooth flank fracture, fisheye of constant loading [7], fisheye with beachmarksdue to the crack growth under varying loading [1]

Experimental results of test gears are described in the works of Tobie [33], Bruckmeier [8] and Witzig [36]. Witzig did substantial experimental research. Different gear geometries with different materials were tested with varying loading conditions up to 100 million load cycles in an FZG back-to-back test rig. The gear set with module 3 mm and 67/69 teeth of these experimental investigations is possibly the most discussed for the evaluation of TFF calculation approaches. TFF is observed in a range of 1 million up to 100 million load cycles for this gear geometry. In addition, a calculation approach is presented in Witzig based on the Superior FZG-Modell. Nevertheless, this failure mode is still much less researched compared to other failures such as pitting and tooth root breakage.

3 STRESS CALCULATION

While transmitting torque, a single tooth of the gear is loaded with different stresses, which are responsible for a possible occurring failure mode. For subsurface-initiated failure modes, the super-positioning of several loading stresses is possibly relevant.

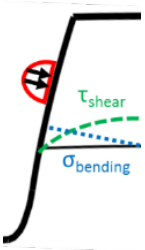


Figure 4: Tooth shear stresses and bending stresses

The main stresses due to loading are the contact stresses after Hertzian theory. Stresses due to the shear of the tooth and bending of the tooth strongly depend on the geometry of the gear set [8, 36]. The stresses due to tooth shear load are maximal in the middle of the tooth and constantly distributed in the tooth height under the contact point. Bending stresses with a maximum at the surface and near zero in the middle of the tooth decrease with increasing tooth height. The mentioned stresses have significantly different distributions as shown in **Figure 4**.

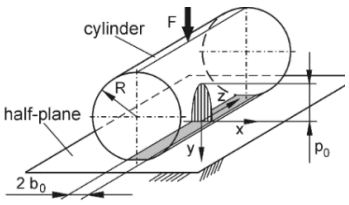


Figure 5: Theory of Hertz

The contact stresses of the rolling and sliding contact between the tooth flanks are described by the Hertzian theory [12]. The stresses depend on the loading of the flank, the local normal radius of relative curvature, the reduced modulus of elasticity and the tooth width of the pinion and the wheel. The loading and the radius of relative curvature depend on the contact point at the transverse path of contact. The normal contact force depends on the number of teeth in contact. Between point B and D, a maximum level of the normal force due the singular contact is reached. The radius of relative curvature is usually increasing until contact point D. This leads to a maximum contact stress

between the contact points B and D.

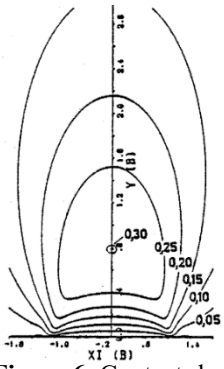


Figure 6: Contact shear stress with maxima [18]

The contact stresses after Hertz are described by the pressure p_H on the contact width $2\times b_H$ and based on a half space approach, where the two radii are combined to a relative radius of curvature, which is forced on a half plane. The elliptical distribution of pressure over the contact width $2\times b_H$ is constant over the contact length or respectively the tooth width. According to the Hertzian theory, the normal stresses are maximal at the surface and the shear stress maximum of $0.3\times p_H$ is at a depth of approximately $0.8\times b_H$ (**Figure 6**). The dependency of p_H on the radius of relative curvature means, that for gears with greater radius of curvature (such as large gears) the maximum shear stress is at a greater depth normal to the flank. These contact stresses can be calculated with the equations of Hertz or by the equations of Johnson [16] dependent on the Hertzian stress p_H and the half contact width b_H.

4 MATERIAL STRENGTH AND CALCULATION OF HARDNESS PROFILES

For the calculation of the material exposure, mostly local approaches are used. The local approach is a comparison of the local stress and the local material strength. The material strength is mostly derived from the hardness profile. Additionally, in some local calculation approaches, the yield strength R_p, tensile strength R_m or other strength parameters such as the alternating strength σ_w are used. These material-dependent parameters are gained by testing specimens under a defined load.

Different calculation approaches for the hardness profile are used in the design phase. The calculation is based on the CHD, the surface hardness and the core hardness, which are usually specified in the design phase. There are different approaches for the hardness profile for different heat treatment processes. In **Figure 7**, approaches for case hardening are compared to a representative measurement of the module 3 mm gear researched in Witzig [36].

The hardness of the material can be calculated with the equations after Lang [19], which is the most common approach. The approach of Lang is suitable for case hardening, induction hardening and nitriding. It requires the CHD, the surface hardness and the core hardness. For the tooth flank hardness profile, the core hardness measured at the flank area should be used for a better alignment with the measured hardness. Another approach for case-hardened gears is proposed by FZG/Thomas [32]. This approach has the ability to represent the hardness plateau in the near surface area, which occurs in large gears due to the case-hardening process. The plateau is calculated by the specification of the maximum hardness depth. Mack Aldner and Olsson proposed a hardness profile calculation [24]. For the approach, the carburization depth in addition to the surface hardness and core hardness is required. Beermann [5] proposed two alternatives for the approach of Lang. The two alternatives (A1 and A2) are mathematical corrections of the Lang equations, where the CHD is positioned at 550 HV.

Figure 7 shows a comparison of the mentioned hardness profile calculation approaches for a surface hardness of 700 HV1 and a core hardness of 440 HV1 with a CHD of 0.5 mm. By all approaches, the hardness measurement is described quite well under the consideration of the uncertainty of hardness measurements. The maximum hardness in the approach of Thomas is

assumed to be 0.0 and 0.08 mm to show the behavior of the approach. Differences in the approaches only exist in the transition to the core hardness, which is the critical area for TFF. For different gears and gear sizes, different approaches can be suitable. Due to the high influence on the material exposure in some existing calculation approaches for TFF, an exact calculation of the hardness profile is mandatory.

5 RESIDUAL STRESSES AND CALCULATION OF RESIDUAL STRESSES

Lang [19] also proposed an approach to calculate the residual stress profile (**Figure 7**). The calculation is only depending on the hardness profile. Improvements of the equations were made by FZG [8, 11] to adjust the residual stress in the surface area when the difference between the hardness profile and the core hardness is higher than 300 HV.

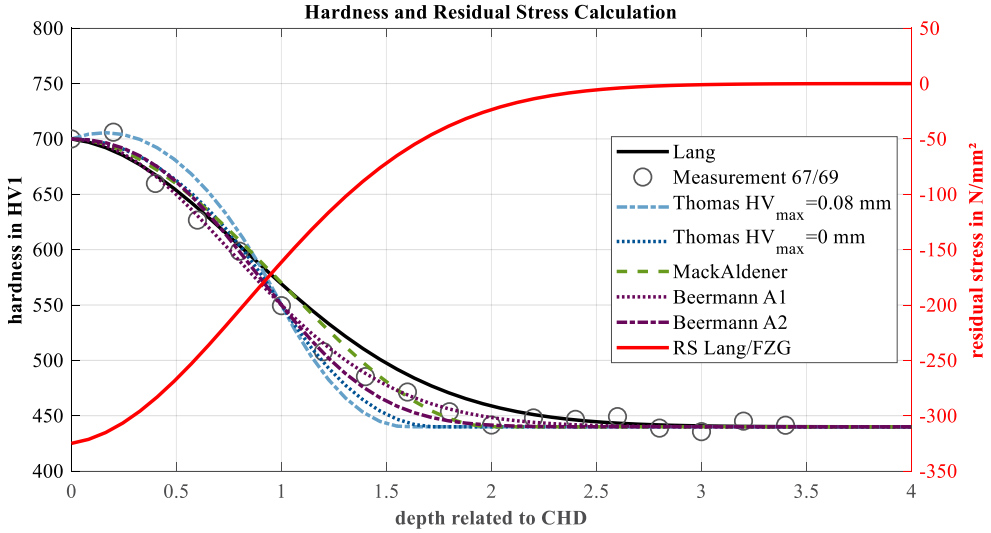


Figure 7: Hardness and residual stress calculation of different approaches compared to hardness measurement

The residual stresses are caused due the transformation of the micro-structure due to the heat treatment. They can be defined as three different kinds after the influenced area [23] . The total residual stress state is a superposition of all three kinds. The residual stresses are self-equilibrating stresses, which means there cannot be a resulting force or moment in the gear. Due to the mechanical equilibrium, compressive residual stresses must be compensated by tensile residual stresses. The calculation of Lang does not consider the tensile residual stresses, which should exist in higher depths of the tooth volume. In addition, the three-dimensional stress state is not considered.

A calculation approach with consideration of the tensile stresses is difficult to prove due to the complicated measurement of the residual stresses at higher depths. Still, calculation approaches with consideration of tensile residual stress are proposed. Konowalczyk [17] and Weber [34] proposed a similar approach. They append a polynomic function to the Lang approach at a depth of 0.5×CHD. The polynomic function is calculated by specified constraints with an algorithm to assure the mechanical equilibrium within the tooth thickness. These two approaches have the disadvantage of using an algorithm that can lead to no result and is difficult for the use in a standard calculation method such as ISO standard. In addition, a small tooth thickness can lead

to a high overestimation of the residual stresses especially in the near tooth addendum area. Furthermore, the three-dimensional stress state is not considered and an equilibrium of the hoop stresses is assumed.

For the validation of the residual stress state, measurements at great depths are necessary. Usually the tangential and axial residual stresses are measured with X-ray diffraction. The X-ray diffraction is applied at the surface of the specimen. By stepwise electrochemical polishing and measuring, a depth profile is gained [29]. The reachable depth is limited by the evenness of the bottom of the crater. Typically, depths up to 1 mm are usually possible. Measurements of greater depths are possible with neutron diffraction. In [27,36], measurements of two different tooth geometries are shown. The measurement results of the module 3 mm gear, which is prone to TFF are shown in **Figure 8**. The measurements at FRM II support the assumptions of Witzig et al. [36,34,20] that in larger material depth the residual stresses in normal (hoop) direction to the flank surface are near zero and the axial and radial stresses show no significant difference with consideration of the error.

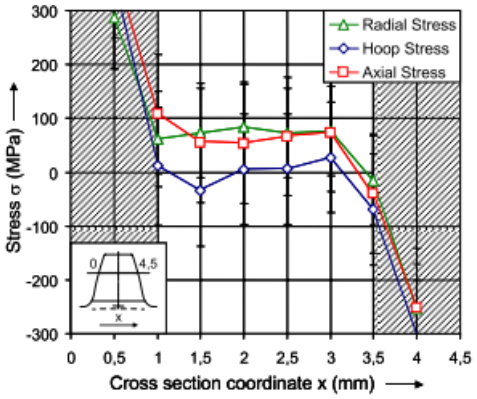


Figure 8: Residual stress measurment of the module 3 gear with neutron diffraction [24]

6 CALCULATION APPROACHES FOR TFF

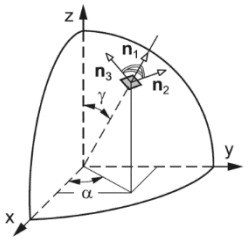


Figure 10: A quarter of sphere with coordinate system [15]

The calculation of subsurface-initiated fractures is based on a comparison of the local stress and local material strength. The quotient is defined as a local material exposure A. The local material strength is described by one-dimensional parameters as described earlier. For material strength, only one-dimensional data is generated e.g. tensile strength by tensile testing. The comparison to a three-dimensional stress state is possible with a multiaxial fatigue criterion.

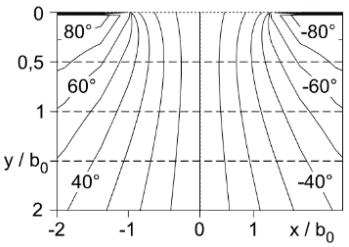


Figure 9: Principal stress direction in rolling and sliding

The loading of the part results in stresses at the planes of the infinite small spherical element. Due to the equilibrium of moment, the shear stresses are the same over the diagonal (symmetry). For the calculation of the stresses in a specific direction a transformation is applied. The direction can be described by a plane at the surface of a sphere, which is described by two angels (α, γ) as shown in **Figure 10**. At specific angles, the stress vector is normal to the plane and the shear stresses are zero. These directions are called principle stress directions. By calculation invariants of the stress tensor, a description of the stress state independent from the body coordinate system is gained. The second invariant is used in the von Mises criterion for the description of failures. It also allows the separation of the hydrostatic stresses and the deviatoric stresses.
The subsurface contact stresses change due to the loading rolling and sliding contact. Also, the principal stress coordinate changes as shown in **Figure 9**. A volume element in a specific depth therefore has a time-dependent stress tensor.

The path of the stresses is described in the planes of the infinite small spheres. The shear stresses change in the direction of the plane and normal stresses change normal to the plane.

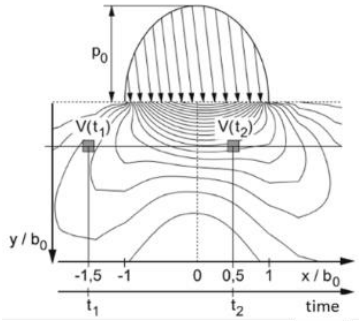


Figure 11: Stress on volume element in the contact area [11].

The stresses in the planes described by alpha and gamma are the basis of the following explanations. The hypotheses can then be divided into hypotheses of the critical plane and integral hypotheses. The critical plane approaches only take the plane with maximum stress into account and ignore the orientation of the micro-structure and assume that the maximum stress is occurring in a slip plane of the micro-structure. The crack initiation is caused by a shear stress high enough to cause plastic deformation when a slip plane is hit. The integral methods regard stresses in all planes.

The shear stress intensity hypothesis (SIH) is an integral criterion. It is based on the interpretation of the von Mises criterion of Novožilov [25] and can be derived from the weakest link theory of Weibull [22, 35]. The SIH is suitable for changing principal stress directions. This criterion satisfies the demands of invariance of the coordinate system on the body and the principal stress coordinate system because all planes are taken into account. [37, 38]. Also after Liu [21] and the SIH after Zenner [38] are the most suitable for the endurance limit of multiaxial stresses with differences in frequency, phase or arbitrarily oscillating loads. The SIH is based on the von Mises criterion. The distortion energy theory (GEH) and shear stress theory (SH) are included when the directions of the principle stresses are constant. The SIH has different forms: the SIH after Simbürger [28] where the failure criterion is the quadratic mean of the material exposure in all planes and after Zenner [38] where the quadratic mean of the effective shear stresses lead to the equivalent stress. The effective shear stress is also used in the SIH variant used by Oster. The SIH used by Hertter for the calculation of the maximum exposure is based on Liu and Zenner. The treatment of residual stresses in these multiaxial criteria is not discussed yet because the influence of residual stresses is usually considered as mean stresses in the material strength.

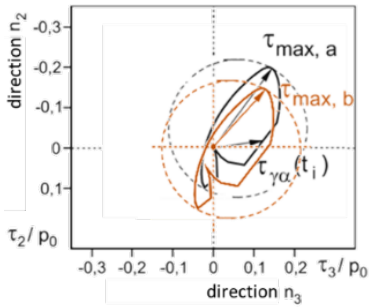


Figure 12: Shear stress path in a plane. a: without compressive residual stress; b: with compressive residual stress [Her03]

For TFF calculation where the residual stresses considered the second highest impact after contact stresses also approaches exist with a superposition of the residual stress state and the loading stress state after the application of a multiaxial stress hypothesis. One of these approaches is after FZG/Oster which results in a good TFF prediction [7]. For TFF prediction with a local approach, the following requirements need to be fulfilled: the height of the calculated material exposure predicts TFF. Thereby the calculated local maximum exposure is at the experimental observed depth of PR and position on the contact path respectively tooth height. Additionally, the calculated material exposure correlates with load cycles in a limited lifetime.

A calculation approach for surface failure and subsurface failure is stated in Oster [26]. Oster describes the shear stress intensity as the quadratic mean value of the maximum shear stress in

all planes which corresponds to the procedure in [38].

$$\tau_{eff} = \sqrt{\frac{1}{4\pi}\int_{\gamma=0}^{\pi}\int_{\alpha=0}^{2\pi}\tau_{\gamma\alpha,max}^{2}\sin\gamma\, d\alpha\, d\gamma} \tag{1}$$

The maximum shear stress in the planes is composed of the normal contact stresses, the shear contact stresses due to friction, the thermal stresses and the residual stresses. The path of the shear stresses in a plane consist of the transition of the Hertzian pressure as shown in **Figure 11**. The effective stress state of the residual stresses is subtracted from the overall effective stress state. The local material exposure A is the quotient of the effective stress state and the allowable shear stress. (2)

$$\tau_{eff\,DA} = \tau_{eff\,Load,RS} - \tau_{eff\,RS}$$

The allowable shear stress is derived from the hardness profile. The constant of proportionality k is approximately 0.4 and further specified for different materials and tooth geometries in [36].

$$\tau_{zul}(y) = k \cdot HV(y) \tag{3}$$

The approach of FZG/Hertter [11] is an extended approach of the approach after FZG/Oster. Hertter separates the dynamic exposure A_{int_a}, which considers the amplitude and mean values of stress and a maximum exposure A_{int} considering the maximum shear and normal stress. Results of calculations show that the maximum material exposure for the evaluation of gears in higher component depths is decisive. The exposure A is calculated in all planes with equation after Liu [21]. The residual stresses are considered in the maximum shear and maximum normal stresses in all planes as shown in in **Figure 12**.

$$A_{max}(\gamma,\alpha) = \sqrt[\mu]{\frac{a\cdot\tau_{max}^{\mu} + b\cdot\sigma_{max}^{\mu}}{R_{p0,2}^{\mu}}} \tag{4}$$

The allowable stress is defined by the yield strength, which is derived from the local hardness after [13]. The local material exposure is calculated by the integration of the exposure in all planes.

$$A_{int} = \sqrt{\frac{15}{8\pi} * \int_{\gamma=0}^{\pi}\int_{\alpha=0}^{2\pi}[A_{max}(\gamma,\alpha)]^2 * \sin\gamma\, d\alpha\, d\gamma} \tag{5}$$

7 INVESTIGATIONS ON THE CRACK INITIATION POINT OF TFF

For the validation of the different calculation approaches, the primary crack starter depth and the corresponding load or the endurance limit need to be investigated for different gears and materials. Due the different depths of maximum stress of the contact, bending and tooth shear stresses, the primary crack initiating point (PR) also gives a hint of which stress is more or less responsible for TFF. In this section, the PR of TFF is further investigated; therefore, the TFF reference gear set with module 3 mm and 67/69 teeth is examined.

Tobie [33] was the first to investigate TFF at the FZG back-to-back test rig for the gear set. The gears were made out of the material 16MnCr5 with an CHD of 0.55 mm. In Stenico [31], the

gear geometry was investigated referring to inclusions in the material. Bruckmeier [8] did test runs with gears of the material 16MnCr5 and 17CrNiMo6. The gears were also case-hardened with a CHD of 0.5-0.55 mm. With the experiments of Witzig [36], the first S-N curves for TFF were completed. He investigated the case-hardened materials 18CrNiMo7-6 and 20MnCr5 with a CHD of ca. 0.5 mm. The endurance limit for 18CrNiMo7-6 was 1460 Nm and for 20MnCr5 1250 Nm. The hardness profile of the gears is comparable with a surface hardness of 690-785 HV and core hardness of 364-440 HV.

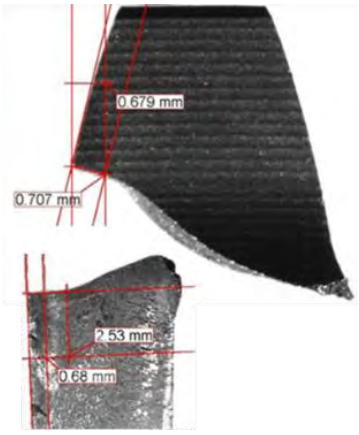


Figure 13: Optical-digital measurement of the PR.

All mentioned authors did research on the PR. The PR is usually identified visually. When observing the fracture surface, a microscope or scanning electron microscope (SEM) can help find the PR. The crack surface usually shows the characteristics of a fatigue fracture with a smooth surface in the area of ductile breakage and a rough surface where the final rupture is. Usually a fisheye is visible in the area of ductile breakage. The PR is usually placed central in the fisheye. For some TFF, a PR is not necessarily detectable.

For this paper, the PRs for the 67/69 gear with module 3 mm and a pressure angle of 20° of these works were summarized and further investigated. The authors [8, 33, 36] measured the PR optical with a digital photo station. For some teeth, the PR was investigated by scanning with an electron microscope with EDX to gain information of a possible nonmetallic inclusion in the material [36]. The depth of the PR was specified in the direction normal to the tooth flank.

The crack initiation points of TFF were further investigated to find the correlation of the PR depth with loading or heat treatment parameters. The residual stress measurements with X-ray diffraction were only up to a depth of 0.32 mm. The investigated PR depth is higher and therefore residual stresses are not considered in the evaluation.
Additional teeth of Witzig were measured digital with a digital photo station. First, the PR was identified by its characteristics. Then photos of the sides of the tooth are taken to digitally measure the exact position normal to the flank as shown in **Figure 13**. The error of the measurement is approximately 0.1 percent due the constraints of the digital photo station and the angle error due to the placement of the teeth in the digital photo station.

For the results, a correlation between PR depth and load or load cycles is not observed. But a dependency on the load is expected when the contact stresses are a main influence. Due to higher loading the maximum contact shear stresses are in greater depths normal to the flank after the theory of Hertz. For correlation with loading parameters (such as the torque), a separation of materials is not necessary because the depth of maximum exposure depends on the contact stresses and the hardness which is comparable. This supports a statement of Konowalczyk [17], who also observed no correlation between loading and the PR depth.

A good correlation of PR depth and the CHD was found as shown in **Figure 14**. The assumption of a normal distribution is possible with a mean of 2.57×CHD (1.29 mm) and standard deviation of 0.68×CHD. Other gear geometries show PRs at higher depths (up to 3.6×CHD in Stenico [31]) or at smaller depths 1-1.5×CHD [2].

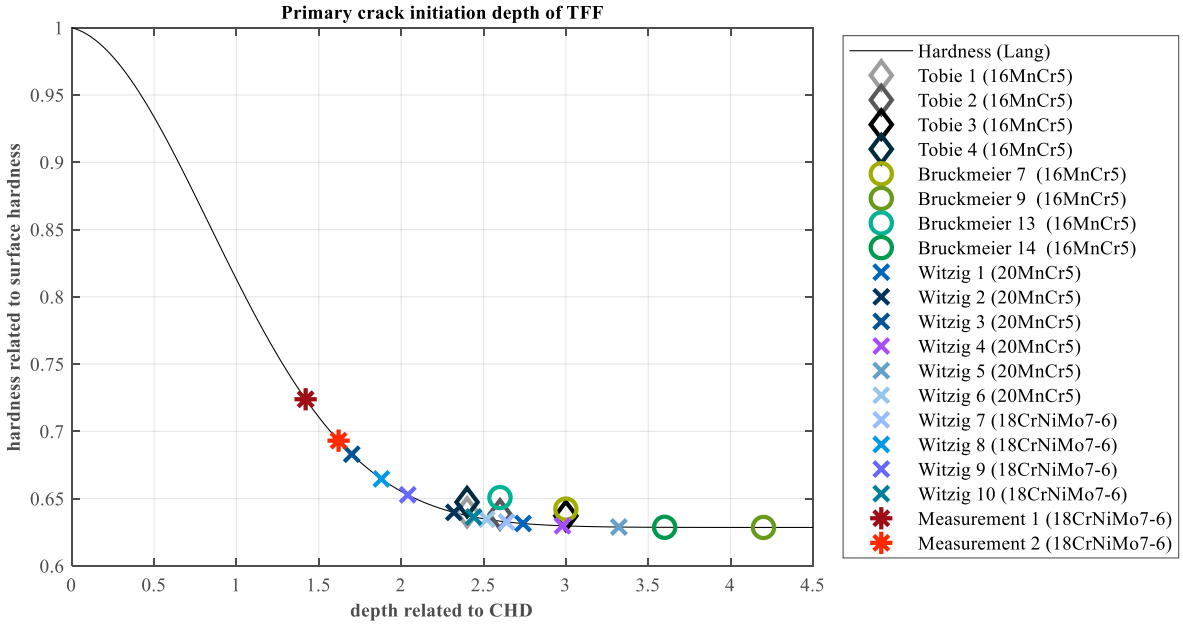


Figure 14: Crack initiation depth of TFF for the module 3 mm 67/69 teeth gear set.

8 CONCLUSIONS

For higher strength in gears, a heat treatment like case hardening is used. Case hardening improves the surface strength due to higher hardness and compressive residual stresses in the surface area. The mechanically required tensile residual stresses in the inner tooth are considered promoting crack initiation and crack growth. TFF is a subsurface-initiated fracture with a primary crack starter in depths of reduced strength. The PR is located deeper than the maximum shear stress after the theory of Hertz and therefore residual stresses are considered a main influence on the crack initiation.

For TFF, several calculation approaches are proposed, which treat the residual stresses differently. For the validation of a local TFF calculation approach, the local residual stress state is required and for the validation the crack initiation point of TFF and the corresponding load are mandatory. This paper summarizes the documented crack initiation depth of the module 3 mm gear set with 67/69 teeth. Also, additional TFFs of this geometry are analyzed and measured by optical-digital measurement. The crack initiation depth is further investigated and correlations with the CHD are shown. However, no correlation with load parameters is found.

More primary crack initiation points of different gear geometries need to be investigated and documented with geometry, load and heat treatment parameters for a statistically verified statement. For the validation of the calculation approaches, further investigations of the three-dimensional residual stress state in the inner tooth and its handling in the multiaxial criteria or the strength within the mean stresses are necessary. For an evaluation of the influence on the crack behavior of TFF in the multiaxial fatigue criteria, it is necessary to exclude additional influences of the microstructure such as carbon content and retained austenite content. Therefore, in Stahl [29], blanked representative parts are manufactured with adjustable residual stress state and without heat treatment. The application of the multiaxial criteria on these parts

will provide a further understanding of the treatment of residual stresses in the subsurface fracture calculation of gears.

ACKNOWLEDGEMENTS

Part of this work is funded by the Deutsche Forschungsgemeinschaft (DFG, German Research Foundation) - VO 1487/30-1; STA 1198/13-1 and is part of the DFG priority program “Targeted Use of Forming Induced Residual Stresses in Metal Components (SPP2013).”

REFERENCES

[1] Annast, R.: Kegelrad-Flankenbruch. Dissertation, Technische Universität München (2003).
[2] Bauer, E.: Flankenbrüche bei Hochleistungsgetrieben Allianz Report 2/98 (1998).
[3] Bauer, E.; Böhl, A.: Flank Breakage on Gears for Energy Systems. Gear Technology 28. Heft: 8, S. 36–42 (2011).
[4] Baydu Al; Langlois, P.: Evaluation of TIFF and TFF Load Carrying Capacities and Comparison Against Other Failure Modes. CTI MAG (2016).
[5] Beermann, S.: Tooth Flank Fracture - Influence of Macro and Micro Geometry. International Conference on Gears, Garching. VDI (2015).
[6] Boiadjiev, I.; Stemplinger, J.-P.; Stahl, K.: New Method for Calculation of the Load Carrying Capacity of Bevel and Hypoid Gears regarding Tooth Flank Fracture. Conference on Gears, Garching (2015).
[7] Boiadjiev, I.; Witzig, J.; Tobie, T.; Stahl, K.: Tooth flank fracture - basic principles and calculation model for a sub surface initiated fatigue failure mode of case hardened gears. International Conference on Gears, Lyon Villeurbanne, France, S. 670–80 (2014).
[8] Bruckmeier, S.: Flankenbruch bei Stirnradgetrieben. Dissertation, Technische Universität München (2006).
[9] Güntner, C.; Tobie, T.; Stahl, K.: Influences of the Residual Stress Condition on the Load Carrying Capacity of Case Hardened Gears Hardened Gears. AGMA (2017).
[10] Hertter, T.: A Calculation Model for Rating the Gear Load Capacity Based on Local Stresses and Local Properties of the Gear Material. International Conference on Gears; 2010; Garching (2010).
[11] Hertter, T.: Rechnerischer Festigkeitsnachweis der Ermüdungstragfähigkeit vergüteter und einsatzgehärteter Stirnräder. Dissertation, Technische Universität München (2003).
[12] Hertz, H.: Über die Berührung fester elastischer Körper (1881).
[13] Ilg, U.: Strukturelle Änderungen in unterschiedlich wärmebehandelten Wälzkörpern aus 100Cr6 und 20MnCr5 bei Wälz- sowie Wälz-Gleitbeanspruchung. Dissertation, Universität Karlsruhe (TH) (1980).
[14] ISO 6336, 2006,2016: Calculation of load capacity of spur and helical gears. (2006,2016).
[15] ISO/DTS 6336-4, 2018: Calculation of load capacity of spur and helical gears - Calculation of tooth flank fracture load capacity (2018).
[16] Johnson, K. L.: Contact mechanics. Cambridge University Press, Cambridge Cambridgeshire, New York, Port Melbourne, Madrid, Cape Town (1985).
[17] Konowalczyk, P.: Grübchen- und Zahnflankenbruchtragfähigkeit großmoduliger Stirnräder - Pitting and tooth flank fracture load capacity of large modul spur gears. Apprimus Verlag, Aachen (2018).
[18] Konowalczyk, P.; Löpenhaus, C.; Brecher, C.: Inclusion Based Calculation Approach for Flank Fracture Load Capacity. 58th Conference "Gear and Transmission Research" of the WZL on May 10/11 (2017).

[19] Lang, O. R.: Berechnung und Auslegung induktiv randschichtgehärteter Bauteile - In: Grosch, J.(Hrsg.), Induktives Randschichthärten, Tagung 23, S. 332-348. (1988).
[20] Liu, H.; Liu, H.; Zhu, C.; He, H.; Wei, P.: Evaluation of Contact Fatigue Life of a Wind Turbine Gear Pair Considering Residual Stress. Journal of Tribology 140-4 (2018).
[21] Liu, J.: Beitrag zur Verbesserung der Dauerfestigkeitsberechnung bei mehrachsiger Beanspruchung. Dissertation, TU Clausthal (1991).
[22] Liu, J.: Weakest Link Theory And Multiaxial Criteria 25, S. 55–68 (1997).
[23] Macherauch, E.: Introduction to Residual Stress. Advances in surface treatments, vol. 4. (1987).
[24] MackAldener, M.; Olsson, M.: Tooth Interior Fatigue Fracture - computational and material aspects. International Journal of Fatigue 23. Heft: 23 // 4, S. 329–40 (2001).
[25] Novožilov, V. V.: Theory of elasticity, Oxford (u.a.), Pergamon Pr., 1961 (1961).
[26] Oster, P.: Beanspruchung der Zahnflanken unter Bedingungen der Elastohydrodynamik. Dissertation, Technische Universität München (1982).
[27] Schwienbacher, S.; Tobie, T.; Höhn, B.-R.; Hofmann, M.: Measurement of Residual Stresses in Case Hardened Test Gears with Neutron-Diffractometer, Proposal No. 397 (2006).
[28] Simbürger, A.: Festigkeitsverhalten zäher Werkstoffe bei einer mehrachsigen, phasenverschobenen Schwingbeanspruchung mit körperfesten und veränderlichen Hauptspannungseinrichtungen. Dissertation, TH Darmstadt (1975).
[29] Stahl, J.; Müller, D.; Tobie, T.; Golle, R.; Volk, W.; Stahl, K.: Residual stresses in parts manufactured by near-net-shape-blanking. Production Engineering 23. Heft: 3, S. 217 (2018).
[30] Stahl, K.; Höhn, B.-R.; Tobie, T.: Tooth flank breakage - influences on subsurface initiated fatigue failures of case hardened gears. DETC2013, Portland, Oregon, USA. ASME (2013).
[31] Stenico, A.: Einfluss von Einschlüssen im Werkstoffgefüge auf den Beanspruchungszustand und das Schadensverhalten einsatzgehärteter Zahnflanken (2001).
[32] Thomas, J.: Flankentragfähigkeit und Laufverhalten von hart-feinbearbeiteten Kegelrädern. Dissertation, Technische Universität München (1998).
[33] Tobie, T.: Zur Grübchen- und Zahnfußtragfähigkeit einsatzgehärteter Zahnräder - Einflüsse aus Einsatzhärtungstiefe, Wärmebehandlung und Fertigung bei unterschiedlicher Baugröße. Dissertation, TU München (2001).
[34] Weber, R.: Auslegungskonzept gegen Volumenversagen bei einsatzgehärteten Stirnrädern. Dissertation, Universität Kassel (2015).
[35] Weibull, W.: A Statistical Theory of Strength of Materials (1939).
[36] Witzig, J.: Flankenbruch - Eine Grenze der Zahnradtragfähigkeit in der Werkstofftiefe. Dissertation, Technische Universität München (2012).
[37] Zenner, H.; Heidenreich, R.: Schubspannungsintensitätshypothese - Erweiterung und experimentelle Abstützung einer neuen Festigkeitshypothese für schwingende Beanspruchung (1979).
[38] Zenner, H.; Richter, I.: Festigkeitshypothese für die Dauerfestigkeit bei beliebigen Beanspruchungskombinationen. Konstruktion 29-1, S. 11–18 (1977).

XIV International Conference on Computational Plasticity. Fundamentals and Applications
COMPLAS 2019
E. Oñate, D.R.J. Owen, D. Peric , M. Chiumenti, and Eduardo de Souza Neto (Eds)

PLASTIC DISLOCATION AND INCOMPATIBILITY DENSITY AS INDICATORS FOR RESIDUAL STRESSES

PHILIPP LANDKAMMER*, PAUL STEINMANN*

* Institute for Applied Mechanics (LTM)
Friedrich-Alexander-Universität Erlangen-Nürnberg (FAU)
Egerlandstrasse 5, 91058 Erlangen, Germany
e-mail: philipp.landkammer@fau.de, paul.steinmann@fau.de, www.ltm.tf.fau.de

Key words: Incompatibility Density, Residual Stresses, Differential Geometry.

Abstract. Residual stresses in forming simulations are typically investigated by analyzing the remaining stress state after removing all external loadings. However, the generation of the stress state during forming remains unknown. As a remedy, we use the plastic and elastic dislocation and incompatibility densities - derived from continuum mechanical and differential geometrical considerations - as indicators to track the generation of residual stresses through out a forming operation. Theoretical backgrounds for small and large strain plasticity are highlighted and practical aspects regarding implementation are provided. Two examples demonstrate the functionality of the approach, whereby the plastic incompatibility density in phenomenological, multiplicative large strain plasticity serves as indicator.

1 INTRODUCTION

During a forming process, residual stresses occur in the manufactured components. In general, these have a decisive influence on their forming, application and failure behaviour. Regarding a workpiece under cyclic bending, compressive residual stresses close to the surface of the workpiece improve its life-time behaviour, whereas tensile residual stresses promote crack initialization. In particular within cold extrusion processes, high residual stresses occur due to the required forming forces. Thereby, a number of forming experiments have been used to investigate the dependencies of residual stresses on contact and friction conditions and geometry changes, see [1] among others. However, a deeper understanding of residual stresses is required to explore the total potential of deliberately influencing the workpiece behaviour through forming-induced residual stresses.

As a common definition, stresses which remain in the component after removing all external loadings are denoted as residual stresses. Therefore, the numerical investigation of residual stresses within the framework of a finite element (FE) simulation is typically based on the quantification and visualization of the remaining stress state within the unloaded component at the end of a forming operation. However, residual stresses arise during the whole forming process, and possibly also reduce again in case of an opposite load application. Since the residual stress generation during forming is not yet captured in the conventional procedure, a post-processing technique for an accompanying tracking of residual stresses would be of major interest to control them within manufacturing.

From a mechanical point of view, incompatible plastic strains in case of an inhomogeneous plastic deformation are responsible for residual stresses. In more detail, residual stresses arise in consequence of elastic lattice distortions, which are required to ensure that no gaps or overlaps occur despite the underlying incompatible plastic strains. By using differential geometrical considerations, Kröner [2] developed a linear continuum theory for residual strains with respect to additive small strain plasticity and further extended the approach also to nonlinearities [3]. For instance, a second order incompatibility density tensor is introduced therein to quantify the incompatible plastic strains.

Our idea is to use the dislocation and incompatibility densities as indicators for residual stresses. The theoretical aspects are transferred even to multiplicative large strain plasticity in [4], which provides the applicability of these indicators also to forming simulations.

The paper is structured as follows: Section 2 provides an overview to classify incompatible plastic strains within plastic deformations. Section 3 reiterates the computation of plastic incompatibilities in small strain plasticity and also recaptures its extension to multiplicative large strain plasticity. The functionality of these indicator for residual stresses is demonstrated by the plastic incompatibility density for two examples of a homogeneous and an inhomogeneous plastic deformation in Section 4. Finally, Section 5 summarizes the findings.

2 MECHANICAL VIEW ON RESIDUAL STRAINS

The theory of crystal plasticity is fundamental for describing the generation of residual stresses. Macroscopically observed plastic deformations within a forming process are the result of dislocation flow at the microscale. Thereby, dislocations partially get stucked within the periodically arranged crystal lattice and remain as additional obstacles for further dislocations flow, which leads to plastic hardening.

As illustrated by the diagram in **Figure 1**, a classification of plastic deformations according to the generated dislocation structure is stated as follows: Homogeneous plastic deformations lead purely to the formation of so-called statistically stored dislocations (SSD), which are responsible for plastic hardening. In case of inhomogeneous plastic deformations, geometrically necessary dislocations (GND) are generated in addition. They are responsible for maintaining the inhomogeneous plastic deformation after removing all external loadings [5]. GNDs are further distinguished, whether they cause macroscopically stress-free lattice curvatures or lead to incompatible plastic strains. Incompatible plastic strains induce incompatible elastic strains as their counterparts to guarantee the continuity of the continuum. These elastic residual strains cause residual stresses.

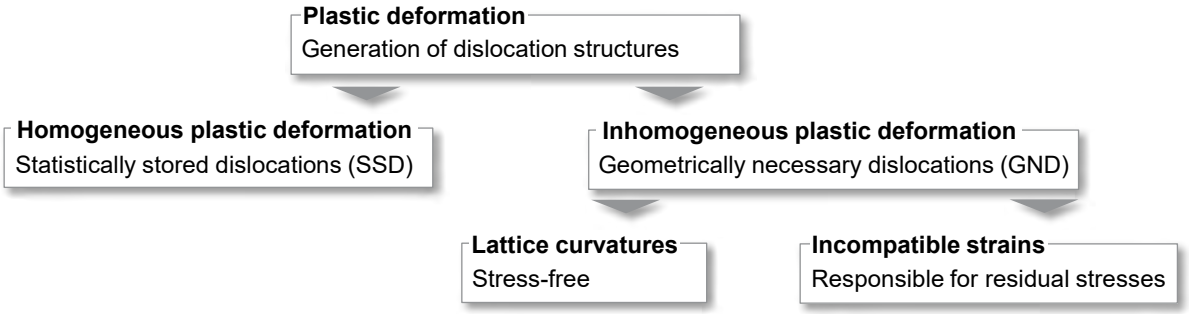


Figure 1: Incompatible strains in case of an inhomogeneous plastic deformation cause residual stresses

3 COMPUTATION OF DISLOCATION AND INCOMPATIBILTY DENSITIES

Concepts of differential geometry and continuum mechanics allow to describe the classification of plastic deformations as depicted in **Figure 1** and enable to quantify inhomogeneities and incompatibilities. Subsequently, the relationships are reiterated in detail.

An unique deformation map $\boldsymbol{\varphi}: \boldsymbol{X} \in \mathcal{B}_0 \rightarrow \boldsymbol{x} \in \mathcal{B}_t$ requires that no closure failure along an arbitrary closed material or spatial line path, $\mathcal{C}$ or $\mathcal{C}_0$, exists. This requirement is called the integrability condition for the deformation gradient $\boldsymbol{F} := \mathrm{Grad}\,\boldsymbol{\varphi}$ and is formulated based on the Stokes theorem as

$$\oint_{\mathcal{C}} \mathrm{d}\boldsymbol{x} = \oint_{\mathcal{C}_0} \boldsymbol{F} \cdot \mathrm{d}\boldsymbol{X} = \boldsymbol{0} \quad \overset{\text{Stokes}}{\Longrightarrow} \quad \int_{\mathcal{A}_0} \mathrm{Curl}^{\mathrm{T}} \boldsymbol{F} \cdot \boldsymbol{N} \mathrm{d}A = \boldsymbol{0}. \tag{1}$$

From Eq. (1), the stronger pointwise compatibility condition follows, which ensure that no gaps or overlaps arise within the deformation of the configuration:

$$\mathrm{Curl}^{\mathrm{T}} \boldsymbol{F} \overset{!}{=} \boldsymbol{0}. \tag{2}$$

In contrast, the rotation field of purely the plastic (or elastic) part of the deformation gradient, called plastic (or elastic) dislocation density, only vanishes in case of a homogeneous deformation, but do not vanish in the presence of an inhomogeneous elasto-plastic deformation. Thus, the plastic (or elastic) dislocation density expresses the non-integrability of inhomogeneous elasto-plastic deformations. In a similar manner, the plastic (or elastic) incompatibility density, which is recaptured for additive small and multiplicative large strain plasticity in the subsequent sections, indicates incompatible plastic strains, which are responsible for residual stresses.

3.1 Small strain

In the linearized theory of small strain elasto-plasticity, the deformation gradient is approximated by $\boldsymbol{F} \approx \boldsymbol{I} + \boldsymbol{\beta}$. The displacement gradient $\boldsymbol{\beta} := \mathrm{Grad}\boldsymbol{u}$, also denoted in this context as distortion, additively decomposes into the symmetric strain tensor $\boldsymbol{\epsilon} = \frac{1}{2}[\mathrm{Grad}\boldsymbol{u} + \mathrm{Grad}^{\mathrm{T}}\boldsymbol{u}]$ and the antisymmetric rotation tensor $\boldsymbol{\omega} = \frac{1}{2}[\mathrm{Grad}\boldsymbol{u} - \mathrm{Grad}^{\mathrm{T}}\boldsymbol{u}]$, whereby both additively decompose further into elastic and plastic parts:

$$\boldsymbol{\beta} = \boldsymbol{\epsilon} + \boldsymbol{\omega} = [\boldsymbol{\epsilon}^{\mathrm{e}} + \boldsymbol{\epsilon}^{\mathrm{p}}] + [\boldsymbol{\omega}^{\mathrm{e}} + \boldsymbol{\omega}^{\mathrm{p}}] = [\boldsymbol{\epsilon}^{\mathrm{e}} + \boldsymbol{\omega}^{\mathrm{e}}] + [\boldsymbol{\epsilon}^{\mathrm{p}} + \boldsymbol{\omega}^{\mathrm{p}}] = \boldsymbol{\beta}^{\mathrm{e}} + \boldsymbol{\beta}^{\mathrm{p}} \tag{3}$$

The integrability condition guarantees:

$$\mathrm{Curl}^{\mathrm{T}} \boldsymbol{\beta} = \boldsymbol{0}. \tag{4}$$

Since the $\mathrm{Curl}\{\cdot\}$-operator is distributive,

$$\mathrm{Curl}\boldsymbol{\beta} = \mathrm{Curl}(\boldsymbol{\beta}^{\mathrm{e}} + \boldsymbol{\beta}^{\mathrm{p}}), \tag{5}$$

it follows for the plastic dislocation density

$$\boldsymbol{\alpha}^{\mathrm{p}} := \mathrm{Curl}\boldsymbol{\beta}^{\mathrm{p}} = -\mathrm{Curl}\boldsymbol{\beta}^{\mathrm{e}} \neq \boldsymbol{0} \ \text{(in general)}. \tag{6}$$

As describe above and according to the pioneering works of Kröner, see [2] among others, $\boldsymbol{\alpha}^{\mathrm{p}}$ quantifies the inhomogeneity of plastic deformations and exclusively equals to zero in case of homogeneous plastic deformations.

Furthermore, the incompatibility density tensor $\mathrm{Inc}\{\cdot\}$ with respect to the strain tensor of the total deformation requires

$$\mathrm{Inc}\boldsymbol{\epsilon} \coloneqq \mathrm{Curl}^{\mathsf{T}}\mathrm{Curl}^{\mathsf{T}}\boldsymbol{\epsilon} = \mathbf{0}, \tag{7}$$

but for its plastic and elastic parts, it yields in accordance to Eq. (6):

$$\boldsymbol{\eta}^{\mathrm{p}} \coloneqq \mathrm{Inc}\boldsymbol{\epsilon}^{\mathrm{p}} = \mathrm{Curl}^{\mathsf{T}}\mathrm{Curl}^{\mathsf{T}}\boldsymbol{\epsilon}^{\mathrm{p}} = \left[\mathrm{Curl}^{\mathsf{T}}\boldsymbol{a}^{\mathrm{p}\,\mathsf{T}}\right]^{\mathrm{sym}} = -\mathrm{Inc}\boldsymbol{\epsilon}^{\mathrm{e}} \neq \mathbf{0} \ \text{(in general)}. \tag{8}$$

Here, the plastic incompatibility density $\boldsymbol{\eta}^{\mathrm{p}}$ serves as a measure for plastic strains, which result from the non-vanishing plastic dislocation density $\boldsymbol{a}^{\mathrm{p}}$, see Eq. (6). Since $\boldsymbol{\eta}^{\mathrm{p}}$ quantifies incompatible plastic (or elastic) strains, the plastic (or elastic) incompatibility density serves as indicator for residual stresses.

Remark 1: For the sake of implementation and according to Steinmann [10] the $\mathrm{Curl}\{\cdot\}$-operation rewrites as:

$$\mathrm{Curl}\{\cdot\} = \begin{bmatrix} \{\cdot\}_{13,2} - \{\cdot\}_{12,3} & \{\cdot\}_{23,2} - \{\cdot\}_{22,3} & \{\cdot\}_{33,2} + \{\cdot\}_{32,3} \\ \{\cdot\}_{11,3} - \{\cdot\}_{13,1} & \{\cdot\}_{21,3} - \{\cdot\}_{23,1} & \{\cdot\}_{31,3} + \{\cdot\}_{33,1} \\ \{\cdot\}_{12,1} - \{\cdot\}_{11,2} & \{\cdot\}_{22,1} - \{\cdot\}_{21,2} & \{\cdot\}_{32,1} + \{\cdot\}_{31,2} \end{bmatrix}. \tag{9}$$

3.2 Large strain

According to Lee [6], the nonlinear large strain elasto-plasticity theory is based on the multiplicative decomposition of the deformation gradient into its elastic and plastic part:

$$\boldsymbol{F} = \boldsymbol{F}^{\mathrm{e}} \cdot \boldsymbol{F}^{\mathrm{p}} \tag{10}$$

As illustrated in **Figure 2**, the plastic part of the deformation gradient, $\boldsymbol{F}^{\mathrm{p}}$, represents the deformation due to the motion of dislocations (depicted as red circles) in the periodically arranged crystal lattice. The lattice orientation remains unchanged in the plastic intermediate configuration $\overline{\mathcal{B}}$. The elastic part $\boldsymbol{F}^{\mathrm{e}}$ then causes the corresponding lattice distortion.

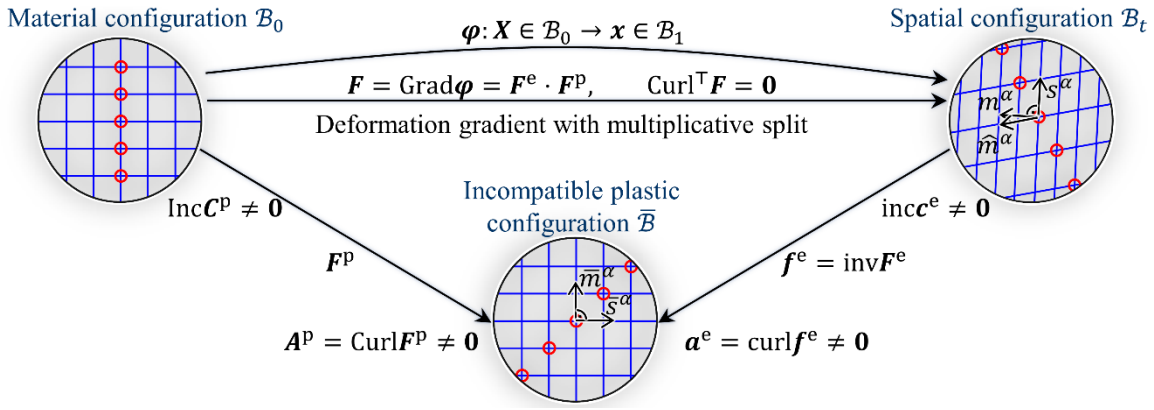


Figure 2: Multiplicative elasto-plasticity modelling includes an incompatible plastic intermediate configuration

Remark 4: Within multiplicative modelling, purely the elastic part of the deformation transforms the slip systems. The elastic part of the deformation gradient and the left Cauchy Green Tensor, $\boldsymbol{F}^{\mathrm{e}}$ and $\boldsymbol{b}^{\mathrm{e}} = \boldsymbol{F}^{\mathrm{e}} \cdot \boldsymbol{F}^{\mathrm{e}\mathsf{T}}$, allow to compute the slip direction $\boldsymbol{s}^{\alpha}$ and the slip plane normal $\boldsymbol{m}^{I}$ in the spatial configuration in dependency of their counterparts in the plastic intermediate configuration: $\boldsymbol{s}^{\alpha} = \boldsymbol{F}^{\mathrm{e}} \cdot \bar{\boldsymbol{s}}^{\alpha}$, $\hat{\boldsymbol{m}}^{\alpha} = \boldsymbol{b}^{\mathrm{e}} \cdot \boldsymbol{m}^{\alpha}$ and $\boldsymbol{m}^{\alpha} = \boldsymbol{F}^{\mathrm{e}-\mathsf{T}} \cdot \bar{\boldsymbol{m}}^{\alpha}$. The transformation of a slip system is additionally depicted in **Figure 2**.

Plastic and elastic dislocation density

The rotation field with respect to the plastic part of the deformation gradient, which is again denoted as plastic dislocation density, is defined as:

$$\boldsymbol{A}^{\mathrm{p}} := \mathrm{Curl}\boldsymbol{F}^{\mathrm{p}} \neq \boldsymbol{0} \text{ (in general).} \tag{11}$$

In accordance to the additive small strain theory, $\boldsymbol{A}^{\mathrm{p}}$ differs from zero in case of inhomogeneous plastic deformations. Thus, the plastic intermediate configuration $\overline{\mathcal{B}}$ is in general incompatible and the plastic dislocation density $\boldsymbol{A}^{\mathrm{p}}$ is directly linked to the GNDs, which arise during inhomogeneous plastic deformations. An incompatible plastic configuration induces incompatible elastic distortions to guarantee the continuity of the continuum. Therefore, it follows for the counterparts in the elastic regime:

$$\boldsymbol{a}^{\mathrm{e}} := \mathrm{curl}\boldsymbol{f}^{\mathrm{e}} \neq \boldsymbol{0} \text{ (in general).} \tag{12}$$

The relationship between the elastic and plastic dislocation density, $\boldsymbol{A}^{\mathrm{p}}$ and $\boldsymbol{a}^{\mathrm{e}}$, which is proposed [5] and further extensively investigated by Cermelli and Gurtin [7], results in:

$$\frac{1}{\det\boldsymbol{F}^{\mathrm{p}}}\boldsymbol{F}^{\mathrm{p}} \cdot \boldsymbol{A}^{\mathrm{p}} = \frac{1}{\det\boldsymbol{f}^{\mathrm{e}}}\boldsymbol{f}^{\mathrm{e}} \cdot \boldsymbol{a}^{\mathrm{e}}. \tag{13}$$

Remark 2: The plastic dislocation density $\boldsymbol{A}^{\mathrm{p}}$ provides further background information: Its diagonal entries arise with the occurrence of screw dislocations, whereby non-diagonal entries are linked with edge dislocations. In addition, a multiplication with a direction vector $\boldsymbol{t}$ of an assumed dislocation line leads to the associated Burgers vector $\boldsymbol{b}$, which describes the closure failure: $\boldsymbol{b} = \boldsymbol{A}^{\mathrm{p}\top} \cdot \boldsymbol{t}$.

Remark 3: The plastic part of the deformation gradient, $\boldsymbol{F}^{\mathrm{p}}$, which is necessary for the computation of the plastic dislocation density $\boldsymbol{A}^{\mathrm{p}}$, is only accessible if crystal plasticity modelling is applied. Unfortunately, in commonly used commercial FE software packages, for example *Marc/Mentat* or *Abaqus*, only a phenomenological multiplicative approach for large strain plasticity as described in Simo and Hughes [8] is implemented and so, the plastic part of the deformation gradient remains still unknown. However, a possible option to incorporate crystal plasticity modelling in the above mentioned FE packages is the usage of the *Fortran* library *DAMASK* [9].

Plastic and elastic incompatibility density

The compatibility relations and their correlations with dislocation densities within the linear theory of small strains, see Kröner [2], are extended by Steinmann [4] to the general nonlinear case of large strains. Applying the multiplicative large strain modelling, the incompatibilities of the continuum rotations contained in $\boldsymbol{F}^{\mathrm{e}} = \mathrm{inv}\boldsymbol{f}^{\mathrm{e}}$ lead to stress-free lattice curvatures, while the incompatibilities of the elastic part of the left Cauchy-Green strain tensor $\boldsymbol{b}^{\mathrm{e}}$ cause the lattice distorsions, which result in residual stresses.

The theories of differential geometry is exploited in [4] to show that the non-integrability of plastic and elastic strains metrics $\boldsymbol{C}^{\mathrm{p}}$ (plastic part of the right Cauchy-Green tensor) and $\boldsymbol{c}^{\mathrm{e}} = \mathrm{inv}\boldsymbol{b}^{\mathrm{e}}$ (elastic part of the left Cauchy-Green tensor) coincides with the non-vanishing plastic and elastic Riemann curvatures $\boldsymbol{H}^{\mathrm{p}}$ and $\boldsymbol{h}^{\mathrm{e}}$. According to these considerations, the plastic incompatibility density (in Euclidean space) is computed by,

$$2\boldsymbol{H}^{\mathrm{p}} = \mathrm{Ink}\boldsymbol{C}^{\mathrm{p}} \coloneqq \mathrm{Curl}^{\mathsf{T}}\mathrm{Curl}^{\mathsf{T}}\boldsymbol{C}^{\mathrm{p}} + \{\mathrm{Grad}\boldsymbol{C}^{\mathrm{p}}\}\bowtie\{\mathrm{Grad}\boldsymbol{C}^{\mathrm{p}}\} \neq \boldsymbol{0}\ (\text{in general}), \tag{14}$$

whereby $\{\cdot\}\bowtie\{\cdot\}$ describes a special product of third-order tensors, see the implementation guidance in the subsection 3.3. Analogously, it follows for the elastic regime,

$$-2\boldsymbol{h}^{\mathrm{e}} = \mathrm{ink}\boldsymbol{c}^{\mathrm{e}} \coloneqq \mathrm{curl}^{\mathsf{T}}\mathrm{curl}^{\mathsf{T}}\boldsymbol{c}^{\mathrm{e}} + \{\mathrm{grad}\boldsymbol{c}^{\mathrm{e}}\}\bowtie\{\mathrm{grad}\boldsymbol{c}^{\mathrm{e}}\} \neq \boldsymbol{0}\ (\text{in general}). \tag{15}$$

As in small strain plasticity, the plastic and elastic incompatibility densities are a measure for the incompatibility of the plastic strains and their elastic counterparts. Since the latter cause residual strains, both incompatibility densities are suited as residual stress indicators.

Remark 5: In commercial FE-software packages, for example *Marc/Mentat* or *Abaqus*, access to the elastic part of the left Cauchy-Green tensor, $\boldsymbol{b}^{\mathrm{e}}$, is provided via subroutines in case of using their phenomenological large strain plasticity modelling. The plastic part of the right Cauchy-Green tensor then follows with $\boldsymbol{C}^{\mathrm{p}} = \boldsymbol{F}^{\mathsf{T}} \cdot \mathrm{inv}\boldsymbol{b}^{\mathrm{e}} \cdot \boldsymbol{F}$. Consequently, the plastic and elastic incompatibility densities, $\mathrm{Inc}\boldsymbol{C}^{\mathrm{p}}$ and $\mathrm{inc}\boldsymbol{c}^{\mathrm{e}}$ – indicators for residual stresses, are even computable without using crystal plasticity.

A relation between the elastic and plastic incompatibility densities, see Eq. (14) and (15), is derived in Steinmann [4] as:

$$\frac{\det\left(\boldsymbol{F}^{\mathrm{p}^{-1}}\right)}{\det\boldsymbol{F}^{\mathrm{p}}}\boldsymbol{F}^{\mathrm{p}} \cdot \boldsymbol{H}^{\mathrm{p}} \cdot \boldsymbol{F}^{\mathrm{p}^{\mathsf{T}}} = \frac{\det\left(\boldsymbol{f}^{\mathrm{e}^{-1}}\right)}{\det\boldsymbol{f}^{\mathrm{e}}}\boldsymbol{f}^{\mathrm{e}} \cdot \boldsymbol{h}^{\mathrm{e}} \cdot \boldsymbol{f}^{\mathrm{e}^{\mathsf{T}}} \tag{16}$$

Unfortunately, Eq. (16) again requires an access to the plastic and elastic deformation gradient, respectively.

3.3 An implementation scheme for the plastic incompatibility density

While in the previous subsection focus is put on the relationships between the plastic and elastic dislocation and incompatibility densities, some hints for implementation are given subsequently.

Computation of the plastic incompatibility density from Riemann curvatures

The steps to compute the incompatibility density is described for the plastic regime, whereby Einstein summation is used as in [4].

After differentiation of the plastic part of the Cauchy Green tensor, $\boldsymbol{C}^{\mathrm{p}}$, with respect to the material coordinates $\boldsymbol{X}$, the plastic Riemann connection is achieved by

$$\mathcal{M}^{\mathrm{p}}_{IJK}(\boldsymbol{C}^{\mathrm{p}}) := \tfrac{1}{2}\left[C^{\mathrm{p}}_{IJ,K} - C^{\mathrm{p}}_{JK,I} + C^{\mathrm{p}}_{KI,J}\right] \tag{17}$$

Next, the plastic material Riemann curvature tensor is computed, whereby differentiation of the Riemann connection $\mathcal{M}^{\mathrm{p}}_{IJK}$, again with respect to the material coordinates $\boldsymbol{X}$, is required:

$$M^{\mathrm{p}}_{IJKL}(\boldsymbol{C}^{\mathrm{p}}) := -2\left[\mathcal{M}^{\mathrm{p}}_{IJK,L} + \mathcal{M}^{\mathrm{p}}_{AIK}\mathcal{M}^{\mathrm{p}\,A}_{\ \ JL}\right]. \tag{18}$$

Finally, the plastic incompatibility tensor is obtained by

$$H^{\mathrm{p}MN}(\boldsymbol{C}^{\mathrm{p}}) \coloneqq -\tfrac{1}{4}\mathcal{E}^{MIJ}M^{\mathrm{p}}_{IJKL}\mathcal{E}^{KLN} = \tfrac{1}{2}\mathcal{E}^{MIJ}\mathcal{M}^{\mathrm{p}}_{IJK,L}\mathcal{E}^{KLN} + \tfrac{1}{2}\mathcal{E}^{MIJ}\mathcal{M}^{\mathrm{p}}_{AIK}\mathcal{M}^{\mathrm{p}\,A}_{\ \ JL}\mathcal{E}^{KLN}, \tag{19}$$

whereby $\mathcal{E}$ refers to the third-order Levi-Cita-Symbol with

$$\mathcal{E}^{123} = \mathcal{E}^{231} = \mathcal{E}^{321} = 1, \;\; \mathcal{E}^{132} = \mathcal{E}^{321} = \mathcal{E}^{231} = -1 \tag{20}$$

and 0 else. Within Euclidean space the first term in Eq. (19) equals

$$\mathcal{E}^{MIJ}\mathcal{M}^{\mathrm{p}}_{IJK,L}\mathcal{E}^{KLN} = \mathrm{Curl}^{\mathsf{T}}\mathrm{Curl}^{\mathsf{T}}\boldsymbol{C}^{\mathrm{p}}, \tag{21}$$

whereas the second term in Eq. (19) can be formulated as

$$\mathcal{E}^{MIJ}\mathcal{M}^{\mathrm{p}}_{AIK}\mathcal{M}^{\mathrm{p}\,A}_{\;\;JL}\mathcal{E}^{KLN} = \{\mathrm{Grad}\boldsymbol{C}^{\mathrm{p}}\}\bowtie\{\mathrm{Grad}\boldsymbol{C}^{\mathrm{p}}\}. \tag{22}$$

Thus, Eq. (14) follows from Eq. (19). The computation of the elastic incompatibility density $\mathrm{ink}\boldsymbol{c}^{\mathrm{e}}$ from the elastic part of the left Cauchy Green tensor works in an analogous way. For further details, the interested reader is referred to [4].

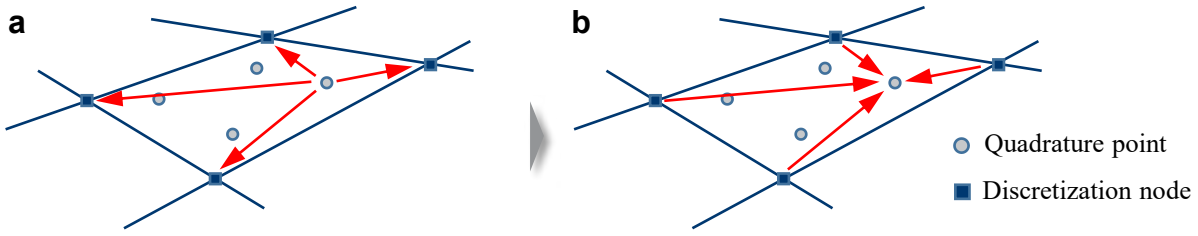
Remark 6: For the sake of implementation and according to Kaiser and Menzel [10] the $\mathrm{Curl}^{\mathsf{T}}\mathrm{Curl}^{\mathsf{T}}\{\cdot\}$-operation rewrites as:

$$\begin{aligned}\mathrm{Curl}^{\mathsf{T}}\mathrm{Curl}^{\mathsf{T}}\{\cdot\} \;=\; &\begin{bmatrix}\{\cdot\}_{12,12}+\{\cdot\}_{13,13} & \{\cdot\}_{11,21}+\{\cdot\}_{13,23} & \{\cdot\}_{11,31}+\{\cdot\}_{12,32}\\ \{\cdot\}_{22,12}+\{\cdot\}_{23,13} & \{\cdot\}_{21,21}+\{\cdot\}_{23,23} & \{\cdot\}_{21,31}+\{\cdot\}_{22,32}\\ \{\cdot\}_{32,12}+\{\cdot\}_{33,13} & \{\cdot\}_{31,21}+\{\cdot\}_{33,23} & \{\cdot\}_{31,31}+\{\cdot\}_{32,32}\end{bmatrix}\\ -\;&\begin{bmatrix}\{\cdot\}_{11,22}+\{\cdot\}_{11,33} & \{\cdot\}_{12,11}+\{\cdot\}_{12,33} & \{\cdot\}_{13,11}+\{\cdot\}_{13,22}\\ \{\cdot\}_{21,22}+\{\cdot\}_{21,33} & \{\cdot\}_{22,11}+\{\cdot\}_{22,33} & \{\cdot\}_{23,11}+\{\cdot\}_{23,22}\\ \{\cdot\}_{31,22}+\{\cdot\}_{31,33} & \{\cdot\}_{32,11}+\{\cdot\}_{32,33} & \{\cdot\}_{33,11}+\{\cdot\}_{33,22}\end{bmatrix}.\end{aligned} \tag{23}$$

Differentiation of quadrature point quantities

For the differentiation of quadrature point quantities – for example the tensor components $C^{\mathrm{p}}_{IJ,K}$ within $\mathrm{Grad}\boldsymbol{C}^{\mathrm{p}}$ – a two-step technique is applied as already proposed in Steinmann [5] for a post-processing approach with respect to the plastic dislocation density:

Firstly, the tensor components are mapped from the quadrature points to the discretization nodes, see **Figure 3 a**. Therefore, the *Superconvergent Patch Recovery Procedure* (*SPR*) [11] as an alternative to the *global L^2-smoothing* [12] is applied. The mapped tensor quantities at each discretization node are indicated in the following by a tilde.



Extrapolation via patch-recovery **Differentiation** via shape functions

Figure 3: A two-step technique for the differentiation of integration point quantities

Secondly, as illustrated in **Figure 3 b**, the differentiation of a tensor component is evaluated at quadrature points by the help of shape functions:

$$\mathrm{Grad}\boldsymbol{C}^{\mathrm{p}\,j} = \sum_{a=1}^{n_{\mathrm{en}}} \left[\widetilde{\boldsymbol{C}}^{\mathrm{p}\,a} \otimes \frac{\partial N^a(\xi^j)}{\partial \xi}\right] \cdot \left[\boldsymbol{X}^a \otimes \frac{\partial N^a(\xi^j)}{\partial \xi}\right]^{-1}, \tag{24}$$

whereby j refers to the quadrature point, a refers to the elementwise discretization node, n_{en} denotes the number of element nodes and $N(\boldsymbol{\xi})$ refers to the shape functions with respect to its natural coordinates.

4 COMPUTATIONAL EXAMPLES

The functional principle of the plastic incompatibility density $\mathrm{Inc}\boldsymbol{C}^{\mathrm{p}}$ as an accompanying indicator for residual stresses during forming simulations is demonstrated for two examples of a homogeneous and an inhomogeneous elastoplastic deformation.

As a representative of FE-packages with phenomenological, multiplicative large strain plasticity modelling, *Marc/Mentat* is used for both examples. Here, the deformation gradient $\boldsymbol{F}$ and the elastic part of left Cauchy Green tensor, $\boldsymbol{b}^{\mathrm{e}}$, are accessible for each quadrature point through subroutines. The plastic part of the right Cauchy Green tensor then follows as:

$$\boldsymbol{C}^{\mathrm{p}} = \boldsymbol{F}^{\mathrm{T}} \cdot \boldsymbol{c}^{\mathrm{e}} \cdot \boldsymbol{F} \qquad \text{with} \quad \boldsymbol{c}^{\boldsymbol{e}} = \mathrm{inv}\boldsymbol{b}^{\mathrm{e}} \tag{25}$$

The plastic incompatibility density as in Eq. (14) is then computed according to the techniques presented in subsection 3.3.

The same elasto-plastic material modelling is applied in both examples. The elastic constants are set to $E = 210.000$ MPa and $\nu = 0.3$. The isotropic plastic hardening, which is modelled by the Hockett-Sherby function with respect to the equivalent plastic strain $\bar{\epsilon}^{\mathrm{p}}$, is used as follows:

$$\sigma_{\mathrm{yield}}(\bar{\epsilon}^{\mathrm{p}}) = 185.2 + [577.1 - 185.2]\left[1 - \exp\left(-2.18\bar{\epsilon}^{\mathrm{p}\,0.667}\right)\right] \tag{26}$$

4.1 Example for homogeneous elasto-plastic deformation: Tension

As the first example, an elasto-plastic deformation by a pure tension is considered. In a two-dimensional model, a bar (height: 180 mm, length: 200 mm) is drawn force-controlled in e_1-direction until an enlargement of 100 mm is reached, see **Figure 1 a**. The resulting constant Cauchy stress equals to 473 MPa (v.Mises coincides with the 11-component) in the fully loaded stated and the equivalent plastic strain computes to 0.47. After reducing the loading back to zero, also the stresses vanish. Thus, no residual stresses are generated. In accordance, since tension leads to a purely homogeneous deformation, the plastic incompatibility density also remains zero through all stages, see **Figure 1 b**.

4.2 Example for inhomogeneous elasto-plastic deformation: Bending

Pure bending, as a benchmark for an inhomogeneous deformation, is considered in the second example. The two-dimensional model consists of a bar (height: 40 mm, length: 150 mm) and is bended by a punch with a travel way of 50 mm, see **Figure 5 a**. The maximal Cauchy stress is computed to 474 MPa (v.Mises) when fully loaded and equivalent plastic strains are computed up to maximal 0.48. When the punch is removed, the stresses reduces only to 437 MPa. The remaining stresses are residual stresses, which are generated through the inhomogeneous plastic deformation. In contrast to the previous examples, the plastic incompatibility density arises (during forming) to a maximum of 0.42 in the L^2-norm when

fully loaded. Thus, the plastic incompatibility density indicates the generation of residual stresses even during forming and despite application of external loading, see **Figure 5 b**.

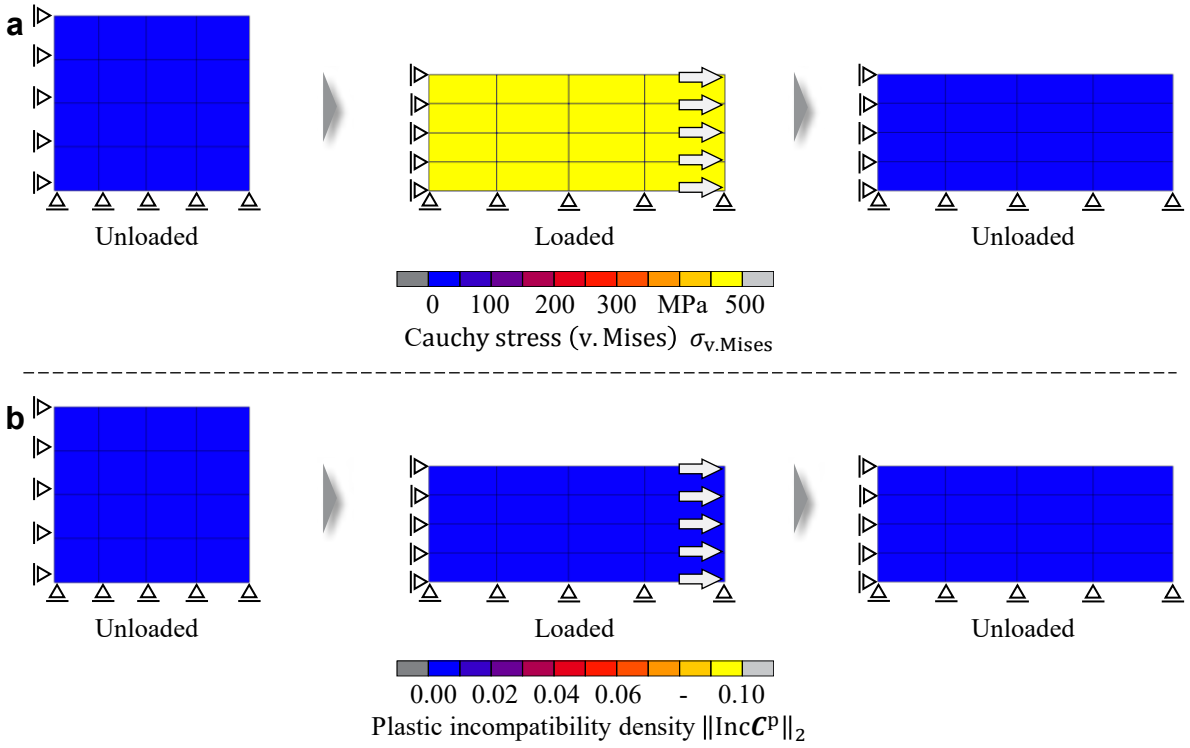


Figure 4: No plastic incompatibility density is computed within a homogeneous deformation

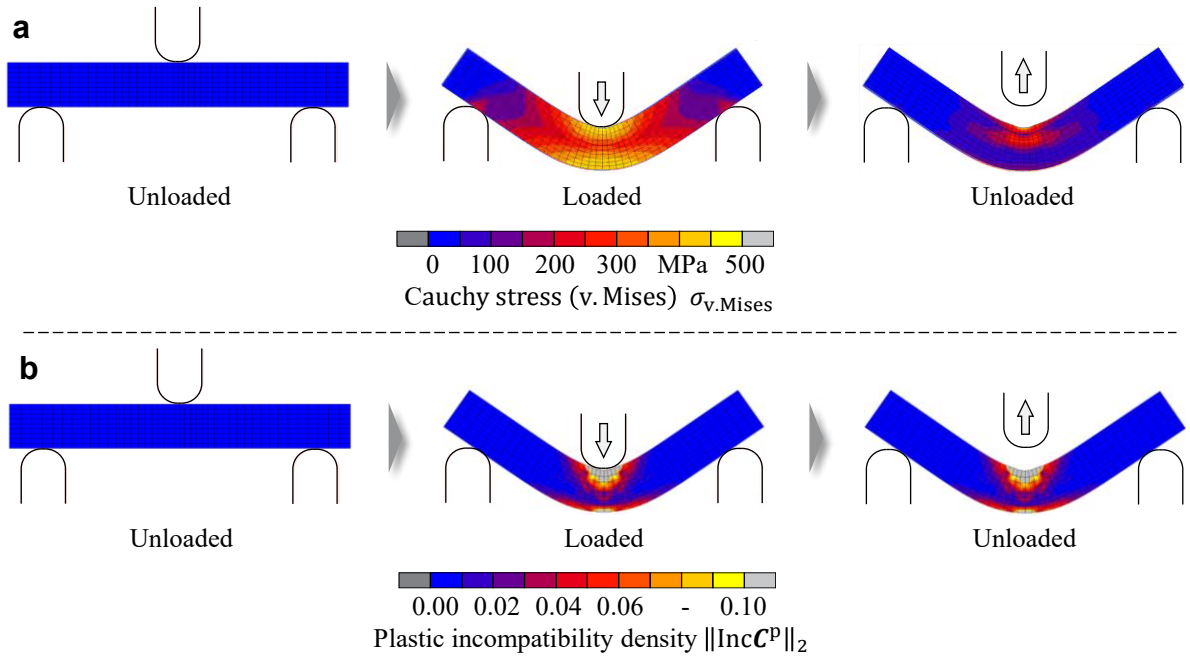


Figure 5: Plastic incompatibility density arise during forming in case of an inhomogeneous deformation

5 CONCLUSION

Residual stresses are of major interest in manufacturing of functional components. However, the generation of residual stresses is not able to be tracked during forming. Typically, purely the remaining stress state after removing all external loads is investigated. However, residual stresses are the result of incompatible plastic strains in case of an inhomogeneous plastic deformation. Further, the plastic dislocation density measures the incompatibility of the plastic intermediate configuration. Thus, the plastic and elastic dislocation and incompatibility densities are exploited to indicate the generation of residual stresses even during the application of external loadings. Theoretical aspects regarding dislocation and incompatibility densities in small and large strain plasticity are reiterated and hints for implementation are provided. Two examples with a homogeneous and an inhomogeneous plastic deformation demonstrated the functionality of the indicators.

ACKNOWLEDGMENT

Our research activities are funded by the *Deutsche Forschungsgemeinschaft* (*DFG*) within the scope of the priority program *SPP2013 - P10* (project number: 374688875).

REFERENCES

[1] Tekkaya, A.E. and Gerhardt, J. *Residual Stresses in Cold-Formed Workpieces*. Annals of the CIRP (1985), **34-1**:225-230.

[2] Kröner, E.: *Allgemeine Kontinuumstheorie der Versetzungen und Eigenspannungen*. Arch. Ration. Mech. Anal., (1959), **4-1**:273-334.

[3] Kröner, E. and Seeger, A. *Nichtlineare Elastizitätstheorie der Versetzungen und Eigenspannungen.* Arch. Rat. Mech. Anal., (1959) **3**:97–119.

[4] Steinmann, P. *Geometrical Foundations of Continuum Mechanics: An Application to First- and Second-Order Elasticity and Elasto-Plasticity*. Berlin: Springer Verlag (2015).

[5] Steinmann, P. *Modellierung und Numerik duktiler kristalliner Werkstoffe*. Forschungs- und Seminarberichte aus dem Bereich der Mechanik der Universität Hannover, Bericht **F97/1**, Habilitationsschrift, (1996).

[6] Lee, E.H. *Elastic-plastic deformations at finite strains*. J. Appl. Mech., (1969) **36**:1-6.

[7] Cermelli, P. and Gurtin, M.E. *Geometrically necessary dislocations in finite plasticity*. J. Mech. Phys. Solids, (2000) **49**:1539-1568.

[8] Simo, J.C. and Hughes, T.J.R. *Computational Inelasticity*. New York: Springer (1998).

[9] Roters, F. and Eisenlohr, P. and Kords, C. and Tjahjanto, D.D. and Diehl, M. and Raabe, D. *DAMASK: Düsseldorf Advanced Material Simulation Kit for studying crystal plasticity using an FE based or a spectral numerical solver*, Procedia IUTAM, (2012) **3**:3-10.

[10] Kaiser, T. and Menzel, A. *An incompatibility tensor-based gradient plasticity formulation - theory and numerics.* Comp. Methods Appl. Mech. Eng., (2019) **345**:671-700.

[11] Zienkiewicz, O.C. and Zhu, J.Z. *The superconvergent patch recovery and a posteriori error estimates. Part 1: the recovery technique*. Int. J. Numer. Methods Eng., (1992) **33**:1331-1364.

[12] Hinton, E. and Campbell, J.S. *Local and global smoothing of discontinuous finite element functions using a least-squares method.* Int. J. Numer. Methods Eng., (1974) **3**:461-480.

XIV International Conference on Computational Plasticity. Fundamentals and Applications
COMPLAS 2019
E. Oñate, D.R.J. Owen, D. Peric , M. Chiumenti, and Eduardo de Souza Neto (Eds)

MACROSCOPIC FE-SIMULATION OF RESIDUAL STRESSES IN THERMO-MECHANICALLY PROCESSED STEELS CONSIDERING PHASE TRANSFORMATION EFFECTS

B.-A. BEHRENS, A. CHUGREEV AND C. KOCK*

Institut für Umformtechnik und Umformmaschinen (IFUM)
Leibniz Universität Hannover (LUH)
An der Universität 2, Garbsen 30823, Germany
*e-mail: kock@ifum.uni-hannover.de, web page: http://www.ifum.uni-hannover.de

Key words: thermo mechanical forming process, finite element analysis, residual stresses, phase transformation effects, transformation induced plasticity, X-ray diffraction.

Abstract. Residual stresses are an important issue as they affect both the manufacturing processes as well as the performance of the final parts. Taking into account the whole process chain of hot forming, the integrated heat treatment provided by a defined temperature profile for cooling of the parts offers a great potential for the targeted adjustment of the desired residual stress state. However, in addition to elastic, plastic and linear thermal strain components, the complex material phenomena arising from phase transformation effects of the polymorphic steels have to be considered in order to predict the residual stresses. These transformation strains account for the plastic deformation at the phase boundary between the emerging and the parent phase. In addition, they are strongly related to the transformation induced plasticity (TRIP) phenomena which depend on the stress state. The aim of this study is the investigation of TRIP effects and their impact on residual stresses regarding the typical hot forming steels 1.7225 (DIN: 42CrMo4) and 1.3505 (DIN: 100Cr6) by means of an experimental-numerical approach. The TRIP behaviour of the materials under consideration is integrated into an FE simulation model in the commercial software Simufact.forming for the purpose of residual stress prediction. The experimental thermo-mechanical investigations are carried out using a quenching and forming dilatometer. These experiments are numerically modelled by means of FEM which allows TRIP coefficients to be determined phase-specifically by numerical identification. For validation of the improved FE-model, an experimental thermo-mechanical reference process is considered, in which cylindrical specimens with an eccentric hole are hot formed and subsequently cooled by different temperature routes. Finally, the numerical model is validated by means of a comparison between residual stress states determined with X-ray diffraction and predicted residual stresses from the simulation.

1 INTRODUCTION

In metal forming, the arising residual stresses influence the material behaviour during and

after manufacturing as well as the performance of the final component [1]. In the past, the focus of forming process design was on minimizing or eliminating residual stresses. However, the residual stress can also serve to improve the properties of the components through targeted use, for example with regard to distortions or wear behaviour [2]. The cost-efficient virtual process design of individual process steps or even an entire process chain is gaining in importance due to economic globalization, continuously rising energy costs and growing competition in the manufacturing industry. Especially in the field of hot forming, process design in trial and error approaches represents a substantial cost and time expenditure [3]. At the same time, hot forming offers great potential for energy-efficient production of components by integrated heat treatment in the cooling phase after forming. The parameters of the forming process in combination with the temperature control over the entire process chain of the hot forming process result in many control parameters influencing the resulting residual stress condition. Nevertheless, the FE simulation-supported design of hot forming processes using polymorphic steels is very challenging. As shown in **FIGURE 1a**, numerous influencing parameters from thermal, metallurgical and mechanical fields exist, which affect each other in complex interactions [4, 5].

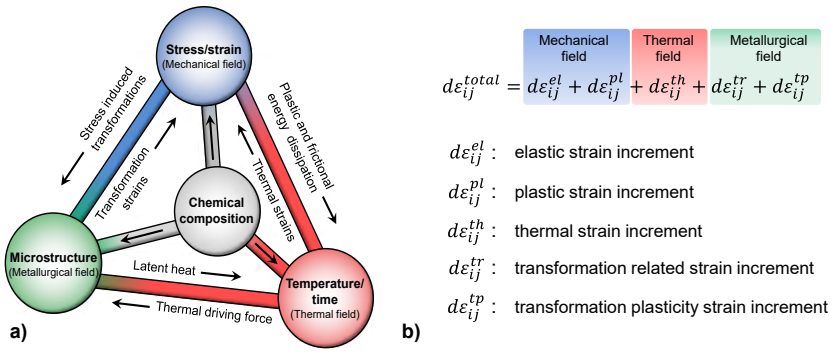


Figure 1: Interrelated thermo-mechanical-metallurgical material phenomena during thermo-mechanical processing of steel [6] (a); basic principles of the additive strain decomposition method (b).

For realistic process simulation, an appropriate mathematical model capable of consistently describing the polymorphic material behaviour is required. For this purpose, fully coupled thermo-mechanical-metallurgical FE-simulations based on the theory of additive strain decomposition method are often used in the literature [7, 8]. The components of such a method are structured in **FIGURE 1b** according to their physical origin. In addition to the elasto-viscoplastic strain increments and the thermal strain increments, transformation related strains occur due to the microstructural phase transformation. The transformation related strains are caused by volume changes due to different lattice constants of the parent and the emerging microstructural phase. In general, the transformation behaviour for calculation of transformation related strains is described by continuous-cooling-transformation (CCT) diagrams and time-temperature-transformation (TTT) diagrams. Thereby, CCT diagrams describe the transformation behaviour of the material during continuous cooling, whereas TTT diagrams represent the transformation behaviour after quenching and subsequent holding at a certain test temperature [9]. For phase transformation simulations TTT diagrams are required according to the mathematical approaches, while CCT diagrams provide a vivid diagram for reading the phase transformations occurring during continuous cooling. At a

given stress state, according to the definition of [10], an additional plastic strain increment in relation to the transformation related strains in the stress free state occurs, which is referred to as transformation plasticity (TRIP). The resulting strain composition acts as driving force for residual stresses and thermal distortions in the final components. The TRIP strains in particular have a special influence on the total strain and thus on the resulting residual stresses, since they are significantly dependent on the prevailing stress state. According to [11], there is a linear relationship between the applied mechanical stress and the TRIP strain. In addition, several authors [12, 13, 14] have shown that, besides the amount, the direction of the stresses also influences the magnitude of the TRIP strain. In the literature for the description of the transformation plasticity strain, a mathematical basic equation is assumed, which generally can be expressed as follows according to [15]:

$$\boldsymbol{d\varepsilon_{ij}^{tp}} = \frac{3}{2}\sum_{n=1}^{m} K_n f_n(\zeta_n) s \tag{1}$$

The total TRIP strain is calculated as the sum of the TRIP strains of the individual phases n, whereby m is the total number of phases involved. The stress deviator is designated by s and the factor K_n is the material and phase specific coefficient of the transformation plasticity. Some authors have already reported values for the coefficient K_n for the martensitic transformation. Hence, for 1.7225 $K = 4.2 \times 10^{-5}$ MPa^{-1} [16] and for 1.5528 $K = 8.68 \times 10^{-5}$ MPa^{-1} for tensile stresses and $K = 9.33 \times 10^{-5}$ MPa^{-1} for compressive stresses [17], respectively, are indicated. The term $f_n(\zeta_n)$ denotes a monotonous function depending on the already transformed volume fraction of the emerging phase ζ_n, whereby the conditions $f_n(\zeta_n = 0) = 0$ (start of transformation) and $f_n(\zeta_n = 1) = 1$ (end of transformation) must be satisfied. An outline of the approaches from the literature of this function is given in [18].

This article presents the design and validation of an FE-simulation model for the numerical investigation of residual stresses in hot forming processes regarding the materials 1.7225 (DIN designation: 42CrMo4 [19]) and 1.3505 (DIN designation: 100Cr6 [20]). In Section 2 particular emphasis is placed on the experimental investigation of phase transformation effects with respect to TRIP strains. A numerical study is used to determine the characteristic TRIP coefficients of the different microstructural phases in Section 3. Finally, a hot forming process is designed in the FE software Simufact.forming and the model is validated by experimental tests in Section 4.

2 MATERIAL CHARACTERISATION

2.1 Thermo-mechanical material data for hot forming simulation applications

As described introductory, extensive material data are required for the fully coupled simulation of a thermo-mechanical forming process. In order to simulate the hot forming step, information on the flow behaviour of the material at corresponding temperatures and strain rates must be available. For this purpose, flow curves of the investigated steels were determined by cylinder compression tests using the servo hydraulic forming simulator Gleeble 3800-GTC. The cylindrical samples had the dimensions Ø10 mm in diameter and

15 mm in height. The tests were performed at the relevant temperatures (900, 1000, 1100 and 1200 °C) with an equivalent plastic strain rate of 1 s^{-1}. In addition, the tests were carried out at a temperature of 1000 °C with the equivalent plastic strain rates of 10 s^{-1} and 50s^{-1}. The determined flow curves are shown in **Figure 2**. For a continuous description of the flow stress k_f, multidimensional functions according to the approach of Hensel and Spittel [21] were calibrated with respect to equivalent plastic strain ε_{eq}, equivalent plastic strain rate $\dot{\varepsilon}_{eq}$ and temperature T. **Equation (2)** shows the formula for calculating the flow stress, with the regression coefficients (A, m_1, m_2, m_3, m_4) listed in **Table 1**.

$$k_f = Ae^{(m_1 T)}\varepsilon_{eq}^{m_2} e^{\frac{m_4}{\varepsilon_{eq}}}\dot{\varepsilon}_{eq}^{m_3} \tag{2}$$

Table 1: Parameters determined for the calculation of the flow stress k_f of the considered steel alloys 1.7225 and 1.3505 according to [19].

Material	A [MPas]	m_1 [°C^{-1}]	m_2 [-]	m_3 [-]	m_4 [-]
1.7225	3805	-0.003458	-0.1083	0.1497	-0.04373
1.3505	2208	-0.003068	-0.179	0.1695	-0.04383

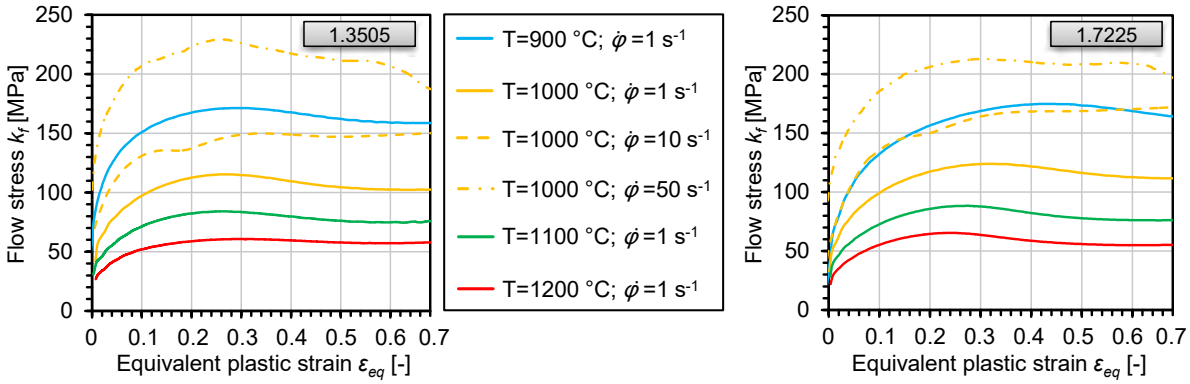


Figure 2: Determined flow curves of the investigated materials 1.7225 (left) and 1.3505 (right) for hot forming applications from the servo hydraulic forming simulator Gleeble 3800-GTC.

For the numerical modelling of the phase transformations during cooling from the forging heat, TTT diagrams of the examined materials were generated using an experimental-numerical approach. In order to visualise the phase transformations that occur during continuous cooling, CCT diagrams of the alloys are shown in **Figure 3**. More detailed information on the experimental-numerical procedure for analysing the phase transformation behaviour of the batches used in this study for the materials 1.7225 and 1.3505 can be found in [22].

Besides hot forming flow curves and TTT diagrams, further phase-specific material data such as specific heat capacity, latent heat or phase specific flow curves are required for thermo-mechanical process simulation. In most cases, it is difficult to generate experimental material data for pure microstructural phases [23]. For this reason, material data has been generated with the thermodynamic simulation software JMatPro [24] as an initial estimation. With help of this software, it is possible to generate mechanical and thermal material data by means of thermodynamic calculation approaches from [25] and [26] based on the chemical composition (see **Table 2**) of the steel alloys. Further details on the material data can be found in [27].

Table 2: Chemical composition of steel alloys 1.7225 and 1.3505 according to international standards [17, 18] used for material data generation with JMatPro.

[wt%]	C	Si	Mn	P	S	Cr	Mo	Fe
1.7225	0.42	0.25	0.75	0.025	0.035	1.10	0.22	balance
1.3505	0.99	0.25	0.35	0.025	0.015	1.475	0.10	balance

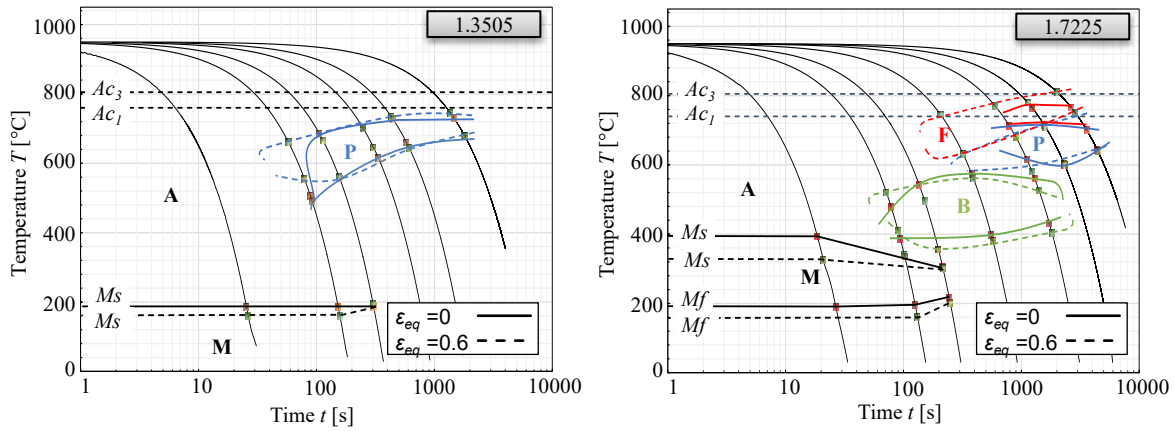


Figure 3: CCT-diagrams for the investigated materials 1.7225 (left) and 1.3505 (right) without and with a previous austenite deformation ε_{eq}.

2.2 Experimental study on the transformation induced plasticity

For the thermo-mechanical physical simulations of the transformation induced plasticity effects, a quenching-deformation dilatometer system DIL 805A/D+T (TA Instruments Inc.) was used. **Figure 4a** shows the principle test setup. A specimen is mounted in two grips, whereby one of them is coupled to a hydraulic system allowing tensile and compressive forces to be applied to the specimen. The specimen can be inductively heated by means of the outer coil. The integrated cooling channels in the inner coil enable the sample to be cooled with the medium helium. The dimensions of the specimens are shown in **Figure 4b**. These specimens were taken from the bulk material by means of electrical discharge machining (EDM). The experimental temperature-force-time profile is illustrated in **Figure 4c** for material 1.7225 as an example. The specimen is heated to 1000 °C with a heating rate of 50 Ks^{-1} and held for a ten minutes soaking time.

Afterwards the specimen is cooled down to room temperature according to the specified cooling rate ϑ. Throughout the test, the temperature is controlled by means of a type k thermocouple welded onto the specimen. Immediately before the start of the phase transformation under investigation, the force F is applied and maintained until the end of the test to gain a constant load L_F. The change in length of the testing area from the specimen is detected via push rods and the total strain ε^{total} is calculated relative to the initial length of 10 mm. The parameters of the experiments performed are listed in **Table 3**. The cooling rates of 30 Ks^{-1} and 1 Ks^{-1} were selected using the CCT diagrams in **Figure 3**. At these conditions, the transformation induced plasticity of the microstructural phases martensite and bainite are investigated for the material 1.7225, and the transformation induced plasticity of the microstructural phases martensite and pearlite for the material 1.3505.

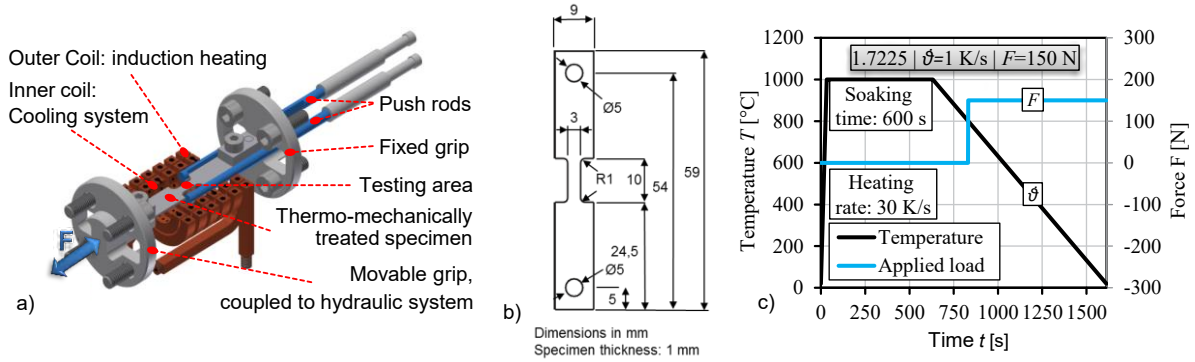


Figure 4: Experimental setup for analyses of TRIP effects in thermo-mechanical processes (a); dimensions of the used specimen (b) and exemplarily temperature as well as force profile of the conducted experiments.

As previous metallographic investigations of the microstructure have shown [27], these are the relevant phases which result from the cooling of the materials after hot forming for model validation in Section 3. Specifically, these microstructural phases will primarily be formed in the materials during the validation tests in Section 4. The temperature at which the load is applied was also selected for each experiment according to the CCT diagrams. The constant load L_F of each experiment was varied in the tension and compression range according to the **Table 3**. The TRIP strain ε^{tp} was calculated as the difference of total strain from the experiment under consideration to the total strain from a reference experiment without load, subtracting the elastic strain component due to the load. The evaluation of the total strain was in each case carried out for the specimen after cooling down to 20°C. The results of the determined TRIP strains can be found in **Table 3**. The experimental length change temperature profiles served as input data for the numerical calibration of the TRIP coefficients in Section 2.3.

Table 3: Parameters and results of the conducted TRIP investigations.

1.7225 (DIN: 42CrMo4)				**1.3505 (DIN: 100Cr6)**			
Cooling rate $\dot{\vartheta}$ [Ks^{-1}]	Onset of load [°C]	Load L_F [MPa]	TRIP strain ε^{tp} [%]	Cooling rate $\dot{\vartheta}$ [Ks^{-1}]	Onset of load [°C]	Load L_F [MPa]	TRIP strain ε^{tp} [%]
		+ 100	+ 0.45			+ 100	+ 0.69
		+ 50	+ 0.24			+ 50	+ 0.32
30	400	0	0	30	200	0	0
		- 50	- 0.19			- 50	- 0.23
		- 100	- 0.38			- 100	- 0.56
		+ 50	+ 0.22			+ 50	- 0.2
1	600	0	0	1	750	0	0
		- 50	- 0.54			- 50	- 0.29
						+ tension	
						- compression	

2.3 Numerical study on the transformation induced plasticity

The experiments for analysis of the TRIP effects were numerically modelled in the simulation software Simufact.forming 15 based on MSC.Marc solver. The material data presented in Section 2.1 were implemented into the simulation model according to [27]. In the heat treatment module of the Simufact.forming software, a one-eighth FE-model of the test area on the used specimen was then created as shown in **Figure 5a**. The boundary conditions of the various tests from **Table 3** were defined on the basis of experimentally measured values for the temperature and load profiles. Since the exact experimental test setup can be reproduced with this FE-model, the length change temperature profiles from experiment and simulation could be compared for each test. The TRIP coefficients K according to **Equation 1** were adjusted iteratively in the simulation model until the calculated curve showed a good agreement with the corresponding experimental curves. **Figure 5b** shows a comparison of the length change versus temperature curves for the material 1.7225 at a cooling rate $\dot{\vartheta} = 30$ Ks^{-1} under different load conditions after adjusting the TRIP coefficient. The numerically identified values of the TRIP coefficients per microstructural phase are listed in **Table 4**. The comparison of the length change temperature profiles from the simulated and experimental TRIP tests shows that the developed material model is able to accurately consider the TRIP effect in thermo-mechanic processes under stress conditions of various directions and amounts. In Section 3, to validate the model for the residual stress calculation a hot forming process with different cooling routes is simulated.

Table 4: Numerically identified phase specific TRIP coefficients.

1.7225 (DIN: 42CrMo4)		1.3505 (DIN: 100Cr6)	
Phase	TRIP coefficient K_n [MPa^{-1}]	Phase	TRIP coefficient K_n [MPa^{-1}]
Martensite	$1.5444*10^{-4}$	Martensite	$6.92011*10^{-5}$
Bainite	$1.009*10^{-4}$	Pearlite	$6.17485*10^{-5}$

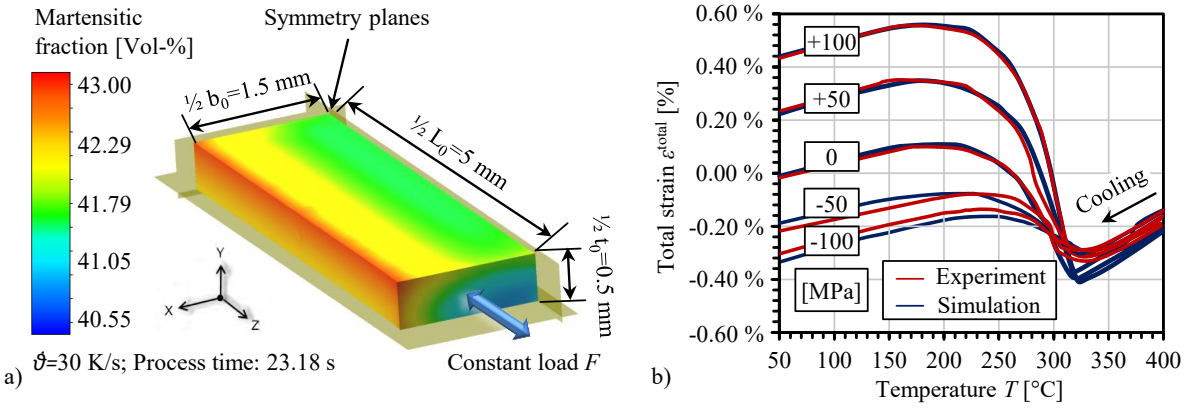


Figure 5: Schematics of the FE-model used for numerical study on the transformation-induced plasticity (a) and comparison of experimental and numerical longitudinal dilatations under different load scenarios (b) for 1.7225.

3 EXPERIMENTAL UPSETTING TESTS AND FE-MODEL VALIDATION

An experimental reference process was realized and subsequently modelled in FE simulations in order to validate the generated material models. Hereby, specimens with eccentric holes as shown in **Figure 6** are heated by an oven to the forming temperature of 1000 °C in a thermobox. After a ten minute holding time, the thermobox with the specimen including the tools is transferred to the servo-hydraulic forming simulator VHS8800 from Instron GmbH. In this way, the specimens can be compressed quasi isothermally to a final height of 28 mm at a punch speed of 200 mms^{-1}. Afterwards the specimens are removed from the thermobox and cooled either in water or in air. Due to the asymmetrical specimen geometry and the different cooling media, various resulting residual stresses on the surfaces of the specimens are aimed at. In order to make a sufficient statistical statement on the residual stresses resulting, the tests for both materials were carried out five times for each cooling medium. Subsequently, the tangential residual stresses σ_t were measured on the surface at the mid-height of the specimen with an X-Ray diffractometer X3000G2 (Stresstech GmbH) according to the corresponding DIN norm [28]. As shown schematically in **Figure 8** illustrating the specimen in sectional view, there is one measuring point on the thick-walled (MP1) side and one measuring point on the thin-walled side (MP2) of the specimen. The surface of the specimen at the locus of the measuring point was electrolytically polished, in order to avoid the influence of scale layers on the measurement. The measuring point was determined by the aperture of a 2 mm collimator. Stress measurements were performed by varying the tilting area with a total of nine tilting positions. Afterwards the measurements were evaluated with the software XTronic (Stresstech GmbH).

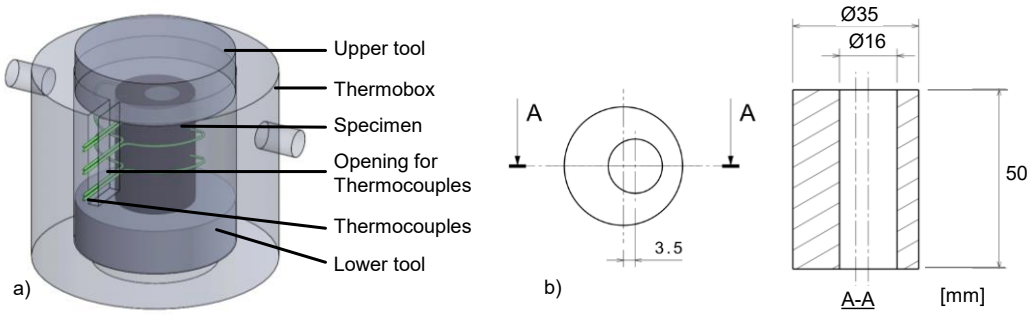


Figure 6: Principal representation of the specimen prepared with thermocouples in the thermobox (a) and shape of the investigated specimen with dimensions in mm (b).

The previously described thermo-mechanical cylinder upsetting tests were numerically modelled with the commercial FE software Simufact.forming 15 based on MSC.Marc solver. When heated to 1000 °C, a homogeneous austenitic structure is formed in the materials, whereby the previously existing residual stresses are almost completely dissolved. From this point on, a new residual stress profile can be generated by the thermo-mechanical forming process. Accordingly, the process simulation is started with a thermally expanded workpiece at 1000 °C with the initial condition of a 100% austenitic microstructure. The FE-model for the simulation of the reference process including the boundary conditions is shown in **Figure 7**. The tools are considered as heat conducting rigid bodies and provided with a mesh of 1 mm element edge length. For the tools of the material 2.4668 (DIN: NiCr19NbMo) constant values of the specific heat capacity $c_p = 435$ J/kgK and heat conductivity $\lambda = 11.4$ $Wm^{-1}K^{-1}$

were taken from the data of the supplier [29]. The workpiece is assigned with an adaptive hexagonal mesh with the minimum element edge length of 0.5 mm, which was determined in a mesh sensitivity analysis. The simulation model consists in total of 56500 hex elements for the tools and 24000 hex elements of the workpiece.

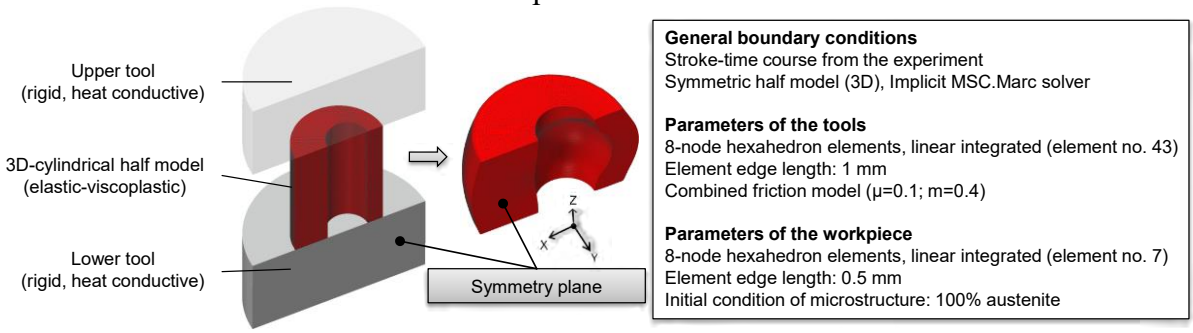


Figure 7: Design of the investigated FE-simulation model and the boundary conditions.

The results of the FE-simulations were compared with the experimentally measured residual stress values. As can be seen in the **Figure 8a** and **b**, the residual stresses due to rapid cooling in water are higher than those after cooling in air. For cooling in water, 1.7225 tangential residual stresses of σ_t=212 MPa at MP1 and σ_t=192 MPa at MP2 were determined. The stresses resulting from the cooling in air are σ_t=27 MPa at MP1 and σ_t=19 MPa at MP2. The residual stresses σ_t=216 MPa for MP1 and σ_t=138 MPa for MP2 during cooling in water were measured on the specimens of the material 1.3505. After cooling in air, compressive residual stresses of σ_t=-83 MPa were measured for MP1 and σ_t=-52 MPa for MP2. At high cooling rates, a diffusion-free transformation of the austenitic into the martensitic phases takes place in the material, which leads to severe stresses in the crystal lattice. During diffusion-controlled phase transformation, which occurs during cooling in air, comparatively lower residual stresses in the range of zero can be observed.

The comparison of the experimentally measured residual stresses and the values obtained from simulations shows that the developed FE-model was suitable for a good prediction accuracy of the residual stresses. In particular, the differences in the amount of residual stresses during cooling in the water between the thick-walled side (MP1) and the thin-walled side (MP2) of the specimen were calculated properly in the simulations. In order to further improve the simulation model, the TRIP coefficients could be identified in additional studies both temperature and load dependent.

With this experimental reference test of hot forming the developed FE simulation model could be validated for different cooling conditions at different measuring points of the specimen with eccentric hole.

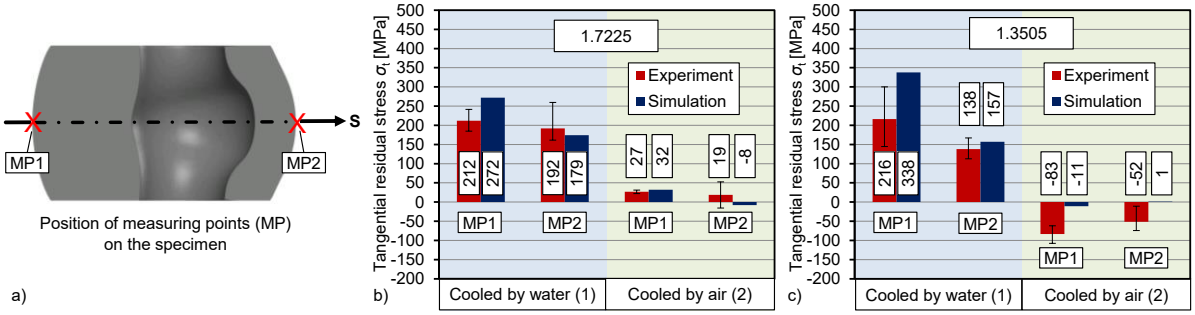


Figure 8: Positions for residual stress evaluation on the principally depicted sectional view of the thermo-mechanically processed specimen (a) as well as results from experiements and simulations for 1.7225 (b) and 1.3505 (c).

4 SUMMARY AND OUTLOOK

In this work material models as well as simulation methods for the calculation of residual stresses in a hot forming process with different cooling routes were developed. In order to characterise the TRIP effect in the considered materials 1.7225 and 1.3505, TRIP coefficients were determined using an experimental-numerical approach and implemented in the FE-model. A simplified hot forming process for the investigation of the residual stress development, using cylindrical specimens with eccentric holes, was experimentally realised and subsequently residual stress measurements on the specimen surfaces were performed using X-ray diffraction. These measurements finally led to validation of the developed FE-models.

In a next step, the influences of the residual stresses of the second and third type from the microscale on the macroscopic residual stresses are to be investigated using multi-scale simulation approaches. In this way, new insights into the effects of the local stress gradients in the component can be gathered and the simulations can then be further improved. Finally, the developed FE-models are to be verified in the context of an industrial forging process.

Acknowledgement

Funded by the Deutsche Forschungsgemeinschaft (DFG, German Research Foundation) - 374871564 (BE 1691/223-1) within the priority program SPP 2013.

REFERENCES

[1] Verlinden B, Driver J, Samajdar J and Doherty RD, 2007. Thermo-mechanical processing of metallic materials, Elsevier Science 11, ISBN: 9780080444970.

[2] Brands, D.; Chugreev, A.; Kock, C.; Niekamp, R.; Scheunemann, L.; Uebing, S.; Behrens, B.-A.; Schröder, J., 2018. On the analysis of microstructural residual stresses in hot bulk forming parts under specific cooling. Proc. Appl. Math. Mech., 18: e201800256.

[3] Behrens, B.-A.; Bouguecha, A.; Vucetic, M.; Chugreev, A., 2016. Advanced Wear Simulation for Bulk Metal Forming Processes, MATEC Web of Conferences, 80, 04003, DOI: http://dx.doi.org/10.1051/matecconf/20168004003.

[4] Behrens, B.-A., Olle, P., 2007. Consideration of phase transformations in numerical simulation of press hardening. Steel Research International, 78 (10-11), 784-790.

[5] Behrens, B.A.; Bouguecha, A.; Bonk, C.; Chugreev, A., 2017. Experimental investigations on the transformation induced plasticity in a high tensile steel under varying thermo-mechanical loading, Computer Methods in Materials Science 17 (1), 36-43.
[6] Behrens, B.-A.; Chugreeva, A.; Chugreev, A., 2018. FE-simulation of hot forging with an integrated heat treatment with the objective of residual stress prediction. AIP Conference Proceedings, 1960 (1), 040003, DOI: https://doi.org/10.1063/1.5034857.
[7] Denis, S.; Gautier, E.; Simon, A.; Beck, G., 1985. Stress-phase-transformation interactions - basic principles, modelling and calculation of internal stresses. Materials Science and Technology, 1, 805–814.
[8] Mitter, W., 1987. Umwandlungsplastizität und ihre Berücksichtigung bei der Berechnung von Eigenspannungen; Vol. 7, Materialkundlich-Technische Reihe, Gebrüder Bornträger Verlag, Berlin.
[9] Behrens, B.-A.; Bach, Fr.-W.; Bouguecha, A.; Nürnberger, F.; Schaper, M.; Yu, Z.; Klassen, A, 2012. Numerical calculation of an integrated heat-treatment process for precision forged parts. Journal of Heat Treatment and Materials, 67 (5), 337-343.
[10] Besserdich, G., 1993. Untersuchungen zur Eigenspannungs- und Verzugsbildung beim Abschrecken von Zylindern aus den Stählen 42CrMo4 und Ck45 unter Berücksichtigung der Umwandlungsplastizität. Dissertation, Universität Karlsruhe.
[11] Gautier, E.; Simon, A.; Beck, G.: Deformation of eutectoid steel during pearlitic transformation under tensile stress. In: Strength of metals and alloys. Proc. 6th Int. Conf., ICSMA 5, 27.-31.8.1979 in Aachen, 2, S. 867-873.
[12] Mahnken, R., Schneidt, A., Antretter, T., 2009. Macro modelling and homogenization for transformation induced plasticity of a low-alloy steel. Int. J. Plast., 25 (2), 183-204.
[13] Lütjens, J., Hunkel, M., 2013. □e in□uence of the transformation plasticity effect on the simulation of partial press-hardening, HTM J. Heat Treatm. Mat., 68 (4), 171-177.
[14] Leblond, J.B., 1989. Mathematical modelling of Transformation Plasticity in Steel II. Coupling with strain hardening phenomena, Int. J. Plast., 5 (6), 573-591.
[15] Böhm M., Wolff M., 2003. Umwandlungsplastizität bei Stählen im Konzept der Thermoelasto-Plastizität. J. Mech. Phys. Solids, 29-48.
[16] Fischer F. D., Sun Q. P., Tanaka K., 1996. Transformation-induced plasticity (TRIP). Appl. Mech. Rev., 49, 317-364.
[17] Turetta A., Ghiotti A., Bruschi S., 2007. Investigation of 22MnB5 mechanical and phase transformation behaviour at high temperature. Proceedings of IDDRG-conference, 147-153.
[18] Behrens, B.-A.; Bouguecha, A.; Bonk, C.; Chugreev, A., 2017. Numerical and experimental investigations of the anisotropic transformation strains during martensitic transformation in a low alloy Cr-Mo steel 42CrMo4. Proc. Eng., 207, 1815–1820.
[19] DIN EN 10083-3 (2007) Steels for quenching and tempering – Part 3: Technical delivery conditions for alloy steels, Beuth-Verlag.
[20] DIN EN ISO 683-17 (2014) Heat-treated steels, alloy steels and free-cutting steels – Part 17: Ball and roller bearing steels, Beuth-Verlag.
[21] Hensel A.; Spittel T, 1978. Kraft- und Arbeitsbedarf bildsamer Formgebungsverfahren; Deutscher Verlag für 542 Grundstoffindustrie.
[22] Behrens B.A.; Chugreev A.; Kock, C., 2018. Experimental-numerical approach to efficient TTT-generation for simulation of phase transformations in thermomechanical

forming processes. IOP Conference Series, Materials Science and Engineering, 461, 012040.

[23] Acht C., Dalgic M., Frerichs F., Hunkel H., Irretier A., Lübben T., Surm H., 2008. Ermittlung der Materialdaten zur Simulation des Durchhärtens von Komponenten aus 100Cr6. Journal of Heat Treatment and Materials, 63, 234–244.

[24] JMatPro. Practical software for materials properties, https://www.sentesoftware.co.uk/jmatpro, 2018.

[25] Saunders N., Guo U.K.Z., Li X., Miodownik A.P., Schillé J.P, 2003. Using JMatPro to Model Materials Properties and Behavior. JOM, 55, 60–65.

[26] Guo Z., Saunders N., Schillé J.P., Miodownik A.P, 2009. Material properties for process simulation. Materials Science and Engineering: A 1-2, 7–13.

[27] Behrens B.-A., Schröder J., Brands D., Scheunemann L., Niekamp R., Chugreev A., Sarhil M., Uebing S., Kock C, 2019. Experimental and numerical investigations on the development of residual stresses in thermo-mechanically processed Cr-alloyed steel 1.3505. Metals, 9(4), 480, DOI: https://doi.org/10.3390/met9040480

[28] DIN EN 15305:2009-1, Non-destructive testing - Test method for residual stress analysis by X-ray diffraction, Beuth Verlag, 2008

[29] Special Metals Co.. New Hartford, New York, USA, http://www.specialmetals.com/assets/smc/540 documents/pcc-8064-sm-alloy-handbook-v04.pdf, 2018.

XV International Conference on Computational Plasticity. Fundamentals and Applications
COMPLAS 2019
E. Oñate, D.R.J. Owen, D. Peric, M. Chiumenti & Eduardo de Souza Neto (Eds)

NUMERICAL THERMO-ELASTO-PLASTIC ANALYSIS OF RESIDUAL STRESSES ON DIFFERENT SCALES DURING COOLING OF HOT FORMING PARTS

S. UEBING, L. SCHEUNEMANN, D. BRANDS AND J. SCHRÖDER

Institute of Mechanics, Departement of Civil Engineering
University Duisburg-Essen, Campus Essen
45141 Essen, Germany
e-mail: sonja.uebing@uni-due.de, web page: http://www.uni-due.de/mechanika

Key words: Residual stresses, Multiscale simulation, FE^2-method, Multi-Phase-Field method, Austenite-to-martensite transformation

Abstract. In current research, more and more attention is paid to the understanding of residual stress states as well as the application of targeted residual stresses to extend e.g. life time or stiffness of a part. In course of that, the numerical simulation and analysis of the forming process of components, which goes along with the evolution of residual stresses, play an important role. In this contribution, we focus on the residual stresses arising from the austenite-to-martensite transformation at microscopic and mesoscopic level of a Cr-alloyed steel. A combination of a Multi-Phase-Field model and a two-scale Finite Element simulation is utilized for numerical analysis. A first microscopic simulation considers the lattice change, such that the results can be homogenized and applied on the mesoscale. Based on this result, a polycrystal consisting of a certain number of austenitic grains is built and the phase transformation from austenite to martensite is described with respect to the mesoscale. Afterwards, in a two-scale Finite Element simulation the plastic effects are considered and resulting residual stress states are computed.

1 INTRODUCTION

In the works of [1], [2] and [3], the benefits from hot forming processes in course of generating targeted residual stress states have been established in research. Subsequent heat treatment leads to predefined properties of the component, see [4]. In contrast, specific cooling starting from the forging heat offers the opportunity to adjust material parameters, such as the deformation state, the temperature profile or cooling media, cf. [5]. During such or similar forming processes, residual stresses occur in the material. The classification of residual stresses in three different types relies on [6]. There, the characterization follows the scale under observation. Thus, residual stresses of first type correspond to the complete component and are referred to as macroscopic. Residual stresses of second and third type are in equilibrium concerning the microstructure of the

component, i.e. stresses of second type distinguish between the mean stress of a grain and stresses of first type. Sstresses of third type show location-dependent deviations of the stresses within the grain and the sum of first and second type. Hence, residual stresses of second and third type can be called microscopic.

In the last decades, residual stresses in a component, which result from the forming process, were often minimized or even canceled out to avoid undesired influence on the final properties regarding, for example, lifetime. But in current research, desired effects of residual stress states are targeted, such as enhanced fatigue life, see [7]. Since it is possible to influence the behavior of components decisively, for example with regard to distortion or wear behavior, the overall aim of the paper is to analyze the development of microscopic residual stresses during cooling of hot formed parts.

On that, the computational approach proposed in [8] is followed, where the combination of a Multi-Phase-Field (MPF) model and a two-scale Finite Element (FE) simulation is used. The MPF model enables the numerical computation of different physical phenomena during phase transformations, in general. The theory was introduced by [9], [10] and [11], among others. An advantage of such MPF models in contrast to dual phase-field models is to describe martensitic transformation or grain growth. Furthermore, it is possible to consider an arbitrary number of phases, which differ from each other by e. g. lattice orientation or material properties. It is possible to calculate elastic stresses as well as thermodynamic quantities in terms of phase transformations. Thus, following [12] and [13], the austenite-to-martensite (A-M) phase transformation, which occurs during rapid cooling, can be investigated. Further approaches and application of MPF models can be found in [14], [15] and [16], which analyze elastic modelling of crack growth, while plastic effects are included in [17] and [18] and a viscoplastic material is used in [19]. Additionally, elastic and plastic models for the A-M phase transformation in connection to crack growth have been formulated in [20] and [21].

Afterwards, the two-scale FE simulation is utilized to consider effects of elastic and plastic strains, see e.g. [22] or [23]. Such multiscale approaches provide the opportunity to describe the macroscopic behavior of materials depending on properties of mesoscale or microscale. Thus, thermal anisotropy or microstructural heterogeneity can be expressed. For example, in [24] an approach to consider microstructural graded properties due to A-M transformation in a two-scale simulation has been proposed.

Within the scope of this publication, the model for the computation of mesoscopic residual stresses presented in [8] is used. Therefore, section 2 describes the macroscopic experimental setup and additional simulations, which provides necessary data for the investigation on lower scales. In section 3, a combination of a MPF and a FE simulation is utilized to describe the A-M phase transformation due to cooling and to calculate related residual stresses. Afterwards, section 4 concludes the paper and gives an outlook.

2 MACROSCOPIC EXPERIMENTS AND SIMULATIONS

The numerical analysis of the evolving residual stresses on minor scales depends on macroscopic data which is obtained during the work on the project “Experimental and numerical modeling and analysis of microstructural residual stresses in hot bulk forming

parts under specific cooling" as part of the DFG priority program SPP 2013. This section introduces briefly the experimental set up as well as related macroscopic simulations. For further details, the interested reader is referred to [8].

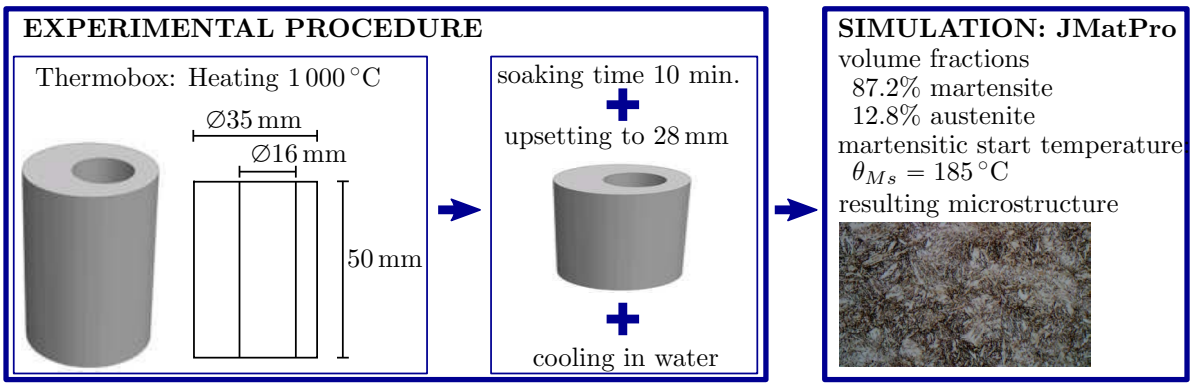


Figure 1: Experimental procedure of upsetting test for a cylindrical specimen and the related macroscopic Finite Element simulation with JMatPro.

The considered specimen, shown in figure 1, is a cylinder made of steel alloy 1.3505 (DIN 100Cr6). Its inital height is 50 mm and the outer diameter equals 35 mm. A hole with a diameter of 16 mm and an eccentricity of 3.5 mm are chosen according to [25], since thereby inhomogeneous residual stress states can be expected. Firstly, the cylinder is heated up to 1 000 °C in a thermobox, such that a stress free austenitic state is formed. After a suitable soaking time of ten minutes, the specimen is upset to a height of 28 mm, still exhibited to the high temperature, before it is rapidly cooled in water. Thus, a diffusionless phase transformation occurs, which results in a martensitic, body-centered tetragonal lattice structure.

In addition to the experiments, the thermodynamic simulation software JMatPro [26] provides further material data based on the chemical composition of the steel alloy 1.3505, given in table 1. Following [27] and [28], mechanical and thermal data such as Poisson's ratio or Young's modulus are computed depending on the temperature. Moreover, the martensitic start temperature is determined at 185 °C. The volume fractions after phase transformation and the needle-like microstructure are determined as approximately 87.2% martensite and 12.8% retained austenite.

Table 1: Chemical composition of the steel alloy 1.3505 for material data generation using JMatPro.

Chemical composition [wt%]	**C**	**Si**	**Mn**	**P**	**S**	**Cr**	**Mo**	**Fe**
1.3505 (DIN 100Cr6) [29]	0.99	0.25	0.35	0.025	0.015	1.475	0.1	balance

3 NUMERICAL ANALYSIS OF MESOSCOPIC RESIDUAL STRESSES DUE TO PHASE TRANSFORMATION ON THE MICROSCALE

Based on data obtained from the experimental and numerical investigations regarding the macroscale presented in section 2, the numerical model originally proposed in [8] is summarized. For details and further illustrations of the workflow, it is referred to the mentioned reference. It accounts for the austenite-to-martensite (A-M) phase transformation during rapid cooling in water and investigates the resulting residual stress distribution on a mesoscopic level, see section 3.4. Therefore, Multi-Phase-Field (MPF) simulations in combination with Finite Element (FE) simulation are utilized and applied to the investigated material 1.3505 (DIN 100Cr6).

3.1 Multi-Phase-Field theory

The Multi-Phase-Field (MPF) model, which is used to describe the austenite-to-martensite (A-M) phase transformation during rapid cooling, was introduced by [9], [10] and [11], among others. An open source implementation is available, see [30]. A general free energy description is utilized that distinguishes between different physical phenomena. In a domain Ω, the free energy density F can be divided into the interfacial energy density f^{intf}, the chemical energy density f^{chem} and the elastic energy density f^{elast}, thus

$$\begin{aligned} F &= \int_\Omega f^{\text{intf}} + f^{\text{chem}} + f^{\text{elast}} \,\mathrm{d}\Omega\,, \\ f^{\text{intf}} &= \sum_{\alpha,\beta=1,\dots,N,\alpha\neq\beta} \frac{4\sigma_{\alpha\beta}}{\eta_{\alpha\beta}} \left[-\frac{\eta_{\alpha\beta}^2}{\pi^2} \nabla\phi_\alpha \cdot \nabla\phi_\beta + \phi_\alpha\phi_\beta \right] , \\ f^{\text{chem}} &= \sum_{\alpha=1,\dots,N} h(\phi_\alpha) f_\alpha(c_\alpha^i) + \tilde{\mu}^i (c^i - \sum_{\alpha=1,\dots,N} \phi_\alpha c_\alpha^i)\,, \\ f^{\text{elast}} &= \frac{1}{2} \Big[\sum_{\alpha=1,\dots,N} h(\phi_\alpha) (\boldsymbol{\varepsilon}_\alpha - \boldsymbol{\varepsilon}_\alpha^* - c_\alpha^i \boldsymbol{\varepsilon}_\alpha^i) : \mathbb{C}_\alpha : (\boldsymbol{\varepsilon}_\alpha - \boldsymbol{\varepsilon}_\alpha^* - c_\alpha^j \boldsymbol{\varepsilon}_\alpha^j) \Big] . \end{aligned} \tag{1}$$

The phase-field parameter for an individual phase α is labeled as ϕ_α. The diffusion equation

$$\dot{\phi}_\alpha = \sum_{\beta=1,\dots,N} \frac{\pi^2 \mu_{\alpha\beta}}{8\eta N} \Big(\frac{\partial F}{\partial \phi_\beta} - \frac{\partial F}{\partial \phi_\alpha} \Big) \tag{2}$$

controls its evolution. Additional physical quantites occurring in the stated formula are listed in table 2.

3.2 Homogenization of eigenstrains in one martenstitic grain

Rapid cooling from forging heat triggers the formation of martensite when reaching the martensitic start temperature. Each grain changes separately due to orientation and evolving martensite variant, i.e. it is necessary to take different martensitic variants into account, see [31]. Moreover, the different lattice types for austenite and martensite have to be embedded. Austenite consists of face-centered cubic unit cells, but diffusionless phase

Table 2: Quantities governing the MPF model in equations (1) and (2).

i, j	components
α, β	identifier of phase-fields
N	total number of phase-fields
$\sigma_{\alpha\beta}$	energy of the interface between phase-fields α and β
$\eta_{\alpha\beta}$	interface width between phase-fields α and β
$f_\alpha(c_\alpha^i)$	chemical potential for phase-field α
c_α^i	concentration of component i in phase-field α
$\tilde{\mu}^i$	generalized chemical potential or diffusion potential as Lagrange multiplier for satisfying the balance of mass for each component ($c^i = \sum_{\alpha=1,\dots,N} \phi_\alpha c_\alpha^i$)
$\boldsymbol{\varepsilon}_\alpha$	total strain of phase-field α
$\boldsymbol{\varepsilon}_\alpha^*$	eigenstrain of phase-field α
$\boldsymbol{\varepsilon}_\alpha^i$	strain of component i in phase-field α
$\mathbb{C}_\alpha$	elasticity tensor of phase-field α
$h(\phi_\alpha)$	polynomial function fulfilling $h(1) = 1$ and $h(0) = 0$ with $h(\phi_\alpha) = \phi_\alpha$
$\mu_{\alpha\beta}$	effective interfacial mobility between phase-fields α and β

transformations result in martensite with body-centered tetragonal lattice structure. Such shifting can be expressed by the socalled Bain-groups, which enable to describe in total all 24 variants of martensite forming from austenite. It is to be noticed that up to now shearing and rotation are neglected, such that only three variants are included in this model, see figure 2a.

In a first step, this microscopic transformation in one grain is analyzed. Therefore, a MPF simulation with following initial configuration is done. A cube made from austenite with three martensitic nulcei is taken into account. Each nucleus represents one of the three considered variants, I, II or III. Transversally isotropic eigenstrain tensors representing the volume change during transformation are applied according to the variant number, which are given by

$$\begin{aligned} \operatorname{diag} \boldsymbol{\varepsilon}_{\mathrm{I}}^* &= [-0.2 \quad 0.12 \quad 0.12]\,, \\ \operatorname{diag} \boldsymbol{\varepsilon}_{\mathrm{II}}^* &= [\ 0.12 \quad -0.2 \quad 0.12]\,, \\ \operatorname{diag} \boldsymbol{\varepsilon}_{\mathrm{III}}^* &= [\ 0.12 \quad 0.12 \quad -0.2]\,. \end{aligned} \tag{3}$$

Due to high temperatures, it is possible to consider the occurring transformation in the framework of small strains. The simulation follows the principle of minimizing the total energy in the system and results in a microscopic laminate consisting of two of the three variants, shown in figure 2b. To obtain information regarding the mesoscale and, in particular, the mechanical energy and mechanical driving force, a partial-rank one homogenization scheme is applied. It is described in [32], [33] and [34] and successfully applied to OpenPhase in [35]. Thus, the static equilibrium as well as strain compatibility condition at the interfaces are ensured. With that, the effective (homogenized) eigenstrain tensor can be calculated by application of a volume averaging scheme

$$\begin{aligned} \operatorname{diag} \overline{\boldsymbol{\varepsilon}}^*_{\mathrm{II,III}} &= [\ 0.12 \quad -0.04 \quad -0.04]\,, \\ \operatorname{diag} \overline{\boldsymbol{\varepsilon}}^*_{\mathrm{I,III}} &= [-0.04 \quad 0.12 \quad -0.04]\,, \\ \operatorname{diag} \overline{\boldsymbol{\varepsilon}}^*_{\mathrm{I,II}} &= [-0.04 \quad -0.04 \quad 0.12]\,. \end{aligned} \tag{4}$$

It is assumed that the volume fraction of each variant in the laminate equals 50%. Now, these tensors can be utilized for mesoscopic calculation, representing microscopic effects such as the internal laminate structure of martensitic grains.

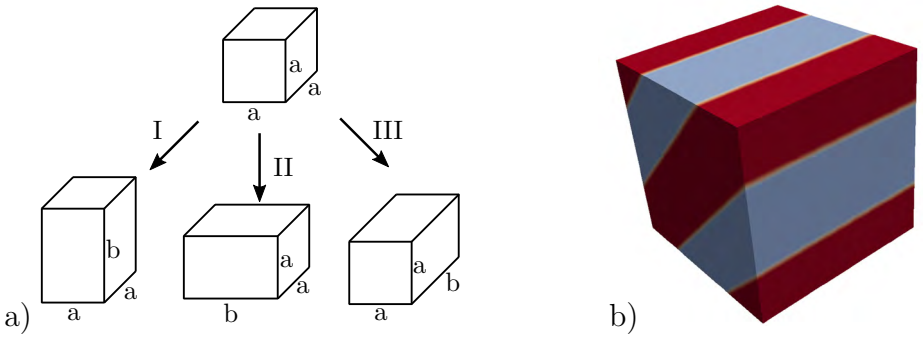


Figure 2: a) Three considered martensitic variants, cf. [31], with a_0 as edge length of an austenitic unit cell and a, b as edge length of a tetragonally transformed martensitic unit cell and b) laminate consisting of two variants of martensite, namely I+II or II+III or I+III.

3.3 Austenite-to-martensite phase transformation

The mesoscopic structure of steels such as 1.3505 (DIN 100Cr6) can be represented by a polycrystal, which can be obtained from a MPF model. Thus, a matrix with 24 arbitrarily placed nuclei is considered in a cube of edge length 121 grid points. Those nuclei differ by the orientations of their crystallographic lattice, which have been defined with help of a geodesic dome leading to overall isotropic orientation of the polycrystal. Applying a MPF simulation controlled by normal grain growth to the initial set up, which is stopped when the matrix has vanished completely, leads to an austenitic polycrystal of 24 grains, see figure 3a. Afterwards, this polycrystal is exposed to a linear mapping, which reduces the height to 50% of its initial value and thus describes the experimental upsetting, see section 2. Fulfilling volume preservation, the new grid has $171 \times 171 \times 61$ grid points, illustrated in figure 3b.

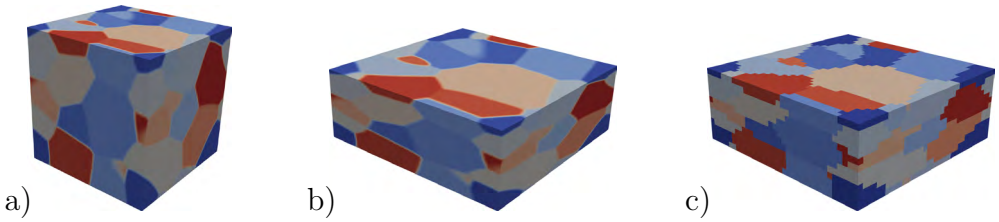


Figure 3: Polycrystal a) before and b) after deformation and c) after coarsening.

In a next step, the phase transformation itself has to be depicted. The volume fractions of austenite and martensite after transformation are considered as a result of the macroscopic experiments and simulations, cf. section 2. From initially 100% austenite, approximately 12.8% remain as retained austenite, while the other 87.2% of the volume undergo phase transformation to martensite. Analyzing the volume fractions of all 24 grains in comparison with the total volume, four grains are taken into account as a good fit to represent the retained austenite, since their combined volume equals exactly 12.8%. They are not taken into account for the transformation scheme, while the other 20 grains are considered to undergo transformation to martensite. At first, one of the effective eigenstrain tensors $\bar{\boldsymbol{\varepsilon}}_i^*$, cf. equation (4), is assigned arbitrarily to each considered grain. The set of all eigenstrain states for the 20 grains is given by

$$\boldsymbol{V} \;=\; \{\bar{\boldsymbol{\varepsilon}}_1^*, ..., \bar{\boldsymbol{\varepsilon}}_{20}^*\} \quad \text{for} \quad \bar{\boldsymbol{\varepsilon}}_i^* \in \{\overline{\boldsymbol{\varepsilon}}_{\mathrm{II,III}}^*\,, \overline{\boldsymbol{\varepsilon}}_{\mathrm{I,III}}^*\,, \overline{\boldsymbol{\varepsilon}}_{\mathrm{I,II}}^*\}\,. \tag{5}$$

Then, an iterative optimization procedure is applied grain by grain following the principle of minimizing the elastic energy f^{elast} in the system, which has been introduced in [8] as

$$\tilde{\boldsymbol{V}} \;=\; \arg\Big[\min_{\boldsymbol{V}}[f^{\mathrm{elast}}(\boldsymbol{V})]\Big]\,, \tag{6}$$

with $\tilde{\boldsymbol{V}}$ as optimized set of eigenstrain states leading to the minimized elastic energy. In relation to $\tilde{\boldsymbol{V}}$, a mesoscopic strain distribution $\boldsymbol{\varepsilon}^{\mathrm{MPF}}(\boldsymbol{x})$ is obtained, which stands for strains occurring in the A-M phase transformation in a polycrystal.

3.4 Residual stress calculation

All MPF models used here only consider elastic strains, such that the utilization of an elasto-plastic FE simulation is inevitable. The mechanical behavior is defined by an elasto-plastic material law with a von Mises yield criterion with exponential hardening, cf. [36]. In table 3 the used material parameters are given for austenite and martensite at the predefined martensitic start temperature of 185° C.

Table 3: Material parameters for austenite (A) and martensite (M) at temperature 185 °C: Youngs's modulus E in MPa and Poisson's ratio ν, initial yield strength y_0 in MPa, limiting yield strength y_∞ in MPa, parameter for exponential hardening δ, linear hardening parameter h in MPa.

	E in MPa	ν	y_0 in MPa	y_∞ in MPa	δ	h in MPa
A	186,610.988	0.301141	333.766	713.135	35	520
M	200,372.074	0.295635	2 609.125	3 057.886	20	500

Equation (7) describes how the mesoscopic strain distribution $\boldsymbol{\varepsilon}^{\mathrm{MPF}}(\boldsymbol{x})$ resulting from the optimal set of eigenstrain states $\tilde{\boldsymbol{V}}$, representing the strains resulting from the A-M phase transformation, is applied as driving force on finite element level. The strain state is incrementally assigned to the total strain field over a pseudo-time t, in which t^n and t^{n+1} stand for the last and actual time step, respectively,

$$\boldsymbol{\varepsilon}(\boldsymbol{u}, \boldsymbol{x}, t^{n+1}) \Leftarrow \boldsymbol{\varepsilon}(\boldsymbol{u}, \boldsymbol{x}, t^{n}) - \boldsymbol{\varepsilon}^{\mathrm{MPF}}(\boldsymbol{x}, t^{n+1})\,. \tag{7}$$

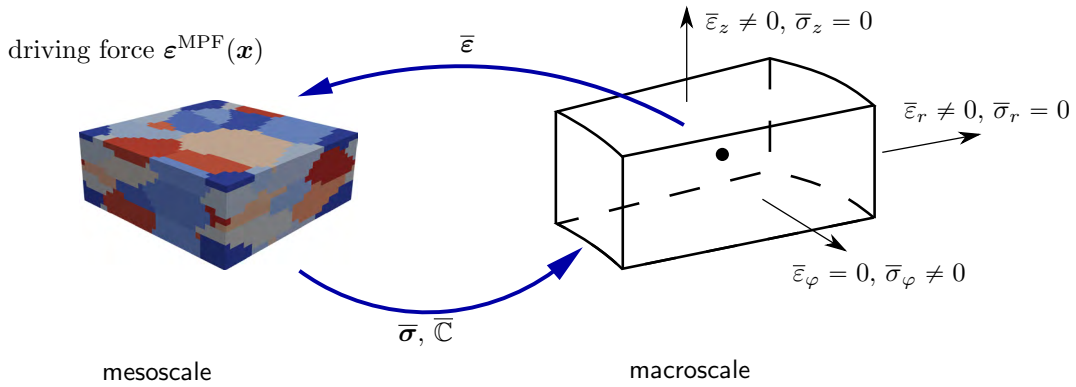


Figure 4: Two-scale boundary value problem for the incorporation of the strains $\boldsymbol{\varepsilon}^{\mathrm{MPF}}(\boldsymbol{x})$ in the FE-model. Macroscopic quantities are denoted by an overline.

For the incorporation of $\boldsymbol{\varepsilon}^{\mathrm{MPF}}(\boldsymbol{x})$ and the phase-field parameter ϕ, a one to one mapping of the grid points from OpenPhase to hexahedral finite elements is chosen. This voxel-like representation accounts for an element wise constant strain distribution. Furthermore, to obtain a better numerical performance, the MPF grid is coarsened by a factor of 5 to $35 \times 35 \times 13$ elements, cf. figure 3c. This discretization of the granular structure is utilized for a two-scale FE calculation, following e.g. [22] or [23]. On the macroscale, a section of the cylindrical specimen with the enforced boundary conditions is considered, see figure 4. There, r, φ and z indicate the radial direction, the tangential direction and the height, respectively. For the lower scale, i.e. mesoscale, the polycrystal with the mesoscopic strain distribution from the MPF simulation as driving force is used. This boundary value problem is solved at each macroscopic intergration point under application of periodic boundary conditions.

Figure 5a-c displays the radial and tangential stresses on the mesoscale as well as the mesoscopic axial stresses with respect to the height. During the simulation, no outer forces have been applied. Hence, these stress distribution can be interpreted as residual stresses instead of mechanically induced stress. The tangential stresses σ_φ are most relevant when investigating the durability or strength of a component, since those are the only stresses not enforced to be zero on average. Furthermore, it should be noticed that the other stress components, namely σ_r and σ_z, level out over the complete domain, since it holds $\bar{\sigma}_r = -0.424\,10^{-12} \approx 0$ and $\bar{\sigma}_z = -0.161\,10^{-11} \approx 0$. Additionally, the equivalent plastic strains, the von Mises stress and the phase distribution after transformation are shown in figure 5d-f. The retained austenite is presented as red islands in a martensitic matrix.

4 CONCLUSIONS

In this work, a model for the analysis of residual stresses on the mesoscale due to austenite-to-martensite phase transformation was introduced. Based on experiments and macroscopic Finite-Element (FE) simulations as well as predefined material data, a mesoscopic model was built. Elastic Multi-Phase-Field (MPF) models in combination with two-scale elasto-plastic FE simulation have been utilized. Based on mesoscopic stresses

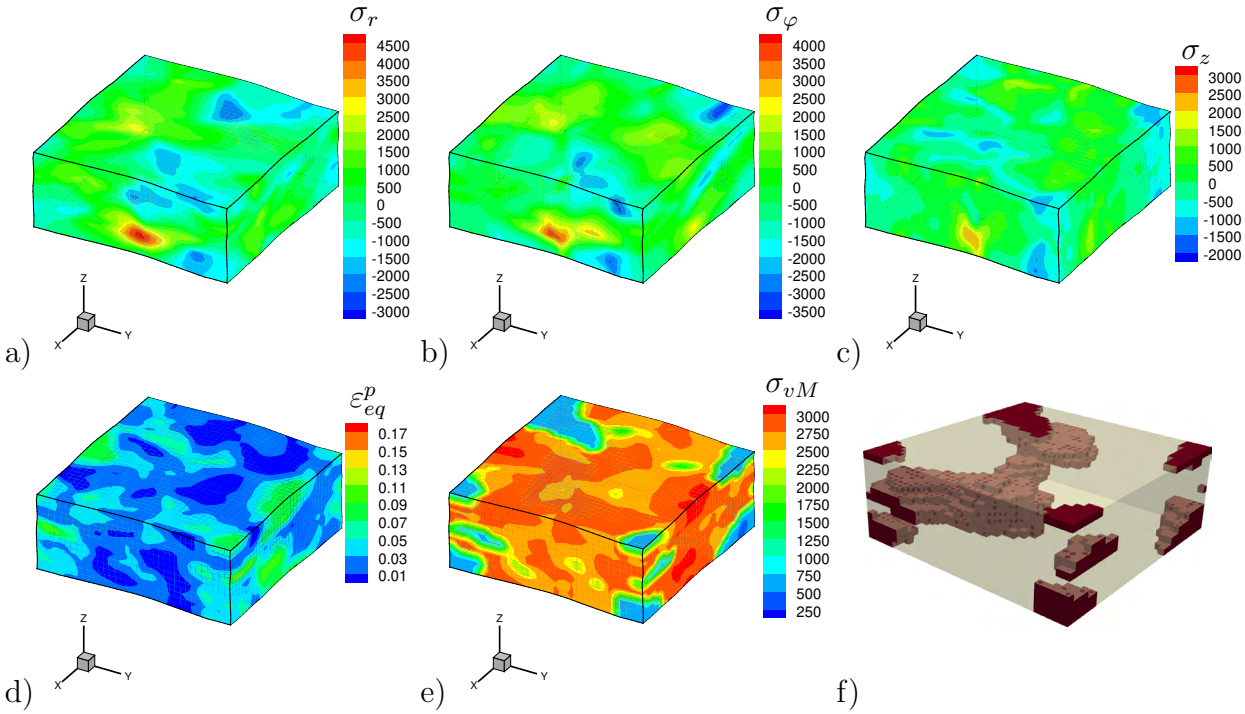


Figure 5: a) Radial stresses σ_r in MPa, b) tangential stresses σ_φ in MPa, c) axial stresses σ_z in MPa, d) equivalent plastic strains and e) von Mises stress in MPa. e) Phase distribution after transformation: red for austenite and yellow for martensite.

due to the austenite-to-martensite phase transformation on the microscale, the development of mesoscopic residual stresses due to phase transformation has been described.

In future steps, the MPF model for the laminates of one martenstitic grain should be revised to be more realistic. Moreover, the relaxation of the elastic energy to find a suitable eigenstrain distribution should be executed in a semi automated manner and the residual stress calculation with finite elements should involve the complete thermo-elasto-plastic cooling process. By validation of the results based on the interactions of the thermo-mechanical investigations on all scales, an improvement of the residual stress calculation and a prediction of targeted residual stress states should be enabled.

Acknowledgment: Funded by the Deutsche Forschungsgemeinschaft (DFG, German Research Foundation) - 374871564 (BE 1691/223-1, BR 5278/3-1, SCHR 570/33-1) within the priority program SPP 2013. The authors thank Prof. Dr.-Ing. Bernd-Arno Behrens, Dipl.-Ing. Alexander Chugreev and Christoph Kock from IFUM (Institute of Forming Technology and Machines) at the Leibniz Universität Hannover as well as their colleagues Dr.-Ing. Rainer Niekamp and Mohammad Sarhil from Universität Duisburg-Essen for the inspiring collaboration. Furthermore, the authors thank Prof. Dr. Ingo Steinbach and Dr. Oleg Shchyglo from ICAMS (Interdisciplinary Center for Advanced Materials Simulation) at the Ruhr-Universität Bochum for their scientific support.

REFERENCES

[1] A.E. Tekkaya, J. Gerhardt, and M. Burgdorf. Residual Stresses in Cold-Formed Workpieces. *Manufacturing Technology*, 34:225–230, 1985.

[2] M.P. Mungi, S.D. Rasane, and P.M. Dixit. Residual stresses in cold axisymmetric forging. *Journal of Materials Processing Technology*, 142(1):256–266, 2003.

[3] D. von Mirbach. Hole-drolling method for residual stress measurement - consideration of elastic-plastic material properties. *Material Science Forum*, 768-769:174–181, 2014.

[4] W. Seidel. *Werkstofftechnik - Werkstoffe, Eigenspannungen, Prüfung, Anwendungen*. Hanser Verlag, 7 edition, 2007.

[5] B.-A. Behrens and J. Schrödter. Numerical Simulation of Phase Transformation during the Hot Stamping Process. In *Thermal Process Modeling: Proceedings from the 5th International Conference on Thermal Process Modeling and Computer Simulation*, pages 179–190, 2014.

[6] E. Macherauch, H. Wohlfahrt, and U. Wolfstied. *Härterei-Technische Mittelungen - Zeitschrift für Werkstoffe, Wärmebehandlung, Fertigung*, 28(3):201–211, 1973.

[7] M.A.S. Torres and H.J.C. Voorwald. An evaluation of shot peening, residual stress and stress relaxation on the fatigue life of ASIS 4340 steel. *International Journal of Fatigue*, 24:877–886, 2002.

[8] B.-A. Behrens, J. Schröder, D. Brands, L. Scheunemann, R. Niekamp, M. Sarhil, S. Uebing, and C. Kock. Experimental and Numerical Investigations of the Development of Residual Stresses in Thermo-Mechanically Processed Cr-Alloyed Steel 1.3505. *Metals*, 9(4):480 (28 pages), 2019.

[9] I. Steinbach, F. Pezzolla, B. Nestler, M. Seeßelberg, R. Prieler, G.J. Schmitz, and J.L.L. Rezende. A phase field concept for multiphase systems. *Physica D: Nonlinear Phenomena*, 94(3):135–147, 1996.

[10] J. Tiaden, B. Nestler, H.J. Diepers, and I. Steinbach. The multiphase-field model with an integrated concept for modelling solute diffusion. *Physica D: Nonlinear Phenomena*, 115(1):73–86, 1998.

[11] I. Steinbach and F. Pezzolla. A generalized field method for multiphase transformations using interface fields. *Physica D: Nonlinear Phenomena*, 134(4):385–393, 1999.

[12] I. Steinbach and M. Apel. Multi phase field model for solid state transformation with elastic strain. *Physica D*, 217:153–160, 2006.

[13] I. Steinbach. Phase-field models in materials science. *Modelling and Simulation in Materials Science and Engineering*, 17:073001 (31 pages), 2009.

[14] D. Schneider, S. Schmid, M. Selzer, T. Böhlke, and B. Nestler. Small strain elasto-plastic multiphase-field model. *Computational Mechanics*, 55:27–35, 2015.

[15] D. Schneider, F. Schwab, E. Schoof, A. Reiter, C. Herrmann, M. Selzer, T. Böhlke, and B. Nestler. On the stress calculation within phase-field approaches: a model for finite deformations. *Computational Mechanics*, 60:203–217, 2017.

[16] D. Schneider, E. Schoof, O. Tschukin, A. Reiter, C. Herrmann, F. Schwaab, M. Selzer, and B. Nestler. Small strain multiphase-field model accounting for configurational forces and mechanical jump conditions. *Computational Mechanics*, 61:277–295, 2018.

[17] E. Schoff, D. Schneider, N. Streichhan, T. Mittnacht, M. Selzer, and B. Nestler. Multiphase-field modeling of martensitic phase transformation in a dual-phase microstructure. *International Journal of Solids and Structures*, 134:181–194, 2017.

[18] C. Herrmann, E. Schoof, D. Schneider, F. Schwab, A. Reiter, M. Selzer, and B. Nestler. Multiphase-field model of small strain elasto-plasticity according to the mechanical jump conditions. *Computational Mechanics*, 62(6):1399–1412, 2018.

[19] E. Schoof, C. Herrmann, N. Streichhan, M. Selzer, D. Schneider, and B. Nestler. On the multiphase-field modeling of martensitic phase transformation in dual-phase steel using J2-viscoplasticity. *Modelling and Simulation in Materials Science and Engineering*, 27:025010 (24 pages), 2019.

[20] R. Schmitt, C. Kuhn, R. Müller, and K. Bhattacharya. Crystal Plasticity and Martensitic Transformations - A Phase Field Approach. *Technische Mechanik*, 34:23–28, 2014.

[21] R. Schmitt. *A Phase Field Model for Martensitic Transformations and Crystal Plasticity*. PhD thesis, TU Kaiserslautern, 2015.

[22] C. Miehe, J. Schröder, and J. Schotte. Computational homogenization analysis in finite plasticity. Simulation of texture development in polycrystalline materials. *Computer Methods in Applied Mechanics and Engineering*, 171(3-4):387–418, 1999.

[23] J. Schröder. A numerical two-scale homogenization scheme: the FE^2-method. In *Plasticity and Beyond - Microstructures, Crystal-Plasticity and Phase Transitions (CISM Lecture Notes 550, Eds. J. Schröder, K. Hackl)*, pages 1–64. Springer, 2014.

[24] D. Brands, D. Balzani, L. Scheunemann, J. Schröder, H. Richter, and D. Raabe. Computational modeling of dual-phase steels based on representative three-dimensional microstructures obtained from EBSD data. *Archive of Applied Mechanics*, 86:575–598, 2016.

[25] C. Simsir and C.H. Gür. 3D FEM simulation of steel quenching and investigation of the effect of asymmetric geometry on residual stress distribution. *Journal of Materials Processing Technology*, 207:211–221, 2008.

[26] JMatPro. Practical software for materials properties, https://www.sentesoftware.co.uk/jmatpro. August 2018.

[27] N. Saunders, U.K.Z. Guo, X. Li, A.P. Miodownik, and J.-P. Schillé. Using JMatPro to Model Materials Properties and Behavior. *JOM*, 55(12):60–65, 2003.

[28] Z. Guo, N. Saunders, J.-P. Schillé, and A.P. Miodownik. Material properties for process simulation. *Materials Science and Engineering: A*, 1-2:7–13, 2009.

[29] DIN EN ISO 683-17. Heat-treated steels, alloy steels and free-cutting steels - Part 17: Ball and roller bearing steels. Technical report, Beuth-Verlag, 2014.

[30] OpenPhase. http://www.openphase.de/. August 2018.

[31] K. Bhattacharya. *microstructure of martensite: why it forms and how it gives rise to the shape-memory effect*. Oxford University Press, Oxford, 2003.

[32] J. Mosler, O. Shchyglo, and H. Montazer Hojjat. A novel homogenization method for phase field approaches based on partial rank-one relaxation. *Journal of the Mechanics and Physics of Solids*, 68:251–266, 2014.

[33] A. Bartels and J. Mosler. Efficient variational constitutive updates for Allen-Cahn-type phase field theory coupled to continuum mechanics. *Computer Methods in Applied Mechanics and Engineering*, 317:55–83, 2017.

[34] B. Kiefer, T. Furlan, and J. Mosler. A numerical convergence study regarding homogenization assumptions in phase field modeling. *International Journal for Numerical Methods in Engineering*, 112:1097–1128, 2017.

[35] M. Sarhil. Constitutive Relations and Homogenization Assumptions in Phase-Field Models with Elasticity: Martensite Transformation as an Example. Master's thesis, Universität Duisburg-Essen and Ruhr-Universität Bochum, Essen, 2018.

[36] C. Miehe. *Kanonische Modelle Multiplikativer Elasto-Plastizität - Thermodynamische Formulierung und Numerische Implementation*. Forschungs- und Seminarberichte aus dem Bereich der Mechanik der Universität Hannover, Hannover, 1992.

XV International Conference on Computational Plasticity. Fundamentals and Applications
COMPLAS 2019
E. Oñate, D.R.J. Owen, D. Peric, M. Chiumenti & Eduardo de Souza Neto (Eds)

A VIRTUAL ELEMENT APPROACH FOR MICROPOLAR CONTINUA

M. PINGARO*, M. L. DE BELLIS† AND P. TROVALUSCI*

* Department of Structural and Geotechnical Engineering
Sapienza University of Rome
Via Gramsci 53, 00197 Rome, Italy
e-mail: marco.pingaro@uniroma1.it, patrizia.trovalusci@uniroma1.it - Web page: http://www.uniroma1.it

† Department of Engineering and Geology
Gabriele dAnnunzio University
Viale Pindaro 42, 65122 Pescara, Italy
e-mail: marialaura.debellis@unich.it - Web page: http://www.unich.it

Key words: Cosserat Continua, Virtual Element Method (VEM)

Abstract. In this work we propose a novel virtual element approach for solving boundary value problems in 2D linear isotropic micropolar elasticity. Following the basic idea of the Virtual Element Method (VEM), the degrees of freedom of each material point, i.e. the displacement and rotation fields, are decomposed into both a polynomial space, either linear or quadratic, and a remaining space that is kept virtual in the formulation. Generalized consistency and stabilization terms are consistently derived.
Different patch tests, properly conceived for micropolar continua, are proposed and compared to reference solutions present in literature. The obtained results are in good agreement with these solutions, confirming the capability of the proposed elements in the modelling of the expected responses.
The expected applications of this methodology concern the mechanical study of microstructured materials, inherently characterized by nonlocal response, which has been widely proven to be effectively represented by micropolar continua.

1 INTRODUCTION

A wide range of microstructured materials, commonly adopted in different engineering applications, is strongly characterized by nonlocal response, due to the presence of internal lengths and related dispersion properties [37, 32, 30]. This behaviour is especially evident for materials with characteristic sizes at the microstructure that are comparable to a structural length. Examples include fiber-beam networks, polycristals, foams, cancellous bones, but also metal matrix composites or masonry-like materials [34, 29, 19]. In all such cases, the overall constitutive behaviour is influenced by scale parameters, directly

related to the dimension of heterogeneities, that are typically non negligible with respect to the characteristic structural size.
In this context, the micropolar continuum, that belongs to the class of generalized continua [11], is able to retain memory of an inherent microstructure, providing an enriched constitutive behaviour, with respect to the classical Cauchy continuum. Each material point is, indeed, provided with displacement and rotation degrees of freedom, thus resulting in additional strains and stresses: besides the classical components, micropolar ones include curvatures (work conjugate to couple stresses) and skew-symmetric strains (work conjugate to skew-symmetric stresses).
From the experimental point of view, micropolar effects have been captured and identified in several materials ranging from natural materials [17, 28, 27, 18], up to engineered materials obtained via 3D printing techniques [26]. On the other hand, from the numerical modelling point of view different approaches have been proposed including micromechanical modelling [24, 13, 1, 4, 12, 19] and multi-scale modelling [31, 35, 16, 33, 21, 15, 36]. In most cases finite element analyses have been performed in order to solve boundary value problems at different scales of interest [12, 19]. As an alternative to the Finite element method, the Virtual Element Method (VEM) has been recently proposed [5, 6], representing an extension of mimetic finite difference approaches to deal with very general polygonal elements with generic number of nodes. The VEM is proving to be a very effective numerical tool, characterized by high flexibility especially concerning the modelling of very complex geometries, hanging nodes and very robust with respect to mesh distortion. Many applications have been presented so far ranging from linear elasticity [23, 22, 25, 8, 20] up to non-linear problems [10, 2, 3, 14].
In this work, we propose a virtual element approach for solving boundary value problems in 2D linear isotropic micropolar elasticity. Following the basic idea of the method, here, the displacement and rotation fields are decomposed into a polynomial space, either linear or quadratic, and a remaining space that is kept virtual in the formulation. Generalized consistency and stabilization terms are consistently derived.
Different applications are proposed [24], ranging from a patch test, properly conceived for micropolar continua, to various engineering applications. The obtained results are in good agreement with reference solutions, confirming the capability of the proposed elements in modelling the expected responses.

2 VIRTUAL FORMULATION FOR COSSERAT MEDIA

In this section we recall the governing equations of 2D linear elastic Cosserat continuum adopted in the presented study and describe the related virtual element space [5, 6], as well as the construction of the bilinear forms resulting from the weak form.
We consider a two–dimensional domain in the space $\mathbf{R}^2$, where the Cartesian coordinate system (O, x, y) is introduced. The body is subjected to the volume force, represented by the vector $\boldsymbol{f} \in (L^2(\Omega))^2$, $\boldsymbol{f} = \{f_1, f_2\}^T$, and body couple represented by the scalar $m \in L^2(\Omega)$, $m = m_3$, where $L^2(\Omega)$ is the standard Lebesgue space. For the sake of simplicity we use homogeneous Dirichlet boundary conditions and consider the Sobolev spaces, $Q := H_0^1(\Omega)$ and $\boldsymbol{V} := [Q]^2$. We introduce the admissible displacement fields

$\boldsymbol{v} \in \boldsymbol{V}$ and the admissible rotation fields $\varphi_3 \in Q$.

Under the hypothesis of small deformations, the kinematical descriptors are the displacement field vector $\boldsymbol{u} = \{u_1,\, u_2\}^T$ and the scalar rotation field $\omega = \omega_3$. The corresponding strain measures are the strain vector $\boldsymbol{\varepsilon} = \{\varepsilon_{11},\, \varepsilon_{22},\, \varepsilon_{12},\, \varepsilon_{21}\}^T$ and the curvature vector $\boldsymbol{\kappa} = \{\kappa_1,\, \kappa_2\}^T$. The compatibility equations write:

$$\begin{cases} \varepsilon_{ij} = u_{j,i} + e_{ji}\,\omega\,, \\ \kappa_j = \omega_{,j}\,, \end{cases} \tag{1}$$

where e_{ij} is the two-dimensional permutation tensor. Whereas the equilibrium equations are:

$$\begin{cases} \sigma_{ij,i} + f_j = 0\,, \\ \mu_{i,i} + e_{jk}\,\sigma_{jk} + m = 0\,, \end{cases} \tag{2}$$

where $\boldsymbol{\sigma}$ is the non–symmetric stress vector $\boldsymbol{\sigma} = \{\sigma_{11},\, \sigma_{22},\, \sigma_{12},\, \sigma_{21}\}^T$ and $\boldsymbol{\mu}$and the and couple stress vector is $\boldsymbol{\mu} = \{\mu_1,\, \mu_2\}^T$.

In the case of 2D isotropic linear elasticity we adopt the following constitutive equations [24]

$$\begin{aligned} \sigma_{ij} &= \mathbb{A}_{ijhk}\,\varepsilon_{hk}\,, \\ \mu_i &= 4Gl^2\,\kappa_i\,, \end{aligned} \tag{3}$$

where the elastic tensor of the fourth order $\mathbb{A}$ is:

$$\mathbb{A} = G \begin{bmatrix} \frac{2(1-\nu)}{1-2\nu} & \frac{2\nu}{1-2\nu} & 0 & 0 \\ \frac{2\nu}{1-2\nu} & \frac{2(1-\nu)}{1-2\nu} & 0 & 0 \\ 0 & 0 & 1+k & 1-k \\ 0 & 0 & 1-k & 1+k \end{bmatrix}, \tag{4}$$

where G is the shear modulus, ν is the Poisson modulus, and l is the length scale material constant. $k = G_c/G$ is the ratio between the Cosserat shear modulus G_c and the standard shear modulus G. The weak form of the linear elastic problem reads:

$$\begin{cases} \text{Find } (\boldsymbol{u}, \omega) \in \boldsymbol{V} \times Q \text{ such that :} \\ a(\boldsymbol{u}, \boldsymbol{v}) + b(\omega, \boldsymbol{v}) = <\boldsymbol{f}, \boldsymbol{v}> \quad \forall \boldsymbol{v} \in \boldsymbol{V} \\ b(\boldsymbol{u}, \varphi) + c(\omega, \varphi) = <m, \varphi> \quad \forall \varphi \in Q \end{cases} \tag{5}$$

where:

$$\begin{aligned} a(\boldsymbol{u}, \boldsymbol{v}) &= \int_\Omega \mathbb{A}_{ijhk}\, u_{h,k}\, v_{i,j}\, d\Omega\,, \\ b(\omega, \boldsymbol{v}) &= \int_\Omega \mathbb{A}_{ijhk}\, e_{hk}\, \omega\, v_{i,j}\, d\Omega\,, \\ c(\omega, \varphi) &= \int_\Omega \left(\mathbb{A}_{ijhk}\, e_{hk}\, e_{ij}\, \omega\, \varphi\right) + \left(2Gl^2\, \omega_{,n} \varphi_{,n}\right)\, d\Omega\,, \\ <\boldsymbol{f}, \boldsymbol{v}> &= \int_\Omega f_i\, v_i\, d\Omega\,, \\ <m, \varphi> &= \int_\Omega m\, \varphi\, d\Omega\,. \end{aligned} \tag{6}$$

In order to approximate the solution of the problem (5) we consider a decomposition $\mathcal{T}_h$ of the domain Ω into non overlapping polygonal elements E. In the following, we denote by e the straight edges of the mesh $\mathcal{T}_h$ and, for all $e \in \partial E$, $\boldsymbol{n}_i$ denotes the outward unit normal vector to e_i. The symbol n_e represents the number of the edges of the polygon E, that coincides with the number of the element vertices.

Let k be an integer ≥ 1. Let us denote by $P_k(\Omega)$ the space of polynomials, living on the set $\Omega \subseteq \mathbb{R}^2$, of degree less than or equal to k.

By the discretization introduced, it is possible to write the bilinear forms (5), as in the finite element methodology, in the following way:

$$\begin{aligned} a(\boldsymbol{u}, \boldsymbol{v}) &= \sum_{E \in \mathcal{T}_h} a^E(\boldsymbol{u}, \boldsymbol{v}) \quad \forall \boldsymbol{v} \in \boldsymbol{V} \,, \\ b(\omega, \boldsymbol{v}) &= \sum_{E \in \mathcal{T}_h} b^E(\omega, \boldsymbol{v}) \quad \forall \boldsymbol{v} \in \boldsymbol{V} \,, \\ c(\omega, \varphi) &= \sum_{E \in \mathcal{T}_h} c^E(\omega, \varphi) \quad \forall \varphi \in Q \,, \end{aligned} \tag{7}$$

The discrete virtual element spaces, $\boldsymbol{V}_h$ and Q_h, are:

$$\begin{aligned} \boldsymbol{V}_h &:= \left\{ \boldsymbol{v} \in \boldsymbol{V} \,:\, \boldsymbol{v} \,|_E \in \boldsymbol{V}_{h|E} \, \forall E \in \mathcal{T}_h \right\} \,, \\ Q_h &:= \left\{ q \in Q \,:\, q \,|_E \in \; Q_{h|E} \, \forall E \in \mathcal{T}_h \right\} \,, \end{aligned} \tag{8}$$

where $\boldsymbol{V}_{h|E} := \left(V_{h|E}\right)^2$ and the local spaces $V_{h|E}$ and $Q_{h|E}$ are defined as

$$\begin{aligned} V_{h|E} &:= \left\{ v_h \in H^1(E) \cap C^0(E) : \, \triangle v_h \in P_{k-2}(E), \, v_h \,|_e \in P_k(e) \, \forall e \in \partial E \right\} \,, \\ Q_{h|E} &:= \left\{ q_h \in H^1(E) \cap C^0(E) : \, \triangle q_h \in P_{k-2}(E), \, q_h \,|_e \in P_k(e) \, \forall e \in \partial E \right\} \,. \end{aligned} \tag{9}$$

By the definition of the local spaces (9), we can observe that, in contrast to the standard finite element approach, the local spaces, $\boldsymbol{V}_{h|E}$ and $Q_{h|E}$, are not fully explicit, in fact $\boldsymbol{V}_{h|E}$ and $Q_{h|E}$ contain all the polynomials of degree $\leq k$, plus other functions that, in general, will not be polynomials. Moreover $\boldsymbol{v}_h$ is a polynomial of degree k on each edge e of E and globally continuous on ∂E.

The problem (5) restricted to the discrete spaces $\boldsymbol{V}_h$ and Q_h becomes:

$$\begin{cases} \text{Find } (\boldsymbol{u}_h, \omega_h) \in \boldsymbol{V_h} \times Q_h \text{ such that} \\ a_h(\boldsymbol{u}_h, \boldsymbol{v}_h) + b(\omega_h, \boldsymbol{v}_h) = < \boldsymbol{f}, \boldsymbol{v}_h > \quad \forall \boldsymbol{v}_h \in \boldsymbol{V_h} \,, \\ b(\boldsymbol{u}_h, \varphi_h) + c(\omega_h, \varphi_h) = < m, \varphi_h > \quad \forall \varphi \in Q_h \,, \end{cases} \tag{10}$$

where $a_h(\cdot,\cdot) : \boldsymbol{V}_h \times \boldsymbol{V}_h \to \mathbb{R}$, $b_h(\cdot,\cdot) : \boldsymbol{V}_h \times Q_h \to \mathbb{R}$ and $c_h(\cdot,\cdot) : Q_h \times Q_h \to \mathbb{R}$ are the discrete bilinear forms approximating the continuous forms $a(\cdot,\cdot)$, $b(\cdot,\cdot)$ and $c(\cdot,\cdot)$ respectively. $< \boldsymbol{f}, \boldsymbol{v}_h >$ and $< m, \varphi_h >$ are the terms approximating the virtual work of external loads.

Table 1: Patch test: coordinates nodes

Node	x	y
1	0.04	0.02
2	0.18	0.03
3	0.16	0.08
4	0.08	0.08
5	0.00	0.00
6	0.24	0.00
7	0.24	0.12
8	0.00	0.12

The discrete bilinear forms are constructed element by element as:

$$\begin{aligned} a_h(\boldsymbol{u}_h, \boldsymbol{v}_h) &= \sum_{E \in \mathcal{T}_h} a_h^E(\boldsymbol{u}_h, \boldsymbol{v}_h) \quad \forall \boldsymbol{u}_h,\ \boldsymbol{v}_h \in \boldsymbol{V}_h\ , \\ b_h(\omega_h, \boldsymbol{v}_h) &= \sum_{E \in \mathcal{T}_h} b_h^E(\omega_h, \boldsymbol{v}_h) \quad \forall \omega_h \in Q_h,\ \ \forall \boldsymbol{v}_h \in \boldsymbol{V}_h\ , \\ c_h(\omega_h, \varphi_h) &= \sum_{E \in \mathcal{T}_h} c_h^E(\omega_h, \varphi_h) \quad \forall \omega_h,\ \varphi_h \in Q_h\ . \end{aligned} \tag{11}$$

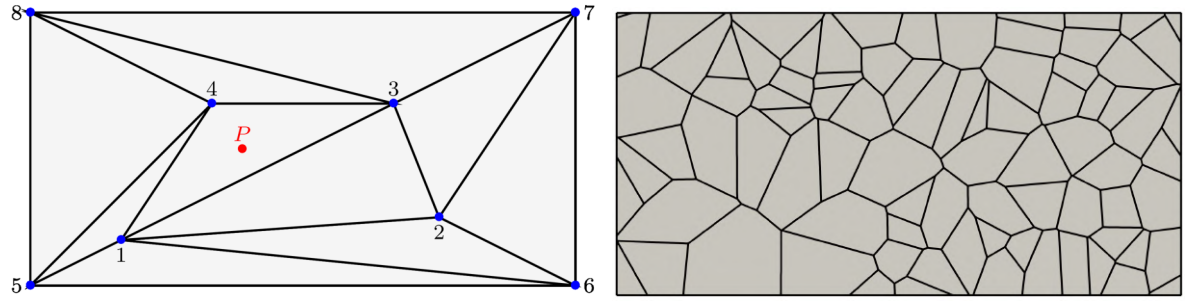
The local stiffness matrices can be derived, consistently with [6, 9], after introducing the local L^2-projection operators $\boldsymbol{\Pi}_E^\nabla : \boldsymbol{V}_h(E) \to (\mathbb{P}_k(E))^2$, $\Pi_E^\nabla : Q_h(E) \to \mathbb{P}_k(E)$ and $\Pi_E^0 : Q_h(E) \to \mathbb{P}_k(E)$.

The details on the construction of the local stiffness matrix are presented in [6, 9, 7, 22], while are here omitted for the sake of brevity.

3 NUMERICAL RESULTS

In this section we report a patch test to prove the reliability and the performances of the developed VEM Cosserat element. The patch test presented has been proposed by [24] and it was specifically conceived for Cosserat finite elements.

We consider a rectangular region discretized using two type of mesh: the first type is made by non-overlapping distorted triangular elements, Fig. 1(a), while the second by Voronoi elements, Fig. 1(b). The coordinates of the nodes for the triangular mesh are reported in the Tab. 1. We impose different boundary conditions (three different cases are analysed in the following) and both strains and stresses are checked [24]. Satisfaction of the patch tests guarantees stability and convergence of the element's solution [38] when used for the solution of real problems. For all tests we set the elastic constants: $G = 1000$, $\nu = 0.25$, $l = 0.1$ and $k = 0.5$.



(a) Triangular element mesh (b) Voronoi mesh

Figure 1: Domain problem and the two relative mesh adopted

3.1 Patch Test 1

The first test is developed to check the capabilities of the element to reproduce the linear elastic Cauchy continuum. We impose the following boundary conditions in terms of displacements, $\boldsymbol{u}$, and rotation, ω

$$\begin{aligned} u_1 &= 10^{-3}\left(x_1 + (1/2)x_2\right) \,, \\ u_2 &= 10^{-3}\left(x_1 + x_2\right) \,, \\ \omega &= (1/4)\, 10^{-3} \,, \\ f_1 &= f_2 = 0 \,, \\ m &= 0 \,, \end{aligned} \tag{12}$$

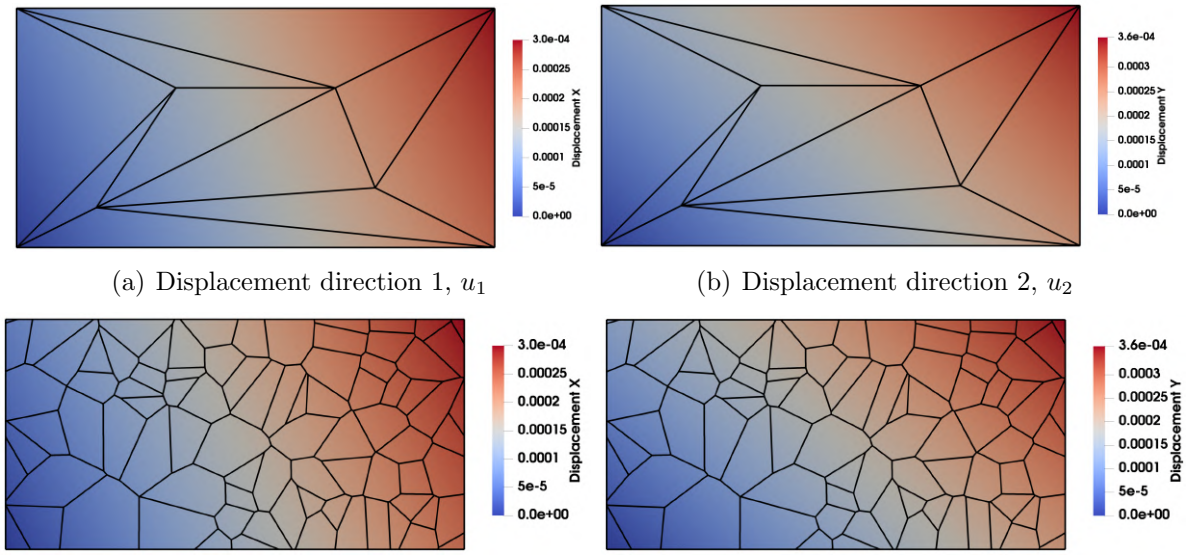
and the relative analytical solution are:

$$\begin{aligned} \sigma_{11} &= \sigma_{22} = 4 \,, \\ \sigma_{12} &= \sigma_{21} = 1.5 \,, \\ \mu_1 &= \mu_2 = 0 \,. \end{aligned} \tag{13}$$

The stress, $\boldsymbol{\sigma}$, is constant and symmetric and the couple, $\boldsymbol{\mu}$, is identically null. In Fig. 2 we report the solution in terms of displacements for the two type of meshes adopted. In Figs. 3 and 4 the map color of the stresses for the two different mesh adopted are reported.

3.2 Patch Test 2

The following patch test was suited to check the capabilities to account for constant non-symmetric stress and identically null couple. We impose the following boundary



(a) Displacement direction 1, u_1

(b) Displacement direction 2, u_2

(c) Displacement direction 1, u_1

(d) Displacement direction 2, u_2

Figure 2: Displacement solution obtained for all tests with triangular and Voronoi meshes, respectively

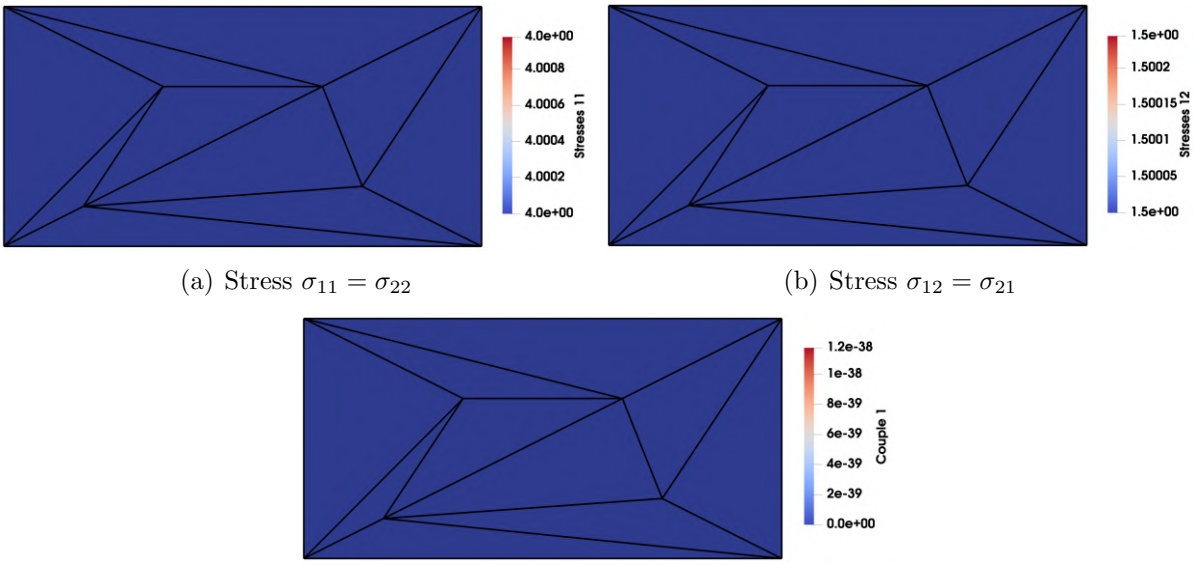
conditions

$$\begin{aligned} u_1 &= 10^{-3}\left(x_1 + (1/2)x_2\right) \,, \\ u_2 &= 10^{-3}\left(x_1 + x_2\right) \,, \\ \omega &= \left(1/4 + 1/(4\alpha)\right) 10^{-3} \,, \\ f_1 &= f_2 = 0 \,, \\ m &= 1 \,, \end{aligned} \tag{14}$$

where the parameter α is $1 - k$. The relative analytical solution in terms of stresses are:

$$\begin{aligned} \sigma_{11} &= \sigma_{22} = 4 \,, \\ \sigma_{12} &= 1 \,, \\ \sigma_{21} &= 2 \,, \\ \mu_1 &= \mu_2 = 0 \,. \end{aligned} \tag{15}$$

The solution obtained are shown in Figs. 5 and 6.



(a) Stress $\sigma_{11} = \sigma_{22}$

(b) Stress $\sigma_{12} = \sigma_{21}$

(c) Couple $\mu_1 = \mu_2$

Figure 3: Stress solution for path test 1 with triangular mesh

3.3 Patch Test 3

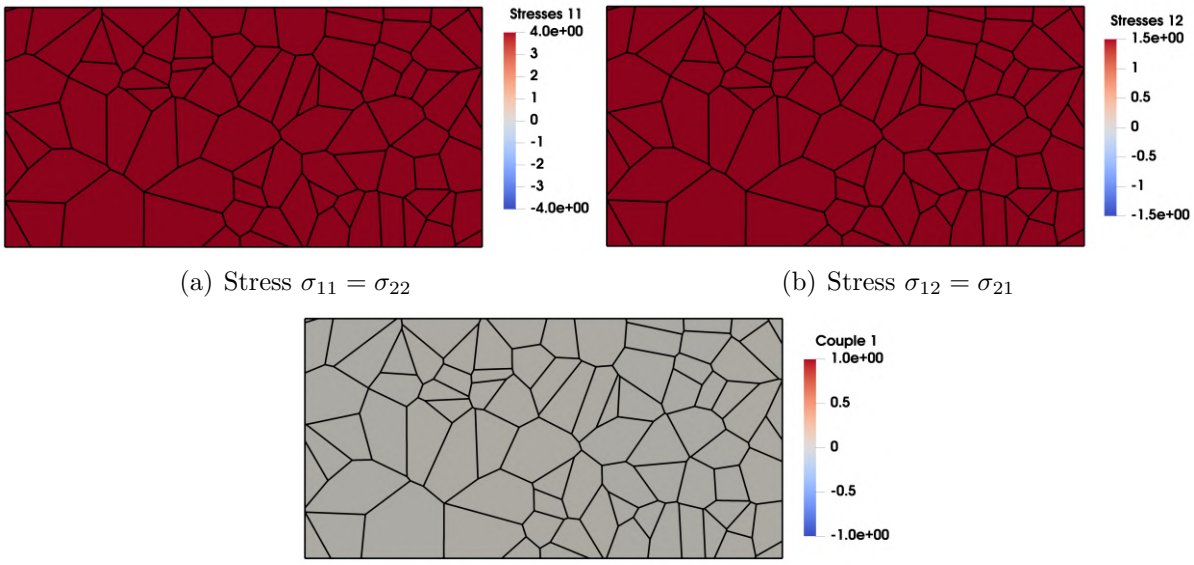
The *patch test 3* tests a general case of Cosserat continuum. The following boundary conditions are imposed

$$\begin{aligned} u_1 &= 10^{-3}\,(x_1 + (1/2)x_2)\ , \\ u_2 &= 10^{-3}\,(x_1 + x_2)\ , \\ \omega &= (1/4 + 1/(2\alpha)(x_1 - x_2))\,10^{-3}\ , \\ f_1 &= f_2 = 1\ , \\ m &= 2(x_1 - x_2)\ , \end{aligned} \tag{16}$$

and the relative solution:

$$\begin{aligned} \sigma_{11} &= \sigma_{22} = 4\ , \\ \sigma_{12} &= 1.5 - (x_1 - x_2)\ , \\ \sigma_{21} &= 1.5 + (x_1 - x_2)\ , \\ \mu_1 &= -\mu_2 = (2l^2/\alpha)\ . \end{aligned} \tag{17}$$

The contour plot of the stresses for triangular and Voronoi meshes are shown in Fig. 7 and Fig. 8 respectively. In Tab. 2 the displacements and the stresses at the point P (see Fig. 1(a)) are reported and compared with the exact solution. All results in the Tab. 2 are refereed to the triangular mesh. The Virtual Element (VEM), here proposed, shows improved performances compared with the MLINT (linear displacement and rotation), MQLT (quadratic displacement and linear rotation) and MQUAT (quadratic displacement and rotation) elements proposed by [24].



(a) Stress $\sigma_{11} = \sigma_{22}$

(b) Stress $\sigma_{12} = \sigma_{21}$

(c) Couple $\mu_1 = \mu_2$

Figure 4: Stress solution for path test 1 with Voronoi mesh

Table 2: Patch test 3: displacements at node 2 and stresses at $P = (0.0933, 0.06)$ using triangular mesh

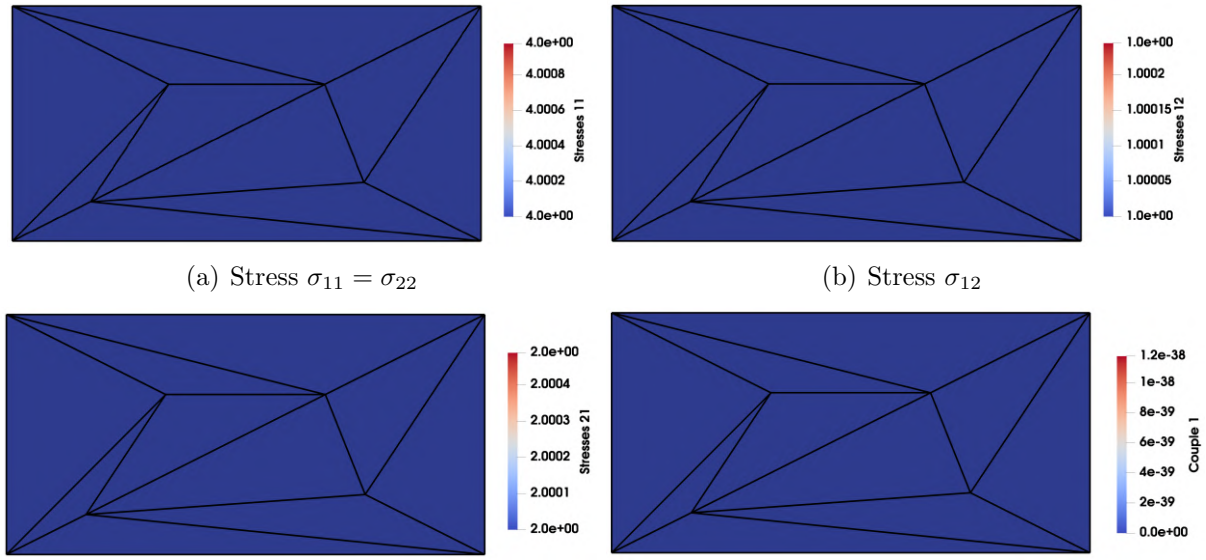
	$u_1 \times 10^3$	$u_2 \times 10^3$	$\omega \times 10^3$	σ_{11}	σ_{12}	μ_1
MLINT	0.1944	0.2096	0.4001	3.9928	1.4634	0.0400
MQLT	0.1945	0.2097	0.4001	3.9956	1.4668	0.0400
MQUAT	0.1945	0.2097	0.3960	3.9956	1.4707	0.0392
VEM	0.1950	0.2100	0.3998	4.0000	1.4668	0.0399
Exact	0.1950	0.2100	0.4000	4.0000	1.4667	0.0400

4 FINAL REMARKS

In the present work we developed a novel formulation of the Virtual Element methodology for 2D micropolar linear elastic continuum. In particular we adopt linear Virtual Element Method both for displacements and rotations. The formulation developed and implemented is in good agreement with the patch tests presented in literature and all tests are passed for the standard triangular mesh and for distorted Voronoi mesh.

Acknowledgment

This research was supported by Italian Ministry of University and Research: PRIN 2015, project 2015JW9NJT (B86J16002300001); Sapienza Research Grants 'Grandi Progetti' 2016 (B82F16005920005) and 'Progetti Medi' 2017 (B83C17001440005).



(a) Stress $\sigma_{11} = \sigma_{22}$ (b) Stress σ_{12}

(c) Stress σ_{21} (d) Couple $\mu_1 = \mu_2$

Figure 5: Stress solution for path test 2 with triangular mesh

REFERENCES

[1] D. Addessi, M. De Bellis, and E. Sacco. Micromechanical analysis of heterogeneous materials subjected to overall Cosserat strains. *Mechanics Research Communications*, 54:27–34, 2013.

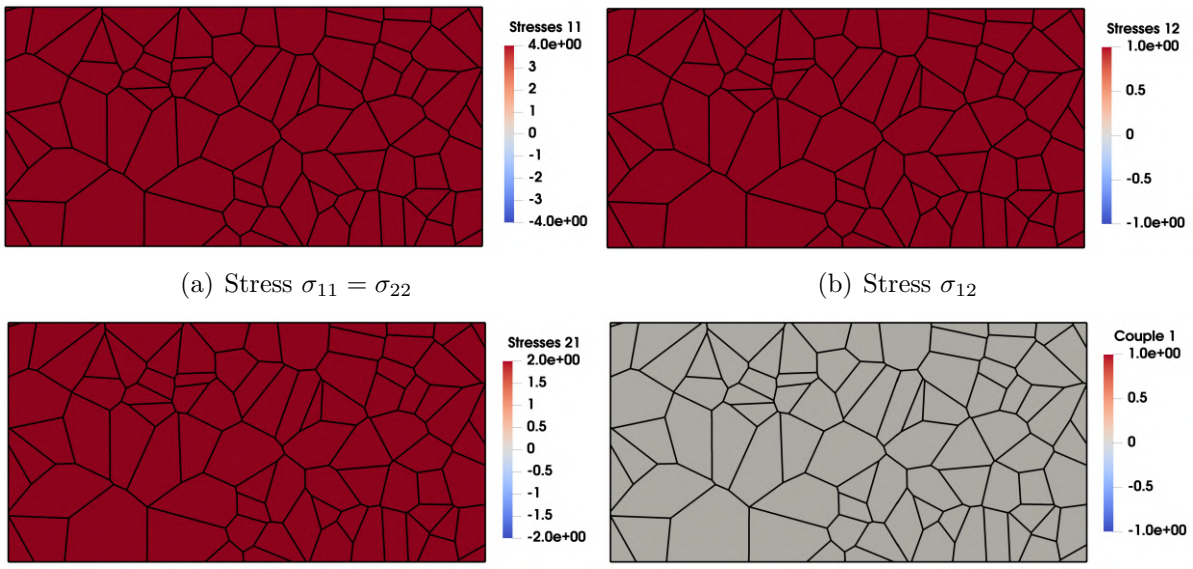
[2] E. Artioli, L. Beiro da Veiga, C. Lovadina, and E. Sacco. Arbitrary order 2D virtual elements for polygonal meshes: part II, inelastic problem. *Computational Mechanics*, 60(4):643–657, 2017.

[3] E. Artioli, S. Marfia, and E. Sacco. High-order virtual element method for the homogenization of long fiber nonlinear composites. *Computer Methods in Applied Mechanics and Engineering*, 341:571–585, 2018.

[4] A. Ask, S. Forest, B. Appolaire, and K. Ammar. A Cosseratphase-field theory of crystal plasticity and grain boundary migration at finite deformation. *Continuum Mechanics and Thermodynamics*, 2018. Article in Press, DOI: 10.1007/s00161-018-0727-6.

[5] L. Beiro Da Veiga, F. Brezzi, A. Cangiani, G. Manzini, L. Marini, and A. Russo. Basic principles of virtual element methods. *Mathematical Models and Methods in Applied Sciences*, 23(1):199–214, 2013.

[6] L. Beiro Da Veiga, F. Brezzi, and L. Marini. Virtual elements for linear elasticity problems. *SIAM Journal on Numerical Analysis*, 51(2):794–812, 2013.



(a) Stress $\sigma_{11} = \sigma_{22}$ (b) Stress σ_{12}

(c) Stress σ_{21} (d) Couple $\mu_1 = \mu_2$

Figure 6: Stress solution for path test 2 with Voronoi mesh

[7] L. Beiro Da Veiga, F. Brezzi, L. Marini, and A. Russo. Mixed virtual element methods for general second order elliptic problems on polygonal meshes. *ESAIM: Mathematical Modelling and Numerical Analysis*, 50(3):727–747, 2016.

[8] H. Chi, L. Beiro da Veiga, and G. Paulino. A simple and effective gradient recovery scheme and a posteriori error estimator for the Virtual Element Method (VEM). *Computer Methods in Applied Mechanics and Engineering*, 347:21–58, 2019.

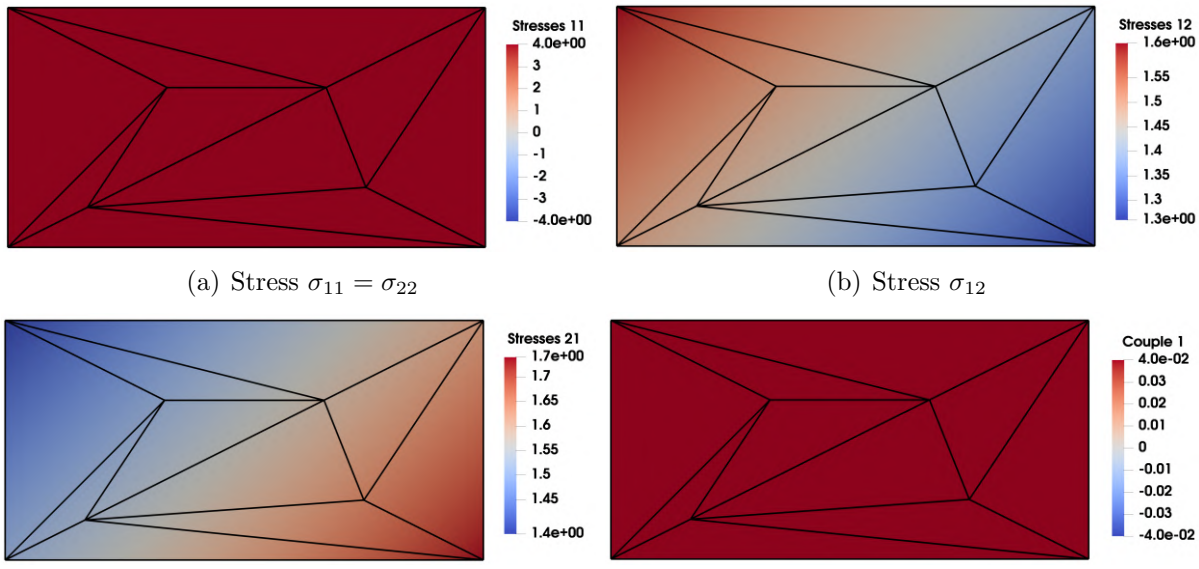
[9] L. Da Veiga, F. Brezzi, L. Marini, A. Russo, F. Brezzi, and G. Manzini. The Hitchhiker's guide to the virtual element method. *Mathematical Models and Methods in Applied Sciences*, 24(8):1541–1573, 2014.

[10] M. De Bellis, P. Wriggers, B. Hudobivnik, and G. Zavarise. Virtual element formulation for isotropic damage. *Finite Elements in Analysis and Design*, 144:38–48, 2018.

[11] A. Eringen. *Microcontinuum field theories*. Springer-Verlag, New York, 1999.

[12] N. Fantuzzi, L. Leonetti, P. Trovalusci, and F. Tornabene. Some Novel Numerical Applications of Cosserat Continua. *International Journal of Computational Methods*, 15(6), 2018.

[13] J. Fatemi, P. Onck, G. Poort, and F. Van Keulen. Cosserat moduli of anisotropic cancellous bone: A micromechanical analysis. volume 105, pages 273–280, 2003.



(a) Stress $\sigma_{11} = \sigma_{22}$ (b) Stress σ_{12}

(c) Stress σ_{21} (d) Couple $\mu_1 = -\mu_2$

Figure 7: Stress solution for path test 3 with triangular mesh

[14] B. Hudobivnik, F. Aldakheel, and P. Wriggers. A low order 3d virtual element formulation for finite elastoplastic deformations. *Computational Mechanics*, 63(2):253–269, 2019.

[15] G. Htter. On the micro-macro relation for the microdeformation in the homogenization towards micromorphic and micropolar continua. *Journal of the Mechanics and Physics of Solids*, 127:62–79, 2019.

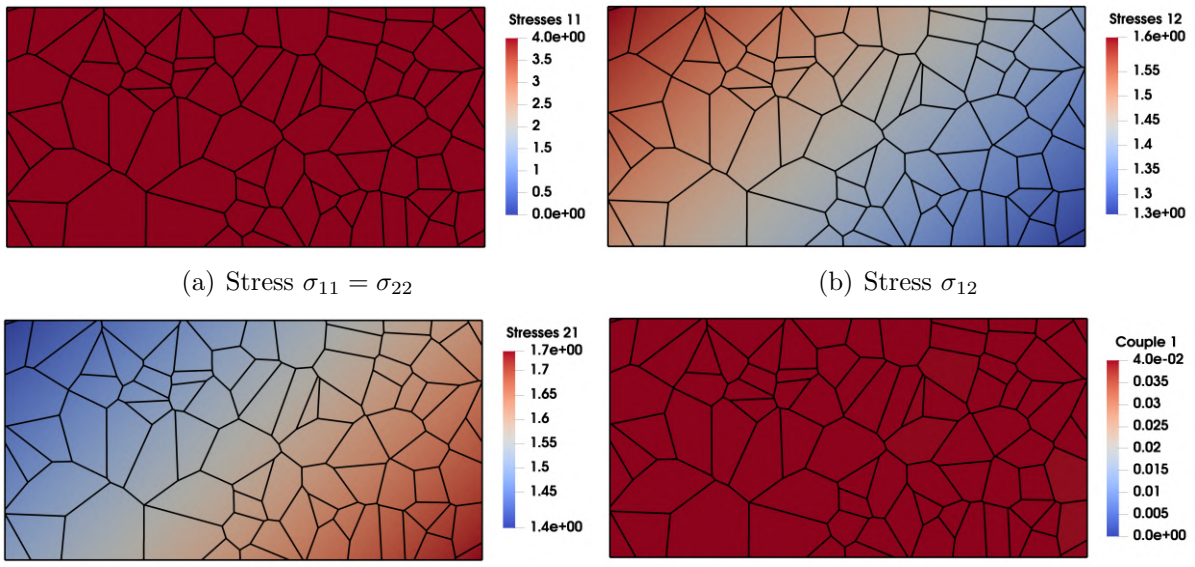
[16] G. Htter, U. Mhlich, and M. Kuna. Micromorphic homogenization of a porous medium: elastic behavior and quasi-brittle damage. *Continuum Mechanics and Thermodynamics*, 27(6):1059–1072, 2015.

[17] R. Lakes. Experimental microelasticity of two porous solids. *International Journal of Solids and Structures*, 22(1):55–63, 1986.

[18] R. Lakes. Elastic and viscoelastic behavior of chiral materials. *International Journal of Mechanical Sciences*, 43(7):1579–1589, 2001.

[19] L. Leonetti, N. Fantuzzi, P. Trovalusci, and F. Tornabene. Scale effects in orthotropic composite assemblies as micropolar continua: A comparison between weak and strong-form finite element solutions. *Materials*, 12(5), 2019.

[20] V. Nguyen-Thanh, X. Zhuang, H. Nguyen-Xuan, T. Rabczuk, and P. Wriggers. A Virtual Element Method for 2d linear elastic fracture analysis. *Computer Methods in Applied Mechanics and Engineering*, 340:366–395, 2018.



(a) Stress $\sigma_{11} = \sigma_{22}$ (b) Stress σ_{12}

(c) Stress σ_{21} (d) Couple $\mu_1 = -\mu_2$

Figure 8: Stress solution for path test 3 with Voronoi mesh

[21] P. Onck. Cosserat modeling of cellular solids. *Comptes Rendus - Mecanique*, 330(11):717–722, 2002.

[22] M. Pingaro, E. Reccia, and P. Trovalusci. Homogenization of random porous materials with low order Virtual Elements. *ASCE-ASME Journal of Risk and Uncertainty in Engineering Systems Part B: Mechanical Engineering*, 2019. Article in Press, DOI: 10.1115/1.4043475.

[23] M. Pingaro, E. Reccia, P. Trovalusci, and R. Masiani. Fast statistical homogenization procedure (FSHP) for particle random composites using virtual element method. *Computational Mechanics*, 2019. Article in Press, DOI: 10.1007/s00466-018-1665-7.

[24] E. Providas and M. Kattis. Finite element method in plane Cosserat elasticity. *Computers and Structures*, 80(27-30):2059–2069, 2002.

[25] B. Reddy and D. van Huyssteen. A virtual element method for transversely isotropic elasticity. *Computational Mechanics*, 2019. Article in Press, DOI: 10.1007/s00466-019-01690-7.

[26] Z. Rueger, C. Ha, and R. Lakes. Cosserat elastic lattices. *Meccanica*, 2019.

[27] Z. Rueger and R. Lakes. Experimental Cosserat elasticity in open-cell polymer foam. *Philosophical Magazine*, 96(2):93–111, 2016.

[28] Z. Rueger and R. Lakes. Strong Cosserat Elasticity in a Transversely Isotropic Polymer Lattice. *Physical Review Letters*, 120(6), 2018.

[29] V. Sansalone, P. Trovalusci, and F. Cleri. Multiscale modeling of materials by a multifield approach: Microscopic stress and strain distribution in fiber-matrix composites. *Acta Materialia*, 54(13):3485–3492, 2006.

[30] V. Settimi, P. Trovalusci, and G. Rega. Dynamical properties of a composite microcracked bar based on a generalized continuum formulation. *Continuum Mechanics and Thermodynamics*, 2019. Article in Press, DOI: 10.1007/s00161-019-00761-7.

[31] I. Stefanou, J. Sulem, and I. Vardoulakis. Three-dimensional Cosserat homogenization of masonry structures: Elasticity. *Acta Geotechnica*, 3(1):71–83, 2008.

[32] P. Trovalusci. Molecular Approaches for Multifield Continua: origins and current developments. *CISM International Centre for Mechanical Sciences, Courses and Lectures*, 556:211–278, 2014. Springer, Vienna.

[33] P. Trovalusci, M. De Bellis, M. Ostoja-Starzewski, and A. Murrali. Particulate random composites homogenized as micropolar materials. *Meccanica*, 49(11):2719–2727, 2014.

[34] P. Trovalusci and R. Masiani. Non-linear micropolar and classical continua for anisotropic discontinous materials. *International Journal of Solids and Structures*, 40(5):1281–1297, 2003.

[35] P. Trovalusci, M. Ostoja-Starzewski, M. De Bellis, and A. Murrali. Scale-dependent homogenization of random composites as micropolar continua. *European Journal of Mechanics, A/Solids*, 49:396–407, 2015.

[36] P. Trovalusci and A. Pau. Derivation of microstructured continua from lattice systems via principle of virtual works: The case of masonry-like materials as micropolar, second gradient and classical continua. *Acta Mechanica*, 225(1):157–177, 2014.

[37] P. Trovalusci, V. Varano, and G. Rega. A generalized continuum formulation for composite microcracked materials and wave propagation in a bar. *Journal of Applied Mechanics*, 77(6), 2010.

[38] O. Zienkiewicz and R. Taylor. *Finite Element Method: Volume 1 - The Basis*. Butterworth-Heinemann, Oxford, 5th edition, 2000.

XV International Conference on Computational Plasticity. Fundamentals and Applications
COMPLAS 2019
E. Oñate, D.R.J. Owen, D. Peric, M. Chiumenti & Eduardo de Souza Neto (Eds)

A FINITE STRAIN THERMO-MECHANICALLY COUPLED MATERIAL MODEL FOR SEMI-CRYSTALLINE POLYMERS

SEBASTIAN FELDER*, HAGEN HOLTHUSEN*, STEFAN HESSELER†, FELIX POHLKEMPER†, JAAN-WILLEM SIMON*, THOMAS GRIES† AND STEFANIE REESE*

* Institute of Applied Mechanics (IFAM)
RWTH Aachen University
Mies-van-der-Rohe-Str. 1, 52074 Aachen, Germany
e-mail: sebastian.felder@rwth-aachen.de, web page: https://www.ifam.rwth-aachen.de/

† Institut für Textiltechnik (ITA)
RWTH Aachen University
Otto-Blumenthal-Str. 1, 52074 Aachen, Germany
web page: https://www.ita.rwth-aachen.de

Key words: Semi-crystalline polymers, Thermo-mechanical coupling, Finite strains, Crystallisation kinetics

Abstract. In this work, a thermo-mechanically coupled constitutive model for semi-crystalline polymers is derived in a thermodynamically consistent manner. In general, the macroscopic material behaviour of this class of materials is dictated by the underlying microstructure, i.e. by the distribution and structure of crystalline regimes, which form up after cooling from the amorphous melt. In order to account for the latter, the total degree of crystallinity is incorporated as an internal variable and its evolution is prescribed by means of a non-isothermal crystallisation kinetics model. The numerically efficient and robust framework is characterised based on experimental data for Polyamide 6 and shows a promising potential to predict the hyperelastic, visco-plastic material behaviour at various temperatures.

1 INTRODUCTION

Thermoplastic polymers are an important class of materials for many technically relevant applications. In contrast to thermosets, which form irreversible chemical bonds, they can be repeatedly reshaped after heating above the melting point. As a consequence, they are well-suited for forming processes. A specific class of thermoplastics are semi-crystalline polymers (e.g. Polyamide 6, which is the considered polymer in this work), which partly crystallise after cooling from the melt. The degree and structure of the crystalline regimes depends on the thermal conditions and applied stress. The relative degree of crystallinity χ_c can be determined by the heat flow rate $(dh)/(dt)$, which is measured by differential

scanning calorimetry (DSC) (cf. chapter 3) and lays between zero (100% amorphous, $t < t_{On}$) and one (at the end of the crystallisation process, $t > t_{End}$).

$$\chi_c = \frac{\int_{t_{\mathrm{On}}}^{t} \frac{dh}{dt} dt}{\int_{t_{\mathrm{On}}}^{t_{\mathrm{End}}} \frac{dh}{dt} dt} := \frac{\Delta h_t}{\Delta h_m}, \quad \chi = \frac{\int_{t_{\mathrm{On}}}^{t} \frac{dh}{dt} dt}{\Delta h_f^{100}} = \chi_c \, \frac{\Delta h_m}{\Delta h_f^{100}} \tag{1}$$

Here, the change in enthalpy during the whole crystallisation process $\Delta h_m(\dot{\theta})$ is introduced, which is depending on the cooling rate. To obtain the absolute degree of crystallinity χ, the material constant Δh_f^{100} corresponding to the specific fusion enthalpy of a 100% crystalline material, must be determined. For Polyamide 6 the latter can be computed from the average of the values corresponding to the α-form (241 J/g) and γ-form (239 J/g) as suggested by Fornes et al. [1].
Naturally, the morphology of the underlying microstructure (i.e. the degree of crystallinity) has a significant influence on the mechanical behaviour of semi-crystalline polymers (cf. chapter 3). Furthermore, the mechanical response of Polyamide 6 is characterised by non-linear, visco-plastic behaviour, depending on the thermal conditions and accompanied by large elastic and plastic strains (cf. section 3). In order to avoid cost- and time-consuming trial and error approaches, a strong demand for computational models arises, which accurately predict the complex material and structural response of parts during and after thermoforming processes.
To this end, a continuum-mechanical, phenomenological material model is presented in this work. The thermo-mechanically coupled, visco-plastic constitutive framework is derived in a thermodynamically consistent manner (cf. chapter 2) and valid for large deformation. In order to account for the underlying microstructure, the total degree of crystallinity χ is treated as an additional internal variable. Crystallisation from a relaxed, static melt is assumed and the evolution of χ is modelled by means of a non-isothermal representation of the Avrami equation (see section 2.1). In section 3, the model is characterised by isothermal and non-isothermal DSC analysis and uniaxial tensile tests for different loading rates and degrees of crystallinity at varying temperatures .

2 MATERIAL MODEL FORMULATION

In line with e.g. the work [2] the resistance of deformation is decomposed into an intermolecular and a network contribution. For the intermolecular resistance, a finite strain elasto-plastic model with non-linear isotropic hardening and non-linear kinematic hardening of Frederick Armstrong type is considered. To account for the molecular orientation and relaxation, the molecular network resistance is represented by a finite strain visco-elastic model. Quantities corresponding to the elasto-plastic model and to the viscous model will be denoted with index $\mathtt{1}$ and $\mathtt{2}$, respectively.
The total deformation gradient $\boldsymbol{F}$ is multiplicatively decomposed separately for both models. For the elasto-plastic constitutive framework the classical split of the deformation gradient, $\boldsymbol{F} = \boldsymbol{F}_{e\mathtt{1}} \boldsymbol{F}_p$, into its elastic part $\boldsymbol{F}_{e\mathtt{1}}$ and plastic part $\boldsymbol{F}_p$ is proposed To account for non-linear kinematic hardening, a physically motivated additional split of the plastic part $\boldsymbol{F_p} = \boldsymbol{F}_{pe} \boldsymbol{F}_{pi}$ is performed. Noteworthy, these decompositions result in

the intermediate plastic configuration ic_{1a} and the so-called intermediate configuration of kinematic hardening ic_{1b}. The kinematic relations corresponding to the viscous model are based on a multiplicative decomposition of the deformation gradient, $\boldsymbol{F} = \boldsymbol{F}_{e2}\boldsymbol{F}_i$, into its elastic $\boldsymbol{F}_{e2}$ and inelastic part $\boldsymbol{F}_i$. Thus, an additional, inelastic intermediate configuration ic_2 is introduced.
The Helmholtz free energy depends on the deformation only through the elastic right Cauchy-Green deformation tensors $\boldsymbol{C}_{e1}$, $\boldsymbol{C}_{e2}$, and $\boldsymbol{C}_{pe}$, in agreement with the principal of material frame invariance.

$$\boldsymbol{C}_{e1} = \boldsymbol{F}_{e1}^T\boldsymbol{F}_{e1} = \boldsymbol{F}_p^{-T}\boldsymbol{C}\boldsymbol{F}_p^{-1}, \quad \boldsymbol{C}_{e2} = \boldsymbol{F}_{e2}^T\boldsymbol{F}_{e2} = \boldsymbol{F}_i^{-T}\boldsymbol{C}\boldsymbol{F}_i^{-1}, \quad \boldsymbol{C}_{pe} = \boldsymbol{F}_{pe}^T\boldsymbol{F}_{pe} = \boldsymbol{F}_{pi}^{-T}\boldsymbol{C}_p\boldsymbol{F}_{pi}^{-1} \tag{2}$$

Here the right Cauchy-Green tensor $\boldsymbol{C} = \boldsymbol{F}^T\boldsymbol{F}$ and the plastic right Cauchy-Green tensor $\boldsymbol{C}_p = \boldsymbol{F}_p^T\boldsymbol{F}_p$ are introduced. The total, specific Helmholtz free energy is additively decomposed into a contribution stemming from the intermolecular resistance ψ_1, a contribution from the molecular network resistance ψ_2 and an energy term ψ_χ associated with the crystallisation process.

$$\psi = \underbrace{\psi_{e1}(\boldsymbol{C}_{e1}, \chi, \theta) + \psi_{kin}(\boldsymbol{C}_{pe}, \theta) + \psi_{iso}(\kappa, \chi, \theta)}_{\psi_1} + \psi_2(\boldsymbol{C}_{e2}, \chi, \theta) + \psi_\chi(\chi, \theta) \tag{3}$$

To account for the dependence of the material response on the temperature θ and the morphology of the underlying microstructure, the energy terms are functions of the temperature θ and the total degree of crystallinity χ. In this work, no differentiation between crystal configurations nor morphology (lamella thickness) is made. Furthermore, non-isothermal crystallisation processes from a static, relaxed melt are assumed. Consequently, $\chi(\theta, \dot{\theta})$ is introduced as an additional internal variable and assumed to be a function of the temperature and cooling rate $\dot{\theta}$. Hence, the free energy is an implicit function of the cooling rate. In equation (3), ψ_{e1} and ψ_{e2} denote the elastic energy contributions of the intermolecular and molecular network resistances, respectively. To phenomenologically account for Bauschinger-like phenomena, ψ_{kin}, a defect-energy associated with plastic deformations, is introduced. The stored energy due to isotropic hardening is defined as ψ_{iso} and is a function of the accumulated plastic strain κ.

2.1 Derivation based on the Clausius-Duhem inequality

Starting point of the thermodynamic consistent derivation of the constitutive framework is the Clausius-Duhem form of the entropy inequality with respect to the reference configuration (rc).

$$\boldsymbol{S} : \frac{1}{2}\dot{\boldsymbol{C}} - \rho_0(\dot{\psi} + \eta_S\dot{\theta}) - \frac{1}{\theta}\boldsymbol{q}_0 \cdot \mathrm{Grad}(\theta) \geq 0 \tag{4}$$

Here, $\boldsymbol{S}$ denotes the second Piola-Kirchhoff stress, η_S is the specific entropy, ρ_0 is the density in the rc and $\boldsymbol{q}_0$ the heat flux with respect to the rc. Assuming that ψ_{e1}, ψ_{e2} and ψ_{kin} are isotropic functions of $\boldsymbol{C}_{e1}$, $\boldsymbol{C}_{e2}$, and $\boldsymbol{C}_{pe}$, respectively, and inserting the total time derivative of the Helmholtz free energy (3) into the latter expression yields, after several

mathematical transformations, the following form of the Clausius-Duhem inequality.

$$\begin{aligned}&(\boldsymbol{S}-\boldsymbol{S}_1-\boldsymbol{S}_2):\frac{1}{2}\dot{\boldsymbol{C}}-\rho_0\left(\frac{\partial\psi}{\partial\theta}+\eta_S\right)\dot{\theta}-\frac{1}{\theta}\boldsymbol{q}_0\cdot\mathrm{Grad}(\theta)\\&-\rho_0\frac{\partial\psi}{\partial\chi}\dot{\chi}+\boldsymbol{M}_2:\boldsymbol{D}_i+\left(\boldsymbol{M}_1-\bar{\boldsymbol{X}}\right):\boldsymbol{D}_p+\boldsymbol{M}_{kin}:\boldsymbol{D}_{pi}+R\dot{\kappa}\geq 0\end{aligned}\tag{5}$$

The inequality (5) is an expression of the evolution of the internal variables (i.e. $\dot{\chi}$, $\boldsymbol{D}_i$, $\boldsymbol{D}_p$, $\boldsymbol{D}_{pi}$, and $\dot{\kappa}$) and the thermodynamic conjugated forces. Here, $\boldsymbol{D}_{(*)}=\mathrm{sym}(\boldsymbol{L}_{(*)})$ denotes the symmetric part of the corresponding velocity gradient $\boldsymbol{L}_{(*)}=\dot{\boldsymbol{F}}_{(*)}\boldsymbol{F}_{(*)}^{-1}$, with $(*)=i,p,pi$. The second Piola-Kirchhoff stress tensors corresponding to the intermolecular and molecular network resistance are

$$\boldsymbol{S}_1=2\rho_0\boldsymbol{F}_p^{-1}\frac{\partial\psi_{e1}}{\partial\boldsymbol{C}_{e1}}\boldsymbol{F}_p^{-T},\quad \boldsymbol{S}_2=2\rho_0\boldsymbol{F}_i^{-1}\frac{\partial\psi_2}{\partial\boldsymbol{C}_{e2}}\boldsymbol{F}_i^{-T}\tag{6}$$

respectively. The Mandel stress tensors

$$\boldsymbol{M}_1=2\rho_0\boldsymbol{C}_{e1}\frac{\partial\psi_{e1}}{\partial\boldsymbol{C}_{e1}},\quad \boldsymbol{M}_2=2\rho_0\boldsymbol{C}_{e2}\frac{\partial\psi_2}{\partial\boldsymbol{C}_{e2}}\tag{7}$$

are defined with respect to the intermediate states ic_1 and ic_2, respectively. In addition, the back stress $\bar{\boldsymbol{X}}$ in ic_{1a}, the Mandel stress corresponding to kinematic hardening $\boldsymbol{M}_{kin}$ in ic_{1b}, and the stress-like driving force of isotropic hardening R read

$$\bar{\boldsymbol{X}}=2\rho_0\boldsymbol{F}_{pe}\frac{\partial\psi_{kin}}{\partial\boldsymbol{C}_{pe}}\boldsymbol{F}_{pe}^T,\quad \boldsymbol{M}_{kin}=2\rho_0\boldsymbol{C}_{pe}\frac{\partial\psi_{kin}}{\partial\boldsymbol{C}_{pe}},\quad R=-\rho_0\frac{\partial\psi_{iso}}{\partial\kappa}\tag{8}$$

In order to fulfil the first line of the inequality (5) for arbitrary processes, the following relations for the total second Piola-Kirchhoff stress and entropy must hold

$$\boldsymbol{S}=\boldsymbol{S}_1+\boldsymbol{S}_2,\qquad \eta_S=-\frac{\partial\psi}{\partial\theta}\tag{9}$$

Fourier's law , $\boldsymbol{q}_0=-J\lambda_T\boldsymbol{C}^{-1}\mathrm{Grad}(\theta)$, is applied in addition for the heat flux, referring to the rc, where λ_T denotes the heat conductivity and $J=\det\boldsymbol{F}$ holds.
To guarantee the non-negativeness of internal dissipation (the second line in inequality (5)), a set of evolution equations for the internal variables is presented, which fulfils the inequality. Based on the proposed formulation of Reese and Govindjee [3], the evolution of the inelastic deformation is given by

$$\boldsymbol{D}_i=\frac{1}{2\tau\mu_2}\left(\boldsymbol{M}_2-\frac{1}{3}\mathrm{tr}(\boldsymbol{M}_2)\boldsymbol{I}\right)+\frac{1}{9\tau K_2}\mathrm{tr}(\boldsymbol{M}_2)\boldsymbol{I}.\tag{10}$$

In the latter expression, the bulk modulus and shear modulus corresponding to the molecular network resistance are denoted by $K_2(\theta)$ and $\mu_2(\theta)$, respectively. The relaxation time $\tau(\boldsymbol{S}_2,\boldsymbol{C},\theta,\chi)$ must be greater than zero and is in general a non-linear function of $\boldsymbol{S}_2$, $\boldsymbol{C}$,

θ, and χ.
In this work no pressure dependence, nor tension-compression asymmetry of the yield behaviour is assumed. Hence, a yield function of von Mises type is proposed

$$\Phi = ||\mathrm{dev}(\boldsymbol{M}_1) - \mathrm{dev}(\bar{\boldsymbol{X}})|| - \sqrt{\frac{2}{3}}(\sigma_y - R) \tag{11}$$

Here, the initial yield stress $\sigma_y(\theta, \chi)$ is introduced and dev$(*)$ denotes the deviatoric part of a quantity. The associative plastic flow rule and the evolution equations for kinematic and isotropic hardening are

$$\boldsymbol{D}_p = \dot{\lambda}\frac{\partial \Phi}{\partial \boldsymbol{M}_1} = \dot{\lambda}\frac{\mathrm{dev}(\boldsymbol{M}_1) - \mathrm{dev}(\bar{\boldsymbol{X}})}{||\mathrm{dev}(\boldsymbol{M}_1) - \mathrm{dev}(\bar{\boldsymbol{X}})||}, \quad \boldsymbol{D}_{pi} = \dot{\lambda}\frac{b}{c}\mathrm{dev}(\boldsymbol{M}_{kin}), \quad \dot{\kappa} = \dot{\lambda}\frac{\partial \Phi}{\partial R} = \sqrt{\frac{2}{3}}\dot{\lambda} \tag{12}$$

respectively, where $\dot{\lambda}$ is the plastic multiplier. The equation for $\boldsymbol{D}_{pi}$ represents nonlinear kinematic hardening of Armstrong-Frederick type in which $b(\theta)$ and $c(\theta)$ are material parameters. Finally, the elasto-plastic model is supplemented by the Kuhn-Tucker conditions $\Phi \leq 0$, $\dot{\lambda} \geq 0$, and $\Phi\dot{\lambda} = 0$.
To predict the relative degree of crystallinity χ_c, the non-isothermal representation of the Avrami equation by means of the modified Nakamura-Ziabicki framework [4] was found to be a well-suited model (cf. chapter 3). Inserting the proposed form into the relation for the total degree of crystallinity χ (cf. equation 1) and differentiating the latter with respect to time yields the evolution equation for χ.

$$\dot{\chi} \approx \dot{\chi}_c\frac{\Delta h_m}{\Delta h_f^{100}} = n\ K_c(1-\chi_c)\left(\int_{t_{on}}^{t} K_c dt\right)^{n-1}\frac{\Delta h_m}{\Delta h_f^{100}} \geq 0 \tag{13}$$

The Avrami exponent n represents the nucleation mechanism and growth dimension and is assumed to be temperature independent. The temperature and cooling rate dependent parameter K_c is given by an empirical function proposed by [5]

$$K_c = K_{max}\ \exp\left(-\frac{4\ln(2)(\theta - \theta_{max})^2}{D^2}\right) \tag{14}$$

where the Nakamura-Ziabicki crystallisation parameters $K_{max}(\dot{\theta})$, $\theta_{max}(\dot{\theta})$ and $D(\dot{\theta})$ are depending on the cooling rate. The starting time of the crystallisation process t_{on} is determined by the cooling rate depending onset temperature $\theta_{on}(\dot{\theta})$.
It can be shown, that the set of evolution equations (10) and (12) fulfils the non-negativeness requirement of the Clausius-Duhem inequality (5) (cf. [3] and [6]). The thermodynamic consistency of the chosen evolution law for $\dot{\chi}$, will be discussed briefly. Concomitant with the assumption of a crystallisation process from a relaxed, static melt, the energy terms depending on the deformation (i.e. ψ_{e1}, ψ_{kin}, ψ_{iso}, and ψ_2) are zero if $\dot{\chi} > 0$. In addition, for the energy associated with transformation $\partial\psi_\chi/\partial\chi < 0$ holds if $\theta < \theta_{On}$ (cf. equation (20)) and thus the remaining inequality $-\rho_0(\partial\psi_\chi/\partial\chi)\dot{\chi} \geq 0$ is always fulfilled.

2.2 Specific choices for energy terms

To conclude the constitutive framework, a set of volumetric energy terms Ψ is specified in this section. For the elastic energy contribution of the molecular network resistance a compressible version of the widely used Arruda-Boyce model [7] is chosen

$$\Psi_2(\boldsymbol{C}_{e2},\theta) = K_2\left(\frac{J_{e2}^2-1}{4} - \ln(J_{e2})\left(\frac{1}{2}+3\alpha_{T2}(\theta-\theta_0)\right)\right) + \mu^*\sum_{i=1}^{5}\frac{C_i}{\lambda_m^{2i-2}}\left(\mathrm{tr}(\bar{\boldsymbol{C}}_{e2})^i - 3^i\right) \tag{15}$$

The latter expression is a function of the isochoric part $\bar{\boldsymbol{C}}_{e2} = \bar{\boldsymbol{F}}_{e2}^T\bar{\boldsymbol{F}}_{e2}$ of the elastic right Cauchy-Green tensor, where $\bar{\boldsymbol{F}}_{e2} = J_{e2}^{-\frac{1}{3}}\boldsymbol{F}_{e2}$ and $J_{e2} = \det\boldsymbol{F}_{e2} = \sqrt{\det\boldsymbol{C}_{e2}}$ holds. The constant parameter λ_m relates to the locking stretch of a fully extended chain, $\alpha_{T2}(\theta,\chi)$ is the coefficient of thermal expansion corresponding to the network resistance and θ_0 is a reference temperature. The parameter μ^* and the tuple C_i are defined as

$$\mu^* = \mu_2\frac{1}{1+\frac{3}{5\lambda_m^2}+\frac{99}{175\lambda_m^4}+\frac{513}{875\lambda_m^6}+\frac{42039}{67375\lambda_m^8}}, \quad C_i = \left(\tfrac{1}{2} \quad \tfrac{1}{20} \quad \tfrac{11}{1050} \quad \tfrac{19}{7000} \quad \tfrac{519}{67375}\right) \tag{16}$$

For the intermolecular resistance a Neo-Hookean material with combined linear and non-linear isotropic hardening of Voce type and non-linear kinematic hardening of Armstrong-Frederick type is considered. The corresponding energy terms are

$$\begin{aligned}\Psi_{e1} =& \frac{\mu_1}{2}\left(\mathrm{tr}(\boldsymbol{C}_{e1})-3\right) - \mu_1\ln(J_{e1}) + \frac{\Lambda_1}{4}\left(\det(\boldsymbol{C}_{e1}) - 1 - 2\ln(J_{e1})\right)\\ &- 3K_1\alpha_{T1}(\theta-\theta_0)\ln(J_{e1})\end{aligned} \tag{17}$$

$$\Psi_{kin} = \frac{c}{2}(\mathrm{tr}(\boldsymbol{C}_{pe})-3) - c\ln(J_{pe}) \tag{18}$$

$$\Psi_{iso} = (\sigma_\infty-\sigma_y)\left(\kappa+\frac{\exp(-\beta\kappa)}{\beta}\right) + \frac{1}{2}H\kappa^2 \tag{19}$$

where $J_{e1} = \det\boldsymbol{F}_{e1}$ is defined. The material parameters $\mu_1(\theta,\chi)$, $\Lambda_1(\theta,\chi)$, $K_1(\theta,\chi)$, $\alpha_{T1}(\theta,\chi)$, $\sigma_\infty(\theta,\chi)$, $\beta(\theta,\chi)$, and $H(\theta,\chi)$ corresponding to the elasto-plastic model, are the Lamé constants, bulk modulus, coefficient of thermal expansion, and isotropic hardening parameters, respectively. It is of note, that the specific functions for the introduced material parameters are provided in chapter 3. The specific energy associated with crystallisation, which contributes in an important manner to the heat release of fusion (cf. equation (21)), is given by

$$\psi_\chi = \Delta h_f^{100}\frac{\theta-\theta_{On}}{\theta_{On}}\chi \tag{20}$$

2.3 Heat generation due to dissipation and crystallisation

The heat generation r_t due to plastic r_1 and viscous dissipation r_2 and due to exothermic crystallisation r_χ is briefly discussed in this paragraph. The terms can be derived in a

consistent manner from the local form of the energy balance and the Helmholtz free energy

$$r_t = \underbrace{\left(\boldsymbol{M}_1 - \theta\frac{\partial \boldsymbol{M}_1}{\partial\theta} - \bar{\boldsymbol{X}} + \theta\frac{\partial \bar{\boldsymbol{X}}}{\partial\theta}\right) : \boldsymbol{D}_p + \left(\boldsymbol{M}_{kin} - \theta\frac{\partial \boldsymbol{M}_{kin}}{\partial\theta}\right) : \boldsymbol{D}_{pi} + \left(R - \theta\frac{\partial R}{\partial\theta}\right)\dot{\kappa}}_{r_1}$$
$$+ \underbrace{\left(\boldsymbol{M}_2 - \theta\frac{\partial \boldsymbol{M}_2}{\partial\theta}\right) : \boldsymbol{D}_i}_{r_2} + \underbrace{\rho_0\ \Delta h_f^{100}\ \dot{\chi}}_{r_\chi} \tag{21}$$

Noteworthy, the dissipation due to thermo-elastic coupling $(\partial \boldsymbol{S}/\partial\theta) : (1/2\dot{\boldsymbol{C}})$ is assumed to be negligibly small and is thus omitted in the latter expression.

2.4 Aspects of numerical implementation

For convenience the derivation of the constitutive equations was carried out in the intermediate configurations. However, for the numerical implementation as an user material subroutine *UMAT* into the commercial FEM software *ABAQUS*/Standard, the model equations need to be represented in the current configuration. To this end, several tensorial pull-back and push-forward operations are applied. The algorithmic implementation is based on the works of Dettmer and Reese [8] and Vladimirov et al. [6]. For the numerical integration of the evolution equations (10) and (12) the exponential map algorithm, which preserves plastic volume and the symmetry of the internal variables, is applied and a local system of 16 non-linear scalar equations is solved in an efficient manner. The evolution equation of the total degree of crystallinity is discretized by means of the implicit Euler method and the trapezoidal scheme is used to numerically approximate the integral in equation (13).

3 PARAMETER CALIBRATION

In this section, the characterisation procedure to obtain the material parameter set is discussed briefly. During the computational solution procedure, cubic spline interpolation is applied to interpolate between the parameters presented in the following.
In order to investigate the crystallisation kinetics of Polyamide 6 (*Ultramid B40*, kindly provided by BASF), isothermal (crystallisation at 192°C, 194°C, 196°C and 198°C) and non-isothermal DSC analysis (constant cooling rates of 5°C/min, 10°C/min, 20°C/min, 40°C/min, 60°C/min, and 100°C/min) are conducted with the *DSC 1* from *Mettler Toledo*. Based on the DSC data, the relative degree of crystallinty χ_c over time is computed (cf. equation 1). The constant Avrami exponent n =2.38 is obtained from linear regression of the classical double logarithmic form of the isothermal and non-isothermal DSC data. The remaining, cooling rate dependent parameters of the non-isothermal model (cf. equations (13) and (14)) are obtained from non-linear optimization of the non-isothermal DSC data and are depicted in table 1. The non-isothermal experimental data and the corresponding fit of the proposed model is shown in figure 1.

The mechanical parameters are obtained from uniaxial tensile test. Different loading

Table 1: Parameters for modified Nakamura-Ziabicki model determined by non-linear optimization

$\dot{\theta}$ [K/min]	K_{max} [1/min]	θ_{max} [K]	D [K]	Δh_m [J/g]
5	9.51	348.22	102.27	56.89
10	13.73	348.46	100.48	54.57
20	9.28	351.10	109.52	54.16
40	7.77	355.17	116.97	50.48
60	5.54	362.99	128.31	48.24
100	4.80	359.49	125.64	43.92

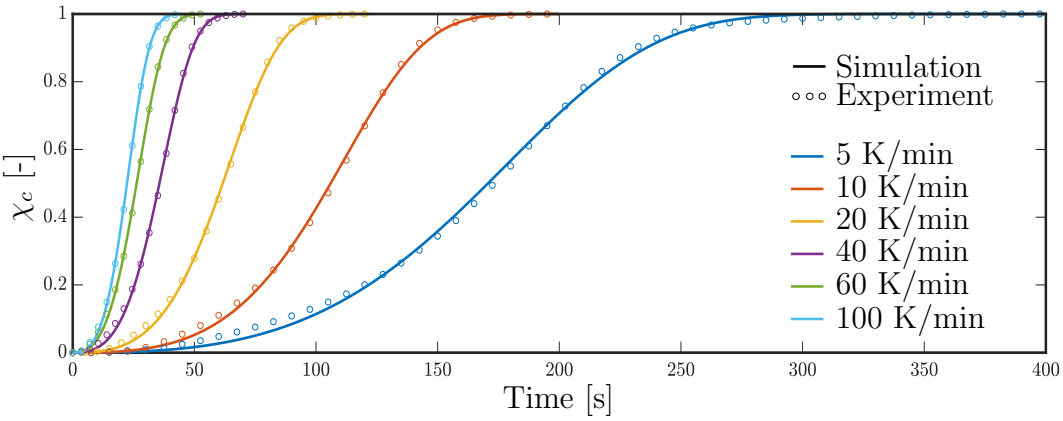


Figure 1: Non-isothermal DSC data and corresponding model response

procedures (monotonic loading, cyclic loading, and relaxation tests) at different loading rates ($v_{min} = 1$ mm/min and $v_{max} = 10$ mm/min) are performed at varying temperatures below and above the glass transition temperature ($\theta_g \approx 80$°C) at 20°C, 50°C, 120°C, and 160°C. Dried specimens (type 5A in accordance with ISO 527-2:2012), which have been produced by injection moulding, are tested for two different degrees of crystallinity (χ_{min}= 23 % and χ_{max}= 28 %). Digital image correlation (DIC) is applied to obtain the true stress (Cauchy stress σ_1) over stretch λ_1 relation in longitudinal 1-direction (cf. figure 2). Based on these results a staggered characterisation scheme is developed, in order to obtain a unique set of mechanical parameters for each considered temperature (cf. table 2). It should be noted that due to the lack of compression data no information about the Bauschinger effect is available. Consequently, only isotropic hardening is considered and the parameters corresponding to kinematic hardening i.e. c and b are set to very small values. Infrared thermography (IR) revealed a significant temperature increase, related to adiabatic self-heating, accompanied by thermal softening, for higher loading rates at moderate stretch levels of 5 %. Due to this fact, the (isothermal) material parameters are only fitted up to this point for v_{max}.

The experimental data for monotonic tensile test at different loading rates and for varying temperatures and degrees of crystallinity is depicted in figure 2, together with the

Table 2: Set of mechanical parameters at different temperatures

Function	Parameter at:	20 °C	50 °C	120 °C	160 °C
$E_1 = \chi E_{1,0}(\theta)$	$E_{1,0}$ [MPa]	5510	3923	1040	851
$E_2 = E_2(\theta)$	E_2 [MPa]	1210	703	130	75
$\nu_1 = \nu_2$	ν_1 [-]	0.35	0.35	0.35	0.35
$\sigma_y = \chi\sigma_{y,0}(\theta)$	$\sigma_{y,0}$ [MPa]	120	45	24	22
$\beta = \chi\beta_0(\theta)$	β_0 [-]	2712	2021	200	195
$H = \chi H_0(\theta)$	H_0 [MPa]	239	669	181	171
$\sigma_\infty = \chi^{\alpha(\theta)}\sigma_{\infty,0}(\theta)$	$\sigma_{\infty,0}$ [MPa]	57.5	66.0	715.0	716.0
	α [-]	0.154	0.682	2.651	2.425
$\tau = \tau_0(\theta)\|\boldsymbol{B}\|^{\varphi(\theta)}\exp(\|\boldsymbol{\sigma}_2\|)^{-\delta(\theta)}$	τ_0 [s]	463	220	96	72
	φ [-]	6.624	5.014	2.525	2.425
	δ [-]	0.196	0.277	0.421	0.621

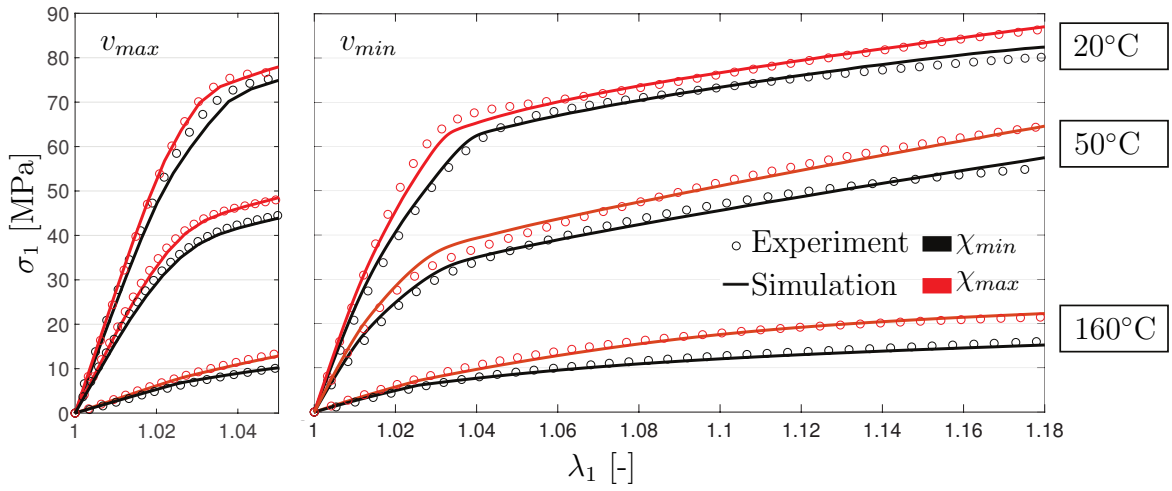


Figure 2: Monotonic, uniaxial extension - Experimental data and corresponding model response

corresponding fit of the proposed model.

The thermal material properties are obtained from the literature. Based on experimental investigations a constant heat conductivity is considered $\lambda_T = 0.27$ W/Km [9]. In line with the data provided in [1], the following function for the density is assumed $\rho_0 = \chi\, 0.001195 + (1-\chi)0.00109$ g/mm^3. For simplicity, the coefficient of thermal expansion is assumed to be constant $\alpha_1 = \alpha_2$=0.876·10^{-4} (cf. [10]). In line with the work [11], the following relation for the heat capacity is assumed $c_p = 4.502\theta + 138.7$ mJ/gK.

4 COMPUTATIONAL EXAMPLE

In order to investigate the crystallisation process and structural response, a thermo-mechanically coupled boundary value problem is considered. In two separate computations, the surface of a plate is subjected to different cooling rates (80 K/min and 15 K/min) until a temperature of 120 °C is reached at t_h (cf. figure 3). Next, the temperature is held constant for 50 s to obtain a homogeneous temperature field. Subse-

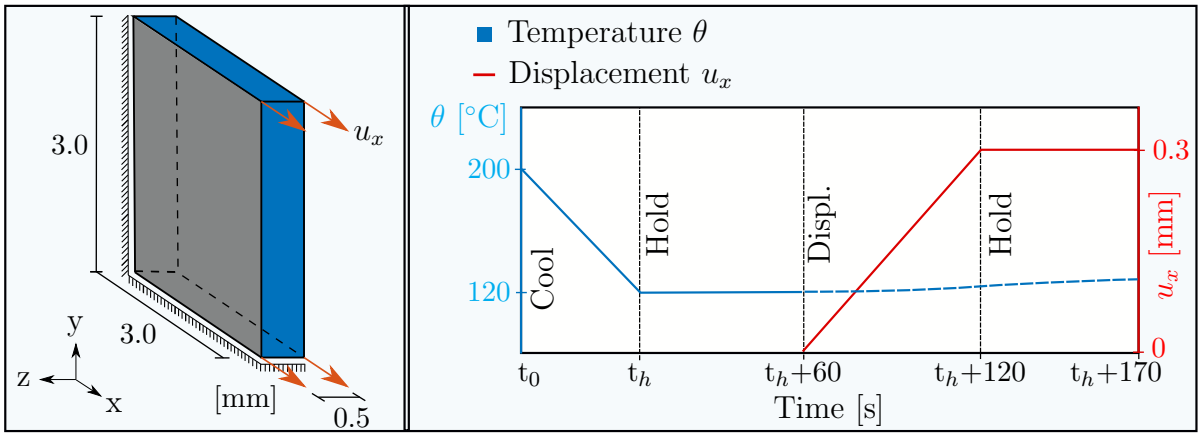


Figure 3: Geometry, boundary conditions and applied loading procedure

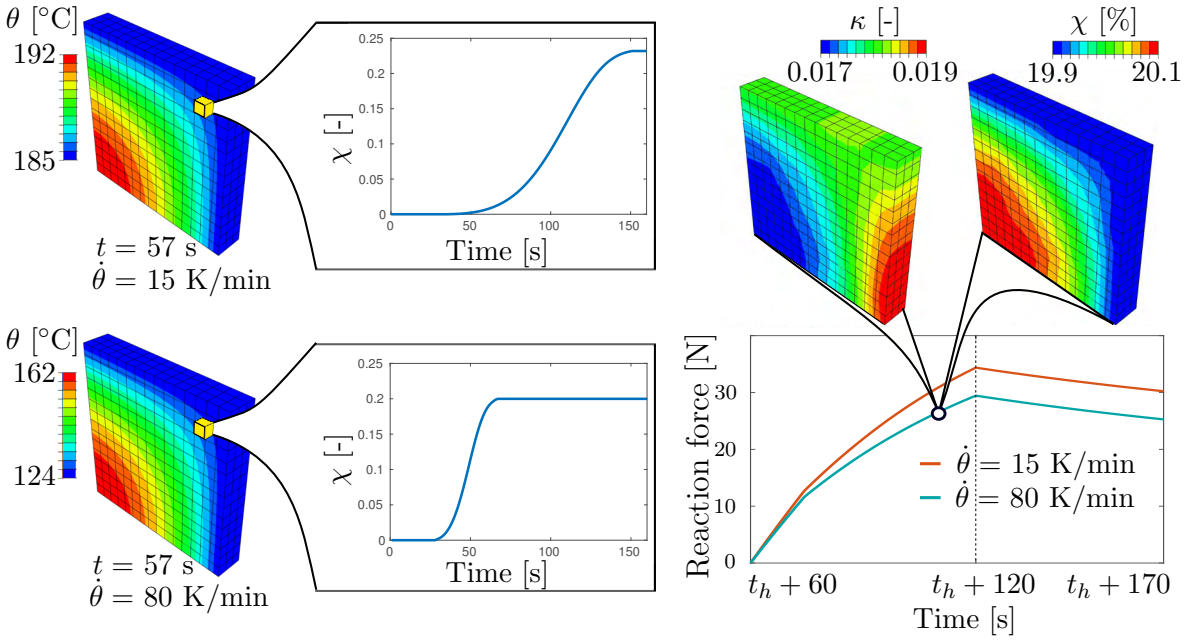


Figure 4: Reaction force, temperature θ, (evolution of) total degree of crystallinity χ and accumulated plastic strain κ

quently, a displacement is linearly increased over time until a final value of $u_x = 0.3$ mm is

prescribed. In this step, the temperature boundary conditions are removed to investigate adiabatic heating. In the last step, the displacement is held constant for 50 s to allow for relaxation. The reaction force - time relation, the total degree of crystallinity χ, the temperature θ, and the accumulated plastic strain κ for selected time steps are displayed in figure 4, for the two different loading procedures.
During the cooling phase, temperature gradients and non-constant cooling rates arise, which result in locally varying crystallisation conditions and thus in a (slightly) varying crystallinity of the structure. Consequently, the stress distribution is heterogeneous as well. Naturally, the different thermal treatments lead to a difference in the absolute degree of crystallinity for the two considered examples. The dependence of the macroscopic material behaviour on the underlying microstructure is clearly visible from the reaction force - time relation (i.e. increasing stiffness, hardening and yield stress with increasing degree of crystallinity). Furthermore, moderate adiabatic heating due to plastic and viscous dissipation is observed.

5 CONCLUSION

In the present work, a thermo-mechanically coupled and thermodynamically consistent constitutive framework at finite strains was proposed, to predict the material response of semi-crystalline polymers in the context of thermoforming processes. To account for the morphology of the underlying microstructure, the total degree of crystallinity was introduced as an additional internal variable, which contributes in an important manner to the elastic, viscous and plastic response of the material. The crystallisation kinetics during cooling from the melt are modelled by a non-isothermal modification of the Avrami model, where a static, relaxed melt is presumed. The set of material parameters is characterized for Polyamide 6 (*Ultramid B40*) and obtained from isothermal and non-isothermal DSC analysis and numerous, uniaxial tensile experiments. The experimental data and simulated behaviour is in good agreement.
The model response is demonstrated in a thermo-mechanically-coupled boundary value problem. The phenomenological approach allows to account for the complex crystallisation phenomena on the micro-scale, with sufficient accuracy. In addition, the model exhibits great convergence behaviour and numerical robustness. To the authors' knowledge, there is no comparable model available in the literature, which accounts for the thermal, mechanical and crystallisation behaviour and the corresponding complex interactions.

Acknowledgements: Financial support of the project RE 1057/41 by the German Science Foundation (DFG) is gratefully acknowledged. Furthermore, the authors are grateful for the provision of *Ultramid B40* by BASF SE.

References

[1] T.D. Fornes and D.R. Paul. Crystallization behavior of nylon 6 nanocomposites. *Polymer*, (2003) **44**:3945–3961.

[2] G. Ayoub, F. Zaïri, C. Fréderix, J.M. Gloaguen, M. Naït-Abdelaziz, R. Seguela and J.M. Lefebvre. Effects of crystal content on the mechanical behaviour of polyethylene under finite strains: Experiments and constitutive modelling. *Int. J. Plasticity*, (2011) **27**:492–511.

[3] S. Reese and S. Govindjee. A theory of finite viscoelasticity and numerical aspects. *Int. J. Solids Struct.*, (1998) **35**:3455–3482.

[4] K. Nakamura, K. Katayama and T. Amano. Some aspects of nonisothermal crystallization of polymers. II. Consideration of the isokinetic condition. *J. Appl. Polym. Sci.*,(1973) **17**:1031–1041.

[5] A. Ziabicki. *Fundamentals of Fibre Formation: The Science of Fibre Spinning and Drawing*. John Wiley & Sons Ltd, Vol. I. (1976).

[6] I. N. Vladimirov, M. P. Pietryga and S. Reese. On the modelling of non-linear kinematic hardening at finite strains with application to springback – Comparison of time integration algorithms. *Int. J. Numer. Meth. Eng.*, (2008) **75**:1–28.

[7] E. M. Arruda and M. C. Boyce. A three-dimensional constitutive model for the large stretch behavior of rubber elastic materials. *J. Mech. Phys. Solids*, (1993) **41**:389–412.

[8] W. Dettmer and S. Reese. On the theoretical and numerical modelling of Armstrong-Frederick kinematic hardening in the finite strain regime. *Comput. Method. Appl. M.*,(2004) **193**:87–116.

[9] M. Li, Y. Wan, Z. Gao, G. Xiong, X. Wang, C. Wan and H. Luo. Preparation and properties of polyamide 6 thermal conductive composites reinforced with fibers. *Mater. Design.*, (2013) **51**:257–261.

[10] B. Jurkowski, Y. A. Olkhov, K. Kelar and O. M. Olkhova. Thermomechanical study of low-density polyethylene, polyamide 6 and its blends. *Eur. Polym. J.*, (2002) **38**:1229–1236.

[11] C. Millot, L.-A. Fillot, O. Lame, P. Sotta and R. Seguela. Assessment of polyamide-6 crystallinity by DSC. *J. Therm. Anal. Calorim.*, (2015) **112**:307–314.

XV International Conference on Computational Plasticity. Fundamentals and Applications
COMPLAS 2019
E. Oñate, D.R.J. Owen, D. Peric, M. Chiumenti & Eduardo de Souza Neto (Eds)

CRYSTAL PLASTICITY FINITE ELEMENT SIMULATIONS OF CAST α-URANIUM

NICOLÒ GRILLI*, ALAN C.F. COCKS* AND EDMUND TARLETON†

* Department of Engineering Science
University of Oxford
Parks Road, OX1 3PJ, UK
e-mail: nicolo.grilli@eng.ox.ac.uk, web page: http://www2.eng.ox.ac.uk/solidmech/

† Department of Materials
University of Oxford
Parks Road, OX1 3PH, UK
e-mail: edmund.tarleton@materials.ox.ac.uk - Web page: https://omg.web.ox.ac.uk

Key words: Uranium, Crystal Plasticity, Finite Element method, Twinning, Thermal residual strains

Abstract. α-uranium, the stable phase of uranium up to 670°C, has a base-centred orthorombic crystal structure. This crystal structure gives rise to elastic and thermal anisotropy, meaning α-uranium exhibits complex deformation and fracture behaviour. Understanding the relationship between the microstructure and mechanical properties is important to prevent fracture during manufacture and usage of components. The lattice of α-uranium corresponds to a distorted close-packed-hexagonal crystal structure and it exhibits twins of both the 1st and 2nd kind. Therefore, detailed examination of the behaviour of α-uranium can also contribute to the general understanding of the interaction between plasticity, twinning and fracture in hcp crystals. Plastic deformation in α-uranium can be accommodated by 4 slip systems and 3 twin systems, previously identified by McCabe et al. These deformation modes are implemented into a crystal plasticity finite element (CPFE) material model. A temperature dependent, dislocation density based law is implemented to describe the critical resolved shear stress on the different slip/twin systems. The strong anisotropic thermal expansion behaviour is taken into account to simulate the development of internal residual stresses following casting of the material. During cooling, the internal stresses in α-uranium are sufficient to induce plasticity. This effect is quantified using polycrystal simulations, in which first the temperature is decreased, then plastic relaxation takes place, followed by application of a mechanical load. The asymmetry between mechanical properties in tension and compression, due to the presence of twins, is investigated. The model is calibrated using stress strain curves and the lattice strain found from published neutron diffraction experiments carried out on textured samples at ISIS. The strength of the slip systems is found to be lower than in fine

©British Crown Owned Copyright 2019/AWE

grained material, while the strength of the twin system is similar to single crystals. The CPFE method allows the heterogeneity of the strain between neighbouring grains and its influence on the evolution of the internal stress state to be investigated.

1 Introduction

α-uranium is the stable phase of uranium up to 670°C and it is used for armour, projectiles and radiation shielding due to its high density (19.1 g/cm^3). The highly anisotropic crystal structure of α-uranium leads to anisotropic elastic coefficients [1] and thermal expansion coefficients [2]. Large thermal residual stresses develop during the casting process [3] that can facilitate fracture. The lattice of α-uranium is orthorhombic.

Dislocation glide and twinning create plastic deformation in α-uranium [4], depending on the temperature [5], loading conditions [6], grain shape [7] and size [6]. 8 active slip systems and 10 twin variants are present, which have very different critical resolved shear stresses (CRSS) [4, 8]. However, only the 2 variants of $\{130\}\langle 3\bar{1}0\rangle$ occupy a significant volume fraction of the crystal [9]. Fracture parallel to $\{172\}$ twin planes is observed [10], leading to the hypothesis that twin parting, similar to some minerals, is the main fracture initiation mechanism. However, cracks are also observed at the tip of twins and at the intersection between twins and grain boundaries [11]. To design and manufacture safe components, a quantitative model is necessary to predict the deformation and fracture behaviour of polycrystalline α-uranium.

Cast α-uranium has a mixed grain size, ranging from millimetres to hundreds of micrometres [12]. The grains are clustered into areas in which the misorientation is within 5°[13]. The recrystallization kinetics during heat treatment is affected by the texture [14] and rolling can transform the material into fine grained α-uranium [15], with grain sizes between 15 and 25 μm [15, 9]. Therefore, the effect of the grain size, spatial arrangement and texture needs to be quantified.

Previously, the elasto-plastic and visco-plastic self-consistent frameworks (EPSC and VPSC) have been used to model plastic deformation in α-uranium [16, 3]. These methods approximate a grain as a spherical inclusion inside a homogenised effective medium (HEM) [17]. In this paper, the crystal plasticity finite element (CPFE) method is used, which is able to model strain field inhomogeneities between neighbouring grains [18, 19]. The constitutive model is calibrated using stress strain curves and in-situ neutron diffraction experiments [13] carried out at the ENGIN-X beamline of the ISIS Neutron Source, Rutherford Appleton Laboratory, on coarse-grained α-uranium, with an average grain size of 200 μm.

A calibration of the values of the critical resolved shear stress (CRSS) for slip and twinning is carried out using polycrystal simulations. It shows that the CRSS for slip is lower than in fine grained specimens [16], while the CRSS for twinning is similar to single crystal specimens [5]. The Hall-Petch relationship turns out to be different for slip and twinning. Simulations of the quenching process are carried out to find the magnitude of the thermal residual stress for different textures. Finally, it is shown that grain clustering

leads to higher axial stresses.

2 Material Model

The finite strain crystal plasticity finite element framework is used [20], in which the deformation gradient is decomposed into elastic and plastic parts:

$$\boldsymbol{F} = \boldsymbol{F}_e \boldsymbol{F}_p \ . \tag{1}$$

The evolution of $\boldsymbol{F}_p$ takes into account the activity of the slip and twin systems [21]. The plastic velocity gradient is:

$$\boldsymbol{L}_p = \dot{\boldsymbol{F}}_p \boldsymbol{F}_p^{-1} = \left(1 - \sum_{\beta=1}^{N_{\text{twin}}} f_\beta\right) \sum_{\alpha=1}^{N_{\text{slip}}} \dot{\gamma}_\alpha \left(\boldsymbol{\sigma}\right) \boldsymbol{s}_\alpha \otimes \boldsymbol{n}_\alpha + \sum_{\beta=1}^{N_{\text{twin}}} \dot{f}_\beta \left(\boldsymbol{\sigma}\right) \gamma_\beta^{\text{twin}} \boldsymbol{s}_\beta \otimes \boldsymbol{n}_\beta \ , \tag{2}$$

where $\dot{\gamma}_\alpha$ is the shear rate on the slip system α, $\dot{f}_\beta$ is the rate of increase of the twin volume fraction on the twin system β and $\gamma_\beta^{\text{twin}}$ is the constant shear on the twin system β. Both $\dot{\gamma}_\alpha$ and $\dot{f}_\beta$ depend on the Cauchy stress $\boldsymbol{\sigma}$. $\dot{\gamma}_\alpha$ and $\dot{f}_\beta$ are described by a power law dependence on the resolved shear stress τ_α [16]. The twin volume fraction increases only if the resolved shear stress τ_β is positive. $\boldsymbol{s}_\alpha$ and $\boldsymbol{n}_\alpha$ are the slip direction and slip plane normal of the slip system α. $\boldsymbol{s}_\beta$ and $\boldsymbol{n}_\beta$ are the twin direction and twin plane normal of the twin system β. Table 1 contains the slip and twin systems used in the simulations and the lattice constants of α-uranium are reported in Table 3.

The Cauchy stress increment $\Delta\boldsymbol{\sigma}$ at every time step is proportional to the elastic strain increment [22]. The stiffness tensor of α-uranium at room temperature is [1]:

$$\mathbb{C} = \begin{bmatrix} 214.74 & 46.49 & 21.77 & 0 & 0 & 0 \\ 46.49 & 198.57 & 107.91 & 0 & 0 & 0 \\ 21.77 & 107.91 & 267.11 & 0 & 0 & 0 \\ 0 & 0 & 0 & 124.44 & 0 & 0 \\ 0 & 0 & 0 & 0 & 73.42 & 0 \\ 0 & 0 & 0 & 0 & 0 & 74.33 \end{bmatrix} \text{ GPa} \ , \tag{3}$$

and a linear decrease of the entries with temperature is imposed, as found in single crystals [5]. Thermal eigenstrains are considered using temperature dependent thermal expansion coefficients, as reported in [2]. The temperature dependent critical resolved shear stress $\tau_\alpha^c(T)$ of the slip systems is calculated using a dislocation density based model, developed by McCabe et al. [16]:

$$\tau_\alpha^c(T) = \left[\tau_\alpha^0 + 0.9 \ b_\alpha \mu_\alpha \sqrt{\rho_\alpha^{\text{for}}} - 0.086 \ b_\alpha \mu_\alpha \sqrt{\rho^{\text{sub}}} \log\left(b_\alpha \sqrt{\rho^{\text{sub}}}\right)\right] \exp\left(-\frac{(T - T_0)}{B_\alpha}\right) \ . \tag{4}$$

This represents the resolved shear stress at which the shear rate $\dot{\gamma}_\alpha$ has the same magnitude as the externally applied deformation shear rate. ρ_α^{for} is the forest dislocation density on the slip system α and ρ^{sub} the dislocation density in the substructures [23]. The critical

Slip system	$\boldsymbol{s}_\alpha^0$	$\boldsymbol{n}_\alpha^0$	b_α (nm)	μ_α (GPa)
$\alpha = 1$ (wall)	$[100]$	(010)	0.285	74.330
$\alpha = 2$ (floor)	$[100]$	(001)	0.285	73.420
$\alpha = 3$ (chimney)	$[1\bar{1}0]$	(110)	0.651	92.255
$\alpha = 4$ (chimney)	$[110]$	$(1\bar{1}0)$	0.651	92.255
$\alpha = 5$ (roof)	$[1\bar{1}2]$	(021)	1.185	115.67
$\alpha = 6$ (roof)	$[\bar{1}\bar{1}2]$	(021)	1.185	115.67
$\alpha = 7$ (roof)	$[112]$	$(0\bar{2}1)$	1.185	115.67
$\alpha = 8$ (roof)	$[1\bar{1}\bar{2}]$	$(0\bar{2}1)$	1.185	115.67

Twin system	$\boldsymbol{s}_\beta^0$	$\boldsymbol{n}_\beta^0$
$\beta = 1$	$[3\bar{1}0]$	(130)
$\beta = 2$	$[\bar{3}\bar{1}0]$	$(\bar{1}30)$

Table 1: Miller indices of the slip and twin systems used in the model [16]. Burgers vectors and projected shear moduli [1, 16].

resolved shear stress, τ_β, of the twin systems is assumed to be constant. The time evolution of the dislocation densities is based on a multiplication-annihilation formalism, as reported in [16], and is calibrated to reproduce the hardening rate [16]. b_α is the Burgers vector and μ_α the projected shear modulus of the slip system α [23, 16]. The values are in Table 1.

Three different sets of parameters for the constant friction stresses τ_α^0 and τ_β, for plastic slip and twinning, are compared in the present study. They are reported in Table 2. The fine grained parameters correspond to 12.5 μm grain size [16], while the single crystal parameters have been obtained using specimens of length 2.5-3 mm [5]. The present material has an average grain size of 200 μm [13] and the parameters in the present study have been calibrated using stress-strain curves and neutron diffraction experiments. The

τ_α^0 (MPa)	Wall	Floor	Chimney	Roof	{130} Twin
Fine grained (McCabe et al. [16])	60	270	295	270	300
Single crystal (Daniel et al. [5])	4	80	168	N/A	25
Coarse grained (present study)	7	10	35	235	25

Table 2: Constant friction stress for the different models.

CRSS for dislocation slip decreases exponentially with temperature, as in equation (4). B_α is a thermal activation parameter [24] and $T_0 = 293$ K is the reference temperature. Model parameters are reported in Table 3.

Polycrystal simulations are carried out by assigning a different rotation matrix $\boldsymbol{R}$ to every grain, which is used to rotate the directions and normals of the slip and twin systems in Table 1.

The model is implemented as a UMAT (user material subroutine) for Abaqus [18], which solves the stress equilibrium equation. The variables ρ_α^{for}, ρ^{sub} and f_β are updated at every time increment. A Newton-Raphson algorithm is used to find the plastic velocity gradient $\boldsymbol{L}_p$ that is compatible with the stress increment and with the elasto-plastic decomposition in equation (1). At every time step the crystal rotation matrix $\boldsymbol{R}$ is updated

Lattice constant (a) [26]	0.2852 nm
Lattice constant (b) [26]	0.5865 nm
Lattice constant (c) [26]	0.4945 nm
Magnitude of shear due to twinning ($\gamma_\beta^{\text{twin}}$) [4]	0.299
Thermal activation parameter for slip (B_α) [24]	140 K

Table 3: Model parameters.

using the continuum elastic spin matrix [25].

3 Polycrystal simulations and elastic lattice strain

To introduce thermal residual stresses, simulations are divided into three phases: first a polycrystal with 8000 ($20 \times 20 \times 20$) cubic grains is cooled down from 400°C to room temperature in 10 s [27], as shown in Figure 1 (a); then, 7000 external grains are removed and the system relaxes for 100 s; finally, deformation is applied along the x axis on the 1000 ($10 \times 10 \times 10$) grains that are in the centre of the original geometry, as shown in Figure 1 (b). The original size of the cubic representative volume is 6000 μm.

The boundary conditions during the three phases are the following. Given the origin O in Figure 1 (a), the surfaces $x = 0$, $y = 0$ and $z = 0$ have zero perpendicular displacement during quenching. During the relaxation phase, given the origin O in Figure 1 (b), the newly created free surfaces $x = 0$, $y = 0$ and $z = 0$ have zero velocity along x, y and z respectively. Finally, pure axial tension or compression along the x axis is applied, up to 1% strain, as shown in Figure 1 (b). The initial value of the dislocation densities ρ_α^{for} and ρ^{sub} is 10^{10} m^{-2} and no twins are present at the beginning of the simulations.

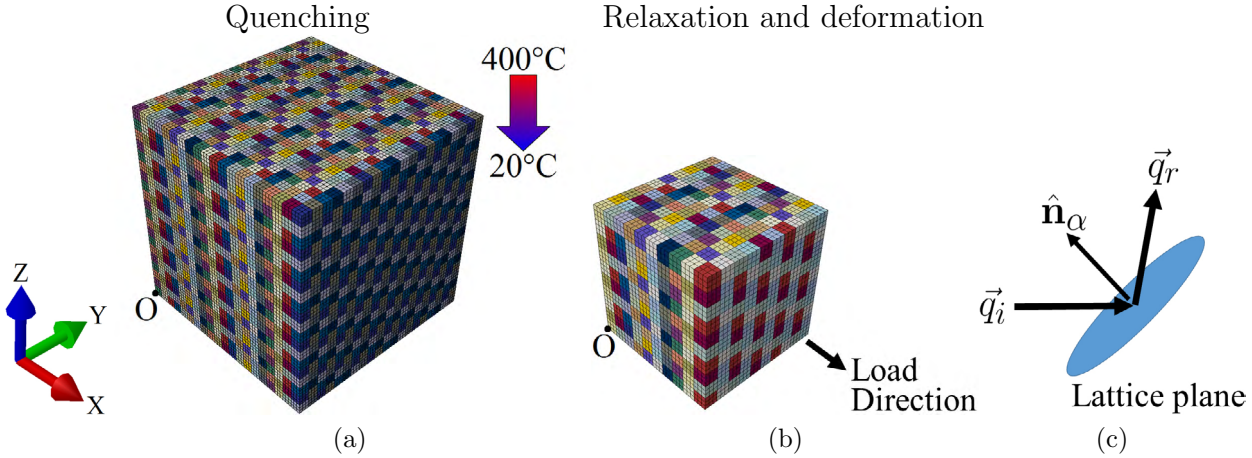
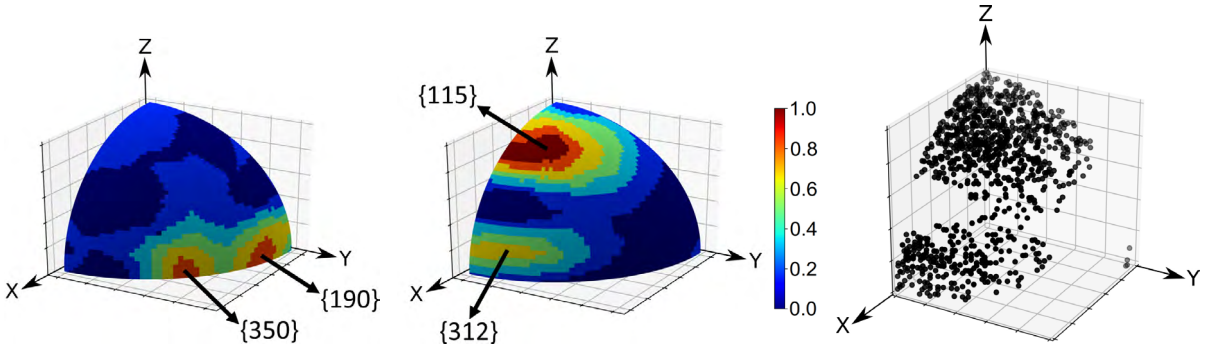


Figure 1: (a) 8000 grains representative volume and mesh during quenching. (b) 1000 grains in the inner part of the representative volume during deformation and load direction. (c) Directions $\vec{\boldsymbol{q}}_i$ and $\vec{\boldsymbol{q}}_r$ of the incident and diffracted neutron beam.

The Green-Lagrange elastic strain tensor is calculated in the crystal lattice coordinate system and its diagonal components are compared with the neutron diffraction experi-

ments. These components will be called (100), (010) and (001) lattice strain in this paper. A grain selection algorithm is developed that selects the grains in which a specific family of lattice planes reflects the neutron beam towards the detector area. The incident neutron beam has direction $\vec{\boldsymbol{q}}_i = \left[1/\sqrt{2}; 1/\sqrt{2}; 0\right]$ and it is reflected by a lattice plane towards the direction $\vec{\boldsymbol{q}}_r$, as shown in Figure 1 (c). The direction $\vec{\boldsymbol{q}}_d = \left[-1/\sqrt{2}; 1/\sqrt{2}; 0\right]$, which is perpendicular to the incident beam, points towards the centre of the detector. Thus, only neutrons diffracted by lattice planes with normals approximately parallel to the load axis are detected. The horizontal detector coverage in the x-y plane is $\pm 14°$, while the vertical coverage, out of the x-y plane, is $\pm 21°$. The simulated Green-Lagrange elastic strain tensor is averaged over the selected grains. For instance, the (100) elastic lattice strain is averaged over grains in which the (100) lattice planes reflect the neutron beam towards the detector.

In the present study, two specimens with different textures C1 and T1 are analysed, as shown in Figure 2 (a) and (b). From these textures, a distribution for the orientations of the 1000 grains in the central part of the representative volume can be obtained, as depicted in Figure 2 (c) for the T1 texture. Each point represents the orientation of the load direction (x axis in the sample coordinate system) in the crystal lattice coordinate system. The outer 7000 grains have a random texture. Two types of spatial arrangement of the 1000 central grains are investigated to understand the effect of grain clustering observed experimentally [13]: the first one has a spatially random grain distribution (RGD); in the second one (GC), the orientations belonging to the two peaks of the probability distribution functions in Figures 2 (a)-(b) ({350} and {190} for the C1 texture, {115} and {312} for the T1 texture) are assigned to grains with low and high z coordinates in Figure 1 (b) respectively. In this second case, the representative volume is similar to a bicrystal with two grains arranged parallel to the load direction.



(a) (b) (c)

Figure 2: (a) Texture of the sample C1, deformed in compression. (b) Texture of the sample T1, deformed in tension. (c) Random distribution of grain orientations, generated with the probability distribution function in (b).

4 Results

4.1 Stress-strain curves

The simulated axial stress on the load surface in Figure 1 (b) is shown in Figure 3 using different material parameters. The parameters for the present study on coarse grained α-uranium in Table 2 are calibrated to fit both the tension and compression experiments. The fine grained parameters lead to the highest stress and also using single crystal parameters the stress is overestimated. If the grain clustering is considered, a higher stress is obtained for the T1 texture.

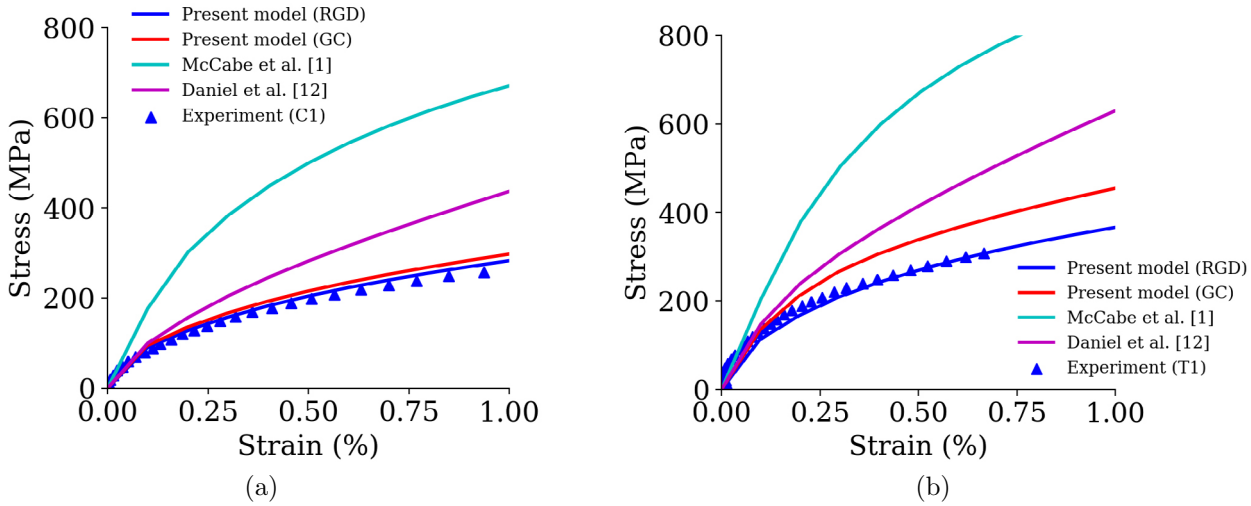


Figure 3: Simulated and experimental stress-strain curves (a) for compression (C1 texture) and (b) for tension (T1 texture).

The T1 texture shows higher stress because of the presence of the {115} grains, which have less active slip and twin modes. The {130} twin system is active in tension for (100)-oriented grains, prevalent in the T1 texture, and in compression for (010)-oriented grains, prevalent in the C1 texture. In the present model, the twin system gives the highest contribution to plastic deformation, followed by wall and floor slip.

The simulated twin volume fraction after quenching, between 5% and 6%, is comparable to that observed by EBSD measurements on the same sample [13]. This provides another validation for the model parameters for coarse grained α-uranium in Table 2.

4.2 Elastic lattice strain

The simulated (100) and (010) elastic lattice strain as a function of the axial stress is shown in Figures 4 and 5. The elastic lattice strain is a measure of the microscopic stress in a grain family; therefore, saturation of the elastic lattice strain indicates that plastic deformation has started only in that grain family.

The present model, without the grain clustering, is the one that best fits the (100)

elastic lattice strain data. The saturation behaviour in the T1 sample is explained with the activation of the {130} twin system, which is not active in compression (sample C1). No saturation of the elastic lattice strain is present if the fine grained material parameters (McCabe et al. [16]) are used because the CRSS for twinning is higher than for slip.

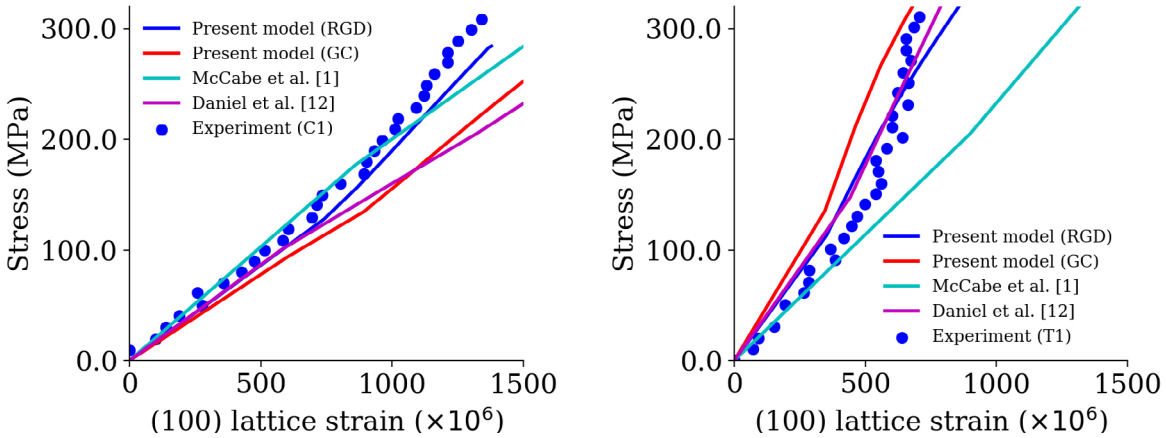


Figure 4: Simulated and measured (100) elastic lattice strain for (a) C1 sample (compression) and (b) T1 sample (tension).

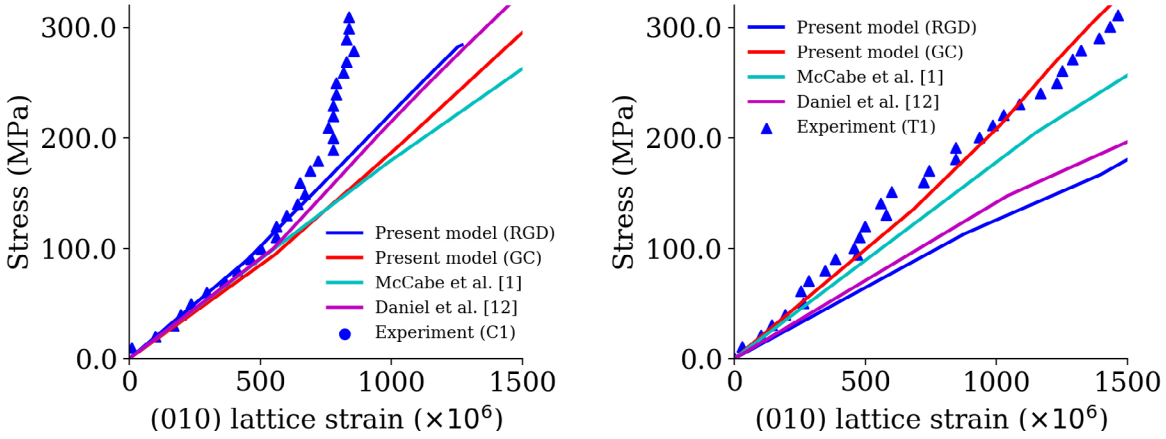
The present model with the grain clustering is the one that best fits the (010) elastic lattice strain of the T1 sample, as shown in Figure 5 (b); however, the saturation behaviour of the C1 sample is not well captured. Twinning is expected in (010)-oriented grains in compression; however, the simulations indicate that both grain families {350} and {190} in Figure 2 (a) have similar plastic deformation due to twinning. Therefore, the simulated mechanical behaviour of the C1 texture is more similar to a single crystal and the microscopic elastic lattice strain is always proportional to the macroscopic stress.

4.3 Thermal residual stress

The calibrated model is used to study the thermal residual stress development during quenching. The Von Mises stress averaged over the 1000 grains in the central part of the representative volume is shown in figure 6 as a function of temperature. The stress reached after cooling is enough to activate the easiest slip modes as well as twinning. It is negligibly higher for the C1 texture and does not depend strongly on the spatial arrangement of the grains.

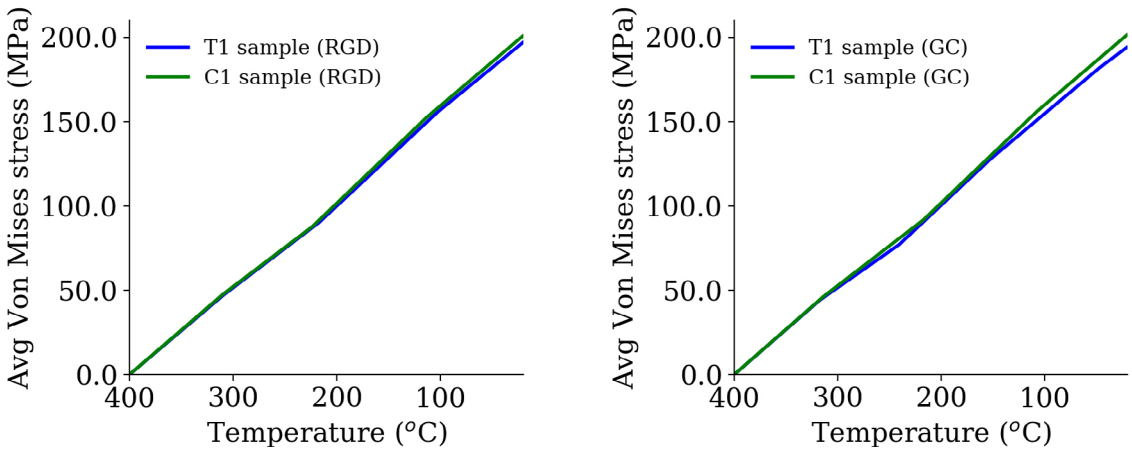
5 Discussion and conclusions

The agreement between the present model and the experimental results for coarse grained α-uranium shows that the CRSS for slip is smaller than for fine grained α-uranium



(a) (b)

Figure 5: Simulated and measured (010) elastic lattice strain for (a) C1 sample (compression) and (b) T1 sample (tension).



(a) (b)

Figure 6: Simulated average Von Mises stress during quenching in case of (a) spatially random grain distribution (RGD) and (b) grain clustering (GC) for the C1 and T1 textures.

[16]. As shown in Section 4.2, the activation of the {130} twin system leads to the tension-compression asymmetry in the (100) elastic lattice strain. This asymmetry is reproduced by the simulations only if the CRSS for twinning is smaller than for chimney and roof slip. The calibrated value of the twinning CRSS (25 MPa) is the same as the value found in single crystals [5] and leads to a twin volume fraction after quenching comparable to the value measured with EBSD [13]. The saturation of the (100) elastic lattice strain in tension

takes place at a macroscopic stress close to 115 MPa, corresponding to a resolved shear stress on the twin system of approximately 54 MPa. This stress is higher than the CRSS (25 MPa) for twinning and shows CPFE simulations are needed to avoid overestimation of the CRSS when analysing neutron diffraction data.

The present simulations suggest that the Hall-Petch dependence [28, 6] is strong for the slip and twin systems of α-uranium for grain size between 12.5 μm and 200 μm. However, there is little grain size dependence of the CRSS for twin formation from 200 μm to millimetre sized single crystals [5].

The formation of grain clusters can significantly change the mechanical properties, as shown by the simulated stress-strain curves in Figure 3 and by the elastic lattice strain in figure 5. The saturation behaviour of the (010) elastic lattice strain in compression, which is not captured by the simulations, may be due to the presence of harder grains, bearing part of the macroscopic stress but placed outside of the neutron beam cross section. The simulations show that the C1 texture, with two grain families at {350} and {190}, has a behaviour similar to a single crystal and the plastic deformation distribution is almost uniform in the two grain families.

In conclusion, a crystal plasticity model is outlined to describe slip and twinning in coarse grained α-uranium. The model predicts not only the stress-strain curves, but also the elastic lattice strain in textured samples, as measured by neutron diffraction experiments. The constitutive model can be applied to find the thermal residual stress after quenching and represents a first step towards understanding the interplay between plasticity and fracture in α-uranium.

Acknowledgements

The authors acknowledge financial support of AWE plc for this research, program manager: Dr John Askew. The authors would like to thank Philip Earp and Prof James Marrow for discussion about their experimental techniques and results. ET acknowledges support from the Engineering and Physical Sciences Research Council under Fellowship grant EP/N007239/1.

REFERENCES

[1] E. S. Fisher and H. J. McSkimin. Adiabatic elastic moduli of single crystal alpha uranium. *Journal of Applied Physics*, 29(10):1473–1484, 1958.

[2] Lowell T. Lloyd and C.S. Barrett. Thermal expansion of alpha uranium. *Journal of Nuclear Materials*, 18(1):55 – 59, 1966.

[3] C.A. Calhoun, J.A. Wollmershauser, D.W. Brown, R.P. Mulay, E. Garlea, and S.R. Agnew. Thermal residual strains in depleted α-U. *Scripta Materialia*, 69(8):566 – 569, 2013.

[4] R.W Cahn. Plastic deformation of alpha-uranium; twinning and slip. *Acta Metallurgica*, 1(1):49 – 70, 1953.

[5] J.S Daniel, B Lesage, and P Lacombe. The influence of temperature on slip and twinning in uranium. *Acta Metallurgica*, 19(2):163 – 173, 1971.

[6] H. Inouye and S.C. Schaffhauser. Low-temperature ductility and hydrogen embrittlement of uranium - a literature review. *ORNL-TM-2563*, 1969.

[7] D.M.R. Taplin and J.W. Martin. The effect of grain shape on the tensile properties of α uranium. *Journal of Nuclear Materials*, 10(2):134 – 139, 1963.

[8] C.A. Calhoun, E. Garlea, T.A. Sisneros, and S.R. Agnew. In-situ neutron diffraction characterization of temperature dependence deformation in -uranium. *Journal of Nuclear Materials*, 502:60 – 67, 2018.

[9] D.W. Brown, M.A.M. Bourke, B. Clausen, D.R. Korzekwa, R.C. Korzekwa, R.J. McCabe, T.A. Sisneros, and D.F. Teter. Temperature and direction dependence of internal strain and texture evolution during deformation of uranium. *Materials Science and Engineering: A*, 512(1):67 – 75, 2009.

[10] R.D. Field, R.J. McCabe, D.J. Alexander, and D.F. Teter. Deformation twinning and twinning related fracture in coarse-grained -uranium. *Journal of Nuclear Materials*, 392(1):105 – 113, 2009.

[11] D.M.R. Taplin. *J. Aust. Inst. Met.*, 12:32, 1967.

[12] E. Garlea, R.L. Bridges, V.O. Garlea, D.A. Carpenter, M.A. Hemphill, and J.S. Morrell. Characterization of a grain size refinement process in cast uranium. *Materials Science and Engineering: A*, 559:210 – 216, 2013.

[13] P Earp, S Kabra, J Askew, and T J Marrow. Lattice strain and texture development in coarse-grained uranium a neutron diffraction study. *Journal of Physics: Conference Series*, 1106(1):012012, 2018.

[14] R.J. McCabe, A.W. Richards, D.R. Coughlin, K.D. Clarke, I.J. Beyerlein, and M. Knezevic. Microstructure effects on the recrystallization of low symmetry alpha-uranium. *Journal of Nuclear Materials*, 465:189 – 195, 2015.

[15] Miroslav Zecevic, Marko Knezevic, Irene J. Beyerlein, and Rodney J. McCabe. Origin of texture development in orthorhombic uranium. *Materials Science and Engineering: A*, 665:108 – 124, 2016.

[16] R.J. McCabe, L. Capolungo, P.E. Marshall, C.M. Cady, and C.N. Tom. Deformation of wrought uranium: Experiments and modeling. *Acta Materialia*, 58(16):5447 – 5459, 2010.

[17] J. W. Hutchinson and Robert Hill. Elastic-plastic behaviour of polycrystalline metals and composites. *Proceedings of the Royal Society of London. A. Mathematical and Physical Sciences*, 319(1537):247–272, 1970.

[18] T.O. Erinosho, A.C.F. Cocks, and F.P.E. Dunne. Texture, hardening and non-proportionality of strain in bcc polycrystal deformation. *International Journal of Plasticity*, 50:170 – 192, 2013.

[19] F. Roters, M. Diehl, P. Shanthraj, P. Eisenlohr, C. Reuber, S.L. Wong, T. Maiti, A. Ebrahimi, T. Hochrainer, H.-O. Fabritius, S. Nikolov, M. Frik, N. Fujita, N. Grilli, K.G.F. Janssens, N. Jia, P.J.J. Kok, D. Ma, F. Meier, E. Werner, M. Stricker, D. Weygand, and D. Raabe. DAMASK the Düsseldorf advanced material simulation kit for modeling multi-physics crystal plasticity, thermal, and damage phenomena from the single crystal up to the component scale. *Computational Materials Science*, 2018.

[20] Suchandrima Das, Felix Hofmann, and Edmund Tarleton. Consistent determination of geometrically necessary dislocation density from simulations and experiments. *International Journal of Plasticity*, 109:18 – 42, 2018.

[21] Surya R. Kalidindi. Incorporation of deformation twinning in crystal plasticity models. *Journal of the Mechanics and Physics of Solids*, 46(2):267 – 290, 1998.

[22] F.P.E. Dunne, D. Rugg, and A. Walker. Lengthscale-dependent, elastically anisotropic, physically-based hcp crystal plasticity: Application to cold-dwell fatigue in ti alloys. *International Journal of Plasticity*, 23(6):1061 – 1083, 2007.

[23] L. Capolungo, I.J. Beyerlein, G.C. Kaschner, and C.N. Tom. On the interaction between slip dislocations and twins in hcp zr. *Materials Science and Engineering: A*, 513-514:42 – 51, 2009.

[24] Miroslav Zecevic, Marko Knezevic, Irene J. Beyerlein, and Rodney J. McCabe. Texture formation in orthorhombic alpha-uranium under simple compression and rolling to high strains. *Journal of Nuclear Materials*, 473:143 – 156, 2016.

[25] Fionn Dunne and Nik Petrinic. *Introduction to computational plasticity*. Oxford university press, 2006.

[26] C. W. Tucker. The crystal structure of the β phase of uranium. *Acta Crystallographica*, 4(5):425–431, Sep 1951.

[27] Marko Knezevic, Laurent Capolungo, Carlos N. Tom, Ricardo A. Lebensohn, David J. Alexander, Bogdan Mihaila, and Rodney J. McCabe. Anisotropic stress strain response and microstructure evolution of textured α-uranium. *Acta Materialia*, 60(2):702 – 715, 2012.

[28] E O Hall. The deformation and ageing of mild steel: III discussion of results. *Proceedings of the Physical Society. Section B*, 64(9):747–753, sep 1951.

XV International Conference on Computational Plasticity. Fundamentals and Applications
COMPLAS 2019
E. Oñate, D.R.J. Owen, D. Peric, M. Chiumenti & Eduardo de Souza Neto (Eds)

EXTENDED CONCEPT OF REPRESENTATIVE DIRECTIONS TO DESCRIBE INELASTIC BEHAVIOUR OF ELECTROSPUN POLYMERS

ALEXEY V. SHUTOV[*] [†]

[*] Lavrentyev Institute of Hydrodynamics
pr. Lavrentyeva 15, 630090 Novosibirsk, Russia
e-mail: alexey.v.shutov@gmail.com, web page: http://sites.google.com/site/materialmodeling

[†] Novosibirsk State University
ul. Pirogova 1, 630090 Novosibirsk, Russia

Key words: Large Strain, Representative Directions, Plasticity, Electrospun Polymers

Abstract. The concept of representative directions allows one to generalize one-dimensional uniaxial material models to more general constitutive equations, suitable for arbitrary multi-axial loading scenarios. The procedure preserves the thermodynamic consistency and the resulting material model satisfies the principle of objectivity. In the current paper, the concept is modified by the introduction of new kinematics. Some features of the resulting constitutive equations as well as the applicability of the extended concept to real materials are discussed. For demonstration purposes, the plastic behaviour of an electrospun polymer is modelled under large strain non-monotonic loading.

1 INTRODUCTION

The development of advanced material models is a multifaceted task, since a number of requirements must be met. First, the developed model must satisfy the general principles of constitutive mechanics, like objectivity, thermodynamic consistency, and preservation of material symmetries. Second, the model must describe the real stress response with a sufficient accuracy for a broad spectrum of loading conditions. Third, a robust identification of material parameters must be possible based on a limited number of experiments. Finally, the model must allow for an efficient and reliable numerics. At the conceptual stage of constitutive modelling one may develop a simplified one-dimensional version of the model which is suitable for uniaxial loading scenarios only. Classical examples are the uniaxial Hooke law in elasticity and the Masing rule in cyclic plasticity [12]. Unfortunately, these one-dimensional laws can not be used for the analysis of general application involving multi-axial loading conditions. To generalize the one-dimensional model, a number of techniques were developed. The current paper focuses on the concept of representative directions (see [16, 4, 15, 5]). It is based on the assumption that for each material particle

the stress power is equal to the sum of stress powers of individual material directions (see Section 2.1). Dealing with one-dimensional laws of hyperelastic type, this assumption is equivalent to the "angular integrations approach" from [9] (see also [3], [10], [7], [11], [8]). In the hyperelastic case the overall free energy is assumed as a sum of energies of individual material directions. In order to obtain a stress tensor as a function of the strain history, an integration over all possible directions is required which is equivalent to the integration over a unit sphere (semi-sphere). Other approaches which also involve the integration over a unit sphere are the micro-plane approach from [2] and the micro-sphere approach [13], [14], [6].

In the current contribution, a modified version of the concept of representative directions is discussed. The main difference from the classical concept lies in a new definition of the strain for each representative direction. Just as for the original approach, the extended concept preserves the thermodynamic consistency and objectivity. It is shown that if the representative directions are equipped with the one-dimensional Hooke law, the new concept yields the well-known Hencky material. The applicability of the concept to real materials is demonstrated; the behaviour of an electrospun polymer subjected to non-monotonic loading is modelled.

2 CONCEPT OF REPRESENTATIVE DIRECTIONS

2.1 Classical method: C-approach

For simplicity, all the considerations are restricted to incompressible material behaviour.

$$\det(\mathbf{F}) \equiv 1 \;\Rightarrow\; \det \mathbf{C} \equiv 1 \;\Rightarrow\; \dot{\mathbf{C}} : \mathbf{C}^{-1} = 0. \tag{1}$$

By $\mathbf{C}(t)$, $t \in [0, T]$ we denote the local deformation history described in terms of the right Cauchy-Green tensor. Assume that each material particle consists of N fibres. In this subsection the term "fibre" will be used along with the term "representative material direction". For each fibre we introduce a unit vector $\mathbf{e}_\alpha$ ($\alpha = 1, 2, ..., N$) which is directed along the fibre in the reference configuration. The stretch of each fibre α is computed through

$$\lambda_\alpha = \sqrt{\overline{\mathbf{C}} : (\mathbf{e}_\alpha \otimes \mathbf{e}_\alpha)}, \quad \overline{\mathbf{C}} = (\det \mathbf{C})^{-1/3} \cdot \mathbf{C}. \tag{2}$$

Assume that a one-dimensional uniaxial constitutive law is given, which provides uniaxial true stress $\sigma_\alpha(t)$ as a function of the stretch history $\lambda_\alpha(t')$, $t' \in [0, t]$.

Since the true stress σ_α is power conjugate to the true strain $\varepsilon_\alpha = \ln(\lambda_\alpha)$ in incompressible case, $\sigma_\alpha \cdot \dot{\varepsilon}_\alpha$ equals the stress power of the fibre. By $\tilde{\mathbf{T}}$ we denote the second Piola-Kirchhoff stress tensor. We assume that the stress power of the material is equal to the average of individual stress powers of the fibres:

$$\tilde{\mathbf{T}} : \frac{1}{2}\dot{\mathbf{C}} = \frac{1}{N}\sum_{\alpha=1}^{N} \sigma_\alpha \cdot \frac{d}{dt}(\ln \lambda_\alpha), \text{ for all } \dot{\mathbf{C}}, \text{ such that } \dot{\mathbf{C}} : \mathbf{C}^{-1} = 0. \tag{3}$$

Obviously,

$$\dot{\varepsilon}_\alpha = \frac{d}{dt}(\ln \lambda_\alpha) = \frac{1}{2\lambda_\alpha^2}(\mathbf{e}_\alpha \otimes \mathbf{e}_\alpha) : \dot{\overline{\mathbf{C}}}. \tag{4}$$

Combining this equation with (3) we obtain the second Piola-Kirchhoff stress in the following form

$$\tilde{\mathbf{T}} = \frac{1}{N}\sum_{\alpha=1}^{N}\frac{\sigma_\alpha}{\lambda_\alpha^2}(\mathbf{e}_\alpha\otimes\mathbf{e}_\alpha) + \tilde{p}\mathbf{C}^{-1}, \tag{5}$$

where $\tilde{p}\in\mathbb{R}$ is a real number; the term $\tilde{p}\mathbf{C}^{-1}$ naturally appears due to the incompressibility constraint $\dot{\mathbf{C}}:\mathbf{C}^{-1}=0$. The method based on (5) will be called C-approach, since the stretches λ_α of individual fibres are calculated using the right Cauchy-Green tensor $\mathbf{C}$.

2.2 Extended method: H-approach

By $\mathbf{H} := \frac{1}{2}\ln(\mathbf{C})$ we denote the referential Hencky strain measure (logarithmic strain tensor). Within the extended approach, we abandon the straightforward definition of the stretch previously adopted for individual directions. A generalized true strain pertaining to certain direction is now defined using $\mathbf{H}$:

$$\varepsilon_\alpha := \mathbf{H}^{\mathrm{D}} : (\mathbf{e}_\alpha\otimes\mathbf{e}_\alpha) = \mathbf{H} : (\mathbf{e}_\alpha\otimes\mathbf{e}_\alpha)^{\mathrm{D}}. \tag{6}$$

Now the term "representative direction" is not identical to the term "fibre" in the common sense since material fibres and representative directions experience different strains.

The generalized true strain rate for each representative direction equals

$$\dot{\varepsilon}_\alpha = (\mathbf{e}_\alpha\otimes\mathbf{e}_\alpha)^{\mathrm{D}} : \dot{\mathbf{H}} = (\mathbf{e}_\alpha\otimes\mathbf{e}_\alpha)^{\mathrm{D}} : \frac{1}{2}\frac{\partial\ln(\mathbf{C})}{\partial\mathbf{C}} : \dot{\mathbf{C}}. \tag{7}$$

Since the fourth-rank tensor $\frac{\partial\ln(\mathbf{C})}{\partial\mathbf{C}}$ exhibits the full symmetry, we have

$$\dot{\varepsilon}_\alpha = \frac{1}{2}\Big(\frac{\partial\ln(\mathbf{C})}{\partial\mathbf{C}} : (\mathbf{e}_\alpha\otimes\mathbf{e}_\alpha)^{\mathrm{D}}\Big) : \dot{\mathbf{C}}. \tag{8}$$

Just as in the previous subsection, assume that σ_α is the uni-axial stress of a fibre-like object and σ_α is power-conjugate to the generalized true strain ε_α. Following the general concept, we assume that the stress power per unit volume of the material equals the average of individual stress powers of representative directions:

$$\tilde{\mathbf{T}} : \frac{1}{2}\dot{\mathbf{C}} = \frac{1}{N}\sum_{\alpha=1}^{N}\sigma_\alpha\cdot\dot{\varepsilon}_\alpha, \text{ for all } \dot{\mathbf{C}}, \text{ such that } \dot{\mathbf{C}}:\mathbf{C}^{-1}=0. \tag{9}$$

Combining this with (8), we obtain the second Piola-Kirchhoff stress in the form

$$\tilde{\mathbf{T}} = \frac{\partial\ln(\mathbf{C})}{\partial\mathbf{C}} : \Big(\frac{1}{N}\sum_{\alpha=1}^{N}\sigma_\alpha(\mathbf{e}_\alpha\otimes\mathbf{e}_\alpha)^{\mathrm{D}}\Big) + \tilde{p}\mathbf{C}^{-1}. \tag{10}$$

Here, just as in the classical concept, $\tilde{p}\mathbf{C}^{-1}$ appears due to the incompressibility constraint; this term stands for the unknown hydrostatic component of the stress tensor. Since the

generalized true strains of individual representative directions are computed now using the Hencky strain, we call this method H-approach.

In a general plastic (viscoplastic) case, $\sigma_\alpha(t)$ depends on the strain history $\varepsilon_\alpha(t')$, $t' \leq t$:

$$\sigma_\alpha(t) = \sigma(\varepsilon_\alpha(t'), t' \leq t). \tag{11}$$

Note that in both approaches the second Piola-Kirchhoff stress $\tilde{\mathbf{T}}$ depends on the history of the right Cauchy-Green tensor $\mathbf{C}$. Therefore, the objectivity constraint is a priory satisfied. Another advantage of both methods is the automatic preservation of thermodynamic consistency, if the used one-dimensional material laws are thermodynamically consistent as well (for the C-approach it was already shown in [15]).

3 SPECIAL CASE OF LINEAR ELASTICITY

In this section we analyze the performance of the H-approach when the one-dimensional material behaviour is governed by the linear relation between the generalized true stress σ_α and the corresponding true strain ε_α:

$$\sigma_\alpha = E \cdot \varepsilon_\alpha. \tag{12}$$

Here, $E \geq 0$ is the Young modulus of generalized fibres (representative directions). For each direction we introduce the corresponding free energy function ψ_α. In order to ensure that the stress power $\sigma_\alpha \cdot \dot{\varepsilon}_\alpha$ equals $\dot{\psi}_\alpha$ for arbitrary processes, it is necessary and sufficient to assume that

$$\sigma_\alpha = \frac{d\psi_\alpha(\varepsilon_\alpha)}{d\varepsilon_\alpha}, \quad \psi_\alpha(\varepsilon_\alpha) = \frac{1}{2} E \varepsilon_\alpha^2. \tag{13}$$

In other words, the linear relation (12) is of hyperelastic type. Next, recall that the overall stress power equals the average of stress powers of representative directions. Thus, we obtain for all isochoric deformation processes

$$\tilde{\mathbf{T}} : \frac{1}{2}\dot{\mathbf{C}} = \frac{1}{N}\sum_{\alpha=1}^{N} \sigma_\alpha \cdot \dot{\varepsilon}_\alpha = \frac{1}{N}\sum_{\alpha=1}^{N} \dot{\psi}_\alpha = \dot{\psi}, \text{ where } \psi = \frac{1}{N}\sum_{\alpha=1}^{N} \psi_\alpha. \tag{14}$$

Thus, the H-approach yields in this case a hyperelastic material with the free energy

$$\psi = \frac{1}{N}\sum_{\alpha=1}^{N} \psi_\alpha = \frac{1}{N}\sum_{\alpha=1}^{N} \frac{1}{2} E \varepsilon_\alpha^2 = \frac{E}{2N}\sum_{\alpha=1}^{N} (\mathbf{H}^{\mathrm{D}} : (\mathbf{e}_\alpha \otimes \mathbf{e}_\alpha))^2. \tag{15}$$

Assume that the representative directions $\mathbf{e}_\alpha$ are (nearly) equally spaced and the number of directions is large. Thus, in the limiting case as $N \to \infty$, the right-hand side of (15) is an *isotropic quadratic form* of $\mathbf{H}^{\mathrm{D}}$. Using the representation theorem for isotropic quadratic forms, and taking into account that $\mathrm{tr}(\mathbf{H}^{\mathrm{D}}) = 0$, the free energy simplifies to

$$\psi = \frac{\mu}{2}\mathbf{H}^{\mathrm{D}} : \mathbf{H}^{\mathrm{D}}, \tag{16}$$

where μ is a suitable constant (shear modulus). Thus, in the special case of linear elasticity, the H-approach yields the well-known hyperelasticity of Hencky type, where the free energy is a quadratic function of $\mathbf{H}^{\mathrm{D}}$.

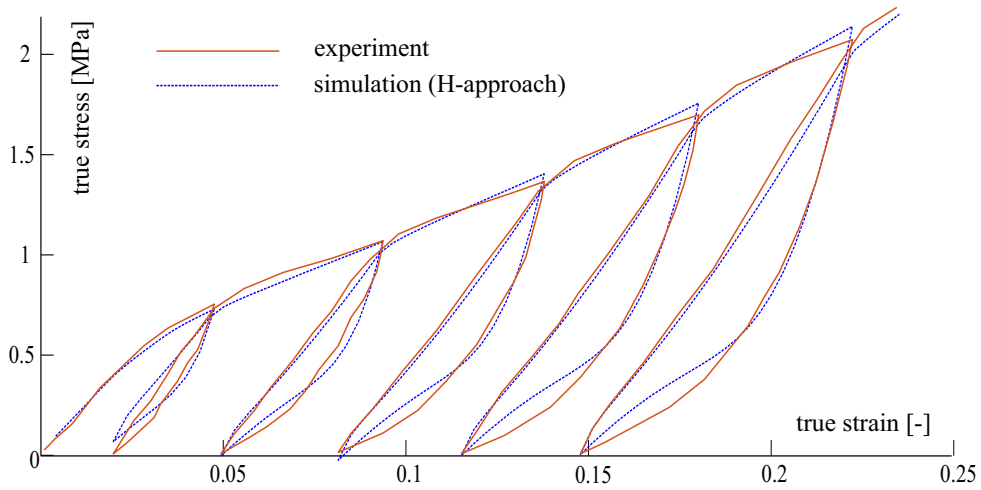


Figure 1: Experimental results taken from [17] on the uniaxial deformation of the electrospun material and corresponding simulation results obtained using the H-approach.

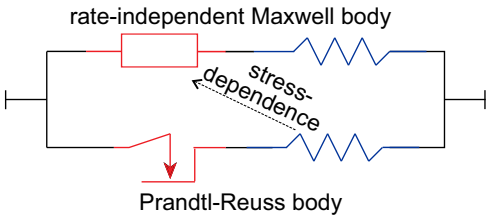


Figure 2: Rheological explanation of the uniaxial material model, used to capture the mechanical response of the electrospun polymer.

4 ELECTROSPUN POLYMER IN THE PLASTIC RANGE

Here we test the performance of the H-approach in terms of a special one-diemensional plasticity model. As a motivation for the studies we start from the experimental results presented in [17] dealing with a uniaxial deformation of an electrospun polymer, see Fig. 1. Clearly, the stress response of the analyzed material is inelastic with a complex form of the hysteresis loops.

As a vivid explanation of the underlying uniaxial material model we use the rheological device presented in Fig. 2. This one-dimensional rheological model consists of the friction element which is attached in series to an elastic spring. We call the obtained elasto-plastic element one-dimensional Prandtl-Reuss body. Next, the rate-independent dashpot (shown as a box in the figure) is attached in series to another elastic spring. The obtained element is referred to as the rate-independent Maxwell body. The overall uniaxial model is a parallel connection of the Prandtl-Reuss body and the rate-independent Maxwell body. Denote by σ_{PR} and σ_{M} the stresses which act in these bodies. Thus, we have

$$\sigma = \sigma_{\mathrm{PR}} + \sigma_{\mathrm{M}}. \tag{17}$$

The behaviour of the Prandtl-Reuss body is governed by the following relations:

$$\sigma_{\mathrm{PR}} = E_{\mathrm{PR}} \cdot \varepsilon_{\mathrm{e}}, \tag{18}$$

$$\varepsilon_{\mathrm{e}} = \varepsilon - \varepsilon_{\mathrm{p}}, \tag{19}$$

$$\dot{\varepsilon}_{\mathrm{p}} = |\dot{\varepsilon}_{\mathrm{p}}| \cdot \mathrm{sign}(\sigma_{\mathrm{PR}}). \tag{20}$$

A linear isotropic hardening is considered:

$$|\sigma_{\mathrm{PR}}| \leq \ K_0 + \gamma s. \tag{21}$$

Here, E_{PR}, K_0, and γ are material parameters; s is the accumulated plastic strain:

$$s(t) = \int_{\tilde{t}=0}^{\tilde{t}=t} |\dot{\varepsilon}_{\mathrm{p}}| d\tilde{t}. \tag{22}$$

Next, we use the following viscous flow rule

$$|\dot{\varepsilon}_{\mathrm{p}}| = \frac{1}{\eta}\big\langle |\sigma_{\mathrm{PR}}| - (K_0 + \gamma s)\big\rangle, \tag{23}$$

where η is a material parameter (viscosity); $\langle x\rangle = \max(0, x)$ is the Macaulay bracket. The rate-independent case is restored as $\eta \to 0$.

The equations of the rate-independent Maxwell body are the same as for the classical rate-dependent one, the only difference is that the physical time t is replaced by the monotonically increasing accumulated strain. Thus we have

$$\dot{\sigma}_{\mathrm{M}} = E_{\mathrm{M}} \cdot \dot{\varepsilon} - b \cdot |\dot{\varepsilon}| \cdot \sigma_{\mathrm{M}}, \tag{24}$$

where $E_{\mathrm{M}} \geq 0$ is a fixed parameter, $b \geq 0$ is a process-dependent "viscosity". In this study we assume

$$b = \frac{b_0}{|\sigma_{\mathrm{PR}}|^2 + b_1}, \tag{25}$$

where b_0 and b_1 are fixed positive parameters. Thus, the generalized viscosity depends on the stresses from the Prandtl-Reuss body. Simple and efficient numerical algorithms can be constructed for the one-dimensional model (17) – (25).

Recall that within the H-approach σ_α and ε_α are (generalized) true stresses and strains. Unfortunately, computations using the uniaxial model (17) – (25) where σ and ε are interpreted as true stresses and strains were not satisfying. The accuracy of the material modelling can be improved when σ and ε which appear in (17) – (25) are seen as engineering stresses and strains. Therefore, the following (geometric) pre- and post-processing is used here: $\varepsilon := e^{\varepsilon_\alpha} - 1$, $\sigma_\alpha := \sigma(1 + \varepsilon)$.

A total number of 100 (nearly) equally spaced directions is used for testing purposes. The unknown material parameters are identified by fitting the predicted stress response to the available experimental data. The fitted parameters are listed Table 1. As is seen from Fig. 1, the H-approach to the concept of representative direction reproduces the real material behaviour with a good accuracy.

Table 1: Identified material constants

K_0 [MPa]	γ [MPa]	η [MPa s]	E_{PR} [MPa]	E_{M} [MPa]	b_0 [MPa^2]	b_1 [MPa^2]
1.38	28.9	0.0	82.5	179.9	1258.0	0.618

5 CONCLUSION

Within the classical C-approach the individual directions can be understood as fibres, whose stretch is naturally defined by (2). Unfortunately, this simple interpretation is lost for the generalized H-approach, since a more complex kinematics is used to define the strain of individual directions, see Eq. (6). At the same time, this assumption is a part of an extended approach which respects the thermodynamic consistency and objectivity. It is shown that in the case of a linear relation between true stresses and strains in the one-dimensional model, the H-approach yields the well-known Hencky material. It is a hyperelastic material with the strain energy given by a quadratic function of the referential Hencky strain. The applicability of the H-approach to a real material is tested. The mechanical behaviour of the electrospun polymer is rendered with a good accuracy.

In the follow-up paper, second order effects like the Swift and Poynting will be discussed and the modelling of initial isotropy will be thoroughly analyzed.

Acknowledgement. The financial support provided by the RFBR (grant no. 17-08-01020) and by the integration project of SB RAS (project 0308-2018-0018) is acknowledged.

REFERENCES

[1] Idelsohn, S.R. and Oñate, E. Finite element and finite volumes. Two good friends. *Int. J. Num. Meth. Engng.* (1994) **37**:3323–3341.

[2] Bažant, Z.P. and Oh, B.H. Microplane model for progressive fracture of concrete and rock. *Journal of Engineering Mechanics* (1985) **111**:559–582.

[3] Federico, S. and Herzog, W. Towards ananalytical model of soft biological tissues. *Journal of Biomechanics* (2008) **41**:3309–3313.

[4] Freund, M. and Ihlemann, J. Generalization of one-dimensional material models for the finite element method. *ZAMM* (2010) **90**(5):399–417.

[5] Freund, M., Shutov, A.V. and Ihlemann, J. Simulation of distortional hardening by generalizing a uniaxial model of finite strain viscoplasticity. *International Journal of Plasticity* (2012) **36**:113–129.

[6] Göktepe, S. and Miehe, C. A micro-macro approach to rubber-like materials. Part III: The micro-sphere model of anisotropic Mullins-type damage. *Journal of the Mechanics and Physics of Solids* (2005) **53**:2259–2283.

[7] Holzapfel, G.A. and Ogden, R.W. On the tensionecompression switch in soft fibrous solids. *European Journal of Mechanics A/Solids* (2015) **49**:561–569.

[8] Holzapfel, G.A. and Ogden R.W. Comparison of two model frameworks for fiber dispersion in the elasticity of soft biological tissues. *European Journal of Mechanics A/Solids* (2017) **66**:193–200.

[9] Lanir, Y. Constitutive equations for fibrous connective tissues. *Journal of Biomechanics* (1983) **16**:1–12.

[10] Lanir, Y. and Namani, R. Reliability of structure tensors in representing soft tissues structure. *Journal of The Mechanical Behavior of Biomedical Materials* (2015) **46**:222–228.

[11] Li, K., Ogden, R.W. and Holzapfel, G.A. Computational method for excluding fibers under compression in modeling soft fibrous solids. *European Journal of Mechanics A/Solids* (2016) **57**:178–193.

[12] Masing, G.E. Eigenspannungen und Verfestigung beim Messing. *Proc. 2nd Int. Conf. Applied Mech., Zürich* (1926), 332–335.

[13] Miehe, C., Göktepe, S. and Lulei, F. A micro-macro approach to rubber-like materials. Part I: the non-a,ne micro-sphere model of rubber elasticity. *Journal of the Mechanics and Physics of Solids* (2004) **52**:2617–2660.

[14] Miehe, C. and Göktepe, S. A micro-macro approach to rubber-like materials. Part II: The micro-sphere model of finite rubber viscoelasticity. *Journal of the Mechanics and Physics of Solids* (2005) **53**:2231–2258.

[15] Naumann, C. and Ihlemann, J. Thermomechanical material behaviour within the concept of representative directions. *In: Jerrams, S., Murphy, N. (Eds.), Constitutive Models for Rubber VII. Balkema, Leiden* (2011) 107–112.

[16] Pawelski, H., *Eigenschaften von Elastomerwerkstoffen mit Methoden der statistischen Physik*. Shaker-Verlag (1998).

[17] Wong, D., Andriyana, A., Ang, B.C. and Verron, E. Surface morphology and mechanical response of randomly oriented electrospun nanofibrous membrane. *Polymer Testing* (2016) **53**:108–115.

XV International Conference on Computational Plasticity. Fundamentals and Applications
COMPLAS 2019
E. Oñate, D.R.J. Owen, D. Peric, M. Chiumenti & Eduardo de Souza Neto (Eds)

SOME NUMERICAL VERIFICATION EXAMPLES FOR PLANE STRESS ELASTO-VISCOPLASTICITY

ANDREY BREZOLIN[†], TIAGO DOS SANTOS[††], PEDRO A. R. ROSA[†††] AND RODRIGO ROSSI[†]

[†]Departamento de Engenharia Mecânica, Universidade Federal do Rio Grande do Sul
Rua Sarmento Leite, 425, Porto Alegre, RS, 90046-902, Brazil
e-mail: andreybrezolin@gmail.com, rrossi@ufrgs.br

[†]Departamento de Engenharia Mecânica, Universidade Federal de Santa Maria
Av. Roraima, 1000, Prédio 7, Santa Maria, RS, 97105-900, Brazil
e-mail:tsantos.dem@smail.ufsm.br

[†††]Instituto de Engenharia Mecânica, Instituto Superior Técnico, Universidade de Lisboa
Lisboa, Portugal - 1049-001
e-mail: pedro.rosa@tecnico.ulisboa.pt

Key words: Verification examples, Viscoplastic material, Plane stress, Stress projected algorithms, Strain-rate hardening, Overstress function

Abstract. This paper presents analytical, semi-analytical and numerical reference examples which can be employed for code verification of elasto-viscoplastic models under plane stress conditions. Mainly because of the overstress function the algorithms traditionally employed in elasto-plastic implementations must be rewritten to correctly impose the plane stress state along with the viscoplastic flow. The viscoplastic formulation presented here considers the strain-rate hardening effects by means of a hardening law that are assumed to have terms depending on the strain rate, which removed can represent a Voce type hardening. The proposed verification tests were employed for the numerical verification of an in-house implementation of the so-called stress-projected procedure inside the finite element method context. Although the focus of this paper is on the stress-projected algorithms the examples presented here can be employed for the verification of other algorithms intended to impose the plane stress state in viscoplasticity.

1 INTRODUCTION

In many engineering practical applications, depending on specific physical and geometric characteristics, useful simplifications can be conveniently assumed. For example, either axisymmetric, plane strain or plane stress assumptions can be referred to. From a general point of view, such assumptions greatly simplifies the problem solution since a reduced number of variables has to be taken into account. Particularly, plane stress

conditions can be adopted in specific engineering situations in which, by suitable mathematical idealization, the out-of-plane stress components are assumed to be null. Practical applications which allow such an assumption are those involving e.g. thin membranes, load-free surfaces, etc.

Particularly, a straightforward formulation can be obtained when isotropic linear elasticity is employed. In this simple case, conditions satisfying null out-of-plane stress components are readily imposed both on analytical and numerical frameworks. In contrast to the linear elastic cases, imposing the corresponding plane stress conditions in inelastic formulations is more complex from both analytical and numerical points of views. It is worth mentioning that imposing the correct constraints to the plastic flow under plane stress assumption is far more complicated when compared to other simplifications, as axisymmetric or plane strain cases, or even when a full three dimensional approach is employed.

This paper focus on development of verification examples which can be applied especially for code verification involving viscoplasticity and in some conditions elasto-viscoplasticity problems. In a first moment, focus is given in some simple, but very important, verification examples in which numerical results are confronted against with analytical and semi-analytical rigid viscoplastic solutions. The term semi-analytical is used here to enforce that some approximation is involved in the development of the evolution of the viscoplastic flow. Secondly, it is presented some comparisons considering a more sophisticated plane stress example, also considered by other researches, serving as reference solutions.

In this paper the enforcement of the plane stress viscoplastic flow is given by a version of the *stress-project algorithm*. Although the stress-projected algorithm is very common in elasto-plasticity, the same does not appear to be true in elasto-viscoplasticity, and few papers on the subject are found in the literature, see subsection 3.2 for more details. The viscoplastic formulation is given in terms of an overstress function which couples viscid and inviscid flow. It is shown that to employ the stress-projected procedure some terms must arise in order to assure the correct evolution of the plane stress state along the viscoplastic flow. The elasto-viscoplastic model considered in this paper is equipped with an internal variable that accounts for the strain-rate hardening, which removed can lead to a Voce type of hardening, thus the procedure presented here can be employed when enforcing the plane stress state not only when using the stress-projected algorithm but also for other algorithms in regular viscoplastic models.

This paper is presented in a very concise manner in 6 sections, including this introduction. In section 2 the formulation of the elasto-viscoplastic constitutive model is briefly depicted. The formulation of the stress-projected algorithm is presented in section 3 and section 4 is devoted to the numerical aspects involved in the local integration procedure and tangent modulus derivation. Numerical results are presented in section 5. Closing this paper we present our conclusions in section 6.

2 CONSTITUTIVE FRAMEWORK

This section addresses the main features of the constitutive model and some important aspects associated with the plane stress particularization. In a first step, the adopted elasto-viscoplastic model is outlined. It is worth mentioning that this model was formulated and and adjusted within a multidimensional context in previous work [1]. The present development has the aim of emphasizing specific aspects related to both analytical and numerical formulations to employ the whole model (whose parameters were adjusted in a 3D setup) in a plane stress-projected framework.

2.1 Elasto-viscoplastic model

The model adopted in this work employs a von Mises material, whose yield function is given by

$$f(\boldsymbol{\sigma}, A) = \|\mathbf{s}\| - \underbrace{\sqrt{\frac{2}{3}}(\sigma_y + A)}_{R(A)}, \tag{1}$$

in which σ_y is the initial yield stress, $A = A_1 + A_2$ is the isotropic stress hardening, $||\mathbf{s}|| = \sqrt{\mathbf{s} : \mathbf{s}} = \sqrt{s_{ij} s_{ij}}$, being $\mathbf{s}$ the deviatoric part of the $\boldsymbol{\sigma}$. Assuming a linear elastic isotropic material, $\boldsymbol{\sigma}$ relates to an elastic strain measure $\boldsymbol{\varepsilon}^e$, by

$$\boldsymbol{\sigma} = \mathbf{D}^e \boldsymbol{\varepsilon}^e, \tag{2}$$

where

$$\mathbf{D}^e = 2\mu \mathbf{I} + \lambda \mathbf{I} \otimes \mathbf{I}, \tag{3}$$

being μ and λ the Lamé constants, which are related to standard elastic parameters as the shear G and bulk K moduli by $\mu = G$ and $\lambda = K - \frac{2}{3}\mu$. In Eq. (3), $\mathbf{I}$ is the *symmetric part* of the fourth order identity tensor, and $\mathbf{I}$ is the second order identity tensor. In components, they are given respectively by $\mathbf{I}_{ijkl} = \frac{1}{2}\left(\delta_{ik}\delta_{jl} + \delta_{il}\delta_{jk}\right)$ and $(\mathbf{I} \otimes \mathbf{I})_{ijkl} = \delta_{ij}\delta_{kl}$.

Inelastic evolution equations are given in the form

$$\dot{\boldsymbol{\varepsilon}}^{vp} = \dot{\lambda}\frac{\partial f}{\partial \boldsymbol{\sigma}} = \dot{\lambda}\frac{\mathbf{s}}{\|\mathbf{s}\|}, \;\; \dot{A}_1 = \delta\left(A_\infty - A_1\right)\dot{\bar{\varepsilon}}, \;\; A_2 = cA_\infty\bar{\varepsilon}, \tag{4}$$

where $\dot{\boldsymbol{\varepsilon}}^{vp} = \dot{\boldsymbol{\varepsilon}} - \dot{\boldsymbol{\varepsilon}}^e$ is the viscoplastic strain-rate, δ, A_∞ and c are model parameters, $\bar{\varepsilon}$ is the accumulated viscoplastic strain , whose rate is defined given by (see Eqs. (1) and (4))

$$\dot{\bar{\varepsilon}} = \sqrt{\frac{2}{3}}\,\|\dot{\boldsymbol{\varepsilon}}^{vp}\| = \sqrt{\frac{2}{3}}\dot{\lambda}. \tag{5}$$

For a constant strain-rate, from Eqs. $(4)_{2-3}$ a closed expression for the hardening variable $A = A_1 + A_2$ can be obtained

$$A = A_\infty\left[1 + c\bar{\varepsilon} - \exp\left(-\delta\bar{\varepsilon}\right)\right]. \tag{6}$$

Furthermore, the present model assumes rate-dependence on A_∞, as presented in [2], given by

$$A_\infty = [1 - \beta(\dot{\bar{\varepsilon}})] A_\infty^{lwr} + \beta(\dot{\bar{\varepsilon}}) A_\infty^{up}, \tag{7}$$

where A_∞^{lwr} and A_∞^{up} are model constants. Parameters $(\cdot)^{lwr}$ and $(\cdot)^{up}$ are related to a lower $\dot{\bar{\varepsilon}}_{lwr} \ll 1$ and an upper $\dot{\bar{\varepsilon}}_{up} \gg 1$ reference strain-rates, respectively. In Eq. (7), functions β, are given by

$$\beta(\dot{\bar{\varepsilon}}) = \left(\frac{\langle \dot{\bar{\varepsilon}} - \dot{\bar{\varepsilon}}_{lwr} \rangle}{\dot{\bar{\varepsilon}}_{up} - \dot{\bar{\varepsilon}}_{lwr}} \right)^{\xi}, \tag{8}$$

satisfying $\beta(\dot{\bar{\varepsilon}}_{lwr}) = 0$ and $\beta(\dot{\bar{\varepsilon}}_{up}) = 1$. The parameter $\xi > 0$ is a model constant. In the last equation, operator $\langle x \rangle = \frac{1}{2}(x + |x|)$ is the Macaulay bracket.

Within a viscoplastic framework, multiplier $\dot{\lambda} \geq 0$ of Eq. $(4)_1$ is assumed to have a relationship with the yield function f and hardening variable A given by a constitutive equation [3, 4]

$$\dot{\lambda} = \Theta(\langle f \rangle, A), \tag{9}$$

where $\Theta \geq 0$ is an overstress function complying with condition $\Theta(0, A) = 0$. Considering a viscoplastic loading, in which $f > 0$ and $\dot{\lambda} > 0$, the Eq. (9) can be rewritten as

$$f = \Theta^{-1}\left(\dot{\lambda}, A\right). \tag{10}$$

In this work, function Θ^{-1} is assumed to have the following specific form

$$f = R(A)\left[\left(1 + \vartheta\dot{\lambda}\right)^{1/m} - 1\right], \tag{11}$$

where $\vartheta > 0$ and $1/m > 0$ are constants. The Eq. 11 is a variation of the Perzyna model, [3, 4], and was proposed by [5].

3 ELASTO-VISCOPLASTICITY UNDER PLANE STRESS CONDITION

3.1 Some preliminaries

Let $\boldsymbol{\sigma} \in \mathcal{S}$ be the Cauchy stress tensor, $\mathcal{S}$ being the second-order symmetric tensor space satisfying $\dim[\mathcal{S}] = 6$. The plane stress condition may be stated by using the Cauchy traction vector, $\boldsymbol{t}$, as those sections planes, for a fixed unitary normal $\boldsymbol{n}$, where

$$\boldsymbol{t}(\boldsymbol{n}) = \boldsymbol{\sigma}\boldsymbol{n} = \boldsymbol{0}. \tag{12}$$

For the sake of simplification, let $\boldsymbol{n} = \boldsymbol{e}_3$ and let $\mathcal{S}^p \subset \mathcal{S}$ be conveniently defined as the stress vector subspace satisfying the planes stress constrains such that

$$\mathcal{S}^p = \{\boldsymbol{\sigma} \in \mathcal{S} | \sigma_{13} = \sigma_{23} = \sigma_{33} = 0\}, \tag{13}$$

where $\dim[\mathcal{S}^p] = 3$.

3.2 Plane stress in viscoplasticity

Appropriate procedures have been proposed in the literature to enforce the plane stress state in *elasto-plasticity* following either local or global procedures, see [6, Chap. 9] for a review. One of these approaches is plane stress-projection algorithm, apparently first reported in [7] but well developed in [8] and especially in [9] for a von Mises yield criterion.

Due to its complexity, the plane stress-projection has been employed mainly in works considering a J_2 yield function within elasto-plasticity, where there are "uncountable" works published so far, and also in viscoplasticity, but in contrast, here one founds very few works [10, 11, 12, 13]. Also, few works employing such strategy using other yield criteria are found [14, 15, 16]. From a full three-dimensional framework, [15, 16] have developed a general consistent projected return mapping algorithm for plane stress isotropic plasticity. They have shown that, in contrast to previous approaches [7, 8, 9, 14, 17], both the stress return algorithm and the consistent tangent operator can be obtained by particularizing the three dimensional formulation to a bi-dimensional stress space. However, for constitutive approaches not employing the von Mises yield function, obtaining the corresponding plane stress-projected formulation can become very complex or even impracticable. Thus, other procedures shall be recommended [6], [15] has pointed out that it could be limited to isotropic plasticity theories.

Now focusing in (elasto-)viscoplasticity, one of the first reports of plane stress state imposition in viscoplasticity was given by [11]. In this paper the authors follows the ideas presented in [9] to reformulate the so-called Robinson's viscoplastic model. More recently, in [12] an elastic–viscoplastic implicit integration algorithm was presented based on the ideas developed for elasto-plasticity. The algorithm was developed for three-dimensional stress states but can approach the plane stress state in viscoplasticity by introducing corrections in the implicit integration evolution equations. However, it is in [13] that a more comprehensive analysis about the imposition of the plane stress state in viscoplasticity is delivered. Different time integration schemes are investigated and compared in a constitutive formulation that considers isotropic and kinematic hardening and damage. The viscous effect is introduced by a power or an hyperbolic sine function.

3.2.1 Plane stress projection framework

In order to formulated the corresponding plane stress framework, the Voigt notation is conveniently adopted. Thus, constitutive relation given in Eq. (2) is rewritten as[1]

$$\begin{bmatrix} \sigma_{11} \\ \sigma_{22} \\ \sigma_{33} \\ \sigma_{23} \\ \sigma_{13} \\ \sigma_{12} \end{bmatrix} = \frac{E}{(1+\nu)(1-2\nu)} \begin{bmatrix} 1-\nu & \nu & \nu & 0 & 0 & 0 \\ \nu & 1-\nu & \nu & 0 & 0 & 0 \\ \nu & \nu & 1-\nu & 0 & 0 & 0 \\ 0 & 0 & 0 & \frac{1-2\nu}{2} & 0 & 0 \\ 0 & 0 & 0 & 0 & \frac{1-2\nu}{2} & 0 \\ 0 & 0 & 0 & 0 & 0 & \frac{1-2\nu}{2} \end{bmatrix} \begin{bmatrix} \varepsilon^e_{11} \\ \varepsilon^e_{22} \\ \varepsilon^e_{33} \\ \gamma^e_{23} \\ \gamma^e_{13} \\ \gamma^e_{12} \end{bmatrix}, \quad (14)$$

[1]Notice that $\boldsymbol{\sigma}$, $\boldsymbol{\varepsilon}^e$, $\mathbf{s}$ are second order tensors while $\boldsymbol{\sigma}$, $\boldsymbol{\varepsilon}^l$, and $\boldsymbol{s}$ are column matrices.

in which E and ν are the Young modulus and Poisson ratio, respectively. To impose the associated plane stress conditions, the in-plane stress components are assumed to be σ_{11}, σ_{22} and σ_{12} . Therefore, Eq. (14) reduces to

$$\begin{bmatrix} \sigma_{11} \\ \sigma_{22} \\ \sigma_{12} \end{bmatrix} = \frac{E}{1-\nu^2} \begin{bmatrix} 1 & \nu & 0 \\ \nu & 1 & 0 \\ 0 & 0 & \frac{1-\nu}{2} \end{bmatrix} \begin{bmatrix} \varepsilon^e_{11} \\ \varepsilon^e_{22} \\ \gamma^e_{12} \end{bmatrix} \rightarrow \boldsymbol{\sigma} = \mathbf{D}^e \boldsymbol{\varepsilon}^e, \tag{15}$$

with the out-of-plane strain component given by $\varepsilon^e_{33} = \frac{-\nu}{E}(\sigma_{11} + \sigma_{22})$. Seeking for a compact notation, a plane stress vector $\boldsymbol{\sigma} \in \mathcal{S}^p \subset \mathcal{S}$ is conveniently defined

$$\boldsymbol{\sigma} = [\sigma_{11}\ \sigma_{22}\ \sigma_{12}]^T. \tag{16}$$

Consistently, a strain vector is accordingly defined

$$\boldsymbol{\varepsilon}^l = [\varepsilon^l_{11}\ \varepsilon^l_{22}\ 2\varepsilon^l_{12}]^T, \tag{17}$$

where the superscript l has to be set depending on the deformation regime, elastic or inelastic. The out-of-plane component ε^l_{33} is left to be specified along the work.

Under plane stress conditions, following the previous notation, the deviatoric stress is assumed to belong to the vector subspace

$$\mathcal{S}^d = \{\mathbf{s} \in \mathcal{S} | \mathrm{s}_{13} = \mathrm{s}_{23} = 0,\ \mathrm{tr}\,(\mathbf{s}) = 0\}. \tag{18}$$

Being $\overline{\mathbf{P}}$ a linear mapping $\overline{\mathbf{P}} : \mathcal{S}^p \longrightarrow \mathcal{S}^d$, it is possible to determine the deviatoric stress vector performing

$$\boldsymbol{s} = \overline{\mathbf{P}}\boldsymbol{\sigma}\ , \tag{19}$$

where

$$\boldsymbol{s} = [s_{11}\ s_{22}\ s_{12}]^T, \tag{20}$$

and

$$\overline{\mathbf{P}} := \frac{1}{3}\begin{bmatrix} 2 & -1 & 0 \\ -1 & 2 & 0 \\ 0 & 0 & 3 \end{bmatrix}. \tag{21}$$

Note that the out of plane deviatoric stress is calculated as $s_{33} = -(s_{11} + s_{22})$. In a similar manner, the deviatoric strain vector, denoted by

$$\boldsymbol{\epsilon} = [\epsilon_{11}\ \epsilon_{22}\ 2\epsilon_{12}]^T, \tag{22}$$

with $\epsilon_{11} = \varepsilon_{11} - \frac{1}{3}\mathrm{tr}\,(\boldsymbol{\varepsilon})$ and $\epsilon_{22} = \varepsilon_{22} - \frac{1}{3}\mathrm{tr}\,(\boldsymbol{\varepsilon})$, can be obtained from the mapping

$$\boldsymbol{\epsilon} = \mathbf{P}\boldsymbol{\varepsilon}, \tag{23}$$

where

$$\mathbf{P} = \frac{1}{3}\begin{bmatrix} 2 & -1 & 0 \\ -1 & 2 & 0 \\ 0 & 0 & 6 \end{bmatrix}. \tag{24}$$

3.2.2 Viscoplastic considerations

When the plane stress condition is imposed, $\boldsymbol{\sigma} \in \mathcal{S}^p$ and $\boldsymbol{s} \in \mathcal{S}^d$, specialization of the yield function Eq. (1) reads

$$f_{ps}(\boldsymbol{\sigma}, A) = \sqrt{\frac{2}{3}\left(\sigma_{11}^2 + \sigma_{22}^2 - \sigma_{11}\sigma_{22} + 3\sigma_{12}^2\right)} - R(A), \tag{25}$$

which can be compactly rewritten using the operator $\mathbf{P}$ as

$$f_{ps}(\boldsymbol{\sigma}, A) = \sqrt{\boldsymbol{\sigma}^T \mathbf{P} \boldsymbol{\sigma}} - R(A)\ . \tag{26}$$

It is worth mentioning that, although they have a different functional form, both the yield functions defined in Eqs. (1) and (26) return the same numerical value for a given plane stress state. Thus, the viscoplastic equation defined in Eq. (11) can be readily applied in the plane stress formulation

$$\begin{aligned} f_{ps} &= \Theta^{-1}\left(\dot{\lambda}, A\right), \\ &= R(A)\left[\left(1 + \vartheta\dot{\lambda}\right)^{1/m} - 1\right], \end{aligned} \tag{27}$$

or

$$f_{ps} + R(A) = R(A)\left[\left(1 + \vartheta\dot{\lambda}\right)^{1/m}\right]. \tag{28}$$

Notice that the last equation is a direct particularization of the full viscoplastic function whose argument is the multiplier $\dot{\lambda}$ employing model parameters (ϑ, m) adjusted in a 3D context. However, in an effort to employ the 3D adjusted model in a particular plane stress implementation, attention is needed in the mathematical manipulation of the model equations. Following the procedure presented in [18], it is useful to rewrite Eq. (28) as

$$f_{ps} + R(A) = \sqrt{2\tilde{f}_{ps}\left(\boldsymbol{\sigma}\right)} = R(A)\left[\left(1 + \vartheta\dot{\lambda}\right)^{1/m}\right], \tag{29}$$

where $2\tilde{f}_{ps}\left(\boldsymbol{\sigma}\right) = \boldsymbol{\sigma}^T \mathbf{P} \boldsymbol{\sigma}$. Thus, the following relation is obtained

$$\tilde{f}_{ps} = \frac{1}{3}(\sigma_y + A)^2\left[\left(1 + \vartheta\dot{\lambda}\right)^{1/m}\right]^2. \tag{30}$$

Based on the plane stress restriction and according to the adopted Voigt notation, the evolution equation $(4)_1$ is rewritten as (see Eq. (26))

$$\dot{\boldsymbol{\varepsilon}}_{ps}^{vp} = \frac{1}{\sqrt{\boldsymbol{\sigma}^T \mathbf{P} \boldsymbol{\sigma}}}\dot{\lambda}\mathbf{P}\boldsymbol{\sigma}, \tag{31}$$

or in a convenient compact form as

$$\dot{\boldsymbol{\varepsilon}}_{ps}^{vp} = \dot{\tilde{\lambda}}\mathbf{P}\boldsymbol{\sigma}, \tag{32}$$

in which $\dot{\boldsymbol{\varepsilon}}_{ps}^{vp} = [\dot{\varepsilon}_{ps_{11}}^{vp} \; \dot{\varepsilon}_{ps_{22}}^{vp} \; 2\dot{\varepsilon}_{ps_{12}}^{vp}]^T$. Notice that in Eq. (32), since $\mathbf{P}\boldsymbol{\sigma}$ is not a unit vector, the multiplier $\dot{\tilde{\lambda}}$ does not represent the magnitude of $\dot{\boldsymbol{\varepsilon}}_{ps}^{vp}$. Therefore, $\dot{\tilde{\lambda}}$ is related to the original (3D) viscoplastic multiplier $\dot{\lambda}$ by means of

$$\dot{\tilde{\lambda}} = \frac{1}{\sqrt{\boldsymbol{\sigma}^T \mathbf{P} \boldsymbol{\sigma}}} \dot{\lambda} \; . \tag{33}$$

In this context, in view of Eqs. (5) and (33), the accumulated viscoplastic strain rate $\dot{\bar{\varepsilon}}$ can be given in terms of $\dot{\tilde{\lambda}}$ according to

$$\dot{\bar{\varepsilon}} = \dot{\tilde{\lambda}} \sqrt{\frac{2}{3} \boldsymbol{\sigma}^T \mathbf{P} \boldsymbol{\sigma}}. \tag{34}$$

Relation given in Eq. (33) is an important point to be highlighted in the present plane stress particularization. Keeping in mind that $\dot{\lambda}$ is the original argument of the 3D viscoplastic function given in Eq. (11), *it is not possible to simply replace* $\dot{\lambda}$ by $\dot{\tilde{\lambda}}$, in manner that

$$f_{ps} = R(A) \left[\left(1 + \vartheta \dot{\tilde{\lambda}} \right)^{1/m} - 1 \right].$$

If this direct replacement is done, the parameters adjusted in a 3D framework cannot be used within the plane stress particularization, otherwise unexpected results will be obtained.

4 NUMERICAL ASPECTS

4.1 Local integration algorithm

Once the constitutive equations under plane stress assumption have been obtained, this section outlines the incremental counterpart and the corresponding integration algorithm used to solve the numerical problem. Adopting a fully implicit integration (backward Euler) procedure, the whole time interval is subdivided into time increments $\Delta t = t_{n+1} - t_n$ and the time rate of each quantity $(\cdot)$ is calculated by an increment $\Delta(\cdot) \coloneqq (\cdot)_{n+1} - (\cdot)_n$, being $(\cdot)_{n+1}$ and $(\cdot)_n$ the values at instants t_{n+1} and t_n, respectively. In this sense, Eq. (34) becomes

$$\bar{\varepsilon}_{n+1} = \bar{\varepsilon}_n + \Delta\tilde{\lambda} \sqrt{\frac{2}{3} \boldsymbol{\sigma}_{n+1}^T \mathbf{P} \boldsymbol{\sigma}_{n+1}}, \tag{35}$$

in which $\Delta\tilde{\lambda} \geq 0$ plays the role of a incremental viscoplastic multiplier.

Considering a viscoplastic loading $\left(f_{ps_{n+1}} > 0\right)$, based on Eq. (29) the following particular plane stress relation is obtained

$$\tilde{f}_{ps} = \frac{1}{2} \boldsymbol{\sigma}_{n+1}^T \mathbf{P} \boldsymbol{\sigma}_{n+1} - \frac{1}{3} (\sigma_y + A_{n+1})^2 \left(1 + \vartheta \frac{\Delta\tilde{\lambda}}{\Delta t} \sqrt{\boldsymbol{\sigma}_{n+1}^T \mathbf{P} \boldsymbol{\sigma}_{n+1}} \right)^{2/m} = 0. \tag{36}$$

In addition, the stress hardening variable A at t_{n+1} can be accounted for by means of the following incremental equation obtained from Eqs. $(4)_{2-3}$ (see also [1])

$$A_{n+1} = A_n + A_{\infty_{n+1}} c(\bar{\varepsilon}_{n+1} - \bar{\varepsilon}_n) + \\ + \left[A_{\infty_{n+1}}(1 + c\bar{\varepsilon}_n) - A_n\right] \left\{1 - \exp\left[-\delta(\bar{\varepsilon}_{n+1} - \bar{\varepsilon}_n)\right]\right\}, \quad (37)$$

in which $A_{\infty_{n+1}}$ is given by

$$A_{\infty_{n+1}} = A_\infty^{lwr} + \left[\frac{1}{\Delta t}\left(\frac{\langle \bar{\varepsilon}_{n+1} - \bar{\varepsilon}_n - \Delta t \dot{\bar{\varepsilon}}_{lwr} \rangle}{\dot{\bar{\varepsilon}}_{up} - \dot{\bar{\varepsilon}}_{lwr}}\right)\right]^\xi (A_\infty^{up} - A_\infty^{lwr}) \, . \quad (38)$$

4.1.1 Elastic predictor-plastic corrector algorithm in plane stress state

In order to solve the set of nonlinear algebraic equations (35)-(38), an elastic predictor-plastic corrector algorithm is employed. The strategy solution is performed into two steps: **(i)** a trial elastic state is assumed, if the condition $f_{ps}(\boldsymbol{\sigma}_{n+1}^{trial}, A_{n+1}^{trial}) \leq 0$ is satisfied, the solution at t_{n+1} is updated, $(\cdot)_{n+1} = (\cdot)_{n+1}^{trial}$; **(ii)** otherwise, if $f_{ps}(\boldsymbol{\sigma}_{n+1}^{trial}, A_{n+1}^{trial}) > 0$, a viscoplastic correction has to be performed. The elastic deformation for plane stress state, at t_{n+1}, can be written as

$$\boldsymbol{\varepsilon}_{n+1}^e = \boldsymbol{\varepsilon}_{n+1}^{e^{trial}} - \Delta\tilde{\lambda}\mathbf{P}\boldsymbol{\sigma}_{n+1}, \quad (39)$$

or equivalently in term of stresses

$$\boldsymbol{\sigma}_{n+1} = \mathbf{H}\left(\Delta\tilde{\lambda}\right)\boldsymbol{\sigma}_{n+1}^{trial}, \quad (40)$$

in which

$$\mathbf{H}\left(\Delta\tilde{\lambda}\right) = \left(\mathbf{D}^{e^{-1}} + \Delta\tilde{\lambda}\mathbf{P}\right)^{-1}\mathbf{D}^{e^{-1}}. \quad (41)$$

The nonlinear set of equations to be solved in the plastic corrector phase is composed by (35), (36), (37), (38), and (39) for the following variables $\left\{\boldsymbol{\varepsilon}_{n+1}^e, \bar{\varepsilon}_{n+1}, \Delta\tilde{\lambda}, A_{n+1}, A_{\infty_{n+1}}\right\}$. It is possible to reduce the number of equations by a simple mathematical manipulation of Eq. 36 and Eq. (39) (or Eq. (40)). These last two equations can be reduced to one equation having as unknown $\Delta\tilde{\lambda}$. To perform such a task let us first write

$$\boldsymbol{\sigma}_{n+1}^T\mathbf{P}\boldsymbol{\sigma}_{n+1} = \gamma\left(\Delta\tilde{\lambda}\right) \, , \quad (42)$$

where the function $\gamma\left(\Delta\tilde{\lambda}\right)$ is given in terms of the trial state as

$$\gamma\left(\Delta\tilde{\lambda}\right) = \left(\boldsymbol{\sigma}_{n+1}^{trial}\right)^T\mathbf{H}^T\left(\Delta\tilde{\lambda}\right)\mathbf{P}\mathbf{H}\left(\Delta\tilde{\lambda}\right)\boldsymbol{\sigma}_{n+1}^{trial}. \quad (43)$$

Previous equation has to be solved in terms of a single scalar unknown: $\Delta\tilde{\lambda}$. However, as pointed out by [6], given the fact that Eq. (43) involves the multiplication and inversion of

other matrices, its solution can lead to a cumbersome calculation. Therefore, in an effort to avoid such operations one can take the advantage of specific characteristic associated with an elastic and isotropic material. That means $\mathbf{P}$ and $\mathbf{D}^e$ share the same eigenvectors, i.e. both have diagonal representation on the same basis, as well as $\mathbf{D}^{e^{-1}}$ and $\mathbf{H}$. The orthogonal matrix $\mathbf{Q}$ representing such transformation is

$$\mathbf{Q} = \begin{bmatrix} \frac{1}{\sqrt{2}} & \frac{1}{\sqrt{2}} & 0 \\ -\frac{1}{\sqrt{2}} & \frac{1}{\sqrt{2}} & 0 \\ 0 & 0 & 1 \end{bmatrix}, \tag{44}$$

implying in the following results

$$\mathbf{P}^* \equiv \mathbf{Q}\mathbf{P}\mathbf{Q}^T = \begin{bmatrix} \frac{1}{3} & 0 & 0 \\ 0 & 1 & 0 \\ 0 & 0 & 2 \end{bmatrix}, \tag{45}$$

$$\mathbf{D}^{e*} \equiv \mathbf{Q}\mathbf{D}^e\mathbf{Q}^T = \begin{bmatrix} \dfrac{E}{1-\nu} & 0 & 0 \\ 0 & 2G & 0 \\ 0 & 0 & G \end{bmatrix}, \tag{46}$$

$$\begin{aligned} \mathbf{H}^*\left(\Delta\tilde{\lambda}\right) &\equiv \left(\mathbf{D}^{*e^{-1}} + \Delta\tilde{\lambda}\mathbf{P}^*\right)^{-1}\mathbf{D}^{*e^{-1}} \\ &= \begin{bmatrix} \dfrac{3(1-\nu)}{3(1-\nu)+E\Delta\tilde{\lambda}} & 0 & 0 \\ 0 & \dfrac{1}{1+2G\Delta\tilde{\lambda}} & 0 \\ 0 & 0 & \dfrac{1}{1+2G\Delta\tilde{\lambda}} \end{bmatrix}, \end{aligned} \tag{47}$$

and the trial stress can be written as

$$\boldsymbol{\sigma}_{n+1}^{trial^*} \equiv \mathbf{Q}\boldsymbol{\sigma}_{n+1}^{trial} = \begin{bmatrix} \frac{1}{\sqrt{2}}\left(\sigma_{11}^{trial} + \sigma_{22}^{trial}\right) \\ \frac{1}{\sqrt{2}}\left(\sigma_{22}^{trial} - \sigma_{11}^{trial}\right) \\ \sigma_{12}^{trial} \end{bmatrix}, \tag{48}$$

and Eq. (43) is rewritten as

$$\begin{aligned} \boldsymbol{\sigma}_{n+1}^T\mathbf{P}\boldsymbol{\sigma}_{n+1} &= \gamma\left(\Delta\tilde{\lambda}\right) \\ &= \frac{\left(\sigma_{11}^{trial} + \sigma_{22}^{trial}\right)^2}{6\left[1 + \dfrac{E\Delta\tilde{\lambda}}{3(1-\nu)}\right]^2} + \frac{\frac{1}{2}\left(\sigma_{22}^{trial} - \sigma_{11}^{trial}\right)^2 + 2\left(\sigma_{12}^{trial}\right)^2}{\left(1 + 2G\Delta\tilde{\lambda}\right)^2} \end{aligned} \tag{49}$$

The matrix $\mathbf{H}\left(\Delta\tilde{\lambda}\right)$ may be now written as

$$\mathbf{H}\left(\Delta\tilde{\lambda}\right) = \mathbf{Q}^T\mathbf{H}^*\left(\Delta\tilde{\lambda}\right)\mathbf{Q}, \tag{50}$$

and using Eq. (44) and (47), one can derive a simpler form as

$$\mathbf{H}(\Delta\tilde{\lambda}) = \begin{bmatrix} \frac{1}{2}(H^*_{11}+H^*_{22}) & \frac{1}{2}(H^*_{11}-H^*_{22}) & 0 \\ \frac{1}{2}(H^*_{11}-H^*_{22}) & \frac{1}{2}(H^*_{11}+H^*_{22}) & 0 \\ 0 & 0 & H^*_{33} \end{bmatrix}, \tag{51}$$

in which

$$H^*_{11} = \frac{3\,(1-\nu)}{3\,(1-\nu)+E\Delta\tilde{\lambda}},\; H^*_{22} = \frac{1}{1+2G\Delta\tilde{\lambda}},\; H^*_{33} = H^*_{22}. \tag{52}$$

It is also possible rewrite Eq. (35) and (36) in terms of $\Delta\tilde{\lambda}$ only, that is

$$\frac{1}{2}\gamma\left(\Delta\tilde{\lambda}\right) - \frac{1}{3}(\sigma_y + A_{n+1})^2\left[1+\vartheta\frac{\Delta\tilde{\lambda}}{\Delta t}\sqrt{\gamma\left(\Delta\tilde{\lambda}\right)}\right]^{2/m} = 0, \tag{53}$$

and

$$\bar{\varepsilon}_{n+1} = \bar{\varepsilon}_n + \Delta\tilde{\lambda}\sqrt{\frac{2}{3}\gamma\left(\Delta\tilde{\lambda}\right)}. \tag{54}$$

Moreover, by substituting Eq. (54) in Eqs. (37) and (38) one writes

$$\begin{aligned} A_{n+1} = A_n + A_{\infty_{n+1}} c\left[\Delta\tilde{\lambda}\sqrt{\frac{2}{3}\gamma\left(\Delta\tilde{\lambda}\right)}\right] + \\ + \left[A_{\infty_{n+1}}\left(1+c\bar{\varepsilon}_n\right) - A_n\right]\left\{1-\exp\left[-\delta\Delta\tilde{\lambda}\sqrt{\frac{2}{3}\gamma\left(\Delta\tilde{\lambda}\right)}\right]\right\}, \end{aligned} \tag{55}$$

with

$$A_{\infty_{n+1}} = A^{lwr}_{\infty} + \left[\frac{1}{\Delta t}\frac{\left\langle \Delta\tilde{\lambda}\sqrt{\frac{2}{3}\gamma\left(\Delta\tilde{\lambda}\right)} - \Delta t\dot{\bar{\varepsilon}}_{lwr}\right\rangle}{\dot{\bar{\varepsilon}}_{up}-\dot{\bar{\varepsilon}}_{lwr}}\right]^{\xi}\left(A^{up}_{\infty}-A^{lwr}_{\infty}\right). \tag{56}$$

In conclusion, the system of nonlinear equations related to the viscoplastic prediction phase is (53), (55), and (56) which has to be solved in terms of $\left\{\Delta\tilde{\lambda},\, A_{n+1},\, A_{\infty_{n+1}}\right\}$.

Consequently, once the solution is obtained, the stress $\boldsymbol{\sigma}_{n+1}$ and elastic strain $\boldsymbol{\varepsilon}^{e}_{n+1}$ are updated respectively as (see Eq. (40))

$$\boldsymbol{\sigma}_{n+1} = \mathbf{H}\left(\Delta\tilde{\lambda}\right)\boldsymbol{\sigma}^{trial}_{n+1},$$

and

$$\boldsymbol{\varepsilon}^{e}_{n+1} = \mathbf{D}^{e^{-1}}\boldsymbol{\sigma}_{n+1}.$$

4.2 Viscoplastic tangent operator for plane stress state

The viscoplastic tangent operator for plane stress state shall be derived $\mathbf{D}^{vp}_{ps}$ from the linearization of equations (36), (39), and (55). After a straightforward mathematical manipulation of this algebraic equations one identifies

$$\mathbf{D}^{vp}_{ps} = \frac{\partial\boldsymbol{\sigma}_{n+1}}{\partial\boldsymbol{\varepsilon}^{e^{trial}}_{n+1}} = \left[\mathbf{D}^{e^{-1}} + \frac{\mathbf{P}\boldsymbol{\sigma}_{n+1}\otimes\mathbf{P}\boldsymbol{\sigma}_{n+1}}{-\left(a_0\dfrac{\partial\tilde{f}_{ps}}{\partial A_{n+1}} + \dfrac{\partial\tilde{f}_{ps}}{\partial\Delta\tilde{\lambda}}\right)} + \Delta\tilde{\lambda}\mathbf{P}\right]^{-1}, \tag{57}$$

where

$$\begin{aligned} a_0 = \Big\{\delta\exp\left(-a_1\delta\Delta\tilde{\lambda}\right)\left[A_{\infty_{n+1}}\left(1+c\bar{\varepsilon}_n\right) - A_n\right] + \\ + A_{\infty_{n+1}}c\Big\}\left(a_1 + \frac{\Delta\tilde{\lambda}}{3a_1}\frac{\partial\gamma}{\partial\Delta\tilde{\lambda}}\right) + \\ + \left\{ca_1\Delta\tilde{\lambda} + \left(1+c\bar{\varepsilon}_n\right)\left[1-\exp\left(-\delta a_1\Delta\tilde{\lambda}\right)\right]\right\}\frac{\partial A_{\infty_{n+1}}}{\partial\Delta\tilde{\lambda}}, \end{aligned} \tag{58}$$

and

$$a_1 = \sqrt{\frac{2}{3}\gamma\left(\Delta\tilde{\lambda}\right)}. \tag{59}$$

5 NUMERICAL RESULTS

This section has the aim to assess the corresponding constitutive and numerical aspects associated with the present development. In this respect, with a view to evaluating the whole finite element framework, simple cases, such as uniaxial tension, simple shear and biaxial stretching, are simulated. Obtained numerical solutions are then compared to specific analytical solutions. A more detailed explanation on the derivation of the analytical and semi-analytical solutions employed in this section is presented in [19]. Comparisons consider strain-rates ranging from $10^{-2}\,\mathrm{s}^{-1}$ to $10^{4}\,\mathrm{s}^{-1}$. In the sequence, in order to evaluate the present approach considering the structural response of more complex problem with a non-homogeneous deformation field, the stretching of a perforated plate is also

simulated. Since this case has been considered in the literature, the present framework is adapted to reproduce the same constitutive formulation proposed in the works in literature allowing the comparison of the results with previous researches. After the numerical verification of the present proposal, specific constitutive features associated with the constitutive model employed herein can be further explored. For example, the strain-induced hardening which is expected to play a major role during the high rate loading of metallic materials. Thereby, specific simulations considering strain-rate hardening effects in plane stress conditions are finally performed.

5.1 Monoelements - Homogeneous results

The material parameters to be employed in the following analysis are those adjusted by [2], where annealed OFHC cooper samples were considered. Parameters values are presented in Table 1. A standard Newton-Raphson method was employed for the numerical solution of the nonlinear system of equations in the returning mapping phase. The minimum error tolerance for the residue norm of 10^{-6} was employed. All the analysis in this subsection were carried out considering a fixed number of iterations in time of $N = 20$ but varying the rates of deformation K.

Table 1: Material properties and model parameters for annealed OFHC cooper, with $\dot{\bar{\varepsilon}}_{lwr} = 10^{-4}$ s^{-1} and $\dot{\bar{\varepsilon}}_{up} = 10^{4}$ s^{-1}. Source: [2]

E (GPa)	ν	σ_y (MPa)	δ	c	A_∞^{lwr} (MPa)	A_∞^{up} (MPa)	ξ	ϑ (s)	m
112	0.33	35	6.46	0.42	233	420	3.16	1.2×10^3	105

5.1.1 Homogeneous compression

The problem addressed in this section consists in the solution of the application of a homogeneous compression in a geometry with quadrilateral shape where the plane stress state is imposed. The analyzed numerical model is formed by a single quadrilateral element of equal side $l_0 = 6$ mm of four nodes. The geometry and boundary conditions are presented in Fig. 1. Also, just for sake of comparison, a single brick element was also considered for analysis aiming to show that under the conditions specified in Fig. 1 the multiaxial element will reproduce the plane stress state and the results have to remain the same.

The analysis was performed by imposing a total homogeneous compression deformation of $\varepsilon_{22_f} = -0.5$ at the final time t_f, which is obtained by applying a total prescribed displacement of $\bar{u}_2 = -2.3608$ mm on the upper face of the element in Fig. 1. The analytical response was derived considering the condition of a rigid-viscoplastic material, resulting in the following stress evolution equation

$$|\sigma_{22}| = (\sigma_y + A)\left(1 + \sqrt{\frac{3}{2}}\vartheta|K|\right)^{1/m} . \tag{60}$$

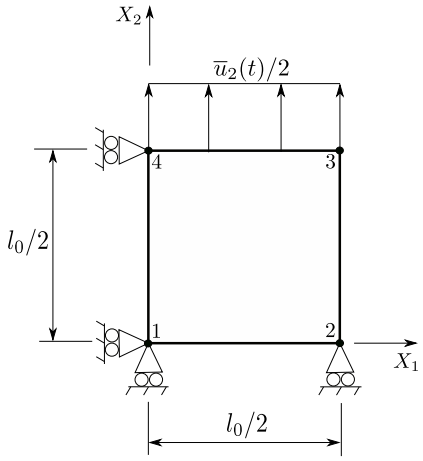


Figure 1: Homogeneous compression - Finite element mesh and boundary conditions.

The comparisons for the stress evolution and hardening evolution for different deformation rates are presented in Figs. 2 and 3. While analyzing the results of these figures it is clear that there is a good approximation between the numerical results with respect to the analytical solution. Due to the rigid-viscoplastic analytical solution, a slight deviation between numerical and analytical response is evidenced at earlier deformation stages. This difference is explained due to the significant contribution of the elastic deformation part at the beginning of the deformation process, which is not taken into account in the rigid viscoplastic analytical model.

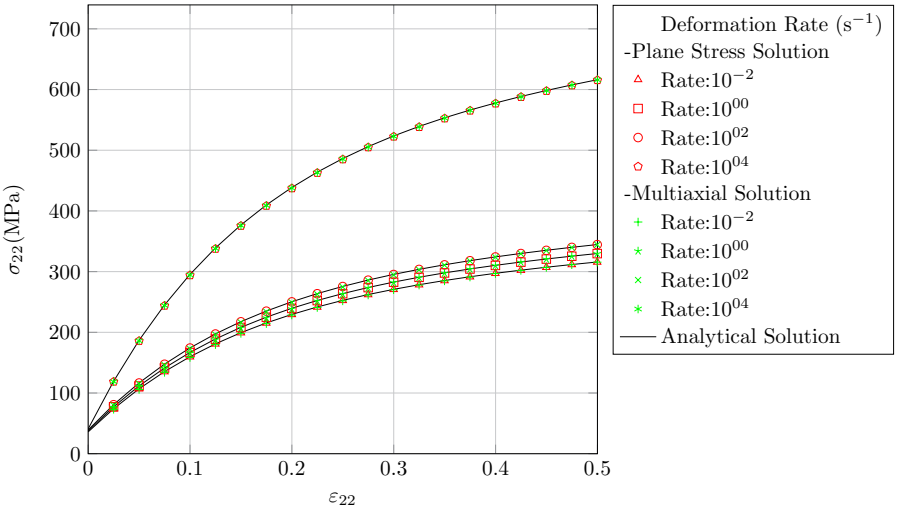


Figure 2: Comparison of flow stress-strain results for homogeneous compression.

It is also possible to observe that in the comparison between responses for the multiaxial stress state and for the plane stress state the result found also agrees with the expected response. Thus, the result indicates that the models developed respect the hypothesis that in the plane, for a given field of homogeneous strain/stress, the stress responses between

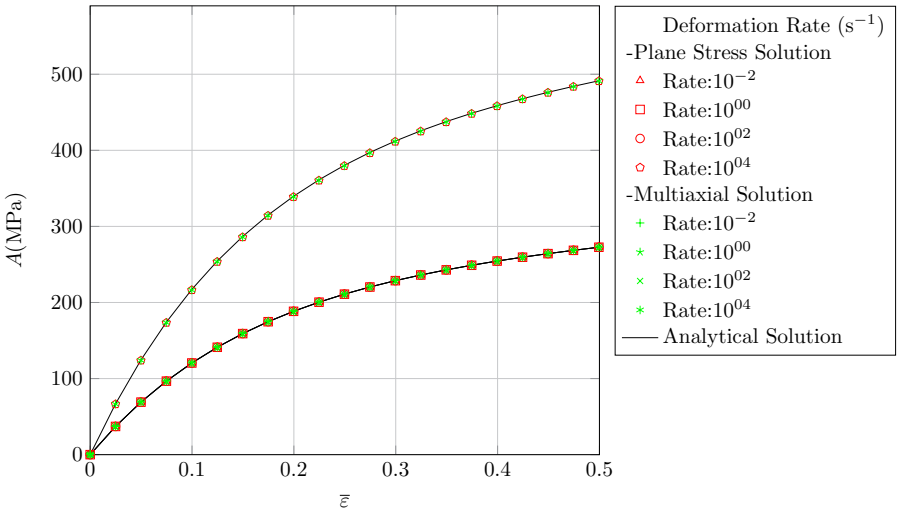


Figure 3: Comparison of hardening versus accumulated viscoplastic strain for homogeneous compression.

both cases must be the same.

5.1.2 Simple Shear

Here, we seek to find the same characteristics mentioned in the previous section, but now in front of a problem where the shear components are preponderant with respect to the normal components. The numerical model is formed by a single quadrilateral element of equal side $l_0 = 6$ mm of eight nodes. Figure 4 shows the geometry and boundary conditions employed for this example. A brick element was also considered for the multiaxial response.

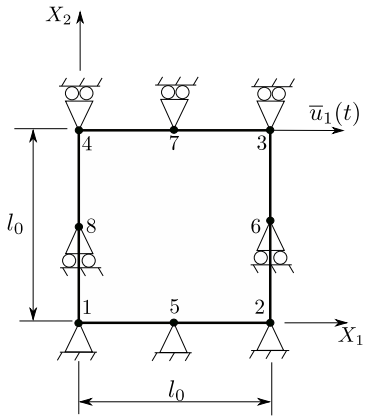


Figure 4: Simple shear - Finite element mesh and boundary conditions.

A total shear deformation of $2\varepsilon_{12} = 0.5$ at final time t_f was imposed, obtained from a prescribed displacement of $\overline{u}_1 = 3.124$ mm on the upper face of the element in Fig.

4. For this case, the developed approximate[2] response for the stress evolution, also for a rigid-viscoplastic material, is

$$|\sigma_{12}| = \sqrt{\frac{1}{3}}(\sigma_y + A)\left(1 + \frac{1}{\sqrt{2}}\vartheta|K|\right)^{1/m} . \tag{61}$$

Figures 5 and 6 show the evolution of the in-plane shear stress component versus the shear deformation and of the hardening in terms of the accumulated viscoplastic strain, respectively. Notice that, as for the first case, there is a very good agreement among the results.

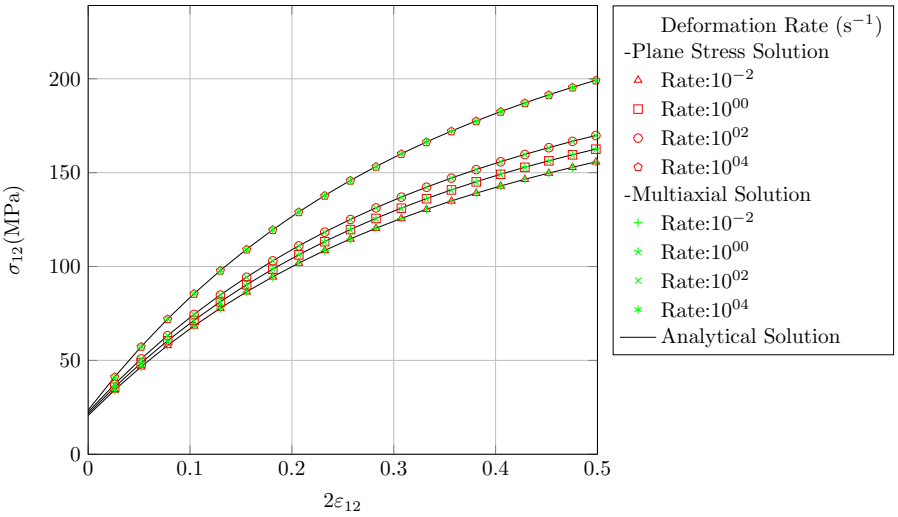


Figure 5: Comparison of flow stress-strain results for simple shear.

5.1.3 Biaxial stretching with finite rotation

The case analyzed in this section consists in the application of a simultaneous biaxial stretching and finite rotation on a single four node quadrilateral finite element of size $l_0 = 1$ mm, as depicted in Fig. 7 where the geometry and boundary conditions are presented. The biaxial stretching occurs in the X_1-X_2 plane while the rotation is around the X_3 axis.

The displacement field applied for this case is given by

$$\bar{u}_1 = \varpi X_2 \quad \text{and} \quad \bar{u}_2 = -\varpi X_1 . \tag{62}$$

At the final time the multiplier assumes the value of $\varpi = 0.7013$ resulting in a homogeneous deformation state of 0.5.

[2]During the development of the analytical solution, under finite deformation, the normal stress components were considered small with relation to the shear component. Therefore the normal components were disregarded.

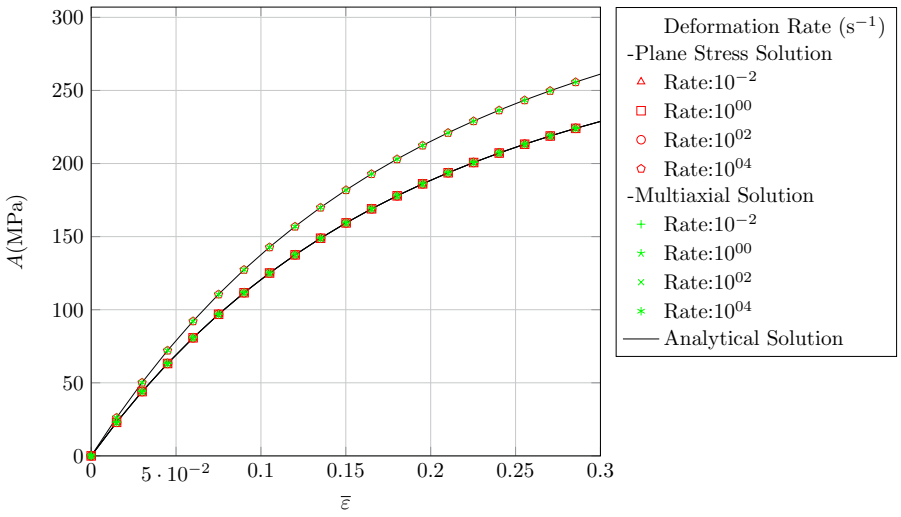


Figure 6: Comparison of hardening versus accumulated viscoplastic strain for simple shear.

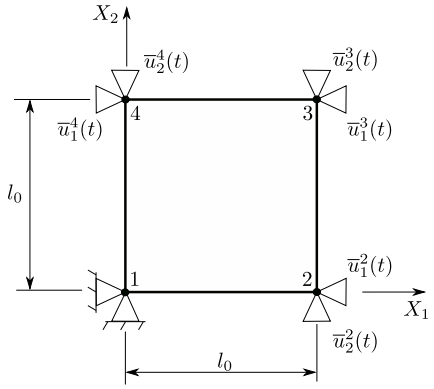


Figure 7: Stretching with rotation - Finite element mesh and boundary conditions.

The stress evolution equation, also under rigid-viscoplastic material hypothesis, is approximated by

$$|\sigma_{11,22}| = (\sigma_y + A)\left(1 + 2\sqrt{\frac{3}{2}}\vartheta\frac{K^2t}{K^2t^2+1}\right)^{1/m}. \tag{63}$$

The comparisons between analytical and numerical for the stress and hardening evolution for different deformation rates are presented in Figs. 8 and 9. The results depicted in these figures show a very good agreement between the analytical and numerical data. As for the last two subsections a brick element was considered in the analysis, see the multiaxial solution.

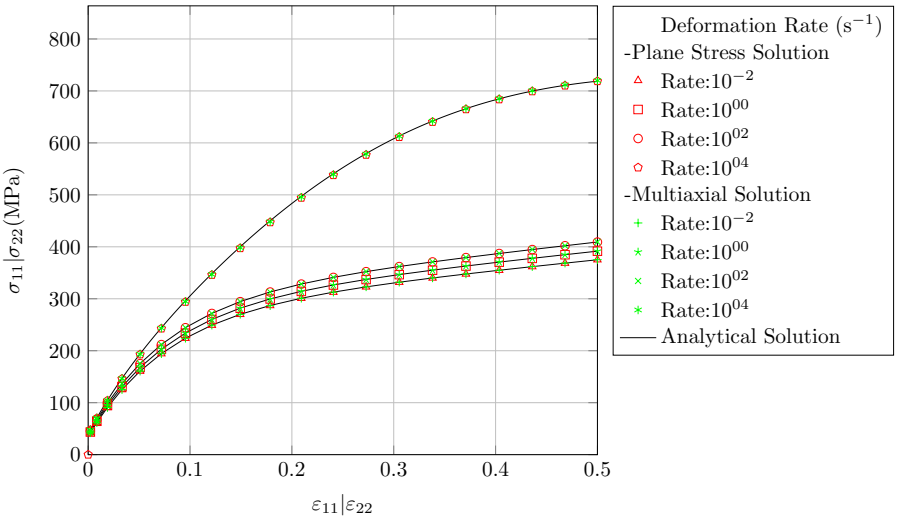


Figure 8: Comparison of flow stress-strain results viscoplastic strain for biaxial stretching with finite rotation.

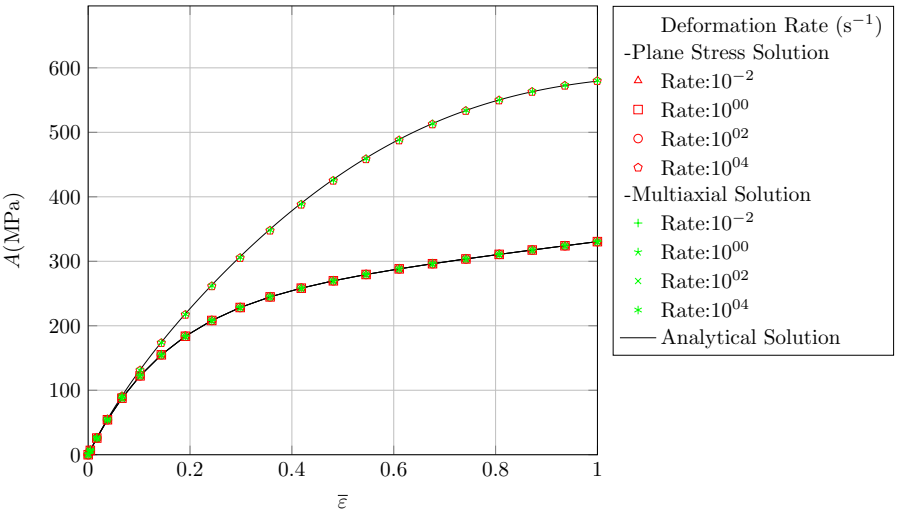


Figure 9: Comparison of hardening versus accumulated viscoplastic strain for biaxial stretching with finite rotation.

5.2 Stretching a perforated plate

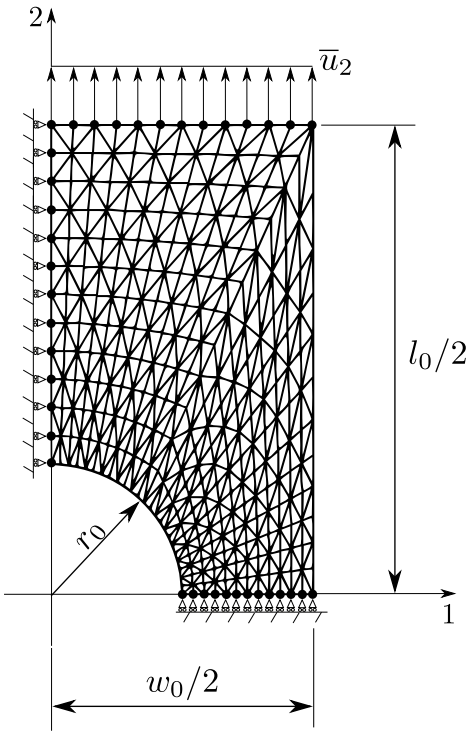
This subsection describes an elasto-viscoplastic problem of a stretching of a perforated plate. Unlike the simple problems analyzed previously, which develop homogeneous stress-strain fields, in the present problem this does not happen.

5.2.1 Verification example using a rate-insensitive hardening

The idea here is to compare the numerical results achieved using the proposed framework with those already published by other authors who employed different strategies to

impose the plane stress state. After an extensive research in the bibliography, we found the *plane stress* numerical results for the *elasto-viscoplastic* problem of a stretching a perforated plate published by [5] and [6]. Accordingly [6] the numerical solution for this problem was achieved by using the *nested iteration algorithm* to impose the plane stress state, see [6], page 469, for more details. Therefore, such results serve as the reference solution for the implementation using the stress-projected algorithm presented in this work.

The model used for this analysis is shown in Fig. 10, in which the dimensions, boundary conditions, discretization and material properties are shown. Also in this figure, the hardening law employed by [5] and [6] is stated. The model was discretized with 576 triangular elements having three nodes per element. It was constructed by applying appropriate boundary conditions to reproduce symmetry conditions resulting in only one quarter of the plate. In this example the Perić overstress function was employed for analysis.



Geometry:
$w_0 = 20$ mm
$l_0 = 36$ mm
$r_0 = 5$ mm

Material properties:
$E = 70$ GPa
$\nu = 0.2$

Hardening law:
$\sigma_y(\overline{\varepsilon}) = 0.243 + 0.2\overline{\varepsilon}$ (GPa)

Viscosity parameter:
$\vartheta^{-1} = 0.002$ s^{-1}

Figure 10: Stretching of a perforated plate - Geometry, boundary conditions and finite element mesh.

For the hardening response to be compatible with the aforementioned publications, the parameters A_∞^{lwr} and A_∞^{up} were set to be unitary in Eq. (7), having $c = 0.2$ in Eq. (6). Also, the initial yield stress was set to $\sigma_y = 0.243$ in Eq. (1). Regarding the overstress function, it was necessary to multiply the parameter related to viscosity for the *Perić* model, ϑ, by $\sqrt{2/3}$. Such modification was necessary because the format of the equations in the cited works differs from the constitutive model used in this work.

The numerical analysis was carried out applying a total vertical displacement of $\overline{u}_2 = 6.15$ mm at the upper face of the plate, as shown in Fig. 10. Different constant rates were employed by varying the velocity v_2. The comparison with the works of [5] and [6] was established in terms of the reaction force in the direction 2 where the vertical displacement is prescribed. The total reaction force was obtained by the summation of the nodal reaction forces in the direction 2 considering loading rates varying from $2v_2/l_0 = 0.555\text{E}^{-4}$ to $2v_2/l_0 = 0.555\text{E}^{+2}$ s^{-1} for the cases where the exponent m in Eq. 28 is 1, 10 and 100.

In order to compare the results obtained in this work with those presented by [5] and [6], a careful digitization process was performed of the graphs presented by these respective authors. Then, with help of a software, we have extracted some data points on the curves from the digitization graph image. Of course, the process of digitization implies introducing some uncertainties in relation to the data obtained in comparison with the originals.

The comparison results for the stretching of the perforated plate are presented in terms of the total reaction force versus edge displacement in the graphs of Figs. 11, 12 and 13. Notice that, despite the uncertainties of the digitization process, the numerical results obtained with the proposed stress projected algorithm are very close to those presented by [5] and [6].

In addition to the rate dependent results we have also plotted the strain rate independent response in Figs. 11, 12 and 13 which was found using the present implementation, which serves as an illustrative and comparative feature of the proposed model. The rate independent case was model by increasing the exponent m to be a large value.

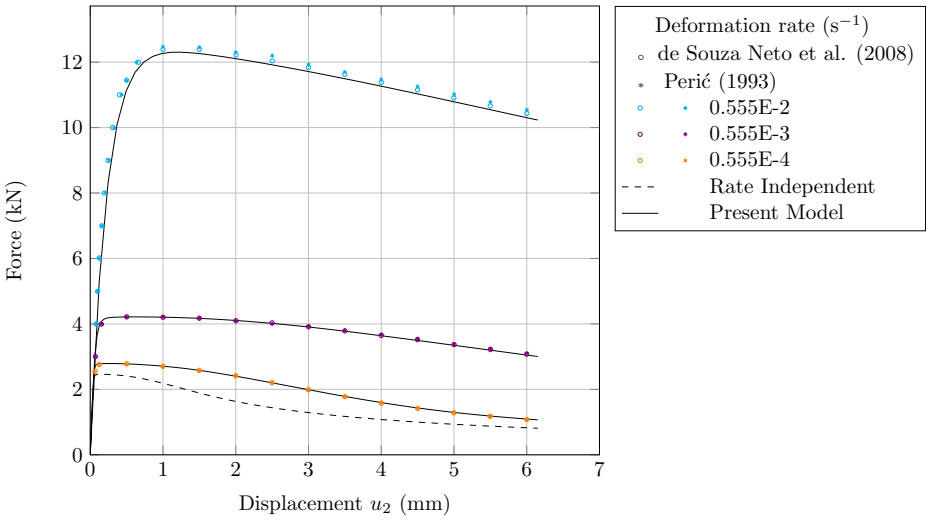


Figure 11: Results for stretching of a perforated plate - Force versus edge displacement for rate sensitivity exponent $m = 1$.

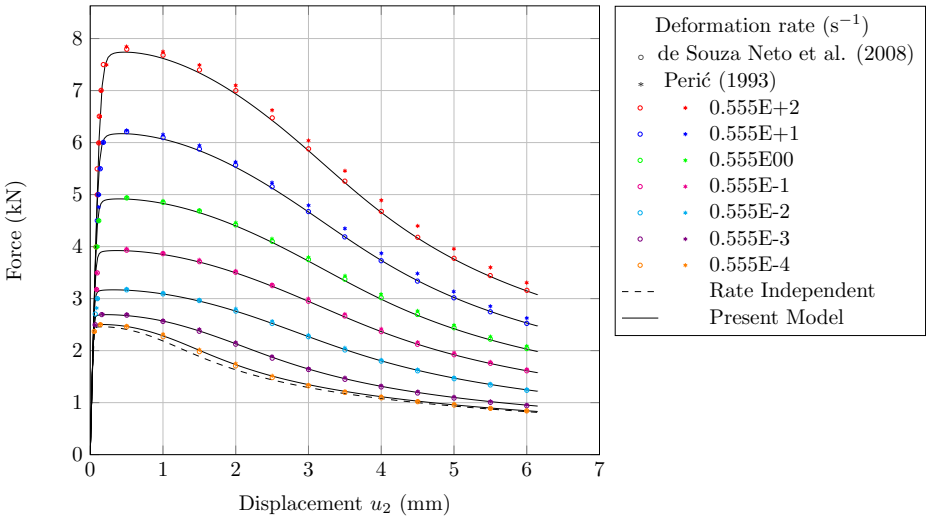


Figure 12: Results for stretching of a perforated plate - Force versus edge displacement for rate sensitivity exponent $m = 10$.

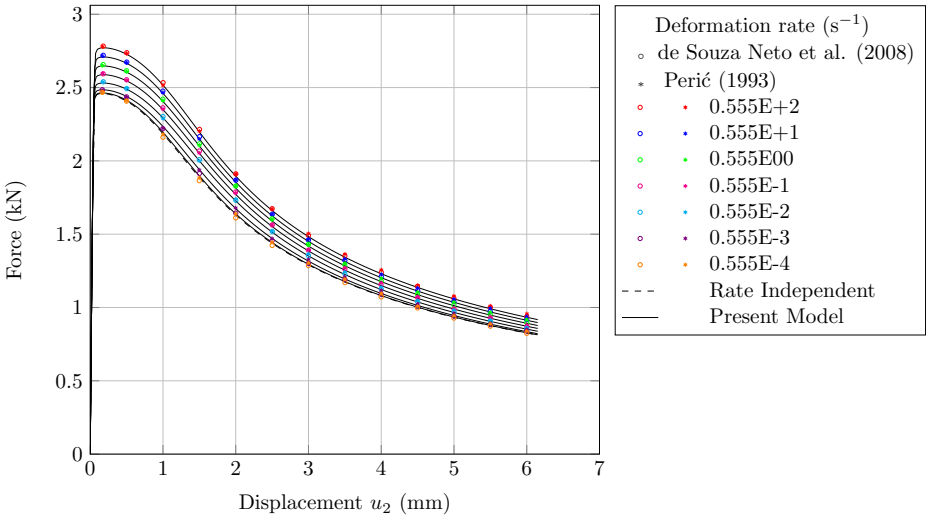


Figure 13: Results for stretching of a perforated plate - Force versus edge displacement for rate sensitivity exponent $m = 100$.

5.2.2 Rate-dependent hardening results

Now we turn our attention to the rate-dependent hardening effects on the response of components and structures. For this purpose, we consider the same discretization and boundary conditions shown in Fig. 10 but uses the full strain-rate hardening model described in subsection 2.1 together with the Perić overstress function Eq. (11) and the material parameters for OFHC cooper presented in Table 1.

The results for stretching of a perforated plate in terms of reaction force versus edge

displacement, for different rates of loading, and considering hardening strain-rate dependence and independence are presented in Fig. 14. Note that the higher the loading rate the greater is the difference between the formulations that consider strain-rate dependent hardening to that for which the hardening is insensitive to the strain-rate. For the higher rate consider in this case, 10^4 s^{-1}, this difference is high, showing the importance of such consideration in viscoplastic analysis of structures.

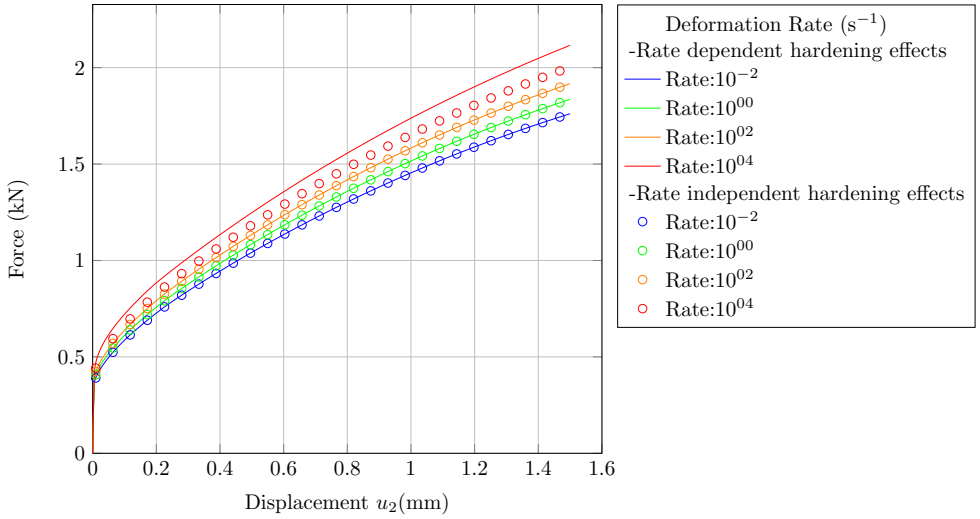


Figure 14: Results for stretching of a perforated plate - Force versus edge displacement for strain-rate dependence and independence hardening formulations.

6 CONCLUSIONS

This paper presented verification examples in elasto-viscoplasticity that shall be considered for code checking, a very important issue during the development of numerical algorithms and further implementation in the nonlinear world. Such verification examples were developed and used to verify the numerical accuracy and precision of an in-house implementation of the stress projected algorithm routines inside the context of elasto-viscoplasticity and the finite element method. During the studying and developing of own constitutive models for elasto-viscoplasticity we faced the necessity to check the program and noticed, quite surprisingly, that there are very few works in the literature treating of the imposition of the plane stress state inside the context of elasto-viscoplasticity. A version of the so-called stress-projected framework to enforce the plane stress state inside the context of viscoplasticity is presented in details. It has been demonstrated that this strategy can be used within the viscoplasticity approach provided that special attention is given to the treatment of the overstress function.

ACKNOWLEDGMENTS

The author Andrey Brezolin wishes to acknowledge the master scholarship supported by *CAPES*, Coordenação de Aperfeiçoamento de Pessoal de Nível Superior. The au-

thor Rodrigo Rossi wishes to acknowledge the support of *CNPq*, Conselho Nacional de Desenvolvimento Científico e Tecnológico (Grant number 306058/2018-9).

REFERENCES

[1] dos Santos, T. *Experimental characterization and constitutive modeling of a viscoplastic effects in high strain-rate deformation of polycrystalline FCC metals*. PhD thesis, Universidade Federal do Rio Grande do Sul, (2016).

[2] dos Santos, T., Rosa, P. A., Maghous, S., and Rossi, R. A simplified approach to high strain rate effects in cold deformation of polycrystalline fcc metals: Constitutive formulation and model calibration. *International Journal of Plasticity* **82**, 76 – 96 (2016).

[3] Perzyna, P. Fundamental problems in viscoplasticity. volume 9 of *Advances in Applied Mechanics*, 243–377. Elsevier (1966).

[4] Perzyna, P. Thermodynamic theory of viscoplasticity. volume 11 of *Advances in Applied Mechanics*, 313–354. Elsevier (1971).

[5] Perić, D. On a class of constitutive equations in viscoplasticity: Formulation and computational issues. *International Journal for Numerical Methods in Engineering* **36**(8), 1365–1393 (1993).

[6] de Souza Neto, E., Peric, D., and Owen, D. *Computational Methods for Plasticity: Theory and Applications*. Wiley, (2008).

[7] Schreyer, H. L., Kulak, R. F., and Kramer, J. M. Accurate numerical solutions for elastic-plastic models. *Journal of Pressure Vessel Technology* **101**(3), 226–234 (1979).

[8] Jetteur, P. Implicit integration algorithm for elastoplasticity in plane stress analysis. *Engineering Computations* **3**(3), 251–253 (1986).

[9] Simo, J. C. and Taylor, R. L. A return mapping algorithm for plane stress elastoplasticity. *International Journal for Numerical Methods in Engineering* **22**(3), 649–670 (1986).

[10] Hornberger, K. and Stamm, H. An implicit integration algorithm with a projection method for viscoplastic constitutive equations. *International Journal for Numerical Methods in Engineering* **28**(10), 2397–2421 (1989).

[11] Walz, G., Hornberger, K., and Stamm, H. An implicit integration algorithm for plane stress viscoplastic constitutive equations. *Computers & Structures* **36**(3), 539 – 546 (1990).

[12] Ohno, N., Tsuda, M., Sugiyama, H., and Okumura, D. Elastic-viscoplastic implicit integration algorithm applicable to both plane stress and three-dimensional stress states. *Finite Elements in Analysis and Design* **109**, 54 – 64 (2016).

[13] Paris, T. and Saanouni, K. Damaged behavior under plane stress. *European Journal of Computational Mechanics* **20**(5-6), 341–368 (2011).

[14] Lee, S., Yoon, J., and Yang, D. A stress integration algorithm for plane stress elastoplasticity and its applications to explicit finite element analysis of sheet metal forming processes. *Computers & Structures* **66**(2), 301 – 311 (1998).

[15] Valoroso, N. and Rosati, L. Consistent derivation of the constitutive algorithm for plane stress isotropic plasticity. part I: Theoretical formulation. *International Journal of Solids and Structures* **46**(1), 74 – 91 (2009).

[16] Valoroso, N. and Rosati, L. Consistent derivation of the constitutive algorithm for plane stress isotropic plasticity. part II: Computational issues. *International Journal of Solids and Structures* **46**(1), 92 – 124 (2009).

[17] Montáns, F. J. Implicit plane stress algorithm for multilayer j2-plasticity using the prager-ziegler translation rule. *International Journal for Numerical Methods in Engineering* **59**(3), 409–418 (2003).

[18] Simo, J. and Hughes, T. *Computational Inelasticity*. Interdisciplinary Applied Mathematics. Springer New York, (1998).

[19] Brezolin, A. Avaliação numérica de um modelo de viscoplasticidade com endurecimento dependente da taxa de deformação. Master's thesis, Universidade Federal do Rio Grande do Sul, (2018).

XV International Conference on Computational Plasticity. Fundamentals and Applications
COMPLAS 2019
E. Oñate, D.R.J. Owen, D. Peric, M. Chiumenti & Eduardo de Souza Neto (Eds)

ELASTIC PROPERTIES OF ISOTROPIC DISCRETE SYSTEMS WITH SKEW CONTACT NORMALS

JAN ELIÁŠ*

* Brno University of Technology
Faculty of Civil Engineering
Institute of Structural Mechanics
Veveří 331/95, Brno, 60200, Czech Republic
e-mail: jan.elias@vut.cz

Key words: Discrete model, homogenization, elasticity, Poisson's ratio, normal vector

Abstract. The macroscopic elastic properties of discrete assemblies are fundamental characteristics of such systems. The contribution uses homogenization procedure based on equivalence of virtual work between the isotropic elastic continuum and the discrete system to develop analytical formulas for estimation of macroscopic elastic modulus and Poisson's ratio.

Such homogenization was recently used to derive formulas for discrete assemblies where (i) there is no vacant space between the discrete units, (ii) the orientation of contacts is uniformly distributed and (iii) the contact normals are parallel to contact vectors (directions connecting centers of discrete units). The third assumption is now removed, three dimensional systems with arbitrary relation between contact vectors and contact normals are studied here.

It is shown that the limits of Poisson's ratio of such system depends on the relation between contact normal and contact vector. The widest limits are however obtained when these two vectors are parallel. This means that arbitrary manipulations with discrete geometry cannot extend Poisson's ratio of the system outside the known boundaries.

1 INTRODUCTION

Discrete modeling allows to explain or predict complex behavior of heterogeneous, cohesive or granular materials. It represents material random heterogeneity and also directly works with discrete and oriented nature of cracks. Its elastic behavior still posses open challenges. Besides the minor issue of inevitable boundary layer [1], the major problem lies in inability to exhibit Poisson's ratios greater than 1/4 for three dimensional models. The usage of the discrete models is therefore limited to materials with relatively low Poisson's ratio.

This paper is motivated by long belief of the author that Poisson's ratio of discrete systems can be increased by changing model geometry. Models described in literature

usually use contact faces between discrete units perpendicular to contact vectors [2, 3]. This restriction is here abandoned allowing to construct model of completely arbitrary geometry. Poisson's ratio is then analyzed using strong assumptions about rotations and translations in the model according to [4]. The paper unfortunately proves that geometrical changes lead only to shrinking of the interval of achievable Poisson's ratios. The previously published results derived for 2D models [5] are extended here into 3D.

The studied system is composed of ideally rigid bodies filling a domain continuously without gaps or overlapping. It is assumed that the system is isotropic in statistical sense – there is no directional dependence. The rigid bodies interact at their borders, where normal and tangential displacement discontinuities $\boldsymbol{\Delta}$ results in normal and tangential forces. Critical parameter governing the macroscopic Poisson's ratio is the ratio between tangential and normal contact stiffness denoted α hereinafter.

Equations are derived from virtual work equality between the discrete system and Boltzmann continuum subjected to equal straining. The discrete system yields non-symmetric stress tensor on contrary to the Boltzmann continuum symmetric stress quantity. The virtual work equivalence is therefore accomplished with help of symmetrization of the tensor of elastic constants from the discrete model. To simplify the notation, we introduce operation transposition T_{ij} on arbitrary tensor $\boldsymbol{A}$ of sufficient order by swapping indices i and j.

$$A^{T_{ij}}_{\ldots i\ldots j\ldots} = A_{\ldots j\ldots i\ldots} \tag{1}$$

2 FUNDAMENTAL GEOMETRIC RELATIONS

Each if the rigid bodies have 6 degrees of freedom associated with translations and rotations of some inner node, $\boldsymbol{x}_a$. The contact element between two nodes $\boldsymbol{x}_a$ and $\boldsymbol{x}_b$ has contact area A, length l, unit normal vector $\boldsymbol{n}$ and contact vector $\boldsymbol{t}$. The situation is sketched in Fig. 1a in two dimensions.

The vector $\boldsymbol{n}$ is here defined in Cartesian coordinate system by two angles, ξ and ζ

$$\boldsymbol{n} = (\cos\xi \sin\zeta,\ \sin\xi \sin\zeta,\ \cos\zeta) \tag{2}$$

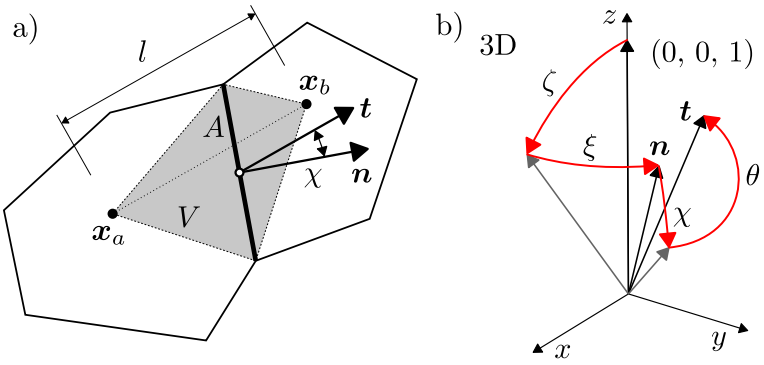


Figure 1: a) Contact between two rigid bodies, its normal and contact vector, area and volume; b) angles determining directions of normal and contact vector.

where ζ is angle between z axis and normal and ξ is the rotation of $\boldsymbol{n}$ around the z axis - see Fig. 1. We assume that the system has no directional bias, therefore all normal directions share the same probability of occurrence. Therefore, ξ must be uniform over interval from 0 to 2π and ζ has the following probability density function

$$f_\xi(\xi) = \begin{cases} \dfrac{1}{2\pi} & \text{for } \xi \in (0, 2\pi) \\ 0 & \text{otherwise} \end{cases} \qquad f_\zeta(\zeta) = \begin{cases} \dfrac{\sin\zeta}{2} & \text{for } \zeta \in (0, \pi) \\ 0 & \text{otherwise} \end{cases} \tag{3}$$

The contact vector $\boldsymbol{t}$ is defined relatively to normal vector $\boldsymbol{n}$ by angles χ and θ - see Fig. 1b. To ensure isotropic, directionally unbiased 3D structure θ is required to be uniformly distributed over 0–2π interval, probability distribution of f_χ can be arbitrary.

$$f_\theta(\theta) = \begin{cases} \dfrac{1}{2\pi} & \text{for } \theta \in (0, 2\pi) \\ 0 & \text{otherwise} \end{cases} \tag{4}$$

For sake of simplicity, it will be assumed now that the maximum angle between $\boldsymbol{n}$ and $\boldsymbol{t}$ is $\gamma \in (0,\ \pi)$ and all directions within this range are equally probable.

$$f_\chi(\chi) = \begin{cases} \dfrac{\sin\chi}{1-\cos\gamma} & \text{for } \theta \in (0, \gamma) \\ 0 & \text{otherwise} \end{cases} \tag{5}$$

Rotation matrix is the second order tensor that provides the following relation between $\boldsymbol{n}$ and $\boldsymbol{t}$

$$\boldsymbol{t} = \boldsymbol{R} \cdot \boldsymbol{n} \tag{6}$$

One can imagine construction of $\boldsymbol{n}$ via taking the vector $\begin{pmatrix} 0 & 0 & 1 \end{pmatrix}$, rotate it along the y axis by angle ζ and then along z axis by angle ξ (Fig. 1b). In the same way, the construction of $\boldsymbol{t}$ is done by four successive rotations along axes y, z, y and z by angles χ, θ, ζ and ξ, respectively.

$$\boldsymbol{n} = \boldsymbol{R}_z(\xi) \cdot \boldsymbol{R}_y(\zeta) \cdot \begin{pmatrix} 0 & 0 & 1 \end{pmatrix} \quad \boldsymbol{t} = \boldsymbol{R}_z(\xi) \cdot \boldsymbol{R}_y(\zeta) \cdot \boldsymbol{R}_z(\theta) \cdot \boldsymbol{R}_y(\chi) \cdot \begin{pmatrix} 0 & 0 & 1 \end{pmatrix} \tag{7}$$

The rotation matrix from Eq. (6) is therefore

$$\boldsymbol{R}(\xi, \zeta, \chi, \theta) = \boldsymbol{R}_z(\xi) \cdot \boldsymbol{R}_y(\zeta) \cdot \boldsymbol{R}_z(\theta) \cdot \boldsymbol{R}_y(\chi) \cdot \boldsymbol{R}_y^T(\zeta) \cdot \boldsymbol{R}_z^T(\xi) \tag{8}$$

The cosine of angle χ between $\boldsymbol{n}$ and $\boldsymbol{t}$ reads

$$\cos\chi = \boldsymbol{n} \cdot \boldsymbol{t} = \boldsymbol{n} \cdot \boldsymbol{R} \cdot \boldsymbol{n} = \boldsymbol{R} : (\boldsymbol{n} \otimes \boldsymbol{n}) = \boldsymbol{R} : \boldsymbol{N} \tag{9}$$

where the second order tensor $\boldsymbol{N}$ is according to Kuhl et al. [4] defined as $\boldsymbol{N} = \boldsymbol{n} \otimes \boldsymbol{n}$. Since no gaps or overlaps exist between the rigid bodies, the volume of the domain is summation over volume of individual mechanical elements

$$V = \sum_e V_e = \sum_e \cos\chi_e \frac{A_e l_e}{3} = \sum_e \boldsymbol{R}_e : \boldsymbol{N}_e \frac{A_e l_e}{3} \tag{10}$$

Note that the volume of individual element is negative whenever $\chi > \pi/2$.

3 TENSOR OF EQUIVALENT ELASTIC CONSTANTS

Let us strain the discrete system in macroscopic sense by constant strain tensor $\boldsymbol{\varepsilon}$. According to [4], it is assumed that all the rotations are zeros and differences in translations are dictated by differences in position

$$\varphi = 0 \qquad\qquad \boldsymbol{u}_b - \boldsymbol{u}_a = \boldsymbol{\varepsilon} \cdot (\boldsymbol{x}_b - \boldsymbol{x}_a) \tag{11}$$

The displacement jump on contact between cells a and b reads

$$\boldsymbol{\Delta} = \boldsymbol{u}_b - \boldsymbol{u}_a = l\boldsymbol{\varepsilon} \cdot \boldsymbol{t} \tag{12}$$

where l and $\boldsymbol{t}$ are length and contact vector belonging to element connecting bodies a and b. The normal and shear strain and stress directly follow

$$e_N = \frac{\boldsymbol{n} \cdot \boldsymbol{\Delta}}{l} = \boldsymbol{n} \cdot \boldsymbol{\varepsilon} \cdot \boldsymbol{t} \qquad\qquad \boldsymbol{e}_T = \frac{\boldsymbol{\Delta}}{l} - e_N \boldsymbol{n} = \boldsymbol{\varepsilon} \cdot \boldsymbol{t} - (\boldsymbol{n} \cdot \boldsymbol{\varepsilon} \cdot \boldsymbol{t})\, \boldsymbol{n} \tag{13}$$

$$s_N = E_0 e_N \qquad\qquad \boldsymbol{s}_T = E_0 \alpha \boldsymbol{e}_T \tag{14}$$

where E_0 is the normal stiffness coefficient and α is the tangential/normal stiffness ratio considered constant in the whole domain.

The virtual work done by single element reads

$$\delta W = Al\,(s_N \delta e_N + \boldsymbol{s}_T \cdot \delta \boldsymbol{e}_T) \tag{15}$$

and summation of individual contributions provides the total virtual work in the discrete system.

Let us now define two additional tensors: the fourth order tensor $\boldsymbol{\mathscr{I}}^{\mathrm{vol}}$ and the third order tensor $\boldsymbol{T}$.

$$\boldsymbol{\mathscr{I}}^{\mathrm{vol}} = \frac{\mathbf{1} \otimes \mathbf{1}}{3} \tag{16}$$

$$\boldsymbol{T} = 3\boldsymbol{n} \cdot \left(\boldsymbol{\mathscr{I}}^{\mathrm{vol}}\right)^{T_{13}} - \boldsymbol{n} \otimes \boldsymbol{n} \otimes \boldsymbol{n} \tag{17}$$

where $\mathbf{1}$ is the identity matrix of size 3. Note that $\boldsymbol{T}$ is different from definition in [4, 1] because the symmetry implied by equality $\boldsymbol{t} = \boldsymbol{n}$ is no longer present. The transposition T_{13} means that dimensions 1 and 3 are swapped. Eq. (13) can be rewritten as

$$e_N = \left(\boldsymbol{N} \cdot \boldsymbol{R}^T\right) : \boldsymbol{\varepsilon} \qquad\qquad \boldsymbol{e}_T = \left(\boldsymbol{T} \cdot \boldsymbol{R}^T\right) : \boldsymbol{\varepsilon} \tag{18}$$

using transposition T of the second order tensor swapping its two dimensions $T = T_{12}$.

The virtual work of single element expressed in Eq. (15) can be rewritten as well

$$\begin{aligned}
\delta W &= Al\,(s_N \delta e_N + \boldsymbol{s}_T \cdot \delta \boldsymbol{e}_T) \\
&= AlE_0 \left(\left[\left(\boldsymbol{N} \cdot \boldsymbol{R}^T\right) : \boldsymbol{\varepsilon}\right] \left[\left(\boldsymbol{N} \cdot \boldsymbol{R}^T\right) : \delta\boldsymbol{\varepsilon}\right] + \alpha \left[\left(\boldsymbol{T} \cdot \boldsymbol{R}^T\right) : \boldsymbol{\varepsilon}\right] \cdot \left[\left(\boldsymbol{T} \cdot \boldsymbol{R}^T\right) : \delta\boldsymbol{\varepsilon}\right]\right) \\
&= AlE_0 \left[\boldsymbol{\varepsilon} : \left(\boldsymbol{R} \cdot \boldsymbol{N} \otimes \boldsymbol{N} \cdot \boldsymbol{R}^T\right)^{T_{12}} : \delta\boldsymbol{\varepsilon} + \alpha\boldsymbol{\varepsilon} : \left(\boldsymbol{R} \cdot \boldsymbol{T}^{T_{13}} \cdot \boldsymbol{T} \cdot \boldsymbol{R}^T\right) : \delta\boldsymbol{\varepsilon}\right] \\
&= AlE_0\boldsymbol{\varepsilon} : \left(\left(\boldsymbol{R} \cdot \boldsymbol{N} \otimes \boldsymbol{N} \cdot \boldsymbol{R}^T\right)^{T_{12}} + \alpha \boldsymbol{R} \cdot \boldsymbol{T}^{T_{13}} \cdot \boldsymbol{T} \cdot \boldsymbol{R}^T\right) : \delta\boldsymbol{\varepsilon} \\
&= AlE_0\boldsymbol{\varepsilon} : (\boldsymbol{\mathscr{N}} + \alpha\boldsymbol{\mathscr{T}}) : \delta\boldsymbol{\varepsilon}
\end{aligned} \tag{19}$$

where

$$\boldsymbol{\mathscr{N}} = \left(\boldsymbol{R}\cdot\boldsymbol{N}\otimes\boldsymbol{N}\cdot\boldsymbol{R}^T\right)^{T_{12}} \qquad \boldsymbol{\mathscr{T}} = \boldsymbol{R}\cdot\boldsymbol{T}^{T_{13}}\cdot\boldsymbol{T}\cdot\boldsymbol{R}^T \tag{20}$$

The total virtual work of reads

$$\delta W^{\mathrm{dis}} = \sum_e \delta W_e = \sum_e A_e l_e E_0 \boldsymbol{\varepsilon} : (\boldsymbol{\mathscr{N}}_e + \alpha\boldsymbol{\mathscr{T}}_e) : \delta\boldsymbol{\varepsilon} \tag{21}$$

The discrete system is now related to equally strained elastic isotropic Boltzmann Boltzmann continuum occupying the same domain of volume V. Stress in the continuum is provided by constitutive equation $\boldsymbol{\sigma} = \boldsymbol{D} : \boldsymbol{\varepsilon}$, where $\boldsymbol{D}$ is fourth order tensor of elastic constants. The virtual work of the continuum is

$$\delta W^{\mathrm{con}} = V\boldsymbol{\sigma} : \delta\boldsymbol{\varepsilon} = V\boldsymbol{\varepsilon} : \boldsymbol{D} : \delta\boldsymbol{\varepsilon} \tag{22}$$

The equivalence of the discrete and continuous system implies equality of virtual works

$$\delta W^{\mathrm{dis}} = \delta W^{\mathrm{con}} \tag{23}$$

Substituting Eqs. (21) and (22) into Eq. (23), expression for tensor of elastic constants is derived

$$\boldsymbol{D} = \left\langle \frac{1}{V}\sum_e A_e l_e E_0 \left(\boldsymbol{\mathscr{N}}_e + \alpha\boldsymbol{\mathscr{T}}_e\right) \right\rangle^{\mathrm{SYM}} \tag{24}$$

The symmetrization is needed because the tensors $\boldsymbol{\mathscr{N}}$ and $\boldsymbol{\mathscr{T}}$ do not posses the symmetries required for Boltzmann continuum, which are the *major* symmetry (derived from equivalence of mixed derivatives of elastic potential) and the *minor* symmetry (derived from symmetry of stress and strain tensors). The symmetric part can be easily obtained using transposition T_{34}.

$$\langle\bullet\rangle^{\mathrm{SYM}} = \frac{\bullet + \bullet^{T_{34}}}{2} \tag{25}$$

Thanks to assumed statistical independence between normal and contact vector and elemental area and length, the summation in Eq. (24) can be broken into the following expression

$$\boldsymbol{D} = \frac{E_0}{V}\left\langle \mathrm{E}\left[\boldsymbol{\mathscr{N}}\right] + \alpha\mathrm{E}\left[\boldsymbol{\mathscr{T}}\right]\right\rangle^{\mathrm{SYM}} \sum_e A_e l_e \tag{26}$$

where $\mathrm{E}\left[\bullet(\boldsymbol{x})\right]$ is the mean value of function $\bullet$ dependent on vector $\boldsymbol{x}$ with distribution function $f_{\boldsymbol{X}}(\boldsymbol{x})$

$$\mathrm{E}\left[\bullet(\boldsymbol{x})\right] = \int_{-\infty}^{\infty}\cdots\int_{-\infty}^{\infty} \bullet(\boldsymbol{x}) f_{\boldsymbol{X}}(\boldsymbol{x})\,\mathrm{d}\boldsymbol{x} \tag{27}$$

Substituting V from Eq. (10) and utilizing the statistical independence again, one obtains

$$\boldsymbol{D} = \frac{3E_0}{\mathrm{E}[\boldsymbol{R} : \boldsymbol{N}]}\left\langle \mathrm{E}\left[\boldsymbol{\mathscr{N}}\right] + \alpha\mathrm{E}\left[\boldsymbol{\mathscr{T}}\right]\right\rangle^{\mathrm{SYM}} \tag{28}$$

4 EVALUATION OF EXPECTATIONS

The integration of mean values from Eq. (28) is tedious. It was analytically done in [5] in two dimensions over two independent variable. For three dimensions it has to be performed over four independent angles and the integration cannot be separated since rotation matrix $\boldsymbol{R}$ depends on all four angles. The calculation was performed by computer with a help of Python library for symbolic mathematics SymPy [6]. The following three integrations were delivered.

$$\mathrm{E}\left[\boldsymbol{R}:\boldsymbol{N}\right] = \int_{-\gamma}^{\gamma}\int_{0}^{2\pi}\int_{0}^{\pi}\int_{0}^{2\pi} \boldsymbol{R}:\boldsymbol{N}\frac{1}{2\pi}\frac{\sin\zeta}{2}\frac{1}{2\pi}\frac{\sin\chi}{1-\cos\gamma}\,\mathrm{d}\xi\,\mathrm{d}\zeta\,\mathrm{d}\theta\,\mathrm{d}\chi = \cos^2\left(\frac{g}{2}\right) \tag{29}$$

$$\begin{aligned}\mathrm{E}\left[\boldsymbol{\mathcal{N}}\right] =& \int_{-\gamma}^{\gamma}\int_{0}^{2\pi}\int_{0}^{\pi}\int_{0}^{2\pi} \boldsymbol{\mathcal{N}}\frac{1}{2\pi}\frac{\sin\zeta}{2}\frac{1}{2\pi}\frac{\sin\chi}{1-\cos\gamma}\,\mathrm{d}\xi\,\mathrm{d}\zeta\,\mathrm{d}\theta\,\mathrm{d}\chi = \\ =& \frac{1}{3}\left(\boldsymbol{\mathcal{I}}^{\mathrm{vol}}\right)^{T_{23}} + \frac{2\cos\gamma+\cos 2\gamma+1}{20}\left(\boldsymbol{\mathcal{I}}^{\mathrm{vol}} + \left(\boldsymbol{\mathcal{I}}^{\mathrm{vol}}\right)^{T_{24}} - \frac{2}{3}\left(\boldsymbol{\mathcal{I}}^{\mathrm{vol}}\right)^{T_{23}}\right)\end{aligned} \tag{30}$$

$$\begin{aligned}\mathrm{E}\left[\boldsymbol{\mathcal{T}}\right] =& \int_{-\gamma}^{\gamma}\int_{0}^{2\pi}\int_{0}^{\pi}\int_{0}^{2\pi} \boldsymbol{\mathcal{T}}\frac{1}{2\pi}\frac{\sin\zeta}{2}\frac{1}{2\pi}\frac{\sin\chi}{1-\cos\gamma}\,\mathrm{d}\xi\,\mathrm{d}\zeta\,\mathrm{d}\theta\,\mathrm{d}\chi = \\ =& \frac{2}{3}\left(\boldsymbol{\mathcal{I}}^{\mathrm{vol}}\right)^{T_{24}} - \frac{2\cos\gamma+\cos 2\gamma+1}{20}\left(\boldsymbol{\mathcal{I}}^{\mathrm{vol}} + \left(\boldsymbol{\mathcal{I}}^{\mathrm{vol}}\right)^{T_{23}} - \frac{2}{3}\left(\boldsymbol{\mathcal{I}}^{\mathrm{vol}}\right)^{T_{24}}\right)\end{aligned} \tag{31}$$

Only the symmetric parts of these expectations are needed (Eq. 25). The symmetric parts of involved tensors are

$$\left\langle\left(\boldsymbol{\mathcal{I}}^{\mathrm{vol}}\right)^{T_{23}}\right\rangle^{\mathrm{SYM}} = \left\langle\left(\boldsymbol{\mathcal{I}}^{\mathrm{vol}}\right)^{T_{24}}\right\rangle^{\mathrm{SYM}} = \frac{\boldsymbol{\mathcal{I}}}{3} \tag{32}$$

where the fourth order tensor $\boldsymbol{\mathcal{I}} = \mathcal{I}_{ijkl} = (\delta_{ik}\delta_{jl} + \delta_{il}\delta_{jk})/2$ with $\delta_{ij} \equiv \mathbf{1}$ being the Kronecker delta is employed. The symmetric part of expectations reads

$$\left\langle\mathrm{E}\left[\boldsymbol{\mathcal{N}}\right]\right\rangle^{\mathrm{SYM}} = \frac{2\cos\gamma+\cos 2\gamma+21}{180}\boldsymbol{\mathcal{I}} + \frac{2\cos\gamma+\cos 2\gamma+1}{20}\boldsymbol{\mathcal{I}}^{\mathrm{vol}} \tag{33}$$

$$\left\langle\mathrm{E}\left[\boldsymbol{\mathcal{T}}\right]\right\rangle^{\mathrm{SYM}} = \frac{39-2\cos\gamma-\cos 2\gamma}{180}\boldsymbol{\mathcal{I}} - \frac{2\cos\gamma+\cos 2\gamma+1}{20}\boldsymbol{\mathcal{I}}^{\mathrm{vol}} \tag{34}$$

5 MACROSCOPIC ELASTIC CHARACTERISTICS

The mechanical behavior of linearly elastic isotropic solid is determined by two independent constants (here we choose elastic modulus E and Poisson's ratio ν) defining tensor of elastic constants

$$\boldsymbol{D} = \frac{E}{1+\nu}\boldsymbol{\mathcal{I}} + \frac{3E\nu}{(1+\nu)(1-2\nu)}\boldsymbol{\mathcal{I}}^{\mathrm{vol}} \tag{35}$$

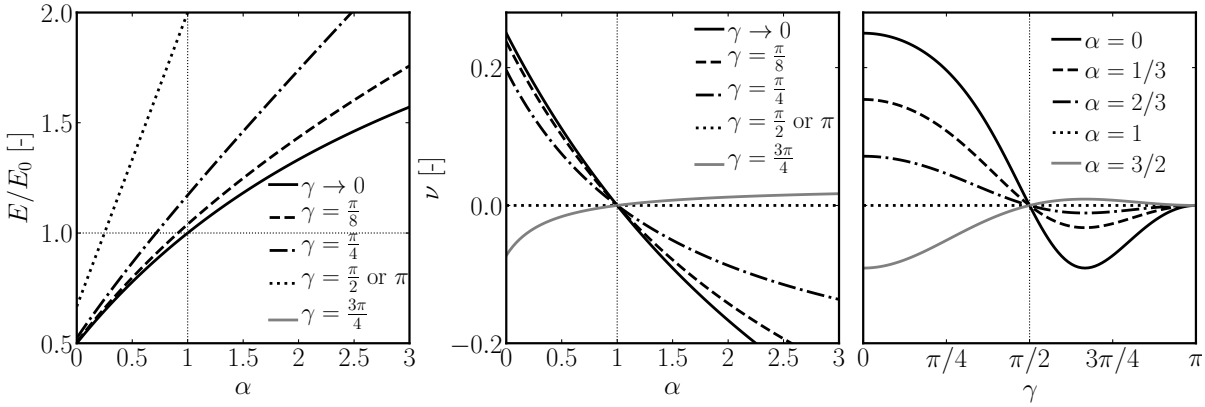


Figure 2: Macroscopic elastic characteristics according to Eqs. (38) and (37).

Equation (28) along with symmetrized expectations (29), (33) and (34) provides

$$\boldsymbol{D} = E_0 \left[\frac{(1-\alpha)(2\cos\gamma + \cos(2\gamma) - 39) + 60}{30(\cos\gamma + 1)} \boldsymbol{\mathscr{I}} + \frac{3(1-\alpha)}{5} \cos\gamma \boldsymbol{\mathscr{I}}^{\mathrm{vol}} \right] \tag{36}$$

Equality between respective scalar multipliers of tensors $\boldsymbol{\mathscr{I}}^{\mathrm{vol}}$ and $\boldsymbol{\mathscr{I}}$ in Eqs. (36) and (35) provides relations between macroscopic parameters E and ν and mesoscopic parameters E_0, α and γ.

$$\nu = \frac{3(1-\alpha)(\cos\gamma + \cos^2(\gamma))}{(1-\alpha)(7\cos\gamma + 7\cos^2\gamma - 20) + 30} \tag{37}$$

$$E = E_0 \frac{2\left[(1-\alpha)(\cos\gamma + \cos^2\gamma - 20) + 30\right]\left[(1-\alpha)(\cos\gamma + \cos^2\gamma - 2) + 3\right]}{(1-\alpha)(7\cos\gamma + 7\cos^2\gamma - 20) + 30} \tag{38}$$

These equations are plotted in Fig. 2 for range $\alpha \in (0, 3)$.

Calculation limit for $\gamma \to 0$ must yield relations for discrete system with $\boldsymbol{n} = \boldsymbol{t}$.

$$\lim_{\gamma\to 0} \nu = \frac{1-\alpha}{4+\alpha} \qquad\qquad \lim_{\gamma\to 0} E = E_0 \frac{2+3\alpha}{4+\alpha} \tag{39}$$

Indeed, the calculation of limits provides correct expressions derived in e.g. [1] under assumption of perpendicularity of contact vector and contact face. They are also identical to those from microplane theory [7].

By differentiate the expression with respect to γ and search for stationary point, the maximum and minimum possible values of Poisson's ratio can be found. The stationary points are $\gamma = 0$, π and $\arccos(-0.5)$ (≈ 2.09440). Plotting the Poisson's ratio with respect to the limit angle γ (Fig. 2 on the right hand side) shows that the maximum range of ν is obtained for $\gamma = 0$, i.e. when the contact vector equals the normal vector. This is the classic solution stated in Eq. (39). Increasing γ towards $\pi/2$ shrinks the interval of achievable Poisson's ratios to zero. The interval opens again beyond $\pi/2$ with opposite signs; its width maximizes at $\gamma = \arccos(-0.5)$. The limiting values at this point are obtained at $\alpha = 0$ and $\alpha \to \infty$ as $(-0.091, 0.034)$. The maximum values of Poisson's ratio are achieved for $\boldsymbol{n} = \boldsymbol{t}$, any deviation of the model geometry from this relation causes narrowing of the Poisson's ratio limits.

6 CONCLUSIONS

- It has been proven that under assumption (5) one cannot increase the Poisson's ratio limits beyond what is provided by model with $\boldsymbol{n} = \boldsymbol{t}$ in Eq. (39).
- The formulas are derived from strong and unrealistic assumption about rotations and displacements in the model (Eq. 11). Behavior of the real model will be less rigid, however the overall effect on macroscopic elastic constants should be qualitatively the same.
- The same conclusions were found for 2D models under the same assumptions in [5].
- The theory will be extended to arbitrary distribution of χ and verified by comparison with real behavior of discrete systems.

ACKNOWLEDGEMENT

Financial support provided by the Czech Science Foundation under project No. GA19-12197S is gratefully acknowledged.

REFERENCES

[1] Jan Eliáš. Boundary layer effect on behavior of discrete models. *Materials*, 10:157, 2017. ISSN 1996-1944. doi:10.3390/ma10020157.

[2] Peter Grassl and John E. Bolander. Three-dimensional network model for coupling of fracture and mass transport in quasi-brittle geomaterials. *Materials*, 9(9):782, 2016. ISSN 1996-1944. doi:10.3390/ma9090782.

[3] John E. Bolander and Shigehiko Saito. Fracture analyses using spring networks with random geometry. *Engineering Fracture Mechanics*, 61(5-6):569–591, 1998. ISSN 0013-7944. doi:10.1016/S0013-7944(98)00069-1.

[4] Ellen Kuhl, Gian Antonio D'Addetta, Hans J. Herrmann, and Ekkehard Ramm. A comparison of discrete granular material models with continuous microplane formulations. *Granular Matter*, 2(3):113–121, 2000. ISSN 1434-5021. doi:10.1007/s100350050003.

[5] Jan Eliáš. On macroscopic elastic properties of isotropic discrete systems: effect of tessellation geometry. In *Proceedings of the Tenth International Conference on Fracture Mechanics of Concrete and Concrete Structures - FraMCoS-X held in Bayonne, France*, 2019.

[6] Aaron Meurer, Christopher P. Smith, Mateusz Paprocki, Ondřej Čertík, Sergey B. Kirpichev, Matthew Rocklin, AMiT Kumar, Sergiu Ivanov, Jason K. Moore, Sartaj Singh, Thilina Rathnayake, Sean Vig, Brian E. Granger, Richard P. Muller, Francesco Bonazzi, Harsh Gupta, Shivam Vats, Fredrik Johansson, Fabian Pedregosa, Matthew J. Curry, Andy R. Terrel, Štěpán Roučka, Ashutosh Saboo, Isuru Fernando,

Sumith Kulal, Robert Cimrman, and Anthony Scopatz. Sympy: symbolic computing in Python. *PeerJ Computer Science*, 3:e103, 2017. ISSN 2376-5992. doi:10.7717/peerj-cs.103.

[7] Ignacio Carol and Zdeněk P. Bažant. Damage and plasticity in microplane theory. *International Journal of Solids and Structures*, 34(29):3807–3835, 1997. ISSN 0020-7683. doi:10.1016/S0020-7683(96)00238-7.

XIV International Conference on Computational Plasticity. Fundamentals and Applications
COMPLAS 2019
E. Oñate, D.R.J. Owen, D. Peric , M. Chiumenti, and Eduardo de Souza Neto (Eds)

ON THE ACCURACY OF THE NUMERICAL INTEGRALS OF THE NEWMARK'S METHOD FOR COMPUTING INELASTIC SEISMIC RESPONSES

NOBUTERU YOSHIZAKI [*], KATSUSHI IJIMA[†], HIROYUKI OBIYA[†] AND NIZAM M. ZAKARIA[†]

[*]Department of Civil Engineering and Architecture
Graduate school of Science and Engineering
Saga University
1, Honjo, Saga, 840-8502, Japan
e-mail :18577015@edu.cc.saga-u.ac.jp

[†]Department of Civil Engineering and Architecture
Graduate school of Science and Engineering
Saga University
1, Honjo, Saga, 840-8502, Japan
e-mail :ijimak@cc.saga-u.ac.jp, Web page : http://toshi1.civil.saga-u.ac.jp/ijimak/index.html

Key words: Inelastic Seismic Response, Numerical Integral, Newmark's Method, Modal Analysis.

Abstract. *The paper proposes an algorithm of the numerical integration with the modal analysis for computing inelastic seismic responses, and furthermore, the accuracy of the numerical integration with the Newmark's β=1/4 method that is most popular in the earthquake engineering is discussed by comparing with the response computed by the proposed method.*

1 INTRODUCTION

In nations exposed by great earthquakes, the seismic proofs of structures against those earthquakes permit that the state of a structure may excess the yield strength by bending moment, but it must not reach to the collapse. Therefore, the verification in computing inelastic seismic responses needs the maximum of the response after excessing the yield point and the residual deformation of the structure.

These inelastic analyses do not need only using a correct inelastic characteristics model but also adopting an accurate algorithm for numerically integrating the equation of the motion. In the numerical integrals for that, the Newmark's β=1/4 method is most popular and it has been using since before more than 30 years. The method is to obtain the incremental response in the incremental time from solving only the linear equation derived from the Newmark's β=1/4 method. However, verifying the validity of the method does not seem enough, because there is no comparison with the exact solution or more accurate solution.

The authors recently developed an algorithm with the modal analysis that enabled

eliminating high frequency components certainly including errors from seismic response. The elimination of the high frequency components to advantage of the modal analysis makes the methods of numerical integrals giving accurate solutions usable. Those methods namely cannot directly solve the linear equation of the incremental response, because the linear equation always includes components with smaller period than the limitation of a time interval existing in those methods. The components with very small period do not contribute to the inelastic seismic response but breed divergence in those methods.

It has been published that there were the differences between the response computed by the modal analysis and that by the direct method with the Newmark's β=1/4 method. The paper is to show more amply the differences, the case of the agreement, comparing both responses of acceleration and so on.

2 THEORY OF NUMERICAL INTEGRALS WITH THE NEWMARK'S METHOD

The motion of an inelastic structure at the time t_m during an earthquake can be expressed by the following equation.

$$\mathbf{M}\ddot{\mathbf{u}}_m + \mathbf{C}_m\dot{\mathbf{u}}_m + \sum_e \boldsymbol{\alpha}_e\mathbf{S}_{e,m} = -\mathbf{M}\mathbf{J}\ddot{\boldsymbol{\phi}}_m . \tag{1}$$

In the equation (1), $\mathbf{M}$ is the mass matrix of the structure, and $\mathbf{C}_m$ is the damping matrix possible to be arbitrarily composed though the paper uses the Rayleigh damping $\mathbf{C}_m = \nu\mathbf{M} + \mu\mathbf{K}_m$ where ν is a constant as well as μ and $\mathbf{K}_m$ is the tangent stiffness of the structure at the time t_m or the secant stiffness joining the two states at the times of t_m and t_{m+1}. Moreover, $\mathbf{S}_{e,m}$ is the end force vector of the element e, $\boldsymbol{\alpha}_e$ is the transforming matrix that changes the element end forces to the forces in the universal coordinates, $\mathbf{J}\ddot{\boldsymbol{\phi}}_m$ is to give the input acceleration of the ground motion to all the nodes in the structure, and $\dot{\mathbf{u}}_m$ and $\ddot{\mathbf{u}}_m$ are the nodal velocity vector and the nodal acceleration vector respectively.

The method proposed in the paper applies the modal analysis with the Newmark's method to the equation (1) and then the existing methods directly apply the Newmark's method to the equation (1).

2.1 The method of modal analysis with the predictor-corrector method

Displacement modes and natural frequencies used in the modal analysis are derived from the eigenvalue analysis with the mass matrix $\mathbf{M}$ in the equation (1) and the tangent stiffness matrix $\mathbf{K}_{\mathrm{T}m}$ given by differentiating the third term in the equation (1) as follows.

$$\delta\left(\sum_e \boldsymbol{\alpha}_e\mathbf{S}_{e,m}\right) = \mathbf{K}_{\mathrm{T}m}\delta\mathbf{u} , \tag{2}$$

where δ expresses the differential operator, and $\delta\mathbf{u}$ is the infinitesimal displacement from the nodal position at the time t_m.

The generalized eigenvalue analysis using $\mathbf{M}$ and $\mathbf{K}_{\mathrm{T}m}$ gives the diagonal matrix $\boldsymbol{\Omega}_m^{(0)}$ composed by the squared natural circular frequencies and the matrix $\mathbf{X}_m^{(0)}$ composed by the displacement modes. The modes can transform the increment displacement $\Delta\mathbf{u}^{(0)}$ in the time

interval Δt between the times of t_m and t_{m+1} to the increment of the normal coordinates $\Delta\boldsymbol{\psi}^{(0)}$ as follows.

$$\Delta\mathbf{u}^{(0)} = \mathbf{X}_m^{(0)}\Delta\boldsymbol{\psi}^{(0)}, \tag{3}$$

where the upper suffix $^{(0)}$ attached to the variables means to relate with the predictor.

Applying the equation (3) and the Newmark's β method changes the equation (1) to the equation of $\Delta\boldsymbol{\psi}^{(0)}$, so that the equation of $\Delta\boldsymbol{\psi}^{(0)}$ is,

$$\begin{aligned}\left\{\frac{1}{\beta\Delta t}\left(\frac{1}{\Delta t}+\frac{\nu}{2}\right)\mathbf{I}+\left(\frac{\mu}{2\beta\Delta t}+1\right)\boldsymbol{\Omega}_m^{(0)}\right\}\Delta\boldsymbol{\psi}^{(0)} &= -\boldsymbol{\zeta}_m^{(0)}\Delta\ddot{\boldsymbol{\phi}}+\frac{1}{\beta}\left\{\left(\frac{1}{\Delta t}+\frac{\nu}{2}\right)\mathbf{I}+\frac{\mu}{2}\boldsymbol{\Omega}_m^{(0)}\right\}\dot{\boldsymbol{\psi}}_m \\ &+\left\{\left(\frac{1}{2\beta}+\frac{\nu\Delta t}{4\beta}-\nu\Delta t\right)\mathbf{I}+\mu\Delta t\left(\frac{1}{4\beta}-1\right)\boldsymbol{\Omega}_m^{(0)}\right\}\ddot{\boldsymbol{\psi}}_m,\end{aligned} \tag{4}$$

where $\boldsymbol{\zeta}_m^{(0)} = \mathbf{X}_m^{(0)\mathrm{T}}\mathbf{M}\mathbf{J}$ is the matrix composed by the participation factors, and $\mathbf{I}$ is the unit matrix.

Since all the matrices in the equation (4) are diagonal, the normal coordinates $\Delta\boldsymbol{\psi}^{(0)}$ are easily obtained. Then, the increment displacement $\Delta\mathbf{u}^{(0)}$ comes from the equation (3), and the displacement as the predictor at the time t_{m+1} is given by $\mathbf{u}_{m+1}^{(0)} = \mathbf{u}_m^{(0)} + \Delta\mathbf{u}^{(0)}$.

Those responses predicted, however, do not ordinarily satisfy the equation of the motion in changing the stiffness of the inelastic structure. Therefore, iterative computations are needed to correct them. In the computations of the iterative time number r, the variables of the response are provided with the upper suffix $^{(r)}$, e.g. the normal coordinates as corrector $\delta\boldsymbol{\psi}^{(r)}$, the matrix of the displacement modes $\mathbf{X}_{m+1}^{(r)}$, the diagonal matrix of the squares of the natural circular frequencies $\boldsymbol{\Omega}_{m+1}^{(r)}$ and so on.

The normal coordinates $\delta\boldsymbol{\psi}^{(r)}$ are obtained from solving the following equation.

$$\left\{\frac{1}{\beta\Delta t}\left(\frac{1}{\Delta t}+\frac{\nu}{2}\right)\mathbf{I}+\left(\frac{\mu}{2\beta\Delta t}+1\right)\boldsymbol{\Omega}_{m+1}^{(r)}\right\}\delta\boldsymbol{\psi}^{(r)} = \mathbf{X}_{m+1}^{(r)\mathrm{T}}\delta\mathbf{U}_{m+1}^{(r)}, \tag{5}$$

where $\delta\mathbf{U}_{m+1}^{(r)}$ is the unbalanced force as insufficiency in the equation of the motion at the time t_{m+1} as follows.

$$\delta\mathbf{U}_{m+1}^{(r)} = -\mathbf{M}\left(\mathbf{J}\ddot{\boldsymbol{\phi}}_{m+1}+\ddot{\mathbf{u}}_{m+1}^{(r)}\right)-\mathbf{C}_{m+1}^{(r)}\dot{\mathbf{u}}_{m+1}^{(r)}-\sum_e \alpha_e\mathbf{S}_{e,m+1}^{(r)}. \tag{6}$$

Then, the normal coordinates are corrected by the following equation,

$$\Delta\boldsymbol{\psi}^{(r)} = \mathbf{X}_{m+1}^{(r)\mathrm{T}}\mathbf{M}\mathbf{X}_{m+1}^{(r-1)}\Delta\boldsymbol{\psi}^{(r-1)}+\delta\boldsymbol{\psi}^{(r)}. \tag{7}$$

2.2 The direct method with the Newmark's β=1/4 method

There are the two of the typical direct methods that derive the responses fulfilling the equation of the motion at the time t_{m+1}. One uses the predictor-corrector method, and the other uses the secant stiffness given by joining the two quantities of structural states at the times of t_m and t_{m+1}. Though the methods are popular and famous, the paper briefly describes the

theories used in the computation to compare the proposed method.

(1) The predictor-corrector method, hereinafter shortened to PCM

Applying Newmark's β=1/4 method to the equation (1) gives the predictor of the increment displacement as follows.

$$\left(\frac{4}{\Delta t^2}\mathbf{M}+\frac{2}{\Delta t}\mathbf{C}_m+\mathbf{K}_{\mathrm{T}m}\right)\Delta\mathbf{u}^{(0)}=\mathbf{M}\left(\frac{4}{\Delta t}\dot{\mathbf{u}}_m+2\ddot{\mathbf{u}}_m-\mathbf{J}\Delta\ddot{\phi}\right)+2\mathbf{C}_m\dot{\mathbf{u}}_m. \tag{8}$$

The corrector is derived from the equation of the motion and the unbalanced force at the time t_{m+1} given by the predictor or the corrector at the iterative time number r-1.

$$\left(\frac{4}{\Delta t^2}\mathbf{M}+\frac{2}{\Delta t}\mathbf{C}_{m+1}^{(r)}+\mathbf{K}_{\mathrm{T}\,m+1}^{(r)}\right)\delta\mathbf{u}^{(r)}=\delta\mathbf{U}_{m+1}^{(r)}, \tag{9}$$

where $\delta\mathbf{U}_{m+1}^{(r)}$ is the unbalanced force at the time t_{m+1}.

The increment of the nodal displacement is renewed by $\Delta\mathbf{u}^{(r)}=\Delta\mathbf{u}^{(r-1)}+\delta\mathbf{u}^{(r)}$.

(2) The secant stiffness method, hereinafter shortened to SSM

First computing the response at the time t_{m+1} uses the tangent stiffness at the time t_m, and then the second afterward in the iterative computation uses the secant stiffness. The increment of the nodal displacement in the time interval Δt is obtained from the following equation.

$$\left(\frac{4}{\Delta t^2}\mathbf{M}+\frac{2}{\Delta t}\mathbf{C}_m^{(r)}+\mathbf{K}_{\mathrm{S}m}^{(r)}\right)\Delta\mathbf{u}^{(r)}=\mathbf{M}\left(\frac{4}{\Delta t}\dot{\mathbf{u}}_m+2\ddot{\mathbf{u}}_m-\mathbf{J}\Delta\ddot{\phi}\right)+2\mathbf{C}_m^{(r)}\dot{\mathbf{u}}_m\ , \tag{10}$$

where $\mathbf{K}_{\mathrm{S}m}^{(r)}$ is the secant stiffness.

3 COMPUTATIONAL MODEL AND THE INELASTIC VIBRATION CHARACTERISTIC

The paper uses the same frame structure as that used to be computed in the paper [5]. The structure is the steel pier for supporting the girder as shown in **Figure 1**. The pier fixed at the base plate is 11m in height and the upper part on the ground is 126kN in weight. The pier supports the girder of 957kN in weight and the mass is added to the top node, so that the structure is comparatively a top-heavy model. The computational model is axially divided to 19 elements of the bar models that the bending behavior is only inelastic and the others are elastic. All the deformation of bending, shear and elongation is assumed to be uniform in the elements. Consequently, the element model is the simplest in various inelastic models ever proposed, whereas it could be allowable to use the model because the purpose of the paper is to discuss the accuracy of numerical integrations, and because the fine division of a structure by using the inelastic model keeps enough accuracy.

The steel pier has the cross section of the box shape and the bending stiffness before/after the yielding are 49021.56 MNm^2 and 5071.8 MNm^2 respectively, and the bending moment at the yielding is 5MNm. The law of kinematic work-hardening applies to the bending behavior of the inelasticity of the computational model, as shown in **Figure 2** describing the hysteresis of the bending moment vs. the curvature at the base in an example of seismic responses.

When the bending stiffness in the pier changes like **Figure 2**, the natural frequencies of the

structure used in the modal analysis fluctuate as shown in **Figure 3**. **Figure 3(a)** shows the first natural frequency, and **Figure 3(b)** shows the third natural frequency. The figures indicate that the deterioration of the bending stiffness remarkably decreases the natural frequencies. Therefore, inelastic seismic computations should take care to adopt the modes that the natural frequencies are higher than a main frequency area of a seismic wave but the decreasing natural frequencies come within the frequency area. By the way, since the second mode relates to the vertical vibration of the structure, the natural frequency is almost flat even after the bending yielding and then omitted.

The damping constant defined by the Rayleigh damping in the paper is determined by the tow constants of ν=0.114 sec^{-1} and μ=0.001157sec. The values of the two constants keep the damping constant of 0.02 at the two frequencies of 0.5Hz and 10Hz, and then the pier has around 0.02 of the damping constant in a main frequency area of the seismic vibration used in the paper.

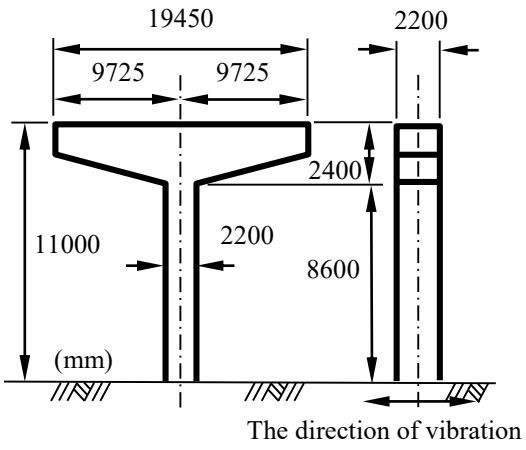


Figure 1: The steel pier used in the computation

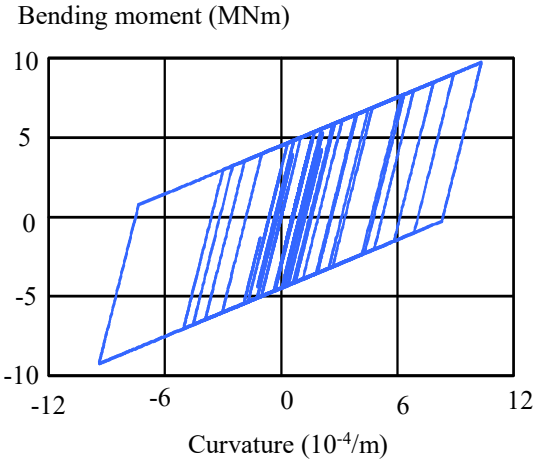


Figure 2: The hysteresis loop in the bending behavior of the element on the base

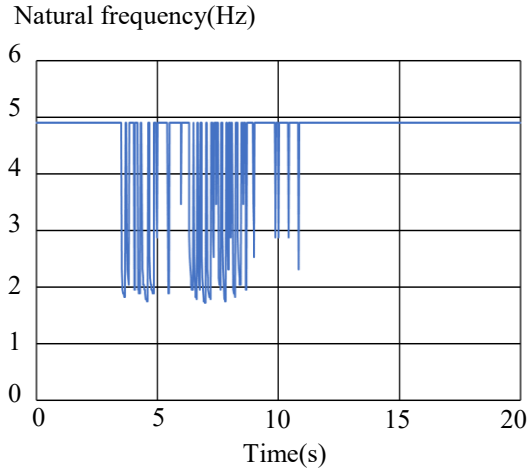


Figure 3(a): Fluctuation of the first natural frequency

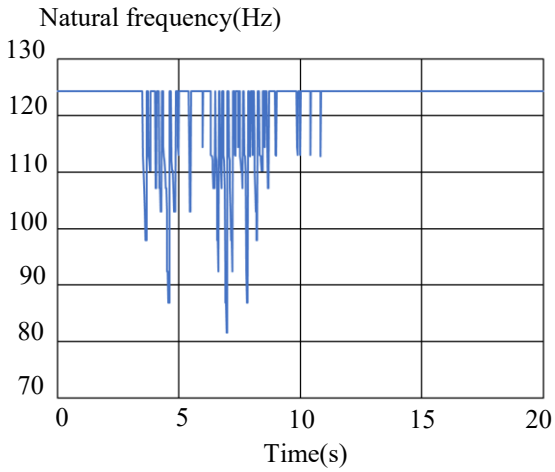


Figure 3(b): Fluctuation of the third natural frequency

4 COMPUTATIONAL RESULTS AND DISCUSSIONS

The input acceleration of the ground motion used in the computations is the acceleration record of Hyogo-ken Nanbu earthquake (1997). The acceleration of the digital data was recorded at the time interval of 0.02sec., and the computation applies the Fourier transformation to the record and the Fourier inverse transformation is used for the interpolation of the input acceleration. Most of the computations in the paper use the time interval of 0.002sec.. The reason for adopting so small time interval compared to that of the record is why the response displacement by the direct method with PCM converges at the time interval. The design criterion in Japan prescribes the convergence by the time interval. Additionally, the main frequency area of the input acceleration is around 0.5Hz to 5Hz.

The time histories of the horizontal component of the displacement at the top of the pier are shown in **Figure 4**. The figure compares the three waves of the time histories that the green line is the result by the direct method with PCM, the blue line is the results by the direct method with SSM and the dotted orange line is the result by the modal analysis with PCM.

The figure shows that the time history by the direct method with PCM is almost identical with that by the modal analysis and the direct method with SSM is only different from the others. Since the pier used for computing is a top-heavy structure, the first mode only is dominant and the third mode or higher mode in bending vibration does not almost affect the seismic response of the displacement. Therefore, although the direct method cannot filter high frequency components, the components may be so small that the direct method with PCM results in nearly equaling to the modal analysis. The reason why SSM gradually differ from PCM with the progress of time should be that a little difference of the bending stiffness affects the inelastic seismic response.

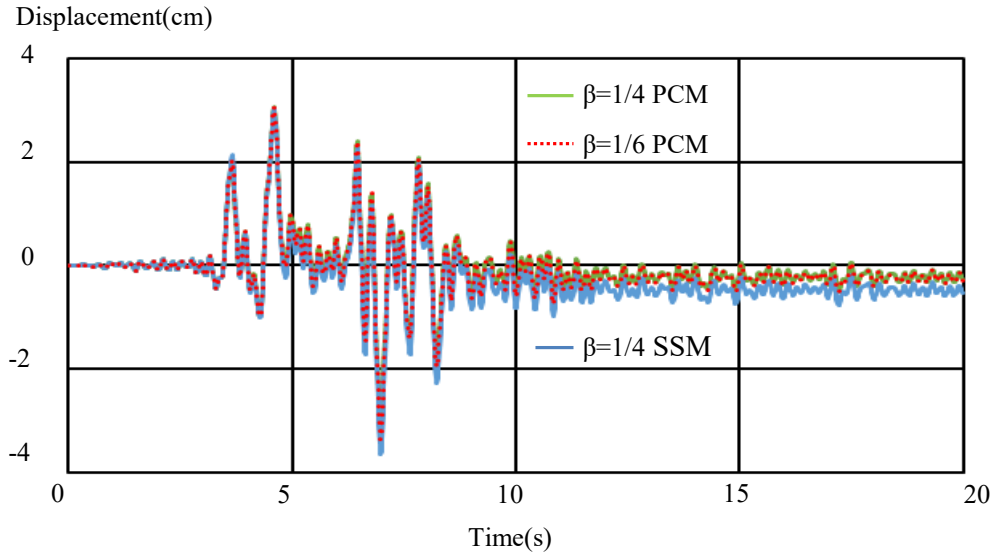


Figure 4: The time history responses of the displacement at the top in the pier

The lines in **Figure 5(a)** join the maximums of the horizontal component of displacement at all the nodes and the lines in **Figure 5(b)** join the maximums of the horizontal acceleration of all the nodes. The vertical axes in the figures indicate height in the pier.

The maximums of the horizontal displacement indicate that the result by the direct method with PCM almost agrees with that by the modal analysis but differs from the direct method with SSM as well as the time histories of the displacement.

The maximums of the horizontal acceleration indicate that the three results largely differ together except the maximums at the top of the pier. The mass at the top of the pier is especially so large that the top slowly oscillates, but the intermediate part of the pier vibrates with high frequencies. The modal analysis uses only the two modes and then the response does not include components of higher frequency more than around 125Hz. The response by direct method, however, includes the components of very high frequency and the components will contain errors.

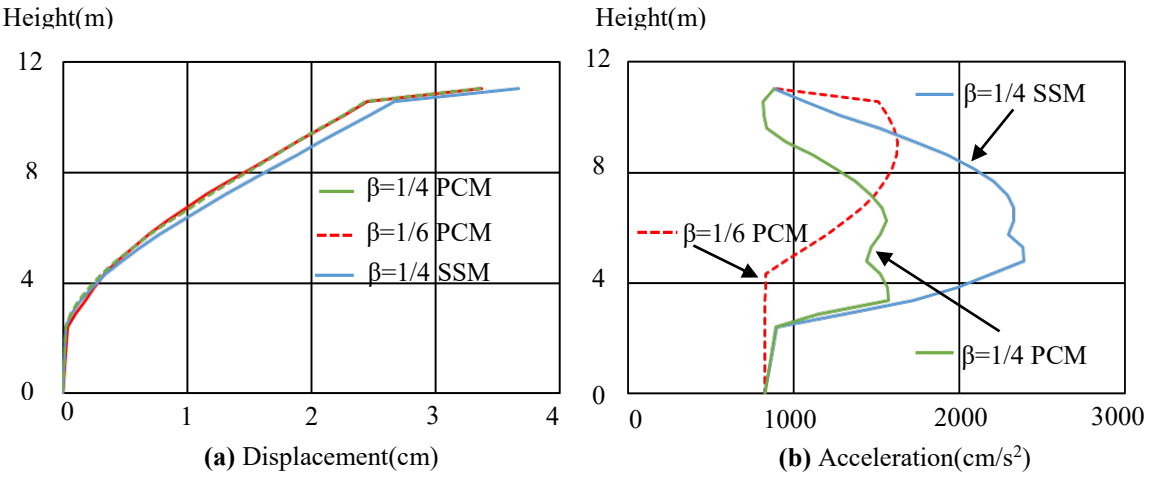


Figure 5: The maximums of the responce of the pier in height

12 CONCLUSIONS

- The paper proposed a method of the time integral with the modal analysis for computing seismic responses of inelastic structures. The advantage of the method is that the method can filter out components of high frequency from the seismic responses. The components of high frequency in the direct method tend to become errors included in the seismic responses.
- A typical steel pier with the inelasticity of bilinear characteristic was used for comparing seismic responses by the proposed method with that by existing methods.
- Since the pier was a top-heavy structure, the first mode only is dominant in the response, and then the displacement by the proposed method well agreed with the direct method with the predictor-corrector method but did not with the secant stiffness method.
- The acceleration responses of the pier computed by the three methods all differed each other.

REFERENCES

[1] Japan Road Association, *Specifications for Highway Bridges Part V Seismic Design*, Japan Road Association, Tokyo, (2012).

[2] The Building Center of Japan, *The Building Standard Law of Japan,* CD-ROM, The Building Center of Japan, Tokyo, (2016).

[3] N. M. Newmark, "A Method of Computation for Structural Dynamics", Proc. ASCE, Vol. 85, No. EM3, (1959), 67-94

[4] M. Miyahara, K. Ijima, H. Obiya and Nizam Z. M., "An accurate algorithm of numerical integration for computing seismic responses of inelastic structures", International Journal of Integrated Engineering, Special Issue 2018: Civil & Environmental Engineering, Vol. 10, No. 2, (2018), 82-86

XV International Conference on Computational Plasticity. Fundamentals and Applications
COMPLAS 2019
E. Oñate, D.R.J. Owen, D. Peric, M. Chiumenti & Eduardo de Souza Neto (Eds)

THE BREZIS-EKELAND-NAYROLES MINIMIZATION PRINCIPLE WITH MIXED FINITE ELEMENT METHOD FOR ELASTOPLASTIC DYNAMIC PROBLEMS

X. CAO*, A. OUESLATI*, A.D. NGUYEN†, M. STOFFEL†, B. MARKET† AND G. DE SAXCÉ*

* Univ. Lille, CNRS, Centrale Lille, FRE 2016 - LaMcube - Laboratoire de mécanique multiphysique et multiéchelle, F-59000, Lille, France
e-mail: xiaodan.cao@univ-lille.fr, abdelbacet.oueslati@univ-lille.fr, gery.de-saxce@univ-lille.fr

† Institute of General Mechanics, RWTH-Aachen University, Germany
e-mail: : andanh@iam.rwth-aachen.de, stoffel@iam.rwth-aachen.de, markert@iam.rwth-aachen.de

Key words: Numerical simulations, Elastic plastic materials, Variational principal, Brezis-Ekeland-Nayroles principle, Constrained optimization

Abstract. We propose a modification of the Hamiltonian formalism which can be used for dissipative systems, the Brezis-Ekeland-Nayroles principle. The formalism is specialized to the standard plasticity in small strains and dynamics. We apply it to solve the classical problem of a thin tube in plane strain subjected to an internal pressure. The continuum is discretized with mixed finite elements.

1 INTRODUCTION

There are two types energy loss, one originated from external actions, another derived from the internal effect. If the cause is internal, such as plasticity etc., we call them dissipative system. Hamilton's variational principle does not work in this case. The proposition, the Brezis-Ekeland-Nayroles principle (in short, BEN principle) is presented in the paper. For more detail of the BEN principle, see [1, 2, 3, 4, 5].

The symplectic version of the Brezis-Ekeland-Nayroles variational principle is proposed in [4]: *The natural evolution curve* $z : [t_0, t_1] \to X \times Y$ *minimizes the functional:*

$$\Pi(z) := \int_{t_0}^{t_1} \left[\phi(\dot{z}) + \phi^{*\omega}(\dot{z} - XH) - \omega(\dot{z} - XH, \dot{z})\right] \, \mathrm{dt} \tag{1}$$

among all the curves verifying the initial conditions $z(t_0) = z_0$ *and, remarkably, the minimum is zero.*

With ϕ dissipation potential, $\phi^{*\omega}$ its Fenchel transform, and ω a natural symplectic form. Observing that $\omega(\dot{z}, \dot{z})$ vanishes and integrating by part, we have also the variant:

$$\Pi(z) = \int_{t_0}^{t_1} [\phi(\dot{z}) + \phi^{*\omega}(\dot{z} - XH) - \frac{\partial H}{\partial t}(t, z)] \text{ dt} + H(t_1, z(t_1)) - H(t_0, z_0) \tag{2}$$

One advantage of the BEN principle is its ability in solving a mechanical problem simultaneously for all time steps. It can avoid the usual computation failures in the step-by-step method. Objective of this paper is to numerically test the feasibility of the BEN principle by modeling a simple mechanical problem, the tube subjected to an internal pressure in dynamics.

2 APPLICATION TO THE STANDARD PLASTICITY AND VISCOPLASTICITY IN DYNAMICS

Application of the BEN principle in statics case is discussed in [4, 5]. The small difference for the BEN principle between the case of statics and dynamics in the mechanical sense is the consideration of the inertia term $\dot{\boldsymbol{p}}$. In dynamics, the equilibrium equations

$$\nabla \cdot \boldsymbol{\sigma} + \boldsymbol{f} = \dot{\boldsymbol{p}} \quad \text{on} \quad \Omega, \qquad \boldsymbol{\sigma} \cdot \boldsymbol{n} = \bar{\boldsymbol{f}} \quad \text{on} \quad \partial\Omega_1 \tag{3}$$

are satisfied. This expression can be transformed as follows. For sake of easiness, let us put:

$$\langle \boldsymbol{l}(t), u \rangle = \int_{\Omega} \boldsymbol{f}(t) \cdot \boldsymbol{u} + \int_{\partial\Omega_1} \bar{\boldsymbol{f}}(t) \cdot \boldsymbol{u}$$

Then,

$$\frac{\partial H}{\partial t}(t, z) = -\langle \dot{\boldsymbol{l}}(t), \boldsymbol{u} \rangle$$

On the other hand

$$\frac{d}{dt} [H(t, z(t))] = \langle \frac{\boldsymbol{p}}{\rho}, \dot{\boldsymbol{p}} \rangle + \langle \boldsymbol{\sigma}, \nabla \dot{\boldsymbol{u}} - \dot{\boldsymbol{\varepsilon}}_I \rangle - \langle \boldsymbol{l}(t), \dot{\boldsymbol{u}} \rangle - \langle \dot{\boldsymbol{l}}(t), \boldsymbol{u} \rangle$$

For the minimizer, the kinematical conditions on $\partial\Omega_0$ and the balance of linear momentum (3) are satisfied and using Green's formula:

$$\langle \boldsymbol{\sigma}, \nabla \dot{\boldsymbol{u}} \rangle = \langle \boldsymbol{l}(t), \dot{\boldsymbol{u}} \rangle - \langle \dot{\boldsymbol{p}}, \dot{\boldsymbol{u}} \rangle \tag{4}$$

that leads to

$$\frac{d}{dt} [H(t, z(t))] - \frac{\partial H}{\partial t}(t, z) = -\langle \boldsymbol{\sigma}, \dot{\boldsymbol{\varepsilon}}_I \rangle \tag{5}$$

Putting (5) in (2) and time-integrating, we have:

$$\Pi(\boldsymbol{\sigma}, \dot{\boldsymbol{u}}) = \int_{t_0}^{t_1} \{\varphi(\boldsymbol{\sigma}) + \varphi^*(\nabla \dot{\boldsymbol{u}} - \boldsymbol{S}\dot{\boldsymbol{\sigma}}) - \langle \boldsymbol{\sigma}, \nabla \dot{\boldsymbol{u}} - \boldsymbol{S}\dot{\boldsymbol{\sigma}} \rangle\} \text{ dt} \tag{6}$$

among all curves $\boldsymbol{u} : [t_0, t_1] \to U$ satisfying the kinematical conditions on $\partial\Omega_0$ and all curves $\boldsymbol{\sigma} : [t_0, t_1] \to E$ such that $\boldsymbol{\sigma}(0) = \boldsymbol{\sigma}_0$ and the balance of linear momentum (3) are satisfied.

3 THE TUBE PROBLEM

We consider a tube of internal radius a and external one b within the plane strain hypothesis. Its internal wall is subjected to an internal pressure $\tilde{p} > 0$ monotonic increasing from zero. The material is elastic perfectly plastic and isotropic with von Mises model and yield stress σ_Y. The initial stresses, displacements and velocities are null. The problem is assumed to be axisymmetric, the stress tensor is diagonal in the local basis of the cylindrical coordinates. The axial tensile stress being supposed as usual to be the intermediate principal stress. We consider the elastic domain:

$$K = \{\boldsymbol{\sigma} \quad \text{such that} \quad f(\boldsymbol{\sigma}) - \sigma_Y \leq 0\}$$

The dissipation potential is:

$$\varphi(\boldsymbol{\sigma}) = \int_\Omega \chi_K(\boldsymbol{\sigma})$$

In the sequel, the inelastic strain $\dot{\boldsymbol{\varepsilon}}_I$ is plastic and denoted $\dot{\boldsymbol{\varepsilon}}^p$. The Fenchel conjugate is obtained conbining this rule with the expression of the dissipation power by unit volume and the yield condition:

$$D = \boldsymbol{\sigma} : \dot{\boldsymbol{\varepsilon}}^p = \sigma_Y \dot{\varepsilon}^p_{\theta\theta} \tag{7}$$

As $\dot{\varepsilon}^p_{\theta\theta}$ must be non negative, the Fenchel conjugate function is:

$$\varphi^*(\dot{\boldsymbol{\varepsilon}}^p) = \int_\Omega \left\{\sigma_Y \dot{\varepsilon}^p_{\theta\theta} + \chi_{\mathbb{R}_+}(\dot{\varepsilon}^p_{\theta\theta})\right\}$$

In plane strain and axisymmetry, the displacement is radial. The only non vanishing components of the strain rate tensor are:

$$\dot{\varepsilon}_{rr} = \frac{d\dot{u}_r}{dr}, \qquad \dot{\varepsilon}_{\theta\theta} = \frac{\dot{u}_r}{r} \tag{8}$$

In plane strain, Hooke's law reads:

$$\varepsilon_{rr} = \frac{1}{\bar{E}}\left(\sigma_{rr} - \bar{\nu}\,\sigma_{\theta\theta}\right), \qquad \varepsilon_{\theta\theta} = \frac{1}{\bar{E}}\left(\sigma_{\theta\theta} - \bar{\nu}\,\sigma_{rr}\right)$$

with: $\bar{E} = \frac{E}{1-\nu^2}, \bar{\nu} = \frac{\nu}{1-\nu}$. Hence the compliance operator reads:

$$\boldsymbol{S} = \frac{1}{\bar{E}} \begin{bmatrix} 1 & -\bar{\nu} \\ -\bar{\nu} & 1 \end{bmatrix}$$

In this problem, there is no supports ($\partial\Omega_0 = \emptyset$). As the minimum is certainly finite, the functional (6) becomes:

$$\bar{\Pi}(\boldsymbol{\sigma}, \boldsymbol{u}) = \int_{t_0}^{t_1} \left\{ \left(\int_\Omega \sigma_Y \dot{\varepsilon}^p_{\theta\theta}\right) - \langle \boldsymbol{\sigma}, \nabla\dot{\boldsymbol{u}} - \boldsymbol{S}\dot{\boldsymbol{\sigma}}\rangle \right\} \,\mathrm{dt} \tag{9}$$

where $\dot{\varepsilon}^p_{\theta\theta}$ is given by normality rule, among all the curves among all curves $(\boldsymbol{\sigma}, \boldsymbol{u})$: $[t_0, t_1] \to U \times E$ such that $\boldsymbol{\sigma}(t_0) = \mathbf{0}$, $\boldsymbol{u}(t_0) = \mathbf{0}$, satisfying the yield condition $f(\boldsymbol{\sigma}) - \sigma_Y \leq 0$ and the normality rule and the balance of linear momentum:

$$\begin{aligned} \frac{d}{dr}\sigma_{rr} + \frac{1}{r}\left(\sigma_{rr} - \sigma_{\theta\theta}\right) = \rho\,\ddot{u}_r \quad \text{for} \quad a < r < b, \\ \sigma_{rr}(a,t) = -\tilde{p}(t), \qquad \sigma_{rr}(b,t) = 0 \end{aligned} \tag{10}$$

4 MIXED FINITE ELEMENT OF TUBE PROBLEM

The continuum is discretized with mixed finite elements. There are two methods to model the tube problem: (i) Method A: balance of linear momentum satisfied exactly, (ii) Method B: balance of linear momentum satisfied in Gauss points.

4.1 Method A

Displacement field. We choose the displacement field:

$$u_r = v_1 + v_2 r + v_3 r^2 + v_4 r^3 \tag{11}$$

which provides the strain field:

$$\varepsilon_{rr} = \frac{du_r}{dr} = v_2 + 2\,v_3 r + 3\,v_4 r^2, \qquad \varepsilon_{\theta\theta} = \frac{u_r}{r} = \frac{v_1}{r} + v_2 + v_3 r + v_4 r^2$$

There is two connectors:

$$q_1 = u_r\,|_{r=\alpha}, \qquad q_2 = u_r\,|_{r=\beta}, \tag{12}$$

Considering two intermediate equidistant nodes of position, $\gamma = \frac{2\,\alpha+\beta}{3}, \delta = \frac{\alpha+2\,\beta}{3}$, we introduce two extra degrees of freedom internal to the element (not connected with the other ones):

$$q_3 = u_r\,|_{r=\gamma}, \qquad q_4 = u_r\,|_{r=\delta}$$

that defines a cubic Lagrange interpolation:

$$u_r(r) =$$

$$\frac{1}{16}\,[-(1-\bar{r})\,(1-9\,\bar{r}^2),\ -(1+\bar{r})\,(1-9\,\bar{r}^2),\ 9\,(1-\bar{r}^2)\,(1-3\,\bar{r}),\ 9\,(1-\bar{r}^2)\,(1+3\,\bar{r})\,] \begin{bmatrix} q_1 \\ q_2 \\ q_3 \\ q_4 \end{bmatrix} \tag{13}$$

where $\bar{r} = \frac{2\,r-(\beta+\alpha)}{\beta-\alpha}$. In short, we have:

$$u_r(r) = \boldsymbol{N}_e(r)\,\boldsymbol{q}_e$$

The corresponding strain field can be expressed in term of the nodal displacement:

$$\boldsymbol{\varepsilon}(r) = \begin{bmatrix} \varepsilon_{rr} \\ \varepsilon_{\theta\theta} \end{bmatrix} = \begin{bmatrix} \dfrac{d\boldsymbol{N_e}}{d\bar{r}}\,\dfrac{d\bar{r}}{dr} \\ \dfrac{\boldsymbol{N_e}}{r} \end{bmatrix} \boldsymbol{q}_e = \boldsymbol{B}_e(r)\,\boldsymbol{q}_e$$

After calculation, one has:

$$\boldsymbol{B}_e(r) =$$

$$\frac{1}{16}\begin{bmatrix} J\,(1+18\,\bar{r}-27\,\bar{r}^2) & J\,(-1+18\,\bar{r}+27\,\bar{r}^2) & J\,(-27-18\,\bar{r}+81\,\bar{r}^2) & J\,(27-18\,\bar{r}-81\,\bar{r}^2) \\ -\dfrac{1}{r}(1-\bar{r})\,(1-9\,\bar{r}^2) & -\dfrac{1}{r}(1+\bar{r})\,(1-9\,\bar{r}^2) & \dfrac{9}{r}\,(1-\bar{r}^2)\,(1-3\,\bar{r}) & \dfrac{9}{r}\,(1-\bar{r}^2)\,(1+3\,\bar{r}) \end{bmatrix}$$

with $J = \dfrac{d\bar{r}}{dr} = \frac{2}{\beta-\alpha}$.

Stress field. We consider an axisymmetric element occupying a volume $\alpha < r < \beta$ with four stress connectors:

$$g_1 = \sigma_{rr} \mid_{r=\alpha}, \qquad g_2 = \sigma_{\theta\theta} \mid_{r=\alpha}, \qquad g_3 = \sigma_{rr} \mid_{r=\beta}, \qquad g_4 = \sigma_{\theta\theta} \mid_{r=\beta} \tag{14}$$

The choice of a polynomial statically admissible stress field is guided by the aim to avoid the global (or structural) equations of linear momentum balance in the constrained minimization problem. Only remains the local yield condition. The general solution of:

$$\nabla \cdot \boldsymbol{\sigma} = \dot{\boldsymbol{p}}$$

is the sum of the general solution $\boldsymbol{\sigma}_h$ of the homogeneous equation and a particular solution $\boldsymbol{\sigma}_d$ of the non homogeneous equation. Following a method due to Schaefer ([6, 7]), this last one is of the form:

$$\boldsymbol{\sigma}_d = 2\,\nabla \boldsymbol{w} - (\nabla \cdot \boldsymbol{w})\,\boldsymbol{I}\ , \tag{15}$$

where the vector potential $\boldsymbol{w}$ is solution of $\nabla^2 \boldsymbol{w} = \dot{\boldsymbol{p}}$. For the displacement field, we seek a radial vector potential. The previous equation reduces to:

$$\frac{d^2 w_r}{dr^2} + \frac{1}{r}\frac{dw_r}{dr} - \frac{w_r}{r^2} = \rho\,(\dot{v}_1 + \dot{v}_2 r + \dot{v}_3 r^2 + \dot{v}_4 r^3)$$

Clearly, a solution is given by a homogeneous polynomial in r of degree five. Introducing it in the previous equation, we obtain by identification:

$$w_r = \rho\left(\frac{\dot{v}_1}{3}\,r^2 + \frac{\dot{v}_2}{8}\,r^3 + \frac{\dot{v}_3}{15}\,r^4 + \frac{\dot{v}_4}{24}\,r^5\right)$$

condition (15) reads in polar coordinates:

$$\sigma_{rr} = 2\,\frac{dw_r}{dr} - \frac{1}{r}\,\frac{d}{dr}(r\,w_r), \quad \sigma_{\theta\theta} = 2\,\frac{w_r}{r} - \frac{1}{r}\,\frac{d}{dr}(r\,w_r)$$

leads to the expression of $\boldsymbol{\sigma}_d$:

$$\sigma_{rr} = -\sigma_{\theta\theta} = \rho\left(\frac{\dot{v}_1}{3}\,r + \frac{\dot{v}_2}{4}\,r^2 + \frac{\dot{v}_3}{5}\,r^3 + \frac{\dot{v}_4}{6}\,r^4\right)$$

Besides, the stress field being defined by four connectors, we choose for $\boldsymbol{\sigma}_h$:

$$\sigma_{rr} = h_1 + h_2 r + h_3 r^2 + h_4 r^3$$

Using the internal equilibrium equation in (10), the hoop stress is:

$$\sigma_{\theta\theta} = h_1 + 2\,h_2 r + 3\,h_3 r^2 + 4\,h_4 r^3$$

In matrix form, the total stress field in terms of stress and displacement parameters reads:

$$\left[\begin{array}{c} \sigma_{rr} \\ \sigma_{\theta\theta} \end{array}\right] = \boldsymbol{\sigma}_e(r) = \boldsymbol{R}_e(r)\,\boldsymbol{h}_e + \boldsymbol{S}_e(r)\,\dot{\boldsymbol{v}}_e$$

$$= \begin{bmatrix} 1 & r & r^2 & r^3 \\ 1 & 2\,r & 3\,r^2 & 4\,r^3 \end{bmatrix} \begin{bmatrix} h_1 \\ h_2 \\ h_3 \\ h_4 \end{bmatrix} + \rho \begin{bmatrix} \frac{r}{3} & \frac{r^2}{4} & \frac{r^3}{5} & \frac{r^4}{6} \\ -\frac{r}{3} & -\frac{r^2}{4} & -\frac{r^3}{5} & -\frac{r^4}{6} \end{bmatrix} \begin{bmatrix} \dot{v}_1 \\ \dot{v}_2 \\ \dot{v}_3 \\ \dot{v}_4 \end{bmatrix}$$

stress connectors (14) are linearly depending on the stress and displacement parameters:

$$\boldsymbol{g}_e = \boldsymbol{C}_e \boldsymbol{h}_e + \boldsymbol{D}_e \dot{\boldsymbol{v}}_e$$

with the connection matrix:

$$\boldsymbol{C}_e = \begin{bmatrix} 1 & \alpha & \alpha^2 & \alpha^3 \\ 1 & 2\,\alpha & 3\,\alpha^2 & 4\,\alpha^3 \\ 1 & \beta & \beta^2 & \beta^3 \\ 1 & 2\,\beta & 3\,\beta^2 & 4\,\beta^3 \end{bmatrix} \qquad \boldsymbol{D}_e = \rho \begin{bmatrix} \frac{\alpha}{3} & \frac{\alpha^2}{4} & \frac{\alpha^3}{5} & \frac{\alpha^4}{6} \\ -\frac{\alpha}{3} & -\frac{\alpha^2}{4} & -\frac{\alpha^3}{5} & -\frac{\alpha^4}{6} \\ \frac{\beta}{3} & \frac{\beta^2}{4} & \frac{\beta^3}{5} & \frac{\beta^4}{6} \\ -\frac{\beta}{3} & -\frac{\beta^2}{4} & -\frac{\beta^3}{5} & -\frac{4}{6} \end{bmatrix}$$

Hence, one has: $\boldsymbol{h}_e = \boldsymbol{C}_e^{-1}(\boldsymbol{g}_e - \boldsymbol{D}_e \dot{\boldsymbol{v}}_e)$. By identification of (11) with (13), we obtain the relation between displacement parameters and connectors:

$$\boldsymbol{v}_e = \boldsymbol{A}_e \dot{\boldsymbol{q}}_e$$

$$\boldsymbol{A}_e^T =$$

$$\begin{bmatrix} \frac{1}{16}\left(9[\frac{\hat{\alpha}}{\hat{\beta}}]^3 + 9[\frac{\hat{\alpha}}{\hat{\beta}}]^2 - \frac{\hat{\alpha}}{\hat{\beta}} - 1\right) & \frac{1}{8}\left(-27\frac{\hat{\alpha}^2}{\hat{\beta}^3} - 18\frac{\hat{\alpha}}{\hat{\beta}^2} + \frac{1}{\hat{\beta}}\right) & \frac{1}{4}\left(27\frac{\hat{\alpha}}{\hat{\beta}^3} + 9\frac{1}{\hat{\beta}^2}\right) & \frac{-9}{2\hat{\beta}^3} \\ \frac{1}{16}\left(-9[\frac{\hat{\alpha}}{\hat{\beta}}]^3 + 9[\frac{\hat{\alpha}}{\hat{\beta}}]^2 + \frac{\hat{\alpha}}{\hat{\beta}} - 1\right) & \frac{1}{8}\left(27\frac{\hat{\alpha}^2}{\hat{\beta}^3} - 18\frac{\hat{\alpha}}{\hat{\beta}^2} - \frac{1}{\hat{\beta}}\right) & \frac{1}{4}\left(-27\frac{\hat{\alpha}}{\hat{\beta}^3} + 9\frac{1}{\hat{\beta}^2}\right) & \frac{9}{2\hat{\beta}^3} \\ \frac{1}{16}\left(-27[\frac{\hat{\alpha}}{\hat{\beta}}]^3 - 9[\frac{\hat{\alpha}}{\hat{\beta}}]^2 + 27\frac{\hat{\alpha}}{\hat{\beta}} + 9\right) & \frac{1}{8}\left(81\frac{\hat{\alpha}^2}{\hat{\beta}^3} + 18\frac{\hat{\alpha}}{\hat{\beta}^2} - \frac{27}{\hat{\beta}}\right) & \frac{1}{4}\left(-81\frac{\hat{\alpha}}{\hat{\beta}^3} - 9\frac{1}{\hat{\beta}^2}\right) & \frac{27}{2\hat{\beta}^3} \\ \frac{1}{16}\left(27[\frac{\hat{\alpha}}{\hat{\beta}}]^3 - 9[\frac{\hat{\alpha}}{\hat{\beta}}]^2 - 27\frac{\hat{\alpha}}{\hat{\beta}} + 9\right) & \frac{1}{8}\left(-81\frac{\hat{\alpha}^2}{\hat{\beta}^3} + 18\frac{\hat{\alpha}}{\hat{\beta}^2} + \frac{27}{\hat{\beta}}\right) & \frac{1}{4}\left(81\frac{\hat{\alpha}}{\hat{\beta}^3} - 9\frac{1}{\hat{\beta}^2}\right) & \frac{-27}{2\hat{\beta}^3} \end{bmatrix}$$

where: $\hat{\alpha} = \alpha + \beta$, $\hat{\beta} = \beta - \alpha$. Eliminating the stress parameters provides the stress field in terms of stress and displacement connectors:

$$\boldsymbol{\sigma}_e(r) = \boldsymbol{T}_e(r)\boldsymbol{g}_e + \boldsymbol{U}_e(r)\ddot{\boldsymbol{q}}_e$$

where:

$$\boldsymbol{T}_e(r) = \boldsymbol{R}_e(r)\boldsymbol{C}_e^{-1}, \qquad \boldsymbol{U}_e(r) = (\boldsymbol{S}_e(r) - \boldsymbol{R}_e(r)\boldsymbol{C}_e^{-1}\boldsymbol{D}_e)\,\boldsymbol{A}_e$$

4.1.1 Space discretization of the principle

Introducing the plastic multiplier $\lambda \geq 0$, the yield rule reads:

$$\dot{\boldsymbol{\varepsilon}}^p = \lambda \frac{\partial f(\boldsymbol{\sigma})}{\partial \boldsymbol{\sigma}}$$

and the dissipation power (7) becomes:

$$D = \sigma_Y \lambda$$

As usual, the integral are approximated by numerical integration on every element:

$$\int_\alpha^\beta \boldsymbol{A}(r)\, 2\,\pi\, r\, dr \cong \sum_{g=1}^{n_e} w_g\, \boldsymbol{A}(r_g)\, 2\,\pi\, r_g$$

In particular, the total dissipation power in the element reads:

$$\int_\alpha^\beta D(r)\, 2\,\pi\, r\, dr = \Lambda_e^T \lambda_e$$

where:

$$\boldsymbol{\Lambda}_e = \sigma_Y \begin{bmatrix} w_1\, 2\,\pi\, r_1 \\ \cdots \\ w_{n_e}\, 2\,\pi\, r_{n_e} \end{bmatrix}, \qquad \boldsymbol{\lambda}_e = \begin{bmatrix} \dot{\lambda}_1 \\ \cdots \\ \dot{\lambda}_{n_e} \end{bmatrix}$$

Performing the assembling thanks to the localization matrices $\boldsymbol{L}_e, \boldsymbol{M}_e, \boldsymbol{P}_e$ such that:

$$\boldsymbol{g}_e = \boldsymbol{M}_e \boldsymbol{g}, \qquad \boldsymbol{q}_e = \boldsymbol{L}_e \boldsymbol{q}, \qquad \boldsymbol{\lambda}_e = \boldsymbol{P}_e \boldsymbol{\lambda}$$

the discretized form of the functional is:

$$\begin{aligned} \bar{\Pi}(\boldsymbol{g}, \boldsymbol{q}, \boldsymbol{\lambda}) = \int_{t_0}^{t_1} \Big[& \boldsymbol{\Lambda}^T \boldsymbol{\lambda}(t) - \dot{\boldsymbol{q}}^T(t)\, (\boldsymbol{G}\, \boldsymbol{g}(t) + \tilde{\boldsymbol{G}}\, \ddot{\boldsymbol{q}}(t)) \\ & + \boldsymbol{g}^T(t)\, \boldsymbol{F_1}\, \dot{\boldsymbol{g}}(t) + \ddot{\boldsymbol{q}}^T(t)\, \boldsymbol{F_2}\, \dot{\boldsymbol{g}}(t) + \boldsymbol{g}^T(t)\, \boldsymbol{F_3}\, \ddot{\boldsymbol{q}}(t) + \ddot{\boldsymbol{q}}^T(t)\, \boldsymbol{F_4}\, \ddot{\boldsymbol{q}}(t) \Big]\, dt \end{aligned} \tag{16}$$

with:

$$\boldsymbol{\Lambda} = \sum_{e=1}^{n} \boldsymbol{P}_e^T \boldsymbol{\Lambda}_e,$$

$$\boldsymbol{G} = \sum_{e=1}^{n} \int_\alpha^\beta \boldsymbol{L}_e^T \boldsymbol{B}_e^T(r)\, \boldsymbol{T}_e(r)\, \boldsymbol{M}_e\, 2\,\pi\, r\, dr, \quad \tilde{\boldsymbol{G}} = \sum_{e=1}^{n} \int_\alpha^\beta \boldsymbol{L}_e^T \boldsymbol{B}_e^T(r)\, \boldsymbol{U}_e(r)\, \boldsymbol{L}_e\, 2\,\pi\, r\, dr,$$

$$\boldsymbol{F_1} = \sum_{e=1}^{n} \int_\alpha^\beta \boldsymbol{M}_e^T \boldsymbol{T}_e^T(r)\, \boldsymbol{S}\, \boldsymbol{T}_e(r)\, \boldsymbol{M}_e\, 2\,\pi\, r\, dr \quad \boldsymbol{F_2} = \sum_{e=1}^{n} \int_\alpha^\beta \boldsymbol{L}_e^T \boldsymbol{U}_e^T(r)\, \boldsymbol{S}\, \boldsymbol{T}_e(r)\, \boldsymbol{M}_e\, 2\,\pi\, r\, dr$$

$$\boldsymbol{F_3} = \sum_{e=1}^{n} \int_\alpha^\beta \boldsymbol{M}_e^T \boldsymbol{T}_e^T(r)\, \boldsymbol{S}\, \boldsymbol{U}_e(r)\, \boldsymbol{L}_e\, 2\,\pi\, r\, dr \quad \boldsymbol{F_4} = \sum_{e=1}^{n} \int_\alpha^\beta \boldsymbol{L}_e^T \boldsymbol{U}_e^T(r)\, \boldsymbol{S}\, \boldsymbol{U}_e(r)\, \boldsymbol{L}_e\, 2\,\pi\, r\, dr$$

The Brezis-Ekeland-Nayroles claims that we have to find the minimum of (16) with respect to the path $t \mapsto (\boldsymbol{g}(t), \boldsymbol{q}(t), \boldsymbol{\lambda}(t))$ under the constrains of:

- equilibrium (on the boundary, the internal equilibrium being satisfies *a priori*):

$$g_{r=a}(t) = -p(t), \quad g_{r=b}(t) = 0$$

- plasticity (at every integration point g of every element e):

$$f_g(\boldsymbol{g}, \ddot{\boldsymbol{q}}) - \sigma_Y \leq 0, \qquad \lambda_g \geq 0 \qquad \boldsymbol{N}_Y \lambda_g = \boldsymbol{B}_e(r_g)\, \dot{\boldsymbol{q}}_e - \boldsymbol{S}\left(\boldsymbol{T}_e(r_g)\, \dot{\boldsymbol{g}}_e + \boldsymbol{U}_e(r) \dddot{\boldsymbol{q}}_e\right)$$

- initial conditions:

$$\begin{aligned} &\boldsymbol{g}(t_0) = \boldsymbol{0}, \qquad \boldsymbol{q}(t_0) = \boldsymbol{0}, \qquad \boldsymbol{\lambda}(t_0) = \boldsymbol{0} \\ &\dot{\boldsymbol{g}}(t_0) = \boldsymbol{0}, \qquad \dot{\boldsymbol{q}}(t_0) = \boldsymbol{0}, \qquad \ddot{\boldsymbol{q}}(t_0) = \boldsymbol{0}, \qquad \dddot{\boldsymbol{q}}(t_0) = \boldsymbol{0} \end{aligned}$$

4.1.2 Time discretization of the functional

For the time discretization of any physical quantity a, we put:

$$a_j = a(t_j), \quad \dot{a}_j = \dot{a}(t_j), \quad \cdots$$

On each step, we approximate the time rates at $t = t_j$ by:

$$\dot{a}_j = \frac{a_j - a_{j-1}}{t_j - t_{j-1}}, \qquad \ddot{a}_j = \frac{\dot{a}_j - \dot{a}_{j-1}}{t_j - t_{j-1}}, \qquad \dddot{a}_j = \frac{\ddot{a}_j - \ddot{a}_{j-1}}{t_j - t_{j-1}}$$

Considering m time step from t_0 to t_m and enforcing the yield condition only at the beginning and the end of the step, we have to minimize the objective function:

$$\begin{aligned} \bar{\Pi}(\boldsymbol{g}_0, \cdots, \boldsymbol{g}_m, \boldsymbol{q}_0, \cdots, \boldsymbol{q}_m, \boldsymbol{\lambda}_0, \cdots, \boldsymbol{\lambda}_m) = \sum_{j=1}^{j=m} \Big[& \boldsymbol{\Lambda}^T \boldsymbol{\lambda}_j - \dot{\boldsymbol{q}}_j^T \left(\boldsymbol{G}\, \boldsymbol{g}_j + \tilde{\boldsymbol{G}}\, \ddot{\boldsymbol{q}}_j \right) + {\boldsymbol{g}_j}^T(t)\, \boldsymbol{F_1}\, \dot{\boldsymbol{g}}_j(t) \\ & + \ddot{\boldsymbol{q}}_j{}^T(t)\, \boldsymbol{F_2}\, \dot{\boldsymbol{g}}_j(t) + {\boldsymbol{g}_j}^T(t)\, \boldsymbol{F_3}\, \dddot{\boldsymbol{q}}_j(t) + \ddot{\boldsymbol{q}}_j{}^T(t)\, \boldsymbol{F_4}\, \dddot{\boldsymbol{q}}_j(t) \Big] \left(t_j - t_{j-1} \right) \end{aligned} \tag{17}$$

under the constrains of:

- equilibrium (on the boundary, at each time step):

$$g_{r=a,j}(t_j) = -p(t), \quad g_{r=b,j}(t_j) = 0$$

- plasticity (at every integration point g of every element e and at every time step):

$$f_{g,j}(\boldsymbol{g}, \ddot{\boldsymbol{q}}) - \sigma_Y \leq 0, \quad \lambda_{g,j} \geq 0, \quad \boldsymbol{N}_Y \lambda_{g,j} = \boldsymbol{B}_e(r_g)\, \boldsymbol{L}_e \dot{\boldsymbol{q}}_j^T - \boldsymbol{S}\, \left[\boldsymbol{T}_e(r_g)\, \boldsymbol{M}_e \dot{\boldsymbol{g}}_j + \boldsymbol{U}_e(r_g)\, \boldsymbol{L}_e \dddot{\boldsymbol{q}}_j \right]$$

- initial conditions:

$$\boldsymbol{g}_0 = \boldsymbol{0}, \qquad \boldsymbol{q}_0 = \boldsymbol{0}, \qquad \boldsymbol{\lambda}_0 = \boldsymbol{0}, \qquad \dot{\boldsymbol{g}}_0 = \boldsymbol{0}, \qquad \dot{\boldsymbol{q}}_0 = \boldsymbol{0}, \qquad \ddot{\boldsymbol{q}}_0 = \boldsymbol{0}, \qquad \dddot{\boldsymbol{q}}_0 = \boldsymbol{0}$$

4.2 Method B

The balance of linear momentum is satisfied in Gauss points.

Displacement field. Same as Method A.

Stress field. We choose the same position for the radial and hoop stress field.

$$\sigma_{rr} = h_1 + h_2\, r + h_3\, r^2 + h_4\, r^3 \qquad \sigma_{\theta\theta} = h_5 + h_6\, r + h_7\, r^2 + h_8\, r^3$$

There are four degrees of freedom for each stress:

$$g_1 = \sigma_{rr}\mid_{r=\alpha}, \qquad g_2 = \sigma_{rr}\mid_{r=\beta}, \qquad g_3 = \sigma_{rr}\mid_{r=\gamma}, \qquad g_4 = \sigma_{rr}\mid_{r=\delta} \tag{18}$$

$$s_1 = \sigma_{\theta\theta}\mid_{r=\alpha}, \qquad s_2 = \sigma_{\theta\theta}\mid_{r=\beta}, \qquad s_3 = \sigma_{\theta\theta}\mid_{r=\gamma}, \qquad s_4 = \sigma_{\theta\theta}\mid_{r=\delta} \tag{19}$$

In matrix form, we have:

$$\sigma_{rr}(r) = \boldsymbol{N}_e(r)\, \boldsymbol{g}_e \qquad \sigma_{\theta\theta}(r) = \boldsymbol{N}_e(r)\, \boldsymbol{s}_e$$

Thus:

$$\boldsymbol{\sigma}(r) = \begin{bmatrix} \sigma_{rr} \\ \sigma_{\theta\theta} \end{bmatrix} = \begin{bmatrix} \boldsymbol{N}_e(r) & \boldsymbol{0} \\ \boldsymbol{0} & \boldsymbol{N}_e(r) \end{bmatrix} \begin{bmatrix} \boldsymbol{g}_e \\ \boldsymbol{s}_e \end{bmatrix} = \boldsymbol{T}_e(r)\, \boldsymbol{t}_e$$

4.2.1 Space discretization of the principle

Same as Method A.

Performing the assembling thanks to the localization matrices $\boldsymbol{L}_e, \boldsymbol{M}_e, \boldsymbol{P}_e$ such that:

$$\boldsymbol{t}_e = \boldsymbol{M}_e \boldsymbol{t}, \qquad \boldsymbol{q}_e = \boldsymbol{L}_e \boldsymbol{q}, \qquad \boldsymbol{\lambda}_e = \boldsymbol{P}_e \boldsymbol{\lambda}$$

the discretized form of the functional is:

$$\bar{\Pi}(\boldsymbol{t}, \boldsymbol{q}, \boldsymbol{\lambda}) = \int_{t_0}^{t_1} (\boldsymbol{\Lambda}^T \boldsymbol{\lambda}(t) - \dot{\boldsymbol{q}}^T(t) \boldsymbol{G}\, \boldsymbol{t}(t) + \dot{\boldsymbol{t}}^T(t) \boldsymbol{F}\, \boldsymbol{t}(t))\ \mathrm{dt} \tag{20}$$

with:

$$\boldsymbol{\Lambda} = \sum_{e=1}^{n} \boldsymbol{P}_e^T \boldsymbol{\Lambda}_e,$$

$$\boldsymbol{G} = \sum_{e=1}^{n} \int_{\alpha}^{\beta} \boldsymbol{L}_e^T \boldsymbol{B}_e^T(r)\, \boldsymbol{T}_e(r)\, \boldsymbol{M}_e\, 2\,\pi\, r\, dr \quad \boldsymbol{F} = \sum_{e=1}^{n} \int_{\alpha}^{\beta} \boldsymbol{M}_e^T \boldsymbol{T}_e^T(r)\, \boldsymbol{S}\, \boldsymbol{T}_e(r)\, \boldsymbol{M}_e\, 2\,\pi\, r\, dr$$

The Brezis-Ekeland-Nayroles claims that we have to find the minimum of (20) with respect to the path $t \mapsto (\boldsymbol{t}(t), \boldsymbol{q}(t), \boldsymbol{\lambda}(t))$ under the constrains of:

- equilibrium (on the boundary, the internal equilibrium being satisfies *a priori*):

$$g_{r=a}(t) = -p(t), \quad g_{r=b}(t) = 0, \quad \frac{d}{dr}\sigma_r(r_g) + \frac{1}{r_g}\left[\sigma_r(r_g) - \sigma_\theta(r_g)\right] = \rho \ddot{u}_r(r_g)$$

- plasticity (at every integration point g of every element e):

$$f_g(\boldsymbol{t}) - \sigma_Y \leq 0, \qquad \lambda_g \geq 0, \qquad \boldsymbol{N}_Y \lambda_g = \boldsymbol{B}_e(r_g)\, \dot{\boldsymbol{q}}_e - \boldsymbol{S}\, \boldsymbol{T}_e(r_g)\, \dot{\boldsymbol{t}}_e$$

- initial conditions:

$$\boldsymbol{g}(t_0) = \boldsymbol{0}, \qquad \boldsymbol{q}(t_0) = \boldsymbol{0}, \qquad \boldsymbol{\lambda}(t_0) = \boldsymbol{0}, \qquad \dot{\boldsymbol{g}}(t_0) = \boldsymbol{0}, \qquad \dot{\boldsymbol{q}}(t_0) = \boldsymbol{0}, \qquad \ddot{\boldsymbol{q}}(t_0) = \boldsymbol{0}$$

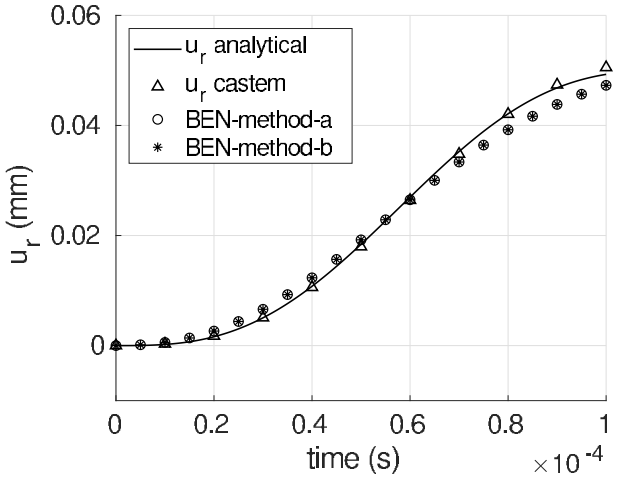


Figure 1: Comparison of radial displacement history of different data when $\tilde{p} = 1$ MPa in elastic case (i) analytical solution (ii) reference numerical solution (Cast3M software) with 10 time steps (iii) BEN method A solution with 20 time steps (iv) BEN method B solution with 20 time steps

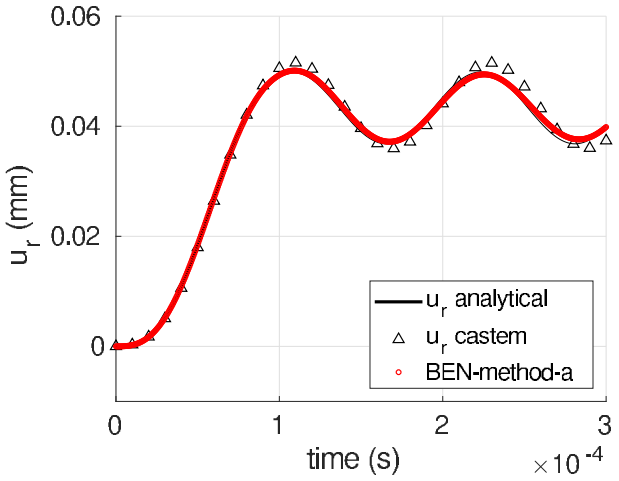


Figure 2: Comparison of radial displacement history of different data when $\tilde{p} = 1$ MPa in elastic case (i) analytical solution (ii) reference numerical solution (Cast3M software) with 30 time steps (iii) BEN method A solution with 600 time steps

4.2.2 Time discretization of the functional

Same as Method A.

Considering m time step from t_0 to t_m and enforcing the yield condition only at the beginning and the end of the step, we have to minimize the objective function:

$$\bar{\Pi}(\boldsymbol{t}_0, \cdots, \boldsymbol{t}_m, \boldsymbol{q}_0, \cdots, \boldsymbol{q}_m, \boldsymbol{\lambda}_0, \cdots, \boldsymbol{\lambda}_m) = \sum_{j=1}^{j=m} (\boldsymbol{\Lambda}^T \boldsymbol{\lambda}_j - \dot{\boldsymbol{q}}_j^T \boldsymbol{G}\, \boldsymbol{t}_j + \dot{\boldsymbol{t}}_j^T \boldsymbol{F}\, \boldsymbol{t}_j) \tag{21}$$

under the constrains of:

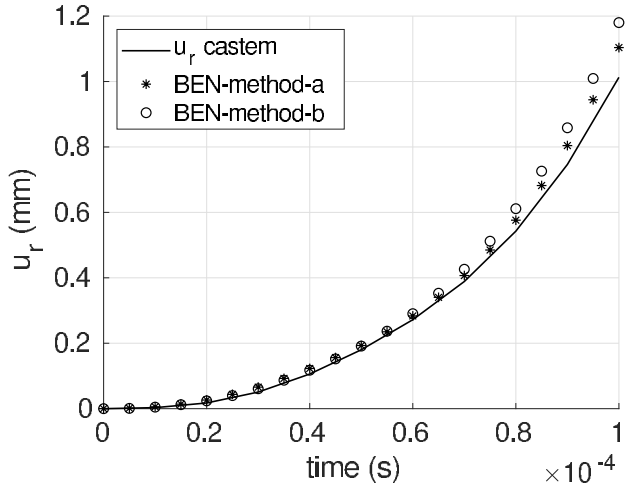


Figure 3: Comparison of radial displacement history of different data when $\tilde{p} = 10$ MPa in plastic case (i) analytical solution (ii) reference numerical solution (Cast3M software) (iii) BEN method A solution with 400 time steps

- equilibrium (on the boundary, at each time step):

$$g_{r=a,j} = -p(t_j), \quad g_{r=b,j} = 0, \quad \frac{d}{dr}\sigma_r(r_{g,j}) + \frac{1}{r_{g,j}}\left[\sigma_r(r_{g,j}) - \sigma_\theta(r_{g,j})\right] = \rho\ddot{u}_r(r_{g,j})$$

- plasticity (at every integration point g of every element e and at every time step):

$$f_{g,j}(\boldsymbol{t}) - \sigma_Y \leq 0, \qquad \lambda_{g,j} \geq 0, \qquad \boldsymbol{N}_Y(r_g)\lambda_{g,j} = \boldsymbol{B}_e(r_g)\,\boldsymbol{L}_e\dot{\boldsymbol{q}}_j - \boldsymbol{S}\,\boldsymbol{T}_e(r_g)\,\boldsymbol{M}_e\dot{\boldsymbol{t}}_j$$

- initial conditions:

$$\boldsymbol{g}_0 = \boldsymbol{0}, \qquad \boldsymbol{q}_0 = \boldsymbol{0}, \qquad \boldsymbol{\lambda}_0 = \boldsymbol{0}, \qquad \dot{\boldsymbol{g}}_0 = \boldsymbol{0}, \qquad \dot{\boldsymbol{q}}_0 = \boldsymbol{0}, \qquad \ddot{\boldsymbol{q}}_0 = \boldsymbol{0}$$

4.3 Simulation results

The program is coded in *Matlab*, the solver *fmincon* is applied to find the local minimum of the constrained functional (17, 21). Material parameters are, $E = 210$ GPa, $\nu = 0.3$, $\sigma_Y = 360$ MPa, $a = 100$ mm, $b = 101$ mm, $\rho = 7.8\,e^{-9}$ Kg/mm^3. Simulation results are displayed in figure (1), (2) and (3) for elastic and plastic cases. There is a good consistence between the BEN principle solution and the analytical or numerical solution. The BEN principle requires sufficient time steps to have a better precision than the one step-by-step. The method A and B does not change the simulation results.

5 CONCLUSIONS AND PERSPECTIVES

Thanks to the simulation results, the BEN method is numerically confirmed in dynamics. The BEN method allows to have a global view of all time steps which can avoid

the usual difficulties in step-by-step method. As the computation time is significantly expansive, application of the Proper Generalized Decomposition (PGD) is the concept to obtain of a more effective program. Final objective of the present work is to apply the symplectic BEN principle in finite displacement to observe its ability in avoiding usual step-by-step method convergence problem.

6 ACKNOWLEDGMENT

This work was performed thanks to the international cooperation project *Dissipative Dynamical Systems by Geometrical and Variational Methods and Application to Viscoplastic Structures Subjected to Shock Waves* (DDGV) supported by the *Agence Nationale de la Recherche* (ANR) and the *Deutsche Forchungsgemeinschaft* (DFG).

REFERENCES

[1] Brezis, H., Ekeland I. *Un principe variationnel associé à certaines équations paraboliques. I. Le cas indépendant du temps.* C. R. Acad. Sci. Paris Série A-B 282, 971-974 (1976)

[2] Nayroles, B. *Deux théorèmes de minimum pour certains systèmes dissipatifs.* C. R. Acad. Sci. Paris Série A-B 282:A1035-A1038 (1976)

[3] Buliga M. *Hamiltonian inclusions with convex dissipation with a view towards applications.* Mathematics and its Applications 1(2), 228-25 (2009)

[4] Buliga, M., & de Saxcé, G. (2017). *A symplectic Brezis-Ekeland-Nayroles principle.* Mathematics and Mechanics of Solids, 22(6), 1288-1302.

[5] Cao, X., Oueslati, A and de Saxcé, G , *The Brezis-Ekeland-Nayroles variational principle for elastoplastic problems.* (2018).

[6] Schaefer, H.*Die Spannungsfuncktionen des dreidimensionalen Kontinuums und des elastischen Körpers.* Z. Angew. Math. Mech. 33, 356-362 (1953)

[7] Gurtin, M. *The linear theory of elasticity, Encyclopedia of Physics.* S. Flügge, Vol VIa/2, Mechanics of Solids II (Berlin: Springer-Verlag, 1972)

XV International Conference on Computational Plasticity. Fundamentals and Applications
COMPLAS 2019
E. Oñate, D.R.J. Owen, D. Peric, M. Chiumenti & Eduardo de Souza Neto (Eds)

COMPUTATIONAL MODELLING OF THE BEHAVIOUR OF BIOMARKER PARTICLES OF COLORECTAL CANCER IN FECAL MATTER

SUÁREZ G.*, VALLEJO E.* AND HOYOS L.†

*Grupo de Investigación en Matemáticas (GMAT), Engineering School
Universidad Pontificia Bolivariana
Cir.1 #70-01, 050031 Medellín, Colombia
gustavo.suarez@upb.edu.co, esteban.vallejomo@upb.edu.co, http://www.upb.edu.co/

† Grupo de Investigación en Biología de Sistemas, Medicine School
Universidad Pontificia Bolivariana
Cir.1 #70-01, 050031 Medellín, Colombia
lina.hoyos@upb.edu.co, http://www.upb.edu.co

Key words: Colorectal adenocarcinoma, mathematical model, computational simulation, human feces, biomarker substance.

Abstract. Colorectal adenocarcinoma is one of the carcinogenic diseases that is increasing the morbidity and mortality rates worldwide. The disease initially occurs through the segregation of biomarker substances in the human system without manifesting symptoms that affect the health of the carrier. Early detection would allow the application of more effective treatments, less invasive procedures and reduce the development of cancer. The purpose of this investigation was the elaboration of a mathematical model and the development of computational simulations to visualize the behavior of biomarker particles in transit through the colon. The flow conditions, properties of the viscous medium and biological regions of interest were established. Constitutive models, numerical conditions and solution strategies were determined. A numerical grid was used to represent the model of the colon and the human feces that carry the bioparticles (biomarkers). The results indicated the trajectories of the bioparticles in the fecal mass and the interactive movement with the natural contractions of the colon. The analysis of the movement of the biomarker particles can provide future less invasive alternatives for the detection in real time of the cancer by means of the implantation of biosensors in the walls of the colon.

1 INTRODUCTION

Worldwide, colorectal cancer (CRC) is one of the most frequently diagnosed degenerative diseases in the population [12, 10]. Despite the fact that some countries have improved their preventive systems for the detection of the disease, a high morbidity and

mortality rate persists due to late detection factors. [20, 18, 17]. In Colombia, for the year 2012, the CRC ranked fourth (7.8 %) in the estimated number of cases of incidence, being also the third cause of death (8.5 %) associated with cancer for both sexes. Globally, however, the CRC ranked third (9.7 %) in the estimated number of incident cases and fourth (8.5 %) in the estimated number of death cases [19, 17].

CRC generally develop as a result of neoplastic progression from adenomas into adenocarcinomas, which are defined as neoplasia derived from the lining of the gut. It is widely accepted that this transformation is triggered by the accumulation of both genetic and epigenetic alterations. The progression from an adenoma to carcinoma may take decades, which provides an opportunity for early CRC detection. Mass screening would therefore greatly contribute to the early diagnosis and timely treatment of CRC [7]. On account of that it is known that CRC develops from the accumulation of genetic and epigenetic changes in the epithelial cells of the colon, molecular markers directed to genetic alterations in tumor tissues and peripheral blood have been evolved [8].

Several research groups have developed mathematical modeling and computational simulations specifically to predict the growth of the advanced middle stage tumor, as well as to study the generation of metastases during different periods of the disease in the patients [3, 6].

Large intestine is composed of six representative parts: Cecum and apendix, ascending colon, transverse colon, descending colon, sigmoid colon and rectum. Rectum was selected to perform the analysis due its easier and more secure access in case of insert a measuring device. A complete reference image is provided in Figure 2 to identify the colorectal zone selected in this research.

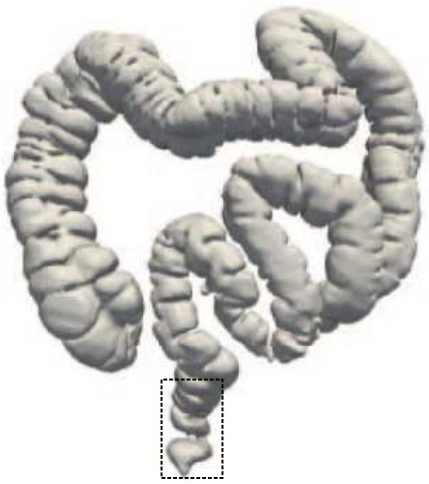


Figure 1: Complete 3D colon image and colorectal analysis section. Taken from [1]

2 MATERIALS AND METHODS

2.1 Definition of the study region

The gastrointestinal tract comprises of several distinct organs in sequence, extending over 7 meters in the human abdomen [13]. In this paper, a biological region of interest has been selected: colorectal section.

The colorectal region is composed of the walls of the colon that transport the fecal viscous mass inside. Based on the above description, a three-dimensional geometric model was constructed to represent the shape of the colorectal region for the development of the required studies. In the elaborated model, the folds and the biological diametral changes of the intestinal area were considered and the dimensions and radiuses obtained clinically indicated were incorporated.

2.2 Determination of biomaterials in colorectal region

The large intestine performs complex biological processes, such as: the absorption of fluids, electrolytes and vitamins, and the evacuation of fecal material [14]. The biomechanical properties and the geometric shape of the colon directly affect the proper behavior of this biological organ. Different models used to characterize the biomechanical properties of the walls of the intestine have been found, especially models of elastic-linear behavior, however in this investigation, a model of hyperelastic Neo-Hookean material of non-linear behavior was determined, since it would allow to reach a similarity with the natural peristatic movement of the organ. The mathematical model of the material implemented was:

$$W = \frac{\mu}{2}(\bar{I}_1 - 3) + \frac{1}{d}(J-1)^2 \tag{1}$$

It is the simplest form of deformation potential that exists for hyperelastic materials. The Neo-Hookean model allows to properly characterize the behavior of the material. Initial values of values of $\mu = 27104\ Pa$ and $d = 1.499e-7\ Pa^{-1}$ were implemented. This model requires the shear modulus and can only be subjected to uni-axial tension with deformation values ranging between 30% and 40%, and pure shear stresses with values of deformation ranging between 80% and 90%.

Human stool is modeled as a high viscous mass that is transported by peristaltic wave and physical parameters [11] were defined in table 1.

Table 1: Stool parameters.

Parameter	Symbol	Value	Unit
Density	μ	1060.00	kg/m^3
Viscosity	ν	5.00	Pa s

2.3 Biofunctionality conditions

There are several motor patterns that ensure that movements and propulsion are appropriate for the breakdown of food, absorption of nutrients and excretion of waste. These movements (peristalsis) are due to coordinated contractions and relaxations of circular and longitudinal smooth muscle layers [13].

Peristaltic movements in rectum allows to transport the waste to store it before the excretion process. Travelling peristaltic waves are generated in the intestinal wall and travel in the antegrade direction. The wave consists of contraction and relaxation components that modify the instantaneous wall tensions in each longitudinal slice [13]. This motion may be mathematically modeled as:

$$h(z,t) = a - 0.5\phi\left[1 + cos\frac{2\pi}{\lambda}(z - ct)\right]. \tag{2}$$

Where z, t, a, ϕ, λ, c y h are respectively axial coordinate, time, radius of the tube, amplitude of wave, wavelength, wave-speed and radial displacement of the walls from the center line [16].

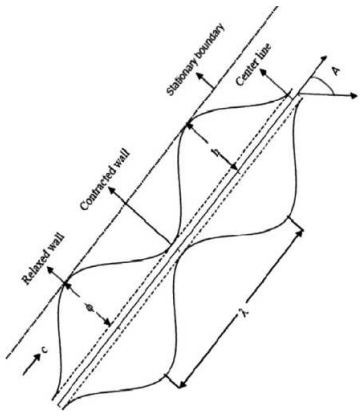


Figure 2: Radial displacement of the colon walls from the central line. Taken from [16].

A peristaltic wave was modeled in order to represent the pressure that travels along colorectal wall and whose function is transport stool during 6 seconds of simulation. Peristaltic pressure wave was plotted to represents its behavior with a pression value of 1893.17 Pa in figure 3 according to several intraluminal pressures reported in [2, 9, 4]:

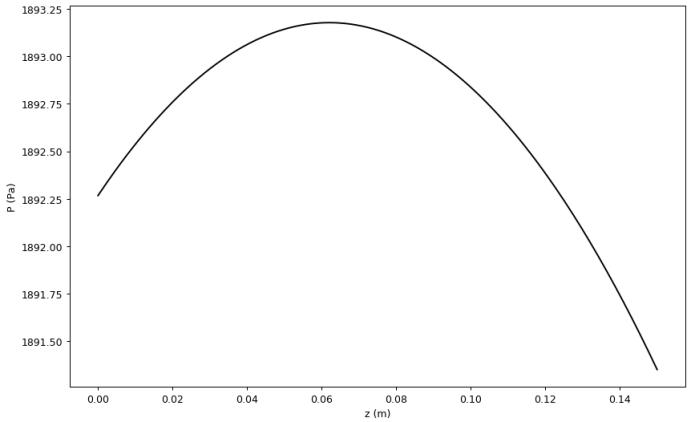


Figure 3: Pressure distribution on the entire wall (0.15 m) at t = 6.0 s.

2.4 Mesh configuration of region

The hexahedric configuration element was defined as the most adjusted and functional to represent the behavior of the biostructure. It was also considered that the eight-node hexahedral element met the physical and numerical conditions to represent the phenomenon. A mesh was constructed for the fluid and a mesh for the structure independently. The overall process of meshing was complex because of the particular shape of the colon (see fig 4). The dimensions chosen corresponds to 15 cm of length and a max diameter of 7 cm.

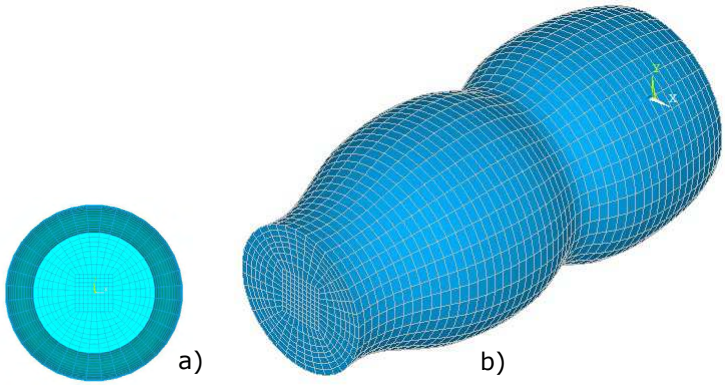


Figure 4: Geometric model meshed inside (fecal material) and in the structure (correctal surface). a) Front view of the geometry, b) perspective view of the geometry.

3 RESULTS AND ANALYSIS

Next, the results that indicate the dynamic behavior of the bio structure are presented, considering the peristaltic pressure, properties of the fecal matter and the characteristics and properties of the colorectal surface. Figure 5 represents the large deformations that occur in the dynamics of the phenomenon in three timesteps (t = 0.5, 2.0 and 6.0 seconds)

giving as a maximum value of radial displacement 6.34e-3 m. We observed a push behavior generated by the peristatic wave on the walls co-assisted by the geometric shape of the colon. There is evidence of an ease of mass displacement due to the biostructural form to the interior, which is formed by a folds and a diametrial variability, which favors the pushing force:

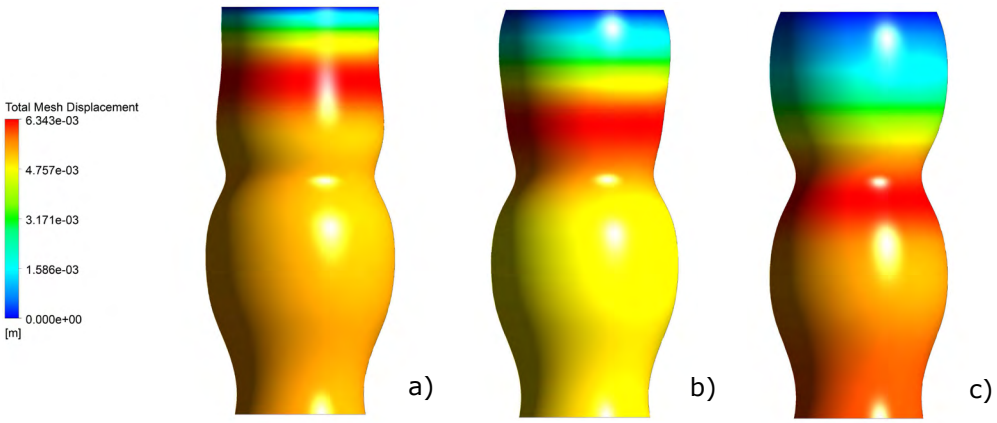


Figure 5: Total mesh displacement due to peristaltic wave in colorectal section at a) 0.5 seconds, b) 2.0 seconds and c) 6.0 seconds.

The behavior of the biological mass inside the colorectal model and the generation of mass flow orientation in time: 0.5, 2.0, 6.0 seconds, with maximum velocity values of 3.5e-3 m/s are presented in figure 6. The results indicated a random movement of the fecal mass into the colon where the greatest dynamic activity towards the inner wall of the colon occurs in some moments of greater compression, which would facilitate the capture of indicator particles of the colorectal disease. This behavior of greater pressure and speed towards the inner walls of the colon is the one of greater interest in the present investigation.

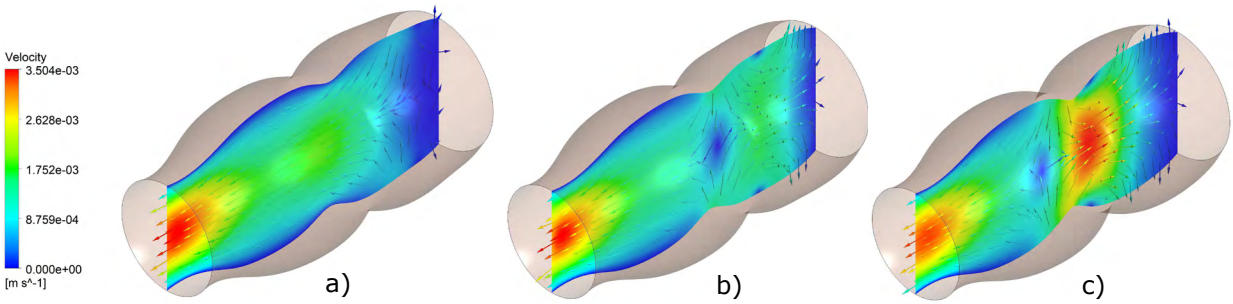


Figure 6: Stool velocity results by peristaltic wave in rectal section at a) 0.5 seconds, b) 2.0 seconds and c) 6.0 seconds.

In order to analyze the magnitude and direction of the mass flow, three cross sections were established, whose generated planes allow the estimation of the flow passing through

them. The first plane, located 0.01785 m from the inlet boundary, presents a flow that goes to the outlet boundary during the first 1.5 seconds, however, after 2 seconds, its direction changes towards the inlet boundary as can be observed in the figures 7-a, having as a maximum recoil value a positive mass flow of $1.3e-3$ kg/s. In the figures 6-b and 6-c, the vector field points in the sense of inlet boundary. It is important to note that as the time progresses, the magnitude of the mass flow begins to decrease after 3 seconds, which indicates that in the time after the second 6 could change the direction of flow again.

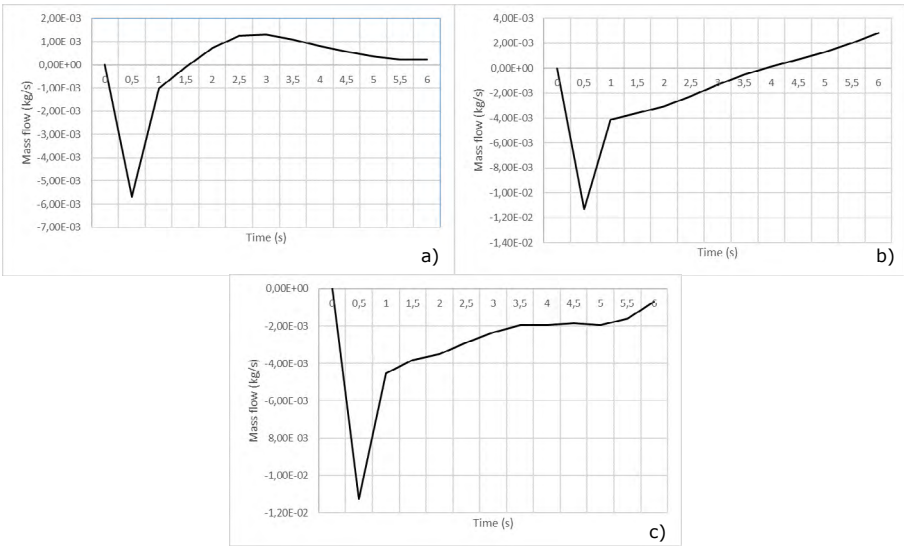


Figure 7: a) Mass flow through transversal slice plane at 0.01785 m of rectal inlet. b)Mass flow through transversal slice plane at 0.06 m of rectal inlet. c) Mass flow through transversal slice plane at 0.1137 m of rectal inlet. Simulation was performed during 6.0 seconds.

The second plane, located 0.06 m from the inlet boundary, presents a flow in the direction of outlet for a longer time, however, it also presents a backward movement from the second 4, as can be seen in the figure 7-b. In the figure 6-b (2 seconds), a significant decrease in the velocity of the flow can be identified because the system is approaching the instant in which the flow changes direction. The flow value for the plane analyzed at time t = 2 corresponds to $-3.07e-3$ kg/s in the direction of outlet.

The third plane, located 0.1137 m from the inlet boundary, has a flow in the direction of outlet permanently, as can be seen in the figure 7-c. However, a small decrease in velocity is noted, which could become a setback at the time of maximum pressure caused by the peristaltic pressure wave at that location.

4 CONCLUSIONS

- The Neo-Hokean model was appropiate to interact with pressure wave and it allowed an adequate displacement of the fecal mass, obtaining as a result the vector field of velocities in which the biomarker particles would be contained.

- Mass flow analized presents the backward behavior expected acording to pressure

wave applied. This behavior provides information about vector field direction and sense, and it allows identify the most interesesting region, which is located in the narrowest zone where highest velocities were found.

- The present research provides a significant contribution to the knowledge of the behavior of the fecal mass flow that contains biomarker particles for the search of early detection mechanisms, such as a possible implantation of a biosensor on the high contact areas.

REFERENCES

[1] Dongqing Chen, Rachid Fahmi, Aly A. Farag, Robert L. Falk, ja Gerald W. Dryden. Accurate and fast 3D colon segmentation in CT colonography. *Proceedings - 2009 IEEE International Symposium on Biomedical Imaging: From Nano to Macro, ISBI 2009*, (June):490–493, 2009.

[2] Ji Hong Chen, Yuanjie Yu, Zixian Yang, Wen Zhen Yu, Wu Lan Chen, Hui Yu, Marie Jeong Min Kim, Min Huang, Shiyun Tan, Hesheng Luo, Jianfeng Chen, Jiande D.Z. Chen, ja Jan D. Huizinga. Intraluminal pressure patterns in the human colon assessed by high-resolution manometry. *Scientific Reports*, 7:1–16, 2017.

[3] P. Ferreira, M. Baptista, S Di Maria, P. Vaz, S. Di Maria, ja P. Vaz. Cancer risk estimation in Digital Breast Tomosynthesis using GEANT4 Monte Carlo simulations and voxel phantoms. *Physica Medica*, 32(5):717–723, 2016.

[4] Christopher P Gayer ja Marc D Basson. The effects of mechanical forces on intestinal physiology and pathology. 21(8):1237–1244, 2010.

[5] Maria Gonzalez-Pons ja Marcia Cruz-Correa. Colorectal Cancer Biomarkers: Where Are We Now? *BioMed Research International*, 2015(Table 1), 2015.

[6] Guiyeom Kang, Claudio Márquez, Ana Barat, Annette T. Byrne, Jochen H M Prehn, Joan Sorribes, ja Eduardo César. Colorectal tumour simulation using agent based modelling and high performance computing. *Future Generation Computer Systems*, 67:397–408, 2017.

[7] Kevin Lam, Kathy Pan, Janneke Fiona Linnekamp, Jan Paul Medema, ja Raju Kandimalla. DNA methylation based biomarkers in colorectal cancer: A systematic review. *Biochimica et Biophysica Acta - Reviews on Cancer*, 1866(1):106–120, 2016.

[8] Hye Seung Lee, Sang Mee Hwang, Taek Soo Kim, Duck-Woo Kim, Do Joong Park, Sung-Bum Kang, Hyung-Ho Kim, ja Kyoung Un Park. Circulating Methylated Septin 9 Nucleic Acid in the Plasma of Patients with Gastrointestinal Cancer in the Stomach and Colon. *Translational Oncology*, 6(3):290–IN4, 2013.

[9] S. Metry, P. Arhan, ja G. Chauvet. A mathematical analysis of intestinal peristaltic waves. *Medical Engineering and Physics*, 17(3):204–214, 1995.

[10] Jessica B. O'Connell, Melinda A. Maggard, ja Clifford Y. Ko. Colon cancer survival rates with the new American Joint Committee on Cancer sixth edition staging. *Journal of the National Cancer Institute*, 96(19):1420–1425, 2004.

[11] Roni Penn, Barbara J. Ward, Linda Strande, ja Max Maurer. Review of synthetic human faeces and faecal sludge for sanitation and wastewater research. *Water Research*, 132:222–240, 2018.

[12] Satya Prakash, Meenakshi Malhotra, Wei Shao, Catherine Tomaro-Duchesneau, ja Sana Abbasi. Polymeric nanohybrids and functionalized carbon nanotubes as drug delivery carriers for cancer therapy. *Advanced Drug Delivery Reviews*, 63(14-15):1340–1351, 2011.

[13] M. D. Sinnott, P. W. Cleary, J. W. Arkwright, ja P. G. Dinning. Investigating the relationships between peristaltic contraction and fluid transport in the human colon using Smoothed Particle Hydrodynamics. *Computers in Biology and Medicine*, 42(4):492–503, 2012.

[14] Dimitrios P. Sokolis ja Sofia G. Sassani. Microstructure-based constitutive modeling for the large intestine validated by histological observations. *Journal of the Mechanical Behavior of Biomedical Materials*, 21:149–166, 2013.

[15] Kasif Teker. Bioconjugated carbon nanotubes for targeting cancer biomarkers. *Materials Science and Engineering: B*, 153(1-3):83–87, 2008.

[16] Dharmendra Tripathi. A mathematical model for the peristaltic flow of chyme movement in small intestine. *Mathematical Biosciences*, 233(2):90–97, 2011.

[17] Esteban Vallejo, Gustavo Suárez, William Torres, ja Adolfo Uribe. Mathematical Modeling and Computational Simulation of the Diffusive Behavior of Adenocarcinoma Biomarker Particles. Kirjassa Juan Carlos Figueroa-García, Eduyn Ramiro López-Santana, ja José Ignacio Rodriguez-Molano, toim., *Applied Computer Sciences in Engineering*, ss. 305–316, Cham, 2018. Springer International Publishing.

[18] Qingzhu Wei, Hui Zhou, Ling Zhong, Liyin Shi, Jianghuan Liu, Qiao Yang, ja Tong Zhao. IMP3 expression in biopsy specimens as a diagnostic biomarker for colorectal cancer. *Human Pathology*, 64:137–144, 2017.

[19] World Health Organization. Estimated number of incident cases, both sexes, worldwide (top 10 cancer sites) in 2012, 2012.

[20] Bin Zhang, Yayuan Yan, Qiujuan Shen, Dong Ma, Langhuan Huang, Xiang Cai, ja Shaozao Tan. A colon targeted drug delivery system based on alginate modificated graphene oxide for colorectal liver metastasis. *Materials Science and Engineering C*, 79:185–190, 2017.

XV International Conference on Computational Plasticity. Fundamentals and Applications
COMPLAS 2019
E. Oñate, D.R.J. Owen, D. Peric, M. Chiumenti & Eduardo de Souza Neto (Eds)

MULTISCALE MODELLING OF LIVER PERFUSION

Eduard Rohan[1], **Jana Turjanicová**[1] **and Vladimír Lukeš**[1]

[1] Faculty of Applied Sciences, European Centre of Excellence, NTIS – New Technologies for Information Society, University of West Bohemia, Univerzitní 8, 306 14 Plzeň, Czech Republic, rohan@kme.zcu.cz

Key words: Homogenization, Double Porosity, Liver Tissue, Perfusion, Darcy-Brinkman model

Abstract. We compare two homogenized models of the microcirculation which rely on different assumptions. The first model has been derived by the homogenization of the mesoscopic structure with the double-porosity medium represented by the Biot model with large contrasts in the permeability coefficients constituting the Darcy law. The newly developed so-called Biot-Darcy-Brinkman (BDB) model is described in the paper; it arises from a two-stage homogenization of the fluid-structure interaction problem which requires geometric representations of the sinusoidal and the inter-lobular vasculatures associated with venous compartments, the portal and the hepatic veins. An illustrative example shows a good correspondence between the two models.

1 Introduction

Understanding of liver perfusion on the multiple scales is crucial for the surgical treatment (liver resections, transplantations), but also for understanding how the liver perfusion is modified by diffuse parenchyma diseases such as cirrhosis, steatohepatitis, or the sinusoidal obstruction syndrome. At the macroscopic scale the liver receive blood from the two separated vascular system (trees), one belonging to the hepatic artery and other to the portal vein. These two vascular trees branch repeatedly, until they reach the microcirculation at the level of so-called hepatic units, typically considered as hexagonal lobules separated by thin vascular septum. The lobular structure can be approximated as a "locally" periodic array of honeycomb-like cells constituted by the sinusoidal porosity connecting the vertex and central veins which are the terminal branches of the two trees.

Here we focus on the lobular level perfusion whereby flows in vascular trees of the upper hierarchies can be described by the multi-compartment Darcy flow model [10]. Existing studies of the liver microcirculation [4, 3], i.e. perfusion between the portal track and the central vein at lobular level, usually consider the conception of the regular hexagonal liver lobule as the hepatic functional unit, see e.g. [5]. In [6], a convenient model has been derived by the homogenization of the mesoscopic structure with the double-porosity medium represented by the Biot model with large contrasts in the permeability coefficients

constituting the Darcy law. Within this model, the macroscopic variables represent two pressures associated with the portal and hepatic veins, representing the vertex and central blood vessels, respectively, and the two related interconnecting networks the macroscopic variables.

As the new contribution, in this paper we extend the so-called Biot-Darcy-Brinkman (BDB) model to describe structures wirth two mesoscopic system of separated channels which correspond to the lobular structure arrangement. For only one mesoscopic compartment, the model was derived using a two-level homogenization approach in [11] for rigid porous structures and then extended in [12] to deal with deformable solid phase, *i.e.* deformable hepatic cells.

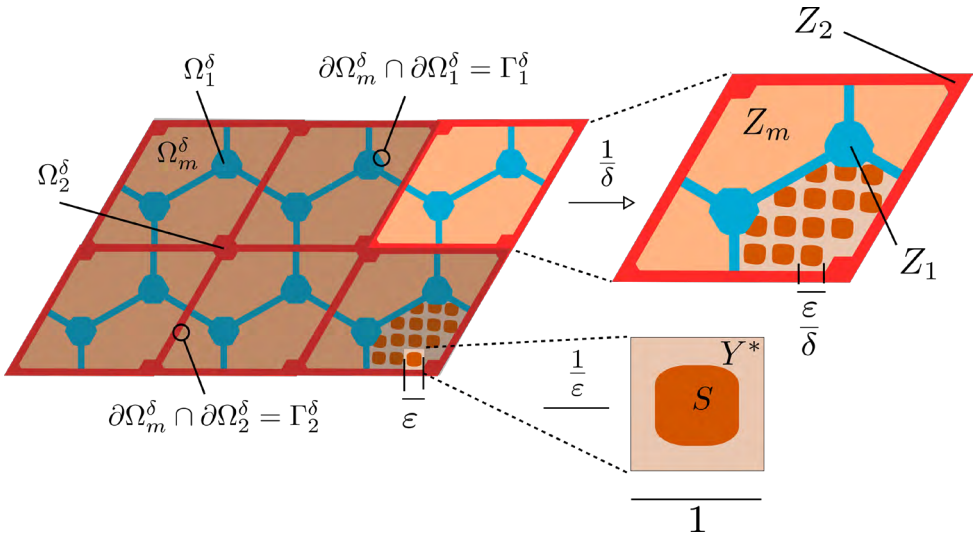


Figure 1: Lobular porous structure parameterized by ε, the characteristic size of the sinusoidal porosity, and δ which describes the size of the mesoscopic heterogeneities.

2 Biot-Darcy-Brinkman model

Two-level homogenization of the fluid-structure interaction with a scaling ansatz related to the viscosity has been applied to treat the geometry with two mesoscopic channels. The macroscopic model is defined in terms of the pressure field associated with flow in the liver sinusoids, the two velocity fields associated with the precapillary vessels of the portal and hepatic vein systems and the displacements.

2.1 Microscopic and mesoscopic structure

The liver tissue can be described using a two-level structured porous material consisting of the solid and fluid phases. These phases occupy an open bounded domain $\Omega \subset \mathbb{R}^3$ which can be decomposed in dual way. According to the phases, Ω splits into the fluid Ω_f and solid Ω_s parts separated by the solid interface $\Gamma_{\rm fs} = \overline{\Omega_f} \cap \overline{\Omega_s}$, whereby both Ω_s and Ω_f are connected domains. The hierarchical structure is periodic at the micro- and meso-scopic

scales related to two small parameters ε and δ, respectively, see Fig. 1. At the mesoscopic scale, the periodic structure is formed by two families of fluid filled channels occupying domains Ω_α^δ, $\alpha = 1, 2$, whereby $\Omega_c^\delta = \bigcup_\alpha \Omega_\alpha^\delta$, and by domain $\Omega_m^\delta = \Omega \setminus \Omega_c^\delta$ which is constituted by a microporous material representing the so-called sinusoidal porosity. In addition, domain $\Omega_p^{\varepsilon,\delta} \subset \Omega_m^\delta$ represents micro pores saturated by fluid, whereas $\Omega_s^{\varepsilon,\delta} = \Omega_m^\delta \setminus \Omega_p^{\varepsilon,\delta}$ is the skeleton. To summarize the decompositions,

$$\begin{aligned} \Omega &= \Omega_m^\delta \cup \Omega_c^\delta \cup \Gamma^\delta \ , \\ \text{solid (hepatic cells)} \quad & \Omega_s^{\varepsilon,\delta} \subset \Omega_m^\delta \ , \\ \text{microporosity (sinusoids)} \quad & \Omega_p^{\varepsilon,\delta} = \Omega_m^\delta \setminus \Omega_s^{\varepsilon,\delta} \ , \\ \text{fluid (blood)} \quad & \Omega_f = \Omega_p^{\varepsilon,\delta} \cup \Omega_c^\delta \cup \Gamma_{cp}^{\varepsilon,\delta} \ . \end{aligned} \tag{1}$$

The mesoscopic channels Ω_α^δ, $\alpha = 1, 2$, are mutually disconnected by the sinusoidal porosity Ω_m^δ, so that also two disconnected interfaces are defined, $\Gamma_\alpha^\delta = \partial\Omega_\alpha^\delta \cap \partial\Omega_m^\delta$.

The sinusoidal porosity (microporous material) Ω_m is generated as a periodic lattice by repeating the representative volume element (RVE) occupying domain $Y^\varepsilon = \varepsilon Y$. The zoomed cell $Y = \Pi_{i=1}^3]0, \bar{y}_i[\subset \mathbb{R}^3$ splits into the solid part (hepatic tissue) occupying domain Y_s and the complementary fluid part Y_fn (the sinusoids), see Fig. 1(a), thus $Y = Y_s \cup Y_f \cup \Gamma_Y$, where $Y_s = Y \setminus Y_f$ and $\Gamma_Y = \overline{Y_s} \cap \overline{Y_f}$ represents the sinusoidal walls on which the chemical transport and diffusion processes take place.

At the mesoscopic level, the lobular structure is generated by the periodic cell δZ representing the lobular unit, see Fig. 1(b). The zoomed cell Z involved in the homogenized model consists of microporous part situated in $Z_m \subset Z$ and of the fluid channels $Z_c = Z \setminus Z_m$, *i.e.* $Z_m \cap Z_c = \emptyset$. According to the split of Ω_c^δ, the two compartments Ω_α^δ are generated by the representative sub-cells Z_α, $\alpha = 1, 2$, whereby two interfaces $\Gamma_\alpha^Z = \overline{Z_m} \cap \overline{Z_\alpha}$ generate Γ_α^δ for a given scale δ.

By virtue of the two-level homogenization, when passing to the limit $\varepsilon \to 0$, the sinusoidal porosity is upscaled, thus yielding the mesoscopic model of the lobular structure. Consequently, pursuing $\delta \to 0$ yields the macroscopic model.

2.2 Microscopic model

At the microscopic level, we consider the fluid-structure interaction problem for a viscous incompressible fluid and elastic solid with linear material response and linear strains; for the displacement field $\boldsymbol{u}(x,t)$ with $x \in \Omega_s^{\varepsilon,\delta}$ and time $t \geq 0$, the strain components are $e_{ij}(\boldsymbol{u}) = 1/2(\partial_j u_i + \partial_i u_j)$. The elasticity tensor $\mathbb{D} = (D_{ijkl})$ satisfies the usual symmetries. saturating the micro- and the mesoscopic pores, see (1). Following the works [2], cf. [11], dealing with models of the rigid double porous media, the viscosity $\eta^{\varepsilon,\delta}$ is given by piece-wise constant function according the micropore size ε:

$$\eta^{\varepsilon,\delta} = \begin{cases} \varepsilon^2 \bar{\eta}_p & \text{in} \quad \Omega_p^{\varepsilon,\delta} \ , \\ \eta_c & \text{in} \quad \Omega_c^\delta \ . \end{cases} \tag{2}$$

This scaling of the viscosity in micropores (sinusoids) is the standard consequence of the assumed non-slip boundary condition for the flow velocity on the pore wall, cf. [1].

The problem imposed in Ω at the microlevel is constituted by the following equations and boundary and interface conditions governing the displacement $\boldsymbol{u}$ of the solid and both the fluid pressure and velocity fields $(\boldsymbol{v}^f, p)$:

$$\begin{aligned} -\nabla\cdot\mathbb{D}\boldsymbol{e}(\boldsymbol{u}) &= \boldsymbol{f}^s \quad \text{in } \Omega_s\ , \\ \boldsymbol{n}\cdot\mathbb{D}\boldsymbol{e}(\boldsymbol{u}) &= \boldsymbol{n}\cdot\boldsymbol{\sigma}^f \quad \text{on } \Gamma_{\rm fs}\ , \\ \boldsymbol{n}\cdot\mathbb{D}\boldsymbol{e}(\boldsymbol{u}) &= \boldsymbol{g}^s \quad \text{on } \partial_\sigma\Omega_s\ , \\ \boldsymbol{u} &= \boldsymbol{0} \quad \text{on } \partial_u\Omega_s\ , \end{aligned} \tag{3}$$

$$\begin{aligned} -\nabla\cdot(2\eta\boldsymbol{e}(\boldsymbol{v}^f) - p\boldsymbol{I}) &= \boldsymbol{f}^f \quad \text{in } \Omega_f\ , \\ \nabla\cdot\boldsymbol{v}^f &= 0 \quad \text{in } \Omega_f\ , \\ \boldsymbol{v}^f &= \dot{\boldsymbol{u}} \quad \text{on } \Gamma_{\rm fs}\ , \\ \boldsymbol{v}^f - \dot{\tilde{\boldsymbol{u}}} =: \boldsymbol{w} &= \bar{\boldsymbol{w}} \quad \text{on } \partial_v\Omega_f\ , \end{aligned} \tag{4}$$

where $\boldsymbol{\sigma}^f = \varepsilon^2\bar{\eta}_p\boldsymbol{e}(\boldsymbol{v}^f) - p\boldsymbol{I}$ is the fluid stress, $\boldsymbol{f}^{s,f}$ denotes the volume forces in the solid, or in the fluid, and $\boldsymbol{g}^s$ is the surface traction stresses acting on the solid part.

Above, to introduce the relative fluid velocity $\boldsymbol{w} = \boldsymbol{v}^f - \dot{\tilde{\boldsymbol{u}}}$ in the fluid-saturated pores $\Omega_f^{\varepsilon\delta}$, we define a smooth extension $\tilde{\boldsymbol{u}}$ of the displacement field $\boldsymbol{u}$ from Ω_s to entire Ω, such that $\tilde{\boldsymbol{u}} \equiv \boldsymbol{u}$ in Ω_s.

2.3 Mesoscopic model relevant to the lobular structure

The mesoscopic model obtained by the first level asymptotic analysis of (3)-(4) with the viscosity (2) for $\varepsilon \to 0$, whereas δ being fixed, is constituted by the following equations,

$$\begin{aligned} -\nabla\cdot(\mathbb{A}\boldsymbol{e}(\boldsymbol{u}^\delta) - \boldsymbol{B}p_m^\delta) &= \phi_s\boldsymbol{f}^s + \phi_f\boldsymbol{f}^f\ , \\ \boldsymbol{B}:\boldsymbol{e}(\dot{\boldsymbol{u}}^\delta) - \nabla\cdot\boldsymbol{K}(\nabla p_m^\delta - \boldsymbol{f}^f) &= 0\ , \quad \text{in } \Omega_m^\delta\ , \\ -\eta_c\nabla^2(\boldsymbol{w}^{\alpha,\delta} + \dot{\tilde{\boldsymbol{u}}}^\delta) + \nabla p_\alpha^\delta &= \boldsymbol{f}^f\ , \quad \text{in } \Omega_\beta^\delta\ , \quad \beta = 1,2\ , \\ \nabla\cdot(\boldsymbol{w}^{\alpha,\delta} + \dot{\tilde{\boldsymbol{u}}}^\delta) &= 0\ , \quad \text{in } \Omega_\beta\ , \\ \boldsymbol{n}^{[\beta]}\cdot\boldsymbol{\sigma}^{m,\delta} - p_m^\delta\boldsymbol{n}^{[\beta]} &= 0\ , \ \text{on } \Gamma_\beta\ , \\ \boldsymbol{n}^{[\beta]}\cdot(\boldsymbol{w}^{m,\delta} - \boldsymbol{w}^{\beta,\delta}) &= 0\ , \quad \text{on } \Gamma\ , \\ \boldsymbol{n}^{[\beta]}\cdot(2\eta_c\boldsymbol{e}(\boldsymbol{w}^{\alpha,\delta} + \dot{\tilde{\boldsymbol{u}}}^\delta) - p_\alpha^\delta\boldsymbol{I}) &= -p_m^\delta\boldsymbol{n}^{[\beta]}\ , \quad \text{on } \Gamma_\beta\ , \end{aligned} \tag{5}$$

where $\boldsymbol{w}^{m,\delta} = -\boldsymbol{K}(\nabla p_m^\delta - \boldsymbol{f}^f)$ is the mesoscopic flow in the sinusoidal microporosity and $\boldsymbol{\sigma}^{m,\delta} := \mathbb{A}\boldsymbol{e}(\boldsymbol{u}^\delta) - \boldsymbol{B}p_m^\delta$ is the total stress in the microporosity. It is worth to note that the interface conditions are obtained as the byproduct of the 1st level homogenization step without any restriction on the curvature of Γ_β.

2.4 Macroscopic model — BDB model for two mesoscopic channels

The macroscopic model is derived using the asymptotic analysis of (5) for $\delta \to 0$. When compared to the model of a mesoscopic structure containing only one channel system treated in [12], *i.e.* when $\alpha = 1$, thus $\Omega_1^\delta = \Omega_c^\delta$, the upscaled mesoscopic structures involving two mesoscopic channels yield two macroscopic velocity fields $\boldsymbol{w}^{0,\alpha}$, $\alpha = 1, 2$ which describe the two parallel flows associated with the portal vein and the hepatic vein compartments.

The local mesoscopic characteristic problems are defined in terms of bilinear forms:

$$\begin{aligned} a_m(\boldsymbol{u},\, \boldsymbol{v}) &= \fint_{Z_m} \mathbb{A}\boldsymbol{e}_z(\boldsymbol{u}) : \boldsymbol{e}_z(\boldsymbol{v}) \,, \\ b_m(p,\, \boldsymbol{v}) &= \fint_{Z_m} p\boldsymbol{B} : \boldsymbol{e}_z(\boldsymbol{v}) \,, \\ c_m(p,\, q) &= \fint_{Z_m} \nabla_z q \cdot \boldsymbol{K} \nabla_z p \,. \end{aligned} \tag{6}$$

Characteristic responses in the matrix part Z_m are defined as solutions of the four uncoupled problems: Find $\boldsymbol{\omega}^{ij}, \boldsymbol{\omega}^P \in \mathbf{H}^1_\#(Z_m)/\mathbb{R}^3$, and $\pi^k, \varphi^k \in H^1_\#(Z_m)$ such that

$$\begin{aligned} a_m\left(\boldsymbol{\omega}^{ij},\, \boldsymbol{v}\right) &= -a_m\left(\boldsymbol{\Pi}^{ij},\, \boldsymbol{v}\right) \quad \forall \boldsymbol{v} \in \mathbf{H}^1_\#(Z_m) \,, \\ a_m\left(\boldsymbol{\omega}^{P},\, \boldsymbol{v}\right) &= b_m(1,\, \boldsymbol{v}) - \fint_{\Gamma_c} \boldsymbol{n}^{[\mathrm{m}]} \cdot \boldsymbol{v} \quad \forall \boldsymbol{v} \in \mathbf{H}^1_\#(Z_m) \,, \\ c_m\left(\pi^k,\, q\right) &= -c_m(z_k,\, q) \quad \forall q \in H^1_\#(Z_m) \,, \\ c_m\left(\varphi^k,\, q\right) &= \fint_{\Gamma_c} q n_k^{[\mathrm{c}]} \quad \forall q \in H^1_\#(Z_m) \,, \end{aligned} \tag{7}$$

where $\Gamma_c = \Gamma_1 \cup \Gamma_2$ employed in $(7)_{2,4}$ includes both the interfaces and $\boldsymbol{\Pi}^{ij} = (\Pi_k^{ij})$ with $\Pi_k^{ij} = z_j \delta_{ik}$ is also employed below.

In each of the mesoscopic channels Z_α, the following problem must be solved. Find $(\boldsymbol{\psi}^{\alpha,ij}, \hat{\varphi}^{\alpha,ij}) \in \mathbf{H}^1_\#(Z_\alpha)/\mathbb{R}^3 \times L^2(Z_\alpha)$, such that,

$$\begin{aligned} 2\eta_c \int_{Z_\alpha} \boldsymbol{e}_z(\boldsymbol{\psi}^{\alpha,ij}) : \boldsymbol{e}_z(\boldsymbol{\vartheta}) - \int_{Z_\alpha} \hat{\varphi}^{\alpha,ij} \nabla_z \cdot \boldsymbol{\vartheta} &= -2\eta_c \int_{Z_\alpha} \boldsymbol{e}_z(\boldsymbol{\Pi}^{ij}) : \boldsymbol{e}_z(\boldsymbol{\vartheta}) \,, \\ \int_{Z_\alpha} q \nabla_z \cdot \boldsymbol{\psi}^{\alpha,ij} &= -\int_{Z_\alpha} q \nabla_z \cdot \boldsymbol{\Pi}^{ij} \,, \end{aligned} \tag{8}$$

for all $(\boldsymbol{\vartheta}, q) \in \mathbf{H}^1_\#(Z_\alpha) \times L^2(Z_\alpha)$.

The set of HC is identified in the two-scale limit equations,

$$
\begin{aligned}
\mathcal{A}_{ijkl} &= \fint_{Z_m} \mathbb{A}\boldsymbol{e}_z(\boldsymbol{\Pi}^{kl}+\boldsymbol{\omega}^{kl}) : \boldsymbol{e}_z(\boldsymbol{\Pi}^{ij}+\boldsymbol{\omega}^{ij}) \,, \\
\mathcal{B}_{ij} &= \phi_c\delta_{ij} + b_m\left(1,\, \boldsymbol{\Pi}^{ij}+\boldsymbol{\omega}^{ij}\right) - \fint_{\Gamma_Z} \boldsymbol{n}^{[\mathrm{m}]}\cdot\boldsymbol{\omega}^{ij} \,, \\
\mathcal{K}_{ij} &= \fint_{Z_m} \nabla_z(z_j+\pi^j)\cdot\boldsymbol{K}\nabla_z(z_i+\pi^i) \,, \\
\mathcal{M} &= \fint_{Z_m} M + b_m\left(1,\, \boldsymbol{\omega}^P\right) + \fint_{\Gamma_Z} \boldsymbol{n}^{[\mathrm{c}]}\cdot\boldsymbol{\omega}^P \,, \\
\mathcal{S}^\alpha_{ijkl} &= 2\eta_c \fint_{Z_\alpha} \boldsymbol{e}_z(\boldsymbol{\Pi}^{ij}+\boldsymbol{\psi}^{ij}) : \boldsymbol{e}_z(\boldsymbol{\Pi}^{kl}+\boldsymbol{\psi}^{kl}) \,, \\
\mathcal{H}^{\alpha\beta}_{ij} &= \fint_{\Gamma_\alpha} \varphi^{j,\beta} n_i^{[\alpha]} = c_m\left(\varphi^{i,\alpha},\, \varphi^{j,\beta}\right) \,, \\
\mathcal{Q}^\alpha_{ij} &= \fint_{Z_m} \nabla_z z_i\cdot\boldsymbol{K}\nabla_z\varphi^{j,\alpha} = -\fint_{Z_m} \nabla_z\pi^i\cdot\boldsymbol{K}\nabla_z\varphi^{j,\alpha} = \fint_{\Gamma_Z} \pi^i n_j^{[\alpha]} \,.
\end{aligned}
\tag{9}
$$

The alternative expressions hold due to the characteristic problems (7) and (8). I addition, the following coefficients are employed,

$$
\begin{aligned}
\mathcal{P}^\alpha_{ij} &= \phi_\alpha\delta_{ij} - \mathcal{Q}^\alpha_{ij} \,, \\
\mathcal{R}^\alpha_{ij} &= \fint_{Z_\alpha} \hat{\varphi}^{ij,\alpha} \,, \quad \mathcal{R}^\alpha_{ij} = \mathcal{R}^\alpha_{ji} \,.
\end{aligned}
\tag{10}
$$

Then the average of the pressure in the α-mesoscopic channels $\hat{p}^\alpha$ can be expressed,

$$
P^0_\alpha(x,t) = \phi_\alpha^{-1} \fint_{Z_\alpha} \hat{p}^\alpha(x,\cdot,t) = \phi_\alpha^{-1}\boldsymbol{\mathcal{R}}^\alpha : \boldsymbol{e}(\boldsymbol{w}^{0,\alpha}+\dot{\boldsymbol{u}}^0) + p^0 \,. \tag{11}
$$

This expression reveals that the mesoscopic pressure P^0_α deviates from the micropore pressure p^0 by the $\boldsymbol{\mathcal{R}}^\alpha$-projection of the mesoscopic fluid velocity deformation.

The macroscopic model involves displacement field $\boldsymbol{u}^0$, two velocity fields $\boldsymbol{w}^{0,\alpha}$, $\alpha=1,2$ associated with the two intralobular venous systems (the portal and the hepatic veins) and the pressure p^0 related to the sinusoidal micro-porosity . The quadruple of functions $(\boldsymbol{u}^0, \boldsymbol{w}^{0,\alpha}, p^0)$ satisfy the following differential equations in domain Ω,

$$
\begin{aligned}
-\nabla\cdot\left(\boldsymbol{\mathcal{A}}\boldsymbol{e}_x(\boldsymbol{u}^0) - p^0\boldsymbol{\mathcal{B}}\right) + \sum_{\beta=1,2}\boldsymbol{h}^{0,\beta} &= \boldsymbol{f}^{\mathrm{blk}} \,, \\
\boldsymbol{\mathcal{B}} : \boldsymbol{e}_x(\dot{\boldsymbol{u}}^0) + \nabla\cdot\boldsymbol{j}^0 + \mathcal{M}\dot{p}^0 &= 0 \,, \\
-\nabla\cdot\boldsymbol{\mathcal{S}}^\alpha\boldsymbol{e}_x(\boldsymbol{w}^{0,\alpha}+\dot{\boldsymbol{u}}^0) - \boldsymbol{h}^{0,\alpha} &= 0 \,, \quad \alpha=1,2 \,,
\end{aligned}
\tag{12}
$$

where $\boldsymbol{f}^{\mathrm{blk}}$ is the bulk volume force (including the forces in the fluid and solid phases) the

fluxes $\boldsymbol{h}^{0,\alpha}$ and $\boldsymbol{j}^0$ are defined, as follows:

$$\begin{aligned} \text{rate of momentum} \quad & \boldsymbol{h}^{0,\alpha} = -(\boldsymbol{\mathcal{P}}^\alpha)^T(\nabla_x p^0 - \boldsymbol{f}^f) - \sum_{\beta=1,2} \boldsymbol{\mathcal{H}}^{\alpha\beta}\boldsymbol{w}^{0,\beta} \,, \\ \text{seepage flow in the sinusoids:} \quad & \boldsymbol{j}^0 = -\boldsymbol{\mathcal{K}}(\nabla_x p^0 - \boldsymbol{f}^f) - \sum_{\beta=1,2} \boldsymbol{\mathcal{P}}^\beta \boldsymbol{w}^{0,\beta} \,. \end{aligned} \tag{13}$$

The boundary conditions are prescribed according to the boundary partitioning of $\partial\Omega$,

$$\begin{aligned} &\partial\Omega = \partial_w^\alpha\Omega \cup \partial_p^\alpha\Omega \,, \quad \partial_w^\alpha\Omega \cap \partial_p^\alpha\Omega = \emptyset \,, \quad \alpha = 1,2 \,, \\ &\partial\Omega = \partial_w^0\Omega \cup \partial_p^0\Omega \,, \quad \partial_w^0\Omega \cap \partial_p^0\Omega = \emptyset \,, \\ &\partial\Omega = \partial_\sigma\Omega \cup \partial_u\Omega \,, \quad \partial_\sigma\Omega \cap \partial_u\Omega = \emptyset \,. \end{aligned} \tag{14}$$

The Dirichlet conditions prescribed for $\boldsymbol{u}^0$, $\boldsymbol{w}^{0,\alpha}$ and p^0 can be imposed,

$$\begin{aligned} \boldsymbol{u}^0 &= \bar{\boldsymbol{u}}^0 \quad \text{on } \partial_u\Omega \,, \\ p^0 &= \bar{p}^0 \quad \text{on } \partial_p^0\Omega \,, \\ \boldsymbol{w}^{0,\alpha} &= \bar{\boldsymbol{w}}^\alpha \quad \text{on } \partial_w^\alpha\Omega \,. \end{aligned} \tag{15}$$

The complementary Neumann-type boundary conditions can be specified through given $\boldsymbol{g}, \bar{p}^0, \bar{W}_n$,

$$\begin{aligned} \boldsymbol{n}\cdot\big(\boldsymbol{\mathcal{A}}\boldsymbol{e}_x(\boldsymbol{u}^0) - p^0\boldsymbol{\mathcal{B}}\big) = \boldsymbol{n}\cdot\boldsymbol{\sigma}^{\rm mp} &= -\bar{\phi}_c\bar{p}^0\boldsymbol{n} + \bar{\phi}_m\bar{\phi}_s\boldsymbol{g} \quad \text{on } \partial_\sigma\Omega \,, \\ \boldsymbol{n}\cdot\boldsymbol{j}^0 = \bar{W}_n^{\rm mes} &= -\bar{\phi}_m\bar{\phi}_f\bar{w}_n^{\rm mic} + \bar{\phi}_c\bar{w}_n^{\rm mes} \quad \text{on } \partial_w^0\Omega \,, \\ \boldsymbol{n}\cdot\boldsymbol{\mathcal{S}}^\alpha\boldsymbol{e}_x(\boldsymbol{w}^{0,\alpha} + \dot{\boldsymbol{u}}^0) - \bar{\phi}_\alpha P_\alpha^0\boldsymbol{n} = \boldsymbol{n}\cdot\boldsymbol{\sigma}^{f,\alpha} &= -\boldsymbol{n}\bar{\phi}_\alpha(\bar{P}^\alpha - \bar{p}^0) \quad \text{on } \partial_p^\alpha\Omega \,. \end{aligned} \tag{16}$$

To explain the meaning of the Neumann conditions, the overall traction stress is by summation of $(16)_1$ and $(16)_3$ which yields $\boldsymbol{n}\cdot(\boldsymbol{\sigma}^{\rm mp} + \sum_\alpha \boldsymbol{\sigma}^{f,\alpha}) = \bar{\phi}_m\bar{\phi}_s\boldsymbol{g} - \boldsymbol{n}\sum_\alpha \bar{\phi}_\alpha\bar{P}_\alpha^0$. The fluid outflow $\bar{W}_n^{\rm mes}$ on $\partial_w^0\Omega$ is given by $\bar{w}_n^{\rm mes} = \sum_\alpha \phi_\alpha\bar{\boldsymbol{w}}^\alpha\cdot\boldsymbol{n}$ lowered by the outflow through the micropores.

We shall now consider special boundary conditions for which the weak formulation will be presented. The microporosity is supposed to be nondrained so that $\partial_p^0\Omega = \emptyset$ and $\boldsymbol{n}\cdot\boldsymbol{j}^0 = 0$ on $\partial_w^0\Omega$. For the two mesoscopic compratments, only the Dirichlet conditions will be prescribed for $\boldsymbol{n}\cdot\boldsymbol{w}^{0,\alpha}$, *i.e.* for the normal component of the velocity on the entire surface $\partial_w^\alpha\Omega = \partial\Omega$. All these assumptions yield vanishing (or natural) Neumann conditions for the flows represented by p^0 and $\boldsymbol{w}^{0,\alpha}$. For the deformation field, the Dirichlet conditions $(15)_1$ are presscribed, whereas the surface tractions $\boldsymbol{g}$ loading the solid phase must be complemented by the microporosity pressure extrapolated by the trace of the solution, *i.e.* $\bar{p}^0 = p^0$ on $\partial_\sigma\Omega$. (Unfortunately, this extra term corrupts symmetry of the entire system.)

The Dirichet conditions are respected by the function spaces,

$$\begin{aligned} V_0(\Omega) &= \{\boldsymbol{v}\in\mathbf{H}^1(\Omega)|\ \boldsymbol{v} = \boldsymbol{0} \ \text{ on } \partial_u\Omega\} \,, \\ Q_0(\Omega) &= \{q\in H^1(\Omega)|\ \int_\Omega q = 0\} \,, \\ W_0^\alpha &= \{\boldsymbol{\psi}\in\mathbf{H}^1(\Omega)|\ \boldsymbol{\psi}\cdot\boldsymbol{n} = 0 \ \text{ on } \partial_w^\alpha\Omega\} \,. \end{aligned} \tag{17}$$

Weak formulation for the BDB model Find $(\boldsymbol{u}^0, p^0, \boldsymbol{w}^{0,1}, \boldsymbol{w}^{0,2})$ such that $\boldsymbol{u}^0 \in \bar{\boldsymbol{u}}^0 + V_0(\Omega)$, $p^0 \in Q_0$ and $\boldsymbol{w}^{0,\alpha} \in \bar{w}_n^\alpha + W_0(\Omega)$ satisfy

$$\int_\Omega \left(\boldsymbol{\mathcal{A}}\boldsymbol{e}_x(\boldsymbol{u}^0) - p^0\boldsymbol{\mathcal{B}}\right) : \boldsymbol{e}_x(\boldsymbol{v}) - \sum_\alpha \int_\Omega \boldsymbol{v}\cdot\left[(\boldsymbol{\mathcal{P}}^\alpha)^T(\nabla_x p^0 - \boldsymbol{f}^f) - \sum_{\beta=1,2}\boldsymbol{\mathcal{H}}^{\alpha\beta}\boldsymbol{w}^{0,\beta}\right] =$$
$$-\int_{\partial_\sigma\Omega}\bar{\phi}_c p^0\boldsymbol{n}\cdot\boldsymbol{v} + \int_\Omega \boldsymbol{f}^{\rm blk}\cdot\boldsymbol{v} + \int_{\partial_\sigma\Omega}\boldsymbol{v}\cdot\bar{\phi}_m\bar{\phi}_s\boldsymbol{g}\ ,$$
$$\int_\Omega q\left(\boldsymbol{\mathcal{B}} : \boldsymbol{e}_x(\dot{\boldsymbol{u}}^0) + \mathcal{M}\dot{p}^0\right) + \int_\Omega \nabla q\cdot\left(\boldsymbol{\mathcal{K}}(\nabla_x p^0 - \boldsymbol{f}^f) + \sum_{\beta=1,2}\boldsymbol{\mathcal{P}}^\beta\boldsymbol{w}^{0,\beta}\right) = 0\ ,$$
$$\int_\Omega \boldsymbol{e}_x(\boldsymbol{\psi}) : \boldsymbol{\mathcal{S}}^\alpha\boldsymbol{e}_x(\boldsymbol{w}^{0,\alpha} + \dot{\boldsymbol{u}}^0) + \int_\Omega \boldsymbol{\psi}\cdot\left[(\boldsymbol{\mathcal{P}}^\alpha)^T(\nabla_x p^0 - \boldsymbol{f}^f) - \sum_{\beta=1,2}\boldsymbol{\mathcal{H}}^{\alpha\beta}\boldsymbol{w}^{0,\beta}\right] = 0\ , \alpha = 1,2\ , \tag{18}$$

for all $\boldsymbol{v} \in V_0(\Omega)$, $q \in Q_0(\Omega)$, and $q \in W_0^\alpha(\Omega)$, $\alpha = 1, 2$.

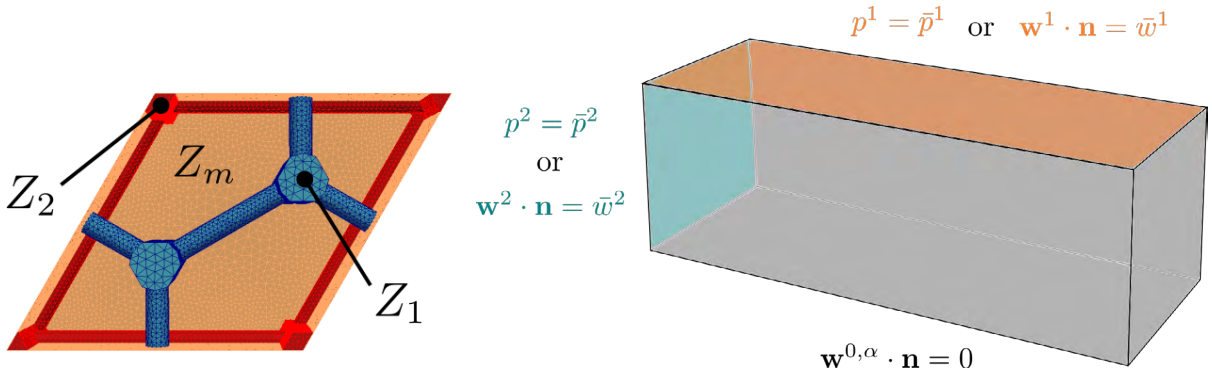


Figure 2: (a) Mesoscopic geometry representing lobular structure; (b) Macroscopic sample with boundary conditions for the two models, BDB and DD. The Dirichlet conditions defined in terms of $\bar{p}^1$ and $\bar{p}^2$ are employed for the DD model, while the normal velocities $\boldsymbol{n}\cdot\boldsymbol{w}^\alpha$, $\alpha = 1, 2$ are employed for the BDB model.

3 Numerical example and comments

In this section we compare steady state responses of the Biot-Darcy-Brinkman (BDB) model presented above with corresponding responses of the two-compartment Darcy flow model derived in [6] by the homogenization of a double-porous medium, as announced in the introduction. Below, this model is referred as the DD model. In the steady state associated with both the models, the flow and fluid pressure is decoupled from the deformation which, thus, is not discussed in this example.

The effective homogenized parameters are calculated using the representative volume element whose the structure, *i.e.* the geometry of the subdomains mimics the hepatic

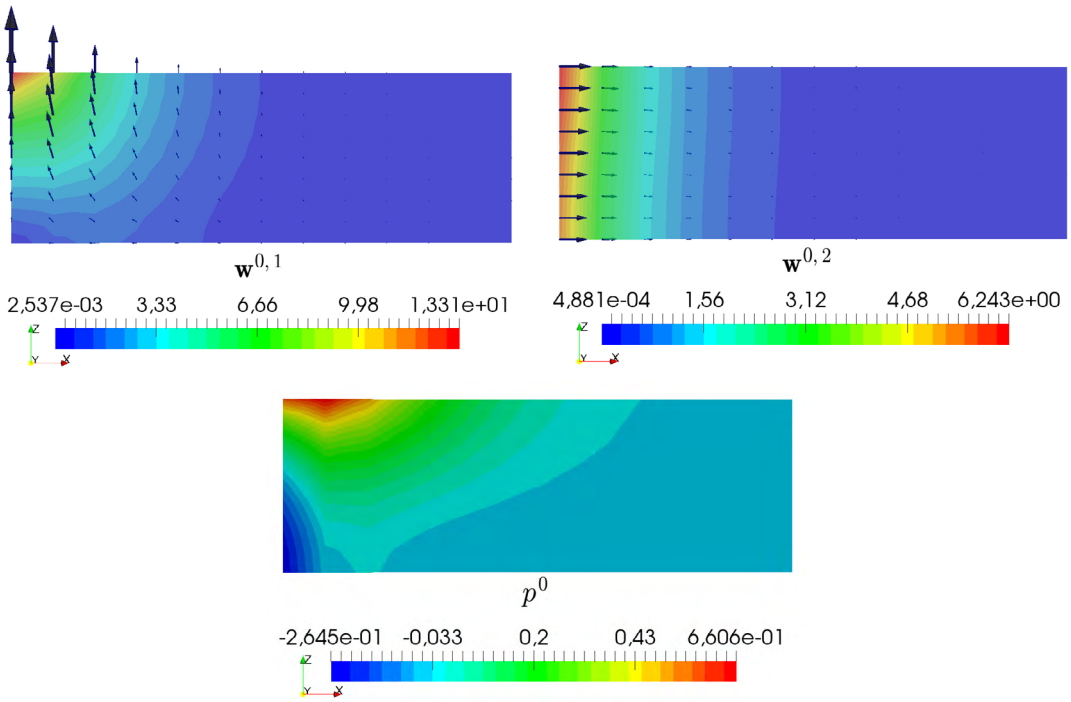


Figure 3: Macroscopic solution of BDB model. The pressure p^0 is related to the sinusoidal microporosity.

vasculature at the lobular level, see Fig. 2a. The periodic representative cell Z consists of the solid porous part Z_m reflecting the sinusoidal microporosity and two fluid parts Z_α, $\alpha = 1, 2$ representing the portal and the hepatic vascular networks in the lobules. Apart of the geometry at both the micro- and meso-scopic levels, the BDB model is defined by the fluid (blood) viscosity, while the DD model requires the permeability tensors to be defined for both the sinusoidal porosity and for the mesoscopic channels representing the precapillary vessels. To be able to compare results provided by both the models, these permeabilities are calculated from the Poiseuille law using viscosities employed in the BDB model. The macroscopic simulation is performed on a block sample, see Fig. 2b. On two distinct faces of the macroscopic sample, we prescribe the two pressures, in the case of the DD model, or normal-projected velocities, in the case of the BDB model. The other faces of the sample are assumed to be impermeable for both the models.

The macroscopic response of the BDB model, *i.e.* the solution of (18), is shown in Fig. 3. It consists of the velocity in the portal system $\boldsymbol{w}^{0,1}$, the velocity in the central system $\boldsymbol{w}^{0,2}$ and the pressure in sinusoidal microporosity p^0. In comparison, the macroscopic solution of DD model, as shown in Fig. 4) consists of the two pressure fields p^1 and p^2 referring to the pressure in the portal and central system, respectively. The velocities $\boldsymbol{w}^{0,1}_{DD}$ and $\boldsymbol{w}^{0,2}_{DD}$ in both system have to be computed from their respective pressure fields. When comparing the preliminary result of velocity $\boldsymbol{w}^{0,1}$ to velocity $\boldsymbol{w}^{0,1}_{DD}$ and velocity $\boldsymbol{w}^{0,2}$ to velocity $\boldsymbol{w}^{0,2}_{DD}$, the satisfactory qualitative and even quantitative agreement can be found. Nonsteady responses of the BDB model will be reported in a forthcoming publication.

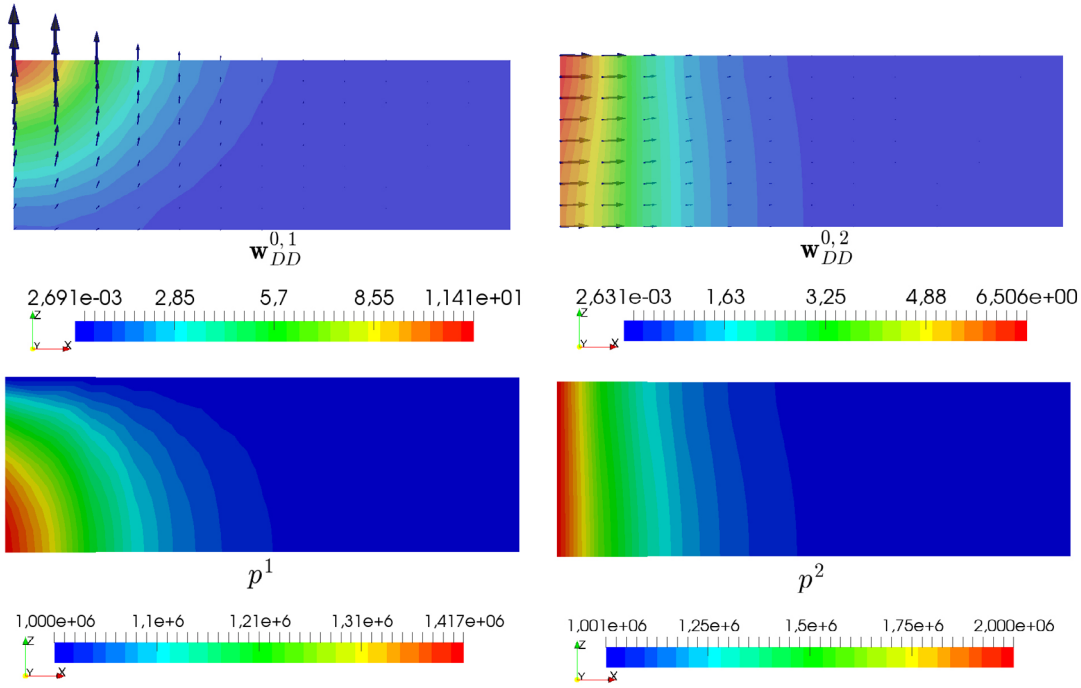


Figure 4: Macroscopic solution of DD model. Velocities $\boldsymbol{w}_{DD}^{0,\alpha}$, $\alpha = 1, 2$ in the mesoscopic porosities are directly related to the pressures p^α through the homogenized Darcy law.

Acknowledgment This research is supported by part by project GACR 19-04956S of the Scientific Foundation of the Czech Republic and by the project LO 1506 of the Czech Ministry of Education, Youth and Sports. The work was also supported from European Regional Development Fund-Project "Application of Modern Technologies in Medicine and Industry" (No. CZ.02.1.01/0.0/0.0/17_048/0007280).

REFERENCES

[1] Arbogast, T., Douglas, Jr, J. and Hornung, U. Derivation of the double porosity model of single phase flow via homogenization theory. *SIAM J. Math. Anal.* (1990) **21**(4):823–836.

[2] D. Cioranescu, A. Damlamian, G. Griso, and et al. The Stokes problem in perforated domains by the periodic unfolding method. new trends in continuum mechanics. *Theta Series in Advanced Mathematics*, **3** (2005): 67–80.

[3] Debbaut, C., Segers, P., Cornillie, P., Casteleyn, C., Dierick, M., Laleman, W. and Monbaliu, D. Analyzing the human liver vascular architecture by combining vascular corrosion casting and micro-CT scanning: a feasibility study. *J. Anat.* (2014) **224**(4):509–517.

[4] Debbaut, C., Vierendeels, J., Casteleyn, C., Cornillie, P., Van Loo, D., Simoens, P., Van Hoorebeke, L., Monbaliu, D. and Segers, P. Perfusion characteristics of the

human hepatic microcirculation based on three-dimensional reconstructions and computational fluid dynamic analysis. *J.Biomech. Eng.* (2012) **134**(1):011003.

[5] Ricken, T., Dahmen, U. and Dirsch, O. A biphasic model for sinusoidal liver perfusion remodeling after outflow obstruction. *Biomechanics and modeling in mechanobiology* (2010) **9**(4):435–450.

[6] Rohan, R. and Cimrman, R. Two-scale modeling of tissue perfusion problem using homogenization of dual porous media. *Int. J. Multiscale Comput. Eng.* (2010) **8**(1):81–102.

[7] Rohan, E., Naili, S., Cimrman, R. and Lemaire, T. Multiscale modeling of a fluid saturated medium with double porosity: Relevance to the compact bone. *J. Mech. Phys. Solids* (2012) **60**(5):857–881.

[8] E. Rohan and V. Lukesš. Modeling nonlinear phenomena in deforming fluid-saturated porous media using homogenization and sensitivity analysis concepts. Applied Mathematics and Computation, 267 (2015) 583-595.

[9] E. Rohan, V. Lukeš, J. Turjanicová, and , and R. Cimrman. Two level homogenization of flows in deforming double porosity media: Biot-Darcy-Brinkman model. In: XIV International Conference on Computational Plasticity. Fundamentals and Applications, COMPLAS XIV, E. Onate, et al. (Eds), CIMNE, Barcelona, 2017.

[10] E. Rohan, V. Lukeš, and A. Jonašová, Modeling of the contrast-enhanced perfusion test in liver based on the multi-compartment flow in porous media. In: Journal of Mathematical Biology 2 (2018), pp. 421-454.

[11] E. Rohan, J. Turjanicová, J. and V. Lukeš, A Darcy-Brinkman model of flow in double porous media – two-level homogenization and computational modelling. Computers & Structures, 207 (2018), pp. 95-110.

[12] E. Rohan, J. Turjanicová, J. and V. Lukeš, The Biot-Darcy-Brinkman model of flow in deformable double porous media; homogenization and numerical modelling. Computers and Mathematics with Applications, *In Press.* DOI:10 1016/j.camwa.2019.04.004. (2019)

XIV International Conference on Computational Plasticity. Fundamentals and Applications
COMPLAS 2019
E. Oñate, D.R.J. Owen, D. Peric , M. Chiumenti, and Eduardo de Souza Neto (Eds)

NUMERICAL EVALUATION OF WEARING PRESSURE AND CLOTH STIFFNESS ON VIBRATION OF HUMAN SKELETAL MUSCLE DURING ATHLETIC MOVEMENT

SHODAI UEDA[*] AND ATSUSHI SAKUMA[†]

[*] Graduate School, Kyoto Institute of Technology
Matsugasaki, Sakyo-ku, Kyoto,606-8585, Japan

[†] Division of Textile Science, Kyoto Institute of Technology
Matsugasaki, Sakyo-ku, Kyoto,606-8585, Japan
email: sakuma@kit.ac.jp, www.fibro.kit.ac.jp

Key words: Compression Wear, FEM, Constitutive Equation, Vibration.

Abstract. *In the design of sportswear which is expected to modify the performance of athletes, it is important to clarify the effects of the wear's rigidity and wearing pressure on the vibrations during exercise because they have been considered to reduce the vibrations of muscles. Therefore, in this study, the relationship between the vibration generated in cyclic movement of thigh with cloth and the physical properties of the wearing cloth is discussed by using a simple FE model of thigh [1, 2]. In the analysis, the FE model consisted of three parts of the thigh muscle, the femur, and the wear in the cross section of thigh. The thigh muscle is fixed to the femur but it is in contact with the wear cloth ignoring friction. The condition of the thigh cyclical movement is set assuming the athlete's 100 m run. Numerical analysis is performed under these conditions, and the variations of vibration behavior due to changing values of muscle, wear and pressure are evaluated by mechanical consideration. In the results of this FE analysis, it is quantitatively confirmed that more flexible cloth has the effect of restraining vibration, and also its effect can also be observed by applying wearing pressure to thigh.*

1 INTRODUCTION

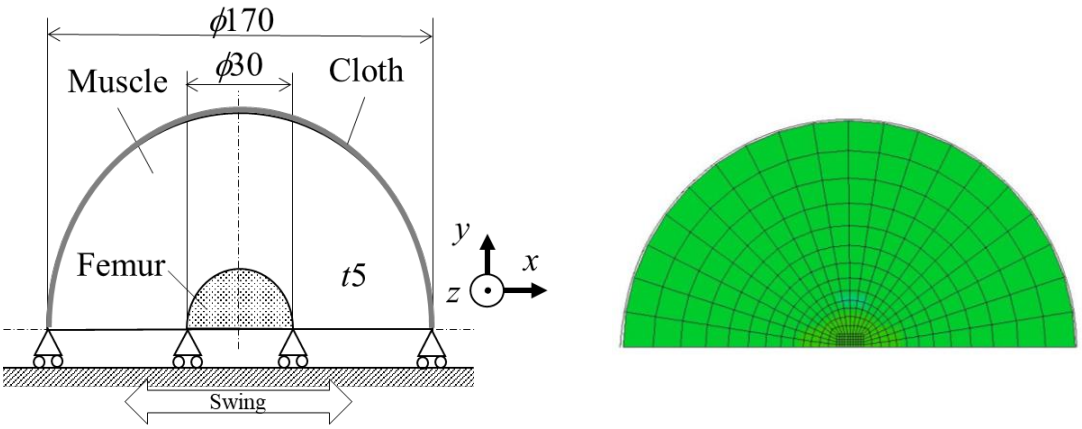
Compression wear is said to have the effect of reducing strain in human body by reducing muscle vibrations, and then it is also said that moderate pressure on the body can improve exercise performance. Here, it was reported that vibration generated in muscle of lower leg can be reduced by compression wear [1]. However, most of these researches are experimentally observed on human being which includes individual differences.

Then, in this study, the simple FE model of the thigh [2, 3] is adopted to analyze the relationship between the vibration generated by the periodic movement of thigh and the physical properties of the clothing precisely.

2 FE MODELING OF HAMSTRING WITH CLOTHE

2.1 Geometry and FE mesh

In this paper, cross section of hamstring is considered to evaluate the deformation behavior of thigh muscle. Figure 1 (a) shows a geometrical model of the hamstring's cross-section with 3 parts of femur, muscle and cloth. Outer diameter of muscle part is 170mm and inner one is 30mm, which is outer diameter of femur part. Half part of the round section is considered to simplify the analysis of defamation behavior by its geometrical symmetricity. The thickness of the section is considered as 5mm with plain strain condition for axis direction z. Movement of hamstring is modeled with the cyclic swing of the femur part which is defined by rigid body mechanically. Other parts of muscle and cloth are defined by elastic body for focusing the objective of this study on the mechanical effect of wearing pressure of cloth. Figure 1 (b) shows FE mesh generated in the geometrical parts, and its specification is shown in Table 1. Here, element type of femur and muscle parts is solid with 8 nodes, and cloth part is shell with 4 nods.



(a) Geometrical condition (b) FE mesh

Figure 1: Geomatical condition and FE mesh for numerical evaluation.

Table 1: FEM specification

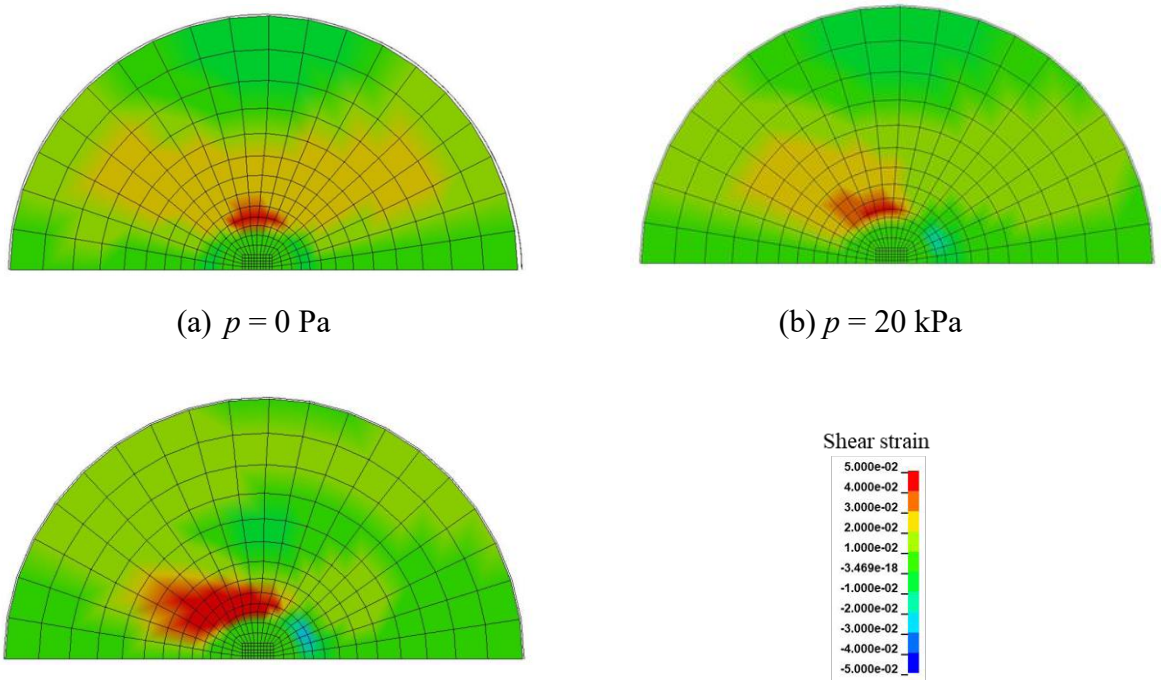
Part	Femur	Muscle	Cloth
Material model	Rigid	Elastic	Elastic
Dimension	Thickness t =5 mm Diameter ϕ =170 mm		
Young's modulus E	—	25 kPa-200 kPa	100kPa-1 MPa
Density	—	1000 kg/m^3	400 kg/m^3
Poisson's ratio ?	—	0.45	0.45
Number of nodes	258	462	122
Number of elements	110	200	60
Solver	Explicit		

Numbers of nodes are 258, 462 and 122, and number of elements are 110, 200 and 60 relatively. FE calculation have done by using LS-Dyna with explicit solver mode.

In the mechanical evaluation of wearing cloth, the modulus of muscle and cloth have changed with the pressure control of wearing cloth as shown in Table 1. The frequency of cyclic swing of thigh is 2.5 Hz because this movement of the swing is estimating 100m dash with 50 steps in 10 seconds. The amplitude of thigh swing is 85mm by considering average physique of human.

2.2 Simulated results

Figure 2 shows the calculated results of FEM, and variation of shear strain due to the pressure caused by cloth shrinkage is compared among figures from (a) to (c). Here, shrinkage for wearing pressure is generated by the function of thermal strain in LS-DYNA with negative coefficient of linear expansion and positive thermal change. Each figure shows the situation at time t = 0.18 s. Here, lift of wearing cloth can be observed in a result of pressure free (p = 0 Pa), but it is not observed in other two pressured condition of p = 20 kPa and 30 kPa. The increase of maximum shear strain due to the increase of wearing pressure can be observed, too.

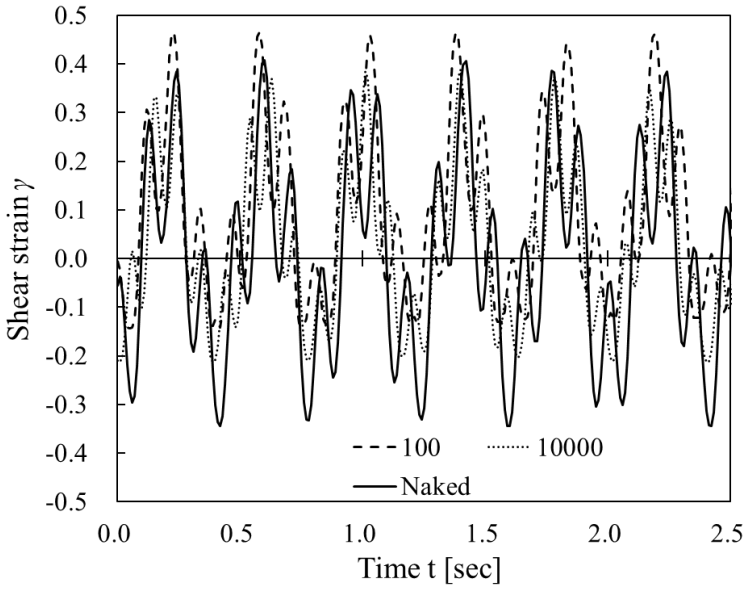


(a) p = 0 Pa

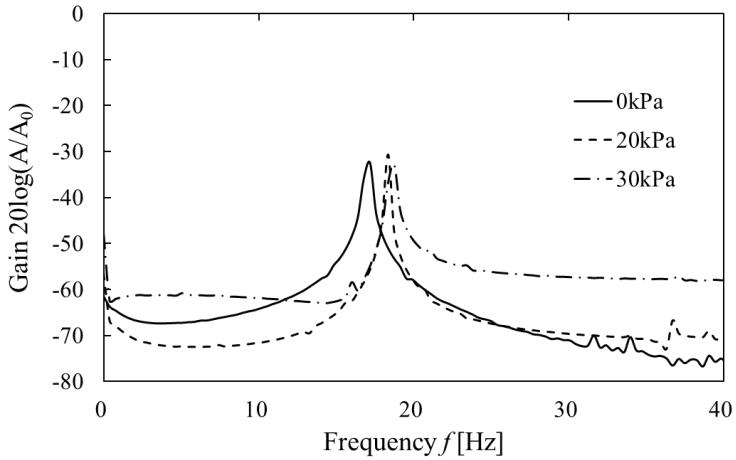
(b) p = 20 kPa

(c) p = 30 kPa

Figure 2: Variation of shear strain distribution induced by wearing pressure.



(a) Variation of strain fluctuation due to cloth rigidity



(b) Frequency analysis

Figure 3: Strain fluctuation and analyzed frequency in pressure p = 50 kPa.

From the results of FEM shown in Figure 2, the fluctuation of strain is derived as shown Figure 3 (a) and result of frequency analysis is shown in Figure 3 (b). In the results of strain fluctuation, the increase of maximum shear strain and due to the increase of cloth rigidity is observed with decrease of minimum shear strain. In the frequency analysis, peak shift to higher range due to increase of the pressure is observed with gain growth in high frequency region. As the result of this Figure 3, not only the amount of shear strain but also the shift of frequency mode are observed by wearing the compression wear.

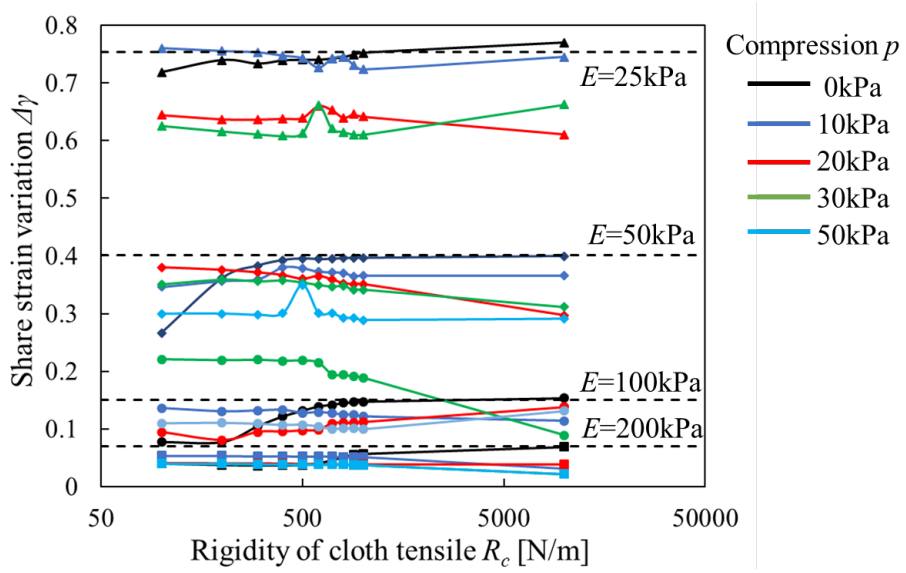


Figure 4: Analysis of shear strain variation

In order to summarize the results of numerical analysis, variation of strain amplitude, which is the difference between maximum and minimum shear strain, is analyzed by changing muscles elasticity E, cloth rigidity Rc, and wearing pressure p. Here, the variation of shear strain $\Delta\gamma$ can be decreased by the increase of muscles elasticity E, and increase of pressure p can decrease the variation of shear strain $\Delta\gamma$. This decrease by the increase of muscles elasticity E can be explained by fundamental Hooke's law or the change of stress wave by pressure p.

3 CONCLUSIONS

- In order to investigate the effect of wearing pressure, a simple cross section model has been developed for the analysis by finite element method, and then the analysis of shear strain in simulated results shows the complexity of deformation behavior change in moving process of muscle.
- The increase of maximum strain can be observed with the decrease of shear strain variation by the increase of wearing pressure.

REFERENCES

[1] Wakeling, M.J., Nigg, B.M and Rozitis A. I. Muscle activity damps the soft tissue resonance that occurs in response to pulsed and continuous vibrations. *Journal of Applied Physiology* (2002)**93**: 1093-1103.

[2] Liu, R. Kwok, Y.L. Li, Y. Lao, T.-T Zhang, X. Dai, X.Q. A three-dimensional biomechanical model for numerical simulation of dynamic pressure functional performances of graduated compression stocking, *Fibers and Polymers* (2006) **7**: 389-397.

[3] Ishimaru, S. Isogai, Y. Matsui, M. Negishi, K. Nonomura, C. Yokoyama, A. Prediction of Clothing Pressure Distribution by Using Finite Element Method -Prediction of Clothing Pressure for Pants-, *Journal of Textile Engineering* (2009) **55**: 179-186.

XIV International Conference on Computational Plasticity. Fundamentals and Applications
COMPLAS 2019
E. Oñate, D.R.J. Owen, D. Peric , M. Chiumenti, and Eduardo de Souza Neto (Eds)

DURABILITY EVALUATION OF MADAKE BAMBOO BY FE ANALYSIS OF FRACTURE WITH CONSIDERATION OF FIBRE DIRECTION

RAVIDUTH RAMFUL [*], ATSUSHI SAKUMA [†] AND HAJIME KIMURA [*]

[*]Graduate School, Kyoto Institute of Technology (KIT)
Matsugasaki, Sakyo-ku, Kyoto, 606-8585, Japan
e-mail: r.ramful@uom.ac.mu

[†] Division of Textile Science, Kyoto Institute of Technology (KIT)
Matsugasaki, Sakyo-ku, Kyoto, 606-8585, Japan
e-mail: sakuma@kit.ac.jp, web page: http://www.fibro.kit.ac.jp/

Key words: Madake Bamboo, Inhomogeneous, Fracture, Pure Bending.

Abstract. *The flexural stiffness of bamboo is inherently influenced by heterogeneous material characteristic owing to its unique hierarchical structure. In addition, low interfacial strength and unequal distribution of fibres lead to a complex fracture behavior in the material. This research study aims to probe into the limited durability of MADAKE bamboo (Phyllostachys bambusoides) by investigating its fracture mechanism through numerical simulation. The influence of functionally graded material (FGM) on the fracture behavior of bamboo culm was evaluated. A half-solid cylindrical model consisting of a rigid section and a 4-layered wall section was simulated in pure bending mode on LS-DYNA. The effects of material homogeneity and inhomogeneity were replicated by inputting elastic and orthotropic-elastic material data comprising of longitudinal to flexural stiffness ratio. These ratios were derived from experimental results of three-point flexural test. Analysis of results, based on maximum principal strain, showed that the homogeneous model displayed fracture characteristics similar to conventional elastic material. In contrast, the inhomogeneous model displayed maximum principal strain on the lateral surface corresponding to fracture mode of bamboo culms observed in nature. Numerical study of material heterogeneity is a step further in understanding the fracture mechanics of functionally graded materials.*

1 INTRODUCTION

As an indispensable construction material to human life, bamboo has been widely used in buildings, bridges and other infrastructures involving structures. In modern times, despite being in an era of highly advanced materials, the growing trend towards sustainable development is reigniting the interest on greener materials. Bamboo has full potential as a sustainable material and could be considered as an alternative to conventional materials used in construction such as steel and concrete. Two factors; (1) a high-strength to weight ratio, and (2) an unrivalled growth rate of up to 100 cm per day, completely outclass other materials of its category [1,2].

The distinct morphology of bamboo culms is composed of cylindrical sections (internodes) reinforced with nodes. Being an organic material with a composite structure, it has been classified as a functionally graded material (FGM). This given structure is the result of millions of years of natural evolution in the natural environment. The inherence of FGM provides excellent material attributes, namely high strength, good stiffness and wear resistance, suitable for structural design. The longitudinally aligned cellulose fibres, which are immersed in a matrix of lignin, forms vascular bundles. These are non-uniformly distributed throughout the thickness resulting in a graded pattern [1].

The vascular bundles, which are smaller and concentrated towards the outermost culm wall and larger and fewer towards the innermost section, account for the increase in effective section moment of inertia. In addition, the volume fraction of vascular bundles increases with height. This large volume fraction compensates for the inferior bending strength inherited by the top most culm section due to a reduction in diameter and wall thickness. This smart structure enables bamboo to withstand extreme flexural loading caused by wind and snow [1,3,4].

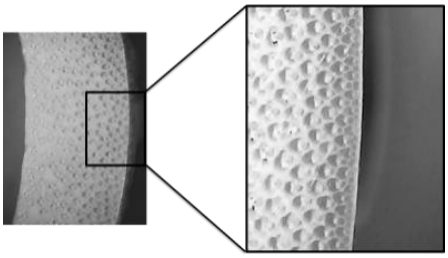


Figure 1: Functionally graded material (FGM)

Mechanical characterization has shown an asymmetric flexural behaviour in bamboo. Unlike fibers strand, parenchyma cells, which displays greater elasticity, can accommodate larger deformation, hence accounting for the substantial flexibility in the culm structure [5,6]. In 4-point bending tests of *Phyllostachys pubescens*, maximum flexural rigidity was noted when the hardest outer part and softest inner part were strained and compressed respectively. Parenchyma cells were found to absorb large compressive deformation and was described as a highly compressible foam-like structure [7]. Recently, engineered bamboo with improved mechanical properties and homogeneity have been produced through advanced techniques [8].

To maximise the integration of bamboo in further engineering application and structures, it is essential to consider certain steps to improve its durability. The average natural durability of raw bamboo culms is about 2 years and up to 7 years if protected from exterior exposure. A noticeable increase in the mechanical strength has been observed in bamboo specimens constituting a lower moisture content than the fiber saturation point (FSP) [9]. By attaining a new state of equilibrium through a series of shrinking and swelling processes, internal stresses are often induced within the material, leading to crack formation and premature split of bamboo culms [1].

Carbonized bamboo has been used over the centuries in building construction owing to its excellent long term durability and preservation of its mechanical properties. In Kyoto, Japan, a traditional craftsmanship technique of wood preservation, known as Shou Sugi Ban, is applied to bamboo to carbonize the outermost layers. In the final product, termed as Yakisugi, moisture is drawn out of the material by thin carbon film, created during a light surface burn process. In the process of drying, whereby fibers gain strength but lose their toughness, bamboo becomes brittle and prone to premature failure by longitudinal split along culm length [1,10].

1.1 Fracture

The flexural stiffness of bamboo is inherently influenced by heterogeneous material characteristic owing to its unique hierarchical structure. Most tissues in this highly anisotropic biomaterial are arranged longitudinally and bound by non-cellulose component. This particular structure, which results in an inferior interfacial strength, surprisingly contributes to the high transverse toughness, making bamboo culms resistant to flexural loads. However, low interfacial strength and unequal distribution of fibres also lead to a complex fracture behavior in the material [5,7,11].

Few research on the fracture toughness has been conducted to elucidate the crack propagation in bamboo. In Moso bamboo, Askarinejad *et al.* found cracks to propagate parallel to the longitudinal direction of fibers irrespective of notch direction and crack bridging was more pronounced in inner fibers [12]. Low fracture toughness parameter in Mode I interlaminar fracture investigation, showed that crack followed an easy path parallel to grain. The resistance against crack propagation, governed by interfacial strength was lower in the outer layer [11]. In Mode II numerical analysis, the interlaminar fracture toughness was found to be unrelated to length of original crack [13].

Typical fracture in bamboo occurs by splitting of culms under the action of stresses, namely impact loads, fatigue loads, creep, internal stresses and external factors [14]. Fracture of bamboo culm by cracking through time-dependent deformation results in creep. Mechano-sorptive is a recurrent creep phenomenon experienced by natural composites as a consequence of cyclic moisture variation on loaded specimens. Creep behaviour of bamboo under various desorption conditions is influenced by; distribution of vascular bundles, density and material anisotropy [15-17].

The inherent FGM structure of bamboo is well adapted to preserve its natural durability against external factors such as wind loadings. When the maximum bending moment threshold is exceeded, failure of culm structure occurs as displayed in Figure 2. Crack is observed to propagate longitudinally along culm length. Several studies have been conducted on the effect of bending moment on cross-sectional deformation of culm structure and onset of fracture [18-20]. During bending of tubular section, cross-sectional inward forces, induced by longitudinal tensile and compressive stresses on the convex and concave sections respectively, have a tendency to ovalize the cross-section [21,20]. This ovalization is amplified by an increase in curvature as a maximum value of bending moment is reached [18].



Figure 2: Natural fracture of bamboo – side culm failure

This deformation by cross-sectional flattening, which was first reported by Brazier on the bending of thin-walled cylinders, leads to a decrease in the second moment of area and stiffness due to instability in the structure [21]. Huang *et al.* identified four modes of failure mechanism of hollow trunks caused by bending. These are Brazier buckling, cracks in the tangent direction/longitudinal split, typical bending failure and shear failure. Key research findings revealed that tangential cracking, followed by longitudinal splitting, is likely to happen as a result of cross-sectional flattening and are initiated at 4 vertices of the ovalized section [19].

In view of further maximizing the external application of bamboo materials, it is essential to improve its durability by considering factors which contribute to its natural rate of degradation. Study of its failure mechanism and defining the fundamental mechanical behaviour is essential in the validation process of material worthiness for design construction. This paper aims to probe into the limited durability of Madake bamboo (*Phyllostachys bambusoides*) by investigating the root cause of material failure by fracture, through numerical analysis.

2 METHODOLOGY

The effects of inhomogeneous material on the failure modes of bamboo culm were investigated by numerical simulation. Figure 3 below, displays the test setup outline of section of bamboo culm model in pure bending mode. The effects of wind loadings on upper section of bamboo culm, were simulated by incorporating a rigid section to the model. The wall-end of the model was constrained in the *z*-direction only. The rigid section was assigned with elastic material data of high modulus of elasticity and constrained in the *x*-direction only.

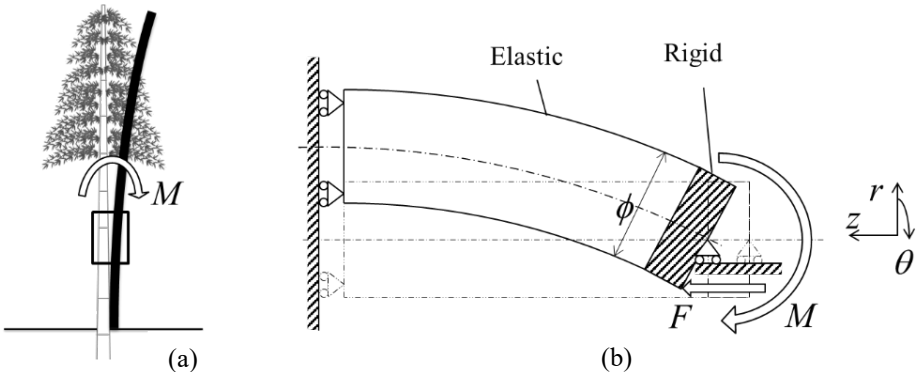
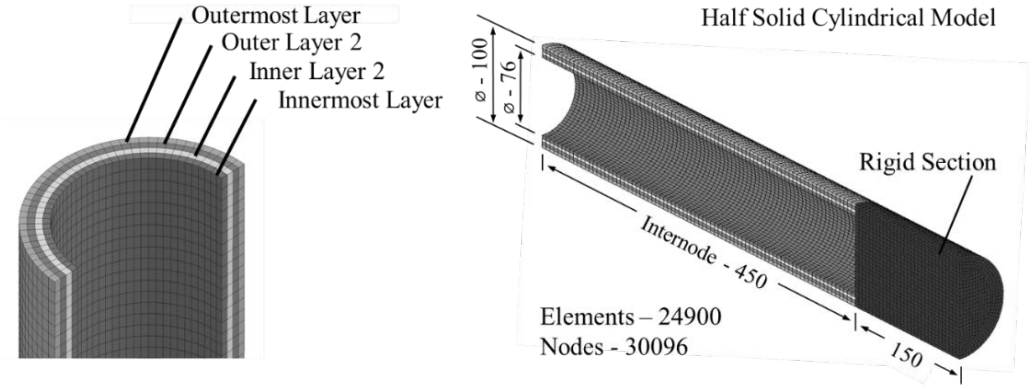


Figure 3: (a) Bending in real bamboo, (b) simulation of pure bending mode

A half-solid cylindrical model, replicating the internodal length of bamboo culm, was modelled to minimize computational time. The model, designed on FEMAP using existing literature data on Madake bamboo, consisted of a rigid solid section and a hollow cross- section composing of a 4-layered wall [1]. Detailed outline of the 3-dimensional model is shown in Figure 4. For an average internode count of 18, the internodal length, outer diameter and wall thickness was determined as 450, 100 and 12 mm respectively. HexMesh solid was used throughout and the model consisted of 24900 elements and 30096 nodes.



(a) (b)

Figure 4: (a) Cross-section of layered model, (b) dimensions outline of culm model

The final model was exported to LS-DYNA and implicit analysis was performed by using appropriate simulation parameters. The effects of material homogeneity and inhomogeneity were replicated by inputting elastic and orthotropic-elastic material data respectively through FE analysis in LS-DYNA. The maximum strength in fibre direction was obtained experimentally through 3-point bending tests and an average value of 15 GPa was taken. Other engineering constants, namely Poisson's ratios and shear moduli were determined by using equations (1) and (2) respectively with respect to their orthogonal directions [22].

$$\frac{v_{ij}}{E_i} = \frac{v_{ji}}{E_j} \qquad i, j = 1, 2, 3 \quad i \neq j \tag{1}$$

$$G_{ij} = \frac{E_i E_j}{E_i + E_j + 2E_j v_{ij}} \qquad i, j = 1, 2, 3 \quad i \neq j \tag{2}$$

The material models were reproduced by assuming a longitudinal to transverse flexural stiffness ratio in the fibre and radial direction respectively. Two material models were investigated in pure bending mode. A homogeneous material model, consisting of uniform isotropic properties in the radial direction, was devised with a uniform modulus of elasticity of 15 GPa throughout as shown in Table 1. A second material model of inhomogeneous nature, consisting of axial reinforced transversely isotropic material, was devised with a longitudinal to transverse stiffness ratio of 100:1 as shown in Table 2.

Table 1: Engineering constants for perfectly isotropic material

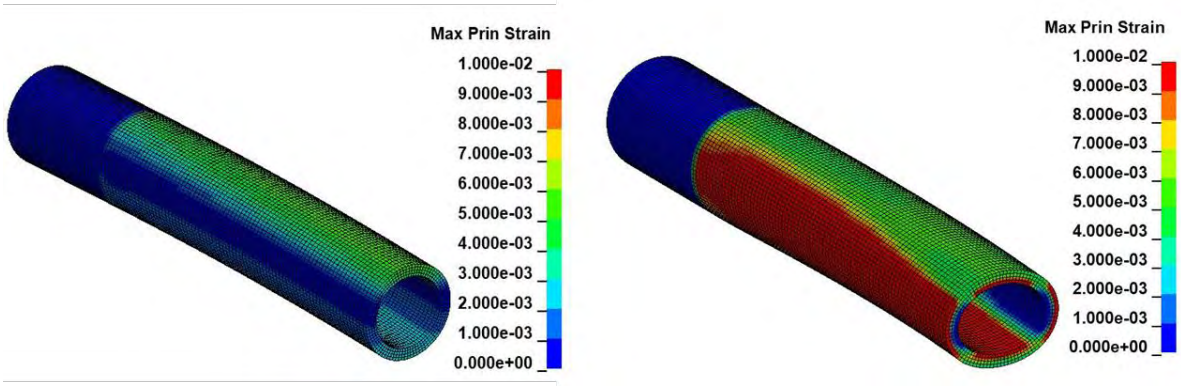
LS-DYNA Material Parameter - MAT_001 Elastic		
Parameter	Elastic Section	Rigid Section
Young's Modulus	E = 15 GPa	$E = 15 \times 10^6$ GPa
Poisson's ratio	ν = 0.3	ν = 0.3

Table 2: Calculator of engineering constants for axial reinforced transversely isotropic material

LS-DYNA Material Parameter - MAT_002 Orthotropic _Elastic					
Defined material data for flexural stiffness ratio longitudinal/transverse - 100:1					
Young's Modulus	Fiber Direction	E_z = 15,000 MPa	Poisson's ratio	Out-Plane	ν_{zr}, $\nu_{z\theta}$ = 0.3
	Radial and Circumferential Direction	E_r, E_θ = 150 MPa		Out-Plane	ν_{rz}, $\nu_{\theta z}$ = 0.003
Shear Modulus		G_{zr}, $G_{\theta z}$ = 148 MPa		In-Plane	$\nu_{r\theta}$, $\nu_{\theta r}$ = 0.003
		$G_{r\theta}$ = 75 MPa			

3 ANALYSIS OF RESULTS

The flexural behavior of 2 material models was investigated by considering the maximum principal strain criterion. The fringe components of selected range of maximum principal strain distribution of both models are displayed in Figure 5. The strain distribution from Figure 5(a), which represents the perfectly isotropic homogeneous model, is found to be greatest at the outermost section of the convex side of the culm. On the other hand, the strain distribution of the axial reinforced transversely isotropic model differed throughout the outer surface of the cross-section. The area of maximum principal strain is located midway on the outer surface and on the inner surface of both convex and concave sides of the culm. From Figure 5(b), ovalization of the cross-section is found to increase with increasing bending moment. Buckling of culm is likely to occur as this cross-sectional flattening weakens the structure [20].



(a) (b)

Figure 5: Comparison of fringe component of selected range of max-principal strain in; (a) perfectly isotropic material, (b) axial reinforced transversely isotropic material

A relative comparison of the maximum principal strain distribution of both material models was derived from Figure 5 and summarized in Figure 6. A local coordinate θ relative to the radial axis (Figure 3(b)) was used to describe the strain distribution across the cylinder cross-

section. The areas more susceptible to failure by fracture in the perfectly isotropic model is located at 0° on the outer surface of the cross-section. This mode of failure is comparable to the strain distribution exhibited by isotropic materials in pure bending mode. In contrast, the distribution of maximum principal strain on the inner and outer circumference of the transversely isotropic model was found to be greatest at 0° and 180° followed by 90° with strain values of 0.032, 0.037 and 0.028 respectively.

Failure by fracture based on maximum principal strain criterion is bound to initiate from the inside sections followed by lateral sides of the culm. As reported in literature, cracks are expected to be initiated at four vertices of the circumference corresponding to the maximum principal strain shown in Figure 5(b) [18-20]. As bending load increases, it is assumed that these cracks will propagate longitudinally along culm length. This anticipated mode of failure corresponds to the fracture behavior of bamboo in nature as described in Figure 2.

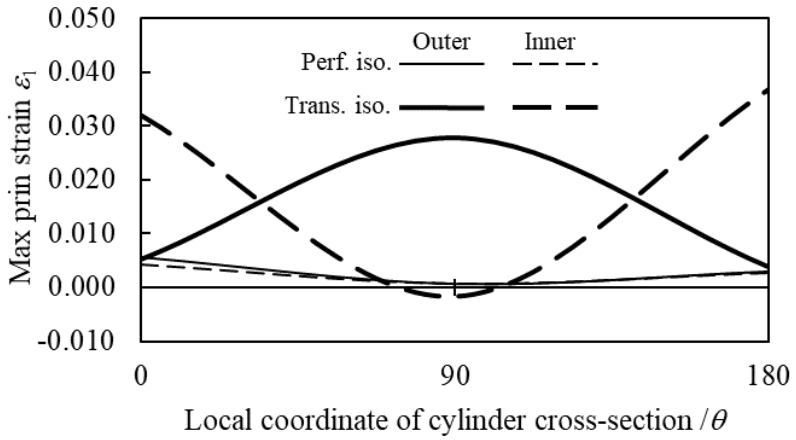


Figure 6: Comparison of maximum principal strain distribution

Modification of the inner culm section at 0° and 180° is a possible consideration to delay the onset of crack initiation by altering the maximum principal strain. This is a potential measure to address fracture from the inside of bamboo culms without requiring modification of its outermost surface. Even though this analysis has been conducted on intermodal length, it is worth mentioning about the contribution of nodes to resist bending. By having small intermodal length at the base of the culm, nodes provides additional reinforcement to the culm structure to resist maximum bending loads. However, as the intermodal length reaches a maximum value in the central part of the culm, this region becomes vulnerable to cross-sectional flattening and buckling [1,18].

4 CONCLUSION

This numerical study highlights the influence of inhomogeneous material on the fracture behavior of culm structure. Fracture behavior of homogeneous material model was found to be analogous to conventional fracture of isotropic material. Significant change in the circumferential distribution of maximum principal strain was observed in simulation of inhomogeneous model as material composition changed from elastic to orthotropic-elastic which comprised of axial reinforced fibres.

Results of this study correlates with natural failure observed in bamboo culms. Based on the criterion of maximum principal strain, cracks, which are likely to be initiated at four vertices of the circumference, are expected to propagate longitudinally.

REFERENCES

[1] Harries, K.A. and Sharma, B. *Nonconventional and vernacular construction materials*. UK: Woodhead Publishing, (2016)

[2] Lakkad, S.C. and Patel, J.M. Technical note Mechanical properties of bamboo, a natural composite. *Fibre Sci and Technol* (1980) **14**:319-322.

[3] Amada, S., Munekata, T., Nagase, Y., Ichikawa, Y., Kirigai, A. and Zhifei, Y. The mechanical structures of bamboos in viewpoint of functionally gradient and composite materials. *Journal of Composite Materials* (1996) **30**:800-819.

[4] Dixon, P.G. and Gibson, L.J. The structure and mechanics of Moso bamboo material. *J. R. Soc. Interface* (2014) **11**. (doi:10.1098/rsif.2014.0321)

[5] Habibi, M.K., Samaei, A.T., Gheshlaghi, B., Lu, J. and Lu, Y. Asymmetric flexural behavior from bamboo's functionally graded hierarchical structure: underlying mechanisms. *Acta Biomaterialia* (2015) **16**:178-186.

[6] Bahtiar, E.T., Nugroho, N. and Nurmadina. Structural grading of Gigantochloa apus bamboo based on its flexural properties. *Construction and Building Materials* (2017) **157**:1173-1189.

[7] Obataya, E., Kitin, P. and Yamauchi, H. Bending characteristics of bamboo (Phyllostachys pubescens) with respect to its fiber-foam composite structure. *Wood Sci Technol* (2007) **41**:385-400.

[8] Archila-Santos, H.F., Ansell, M.P. and Walker, P. Elastic properties of thermo-hydro-mechanically modified bamboo (*Guadua angustifolia* Kunth) measured in tension. *Key Engineering Materials* (2014) **600**:111–120.

[9] Ota, M. Studies on the properties of bamboo stem (part 9). On the relation between compressive strength parallel to grain and moisture content of bamboo splint. *Bulletin of Kyushu University of Forestry* (1953) **22**:87-108.

[10] Kilian, T. Shou-sugi-ban ancient method of charring wood. *Wood Design & Building* (2014) 42-44.

[11] Shao, Z.P., Fang, C.H. and Tian, G.L. Mode I interlaminar fracture property of moso bamboo (Phyllostachys pubescens). *Wood Sci Technol* (2009) **43**:527-536.

[12] Askarinejad, S., Kotowski, P., Youssefian, S. and Rahbar, N. Fracture and mixed-mode resistance curve behavior of bamboo. *Mechanics Research Communications* (2016) **78**:79-85.

[13] Wang, F., Shao, Z. and Wu, Y. Mode II interlaminar fracture properties of Moso bamboo. *Composites: Part B* (2013) **44**:242-247.

[14] Meyers, M.A. and Chawla, K.K. *Mechanical Behavior of Materials*. 2nd ed. UK: Cambridge University Press, (2009).

[15] Norimoto, M., Gril, J. and Rowell, R.M. Rheological properties of chemically modified wood: relationships between dimensional and creep stability. *Wood and Fiber Science* (1992) **24**:25-35.
[16] Tsubaki, T. and Nakano, T. Creep behavior of bamboo under various desorption conditions. *Holzforschung* (2010) **64**:489-493.
[17] Gottron, J., Harries, K.A. and Xu, Q. Creep behaviour of bamboo. *Construction and Building Materials* (2014) **66**:79-88.
[18] Kappel, R., Mattheck, C., Bethge, K. and Tesari, I. Bamboo as a composite structure and its mechanical failure behaviour. Collins, M.W., and Brebbia, C.A., (ed). *Design and Nature II*. UK: WIT Press (2004) 285-293.
[19] Huang, Y.S., Hsu, F.L., Lee, C.M. and Juang, J.Y. Failure mechanism of hollow tree trunks due to cross-sectional flattening. *R. Soc. Open Sci* (2017) **4**. (doi:10.1098/rsos.160972)
[20] Spatz, H.C. and Niklas, K.J. Modes of failure in tubular plant organs. *Am. J. Bot.* (2013) **100**:332-336.
[21] Brazier, L.G. On the flexure of thin cylindrical shells and other thin sections. *Proc. R. Soc. Lond. A* (1927) **116**:104-114.
[22] Jones, R.M. *Mechanics of Composite Materials*. 2nd ed. USA: Taylor & Francis, Inc, (1999) 55:120.

XIV International Conference on Computational Plasticity. Fundamentals and Applications
COMPLAS 2019
E. Oñate, D.R.J. Owen, D. Peric , M. Chiumenti, and Eduardo de Souza Neto (Eds)

ELABORATION AND STUDY OF THE THERMO-MECHANICAL PROPERTIES OF AN ALIGNED CNT - POLYPROPYLENE NANO-COMPOSITE BY TWIN-SCREW MIXER

M. SAHLI[1] AND T. BARRIÈRE[2]

[1] Femto-st Institute/Applied Mechanics Department
Chemin de l'épitaphe, 25000 Besançon, France
e-mail: mohamed.sahli@femto-st.fr

[2] Femto-st Institute/Applied Mechanics Department
Chemin de l'épitaphe, 25000 Besançon, France
email: thierry.barriere@femto-st.fr

Key words: Nano-composite material, Rheology, Microstructures, Multi-walled carbon nanotubes.

Abstract. This study presents first the fabrication of a nanocomposite material based on Multi-Walled Carbon Nanotubes, and on a thermoplastic polymer matrix. First, a twin-screw mixer had been employed for preparing polypropylene nanocomposites loaded at 0.1, 1, 2, and 5wt% of MWCNT. Second, a characterization of rheological behavior for polypropylene as well as polypropylene/multi-walled carbon nanotube mixtures, at three temperatures (180, 200, and 220 °C,) has been carried out using cone and plate rheometer. Then, its thermo-mechanical properties have been studied. The work demonstrates how the addition of functionalized CNTs to a polypropylene will allow it to act as thermal conductor rather than as insulator.

1 INTRODUCTION

Incorporation of nanofiller such as carbon nanofiber, carbon nanotube (CNTs) has been successfully used to improve the matrix dominated and interlaminar properties [1,2]. CNTs exhibit unique structural properties such as exceptionally high specific stiffness and specific strength. Further addition of CNTs to the conventional fiber reinforced polymer composites has its own challenges [3,4]. The main challenge is to uniformly disperse them in the polymer matrix in order to obtain high interfacial area through which stress can be transferred from the weak matrix to the strong nanotubes [5]. Effective stress transfer through the CNTs/polymer interface is the key to obtain superior mechanical properties in the CNTs modified laminated composites [6]. In fact, polymer composites containing conducting fillers such as carbon black, carbon fiber, and metal fiber have been extensively investigated for various applications such as structural reinforcement, electromagnetic interference shielding, electronic packaging, radar absorption, heating element construction and high-charge storage capacitors [7-9].

Many researchers are interested in incorporating carbon nanotubes (CNTs) into polymers,

ceramics and metals to improve their mechanical properties by taking advantages of the superior physical, chemical and electronic properties of CNTs [10-12]. However, because CNTs have high aspect ratios and easily tangle with each other due to high surface energy and strong intrinsic van der Waals force [13,14], their uniform dispersion in a matrix is crucial for the manufacturing of sound nano-composites. The originality of the present study is the assessment of structural performance of these nanocomposites with a range of CNTs loading at various elevated temperature environments.

2 MATERIALS AND EXPERIMENTAL METHODS

2.1 Materials

The polymer matrix used to elaborate the nano-composites was a semicrystalline thermoplastic polypropylene (PP-EP548N) produced by Sabic Company® with melt flow Index (MFI) = 11g/10min (230 °C/2.16 kg) and density = 0.892g/mm3 (see Table 1). Commercially isotactic polypropylene (PP-EP548N) were supplied Multi-walled carbon nanotubes (MWCNTs) - NC7000 were purchased from Nanocyl Company® (Belgium) and were produced with purity higher than 90% and diameter range of 15-30 nm with typical length of 1-10 µm.

Table 1: Material characteristics of Polypropylene

Material	Polypropylene (PP), P548N
Density [g/mm^3]	0.892
Transition temperature [°C]	-10
Melting temperature [°C]	155
Melt flow index (MFI) [g/10min]	[230°C/2.16kg]:11

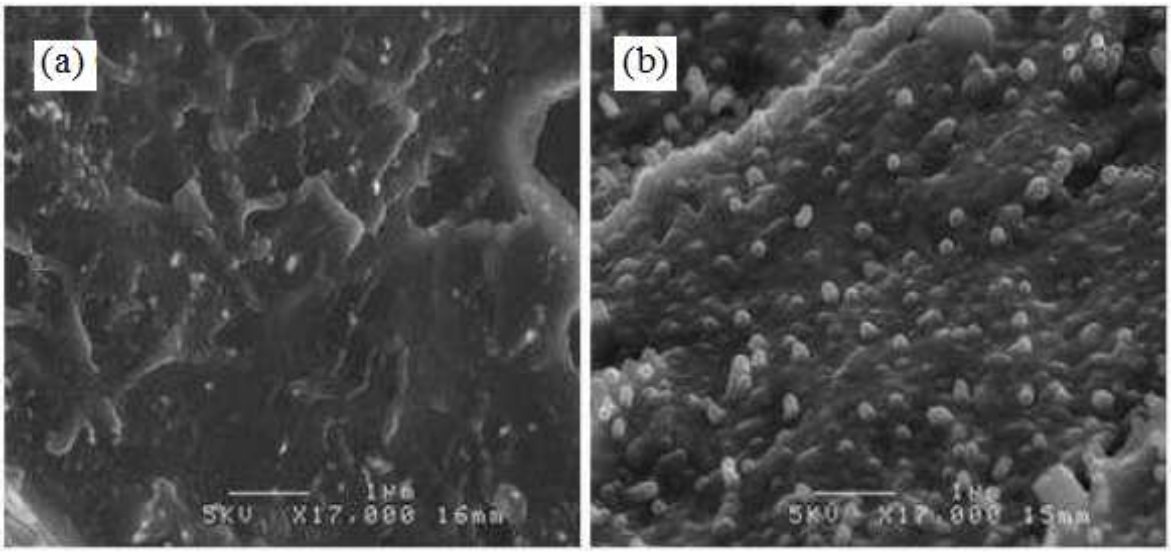


Figure 1: Dispersion of (a) 0.1%, (b) 0.5% MWCNT in nano-composite.

Figure 1 indicates the dispersion state of MWCNTs in the PP matrix of 0.1% and 5% nano-composites. The MWCNTs are mostly isolated from each other and uniformly distributed throughout the matrix of 0.1% MWCNT-composite whereas in 5% MWCNT-composites, local bunches of CNTs are found which form agglomerates as shown in Fig. 1b. The reduction of strength at higher MWCNT content can be attributed towards formation of these agglomerates, reducing the total CNTs/matrix interfacial area.

2.2 Nano-composites preparation

All Prior to the preparation of nano-composites, all of the materials were dried in an oven for 24 h at 80 °C to facilitate the dispersion of CNTs particles into the PP. Firstly PP was introduced in the a Brabender® mixer with a pair of rotor blades (see Fig.2); after the melting of the PP, CNTs were then carried out in. For the melt mixing process, the rotation speed and temperature of the mixing chamber were set at 30 rpm and 180 °C, respectively, and the blending continued for 30 min. After pelletizing, blend granules will be used in the injection process. In order to prepare tensile specimens for measurement of mechanical properties, the mixture PP loaded with the CNTs was injected into a die mould cavities.

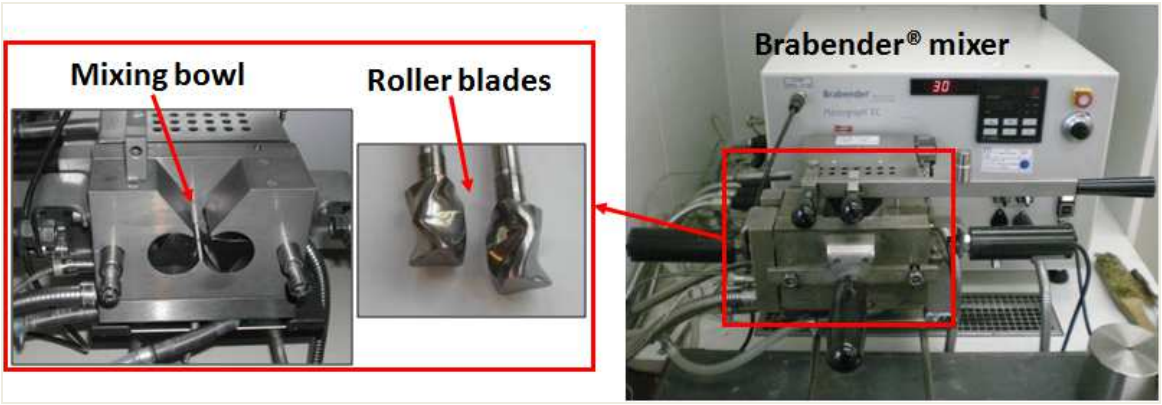


Figure 2: Photograph of Brabender® mixer and its internal structure.

2.3 Characterizations

The morphology of CNTs nano-particles and nano-composites were examined by scanning electron microscopy. The rheological analyses were carried out using rheometer HAAKE MARS III with a cone and plate geometry with the diameter of 35 mm and the cone angle of 2°. The test temperature is set from 180 to 220 °C beyond the melting temperature of polypropylene and below its degradation temperature. The shear rate has been chosen in a range from 10^{-1} to 10^{2} s^{-1}. Dynamic measurements of rheological properties were carried out using the HAAKE MARS III using parallel plate geometry (25 mm diameter and 1 mm gap). Frequencys weeps from 0.1 to 100 rad/s were performed. For rheological measurements, PP/CNTs samples were tested within the linear viscoelastic strain range. Thermo-gravimetric/differential thermal analysis (TG/DTA) of PP/CNTs nano-composite were carried out using a thermobalance Setaram® thermal analyzer from room temperature to 500 °C, at a rate of 10 °C/min in a continuous argon flow.

3 RESULTS AND DISCUSSION

In this paper, different loading ratio of the CNTs have been selected to elaborate the PP/CNTs nano-composite by melt mixing process. The curves in figure 3 shows the final mixing torque variation of the PP and PP/CNTs nano-composite (loading ratio from 0.1 to 5 wt.%), vs. mixing time. Uniform mixing is achieved when the torque reaches a steady state value. From the results, it reveals that:

- the addition of the CNTs can increase effectively the final mixing torque of the nano-composites which means the addition of CNTs decreases the fluidity of the nano-composite;
- increasing the CNTs content can increase the final mixing torque, when the CNTs content is below to 1wt.%, there is no evident difference comparing to the pure PP; when the CNTs content is beyond 1wt.%, an evident increase of the mixing torque for the nano-composite is observed.

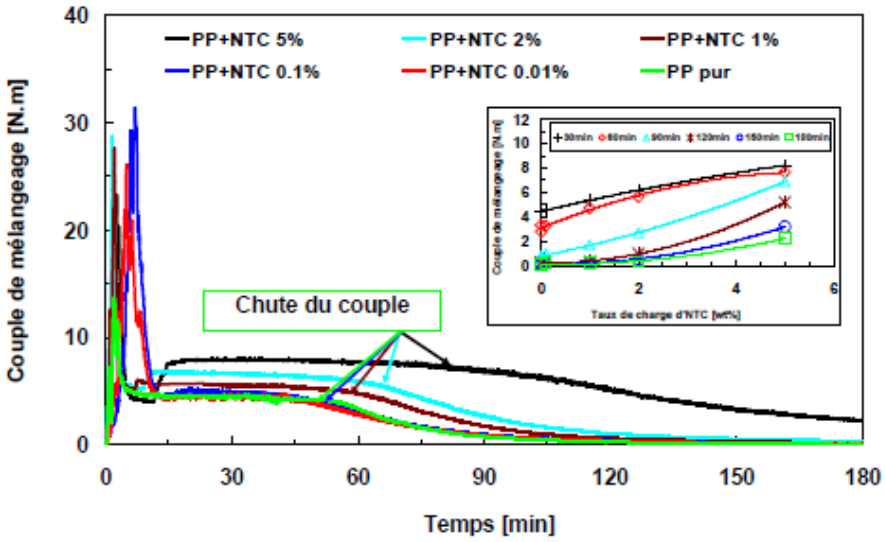


Figure 3: Mixing torque vs. time for PP and PP/CNTs nano-composites at 180°C during 30 min.

Figure 4 illustrates the influence of the CNTs loading ratio to the nano-composites shear viscosity tested at 220°C, the viscosity of composite increases clearly with a rise of the CNTs loading ratio from 0.1% to 1% (For the CNTs loading ratio of 10%, the viscosity is too high beyond the measurement range of the rheometer). Finally, the conclusion can be obtained that increasing the temperature and shear rate can decrease effectively the viscosity of CNTs/PP nano-composites and improve their capacity of filling the mould cavities, but increasing the CNTs loading ratio results in the rise of the nano-composites viscosity which is not conducive to the cavities filling.

Figure 5, it is shown that the storage modulus and loss modulus of the CNTs/PP nano-composites increases lightly with the increase in MWCNT up to 5 wt%. The results shown in Fig. 5 indicate that increasing CNTs concentration leads to a transition from convex to concave curves. Therefore, at sufficiently high concentrations the elastic modulus tends to level off as frequency goes to zero.

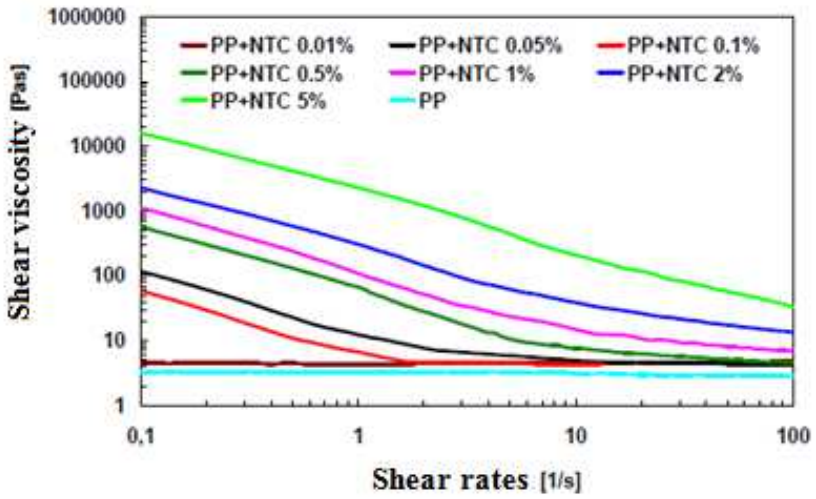


Figure 4: The shear viscosity of PP loaded respectively with 0.1 and 1wt% CNTs vs. shear rate at 220°C.

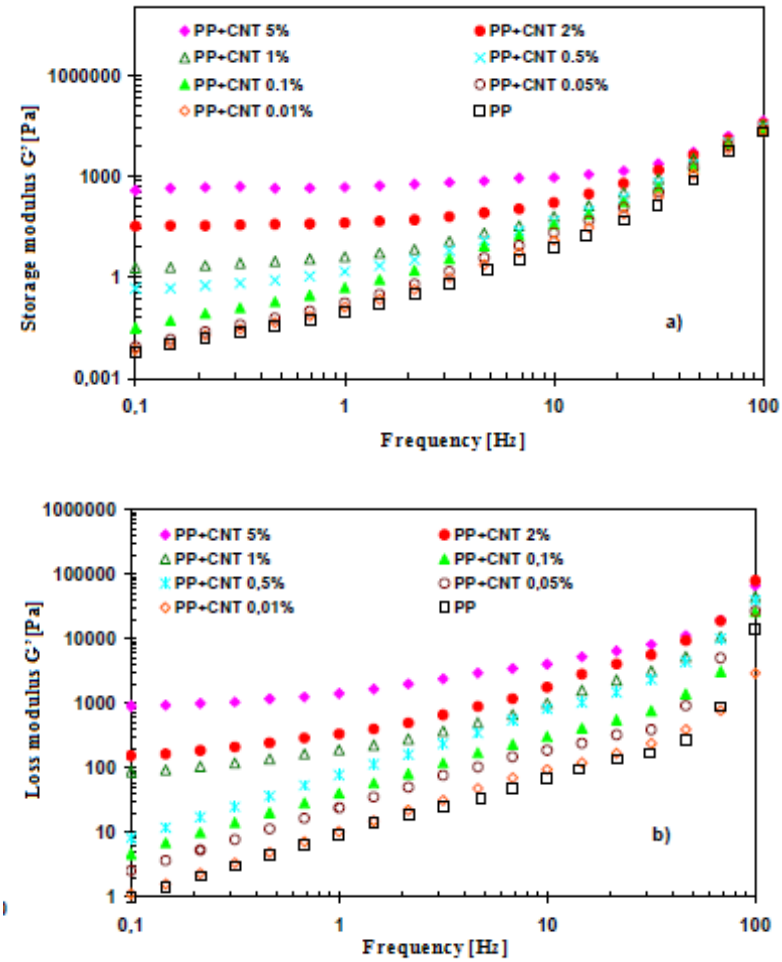


Figure 5: Variation of the viscoelastic modulus with frequency for the indicated compositions (180 °C).

Thermo-gravimetric analysis (TGA) was performed on nano-composites at all concentrations to obtain additional confirmation of both the CNTs content and the structure of the nano-composite, as well as to determine the effects of the CNTs on the thermal stability of the nano-composite. TGA was carried out under a argon atmosphere. The resulting curves are shown in Fig. 6a. In the case of nano-composite, an initial 98% weight loss at > 350 °C revealed the oxidation of amorphous carbon present in the sample and also attributed to the decomposition of PP and was degraded completely at 430 °C. This method can determine the actual CNTs content in the nano-composites. The degradation temperature of the nano-composites increased with CNTs content. A maximum increase of 35 °C was observed for the 5 wt.% nano-composite. This indicates also that the thermal stability of the PP nanoparticles was improved by the addition of CNTs. The incorporation of nano-particles CNTs on PP matrix resulted in an increase in crystallization temperature (Tc). In the case of pristine PP matrix, the Tc was observed at 95 °C and was shifted to 120 °C for the 5 wt.% nano-composite. Such an effect on the Tc obtained there are also observed on the glass transition (Tg) and melting temperatures (Tf).

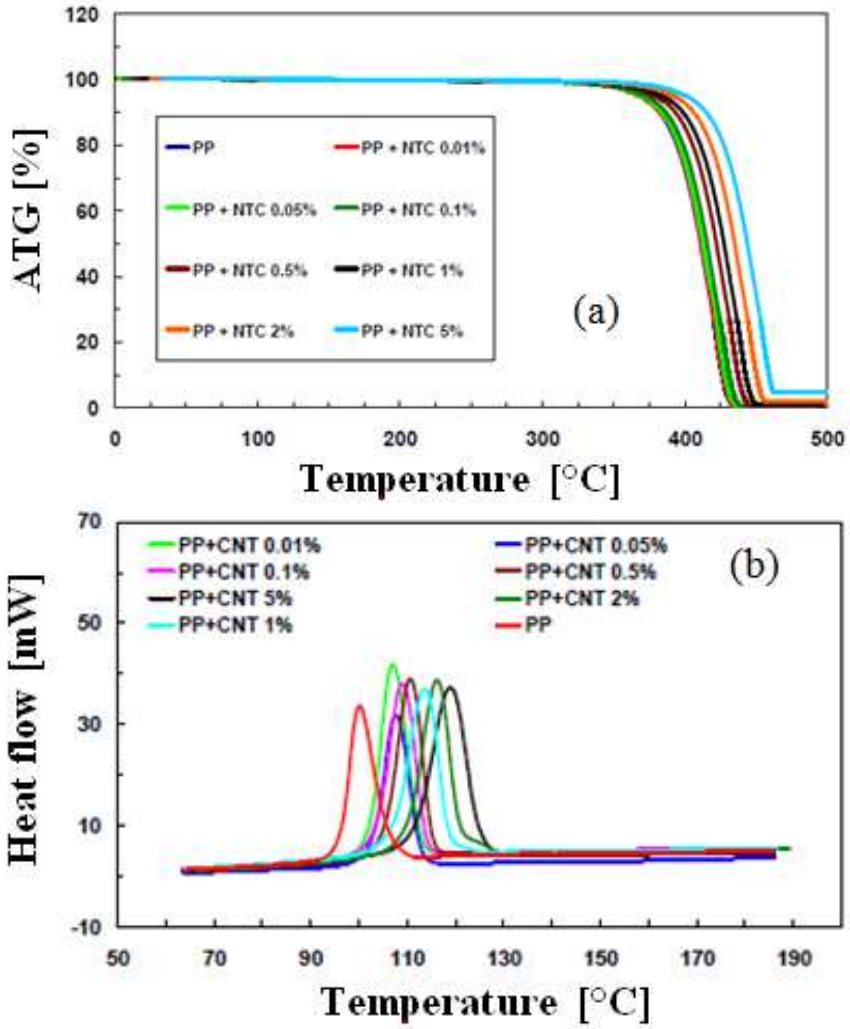


Figure 6: Thermal properties of the CNTs/PP nano-composite: (a) TGA and (b) DSC analysis.

The stress-strain plots for samples with CNTs loading at various in-situ temperatures are shown in Fig. 7a. The service temperature of these materials is limited in accordance with their melting temperature (Tf). Hence the maximum in-situ testing temperature was so chosen that it is under to the Tf of the nano-composites. The impact of various CNTs loading on nano-composites can be noticed from Fig. 7b. The properties obtained from these stress-strain plots are then reported in Table 2. Addition of 1% MWCNT into the nano-composites resulted in enhancement of both modulus and strength by 14.6% and 39.7% respectively when tested at room temperature as shown in Fig. 7b. This huge increment in strength might be attributed to the efficient stress transfer from the polymer matrix to the stiff MWCNT through the subtle S/polymer interface.

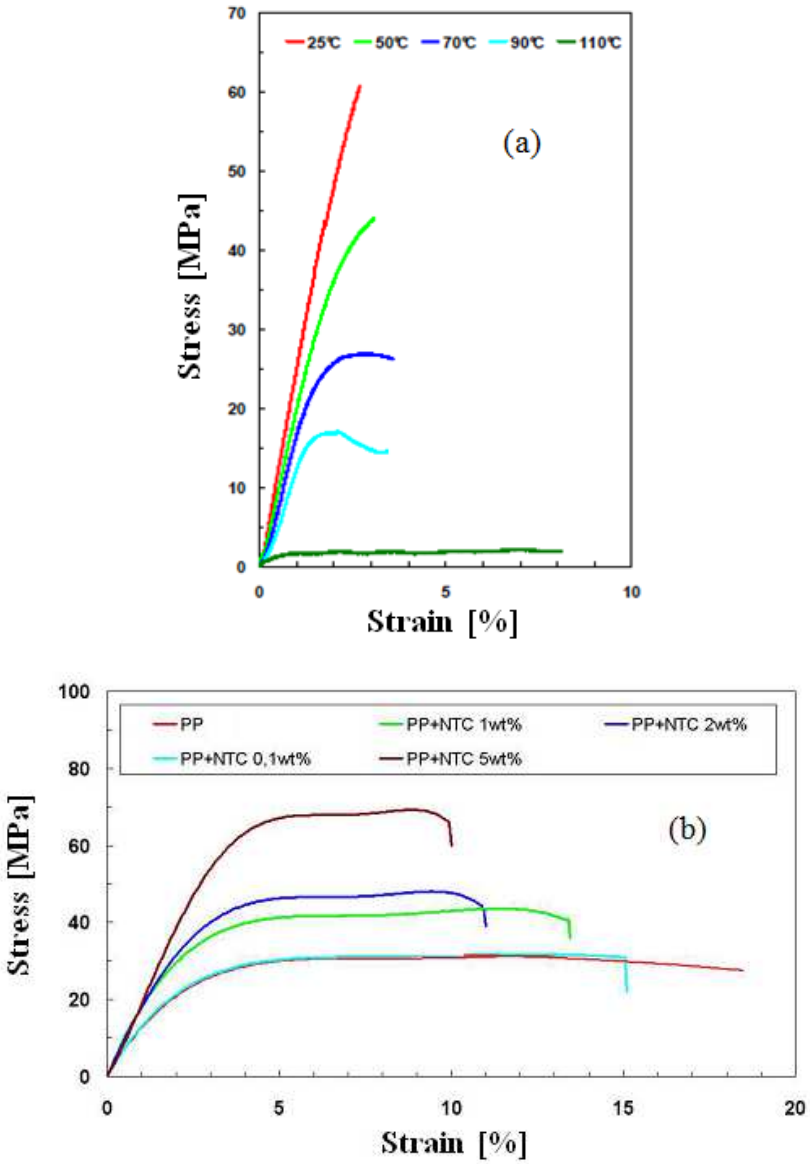


Figure 7: Stress-strain curves for nano-composites at: (a) diffirent temperatures and (b) room temperatures with various CNT contents.

Table 2: Properties of nano-composites with varying CNT content at room temperatures

CNT content (%)	Young Modulus [GPa]	Resistance a la traction [MPa]
0.0	1.37±0.02	31.06±0.02
0.1	1.43±0.03	31.37±0.03
1.0	1.57±0.05	43.36±0.04
2.0	1.63±0.04	47.53±0.02
5.0	1.89±0.03	68.90±0.02

6 CONCLUSIONS

Homogenous multi-wall carbon nanotube/polypropylene nano-composites have been fabricated using a twin-screw Brabender® mixer. Based on experimental investigations of impact behaviour of PP filled with multi-walled carbon nano-tubes (CNTs), the following conclusions can be drawn:

- From the results of the rheological properties of the PP/MWCNT nano-composites, the increase in the viscosity was observed, that may be due to the increase inhomogeneous dispersion of the MWCNT in the PP matrix. The rheological properties of these nano-composites blends were investigated under shear flows. Our small-amplitude dynamic shear rheological studies showed that both the complex viscosity increase monotonically with increasing MWNT content,

- Introduction of CNTs to the PP system can enhance the thermal stability of nano-composites due to an interaction between the outer walls of the CNTs and PP lattices. Moreover, the formation of a barrier of CNT inhibits mass transfer and provides thermal insulation to shield the underlying polymer from the heat source,

- Tensile test measurements show that the tensile strength and Young modulus increases dramatically with the nanotube loading, while the draw-down ratio (drawability) significantly decreases. The addition of MWNTs to PP improves the mechanical, thermal, and wear properties of an already low performance matrix, without harming important characteristics, such as thermal and chemical resistance.

REFERENCES

[1] Wang, B-C. Zhou, X. Ma, K-M. Fabrication and properties of CNTs/carbon fabric hybrid multiscale composites processed via resin transfer molding technique, *Compos Part B Eng* (2013) **46**:123-131.

[2] Fiedler, B. Gojny, FH. Wichmann, MHG. Nolte, MCM. Schulte, K. Fundamental aspects of nano-reinforced composites, *Compos Sci Technol* (2006) 66:3115-3125.

[3] Siddiqui, NA. Khan, SU. Ma, PC. Li, CY. Kim, J-K. Manufacturing and characterization of carbon fibre/epoxy composite prepregs containing carbon nanotubes, *Compos Part Appl Sci Manuf* (2011) **42**:1412-1420.

[4] Ma, P-C. Siddiqui, NA. Marom, G. Kim, J-K. Dispersion and functionalization of carbon nanotubes for polymer-based nanocomposites: a review, *Compos Part Appl Sci Manuf* (2010) **41**:1345-1367.
[5] Li, Q. Zaiser, M. Koutsos, V. Carbon nanotube/epoxy resin composites using a block copolymer as a dispersing agent, *Phys Status Solidi Appl Res* (2004) **201**:89-91.
[6] Ma, P-C. Zheng, Q-B. Mäder, E. Kim, J-K. Behavior of load transfer in functionalized carbon nanotube/epoxy nanocomposites, *Polymer* (2012) **53**:6081-6089.
[7] Al-Saleh, M. Sundararaj, U. Electromagnetic interference (EMI) shielding effectiveness of PP/PS polymer blends containing high structure carbon black, *Macromol Mater Eng* (2008) **293**:621-630
[8] Kim, MG. Moon, JB. Kim, CG. Effect of CNT functionalization on crack resistance of a carbon/epoxy composite at a cryogenic temperature, *Composites Part A* (2012) **43**:1620-6127.
[9] Theilmann, P. Chu, KM. Bandaru, PR. Asbeck, P. Park, SH. Optimisation of microwave absorption of carbon nanotube composites through use of carboxyl-epoxide functional group linkages, *Electron Lett* (2012) **48**:638-648.
[10] Curtin, WA. Sheldon, BW. CNT-reinforced ceramics and metals, *Mater Today* (2004) 7:44-53.
[11] Li, QQ. Rottmair, CA. Singer, RF. CNT reinforced light metal composites produced by melt stirring and by high pressure die casting, *Compos Sci Technol* (2010) 70:2242-2249.
[12] Neubauer, E. Kitzmantel, M. Hulman, M. Angerer, P. Potential and challenges of metal-matrix-composites reinforced with carbon nanofibers and carbon nanotubes, *Compos Sci Technol* (2010) **70**:2228-2236.
[13] Calvert, P. Nanotube composites-a recipe for strength. *Nature* (1999) **399**:210-221.
[14] Coleman, JN. Khan, U. YK. Gun'ko, Mechanical reinforcement of polymers using carbon nanotubes, *Adv Mater* (2006) **18**:689-706.

XV International Conference on Computational Plasticity. Fundamentals and Applications
COMPLAS 2019
E. Oñate, D.R.J. Owen, D. Peric, M. Chiumenti & Eduardo de Souza Neto (Eds)

THE ELASTOPLASTICITY BEHAVIOR OF WIRE IN INHOMOGENEOUS WOVEN METAL MESH

JIANLIANG ZHANG*, HIKARU MIYAKI* and ATSUSHI SAKUMA†

* Graduate School, Kyoto Institute of Technology
Matsugasaki, Sakyo-ku, Kyoto, 606-8585, Japan
e-mail: aeikziron@gmail.com, web page: http://www.fibro.kit.ac.jp/

† Division of Textile Science, Kyoto Institute of Technology
Matsugasaki, Sakyo-ku, Kyoto, 606-8585, Japan
e-mail: sakuma@kit.ac.jp, web page: http://www.fibro.kit.ac.jp/

Key words: Plain Woven Mesh, FEM, Constitutive Equation, Unit Cell, Elastoplasticity

Abstract. *This paper discusses the plastic behavior of wires in metal mesh for discussing the structure of woven warp and weft with their inhomogeneous and homogeneous by using finite element method (FEM). In the FEM, an isotropic plasticity is adopted as constitutive model of woven wire, but inhomogeneous between warp and weft is discussed to evaluate the mechanical characteristic of the mesh as an industrial products. Here, fundamental relation of power law hardening rule is adopted to represent the plasticity, but physical parameters of it will be controlled for the discussion of plasticity on mesh weaving. The inhomogeneous of mesh structure is one of key technology to control the product quality of metal mesh, and the mechanics of plasticity of metal mesh should be discussed to develop the product. In this report, the difference of material parameters and tension during weaving process is targeted on the discussion. Some conditions on the wires of warp and weft are examined in weaving process by FEM.*

1 INTRODUCTION

Woven mesh of warp and weft wires is one of simplest materials to realize controlled structure in industrial field. Its corresponding customer needs are also clear: neatly shaped. According to the experience summarized in industrial production from previously survey, a fact was known that a metal mesh manufactured by inhomogeneous weaving tends to have a more neat appearance than by homogenous weaving method. To explore its theoretical basis of this empirical conclusion, this paper measured the shape of a metal mesh sample[1]. For comparison, some material model were designed, include one elastic model, four bi-linear elastoplastic model and one power law elastoplastic model[2, 3]. And a unit-cell corner model[4, 5] of plain woven structure was build for FEM. Using these models, simulation was performed on both homogeneous and a inhomogeneous case in finite element method.

2 EXPERIMENTAL EVALUATION

2.1 Equipment and Condition

The exact shape of plain woven metal mesh was measured by using a microscope named VR-3100 which made by KEYENCE Corporation. The specification of SUS304 mesh sample is 1.5 mm in diameter and 12.7 mm in woven pitch, which sprayed in blue for reducing optical reflection as shown in Figure 1(a). The height data of mesh sample obtained by using VR-3100 is shown in Figure 1(b). Here some data-lost occurred at wires horizontal sides, but peak position is clear and this part of wire is targeted in evaluating of deformation.

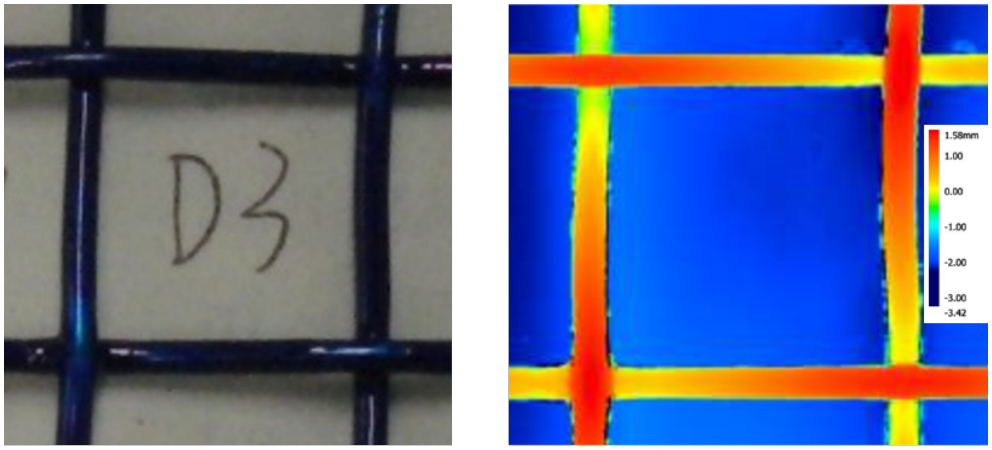


Figure 1: Scope view(a) and height observation(b)

2.2 Evaluation by Digitization

The measured shapes of mesh sample was output as STEP files, STEP files was processed by using processing method in FEM mesh generation. Here, LS-PrePost®is adopted in mesh generation using data from both vertical directions, result is shown in Figure 2.

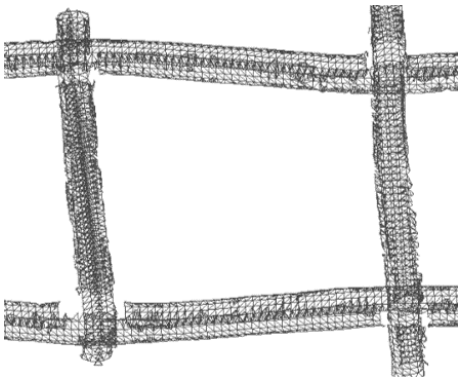


Figure 2: Digitization of experimental data

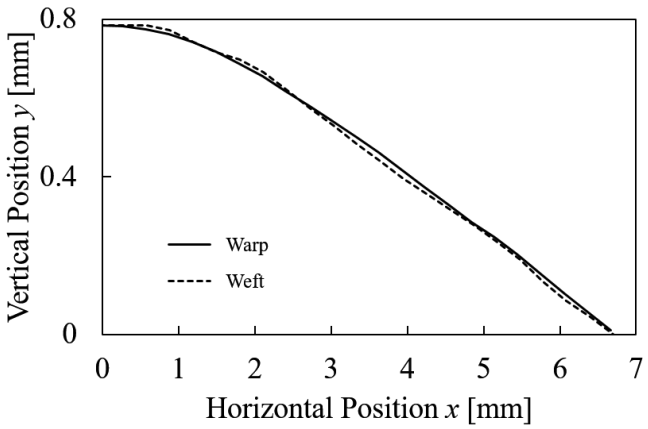


Figure 3: Profile comparison of deformed warp and weft

The digitized data of mesh shape is shown in Figure 3. Here, the deformed shape of warp and weft is duplicated to compare their situation. The difference of their deformation is not significant in this case.

3 NUMERICAL EVALUATION BY FEM

3.1 Geometry of plain woven structure

To detail the shape changes of the plain woven structure in analysis, a FEM model was performed by using corner model[4, 5] as shown in Figure 4(a). In an unit cell, wire diameter $\phi = 1.5$ mm and pitch length $p = 12.7$ mm. Diameter ϕ of warp and weft is considered as same.

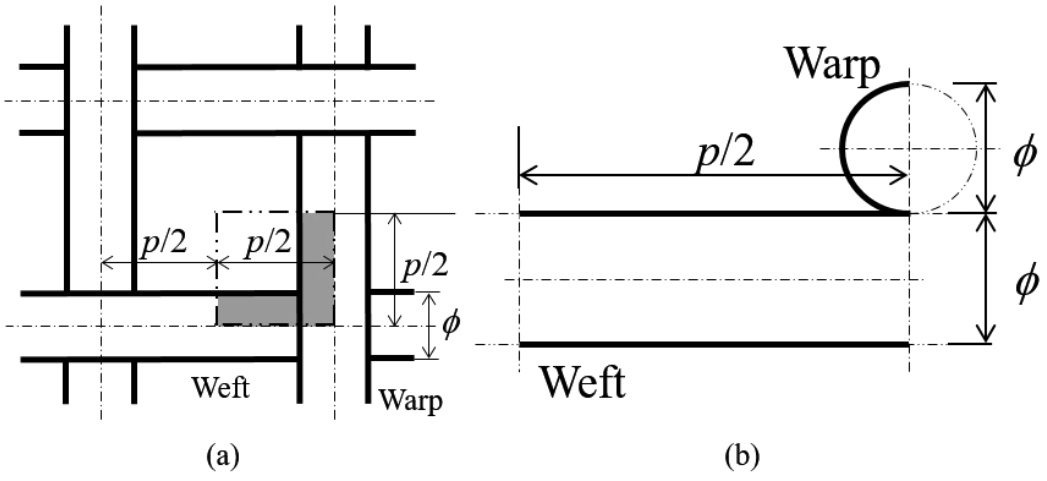


Figure 4: Unit-cell corner model of plain woven structure: top view(a) and sectional view(b)

The finite element is generated as shown in Figure 5. Here, it has 1296 elements, contain hexahedral and pentahedral elements, and its number of nodes is 1848.

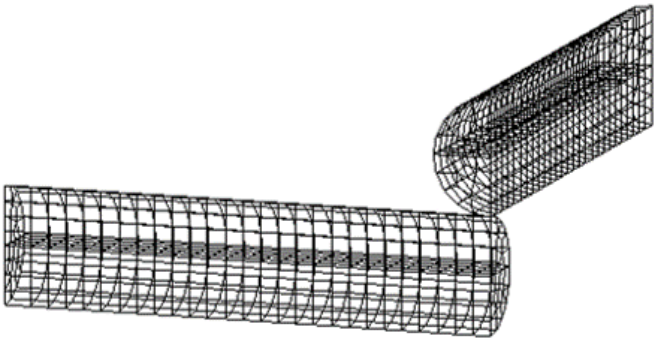


Figure 5: FE model for analysis

3.2 Representation of Plasticity by Bi-linear Constitutive Model

To obtain sufficient data for evaluate the differences in shapes of plain woven structure, some models of elastoplastic behavior are considered in this section.

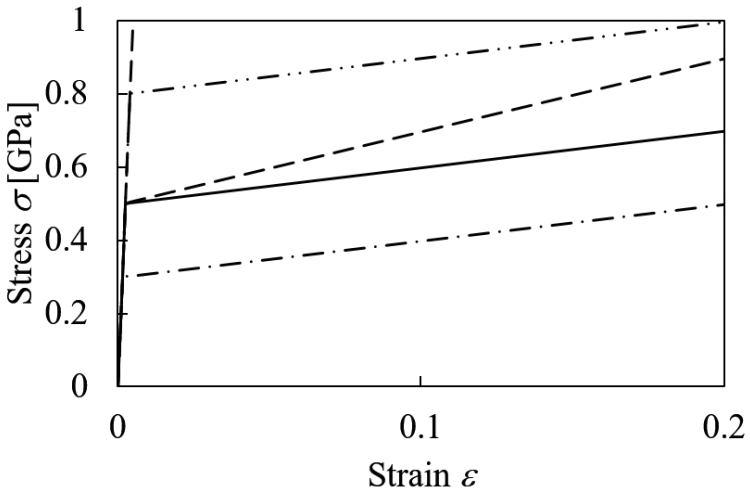


Figure 6: Modeled relationships of stress and strain

Figure 6 shows the stress-strain relationships of 1 elastic model, and 4 elastoplastic models which have same elastic modulus but different strain hardening modulus or yield stress. Three of them have same strain hardening modulus.

3.3 Results of Bi-Linear Material Model in Homogeneous Weaving

Four elastoplastic models and a elastic material model described in section 3.2 was applied in FE analysis. Its results are shown in Figure 7. Figure 7(a) shows a result of an elastoplastic model with a yield stress of 0.5 GPa and a tangent modulus of 1 GPa. In this result, the outermost region of the contact portion of warp and weft has a higher von Mises stress.

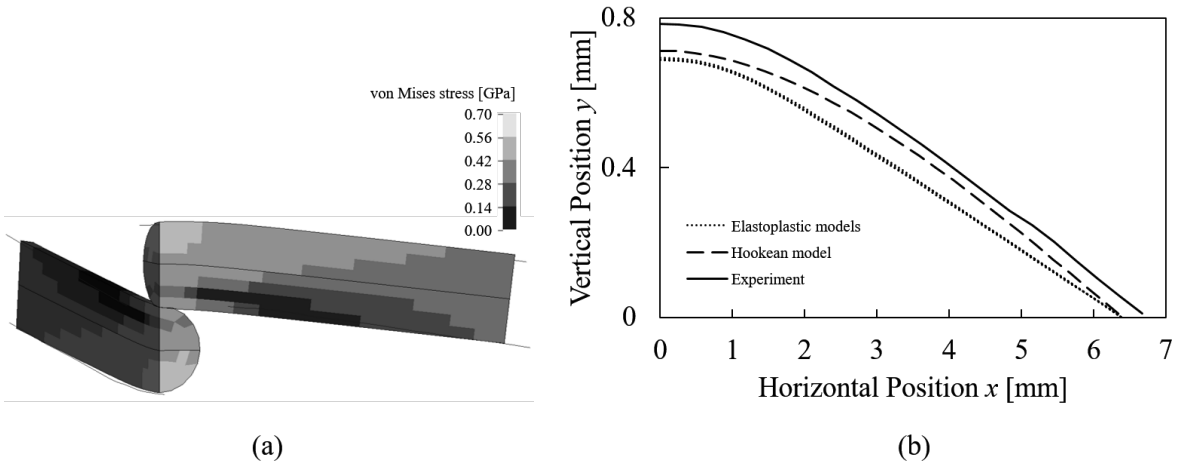


Figure 7: FEA results(a) and comparison of shapes(b)

Figure 7(b) shows the outermost shape of warp in FEM result with the sample data shown in section 2.2. This result shows that: 1) shapes between 4 elastoplastic models are almost same because their tangent modulus of plastic hardening is much smaller than elastic modulus; 2) deformed profile in Hookean model has strong curve unlike the others in Figure 7(b) because plasticity causes low bending moment in weaving process.

3.4 Representation of Plasticity by Power Law Material Model

Here, an elastoplastic model that transfer to plasticity phase with power law at its yield strength is discussed to evaluate the availability of hi-linear model. The stress-strain curve of power model is shown in Figure 8(a), and results of simulation is shown in Figure 8(b).

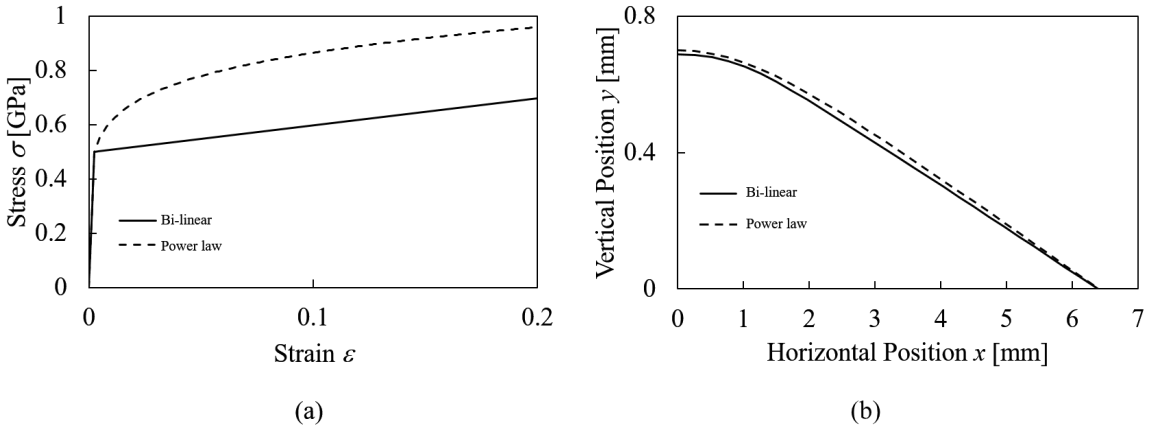


Figure 8: Modeled relationship by bi-linear and power rule (a) and its FEA results (b)

Figure 8(a) shows that power law model which tangent modulus of plastic hardening is decreasing continuously, and bi-linear model only have one tangent modulus of plastic

hardening. It caused their deformed difference as shown in Figure 8(b), and it is known that the slope of power law one's curve is monotonically decreasing continuously because the tangent modulus it associated is monotonically decreasing continuously.

3.5 FEA Results of Bi-Linear Material Model in In-Homogeneous Weaving

To evaluate inhomogeneous weaving with tension will bring what visible changes, the length of warp in corner models was reduced by 0.05mm, and then applied a forced displacement to the boundary at the pitch center, make the length of warp increase 0.05mm before weaving. Its FE result is shown in Figure 9.

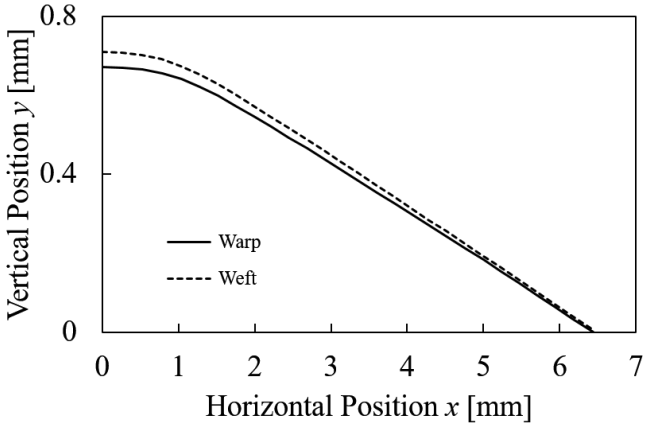


Figure 9: Comparison of Inhomogeneous Condition

The warp in Figure 9 shows less elongation in plain woven than weft. This result is considered that the application of tension caused hardening, make warp got less plastic strain on after woven procedure.

4 Conclusions

- On above, experimental measured result was simplified for comparison and further discussion.
- Results of several material FE models was compared to evaluate elastoplasticity represents in plain woven structure.
- Measured experimental data was compared with FE numerical analysis results for further research.

Acknowledgements

With grateful thanks, this research is supported by Mr.Okugami from OKUGAMI WIRE NETTING Co., Ltd.

REFERENCES

[1] Lee Y.H., Lee B.K., Jeon I. and Kang K.J. Wire-woven bulk Kagome truss cores. *Acta materialia*. (2007) **55**:6084-6094

[2] Liu W.K., Guo Y., Tang S., and Belytschko T. A Multiple-Quadrature Eight-node Hexahedral Finite Element for Large Deformation Elastoplastic Analysis. *Comput. Meths. Appl. Mech. Engrg.* (1998) **154**:69-132

[3] Miyaki H. and Sakuma A. Phantom-Element Technique for Periodic Deformation Analysis of Plain Fabrics using LS-DYNA. *Proc. ASME 2018 IMECE*. (2018) IMECE2018-87459, pp. V009T12A050

[4] Miyaki H. and Sakuma A. Mesoscopic-Structure Modeling of Woven Textile for Deformation Analysis evaluating Softness. *Proc. JSMS Annual Meetings*. (2018) **67**:323-324

[5] Miyaki H. and Sakuma A. Unit-cell Modelling for Multiscale Analysis of Plane Fabric Structure. *Proc. TMSJ Annual Meetings*. (2018) **71**:186-187

XV International Conference on Computational Plasticity. Fundamentals and Applications
COMPLAS 2019
E. Oñate, D.R.J. Owen, D. Peric, M. Chiumenti & Eduardo de Souza Neto (Eds)

MODELING ANISOTROPIC AND RATE-DEPENDENT PLASTICITY IN SHORT-FIBER REINFORCED THERMOPLASTICS

AHMAD AMIRI-RAD[*,†], LEONID V. PASTUKHOV[*,†], LEON E. GOVAERT[*] AND JOHANNES A. W. VAN DOMMELEN[*]

[*] Eindhoven University of Technology, P.O. Box 513, 5600 MB, Eindhoven, the Netherlands

[†] Dutch Polymer Institute (DPI), P.O. Box 902, 5600 AX, Eindhoven, the Netherlands

Key words: Short-Fiber Composites, Rate-Dependent Plasticity, Computational Mechanics, Constitutive Modeling

Abstract. In this study, an anisotropic viscoelastic-viscoplastic macro-mechanical model is presented for short-fiber reinforced thermoplastics (SFRT). In injection molding of SFRT, the fiber orientation is influenced by the flow velocity profile which varies throughout the mold. The flow-induced orientation in the microstructure leads to anisotropy in the mechanical response. In addition to the mechanical anisotropy, SFRTs show time dependent behavior because of the thermoplastic matrix. The developed model captures the effects of both material orientation and loading rate on the yield behavior. In this study, uniaxial tests are performed at different strain rates and material orientations with samples cut from injection molded plaques. The experimental results show that the effects of loading rate and material orientation on the yield are decoupled. The presented model takes advantage of this observation to simplify material characterization. An implicit integration scheme is used for the numerical implementation of the model as a UMAT in ABAQUS. Multiple relaxation times are used in order to capture the nonlinear pre-yield regime. An efficient method for obtaining the model parameters for different modes is proposed. Experimental results are used for validation of the model and a good agreement is observed for the prediction of viscoelastic and viscoplastic behavior.

1 INTRODUCTION

Injection-molded short-fiber composites are used for a variety of load-bearing structures, especially in the automotive industry. Their fast and cost-efficient production, light weight and better mechanical properties compared to unfilled plastics are among the reasons for their popularity. In the injection-molding process, the flow causes the fibers to be oriented, which leads to anisotropic mechanical properties. Also, because of the polymer matrix, the mechanical response is time-dependent. This paper aims to propose a reliable and accurate prediction tool for this complex mechanical response.

In this study, a macro-mechanical continuum-based constitutive model is presented for the components based on short-fiber reinforced thermoplastics. This model is built upon the framework of the Eindhoven Glassy Polymer (EGP) model [1–3] which has been successfully used for modeling time-dependent behavior of unfilled polymers. To describe the rate-dependent plasticity this model does not use a classic explicit yield surface and instead treats the polymer as a fluid with a very high initial viscosity which is exponentially reduced with increasing stress. This model belongs to a class of models which follow the pioneering work of Haward and Thackray [4]. Some other examples from this group are the BPA model [5–7] and OGR model [8–10].

The model presented here aims to capture the anisotropic viscoelastic-viscoplastic response of short-fiber composites. To model the rate-dependent and anisotropic yield behavior the associated flow rule proposed by van Erp et al [11] is incorporated into the framework of EGP. This flow rule uses Hill's anisotropic effective stress along with an Eyring type equation. Also, modifications to the EGP model is made to capture the anisotropy in the viscoelastic response. The model is developed based on the observation that the effects of orientation and loading rate on yield stress are factorizable. Experimental results demonstrating this behavior are presented in the following sections.

In the next sections, first, the experimental observations and the developed constitutive model are presented. Next, numerical implementation and material characterization are discussed. In the end, simulations are performed to investigate the performance of the model.

2 CONSTITUTIVE MODEL

The flow-induced fiber orientation causes anisotropy of the mechanical response of injection-molded short-fiber composites. To investigate the dependence of the elastic and yield behavior on the material orientation and strain rate, uniaxial tests at various constant strain rates are performed on specimens cut from injection molded plaques. The material used in this study is SABIC Lexan® 3412R PC (20 wt% short E-glass fiber-reinforced polycarbonate) from SABIC Innovative Plastics, the Netherlands. Figure 1 (a) shows measured values for yield stress at different strain rates and orientations in a double log plot. Angle ϕ shows the angle with respect to the main mold flow direction at which, the specimens are cut. In Figure 1 (b) stress-strain curves for the strain rate of 10^{-4} s^{-1} is shown. As can be seen in these figures, the mechanical response is dependent on the specimen orientation and loading rate. In the double log plot shown in Figure 1 (a), the curves for different angles have the same slope and only a vertical shift is observed as the orientation is changed. This shows the effect of material orientation and strain-rate on the yield behavior are factorizable. van Erp et al. [11] showed their proposed associated flow rule can capture this property. This makes the characterization process simpler since the effects of orientation and loading rate can be taken apart.

In the EGP model, total stress $\boldsymbol{\sigma}$ consists of two components acting in parallel. The components are called driving stress $\boldsymbol{\sigma}_s$ which is the dominant contribution in the pre-yield regime, and the hardening stress $\boldsymbol{\sigma}_r$ which is more important in the post-yield behavior. The mechanical analog of the model is shown in Figure 2. The hardening stress comes

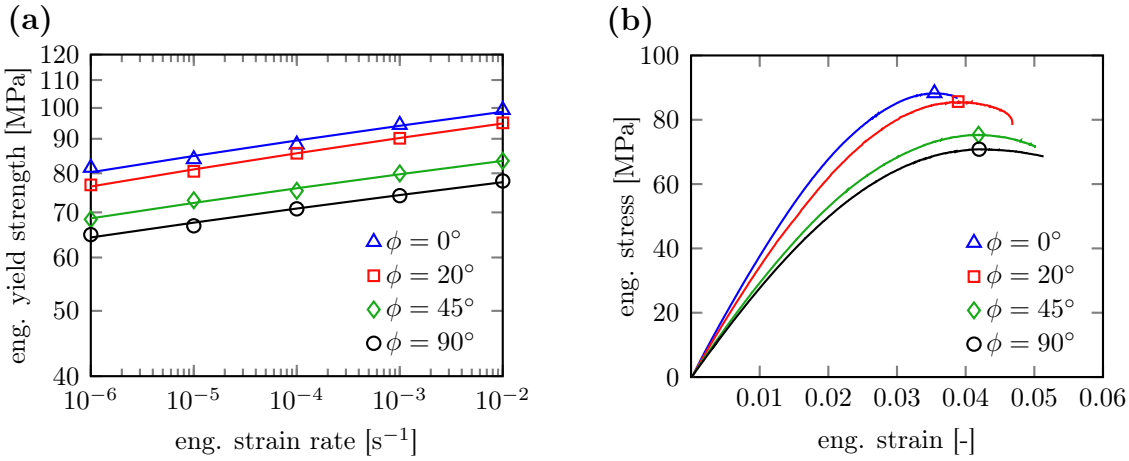


Figure 1: (a) Measured yield stress values at different material orientations and strain rates for polycarbonate with 20 wt% glass fiber; solid lines are guide-to-the-eye (b) stress-strain curves for uniaxial tension tests on polycarbonate with 20 wt% glass fiber at a constant strain rate of 10^{-4} s^{-1} for different material orientations.

from the spring with the modulus G_r and the driving stress is the sum of stress values from all the Maxwell branches. The use of multiple Maxwell branches helps modeling of the nonlinear and rate-dependent pre-yield regime. The total stress is written as:

$$\boldsymbol{\sigma} = \boldsymbol{\sigma}_r + \sum_{i=1}^{n} \boldsymbol{\sigma}_{s,i}, \tag{1}$$

where n is the number of Maxwell elements, $\boldsymbol{\sigma}_{s,i}$ is driving stress component from the ith Maxwell branch and $\boldsymbol{\sigma}_r$ is the hardening stress. The hardening stress is not utilized in the current study since samples fail at relatively low plastic strains. To model the elastic anisotropy, linear orthotropic springs are used in each Maxwell element. To calculate stress in each Maxwell branch, first, a second Piola-Kirchhoff type stress is calculated in the intermediate configuration according to:

$$\hat{\boldsymbol{S}}_{s,i} = {}^4\hat{\boldsymbol{C}}_i : \hat{\boldsymbol{E}}_{e,i}, \tag{2}$$

where $\hat{\boldsymbol{E}}_{e,i}$ shows the Green-Lagrange strain tensor, and ${}^4\hat{\boldsymbol{C}}_i$ represents the 4th order orthotropic elastic stiffness tensor. After the stress is calculated, it is pushed back to the current configuration and Cauchy stress is obtained. It should be noted that, the deformation gradient in each element $\boldsymbol{F}_i$, is decomposed multiplicatively into elastic and plastic components, where first, a rotation-free plastic deformation $\boldsymbol{F}_{p,i}$ brings the material to an intermediate stress-free configuration and then the elastic deformation $\boldsymbol{F}_{e,i}$ is applied and the material comes to its current configuration.

The plastic rate of deformation is defined in the intermediate configuration as follows:

$$\hat{\boldsymbol{D}}_{p,i} = \mathrm{sym}(\dot{\boldsymbol{F}}_{p,i} \cdot \boldsymbol{F}_{p,i}^{-1}). \tag{3}$$

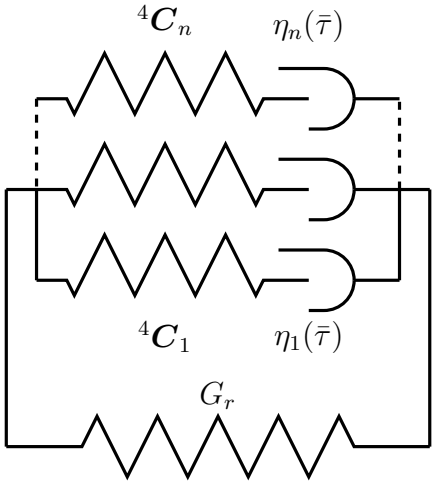


Figure 2: Mechanical analog of the constitutive model consisting of multiple Maxwell elements.

This rate for ith Maxwell element is found through the associated flow rule proposed by van Erp et al. [11]:

$$\hat{\boldsymbol{D}}_{p,i} = \dot{\bar{\gamma}}_{p,i}\hat{\boldsymbol{N}}_i, \tag{4}$$

$$\hat{\boldsymbol{N}}_i = \frac{\partial \bar{\tau}_i}{\partial \hat{\boldsymbol{S}}_{s,i}}, \tag{5}$$

where $\bar{\tau}_i$ is calculated from Hill's effective stress [13] and $\dot{\bar{\gamma}}_{p,i}$ is the equivalent rate of plastic deformation. An Eyring type flow equation [12] is used to find this rate:

$$\dot{\bar{\gamma}}_{p,i} = \frac{\bar{\tau}_i}{\eta_i}, \tag{6}$$

where η_i is the viscosity and is obtained as follows:

$$\eta_i = \eta_{0,i} a(\bar{\tau}), \tag{7}$$

where $\eta_{0,i}$ is the zero shear viscosity, which is modified with the stress shift factor $a(\bar{\tau})$, defined as:

$$a(\bar{\tau}) = \frac{\bar{\tau}/\tau_0}{\sinh(\bar{\tau}/\tau_0)}, \tag{8}$$

where τ_0 is called characteristic stress and $\dot{\gamma}_0$ is the rate constant. It should be noted that the same shift factor is applied to all the branches and the equivalent stress $\bar{\tau}$ in the above equation is calculated from the total driving stress $\boldsymbol{\sigma}_s$ using the Hill's effective stress [13].

For the numerical implementation of the presented model, an implicit scheme is applied. For brevity, the index i, for the ith mode, is eliminated in the following equations. First,

an initial guess is made for the plastic right Cauchy-Green deformation tensor $\boldsymbol{C}_{p_{n+1}}$. Using this value, the plastic right stretch tensor $\boldsymbol{U}_{p_{n+1}}$ is calculated at the end of the time step at t_{n+1}:

$$\boldsymbol{U}_{p_{n+1}} = \sqrt{\boldsymbol{C}_{p_{n+1}}}. \tag{9}$$

Then, the elastic deformation gradient tensor $\boldsymbol{F}_{e_{n+1}}$ is obtained:

$$\boldsymbol{F}_{e_{n+1}} = \boldsymbol{F}_{n+1} \cdot \boldsymbol{U}_{p_{n+1}}^{-1}. \tag{10}$$

Using the elastic deformation gradient tensor $\boldsymbol{F}_{e_{n+1}}$ the driving stress tensor can be calculated from Equation (2). To obtain the stress shift factor a, the equivalent stress $\bar{\tau}_{n+1}$ is obtained from its value at t_n using forward Euler explicit integration. This facilitates the integration process since the stress tensor in each mode can be calculated independent of the other modes at each step:

$$\bar{\tau}_{n+1} = \bar{\tau}_n + \dot{\bar{\tau}}_n \Delta t. \tag{11}$$

After calculating the stress shift factor from Equation (8), the plastic rate of deformation $\hat{\boldsymbol{D}}_{p_{n+1}}$ can be obtained using Equations (4) to (8). In the next step, rate of the plastic right Cauchy-Green deformation tensor $\dot{\boldsymbol{C}}_{p_{n+1}}$ is found as follows:

$$\dot{\boldsymbol{C}}_{p_{n+1}} = 2\boldsymbol{U}_{p_{n+1}} \cdot \hat{\boldsymbol{D}}_{p_{n+1}} \cdot \boldsymbol{U}_{p_{n+1}}. \tag{12}$$

The plastic right Cauchy-Green deformation tensor at the time t_{n+1} is then found according to:

$$\boldsymbol{C}_{p_{n+1}} = \boldsymbol{C}_{p_n} + \Delta t \dot{\boldsymbol{C}}_{p_{n+1}}. \tag{13}$$

This set of equations is solved with the Newton-Raphson scheme. In each iteration of the Newton-Raphson scheme, an initial estimate will be chosen for $\boldsymbol{C}_{p_{n+1}}$ and the residual is obtained by finding the difference between this initial guess and the value calculated from Equation (13). Using the presented implicit integration scheme, the model is implemented in the finite element package ABAQUS as a user material subroutine UMAT.

3 CHARACTERIZATION

Obtaining the input parameters for the proposed constitutive model is discussed in this section. As was explained in the previous section, to obtain the plastic rate of deformation tensor $\hat{\boldsymbol{D}}_p$, Hill's effective stress and an Eyring flow equation is used. One of the kinetics parameters that need to be determined is the characteristic stress τ_0, which determines the slope of yield stress vs. logarithm of strain rate [3]. Because the effects of the loading rate and material orientation are factorizable, this value is the same for all the orientations. Figure 3 (a), shows yield stress vs. logarithm of strain rate for orientation of $\phi = 90°$. By fitting the Eyring equation (Equation (6)) to this data, the value for τ_0 is obtained (Table 1). Plastic anisotropy parameters such as R_{11} and R_{12} are required for calculation of Hill's

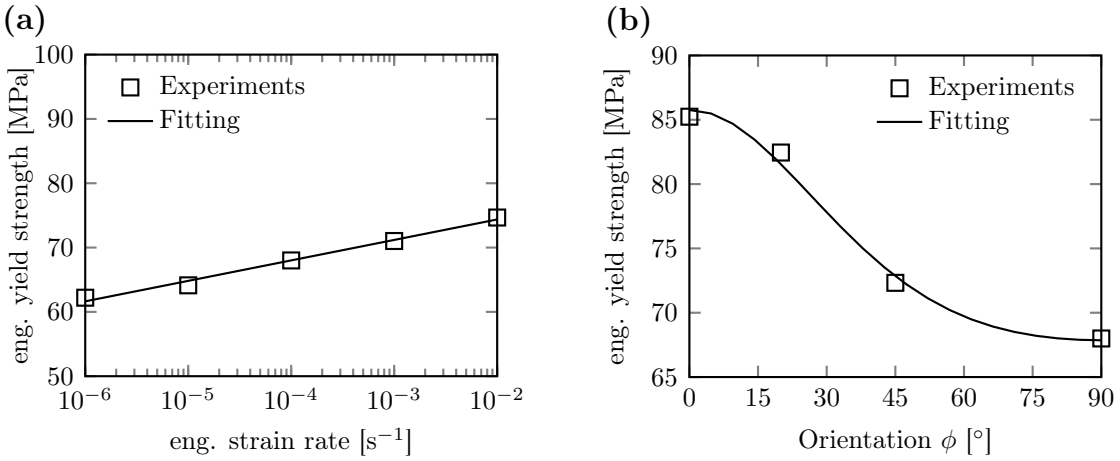


Figure 3: (a) Measured value for yield strength at (a) different rates for the reference orientation of $\phi = 90°$ and at (b) different orientations at a strain rate of 10^{-4} s^{-1}.

Table 1: Model parameters.

characteristic stress	Hill parameters		
τ_0 [MPa]	R_{11}	R_{22}	R_{12}
0.8	1.26	1	1.1

effective stress [11]. The parameter R_{11}, shows the ratio of yield in 1 direction, which here is taken as the main direction of mold flow ($\phi = 0°$) which has the most amount of fiber alignment, to yield in the reference direction. The reference yield direction is chosen as the direction perpendicular to the main mold flow direction ($\phi = 90°$), which has the least amount of fiber alignment, hence $R_{22} = 1$. The value for R_{12} shows, the ratio of shear stress in 12 direction to the reference shear stress. Because of the factorizable behavior shown in the previous section, the values for R_{11}, R_{22} and R_{12} are independent of the strain rate. In Figure 3 (b), Hill function is fitted to yield strength values measured for different orientations at strain rate of 10^{-4} s^{-1}. The obtained values for different Hill parameters are shown in Table 1.

For obtaining the moduli and viscosity for each mode (Figure 2), a procedure similar to [14] is followed. The procedure proposed in [14] is for the isotropic case. The method is extended to the orthotropic response, by first finding the moduli in a reference direction by the same procedure proposed in [14] and then, assuming the same distribution of the elastic parameters between different modes as the reference direction. Here, the direction $\phi = 90°$ is chosen as the reference direction and therefore E_{22} is found for different modes. The obtained values for E_{22} and also viscosities and relaxation times are shown in Table 2. Total values for different elastic parameters are also found from the stress-strain curves for different orientations and shown in Table 3. Sum of E_{22} values for different modes is

Table 2: Normal relaxation times, moduli and zero shear viscosities, fitted using using measurements at $\phi = 90^\circ$ and $\dot{\varepsilon} = 10^{-4}$ s^{-1}.

Mode	$\lambda_i^{norm.}$[s]	$E_{22,i}$[MPa]	$\eta_{0,i}$[MPa s]
1	2.07×10^{22}	1659	1.14×10^{25}
2	1.81×10^{21}	164	9.91×10^{22}
3	2.07×10^{20}	136	9.39×10^{21}
4	2.37×10^{19}	118	9.36×10^{20}
5	2.71×10^{18}	93	8.40×10^{19}
6	3.10×10^{17}	83	8.61×10^{18}
7	3.54×10^{16}	71	8.43×10^{17}
8	4.05×10^{15}	65	8.76×10^{16}
9	4.63×10^{14}	56	8.65×10^{15}
10	5.29×10^{13}	57	9.99×10^{14}
11	6.04×10^{12}	49	9.81×10^{13}
12	6.91×10^{11}	47	1.09×10^{13}
13	7.90×10^{10}	42	1.10×10^{12}
14	9.03×10^{9}	43	1.30×10^{11}
15	1.03×10^{9}	37	1.27×10^{10}
16	1.18×10^{8}	36	1.41×10^{9}
17	1.35×10^{7}	36	1.62×10^{8}
18	1.54×10^{6}	27	1.40×10^{7}
19	1.76×10^{5}	39	2.31×10^{6}
20	2.01×10^{4}	28	1.86×10^{5}
21	2.30×10^{3}	25	1.89×10^{4}
22	2.63×10^{2}	44	3.84×10^{3}
23	3.01×10^{1}	59	5.91×10^{2}

Table 3: Elastic parameters of the model.

E_{11} [MPa]	E_{22} [MPa]	G_{12} [MPa]	$\nu_{12} = \nu_{23}$
4181	2988	1184	0.26

approximately equal to the total E_{22} value shown in Table 3. A dimensionless vector m can be found according to:

$$\begin{aligned} E_{22} &= \sum_{i=1}^{n} E_{22,i} = \sum_{i=1}^{n} m_i E_{22}, \\ \sum_{i=1}^{n} m_i &= 1. \end{aligned} \tag{14}$$

Then using the assumption of the same distribution of elastic properties, one can write:

$$^4\boldsymbol{C}_i = m_i \, ^4\boldsymbol{C}. \tag{15}$$

It should be noted that values of Poisson ratio are assumed to be the same for all the modes.

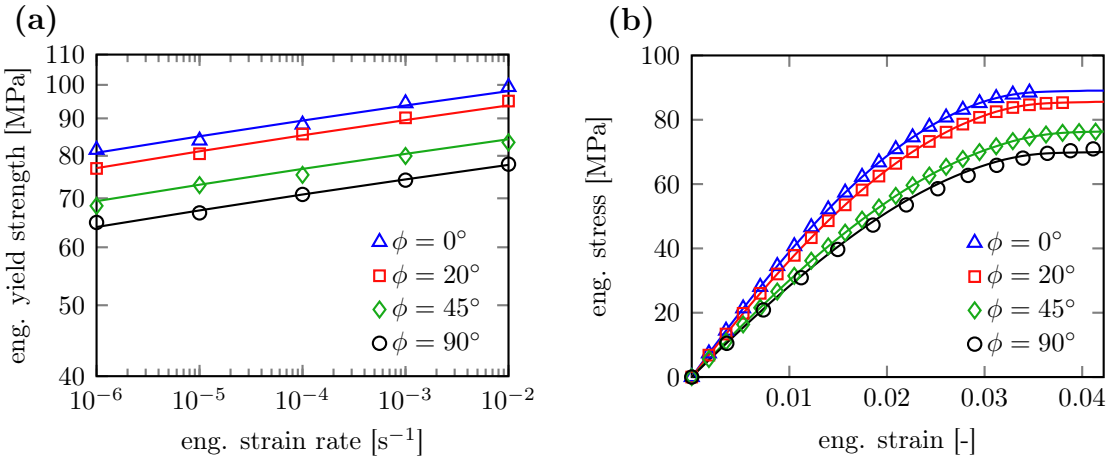


Figure 4: Model predictions (solid lines) and test results (markers) for (a) yield strength at various material orientations and strain rates and (b) stress-strain curves at different material orientations at a strain rate of $\dot{\varepsilon} = 10^{-4}$ s^{-1}.

4 RESULTS AND DISCUSSION

The presented constitutive model is implemented as an ABAQUS user material subroutine using the implicit scheme presented in section 2. After finding the material parameters following the procedure presented in the previous section, uniaxial tension tests are simulated in ABAQUS. As was discussed in the previous section, uniaxial test results at $\phi = 90°$ for different strain rates and also results at a strain rate of 10^{-4} s^{-1} for different orientations were used to find the model parameters. Values for yield stress for other orientations and strain rates are obtained from ABAQUS simulations and are compared to the experimental measurements in Figure 4 (a). In Figure 4 (b), stress-strain curves from ABAQUS simulations are compared with the test results. As can be seen in Figure 4, there is a good match between the model predictions and experimental data for yield strength, and with the use of a spectrum of relaxation times, the model is able to capture the nonlinear pre-yield response with good accuracy.

Figure 5 (a) shows the results for creep simulations. Applied stress is plotted vs. time-to-failure and model predictions (solid lines) are compared with the experimental data (markers). Figure 5 (b) shows strain evolution in time for different stress values from finite element simulations. The failure is considered as the point where plastic localization happens and a very high strain rate is observed. Failure points are shown with the markers in this figure.

The comparison of the model predictions and the experiments shows the capabilities of the model in predicting both the yield and pre-yield behavior. The rate-dependence and anisotropic response are modeled with good accuracy. The factorizable dependence of the yield stress on loading rate and material orientation is also captured.

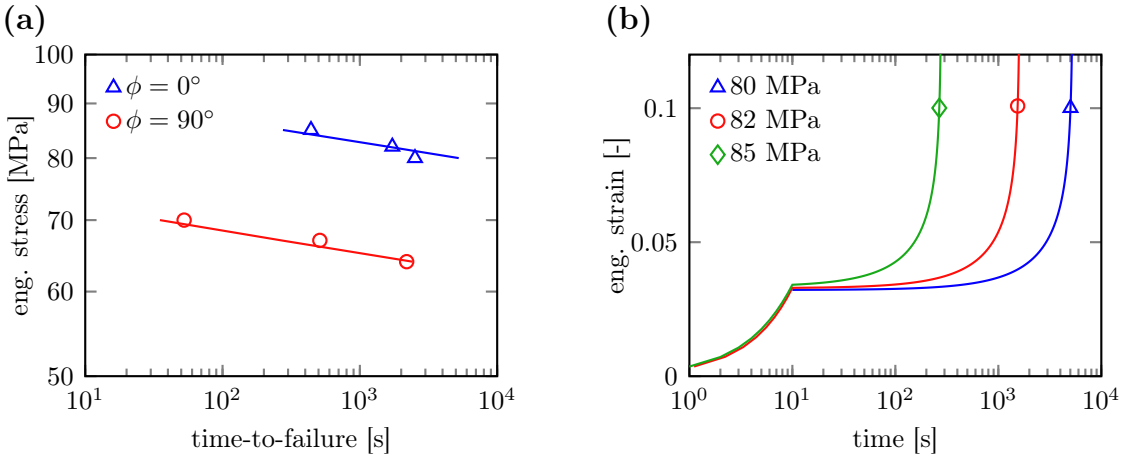


Figure 5: (a) Comparison of model predictions (solid lines) and experimental measurements (markers) for time-to-failure at different stress levels; (b) evolution of engineering strain with time in creep simulations for $\phi = 0°$ with different stress values (markers indicate the failure points).

5 CONCLUSIONS

In this paper, an anisotropic viscoelastic-viscoplastic macro-mechanical model was proposed for short-fiber reinforced thermoplastics. Results for uniaxial tension tests at different strain rates and orientations were presented and it was shown that the effect of strain rate and material orientation on the yield are factorizable. Hill's effective stress and an Eyring type flow equation were used to model the rate-dependent and anisotropic yield behavior. The nonlinear, anisotropic and rate-dependent pre-yield regime was modeled with application of a spectrum of relaxation times and orthotropic springs in each Maxwell element. An implicit scheme was presented for the integration of the constitutive model. It was shown that by use of the factorizability feature, the effects of strain rate and orientation on the yield can be taken apart in the characterization process. An effective method for finding moduli and relaxation times for different modes was also presented. The model predictions for constant strain rate and creep tests were compared with experiments and it was shown that a good agreement exists between the results.

REFERENCES

[1] L.E. Govaert, P.H.M. Timmermans, and W.A.M. Brekelmans. The influence of intrinsic strain softening on strain localization in polycarbonate: modeling and experimental validation. *Journal of Engineering Materials and Technology*, 122(2):177–185, 2000.

[2] T.A. Tervoort, E.T.J. Klompen, and L.E. Govaert. A multi-mode approach to finite, three-dimensional, nonlinear viscoelastic behavior of polymer glasses. *Journal of Rheology*, 40(5):779–797, 1996.

[3] E.T.J. Klompen, T.A.P. Engels, L.E. Govaert, and H.E.H. Meijer. Modeling of the postyield response of glassy polymers: influence of thermomechanical history. *Macromolecules*, 38(16):6997–7008, 2005.

[4] R.N. Haward and G. Thackray. The use of a mathematical model to describe isothermal stress-strain curves in glassy thermoplastics. In *Proc. R. Soc. Lond. A*, volume 302, pages 453–472. The Royal Society, 1968.

[5] M.C. Boyce, D.M. Parks, and A.S. Argon. Large inelastic deformation of glassy polymers. part i: rate dependent constitutive model. *Mechanics of Materials*, 7(1):15–33, 1988.

[6] E.M. Arruda and M.C. Boyce. Evolution of plastic anisotropy in amorphous polymers during finite straining. *International Journal of Plasticity*, 9(6):697–720, 1993.

[7] O.A. Hasan, M.C. Boyce, X.S. Li, and S. Berko. An investigation of the yield and postyield behavior and corresponding structure of poly (methyl methacrylate). *Journal of polymer science part B: polymer physics*, 31(2):185–197, 1993.

[8] C.P. Buckley and D.C. Jones. Glass-rubber constitutive model for amorphous polymers near the glass transition. *Polymer*, 36(17):3301–3312, 1995.

[9] C.P. Buckley, P.J. Dooling, J. Harding, and C. Ruiz. Deformation of thermosetting resins at impact rates of strain. part 2: constitutive model with rejuvenation. *Journal of the Mechanics and Physics of Solids*, 52(10):2355–2377, 2004.

[10] J.J. Wu and C.P. Buckley. Plastic deformation of glassy polystyrene: a unified model of yield and the role of chain length. *Journal of Polymer Science Part B: Polymer Physics*, 42(11):2027–2040, 2004.

[11] T.B. van Erp, C.T. Reynolds, T. Peijs, J.A.W. van Dommelen, and L.E. Govaert. Prediction of yield and long-term failure of oriented polypropylene: Kinetics and anisotropy. *Journal of Polymer Science Part B: Polymer Physics*, 47(20):2026–2035, 2009.

[12] T.A. Tervoort, R.J.M. Smit, W.A.M. Brekelmans, and L.E. Govaert. A constitutive equation for the elasto-viscoplastic deformation of glassy polymers. *Mechanics of Time-Dependent Materials*, 1(3):269–291, 1997.

[13] R. Hill and E. Orowan. A theory of the yielding and plastic flow of anisotropic metals. *Proceedings of the Royal Society of London. Series A. Mathematical and Physical Sciences*, 193(1033):281–297, 1948.

[14] L.C.A. van Breemen, E.T.J. Klompen, L.E. Govaert, and H.E.H. Meijer. Extending the egp constitutive model for polymer glasses to multiple relaxation times. *Journal of the Mechanics and Physics of Solids*, 59(10):2191–2207, 2011.

XIV International Conference on Computational Plasticity. Fundamentals and Applications
COMPLAS 2019
E. Oñate, D.R.J. Owen, D. Peric,M. Chiumenti, and Eduardo de Souza Neto(Eds)

TEMPORAL NATURE OF PLASTICITY IN THE DESIGN OF MATERIALS

N.S. SELYUTINA*† AND Y.V. PETROV*†

* Saint-Petersburg State University (SPbU)
Universitetskaya nab. 7/9, 199034 St. Petersburg, Russia
web page: http://english.spbu.ru/

† Institute of Problems of Mechanical Engineering Russian Academy of Sciences (IPME RAS)
V.O., Bolshoj pr., 61, 199178 St. Petersburg, Russia
email: ipmash.ran@gmail.com, http://www.ipme.ru/en/

Key words: Relaxation Model of Plasticity, Yield drop, Metals.

Abstract. A full spectrum of materials responses to dynamic loading and observed temporal effects of plasticity from a united viewpoint are analyzed. The relaxation model of plasticity with characteristic time idea is capable to effectively predict the instability of the stress-strain dependencies on strain rates. It is shown that empirical models cannot simultaneously simulate the appearance and disappearance of the yield drop unlike the relaxation model of plasticity presented in the paper.

1 INTRODUCTION

The simultaneous growth of the yield point and of the whole stress-strain curve after the beginning of yielding is a typical evidence of the temporal nature of plastic deformation. However, experiments on soft steels [1,2] conducted in a wide range of strain rates exhibit another temporal effect, known as a yield drop phenomenon. The anomalous increase of the peak stress accompanied by a subsequent drop of stresses is ignored by many of existing models of dynamic plasticity (Fig.1.a). The availability of the yield drop phenomena cannot be recognized from the conventional strain rate dependencies of the yield limit. It is necessary to develop approaches that would allow one to consider these effects of strain rate sensitivity of the materials from the united viewpoint.

The structural-temporal approach for determining both brittle strength and yield strength of materials based on the notion of characteristic (incubation) time of the stress relaxation process preceding the macro failure turned out to be an effective alternative approach for describing temporal effects in the high-speed deformation of metals [3,4]. This approach was applied in those strain rate ranges in which the classical Johnson-Cook empirical formula and its modifications do not work [5,6]. These theoretically calculated parameters gave a satisfactory correspondence to the structural-temporal plasticity model with experiment [7,8]. In the work [5], we compared numerical models with the structural-temporal approach considering initial moments of the plastic flow in metals (Fig.1). In this paper, we continue constructing analytical relationships for the entire deformation curve and try to establish

connections between parameters of empirical models and those of the relaxation model of plasticity [8,9].

In this paper, responses of some of the materials to the applied dynamic load are predicted based on the plasticity relaxation model [8,9]. Unlike original and modified Johnson-Cook models, one of the advantages of calculating the yield strength by the relaxation model of plasticity is a limited set of material parameters that do not require further modifications in conditions of high strain rates. The main result is the opportunity to describe the principal temporal effects of high-rate plastic deformation of metals from the united viewpoint.

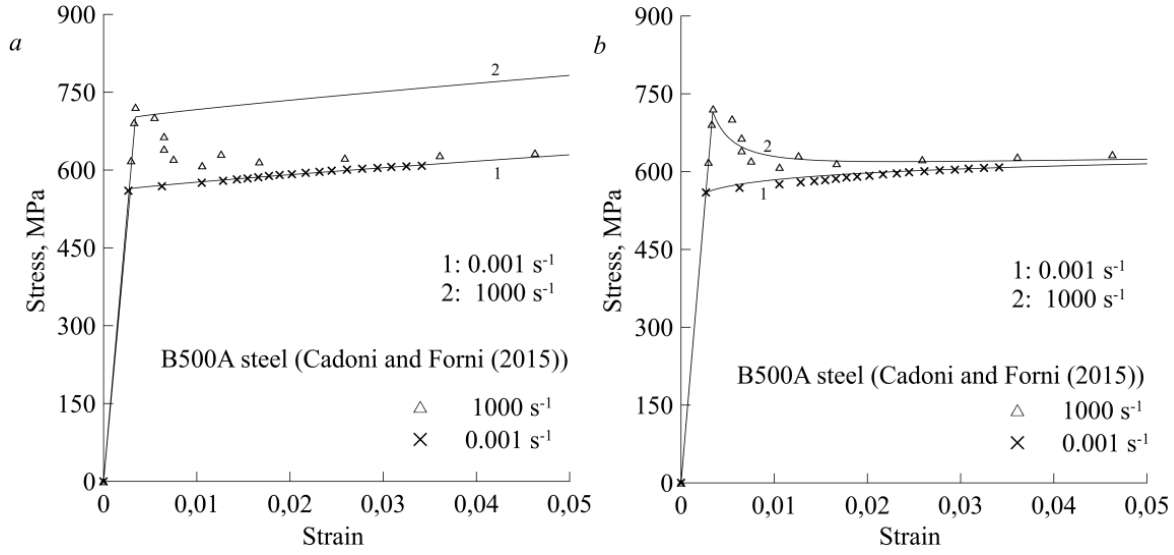


Fig.1. Stress-strain dependences of B500A steel [1] on strain rates 0.001 s^{-1} and 1000 s^{-1}, predicted by the Johnson-Cook model (a) and the relaxation model of plasticity (b).

2 THE RELAXATION MODEL OF PLASTICITY

Many principal temporal effects of yielding influencing stress-strain relations with increase of the strain rate are taken into account by the incubation time concept. To construct the whole set of stress-strain curves in a wide range of strain rates, we proposed the generalized structural-temporal approach to plastic deformation, known as the relaxation model of plasticity previously introduced by Petrov et al [8,9] and based on the notion of incubation time [3].

Let us introduce a dimensionless relaxation function $0<\gamma(t)\leq 1$, defined as follows

$$\gamma(t)=\begin{cases}1, & \dfrac{1}{\tau}\displaystyle\int_{t-\tau}^{t}\left(\frac{\Sigma(s)}{\sigma_y}\right)^{\alpha}ds\leq 1,\\ \left(\dfrac{1}{\tau}\displaystyle\int_{t-\tau}^{t}\left(\frac{\Sigma(s)}{\sigma_y}\right)^{\alpha}ds\right)^{-1/\alpha}, & \dfrac{1}{\tau}\displaystyle\int_{t-\tau}^{t}\left(\frac{\Sigma(s)}{\sigma_y}\right)^{\alpha}ds>1.\end{cases} \tag{1}$$

The equality $\gamma(t)=1$ in (1) corresponds to the case of purely elastic deformation. Gradual decrease of the relaxation function in the range $0<\gamma(t)<1$ describes a transition to the plastic deformation stage. During the plastic stage of deformation, $t\geq t_*$, the relaxation function $\gamma(t)$

satisfies the condition

$$\frac{1}{\tau}\int_{t-\tau}^{t}\left(\frac{\gamma(t)\Sigma(s)}{\sigma_y}\right)^{\alpha} ds = 1. \quad (2)$$

Here, we suppose that the equality (2) is retained from the yield moment $t=t_*$ (the detailed calculation scheme for the t_* is given in [9]) during the subsequent irreversible deformation process in the material ($0<\gamma(t)<1$). We determine the true stresses in the deformed sample at $t\geq t_*$ in the following form:

$$\sigma(t)=E\gamma^{1-\beta}(t)\varepsilon(t) \quad (3)$$

where E is the Young's modulus and β is the scalar parameter ($0\leq\beta\leq1$), which describes the degree of hardening of the material. The case of $\beta=0$ corresponds to the absence of hardening. Considering the stages of elastic and plastic deformations separately, we can obtain from (4) the following stress-strain relation:

$$\sigma\big(\varepsilon(t)\big) = \begin{cases} E\varepsilon(t), & \varepsilon(t)/\dot{\varepsilon} < t_*, \\ E\gamma^{1-\beta}\left(\dfrac{\varepsilon(t)}{\dot{\varepsilon}}\right)\varepsilon(t), & \varepsilon(t)/\dot{\varepsilon} \geq t_*. \end{cases} \quad (4)$$

All parameters α, τ, β are invariant to loading history and only depend on structural transformations in the material. The relaxation model of plasticity can be used for the arbitrary pulse shape, defined by the $\Sigma(s)$ function.

3 THE YIELD DROP PHENOMENON IN THE MATERIALS

Introducing the independent mechanisms controlled by α, β, τ parameters makes it possible to predict the rate sensitivity effect of the material response and the appearance of the "yield drop" effect in both cases in the perfect plasticity (Fig. 2) and that with hardening (Fig. 3). Further materials without hardening (Material WH) and with hardening (Material H) are considered. The sufficiency of the three parameters to describe the effect of the "yield drop" follows from the fact that the effect of the yield drop contains three quantities that correspond to this phenomenon. These include the width of the yield drop, the upper and lower yield stresses.

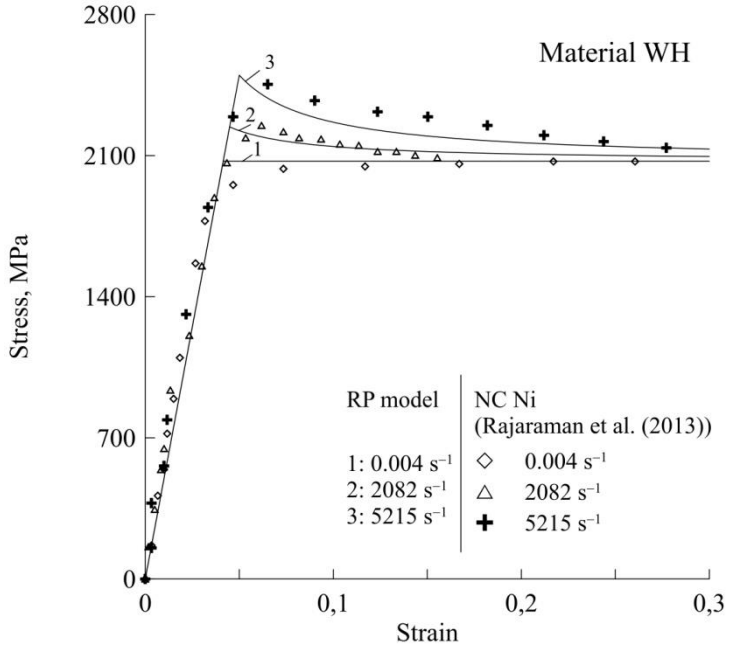


Fig. 2. The responses of nanocrystalline nickel [10] and theoretical stress-strain relations at 0.004 s^{-1}, 2082 s^{-1}, 5215 s–1, plotted by the relaxation model of plasticity (α=1; β=0; τ=3.3 μs; σ_y=2072 MPa; E= 50 GPa).

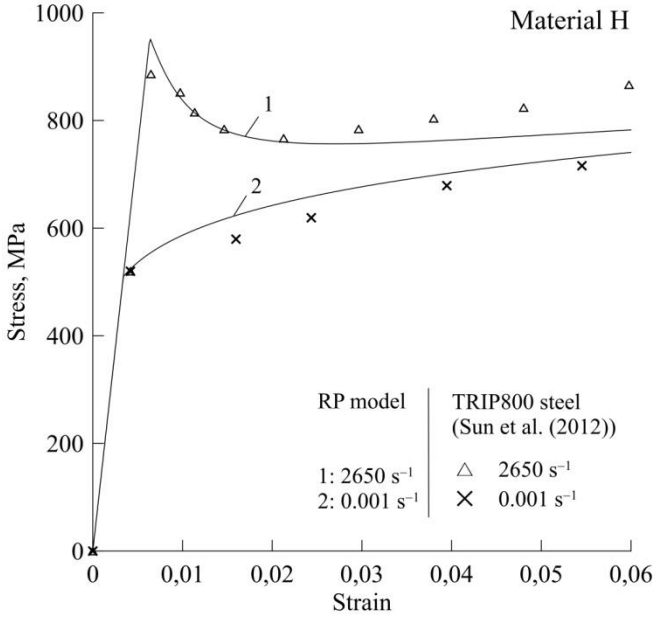


Fig. 3. Stress-strain dependences of TRIP800 steel [2] on strain rates 0.001 s^{-1} and 2650 s^{-1}, predicted by relaxation model of plasticity (E=150 GPa, σ_y=510 MPa; α=2, τ=2.8μs, β=0.13).

4 DIFFERENCE MATERIALS RESPONSES TO DYNAMIC LOADING

The rate sensitivity in the material can be analyzed using the dependence of the limiting stress (initial point of the irreversible deformation, called the yield stress in metal) on the strain rate and a set of responses of the material to the applied load, characterized by different durations and amplitudes. Different types of the material deformation curves in a wide range of strain rates can be predicted from the viewpoint of the relaxation model of plasticity (Fig. 4 and Fig. 5). Particularly, the increase of loading rate can lead to appearance of anomalies, called "yield drops", at the initial stage of the plastic deformation. In this case, the transition to plastic deformation stage is accompanied by the presence of a pronounced maximum stress with a subsequent stress drop on the deformation dependence. The phenomenon of the maximum stress increasing with the applied load can indicate the existence of the material rate sensitivity. Classical dynamic models of the plastic deformation are only able to account for the cases shown in Fig. 6 when loading rate growth increases the yield stress and the stress-strain dependence remains smooth during transition to the stage of irreversible deformation.

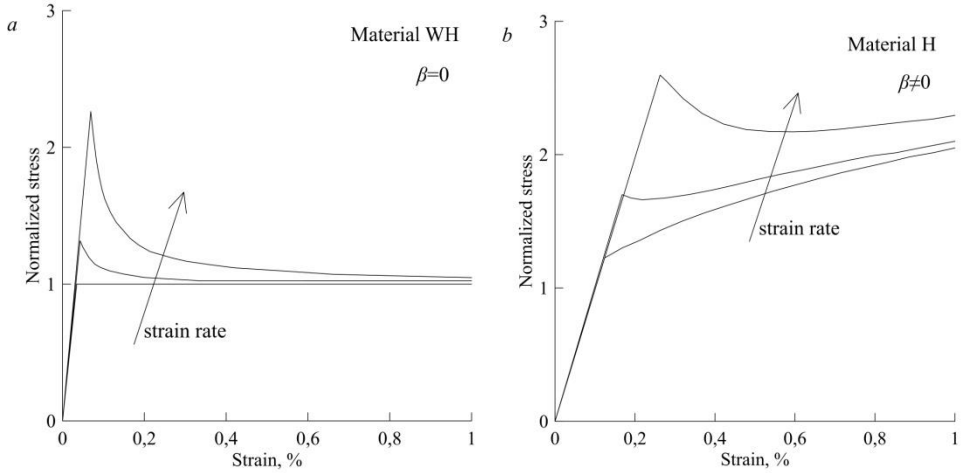


Fig. 4. Prediction of "yield drop" effect with hardening (a) and without hardening (b) using the relaxation model of plasticity.

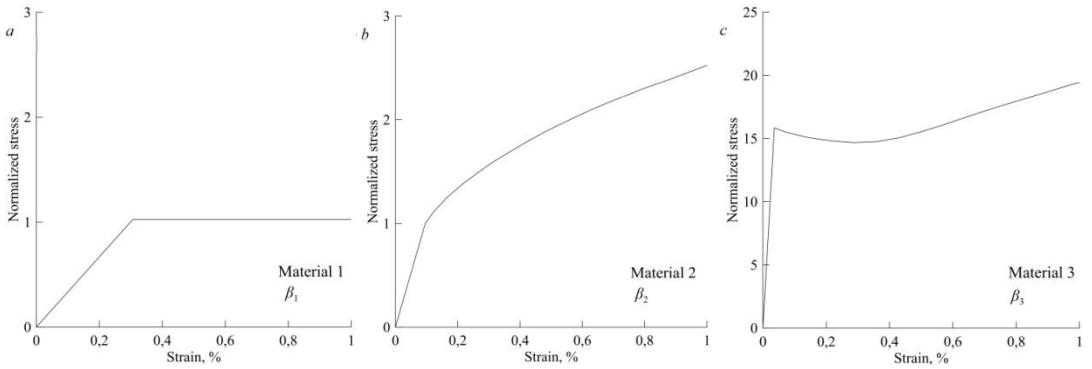


Fig. 5. Full spectrum material responses based on the relaxation model of plasticity: (a) perfect plasticity, (b)

appearance and (c) disappearance of the “yield drop” effect.

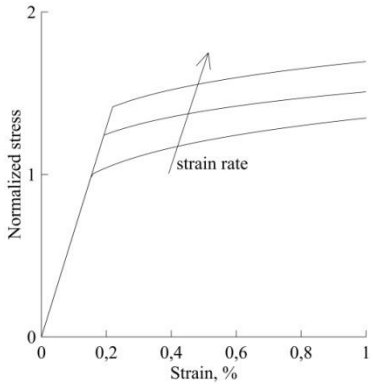


Fig. 6. The increase of the yield stress with disappearance of the “yield drop” effect.

5 CONCLUSIONS

Characteristic (incubation time of plastic deformation) time being considered as a material constant can serve a principal parameter of the integral yield criterion that predicts the dynamic behaviour of the yield strength in a wide range of strain rates. The relaxation model of plasticity is able to describe experimentally observed instabilities of stress-strain dependencies, caused by strain rates, including the yield drop phenomenon. It was shown that utilizing this approach the broad spectrum of material responses to dynamic loading can be obtained (Fig. 4 and Fig. 5).

ACKNOLEGMENTS

The work was supported by the Russian Science Foundation (grant 17-11-01053).

REFERENCES

[1] Cadoni, E. and Forni D. Strain rate effects on reinforcing steels in tension. *EPJ Web of Conferences* (2015) **94**: 01004.

[2] Sun, X., Soulami, A., Choi, K.S., Guzman O. and Chen W. Effects of sample geometry and loading rate on tensile ductility of TRIP800 steel. *Mater. Sci. Engng. A* (2012) 541: 1-7.

[3] Petrov Y.V. On “quantum” nature of dynamic failure of brittle media. *Dokl. Akad. Nauk SSSR* (1991) **321**: 66-68.

[4] Gruzdkov, A.A. and Petrov, Yu.V. On temperature-time correspondence in high-rate deformation of metals. *Dokl. Phys.* (1999) **44** (2): 114-116.

[5] Selyutina, N.S. and Petrov Yu.V. Comparative analysis of dynamic plasticity models. *Rev. Adv. Mater. Sci.* (2018) **57**: 199-211.

[6] Selyutina, N.S. and Petrov, Yu.V. Prediction of the dynamic yield strength of metals using two structural-temporal parameters. *Phys. Solid State* (2018) **60** (2): 244–249.

[7] Gruzdkov, A.A., Petrov, Yu.V. and Smirnov, V.I. An invariant form of the dynamic

criterion for yield of metals. *Phys. Solid State* (2002) **44** (11): 2080-2082.

[8] Petrov, Y.V. and Borodin, E.N. Relaxation mechanism of plastic deformation and its justification using the example of the sharp yield point phenomenon in whiskers. *Phys. Solid State* (2015) **57** (2): 353-359.

[9] Selyutina, N., Borodin, E.N., Petrov, Y. and Mayer, A.E. The definition of characteristic times of plastic relaxation by dislocation slip and grain boundary sliding in copper and nickel. *Int. J. Plasticity* (2016) **82**: 97-111.

[10] Rajaraman, S., Jonnalagadda, K.N., Ghosh, P. Indentation and dynamic compression experiments on microcrystalline and nanocrystalline nickel. In: Conference Proceedings of the Society for Experimental Mechanics Series (2013) **1**: 157-163

XIV International Conference on Computational Plasticity. Fundamentals and Applications
COMPLAS 2019
E. Oñate, D.R.J. Owen, D. Peric , M. Chiumenti, and Eduardo de Souza Neto (Eds)

FORMULATION METHOD OF BALL INDENTATION PROCESS FOR ULTRA-THIN ELASTIC BODY WITH MECHANICS POISSON EFFECT

CHAO LU [*] AND ATSUSHI SAKUMA [†]

[*] Graduate School of Science and Technology
Kyoto Institute of Technology
Matsugasaki, Sakyo-ku, 606-8585 Kyoto, Japan
e-mail: michaellu950609@gmail.com, http://www.fibro.kit.ac.jp/

[†] Division of Textile Science
Kyoto Institute of Technology
Matsugasaki, Sakyo-ku, 606-8585 Kyoto, Japan
email: sakuma@kit.ac.jp, http://www.fibro.kit.ac.jp/

Key words: Finite Element Method, Full Contact Model, Poisson's Effect, Engineering Strain

Abstract. *A new theoretical method for determining the mechanics properties of ultra-thin elastic materials is proposed in this paper. This method is based on a full contact model and Poisson's effect. This study consisted of three steps. First, FE model of indentation problem for ultra-thin specimen is developed by elastic constitutive relationship for precise analysis of problem. Second, the simplified model is used to evaluate the result of FEM, and its availability is discussed by comparison with extended Hertzian theory. Third, an equation is proposed after comparing the results of FEM, extended Hertzian theory and full contact model.*

1 INTRODUCTION

Over the past one hundred years, the indentation technique has been adopted to measure the hardness and elastic modulus of various materials [1-3]. Fundamental ball indentation technology proposed by Heinrich Hertz is regarded as an effective method for deducing the physical properties of semi-infinite elastic bodies [1]. W.C Oliver *et al* proposed a nanoindentation technique applied under small-scale deformation [4]. After that, experiments on nanoindentation were carried out continuously [5-7]. Several researchers have theoretically investigated the mechanical properties for thin film materials. However, the studies of Hertzian theory and nanoindentation technique have limitation when one of the contacting bodies is very thin. A extended Hertzian theory based on nonequivalent indentation strain was proposed by Tani *et al*. to investigate the applicability in this case [8,9]. but this method is not universal and has a certain error when the thickness is too small.

In this paper, therefore, a theoretical full contact theory is studied to solve this theoretically problem. First, the optimal experimental conditions were selected after considering the thickness effect and diameter effect. Then, a simplified model is formulated to derive full contact theory. At last, by using the result of FEM, the difference between extended theory and full contact theory is compared under various thickness conditions.

2. EVALUATION METHOTOLOGY

2.1 Thickness effect by FEM

The FE model of indentation problem is developed by elastic constitutive relationship for precise analysis. The intent of this section is to explore the effects of various dimensions of the diameter and specimen on the experiment and to find optimal experimental conditions. Numerical experiments have been carried out by LS-DYNA and FEMAP V11.4.1.

The boundary conditions for FE model of ultra-thin indentation problem are given in Fig.1.

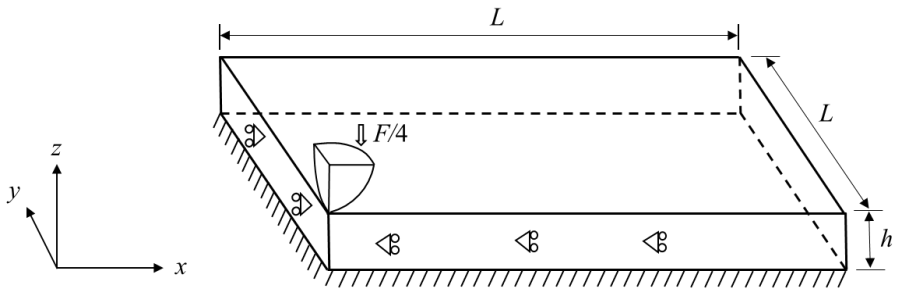
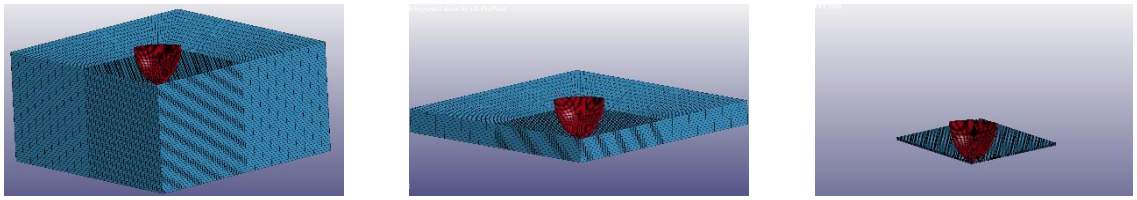


Figure 1: Geometry and boundary conditions of quarter finite element model

The FE models of indenter and specimen were constructed and meshed in FEMAP. The FE models and its meshing at different thickness *h* of specimen are given in Fig.2. The diameter of indenter is 30mm. Since the symmetricity of this model, a quarter of specimen and a spherical shell of indenter are used to reduce computation time. Specimen is a rectangular parallelepiped with a side length of 50mm×50mm. Its thickness *h* is prepared as 50mm, 10mm and 1mm for corresponding to different situations. The regional differential meshing is used for specimen. In particular, the model can be neglect its dimensions as shown in Fig.2 (c) when the thickness of the specimen is very thin.



(a) Thick (Hertzian) (b) Thin (extended) (c) Ultra-thin (full contact)

Figure 2: FE models to analyze the influence of thickness

Fig.3 shows the thickness effect on the experimental results. It indicates that the same indentation depth produces different magnitudes of load force *F* at different thicknesses. On the other hand, this difference becomes more and more noticeable when the thickness becomes thinner.

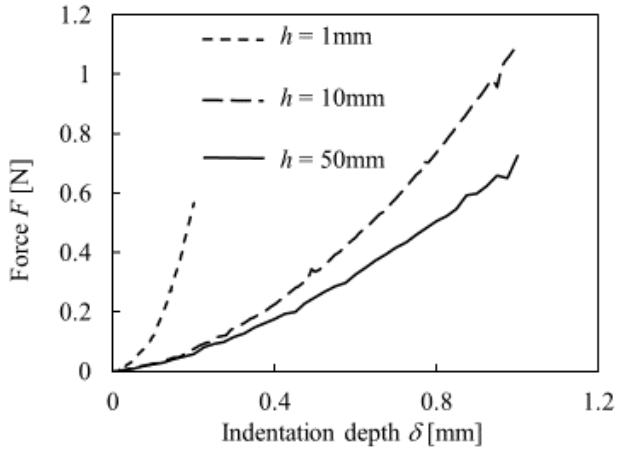
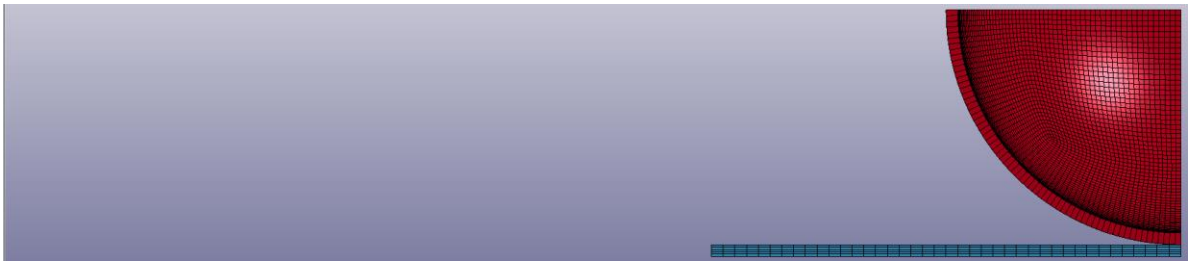


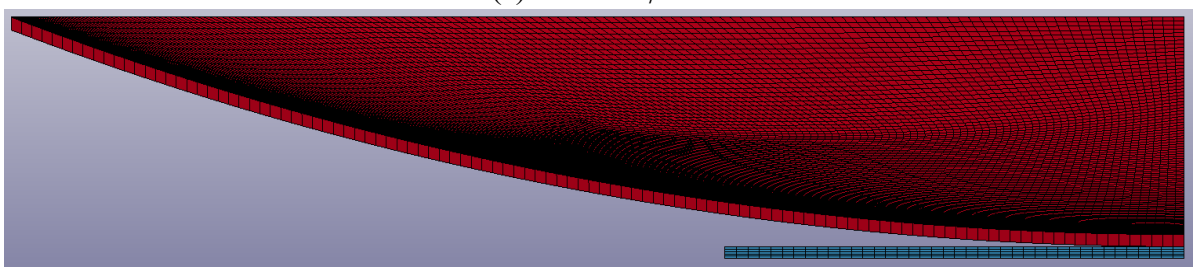
Figure 3: Thickness effect in indentation

2.2 Diameter effect for ultra-thin specimen

The diameter effect is discussed in this section. The FE models are shown in Fig.4. The indenter is a rigid sphere with a diameter of 2mm and 30 mm. Where only a portion of a spherical indenter is taken for the indenter model in order to reduce the simulation time.



(a) Diameter ϕ=2mm



(b) Diameter ϕ=30mm

Figure 4: Finite element mesh of ultra-thin indentation problem at different diameter of indenter

Table 1 represents the conditions of experiment. The Young's modulus E and Poisson's ratio v of indenter are 200GPa and 0.29, respectively. The Young's modulus E of specimen is 100kPa, and the Poisson ratio v is 0.45.

Table 1: Experiment condition

	Unit	Indenter	Specimen
Materials		rigid	elastic
Young's modulus	E [Pa]	200G	100k
Poisson's ratio		0.29	0.45
Diameter/ Thickness	ϕ/h [mm]	2, 30	0.05

Fig.5 shows the diameter effect of thin specimen indentation test. It indicates that the larger diameter h of indenter will cause the bigger load force F under the same experimental conditions. The large diameter indenter is used in this study in order to facilitate the processing and comparison of experiment results.

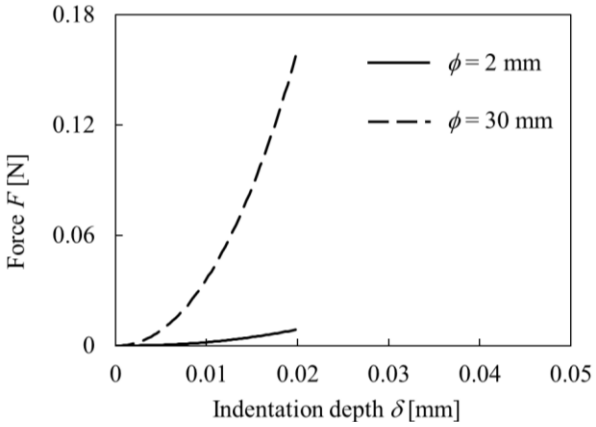


Figure 5: Diameter effect in thin specimen

3. EVALUATION FOR ULTRA-THIN INDENTATION PROBLEM

3.1 Evaluation by extended Hertzian theory

The relationship between the load force F and the indentation depth δ shown in the Fig.1 (a) can be described by Hertzian contact theory [1] as following.

$$F = \frac{4}{3}\frac{E}{1-v^2}\left(\frac{\phi}{2}\right)^{\frac{1}{2}}\delta^{\frac{3}{2}} = A\delta^{\frac{3}{2}} \tag{1}$$

$$A = \frac{4}{3}\frac{E}{1-v^2}\left(\frac{\phi}{2}\right)^{\frac{1}{2}} \tag{2}$$

Here ϕ, E and v are the diameter of indenter, the Young's modulus and Poisson's ratio of specimen, respectively. Equation (3) is the extended Hertzian theory proposed by Tani *et al.* [8,9] as shown in Fig.1 (b). Where coefficient B is the constant determined by the curve fitting method numerically.

$$\hat{F} = A\{\delta(1+B\delta)\}^{\frac{3}{2}} = \hat{A}\delta^{\frac{3}{2}} \tag{3}$$

$$\hat{A} = A(1+B\delta)^{\frac{3}{2}} \tag{4}$$

Therefore, the apparent Young's modulus $\hat{E}$ of the specimen during the experiment can be determined by Equation (5).

$$\hat{E} = E(1 + B\delta)^{\frac{3}{2}} \tag{5}$$

3.2 Formulation of full contact theory

The relationship between load force F and indentation depth δ represents an important material characteristic. However, it is very difficult to analyses the contact mechanics when one of the contacting bodies is very thin. The aim of this section is to seek a theoretical method to express the load force F according to indentation depth δ when thickness h is very thin.

Fig.6 shows a schematic of model named full contact model for the ultra-thin indentation problem. It differs from the Hertzian contact theory in the contact area radius a, which is denoted by α in this paper. The shaded portion in Fig.6 is considered to be the compressed area. A coordinate system is established with the projection point of the indenter on the bottom surface as the origin. Where δ is the indentation depth, h is the thickness of specimen, δ_i and h_i are the indentation depth and thickness of specimen at radius r_i on the r-axis, respectively. α is the radius of the contact area which can be determined by equation (6).

$$\alpha = \sqrt{\phi\delta - \delta^2} \tag{6}$$

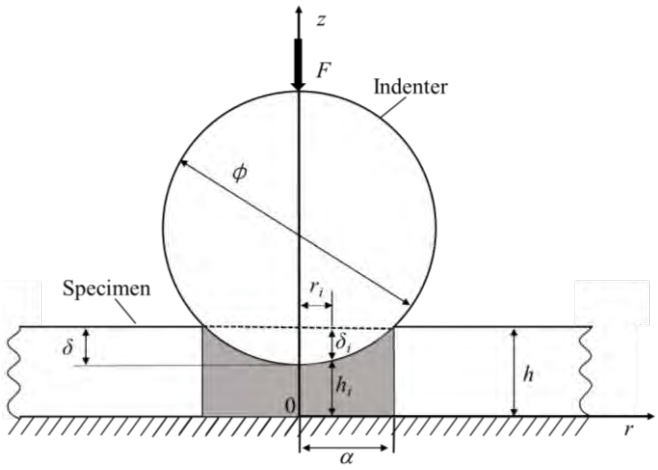


Figure 6: Schematic of full contact theory model

The curve equation of the indenter can be expressed by the equation (7).

$$z = h + \frac{\phi}{2} - \delta - \sqrt{\frac{\phi^2}{4} - r^2} \tag{7}$$

$$r \in [0, \alpha]$$

When the value of r increase from 0 to α, the expressions of δ_i and h_i are as shown in equation (8) and equation (9).

$$\delta_i = \delta - \frac{\phi}{2} + \sqrt{\frac{\phi^2}{4} - r_i^2} \tag{8}$$

$$h_i = h + \frac{\phi}{2} - \delta - \sqrt{\frac{\phi^2}{4} - r_i^2} \tag{9}$$

According to the definition of engineering strain, the strain is the ratio of the shortening or elongation of the specimen to the initial value of the gauge length. Therefore, the strain ε_i at different positions can be defined by equation (10).

$$\varepsilon_i = \frac{\delta - \frac{\phi}{2} + \sqrt{\frac{\phi^2}{4} - r_i^2}}{h} \tag{10}$$

The stress value σ_i at different positions r_i can be obtained by Hooke's law $\sigma = E\varepsilon$, where E is the Young's modulus of the specimen.

$$\sigma_i = E\frac{\delta - \frac{\phi}{2} + \sqrt{\frac{\phi^2}{4} - r_i^2}}{h} \tag{11}$$

In order to simplify the model, the Young's modulus of the specimen is considered as a constant. Therefore, the load force F can be defined by equation (12).

$$F = \int_0^{\alpha} 2\pi\sigma(r)dr = 2\pi E\int_0^{\alpha} r\frac{\delta - \frac{\phi}{2} + \sqrt{\frac{\phi^2}{4} - r_i^2}}{h}dr \tag{12}$$

When the sides of the object is fixed, the boundary creates an extra force on the object during compression process. This effect is called the Poisson effect which can be defined as shown in equation (13). Where v is the Poisson's ratio of specimen.

$$E' = E\frac{1 - v}{(1 + v)(1 - 2v)} \tag{13}$$

In the ultra-thin ball indentation test, the compressed area can be approximated as the shaded portion in Fig. 6. Therefore, the full contact theory is proposed as shown in equation (14).

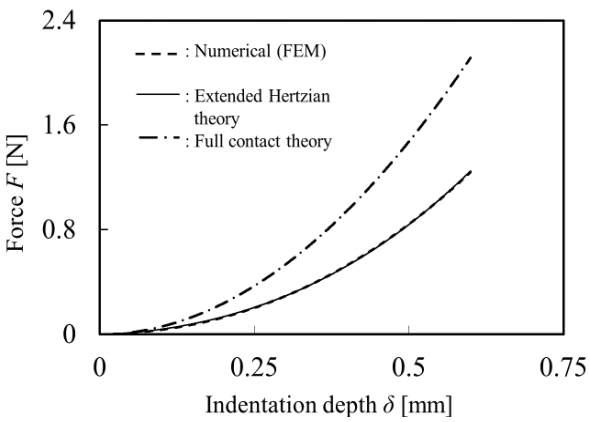
$$F = \frac{\pi E\delta^2}{h}\left(\frac{\phi}{2} - \frac{\delta}{3}\right)\frac{1 - v}{(1 + v)(1 - 2v)} \tag{14}$$

3.3 Evaluation and comparison

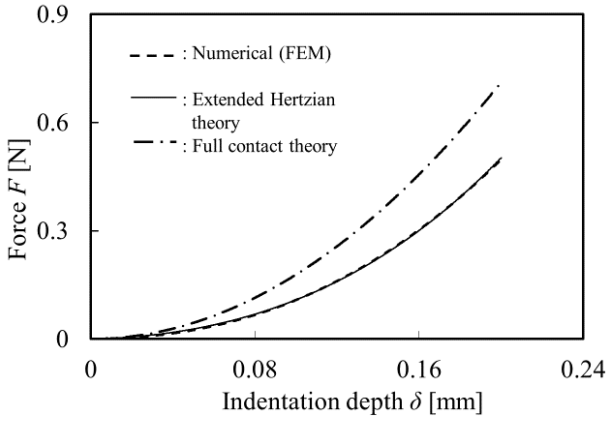
Based on the full contact theory, the fundamental and extended Hertzian theories, a series of experiments were conducted to investigate the differences in various thicknesses h of specimen.

The FE model used in this section is similar to that of Fig.4, and the mechanical properties of the material are the same as in Table.1. The diameter of the indenter is set to 30mm because of the diameter effect, while the thickness h of the specimen is 0.05mm, 0.1mm, 0.3mm, 1mm and 3mm. The direction of indenter is perpendicular to the specimen bottom surface. Since the thickness h of each specimen is different, the maximum indentation depth is set to 20% of the specific thickness h of specimen in order to visually compare the differences.

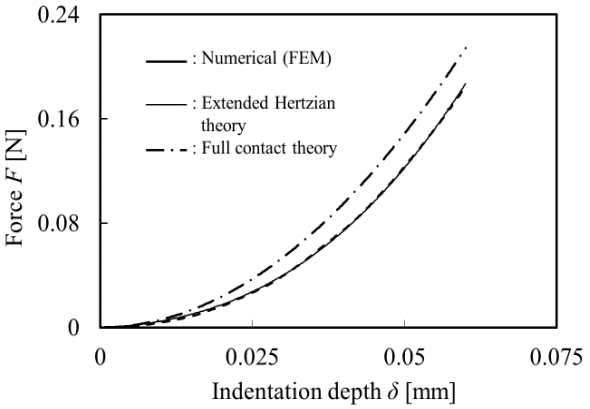
The calculated results are shown in Fig.7. It indicated when the thickness of the specimen is decreasing, the results obtained by the full contact theory are getting closer to the FEM results. The results are almost the same when the thickness reaches 0.1mm or even 0.05mm. On the other hand, the extended Hertzian theory is very close to the FEM results at different thickness h of specimen.



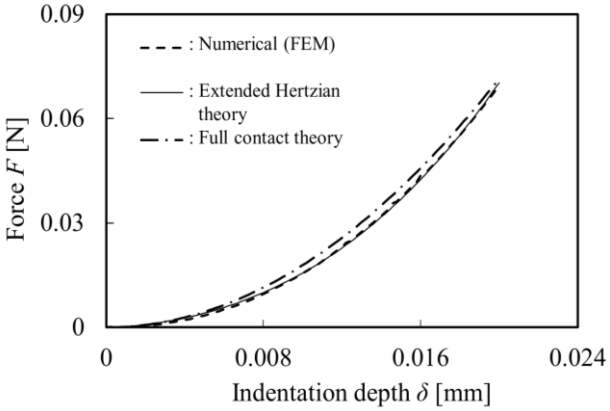
(a) Thickness h=3mm



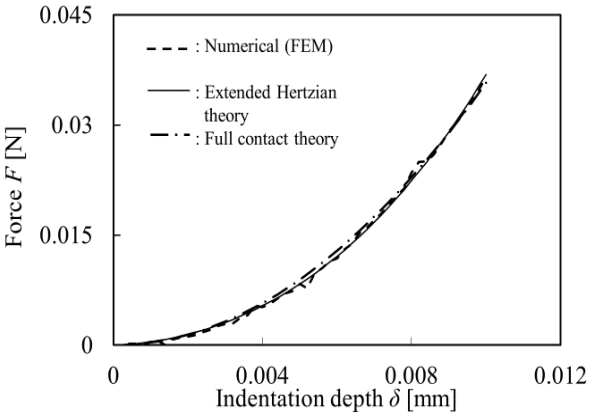
(b) Thickness h=1mm



(c) Thickness h=0.3mm



(d) Thickness h=0.1mm



(e) Thickness h=0.05mm

Figure 7: Comparison of different theories

Fig. 8 shows the variation of E'/E_0 at different thicknesses. Where E_0 is the actual Young's modulus which the value is 100kPa. F' is the load force obtained from FE results. E' is the apparent Young's modulus obtained in the simulation according to the full contact theory. The solution of E' is as shown in equation (15). The abscissa is the thickness h, and the ordinate is the ratio of the apparent Young's modulus E' to the actual Young's modulus E_0. It indicates that the apparent Young's modulus E' decreases as the thickness of the specimen increases.

$$E' = \frac{F'}{C} \tag{15}$$

$$C = \frac{\pi\delta^2}{h}\left(\frac{\phi}{2} - \frac{\delta}{3}\right)\frac{1-\upsilon}{(1+\upsilon)(1-2\upsilon)}$$

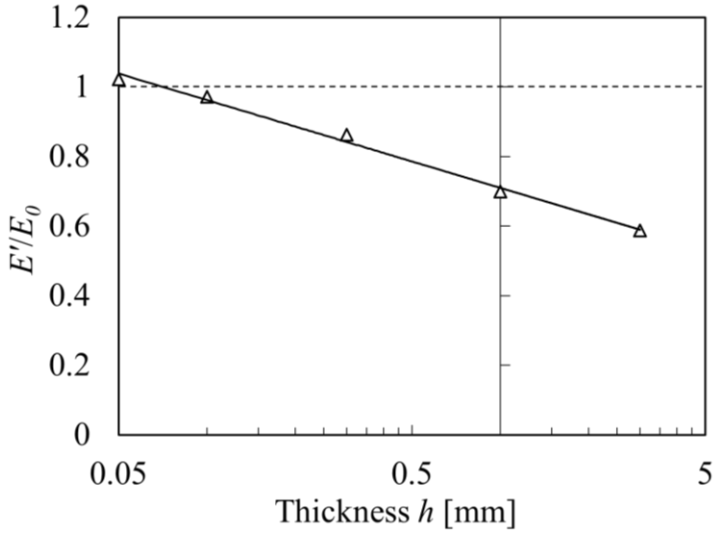


Figure 8: Variation of Young's modulus E' at different thicknesses

The results can be fitted with a logarithmic function as shown in equation (16). The coefficient of determination R^2 is 0.9931.

$$\frac{E'}{E_o} = -0.11\ln(h) + 0.7098 \tag{16}$$

It can be obtained that when h is 0.0715 mm, apparent Young's modulus E' is equal to actual Young's modulus E_0. Therefore, it can be considered that full contact theory is applied when the thickness is less than 0.0715 mm.

$$R_L = \frac{h}{\phi} \tag{17}$$

Here， R_L is the ratio of thickness h to diameter ϕ. In this paper, the full contact theory can be applied when the value range of R_L is 0.0017 which is threshold of applicability of equation (14).

4 CONCLUSION

- The results of the experiment indicate that the extended Hertzian theory has good applicability, and the full contact theory applies only when the thickness h of specimen is very thin.
- By comparing the extended Hertzian theory with the full contact theory, it can be found that the full contact theory can predict the result directly when h is very thin.
- According to the principle of geometric similarity, the full contact theory can be applied when the ratio R_L of the thickness h to the diameter ϕ is under 0.0017 in the case of very thin specimen.

REFERENCES

[1] Hertz, H. R. *Über die Berührung fester elastischer Körper und über die Härte*. Universitätsbibliothek Johann Christian Senckenberg, (2006).

[2] Oliver, W. C., and George M. P. An improved technique for determining hardness and elastic modulus using load and displacement sensing indentation experiments. *Journal of materials research* (1992) **7.6**: 1564-1583.

[3] Oliver, W. C., and George M. P. Measurement of hardness and elastic modulus by instrumented indentation: Advances in understanding and refinements to methodology. *Journal of materials research* (2004) **19.1**: 3-20.

[4] Pharr, G. M., and W. C. Oliver. Measurement of thin film mechanical properties using nanoindentation. *Mrs Bulletin* (1992) **17.7**: 28-33.

[5] Nayebi A, El Abdi R, Bartier O, et al. New procedure to determine steel mechanical parameters from the spherical indentation technique. *Mechanics of Materials*, (2002) **34(4)**: 243-254.

[6] Ma D, Xu K, He J. Numerical simulation for determining the mechanical properties of thin metal films using depth-sensing indentation technique. *Thin Solid Films*, (1998) **323(1-2)**: 183-187.

[7] Waters, N. E. The indentation of thin rubber sheets by spherical indentors. *British Journal of Applied Physics* (1965) **16.4**: 557.

[8] Tani, M., Sakuma, A., and Shinomiya, M. Evaluation of thickness and Young's modulus of soft materials by using spherical indentation testing. *Transactions of the Japan Society of Mechanical Engineers, Series A* (2009) **75.755**: 901-908.

[9] Tani, M., and Sakuma, A. Applicability evaluation of Young's modulus measurement using nonequivalent indentation strain in spherical indentation testing for soft materials. *Transactions of the Japan Society of Mechanical Engineers, Series A* (2010) **76.761**: 102-108.

A ZERO-THICKNESS MORTAR/ INTERFACE FORMULATION WITH APPLICATION TO FRACTURE MECHANICS

M. de Francisco, I. Carol

Div. of Geotechnical Engineering and Geo-Sciences
School of Civil Engineering (ETSECCPB)
Technical University of Catalonia (UPC)
08034 Barcelona
ignacio.carol@upc.edu

Key words: Zero-thickness Interface, Mortar Methods, Fracture Mechanics.

Abstract. A zero-thickness mortar/interface element formulation is briefly described and demonstrated. This element may be considered as an extension of traditional zero-thickness interface element, in order to represent material interfaces located in between subdomains with non-matching FE meshes. In the context of small strain analysis, these elements may be equipped with the same type of constitutive laws as traditional interface elements. Therefore, if friction or fracture-mechanics-based laws are adopted, mortar/interface elements may be used to represent frictional sliding or cracking following the lines (surfaces) along which they have been pre-inserted. Two basic verification examples of this type are presented, showing that the model can correctly represent uniform states of stress and deformation when connecting unmatched mesh subdomains.

1 INTRODUCTION

Since they were first proposed in the late 60s in a geo-mechanical context [1], zero-thickness interface elements have been a very useful tool to represent contacts and discontinuities in a variety of engineering fields, including concrete and other quasi-brittle materials, bone tissue, etc. However, as originally proposed, interface elements are subject to the limitation that nodes on each side must be paired and perfectly matched one-to one. That is, meshes of the continuum on both sides of the interface line have to be perfectly matching and conformal meshes. This may be not a non-trivial requirement in some cases, such as for instance in the case of complex problems containing different subdomains that may be more conveniently meshed independently, or in case of meshes initially matched that may become unmatched due to large opening/sliding of the discontinuities.

One way to deal with unmatched meshes on both sides of the discontinuities, consists of the so called “mortar” elements. The concept was originally introduced by Bernardi et al in 1987 in the context of spectral discretization of domain decomposition methods [2], and was later introduced in the FEM for large-deformation contact-friction analysis and shown to preserve the optimal convergence ratio and fulfil the Babuska-Brezzi condition [3]. Initially, mortar elements were formulated on the basis of Lagrange multipliers, although later formulations are also based on penalty approach [4]. The mortar formulation described here uses a penalty approach, which makes it similar to traditional zero-thickness interface elements and in fact,

the mortar formulation developed may be considered as an extension of those elements to the case of unmatched meshes. Another advantage of the penalty approach is the possibility of using the same constitutive models as used for interface elements, and in particular, the model of normal/shear cracking model developed in [5].

2 STANDARD INTERFACE FORMULATION

The departing point for the formulation of the mortar element is the classical displacement-based zero-thickness interface element [6]. This is why this section includes a summary/reminder of that formulation, although it is recast in a way that is more convenient for the later extension to the mortar case. Figure 1 shows a linear interface element composed of two faces with two nodes per face. Although in the figure the faces are represented at a distance from each other, locations the two faces are generally coincident. A mid-plane line is defined at mid distance between the two faces, or if they coincide, at the same location. For interpolation and integration purposes, a local coordinate ξ varying from -1 to 1, is defined along the mid-plane in such a way that nodes 1 and 3 are located just across the discontinuity at the point $\xi = -1$, which is also denoted as mid-point α, and the same for nodes 2 and 4 at $\xi = 1$, which also denoted as mid-point β.

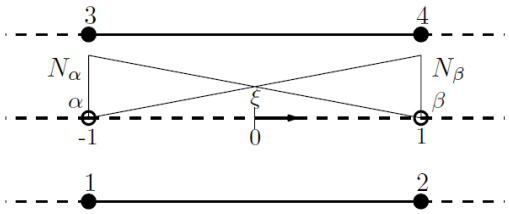


Figure 1: Geometry of standard interface element

Interface nodal relative displacement are then defined as:

$$\begin{aligned} \mathbb{r}_{\alpha}^{xy} &= \boldsymbol{u}_3 - \boldsymbol{u}_1 \\ \mathbb{r}_{\beta}^{xy} &= \boldsymbol{u}_4 - \boldsymbol{u}_2 \end{aligned} \tag{1}$$

where $\boldsymbol{u}_1$, $\boldsymbol{u}_2$, $\boldsymbol{u}_3$, $\boldsymbol{u}_4$ are the standard nodal displacements in Cartesian axes. Expression (1) may be written in matrix form as:

$$\mathbb{r}_{e}^{xy} = \begin{bmatrix} \mathbb{r}_{\alpha}^{xy} \\ \mathbb{r}_{\beta}^{xy} \end{bmatrix} = \left[\begin{array}{cc|cc} -\mathbb{I} & \mathbf{0} & \mathbb{I} & \mathbf{0} \\ \mathbf{0} & -\mathbb{I} & \mathbf{0} & \mathbb{I} \end{array}\right] \begin{bmatrix} \boldsymbol{u}_1 \\ \boldsymbol{u}_2 \\ \boldsymbol{u}_3 \\ \boldsymbol{u}_4 \end{bmatrix} = \begin{bmatrix} \mathbf{T}_A & \mathbf{T}_B \end{bmatrix} \begin{bmatrix} \boldsymbol{u}_A \\ \boldsymbol{u}_B \end{bmatrix} = \mathbf{T}\, \boldsymbol{u}_e \tag{2}$$

where $\mathbf{T}$ and $\boldsymbol{u}_e$ are the overall transfer matrix and nodal displacement vectors, while $\boldsymbol{u}_A$ and $\boldsymbol{u}_B$ are the displacement vectors containing the displacement of nodes on the upper and lower sides of the discontinuity surface, and matrices $\mathbf{T}_A$ and $\mathbf{T}_B$ are the respective transfer matrices. Relative displacements at any point ξ of the mid-plane surface are then interpolated from their mid-point nodal values using the standard shape functions $N_\alpha(\xi)$ and $N_\beta(\xi)$ (Fig.1), as:

$$\mathbb{r}^{xy}(\xi) = \begin{bmatrix} r_x(\xi) \\ r_y(\xi) \end{bmatrix} = \begin{bmatrix} N_\alpha(\xi) & 0 \\ 0 & \mathrm{N}_\alpha(\xi) \end{bmatrix} \begin{bmatrix} r_{\alpha x}(\xi) \\ r_{\alpha y}(\xi) \end{bmatrix} + \begin{bmatrix} N_\beta(\xi) & 0 \\ 0 & N_\beta(\xi) \end{bmatrix} \begin{bmatrix} r_{\beta x}(\xi) \\ r_{\alpha y}(\xi) \end{bmatrix} =$$
$$= \mathbf{N}_\alpha(\xi)\, \mathbb{r}_\alpha^{xy} + \mathbf{N}_\beta(\xi)\, \mathbb{r}_\beta^{xy} = \begin{bmatrix} \mathbf{N}_\alpha(\xi) & \mathbf{N}_\beta(\xi) \end{bmatrix} \begin{bmatrix} \mathbb{r}_\alpha^{xy} \\ \mathbb{r}_\beta^{xy} \end{bmatrix} \tag{3}$$

Combining equations (2) and (3) we obtain:

$$\mathbb{r}^{xy}(\xi) = \begin{bmatrix} \mathbf{N}_\alpha(\xi) & \mathbf{N}_\beta(\xi) \end{bmatrix} \mathbf{T}\, \boldsymbol{u}_e = \mathbf{N}(\xi)\, \boldsymbol{u}_e = [\mathbf{N}_A(\xi) \;\; \mathbf{N}_B(\xi)] \begin{bmatrix} \boldsymbol{u}_A \\ \boldsymbol{u}_B \end{bmatrix} \tag{4}$$

where $\mathbf{N}(\xi)$ is the overall interpolation matrix for the interface element, which can be decomposed in the "upper" and "lower" interpolation matrices $\mathbf{N}_A(\xi)$, $\mathbf{N}_B(\xi)$, with components:

$$\mathbf{N}_A(\xi) = \left[\begin{array}{cc|cc} -N_\alpha(\xi) & 0 & -N_\beta(\xi) & 0 \\ 0 & -N_\alpha(\xi) & 0 & -N_\beta(\xi) \end{array}\right]$$
$$\mathbf{N}_B(\xi) = \left[\begin{array}{cc|cc} N_\alpha(\xi) & 0 & N_\beta(\xi) & 0 \\ 0 & N_\alpha(\xi) & 0 & N_\beta(\xi) \end{array}\right] \tag{5}$$

The relative displacement vector in global coordinates *x,y* is rotated to the local normal and tangential coordinates *n,t* , by means of a local rotation matrix **R**:

$$\mathbb{r}^{nt}(\xi) = \mathbf{R}\, \mathbb{r}^{xy}(\xi) = \mathbf{R}\, \mathbf{N}(\xi)\, \boldsymbol{u}_e = \mathbf{B}(\xi)\, \boldsymbol{u}_e = [\mathbf{B}_A(\xi) \;\; \mathbf{B}_B(\xi)] \begin{bmatrix} \boldsymbol{u}_A \\ \boldsymbol{u}_B \end{bmatrix} \tag{6}$$

where matrix $\mathbf{B}(\xi)$ may also be decomposed into upper and lower side submatrices:

$$\mathbf{B}_A(\xi) = \mathbf{R}\, \mathbf{N}_A(\xi) \quad , \quad \mathbf{B}_B(\xi) = \mathbf{R}\, \mathbf{N}_B(\xi) \tag{7}$$

In order to obtain the element stiffness matrix, the classical procedure is followed. First, the Principle of Virtual Work (PVW) is applied along the element mid-plane surface:

$$(\delta \boldsymbol{u}_e)^T \boldsymbol{F}_e = \int_L (\delta \mathbb{r}^{nt})^T\, \mathbf{t}^{nt}\, dL \tag{8}$$

Replacing the relative displacement vector $\mathbb{r}^{nt}$ with expression (6), grouping terms around $(\delta \boldsymbol{u}_e)^T$ and eliminating this term from the equation, the weak form of equilibrium for the interface element is obtained as:

$$\boldsymbol{F}_e = \int_L \mathbf{B}^T\, \mathbf{t}^{nt} dL \tag{9}$$

The general format of a linear constitutive relation with stiffness $\mathbf{D}$ and initial stress $\mathbf{t}_0^{nt}$ is now considered as:

$$\mathbf{t}^{nt} = \mathbf{D}\, \mathbb{r}^{nt} + \mathbf{t}_0^{nt} \tag{10}$$

Replacing (9) into (8) leads to the expressions of the element stiffness matrix $\mathbf{K}_e$ and the initial force vector $\boldsymbol{F}_e^0$:

$$\boldsymbol{F}_e = \mathbf{K}_e\, \boldsymbol{u}_e + \boldsymbol{F}_e^0 \tag{11}$$

$$\mathbf{K}_e = \int_L \mathbf{B}^T\, \mathbf{D}\, \mathbf{B}\, dL \qquad , \qquad \boldsymbol{F}_e^0 = \int_L \mathbf{B}^T\, \mathbf{t}_0^{nt} dL \tag{12}$$

that may be also rephrased in terms of upper and lower B matrices:

$$\mathbf{K}_e = \int_L \begin{bmatrix}\mathbf{B}_A^T \\ \mathbf{B}_B^T\end{bmatrix} \mathbf{D}\, [\mathbf{B}_A \;\; \mathbf{B}_B] dL \qquad , \qquad \boldsymbol{F}_e^0 = \int_L \begin{bmatrix}\mathbf{B}_A^T \\ \mathbf{B}_B^T\end{bmatrix} \mathbf{t}_0^{nt} dL \tag{13}$$

3 ZERO-THICKNESS MORTAR INTERFACE

3.1 Discretization/Formulation

Zero-thickness mortar/interface elements are defined as the contact in between two continuum body surfaces denoted as "Surface A" and "Surface B", which in the general situation (and as the main difference with standard interface elements) will exhibit "unmatched" meshes (nodes on both sides will not coincide one-to-one). The contact surface itself is considered a separate entity and is called "Surface C". The discretization into mortar/interface elements is achieved by projecting all nodes from each side, surfaces A and B, onto the mid-plane surface C, and then defining one mortar element for each one of the resulting segments (Fig. 2).

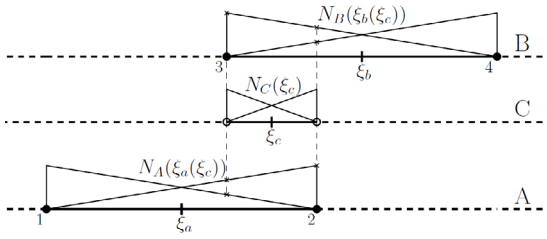


Figure 2. Geometry of mortar interface element

A standard displacement-based interpolation is defined independently for each the two sides of the mortar-interface element, with local coordinates ξ_A and shape functions $N_A^{(i)}(\xi_A)$ for surface A, and local coordinates ξ_B and shape functions $N_B^{(i)}(\xi_B)$. Additionally, a third local coordinate ξ_C also varying in the range [-1,1] is defined along the mid-plane surface of the interface/mortar element segment, as well as the corresponding interpolation functions $N_C^{(i)}(\xi_C)$. This choice of the mortar surface along the mid-plane surface has the advantage of a symmetric treatment of the two sides of the discontinuity [7,8].

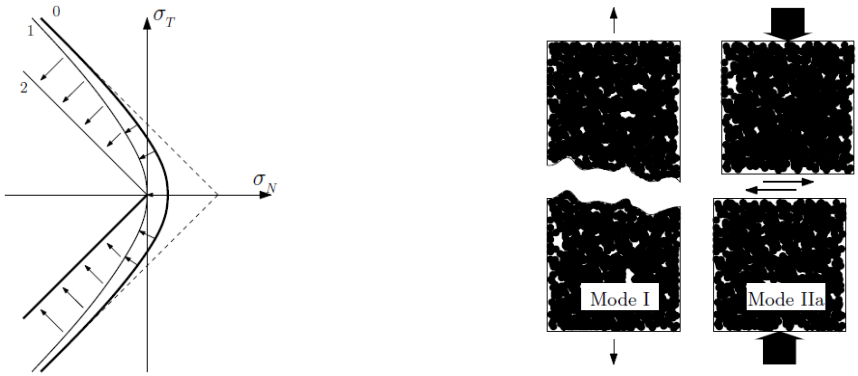
Similarly to the classical interface elements, by assuming general linear constitutive behavior (10), the stiffness matrix and initial force vector of the mortar/interface element may be obtained by direct application of the PVW along the mortar surface. This leads to an expression analogous to (11), in which the stiffness and initial force vector of the mortar/interface element $\mathbf{K}_e$ and $\boldsymbol{F}_e^0$ take the form:

$$\mathbf{K}_e = \int_{L_C} \begin{bmatrix} \mathbf{B}_A^T(\xi_A) \\ \mathbf{B}_B^T(\xi_B) \end{bmatrix} \mathbf{D}[\mathbf{B}_A(\xi_A)\ \ \mathbf{B}_B(\xi_B)]\ dL_C \quad , \quad \boldsymbol{F}_e^0 = \int_{L_C} \begin{bmatrix} \mathbf{B}_A^T(\xi_A) \\ \mathbf{B}_B^T(\xi_B) \end{bmatrix} \mathbf{t}_0^{nt}(\xi_C)\ dL_C \tag{14}$$

Although formally similar to (13), the matrices in expressions (14) exhibit a fundamental difference w.r.t. those: the shape functions involved in their components are now $N_A^{(i)}$ for $\mathbf{B}_A$, which is parametrized in terms of ξ_A, and $N_B^{(i)}$ for $\mathbf{B}_B$, which is parametrized in terms of ξ_B. In spite of that, the integrals in (14) are performed over the domain of the mortar surface C, along which the position of integration points (where and constitutive stiffness, history variables, etc. are evaluated) is parametrized in terms of ξ_C. Therefore, a mapping needs to be established between ξ_C and ξ_A, and also between ξ_C and ξ_B. More details of this derivation may be found in [9].

3.2 Extension to non-linear constitutive behavior

The extension of previous elastic formulation to non-linear constitutive behavior of the mortar/interface contact surface may be achieved by means of an iterative process in which, at each iteration, $\mathbf{K}_e$ and $\boldsymbol{F}_e^0$ are recalculated to represent the new tangential stiffness and residual force vector, respectively. In this study, an existing and extensively verified normal/shear cracking constitutive model is chosen to characterize the behavior of the interface. This model is defined in terms of the normal and shear stresses, with a hyperbolic surface characterized by three geometric parameters: friction angle, cohesion and tensile strength. The evolution of these geometric parameters is controlled by a single history variable: the work spent on fracture processes. The model covers the full range of cracking from uniaxial tension to shear-compression, including those two limit situations, i.e.: (1) cracking under pure tension with zero shear stresses (Mode I) when the surface is reached along the horizontal axis; and (2) cracking under shear and very high compression when the surface is reached in its asymptotic region, where the hyperbola approaches a Coulomb criterion (Mode IIa), as depicted in Figure 3. More details of the constitutive model are given in [5,10]



a) Evolution of cracking surface **b)** Elemental modes of fracture

Figure 3. Hyperbolic cracking model

4 NUMERICAL EXAMPLES

Two simple examples are presented in this section to illustrate that the proposed mortar interface formulation model is capable of reproducing uniform basic stress fields in spite of unmatched meshes on both sides.

4.1 Example 1: uniaxial compression test

The geometry and boundary conditions of the first example are shown in Figure 4. It consists of two horizontal layers of the same material but unmatched meshes, connected with a line of mortar/interface elements. A uniform normal stress is applied on the top face of the mesh while the bottom face remains fixed vertically, and free to expand horizontally. The parameter values used for the continuum elements are: E =10,000 MPa and $\upsilon = 0$. The only relevant interface parameters in this case are normal and tangential elastic stiffness $K_N = K_T = 1e^7$ MPa/m.

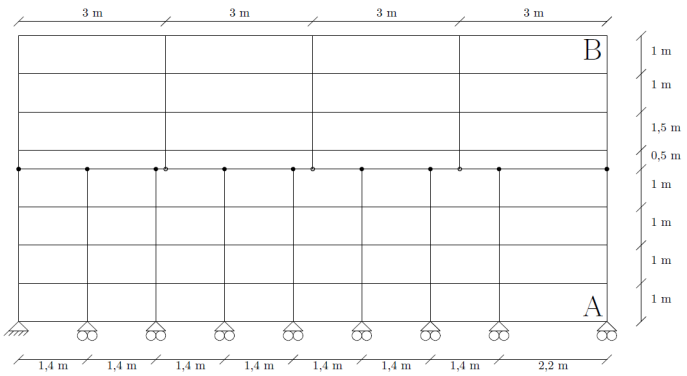


Figure 4. Example 1: geometry and boundary conditions

The results are represented in Figures 5 and 6. Fig.5 depicts the stress distribution obtained along the discontinuity line, and Figure 6 depicts the principal stresses in the continuum elements. As shown, the normal stress turns out constant and with the correct value along all mortar/interface elements and perfectly constant and well aligned in the continuum in spite of the unmatched mesh geometry.

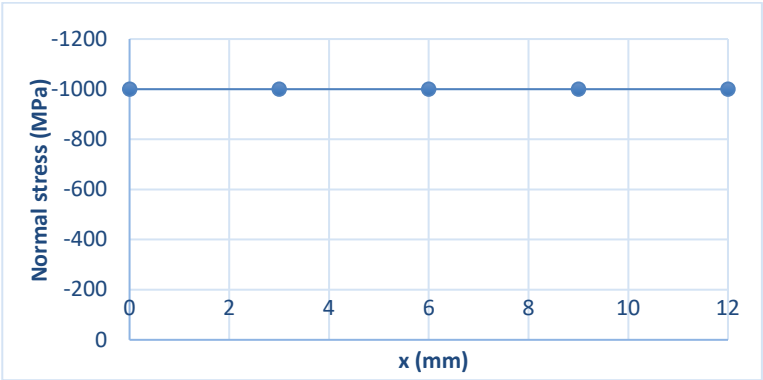


Figure 5. Compression test: normal stress along discontinuity

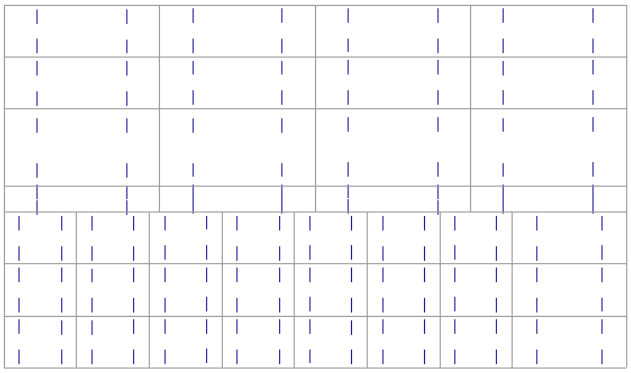


Figure 6. Compression test: principal stresses in the continuum elements.

4.2 Direct shear under high compression

The second example consists of a direct shear test, which is performed on the same geometry and as a continuation of the calculation presented in the previous example, by adding a second load step. This load consists of an increasing tangential displacement up to $\delta_t = 1.0e^{-3}$ m. applied on the nodes on the upper side of the mortar/interface line, while at the same time restricting the horizontal movement of the lower nodes of the same elements. The parameters used for the continuum and for elastic part of the interface are the same as in previous example, and the remaining parameters of the interface (now indeed relevant) are: initial friction angle $\tan\varphi_0 = 0.8785$, initial tensile strength $\chi_0 = 3.0$ MPa, initial cohesion $C_0 = 4.0$ MPa, fracture energy mode I, $G^f_I = 0.2$ MPa·m, energy mode IIa, $G^f_{IIa} = 2$ MPa·m and normal stress at which dilatancy vanishes, $\sigma_{dil} = 0$ MPa.

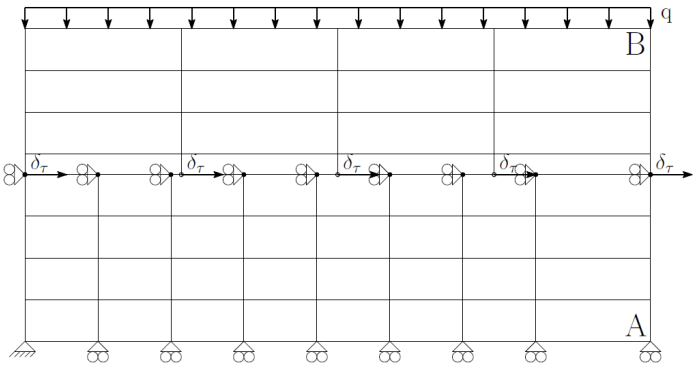


Figure 7. Direct shear under high compression: Geometry and boundary conditions

Figure 8 shows the evolution of the tangential stresses obtained at a point of the mortar/interface contact, as a function of the tangential displacement prescribed. The curve obtained directly reproduces the constitutive prediction. It has to be noted that the results show at all times uniform state of stress and deformation in both the continuum and the mortar/interface contact. Note that the results obtained are not at all trivial since, although tangential displacements may be applied to the mortar nodes directly, the normal stress is

applied on the top surface of the domain, which makes the results totally dependent on the overall correct structural response.

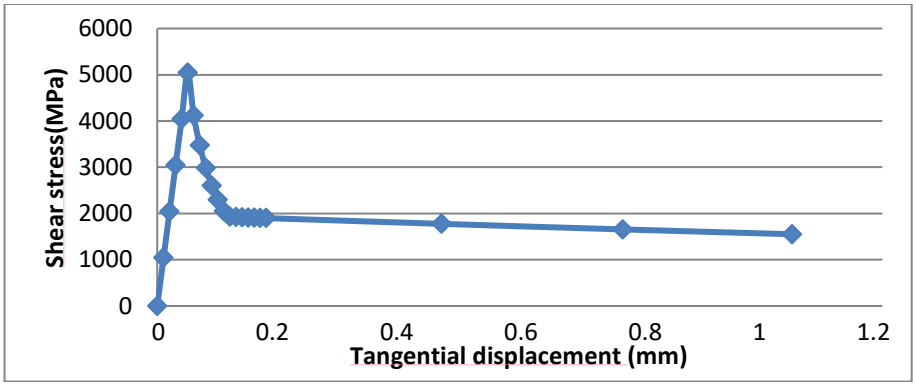


Figure 8. Results of the shear test: shear stress vs. tangential relative displacement.

5 CONCLUDING REMARKS

A general zero-thickness mortar/interface formulation is described in this paper. These elements may be used to connect continuum elements in the general case of non-conforming discretization between the elements of two sides of interface. Simple numerical examples are proposed to test the performance of the approach, and the results obtained turn out correct, that is the mortar/interface element developed succeeds in transmitting properly the compression and shear stresses applied through the interface, even in the scenario of totally unmatched meshes. The results presented are a part of a wider scope research aimed at modeling the transition between fracture of quasi-brittle materials and contact friction between the resulting fragments.

ACKNOWLEDGEMENTS

The work was partially supported by research grants BIA2016-76543-R from MEC (Madrid), which includes FEDER funds, and 2017SGR-1153 from Generalitat de Catalunya (Barcelona). The FPU fellowship from MEC (Madrid) to the first author is also greatfully acknowledged.

REFERENCES

[1] Goodman R.E., Taylor R.L., Brekke T. A model for the mechanics of jointed rock. J Soil Mech. Found. Div. Proc. ASCE (1968) 94.

[2] Bernardi C., Maday Y., Patera A.T. A new nonconforming approach to domain decomposition: the mortar element method. In H.Brezis and J. L. Lios, editors, Nonlinear Partial Differential Equations and Their Applications, Collège de France Seminar, Piman, (1987).

[3] Wohlmuth B.I. Discretization methods and iterative solvers based on domain decomposition. Springer, (2001).

[4] Yang B., Laursen T.A., Meng X.N., Two dimensional mortar contact methods for large deformation frictional sliding, Int. J. Numer. Methods Engrg. (2005) 62 1183–1225.

[5] Carol I., Prat P.C., López C.M. A normal/shear cracking model. Application to discrete crack analysis, ASCE J. Engrg. Mech. 123 (8) (1997) 765–773.
[6] Gens A., Carol I., and Alonso, E. An interface element formulation for the analysis of soil-reinforcement interaction. Computers and Geotechnics. (1988) 7:133-151.
[7] Simo J.C., Wriggers P., Taylor R.L. A perturbed lagrangian formulation for the finite element solution of contact problems. Computer Methods in Applied Mechanics and Engineering; (1985) 50:163–180.
[8] El-Abbasi N. and Bathe K. J. Stability and patch test performance of contact discretizations and a new solution algorithm. Computers and Structures, (2001) 79: 1473-1486.
[9] de Francisco, M., and Carol, I. Displacement-based and hybrid formulations of zero-thickness mortar/interface elements, with application to fracture mechanics. Manuscript in preparation.
[10] Caballero A., Willam K.J., Carol I. Consistent tangent formulation for 3D interface modeling of cracking/fracture in quasi-brittle materials. Comput. Methods Appl. Mech. Engrg. 197 (2008) 2804–2822.

XV International Conference on Computational Plasticity. Fundamentals and Applications
COMPLAS 2019
E. Oñate, D.R.J. Owen, D. Peric , M. Chiumenti, and Eduardo de Souza Neto (Eds)

NEW DEVELOPMENTS IN THE APPLICATION OF CONFIGURATIONAL MECHANICS TO CRACK PROPAGATION

L. CRUSAT, I. CAROL AND D. GAROLERA

ETSECCPB (School of Civil Engineering)
Universitat Politècnica de Catalunya (UPC)
08034 Barcelona, Spain
e-mail: laura.crusat@upc.edu, ignacio.carol@upc.edu, daniel.garolera@upc.edu

Key words: Configurational mechanics, crack propagation, nodes relocation.

Abstract. The numerical description of discrete cracks and their propagation remains one of the main difficulties in the modeling of quasi-brittle materials such as rock or concrete. An emerging powerful approach is the use of Configurational Mechanics concepts, in such a way that crack trajectory really corresponds to a structural energy minimum and is not predetermined by the initial mesh lines. In the implementation developed, discrete cracks, represented by zero-thickness interface elements, are reoriented on the basis of configurational or material forces, calculated in a FEM context by an integration over the elements of the Eshelby energy-momentum tensor. The strategy is illustrated with an application example for which the fracture path is known a priori, and the initial mesh layout is chosen such that the lines zig-zag significantly with respect to it. The results show that the procedure implemented works successfully, that is, mesh lines do succeed in reorienting themselves during configurational iterations, so that the developing crack progressively matches the known physical trajectory.

1 INTRODUCTION

Discontinuities such as cracks or fractures play a fundamental role in the description of mechanical behavior of concrete, rock and other quasi-brittle materials. In the particular cases that the crack trajectory is known a priori (e.g. due to symmetry), accurate numerical descriptions of crack initiation and development may be obtained with the help of Fracture Mechanics principles e.g. using Hillerborg's Fictitious Crack Model [1], or extensions of it via zero-thickness interface elements equipped with appropriate energy-driven constitutive models [2]. In the general case, however, the determination of the crack trajectory itself remains as the main challenge. One solution is to consider all the lines in the mesh as potential crack lines, and let them open/close depending on local stresses [3,4,5]; although this means that cracks can only follow the original mesh lines, which in general may lead to zig-zagging cracks with excessive unrealistic roughness. Alternatively, crack trajectory may be adjusted by modifying the mesh geometry, although the quality of the resulting crack path may be strongly dependent on the criterion used for determining crack orientation. Traditionally, local criteria were used such as direction of maximum tensile stress (e.g. [6]). However, it is well accepted that cracks will develop in the direction that minimizes the global energy of the structure, concept that may be developed and implemented in FE calculations with the help of Configurational Mechanics. The concepts of configurational (or

material) forces and configurational stresses were originally introduced by Eshelby [7]. In the context of the FEM, configurational forces may be understood as derivatives of the global structural energy with respect to the nodal coordinates [8]; thus, as a general idea, moving the nodes in the direction of configurational forces should decrease the global structural energy. Application of the above concepts to mesh optimization and crack propagation has been described in the literature [8-13]. In [14], the authors discussed those concepts with emphasis on the distinction between energy changes due to discretization error ("configurational noise"), and due to physical geometric changes such as dimensions or crack trajectory. In the present paper, recent developments in the application of configurational mechanics to crack propagation are summarized. In the implementation developed, cracks are represented using fracture-based zero-thickness interface elements. During the calculation, configurational forces are evaluated and nodes are relocated to optimize crack trajectory without changing the mesh topology.

2 FEM+Z COMBINED WITH CONFIGURATIONAL MECHANICS

A model based on combining traditional displacement-based FEM including zero-thickness interface elements (FEM+z approach), with the contribution of Configurational Mechanics, is proposed to evaluate crack propagation with non-preestablished paths. FEM+z has been extensively used in the past to describe the behavior of fractures with a fixed position, while configurational mechanics provides information on how to move nodes to reorient interface elements when they start cracking, in order to approach a global energy minimum [14].

The FEM+z approach for non-linear fracture analysis is an existing and extensively-tested methodology. It consists of using traditional zero-thickness interface elements [15] in combination with a fracture-based constitutive law [16], while the continuum remains elastic (or visco-elastic) at all times.

In the context of a general, large-strain formulation of the FEM, global elastic energy is a function of original location as well as final node position after deformation $\mathbf{x}$, i.e. $\psi = \psi(\mathbf{X}, \mathbf{x})$, and configurational nodal forces may be defined as the negative gradient of energy with respect to the original node locations (at constant $\mathbf{x}$), i.e.:

$$\hat{\mathbf{f}} = -\left.\frac{\partial \psi}{\partial \mathbf{X}}\right|_{\mathbf{x}=\mathbf{ct}} \tag{1}$$

Developing this equation with standard FE assumptions, configurational nodal forces may be expressed as:

$$\hat{\mathbf{f}} = \int \hat{\mathbf{B}}^T \boldsymbol{\Sigma}\, dV \tag{2}$$

where $\widehat{\mathbf{B}}$ is the non-symmetric version of the traditional "B" FE matrix, and $\boldsymbol{\Sigma}$ is the "configurational stress" given by Eshelby's energy-momentum tensor [8]:

$$\boldsymbol{\Sigma} = W\mathbf{I} - \mathbf{F}^T\mathbf{P} \tag{3}$$

where W is the elastic energy per unit volume of the undeformed body, $\mathbf{F}$ the deformation gradient and $\mathbf{P}$ the first Piola-Kirchoff stress.

The method implemented basically consists of "moving" the nodes (change their coordinates) by certain magnitude along the directions indicated by configurational forces and, once moved, reevaluate configurational forces and repeat the process iteratively until convergence. Similar to classical deformational analysis, node relocation is subject to some restrictions, such as for instance boundary restrictions not to change the domain geometry.

A peculiarity of zero-thickness interface elements is the presence of double nodes with (generally) the same coordinates. Each pair of nodes may become a cluster of several nodes in the case of interface intersections (Figure 1a). With the purpose of configurational node relocation, all the nodes in a cluser are treated as a single node in a mesh without interfaces (Figure 1b), which is subject to a configurational force equal to the sum of the forces on all the nodes in the cluster.

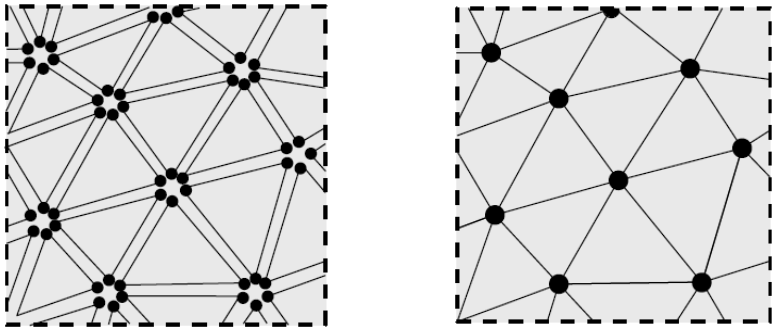


Figure 1: (a) Standard finite element mesh with zero-thickness interface elements in which all nodes in each cluster have the same coordinates, and (b) equivalent mesh without interfaces.

The simultaneous change of nodal coordinates in all the nodes subject to configurational forces has been shown to desestabilize the process. For this reason, only crack tip nodes are allowed to change their coodinates (Figure 2). Every time interface elements have been reoriented, a "mesh relaxation" algorithm (e.g. [17,18]) is applied to improve mesh quality around the modified area.

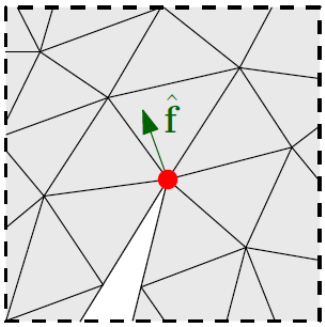


Figure 2: Detail of a deformed FE-mesh. The green arrow represents the configurational force $(\hat{\mathbf{f}})$ direction on a crack tip node.

The relocated nodes require a mapping and update of the corresponding nodal variables in order to maintain consistency of the results. This procedure is done by interpolation of the variables in the new position with respect to the previous mesh configuration. The details of this and other auxiliary procedures involved in the implementation are described in [19].

3 NUMERICAL EXAMPLE

A three-point bending beam test of 5x1m is represented in Figure 3. The three-point bending test is a good example to verify simulations of cracking along non-pre-established path because, due to symmetry, it is known that the crack path should be vertical, along the plane of symmetry and starting from the bottom face of the beam. If the process works correctly, the initial zig-zagging mesh lines should get realigned to this vertical crack path.

Deformational boundary conditions consist of nodes at the lower vertices vertically constrained, and a node at the middle of the upper face with horizontal displacements restricted. The loading consists of vertical displacements at this point prescribed with an increasing value (Figure 3).

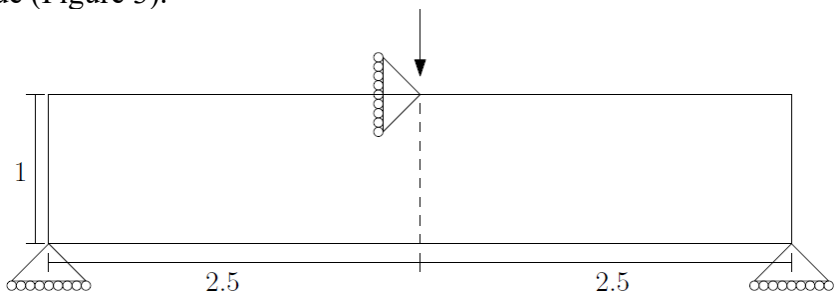


Figure 3: Boundary conditions of three-point bending test example.

The beam is discretized into triangular elements of quadratic order in order to reduce the discretization error (Figure 4). Due to the expected crack trajectory, and to deal with increasing complexity, interface elements are pre-inserted along a single line zig-zagging around the symmetry line of the beam (red line in Figure 4).

The continuum material is assumed linear elastic (small strain), with Young's modulus of E = 15000MPa and Poisson's ratio ν = 0.0.The constitutive model for the interface is the fracture based constitutive model described in [16], with the following parameter values: normal and tangential elastic stiffness $K_N = K_T = 10^7$MPa/m, friction angle tanφ = 0.7, tensile strength χ = 3MPa, cohesion c = 6MPa, energy mode I $G^I_f = 10^{-2}$MPa·m, energy mode IIa $G^{IIa}_f = 10^{-1}$MPa ·m and sigma dilatation σ_{dil} = 30MPa.

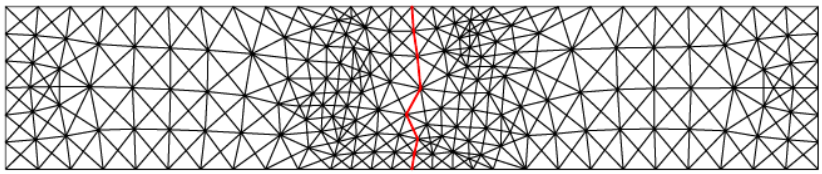


Figure 4: Initial configuration of beam bending realignment.

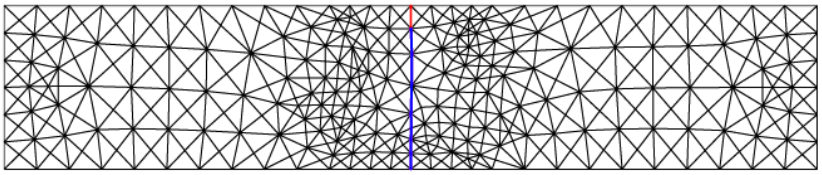


Figure 5: Final configuration of beam bending realignment.

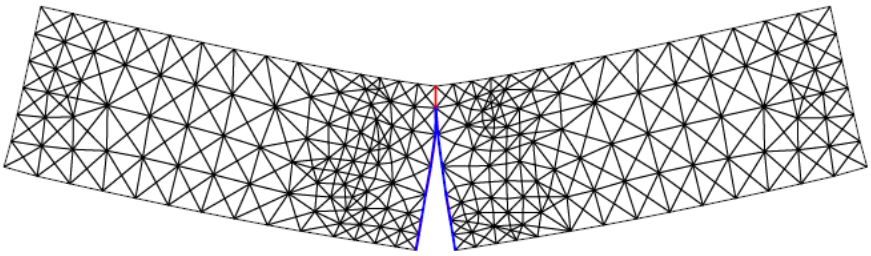


Figure 6: Three-point bending test deformation after solving the deformational and configurational problem (displacement magnification x100).

As Figure 6 depicts, the crack is initiated at the center of the lower face of the beam and propagates upwards. In Figures 5 and 6 the final state of the beam is depicted. These figures show that the iterative configurational process succeeds in orienting the crack along the correct vertical direction.

In the figures, red lines correspond to the zero-thickness interface elements which have not started cracking yet, and therefore, in the scheme implemented they have not triggered the process of moving nodes (although some of them may have changed orientation if they share nodes with an interface which has started cracking, such is the case of the top interface in Figures 5 and 6). Blue lines correspond to the interface elements that have started cracking, and therefore configurational forces may have moved them to an optimal position.

Figure 7 displays two load-displacement curves, the one obtained for the initial configuration fixed (mesh with the distorted crack trajectory), and the other one obtained after crack realignment (solving the FEM problem with the final configuration, mesh with the vertical crack path). As it could be expected, the load-displacement curve obtained from the final configuration exhibits a lower, more realistic peak and post-peak response. This is because in the final configuration interface elements are better oriented and therefore the crack initiates and propagates with lower applied load values.

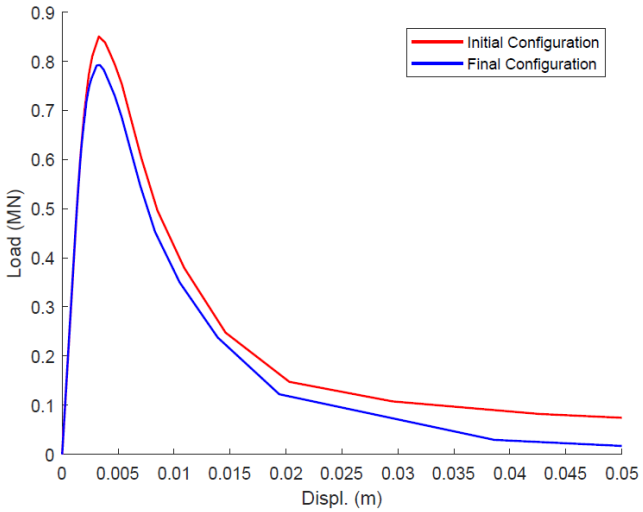


Figure 7: Three-point bending test load-displacement curves.

4 CONCLUDING REMARKS

This article is focused on describing discrete cracks with traditional zero-thickness interface elements of initial random orientation, and obtaining their correct orientation for crack propagation on the basis of concepts of configurational mechanics. In the FEM context, configurational nodal forces indicate the direction in which nodal coordinates should be changed to minimize global energy. An iterative process based on this idea leads to progressive reorientation of interface elements as cracks open and propagate. An example of application consisting of a three-point bending beam shows that the approach proposed succeeds in re-orienting the initially random mesh into a well-aligned crack developing along the symmetry plane of the beam.

ACKNOWLEDGMENTS

This work was partially supported by research grants BIA2016-76543-R from MEC (Madrid), which includes FEDER funds, and 2017SGR-1153 from Generalitat de Catalunya. The FPI fellowship from MEC (Madrid) to the first author is also gratefully acknowledged.

REFERENCES

[1] Hillerborg, K., Modéer, M., and Petersson, P. Analysis of crack formation and crack growth in concrete by means of fracture mechanics and finite elements. *Cement and Concrete Research* (1976) **6(**6): 773-781.

[2] Rots, J. *Computational modeling of concrete fracture*, Doctoral thesis, Technische Universiteit Delft (1988).

[3] Vonk, R.A. *Softening of concrete loaded in compression*. Doctoral thesis, TU Eindhoven, The Netherlands (1992).

[4] Camacho, G. and Ortiz, M. Computational modelling of impact damage in brittle materials. *International Journal of solids and structures* (1996) **33**(20-22): 2899-2938.

[5] Carol, I., López, C.M., and Roa, O. Micromechanical analysis of quasi-brittle materials using fracture-based interface elements. *Int. J. Numerical Methods in Engineering* (2001) **52**(1–2):193–215.

[6] Ingraffea, A.R. and Saouma, V. Numerical modeling of discrete crack propagation in reinforced and plain concrete. *Fracture mechanics of concrete: structural application and numerical calculation*, Springer, Dordrecht (1985) 171-225.

[7] Eshelby, J. D. The force on an elastic singularity *Philosophical Transactions of the Royal Society of London A: Mathematical, Physical and Engineering Sciences* (1951) **244**(877):87-112.

[8] Mueller, R. and Maugin, G. A. On material forces and finite element discretization *Computational mechanics* (2002) **29**(1):52-60.

[9] Maugin, G. A. and Trimarco, C. Psuedomentum and material forces in nonlinear elasticity: variational formulations and application to brittle fracture. *Acta Mechanica* (1992) **94**:1-28.

[10] Mueller, R., Kolling, S. and Gross, D. On configurational forces in the context of the finite element method. *International Journal for Numerical Methods in Engineering* (2002) **53**(7):1557-1574.

[11] Mueller, R., Gross, D. and Maugin, G. Use of material forces in adaptive finite element methods. *Computational Mechanics* (2004) **33**(6):421-434.
[12] Miehe, C. and Gürses, E. A robust algorithm for configurational-force-driven brittle crack propagation with R-adaptive mesh alignment. *International Journal for Numerical Methods in Engineering* (2007) **72**(2):127-155.
[13] Steinmann, P., Scherer, M. and Denzer, R. Secret and joy of configurational mechanics: From foundations in continuum mechanics to applications in computational mechanics *ZAMM-Journal of Applied Mathematics and Mechanics* (2009) **89**(8):614-630.
[14] Crusat, L. and Carol, I. *Application of configurational mechanics to crack propagation,* Proc. of the XIV International Conference on Computational Plasticity. Fundamentals and Applications (COMPLAS), Barcelona, Sept. 2017. International Centre for Numerical Methods in Engineering (CIMNE).
[15] Gens, A., Carol, I. and Alonso, E.E. An interface element formulation for the analysis of soil-reinforcement interaction. *Computers and Geotechnics* (1989) **7**(1-2):133-151.
[16] Carol, I., Prat, P.C. and Lopez, C.M. Normal/shear cracking model: application to discrete crack analysis. *Journal of engineering mechanics* (1997) **123**(8):765-773.
[17] Frey, W.H. and Field, D.A. Mesh relaxation: a new technique for improving triangulations. *International Journal for Numerical Methods in Engineering* (1991) **31**(6):1121-1133.
[18] Schweingruber, M. and Rank, E. *Adaptive mesh generation for triangular or quadrilateral elements.* Proc. of the First European Conference on Numerical Methods, Brussels, Sept. 1992.
[19] Crusat, L. *Numerical modeling of cracking along non-preestablished paths.* Doctoral thesis, Universitat Politècnica de Catalunya (2018).

XIV International Conference on Computational Plasticity. Fundamentals and Applications
COMPLAS 2019
E. Oñate, D.R.J. Owen, D. Peric , M. Chiumenti, and Eduardo de Souza Neto (Eds)

COMPUTATIONAL ANALYSIS OF THE BEHAVIOR OF ATMOSPHERIC POLLUTION DUE TO DEMOGRAPHIC, STRUCTURAL FACTORS, VEHICULAR FLOW AND COMMERCE ACTIVITIES

SUÁREZ G.[1], NIÑO J.A.[2], CHAKIR R.[3], HOYOS J.D.[1,2] AND STREICHENBERGER B.[3]

[1] Grupo de investigación en Matemáticas (GMAT), Escuela de Ingeniería
Universidad Pontificia Bolivariana, Cir.1 #70-01, 050031 Medellín, Colombia,
gustavo.suarez@upb.edu.co, www.upb.edu.co

[2] Grupo de Aeronáutica y Aeroespacial, Escuela de Ingeniería
Universidad Pontificia Bolivariana, Cir.1 #70-01, 050031 Medellín, Colombia, www.upb.edu.co
juliana.nino@upb.edu.co, www.upb.edu.co

[3] Laboratoire Instrumentation, Simulation et Informatique Scientifique (LISIS)
Institut Français des Sciences et Technologies des Transports, de l'Aménagement et des Réseaux (IFSTTAR), 14-20 bd Newton, Francia
rachida.chakir@ifsttar.fr, www.ifsttar.fr/accueil/

Key words: Environmental Pollution, Medellin City model, Mathematical model, Computational Simulation.

Abstract. According to the latest assessments made by the world health organization (WHO-2016), the atmospheric pollution (air), has become one of the main causes of morbidity and mortality in the world, with a steep growth of respiratory diseases, increase in lung cancer, ocular complications, and dermis diseases [1,2,3]. Currently, there are governments which still underestimate investments in environmental care, turning their countries into only consumers and predators of the ecosystem [1,2,3]. Worldwide, several cities have been implementing different regional strategies to decrease environmental pollution, however, these actions have not been effective enough and significant indices of contamination and emergency declarations persist [1,2,3]. Medellín is one of the cities most affected by polluting gases in Latin America due to the high growth of construction sector, high vehicular flow, increase in commerce, besides a little assertive planting trees system, among other reasons [1,2,3]. With the purpose of providing new researching elements which benefit the improvement of air quality in the cities of the world, it is pretended to mathematically model and computationally implement the behavior of the flow of air, e.g., in zones in the city of Medellín to determine the extent of pollution by tightness, impact of current architectural designs, vehicular transport, high commerce flow, and confinement in the public transport system. The simulations allowed to identify spotlights of particulate tightness caused by architectural designs of the city which do not benefit air flow. Also, recirculating gases were observed in different zones of the city. This research can offer greater knowledge around the incidence of pollution generated by structures and architecture. Likewise, these studies can contribute to a better urban, structural and ecological reordering in cities, the implementation

of an assertive arborization system, and the possibility to orientate effective strategies over cleaning (purification) and contaminant extracting systems.

1 INTRODUCTION

In this research, a study was conducted on the dispersion of environmental pollution in several areas of the city of Medellín where there is a high traffic flow, commercial activities, high population density, among other incident factors. The city of Medellín has presented critical environmental conditions that are detrimental to the health of the population, especially in certain periods of the year where air flow is significantly reduced [4,5,6,7].

Medellín is in the region of the Aburrá Valley, composed by a extensive mountainous system, with high demographic density. Another component that has contributed to the accumulation of toxic particulate matter within the city, is the growing development of the construction sector that has not considered the incidence of structural designs (sizes and shapes) in the accumulation of toxic particles. [4,5,6,7].

In order to represent the behavior of air flow, a mathematical-computational model was developed including the detection of the level of particles, the effects of recirculation of the flow, the sealing of the particles by zones, buoyancy of particulate material, between obtained results. A three-dimensional model was elaborated with the structural elements and the urban distribution that make up the city. Conditions such as velocities of the air flow entering the city of Medellín were considered, along the borders of the bored valley, the direction of the wind, velocity profile, sources of gas emission, among others.

The main area where the regions were included for the analysis was established by a surface area of 700m^2. Data and previous studies of METEOBLUE, IDEAM (Institute of Hydrology, Meteorology and Environmental Studies) and SIATA (Early Warning System of Medellín and Aburrá Valley) were collected and analyzed. [4,5,6,7].

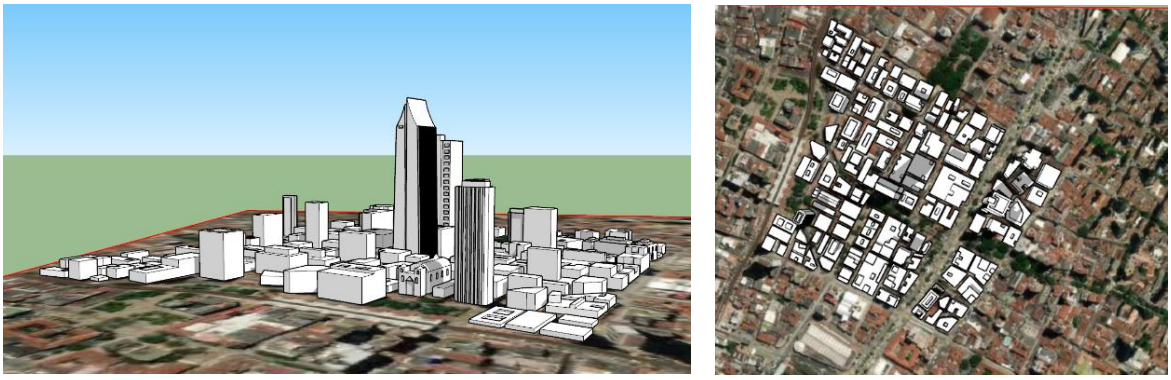


(a) (b)

Figure 1: Aburrá Valley (a) and pollution in the central zone of the city (b).

2 SYSTEM FUNCTIONALITY CONDITIONS

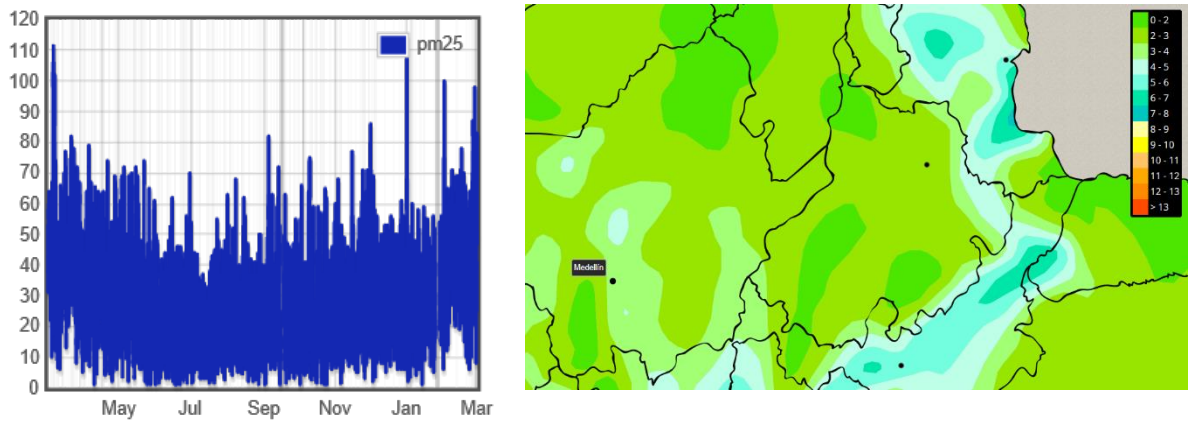
The central zone of the city of Medellín has been chosen for the high automotive, commercial and population flow in it, among other aspects. The structures of the buildings were developed using satellite images and perspectives of the region [8].



(a) (b)

Figure 2: Modeling of the central zone of the city of Medellín, panoramic view (a), aerial view (b).

The inlet conditions of the flows from the Aburrá Valley to the city of Medellín were determined. The levels of pm 2.5 are known for their adverse effects on human health, for this reason they are monitored by the municipal authorities. The SIATA has statistics of the increase of these particles, where it is observed that in July it is the month with the lowest concentration of pm 2.5, while March is the month with the highest concentration, fig. 3 [9,10].

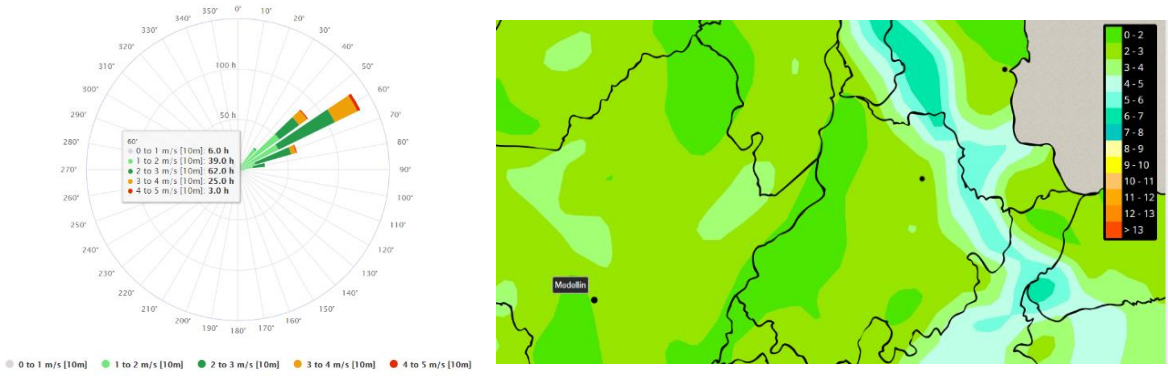


(a) (b)

Figure 3: Levels of pm2.5 in the center of Medellín (a) and wind speed in month of July (b).

It is possible to obtain the wind intensity map for each month of the year from the IDEAM data source. The map showing a higher average wind speed is the month of July with an average of between 3 and 4 m/s at a height of 10m that corresponds to the month with the lowest concentration of pm 2.5 [10,11,12].

According to this relationship, the most desirable scenario to develop the computational model, was the one with the highest concentration of particulate material and lower wind flow velocity. In this way, the acquisition of data from the METEOBLUE global climate database was develop with sampling days between March 11 and 25, 2019 at a height of 10m and 80m, fig. 4 [10,11,12].



(a) (b)

Figure 4: Compass rose 10 m above ground (a) and wind speed in month of March (b).

From the information obtained from METEOBLUE, it was found that the central value of the distribution is 2.3258 m/s at a height of 10m. This data is validated with the map provided by the IDEAM for the month of March in which a speed of between 2 and 3 m/s is observed. The data collection is made on the same date but at 80 m height, obtaining the average value of the distribution of 3 m/s. Once obtained these data, we proceed to modeling the change of speed with height, the power law is used for this purpose commonly [13].

$$U_2 = U_1 \left(\frac{h_2}{h_1}\right)^{\alpha} \tag{1}$$

Where U_2 and U_1 are the wind speeds at heights h_2 and h_1 respectively, and α the roughness index. From the data obtained from METEOBLUE for 10m and 80m, $\alpha = 0.12237$ is found. The wind entry conditions, namely, the profile of speeds at the inlet and the wind direction of 50° given the wind roses obtained from METEOBLUE, was determined.

$$U(h) = 1.755h^{0.12237} \tag{2}$$

3 MATHEMATICAL MODEL

The turbulence model κ-ε, described below, was established for the development of the flow [14]:

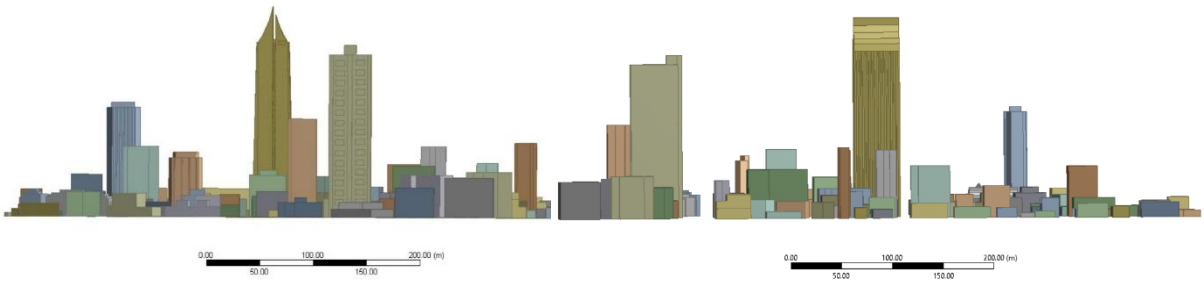
$$\frac{\partial}{\partial t}(\rho k) + \frac{\partial}{\partial x_j}(\rho k u_i) = \frac{\partial}{\partial x_j}\left[\left(\mu + \frac{\mu_t}{\sigma_k}\right)\frac{\partial k}{\partial x_j}\right] + G_k + G_b - \rho\epsilon \tag{3}$$

$$\frac{\partial}{\partial t}(\rho\epsilon) + \frac{\partial}{\partial x_i}(\rho\epsilon u_i) = \frac{\partial}{\partial x_j}\left[\left(\mu + \frac{\mu_t}{\sigma_\epsilon}\right)\frac{\partial \epsilon}{\partial x_j}\right] + C_{1\epsilon}\frac{\epsilon}{k}(G_k + C_{3\epsilon}G_b) - C_{2\epsilon}\rho\frac{\epsilon^2}{k} \quad (4)$$

Where k is defined as the kinetic energy of the turbulent flow, ϵ is the turbulence dissipation rate, ρ is the density, t time, x_i y x_j are the are the Cartesian coordinates, μ_i is the flow speed, μ is the kinetic viscosity, G_k the turbulence production parameter, G_b is the kinetic turbulence energy generated by buoyancy, σ_κ and σ_ϵ are the turbulence coefficients.

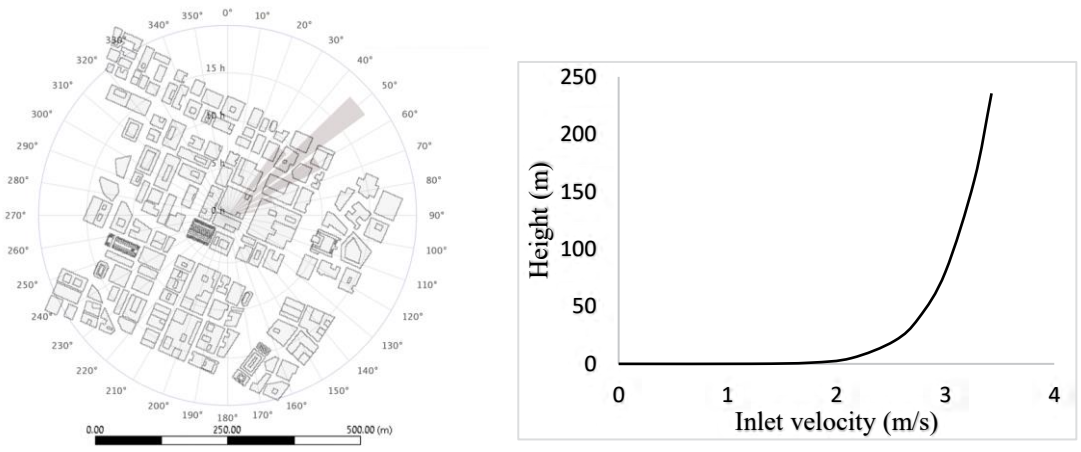
4 COMPUTATIONAL IMPLEMENTATIONS

The three-dimensional architecture of the chosen area of the city of Medellín was built, consisting of several sectors where behavioral studies were carried out. The different orientations of the flow that occur in the city due to the unevenness of the surface were considered [15].



(a) (b)

Figure 5: Architecture model of the chosen area in Medellín, front view (a) and side view (b).



(a) (b)

Figure 6: Wind direction of the area (a) and velocity profile at the inlet (b).

It was implemented as a condition for the inlet of the flow in the Aburrá Valley towards the city by means of the elaboration of a velocity profile provided from the data collection.

A grid with tetrahedral elements was elaborated for a total of 8'017.235 with a controlled

refinement in the areas where the flow was considered to develop with greater speed, it would present turbulence, or also where it was required to evaluate the behavior of the particulate material, fig. 7.

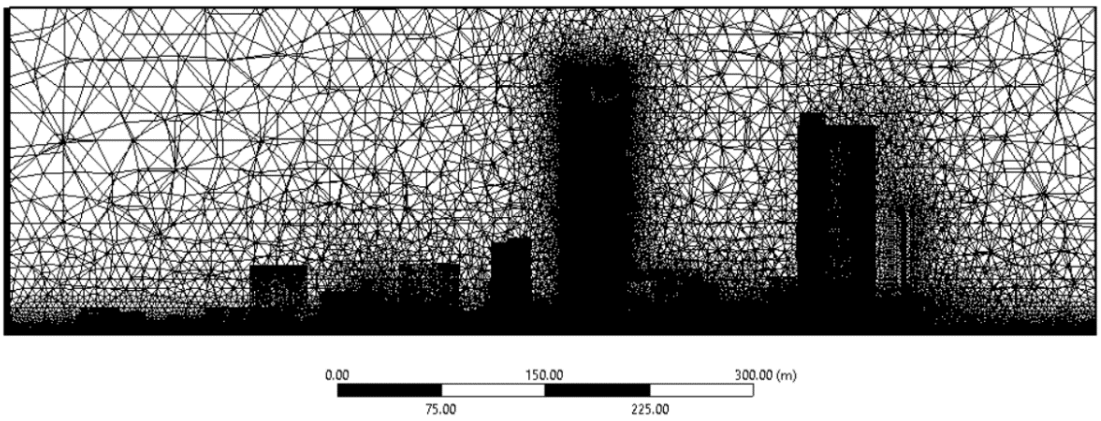
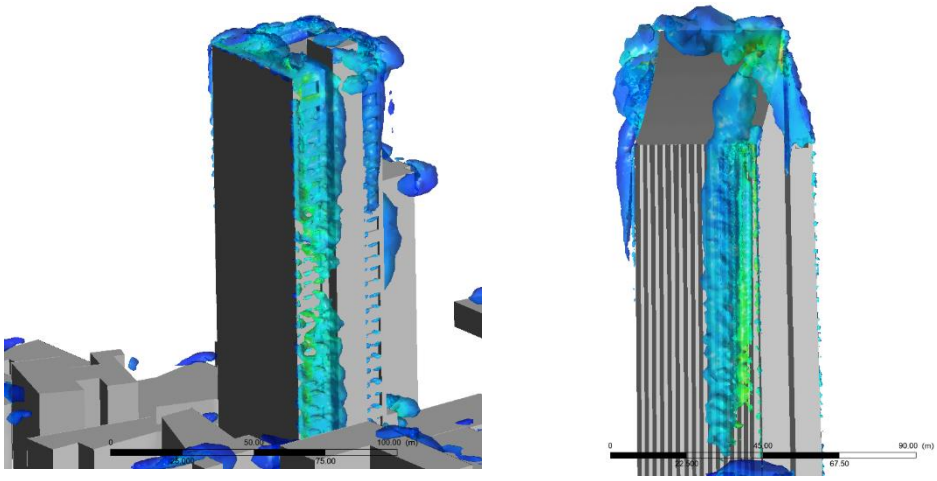


Figure 7: Development of the numerical grid for the volume where fluid behavior was studied within the city.

5 ANALYSIS AND RESULTS

The results have indicated a significant turbulence due to the variability of the architecture in height and sizes and a possible accumulation of contaminating particles in some points of these structures due to recirculation effects. The results are presented below, especially in the *Cámara de Comercio* building and the *Coltejer* building. This behavior is evident in the slenderest buildings.

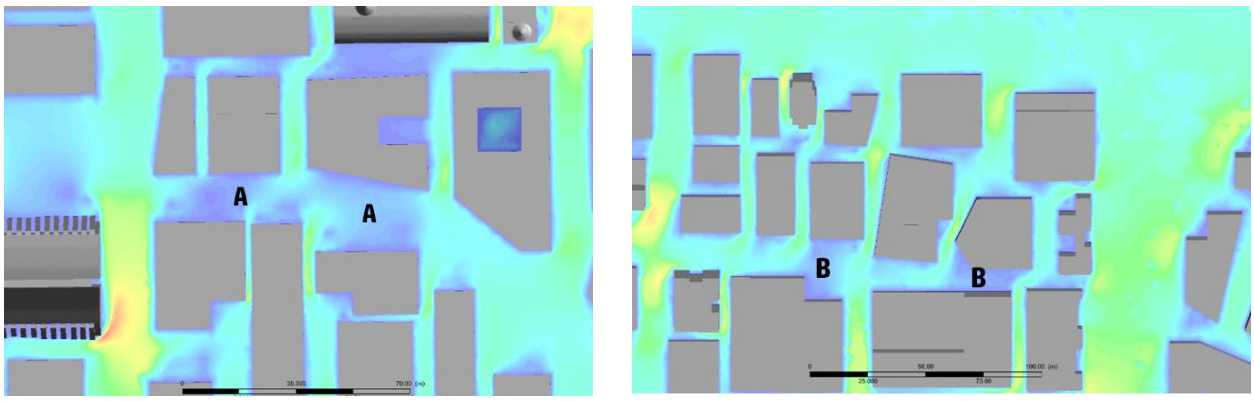


(a) (b)

Figure 8: Simulations of turbulence behavior at specific points and spotlights with recirculation. *Cámara de Comercio* building: Cl. 53 #45 (a), *Coltejer* building: Cl. 52 #42 (b).

Below are some points of accumulation of particulate material where you can also observe sealing points where the air velocity is close to zero. This behavior would not allow polluting emissions to flow and spread. Some streets have an appropriate air circulation (yellow) while

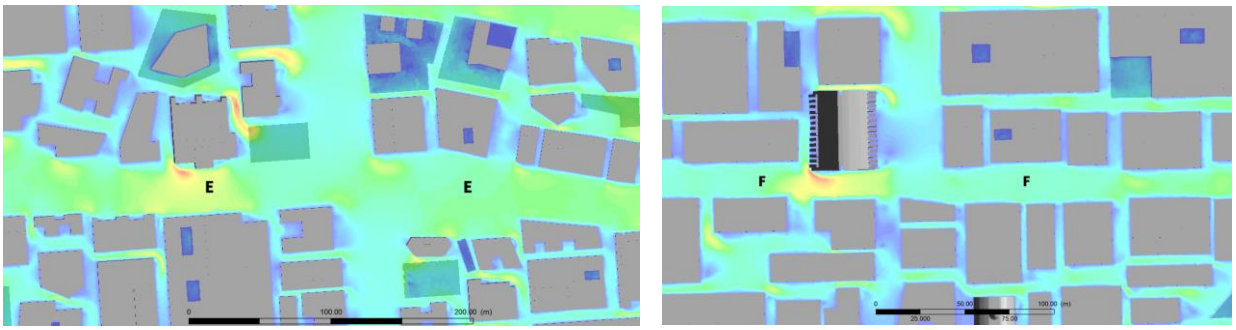
it is visible in different points of stagnation (dark blue), as shown in the fig. 9.



(a) (b)

Figure 9: Computational simulations of flow behavior. Aerial view of the area of the city with stagnation areas Cl. 52 # 50 (A) of the sector (a), and zone Cl. 54 # 47 (B) of the sector (b).

Otherwise, streets that have greater air circulation are shown in fig. 10. Medellín city is composed of narrow and wide streets without a certain order. This irregular urban condition caused a combination in stagnation effects and appropriate circulation in nearby analysis sites.



(a) (b)

Figure 10: High flow areas in Cra 46 *Oriental* Avenue (E), sector (a) and Cra 49 *Junín* Avenue (F), sector (b).

6 CONCLUSIONS

A study of the behavior of air flow in a large area of the city of Medellín was presented. Stagnation areas, turbulence, and recirculation were found, among other elements that contributed to the high contamination index.

It was shown that architecture and its forms hinder air circulation. It was also observed that even when there is a period of high air flow in the city, there are factors such as urban distribution, street dimensions (Cl. 52 # 50, and Cl. 54 # 47) which would not allow the effective dispersion of polluting gases in certain focused areas of the city. The largest recirculation and turbulence were found in the slenderest buildings. The streets Cra 46 *Oriental* Avenue (E) and Cra 49 Junín Avenue presented appropriate flow circulation.

Through the results of this research, it is expected to obtain a greater understanding of the

impact of the effects that are polluting the city of Medellín, including demographic, chronological, structural factors, in addition, the traditional effects such as: the effects of automotive flow, population effects, and commercial among other factors included.

Based on the results, effective solutions can be provided in the future to reduce environmental pollution problems in the city of Medellín and its region.

REFERENCES

[1] Word Health Organization: Ambient air pollution, [https: //www.who. int/gho/phe/ outdoor_air_pollution/en/], 2016.

[2] Aristodemou E. and col, Journal: Environmental Pollution, How tall buildings affect turbulent air flows and dispersion of pollution within a neighbourhood, Volume 233, Pages 782-796, 2018.

[3] Luo M. and col., journal: Science of The Total Environment, Trans-boundary air pollution in a city under various atmospheric conditions, Volume 618, Pages 132-141, 2018.

[4] N. H. Al-Khalidy, «City Scale Pollutant Dispersion Modelling Utilising a Combination of Computational Fluid Dynamics and Standard Air Quality Simulation,» *INTERNATIONAL JOURNAL OF MECHANICS ,* vol. 11, pp. 210-217, 2017.

[5] Blocken, B. Computational Fluid Dynamics for urban physics: Importance, scales, possibilities, limitations and ten tips and tricks towards accurate and reliable simulations. Building and Environment, (2015) 91, 219-245.

[6] E. A. Día, 15 11 2016. [Online]. Available: http://actualidadeducativa.com.co/el-valle-de-aburra-tendra-320-000-arboles-mas/

[7] C. Espanol, 23 03 2017. [Online]. Available: https://cnnespanol.cnn.com/2017/03/23/colombia-declaran-alerta-roja-en-medellin-por-contaminacion-del-aire/

[8] https://www.sketchup.com

[9] SIATA. [Online]. Available: https://siata.gov.co/descarga_siata/index.php/index2/graficador/

[10] IDEAM. [Online]. Available: http://atlas.ideam.gov.co/visorAtlasVientos.html

[11] METEOBLUE. [Online]. Available: https://www.meteoblue.com

[12] https://noticias.caracoltv.com/antioquia/medellin-en-un-nuevo-dia-de-estado-de-alerta-por-su-calidad-del-aire

[13] P. Gousseau, B. Blocken, T. Stathopoulos y G. v. Heijst, «CFD simulation of near-field pollutant dispersion on a highresolution grid: a case study by LES and RANS for a building group in downtown Montreal,» *Atmospheric Environment,* nº 45, pp. 428-438, 2010.

[14] Mei D., Deng Q.H., Wen M., Fang Z. Evaluating Dust Particle Transport Performance within Urban Street Canyons with Different Building Heights. Aerosol. Air Qual. Res. 2016;16:1483–1496. doi: 10.4209/aaqr.2015.07.0436.

[15] https://www.ansys.com/

XV International Conference on Computational Plasticity. Fundamentals and Applications
COMPLAS 2019
E. Oñate, D.R.J. Owen, D. Peric, M. Chiumenti & Eduardo de Souza Neto (Eds)

MODELLING ACID ATTACK OF OIL-WELL CEMENT EXPOSED TO CARBONATED BRINE: EFFECT OF SPECIMEN GEOMETRY ON EXPERIMENTAL RESULTS

L. BARANDIARÁN, J. LIAUDAT, C. M. LÓPEZ AND I. CAROL

School of Civil Engineering of Barcelona (ETSECCPB)
Universitat Politècnica de Catalunya
Campus Nord UPC, 08034 Barcelona, Spain
e-mail: lucia.barandiaran@upc.edu, joaquin.liaudat@upc.edu, carlos.maria.lopez@upc.edu, ignacio.carol@upc.edu

Key words: Carbon sequestration, Oil-well cement, CO_2, Carbon dioxide, Acid attack, Chemical model, Finite Element Method

Abstract. In recent years, the authors and co-workers have developed a diffusion-reaction model for the degradation process of oil-well cements exposed to carbonated brines in the context of CO_2 capture and storage in abandoned oil reservoirs. The model considers two main diffusion-reaction field variables for the concentrations of aqueous calcium and carbon species in the pore solution of the hardened cement paste, complemented by two diffusion-only field variables for chloride and alkalis concentrations. The volume fractions of solid constituents evolve according to the chemical kinetics and chemical equilibrium equations of the reactions involved, determining the diffusivity properties of the material. In this paper, in the framework of an experimental campaign in preparation, this model is used for assessing the effect of different specimen geometries on the kinetics and extent of the acid attack. The results obtained will help to optimize the experimental setup and to the interpretation of the results obtained.

1 INTRODUCTION

Geologic carbon dioxide (CO_2) sequestration represents an effective mitigation action for the stabilization of greenhouse gas concentrations in the atmosphere. The solution consists of the capture and storage of CO_2 generated by industrial processes in geological formations [1]. Among other possibilities, depleted oil and gas fields emerge as the most promising options, mainly because the oil and gas that originally accumulated in the fields traps did not escape for millions of years demonstrating their integrity and safety. However, the presence of abandoned wells that perforate the cap rock may jeopardize the integrity of many mature reservoirs by constituting potential CO_2 leakage pathways [2]. In particular, the long-term chemical stability of the oil-well cements may be affected by the changes in the exposure conditions induced by the CO_2 injections. When ordinary

portland cements, which are alkaline in nature, are exposed to the carbonic acid resulting from the CO_2 dissolution in the water filling the depleted reservoir, a dissolution reaction occurs leading to the decalcification of the cement, with consequent increase of porosity and lost of mechanical strength [3, 4].

In this context, the necessity arises of experimental studies and numerical models for an accurate assessment of the long-term sealing capacity of oil-well cements in the context of carbon sequestration projects. In a previous paper, Liaudat et al. [5] presented a diffusion-reaction model capable of successfully simulating experimental results of Hardened Cement Paste (HCP) degradation of cylindrical samples, carried out by Duguid and Scherer [6]. In a subsequent stage, this diffusion-reaction model is being coupled with a geomechanical model, in order to study possible chemo-mechanical degradation mechanisms of the oil-well cements. For this purpose and as part of the same research project, the fracture mechanical parameters of the degraded HCP will be characterized by means of laboratory experimental tests. In these experiments, prismatic HCP specimens with a central notch will be exposed to a carbonated brine for different time lapses, after which they will be mechanically tested in a three-point bending scheme. With the aim of determining the best notch geometry in order to optimize the time required to produce significant degradation of the HCP around the notch tip, a number of simulations are performed using the model by Liaudat et al. [5]. Additionally, the simulations make it possible to have an estimate of the rate at which calcium is released from the HCP specimens to the chemical reactor, a result which will help to dimension the equipment to be used in the experimental campaign. This paper presents the results obtained in this study.

2 THE MODEL

In the following paragraphs, the diffusion-reaction model proposed by Liaudat et al. [5] is briefly summarized.

2.1 Diffusion-reaction mechanism

As CO_2 dissolves in the brine within the reservoir, carbonic acid (H_2CO_3) is formed and subsequently dissociated mainly into HCO_3^- and CO_3^{2-} (Reactions (1) and (2)). As carbon concentration rises, a diffusion process is generated from the brine into the HCP, increasing the acidity of pore solution in the HCP. In this condition, the portlandite ($Ca(OH)_2$) in contact with the pore solution becomes unstable, dissolving into Ca^{2+} (Reaction (3) towards right). As long as some portlandite remains in contact with the pore solution, the pH will remain high and, consequently, the predominant carbon species will be CO_3^{2-}. Then, the Ca^{2+} ions will react with the CO_3^{2-} ions to form solid calcite (Eq. (4) towards left) within the pore space, locally reducing the porosity of the material. If the carbon concentration in pore solution continues rising, portlandite will be completely depleted and the pH of the pore solution will significantly decline. In consequence, the calcite production will be slowed down and the $CSH_{2.5}$ (cement chemistry notation) will also become unstable, releasing Ca^{2+} to the pore solution (Reaction (5) towards left). For

an additional increment of carbon concentration, further decline of pH will be induced, triggering calcite dissolution (Reaction (4) towards right) and complete decalcification of the $CSH_{2.5}$ (Reaction (5) towards left). The remaining amorphous silicate hydrates $SH_{1.5}$ is considered to be stable in the acidic carbonated brine. In this condition, HCP is totally degraded exhibiting complete mechanical strength loss and high permeability.

$$CO_{2(aq)} + H_2O \leftrightharpoons HCO_3^- + H^+ \tag{1}$$
$$HCO_3^- \leftrightharpoons CO_3^{2-} + H^+ \tag{2}$$
$$Ca(OH)_{2(s)} \leftrightharpoons Ca^{2+} + 2OH^- \tag{3}$$
$$CaCO_{3(s)} \leftrightharpoons Ca^{2+} + CO_3^{2-} \tag{4}$$
$$[Ca(OH)_2][(SiO_2)(H_2O)_{1.5}]_{(s)} \leftrightharpoons Ca^{2+} + 2OH^- + (SiO_2)(H_2O)_{1.5(s)} \tag{5}$$
$$H_2O \leftrightharpoons OH^- + H^+ \tag{6}$$

2.2 Formulation and numerical implementation

The model considers two main diffusion-reaction field equations for the concentrations of aqueous calcium and carbon species in the pore solution of the HCP, complemented by two diffusion-only field variables for chloride and alkalis concentrations, namely:

$$\frac{\partial(\phi c^{ca})}{\partial t} = \nabla(D^{ca}\nabla c^{ca}) + q^{ca} \tag{7}$$
$$\frac{\partial(\phi c^{tc})}{\partial t} = \nabla\left(D^{tc}\nabla c^{tc}\right) + q^{tc} \tag{8}$$
$$\frac{\partial\left(\phi c^{cl}\right)}{\partial t} = \nabla\left(D^{cl}\nabla c^{cl}\right) \tag{9}$$
$$\frac{\partial(\phi c^{r})}{\partial t} = \nabla(D^{r}\nabla c^{r}) \tag{10}$$

where superscripts ca, tc, cl, and r specify calcium, total carbon, chloride, and alkali species, respectively, ϕ is the total porosity, c^β [mol/m^3] is the concentration of aqueous β-species in the pore solution, D^β [m^2/s] is the effective diffusivity of aqueous β-species in the porous medium, and q^β [mol/(m$^3 \cdot$ s)] is the rate of production/consumption of β-species per unit volume of porous medium, which also is a function of the concentration of aqueous species, i.e. $q^\beta = q^\beta(c^{ca}, c^{tc}, c^{cl}, c^r)$, and $\nabla = [\partial/\partial x \ \ \partial/\partial y]^{\mathrm{T}}$. The variable c^{tc} stands for the sum of molar concentrations of each carbonic species present in pore solution, i.e. $c^{tc} = c^{c0} + c^{c1} + c^{c2}$, where $c0$, $c1$ and $c2$ stand for $CO_{2(aq)}$, HCO_3^- and CO_3^{2-}, respectively. Note that the only transport mechanism considered is the Fickian diffusion of the aqueous species. The sink/source terms q^β in Eqs. (7) and (8) are determined by net rates of production/dissolution of the reactive solid species, namely portlandite, calcite, $CSH_{2.5}$ and SH, according to Reactions (3), (4) and (5). In turn, the volume balance of the solid species determine the evolution of the porosity and of the effective diffusivities D^β of the material. The total volume of pore space filled with pore solution includes both the volume of capillary pores and the volume of gel pores within the $CSH_{2.5}$ and SH volume fractions.

It is assumed that the driving force of the dissolution/precipitation reaction of reactive solid α-species is $(1 - \psi^{\alpha})$, where ψ^{α} is the dimensionless saturation index of the pore solution with respect to the solid α-species. Depending on whether $\psi^{\alpha} > 1$, $\psi^{\alpha} = 1$, or $\psi^{\alpha} < 1$, the pore solution is over-saturated, in equilibrium, or under-saturated, respectively, with respect to α-species. The saturation indices are functions of the activities of the primary and secondary aqueous species involved in the corresponding chemical reaction, which are estimated with the well-known Davies equation using the modification on the second term as proposed by Samson and Lemaire [7]. In order to determine the concentration of secondary species, additional calculations need to be performed considering the equilibrium equations of the dissociation Reactions (1), (2) and (6), as well as the electric charge neutrality of the pore solution.

A modified version of the analytical formula proposed by Oh and Jang [8] is used to compute the effective diffusivity of the primary aqueous β-species in the water-saturated HCP (D^{β}). The equation involves four parameters which describe the microstructure of HCP: capillary porosity, percolation threshold, the normalized diffusivity of solid phase, and the percolation exponent. Reduction of tortuosity in pore structure due to $CSH_{2.5}$ dissolution is considered by assuming that the percolation exponent evolves with the decalcification of the $CSH_{2.5}$.

Isothermal and isobaric conditions are assumed at all times, as well as water saturation of the material pores.

The model has been implemented in the Finite Element code DRACFLOW, in-house developed by the group of Mechanics of Materials at UPC (MECMAT/UPC). Formerly, the code has been used to model durability problems in concrete such as drying shrinkage [9], external sulfate attack [10], Alkali-Silica Reaction [11], and high temperatures [12].

3 MODELLING RESULTS

3.1 Model geometry and parameters

For the experimental campaign described in the introduction, prismatic 40 × 40 × 160 mm HCP specimens will be used (Fig. 1a). The specimens will have a central notch to localize fracture in a three-point bending test. In order to optimize the experimental setup, three different possible notch geometries are studied in this paper: 2 × 20 mm rectangular notch, 2 × 10 mm rectangular notch, and a Chevron type notch with the dimensions indicated in Fig. 1b. After curing, the external surfaces of the specimens will be covered with a layer of epoxy resin in order to prevent the acid attack of these zones. In the case of the rectangular notches, all the internal surfaces will remain uncovered, while in the case of the Chevron notch only the 'tip' of the notch will remain uncovered. Under these conditions, the acid attack process may be simulated with two-dimensional geometries as the one schematically represented for the Chevron notch specimen in Fig. 1b, taking advantage of the symmetry plane indicated in Fig. 1a. The models have been spatially discretized with quadrangular linear elements representing the brine and HCP domains, and zero-thickness interface elements representing the brine-HCP interfaces and the internal layer of epoxy in the Chevron notch specimen (Fig. 1b). Simulations have

been performed for a total time of 600 hours (25 days), discretized in increments of 0.2 hours.

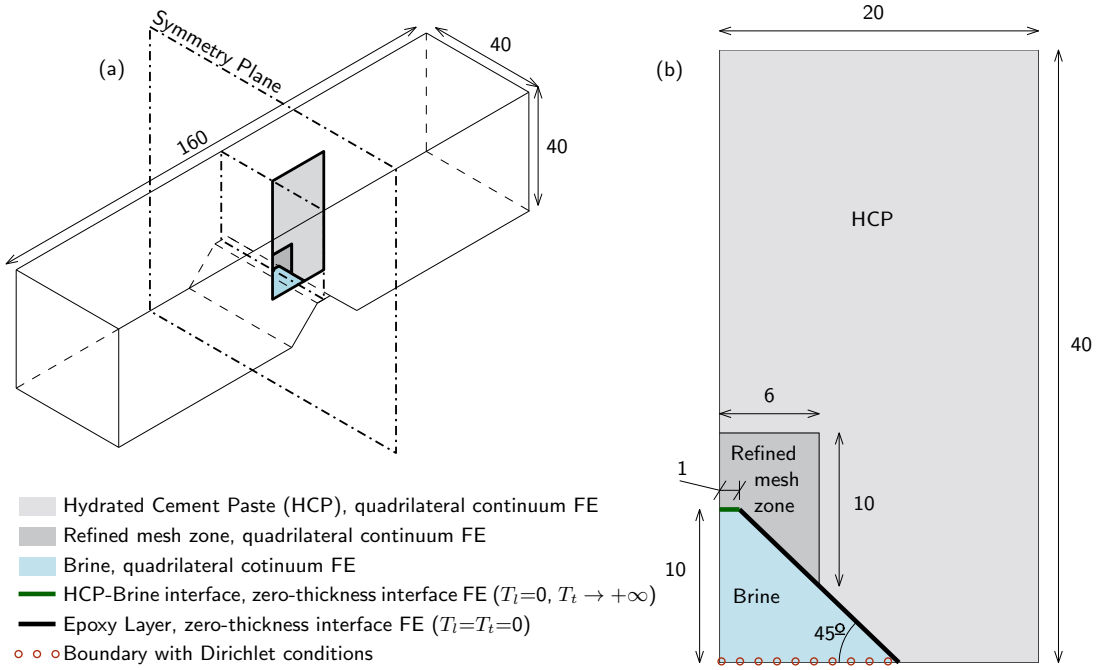


Figure 1: (a) Prismatic specimen geometry. (b) Model geometry and diffusion boundary conditions. Dimensions given in mm.

The specimens will be prepared with cement CEM I 42,5 N-SR 5 [16] and with a water to cement ratio of 0.45. After casting, the specimens will be cured in 0.5 M NaCl brine at 50 °C for 28 days. The initial volume fractions in the HCP are estimated using the expressions given by Brouwers [14, 15], and taking into account the effects of the curing temperature on the gel porosity of the C–S–H reported by Gallucci et al. [17], obtaining the following volume fractions: $CSH_{2.5}$ = 0.206, portlandite = 0.243, Inert Cement Paste = 0.235, Capillary Pores = 0.315, and total (gel + capillary) pores = 0.428.

It is assumed that at the beginning of the exposure to the carbonated brine, the concentrations of alkali and chlorides are homogeneous in the specimens and equal to that of the curing brine, i.e. $c_o^{cl} = c_o^r = 500$ mmol/L. The initial concentration of calcium in pore solution is determined as the saturation concentration of portlandite in 0.5 M NaCl solution at 20 °C, resulting in $c_o^{ca} = 20.95$ mmol/L.

In the reactors, the specimens will be exposed to 0.5 M NaCl solution at 20 °C, saturated with CO_2 at a constant pressure of 1.5 MPa. The total carbon concentration in the brine under these conditions is estimated using the semi-empirical thermodynamic model proposed by Dubacq et al. [13], resulting in 493 mmol/L. Since the brine in the reactor will be continuously renovated, Dirichlet boundary conditions are imposed at the 'mouth' of the notches with $\hat{c}^{ca} = 0$ mmol/L, $\hat{c}^{tc} = 493$ mmol/L, $\hat{c}^{cl} = 500$ mmol/L, and $\hat{c}^r = 500$ mmol/L.

The saturation product constants considered for Reactions (3), (4), and (5) are K_{sp}^{CH} = 7.515E−09, $K_{sp}^{C\bar{C}}$ = 3.554E−09 and K_{sp}^{CSH} = 7.515E−09, for activities in mol/L. The equilibrium constants considered for Reactions (1), (2), and (6) are K_{eq}^{c0}= 4.136E−07, K_{eq}^{c1}= 4.246E−11 and K_{eq}^{w} = 6.893E−15, also for activities in mol/L.

3.2 Results

Figures 2 and 3 show the concentrations of carbon species and calcium in pore solution, respectively, for three different exposure times and for each of the notch geometries considered. Similarly, Figs. 4 and 5 show the volume fractions of portlandite and calcite, respectively, for the same exposure times and notch geometries. The molar rate of calcium leaving the specimen through the notch 'mouth', i.e. the sum of the reactions to the Dirichlet boundary conditions imposed to the nodes at the notch mouth, is plotted as a function of time for each notch geometry in Fig. 6.

In the specimens with rectangular notch, the degradation process progresses mainly in the area close to the notch mouth (where the Dirichlet boundary conditions are applied) and in the horizontal direction. The degradation of the notch tip is slowed down mainly because of two reasons: (i) most of the carbon species flowing into the notch are captured in the formation of calcite in the notch mouth zone, leaving only a small remnant to attack the notch tip zone (Fig. 2); (ii) as calcium ions are released into the notch from the lateral surfaces, the calcium concentration is locally risen reducing or even inverting the calcium concentration gradient from the tip to the mouth of the notch (Fig. 3). These effects are more clearly observed for the 20-mm notch, but can be also be appreciated for the 10-mm notch. In contrast, in the specimen with the Chevron notch and the internal lateral surfaces covered with epoxy resin, none of these mechanisms are developed and, consequently, the degradation front at the notch tip zone progresses at a significantly higher velocity. It must be noted that the better performance of the Chevron notch specimen is mainly because of the layer of epoxy resin covering the internal lateral surface rather than because of the Chevron geometry itself.

Since, from the point of view of the experimental tests that motivated this numerical study (see Sec. 1), the main interest is maximizing the velocity of advancement of the degradation front at the notch tip zone of the specimens, the Chevron notch emerges as the best option. Furthermore, the rate at which calcium is released from the Chevron notch specimen is less than a half of that of the specimens with rectangular notch (Fig. 6). This implies that specimens with Chevron notch will require a much lower flow of fresh carbonated brine in order to keep the calcium concentration in the reactor under a certain maximum value.

4 CONCLUDING REMARKS

- In the context of an experimental campaign in preparation, the diffusion-reaction model developed by Liaudat et al. [5] has been used for preliminary assessing different possible notch geometries for $40 \times 40 \times 160$ mm prismatic specimens to be used in three-point bending tests after being exposed to carbonated brine.

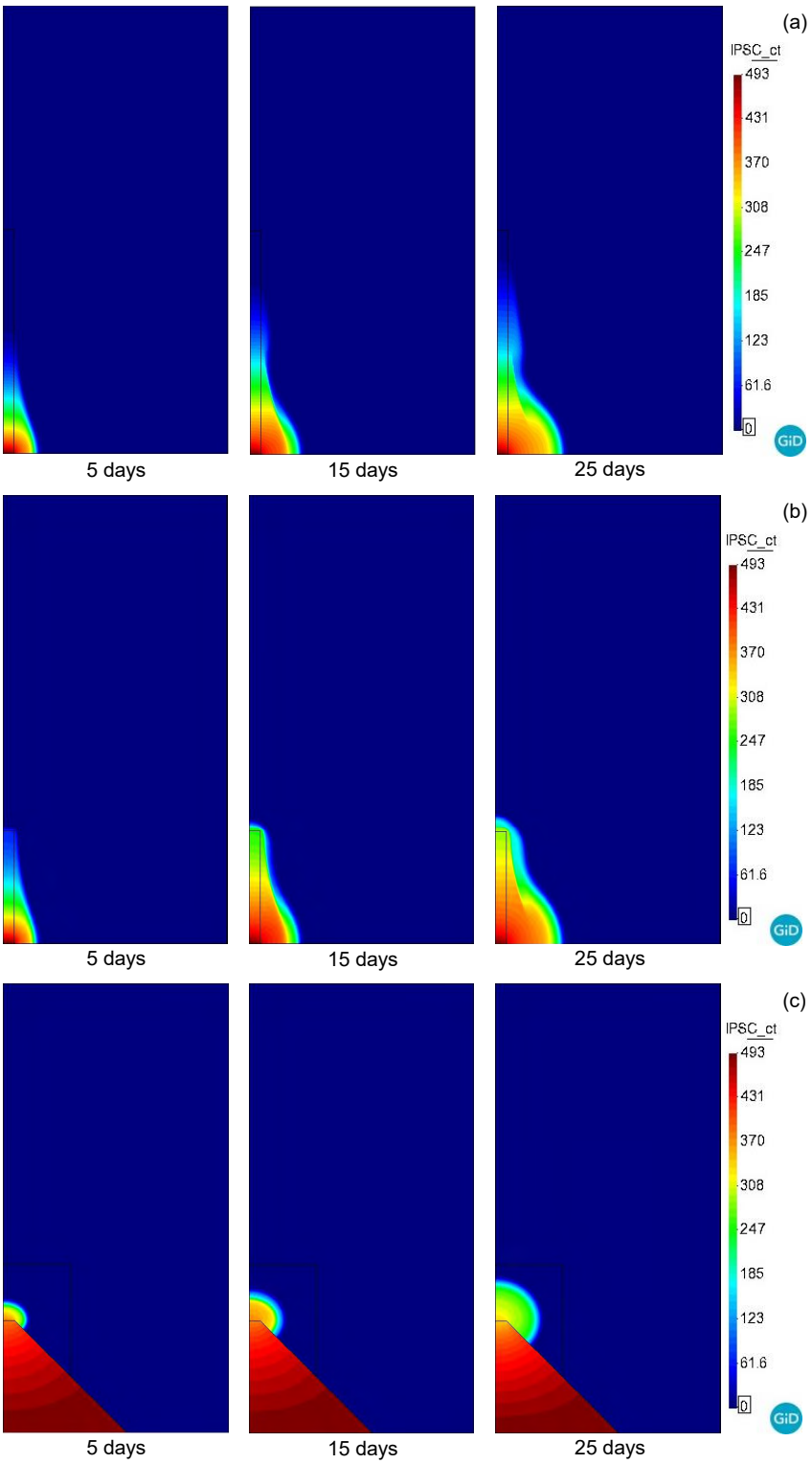


Figure 2: Concentration of carbon species in pore solution [mmol/L]. (a) 2 × 20 mm rectangular notch. (b) 2 × 10 mm rectangular notch. (c) Chevron type notch.

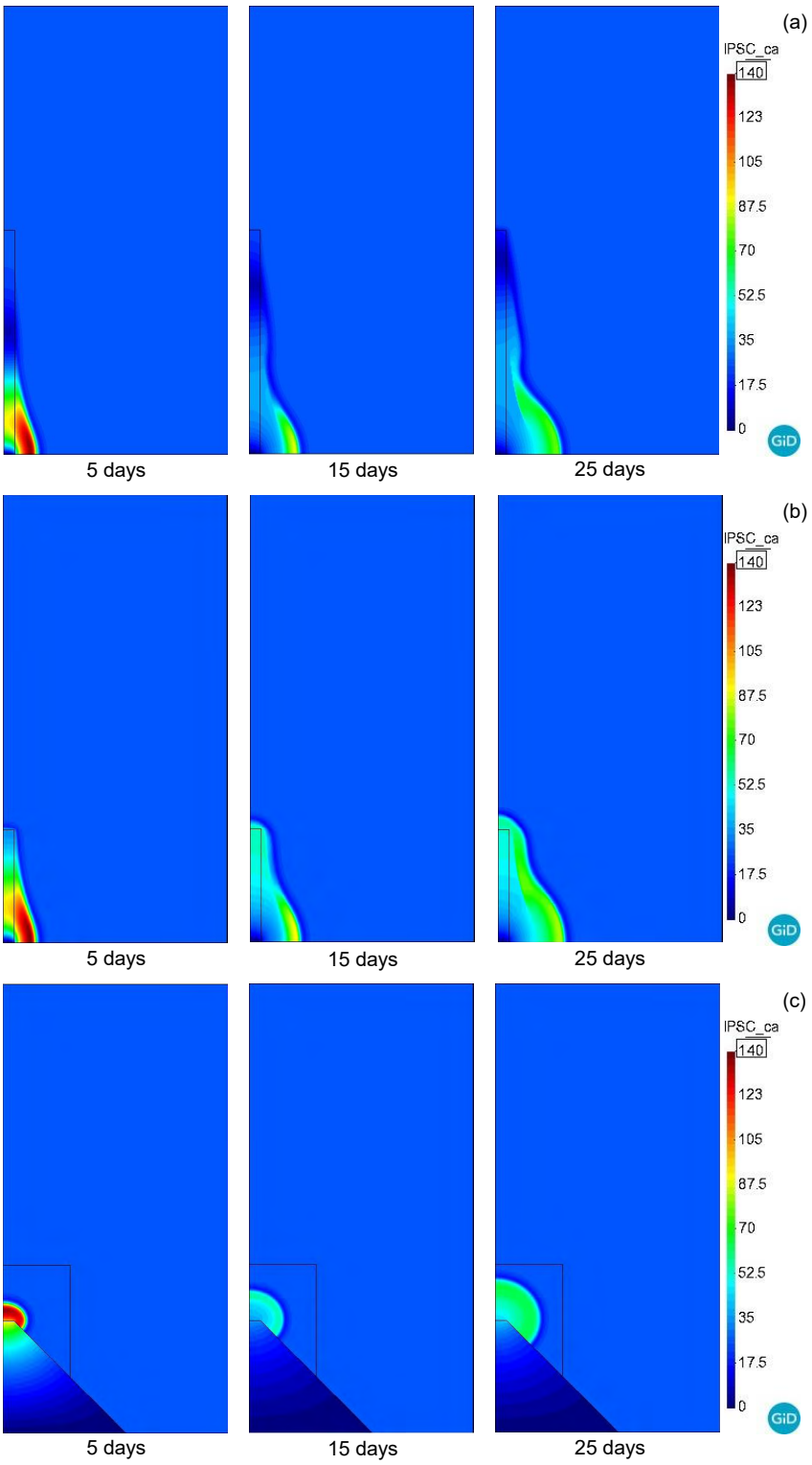


Figure 3: Calcium concentration in pore solution [mmol/L]. (a) 2×20 mm rectangular notch. (b) 2×10 mm rectangular notch. (c) Chevron type notch.

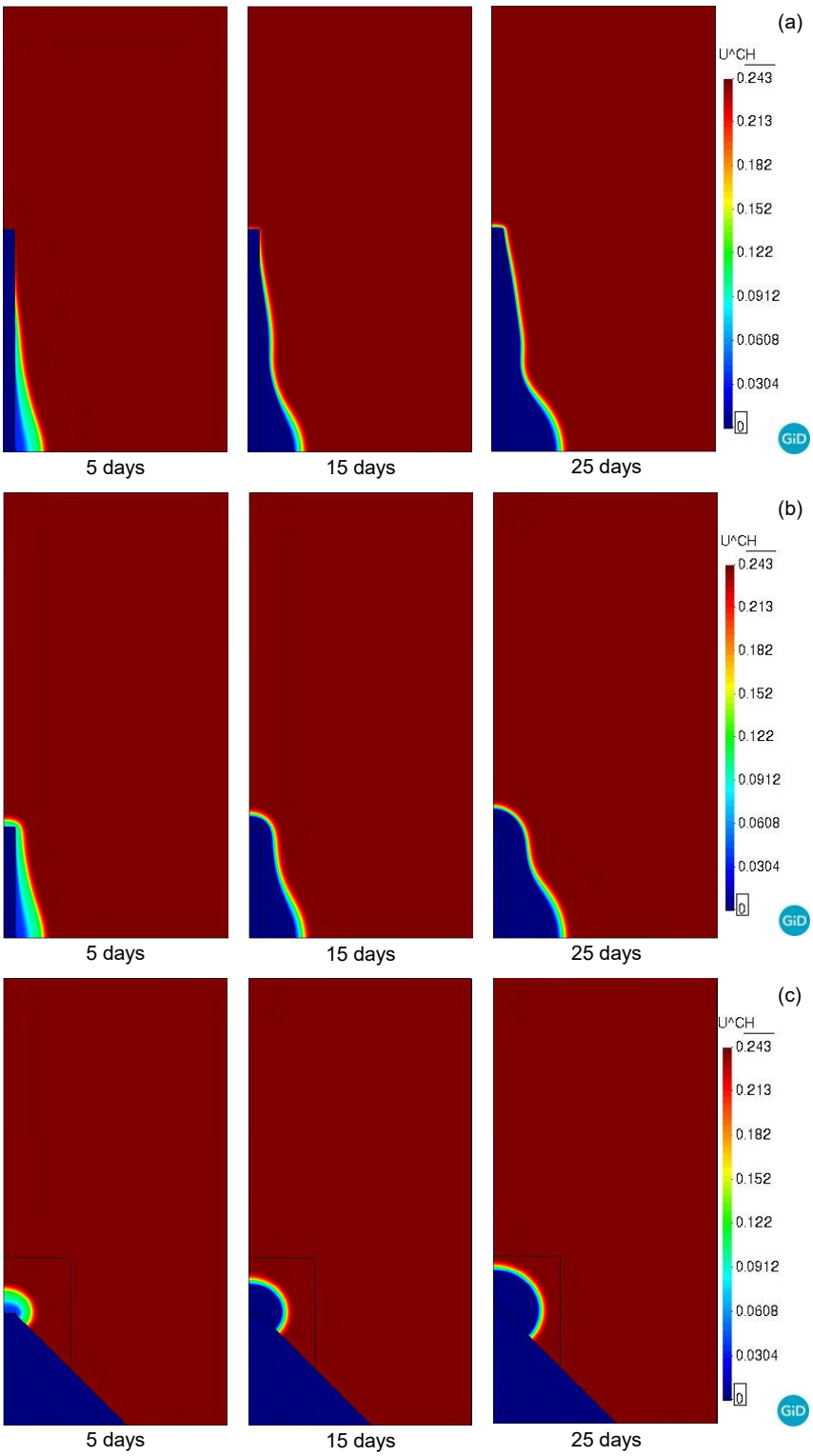


Figure 4: Portlandite volume fraction [m^3/m^3]. (a) 2×20 mm rectangular notch. (b) 2×10 mm rectangular notch. (c) Chevron type notch.

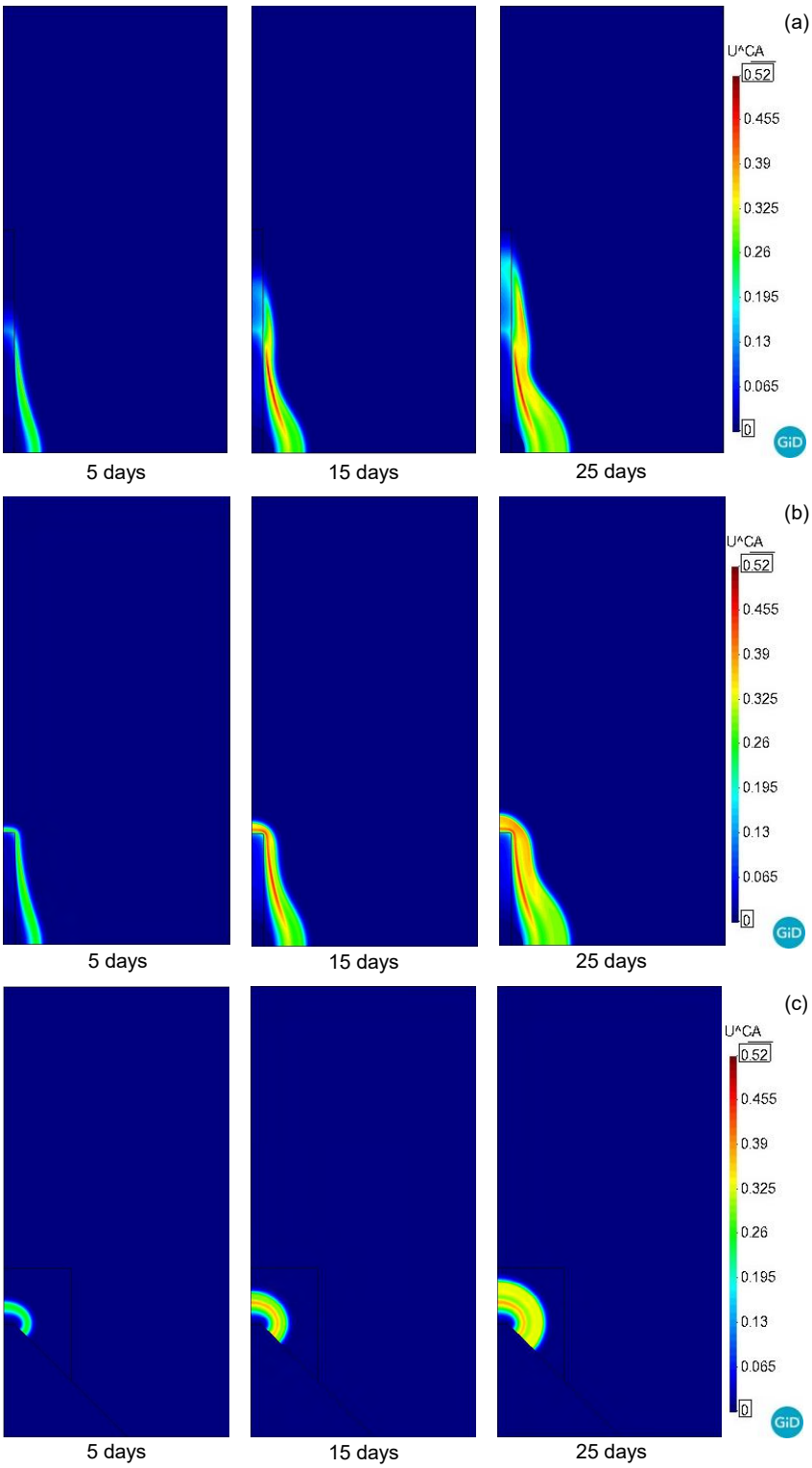


Figure 5: Calcite volume fraction [m^3/m^3]. (a) 2×20 mm rectangular notch. (b) 2×10 mm rectangular notch. (c) Chevron type notch.

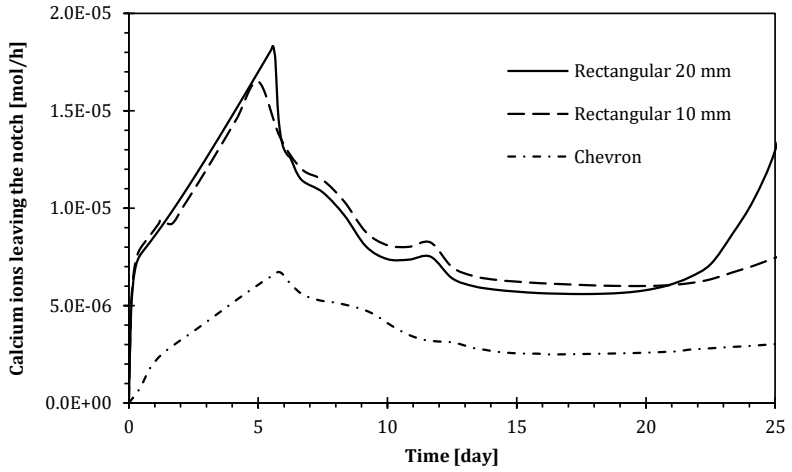


Figure 6: Molar rate of calcium ions leaving the notch at nodes with Dirichlet boundary conditions. Results have been multiplied by 2 and by 0.40 in order to represent the calcium released by a full-size prismatic specimen.

- The simulations have helped to identify the mechanisms determining the advancement velocity of the degradation front at the zone of interest (notch tip zone) in specimens with rectangular notches, leading to the adoption of a more convenient Chevron type notch geometry.

- The simulations have provided an estimate of the rate at which calcium will be released to the surrounding carbonated brine. This value will be used for dimensioning the testing equipment.

ACKNOWLEDGEMENT

This work was partially supported by research grant BIA2016-76543-R from MEC (Madrid), which includes European FEDER funds, and 2017SGR-1153 from Generalitat de Catalunya (Barcelona). The first author also acknowledges her FPI scholarship (BES-2017-083000) from MEC (Madrid).

REFERENCES

[1] IPCC. Special Report on Carbon Dioxide Capture and Storage. Prepared by Working Group III of the Intergovernmental Panel on Climate Change. Cambridge University Press, Cambridge, United Kingdom and New York, NY, USA (2005).

[2] Gasda, S. E., Bachu, S. and Celia, M. A. The potential for CO_2 leakage from storage sites in geological media: analysis of well distribution in mature sedimentary basins. *Environmental Geology* (2004) **46**:6–7.

[3] Kutchko, B. G., Strazisar, B. R., Dzombak, D. A., Lowry, G. V. and Thaulow, N. Degradation of well cement by CO_2 under geologic sequestration conditions. *Environmental Science and Technology* (2007) **41**:4787–4792.

[4] Carey, J. W., Wigand, M. Chipera, S. J., WoldeGabriel, G. Pawar, R., Lichtner, P. C., Wehner, S. C., Raines, M. A. and Guthrie, G. D. Analysis and performance of oil well cement with 30 years of CO_2 exposure from SACROC Unit, West Texas, USA. *International Journal of Greenhouse Gas Control* (2007) **1**:75–85.

[5] Liaudat, J., Martínez, A., López, C. M. and Carol, I. Modelling acid attack of oilwell cement exposed to carbonated brine. *International Journal of Greenhouse Gas Control* (2018) **68**:191–202.

[6] Duguid, A. and Scherer, G.W. Degradation of oilwell cement due to exposure to carbonated brine. *International Journal of Greenhouse Gas Control* (2010) **4**:546–560.

[7] Samson, E. and Lemaire, G. Modeling chemical activity effects in strong ionic solutions. *Computational Materials* (1999) **15**:285–294.

[8] Oh, B. H. and Jang, S. Y. Prediction of diffusivity of concrete based on simple analytic equations. *Cement and Concrete Research* (2004) **34**:463–480.

[9] Idiart, A. E., López, C. M. and Carol, I. Modeling of drying shrinkage of concrete specimens at the meso-level. *Material and Structures*. (2011a) **44**:415-435.

[10] Idiart, A. E., López, C. M. and Carol, I. Chemo-mechanical analysis of concrete cracking and degradation due to external sulfate attack: A meso-scale model. *Cement and Concrete Composites*. (2011b) **33**:411–423.

[11] Liaudat, J., López, C. M. and Carol, I. Coupled C-M meso-scale model for ASR expansion in concrete, in Meschke, G., Pichler, B., Rots, J.G. (Eds.). *Computational Modelling of Concrete Structures: Proceedings of the Conference on Computational Modelling of Concrete and Concrete Structures (EURO-C 2018)*, Bad Hofgastein, Austria (2018), pp. 363–370.

[12] Rodríguez, M., López, C. M. and Carol, I. Modeling of Heat and Mass Transfer Induced by High Temperature in Concrete. In: Oñate E., Owen D.R.J., Peric D., Chiumeti M. (eds). *XIII International Conference on Computational Plasticity. Fundamentals and Applications COMPLAS XIII*. CIMNE, Barcelona (2015), pp 346-353.

[13] Dubacq, B., Bickle, M. J. and Evans, K. A. An activity model for phase equilibria in the H_2O-CO_2-NaCl system. *Geochimica et Cosmochimica Acta* (2013) **110**: 229–252.

[14] Brouwers, H. J. H. The work of Powers and Brownyard revisited: Part 1. *Cement and Concrete Research* (2004) **34**:1697–1716.

[15] Brouwers, H. J. H. The work of Powers and Brownyard revisited: Part 2. *Cement and Concrete Research* (2005) **35**:1922–1936.

[16] AENOR, Cement-part 1: Composition, Specifications and Conformity Criteria for Common Cements UNE-EN 197-1 (2011), AENOR, Madrid.

[17] Gallucci, E., Zhang, X., Scrivener, K.L. Effect of temperature on the microstructure of calcium silicate hydrate (C–S–H). *Cement and Concrete Research* (2013) **53**: 185—195.

XV International Conference on Computational Plasticity. Fundamentals and Applications
COMPLAS 2019
E. Oñate, D.R.J. Owen, D. Peric , M. Chiumenti, and Eduardo de Souza Neto (Eds)

VISCOPLASTIC CONSTITUTIVE MODELS FOR ZERO-THICKNESS INTERFACE ELEMENTS, FORMULATION AND APPLICATIONS

I. JAQUÉS[*] AND I. CAROL[*]

[*] ETSECCPB (School of Civil Engineering)
Universidad Politécnica de Cataluña
Campus Norte UPC, 08034 Barcelona, Spain
e-mail: ignacio.carol@upc.edu

Key words: Viscoplasticity, Interface elements, Finite Element Method (FEM), Viscoplastic relaxation.

Abstract. An energy-based work-softening visco-plastic model for zero-thickness interface elements has been developed as an extension of an existing elastic-perfectly-viscoplastic formulation. In the inviscid limit the model also collapses into a well-established fracture mechanics-based elasto-plastic model. The new model is verified satisfactorily for common loading cases at interfaces such as pure tension (mode I) opening, and shear-compression (mixed-mode) sliding, with results that in the long term match the predictions of the fracture mechanics inviscid model.

1 INTRODUCTION

Zero–thickness interface elements, sometimes also called “cohesive elements”, were introduced by Goodman [1] for geotechnical analysis using the FEM, and in more recent times are becoming popular for their many possible applications. In the simplest scenario of linear elastic behaviour, interface elements inserted in between standard continuum elements may be used to represent the presence of a thin, deformable layer without the need to use extremely fine meshes. If considered linear elastic but assuming sufficiently high stiffness values, interface elements may lead to stresses and deformations of the continuum elements practically identical to those that would be obtained in the same domain without any interface elements inserted. And that may be used as a means to obtain, besides the regular stresses and deformations of the continuum, also the normal and shear stress tractions transmitted across the planes in which interface elements have been inserted. Stress tractions may be of high interest for instance along interfaces in between different material layers or in between different materials. If equipped with non-linear constitutive laws exhibiting a maximum strength condition, interface elements may also be used to represent frictional sliding planes, cracks or fractures. For this purpose, the precise type and characteristics of the constitutive law are essential. A frictional contact surface may be represented with perfect plasticity, while a developing crack will require a constitutive model with softening which incorporates fracture energy parameters. In the late 90s, a model of this type was proposed by the research group [2],

and the same model was later developed further and improved [3].

A useful extension of the zero-thickness interface elements and constitutive laws is in the field of visco-plasticity [4]. Potential applications range from representation of physical time-dependent behavior (such as for instance failure under sustained load), to purely numerical strategies such as visco-plastic relaxation. In recent years, an elastic-perfectly visco-plastic interface model was proposed [5], together with a discussion on the schemes necessary for the various possible applications. In the inviscid limit (time tending to infinity) the model response approached an elastic-perfectly plastic version of the group's fracture model.

The rate-dependent (viscoplastic) formulation requires a time integration strategy to discretize time in increments and evaluate linearized relation between stress and strain increments for each time step. Usually, the algorithms proposed in the literature are strain-driven, i.e. they are based on the initial stress scheme used in Finite Elements, in which the strain increments are prescribed to the constitutive equations, which then return the resulting stress [6-7-8].

In contrast, stress-driven schemes are less common. After the original constant-stress implementation of Zienkiewicz and Cormeau [9] that may be considered the most elementary form of stress-driven viscoplastic schemes, to the knowledge of the authors, the only previous proposals of this type are [4]. The implementation of stress-prescribed schemes is conceptually much simpler and numerically advantageous (explicit integration of the constitutive equations and simple coding).

The main objective of this paper is to describe and demonstrate an energy-based softening visco-plastic model for zero-thickness interface elements using a stress-prescribed integration algorithm for Perzyna viscoplasticity in a FE framework. In the inviscid limit the predictions of the model approach those of the full version of the fracture-based elasto-plastic model previously proposed by the group.

2 ENERGY-BASED WORK-SOFTENING VISCO-PLASTIC MODEL FOR ZERO-THICKNESS INTERFACE ELEMENTS

As already mentioned, the new energy-based softening visco-plastic model for zero-thickness interface elements is developed as an extension of an existing elastic-perfectly-viscoplastic formulation [5], which is based on a hyperbolic cracking surface. This model was proposed originally for the behaviour of geotechnical interfaces [10], later modified for fracture energy-based opening and development of cracks in quasi-brittle materials (concrete, rock, etc) [2], and more recently extended to 3D and reformulated more efficiently [3].

2.1 Elasto-plastic interface constitutive model

The existing fracture-based interface constitutive law, named *Normal/Shear Cracking Model*, is based on the theory of elasto-plasticity and it incorporates concepts of fracture mechanics and fracture energies. Its behavior is formulated in terms of normal and shear components on the interface plane $\boldsymbol{\sigma} = [\sigma_N, \sigma_T]^T$ and their respective relative displacements $\boldsymbol{r} = [r_N, r_T]^T$. The interface fracture model is based on a hyperbolic cracking surface [2], Fig.1a. The corresponding yield (cracking) function F is defined in terms of normal and shear stresses and three geometric parameters included in vector $\boldsymbol{p}$: the strength parameters cohesion (c), uniaxial tensile strength (χ) and internal friction angle $(tan\phi)$. The algebraic expression of F

has been changed in some versions of the model, the most convenient [3] being:

$$F(\boldsymbol{\sigma}, \boldsymbol{p}) = -(c - \sigma_N tan\phi) + \sqrt{\sigma_T^2 + (c - \chi tan\phi)^2} \tag{1}$$

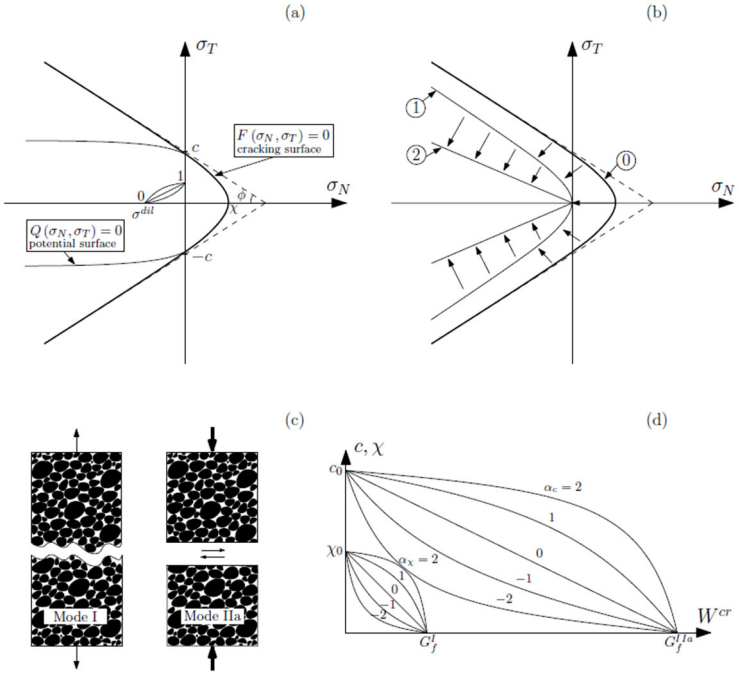


Figure 1 Interface model: (a) cracking surface and plastic potential, (b) evolution of cracking surface, (c) fundamental modes of fracture and (d) softening laws for c and χ.

The hardening/softening laws (evolution laws of the surface geometric parameters $c, \chi, tan\phi$) are formulated in terms of a single history variable, W^{cr}, defined as the energy spent in fracture processes. These laws, represented in Fig.1d, include as parameters the classical fracture energy in Mode I, G_f^{I} (pure tension) and a second mode named Mode IIa defined under shear and high compression without dilatancy, G_f^{IIa} (Fig.1c). The history variable work is defined incrementally as:

$$dW^{cr} = \begin{cases} \boldsymbol{\sigma} : d\boldsymbol{r^{cr}} & \sigma_N \geq 0 \ (tension) \\ (\sigma_T + \sigma_N tan\phi) dr_T^{cr} & \sigma_N < 0 \ (compression) \end{cases} \tag{2}$$

Equations (2) show that, in the case of tensile-dominated cracking, all plastic work dissipated counts towards the history variable, while in compression-shear cracking, there is also a frictional part which is excluded from W^{cr} (Eq.2). Note that, with the definitions above, the evolution of the cracking surface is as depicted in Fig. 1b: from configuration "0" with initial tensile strength χ_0 and asymptotic cohesion c_0, as the history variable reaches $W^{cr} = G_f^{\mathrm{I}}$ the surface moves to configuration "1" with zero tensile strength, and as it approaches $W^{cr} = G_f^{\mathrm{IIa}}$ the surface moves toward configuration "2" which corresponds to a pair of straight lines of residual friction and no cohesion.

2.2 Perzyna viscoplastic constitutive model for the interface.

The visco-plastic version of the interface model is based on the assumption that the total visco-plastic "strain" (relative displacements) can be split into the elastic part $\boldsymbol{r}^{el}$ and the viscoplastic part $\boldsymbol{r}^{vp}$ [5]:

$$\boldsymbol{r} \quad = \boldsymbol{r}^{el} + \boldsymbol{r}^{vp} \tag{3}$$

The elastic part is assumed to be related to stresses via isotropic linear elasticity:

$$\boldsymbol{r}^{el} = \boldsymbol{D_0^{-1}} : \boldsymbol{\sigma} \tag{4}$$

where $\boldsymbol{D_0}$ is the elastic stiffness matrix, symmetric and positive definite, and $\boldsymbol{D}_0^{-1}$ indicates its inverse, which is the elastic compliance matrix and it may be also denoted as $\boldsymbol{C_0}$.

The main change with respect to the previous perfect visco-plastic model proposed [5] is that in the current implementation the geometric parameters of the surface will evolve in a way similar to the inviscid elasto-plastic model of the previous section. A history variable W^{vp} is defined which is similar to the previous W^{cr}(except that visco-plastic "strain" replaces plastic strain), i.e.:

$$dW^{vp} = \begin{cases} \boldsymbol{\sigma} : d\boldsymbol{r}^{vp} & \sigma_N \geq 0 \ (tension) \\ (\sigma_T + \sigma_N tan\phi)\mathrm{d}r_T^{vp} & \sigma_N < 0 \ (compression) \end{cases} \tag{5}$$

and the geometric parameters of the surface $\boldsymbol{p}$ (composed by $c, \chi, tan\phi$) are assumed to evolve with W^{vp}in a way identical as they did with W^{cr} in the inviscid elasto-plastic model (Fig. 1d).

The cracking surface $F(\boldsymbol{\sigma}, \boldsymbol{p}) = 0$ determines the limit between elastic state ($F \leq 0$) and the visco-plastic state ($F > 0$) state, in which a Perzyna visco-plastic "strain" rate is assumed:

$$\dot{\boldsymbol{r}}^{vp} = \frac{1}{\eta}\left\langle \psi\left(\frac{F(\boldsymbol{\sigma}, \boldsymbol{p})}{F_0}\right)\right\rangle \boldsymbol{m} \tag{6}$$

where η is the viscosity of the material, F_0 is a reference value of the yield surface, Q is the visco-plastic potential typical of non-associated formulations and the flow rule is $\boldsymbol{m} = \partial Q/\partial \boldsymbol{\sigma}$.

Finally, the accumulated visco-plastic strain $\Delta \boldsymbol{r}^{vp}$ (Eq.3) can be obtained by integrating in time the visco-plastic strain rate, i.e.:

$$\Delta \boldsymbol{r}^{vp} = \int_{t_0}^{t_1} \dot{\boldsymbol{r}}^{vp}\, dt = \int_{t_0}^{t_1} \frac{1}{\eta}\left\langle \left(\frac{F(\boldsymbol{\sigma}, \boldsymbol{p})}{F_0}\right)\right\rangle \boldsymbol{m} \quad dt \tag{7}$$

For the numerical integration of the new interface visco-plastic constitutive model, the methodology is a generalization of the procedure previously proposed for perfect visco-plasticity [5]. In that integration scheme it is assumed that the stress increment $\Delta\boldsymbol{\sigma}$ (that takes place during a time increment Δt) is prescribed, and the corresponding "strain" (relative

displacement) is calculated. In this case, though, the geometric parameters of the yield function, $\boldsymbol{p}$ (composed by $c, \chi, tan\phi$) are not constant, but have to be continuously updated using the softening laws in terms of W^{vp}, which is also continuously changing. This requires a sub-stepping scheme. In the case that for a given substep $F(\boldsymbol{\sigma}_{fin}, \boldsymbol{p}_{fin}) > 0$, the integral of Eq.(7) is approximated by first order expansion as:

$$\Delta \boldsymbol{r}^{vp} = \frac{\Delta t}{\eta F_0}\Big((1-\theta)F(\boldsymbol{\sigma}_{ini}, \boldsymbol{p}_{ini})\, \boldsymbol{m}(\boldsymbol{\sigma}_{ini}, \boldsymbol{p}_{ini}) + \theta F\left(\boldsymbol{\sigma}_{fin}, \boldsymbol{p}_{fin}\right)\, \boldsymbol{m}\left(\boldsymbol{\sigma}_{fin}, \boldsymbol{p}_{fin}\right)\Big) \qquad (8)$$

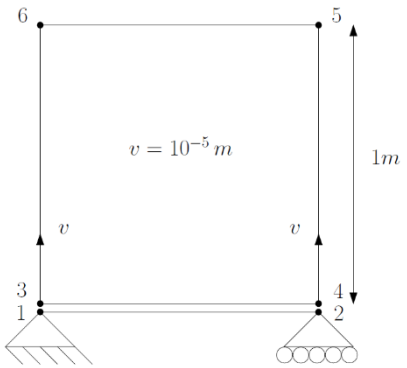
where $\boldsymbol{n} = \partial F/\partial \boldsymbol{\sigma}$ and θ is a constant scalar factor that may take a fixed value between 0 and 1. This expression, properly developed, leads to the relation between $\Delta\boldsymbol{\sigma}$ and $\Delta\boldsymbol{r}$, which provides the constitutive tangential compliance and initial strain vector necessary for the iterative calculations. If $\theta = 0$, the formula above is equivalent to the forward Euler scheme. The other limit case is when $\theta = 1$ and the formula is equivalent to the traditional backward Euler scheme. Note also that, except for the case $\theta = 0$ in which all variables are known at the beginning of the increment, for any other value of $\theta > 0$ the calculation will require iterations at structural level, because the expression involves the stresses at the end of the increment, which are not known *a priori*.

3 VERIFICATION EXAMPLES

A pure tension and shear-compression simple examples have been considered in this section for verification purposes, and the results have been compared with those that would be obtained with the elastoplastic law, with which they should coincide for long visco-plastic times (inviscid limit of the visco-plastic model).

3.1 Uniaxial tension opening

The first example consists of a single interface element subject to uniaxial tension (Fig.2). A square continuum element has been also included in the discretization, although it does not play any mechanical role. Loading is composed of an alternate sequence of two kinds of steps, the first one consisting of a prescribed displacement increment (applied instantaneously), followed by the pass of a long time (which takes place at constant nodal displacements).



Interface properties

$Kn = Kt = 10^6\, kPa/m$
$TanPhi = 0.7$
$Xi = 2.0\, kPa$
$C = 2.0\, kPa$
$GfI = 0.00001\, kN/m$
$GfIIa = 0.0001\, kN/m$
$\eta = 10^6\, kPa \cdot s$

Figure 2. Geometry and properties of the uniaxial tension example. Prescribed displacements are imposed on nodes 3 and 4.

The results of the visco-plastic calculation are represented in Fig.3 in red color lines, together with the results obtained with the elastoplastic interface constitutive law in blue [2]. As shown in the figure, for each instantaneous load step, the visco-plastic response consists first of an elastic stress increment, which is then followed by progressive relaxation as time passes, leading in the long term to the same stress value as predicted by the fracture mechanics inviscid model for the same relative displacement. Similar behaviour is observed for each one of the prescribed displacement increments. Therefore, it can be concluded that in this case the proposed visco-plastic model in the visco-plastic limit clearly coincides with the existing elasto-plastic model.

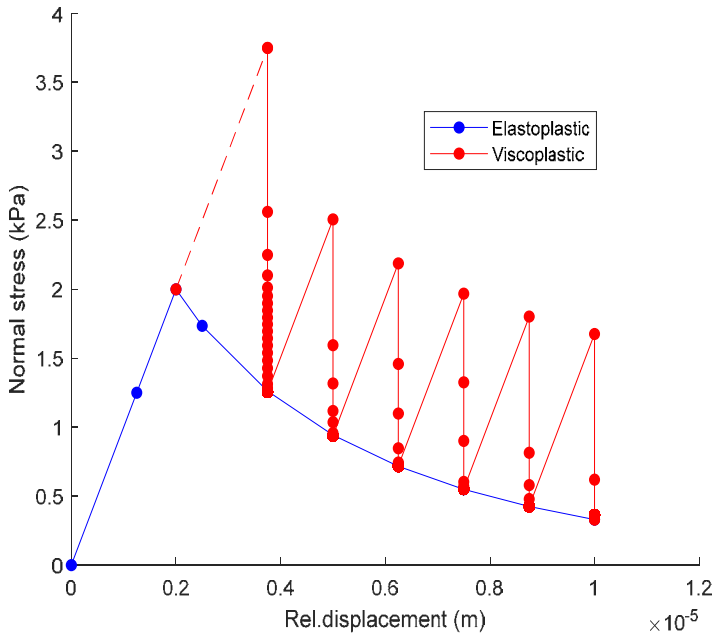


Figure 3. Normal stress-normal relative displacement evolution curve of the interface element. Viscoplastic results in the long term match the predictions of the fracture mechanics inviscid model.

The formulation proposed also provides the energy spent in the fracture process. The following table (Table 1) shows the comparison between the energies obtained with the elasto-plastic and with the visco-plastic models. As it can be seen, these values turn out very similar as expected.

Table 1: Comparison between energy values computed in both cases elastoplastic and viscoplastic. The total energy obtained in both cases are very similar as expected.

	Elasto-plastic model (kPa·m) W^{cr}	**Visco-plastic model (kPa·m)** W^{vp}
Energy dissipated in fracture processes	$8.35067 \cdot 10^{-6}$	$8.34314 \cdot 10^{-6}$

3.2 Shear-compression sliding

The second example consists of a shear test applied on the same geometry and with the same material parameters as in previous section. The loading (Fig.4) consists of two parts: first, applying an instantaneous vertical stress on the top face of the continuum element (Fig.4a) and, second, applying the horizontal loading. Similarly as in example one, the horizontal loading (Fig.4b) is applied as a sequence of small horizontal displacements prescribed to nodes 3 and 4 instantaneously, followed each of them by a number of time increments until stresses would be totally relaxed.

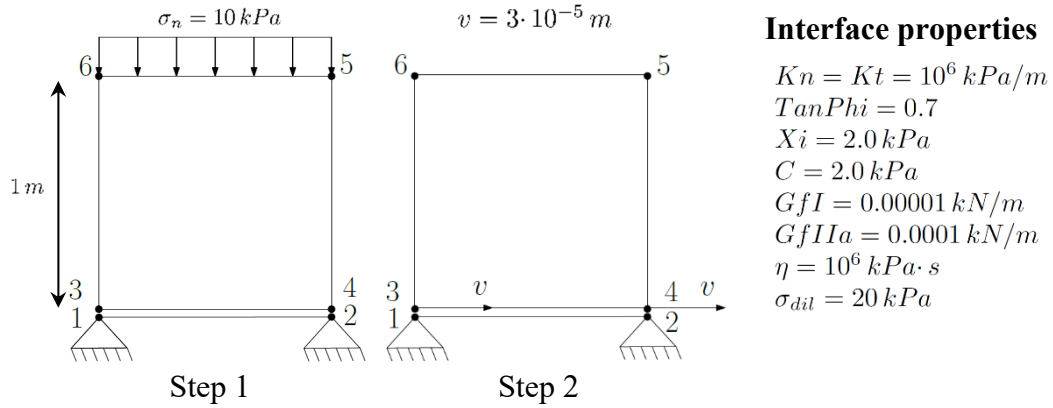


Figure 4. Geometry of the shear-compression sliding example. An instantaneous vertical stress is applied on the top face and also an instantaneous displacement is imposed on nodes 3 and 4. Also interface properties are shown.

The results of the visco-plastic calculations are represented in Fig.5a (red color lines), together with the results obtained with the existing elasto-plastic model (in blue) [2]. Fig.5b shows the evolution of the dilatancy, also computed with both elastoplastic and viscoplastic models. Similar to the previous case, the results show that in the inviscid limit the visco-plastic formulation approaches nicely the predictions of the corresponding elasto-plasticity.

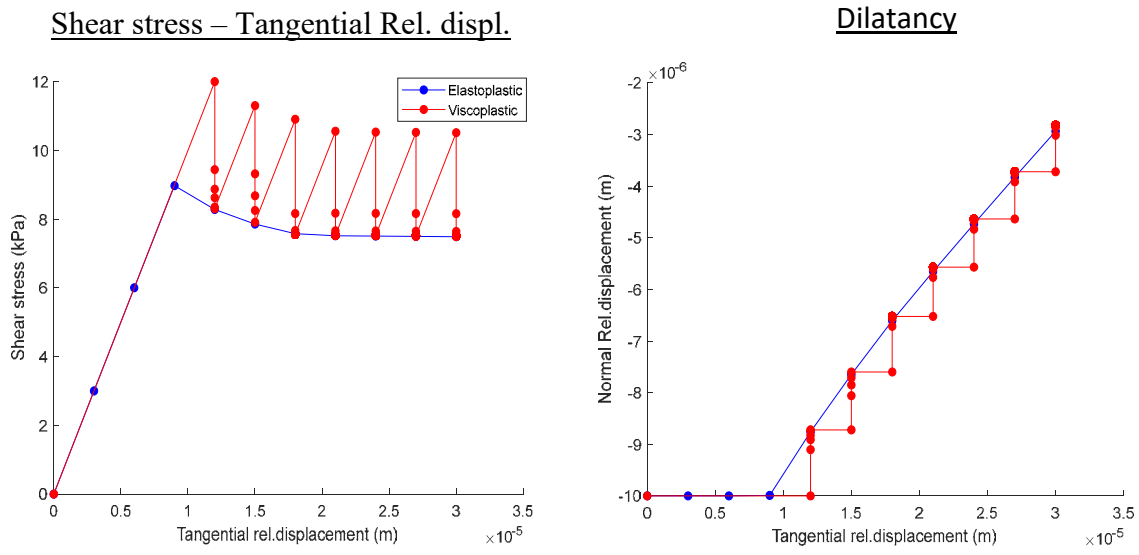


Figure 5. (a) Shear stress-tangential relative displacement evolution curve of the interface element. (b) Evolution of the dilatancy. Viscoplastic results in the long term match the predictions of the fracture mechanics inviscid model.

As in the previous example, the energy spent in the fracture process also has been calculated in this case. The following table (Table 2) shows the comparison between the energies obtained with the elastoplastic model and with the viscoplastic one, which turn out very similar as expected.

Table 2: Comparison between energy values computed in elastoplastic and viscoplastic models.

	Elasto-plastic model (kPa·m) W^{cr}	**Visco-plastic model (kPa·m)** W^{vp}
Energy dissipated in fracture processes	$1.56693 \cdot 10^{-5}$	$1.58374 \cdot 10^{-5}$

4 CONCLUDING REMARKS

In the present paper, an energy-based softening visco-plastic model of the Perzyna type for zero-thickness interface elements has been described, as well as its basis for numerical implementation using a stress-prescribed integration algorithm. Numerical results have been also presented for two simple examples of application, the first one consisting of a uniaxial tensile interface opening (mode I), and the second one a shear-compression (mixed-mode) failure with sliding. Both may represent academic problems of rock samples with discontinuities. The results show that in the long term the visco-plastic results match very well the predictions of the fracture mechanics inviscid model.

ACKNOWLEDGEMENTS

This research work was partially supported by research grants BIA2016-76543-R from MEC (Madrid), which includes FEDER funds, and 2017SGR-1153 from Generalitat de Catalunya (Barcelona). The first author also acknowledges her FI doctoral fellowship (2017FI_B_00759) received from AGAUR-Generalitat de Catalunya.

REFERENCES

[1] Goodman, R.E. and Taylor, R.L. and Brekke, T.L. A model for the mechanics of jointed rock. ASCE J. Soil Mech. and Found. Div. (1968) **94**:637-659.

[2] Carol, I., Prat, P. and López, C.M. Normal/shear cracking model: application to discrete crack analysis. *Journal of engineering mechanics* (1997) **123(8)**:765-773.

[3] Caballero, A., Willam, K.J. and Carol, I. Consistent tangent formulation for 3D interface modeling of cracking/fracture in quasi-brittle materials. *Computer Methods in Applied Mechanics and Engineering* (2008) **197(33)**:2804-2822.

[4] Caballero, A, Garolera, D., Carol, I. and Gens, A. Viscoplastic multilaminate model for jointed rock with stress-prescribed using a stress-prescribed LEGI scheme. *International Journal of Solids and Structures* (2009) **45(9)**:2686-2705.

[5] Aliguer, I., Carol, I. and Sture, S. Stress-driven integration strategies and m-AGC tangent operator for Perzyna viscoplasticity and viscoplastic relaxation: application to

geomechanical interfaces. *International journal for numerical and analytical methods in geomechanics* (2016) **41(6)**:918-939.

[6] Hughes, T.J.R. and Taulor, R.L. Unconditionally stable algorithms for quasi-static elasto/viscoplastic finite element analysis. *Computers & Structures* (1978) **8**:169-173.

[7] Peric, D. On a class of constitutive equations in viscoplasticity: formulation and computational issues. *International Journal for Numerical Methods Engineering* (1993) **36**:1365-1393.

[8] Ponthot, J.P. Unified stress update algorithms for the numerical simulation of large deformation elasto-plastic an elasto-viscoplastic processes. *International Journal of Plasticity* (2002) **18(1)**:91-126.

[9] Zienkiewicz, O.C. and Cormeau, I.C. Visco-plasticity - plasticity and creep, a unified numerical solution approach. *International Journal for Numerical Methods Engineering* (1974) **8**:821-845.

[10] Gens, A., Carol, I. and Alonso, E.E. An interface element formulation for the analysis of soil-reinforcement interaction. Computers and Geotechnics (1989) **7**:133-151.

XV International Conference on Computational Plasticity. Fundamentals and Applications
COMPLAS 2019
E. Oñate, D.R.J. Owen, D. Peric , M. Chiumenti, and Eduardo de Souza Neto (Eds)

ZERO-THICKNESS INTERFACE MODEL WITH CHEMICAL DEGRADATION BY ACID ATTACK

A. MARTÍNEZ, J. LIAUDAT, C. M. LÓPEZ AND I. CAROL

School of Civil Engineering (ETSECCPB)
Universitat Politècnica de Catalunya (UPC)
Campus Nord UPC, 08034 Barcelona, Spain
e-mail: ariadna.martinez.e@upc.edu, joaquin.liaudat@upc.edu, carlos.maria.lopez@upc.edu, ignacio.carol@upc.edu

Key words: oil-well cement, acid attack, CO_2, interface elements, constitutive law, C-M coupling

Abstract. Carbon dioxide (CO_2) storage in abandoned oil/gas reservoirs is considered a viable alternative to reduce greenhouse gas emissions to the atmosphere. An important element of the risk associated with long-term CO_2 storage is the loss of integrity of the cement seals of the abandoned wells in the reservoir. Among others, one possible cause of loss of integrity is the degradation of the oil-well cement due to the acid attack of the carbonated brine in the reservoir. In previous studies, the authors have developed a diffusion-reaction model for simulating this degradation process. In order to study possible coupled Chemo-Mechanical (C-M) mechanisms, this model will be coupled with an existing mechanical model. For this purpose, in this paper, an existing constitutive law for zero-thickness interface, based on the theory of elasto-plasticity with concepts of fracture mechanics, is modified to incorporate the effect of chemical degradation on the mechanical strength parameters. Preliminary results obtained with this new constitutive law are presented, in order to illustrate the main aspects of the proposed constitutive law, as well as a possible C-M degradation mechanism that should be considered in the long-term safety assessment of CO_2 geological storage projects.

1 INTRODUCTION

Carbon dioxide (CO_2) storage in depleted oil/gas reservoirs is considered a viable alternative to reduce greenhouse gas emissions to the atmosphere. One of the major sources of concern with this type of projects is the presence of abandoned wells which perforate the caprock of the reservoir and which may potentially constitute CO_2 leakage pathways. In many cases, the plugging of abandoned wells began decades ago when CO_2 storage was not under consideration and, therefore, the primary cement used for the casing and/or the plug cement in the well were regular Portland cements (e.g. API Class G and H oilwell cement). These cements, which are basic in nature, are chemically unstable in acidic environments as the one resulting from the injection of CO_2 into the reservoir [1–6].

The CO_2 injected progressively dissolves in the water or brine filling the depleted reservoir, leading to the formation of carbonic acid, with a consequent decrease of the pH. As the carbonated brine reaches the oil-well cement, a number of chemical reactions occur between

the aqueous carbon species and the Hydrated Cement Paste (HCP). These reactions combined with the diffusion of aqueous species in the HCP pore solution leads to the development of a decalcification front, which advances into the material. In the decalcified zones of the HCP, only an amorphous silica gel remains, which shows practically no mechanical strength and very high permeability [7]. A detailed discussion of this chemical degradation process may be found in Ref. [8].

The velocity of advancement of the degradation front is relatively slow (a few millimetres per month) and decreases as the degradation front moves into the HCP [3, 6]. If compared with typical well cementation lengths of tens of meters, the advancement of the degradation front *per se* does not seem to have the potential of compromising the integrity of the well seals. However, if the acid attack is considered in combination with the mechanical loads acting on the well cement in the reservoir, the picture could be different.

The time evolution of the pore pressure in the reservoir because of the injection/extraction of fluids, combined with the fact that well cementing is done in different times of the well life, may induce significant stresses on the well cement, including tensile stresses [9]. These stresses may induce the propagation of cracks, in particular in the interfaces between the cement and the steel case and between the cement and the rock. If the carbonated brine penetrates these cracks, the strength reduction due to the acid attack of the crack tip may induce subcritical crack growth with consequent risk for the integrity of the well.

In order to study this Chemo-Mechanical (C-M) degradation mechanism, a numerical model is being developed by the authors in the context of an ongoing research project. For this purpose, a diffusion-reaction model for simulating acid attack on oil-well cements exposed to carbonated brine, recently developed by the authors [8, 10, 11], will be coupled with an existing mechanical model. This mechanical model has the characteristic ingredient of using zero-thickness interface elements with double nodes for representing cracks, e.g. [12-14]. As a necessary intermediate step, in this paper, a new constitutive law for the interface elements is briefly described which makes it possible to incorporate the effect of degradation of the mechanical strength by the acid attack. This constitutive law is obtained by modifying an existing one based on the theory of elasto-plasticity, with concepts and parameters from the non-linear fracture mechanics theory [12-14]. Preliminary results obtained with this new constitutive law are presented, in order to illustrate the main aspect of the new constitutive law, as well as coupled C-M degradation mechanisms that should be considered in the long-term safety assessment of CO_2 geological storage projects.

2 CONSTITUTIVE LAW FOR ZERO-THICKNESS INTERFACE ELEMENTS WITH CHEMICAL DEGRADATION

The constitutive law is formulated in terms of the normal and tangential stress components in the mid-plane of the interface element $\boldsymbol{\sigma} = [\sigma_N, \sigma_T]^{\mathrm{t}}$ and the conjugate relative displacements $\mathbf{u} = [u_N, u_T]^{\mathrm{t}}$ ($^{\mathrm{t}}$ = transposed). The law is based on the theory of elasto-plasticity and introduces nonlinear fracture mechanics concepts in order to define the softening behaviour due to the work dissipated in the fracture process (denoted W^{cr}).

The fracture surface $F(\boldsymbol{\sigma}) = 0$ is defined by a hyperbola of three parameters (Fig. 1a):

$$F(\boldsymbol{\sigma}) = -(c - \sigma_N \tan\phi) + \sqrt{\sigma_T^2 + (c - \chi \tan\phi)^2} = 0 \tag{1}$$

where χ is the tensile strength, c is the apparent cohesion, and ϕ is the asymptotic friction angle. Cracking starts when the fracture surface is reached. As the fracture process and/or the chemical degradation progress, the fracture surface shrinks. In order to control the evolution process of the fracture surface, the model incorporates two parameters, G_F^I and G_F^{IIa}, that represent the specific fracture energy in Mode I and in Mode II under high confinement, respectively (Fig. 1b). These two parameters are reduced by the chemical degradation of the material. Total exhaustion of tensile strength ($\chi = 0$) is reached either for $W^{cr} = G_F^I$ or for $\eta = 1$ (curve "1" in Fig. 1c), and residual frictional strength ($c = 0$ and $\tan\phi = \tan\phi_r$) is obtained for $W^{cr} = G_F^{IIa}$ (curve "2" in Fig. 1c).

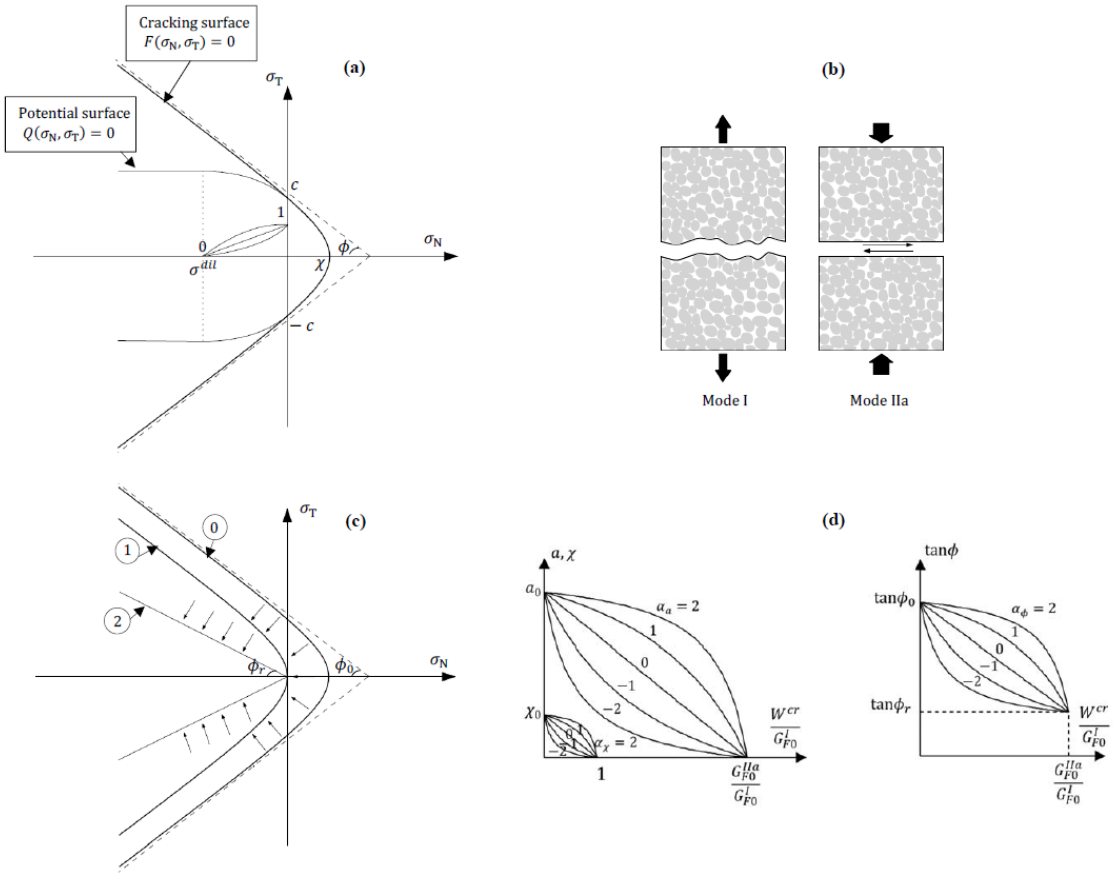


Figure 1: Crack laws for material without chemical degradation ($\eta = 0$): (a) cracking surface and potential surface; (b) fundamental modes of fracture; (c) evolution of cracking surface; (d) softening laws for χ, a, and $\tan\phi$. Adapted from [12, 14].

The work spent on the fracture process during the formation of the crack is given by:

$$\begin{aligned} dW^{cr} &= \sigma_N\, du_N^{cr} + \sigma_T\, du_T^{cr} \qquad \text{if } \sigma_N \geq 0 \\ dW^{cr} &= \sigma_T\, du_T^{cr} \left(1 - \left|\frac{\sigma_N \tan\phi}{\sigma_T}\right|\right) \quad \text{if } \sigma_N < 0 \end{aligned} \tag{2}$$

These expressions imply that, in tension, all work dissipated in the crack goes into the fracture process, while, in compression, the contribution of W^{cr} comes only from the shear work by subtracting the basic friction.

The parameters of the fracture surface evolve by means of the following softening laws:

$$\chi = \chi_0[1 - S(\xi_\chi)][1 - S(\eta)] \tag{3}$$

$$\tan\phi = \tan\phi_0[1 - S(\xi_\phi)] + \tan\phi_r\, S(\xi_\phi) \tag{4}$$

$$a = a_0[1 - S(\xi_a)] \tag{5}$$

where ξ_χ, ξ_ϕ, and ξ_a are dimensionless positive internal variables which grow with W^{cr}, η is the dimensionless history variable representing the chemical degradation of the material ($\eta = 0$ for non-degraded material, $\eta = 1$ for completely degraded material). $S(X)$ is a scaling function which makes it possible to obtain a family of evolution curves for different values of the shape parameter α (Fig. 1d). The variable a is the horizontal distance between the vertex of the updated hyperbola and its asymptotes, in such a way that the updated apparent cohesion c is obtained from the following expression:

$$c = (a + \chi)\tan\phi \tag{6}$$

The internal variable ξ_χ is defined in a differential form as follows:

$$d\xi_\chi = \frac{dW^{cr}}{G_F^I(\eta)} \tag{7}$$

The specific fracture energy in Mode I evolves with η according to:

$$G_F^I(\eta) = G_{F_0}^I[1 - S(\eta)] + G_{Fmin}^I\, S(\eta) \tag{8}$$

where $G_{F_0}^I$ and G_{Fmin}^I are the values of G_F^I for $\eta = 0$ (non-degraded material) and $\eta = 1$ (completely degraded material), respectively.

Similarly, the internal variables ξ_ϕ and ξ_a are given by:

$$d\xi_\phi = d\xi_a = \frac{dW^{cr}}{G_F^{IIa}(\eta)} \tag{9}$$

Assuming that the ratio $G_F^{IIa}(\eta)/G_F^I(\eta)$ remains constant for any value of η, the following relationship is obtained from Eqs. (7) and (9):

$$\xi_\phi = \xi_a = \xi_\chi \frac{G_{F0}^I}{G_{F0}^{IIa}} \tag{10}$$

Note that the effect of the increasing chemical degradation (increasing η) on the mechanical strength of the material is considered in two ways: (i) by reducing the tensile strength (Eq. (3)), and (ii) by reducing the specific fracture energies G_F^I and G_F^{IIa} (Eq. (8)).

3 PRELIMINARY RESULTS

In the following sections, a number of simple academic examples are presented in order to illustrate the main features of the proposed constitutive law. In these examples, three different mechanical loading schemes (pure tension, shear under compression, and three-point bending) are considered combined with chemical degradation.

3.1 Pure tension tests

The pure tension tests are simulated considering a single zero-thickness interface element with the following parameters: $K_N = K_T = 100000$ MPa/mm, $\chi_0 = 3$ MPa, $c_0 = 7$ MPa, $G_{F0}^I = 0.03$ N/mm, $G_{F0}^{IIa} = 10G_{F0}^I$, and $G_{Fmin}^I = 0.01G_{F0}^I$. The results obtained for different sequences ("cases") of loading and chemical degradation are shown in Figs. 2–4. In those figures, Case 0 is the reference case corresponding to an interface element subjected to increasing normal relative displacement, without any chemical degradation. Note that because the adopted chemical degradation rates are arbitrary, time is given as a dimensionless variable.

In Cases 1 and 2 (Fig. 2), an initial normal relative displacement (u_N) is imposed until reaching the initial tensile strength of the interface (χ_0). Thereafter, u_N is progressively increased together with the chemical degradation parameter (η), with higher degradation rate for Case 2 than for Case 1. It can be appreciated that a higher rate of chemical degradation implies a faster decrease of the tensile strength of the interface element.

In Case 3 (Fig. 2), an initial u_N is also imposed, but without surpassing the tensile strength. This initial u_N is kept constant while the chemical degradation is increased until $\eta = 0.6$. According with Eq. (3), this leads to a reduction of the tensile strength with consequent cracking (plastification) of the interface element. Thereafter, u_N is progressively increased without additional chemical degradation.

In Cases 4 and 5 (Fig. 3), an initial u_N is imposed which cracks (plastifies) the interface. This initial u_N is kept constant while η is progressively increased, with a different rate in each case. The chemical degradation decreases the normal stress in the interface due to the contraction of the fracture surface. As expected, the higher the chemical degradation rate, the higher the decrease of the normal stress. Thereafter, u_N is progressively increased without additional chemical degradation.

In Cases 6 and 7 (Fig. 4), the same sequences of mechanical and chemical degradation as in Cases 4 and 5 are followed, with the only difference that now the interface elements are partially unloaded before applying the chemical degradation. Note that because K_N is very high, the unloading of the interface implies practically no change in u_N. As expected, the softening branch obtained for Cases 6 and 7 are exactly the same as for Cases 4 and 5, respectively.

3.2 Shear under compression tests

The tests with shear under compression loading are also simulated considering a single interface element, and with the same parameters as in the previous examples. The results obtained for different sequences of loading and chemical degradation are shown in Figs. 5–7. In those figures, Case 0 is the reference case corresponding to an interface element subjected to increasing tangential relative displacement (u_T), without any chemical degradation. A constant normal stress $\sigma_N = -2$ MPa is considered in all cases.

In Case 1 (Fig. 5), an initial u_T is imposed reaching the initial shear strength of the interface (point a). Then, u_T is progressively increased together with the chemical degradation parameter (η).

In Case 2 (Fig. 5), an initial u_T is imposed in the elastic range of the interface (point b). This initial u_T is kept constant while η is increased until reaching complete chemical degradation ($\eta = 1$). Then, u_T is further increased until reaching the residual frictional strength. Note that at point c, the tensile strength of the interface is null ($\chi = 0$), but the shear strength is not completely degraded yet.

In Cases 3 and 4 (Fig. 6), different initial u_T are imposed, which crack the interface element. In Case 3, the work spent in the fracture process (W^{cr}) due to the imposed u_T is lower than the specific fracture energy in mode I, i.e. $W^{cr} < G_{F0}^{I}$, while in Case 4, the initial u_T is such that $W^{cr} > G_{F0}^{I}$. In both cases, the initial u_T is kept constant while η is increased until reaching $\eta = 0.6$. Thereafter, in both cases, u_T is increased without additional chemical degradation. Note that, in both cases, as u_T is increased, the shear strengths tend to the residual frictional strength.

In Cases 5 and 6 (Fig. 7), the same sequences of mechanical and chemical degradation as in Cases 3 and 4 are followed, with the only difference that now the interface elements are partially unloaded before applying the chemical degradation. As expected, the softening branch obtained for Cases 5 and 6 are exactly the same as for Cases 3 and 4, respectively.

3.3 Three-point bending test

This example is intended to simulate the propagation of an initially stable flexural crack in a beam due to the chemical degradation of the tip of the crack. For this purpose, a two-dimensional (plane stress) beam of 0.6 m length and 0.1 m height is considered, with a line of interface elements in the central section (Fig. 8). The continuum elements are assumed linear elastic ($E = 25000$ MPa, $\nu = 0.2$) and the interface elements are equipped with the constitutive law presented in this paper, with the same parameters as for the other examples.

It is considered that the chemical degradation rate is the same at all the integration points of the interface elements, but that it only starts if the integration point has been cracked ($W^{cr} > 0$). This latter assumption is made in order to mimic, in a very simplified manner, the C-M mechanism described in the Introduction, in which the ingress of carbonated brine in pre-existing cracks in the well cement may lead to sub-critical grow due to the acid attack of the tip of the crack.

The beam is initially loaded with a negative vertical displacement which is applied at mid-span, on the upper face of the beam, until the first interface element from the lower face of the beam starts to crack. This initial vertical displacement is kept constant until the end of the test. The deformed mesh and the normal stresses in the interface elements corresponding to this initial condition are indicated with time t = 0 in Fig. 8. In this condition, the chemical degradation starts in the first interface element, leading to the contraction of the fracture (plastic) surface and the consequent reduction of the tensile strength (χ). This reduction of the tensile strength of the first interface element leads to a stress redistribution, which increases the normal stresses in the interface elements above it. Eventually, this stress redistribution causes the cracking of the second interface element, triggering its chemical degradation. As time goes by, this process progresses leading to the propagation of the initial crack, as it is shown in Fig. 8.

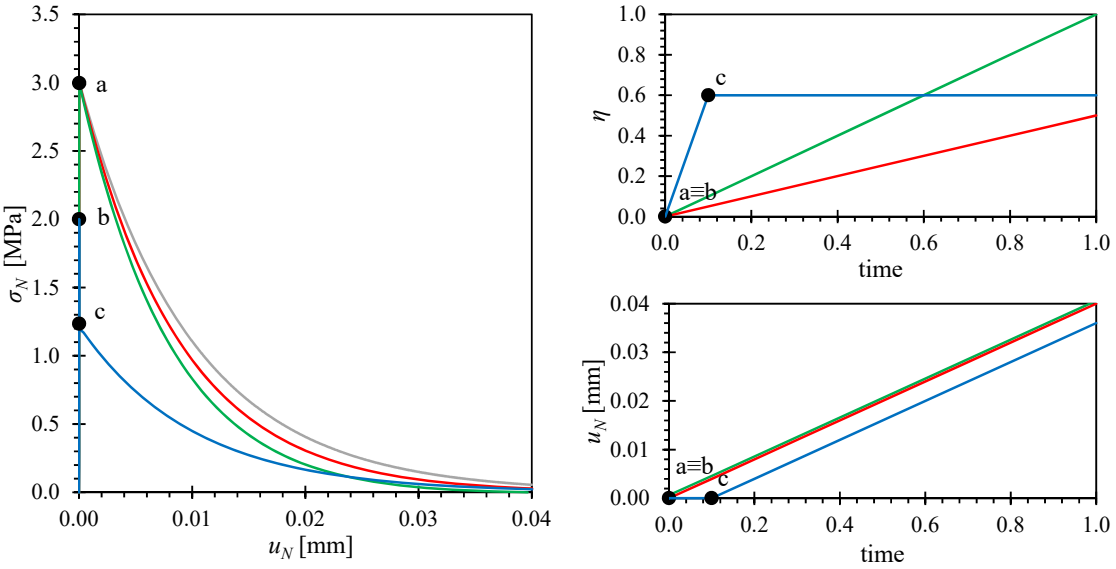


Figure 2: Pure tension tests combined with different cases of chemical degradation described in the body of the text: Case 0 (grey line), Case 1 (red lines), Case 2 (green lines), and Case 3 (blue lines). Left plot, normal stress versus normal relative displacement. Upper-right plot, chemical degradation versus time. Lower-right plot, normal relative aperture versus time. The red line in the lower-right plot has been slightly shifted for the sake of clarity.

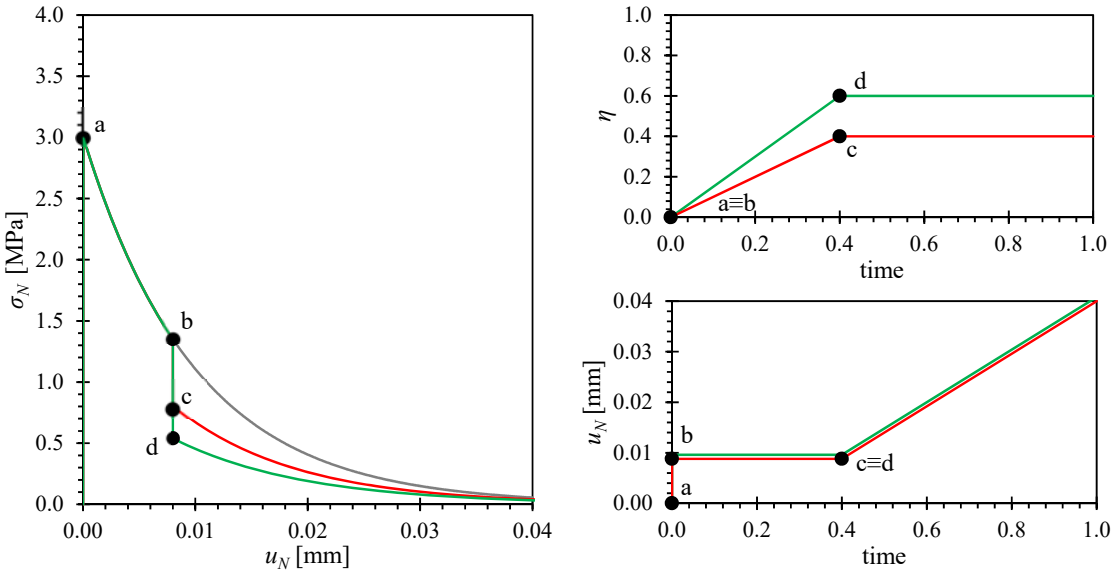


Figure 3: Pure tension tests combined with different cases of chemical degradation described in the body of the text: Case 0 (grey line), Case 4 (red lines), and Case 5 (green lines). Left plot, normal stress versus normal relative displacement. Upper-right plot, chemical degradation versus time. Lower-right plot, normal relative aperture versus time. The green line in the lower-right plot has been slightly shifted for the sake of clarity.

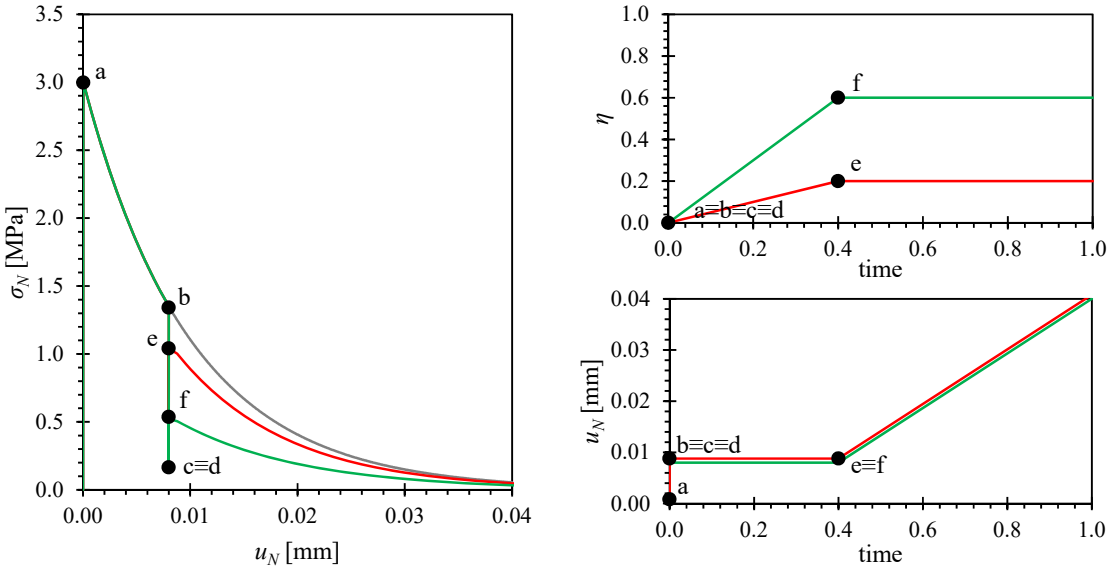


Figure 4: Pure tension tests combined with different cases of chemical degradation described in the body of the text: Case 0 (grey line), Case 6 (red lines), and Case 7 (green lines). Left plot, normal stress versus normal relative displacement. Upper-right plot, chemical degradation versus time. Lower-right plot, normal relative aperture versus time. The green line in the lower-right plot has been slightly shifted for the sake of clarity.

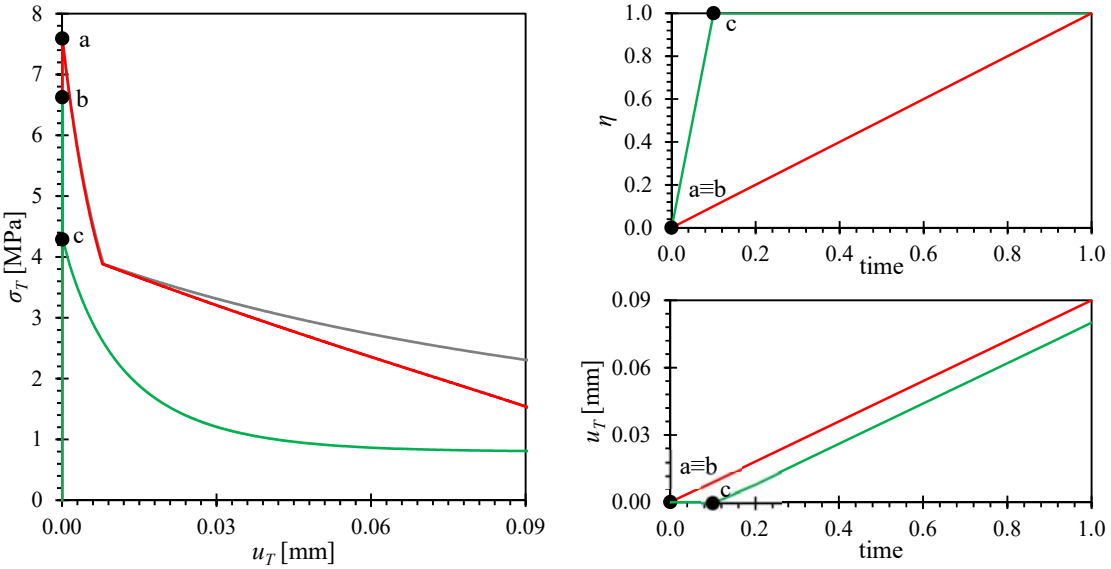


Figure 5: Shear under compression tests combined with different cases of chemical degradation described in the body of the text: Case 0 (grey line), Case 1 (red lines), and Case 2 (green lines). Left plot, normal stress versus normal relative displacement. Upper-right plot, chemical degradation versus time.

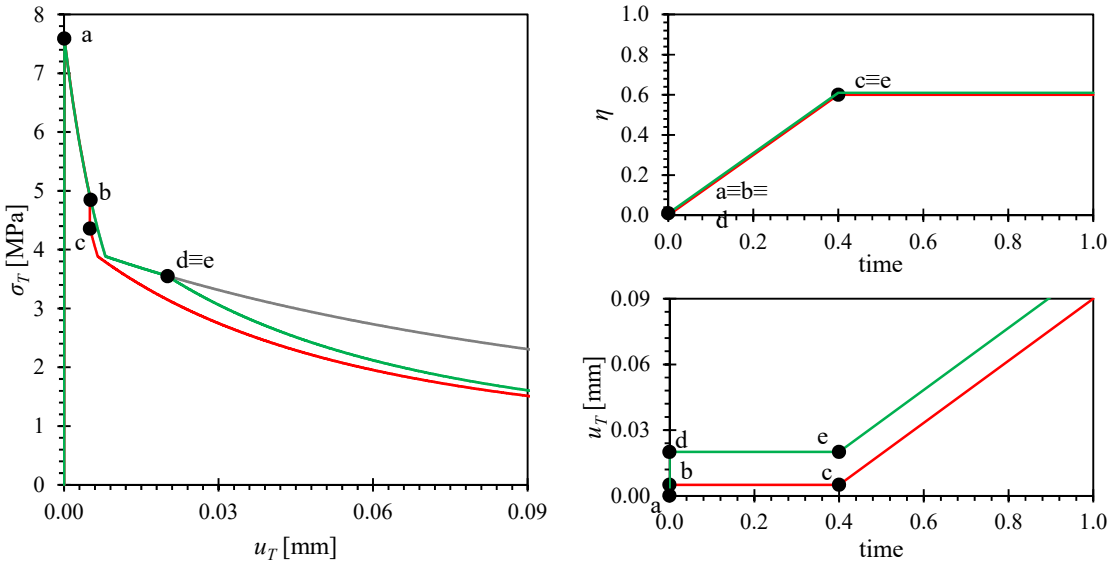


Figure 6: Shear under compression tests combined with different cases of chemical degradation described in the body of the text: Case 0 (grey line), Case 3 (red lines), and Case 4 (green lines). Left plot, normal stress versus normal relative displacement. Upper-right plot, chemical degradation versus time. The green line in the upper-right plot has been slightly shifted for the sake of clarity.

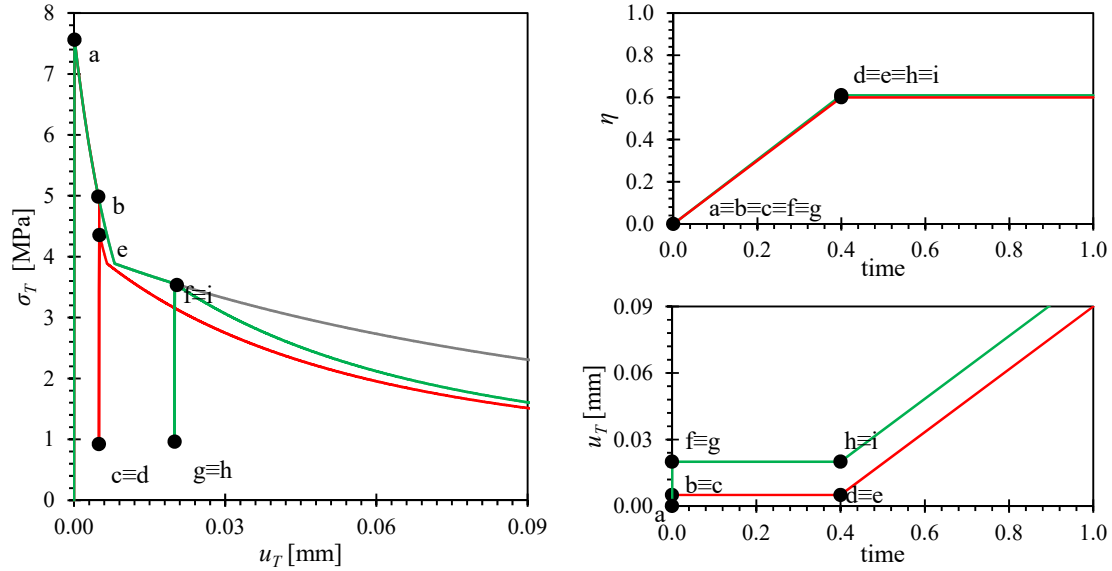


Figure 7: Shear under compression tests combined with different cases of chemical degradation described in the body of the text: Case 0 (grey line), Case 5 (red lines), and Case 5 (green lines). Left plot, normal stress versus normal relative displacement. Upper-right plot, chemical degradation versus time. The green line in the upper-right plot has been slightly shifted for the sake of clarity.

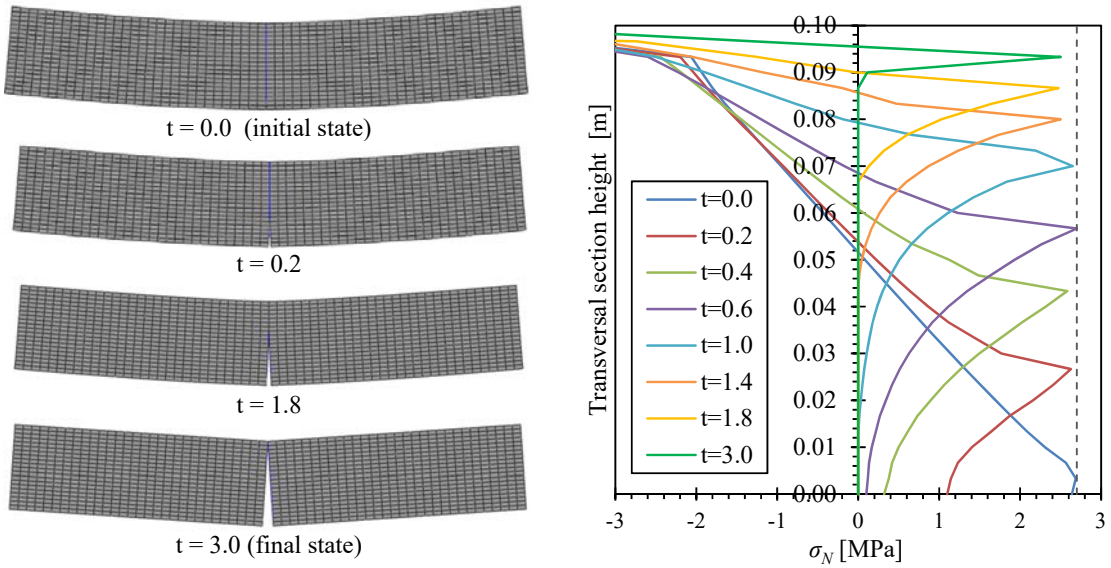


Figure 8: Three-point bending test. An initial vertical displacement is imposed to the mid-span point of the upper face of the beam, and it is kept constant while the chemical degradation of the cracked interface elements makes the flexural crack to grow. Left, deformed FE mesh (× 200) at different times. Right, time evolution of the normal stress profile of the central section of the beam as the fracture progresses due to the chemical degradation.

4 CONCLUDING REMARKS

- A C-M mechanism which may lead to the propagation of cracks in oil-well cements exposed to carbonated brines is proposed.
- In order to reproduce this mechanism with a coupled FE C-M model, a new constitutive law for zero-thickness interface elements is being developed.
- This constitutive law makes it possible to simulate the reduction of the material strength parameters due to chemical degradation processes, such as acid attack of oilwell cements.
- The behaviour of the new law is illustrated by a number of simple academic tests, including pure tensile tests, shear under compression tests, and a three-point bending test.
- The preliminary results obtained seem indicate that the proposed C-M mechanism for sub-critical crack propagation due to acid attack can be simulated with the new constitutive law.

ACKNOWLEDGMENTS

This research has been supported by MEC (Madrid) through project BIA2016-76543-R, which includes European FEDER funds, and 2017SGR-1153 from Generalitat de Catalunya (Barcelona). The first author also acknowledges AGAUR (Barcelona) for her FI doctoral fellowship.

REFERENCES

[1] Gasda, S.E., S. Bachu and M.A. Celia. The potential for CO_2 leakage from storage sites in geological media: analysis of well distribution in mature sedimentary basins. *Environmental Geology* (2004) **46**(6–7):707–720.

[2] Kutchko, B.G., Strazisar, B.R., Dzombak, D.A., Lowry, G.V., Thaulow, N. Degradation of well cement by CO_2 under geologic sequestration conditions. *Environmental Science and Technology* (2007) **41**:4787–4792.

[3] Kutchko, B.G., Strazisar, B.R., Lowry, G.V., Dzombak, D.A., Thaulow, N. Rate of CO_2 Attack on Hydrated Class H Well Cement under Geologic Sequestration Conditions. *Environmental Science and Technology* (2008) **42**:6237–6242.

[4] Rimmelé, G., Barlet-Gouédard, V., Porcherie, O., Goffé, B., Brunet, F. Heterogeneous porosity distribution in Portland cement exposed to CO_2-rich fluids. *Cement and Concrete Research* (2008) **38**:1038–1048.

[5] Carey, J.W., Wigand, M., Chipera, S.J., WoldeGabriel, G., Pawar, R., Lichtner, P.C., Wehner, S.C., Raines, M.A., Guthrie, G.D. Analysis and performance of oil well cement with 30 years of CO_2 exposure from SACROC Unit, West Texas, USA. *International Journal of Greenhouse Gas Control* (2007) **1**:75–85.

[6] Duguid, A., Scherer, G.W. Degradation of oilwell cement due to exposure to carbonated brine. *International Journal of Greenhouse Gas Control* (2010) **4**:546–560.

[7] Duguid, A., Radonjic, M., Scherer, G.W. Degradation of cement at the reservoir/cement interface from exposure to carbonated brine. *International Journal of Greenhouse Gas Control* (2011) **5**:1413–1428.

[8] Liaudat, J., Martínez, A., López, C.M., Carol, I. 2018. Modelling acid attack of oilwell cement exposed to carbonated brine. *International Journal of Greenhouse Gas Control* (2018) **68**:191–202.

[9] Mainguy, M., Longuemare, P., Audibert, A., Lécolier, E. Analyzing the risk of well plug failure after abandonment. *Oil & Gas Science and Technology-Revue de l'IFP* (2007) **62**(3):311-324.

[10] Martínez, A., Liaudat, J., López, C.M., Carol, I. Diffusion-reaction modelling of degradation of oil-well cement exposed to carbonated brine. In *Computational Plasticity XIV - Fundamentals and Applications*, pp.625–635, CIMNE, Barcelona, 2017.

[11] Barandiarán, L., Liaudat, J., López, C.M., Carol, I. Modelling acid attack of oilwell cement exposed to carbonated brine: effect of specimen geometry on experimental results. Submitted to the *XV International Conference on Computational Plasticity - Fundamentals and Applications (COMPLAS XV)*, Barcelona, 2019.

[12] Carol, I, Prat, P.C., López, C.M., A normal/shear cracking model. Application to discrete crack analysis. *Journal of Engineering Mechanics* (1997) **123**(8):765–73.

[13] Carol, I., López, C.M., Roa, O. Micromechanical analysis of quasi-brittle materials using fracture-based interface elements. *International Journal for Numerical Methods in Engineering* (2001) **52**(1-2):193–215.

[14] López, C.M., Carol, I., Aguado, A. Meso-structural study of concrete fracture using interface elements. I: numerical model and tensile behavior. *Materials and structures* (2008) **41**(3):583–599.

XV International Conference on Computational Plasticity. Fundamentals and Applications
COMPLAS 2019
E. Oñate, D.R.J. Owen, D. Peric, M. Chiumenti & Eduardo de Souza Neto (Eds)

A NOVEL INDICATOR FOR KINEMATIC HARDENING EFFECT QUANTIFICATION IN DEEP DRAWING SIMULATION

RÉMI LAFARGE*, NIKLAS KÜSTERS* AND ALEXANDER BROSIUS*

* Chair of Forming and Machining Processes (FF)
Technische Universität Dresden (TUD)
01069 Dresden, Germany
e-mail: remi.lafarge@mailbox.tu-dresden.de, web page: http://www.tu-dresden.de/mw/if/ff

Key words: Sheet metal forming, kinematic hardening

Abstract. Deep drawing simulation techniques reduce tool design costs and improve tool performance and reliability. In terms of strain hardening, mixed models capturing the kinematic effect are sometimes more accurate than isotropic models. Indeed, non-linearity in strain paths can lead to inconsistent simulation results. However, the use of such models requires a greater number of tests including strain path changes. Therefore, the use of such mixed models shall be required only if the simulation includes non-linear strain paths and the material exhibits a pronounced Bauschinger effect. New tools to help engineers choose between models could ease the spread of more advanced models in simulation of deep drawing processes when needed. With this in mind, an indicator predicting the influence of kinematic effects could help to select an adequate model.

In this study, a new indicator is introduced with the idea of characterising strain path non-linearity in order to assess kinematic hardening influence. The indicator is computed using the forming history taken from a purely isotropic simulation – which is easier to set up and parametrise. The ability of the indicator to predict inconsistencies within the isotropic simulation is investigated using U-channel simulations.

1 INTRODUCTION

Simulation techniques as finite element analysis are widely spread in sheet metal forming, as they can be help to enlarge process windows and to develop reliable tools within a short period of time. Furthermore it is well known, that accurate modelling of the material behaviour is crucial for reliable predictions of forming processes [1]. For this purpose, numerous formulations for describing complex material flow were developed in the past, requiring a greater number of tests including strain path changes.

Especially for forming processes where a high amount of cyclic bending is induced by forming through draw beads, isotropic hardening models are insufficient for precise springback prediction. Previous work already studied the influence of kinematic hardening

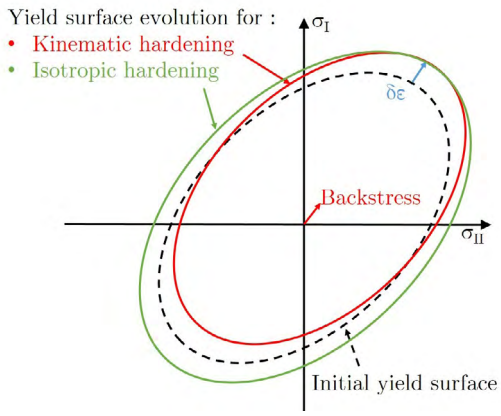


Figure 1: Kinematic and isotropic hardening

in deep drawing processes [2] and showed the importance of this material behaviour for the prediction of springback [3], being crucial for deep drawing tools design. In these cases, mixed isotropic-non-linear kinematic hardening formulations in general [4], but also special formulations of distorsional hardening as shown in [5] are able to capture the springback phenomenon. However, the authors of [6] demonstrated that identification of kinematic hardening behaviour is a difficult task due to ambiguity. Results often provide good predictions, but are not reliable in all cases and, therefore, always have to be verified. For the parametrisation of the yield surface evolution, a smart choice of experimental tests and sophisticated numerical evaluation strategies has to be made as shown in [7]. As a result of precise material modelling, it is subsequently possible to compensate springback by optimisation of tool geometries [8]. In addition to conventional strategies, the recently proposed macro-structured tools by Brosius et al. [9] are not only capable of widening process window regarding drawing depth, but are also helpful to reduce springback angles for specific materials, with a higher amount of kinematic hardening [10].

Despite the great potential for optimisation due to enhanced knowledge of kinematic hardening effects in drawing operations, in industrial applications, an estimation of the extensive efforts is often desired in advance. Additional material characterisation and numerical analysis with these models should only be performed for forming operations with high non-linear strain paths and for materials with a pronounced Bauschinger effect. For this reason evaluation tools for assisting engineers in the choice of adequate material models in simulation of deep drawing processes would be advantageous. In order to quantify non-linearity in strain paths, diverse indicators such as shown by Herault et al. [11] were proposed in the past. In this study, an alternative approach for the quantification of the kinematic hardening effect is proposed and discussed for the analysis of a macro-structured tool as used in [10].

2 CONTEXT

2.1 Hardenings models

The Bauschinger effect describe a lowering of the yield stress upon strain reversal. This change can be permanent or only transient, and the magnitude of this effect is dependent on many parameters including material and prestrain. A model aiming at the simulation of cyclic behaviour must be able to accurately capture the Bauschinger effect as shown in [12]. Strain hardening consists of a yield surface evolution following an initial deformation. The first model to capture this effect was isotropic hardening. It operates by uniformly scaling of the yield surface on increasing plastic hardening. The parameter identification of this hardening model can be realised using the result of simple tensile tests. However, this model fails to capture the Bauschinger effect, as no softening on reversal can be obtained with this family of models. Kinematic hardening was first introduced by Prager [13]. In this model, yield stress evolution is characterised by the translation of the yield surface, which is implemented using a backstress tensor. In Prager's model, backstress increments are calculated by multiplicating the strain increments by a constant c. However, the use of a pure kinematic model, does not enable a correct simulation of the Bauschinger effect within sheet metal, and a mixed model using anisotropic and kinematic hardening should be used [14].

Figure 1 represents the evolution of the yield surface following a strain increment for a isotropic hardening model and a kinematic hardening model. It is quite clear that for non-linear strain paths, the two families of models will lead to different results, in contrast to linear strain paths. Not only does kinematic hardening has a strong influence on stress values, but also on the Lankford coefficient, as the translation of the yield surface will also influence surface normals [15].

The parameter identification for non-linear, mixed models is also more complex than for isotropic models, as tension-compression tests are required. This test is challenging for sheet metal, as buckling might occur during the compression phase [16]. Besides the use of anti-buckling mechanisms supporting specimens on the surface to prevent buckling, the use of miniaturized samples, where geometry makes the tests less prone to buckling as shown in [17], is common technique.

2.2 Kinematic hardening in deep drawing processes

Non-linearity in strain path is to be expected in a deep drawing process. Indeed, the bending and unbending of the blank along the die edge implies strain reversal in the blank at least near the surface (see figure 2). However, the amount of strain path non-linearity is not easily predicted and is non-uniform in the blank for complex drawing parts. Moreover, strain path non-linerarities can be caused by other elements of the tool's geometry.

The influence of kinematic hardening in forming applications has already been studied by Oliveira et al. [18]. They investigated the influences of kinematic hardening for the U-profile and different mild and high strength steel grades (DC06 and DP600). They concluded that springback behaviour depends on strain path non-linearity. In order to study the influence of kinematic hardening, the authors compared two simulations, one imple-

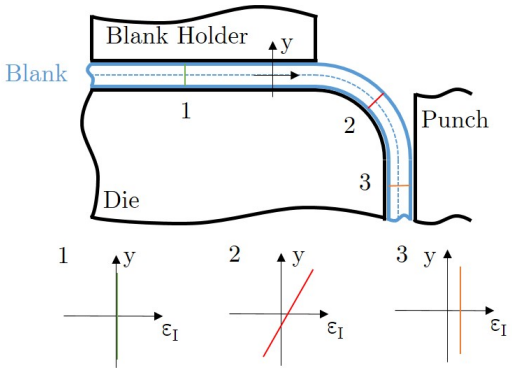


Figure 2: Strain reversal on die edge

mented a simplified isotropic model and the second used a mixed (isotropic-kinematic) hardening model. Liao et al. [3] studied the influences of path dependent behaviour on twist springback for P-channel and C-channel. They concluded that path dependent behaviour has a significant influence on simulated springback results.

2.3 Kinematic indicator

Since the influence of kinematic hardening is non-uniform and difficult to predict, a few indicators have been proposed for evaluating its influence and other strain path dependent behaviour in drawing operations.

First, Schmitt et al. [19] studied the influence of strain path change on crystal formation using the following equation:

$$\theta_{Schmitt} = \frac{\dot{\varepsilon}_1^p : \dot{\varepsilon}_2^p}{\|\dot{\varepsilon}_1^p\|\|\dot{\varepsilon}_2^p\|} \tag{1}$$

where $\dot{\varepsilon}_1^p$ and $\dot{\varepsilon}_2^p$ are two successive plastic strain increment tensors. This parameter take values between -1 and +1, with -1 corresponding to strain reversal and +1 to strain path linearity. Van Riel [20] studied the use of such indicators in FE simulations. He proposed the use of an indicator based on strains increments. However, he noted that this indicator is very sensitive to sampling frequency and converge to 1 for high enough sampling frequencies. A more stable variant was developed:

$$\theta_{VanRiel} = \frac{G : \dot{\varepsilon}^p}{\|G\|\|\dot{\varepsilon}^p\|} \tag{2}$$

where G is defined by the following differential equation:

$$\dot{G} = \dot{\varepsilon}^p - c\|\varepsilon\|G \tag{3}$$

G is named strain history and the c parameter is used to quantify the influence of previous strain states. Herault et al. [11] use this indicator to study strain reversal and cross-hardening (where yield surface is stretched perpendicularly to the strain increment) of DP600 for the reverse redrawing of cylindrical cups. A limit of this indicator is the

absence of a method to select the right value for the parameter c. Moreover, this indicator is not dependent on the material model.

Oliviera et al. [18] propose to use plastic strain direction and a plastic strain reference to develop a new indicator. However, no indication is given on how to choose the plastic strain reference. Based on this work, Clausmeyer et al. [21] introduced a cross hardening indicator and studied the influence of cross hardening for a specific channel profile.

Another proposition was made by Tekkaya at al. [22]. The authors suggest the following indicator:

$$\theta_{LWI} = \frac{\sum_{i=0}^{n}(\Delta\alpha * \delta E)}{E_{o\rightarrow\varepsilon^p_{max}}} \tag{4}$$

where α is the angle between two consecutive strain increments, and E is the plastic deformation energy. The variation of internal energy is used to weight the different changes of direction according to the amount of plastification they represent. The authors linked this indicator with kinematic influences on von Mises stress for the deep drawing of the S-Rail using DP600 steel. This indicator presented the same flaw as the discretised version of $\theta_{Schmitt}$: it is converging to zero for high enough sampling frequencies.

3 A NOVEL INDICATOR

Based on the previously introduced indicators flaws, it is possible to set some specifications for a novel indicator. The output values should be a scalar; it must have a local definition to be calculable for every element in a FE simulation. It should take values between 0 and 1 and converge as the sampling frequency increases.

The following new indicator is proposed :

$$\theta = \frac{\sum_{i=0}^{N} \measuredangle(\alpha_{est}, \dot{\varepsilon}^p) * \delta E}{\pi * w_{max}} \tag{5}$$

where:

- α_{est} is the estimation of the backstress tensor
- δw is the variation of the specific plastic work for the given timestep
- w_{max} is the maximum of the specific plastic work in the part

The angle between the backstress tensor and the plastic strain is defined between 0 and π. This value is meant to represent the non-linearity of the strain path at specific time of the simulation. The use os specific plastic work increment enables to weight the most important evolution of the strain history. The backstress estimation α_{est} is calculated using the strain path produced by an isotropic simulation using:

$$d\alpha_{est} = \dot{\varepsilon}^p * \frac{d\sigma_0}{d\varepsilon^p_{eq}} \tag{6}$$

The backstress is estimated using the hardening law and the strain path, assuming a pure kinematic model. It is therefore possible to validate the convergence condition

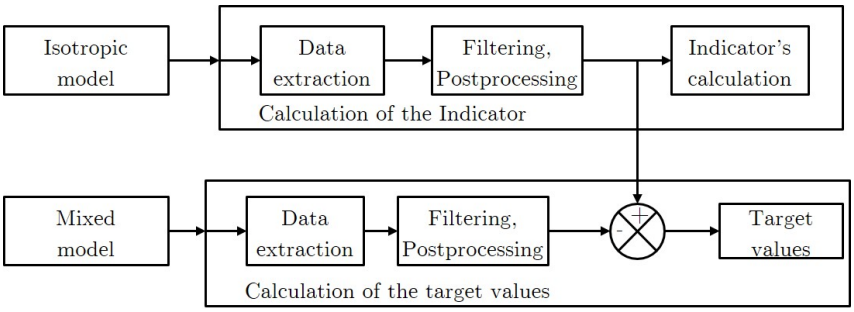


Figure 3: Calculation of indicator and target values

without having specified a fixed reference such as Oliviera et al. [18] or a value constructed from unspecified parameters such as Van Riel [20].

A shell element has different layers, corresponding to different integration points along the section. The strain history depends of the chosen integration point. Therefore, the indicator must be calculated for each integration point. With the software (LS-DYNA) used in this work, three integration point can be used: upper, middle and lower.

4 EVALUATION OF THE INDICATOR

4.1 Evaluation framework

To validate the use of this indicator, a scheme presented figure 3 was employed. First, two simulations are carried out using LS-DYNA; one with a full isotropic model, and a second with a mixed model. Then the isotropic simulation results are used to calculate the indicator. Disparities between two simulations are then used as target value: the deviation between the two simulations is subsequently used as a measure of the influence of kinematic hardening. Different target variables may be used. This work focus on specific accumulated plastic work and von Mises equivalent stress. Both are dependent on the integration point and should be compared with the corresponding value of the indicator, i.e. calculated for the same integration point.

To evaluate the performance of this indicator, a simple U-profile shape is used at first. To create more complex strain paths, macro-structured tools are used. Introduced by Brosius et al. [9] to enable lubricant free deep drawing, the U-profile tool consists of a macro-structured blank holder and die as shown in Figure 4. With this tool, the immersion depth δ (see figure 4), which is the distance between blankholder and die substracted from blank thickness is adjustable. Two configurations will be used in this paper, an immersion depth of $0mm$ and $0.2mm$. The indicator, as well a the target values, should show a significant sensitivity to these features (macro-structured, immersion) of the tool for materials with pronounced kinematic hardening. The material used is an DP600 steel. Sheet thickness was mesured at 1,17mm. Drawing Depth was 90mm. Other geometric properties are shown figure 4.

The simulation are performed using LS-DYNA 11.0.0 using MPP for parallelisation. A high number of elements were used (around 15000 in the blank), as the used proprocessing

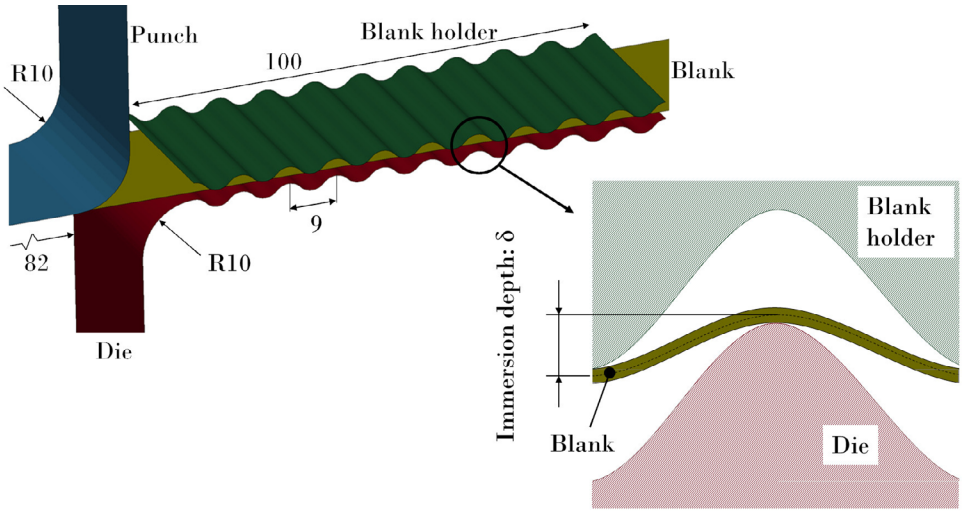


Figure 4: Tools and blank in LS-PREPOST

Table 1: DP600 Parameter for Simulation

Parameter description	Symbol	Value	Unit
Young's Modulus	E	185	MPa
Mass density	ρ	7850	kg^{-3}
Poisson coefficient	ν	0.3	$\varnothing$
Swift parameter	ε_0	$1.822 * 10^{-3}$	$\varnothing$
Swift parameter	k	1060	MPa
Swift parameter	n	0.1741	$\varnothing$
Chaboche modified parameter	a_1	379.0	MPa
Chaboche modified parameter	c_1	11.40	$\varnothing$

libraries are not compatible with active remeshing. Belytschko-Tsay formulation was used ($ELFORM = 2$) with 9 integration point. The material model used is a modified Chaboche (**MAT_133*), for both mixed and isotropic model. The Barlat 2000-2d yield criterion is used.

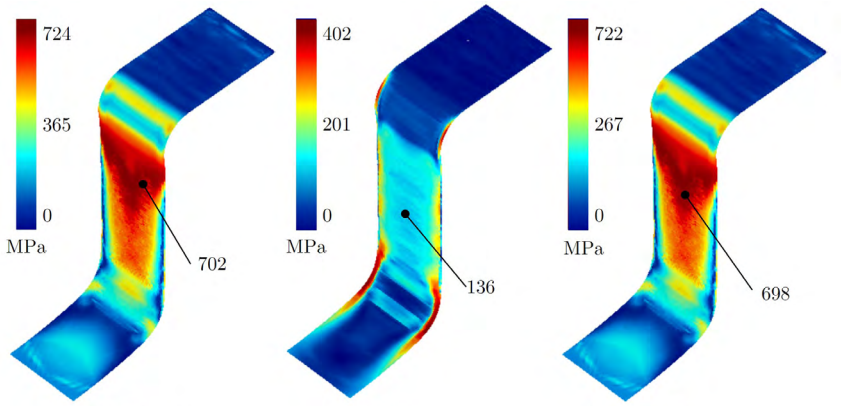
Computation of the indicator is performed in Python using SciPy [23], and qd.cae[1].

For the material characterisation of the DP600, tensile tests in three different rolling directions, a bulge test and a cyclic tension compression test were carried out and used for parameter identification.

4.2 Performance of the indicator

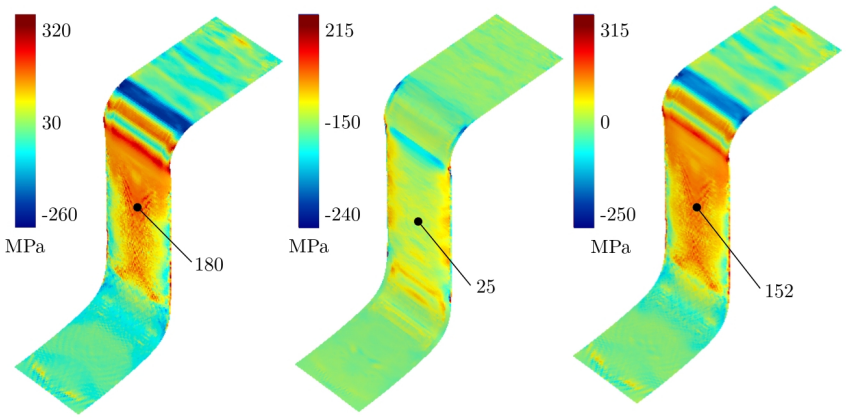
At first, numerical results of the macrostructured U-profile drawing with zero immersion depth ($\delta = 0mm$) depth will be investigated. The figure 5 represents the von Mises equivalent stress for different integration points. Figure 6 represents the differences of the von Mises equivalent stress values between the simulations implementing isotropic and

[1]https://github.com/qd-cae/qd-cae-python



(a) Upper layer (b) Middle layer (c) Lower layer

Figure 5: Values of the von Mises stresses values ($\sigma_{\text{VM, Iso.}}$) for different layers and with a zero immersion depth ($\delta = 0mm$)

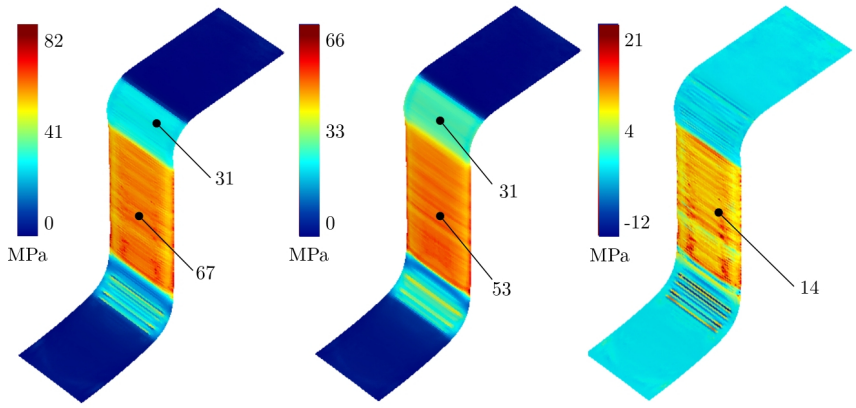


(a) Upper layer (b) Middle layer (c) Lower layer

Figure 6: Values of the difference between simulation for von Mises stresses values ($\sigma_{\text{VM, Iso.}} - \sigma_{\text{VM, Kin.}}$) for different layers and with a zero immersion depth ($\delta = 0mm$)

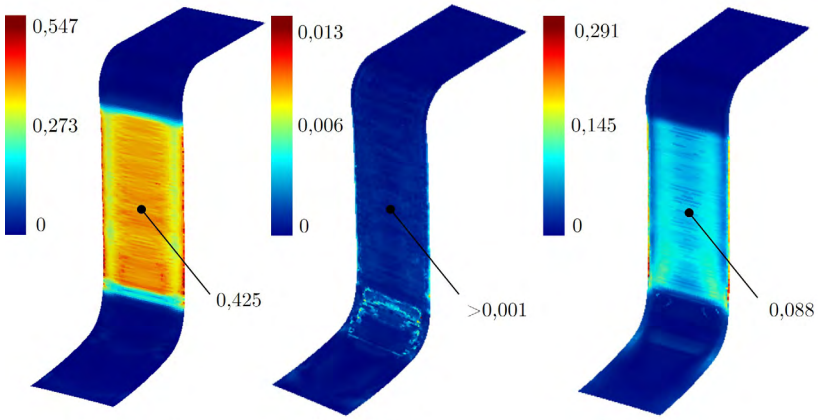
combined isotropic-kinematic hardening model. The figure 7 represents the specific plastic work for the two simulation, and the difference obtained, for the upper layer. Those results are consistent with theory: the influence of kinematic hardening is linked with the bending and unbending along the die radius. As expected, the plastic works after unbending is smaller for the mixed model than for the isotropic model, despite being the same after the first bending.

The figure 8 represents the values obtained for the indicator on different layer. Results imply the indicator is able to accurately predict differences between accumulated specific plastic work. However, it is less suitable for predicting discrepancies concerning the von Mises stress. This is linked to the accumulative definition of the indicator, leading to steadily increasing or constant values, which therefore cannot predict a reduction of stress values. Another error source is likely caused by strain path differences: this indicator can be useful only for process simulations where the characteristics of the strain paths are



(a) Isotropic model (b) Mixed model (c) Difference

Figure 7: Values of the specific accumulated plastic work in the upper layer for the simulation implementing the isotropic model (a), the mixed model and differences between simulation ($w_{\text{pl, Iso.}} - w_{\text{pl, Kin.}}$) for the Upper layer and with a zero immersion depth ($\delta = 0mm$)

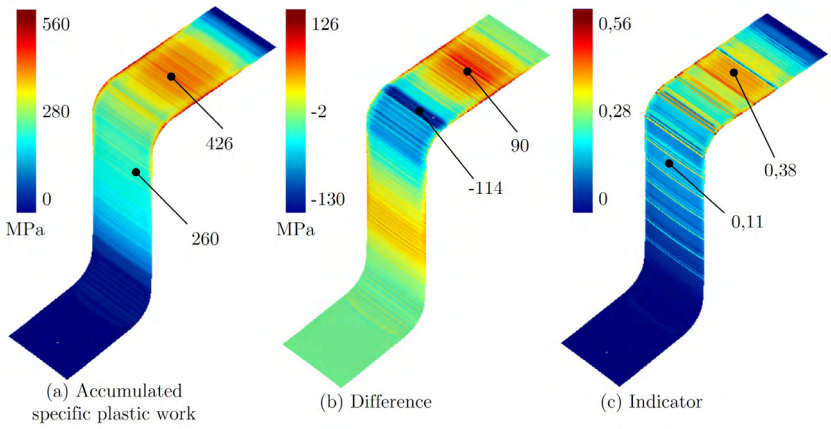


(a) Upper layer (b) Middle layer (c) Lower layer

Figure 8: Values of the indicator θ for different layers and with a zero immersion depth ($\delta = 0mm$)

relatively insensitive regarding the used material model.

When immersion depth is high enough that plastification occurs between blank holder and die, kinematic hardening will play a major role, as bending and unbending occurs in a significant number of times. Figure 9 represents the numerical results computed with a non-zero immersion depth. As expected for this immersion depth, plastification occurs within the blank, which is is visible figure 9 (a). The alternate bending in this zone result in large differences between the two simulations, especially concerning the plastic work as shown figrure 9 (b). Indeed, the upper and lower layers of blank are constantly submitted to reversed loading and deformation. The indicator is able to correctly capture this effect, as presented Figure 9 (c).



(a) Accumulated specific plastic work (b) Difference (c) Indicator

Figure 9: Values of the specific accumulated plastic work in the upper layer for the simulation implementing the isotropic model (a), the differences between both simulation ($w_{\text{pl, Iso.}} - w_{\text{pl, Kin.}}$) (b), and the indicator (θ)(c) for the upper layer and with non-zero immersion depth ($\delta = 0.2mm$)

5 CONCLUSION

In this work, the importance of the kinematic hardening influence is recalled within deep drawing simulation. Based on previous work, a new indicator to predict the influences of kinematic hardening using isotropic simulation results has been proposed. Unlike previous indicators, it is stable for increasing sampling frequencies, but does not require any references or other parameter. Using the additional information provided by the indicator, engineers are able to evaluate material's choice and tool design in early stages of process design and furthermore conclude on the necessity of extensive material characterisation for kinematic hardening for specific forming operations.

The ability of this indicator to predict kinematic hardening has been illustrated using FE-simulation. Future studies will focus on the confirmation of the performance of this new indicator for different, more complex shaped parts. A method to find the smallest sampling frequencies will be investigated. Further developments of the indicator will also be related to springback quantification and an evaluation regarding process limits.

6 ACKNOWLEDGMENT

The authors are grateful to the German Federation of Industrial Research Associations (AiF) for supporting the research project "Relevance analysis for the kinematic hardening in deep drawing processes with closed profiles" (IGF 19973BG). The computations were performed on a PC-Cluster at the Center for Information Services and High Performance Computing (ZIH) at TU Dresden.

REFERENCES

[1] Bruschi, S., Altan, T., Banabic, D., Bariani, P.F., Brosius, A., Cao, J., Ghiotti, A.,Khraisheh, M., Merklein, M., Tekkaya, A.E. (2014) *Testing and modelling of material behaviour and formability in sheet metal forming.* CIRP Ann – Manuf Techn

63/2:727-749.

[2] Haddag, B., Balan, T., and Abed-Meraim, F. (2007). *Investigation of advanced strain-path dependent material models for sheet metal forming simulations.* International Journal of Plasticity, 23(6), 951–979. https://doi.org/10.1016/J.IJPLAS.2006.10.004

[3] Liao, J., Xue, X., Lee, M.-G., Pereira, A. B., Barlat, F., Vincze, G., and Pereira, A. B. (2017). *Constitutive modeling for path-dependent behavior and its influence on twist springback.* International Journal of Plasticity, 93, 64–88. https://doi.org/10.1016/j.ijplas.2017.02.009

[4] Taherizadeh, A., Ghaei, A., Green, D. E., and Altenhof, W. J. (2009). *Finite element simulation of springback for a channel draw process with drawbead using different hardening models.* International Journal of Mechanical Sciences, 51(4), 314-325.

[5] Lee, J. Y., Lee, J. W., Lee, M. G., and Barlat, F. (2012). *An application of homogeneous anisotropic hardening to springback prediction in pre-strained U-draw/bending.* International Journal of Solids and Structures, 49(25), 3562-3572.

[6] Eggertsen, P. A., and Mattiasson, K. (2011). *On the identification of kinematic hardening material parameters for accurate springback predictions.* International journal of material forming, 4(2), 103-120.

[7] Avril S, Bonnet M, Bretelle AS, Grédiac M, Hild F, Ienny P, Latourte F, Lemosse D, Pagano S, Pagnacco E, Pierron F (2008) *Overview of Identification Methods of Mechanical Parameters Based on Full-field Measurements.* Experimental Mechanics 48(4):381.

[8] Meinders, T., Burchitz, I. A., Bonté, M. H., and Lingbeek, R. A. (2008). *Numerical product design: Springback prediction, compensation and optimization.* International Journal of Machine Tools and Manufacture, 48(5), 499-514.

[9] Brosius, A., and Mousavi, A. (2016). *Lubricant free deep drawing process by macro structured tools.* CIRP annals, 65(1), 253-256.

[10] Mousavi, A., Ridolfi, K. S., and Brosius, A. (2018). *Influence of alternating bending on springback behavior of parts in deep drawing process with macro-structured tools.* In MATEC Web of Conferences (Vol. 190, p. 14005). EDP Sciences.

[11] Herault, D., Thuillier, S., Manach, P.-Y., and Duval, J.-L. (2018). *Strain path changes in Reverse Redrawing of DP Steels.* IOP Conference Series: Materials Science and Engineering, 418(1), 012042. https://doi.org/10.1088/1757-899X/418/1/012042

[12] Choteau, M. (1999). *Caractérisation de l'effet bauschinger en sollicitations uniaxiales d'un acier inoxydable austenitique X2CrNiMo17-12-2.*. Retrieved from https://www.theses.fr/1999LIL10209

[13] Prager, W. (1949). *Recent Developments in the Mathematical Theory of Plasticity.* Journal of Applied Physics, 20(3), 235–241. https://doi.org/10.1063/1.1698348

[14] Chun, B. K., Jinn, J. T., and Lee, J. K. (2002). *Modeling the Bauschinger effect for sheet metals, part I: Theory.* International Journal of Plasticity, 18(5–6), 571–595. https://doi.org/10.1016/S0749-6419(01)00046-8

[15] Wagoner, R. H., Lim, H., and Lee, M.-G. (2013). *Advanced Issues in springback.* International Journal of Plasticity, 45, 3–20. https://doi.org/10.1016/J.IJPLAS.2012.08.006

[16] Boger, R. K., Wagoner, R. H., Barlat, F., Lee, M. G., and Chung, K. (2005). *Continuous, large strain, tension/compression testing of sheet material.* International Journal of Plasticity, 21(12), 2319–2343. https://doi.org/10.1016/j.ijplas.2004.12.002

[17] Staud, D., Merklein, M., Borsutzki, M., and Geisler, S. (2009). *Zug-Druck-Versuche an Miniaturproben zur Erfassung von Parametern für kinematische Verfestigungsmodelle.* Tagungsband Werkstoffprüfung, 2, 211-218.

[18] Oliveira, M. C., Alves, J. L., Chaparro, B. M., and Menezes, L. F. (2007). *Study on the influence of work-hardening modeling in springback prediction.* International Journal of Plasticity, 23(3), 516–543. https://doi.org/10.1016/J.IJPLAS.2006.07.003

[19] Schmitt, J. H., Aernoudt, E., and Baudelet, B. (1985). *Yield loci for polycrystalline metals without texture.* Materials Science and Engineering, 75(1–2), 13–20. https://doi.org/10.1016/0025-5416(85)90173-9

[20] Van Riel, M. (2009, August 28). *Strain path dependency in sheet metal. Experiments and models.* Retrieved from https://research.utwente.nl/en/publications/strain-path-dependency-in-sheet-metal-experiments-and-models

[21] Clausmeyer, T., Güner, A., Tekkaya, A. E., Levkovitch, V., and Svendsen, B. (2014). *Modeling and finite element simulation of loading-path-dependent hardening in sheet metals during forming.* International Journal of Plasticity, 63, 64–93. https://doi.org/10.1016/J.IJPLAS.2014.01.011

[22] A. E. Tekkaya, M. Merklein, H. Traphöner, M. Rosenschon, *Identifikation spannungsabhängiger Bauschinger-Koeffizienten*, ISBN: 978-3-86776-480-3

[23] Jones E, Oliphant E, Peterson P, et al. (2001-). *SciPy: Open Source Scientific Tools for Python*, http://www.scipy.org/

XV International Conference on Computational Plasticity. Fundamentals and Applications
COMPLAS 2019
E. Oñate, D.R.J. Owen, D. Peric, M. Chiumenti & Eduardo de Souza Neto (Eds)

FINITE ELEMENT ANALYSIS OF RESIDUAL STRESSES IN LARGE COLD-ROLLED THREADS

Julian Unglaub*, Hendrik Jahns* and Klaus Thiele*

* Institute for Steel Structures
Technische Universität Braunschweig
Beethovenstraße 51, 38106 Braunschweig, Germany
e-mail: j.unglaub@stahlbau.tu-braunschweig.de, web page:
http://www.stahlbau.tu-braunschweig.de/

Key words: Computational Plasticity, Forming Process, Residual Stress, Bolt, Fatigue

Abstract. As a subproject of the DFG Research Training Group *Graduiertenkolleg 2075 - Modelling the constitutive evolution of building materials and structures with respect to aging* (GRK 2075), the fatigue behaviour of rolled-after heat-treatment and hot-dipped galvanized HT-bolts is examined.
Bolted joints are one of the most frequently used joining connections in mechanical and civil engineering. HT-bolts with large diameters (M 30 up to M 72) are widely used in wind power plants both on-shore and off-shore. During the cold-rolling process, compressive residual stresses are generated at the root of the thread in combination with strain hardening. Therefore, bolts rolled-after heat-treatment under tensile loading have a much longer fatigue life than rolled-before heat-treatment ones. In order to calculate the fatigue life of rolled-after heat-treatment bolts with a notch-strain concept, it is necessary to calculate the residual stresses and the material state from the forming process.
A simulation of the forming process of the M 48 thread will be presented. It is investigated if the residual stress and material state from the forming process can be captured with the transient cyclic material model of Chaboche et al.[1] implemented in the commercial FE program `Abaqus`. The forming process is simulated with remeshing and Mesh-to-Mesh-solution-Mapping [3] on an axisymmetric model. The result will be evaluated in terms of geometry, stress and strain state. The determined stress state is compared to measured residual stresses in Unglaub [2] and Fares [4]
The simulation of the forming process gives a good coincidence with the thread geometry in practice. The residual stress path corresponds qualitatively to the measured residual stresses. The plastic equivalent strain in the thread root is overestimated because of the chosen material model and the axisymmetric modeling.

1 Introduction

Bolts as elements are subject to aging. High-tensile (HT) bolts with large diameters (M 30 up to M 72) are widely used in wind power plants both onshore and offshore. Cyclic loading can lead to fatigue failure in the thread. The manufacturing process (rolled, cut, quenched tempered, galvanized) influences the fatigue strength. One of the fatigue strength governing parameters is the processing method used to manufacture those threads, shown in Figure 1 for an rolled-after heat-treatment (SG), hot-dip galvanized (tZn) HT-bolt.

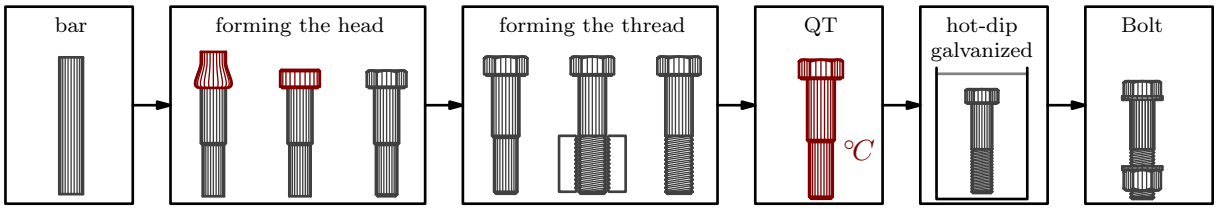


Figure 1: Manufacturing process steps for SG, hot-dip galvanized bolts [2]

During the cold-rolling process, compressive residual stresses are generated at the root of the thread in combination with strain hardening. Nearly all cracking due to cyclic loading occurs in this massively deformed area. Therefore, SG HT-bolts under tensile loading have a much longer fatigue life than rolled-before heat-treatment (SV) HT-bolts.

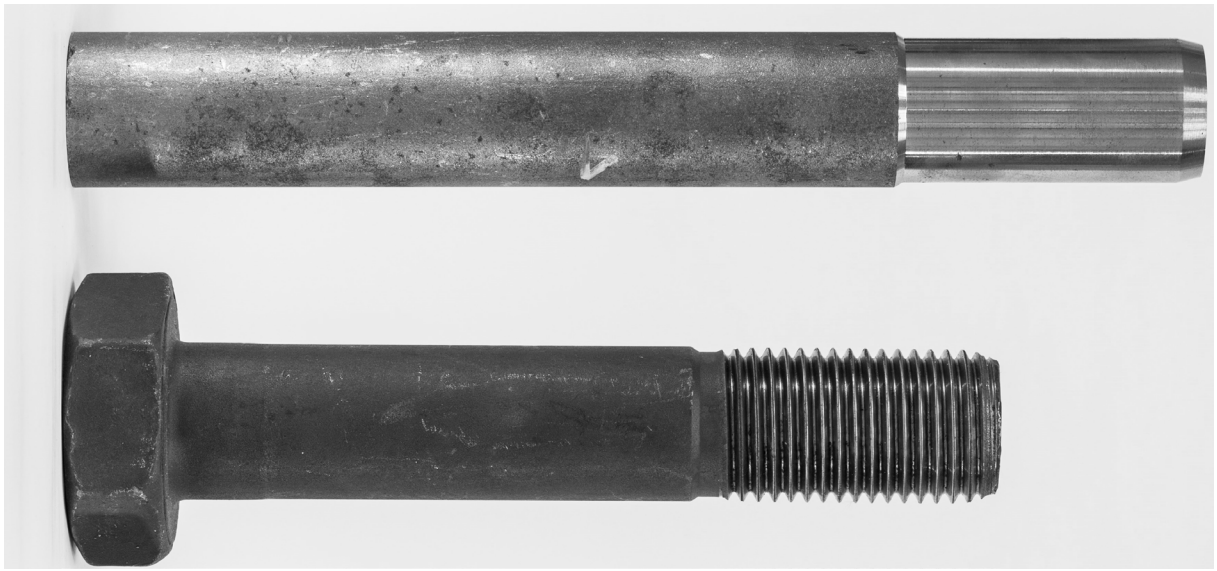


Figure 2: Workpiece for M48x255 SG 10.9 HT-Bolt (above) and final geometry of M48x255 SG 10.9 HT-Bolt (below)

To describe the fatigue behaviour of SV HT-bolts locally, notch-strain-concepts are frequently used [7]. The cyclic transient elastic-plastic material behaviour is estimated with the help of experiments. Previous local concepts for SG bolts take residual stresses

into account via phenomenological parameters [8].
The reason for this situation is the description of the complex residual stress state and hardening condition in the thread root. In order to develop a comprehensive notch-strain-concept for SG bolts, it is necessary in a first step to understand the cyclic transient elastic-plastic behaviour in finite element simulation during the forming process. On this basis a further loading behavior can be investigated.
In the following the calculation of the residual stress state is carried out by means of forming simulation of a M48x255 SG 10.9 HT-bolt, cf. Figure 2. The result will be evaluated in terms of geometry, stress and strain state. The determined stress state is compared to measured residual stresses in Unglaub [2] and Fares [4].

2 Principle of thread rolling

The piercing process rolls the thread on the workpiece by shifting two thread-dies on both sides, cf. Figure 3. The workpiece is mounted on additional rollers so that it can rotate freely in the rolling direction. In addition, the workpiece is continuously lubricated and cooled via suspension. The manufacturing process can be divided into two phases: In a first step, plastic deformation takes place as a result of the displacement and rotation of the die rollers. Once the dies have completely penetrated the workpiece, the displacement is kept constant in a second step and a defined number of roll-overs are applied [2].
The diameter of the raw workpiece is smaller than the diameter of the actual thread, cf. Figure 2. This can be attributed to the volume constancy and the material behaviour. During the forming process, the thread flank is held laterally by contact with the thread-die. Only the first thread is not held laterally. To prevent breakage, the starting area of the raw workpiece is sloped [2].

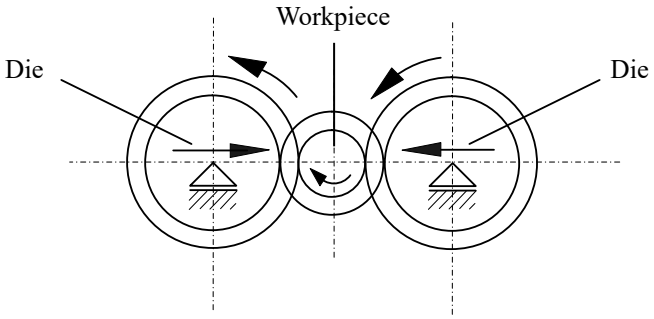


Figure 3: Principle sketch of piercing process for threads [2]

2.1 Review

Fares [4] simulates with a three-dimensional model the forming process of SG M 10 bolt, for which an elastic-plastic material model is used, without hardening and softening effects. Essential parameters such as element type and time step are not specified. Thus, the quality of the simulation cannot be assessed. The axial residual stresses are validated by comparing the calculated stress with a measured residual stress curve. The stresses

are reproduced well in the near-surface area of the thread root, Figure 8.
Furukawa et al. [5] investigate the influence of residual stresses on the fatigue strength of bolts. A two-dimensional FE model (plane strain state) is used to analyse the origin of the residual stresses. In order to reduce the calculation time, only three threads are simulated. The movement of the die is applied by 11 steps of loading and unloading. The elastic springback in the unloading phase and the subsequent loading lead to cyclic loading of the material. However, the used material model only considers isotropic hardening behaviour. The results of the simulation are compared with residual stress measurements. A two-dimensional simulation model can reproduce the residual stresses in an acceptable range. The authors note that a three-dimensional model could reproduce a better stress state. They assume that friction influences the material flow when the die comes into contact with the Workpiece.
Present research mainly focuses on the development of suitable rolling tools and the determination of parameters for bolt manufacturing machines. The correct reproduction of the residual stress state is not the focus of research. Predominantly axial symmetric models with elastic-plastic material behaviour are used in the simulation. Hardening and softening of the material are usually not considered [2].

3 Modeling

3.1 Material Model

In order to describe the material state of SG HT-bolts, it is necessary to describe the Bauschinger effect, cyclic hardening and softening as well as creep and stress-relaxation. A widely used material model that combines these properties is the *Chaboche* material model [1]. The material model implemented in `Abaqus` according to *Chaboche* requires 7 to 25 parameters to describe the material behaviour. The number depends essentially on the number of back stresses (γ_i, C_i), which indicates the nonlinear kinematic hardening. For each occuring back stress, the number of parameters has to be increased by two. A maximum of 10 back stresses can be used. The nonlinear isotropic hardening is determined by three parameters ($\sigma|_0$, Q, b), the elastic by two (E, ν).The used parameters are listed in table 1.

Table 1: Material Parameters [2]

E	ν	$\sigma\|_0$	C_1	γ_1	C_2	γ_2	C_3	γ_3	Q	b
[MPa]	[-]	[MPa]	[MPa]	[-]	[MPa]	[-]	[MPa]	[-]	[MPa]	[-]
192263	0.28	871.69	42796	120.37	187524	1257.5	1759340	31770	-450.85	24.87

The parameters are determined with a incremental step test on un-notched specimens. The evaluation methodology is explained in [2]. A complete adaptation of the material model to the test data is not possible for two reasons: If the parameters are selected in such a way that the cyclic material behaviour is described exactly, the initial load path

cannot be represented correctly. If an adjustment is made to the initial load, the cyclic material behaviour is underestimated. This general problem has been recognized several times [6]. Chaboche et al. [1] publish an extended elastic-plastic material model with a memory surface. However, this improvement is not yet implemented in commercial FE programs such as `Abaqus`. The chosen parameter set represents an acceptable compromise between monotonous and cyclic material behaviour. Since especially the cyclic behaviour is of importance, an overestimation of the monotonous behaviour is accepted[2].

3.2 Modeling Parameters

An implicit simulation of the forming process is carried out using `Abaqus` with the elastic-plastic material model according to *Chaboche*. An axial symmetric model is used according to Furukawa et al.[5]. Since large deformations in relation to the element size occur during the forming process, the model is re-meshed in specified time steps, cf. Figure 5. With Mesh-to-Mesh Solution-Mapping (MTMSM) the solution is transferred to the new mesh. The developed `Python` script for the simulation control is based on the concept of Abbas [3].

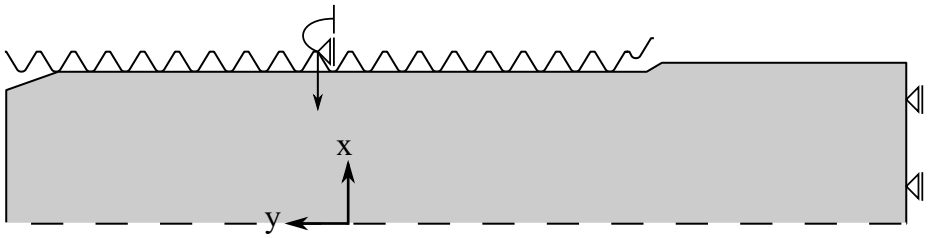


Figure 4: Geometry and boundary condition of the axial-symmetrical model [2]

In the real production process, the thread is rolled via two die rollers using the piercing process. In order to limit the size of calculation, a simplified process model of the forming process is selected for the simulation, cf. Figure 4. The complete thread and the transition area to the shank are taken into account. The die is modeled via a rigid line object. Provided that the deformation of the die is small in relation to the deformation of the Workpiece.

By the use of `General Contact` a new definition of the contact is not necessary. Since the die is modeled as a line object with two surfaces, the contact can be detected incorrectly if it overlaps with the Workpiece. Therefore, the automatic elimination of contact overlaps is omitted. The `Penalty` method is used for the contact kinematics problems.
The displacement in horizontal direction is constrained in the bolt center axis, as is the vertical displacement at the bolt shank. The rigid line object is constrained at the reference point against rotation and horizontal displacement.
The parameters of the thread forming simulations are summarized in Table 2.

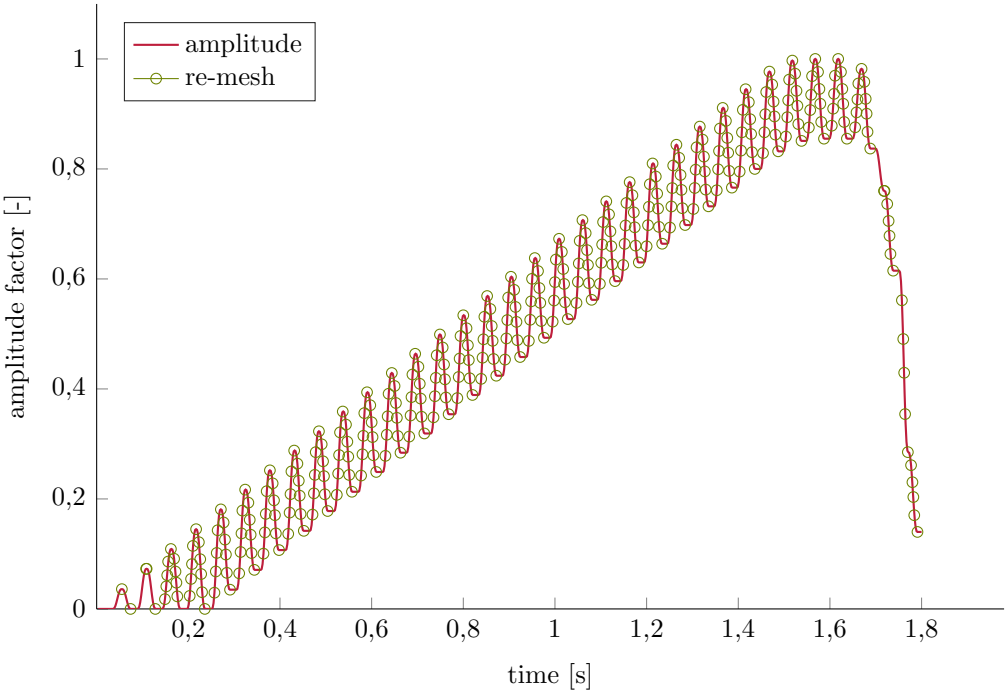


Figure 5: Displacement of the die over time [2]

Table 2: Simulation Parameters [2]

Model	implicit
Workpiece radius	22,5 mm
Contact	General Contact
Friction coefficient	0.015
No. of elements	79,060 - 254,694
No. of nodes	86,734 - 264,740
Edge length smallest element	0.1 - 0.07 mm
Edge length largest element	1 - 0.7 mm
Element type	CAX3 and CAX4

4 Results

In order to reproduce the formed geometry and residual stresses from the forming process for a M 48 HT thread, extensive parameter studies are carried out. Essential parameters are the radius of initial bar, the deformation path of the line object and the friction between the thread-die and the workwpeace.
Although the dimensions of the Workpiece are known, the final geometry cannot be adequately reproduced with this simulation model. Either the thread flank is too short in the final state or the core diameter is too small. This phenomenon indicates an insufficient

reproduction of the material flow due to friction between the workpiece and the die. In reality, friction is negligible due to the continuous lubrication. In simulation, a frictionless contact leads to instability of the model: a chink forms on the thread flank, creating a strong local distortion. In reality, the chink is also present [2]. In order to ensure the stability of the simulation, it is necessary to consider a very small friction. This means that the initial diameter must be increased in order to provide sufficient material for the flank. This phenomena is also observed by Furukawa et al. [5].
A good combination of the initial parameters is given in Figure 7. The simulation result of the stress in bolt longitudinal axis σ_{22}, as well as the final geometry of the HT-bolt are given in Figure 7a. The stress in the thread root is given in Figure 7b. The thread geometry is well reproduced both in the thread root and flank, cf. Figure 6. The transition area from the thread to the shank is described sufficiently.

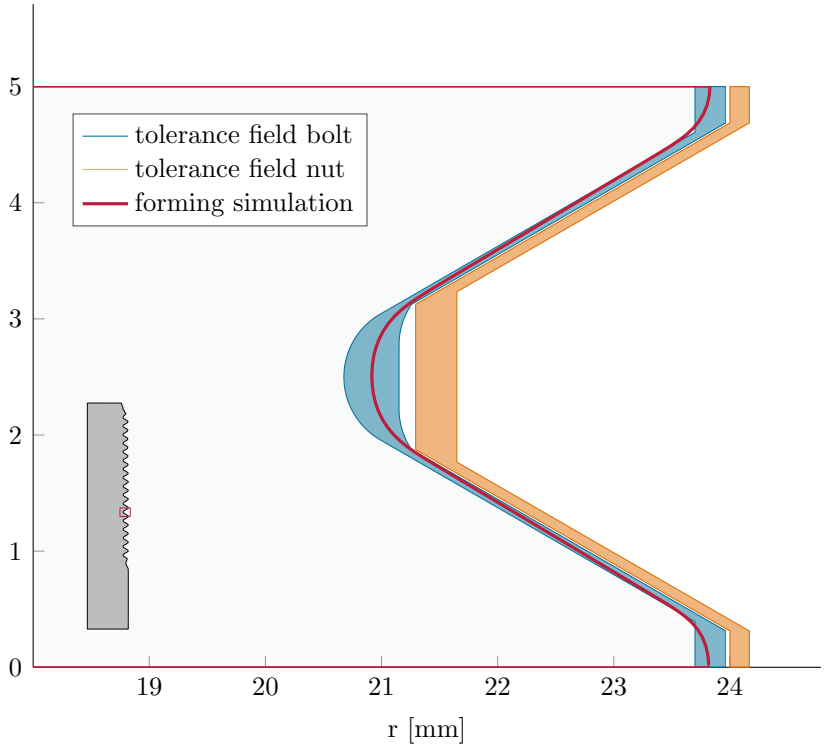
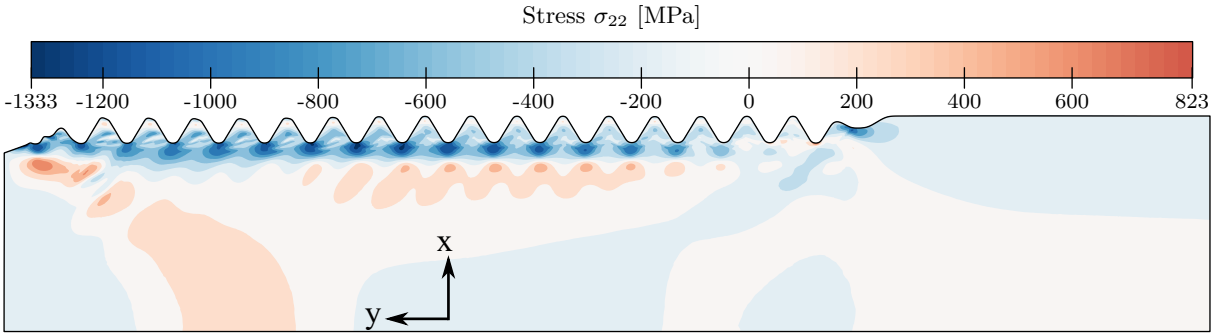


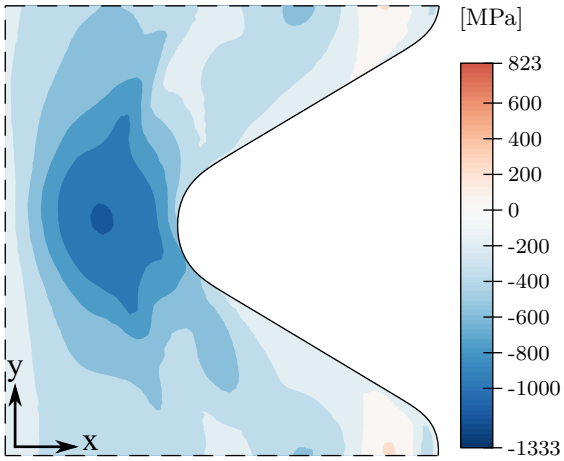
Figure 6: Comparison: Geometry from forming simulation with the permitted tolerance field for M 48 HT thread [2]

There are compressive stresses in the thread root which reach their maximum below the surface. Tensile stresses are present towards the thread core. Stresses tend to change in the direction towards the free bolt end. This is due to the axial symmetric modelling approach: When compression is applied by the die, the material flow can only shift in the direction of the free end. It can also be seen that the stresses vary slightly from thread root to thread root. This behaviour cannot be detected in residual stress measurements on M 48 HT bolts. Here, only slight fluctuations due to the measurement uncertainty

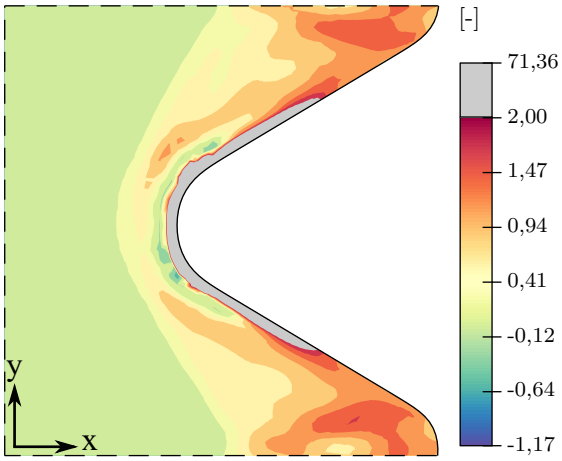
would occur [2].
In Figure 7c the plastic equivalent strain shows a strong increase form to the thread core to the surface. As a result of the lateral strain obstruction in the simulation, the plastic equivalent strain is noticeably overestimated. In reality, there is no lateral strain obstruction of the boundary condition, the material flow can also develop in the circumferential direction of the thread during compression. From hardness measurements it can be seen that there is a hardening of the material, but not as expected from the simulation. Similar observations are confirmed by Fares [4].



(a) Stress state after forming in the M 48 HT bolt



(b) Stress σ_{22}



(c) Strain $\epsilon_{pl,eq}$

Figure 7: Results: Simulation of forming prosess, stress in bolt longitudinal axis and plastic equivalent strain in the thread root [2] .

4.1 Residual Stresses

In Figure 8 a stress path in the thread root is compared with the measurements of Unglaub [2]and the measurement of Fares [4]. The path of the axial stress component

is plotted. The horizontal axis refers to the nominal bolt diameter. It should be noted that size effects are included, especially when compared to the small M 10 bolt. In the simulation and measurement of the M 36 HT bolt, the maximum is located in the pressure area beneath the surface. This is due to the elastic springback of the surface when the dies are retracted. The strong decrease of stresses towards the thread core can be seen more clearly in the measurement data on the M 10 thread. Both the measurements and the simulation show moderate tensile stresses towards the thread core.

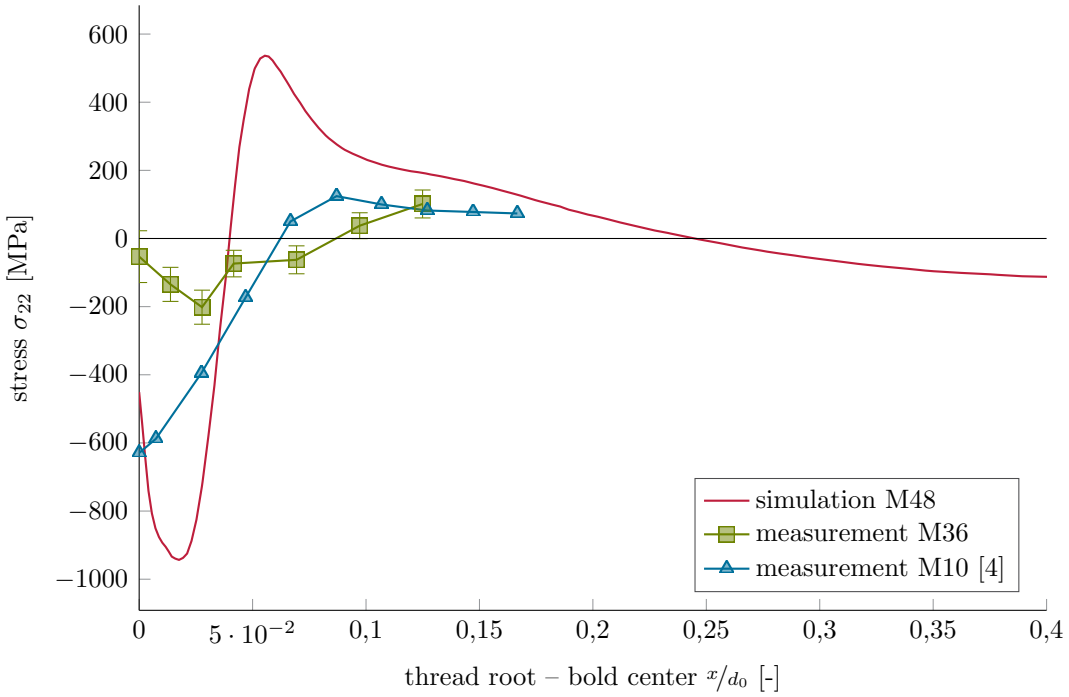


Figure 8: Comparison of the forming simulation with own residual stress measurements of Unglaub [2] and Fares [4]

5 CONCLUSIONS

The final geometry of the forming simulation fulfils an average tolerance field of HT-bolts. The residual stresses from the rolling process are reproduced qualitatively. In the thread root, there are residual compressive stresses, found with SG bolts. The plastic equivalent strain, especially in the area close to the surface, is clearly overestimated. This difference is caused by the drawbacks of the material model on the one hand and on the other hand by the obstruction of the lateral strain due to the axial symmetrical modelling. In summery:

- good achievement of the final thread geometry
- qualitative reproduction of the residual stress state in the thread root
- overestimation of the plastic equivalent strain in the thread root

6 OUTLOOK

In order to improve the results of the forming simulation, further investigations with an modified material model are required. The forming simulation with a three-dimensional model can provide information about the influence of the lateral strain obstruction. A validated simulation model can be used for investigations on fatigue strength with notch-strain-concepts. Further investigation on crack initiation as a result of hot-dip galvanizing and crack propagation in residual stress fields is needed.

REFERENCES

[1] Lemaitre J. and Chaboche, J.-L. *Mechanics of solid materials*, Cambridge, (1990).

[2] Unglaub, J. *Einfluss von Eigenspannungen auf die Ermüdungsfestigkeit von großen Schrauben*, Diss., TU Braunschweig (2019).

[3] Abbas, S. M. *Mesh-To-Mesh Solution Mapping in Abaqus to Simulate Sharp Indention Using Python Scripting and User Element Subroutine*, http://swym.3ds.com/#post:42016 (2016).

[4] Fares, Y. *Dimensionnement en fatigue des assemblages boulonnes a l'aide de criteres de fatigue multiaxiale*. Diss. (2006).

[5] Furukawa, A., Hagiwara, M.: Relationship Between Fatigue Strength of a Bolt and the Residual Stress at the Thread Root. (1st Report, Residual Stress on the Groove-Rolled Specimen). *The Japan Society of Mechanical Engineers* 75 (2009), p. 1049–1055.

[6] Scheibe, H.-J. *Zum zyklischen Materialverhalten von Baustahl und dessen Bercksichtigung in Konstruktionsberechnungen.* Diss., (1990).

[7] Olveda, D., Beyer, J., Panic, D., Beier, T. H. Gewindeverbindungen örtlich II. Vorhaben Nr. 297, *Örtliche Bewertung der Schwingfestigkeit von Gewindeverbindungen II* ; Abschlussbericht. Frankfurt, M (2014).

[8] *FKM-Richtlinie: Rechnerischer Festigkeitsnachweis fr Maschinenbauteile aus Stahl, Eisenguss- und Aluminiumwerkstoffen.* Frankfurt, M (2012).

XIV International Conference on Computational Plasticity. Fundamentals and Applications
COMPLAS 2019
E. Oñate, D.R.J. Owen, D. Peric , M. Chiumenti, and Eduardo de Souza Neto (Eds)

NEW APPROACH FOR DETERMINATION OF STRAIN RATE SENSITIVITY OF MILD STEEL DC01 UNDER STACK COMPRESSION AND UNIAXIAL TENSILE TESTS

PEDRAM FARAHNAK[1,2], MIROSLÁV URBANEK[1], MARTIN RUND[1], JAN DŽUGAN[1], STEFFEN GERKE[2] AND MICHAEL BRÜNIG[2]

[1] COMTES FHT a.s., Průmyslová 995, 33441, Dobřany, Czech Republic

[2] Institut für Mechanik und Statik, Universität der Bundeswehr München, Werner-Heisenberg-Weg 39, D-85577 Neubiberg, Germany

email: pfarahnak@comtesfht.cz, www.comtesfht.com

Key words: Material Characterization, Forming Process, Strain Rate Sensitivity, Tensile Test, Stack Compression Test

Abstract. Deformation under uniaxial tensile loading with using Digital Image Correlations (DIC) is the easiest way to analyze the material behavior in sheet metal forming. In order to determine the plastic parameters such as hardening, anisotropy and strain rate sensitivity at higher strain level, equi-biaxial stress state is prerequisite. As reported in the literature, Bulge tests are frequently used for this purpose, but in this work, stack compression test is used as an alternative. In this experiment, deformation in the middle layer where the friction effect is the lowest was monitored using two pairs of DIC systems in rolling and transversal directions. Uniaxial tensile tests as well as stack compression tests were performed on mild ferritic steel DC01 at different strain rates, from $0.001\ s^{-1}$ to $10\ s^{-1}$. Strain rate sensitivity parameter was investigated at different level of strains for both experiments and strain rate sensitivity profiles were obtained. Results show a decrease of material strain rate sensitivity with increasing the true strain.

1 INTRODUCTION

In sheet metal forming, the quality of the simulation results highly depends on the input data and material parameters. The aim of numerical simulation is to describe the real experiment as accurate as possible. The main parameters for the plastic material behaviour are the yield curve, Lankford ratio and strain rate sensitivity which can be determined by different tests like tensile, Bulge and compression tests. Material hardening is a function of work hardening, strain rate sensitivity and temperature. Since cold forming mainly depends on work hardening and strain rate sensitivity, therefore, the temperature is not considered in the presented paper. Tensile test in sheet metal forming is well-known and frequently used for determination of elastic and plastic parameters. Tensile tests are frictionless and strain rate can be controlled by the test velocity, however, only the uniaxial material behaviour can be described. Therefore, equi-biaxial stress state is prerequisite for determination of plastic parameters at higher strain level. Jocham et al [1] determined the strain rate sensitivity profile for DC06 through tensile and Bulge tests. The Bulge test is a well-known biaxial experiment

and it is standardized in ISO-16808 [2]. In this work, stack layer compression test is used as an alternative to show the material behaviour from strain rate $0.001\ s^{-1}$ to $10\ s^{-1}$.

The stack discs compression was proposed by Pawelski [3]. For stack compression test, a set of stacked discs must be arranged to obtain a correct alignment between the discs. This preserves the material orientations in the stacked discs. This experiment was mainly used to determine the biaxial Lankford ratio which is the division of strain in transversal direction to strain in rolling direction [4,5]. Merklein and Kuppert [6] proposed a method to determine the flow curve at high strain level from stack compression test by measuring the true area during the experiment. For this purpose, two pairs of DIC systems with angle $90°$ towards each other, capture the deformation in the middle layer and in rolling and transversal directions. It is worth noting that in the middle layer the friction effect is less due to the upper and lower disc layers. In this experiment, the extension of the true area can be calculated through two true principal strains, one in rolling and another in transversal directions. Subsequently, true stress can be calculated thanks to load cell and the obtained true area. Similar to Bulge test, it provides the plastic parameters at higher strain levels. Suttner and Merklein [7] performed bulge test on different materials and it was found that for some materials like aluminum and advanced high strength steels, the obtained flow curves are in close agreement with uniaxial flow curve, however, for mild steels the biaxial flow curve is different from uniaxial one and it has to be converted to uniaxial flow curve according to ISO-16808 [2]. In this work, stack compression tests are performed at different velocities for determination of plastic parameter at different strain rates.

Strain rate sensitivity describes the dynamic material behavior and is defined by the average slopes in the logarithmic space of true stress and strain rate. Many definitions are available for the strain rate sensitivity in the literature. Jump test provides the instantaneous value of strain rate sensitivity without consideration of strain path history [8]. The concept of dynamic factors, i.e. the ratio of dynamic to static yield stresses was used in [8, 9]. The strain rate sensitivity is denoted by m and calculated mainly in publications based on the strain rate dependency of flow curves [10-14] and it can be expressed in the form:

$$m = \frac{\partial log\sigma}{\partial log\dot{\varepsilon}} \tag{1}$$

Where σ is the true yield stress and $\dot{\varepsilon}$ is the strain rate.

In this work, the material under investigation is mild ferritic steel DC01 and Table 1 represents the chemical composition of the material. In this work, uniaxial tensile tests are performed at different velocities at which the strain rate varies from $0.001\ s^{-1}$ to $10\ s^{-1}$. On the other hand, stack compression tests are performed as well at the interested strain rate range to provide the plastic parameters at higher strain levels. Finally, results are discussed for mild steel DC01.

Table 1: Chemical composition of mild ferritic steel DC01

C [%]	Mn [%]	P [%]	S [%]
0.12	0.6	0.045	0.045

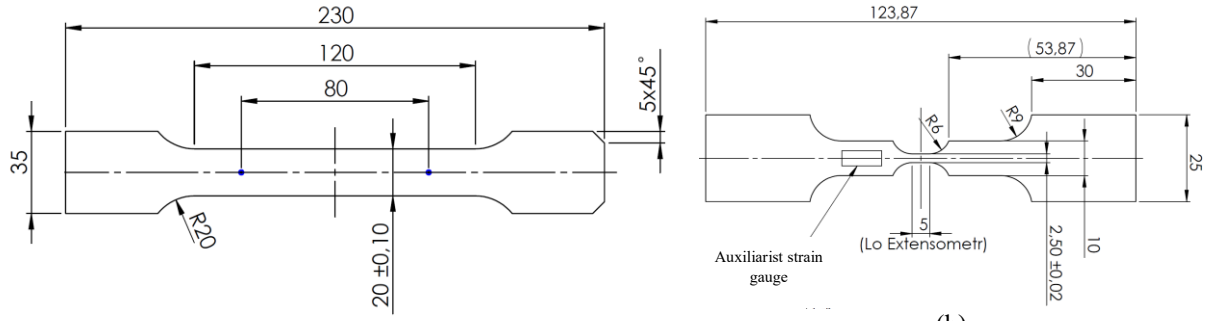
2 EXPERIMENTAL AND NUMERICAL RESULTS

2.1 Uniaxial tensile test

Figure 1 (a) and (b) depict the geometry of standard and non-standard dog-bone specimens, respectively and the sheet thickness is 1.5 mm. Throughout this paper, all the dimensions are presented in terms of mm. Standard specimen is used for static test with strain rate $0.001\ s^{-1}$, while non-standard one for dynamic tests with strain rates 0.1 and $10\ s^{-1}$.

For static test, electro-mechanical testing system, Mayes, is used to conduct the uniaxial tests and the GOM Aramis^{TM} system with a 4 megapixel camera is utilized to monitor $2D$ strain fields with high resolution. The data acquisition rate is set at $100\ Hz$ in the testing system for accurate measuring of the tensile behaviour. For evaluation of the experiments, initial length of extensometers is chosen as $80\ mm$. Farahnak et al [15-17] performed other tensile tests on standard and miniature samples in transversal and diagonal directions to investigate about anisotropic behaviour of the material and it was observed that engineering stress-strain curves as well as Lankford ratios are very close to each other. Therefore, throughout this paper the material is assumed as an isotropic material for numerical simulation.

For dynamic tests, MTS BIONIX machine with $25\ kN$ capacity was used. For strain rates $0.1\ s^{-1}$ and $10\ s^{-1}$ velocities are adjusted to $0.5\ mm/s$ and $50\ mm/s$, respectively. During experiments, $2D$ strain fields are captured using high speed camera Phantom with a 1 megapixel camera. As it is shown in the Figure 1 (b), $5\ mm$ is chosen as the initial length of extensometer. Figure 2 (a) shows the engineering stress- strain curves at different strain rates. As can be seen in the figure, an increase of yield stress for different strain rates display the expected behaviour and the strain rate sensitivity of the material is clear. The extensions at strain rates $0.1\ s^{-1}$ and $10\ s^{-1}$ are bigger than static one, since the geometry is different and the initial length is pretty smaller as well. The strain rate sensitivity m, has to be calculated in terms of true stress and strain values and the range of 0.03 to 0.2 true strain is chosen for m profile determination. Figure 2 (b) indicates the true stress- strain curves for those strain rates.



(a) (b)

Figure 1: (a) standard dog-bone sample for static test (b) Geometry of tensile sample for dynamic test

m Profile is determined by plotting true logarithmic stress versus true logarithmic strain at given true strain values and it is shown in the Figure 2 (c). As can be seen in the figure and according to Equation (1), m is the gradient of linear regression of all points with the same true strain value and resulting m-profile obtained from tensile test is depicted in Figure 2 (d). Therefore, yield curves at aforementioned range of the true strain play an active role of the resulting m profile. As it is shown in Figure 2 (d), strain rate sensitivity decreases with

increasing the true strain level.

For static test, the flow curve is extrapolated using Abaqus FEM based software for numerical simulation with conventional plasticity [18] based on von Mises material. As it was mentioned above, standard dog-bone in Figure 1 (a) was used for numerical simulation. Mesh sizes in the centre of specimen was $0.8\,mm$ and in surrounding area was $1.2\,mm$.with 4 C3D8R elements (according to Abaqus library) along the thickness. Flow curve in Figure 3 (a), is extrapolated using El-Magd hardening law (Equation (2)) and it is calibrated through inverse analysis by comparing numerical and experimental force-displacement curves. Figure 3 (b) compares the numerical and experimental force- displacement curves. As can be seen in the figure, a close agreement is achieved between numerical and experimental results and it proves the appropriate extrapolation of the flow curve. Calibrated parameters for El- Magd hardening law are summarized in Table 2. In next section, stack compression experiment is designed thanks to the characterized parameters from tensile tests.

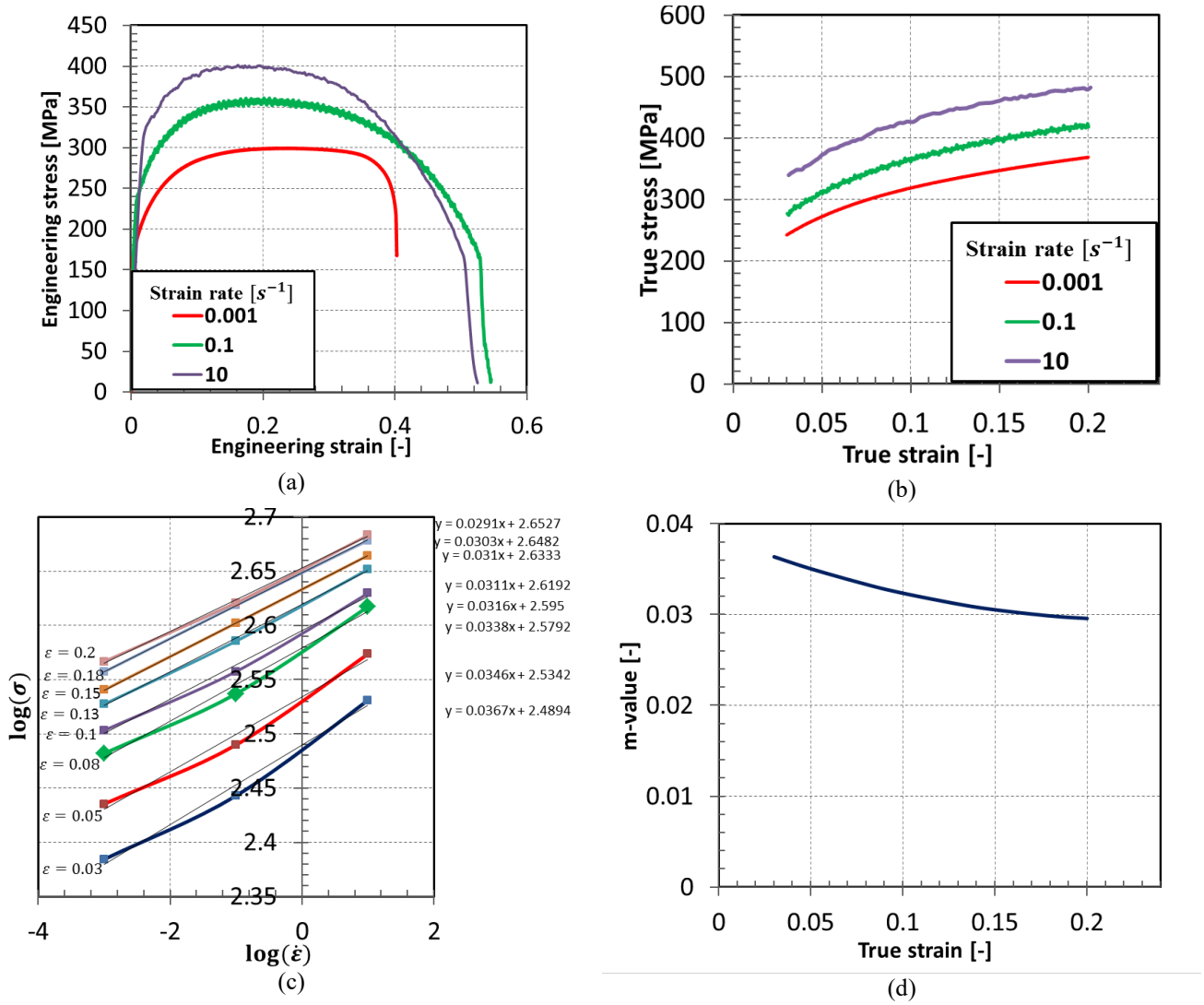
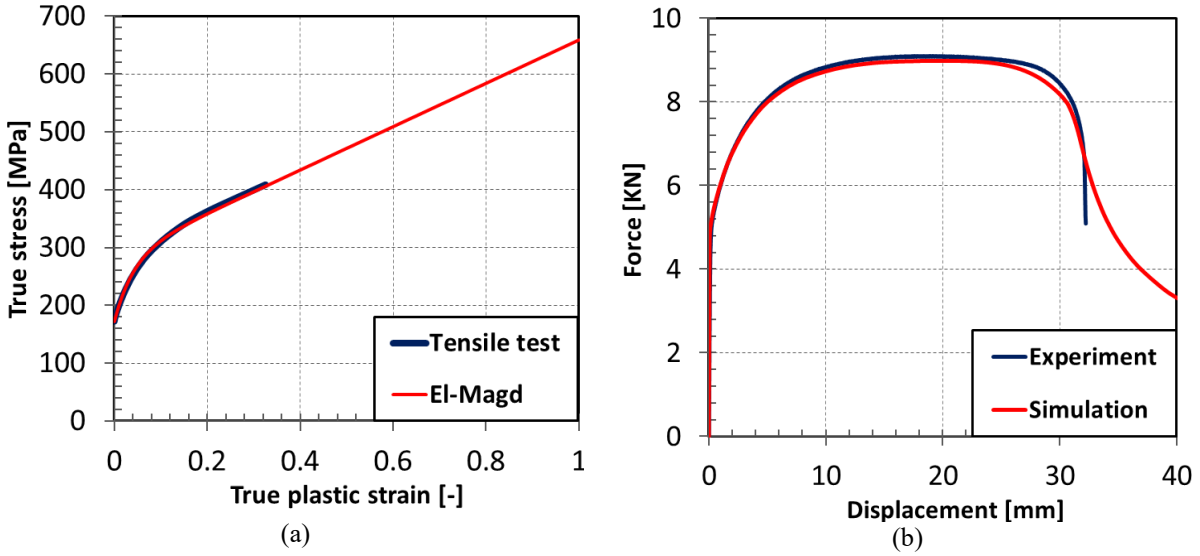


Figure 2: (a) Engineering stress- strain curves (b) True stress- strain curves at interested range (c) Logarithmic stress-strain rate space for m-value determination (d) m profile

$$\sigma_0(\varepsilon) = c_1 + c_2\varepsilon + c_3[1 - e^{-c_4\varepsilon}] \quad (2)$$

Table 2: Calibrated parameters of El-Magd hardening law

c_1	c_2	c_3	c_4
172	375	112	24



(a) (b)

Figure 3: (a) Extrapolation of the flow curve (b) Experimental and numerical force-displacement curves

2.2 Stack compression discs

2.2.1 Experiment design using numerical simulation

In this section, the experiment is designed in order to achieve highest deformation with as low as possible friction effects. In this experiment, a set of stacked discs must be available at which discs are arranged in a tool to obtain a correct alignment between the discs. The ratio of height (H) to diameter (D) should be smaller than 1.5 for stability of the stacked discs. Moreover, the machine load capacity must be taken into account. Therefore, two types of discs with diameters 15 mm and 12 mm are chosen for numerical simulation. The former diameter is simulated with 9 layers while the latter with 13 layers. As it was mentioned above the sheet thickness is 1.5 mm. For the first case of numerical simulation with 15 mm diameter and 9 layers satisfies the stability constrain ($\frac{H}{D} \leq 1.5$), whereas for the second case the ratio a little bit exceeded the limit, but it is not crucial for the real experiment. It is worth noting that the friction effect in the middle layer is the lowest and the goal of the real experiment is to capture the deformation in the middle layer during the experiment using DIC system. Therefore, the number of layers should be odd number.

For stack compression tests, two pairs of DIC system are required to capture deformations in rolling and transversal directions. Merklein and Kuppert [6] proposed a formula for measuring of the real area of the circular discs during the experiment using major strains in each pair of DIC system. Equation (3) provides the real area during stack compression test at which ε_1 and ε_2 are the principal strains in rolling and transversal directions, respectively:

$$A = \left(\left(\frac{e^{\varepsilon_1} + e^{\varepsilon_2}}{2} \right) \frac{D}{2} \right)^2 . \pi \tag{3}$$

For numerical simulations, it is assumed that friction coefficients between plate-disc and disc-disc are considered 0.115 and 0.20, respectively. Figures 4 (a) and (b) show the Mises stress contour of deformation for diameters 15 mm and 12 mm in the half cut view almost at the same level of deformation, respectively. As can be seen in the figures, the Mises stress distribution is more uniform in Figure 4 (b) with 13 layers. Force-displacement curves are presented in Figure 4 (c) in order to evaluate the maximum load level required for the real experiment. As can be seen in the Figure 4 (c), force amplitude can be significantly reduced by reducing the disc diameter. The true area is calculated according to Equation (3) in the middle layer, i.e. 5th and 7th layers, respectively. Afterwards, true stress can be obtained from division of the force to the true area. Subsequently, elastic parts are removed and true plastic stress- strain curves for both curves are depicted in Figure 4 (d) and compared with extrapolated flow curve in section 2.1. In Figure 4 (d), it is obvious that experiments on 13 layers discs with 12 mm diameter can provide more convenient result with wider range of true plastic strain, however, it is worth noting that the alignment of the stacked discs in practice can become more difficult by reducing the diameter.

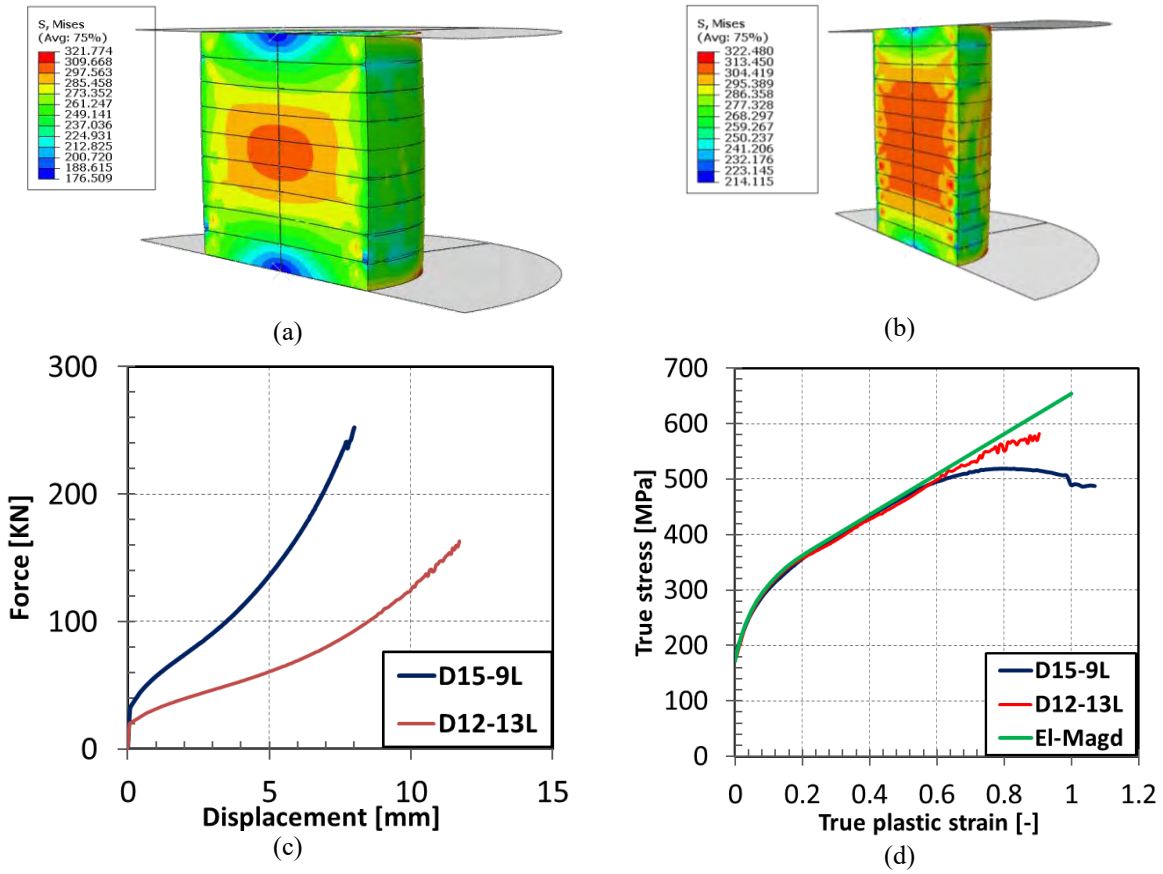


Figure 4: (a) Contour of Mises stress on 9 layers stacked discs with diameter 15 mm (b) Contour of Mises stress on 9 layers stacked discs with diameter 15 mm (c) Comparison of force- displacement curves (d) obtained numerical flow curves and comparison with El-Magd curve

2.2.2 Experimental setup

According to the obtained numerical results in Figure 4, 13 layers with 12 mm diameter are stacked and arranged to obtain a correct alignment. As it was mentioned above, two pairs of GOM Aramis^{TM} DIC systems with 12 and 4 megapixels are utilized to monitor $3D$ strain fields during the experiment in rolling and transversal directions, respectively. Figure 5 (a) represents the experimental setup. Experiments were conducted at different strain rates 0.001 s^{-1}, 0.1 s^{-1} and 10 s^{-1} which are corresponding to the velocities 0.013 $^{mm}/_{s}$, 1.5 $^{mm}/_{s}$ and 13.82 $^{mm}/_{s}$, respectively. For each strain rate three experiments were performed. For strain rate 10 s^{-1}, two pairs of high speed Phantom cameras with 1 megapixel resolution were used; however, the results were not acceptable due to the low resolutions of the cameras. Thus, material behaviour at strain rate 10 s^{-1} is excluded for stack compression test. For strain rates 0.001 s^{-1} and 0.1 s^{-1} frequency was adjusted to 1 Hz and 50 Hz, respectively. Discs are glued together for better stability and it is quite useful, especially for high strain rate experiments in which initial machine impact on stacked discs can cause eliminate the alignment. As it was mentioned, the true area is calculated using Equation (3) and Figure 5 (b) shows true stress- strain curves for those strain rates. As can be seen in Figure 5 (b), the range of 0.08 to 0.6 true strains is chosen for m profile determination. Similar to uniaxial tensile test in Section 2.1, m profile is the gradient of linear regression of all points with the same true strain value and it is illustrated in Figure 5 (c).

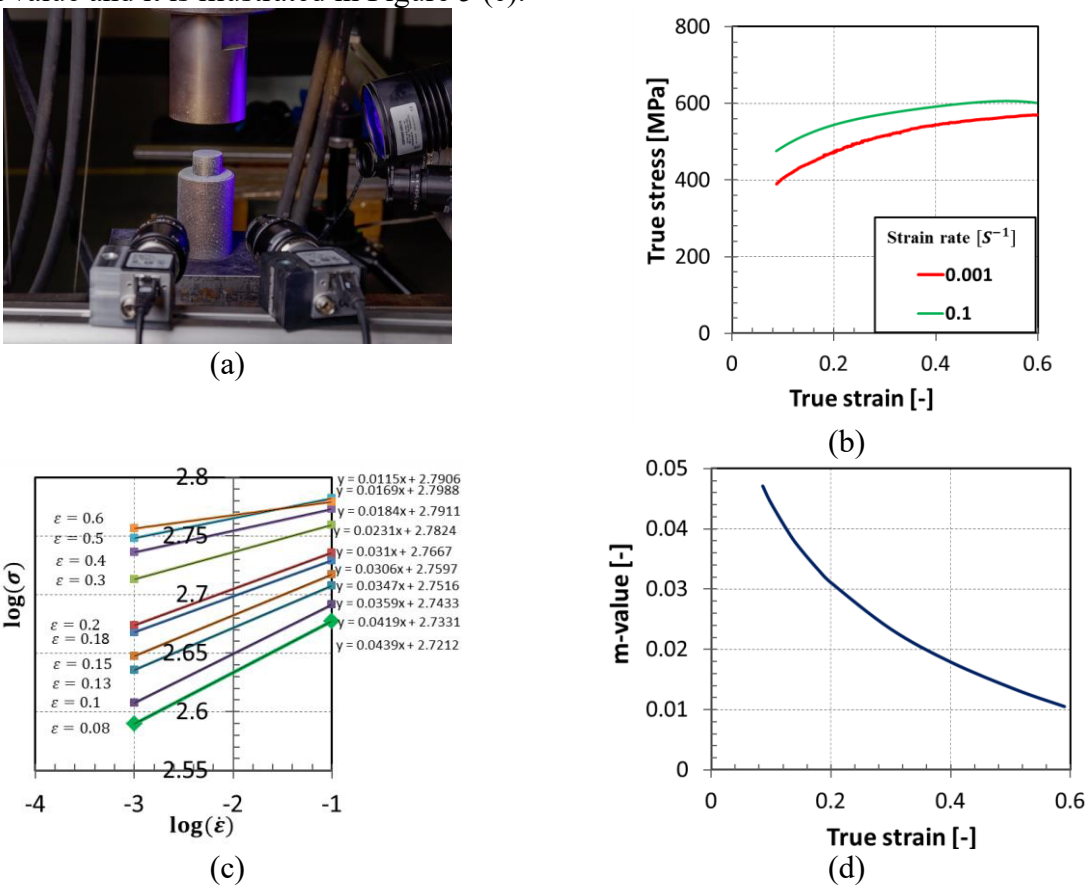


Figure 5: (a) Experimental setup (b) True stress- strain curves at interested range (c) Logarithmic stress- strain rate space for m-value determination (d) m profile

Finally, Figure 5 (d) represents obtained m profile from stack compression test. It is obvious in Figure 5 (d) that the material strain rate sensitivity is decreasing with increasing the deformation level and similar result was observed from uniaxial results (Figure 3 (d)).

3 MATERIAL HARDENING INTEGRATED WITH STRAIN RATE SENSITIVITY

Strain rate sensitivity has a significant influence on the material behaviour, especially during forming simulations. Therefore, the obtained m profiles from uniaxial tensile and stack compression tests can be integrated in the material hardening model. Work hardening was presented in Equation (2) and Johnson-Cook (J-C) model for strain rate sensitivity can be utilized as well in equation (4):

$$\sigma(\varepsilon, \dot{\varepsilon}) = \sigma_0(\varepsilon).(1 + c_{J-c} ln\left(\frac{\dot{\varepsilon}}{\dot{\varepsilon}_0}\right)) \tag{4}$$

Where c_{J-c} is corresponding to the m value, $\dot{\varepsilon}$ is the strain rate and $\dot{\varepsilon}_0$ is the reference strain rate. The m-values from uniaxial tensile and stack compression tests which were already presented above in Figures 2 (d) and 5 (d) can be denoted by $m_{tensile}(\varepsilon)$ and $m_{stack\ test}(\varepsilon)$, respectively. Both curves are modelled using logarithmic equations and are expressed in Equation (5):

$$\begin{aligned} m_{tensile}(\varepsilon) &= A.\ln(\varepsilon) + B \\ m_{stack\ test}(\varepsilon) &= C.\ln(\varepsilon) + D \end{aligned} \tag{5}$$

Table 3 summarizes the coefficient values in Equation (5). Finally, m-values from Equation (5) can be combined into one equation. Equation (6) takes into account work flow and strain rate sensitivity from tensile and stack tests.

Table 3: Coefficients of logarithmic equations

Tensile test		Stack compression test	
A	B	C	D
-0.0399	0.0369	-0.0190	0.0005

$$\begin{aligned} \sigma\left(\varepsilon, \dot{\varepsilon}, \frac{\sigma_2}{\sigma_1}\right) = \sigma_0(\varepsilon).\Bigg[\left(1 - \frac{\sigma_2}{\sigma_1}\right).\left(1 + (A.\ln(\varepsilon) + B).ln\left(\frac{\dot{\varepsilon}}{\dot{\varepsilon}_0}\right)\right) \\ + \left(\frac{\sigma_2}{\sigma_1}\right).\left(1 + (C.\ln(\varepsilon) + D).ln\left(\frac{\dot{\varepsilon}}{\dot{\varepsilon}_0}\right)\right)\Bigg] \end{aligned} \tag{6}$$

Where σ_1 and σ_2 are the principal stresses. Equation (6) describes the material hardening depending on true strain, strain rate and loading condition with consideration of $0 < \varepsilon \leq 0.6$. It is clear that for uniaxial tensile $\sigma_2 = 0$ and for equi-biaxial $\sigma_1 = \sigma_2$, therefore, Equation (6) can be reduced according to the loading condition to the relevant form.

4 CONCLUSIONS AND FUTURE RESEARCH

In this work, strain rate sensitivity of mild ferritic steel DC01 was investigated under uniaxial tensile and stack compression tests. Uniaxial tensile tests were performed at different strain rates and m profile was discovered, however, at low strain level. In order to observe the material strain rate sensitivity at higher level of deformation, stack compression test was used as an alternative for Bulge test in the present work. First, stack compression test was designed

thanks to the numerical simulation to specify the number of layers, disc's diameter and force amplitude. It was observed that experiment with 13 layers and 12 *mm* disc's diameter can provide uniform deformation along the stacked disc's height. Therefore, stack compression experiments were conducted at different strain rates. Similar to uniaxial tensile test, m profile was obtained, but at higher strain level and it was observed that for both experiments, material strain rate sensitivity decreases with increasing the deformation level. Finally, strain rate sensitivity profiles from both tests, were integrated with material hardening.

In this work, the constant velocity was applied to the stacked discs during the experiment. However, the strain rate during experiment had a little variation. Therefore, for further investigations, the authors would like to impose the velocity profile to keep strain rate constant during the experiment.

ACKNOWLEDGEMENTS

This paper is a result of the project Development of West-Bohemian Centre of Materials and Metallurgy No.: LO1412, financed by the MEYS of the Czech Republic and project methods development for formability assessment of thin sheets considering anisotropy and non-linear loading path No.: TF02000072, financed by Technology Agency of the Czech Republic.

REFERENCES

[1] Jocham, D., Norz, R., & Volk, W. (2017). Strain rate sensitivity of DC06 for high strains under biaxial stress in hydraulic bulge test and under uniaxial stress in tensile test. *International Journal of Material Forming*, *10*(3), 453–461. https://doi.org/10.1007/s12289-016-1293-8

[2] ISO copyright office (2013) Metallic Materials-Sheet and strip determination of biaxial true stress-true strain curve using hydraulic bulge test with optical measurement system. ISO/DIS 16808:2013.

[3] Pawelski, O., (1967), Über das Stauchen von Hohlzylindern und seine Eignung zur Bestimmung der Formänderungsfestigkeit dünner Bleche. Archiv für Eisenhüttenwesen 38, pp. 437-442.

[4] Peters, P.R., (2015), Yield functions taking into account anisotropic effects for an improved virtual representation of deep drawing process, *Doctoral thesis ETH Zurich*.

[5] Chongthairungruang, B., Uthaisangsuk, V., Suranuntchai, S., & Jirathearanat, S. (2013). Springback prediction in sheet metal forming of high strength steels. *Materials and Design*, *50*, 253–266. https://doi.org/10.1016/j.matdes.2013.02.060

[6] Merklein, M., & Kuppert, A. (2009). A method for the layer compression test considering the anisotropic material behavior. *International Journal of Material Forming*, *2*(SUPPL. 1), 483–486. https://doi.org/10.1007/s12289-009-0592-8

[7] Suttner, S., & Merklein, M. (2016). Experimental and numerical investigation of a strain rate controlled hydraulic bulge test of sheet metal. *Journal of Materials Processing Technology*, *235*, 121–133. https://doi.org/10.1016/j.jmatprotec.2016.04.022

[8] Wagoner, R. H., & Wang, N. M. (1983). Operant strain-rate sensitivity during tensile necking. *Metallurgical Transactions A*, *14*(11), 2395–2406. https://doi.org/10.1007/BF02663315

[9] Miura, K., Takagi, S., Furukimi, O., Obara, T., & Tanimura, S. (2010). Dynamic Deformation Behavior of Steel Sheet for Automobile. In *SAE Technical Paper Series* (Vol. 1). SAE International. https://doi.org/10.4271/960019

[10] Wilson, D. V. (2013). Strain-rate sensitivity and effects of strain rate in sheet forming. *Metals Technology*, *7*(1), 282–292. https://doi.org/10.1179/030716980803287297

[11] Ghosh, A. K. (2010). The Influence of Strain Hardening and Strain-Rate Sensitivity on Sheet Metal Forming. *Journal of Engineering Materials and Technology*, *99*(3), 264. https://doi.org/10.1115/1.3443530

[12] Hosford, W.F., (2000), Effect of strain rate exponents on neck shape, *IDDRG*, pp.95-99.

[13] Shi, M. F., & Meuleman, D. J. (1995). On certain aspects of strain rate sensitivity of sheet metals. *Journal of Materials Engineering and Performance*, *4*(3), 321–333. https://doi.org/10.1007/BF02649070

[14] Schindler, I., Hadasik, E., & Kawalla, R. (2016). Strain-Rate Sensitivity in Hot Forming of Steels - Influence of Microstructure, Temperature and Chemical Composition. *Steel Research International*, *74*(10), 617–623. https://doi.org/10.1002/srin.200300241

[15] Farahnak, P., Urbanek, M., & Džugan, J. (2017). Investigation Study on Determination of Fracture Strain and Fractuer Forming Limit Curve Using Different Experimental and Numerical Methods. In *Journal of Physics: Conference Series* (Vol. 896). Institute of Physics Publishing. https://doi.org/10.1088/1742-6596/896/1/012082

[16] Farahnak, P., Prantl, A., Dzugan, J., Konopik, P., & Prochazka, R. (2017). Sheet necking prediction in forming limit diagrams with the anisotropy influence incorporation. In *IOP Conference Series: Materials Science and Engineering* (Vol. 179). Institute of Physics Publishing. https://doi.org/10.1088/1757-899X/179/1/012023

[17] Farahnak, P., Konopik, P., Rund, M., Džugan, J., & Rzepa, S. (2018). Applicability of miniature tensile test in the automotive sector. In *IOP Conference Series: Materials Science and Engineering* (Vol. 461). Institute of Physics Publishing. https://doi.org/10.1088/1757-899X/461/1/012043

[18] Viera, A.F.C. (2017). Material Modelling: Applications, Challenges and Research. *ISBN: 9781536121612. Nova Science Publishers. New York, Chapter 8: The Numerical Non-Linear Analysis of Elastoplastic Materials Using the Radial Point Interpolation Method.*

XIV International Conference on Computational Plasticity. Fundamentals and Applications
COMPLAS 2019
E. Oñate, D.R.J. Owen, D. Peric , M. Chiumenti, and Eduardo de Souza Neto (Eds)

NON-LINEAR MODEL-PREDICTIVE-CONTROL FOR THERMOMECHANICAL RING ROLLING

ALEXANDER BROSIUS, MARC TULKE* AND CHRISTINA GUILLEAUME

* Institute of Manufacturing Technology, Chair of Forming and Machining Processes
Technische Universität Dresden
01062 Dresden, Germany
e-mail: marc.tulke@tu-dresden.de, web page: www.tu-dresden.de/ing/maschinenwesen/if/ff

Key words: Ring rolling, Thermomechanical rolling, Microstructure

Abstract. The authors present a new ring rolling variant that combines a semi-warm forming process of a bearing ring with controlled cooling directly followed by a cold forming process. The aim is to produce near net shape rings with a selected microstructure and high strength without additional consecutive heat treatment. To achieve this, a new and fast control strategy is necessary that not only controls the geometrical forming of the ring, but also considers temperature development and microstructure formation. The proposed control strategy is based on the application of a fast semi-analytical simulation model with a very short response time in combination with a FE-analysis of the thermomechanical ring rolling process. The semi-analytical model is used as a predictor and a parallel FEA or experimental results as a corrector for the control model. The aim is to correctly identify transient process parameters needed to achieve defined product properties as a basis for a later implementation in a non-linear model-predictive-control of thermomechanical ring rolling. The new approach will be described in detail and demonstrated numerically and experimentally.

1 INTRODUCTION

A new process variant of the well-established ring rolling process with a new approach to apply closed-loop control in order to produce rings with selected specific product properties is presented in the following. A short introduction both into the process itself with current control strategies as well as into thermomechanical processes in general will be given in the following.

1.1 Ring rolling

Ring rolling is an incremental process for bulk metal forming for the production of seamless rings which includes a wide range of process variants that can be classified according to the resulting geometry, process route, machine layout, and process temperature [1]. Cold ring rolling is generally suitable to form near net shape metal rings, e.g. for bearings, that have an advantageous microstructure, desired surface hardness and high strength. Ring rolling also offers the possibility of producing hybrid ring-shaped components [2]. The production of hybrid rings has been proven both numerically and experimentally at the RWTH Aachen within the framework of a hot forming process [3]. In contrast, Küsters et al. have demonstrated the feasibility of producing force-locked brass-steel composite rings by cold ring rolling [4]. Within

the scope of these investigations, a radial ring rolling machine, based on the machine concept of PROFIROLL TECHNOLOGIES GMBH, is used originally designed to manufacture outer roller bearing rings. The principle of radial ring rolling is shown in Figure 1. Here, the ring is formed between a main roll and a mandrel in radial direction while two calibration rolls are used to control the ring growth and shaping.

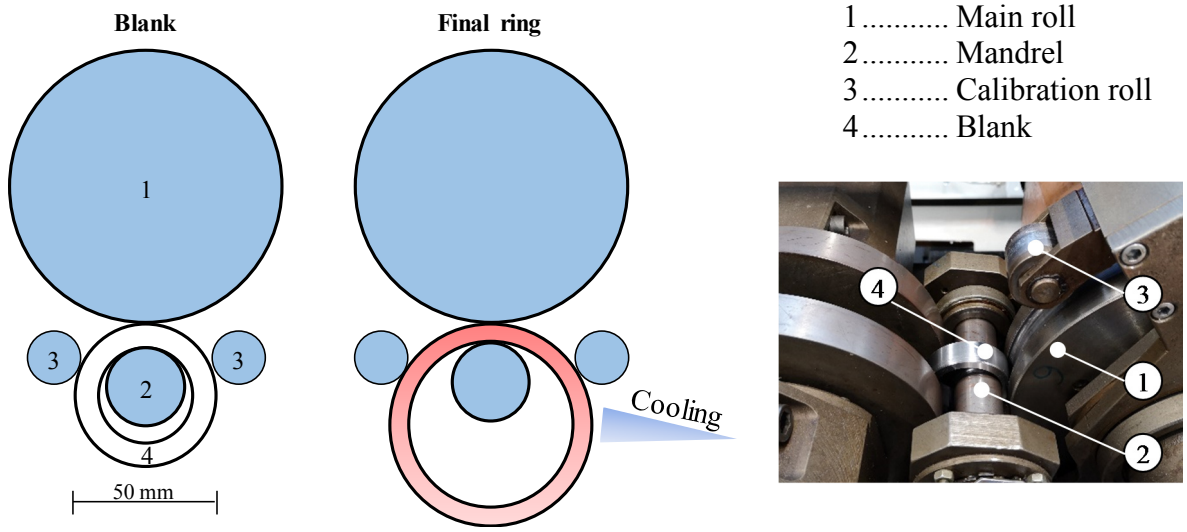


Figure 1: Principle test setup (left) and experimental ring rolling machine (right)

Like all processes, hot and cold ring rolling are subject to uncertainties, which are mainly caused by the cooling conditions and heat generation during forming [5]. Coupled with the forming stages over the process time, these uncertainties not only influence the geometric properties of the manufactured rings, but also the formation of the microstructure and the resulting material properties. For the control of the ring rolling processes, there are various approaches, most of which are exclusively concerned with the geometric shape of the rings produced. Industrial plants usually use a controller based on a kinematic model of Koppers [6] as described by [7]. For radial-axial ring rolling, Choi and Cho [8] present an approach to control the ring geometry adaptively by controlling the infeed of the working roll and the conical support rolls to increase the final accuracy. Due to the non-linear behavior and the uncertainty of the input parameters, they design an adaptive control that can map the dynamic changes over the process time. In further work, the approach for force control of the guide rollers is transferred [9]. By default, hot ring rolling mills do not have thermal actuators such as cooling or heating, only the forming speed can be actively influenced by the roll infeed [5]. Process models must take the transient boundary conditions of the forming into account and thus become too slow to be used for control, so that controllers are essentially used to maintain the tool path [10]. In the field of sensor technology, development is moving towards the use of camera-based geometry acquisition and evaluation, as well as the use of thermographic cameras [11]. FE models show that the influences of the adjustable control variables speed, roll infeed and position of the guide rolls show strong interdependence, although the influenced areas in the ring are very different [5]. Therefore, strongly simplified models appear to be unsuitable for an adequate process analysis. Currently, existing control algorithms within FE models are used to investigate the influence of geometric control on temperature distribution and microstructure, as for example presented by

Jenkouk [12]. An extension of the ring rolling mills with thermal actuators opens up possibilities for setting a desired microstructure, even under interference [5].

1.2 Thermomechanical processes

Due to a large number of manufacturing processes in which both thermal and mechanical processes are interlinked, it is necessary to define thermomechanical manufacturing processes as applied by the authors. Sometimes they are also summarized under the term Thermomechanical Treatment (TMT) and include those processes which "during the process, by means of a targeted combination of temperature and forming conditions, give the end product material properties which are superior to or at least equivalent to those properties which exist after conventional production" [13]. In [14] thermomechanical rolling is defined as "a rolling process with final forming in a certain temperature range which results in a material condition with certain properties which cannot be achieved by heat treatment alone and which cannot be repeated". For the TMT, "temperature and deformation in their temporal sequence" must be controlled according to Stahl-Eisen-Werkstoffblatt 082 (steel iron material data sheet) [15]. The objective here is to achieve a homogeneous microstructure state with defined properties by a targeted combination of temperature and forming conditions, using certain metallurgical mechanisms and phase transformations in the material [13]. The temperature range, degree of forming and cooling speed between 800 °C and 500 °C are relevant process variables for setting lasting effects by thermo-mechanical forming [16]. Multiphase microstructures of ferrite and martensite or ferrite, bainite and retained austenite can be adjusted by material-adapted cooling. Using this method, very good material properties with high tensile and good impact strength can also be achieved on the basis of low-alloy steels [17]. Due to the low carbon content, the weldability remains completely intact, while tensile strengths of up to 1100 MPa can be reached [18]. Von Hehl [13] has demonstrated this in principle for the ring rolling of large rings at high temperatures with guided cooling. The basis for the increase in strength is a temperature treatment according to the transformation-time-temperature diagram of 100Cr6. Based on the state of the art the authors propose the application of a thermomechanical ring rolling process in order to control and improve selected material properties while also expanding the process window and lowering process forces.

2 CONCEPT

The presented approach, similar to [13], is a combination of semi-warm ring rolling with guided cooling with a directly subsequent cold rolling process in order to produce near-net-shape rolling bearing rings with advantageous microstructural properties at high strength without additional heat treatment steps. Due to the relatively low component volume of the rings, active cooling ensures sufficiently rapid cooling for the formation of a martensitic microstructure. Compared to a pure cold rolling process, the advantages lie in the achievement of higher degrees of forming and reduced process forces. The prerequisite for this combined process route is the use of a suitable material and the development of a control system in order to achieve the set microstructure and the resulting work hardening by means of the forming process and cooling curve. The resulting combined process of a first stage of semi-warm rolling directly followed by a cold rolling calibration is significantly shorter than a conventional process chain to achieve the same combination of microstructure and geometry, see Figure 2.

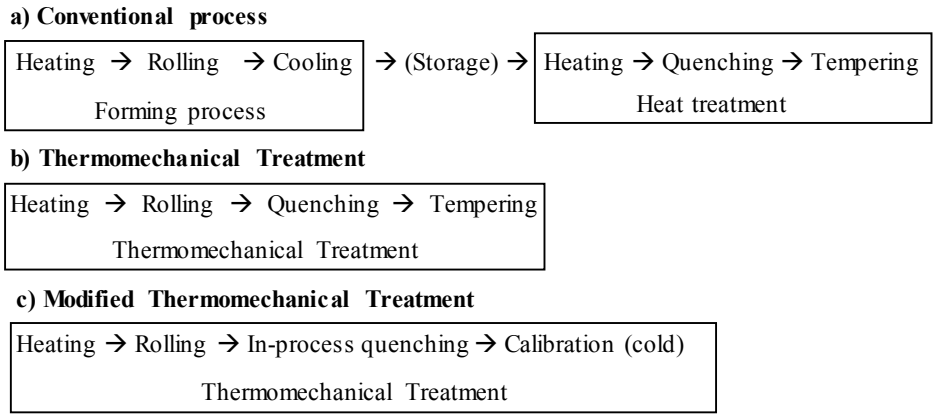


Figure 2: Different manufacturing strategies for rolled rings according to [13]

A prerequisite to fully implement a thermomechanical ring rolling process to specifically choose microstructure and corresponding part properties is a fast process model as a basis for the integration of a closed-loop predictive control. This closed-loop control is necessary for a robust process, because of the numerous interdependent thermal and mechanical parameters. The approach proposed by the authors is a combination of suitable soft-sensors and semi-analytical models to achieve a closed-loop control, depicted in Figure 3. Soft-sensors are aimed at deriving current material properties and process states from secondary measurements. For example, the temperature development in the ring core cannot be measured during the process and therefore has to be modelled via soft sensors from the surface temperature and amount of forming energy induced into the workpiece. Eddy-current sensors can be used to observe microstructure development during the process. This sensor information is then fed into the fast analytical process model which in turn is used for the closed-loop control of the thermal and mechanical process actuators.

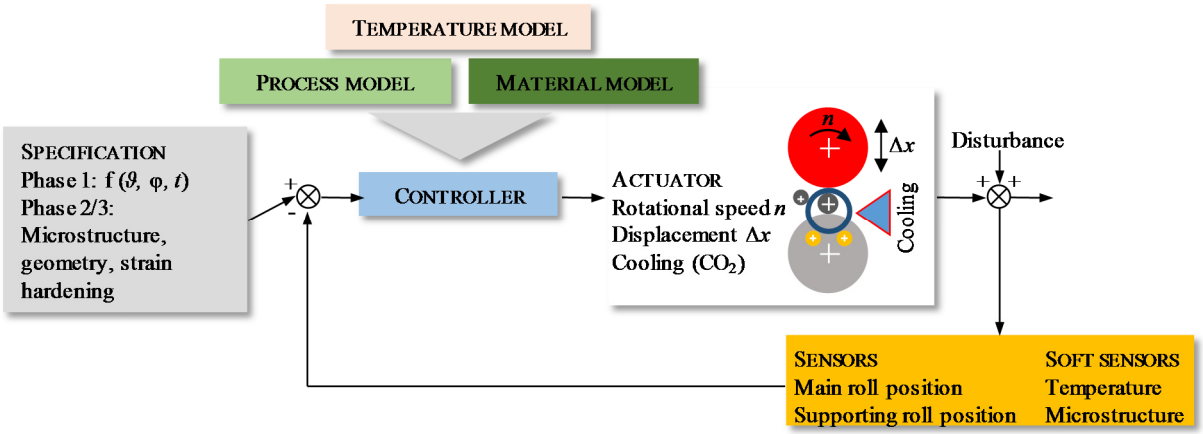


Figure 3: Principle scheme of the control loop with analytical models

The process model to be implemented will consist of the semi-analytical model based on the theory of plasticity for ring rolling as developed by Küsters et al. [4] for hybrid ring rolling.

Specifically, it will be adapted to consider additionally the temperature dependency of the current flow stress as provided by the advanced material and temperature models. In combination with all necessary semi-analytical models for the soft-sensors and control-loop, parameter identification and functional integration, it will serve as the central model for the control-loop. The microstructure model delivers the necessary input for an adaptive material model, the soft-sensor models for temperature and microstructure in the ring core, as well as a model to describe temperature development during forming will feed into the process model. The connection between these models is schematically summarized in Figure 4.

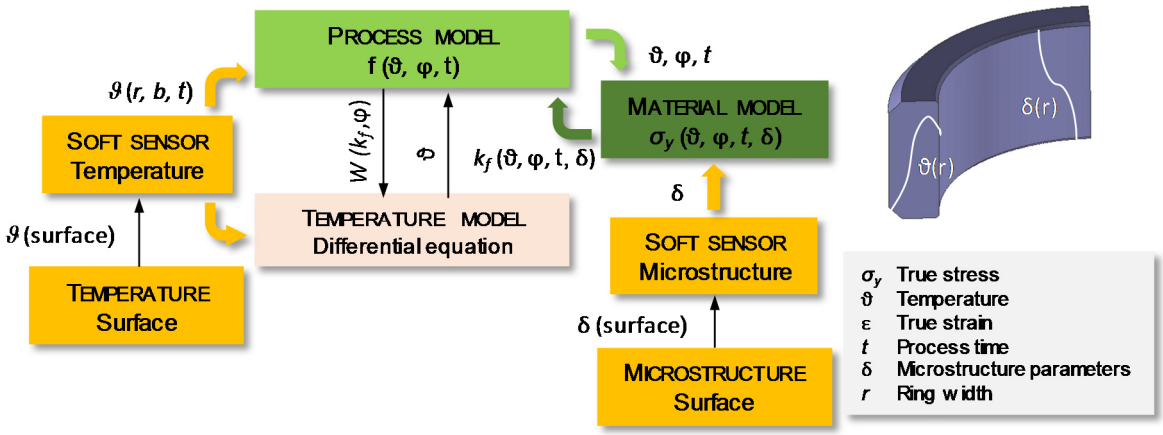


Figure 4: Context of the all interacting models

3 EXPERIMENTAL INVESTIGATION OF THE ROLLING PROCESS

The two main goals of the experimental investigations are to show the feasibility of the proposed process regarding process stability and ability to significantly influence final material properties in the same final near net shape ring geometry via Thermomechanical Treatment. Secondly, the experimental analysis is used to verify the fast process model proposed in the next chapter. As a first step, the influence of the combined forming and cooling on the strength and hardness of the ring will be demonstrated by means of experimental and numerical investigations.

3.1 Experimental set-up

Basic comparative tests are carried out between different process temperature routes. The initial workpiece temperature at the start of the rolling process is varied between room temperature and a semi-warm temperature of about 600 °C. As a second variable, the semi-warm process is carried out with and without additional cooling using liquid nitrogen (LN_2) or compressed air (0.8 MPa) after a certain expired process time. A thermal camera ImageIR® 8340 hp (company INFRATEC GMBH, detector format 640 x 512 pixels, thermal resolution of 20 mK, frame rate up to 1 kHz) is used to visualize the surface temperature of the ring over the process time in order to evaluate the effect of the workpiece cooling, see Figure 9.

The cooling of the workpiece starts after the forming of the ring has begun in order to exploit the reduced flow stress of the material at higher temperatures at the beginning of the process.

The amount of deformation induced during this phase also has an influence on the microstructure evolution during the cooling phase due to the resulting microstructural dislocations and additional heat input from forming energy. Despite the very short process time of five seconds, the heat treatment of the workpieces is expected to result in a change in structure and hardness compared to the ring rolled conventionally at room temperature. Table 1 shows an overview over the selected process parameters for different specimen as well as the final geometry.

Table 1: Process parameters

Specimen	Initial rolling temperature in °C	Cooling	Max. plastic strain φ
0 (Blank)	-	-	-
1	20	None	0.248
2	600	None	0.237
3	600	Compressed air / Liquid N_2	0.250

The roller bearing steel 100Cr6 (1.3505) is used for the thermomechanical ring rolling. The ring geometry is a simple symmetrical ring with a ball track as the inner contour. The geometry of the finished part and the blank are shown in Figure 5. Based on the ttt-diagram, a workpiece temperature of 800 °C is required for austenitization of the workpiece material. In order to achieve the high cooling rate required for martensite formation, cooling with liquid nitrogen (about -200 °C) is used. Due to the experimental conditions, a workpiece temperature of 600 °C can currently be achieved. However, this temperature is sufficient to investigate the cooling strategy with regard to the cooling rate and to influence the microstructure.

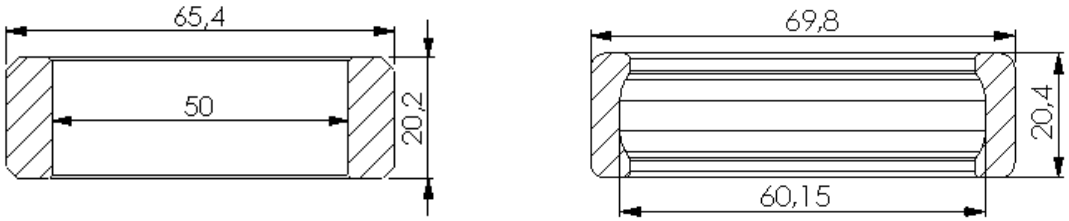


Figure 5: Blank (left) and final ring (right)

3.2 Evaluation

In the following, the results of the thermomechanical investigations compared to conventional cold and semi-hot rolled rings are presented and discussed. Figure 6 shows the different rolling strategies, cold formed, semi-warm formed and thermomechanical formed (semi-warm forming and cooling). On average, the rings have an outside diameter of 69.80 mm and an inside diameter of 56.7 mm for the ball track. In comparison, cold and thermomechanical rolled rings show no significant differences in the geometric dimensions, compare Figure 6. In addition to the geometric dimensions, the surface roughness over the width of the rings is measured. Differences are shown with regard to the average roughness R_a achieved, see Figure 6 (right). In general, the roughness of the blank is reduced by the forming process. The smallest measured

roughness, however, is with the cold-rolled ring at approx. 0.6 µm. The hot-rolled ring, on the other hand, has a roughness value of 1.0 µm, which is still significantly lower than that of the blank (specimen 0). The increase compared to the cold rolled rings is at least partially due to some scaling occurring during the heating process. Thermomechanical rolled rings have a mean roughness of 0.8 µm. These results show that the rolling process improves surface roughness and the effects of scaling can be limited. Additionally, these results give a first indications that the process is suitable for influencing the material properties.

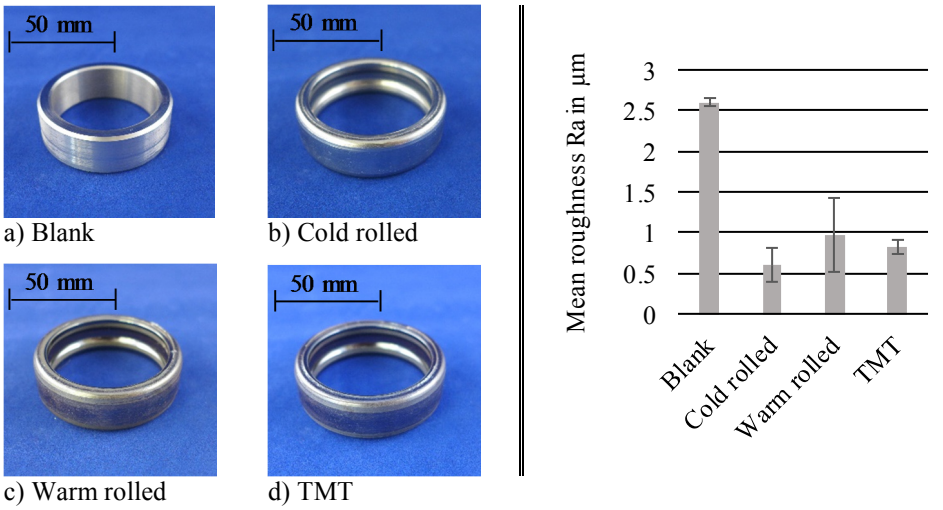


Figure 6: Final ring geometrie (left) and mean surface roughness (right)

The decisive criterion for the approach presented is the development of the microstructure and the hardness of the ring material as a result of thermomechanical ring rolling in contrast to conventional cold ring rolling. In general, it can be said that an increase in hardness occurs just as a result of forming. While there is a uniform hardness of 206 to 212 HV0.1 over the cross-section of the blank, the hardness increases to values between 260 and 272 HV0.1 for the cold-formed ring. As explained and aimed for in the concept chapter, there is an additional increase in the hardness values as a result of the combination of heat treatment and forming. While the cold formed ring achieves an average hardness of 265 HV0.1, the value is even increased up to 314 HV0.1 as a result of the in-process heat treatment during ring rolling.

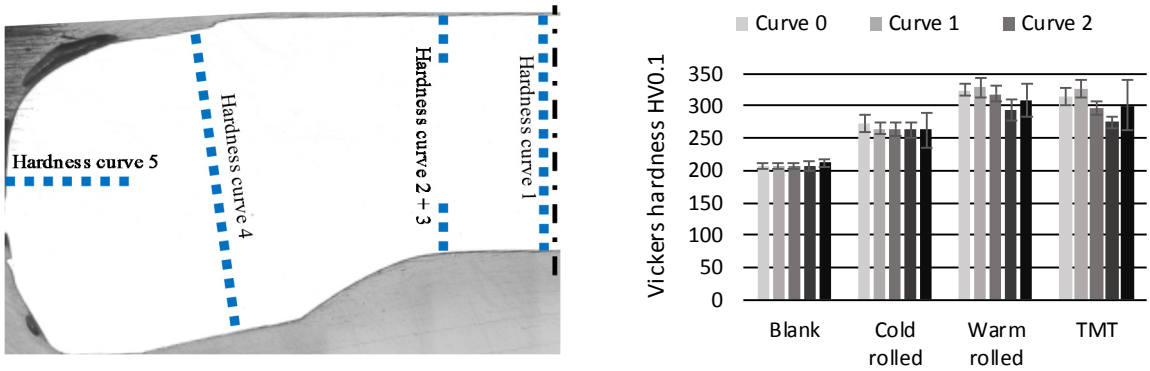
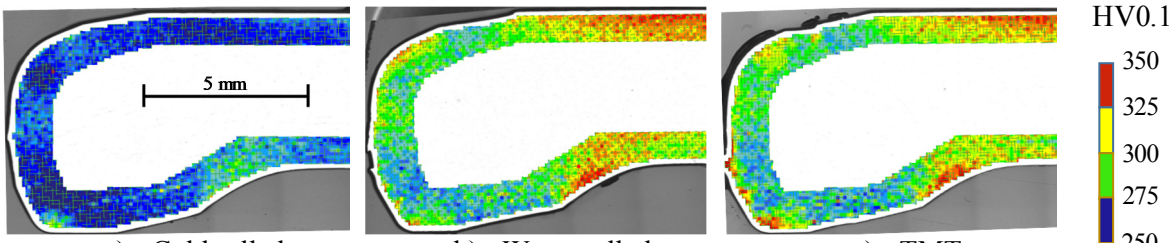


Figure 7: Cross section of final ring and hardness

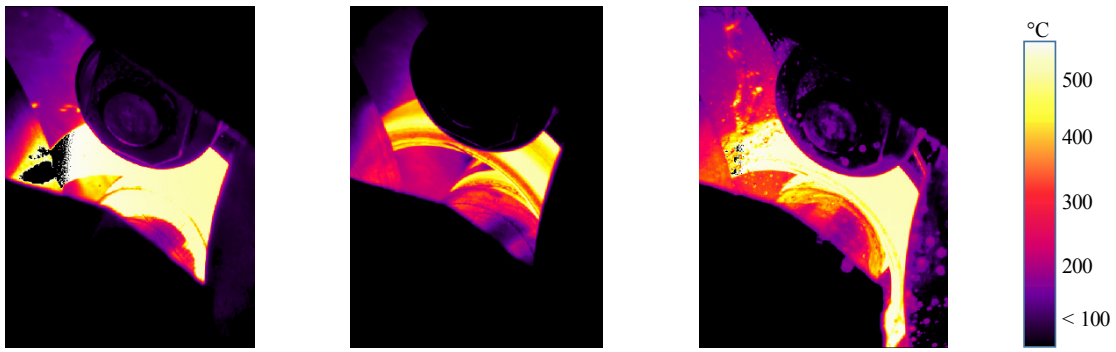
The distribution of the hardness over the cross section after forming and thermomechanical forming is shown in Figure 8. The increase in hardness as a result of the work hardening is clearly visible, whereby regions with higher forming strain also exhibit greater hardness. The influence of simultaneous heat treatment during forming can also be seen in form of an additionally increased hardness, shown in Figure 8 b) and c) compared to Figure 8 a). However, there are no differences in the hardness values when comparing the hot-rolled and thermomechanical rolled rings, Figure 8 b) and c).



a) Cold rolled b) Warm rolled c) TMT

Figure 8: Distribution of hardness in different formed rings

The main reason for this is the insufficient cooling rate of the workpiece core, so that no thermal transformation of the microstructure across the cross section of the ring occurs due to the cooling. The initial and final temperature of the thermomechanical rolled rings are shown in Figure 9. Only for air-cooled rings a change in temperature of approx. 90 K during the ring rolling process can be detected on the outer diameter, which results in a structural change, as already mentioned. The change in microstructure manifests itself in a change in strength or hardness of the material, particularly in the edge area, as shown in the Figure 9. The numerical results show a similar distribution of the strength compared to the experimental determined hardness.



a) Initial condition b) Final state of compressed air cooling c) Final state of LN_2-cooling

Figure 9: Temperature development due to chosen cooling strategy

4 PROCESS MODEL

4.1 FE-Modelling

In order to investigate the relevant mechanisms and effects during this thermo-mechanical transient deformation process, a simplified finite-element-model was build using the FE-code msc.marc v2013.1 with an implicit time integration schema. To achieve a short simulation time, a 2D model was generated using the plane strain assumption. Therefore, the model neglects the cross section deformation at the inner side of the ring caused by the mandrel. Nevertheless, the effects of the local and time depending cooling, realized by pressurized air or liquid nitrogen can be observed. For this reason, a subroutine is implemented to ensure a constant heat transfer coefficient of $3 \cdot 10^{-3}$ W·m^{-2}·K^{-1} at a defined single position at the outer diameter and a heat loss due to the contact to the roll with a heat transfer coefficient of 10^{-4} W·m^{-2}·K^{-1}. Friction was realized by the shear factor model with the friction coefficient $m = 0.9$. The material behavior is modelled temperature dependent by the equation of Johnson-Cook:

$$\sigma(\varphi,\vartheta) = (504\ \text{MPa} + 370\ \text{MPa} \cdot \varphi^{0.17}) \cdot \left(1 + 0.025 \cdot ln\left(\frac{\dot{\varepsilon}}{1\ \text{s}^{-1}}\right)\right)\left(1 - \left(\frac{(\vartheta - 20°)}{\vartheta_{\text{melt}} - 20°}\right)^{0.793}\right) \quad (1)$$

Figure 10 shows the geometry of the model (a) and the results of the temperature distribution at the process time of 0.25 sec, 0.50 sec, and 1 sec (b to d).

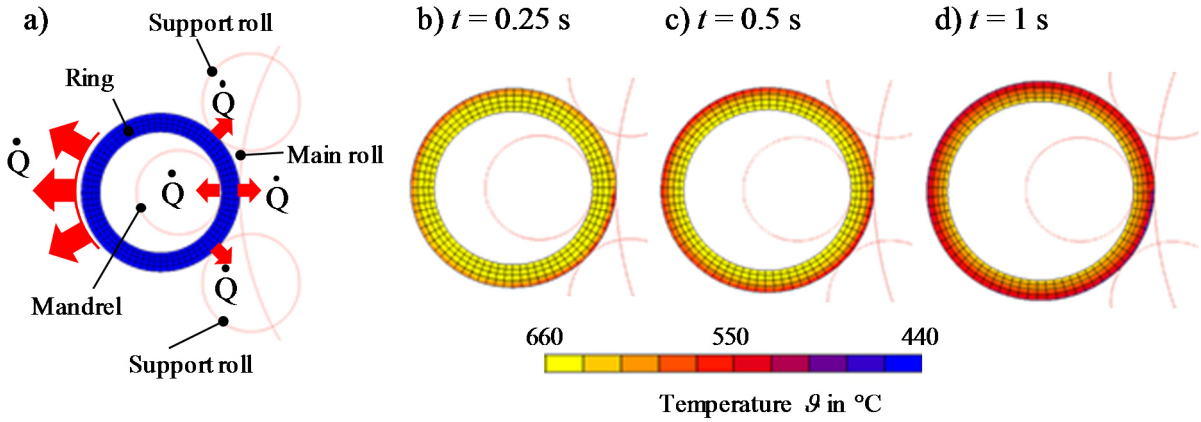
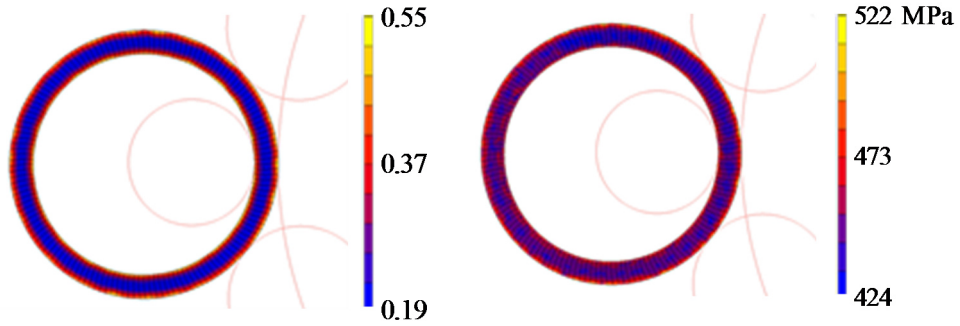


Figure 10: FE results of the temperature distribtion during thermo-mechanical ring rolling

As can be seen, the process runs without any instabilities the might occur during warm ring rolling. The local heat flux is realized by the contact on the right position and the location of applied fluid at the left position. The observed temperature drop is in the range of 110°C at a process time of 1 sec, which ensures the desired effects of thermo-mechanical ring rolling. Starting from an initial yield stress of 260 MPa, an increase in strength is achieved throughout the ring, with a significant increase in the outer ring area. The results of the numerical simulation show a similar distribution of the degree of deformation and the yield stress over the ring cross-section as the distribution of the hardness values in the experimental investigations. The highest strength is achieved at the outer diameter. The results are summarized in Figure 11.



a) Plastic strain b) True strain

Figure 11: Distribution of plastic strain and true strain in the final ring

5 Conclusion and Outlook

In the course of the experimental and numerical investigations on thermomechanical ring rolling, an approach was implemented which enables the material properties to be influenced as a result of a forming process and simultaneous thermal treatment. A comparison of the experimentally measured micro hardness and the numerically determined strength in the ring cross-section shows that the areas with the largest deformation and highest strength also have the greatest hardness values and a comparable distribution exists. It can be shown that not only geometrical dimensions of the ring but also roughness as well as strength and hardness values can be adjusted by targeted Thermomechanical Treatment.

Further work concerns the development of a soft sensor in order to deduce the core temperature from the measured surface temperature of the ring during the ring rolling process. This soft sensor in combination with a fast simulation approach provides the basis for a later inline process control. Additionally, the cooling strategy will be improved in order to realise a higher cooling rate and thereby an improved control of the microstructure formation.

REFERENCES

[1] Allwood, J.M.; Tekkaya, A.E. and Stanistreet, T.F. The development of ring rolling technology. *Steel research international* Vol. 56 (2005) 111-120.

[2] Kluge, A.; Wiegels, H. and Kopp, R.: Ringwalzen von Werkstoffverbunden. *Stahl und Eisen* Vol. 7 (1995) 37-38.

[3] Seitz, J.; Schwich, G.; Guenther and S.; Hirt, G. Investigation of a composite ring rolling process by FEM and experiment. *Saanouni, K. MATEC Web of Conferences* Vol. 80: EDP Sciences (2016) 15011.

[4] Küsters, N.; Schomäcker, M. and Brosius, A. Herstellung kraftschlüssiger Messing-Stahl-Verbindungen durch Verbundkaltringwalzen - Verfahrensprinzip und Einflussfaktoren. *SFU 2017 - Werkstoffe und Komponenten im Fahrzeugbau.* Freiberg. ACATRAIN e.V. (2017)

[5] Allwood, J.M.; Duncan, S.R.;Cao, J.; Groche, P.; Hirt, G.; Kinsey, B.; Kuboki, T. and Liewald, M. Closed-loop control of product properties in metal forming. *CIRP Annals – Manufacturing Technology* Vol. 65 (2016) 573-596.

[6] Koppers, U. Geometrie, Kinematik und Statik beim Walzen von Ringen mit Rechteckquerschnitten. RWTH Aachen (1987).
[7] Polyblank, J.A; Allwood, J.M. and Duncan, S.R. Closed-loop control of product properties in metal forming. A review and prospectus. *Journal of Materials Processing Technology* Vol. 214. Elsevier BV (2014) 2333-2348.
[8] Choi, H., Cho and H. An adaptive control approach to the ring geometry control for radial-axial ring rolling processes. *Proceedings of the institution of mechanical engineering. Part C: Mechanical Engineering Science* Vol. 203*,* SAGE Publications (1989) 243-254.
[9] Choi, H.D., Cho, H.S. and Lee, C.O. Application of an adaptive control method to the guide roll force control for ring rolling processes. *IFAC Proceedings* Vol. 23. Tallin, Estonia. Elsevier BV (1990) 335-340.
[10] Kopp, R.; Koppers, U. and Wiegels, H. New control system for ring rolling. *Advanced Technology Plasticity* Vol. 2 (1984) 803-807.
[11] Husmann, T. and Meier, H. Use of image processing to evaluate radial-axial rolled rings. *Procedia Engineering* Vol. 81, Elsevier BV (2014) 304-309.
[12] Jenkouk, V. Integration von Regelungsalgorithmen in die Finite-Elemente-Simulation von Ringwalzprozessen. RWTH Aachen (2009).
[13] Hehl, A. Thermomechanische Behandlung beim Ringwalzen – Modelle zur schnellen Simulation der Gefügeevolution, RWTH Aachen. DISS (2009).
[14] DIN EN 10025-4 Warmgewalzte Erzeugnisse aus Baustählen - Teil 4: Technische Lieferbedingungen für thermomechanisch gewalzte schweißgeeignete Feinkornbaustähle (2005).
[15] Stahl-Eisen-Werkstoffblatt SEW 082: Begriffsbestimmungen. Normalisierendes Umformen und Thermomechanisches Umformen. Beuth Verlag GmbH (1989).
[16] Hartmut, H.; Neugebauer, R. and Spur, S. *Handbuch Umformen*. Carl Hanser Verlag, München (2012).
[17] Tanaka, T. Development of thermo-mechanical controlled processing of high-strength low alloy steel. *Key Engineering Material* Vol. 84-85, Trans Tech Publicatio*n* (1993) 331-355.
[18] Klein, M.; Rauch, R.; Spindler, H. and Stiaszny, P. Ultra High Strength Steels Produced by Thermomechanical Hot Rolling – Advanced Properties and Applications. *BHM Berg- und Hüttenmännische Monatshefte* Vol. 157, Springer Nature (2012) 108-112.

XV International Conference on Computational Plasticity. Fundamentals and Applications
COMPLAS 2019
E. Oñate, D.R.J. Owen, D. Peric, M. Chiumenti & Eduardo de Souza Neto (Eds)

THE BREAKAGE PREDICTION FOR HYDROMECHANICAL DEEP DRAWING BASED ON LOCAL BIFURCATION THEORY

H. LU*, W. HUANG, H. B. YU*** AND S. J. QIN†**

* Key Laboratory of Advanced Forging and Stamping Technology and Science, Ministry of Education
Yanshan University
066004 Qinhuangdao, China
e-mail: honglu@ysu.edu.cn

** National Engineering Research Center for Equipment and Technology of Cold Strip Rolling (NECSR)
Yanshan University
066004 Qinhuangdao, China
e-mail: huangwen@ysu.edu.cn

***Tianjin Heavy Industry Co. Ltd.
First Heavy Machinery Group Co.
300457 Tianjin, China

† Key Laboratory of Advanced Forging and Stamping Technology and Science, Ministry of Education
Yanshan University
066004 Qinhuangdao, China
e-mail: plastic@ysu.edu.cn

Key words: Forming Limit, Bifurcation Theory, Localized Necking Criterion, Characteristic Curve Theory, FE Simulation, Hydromechanical Deep Drawing

Abstract. A criterion of sheet metal localized necking under plane stress was established based on the bifurcation theory and the characteristics theory of differential equation. In order to be capable to incorporate the directional dependence of the plastic strain rate on stress rate, Ito-Goya's constitutive equation which gave a one to one relationship between stress rate component and plastic strain rate component was employed. The hydromechanical deep drawing process of a cylindrical cup part was simulated using the commercial software ABAQUS IMPLICIT. The onset of breakage of the part during the forming process was predicted by combining the simulation results with the local necking criterion. The proposed method is applied to the hydro-mechanical deep drawing process for A2219 aluminum alloy sheet metal to predict the breakage of the cylindrical cup part. The proposed method can be applied to the prediction of breakage in the forming of the automotive bodies.

1 INTRODUCTION

Due to weight reduction, the application of aluminum alloy sheet metal in automobile industry and aerospace field has been increased. As aluminum alloy is low in r value, breakage defect is easy to occur in the forming process. Hydromechanical deep drawing(HDD) process is paid attention as a process to raise its formability in industry. In HDD, the die design, material properties, friction condition, and process parameters such as pre-bulging pressure, forming pressure, and loading path, and etc. have great influence on the forming results. In order to obtain the adapted process condition, it is needed to predict breakage defect accurately.

Breakage is a phenomenon of material seperation and can't be treated using the continuum mechanics. Therefore, the precursors of sheet breakage i.e. local necking and diffusion are taken as the forming limit. The representative work includes Hill's local necking theory[1], Swift's diffusion necking theory[2], the theory proposed by Marciniak and Kuczynski[3] in which the limiting strain of the sheet metal was analyzed under biaxial stretching, and the theory proposed by Stören and Rice[4] which considers the location of the deformation mode.

Although by using some commercial software, forming limit diagram(FLD) can be given, it is produced under proportional loading condition. However, in industry, the loading condition is complicated. In this study, based on the Hill's bifurcation theory[5] and the characteristics theory of differential equation, a criterion of localized necking of sheet metal under plane stress was given. Ito-Goya's constitutive equation, which gave a one to one relationship between stress rate component and plastic strain rate component was used. By combining the simulation results of HDD with the criterion, the occurrence and location of breakage are predicted.

2 CONDITION OF LOCALIZED NECKING

Localized necking which is taken as the precursor of sheet metal breakage, is treated as bifurcation from basic deformation mode to local deformation mode in plastic mechanics and mathematics. Based on Triantafyllidis's analaysis method, bifurcation is considered by general boundary value problem in incremental form. Due to sheet metal forming endures large deformation, the updated Lagrange formulation is used. The incremental equilibrium equation using nominal stress can be expressed by

$$\nabla \cdot \dot{\mathbf{\Pi}} = 0 \quad in \quad V \tag{1}$$

Boundary conditions are expressed by

$$\begin{aligned} \dot{\mathbf{\Pi}} \cdot \boldsymbol{n} &= \dot{\boldsymbol{f}} \quad on \quad S_F \\ \boldsymbol{v} &= \boldsymbol{V} \quad on \quad S_V \end{aligned} \tag{2}$$

where V denotes the region of body in initial configuration, S_F the surface on which the rate of traction force $\boldsymbol{f}$ is prescribed, S_V the surface on which the velocity $\boldsymbol{v}$ is prescribed, $\boldsymbol{n}$ the unit normal to the surface S_F, and $\dot{\mathbf{\Pi}}$ denotes nominal stress rate, which is related

to Cauthy stress as shown in Eq. (3).

$$\begin{aligned} \dot{\boldsymbol{\Pi}} &= \overset{\triangledown}{\boldsymbol{\sigma}} + \boldsymbol{w}\cdot\boldsymbol{\sigma} - \boldsymbol{\sigma}\cdot\boldsymbol{w} - \boldsymbol{L}\cdot\boldsymbol{\sigma} \\ &= \boldsymbol{A} : \boldsymbol{L} \end{aligned} \tag{3}$$

where $\boldsymbol{\sigma}$ denotes Cauchy stress, $\overset{\triangledown}{\boldsymbol{\sigma}}$ the Jaumann rate of the Cauchy stress, $\boldsymbol{L}$ the velocity gradient tensor, $\boldsymbol{w}$ the spin tensor. The components of $\boldsymbol{A}$ are given as Eq. (4):

$$A_{ijkl} = D_{ijkl} + \frac{1}{2}\left(\sigma_{il}\delta_{jk} - \sigma_{jl}\delta_{ik} - \sigma_{ik}\delta_{jl} - \sigma_{jk}\delta_{il}\right) + \sigma_{ij}\delta_{kl} \tag{4}$$

Substituting Eq.(3) into Eq.(1) and (2), the incremental boundary value problem of elasto-plastic material can be written as

$$\begin{aligned} \nabla\cdot(\boldsymbol{A}:\boldsymbol{L}) &= 0 \quad in \quad V \\ (\boldsymbol{A}:\boldsymbol{L})\cdot\boldsymbol{n} &= \dot{\boldsymbol{f}} \quad on \quad S_F \\ \boldsymbol{v} &= \boldsymbol{V} \quad in \quad S_V \end{aligned} \tag{5}$$

From the first equation of Eqs. (5), we can obtain

$$\nabla\cdot(\boldsymbol{A}:\Delta\boldsymbol{L}) = 0 \quad in \quad V \tag{6}$$

where $\Delta(\cdots)$ denotes the difference of two solution sets. Using $\boldsymbol{A}^L$ as the tensor for the linear comparison solid of $\boldsymbol{A}$[5], we obtain

$$\nabla\cdot\left(\boldsymbol{A}^L:\Delta\boldsymbol{L}\right) = 0 \quad in \quad V \tag{7}$$

Considering the deformation of sheet metal under plane stress, denoting the velocity components corresponding to rectangular coordinate system $x_\alpha\,(\alpha=1,2)$ within the sheet plane as $v_\alpha,(\alpha=1,2)$, Eq. (7) can be written as following differential equations[6]:

$$\begin{aligned} b_1\frac{\partial^2(\Delta v_1)}{\partial x_1^2} &+ b_2\frac{\partial^2(\Delta v_1)}{\partial x_1\partial x_2} + b_3\frac{\partial^2(\Delta v_1)}{\partial x_2^2} + \\ b_4\frac{\partial^2(\Delta v_2)}{\partial x_1^2} &+ b_5\frac{\partial^2(\Delta v_2)}{\partial x_1\partial x_2} + b_6\frac{\partial^2(\Delta v_2)}{\partial x_2^2} + \phi_1 = 0 \\ c_1\frac{\partial^2(\Delta v_1)}{\partial x_1^2} &+ c_2\frac{\partial^2(\Delta v_1)}{\partial x_1\partial x_2} + c_3\frac{\partial^2(\Delta v_1)}{\partial x_2^2} + \\ c_4\frac{\partial^2(\Delta v_2)}{\partial x_1^2} &+ c_5\frac{\partial^2(\Delta v_2)}{\partial x_1\partial x_2} + c_6\frac{\partial^2(\Delta v_2)}{\partial x_2^2} + \phi_2 = 0 \end{aligned} \tag{8}$$

whereis $\phi_\alpha\,(\alpha=1,2)$ are the function of $\partial(\Delta v_\alpha)/\partial x_\beta\,(\alpha,\beta=1,2)$ and $\partial\sigma_{\alpha\gamma}/\partial x_\beta\,(\alpha,\beta,\gamma=1,2)$. The values of $b_i(i=1,6)$ and $c_i(i=1,6)$ are dependent on stress components, strain components, work-hardening coefficient and tangential stiffness tensor of constitutive equation.

When non-zero solution for Eq.(8) exists, it is possible that bifurcation occurs[5]. The occurrence condition of local bifurcation mode is same as that of existence of characteristic curve of the second-order simultaneous differential equations Eq.(8). Denote the angle between the tangent line of the characteristic curve and x_1-axis by α . Using $\lambda = tan\alpha$, the existence condition for characteristic curve of the simultaneous equations Eq. (8) can be expressed by

$$\begin{vmatrix} b_1\lambda^2 - b_2\lambda + b_3 & b_4\lambda^2 - b_5\lambda + b_6 \\ c_1\lambda^2 - c_2\lambda + c_3 & c_4\lambda^2 - c_5\lambda + c_6 \end{vmatrix} = 0 \tag{9}$$

From Eq.(9), we can obtain the following 4th degree algebraic equation related to λ:

$$A_1\lambda^4 + A_2\lambda^3 + A_3\lambda^2 + A_4\lambda + A_5 = 0 \tag{10}$$

where $A_i(i = 1, 5)$ are related to $b_i(i = 1, 6)$ and $c_i(i = 1, 6)$. After gaining the distribution of stress and strain by FEM simulation, the value of $A_i(i = 1, 5)$ can be determined. By combining Eq. (10) and the results of FEM simulation, we can predict the occurrence of local necking(breakage) in sheet metal forming.

3 CONSTITUTIVE EQUATION

The classical J2-flow rule is not suitable for bifurcation analysis. To use the constitutive rule in which there is a one-to-one relationship between stress rate affects and plastic strain rate affects critical point[7]. A constitutive rule which incorporates the characteristics that the direction of deviatoric stress rate affects the direction of plastic strain rate has been proposed by Goya and Ito[8]. In this study, we use the constitutive rule.

$$d\boldsymbol{\varepsilon}^p = \frac{3}{2H'}\left\{K_c d\boldsymbol{\sigma}' + \frac{3}{2}(1 - K_c)\left[\frac{\boldsymbol{\sigma}'}{\bar{\boldsymbol{\sigma}}} \otimes \frac{\boldsymbol{\sigma}'}{\bar{\boldsymbol{\sigma}}}\right] : d\boldsymbol{\sigma}'\right\} \tag{11}$$

where H' denotes the tangential modulus on the stress-strain curve, K_c is the material coefficient, which denotes the direction dependency degree of plastic strain increment on deviatoric stress increment. For plane stress problem, from Eq.(11) we can obtain

$$\begin{pmatrix} \overset{\triangledown}{\sigma}_{11} \\ \overset{\triangledown}{\sigma}_{12} \\ \overset{\triangledown}{\sigma}_{22} \end{pmatrix} = \begin{pmatrix} \alpha_{11} & \alpha_{12} & \alpha_{13} \\ \alpha_{21} & \alpha_{22} & \alpha_{23} \\ \alpha_{31} & \alpha_{32} & \alpha_{32} \end{pmatrix} \begin{pmatrix} \dot{\varepsilon}_{11} \\ \dot{\varepsilon}_{12} \\ \dot{\varepsilon}_{22} \end{pmatrix} \tag{12}$$

where $\overset{\triangledown}{\sigma}_{\alpha\beta}$ denotes the component of Jaumann rate tensor of Cauchy stress; $\dot{\varepsilon}_{\alpha\beta}$ is the component of strain rate tensor; and α_{ij} denotes the tangential stiffness tensor introduced into the constitutive relation.

4 APPLICATION OF THE LOCAL NECKING CRITERION

The local necking criterion obtained in the previous section is programmed and combined with FEM simulation results. The occurrence of local necking during HDD is investigated.

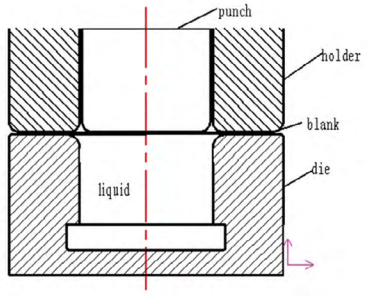


Figure 1: A schematic diagram of the hydromechanical deep drawing

4.1 Finite element model

A schematic diagram of the hydromechanical deep drawing is shown in Fig. 1. The sheet is 200mm in diameter and 1.5mm in thickness. The gap between the die and the holder is constant and is 1.2t(=1.8mm). The diameter of the punch is 100mm and the clearance between the punch and the die is 2mm. The radiuses of the punch, the die and the holder are 10mm respectively. Sheet material A2219 is used. The material parameters are $E = 70.7 \times 10^3 MPa, \nu = 0.3, \sigma_y = 107 MPa, C = 634.7 MPa, n = 0.3$.

FEM simulation is conducted using commercial software ABAQUS IMPLICIT. The simulation model of HMD is shown in Fig. 2. 3-node and 4-node shell elements S3R and S4R are used. Die and holder are analytical rigid bodies. Since the part and load are axis-symmetrical, 11.25° sheet is used in the model. The friction coefficients between the blank and the holder and the die is 0.01 respectively and the friction coefficient between the blank and the punch is 0.15.

4.2 Loading path

The hydromechanical deep drawing consists of two steps. In the first step, the punch is fixed above the blank. The distance between the punch and the top of blank is 2.25mm. Apply 4MPa chamber pressure linearly onto the bottom of the blank. In the second step, apply maximum chamber pressure of 5MPa and 10MPa respectively onto the bottom of the blank while moving the punch down by 70mm. The pressure-stroke curve is shown as Fig. 3.

4.3 Prediction results and analysis

When the maximum chamber pressure is 5MPa and 10MPa, the stress results of the blank after hydromechanical deep drawing are shown in Fig. 4 .

Bifurcation analysis is conducted by combining the stress and strain results obtained by the simulation of HDD and the local necking criterion. The simulation results are input into self-made Matlab program in which the local necking is predicted according to

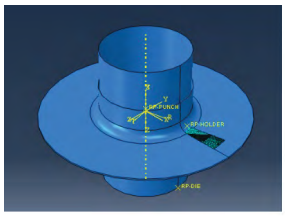


Figure 2: The simulation model of HDD

the criterion obtained in section 2.

When forming pressure is 5MPa, after the HDD, the breakage occurs. The predicted local necking results is shown in Fig. 5. Here coefficient $K_c = 0.3$. When forming pressure is 10MPa, the breakage doesn't occur. The predicted local necking results are compared with experiments[9]. The experiment shows good agreement with the analysis.

5 CONCLUSIONS

- The criterion of localized necking for plane stress has been given by using bifurcation theory. The existing condition of characteristic curve of equilibrium equation in rate form is used. The Ito-Goya's constitutive equation is employed, which gives one-to-one relationship between plastic strain increment component and the stress increment component.

- Combining the proposed criterion that is programmed in Matlab with simulation results of HDD for A2219 aluminum alloy sheet, the occurrence of localized necking is analyzed. The breakage occurs when maximum forming pressure is 5MPa during the analysis. Here, the coeficient K_c is 0.3. The analysis results show good agreement with the experiment.

ACKNOWLEDGEMENTS

The authors acknowledge the financial support by National Natural Science Foundation of China in 2017(Grant no. 51675466). The first and second authors would like to thank the emeritus professor Koichi Ito of Tohoku University of Japan for his instructions and supports.

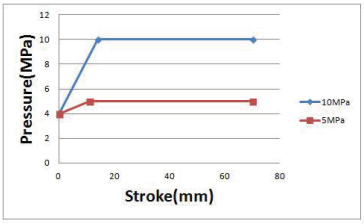


Figure 3: The pressure-stroke curve during forming stage

REFERENCES

[1] HILL, R. On discontinuous plastic states with special reference to localized necking in thin sheets. *Journal of the Mechanics and Physics of Solids* (1952)**1-1**:19–30.

[2] Swift, H. W. Plastic instability under plane stress. J. Mech. Phys. Solids (1952) **1**1-18

[3] Marciniak, Z. and Kuczyński, K. Limit strains in the processes of stretch-forming sheet metal. *Int. J. Mech. Sci.* (1967)**9**: 609-620.

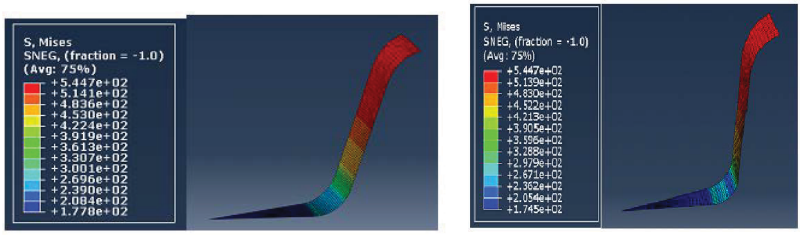
[4] Stören, S. and Rice, J. R. Localized necking in thin sheet. *J. Mech. Phys. Solids*(1975) **23**:421-441.

[5] Hill, R. A general theory of uniqueness and stability in elastic-plastic solids. *J. Mech. Phys. Solids*(1958)**6**:236-249.

[6] Huang, W., Lu, H., Yu, H.B., and et al. The rupture criterion for the sheet metal forming based on local bifurcation theory -the study of enhancing the accuracy of rupture prediction for aluminum alloy sheet metal.*Journal of Plasticity Engineering*(2017)**24(5)**:68-73.

[7] Ito, K., Satoh, K., Goya, M. and Yoshida, T. Prediction of limit strain in sheet metal-forming processes by 3d analysis of localized necking. *Int. J. Mech. Sci.* (2000) **42**:2233-2248.

[8] Goya, M. and Ito, K. An expression of elastic-plastic constitutive law incorporating a stress increment dependence. *Transactions of the Japanese Society of Mechanical Engineering*(1990) **56A(521)**:101-106.



(a) 5MPa (b) 10MPa

Figure 4: The stress distribution in the blank(maximum values of forming pressure are 5MPa and 10MPa)

[9] Chen, Y. Z. Research on hydromechanical deep drawing of 2219 alumimum alloy cylindrical cup. *Dessertation for the Master Degree in Engineering*(2013) :31-50.

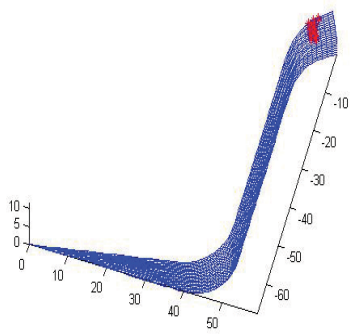


Figure 5: The predicted local necking occurred after HDD(maximum forming pressure is 5MPa)

XV International Conference on Computational Plasticity. Fundamentals and Applications
COMPLAS 2019
E. Oñate, D.R.J. Owen, D. Peric, M. Chiumenti & Eduardo de Souza Neto (Eds)

THERMO-MECHANICAL ANALYSIS OF ADDITIVELY MANUFACTURED HYBRID EXTRUSION DIES WITH CONFORMAL COOLING CHANNELS

C. BERTOLI*, P. STOLL† AND P. HORA*

* Institute of Virtual Manufacturing (IVP)
ETH ZURICH
Tannenstr. 3, 8092 Zurich, Switzerland
e-mail: bertoli@ivp.mavt.ethz.ch, - web page: http://www.ivp.ethz.ch

† Innovation Center for Additive Manufacturing Switzerland (ICAMS)
Inspire AG - ICAMS
Lerchenfeldstr. 3, 9014 St. Gallen, Switzerland
e-mail: stoll@inspire.ethz.ch - web page: https://www.inspire.ethz.ch

Key words: aluminum extrusion, selective laser melting, hybrid extrusion die

Abstract. Profile overheating and surface defects during hot aluminum extrusion can occur when seeking higher productivity rates at increased ram speed velocities. The incorporation of cooling channels in the die-design allows overcoming this process limitation by keeping the profile temperature below the melting point of the alloy used [1]. Selective laser melting (SLM) of conformal cooling channels provides, in contrast to conventional manufacturing techniques, the opportunity to place the cooling circuit inside the mandrel of a porthole-die in a well-defined position to the critical bearing region [2].

In the framework of this study, a preliminary numerical investigation on the extrusion process under the assumption of liquid nitrogen cooling is analysed. The results show, that by combining conformal cooling channels with liquid nitrogen as a cooling media high cooling rates, which are well beyond the state of the art of conventional dies, can be achieved.

In a hybrid extrusion die set-up, a part of the mandrel, that is additively manufactured, is either joined [3] or directly selective leaser melted onto the conventionally manufactured parts [4]. For a proper implementation in the extrusion process, material testing of the welded joint are needed. Thus, in the current study, tensile tests performed at room temperature for hybrid specimens, partially consisting of conventionally processed tool steel 1.2343 and partially additively manufactured 1.2709, will be presented. Moreover, four different heat treatment sequences of the hybrid specimens will be discussed. In addition, for each configuration, micro-structural images are taken to investigate failure at the bonding region. Finally, an optimal manufacturing sequence for a hybrid die with the described material combination is proposed.

1 INTRODUCTION

As for other industrial processes, the main optimization goal is to raise productivity rates by increasing ram speed. During the extrusion process, however, the temperature development in the profile needs to remain below the melting point of the alloy in use, thus, limiting the maximal possible velocity [5, 6]. Therefore, as studied amongst others by Ward et al. [1], to manage the temperature increase in the extruded profile, cooling channels for nitrogen tempering are implemented in the tool design.

During aluminum extrusion, the highest temperatures are encountered in the forming region (see Figure 1), also known as the bearing region, where the material flow reaches its final profile shape [6]. In order to efficiently position the cooling channels inside the tools as close as possible to the bearing region, conformal cooling channels manufactured by selective laser melting (SLM) are implemented in the die design, as proposed by Hölker et. al [2, 7]. The difference to channels conventionally manufactured by milling and drilling operations is that the conformal pipes can follow the contour of the of the heated surfaces and enhance a homogeneous cooling effect.

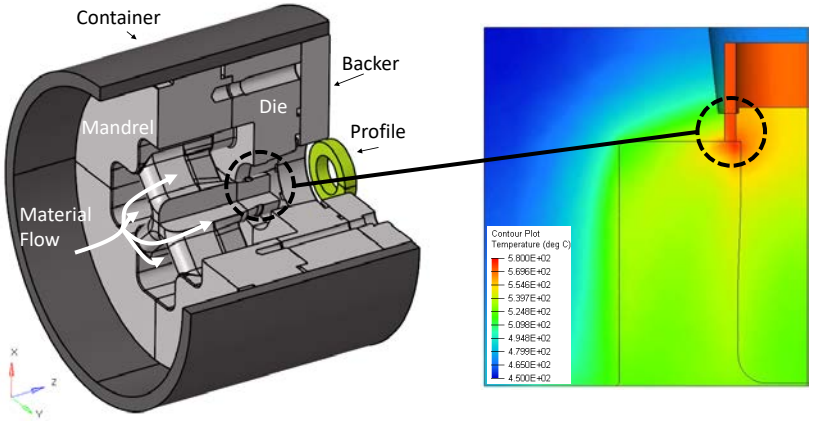


Figure 1: Exemplary critical temperature distribution of a tube profile for a four chamber porthole die

2 MANUFACTURING CONCEPTS FOR HYBRID EXTRUSION DIES

Selective laser melting of a complete extrusion tool set-up would be very cost and time intensive and also difficult to produce due for example to the restricted building chambers of the existing SLM machines, therefore, a hybrid die concept is introduced. Figure 2 pictures two possible ways of building hybrid extrusion tools. As it can be seen, to overcome the manufacturing and cost constraints, the tools can consist of both: additively and conventionally manufactured components. Moreover, the parts can either be joined or welded together. A simplified cost analysis for the production of the additively manufactured parts can be seen in Table 1. The costs are calculated under the assumption of: €$70/kg$ for the material costs and €$120/h$ for the machine costs. It is clear from this

table, that to manufacture the entire mandrel by selective laser melting would not be acceptable in the industrial framework.

Table 1: Cost estimation of additive manufactured parts

	Mass kg	Time h	Material €	Machine €	Total Costs €
Insert (joined)	0.64	10	50.30	1'200	1'250.30
Insert (welded)	0.32	5	25.15	600	625.15
Mandrel (full)	16.75	262.98	1'322.86	31'557.60	32'880.46

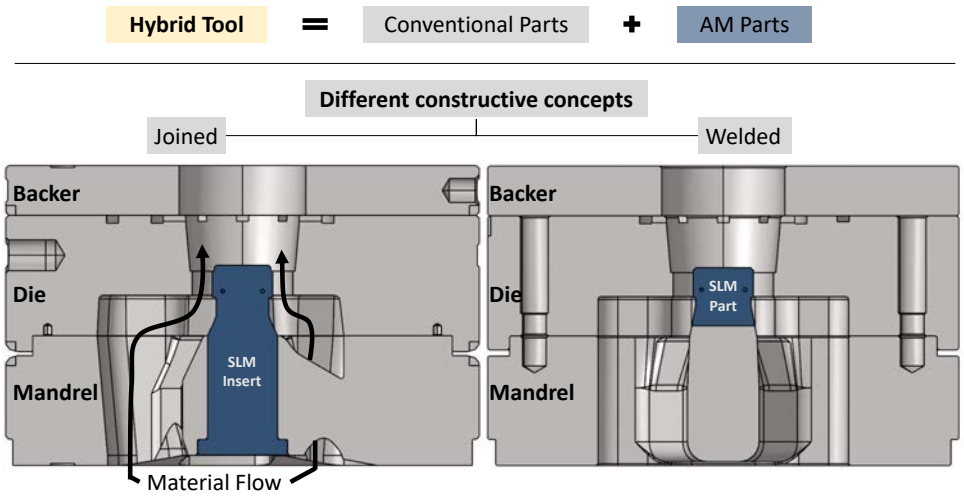


Figure 2: Design concepts for hybrid tools applied on a porthole-die for a tube profile.

There are various arguments in favor and against the hybrid constructive concepts pictured in Figure 2. The joined tool design has the advantage, that the several parts can be manufactured and heat treated separately and therefore, it has a greater flexibility regarding the material choice. However, there are more geometrical constraints because the additively manufactured insert has to fit into the mandrel and therefore, the geometrical freedom, given by the additive manufacturing technique, is more limited than in the welded tool set-up. The welded tool version, on the other hand, is more sensitive to the material selection. When the powder material for the SLM part differs from the material for the conventional part, material tests are needed to ensure the structural integrity of the insert subjected to the extrusion loads. Therefore, after a thermo-mechanical assessment of the extrusion process with and without tool cooling, introduced in Chapter 3, the results of hybrid tensile tests for the analysis of the welded tool set-up will be presented and discussed.

3 NUMERICAL INVESTIGATION OF THE EXTRUSION PROCESS

In this chapter, the results of numerical extrusion simulations are presented to show the potential and discuss the constraints of nitrogen cooling. The simulations are performed for a tube profile with a thickness of $5mm$ extruded through a five chamber porthole-die. The simulations of the extrusion process are computed with the commercial code HyperXtrude of Altair based on the ALE approach. The tools are assumed to be rigid bodies, therefore no tool deflection is computed. For the temperature dissipation into the tools a convective heat transfer coefficient of $11'000W/m^2K$ between the aluminum and the tool surfaces is defined. The workpiece material is set to a AW6060 aluminum alloy for which the Sellars-Tegart material model, implemented in HyperXtrude, is used. The model description is given by Equation 1, where n is the stress exponent, A is the reciprocal strain factor, Q is the activation energy, R is the universal gas constant, α is a constant and T is the reference temperature. The used parameter values can be seen in Table 2. These have been fitted based on material data of compression tests performed for a previous project at the institute on a dilatometer-machine.

$$\sigma = \frac{1}{\alpha}\sinh^{-1}\left(\left[\frac{Z}{A}\right]^{(1/n)}\right) \quad where\ Z = \dot{\epsilon}\exp(Q/RT) \tag{1}$$

Table 2: Parameters for the Sellars-Tegart material model

n	A	Q	R	α
-	-	J/mol	$J/molK$	$1/Pa$
2.6543	1.0989e+012	209631	8.314	1.096e-007

The preliminary study is performed on the joined tool set-up pictured in Figure 2 on the left, where 1.2709 tool steel is used for the additive manufactured insert and 1.2343 tool steel is used for the conventional parts. Since only a thermal evolution is computed for the tools, the relevant material parameters for the simulations are the thermal conductivities of the two steels used. Their values are $\lambda = 20\ W/mK$ for 1.2709 and $\lambda = 28.5\ W/mK$ for 1.2343. The billet length is considered to be $1'000mm$, however to save computational time only about $400mm$ of the entire billet length are simulated. The billet preheat is set to $485°C$ whereas the container and the tools are at $495°C$. Finally, three simulations at $3mm/s$ ram speed with and without cooling are conducted.

For the simulation with tool cooling, the cooling channels are positioned as pictured in Figure 3. As it can be seen, the main inlet channel goes through the mandrel and the insert and is divided in five smaller channels with the ration $d_i/d = 0.45$ at the bearing starting location, where the highest temperatures in the insert occur.

For the planned extrusion experiments, liquid nitrogen will be used as a cooling media for the tools. It is important to consider, that the liquid nitrogen undergoes a critical

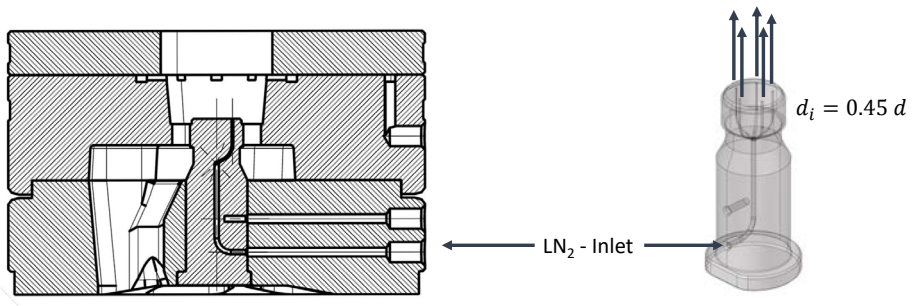
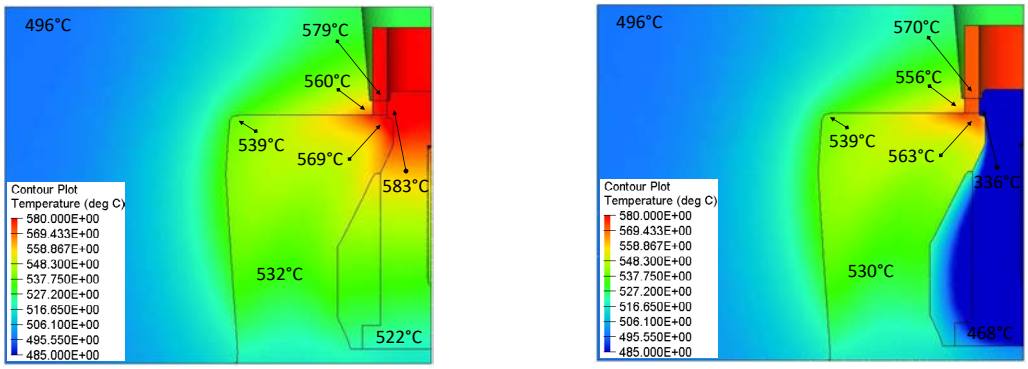


Figure 3: Cooling channel position and geometry for a five-chamber porthole die

phase-change during the cooling process caused by the very high temperature differences between the saturation temperature of the liquid (ca. $-196°C$ at $5bar$) and the wall temperature of the solid (ca. $500°C$). In the case of the extrusion process this temperature change can reach values of about $600°C$, that normally leads to boiling heat transfer characteristics. In the literature for cryogenic machining, several values for the boiling heat transfer coefficient of liquid nitrogen are proposed. However, as mentioned in the work of [8], they change the order of magnitude from $1 \cdot 10^1\ W/m^2K$ [9] up to $1 \cdot 10^4\ W/m^2K$ [10, 11] depending which physical state of the coolant is assumed for the calculations. In the case of aluminum extrusion, most of the studies on liquid nitrogen tool cooling, are based on experimental tests [12, 13, 14] rather than computational temperature prediction. Thus, no knowledge about the possible location of the phase-change or the real physical state of the fluid inside the channels is known. For this reason, while considering the studies on cryogenic machining, two simulations with a heat transfer coefficient of $1'000\ W/m^2K$ and $10'000\ W/m^2K$, assuming cold gas and cold liquid respectively, with a bulk temperature of $-150°C$ are computed.

An exemplary temperature distribution for the tool and workpiece can be found in Figure 4. The extracted temperature values are for the same nodes at the same time-step for the simulation without (left) and with (right) cooling. As it can be seen, the temperatures of the workpiece differ mostly from each other in the profile region. Due to the tool cooling, the heat generated at the bearing location dissipates towards the cooling channels (heat sink), allowing the profile to cool down about $9°C$. A temperature reduction of about $5°C$ is computed instead for the simulation with the surface heat transfer coefficient of $1'000\ W/m^2K$. The average cross-sectional profile exit temperatures are plotted in Figure 5. According to this figure, it can be observed, that the average profile temperature development without tool cooling reaches values above the critical temperature (ca. $560°C$) of the alloy used (AW-6060). Therefore, it can be concluded, that to keep profile quality at the given productivity rate without encountering profile softening, an appropriate tool cooling is necessary. In order to better quantify the cooling capacity and the heat transfer characteristics, a comparison with experimental data will be conducted in a further study. Nevertheless, the potential of nitrogen cooling, more precisely of additively manufactured conformal cooling channels, could be predicted.



(a) No cooling (b) Heat transfer coefficient 10′000 W/m^2K

Figure 4: Temperature distribution for the tool and workpiece at a press stroke of 400mm

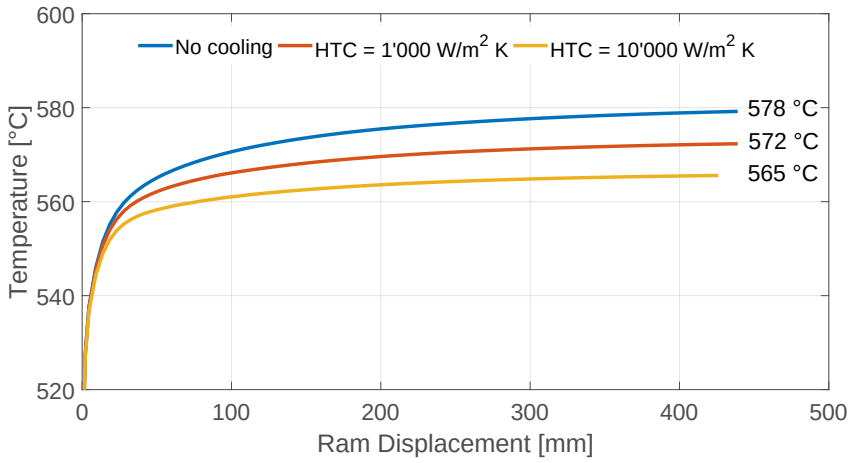


Figure 5: Average profile exit temperature development for the simulations computed with no cooling, 1′000 W/m^2K and 10′000 W/m^2K heat transfer coefficient as a boundary condition

4 EXPERIMENTAL INVESTIGATION OF THE HYBRID SPECIMENS

In Chapter 3, the potentiality of conformal cooling channels has been discussed. The simulations are performed only for the joined tool set-up, because from a computational point of view, under the described model assumptions, the results would not change for the welded tool set-up.

From the manufacturing side however, there are some aspects of the welded tool set-up that need to be addressed. In fact, when using different materials for the additively and the conventionally manufactured parts, the heat treatment strategy plays a relevant role in the manufacturing process of the die-set. Furthermore, the quality of the bonding region

between the two welded parts needs to be investigated. Therefore, in this Chapter: the results of tensile tests performed at room temperature on hybrid specimens for different heat treatment strategies will be presented together with micro-graphs of the bonding regions.

Figure 6 shows the four tested versions of hybrid tensile specimens. The conventional part of the tensile bar is either made of hardened or not hardened 1.2343 tool steel. The additively manufactured parts are then selective laser melted out of 1.2709 metal powder directly onto the conventional manufactured round bars. Afterwords, the specimens, three for each variant, are heat treated as follows:

HT1: specimens are hold at $510°C$ for 8 hours, which is the heat treatment strategy normally used for additively manufactured 1.2709 tool steel

HT2: the other samples undergo a 35 minutes hardening process at $1'020°C$ followed by two times tempering for 2 hours at $600°C$, which is the heat treatment strategy for (forged) 1.2343 tool steel

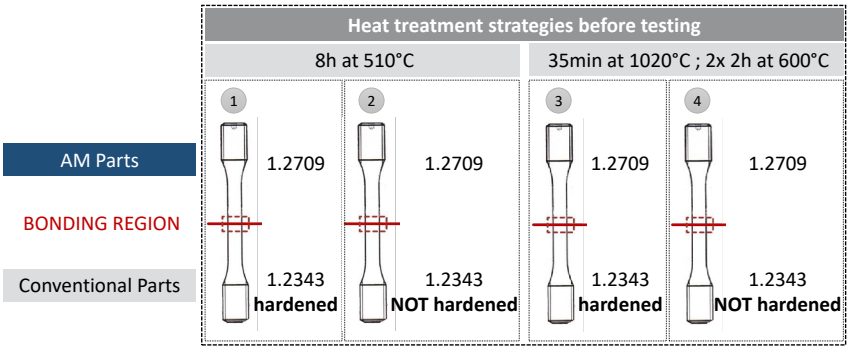


Figure 6: Tested hybrid specimens partially additively (1.2709) and partially conventionally (1.2343) manufactured

In the end, the round bars undergo turning operations to get to the final tensile bar geometry, accordinf to DIN 50125-A, and to remove possible geometry distortions induced by the heat treatment. The results of the tensile tests performed at room temperature are shown in Figure 7. The specimens that were treated based on the first strategy (HT1) show a rather ductile behavior (curves 1 and 2) compared to others (curves 3 and 4). The specimens for curves 1 and 2 show necking at the fracture surface, which lies in the conventional part of specimen made of 1.2343 and not in the selective laser melted part. For the specimens that followed the HT2 strategy, the fracture surfaces lie instead near the bonding region in the selective laser melted part. Figure 8 shows the micro-graphs taken at the bonding region after performing the tensile tests. None of the specimens directly fractured at the bonding layer, hence fulfilling a relevant requirement for the implementation of the welded tool set-up in the industrial framework.

Considering the fact, that the hybrid tool is mainly under tensile loading during the extrusion process, the best results regarding the industrial application are achieved by the

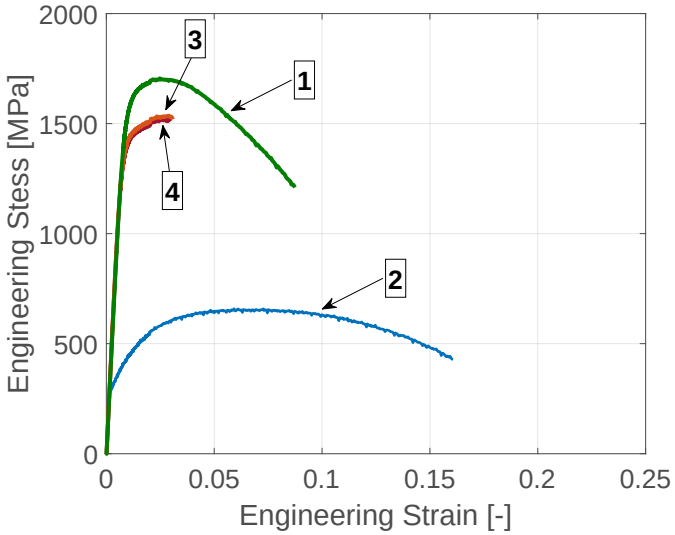


Figure 7: Tensile tests results for hybrid specimens tested at room temperature

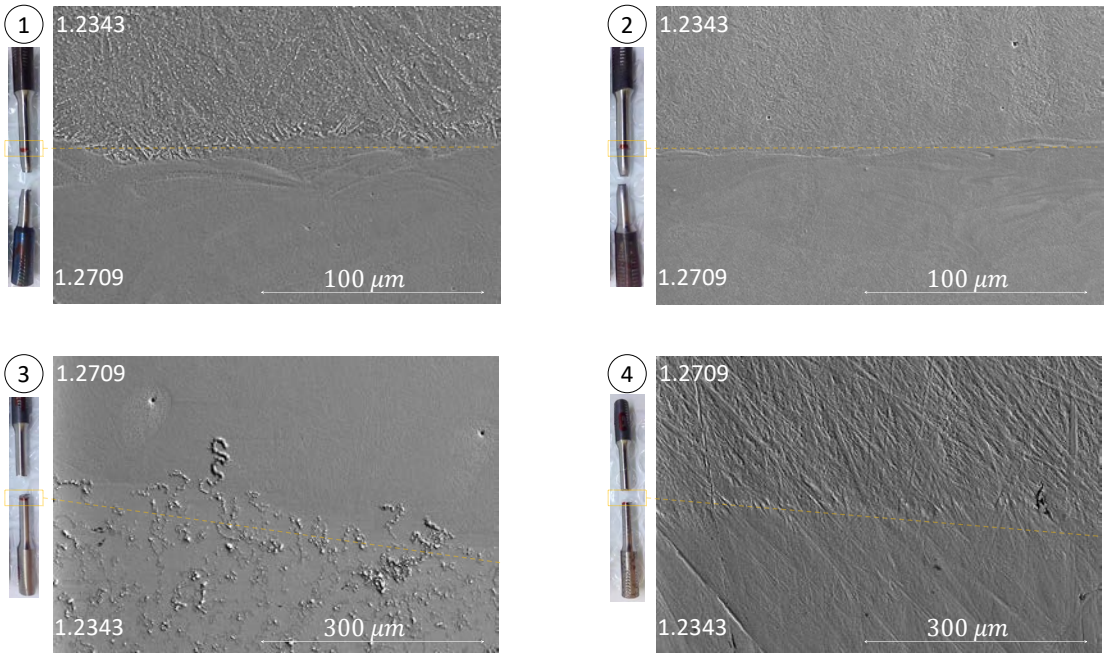


Figure 8: Micro-graphs of the bonding region after tensile testing

manufacturing strategy represented by curve 1 in Figure 7. Thus, for the hybrid tool set-up the conventional parts should be manufactured and hardened as usual. The additively manufactured part should then be directly selective laser melted onto the conventional

parts and in the end the entire hybrid tool should undergo the HT1 strategy in order to reach the required hardness of about 55 HRC for the selective laser melted material.

5 CONCLUSIONS

In this study, the use of two hybrid tool set-ups has been discussed. Simulations with and without liquid nitrogen cooling have been presented. These show promising results for the utilization of the hybrid tools in the industrial framework. However, due to the complexity of the tool cooling caused by the inevitable phase-change of the liquid nitrogen, a further study on the heat transfer characteristics coupling extrusion experiments with a numerical analysis should be performed. Material tests for hybrid tensile specimens, for which two different heat treatment strategies were analyzed, are presented and discussed. The specimen following the HT1 strategy and the first manufacturing sequence pictured in Figure 7 show the most promising performance. Moreover, for each specimen micrographs show that failure is not occurring at the bonding region between the two tool steels used for the hybrid tool set-up.

REFERENCES

[1] Thomas J. Ward, Richard M. Kelly, Gary A. Jones, and James F. Heffron. The effects of nitrogen—liquid and gaseous—on aluminum extrusion productivity. *Journal of Metals*, 36(12):29–33, 1984.

[2] Ramona Hölker, Andreas Jäger, Nooman Ben Khalifa, and A. Erman Tekkaya. New concepts for cooling of extrusion dies manufactured by rapid tooling. volume 491, pages 223–232. Trans Tech Publ, 2012.

[3] Barbara Reggiani and Lorenzo Donati. Additive Manufacturing for Extrusion Dies. *Light Metal Age*, (76):10–17, 2018.

[4] Ramona Hölker, Andreas Jäger, Nooman Ben Khalifa, and A. Erman Tekkaya. Controlling heat balance in hot aluminum extrusion by additive manufactured extrusion dies with conformal cooling channels. *International Journal of Precision Engineering and Manufacturing*, 14(8):1487–1493, 2013.

[5] Eckhart Doege and Bernd-Arno Behrens. Massivumformung. In *Handbuch Umformtechnik: Grundlagen, Technologien, Maschinen*, pages 469–711. Springer Berlin Heidelberg, Berlin, Heidelberg, 2010.

[6] Martin Bauser, Guenter Sauer, and Klaus Siegert. *Strangpressen.* Aluminium-Verlag, Düsseldorf, 2001.

[7] Ramona Hölker, Matthias Haase, Nooman Ben Khalifa, and A. Erman Tekkaya. Hot extrusion dies with conformal cooling channels produced by additive manufacturing. *Materials Today: Proceedings*, 2(10):4838–4846, 2015.

[8] F. Pusavec, T. Lu, C. Courbon, J. Rech, U. Aljancic, J. Kopac, and I. S. Jawahir. Analysis of the influence of nitrogen phase and surface heat transfer coefficient on cryogenic machining performance. *Journal of Materials Processing Technology*, 233:19–28, July 2016.

[9] Tao Jin, Jian-ping Hong, Hao Zheng, Ke Tang, and Zhi-hua Gan. Measurement of boiling heat transfer coefficient in liquid nitrogen bath by inverse heat conduction method. *Journal of Zhejiang University-SCIENCE A*, 10(5):691–696, May 2009.

[10] Shane Y Hong and Yucheng Ding. Cooling approaches and cutting temperatures in cryogenic machining of Ti-6al-4v. *International Journal of Machine Tools and Manufacture*, 41(10):1417–1437, August 2001.

[11] Shane Y. Hong and Y. Ding. Micro-temperature manipulation in cryogenic machining of low carbon steel. *Journal of Materials Processing Technology*, 116(1):22–30, October 2001.

[12] Lorenzo Donati, Antonio Segatori, Barbara Reggiani, Luca Tomesani, and Pietro Alfredo Bevilacqua Fazzini. Effect of liquid nitrogen die cooling on extrusion process conditions. volume 491, pages 215–222. Trans Tech Publ, 2012.

[13] Enea Mainetti, Massimo Bertoletti, S. Wallfish, and A. Ferrentino. Significant Extrusion Speed Increase using Liquid Nitrogen to Eliminate Overheating of Dies During Extrusion Process. volume 1, pages 201–206, 2012.

[14] P. Stratton. Raising productivity of aluminium extrusion with nitrogen. *International Heat Treatment and Surface Engineering*, 2(3-4):105–108, 2008.

XIV International Conference on Computational Plasticity. Fundamentals and Applications
COMPLAS 2019
E. Oñate, D.R.J. Owen, D. Peric , M. Chiumenti, and Eduardo de Souza Neto (Eds)

PREDICTION OF UNSUPPORTED EXCAVATIONS BEHAVIOUR WITH MACHINE LEARNING TECHNIQUES

STEPHANE COMMEND[*], SACHA WATTEL[+], JEAN HENNEBERT[†], PIERRE KUONEN[†] AND LAURENT VULLIET[°]

* Institute of Construction and Environmental Technology - iTEC, HEIA-FR, HES-SO University of Applied Sciences and Arts Western Switzerland, Pérolles 80, CH-1700 Fribourg, Switzerland
Email: stephane.commend@hefr.ch - Web page: https://itec.heia-fr.ch

+ GeoMod ingénieurs conseils SA, Epinettes 32, CH-1007 Lausanne, Switzerland
Email : info@geomod.ch - Web page : http://www.geomod.ch

† Institute of Complex Systems - iCoSys, HEIA-FR, HES-SO University of Applied Sciences and Arts Western Switzerland, Pérolles 80, CH-1700 Fribourg, Switzerland
Emails: jean.hennebert@hefr.ch and pierre.kuonen@hefr.ch - Web page: https://www.icosys.ch

° Laboratory of Soil Mechanics, EPFL - ENAC - LMS, Station 18, CH-1015 Lausanne, Switzerland
Email : laurent.vulliet@epfl.ch - Web page : https://lms.epfl.ch

Key words: geotechnics, excavations, finite elements, neural networks, machine learning.

1 INTRODUCTION

Artificial intelligence and machine learning algorithms have known an increasing interest from the research community, triggering new applications and services in many domains. In geotechnical engineering, for instance, neural networks have been used to benefit from information gained at a given site in order to extract relevant constitutive soil information from field measurements [1]. The goal of this work is to use machine (supervised) learning techniques in order to predict the behaviour of a sheet pile wall excavation, minimizing a loss function that maps the input (excavation's depth, soil's characteristics, wall's stiffness) to a predicted output (wall's deflection, soil's settlement, wall's bending moment).

Neural networks are used to do this supervised learning. A neural network is composed of neurons which apply a mathematical function on their input (see Figure 1, left) and synapses which take the output of one neuron to the input of another one. For our purpose, neural networks can be understood as a set of nonlinear functions which can be fitted to data by changing their parameters. In this work, a simple class of neural networks, called Multi-Layer Perceptron (MLP) are used. They are composed of an input layer of neurons, an output layer, and one or several middle layers (hidden layers) (see Figure 1, right). A neural network learns by adjusting the weights and biases in order to minimize a certain loss function (for instance: the mean squared error) between the desired and the predicted output. Stochastic gradient descent or one of its variations are used to adjust the parameters and the gradients are obtained through backpropagation (an efficient application of the chain rule).

The interest in neural networks comes from the fact that they are universal function estimators, in the sense that they can approximate any continuous function to any precision given enough neurons. However, this can lead to over-fitting problems where the network learns the noise in the data, or worse, where they memorize by rote each sample [2].

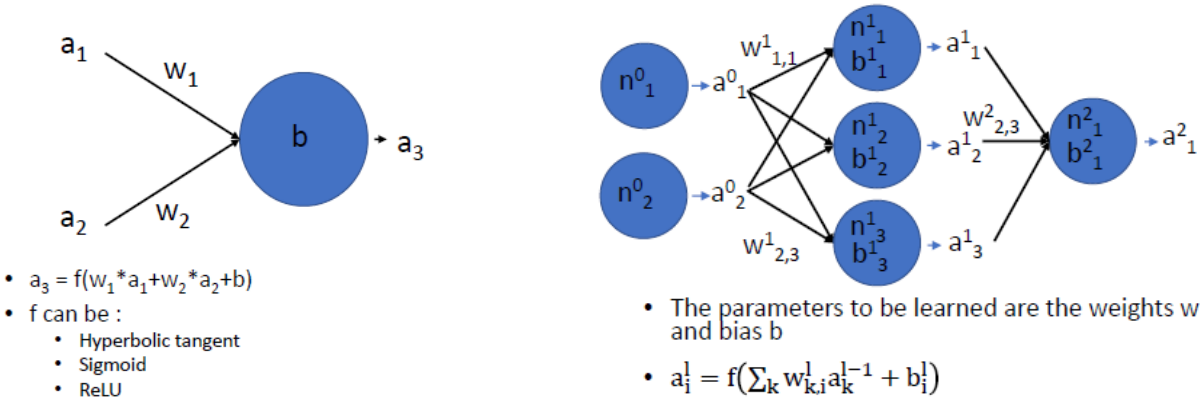


Figure 1: (left) Graph of a neuron with activation (a), bias (b) and weight (w) - (right) MLP graph

2 CREATION OF THE DATASET

For a neural network to learn, a dataset of excavations must first be compiled. The size of the dataset should be in hundreds or thousands of samples, and we do not have at hand such a large number of real excavation results. Thus, the dataset is obtained through numerical simulation using ZSWalls [3], a simple 2D deep excavation retaining wall analysis software based on the finite element method (FEM) program ZSOIL.

ZSOIL has been successfully used throughout the last three decades predicting the behaviour of large excavations in urban environments [4, 5].

In this first attempt to prove the feasibility of the method, the following simplifications have been taken into account: the support system is a free standing sheet pile wall (no anchors or struts), we only consider one soil, without water (unit weight = 20 kN/m^3, Poisson ratio and dilatancy angle are fixed), and the excavation width is proportional to its depth. The remaining meaningful variables (and their ranges, in brackets) are (see Figure 2 left):

- soil's parameters: loading E_{50} modulus [10 MPa; 100 MPa], friction angle phi [28°; 45°] and cohesion c [0 kPa; 10 kPa]. We use here the Hardening soil constitutive model with small strain extension [6], and assume $E_{ur} = 4 \times E_{50}$ and $E_0 = 10 \times E_{50}$
- excavation's depth H [2 m; 8 m]
- wall's length L [1.1; 3.0] x excavation's depth
- sheet pile's characteristics (defining its moment of inertia I): 20 samples from the Arcelor Mittal catalogue [7]. We assume $E_{steel} = 2 \times 10^8$ kN/m^2

From the background ZSOIL computation (Figure 2 right), the results extracted are: the wall's stability (with the hypothesis that a computation that does not converge means that the support system does not hold) and if convergence is obtained, the maximum settlement behind the wall, the maximum horizontal wall's displacement (or deflection) and the maximum bending moment in the sheet pile wall (Figure 3).

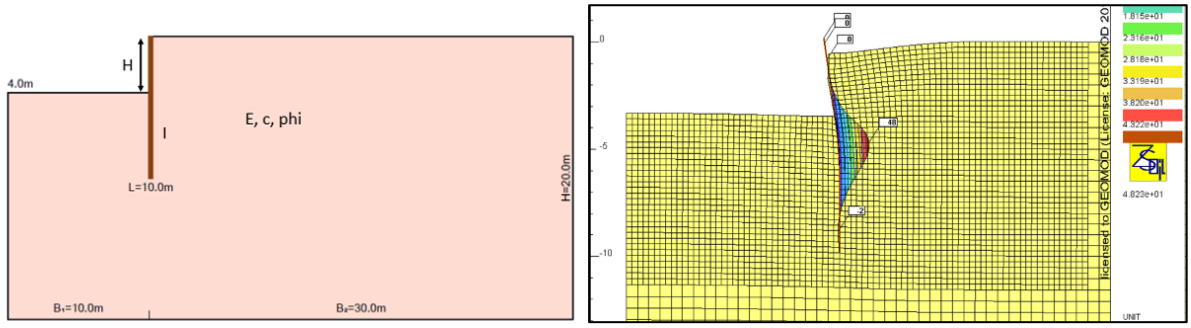


Figure 2: (left) ZSWalls input: definition of the excavation properties – (right) results of ZSOIL background calculation: bending moment and deformed mesh (x50)

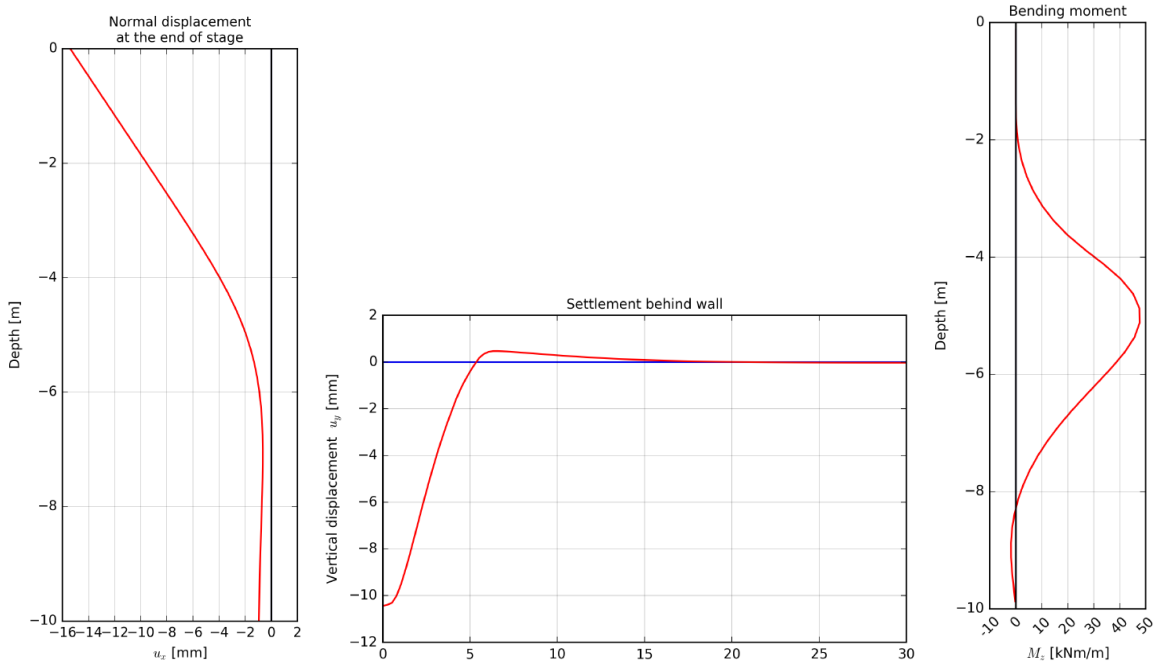


Figure 3: ZSWalls output: wall's deflection, soil's vertical settlement, wall's bending moment

3 ARCHITECTURE OF THE NEURAL NETWORK

The logical choice for the input of the neural network is the set of meaningful variables that defines the sample (soil's parameters, excavation's depth, wall's length and sheet pile's characteristics). Every other variable is either dependent on these ones - and this dependence is left to the neural network to learn, or should not influence the results. As for the output, it is simply the convergence status (yes/no), and three continuous outputs: the maximum settlement, the maximum horizontal wall displacement and the maximum bending moment in the sheet pile wall. Since the continuous outputs don't make sense if there is no convergence, the task should be separated in two: first a classification where the neural network predicts the convergence status, and then, if the convergence status is good, a regression can be done on the continuous variables.

All input values are scaled in order to have an expected value of 0 and a variance of 1. This, associated with the Glorot normal initialization of the weights, helped the network to learn faster. As for the output values, the convergence status is simply represented by a binary variable 0 or 1, and the continuous variables are linearly scaled between 0 and 1. This is necessary since a sigmoid activation function is used.

As mentioned before, a MLP neural network is built. The number of input and output neurons are defined by the number of inputs and output features. Thus, only the number of hidden layers and the number of neurons in each layer have to be decided. When the number of layers and neurons is augmented, the representational power of the network is also higher, but this comes with an increased number of parameters and a bigger risk of over-fitting.

The Tensorflow library for Python as well as the Keras API were used for all the experiments reported here.

4 RESULTS

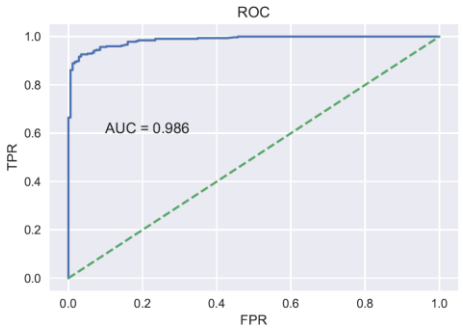
4.1 Classification

The complete dataset contains 5000 random samples, of which 37% did not converge.

The first task to accomplish is to predict whether the excavation is stable, i.e. evaluate the convergence of the FEM model. The architecture used is a simple MLP with one hidden layer of 10 neurons and a sigmoid activation function. No regularization technique is used. The output of the network is a real number between 0 and 1. An output close to 0 means a non-convergence prediction, and the opposite if the output is close 1. While there is a class unbalance, it did not create difficulties in the learning convergence. However, it reduces the meaning of accuracy (percentage of correct predictions) as 63% could be achieved with a network that only predicts convergence.

A preferred measure of the quality of prediction is the Positive Predicted Value (PPV) and the Negative Predicted Value (NPV) which corresponds to the ratio between correct predicted positive (resp. negative) over total predicted positive (resp. negative). Since, in civil engineering, false positives should be most avoided, it is possible to set the cut-off point higher to reduce them, at the cost of an overall decrease of accuracy.

The Receiver Operator Curve (ROC, see Figure 4, left) plots the False Positive Rate (FPR: fraction of negatives classified incorrectly) against the True Positive Rate (TPR: fraction of positives classified correctly). It is useful to show the tradeoff between correctly classifying positives and negatives cases when changing the cut-off point (see Figure 4, right). The Area Under the Curve (AUC) should be the closest possible to 1. It can be interpreted as the probability of correctly classifying a random positive case higher than a random negative case.



Cut-off	PPV	NPV
-	%	%
0.5	94.5	90.3
0.9	98.7	77.7
0.95	99.2	72.4
0.99	100	64.2

Figure 4: Receiver Operator Curve (ROC) and effect of cut-off point on PPV and NPV

4.3 Regression

The regression models were trained on the converged subset of the dataset (3141 samples), with 20% reserved for testing. Several models of increasing complexity were trained and evaluated: "10", with one hidden layer of 10 neurons, "30", with one hidden layer of 30 neurons, and finally "30red" or "30-20-10", with three hidden layers of neurons, containing respectively 30, 20 and 10 neurons.

As stated before, a more complex system has more representational power, as it can learn more complex functions. However, it becomes prone to over-fitting and care should be taken when training and evaluating the network. In this work, to avoid over-fitting, training was stopped when validation performance started to degrade.

As can be seen in Table 2, the performance of the model increases with its complexity: results are given for the different models with the coefficient of determination (R2), mean absolute error (MAE), mean relative error (MRE), 95 percentile of the relative error (RE95), mean relative error truncated (MRE_tr) and 95 percentile of the relative error truncated (RE95_tr). Note that truncation has been applied when absolute errors are below 2 mm (maximal settlement or wall's displacement) or 5 kNm/m' (maximal bending moment).

Table 2: Prediction results for the different models in terms of errors

	Model	R^2	MAE [m]	MRE	RE95	MRE_tr	RE95_tr
Settlement	10	0.983	1.7E-03	1.52	8.21	0.08	0.21
	30	0.988	1.3E-03	1.07	5.90	0.06	0.15
	30-20-10	0.989	1.4E-03	1.40	7.00	0.05	0.12
	Model	**R^2**	**MAE [m]**	**MRE**	**RE95**	**MRE_tr**	**RE95_tr**
Wall deviation	10	0.982	1.3E-03	0.22	0.88	0.04	0.17
	30	0.991	1.1E-03	0.16	0.54	0.02	0.14
	30-20-10	0.991	9.8E-04	0.12	0.37	0.02	0.11
	Model	**R^2**	**MAE [kN]**	**MRE**	**RE95**	**MRE_tr**	**RE95_tr**
Moment	10	0.995	2.7	0.13	0.34	0.02	0.10
	30	0.995	2.6	0.13	0.30	0.01	0.08
	30-20-10	0.994	2.7	0.12	0.30	0.01	0.08

Figure 5 shows the behaviour of the three different models: the predicted values for settlement, deflection and bending moment given by the neural network are compared to the "correct" computed values.

It can be noticed that there is a tendency to predict lower values. This probably comes from the choice of the relative error as a criterion for model selection: smaller predictions are bounded by 100% whereas bigger predictions are unbounded.

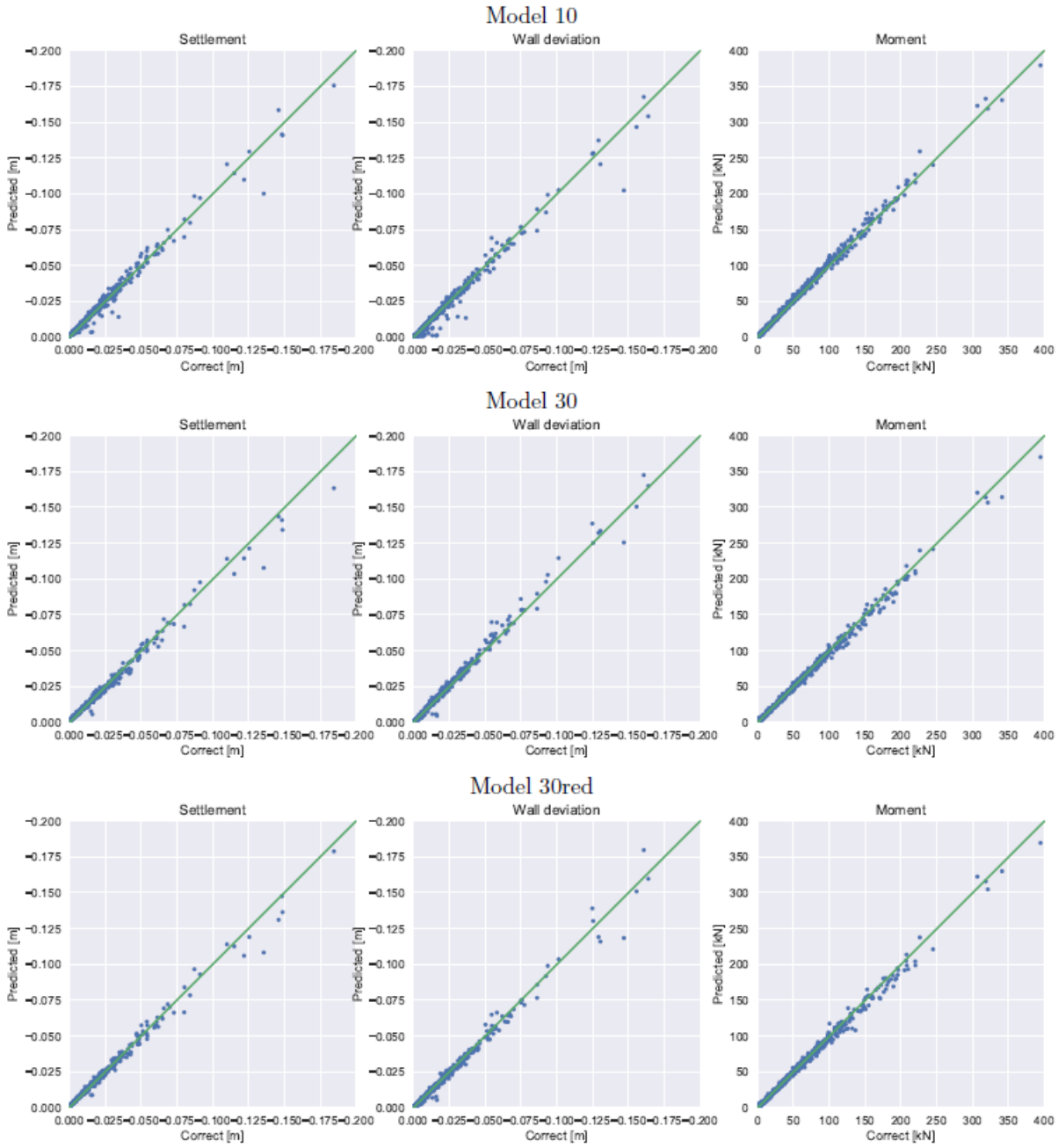


Figure 5: Predicted against computed soil's settlement, wall's horizontal displacement and bending moment

5 CONCLUSIONS

The resulting model can predict accurately if an unsupported excavation is stable. Soil's settlement, wall deflection and maximum bending moment in the sheet pile wall can also be predicted with small relative errors (less than 5%).

In future work, we would like to generalize this approach to real-life cases, building a tool capable of predicting the behaviour of an excavation support (slurry or sheet pile wall, with anchors or struts) for a given set of data (stratigraphy, groundwater table, excavation's depth), without calculating it with conventional engineering software (finite element method), but rather using an existing dataset.

Once this tool will be functional, it could also be used in order to find an optimal excavation design in terms of costs or planning, under constraints (maximal acceptable horizontal displacement for instance).

REFERENCES

[1] Hashash Y., Marulanda C., Ghaboussi J. & Jung S. *Novel Approach to Integration of Numerical Modeling and Field Observations for Deep Excavations*. Journal of Geotechnical and Geoenvironmental Engineering. 132 (2006)

[2] Cybenko G., *Approximation by superpositions of a sigmoidal function*. Mathematics of Control, Signals and Systems 2, 303-314 (1989)

[3] *ZSWalls: a standalone module of ZSoil.PC 2D for deep excavations and retaining walls*, *user guide*. ZACE Services Ltd. (2018)

[4] Commend S., Geiser F., Crisinel J. *Numerical simulation of earthworks for a large excavation*. Advances in Engineering Software 35, 669-678 (2004)

[5] Obrzud R. & Preisig M. *Large scale 3D numerical simulations of deep excavations in urban areas - constitutive aspects and optimization*. Publication de la Géotechnique Suisse 167 (2013)

[6] Obrzud R. & Truty A. *The hardening soil model – a practical guidebook*. Zace Services Ltd. (2013)

[7] *Palplanches, catalogue général*. Arcelor Mittal. (2013)

TEMPORAL CHARACTERIZATION OF ROCK DYNAMIC DESTRUCTION

A.N. Martemyanov*†, Yu.V. Petrov†‡

† Elasticity Department of Mathematics & Mechanics Faculty
Saint-Petersburg State University
Universitetsky pr., 28, Stary Peterhof, 198504 Russia
e-mail*: st021087@student.spbu.ru,
web page: http://www.math.spbu.ru/en/

‡ Research Institute for Mechanics,
National Research Lobachevsky State University of Nizhni Novgorod,
Gagarina str., 23-6 Nijnii Novgorod, 603600, Russia
e-mail: y.v.petrov@spbu.ru

Keywords: structural-time approach, incubation time, dynamic strength, split Hopkinson pressure bar, spalling, rock material.

Abstract. Dynamic strength tests published in literature have been analysed by structural-temporal damage criteria. Parameter τ - incubation time - describing material stability behaviour under high-rate influences have been estimated for Kimachi sandstone, Inada granite and Tage tuff. Two types of dynamic tensile experiments have been used: split Hopkinson pressure bar and spalling. Purely dynamic effect of fracture delay have been observed in the case of Kimachi sandstone and discussed.

1 INTRODUCTION

Nowadays geoscience and mining industry problems require consideration of new physical effects for accurate modelling of flowing processes. Area of rock formation stability problems includes both long-lasting quasistatic processes and rapid influences. Last ones are related with effect of dynamic strength.

It was empirically observed that material under dynamic impulses is able to withstand stresses much bigger than its static strength in both compression and tension. Moreover increasing of loading rate leads to rising of maximum stress went through material at the moment of rupture. Such behaviour was named "dynamic strength effect".

In surrounding world this effect may occur when elastic waves produced by earthquake or charge detonation propagate across rock medium. If characteristics of wave enough to cause destruction than change of material state behind the front should be expected. Another example of dynamic rock strength is fracturing near free surfaces inside tunnels and mines due to spalling.

In laboratory conditions there are several techniques how to measure dynamic strength of rocks under different strain rates [1]. Servo-controlled and pneumatic machines are used to make measurement in relatively small speed range. For higher rates drop-weight machine or modified split Hopkinson pressure bar method are applicable. Extremely big velocities (up to 10^6 s^{-1}) are reached by spall or plane shock wave technique approach.

This work is dedicated to analysis of dynamic destruction tests published in [2, 3] of three types of rocks: Kimachi sandstone, Inada granite and Tage tuff. First material was investigated by two different methods - SHPB and spalling - to obtain dynamic tensile strength. Structural-temporal approach [4, 5, 6] have been chosen as damage criteria. According it every medium is characterized by additional material parameter - incubation time, describing its strength properties under dynamic conditions. Basing on experimental results range of incubation time variation for each rock type have been estimated. Curios dynamic effect of fracture delay when

destruction occurs after phase of stress increasing in rupture plane is discussed.

2 LABORATORY STUDY OF DYNAMIC STRENGTH

Several experimental techniques are used to measure the dynamic strength of materials at present. The most popular is modified split Hopkinson pressure bar (SHPB) allowing to produce loading strain rates up to 10^4 s^{-1}. To get higher rates method of spall is required. A brief overview will be given here, for comprehensive description look [1, 7, 8].

2.1 Split Hopkinson pressure bar

Application of given technique extends classic compression and tensile strength tests to dynamic case. Sample of studying material is put between two metal bars (as demonstrated on fig.1) which dynamic and static mechanical properties well known. Stress impulse produced by striker inside incident bar propagates to bar-sample interface where partially reflects and partially passes through the test material into transmitted bar. Deformations of bars record by strain gauges and easily convert to stresses from both sides of sample. Typical curves of incident, reflected and transmitted signals have shown on fig.2(a).

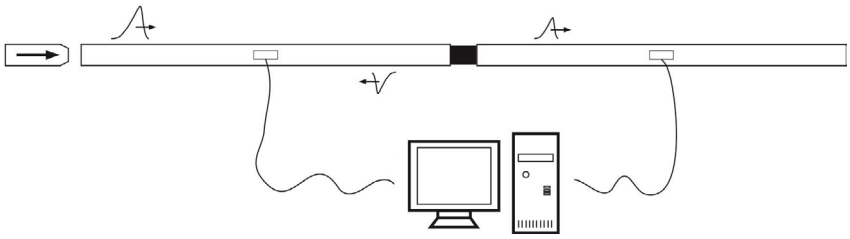
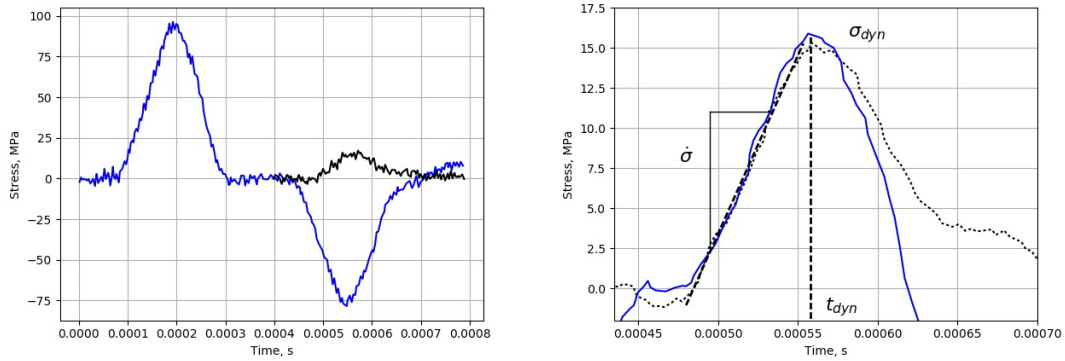


Figure 1: Scheme of split Hopkinson bar installation

Important part of experiment is to reach balance between different sides of sample (see fig.2(b)). If given condition is satisfied then the stress variation along investigated material can be neglected and quasistatic formulas may be used for measurement interpretation.



(a) Signals from incident and transmitted bars

(b) Stress balance

Figure 2: Stress curves obtained through experiment from [3]

In the cases of direct compression or tension test analysis of the loading history allows to determine: dynamic strength as a peak value reached through loading process, fracture time corresponding dynamic strength and stress rate as a slope of the tangent to the graph of the

stress history. For indirect measurements stress curves from bars should be converted previously to internal stress at estimated point of destruction. In the case of Brazilian disc method such point corresponds to disc center, tensile stress σ_t here depends on external load σ by formula

$$\sigma_t(t) = \frac{2 \cdot \pi R^2}{\pi L D} \cdot \sigma(t) \tag{1}$$

where D - diameter of sample, L - its thickness and R is radius of metal bar. Easy to see that maximum tensile stress in the middle of disc will be calculated from peak value of external loading.

2.2 Spalling

Effect of spall appears when elastic wave propagates near the free boundary of material: compression wave reflects as tension wave and causes occurrence of cracks inside body. Although wave analysis can be quite complex laboratory conditions allow to consider one-dimensional problem.

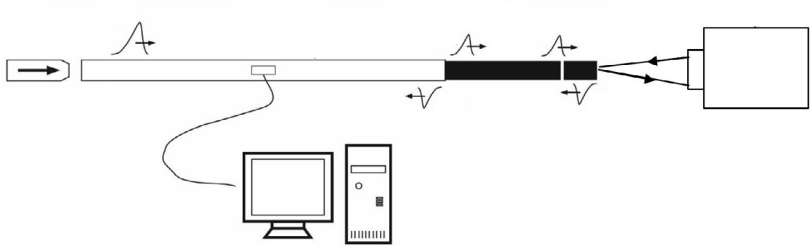
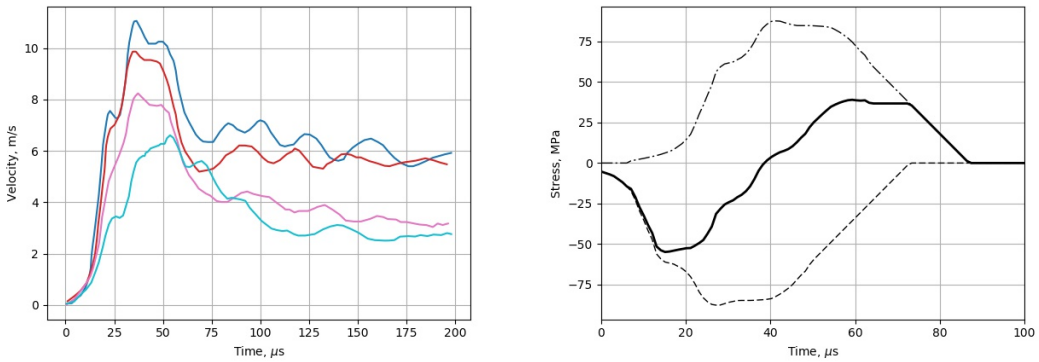


Figure 3: Scheme of spall experiment

For classical spall test extended cylindrical sample uses. Laboratory installation schematically shown on fig.3. Striker produces a stress impulse which propagates toward free end through studying material. Because of all materials significantly stronger in compression then tension damage arises when reflected impulse becomes dominant. Velocity of sample free end $U(t)$ is registered by laser interferometry (fig.4(a)).



(a) Free surface velocity profiles from [2] (b) Stress history at some distance from free surface

Figure 4: Data from spall experiments

According to classical approach it "copies" acting compression stress profile $\sigma(t)$ and following formula is valid:

$$\sigma(t) = -\frac{1}{2}\rho c \cdot U(t). \tag{2}$$

The place and time of fracture appearing may be fixed independently. Stress history reconstruction (fig.4(b)) in crack plane may be done using (2):

$$\sigma(x,t) = \sigma(t - x/c) - \sigma(t + x/c) = \frac{1}{2}\rho c \cdot \Big(U(t - x/c) - U(t + x/c)\Big) \tag{3}$$

here t is measured from the moment when stress impulse first came to free boundary, x - distance from free boundary. Obtained stress curve can be analyzed like in previous case of SHPB.

3 STRUCTURAL-TEMPORAL DAMAGE CRITERIA

Fracture formation in rocks, which lead to a partial or complete loss of material bearing capacity, occurs due to accumulation of damages at the micro level, fused with each other. Processes of growth and coalescence of micro destructions require some time to reach macro effect. By its nature ones close to relaxation process and may be characterized by temporal parameter reflecting the tendency of material to develop microdefects.

In Yu.V. Petrov and N.F. Morozov works have been introduced the notion of incubation time of material and proposed structural-temporal damage criteria based on this parameter. This concept has been successfully used for describing of dynamic strength phenomenon. Let $\sigma(x,t)$ be the stress function in point x inside elastic body subjected external loading. According incubation time criteria rupture of material in x at moment t will observe when following condition satisfied:

$$\frac{1}{\tau}\int\limits_{t-\tau}^{t}\frac{1}{d}\int\limits_{x-d}^{x}\left(\frac{\sigma(y,s)}{\sigma_{st}}\right)^{\alpha} dyds \geqslant 1. \tag{4}$$

Where τ - incubation time of material, d - length parameter describing scale level and $\sigma_s t$ is static strength of material. Parameter α is dimensionless and characterizes reaction of medium on external stress impulse amplitude.

If external influence changes slowly enough, i.e. $\sigma \approx const$, then condition (4) reduces to well-known quasistatic one. At the same moment with rising strain rates time to fracture decreases to τ and even less. Pursuant to relation (4) amplitude of stress acting at given point should grow to cause damage as it is observed in experiments. So it may be said that incubation time controls strength behavior of material under dynamic conditions.

Analysis of experimental results to estimate incubation time of material requires a detailed reconstruction of elastic wave propagation through the sample. For stress impulses close to model, i.e. triangular or trapezoidal, theoretical relation based on condition (4) between dynamic strength σ_{dyn} observed in experiment and external impulse stress or strain rate ($\dot{\sigma}$ or $\dot{\varepsilon}$) (see [9, 10]). This curve depends on value of incubation time τ as on parameter and may be used to define parameter τ from comparison with measured data.

Samples for laboratory investigations are always limited in sizes. Most of them have dimensions from units to tens centimeters. All measured for such samples parameters should be related with this scale level.

Concept of structural-temporal damage criteria based on incubation time has been successfully applied to rock dynamic destruction problem understanding [11, 12].

4 INCUBATION TIME OF ROCKS

4.1 SHPB tests analysis

Brazilian method have been used to obtain tensile strength of three rocks in [3]. Laboratory setting consists of incident bar 2600 m in length and 1600 m transmitted bar. They diameters

equal 37 mm. Incident stress impulse was produced by striker with length 200 mm and diameter 27 mm. Its approximate velocity was 7 m/s. Pulse shaper have been used to reach stress balance.

Tests samples have been made in the form of disc with diameter 50 mm and thickness $24 - 26$ mm. Mechanical properties of studying materials collected in table 1.

Table 1: Mechanical properties of rocks

Rock type	Density, g/cm^3	Compression, velocity, m/s	Young mod., GPa	St. tensile str., MPa	Total porosity
Kimachi sandstone	2.00	2710	6.5	4.82	17%
Inada granite	2.58	3950	56.8	7.3	0.5%
Tage tuff	1.76	2380	4.5	2.29	29%

For our work signal records from setting bars have been used. Incident and reflected impulses have been summed to get acting stress from the left side of the sample. After comparison with transmitted signal peak stress σ_p, corresponding time t_* and stress rate $\dot{\sigma}$ have been found for every dynamic test as was described in section 2. Then value of dynamic tensile strength σ^t_{dyn} have been calculated using peak stress and equation (1). Figures 2(a) and 2(b) demonstrate this procedure for Kimachi sandstone sample with number SB-1.

Series of high-rate measurements supplemented by static strength have been analysed to estimate incubation time for each rock type. Stress acting inside sample during experiment may well approximate by line function: $\sigma(t) \approx const \cdot t$. Such relation united with incubation time criteria (4) allows to obtain theoretical dependence of dynamic strength σ^t_{dyn} from stress rate $\dot{\sigma}$ [5]. Last one have been matched with experimental points to get value of τ.

Table 2: Interpretation of rock dynamic experiments

Rock type	Sample number	t_*, μs	$\dot{\sigma}$, GPa/s	σ_p, MPa	σ^t_{dyn}, MPa	τ, μs
Kimachi sandstone	SB-1	85	108	16.7	9.2	91
	SB-2	88	125	20.2	11.1	
Inada granite	GB-1	76	340	47.2	25.8	107
	GB-2	64	282	32.6	17.9	
Tage tuff	TB-1	94	81	13.9	7.6	150
	TB-2	93	74	12.6	6.9	

Theoretical curves based on structural-temporal approach (see fig. 5) approximate dynamic test results with accuracy 0.6 MPa for Kimachi sandstone, 3 MPa for Inada granite and 0.2 MPa for Tage tuff.

4.2 Spall tests analysis

Kimachi sandstone. Spall test is different from previous case where whole sample is always destroyed after experiment. Due to extended size of sample for spalling fracture plane may occur in various point along the length of the rod depending on produced wave parameters. Sometimes several consecutive cracks are formed dividing the original sample into fragments. So fracture position is additional experiment parameter which should be taken into account for correct results interpretation.

Main data measured in spall test is free surface velocity (see fig. 4(a)) which helps to reconstruct stress impulse produced in experiment and to get some additional information. Whole curve may

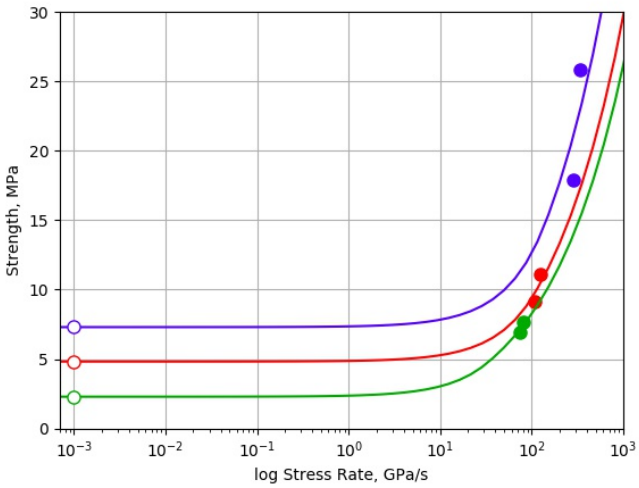


Figure 5: Incubation time curve and experimental data for: Kimachi sanstone (red), Inada granite (blue), Tage tuff(green)

be divided into two parts: trapezoid-like before fracture and oscillations after [7, 8]. First one uses to calculate stress history during experiment and last one to specify the time of destruction. Because of fracture occurred some impulse turns out to be locked in breakaway fragment and circulates between two surfaces which causes oscillations. Its period uses to estimate fracture time.

Author of [2] made several spall tests with Kimachi sandstone samples 60 mm in diameter and 300 mm in length using underwater shock waves. For every type of loading parameters typical free surface velocity and variation of fracture position have been measured. This data together with incubation time criterion is analysed in present work to estimate parameters of dynamic destruction of given rock.

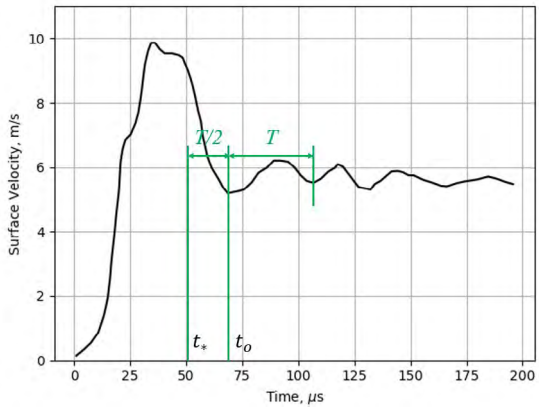
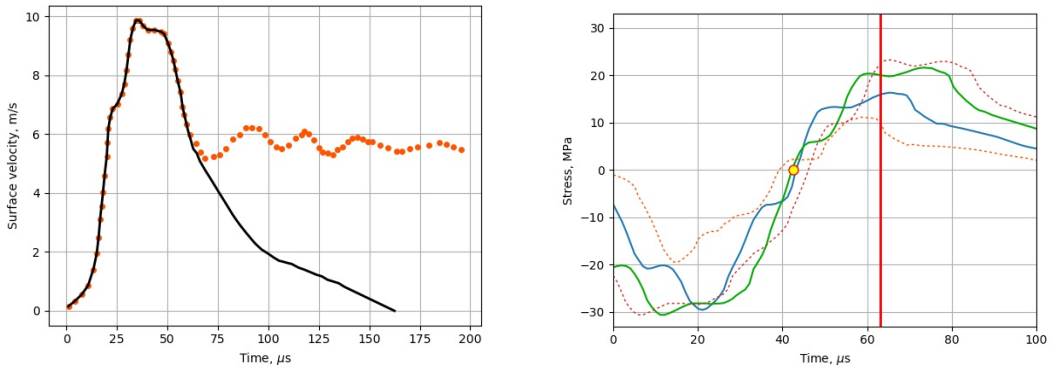


Figure 6: Example of temporal characteristics estimation from test results

Table 3: Spall fracture parameters

Charge lenght	t_o, μs	T, μs	t_*, μs	x, cm
50	72.8	19.3	63.2	4-6.5
70	68.7	38.1	49.6	4.5-6
100	81.5	37.5	62.8	5-8
200	119.6	39.6	99.8	9-11

First minimal value on surface velocity after rapid drop reflects fracture initiation and fact that wave produced in that process has reached free border. Corresponding time is marked for t_o. Then this wave goes through sample fragment from free surface to fracture and back that causes fluctuations in the velocity of the free surface. Period of such oscillations T is equal to double time of wave propagation from fracture to surface. Values of t_o and T are used to get moment t_* when spall fracture occurs. Obtained temporal parameters accompanied with fracture location data from [2] for different loading conditions are contained it the table 3.



(a) Surface velocity profile reconstruction

(b) Stress history at different cross sections

Figure 7: Stress analysis of spall experimental data

To determine magnitude and rate characteristics of stress acting in fracture plane recorded curve should be corrected. In considered case initial impulse continues with a "tail" as on fig. 7(a). Stress curve have been calculated by (2). Negative sign corresponds to compression.

Comparison of stress histories for different cross sections with fracture data shown on fig. 7(b). Case of 50 mm charge length is presented here. Blue and green solid curves describe stress behaviour in sections 4 and 6.5 cm from free end correspondingly, yellow point marks the occurrence of extension, red vertical line is fracture time indicator. Dotted orange and purple lines show stresses in sections 2 and 8 cm. According to experimental results crack arises at any point of the interval $4 - 6.5$ cm equally likely, and stress calculation demonstrates that destruction has come after intensive stress raising when load kept almost constant.

Fig. 7(b) demonstrates the difference in stress histories along laboratory sample: tensile forces arise earlier near the free end, but their magnitude as bigger as they are farther from the edge until it reach the amplitude of the shock pulse. It is also curious that, according to the calculations, destruction in this case occurs after the phase of stress growth when the load in fracture plane is kept at approximately the same level. Such effect is inconsistent with quasistatic representations of failure at a given stress threshold and requires analysis using the dynamic strength criterion.

According to structural temporal approach effect of fracture delay may be considered if amplitude of trapezoid load impulse quite close to value of limiting stress that material is able to withstand at given dynamic conditions. Easy to see that increasing of loading amplitude with constant stress rate will cause the shift of crack plane toward free surface. It follows from relation (4) that signal close to limit value will lead to the situation when integral corresponding some cross section will accumulate due to the stress "shelf". This effect can be measured accurately if every dynamic destruction test will be accompanied by independent fracture location and time measurements.

Because of uncertainty in rupture plane it is not possible to specify the exact value of the incubation time for Kimachi sandstone. Variation of parameter τ in (4) have shown that any value from $55 - 70$ μs can be taken as given material characteristic. Static strength was assumed to be 3.7 MPa according to [2].

5 CONCLUSIONS

Dynamic rock stability behaviour may be successfully described by structural-temporal approach based on incubation time notion. Last one is effective tool for assessing material strength under

high-speed loads.

Incubation time τ for three types of rock have been obtained using SHPB experiment results. These values are 91 μs for Kimachi sandstone, 107 μs for Inada granite and 150 μs for Tage tuff.

Spall test analysis have shown interesting dynamic effect of fracture delay. Experimental observation of given effect is related with accurate analysis of destruction time and stress curve acting in crack cross section. Temporal characteristic τ obtained through spall tests for Kimachi sandstone is less than obtained previously. It may be caused by different stone properties as indicated by static strength.

ACKNOWLEDGEMENTS

The work is supported by the Ministry of Education and Science of the Russian Federation within the FTP for Research and Development for 2014–2020 under the contract No. 14.578.21.0246 (RFMEFI57817X0246).

REFERENCES

[1] Zhang, Q.B. and Zhao, J. A Review of Dynamic Experimental Techniques and Mechanical Behaviour of Rock Materials. *J. Rock Mech Rock Eng.* (2014) **47**:1411–1478.

[2] Kubota, Sh., Ogata, Y., Wada, Y., Simangunsong, G., Shimad, H., Matsui, K. Estimation of dynamic tensile strength of sandstone. *Int J. Rock Mech Min Sci* (2008) **45**:397–406.

[3] Yang, J.H., Ahn, J.L., Kim, S.K., Song, Y.S., Sung, N.H., Lee, Y.K., Cho, S.H. Estimation of Dynamic Brazilian Tensile Strengths of Rocks Using Split Hopkinson Pressure Bar (SHPB) System. *J. Kor Soc Rock Mech* (2011) **21**(2):109–116.

[4] Petrov Yu.V., Utkin A.A. Dependence of the dynamic strength on loading rate. *Mater Sci.* (1989) **25(2)**:153–156.

[5] Petrov, Yu.V. Incubation time criterion and the pulsed strength of continua: fracture, cavitation, and electrical breakdown. *Dokl. Phys.* (2004) **49**:246–249.

[6] Petrov, Yu.V. and Morozov, N.F. On the modeling of fracture of brittle solids. *J. Appl. Mech.* (1994) **61**:710–712.

[7] Volkov, G.A., Petrov, Yu.V., Utkin, A.A. On Some Principal Features of Data Processing of Spall Fracture Tests. *Physics of the Solid State* (2017) **59**(2):310–315.

[8] Mikhailova, N.V., Volkov, G.A., Meshcheryakov, Yu.I., Petrov, Yu.V., Utkin, A.A. Failure-Delay Effect in Destruction of Steel Samples under Spalling Conditions. *Technical Physics* (2017) **62**(4):547–552.

[9] Smirnov, V.I., Petrov, Yu.V. Effect of Pulse Shape On Spall Strength. *J. App Mech Tech Phys* (2018) **59**(2):303–309.

[10] Petrov, Yu.V., Utkin, A.A. Structural-temporal approach and geometry of the fracture zone in spalling. *Procedia Structural Integrity* (2017) **6**:134–139.

[11] Martemyanov, A.N., Selyutina, N.S., Katorina, A.I. Incubation time criterion analysis of rock materials under dynamic loadings. *Procedia Structural Integrity* (2017) **6**:336–343.

[12] Martemyanov, A.N., Petrov, Yu.V. Understanding of Rock Material Behavior Under Dynamic Loadings Based on Incubation Time Criteria Approach. *PMMEEP 2017, SPRINGERGEOL* (2018) P. 233–248.

THERMO-HYDRO-MECHANICAL SIMULATION OF A FULL-SCALE STEEL-LINED MICRO-TUNNEL EXCAVATED IN THE CALLOVO-OXFORDIAN CLAYSTONE

TOURCHI, S.*, VAUNAT, J.* GENS, A.*, VU, M.N†, BUMBIELER, F†

*Department of Geotechnical Engineering and Geosciences
Universidad Politècnica de Catalunya (UPC)
Campus Norte UPC, 08034 Barcelona, Spain
e-mail: saeed.tourchi@upc.edu

† National Radioactive Waste Management Agency (Andra),
1 rue Jean Monnet, 92290 Châtenay-Malabry

Keywords: in situ testing; numerical modelling; radioactive waste disposal; temperature effects.

Abstract. The paper presents an interpretation of the full-scale ALC1604 in situ heating test carried out in Callovo-Oxfordian claystone (COx) in the Meuse/Haute-Marne underground research laboratory (MHM URL). The MHM URL is a site-specific facility planned to study radioactive waste disposal in the COx. The thermo-hydro-mechanical (THM) behaviour of the host rock is significant for the design of the underground radioactive waste disposal facility and for its long-term safety. When subjected to thermal loading, the Callovo-Oxfordian claystone of low permeability (~10^{-20}-10^{-21} m^2) exhibits a strong pore pressure response that significantly affects the hydraulic and mechanical behaviour of the material. The observations gathered in the in situ test have provided an opportunity to examine the integrated thermo-hydro-mechanical (THM) response of this sedimentary clay. Coupled THM numerical analyses have been carried out to provide a structured framework for interpretation, and to enhance understanding of THM behaviour of COx. Numerical analyses have been based on a coupled theoretical formulation that incorporates a constitutive law specially developed for this type of material. The law includes a number of features that are relevant for a satisfactory description of the hydromechanical behaviour. By performing the numerical analysis, it has been possible to incorporate anisotropy of material parameters and of in situ stresses. The performance and analysis of the in situ tests have significantly enhanced the understanding of a complex THM problem and have proved the capability of the numerical formulation to provide adequate predictive capacity.

1 INTRODUCTION

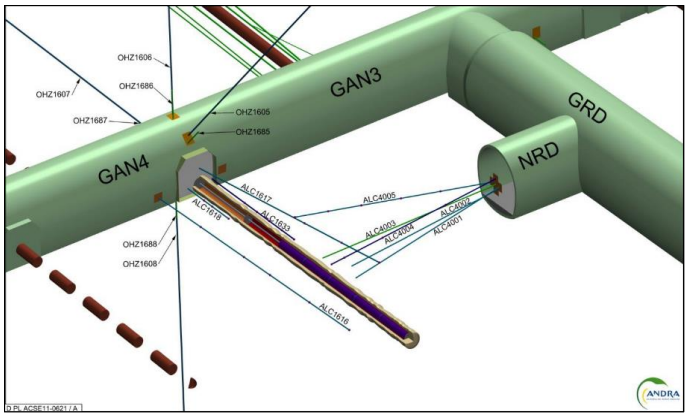
Argillaceous rocks provide the geological background to many civil engineering projects. They exhibit favourable characteristics, such as low permeability, a degree of self-healing capacity when fractured, significant retardation properties for solute transport, and no foreseeable economic value (Gens 2003). This paper concentrates on the response of Callovo-Oxfordian claystone (COx) to thermal loading in the context of the ALC1604 in situ heating test performed in the Meuse/Haute-Marne underground research laboratory. Special attention

is given to the interplay between the thermal, hydraulic and mechanical aspects of the COx behaviour. Callovo-Oxfordian claystone exhibits a strongly bedded structure that results in a distinct anisotropy of several thermo-hydro-mechanical (THM) properties. The observations are interpreted using a coupled THM analysis that accounts for the main features of the generalised COx behaviour, including its anisotropy.

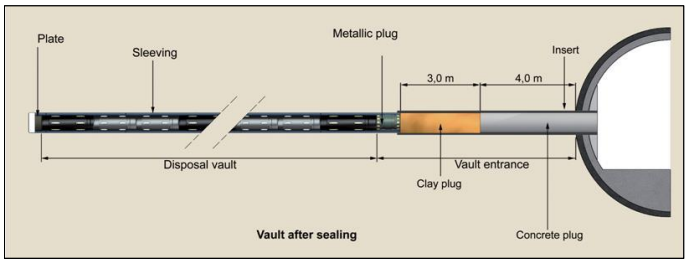
2 APPLICATION TO HA-ALC1604 IN SITU HEATING TEST

The ALC1604 experiment is an in situ heating test performed in the MHM URL where the host rock is Callovo-Oxfordian claystone. It aims to test the 2009 emplacement concept for vitrified HLW in dead-end, horizontal micro-tunnel with an excavated (drilled) diameter of approximately 0.7m and a steel casing (Armand et al. 2017). The micro-tunnel is composed of a body section for package disposal and a head section for cell closure, also called insert. They are favourably aligned with respect to the stress field (Figure 1a).

To prevent rock deformation and enable potential retrieval of waste containers during the reversibility period, both cell body and cell head sections have a non-alloy steel casing (Bumbieler et al. 2015). The diameter of the casing in the body is slightly smaller than that in the insert (Figure 1b). shows the concept of the experiment, with the 25m long micro-tunnel and surrounding boreholes for THM measurements. The excavation rate was around 0.3-0.5 mh^{-1} and the excavation was completed in seven days. The power applied in the deepest 15m was constant and equal to 220 W/m, in order to reach around 85 ºC in two years and continues up to the present.



(a)



(b)

Figure 1: a) 3D view of the demonstration test of HLW cells b) 2009 concept of HLW disposal cell (Armand et al. 2017).

3 MAIN FEATURES OF THE NUMERICAL MODEL

The coupled THM formulation employed herein for the solution of the analysed boundary value problem is a particular case of the general formulation presented in Olivella et al. (1996). It is completed by a special mechanical constitutive law adopted for the description of the stress/strain behaviour of the Callovo-Oxfordian claystone (see Mánica et al. 2016 for more details). The model, developed within the framework of elastoplasticity, includes a number of features that are relevant for a satisfactory description of their hydromechanical behaviour: anisotropy of strength and stiffness, behaviour nonlinearity and occurrence of plastic strains prior to peak strength, significant softening after the peak, time-dependent creep deformations and permeability increase due to damage. Both saturated and unsaturated conditions are handled.

The mesh and main boundary conditions (B.C.) are illustrated in Figure 2a. The model includes the geometry of the steel casings, the gap formed between the casings and the COx, and the host rock domain (**Figure 2**b). For computational purposes, the gap will be dealt with as a continuum provided with the bi-linear elasticity model to represent gap opening and closure. According to the experiment arrangement, the casing is supported at the bottom of the excavation and is thus eccentric with respect to the centreline of the micro-tunnel (Figure 2b).

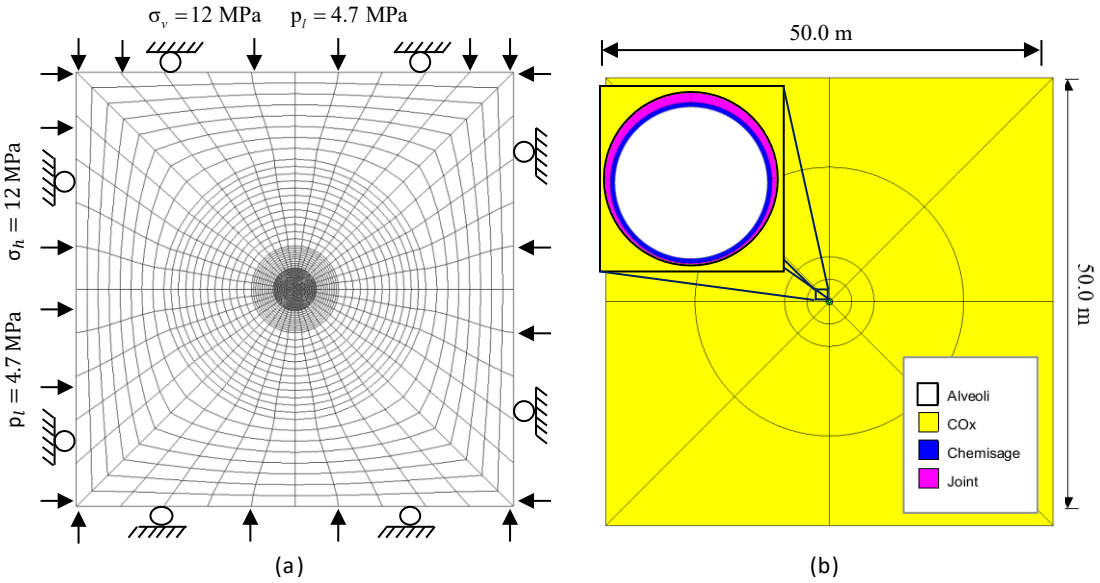


Figure 2: a) Finite element mesh, main boundary conditions b) Geometry and materials.

4 THERMAL RESULTS

Purely thermal analysis has been performed to back-analyse the value of thermal conductivity that achieves the closest agreement between computed and measured temperatures. The observed evolution of temperatures at the three sensors located in section *a* (depth of 17.5 m, see Figure 3b) are shown in Figure 3a together with the computed results from the 2D and 3D analysis. Along this section, located at mid-length, that is in the symmetry plane of the heater, results of both 3D and 2D analyses are close to the measurements for all the three sensors, whatever is their orientation (parallel or perpendicular) with respect to bedding

plane. Maximum temperatures reach values just above 56°C after 1200 days of the heating stage.

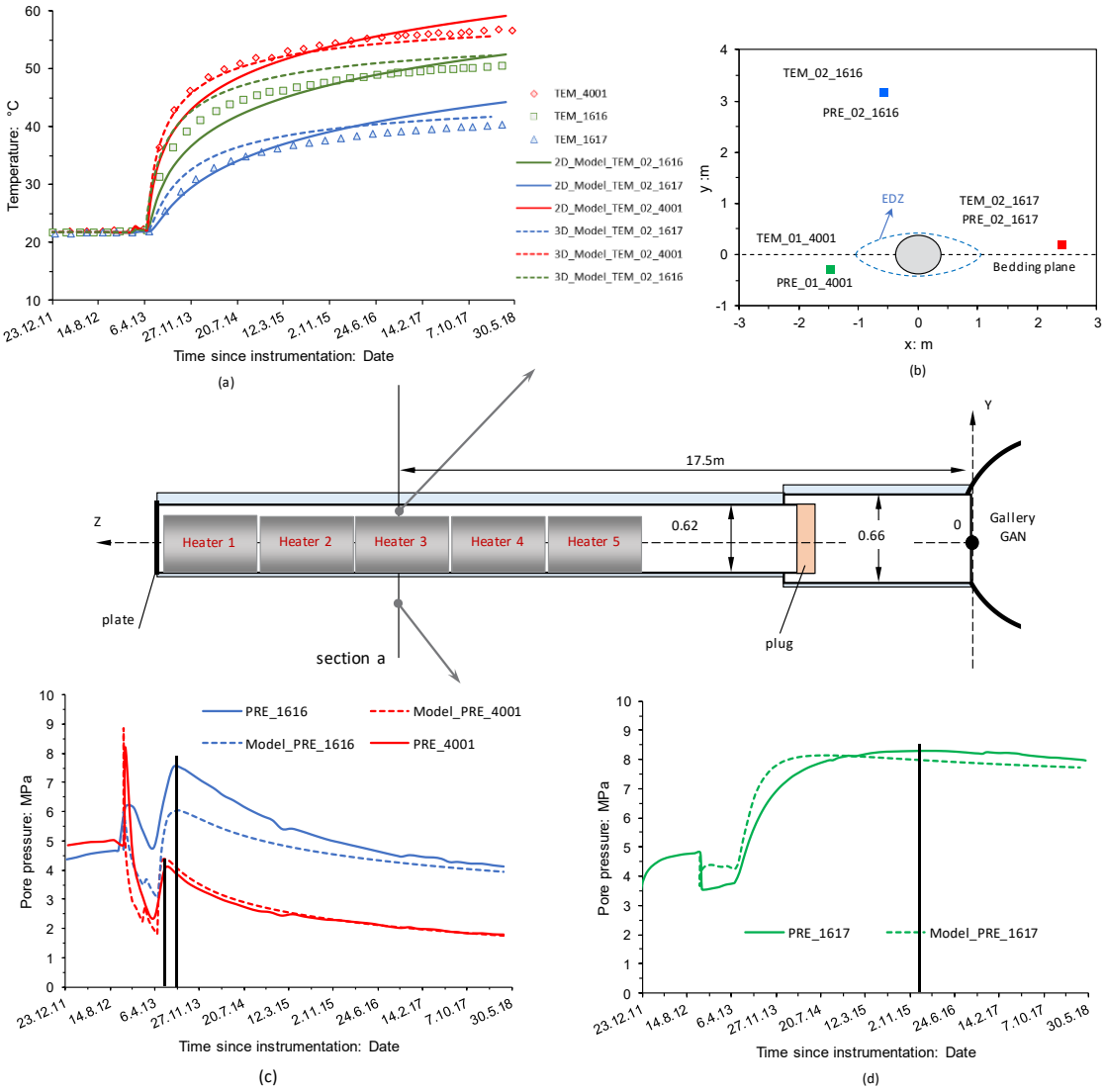


Figure 3: (a) Evolution of temperatures at section *a* (b) Location of observation points at section a (c) Evolution of pore pressure in section *a* at points PRE_1616 and PRE_4001 (c) Evolution of pore pressure in section a, at point PRE_4001

Anisotropic effects are noticeable in the temperatures measured in the rock mass (Figure 4a). Take, for instance, points TEM_1616, TEM_400 and TEM_1617: the first two are oriented in a plane parallel to the bedding with respect and passing through the centreline of the micro-tunnel, while the third is perpendicular to the bedding. They reach different temperatures, about 40, 50 and 55 °C respectively. The anisotropic temperature distribution is apparent, with higher temperatures being reached in the direction of the bedding planes. However as stated above,

the casings are supported at the bottom of the excavation, higher temperature is concentrated at a lower part of the casing (Figure 4b).

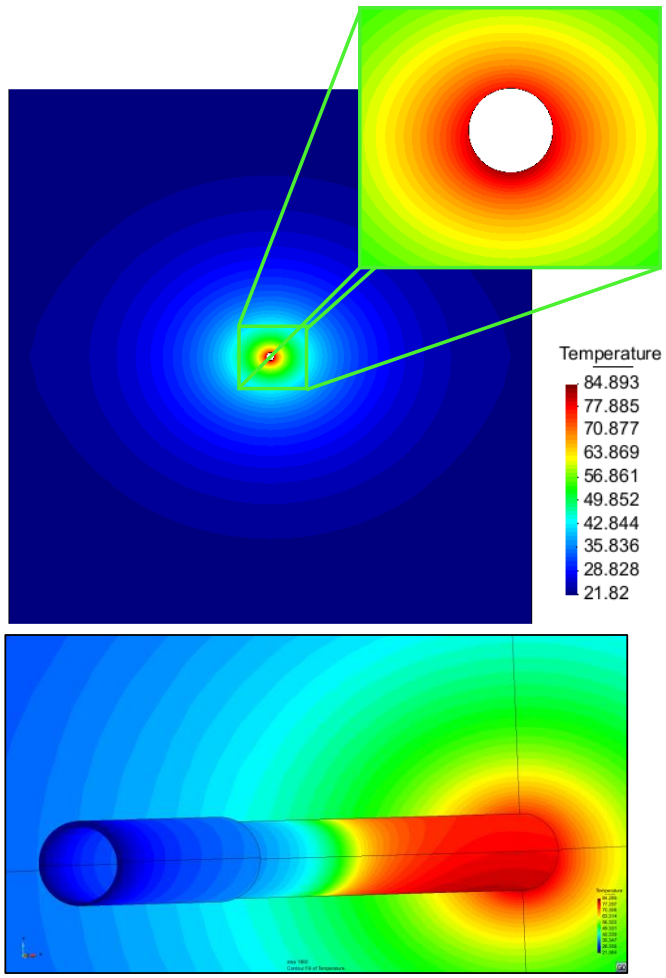


Figure 4: (a) Computed contours of equal temperature (°C) in a cross-section across Heater 3 (b) Three-dimensional view of computed contours of equal temperature (°C) at the end of the computation.

6 EXCAVATION DAMAGE ZONE

The experiments have revealed that excavation operations induce damage and fracturing around the galleries (Armand et al. 2014), creating a zone known as the excavation damaged zone (EDZ), where significant changes in flow and transport properties take place (Tsang et al. 2005). The observed configuration of the EDZ depends on the orientation of the excavation with respect to the anisotropic in situ stress state. The EDZ is identified as one of the key issues affecting the long-term behaviour of the tunnel near-field (Blümling et al. 2007). Major efforts have been thus made to simulate these experimental excavations (Seyedi and Gens 2017) and to gain insights into the design of the actual repository.

As stated above, the ALC1604 cell is drilled in the direction of the major horizontal stress σ_H has a nearly isotropic stress state in the plane normal to the tunnel axis. Despite of that, the

EDZ extends further in the horizontal direction (Figure 5), suggesting strong anisotropic characteristics of the rock mass. An estimate of the configuration of the excavation-damaged zone can be obtained by plotting contours of the cumulative plastic multiplier as it is directly related to the magnitude of irreversible strains (Figure 6). Model results suggest that a plastic zone up to 0.7 m away from the micro-tunnel wall is formed, which agrees with the lateral extension of the shear fractures zone observed in smaller openings (close to 1 diameter, Armand et al. 2014). At the point with the higher plastic multiplier, greater mechanical effects will be noticed on the deformability of rock and hydraulic diffusion. It can be seen that the configuration of the damaged zone is similar to that observed in the previous micro-tunnels with the same orientation, extending more in the horizontal direction (Armand et al. 2014, 2017).

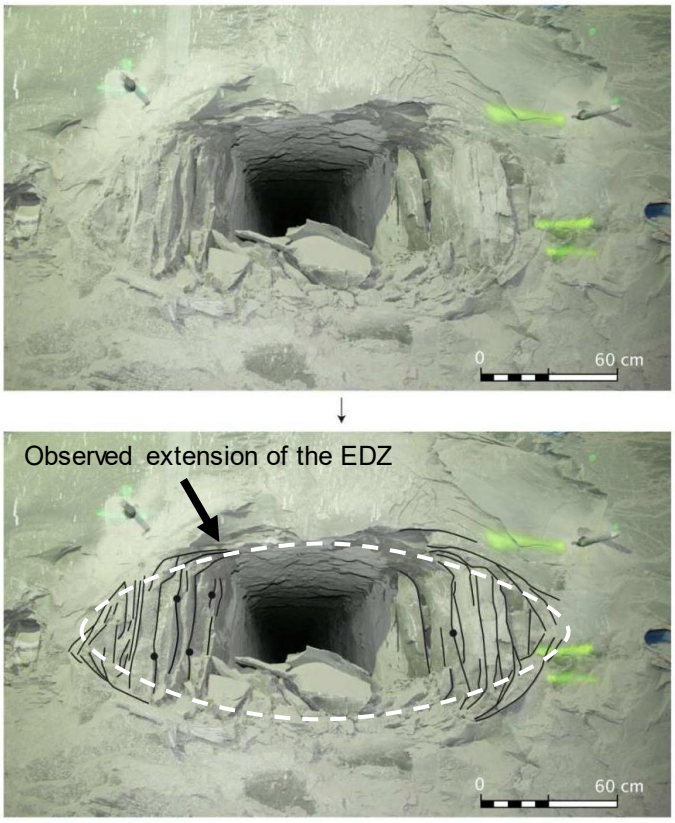


Figure 5: Extension of the damaged zone around a full-scale HLW cell parallel to major horizontal stress.

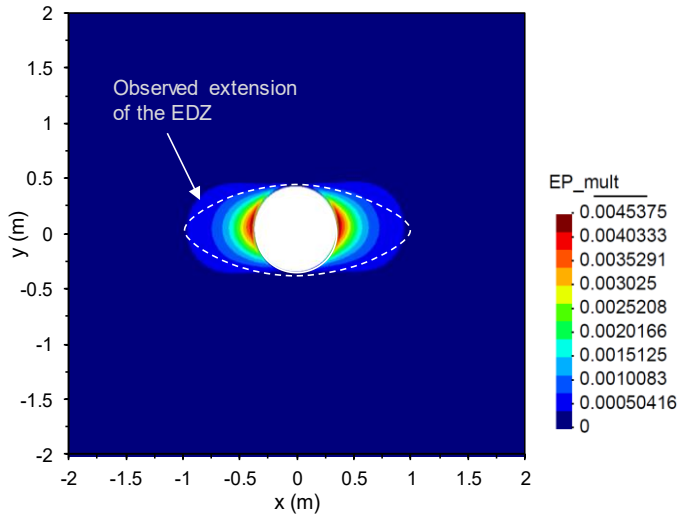


Figure 6: Obtained configuration of the EDZ in terms of plastic multiplier in the section *a* at the end of excavation.

5 PORE PRESSURES

As expected, temperature increases triggered a large upsurge of pore pressures. A typical set of observations is presented in Figure 3c and Figure 3d where the pore pressure recorded in sensors PRE_1616, PRE_1617 and PRE_4001 are plotted. The hydromechanical impact of the cell excavation monitored on the peripheral boreholes is consistent with the measurements taken during the excavation of the previous cells parallel to the major horizontal stress. Indeed, the excavation leads to pore pressure increase in the horizontal plane (Figure 3c) of the cell and to pore pressure drops in the vertical plane (Figure 3d). As was observed in the TED experiment (Garitte et al. 2014), the influence of heating upon the pore pressure firstly results in thermal pressurisation (controlled by the difference between the thermal expansion coefficients of the pore water and of the rock), followed by the dissipation of the overpressure when the speed of the temperature rise decreases. Anisotropic effects are also here noticeable: although the overpressure peak was observed in the cell's horizontal plane (Figure 3c) in the 140 days after the start of heating, peak had not yet been reached in the vertical plane (Figure 3d) after more than 800 days. The difference between the times taken to reach the overpressure peak in the vertical and horizontal planes can be explained by the anisotropic thermal and hydraulic properties of the rock.

A comparison between the results of the 2D analysis and observations, in terms of pore pressure increases, for various points in section "*a"* is presented in Figure 3c and Figure 3d. It is apparent that the maximum pore pressure value at peak is reasonably well captured by the formulation and parameters used. The evolution of pore pressure is also reproduced well, with the noticeable exception of borehole PRE_1616, located in a horizontal plane. This is due to the fact that pore pressure after excavation is not well-captured by the model, which shifts of the further evolution during heating. In Figure 3c and Figure 3d, the time at which the maximum pore pressure increase is calculated is indicated for each measurement point. Time is longer as the distance to the main borehole increases. This comes from the combined effect of the lower temperature rise and lower pore pressure dissipation as the distance from the drainage/heating

condition prevailing at micro-tunnel wall increases.

7 CONCLUSIONS

A full-scale in situ heating test has been performed to simulate the conditions of high-level radioactive waste disposal in a deep geological repository excavated in Callovo-Oxfordian claystone (COx). The test has provided, for a period of up to five years, a large amount of information concerning the thermo-hydro-mechanical behaviour of the COx, sleeve and the air gap. When COx claystones are subjected to thermal loading, they may develop a strong pore pressure response. In turn, the generated pore pressures will affect subsequent thermo-hydro-mechanical behaviour. The performance of a heating test in the Meuse/Haute-Marne underground research laboratory (MHM URL) has provided the opportunity to observe in situ the development of the coupled THM behaviour in this type of material. A priori, the strongly bedded nature of the COx suggested that anisotropy effects could be significant. Performance of three-dimensional thermal analysis has proved very useful in providing a structured framework for interpretation. A 3D simulation has allowed the interpretation of the temperature field obtained during the heating experiment and the determination of the optimum thermal parameters. By comparing the results of the 3D thermal computations with those of 2D analyses, it is possible to conclude that the anisotropic effects are certainly noticeable although not large. The mechanical behaviour of the material has been described by a constitutive model that explicitly developed for this type of material. It is of interest to note that the predicted damaged zone appears to be quite consistent with the test observations. Overall, the theoretical formulation adopted and the analysis performed have been able to provide a satisfactory reproduction of in situ test observations, even from a quantitative point of view.

REFERENCE

Armand, G., Bumbieler, F., Conil, N., de la Vaissière, R., Bosgiraud, J. M., and Vu, M. N. (2017). “Main outcomes from in situ thermo-hydro-mechanical experiments programme to demonstrate feasibility of radioactive high-level waste disposal in the Callovo-Oxfordian claystone.” *Journal of Rock Mechanics and Geotechnical Engineering*, 9(3), 415–427.

Armand, G., Leveau, F., Nussbaum, C., De La Vaissiere, R., Noiret, A., Jaeggi, D., Landrein, P., and Righini, C. (2014). “Geometry and properties of the excavation-induced fractures at the meuse/haute-marne URL drifts.” *Rock Mechanics and Rock Engineering*, 47(1), 21–41.

Blümling, P., Bernier, F., Lebon, P., and Derek Martin, C. (2007). “The excavation damaged zone in clay formations time-dependent behaviour and influence on performance assessment.” *Physics and Chemistry of the Earth*, 32(8–14), 588–599.

Bumbieler, F., Necib, S., Morel, J., Crusset, D., and Armand, G. (2015). “Mechanical And SCC Behavior Of An API5L Steel Casing Within The Context Of Deep Geological Repositories For Radioactive Waste.” *ASME 2015 Pressure Vessels and Piping Conference*, 1–11.

Garitte, B., Gens, A., Vaunat, J., and Armand, G. (2014). “Thermal conductivity of argillaceous rocks: Determination methodology using in situ heating tests.” *Rock Mechanics and Rock Engineering*, 47(1), 111–129.

Gens, A. (2003). *The role of Geotechnical Engineering for nuclear energy utilisation*.

Mánica, M., Gens, A., Vaunat, J., and Ruiz, D. F. (2016). "A time-dependent anisotropic model for argillaceous rocks. Application to an underground excavation in Callovo-Oxfordian claystone." *Computers and Geotechnics*.

Olivella, S., Gens, A., Carrera, J., and Alonso, E. E. (1996). "Numerical formulation for a simulator (CODE_BRIGHT) for the coupled analysis of saline media." *Engineering Computations*, 13(7), 87–112.

Seyedi, D. M., and Gens, A. (2017). "Numerical analysis of the hydromechanical response of Callovo-Oxfordian claystone to deep excavations." *Computers and Geotechnics*, 85, 275–276.

Tsang, C. F., Bernier, F., and Davies, C. (2005). "Geohydromechanical processes in the Excavation Damaged Zone in crystalline rock, rock salt, and indurated and plastic clays - In the context of radioactive waste disposal." *International Journal of Rock Mechanics and Mining Sciences*, 42(1), 109–125.

Finite volume analysis of reinforced concrete structure cracking using a thermo-plastic-damage model

B. Selma[*], M. Chekired[*], J. Côté[*], C. Bessette[†] and L. Jinga[†]

[*] Institut de recherche d'Hydro-Québec
1800 Lionel Boulet Varennes
[†] Hydro-Québec
Réseau de distribution

Key words: Crack, damage, OpenFOAM, fvm, plasticity, elasticity, concrete, rheology, temperature

Abstract This paper proposes modifications to the phenomenological model formulation called CDPM2, developed by Grassl et al. [1]. The proposed modifications are designed to enhance model performance with coupling to temperature effects. A very strong coupling between nonlinear elasticity, plasticity, nonlocal damage evolution and temperature gradient is used to simulate arbitrary crack propagation. The use of FVM to model solid damage is a numerical challenge. This approach presents some advantages such as: ensuring that discretization is conservative even when the geometry is changing; providing a simple formulation that can be obtained directly from a difference method; and employing unstructured meshes. Most authors have neglected the nonlinearity of concrete in the elastic domain from the start of loading to the plastic domain. In this paper we confirm that concrete rheology is not linear even under low loading. Also, since the so-called fracture energy is a key parameter needed to determine the size of cracks and how they propagate in space, we consider that the fracture energy is both material and geometrical parameter dependent. For this reason, we developed a new approach which includes adaptive mesh, nonlinear rheology and thermal effects to re-calculate fracture energy at each time step. Many authors use a constant value obtained from experiments to calculate fracture energy; others use a numerical correlation. In this study, the fracture energy parameter is not constant and can vary with temperature or/and with a change in geometry due to concrete failure. As is well known, the mesh quality of complex geometries is very important for making accurate predictions. A new meshing tool was developed using the C^{++} programming language. This tool is faster, more accurate and produces a high-quality structured mesh. The predictions obtained were compared to a wide variety of experimental data and showed good agreement.

1. Introduction

Concrete is difficult to model because of its quasi-fragility, heterogeneity, porosity and thermal dilation. The literature contains several constitutive models developed to simulate crack formation and propagation. Among them is CDPM2, developed by Grassl et al. [1], which combines damage mechanics and plasticity theory in order to analyze the failure of concrete structures. In the present study, the concept of inelasticity is used instead of plasticity. Inelasticity is close to reality and contains the plastic, elastic and thermal strains, as well as strains due to the effect of time, such as creep. Concrete degradation models are based on the concept of damage, which is often formulated on the basis of mechanical tests on a macro level. However, damage is only one physical parameter and cannot adequately represent crack behavior and random propagation. Crack behavior depends mainly on the damage, crack number and size, mechanical and thermal loading, the initial concrete mix, its age, and the dimensions of the structure. To date, no constitutive models have included all these parameters in the formulation of the damage variable.
In theory, concrete stress has two main causes: damage (highly solicited zones, cracks, microcracks, coalescence problems, aggregate segregation) and plasticity, a mechanism that

is not well understood, especially since plasticity theory was developed from models applied to hyper elastic materials such as plastic and metal. Damage and plasticity are described by continuum mechanics, and their coupling is necessary for concrete degradation modeling. When the thermal gradient is added, the coupling becomes more complex in terms of the discretization of differential equations using, for example, the finite-element method. In the present study, an open-source tool based on the finite-volume method was developed by integrating an algorithm for solving a set of mathematical equations. This tool, coded in OpenFOAM, is in the form of a solver that uses a new library developed specifically for concrete degradation problems.

The finite volume method, recommended by Fryer et al. [2], Demirdzic and Muzaferija [3], Ivankovic et al. [4], Maneeratana [5], and Tukovic et al. [6] for problems related to solid mechanics, was used in the present study to discretize the calculation domain and differential equations. It was chosen because of the complexity of the problem, i.e., the appearance of cracks, their random propagation and the subsequent damage to the structure. Originally developed for fluid mechanics, the finite-volume method has been adapted, with several modifications, to solid mechanics. The work of Menétrey [7]; Grassl et al. [8] and Cervenka and Papanikolaou [9] explains plasticity models based on stress and fracture mechanics. However, as shown in testing, plasticity models are not capable of representing the material's loss of rigidity after cracking. Other researchers, in particular Mazars [10,11]; Grassl and Jirasek [12]; Cicekli et al. [14]; Voyiadjis et al. [13]; and Grassl et al. [1,8], have combined plasticity models with damage mechanics. The present study is based mainly on the work of Grassl et al. [1]. This model is complete enough to be applied to cases involving lower loads (compression or traction) while considering isotropic damage during the deformation process. The damage model, used by Grassl and Jirasek [12], is based on a single parameter for both load types (compression and traction). Those authors nevertheless recognized that their model was inadequate for dealing with a deformation following biaxial compression-traction tests, and recommended using other damage models with several parameters. Recently, Grassl et al. [8] used the model known as CPDM1 (Concrete Plasticity Damage Model 1) to develop an improved version by adding a two-parameter isotropic damage model. In the present work, a damage law was developed based on the work of Mazars [10, 11] and Oliver et al. [15].

2. Mathematical modeling

The general formulation for elasto-plastic with damage is written as follows:

$$\dot{\sigma} = (1 - \mathbf{d})\dot{\bar{\sigma}} = (1 - \mathbf{d})\mathbf{D_e}\colon(\dot{\varepsilon} - \dot{\varepsilon}_p) \tag{1}$$

Where $\dot{\sigma}$ and $\dot{\bar{\sigma}}$ represent the total and effective stresses, respectively, and (**d)** is the isotropic damage variable (**d=0**: healthy structure; **d=1**: damaged structure). In OpenFOAM, **d** is written as follows:

$$\mathbf{d} = \mathrm{d[cell]} \tag{2}$$

The term "cell" defines the index of a finite volume in the mesh. Effective stress is expressed by the following equation:

$$\dot{\bar{\sigma}} = \mathbf{D_e}\colon\left(\dot{\varepsilon} - \dot{\varepsilon}_p\right) \tag{3}$$

The terms $(\dot{\varepsilon})$ and $(\dot{\varepsilon}_p)$ represent the total and plastic deformation rates, respectively. Plastic deformation, $\dot{\varepsilon}_p$, is determined using the concept of plasticity governed by a set of equations and conditions, as follows:

$$\dot{\varepsilon} = \dot{\varepsilon}_e + \dot{\varepsilon}_p \,,\, \dot{\bar{\sigma}} = E\dot{\varepsilon}_e \,,\, \dot{\varepsilon}_p = \dot{\lambda}_p m(\bar{\sigma}, \dot{\kappa}_p) \,,\, \dot{\kappa}_p = \frac{\dot{\lambda}\|m\|}{\dot{X}_h(\bar{\sigma})}(2cos\bar{\theta})^2 \tag{4}$$

Where E is the initial Young modulus, $m(\bar{\sigma}, \dot{\kappa}_p)$ represents the plastic flow vector, and $\dot{\lambda}_p$ is the plastic multiplier rate calculated under the following conditions:

$$F_p(\bar{\sigma}, \kappa_p) \leq 0, \quad \dot{\lambda}_p \geq 0, \quad \text{et} \quad \dot{\lambda}_p F_p(\bar{\sigma}, \kappa_p) = 0 \tag{5}$$

2.1 Failure interface function

Function $F_p(\bar{\sigma}, \kappa_p)$ defines the failure interface, which is a line separating the elastic domain and the cracked area.

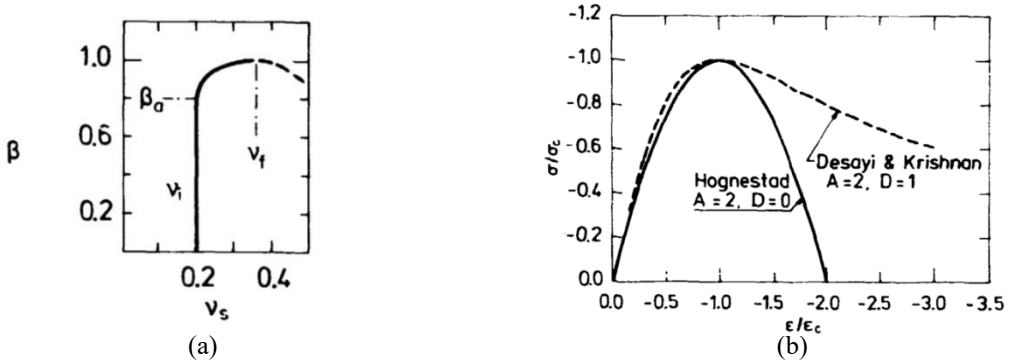
$$F_p(\bar{\sigma}, \dot{\kappa}_p) = \left\{ [1 - q_{h1}] \left(\frac{\bar{\rho}}{\sqrt{6} f_c} + \frac{\bar{\sigma}_V}{f_c} \right)^2 + \sqrt{\frac{3}{2}} \frac{\bar{\rho}}{f_c} \right\}^2 + m_0 q_{h1}^2(\kappa_p) q_{h2}(\kappa_p) \left[\frac{\bar{\rho}}{\sqrt{6} f_c} r(cos\bar{\theta}) + \frac{\bar{\sigma}_V}{f_c} \right] - q_{h1}^2(\kappa_p) q_{h2}^2(\kappa_p) \tag{6}$$

With $\bar{\sigma}_V = \frac{1}{3} tr(\sigma)$

The work of Grassl et al. [1] provides more detail about the CDPM2 model.

2.2 Concrete elasticity

Figure 2 shows the change in the Poisson coefficient and Young modulus based on the work of Ottosen [16]:



(a) (b)

Figure 1 : Change in rheological properties of concrete: (a) Poisson coefficient (b) Influence of parameters A and B (Ottosen [16])

L'évolution du coefficient de Poisson, ν, est donnée par la relation suivante:

$$\nu = \begin{cases} \nu_0 & si\ \beta \leq \beta_0 \\ \nu_f - (\nu_f - \nu_0)\sqrt{1 - \left(\frac{\beta - \beta_0}{1 - \beta_0}\right)^2} & si\ \beta > \beta_0 \end{cases} \tag{7}$$

For any type of concrete or load $\nu_f = 0.36$ and $\beta_0 = 0.8$. Parameter ν_0 represents the initial Poisson coefficient. Variable β defines the ratio of the equivalent stress over the compression withstand limit:

$$\beta = \frac{\varepsilon_{eq}}{f_c'} \tag{8}$$

Absence of a load ($\varepsilon_{eq} = 0$) implies that $\beta = 0$, and only in that case is the concrete response considered elastic-linear. The variation in the elasticity modulus is expressed by the following non-linear equation:

$$E_{nl} = \frac{1}{2} E_0 - \beta \left(\frac{1}{2} E_0 - E_f \right) + \sqrt{\left[\frac{1}{2} E_0 - \beta \left(\frac{1}{2} E_0 - E_f \right) \right]^2 - \beta E_f^2 [A(1 - \beta) - 1]} \tag{9}$$

If $\beta = 0$, equation (33) will give: $E_{nl} = E_0$ (linear response).
The term E_f represents the Young modulus at the fracture point, and is defined as follows:

$$E_f = \frac{E_0}{1+4(B-1)\left(\frac{\sqrt{J_2}}{fc}-\frac{1}{\sqrt{3}}\right)} \tag{10}$$

A and B are parameters of the model (A=1 and B=2 according to Desayi and Krishnan [17]). f_c is the compression withstand limit, and J_2 represents the plasticity criterion defined by:

$$J_2 = \frac{1}{3}(I_1^2 - 3I_2) \tag{11}$$

2.3 Concrete plasticity

The deformations resulting from mechanical loading are shown in Figure 3.

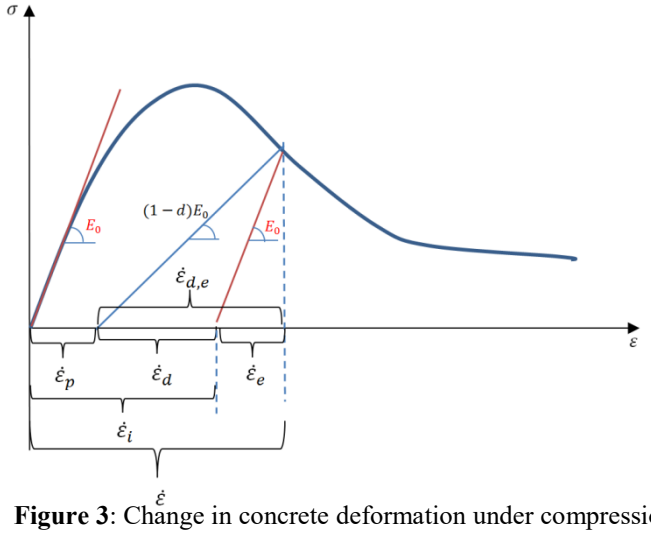


Figure 3: Change in concrete deformation under compression

It can be seen that there are several mathematical formulations in terms of equivalent deformations and in the form of increments for small displacements:

$$\dot{\varepsilon} = \dot{\varepsilon}_e + \dot{\varepsilon}_i \tag{12}$$

$$\dot{\varepsilon}_i = \dot{\varepsilon}_p + \dot{\varepsilon}_d \tag{13}$$

$\dot{\varepsilon}_i$ is the increment of inelastic deformation; $\dot{\varepsilon}_d$ is the increment of deformation due to elasto-plastic damage. In analyzing concrete structure performance, the use of inelastic deformation is the approach closest to reality. Based on Figure 3, deformation due to elasto-plastic damage can be defined. This new parameter is expressed by the following equation:

$$\dot{\varepsilon}_d = \dot{\varepsilon}_{d,e} - \dot{\varepsilon}_e \tag{14}$$

With $\dot{\varepsilon}_{d,e} = \frac{1}{(1-d)}\dot{\varepsilon}_e$

$\dot{\varepsilon}_{d,e}$ define the deformation after concrete damage while remaining in its elastic domain. Finally, Equations (13) and (14) give this result:

$$\dot{\varepsilon}_d = \frac{d}{(1-d)}\dot{\varepsilon}_e \tag{15}$$

By definition, elastic deformation is given by the following equation:

$$\dot{\varepsilon}_e = \frac{\dot{\sigma}}{E_0} \tag{16}$$

The increment of total stress is expressed as a function of inelastic deformation, as follows:

$$\dot{\sigma} = 2\mu(\dot{\varepsilon} - \dot{\varepsilon}_i - \dot{\varepsilon}_T) + \lambda \mathbf{I} tr(\dot{\varepsilon}) \tag{17}$$

Parameters μ and λ are the Lamé coefficients, defined by the following equations:

$$\begin{cases} \mu = \frac{E}{2(1+\nu)} \\ \lambda = \frac{\nu E}{(1+\nu)(1-2\nu)} \end{cases} \tag{18}$$

Consequently, Equations (12), (14) and (15) give the following analytical solution:

$$\dot{\varepsilon}_p = \dot{\varepsilon} - \frac{1}{1-\mathbf{d}}\dot{\varepsilon}_e \tag{19}$$

Equations (12) to (19) are expressed in terms of equivalent deformations in order to calculate the equivalent plastic deformation, which is approximately equal to the plastic multiplier $\dot{\lambda}_p$. The following equation may therefore be concluded:

$$\dot{\varepsilon}^p_{eq} \cong \dot{\lambda}_p \tag{20}$$

Equations (4) and (20) therefore yield this equivalence:

$$\dot{\varepsilon}^p = \dot{\varepsilon}^p_{eq} m(\bar{\sigma}, \kappa_p) \tag{21}$$

The plastic normal (or plastic flow vector), $m\left(\bar{\sigma}, \kappa_p\right)$, is defined by:

$$m\left(\bar{\sigma}, \kappa_p\right) = \frac{\partial}{\partial \bar{\sigma}} G_p(\bar{\sigma}, \kappa_p) \tag{22}$$

2.4 Influence of temperature on concrete degradation

Temperature variations affect rheological parameters (E, f_t, and f_c) as well as the dilation coefficient and thermal conductivity. In this study, the correlations established by Shoukry et al. [23] were incorporated into the numerical tool as follows:

$$f_t(T) = 0.55\sqrt{\acute{f}_t} - 0.018(T-20),\ f_c(T) = \acute{f}_c - 0.13(T-20) \text{ and } E(T) = E_0 - 0.10627(T-20)$$

The concrete dilation coefficient was assumed to be fixed at $\alpha = 6.8{\times}10^{-6}$ 1/C° according to ACI (2019). The rheological parameters are in MPa for (f_t, f_c) and in GPa for Young's modulus. To determine thermal conductivity, the model of Kim et al. [24] was used.

$$k_c = k_0\left[0.293 + 1.01V_g\right]\left[0.8\left(1.62 - 1.54\left(\frac{W}{C}\right)\right) + 0.2R_h\right] \tag{23}$$
$$\times\,[1.05 - 0.0025T][0.86 + 0.0036V_s]$$

Where k_0 is the reference conductivity of concrete (at T=20C°), V_g the volume fraction of the large aggregate, (w/c) the water/cement ratio, R_h the humidity and V_s the volume fraction of the sand. Thermal damage is calculated according to the following correlation, Jirasek and Bazant [25]:

$$D^T = 1 - (0.03931 + \exp(-0.002T)) \tag{24}$$

Equation (24) does not take elastic or plastic deformation into account. This equation is used to correct mechanical damage, as follows:

$$D_{global} = (1 - D^M)(1 - D^T) \tag{25}$$

2.5 Analytical solution proposed to determine plastic deformation

The iterative algorithms proposed in the literature [11,12,27] to calculate the plastic multiplier and deduce the plastic deformation have a number of disadvantages, including high effort calculation and high residuals. The contribution of the present study is of a theoretical nature; it is based on a mathematical development for determining plastic deformation. For concrete, the inelastic definition is used, in which plastic deformation is implicitly included. Figure 3 shows the definition of each variable in terms of stress-deformation curve. Moreover, the following condition was developed and verified:

$$\frac{1}{2}\dot{\varepsilon} \leq \dot{\varepsilon}_p \leq \dot{\varepsilon} \tag{26}$$

Thus, based on the following equations:

$$E_p = (1 - \mathbf{d})E \tag{27}$$

And

$$\dot{\varepsilon} = \dot{\varepsilon}_e + \dot{\varepsilon}_p \tag{28}$$

Using the total stress rate applied as follows:

$$\frac{\dot{\sigma}}{E_{ep}} = \frac{\dot{\sigma}}{E} + \frac{\dot{\sigma}}{E_p} \tag{29}$$

From Equation (29) it may be deduced that:

$$E_{ep} = \frac{EE_p}{E+E_p} \tag{30}$$

Given that:

$$E_{ep} = \frac{\dot{\sigma}}{\dot{\varepsilon}} \tag{31}$$

Equations (27) and (30) give:

$$\dot{\varepsilon}_p = \frac{E}{E+E_p}\dot{\varepsilon} \tag{32}$$

By combining Equations (27) and (32), the following result was obtained:

$$\dot{\varepsilon}_p = \frac{1}{2-\mathbf{d}}\dot{\varepsilon} \tag{33}$$

Using extreme conditions of damage, the following system is found:

$$\begin{cases} \dot{\varepsilon}_p = \frac{1}{2}\dot{\varepsilon} & si\ d = 0 \\ \dot{\varepsilon}_p = \dot{\varepsilon} & si\ d = 1 \end{cases} \tag{34}$$

Based on equation system (34), it may be deduced that the following equation is true at all times:

$$\frac{1}{2}\dot{\varepsilon} \leq \dot{\varepsilon}_p \leq \dot{\varepsilon} \tag{35}$$

This new condition was implemented into the numerical toolbox developed in the present study. Computational stability and convergence are observed during simulation.

2.6 Components of damaged concrete

Mazars' two damage laws [10,11], in their original and modified versions, have been widely used in the study of concrete degradation. In the present work, an exponential law was incorporated into the numerical code (please see those studies for more details). Mathematically, Mazars' laws have exponential form; however, in this model, the exponential law is written explicitly as follows:

$$\mathbf{d_t} = 1 - exp\left(-\frac{\varepsilon_{eq,t}}{\varepsilon_f}\right) \tag{36}$$

$$\mathbf{d_c} = 1 - exp\left(-\frac{\varepsilon_{eq,c}}{\varepsilon_f}\right) \tag{37}$$

This new formulation makes implicit use of fracture energy in the term $\varepsilon_f = G_f/(f_t h_e)$. Mazars' laws do not use this important parameter, considered to be both a physical and geometric property of the material. The overall damage rate is given by the same equation as the one developed by Mazars [10]:

$$\mathbf{D} = \alpha_t\, \mathbf{d}_t + (1-\alpha_t)\mathbf{d}_c \tag{38}$$

The present work uses the following equation from Grassl et al. [1]:

$$\alpha_c = \sum_{i=1}^{3} \frac{\bar{\sigma}_{c,i}(\bar{\sigma}_{t,i}+\bar{\sigma}_{c,i})}{\|\bar{\sigma}_p\|^2} \tag{39}$$

Where

$\alpha_t = (1-\alpha_c)$; $\varepsilon_{eq,t} = \sqrt{\sum_i^3 <\varepsilon_i>_+^2}$; $\varepsilon_{eq,c} = \sqrt{\sum_i^3 <\varepsilon_i>_-^2}$; $\bar{\sigma}_p = \frac{1}{3} tr(\bar{\sigma})\ \bar{\sigma}_{t,i} = <\bar{\sigma}_i>_+$; $\bar{\sigma}_{c,i} = <\bar{\sigma}_i>_-$

Equations (36) and (37) are based on the work of Oliver et al. [53], whose model had limits in terms of biaxial and shear loading. Equivalent deformation is uniform, whether for mode I or mode II. The concept of this development is based on the use of Mazars' laws [10,11], because of their advantages in biaxial tests, and on the exponential law of Oliver et al. [53], which includes fracture energy. Combining these two laws yielded Equations (36) and (37).

2. 9 Cohesive forces on the concrete-concrete interface

According to Xu and Needleman [18], normal and tangential cohesive forces are expressed as follows:

Normal traction:

$$T_n = -\frac{\Phi_n}{\delta_n} exp\left(-\frac{\Delta_n}{\delta_n}\right)\left\{\frac{\Delta_n}{\delta_n} exp\left(-\frac{\Delta_t^2}{\delta_t^2}\right) + \frac{1-q}{r-1}\left[1 - exp\left(-\frac{\Delta_t^2}{\delta_t^2}\right)\right]\left[r - \frac{\Delta_n}{\delta_n}\right]\right\} \quad (40)$$

Tangential traction :

$$T_t = -\frac{\Phi_n}{\delta_n}\left(2\frac{\delta_n}{\delta_t}\right)\frac{\Delta_t}{\delta_t}\left\{q + \left(\frac{r-q}{r-1}\right)\frac{\Delta_n}{\delta_n}\right\} exp\left(-\frac{\Delta_n}{\delta_n}\right) exp\left(-\frac{\Delta_t^2}{\delta_t^2}\right) \quad (41)$$

The parameters are defined in Xu and Needleman [18]. However, the characteristic lengths, δ_n and δ_t, were determined using the equation proposed by Hillerborg et al. [19]:

$$\delta_n = \delta_t = \frac{G_f E}{f_t^2} \quad (42)$$

G_f is the fracture energy expressed by the equation of Bazant and Becq-Giraudon [26]:

$$G_f = (0.0469 h_e^2 - 0.5 h_e + 26) f_c^{0.7} \quad (43)$$

2.10 Estimation of crack opening

Based on the work of Bazant and Oh [27], crack thickness is expressed as follows:

$$w_c = l_{ch}\varepsilon_c \quad (44)$$

l_{ch} is the characteristic length defined by Equation (42), and ε_c is the deformation in the crack area. By combining Equations (42) and (44):

$$w_c = \frac{G_f E}{f_t^2}\varepsilon_c \quad (45)$$

It should be noted that in the present work, the term ε_c has been replaced by equivalent deformation, $\tilde{\varepsilon}$, because of its involvement in the damage parameter calculation. In addition, crack thickness is proportional to equivalent deformation. The following equation was developed and incorporated into the numerical tool: $w_c = \frac{G_f E}{f_t^2}\tilde{\varepsilon}$

3. Development of an open-source toolbox for concrete cracking

As part of this study, a meshing tool was developed. The mesh generated contained two main volume types: hexahedron and prism. Table 1 provides some of the mesh characteristics in the case of beam.

Table 1: Mesh generation and characteristics

Geometry (cm)	Number of FVs	Type of mesh	Time (s)	Max. Skewness	Max. aspect ratio
Beam $20(W) \times 40(H) \times 420(L)$	0.9×10^6	Hex. (96.5%) / Prism (4.5%)	32	0.78	7.95

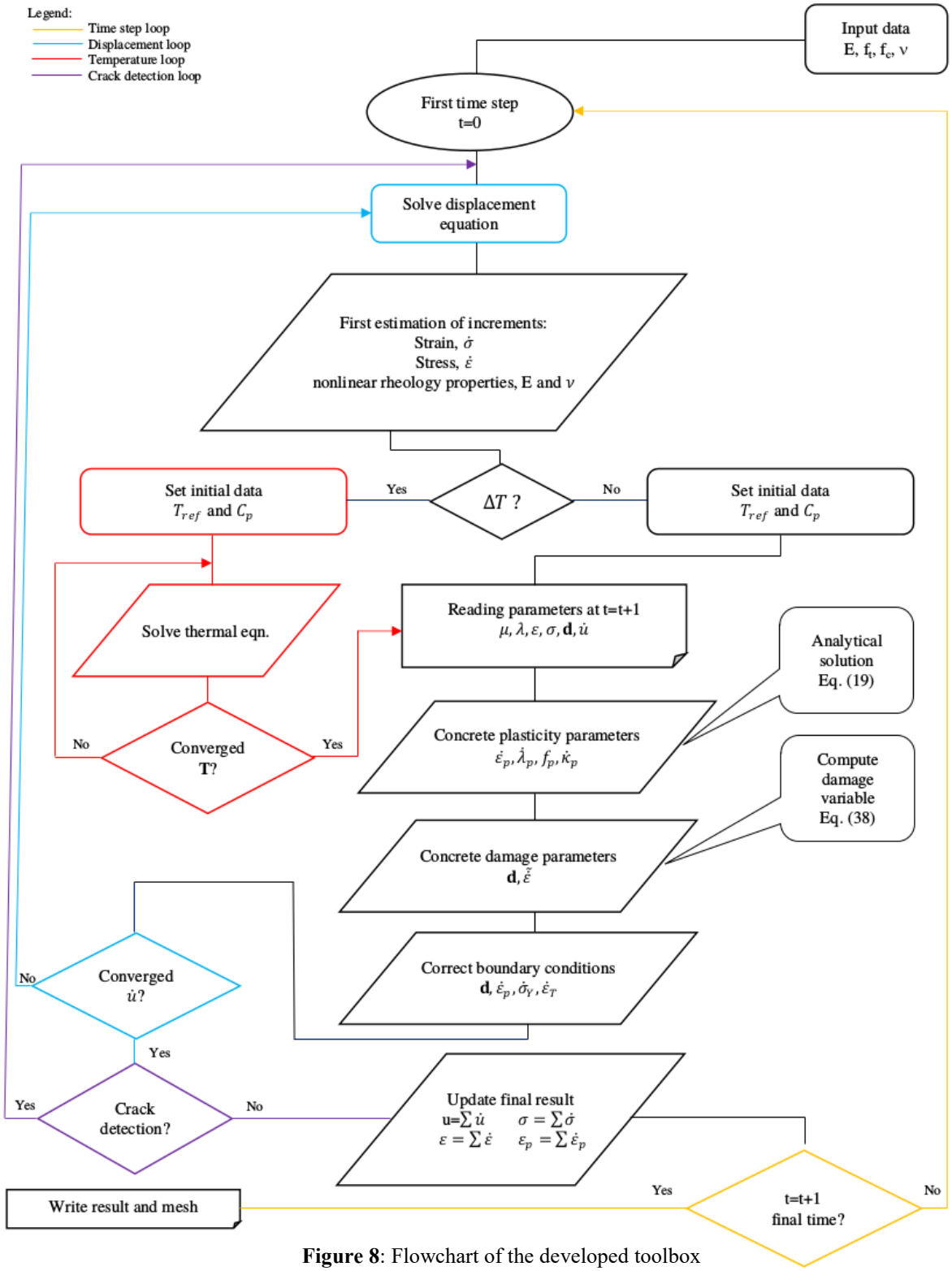
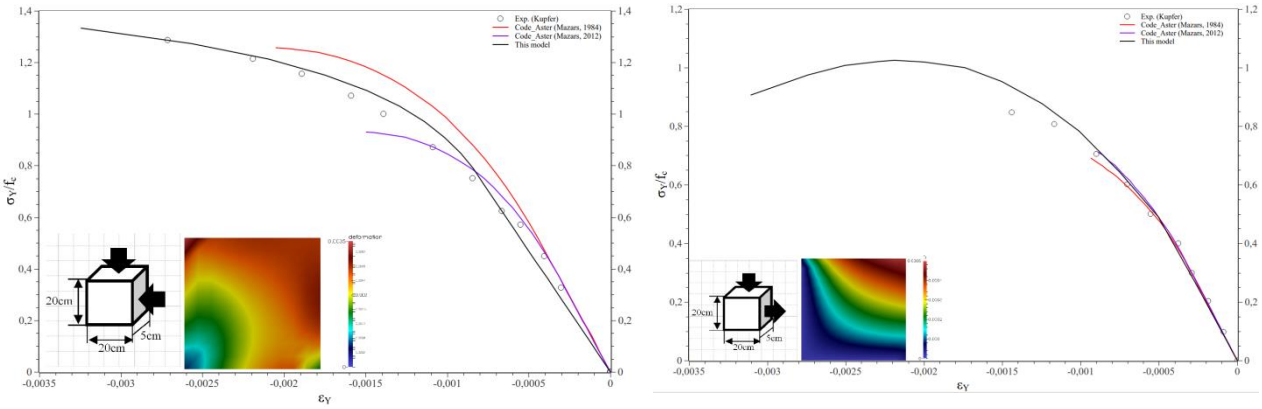


Figure 8: Flowchart of the developed toolbox

4. Experimental validation

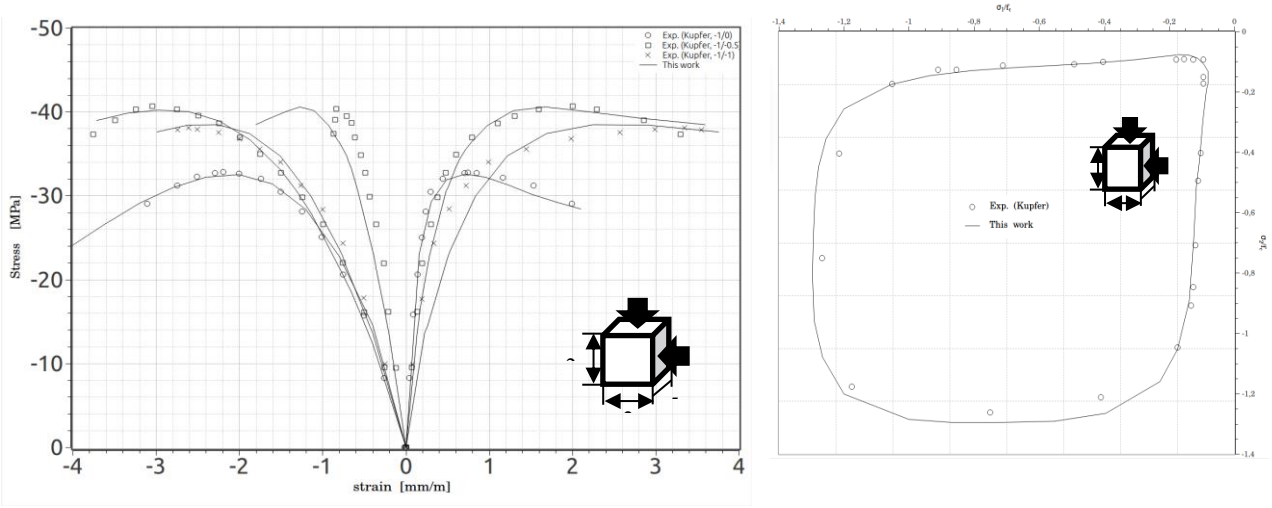
To assess the validity of the proposals developed in this work, the numerical simulation results were compared with lab test results. In this way, the model's ability to reliably predict the response of reinforced concrete to various types of loading was determined. The experimental results used for the validation were those of Kupfer et al. [28] in Figures 11 and 12, of Nooru [20] in Figure 13, of Imran [21] in Figure 14, and of Mirzazadeh and Green [22] in Figure 15. It can be seen that the model's results are very similar to those obtained experimentally, regardless of the type of loading the concrete samples were subjected to.

4.1 Kupfer's biaxial tests



(a) (b)

Figure 11: Comparison between experimental result and model (a) Biaxial compression (b) Compression-Traction



(a) (b)

Figure 12: (a) Uniaxial and biaxial compression (b) Biaxial compression: Axial deformations

4.2 Nooru's shear tests

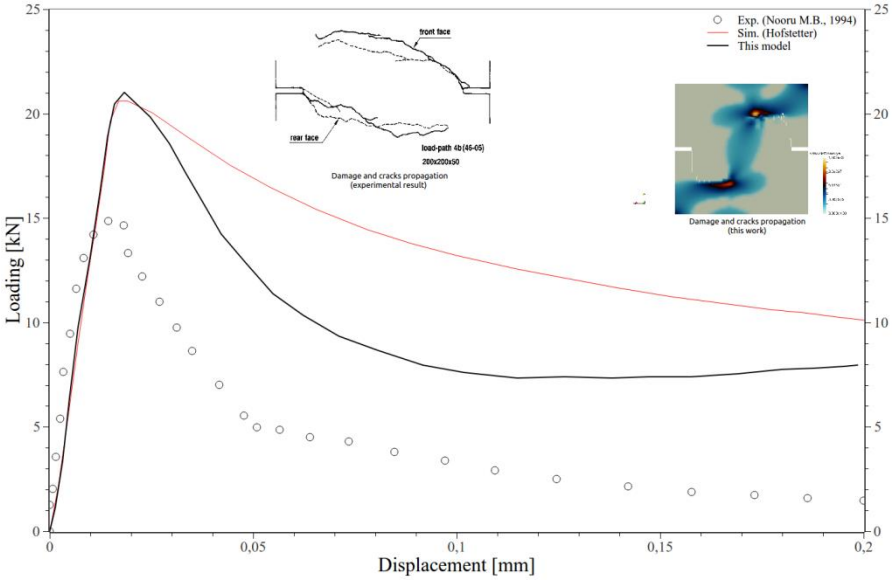


Figure 13: Nooru-Mohamed's shear tests [20] and numerical result

4.3 Imran's confinement tests

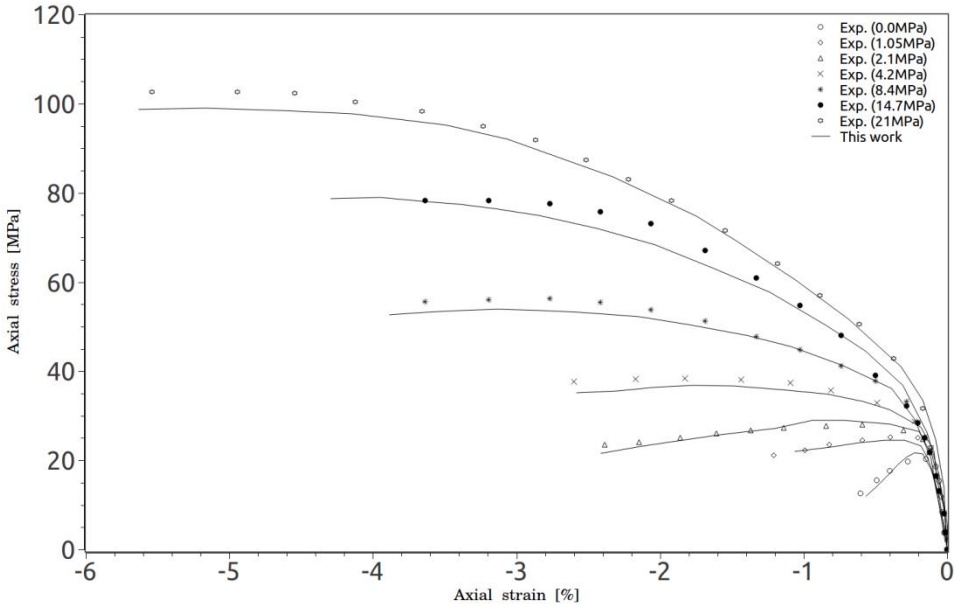


Figure 14: Confinement test on saturated concrete with E/C=0.75

4.4 Mirzazadeh and Green four-point beam [22]

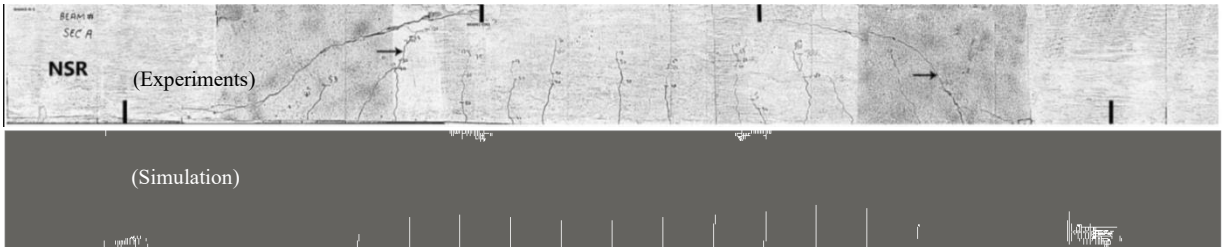


Figure 15: Beams with no stirrups (average temperature inside beam: 30C°)

6. Conclusion

The proposals developed were validated based on experimental results obtained from the literature. The mathematical model resulting from the present work may be considered generic and scalable for the study of concrete degradation. The model also takes into account concrete expansion due to thermal gradient. The effect of fracture energy on fracture behavior is considered to be the most important factor. A number of nonlinear laws and analytical solutions were introduced with the aim of simulating concrete response to cracking but also to reduce calculation effort. The following points were noted during the numerical simulations performed by means of parallel calculations:

- The damage variable has more influence on cracks in compression mode than in strain mode.
- Plastic deformations have a considerable effect on crack direction and opening.
- Plastic deformations are more numerous in mode I (strain) than mode II (compression).
- Nonlinear response was observed in the elastic part (see Kupfer's biaxial tests).
- The degradation of the concrete's Young modulus starts well before its compression or traction withstand limit.
- The following equation applied at all times, regardless of the type of loading:

$$\frac{1}{2}\dot{\varepsilon} \leq \dot{\varepsilon}_p \leq \dot{\varepsilon}$$

- Fracture energy depends on geometry, coarse aggregate size and the material's rheological properties.
- Some of the samples had gouges in them, which accelerated the appearance of cracking.
- Crack thickness is strongly influenced by fracture energy.
- The cohesive forces at the concrete-concrete interface depend on the fracture energy. Consequently, the fracture energy value determines whether or not new cracked surfaces will form.

References:

[1] Grassl P., Xenos D., Nystrom U., Rempling R., and Gylltoft K. *CDPM2: A damage-plasticity approach to modelling the failure*. International Journal of Solids and Structures, Vol. 50, pp. 3805-3816 (2013)

[2] Fryer Y.D., Bailey C., Cross M., and Lai C.H. *A control volume procedure for solving the elastic stress-strain equations on an unstructured mesh*. Appl. Math. Modelling, vol. 15, pp. 639-645 (1991)

[3] Demirdzic I. and Muzaferija S. *Finite volume method for stress analysis in complex domains*. International Journal for numerical Methods in Engineering, vol. 37, pp. 3751-3766 (1994)

[4] Ivankovic A., Demirdzic I., Williams J.G., and Leevers P.S. *Application of the finite volume method to the analysis of dynamic fracture problems*. International Journal of Fracture, vol. 66, pp. 357-371 (1994)

[5] Maneeratana K. *Development of the finite volume method for non-linear structural applications*. Thesis, Imperial College, University of London (2000)

[6] Tukovic Z., Ivankovic A., and Karac A. *Finite-volume stress analysis in multi-materials linear elastic body*. Inter- national Journal for Numerical Methods in Engineering, vol. 93, pp. 400-419 (2013)

[7] Menétrey Philippe. *Numerical analysis of punching failure in reinforced concrete structures*. Thèse doctorat, École Polytechnique Fédérale de Lausanne EPFL, 1994

[8] Grassl P., Lundgren K., and Gylltoft K. *Concrete in compression: a plasticity theory with a novel hardening law*. International Journal of Solids and Structures, Vol. 39, pp 5205–5223 (2002)

[9] Cervenka, J., Pappanikolaou, V. *Three-dimensional combined fracture- plastic material model for concrete*. Int. J. of Plasticity, Vol. 24, 12, 2008, ISSN 0749-6419, pp. 2192-2220

[10] Mazars J. *Application de la mécanique de l'endommagement au comportement non-linéaire et à la rupture du béton de structure*. Thèse de doctorat d'état, Université Paris VI, France (1984)

[11] Mazars J., Hamon F., Grange S. *A new 3D damage model for concrete under monotonic, cyclic and dynamic loadings*. Materials and Structures, 2014 (on line, DOI 10.1617/s11527-014-0439-8)

[12] Grassl P. and Jirasek. *Damage-plastic model for concrete failure*. International Journal of Solids and Structures, Vol. 43, pp. 7166-7196 (2006)

[13] Voyiadjis G.Z., Taqieddine Z.N., and Kattan P.I. *Anisotropic damage-plasticity model for concrete*. International Journal of Plasticity, Vol. 24, pp. 1946-1965, 2008

[14] Cicekli U., Voyiadjis G.Z., and Abu Al-Rub R.K. *A plasticity and anisotropic damage model for plain concrete*. International Journal of Plasticity, Vol. 23, pp. 1874-1900, 2007

[15] Oliver J., Cervera M., Oller S., and Lubliner J. *Isotropic damage models and smeared crack analysis of concrete*. In. Computer Aided Analysis and Design of Concrete Structures, Bicanic N, Mang H (eds), Pineridge Press: Swansea, UK, pp. 945-957 (1990)

[16] Ottosen N.S. *Nonlinear Finite Element Analysis of Concrete Structures*. Risø National Laboratory, DK 4000, Roskilde, Denmark

[17] Desayi, P. and Krishnan, S. (1964). *Equation for the Stress-Strain Curve of Concrete*. Proc. American Concrete Institute ACI, Vol. 61, 345-350.

[18] Xu X.-P and Needleman A. *Numerical simulations of fast crack growth in brittle solids*. J. Mech. Phys. Solids, Vol. 42, No. 9, pp. 1397-1434, 1994

[19] Hillerborg A., Modéer M. and Petersson P-E. *Analysis of crack formation and crack growth in concrete by means of fracture mechanics and finite elements*. Cement and Concrete Research, Vol. 6, pp. 773-782, 1976

[20] Nooru-Mohamed M.B. *Mixed-mode fracture of concrete: an experimental approach*. Thesis, Delft University of technology, Netherlands (1994)

[21] Imran I. and Pantazopoulou S.J. Experimental study of plain concrete under triaxial stress. ACI Materials Journal, Vol. 93, No. 6, 1996

[22] Mirzazadeh M.M. and Green M.F. Non-linear finite element analysis of reinforced concrete beams with temperature differentials, Engineering Structures, Vol. 152 (2017), pp. 920-933

[23] Shoukry S.N., William G.W., Downie B. and Riad M.Y. *Effect of moisture and temperature on the mechanical properties of concrete*. Construction and Building Materials, Vol. 25, pp. 688-696, 2011

[24] Kim K.-H, Jeon S.-E, Kim J.-K and Yang S. *An experimental study on thermal conductivity of concrete*. Cement and Concrete Research, Vol. 33, pp. 363-371, 2003

[25] Jirasek M., and Bazant Z.P. *Inelastic analysis of structures*. John Wiley, ISBN 0-471-98716-6 (2002)

[26] Bazant Z.P. and Becq-Giraudon E. *Statistical prediction of fracture parameters of concrete and implications for choice of testing standard*. Cement and Concrete Research, Vol. 32, pp. 529–556 (2002)

[27] Bazant Z.P. and Oh B.H. *Crack band theory for fracture of concrete*. Materials and Structures, Vol. 16, pp. 155-177 (1983)

[28] Kupfer H., Hilsdorf H.K., and Rusch H. *Behavior of concrete under biaxial stresses*. ACI Journal, vol. 66, pp. 656-666 (1969)

XV International Conference on Computational Plasticity. Fundamentals and Applications
COMPLAS 2019
E. Oñate, D.R.J. Owen, D. Peric , M. Chiumenti, and Eduardo de Souza Neto (Eds)

HEAT TRANSPORT WITH ADVECTION IN FRACTURED ROCK

A. PÉREZ*, I.CAROL* AND P.PRAT*

* Department of Civil and Environmental Engineering
Universitat Politècnica de Catalunya (UPC)
Jordi Girona 1, D2 Building, E-08034 Barcelona, Spain
e-mail: adria.perez@upc.edu, ignacio.carol@upc.edu, pere.prat@upc.edu

Key words: Large advection, heat transport, zero-thickness interface elements, Péclet number, FEM, SUPG.

Abstract. In the transport of heat in porous media, diffusion generally dominates over advection due to slow fluid velocities imposed by low permeability. This is the reason why standard Galerkin formulation leading to extra non-symmetric matrix terms may be still used successfully. However, in the presence of fractures the situation may be different. Fractures constitute preferential flow paths where fluid velocities may be significant and advection may become dominant over diffusion ("large advection" with Péclet number >1). This paper focuses on the formulation, numerical implementation and verification of a model to solve the steady-state heat transport problem with large advection along geomechanical discontinuities represented by zero-thickness interface elements. The fluid velocity field is considered as known input data (no hydraulic coupling). The existing SUPG method is modified for its application to zero-thickness interface elements, and the resulting formulation is implemented in an existing FE geomechanical code. An example of application is presented with large advection along a discontinuity crossing a low permeability domain. The results show that the proposed approach leads to stable results, in contrast to standard Galerkin.

1 INTRODUCTION

The two main mechanisms of heat transport in saturated porous media are diffusion and advection. In the numerical formulation of the problem via the FEM, it is well known that, if advection dominates over diffusion (Péclet number $Pe > 1$), traditional Galerkin formulations cease to work [1]. In many practical engineering situations, however, such as in the case of geological materials, average fluid (Darcy) velocities may remain small due to the low permeability and tortuosity of the pore system, and this problem may be ignored.

But this situation may change in the presence of open fractures or cracks, because these may become preferential paths for fluid circulation with fluid velocities significantly higher than those found in the surrounding porous medium, and therefore exceeding the limit condition $Pe > 1$. Thus, it is important to establish a methodology to solve the large advection problem, especially for fractures or cracks.

1.1 Governing equations

The three-dimensional *transient heat conduction-advection differential equation* may be written as follows [1]:

$$\rho c \left(\frac{\partial \phi}{\partial t} + [\mathbf{v}]^\top \nabla \phi \right) - [\nabla]^\top \mathbf{D}^T \nabla \phi - Q^T = 0 \quad \text{in} \quad \Omega \tag{1}$$

with Dirichlet and Neumann boundary conditions:

$$\phi = \bar{\phi}(x, y, x, t) \quad \text{on} \quad \Gamma_\phi \tag{2}$$

$$q_n^T = \bar{q}_n^T(x, y, z, t) \quad \text{on} \quad \Gamma_q \tag{3}$$

where ϕ is the nodal variable (temperature $[^oC]$), ρ and c are the density $[kg/m^3]$ and the thermal capacity $[J/(kg\ ^oC)]$ of the material, $Q^{(T)}$ is a thermal source term, $\mathbf{v}$ is the average fluid velocity field (e.g. Darcy's velocity of the fluid transporting heat), q_n^T is the flow normal to the boundary, $\mathbf{D}^T$ is the constitutive matrix of the conduction problem $[J/(s\ m\ ^oC)]$, which is a diagonal matrix if the material is thermally isotropic, ∇ is the gradient operator vector $\nabla = \left[\frac{\partial}{\partial x}\ \frac{\partial}{\partial y}\ \frac{\partial}{\partial z}\right]$, and $[\ ]^\top$ denotes the transposed of a vector or a matrix (not to be confused with super index *T* which stands for "thermal").

1.2 FEM standard formulation for the advection problem

Performing the spatial discretization of Eq. (1) in the context of the Finite Element Method (FEM), applying the Divergence Theorem to the first term of the equation, applying the Galerkin weighing ($w = N^{(1)}, N^{(2)}, ...$) and performing the time discretization using the Finite Difference Method (FDM), the following algebraic system of equations is obtained:

$$\left[\frac{1}{\Delta t} \mathbf{C} + \theta\ (\mathbf{K} + \mathbf{K_c}) \right] \Delta \boldsymbol{\phi}_{n+1} = -(\mathbf{K} + \mathbf{K_c}) \boldsymbol{\phi}_n + \mathbf{f} \tag{4}$$

where $\boldsymbol{\phi}$ is the nodal temperature vector, $\mathbf{C}$ is the thermal capacity matrix, $\mathbf{K}$ is the thermal conduction matrix, $\mathbf{K_c}$ is the thermal advective matrix and $\mathbf{f}$ is the thermal force vector, which are obtained by the assembly of the contribution of each element of the mesh and are defined by:

$$\mathbf{C} = \int_\Omega \rho c\ [\mathbf{N}]^\top \mathbf{N}\ \mathrm{d}\Omega \tag{5}$$

$$\mathbf{K} = \int_\Omega [\nabla \mathbf{N}]^\top \mathbf{D}^T \nabla \mathbf{N}\ \mathrm{d}\Omega \tag{6}$$

$$\mathbf{K_c} = \int_\Omega \rho c\ [\nabla \mathbf{N}]^\top \mathbf{v}\, \mathbf{B}\ \mathrm{d}\Omega \tag{7}$$

$$\mathbf{f} = \int_\Omega [\mathbf{N}]^\top Q^T\ d\Omega - \int_{\Gamma_q} [\nabla \mathbf{N}]^\top \bar{\mathbf{q}}^T\ \mathrm{d}\Gamma \tag{8}$$

1.3 Large advection: Péclet number and numerical instabilities

It is well known [1] that the standard Galerkin weighting in FEM is very well suited for diffusion-dominated problems, but it performs badly when transport effects dominate over the conduction (large advection). Determination of whether the fluid velocities are high or low is generally based on the so-called Péclet number [3], a non-dimensional number that relates the velocity of advection and the rate of diffusion, and it is defined for thermal problems as:

$$Pe = \rho c \frac{v\, h_{car}}{2k^T} \tag{9}$$

where v is the average fluid velocity value in the porous medium (i.e Darcy velocity), h_{car} is the characteristic length of the element (length of the element in the direction of the flow) and k^T is the thermal conduction of the material.

A simple academic example in 1-D is presented in order to demonstrate that the standard Galerkin weighting leads to oscillatory results when $Pe > 1$. The geometry (Figure 1) consists of a horizontal rod element divided in 8 segments of equal length L. Boundary conditions are: prescribed temperature to 0ºC at the left-hand side node of the rod, prescribed temperature to 80ºC at the right-hand side node of the rod, and a constant velocity from left to right. With the only variation of the velocity magnitude, four results are obtained with different Péclet numbers (Figure 2), where it is observed that the solutions exhibit oscillations when $Pe > 1$. Thus, when the fluid velocities are high enough and the advection dominates the problem it is necessary to use a more appropriate numerical method that does not result in oscillatory solutions.

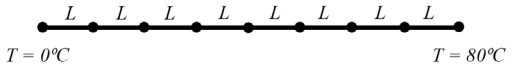


Figure 1: Geometry of the domain and boundary conditions.

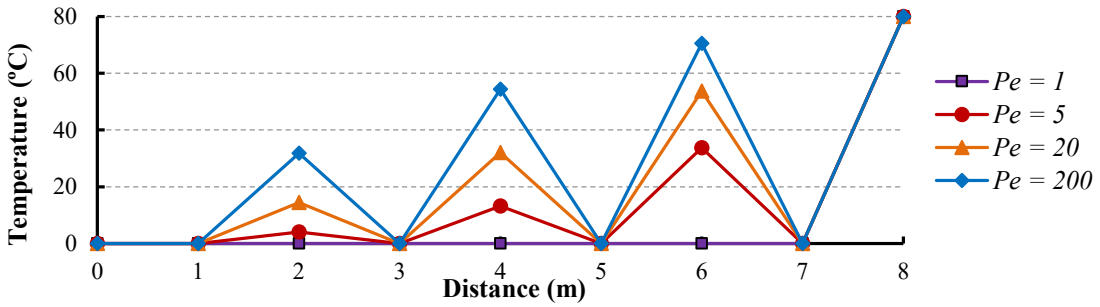


Figure 2: Solutions of the simple academic example for different velocities using the traditional Galerkin weighting method in FEM. Oscillations appears when $Pe > 1$.

2 STEADY-STATE LARGE ADVECTION USING THE SUPG METHOD

The most common method used in order to stabilize the diffusion-advection steady-state problem is the *Streamline Upwind Petrov-Galerkin* (SUPG) method [1]. The first *upwind* approach was proposed and applied in 1976 [4,5,6]. Then a new weighting function was proposed leading to the *Streamline Upwind* (SU) method [7], further developed as the SUPG method [8]. This method is based on the modification of the stiffness matrix by using modified weighting functions ($w \neq N^{(1)}, N^{(2)}, ...$), that are defined (in indicial notation) as:

$$w = N^{(a)} + \frac{\alpha_{opt}\, h_{car}}{2} \frac{v_i}{|\mathbf{v}|} \frac{\partial N^{(a)}}{\partial x_i} \tag{10}$$

where α_{opt} is the optimal value of α that must be used in order to obtain exact nodal values for any Péclet value [1]:

$$\alpha_{opt} = \coth|Pe| - \frac{1}{|Pe|} \tag{11}$$

Performing the spatial discretization of Eq. (1) by using the FEM, applying the Divergence Theorem to the first term of the equation and applying the Petrov-Galerkin weighing defined by Eq. (10), the following system of equations is obtained:

$$(\mathbf{K} + \mathbf{K_c} + \mathbf{K_{SUPG}})\,\boldsymbol{\phi} = (\mathbf{f} + \mathbf{f_{SUPG}}) \tag{12}$$

where $\mathbf{K_{SUPG}}$ and $\mathbf{f_{SUPG}}$ are the thermal stabilization matrix and the thermal force stabilization vector from the SUPG method. These matrices and vectors are obtained by the assembly of the contribution of each element of the mesh and are defined by:

$$\mathbf{K} = \int_{\Omega} [\mathbf{B}]^{\top}\, \mathbf{D}^{T}\, \mathbf{B}\, d\Omega \tag{13}$$

$$\mathbf{K_c} = \int_{\Omega} \rho c\, \mathbf{N}\, [\mathbf{v}]^{\top}\, \mathbf{B}\, d\Omega \tag{14}$$

$$\mathbf{K_{SUPG}} = \int_{\Omega} \left[\rho c \left(\frac{\alpha_{opt}\, h_{car}}{2|\mathbf{v}|}\, [\mathbf{v}]^{\top}\, \mathbf{B} \right) [\mathbf{v}]^{\top}\, \mathbf{B} + \left(\frac{\alpha_{opt}\, h_{car}}{2|\mathbf{v}|}\, [\mathbf{v}]^{\top}\, \boldsymbol{\nabla}\mathbf{B} \right) \mathbf{D}^{T}\, \mathbf{B} \right] d\Omega \tag{15}$$

$$\mathbf{f} = \int_{\Omega} [\mathbf{N}]^{\top}\, Q^{T}\, d\Omega - \int_{\Gamma_q} \mathbf{N}\, \bar{\mathbf{q}}^{T}\, d\Gamma \tag{16}$$

$$\mathbf{f_{SUPG}} = \int_{\Omega} \left[\left(\frac{\alpha_{opt}\, h_{car}}{2|\mathbf{v}|}\, [\mathbf{v}]^{\top}\, \mathbf{B} \right) Q^{T} \right] d\Omega \tag{17}$$

where $\mathbf{B} = \boldsymbol{\nabla}\mathbf{N}$ is the matrix containing the first-order derivatives of the shape functions. It must to be noted that the SUPG method is only applicable to steady-state regime.

2.1 Simple academic example: continuum medium in 2-D using the SUPG method

In order to verify that the SUPG method provides stable solutions when $Pe > 1$, a simple 2-D verification example is presented. The geometry consists of three horizontal layers of two different continuum materials (Figure 3 left). A constant flow velocity field from left to right (Figure 3 left) is imposed in the intermediate layer of the domain. The initial state of the thermal problem is shown in Figure 3 (right) and consists of a linear distribution of temperatures from left to right of the domain. The parameters for the numerical analysis are: heat capacity $\rho c = 1 \cdot 10^{-3}\, J/(m^3\, ^{o}C)$ and thermal conductivity $k^T = 2.5 \cdot 10^{-4}\, J/(s\, m\, ^{o}C)$.

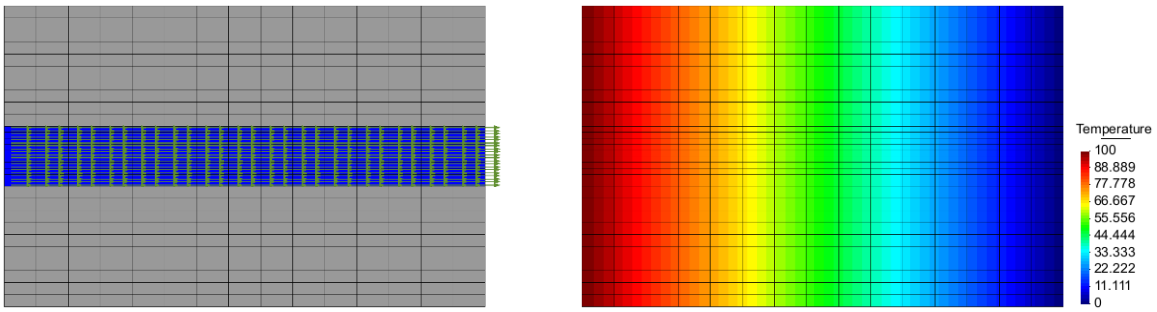


Figure 3: (left) Imposed velocities in the intermediate layer and (right) initial temperature distribution at *t=0* (after velocity application).

In the first calculations (Figure 4), the standard Galerkin weighting is used for a small advection problem, with Péclet numbers of 0.3 ($v = 0.006m/s$) in the left diagram, and 0.9 ($v = 0.017m/s$) in the right diagram. In both cases the SUPG and the standard FEM method both lead to the same stable solution depicted in the figure. Finally, the calculations are repeated using higher fluid velocities corresponding to $Pe = 7.2$ ($v = 0.135m/s$). In that case, Figure 5 (left) shows that the solution becomes oscillatory using the standard Galerkin weighting. However, using the SUPG method, the solution is stabilized (Figure 5 right).

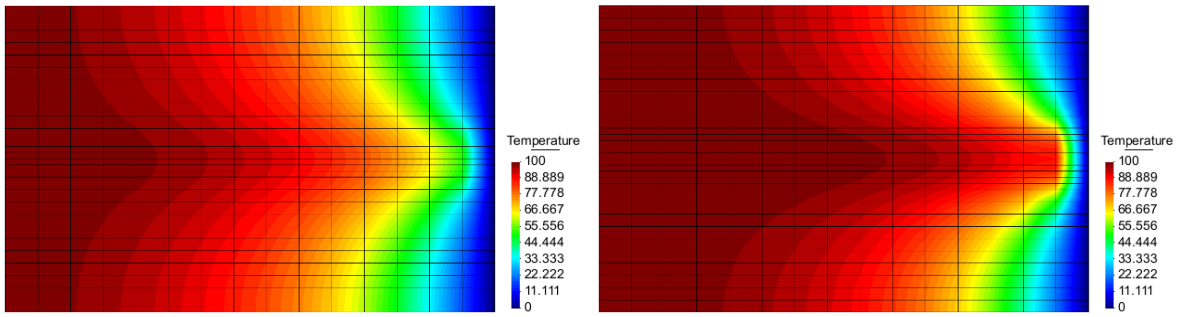


Figure 4: (left) Temperature distribution due to the applied velocities and *Pe = 0.3*. (right) Temperature distribution due to the applied velocities when the Péclet number increases but *Pe < 1* (*Pe = 0.9*).

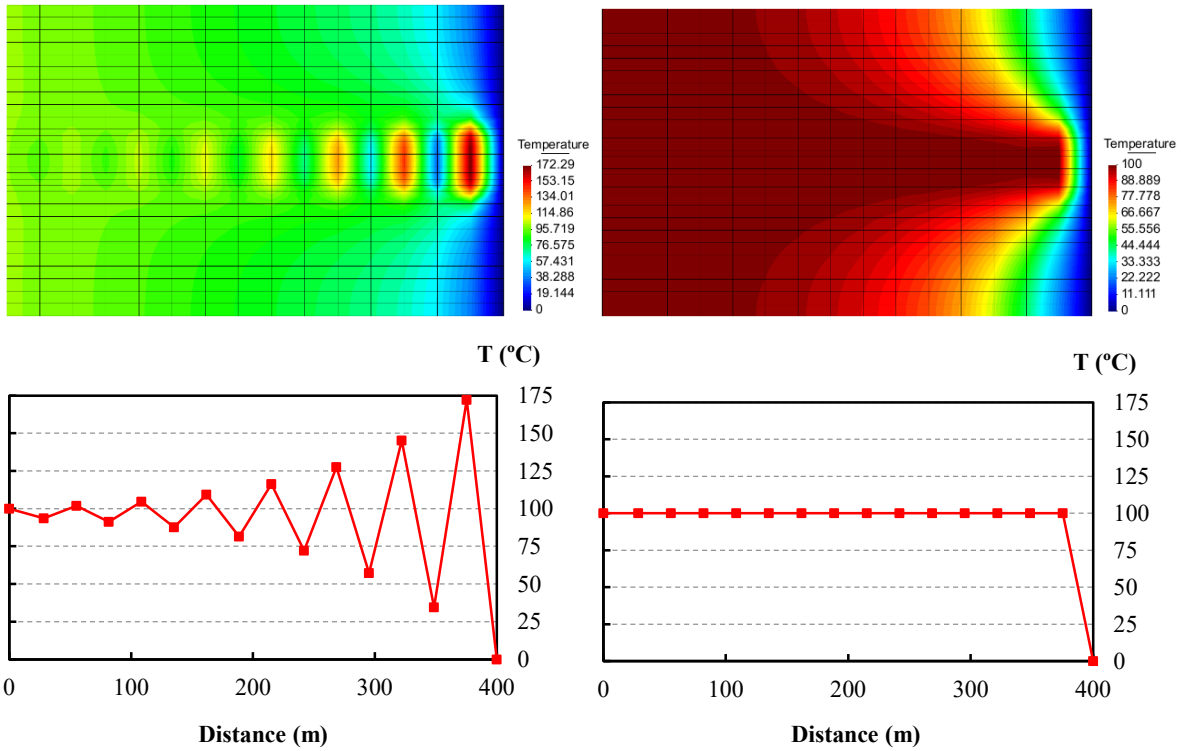


Figure 5: (left) Oscillatory distribution of temperatures using the standard Galerkin weighting when *Pe = 7.2* in the intermediate layer (the rest of the domain *Pe = 0*). (Right) Correct distribution of temperatures using the SUPG method for the same problem. Lower graphs represent the temperature distributions along the horizontal symmetry axis of the figures.

3 STEADY-STATE HEAT TRANSFER PROBLEM WITH LARGE ADVECTION FOR ZERO-THICKNESS INTERFACE ELEMENTS IN 2-D

In a 2D continuum, fractures and discontinuities may be represented individually by using double-nodded zero-thickness interface elements [9]. In this type of elements, one of the dimensions is collapsed to become 1-D line elements of "zero-thickness", and the integration is consequently reduced also by one order. The formulation of zero-thickness interface elements is composed of two parts (Figure 6): the formulation of the longitudinal flow along the interface and the formulation of the transversal flow across the interface, as described by [10,11]. The longitudinal flow is formulated along the mid-plane of the interface, and the nodal temperatures of the element are obtained by assuming that the temperature at each mid-plane node is the average of the temperature of the two nodes of the corresponding pair of the interface. Additional to the longitudinal flow, the existence of a discontinuity may also represent a resistance to the temperature flow in the transversal direction, which would result in a localized temperature drop across the interface. It is important to note that the large advection affects only the longitudinal flow. More details of the variables and geometry aspects that involve the double-nodded zero-thickness interface elements formulation can be found in [10,11,12].

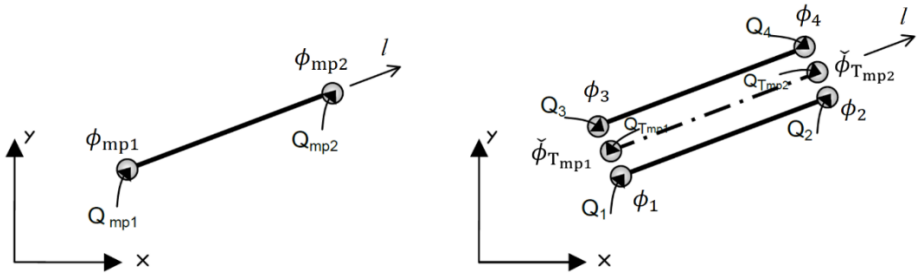


Figure 6: Zero-thickness elements used in the FE formulation with regard to longitudinal flow (left) and transversal flow (right).

3.1 Longitudinal flow

The longitudinal heat flow intensity q_{L}^{T} along the mid-plane of a discontinuity, corresponding to the accumulation of conduction (Fick´s law) plus advection flows in the transient regime, may be written as:

$$q_{\mathrm{L}}^{T} = -k_{\mathrm{L}}^{T} \frac{\partial \phi}{\partial l} + \rho c \phi v_{\mathrm{L}} \tag{18}$$

where k_{L}^{T} is the longitudinal thermal conductivity coefficient and v_{L} is the longitudinal velocity at the mid-plane of the interface element. The above q_{L}^{T} has the meaning of heat flow per unit area; by multiplying it by the interface aperture, r_N, one obtains the total heat flowing along the discontinuity (in 2-D per unit "depth" in the out-of-plane direction):

$$Q_{\mathrm{L}}^{T} = r_N \, q_{\mathrm{L}}^{T} = -r_N k_L^{T} \frac{\partial \phi}{\partial l} + r_N \rho c \phi v_{\mathrm{L}} \tag{19}$$

By enforcing heat conservation in a differential section of the interface element mid-plane (Figure 7), the continuity equation is obtained:

$$-\frac{\partial Q_{\mathrm{L}}^{T}}{\partial l} = r_N \rho c \frac{\partial \phi}{\partial t} \tag{20}$$

where source terms have not been considered for simplicity.

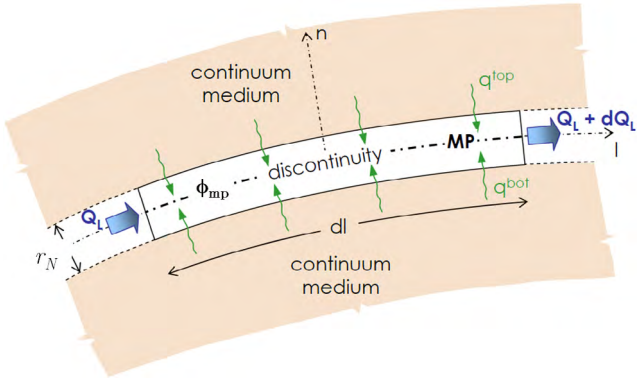


Figure 7: Thermal flow through a differential interface element.

Substituting now (19) into (20), leaving out transient terms, and taking into account that underlying flow is incompressible, leads to:

$$r_N \rho c \left(v_{\mathrm{L}} \frac{\partial \phi}{\partial l}\right) - r_N \frac{\partial}{\partial l}\left(k_L^T \frac{\partial \phi}{\partial l}\right) = 0 \quad \text{in} \quad \Omega_J \tag{21}$$

where Ω_J denotes the interface mid-plane domain. The boundary conditions are described by equations analogous to (2) and (3).

In order to stabilize the numerical solution of the steady-state large advection problem, the SUPG method defined in the previous section is used for zero-thickness interface elements.

Performing the spatial discretization of Eq. (21) along of the mid-plane of the interface by using the FEM, applying the Divergence Theorem to the first term of the equation, applying the Petrov-Galerkin weighing defined by Eq. (12), the following expression for the longitudinal flow along the mid-plane is obtained:

$$\mathbf{Q}_{\mathrm{L_{mp}}} = \left(\mathbf{K}_{\mathrm{L_{mp}}} + \mathbf{K}_{\mathbf{c},\mathrm{L_{mp}}} + \mathbf{K}_{\mathrm{L_{mp}}}^{\mathrm{SUPG}}\right) \boldsymbol{\phi}_{\mathrm{mp}} \tag{22}$$

where

$$\mathbf{K}_{\mathrm{L_{mp}}} = r_N \int_{\Omega_J} \left([\mathbf{B}_J]^{\mathrm{T}}\, k_L^T\, \mathbf{B}_J\right) \mathrm{d}\Omega_J \tag{23}$$

$$\mathbf{K}_{\mathbf{c},\mathrm{L_{mp}}} = r_N \rho c \int_{\Omega_J} \mathbf{N}_J\, v_{\mathrm{L}}\, \mathbf{B}_J\, \mathrm{d}\Omega_J \tag{24}$$

$$\mathbf{K}_{\mathrm{L_{mp}}}^{\mathrm{SUPG}} = r_N \rho c \int_{\Omega_J} \left(\frac{\alpha_{opt} h_{car}}{2|v_{\mathrm{L}}|} v_{\mathrm{L}} \mathbf{B}_J\right) v_{\mathrm{L}} \mathbf{B}_J\, \mathrm{d}\Omega_J + r_N \int_{\Omega_J} \left(\frac{\alpha_{opt} h_{car}}{2|v_{\mathrm{L}}|} v_{\mathrm{L}} \boldsymbol{\nabla}_J \mathbf{B}_J\right) k_L^T\, \mathbf{B}_J\, \mathrm{d}\Omega_J \tag{25}$$

$$\mathbf{B}_J = \frac{\partial \mathbf{N}_J}{\partial l} \qquad \boldsymbol{\phi}_{\mathrm{mp}} = \left[\phi_{mp}^{(1)}\ \phi_{mp}^{(2)}\right]^{\mathrm{T}} \tag{26}$$

In order to obtain the final FEM formulation related to the nodes of the mesh (and not to the mid-plane nodes), it is assumed that the temperature at the mid-plane is the average of the

temperature at the corresponding nodes of the element. Thus, the mid-plane temperatures of two-dimensional interfaces can be written in terms of the element's nodal temperatures (Figure 6) as:

$$\boldsymbol{\phi}_{\mathrm{mp}} = \begin{bmatrix} \phi_{mp}^{(1)} \\ \phi_{mp}^{(2)} \end{bmatrix} = \begin{bmatrix} \dfrac{\phi^{(1)} + \phi^{(3)}}{2} \\ \dfrac{\phi^{(2)} + \phi^{(4)}}{2} \end{bmatrix} = \begin{bmatrix} \frac{1}{2} & \frac{1}{2} \end{bmatrix} \boldsymbol{\phi}_{\mathrm{e}} = \widetilde{\mathbb{T}}_{\mathrm{L}}\, \boldsymbol{\phi}_{\mathrm{e}} \tag{27}$$

where $\widetilde{\mathbb{T}}_{\mathrm{L}} = \begin{bmatrix} \frac{1}{2} & \frac{1}{2} \end{bmatrix}$ is the longitudinal transference matrix and $\boldsymbol{\phi}_{\mathrm{e}}$ is the element temperature vector defined by:

$$\boldsymbol{\phi}_{\mathrm{e}} = \begin{bmatrix} \phi^{(1)} & \phi^{(3)} & \phi^{(2)} & \phi^{(4)} \end{bmatrix}^{\mathrm{T}} \tag{28}$$

Additionally, using the Principle of Virtual Work (PVW) in a discrete form leads to:

$$[\delta\boldsymbol{\phi}_{\mathrm{e}}]^{\mathrm{T}}\, \mathbf{Q}_{\mathrm{L_e}} = \left[\delta\boldsymbol{\phi}_{\mathrm{mp}}\right]^{\mathrm{T}}\, \mathbf{Q}_{\mathrm{L_{mp}}} \tag{29}$$

$$\mathbf{Q}_{\mathrm{L_e}} = \left[\widetilde{\mathbb{T}}_{\mathrm{L}}\right]^{\mathrm{T}} \mathbf{Q}_{\mathrm{L_{mp}}} \tag{30}$$

All the matrices and vectors defined at the mid-plane of the interface have to be transformed using the transference matrix, in order to obtain the similar relations between full element vectors including the pairs of nodes that appear in the FEM mesh. Substituting Eqs. (27) and (30) into Eq. (22) those relations are obtained as follows:

$$\mathbf{Q}_{\mathrm{L_e}} = \left(\mathbf{K}_{\mathrm{L_e}} + \mathbf{K}_{\mathbf{c},\mathrm{L_e}} + \mathbf{K}_{\mathrm{L_e}}^{\mathrm{SUPG}}\right) \boldsymbol{\phi}_{\mathrm{e}} \tag{31}$$

where

$$\mathbf{K}_{\mathrm{L_e}} + \mathbf{K}_{\mathbf{c},\mathrm{L_e}} + \mathbf{K}_{\mathrm{L_e}}^{\mathrm{SUPG}} = \left[\widetilde{\mathbb{T}}_{\mathrm{L}}\right]^{\mathrm{T}} \left(\mathbf{K}_{\mathrm{L_{mp}}} + \mathbf{K}_{\mathbf{c},\mathrm{L_{mp}}} + \mathbf{K}_{\mathrm{L_{mp}}}^{\mathrm{SUPG}}\right) \widetilde{\mathbb{T}}_{\mathrm{L}} \tag{32}$$

3.2 Transversal flow

Additional to the longitudinal flow, the existence of a discontinuity may also represent a resistance to the temperature flow in the transversal direction, which would result in a localized temperature drop across the interface (Figure 8). It is assumed that this temperature drop $\check{\phi}_N$ is related to the transverse heat flow q_N^T by a simple discrete version of Fick's law, in which the temperature drop plays the role of the temperature gradient:

$$q_N^T = \check{k}_N^T\, \check{\phi}_N \tag{33}$$

where $\check{k}_N^T$ is the transversal thermal conductivity of the interface.

The mid-plane potential thermal drop across the discontinuity is defined by the temperature difference between the two sides of the interface (Figure 8) as follows:

$$\check{\phi}_N = \phi_{bot} - \phi_{top} \tag{34}$$

$$\check{\boldsymbol{\phi}}_{\mathrm{N_{mp}}} = \begin{bmatrix} \check{\phi}_{N_{mp}}^{(1)} \\ \check{\phi}_{N_{mp}}^{(2)} \end{bmatrix} = \begin{bmatrix} \phi^{(1)} - \phi^{(3)} \\ \phi^{(2)} - \phi^{(4)} \end{bmatrix} = \begin{bmatrix} 1 & -1 \end{bmatrix} \boldsymbol{\phi}_{\mathrm{e}} = \widetilde{\mathbb{T}}_{\mathrm{N}}\, \boldsymbol{\phi}_{\mathrm{e}} \tag{35}$$

where $\widetilde{\mathbb{T}}_{\mathrm{N}} = [1 \quad -1]$ is the transference transversal matrix. That means that the potential thermal drop at the mid-plane node is the difference of potential between the two actual nodes.

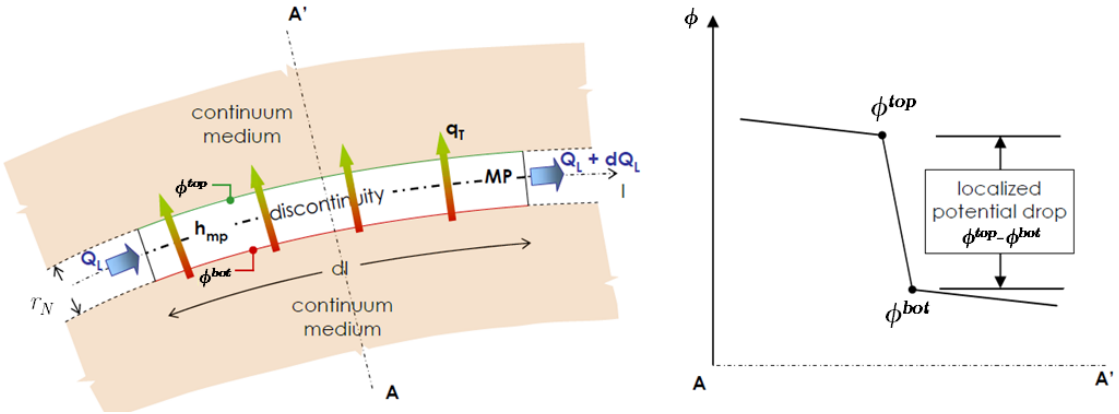


Figure 8: Scheme of the potential thermal drop across a differential interface element.

The FEM formulation for the mid-plane is obtained using the Principle of Virtual Work, which can be expressed for the transverse thermal flow problem as:

$$\left[\delta\check{\boldsymbol{\Phi}}_{\mathrm{Nmp}}\right]^{\mathrm{T}} \mathbf{Q}_{\mathrm{Nmp}} = \int_{\Omega_J} \delta\check{\phi}_{\mathrm{Nmp}}\, q^{T}_{N\mathrm{mp}}\, \mathrm{d}\Omega_J \qquad \forall\delta\check{\boldsymbol{\Phi}}_{\mathrm{Nmp}} \tag{36}$$

And substituting Eq. (33) into (36),

$$\mathbf{Q}_{\mathrm{Nmp}} = \mathbf{K}_{\mathrm{Nmp}}\check{\boldsymbol{\Phi}}_{\mathrm{Nmp}} \tag{37}$$

$$\mathbf{K}_{\mathrm{Nmp}} = \int_{\Omega_J} \left[\mathbf{N}_J\right]^{\mathrm{T}} \check{k}^{T}_{N}\, \mathbf{N}_J\, \mathrm{d}\Omega_J \tag{38}$$

where $\mathbf{K}_{\mathrm{Nmp}}$ is the transversal thermal conductivity matrix at the mid-plane. The vector of temperatures is defined by the same equation as in the longitudinal flow, Eq. (26).

Operating analogously to the longitudinal problem, the transversal thermal conductivity matrix at the nodes of the element is obtained:

$$\mathbf{K}_{\mathrm{N_e}} = \left[\widetilde{\mathbb{T}}_{\mathrm{N}}\right]^{\mathrm{T}} \mathbf{K}_{\mathrm{Nmp}}\, \widetilde{\mathbb{T}}_{\mathrm{N}} \tag{39}$$

3.3 Integrated formulation: longitudinal and transversal flow

To obtain an integrated conductivity matrix it is necessary to combine the longitudinal and the transversal flow as a sum of both, obtaining the final algebraic system of equation for each element as follows:

$$\left(\mathbf{K}_{\mathrm{L_e}} + \mathbf{K}_{\mathbf{c},\mathrm{L_e}} + \mathbf{K}^{\mathrm{SUPG}}_{\mathrm{L_e}} + \mathbf{K}_{\mathrm{N_e}}\right)\boldsymbol{\phi}_{\mathrm{e}} = 0 \tag{40}$$

where $\mathbf{K}_{\mathrm{L_e}}$, $\mathbf{K}_{\mathbf{c},\mathrm{L_e}}$, $\mathbf{K}^{\mathrm{SUPG}}_{\mathrm{L_e}}$ and $\mathbf{K}_{\mathrm{N_e}}$ are the longitudinal and transversal thermal conduction-advection matrices of the element defined by:

$$\mathbf{K}_{\mathrm{L_e}} = \left[\widetilde{\mathbb{T}}_{\mathrm{L}}\right]^{\top}\left(r_N \int_{\Omega_J}\left(\left[\mathbf{B}_J\right]^{\top} k_L^T\, \mathbf{B}_J\right) \mathrm{d}\Omega_J\right)\widetilde{\mathbb{T}}_{\mathrm{L}} \tag{41}$$

$$\mathbf{K}_{\mathbf{c},\mathrm{Le}} = \left[\widetilde{\mathbb{T}}_{\mathrm{L}}\right]^{\top}\left(r_N \rho c \int_{\Omega_J} \mathbf{N}_J\, v_{\mathrm{L}}\, \mathbf{B}_J\, \mathrm{d}\Omega_J\right)\widetilde{\mathbb{T}}_{\mathrm{L}} \tag{42}$$

$$\mathbf{K}_{\mathrm{Le}}^{\mathrm{SUPG}} = \left[\widetilde{\mathbb{T}}_{\mathrm{L}}\right]^{\top}\left(r_N \rho c \int_{\Omega_J}\left(\frac{\alpha_{opt} h_{car}}{2|\mathbf{v}_{\mathrm{L}}|} v_{\mathrm{L}} \mathbf{B}_J\right)\left[\mathbf{v}_{\mathrm{L}}\right]^{\top}\mathbf{B}_J\, \mathrm{d}\Omega_J + r_N \int_{\Omega_J}\left(\frac{\alpha_{opt} h_{car}}{2|\mathbf{v}_{\mathrm{L}}|} v_{\mathrm{L}} \boldsymbol{\nabla}\mathbf{B}_J\right) k_L^T\, \mathbf{B}_J\, \mathrm{d}\Omega_J\right)\widetilde{\mathbb{T}}_{\mathrm{L}} \tag{43}$$

$$\mathbf{K}_{\mathrm{N_e}} = \left[\widetilde{\mathbb{T}}_{\mathrm{N}}\right]^{\top}\left(\int_{\Omega_J}\left[\mathbf{N}_J\right]^{\top} \check{k}_N^T\, \mathbf{N}_J\, \mathrm{d}\Omega_J\right)\widetilde{\mathbb{T}}_{\mathrm{N}} \tag{44}$$

Finally, the global matrices of the system of Eq. (40) are obtained by the assembly of the contribution of each element of the mesh.

3.4 Simple academic example: steady-state large advection thermal problem in 2-D for interfaces using the SUPG method

The objective of this example is to compare some numerical results obtained with the standard Galerkin FEM method and the SUPG method, and verify that the latter provides stable solutions when *Pe >1* in a 2-D simple example using interfaces.

The geometry of this example consists of three horizontal layers with an interface at the symmetry axis (Figure 9 left), composed of 600 continuum elements and 20 interface elements. In order to visualize the heat transport, a known and constant velocity field from left to right ($v_{\mathrm{L}} = 0.057 m/s$, Figure 9 left) is imposed along the discontinuity, as a preferential path through the continuum medium.

The initial state of the thermal problem is shown in Figure 9 (right) and consists in a linear distribution of temperatures from left to right of the domain.

The numerical parameters for the continuum media are $\rho c = 1 \cdot 10^{-3}\, J/(m^3\, {}^{o}C)$ and $k^T = 7 \cdot 10^{-4}\, J/(s\, m\, {}^{o}C)$, and for zero-thickness interfaces $\rho c = 5 \cdot 10^{1}\, J/(m^3\, {}^{o}C)$, $k_L^T = 1 \cdot 10^{1}\, J/(m\, {}^{o}C\, s)$ and $\check{k}_N^T = 1 \cdot 10^{-03}\, J/(m^2\, {}^{o}C\, s)$.

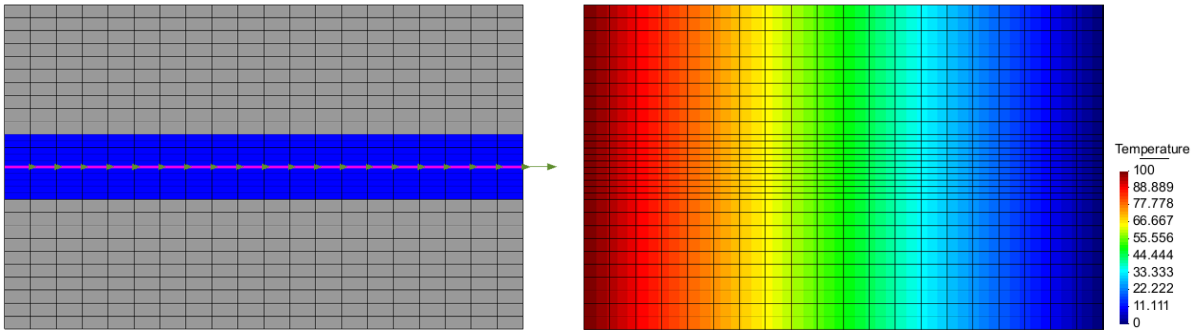


Figure 9: (left) Imposed velocities along the discontinuity (right) steady-state temperature distribution at t=0 (after velocity application).

In the first calculations, standard Galerkin weighing is used for the steady-state large advection problem (*Pe* = 3.8), leading to oscillatory results as shown in Figure 10 (left). However, using the new numerical solution (Petrov-Galerkin weighting, SUPG method) for

the interface element, the steady-state solution is stabilized, as shown in Figure 10 (right). In both cases the characteristic length of the element h_{car} is taken as the length of the element in the direction of the velocities.

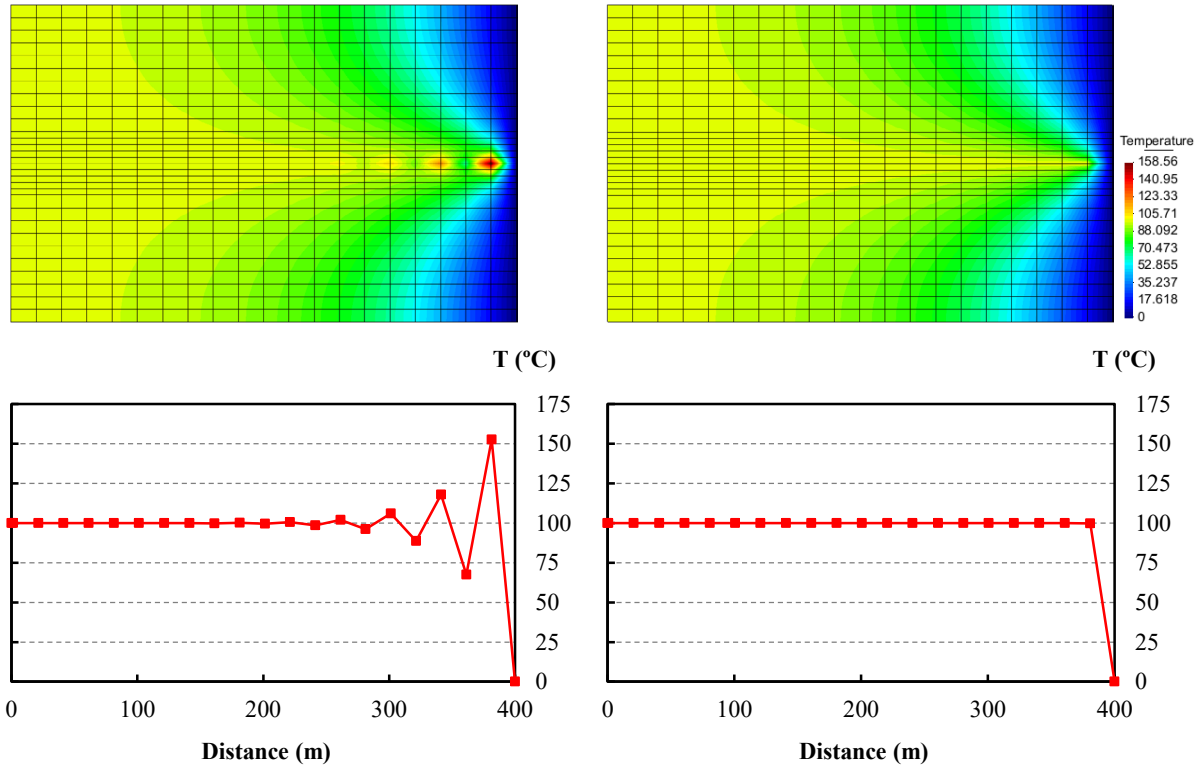


Figure 10: (left) Oscillatory distribution of temperatures using the standard Galerkin weighting when $Pe = 3.8$ along the discontinuity (the rest of the domain $Pe = 0$). (Right) Correct distribution of temperatures using SUPG method for the same problem. Lower graphs represent the temperature profiles along the mid-plane of discontinuity located in the symmetry axis of the problem.

4 CONCLUDING REMARKS

This paper describes the numerical FEM solution of the steady-state problem of heat flow in a porous medium, where a known Darcy velocity field of the pore fluid produces thermal transport with large advection. First, the traditional formulation using the standard Galerkin weighting has been reviewed. In this case a simple academic example shows that the solution becomes unstable when the advection dominates over the conduction ($Pe > 1$). Then, the SUPG method has been introduced, showing that this methodology stabilizes the solution when $Pe > 1$. Finally, the SUPG method has been formulated for 2-D zero-thickness interface elements. A verification example has been presented to show that this method is suitable for this type of elements when the advection is dominant for steady-state problems. Current work aims at the extension of the formulation presented to the transient problem with large advection, on the basis of the Taylor-characteristics method [1].

ACKNOWLEDGEMENTS
This work was partially supported by research grant BIA2016-76543-R from MEC (Madrid), which includes European FEDER funds, and 2017SGR-1153 from Generalitat de Catalunya (Barcelona). The first author also acknowledges his FPU scholarship from MEC (Madrid).

REFERENCES

[1] Zienkiewicz, O. & Taylor, R., *The Finite Element Method: Vol 3. Fluid Dynamics.* Fifth ed. Oxford: Butterworth-Heinemann (2000).
[2] Pérez, A. *THM coupling with large advection in fractured rock masses using zero-thickness interface elements.* Doct. Thesis. Universitat Politècnica de Catalunya, Barcelona (2018).
[3] Huysmans, M. & Dassargues, A. Review of the use of Péclet numbers to determine the relative importance of advection and diffusion in low permeability environments. *Hydrogeology Journal*. **13**:895-904, (2004).
[4] Zienkiewicz, O., Gallagher, R. & Hood, P., Newtonian and non-Newtonian viscous incompressible flow. Temperature induced flows and finite element solutions. *The Mathematics of Finite Element Methods (ed J. Whiteman). Academic Press, London.,* Volume II, (1976).
[5] Christie, I., Griffiths, A. & Zienkiewicz, O. Finite element methods for second orde differential equations with significant first derivatives. *International Journal for Numerical Methods in Engineering.* **10**:1389-96 (1976).
[6] Zienkiewicz, O., Heinrich, J. & Huyakorn, P. M. A., An upwind finite element scheme for two dimensional convective transport equations.. *Int. J. Num. Meth. Eng.,* **10**:131-144, (1977).
[7] Hughes, T. & Brooks, A. A multidimensional upwind scheme with no crosswind diffusion. *In ASME Monograph AMD-34 (Hughes, T.J.R., Ed.). NYC.,* Volume 34 (1979).
[8] Brooks, A. & Hughes, T. Streamline upwind/Petrov-Galerkin formulations for convection dominated flows with particular emphasis on the incompressible Navier-Stokes equations. *Computer Methods in Applied Mechanics and Engineering,* **32**:199-259, (1982).
[9] Goodman, R., Taylor, R. & Brekke, T.,. A model for the mechanics of jointed rock. *ASCE Journal of the Soil Mechanics and Foundations Division,* **94**:637–659, (1968).
[10] Segura, J., Carol, I. On zero-thickness interface elements for diffusion problems. *Int. J. Num. Anal.Meth.Geomech.,* **28**:947-962 (2004).
[11] Segura, J., Carol, I. Coupled H-M analysis using zero-thickness interface elements with double nodes. Part I: Theoretical model, and Part II: Verification and application. *Int. J. Num. Anal.Meth.Geomech.,* **32**:2083-2123 (2008).
[12] Garolera, D. *Zero-thickness interface elements in petroleum geomechanics: sand production and hydraulic fracture.* PhD Thesis. Universitat Politècnica de Catalunya, Barcelona (2017).

XV International Conference on Computational Plasticity. Fundamentals and Applications
COMPLAS 2019
E. Oñate, D.R.J. Owen, D. Peric, M. Chiumenti & Eduardo de Souza Neto (Eds)

AN OPTIMIZATION OF THE LOCAL HALL-PETCH RELATIONSHIP USING SLIP TRACE ANALYSIS TECHNIQUE AND SCALE TRANSITION RULES: APPLICATION IN EQUIAXED TI-6AL-4V TITANIUM ALLOY

FATNA. BENMESSAOUD*, MOHAMMED CHEIKH*, VINCENT. VELAY*, VANESSA. VIDAL*, HIROAKI. MATSUMOTO†,

* ICA, Toulouse University, CNRS, IMT Mines Albi, INSA, UPS, ISAE-SUPAERO
Campus Jarlard, 81013 Albi Cedex 09, France
e-mail: ica@mines-albi.fr, web page: http://www.mines-albi.fr/

† Department of Advanced Materials Science
Faculty of Engineering and Design Kagawa University
2217-20, Hayashi-cho, Kagawa 761-0396, Takamatsu, Japan
e-mail: matsu_h@eng.kagawa-u.ac.jp - Web page: https://www.kagawa-u.ac.jp

Key words: Multi-Scale Optimization, Ti-6Al-4V, Slip Trace Analysis, Scale Transition Rules, Critical Resolved Shear Stress (CRSS), Grain Size Effects.

Abstract. The aim of this work is to optimize the relative and the absolute Critical Resolved Shear Stress (CRSS) of slip mechanism in α-phase of Ti-6Al-4V titanium alloy. The influence of grain size is then modeled through a local Hall-Petch relationship. A slip trace analysis technique coupled with statistical reasoning were used to identify the CRSS ratios of basal $\langle a \rangle$, prismatic $\langle a \rangle$ and pyramidal $\langle c + a \rangle$ slip systems. The multi-scale transition rule of Berveiller-Zaoui was then used to determine the absolute CRSS in three different microstructures; Ti-6Al-4V with ultra fine grains (UFG), fine grains (FG) and standard grains (SD). Finally, the local Hall-Petch relationship was optimized. As expected, plastic deformation is mainly accommodated by prismatic and then basal slip systems. Due to their high CRSS, sliding in pyramidal systems is more difficult. Grain size shows a significant role on the activation of slip systems. By increasing the grain size, the CRSS of each slip system type decreases and thus sliding becomes easier in coarse grains.

1 INTRODUCTION

The multi-scale modeling of mechanical behavior of materials essentially requires to identify the local parameters. An accurate prediction of the material properties at different scales strongly depends on the local model formulation as well as the identification procedure of its parameters .

In Hexagonal Closed Packed (HCP) materials such as pure titanium, the plastic behavior is mainly accommodated by twinning and crystallographic sliding mechanisms. However, addition of some alloying elements such as aluminum limits the role of twinning mechanism [1–4] which is the case of Ti-6Al-4V alloy. In this alloy, three several types of slip systems namely basal $\langle a \rangle$, prismatic $\langle a \rangle$ and pyramidal $\langle c+a \rangle$ can accommodate the plastic strain. The Critical Resolved Shear Stress (CRSS) varies from a type to another [5]. Therefore, the identification of this parameter for titanium and its alloys remains difficult and only the relative values have been estimated in most of previous works [5–9]. Moreover, the CRSS not only depends on the HCP material (Ti, Zr, Mg ...) or the type of slip systems but also on the morphology features such as the grain size.

The present contribution aims to identify the CRSS of basal $\langle a \rangle$, prismatic $\langle a \rangle$ and pyramidal $\langle c+a \rangle$ slip systems types in three microstructures of Ti-6Al-4V titanium alloy. Hence, the Hall-Petch relationship can be optimized. In order to achieve this goal, a slip trace analysis technique was proposed to identify the slip systems by comparing their observed traces with those given by the theoretical rules. Then, a statistical methodology adapted from the work of Li et al. [6] was used to estimate the CRSS ratios. Finally, a multi-scale numerical optimization was proposed to determine the absolute CRSS and therefore the local Hall-Petch relationship.

2 OPTIMIZATION PROCEDURE

Four microstructures of an equiaxed Ti-6Al-4V reported in Tab.1 were used in the optimization procedure. T2-SD is characterized by a weak crystallographic texture and coarse grains, that allows identifying the slip traces of sliding systems after tensile tests and thus estimate their CRSS ratios with lesser effects of crystallographic texture. T1-UFG, T1-FG and T1-SD are characterized by ultra fine grains, fine grains and standard grains microstructures respectively and the same crystallographic texture (all are strongly textured). Consequently, the effects of the grain size on the activation of sliding systems and therefore optimization of their absolute CRSS in relationship with the grain size can be addressed. The morphology as well the crystallographic texture of these Ti-6Al-4V microstructures are illustrated in Fig. 1 and 2.

Table 1: grain size and crystallographic texture of the investigated microstructures of Ti-6Al-4V.

Microstructure	**grain size** (μm)	**Crystallographic texture**
T1-UFG	0.6	Strong
T1-FG	3	Strong
T1-SD	7.5	Strong
T2-SD	7.5	Weak

Tensile test until 5% of strain was performed for T2-SD. Then, experimental slip traces were then observed by Scanning Electron Microscopy (SEM) and identified using the ori-

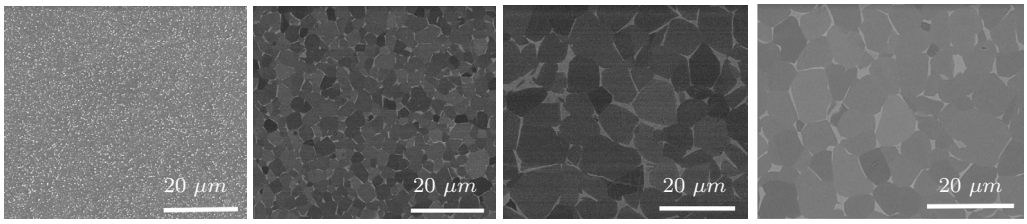


Figure 1: Ti-6A-4V microstructures of (a)T1-UFG, (b) T1-FG, (c) T1-SD and (d) T2-SD

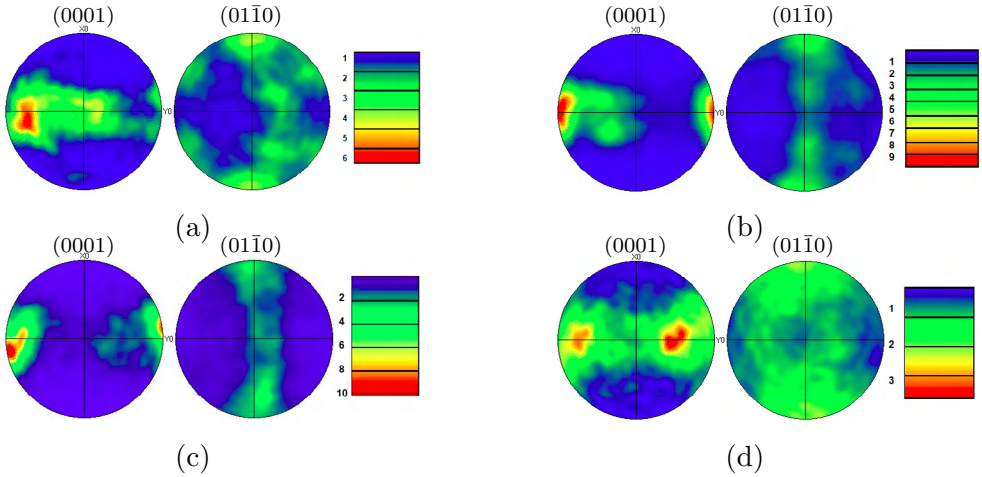


Figure 2: (0001) and $\{10\bar{1}0\}$ pole figures of different Ti-6Al-4V microstructures (a) T1-UFG, (b) T1-FG, (c) T1-SD, (d) T2-SD.

entation data (i.e. Euler angles) provided by Electron Backscatter Diffraction (EBSD) analysis and `ImageJ` software. The prediction of the most likely slip systems to be activated was carried out by comparing the results from theoretical slip trace with the experimental results. An algorithm was developed to calculate the Schmid factor and slip trace angle of each theoretical slip system relative to the orientation of a single grain. The activation of the actual and theoretical slip system was then recorded as a function of slip system type and the Schmid factor as shown in Tab. 2. 3.

230 grains were analyzed, 134 of them present a slip traces (58%). The Schmid factor of 3 basal $\langle a \rangle$, 3 prismatic $\langle a \rangle$ and 6 pyramidal $\langle c+a \rangle$ systems was computed for each yield grain. 1608 values are therefore determined (Tab. 3). The statistical procedure proposed by Li et al. [6] was adapted in this paper for identifying the CRSS ratios. The experimental observed slip systems were compared with those given by the theory by dividing each pair in Tab. 2 designed by O_{ij} with the corresponding theoretical pair T_{ij} in Tab. 3 as:

$$R_{ij} = O_{ij}/T_{ij} \tag{1}$$

Where i is the slip systems type, it can be: basal $\langle a \rangle$ $(i = 1)$, prismatic $\langle a \rangle$ $(i = 2)$ and

Table 2: Distribution of experimental observed slip systems O_{ij} as function of their schmid factor

Schmid factor	**Basal** $\langle a \rangle$ **(34%)**	**Prismatic** $\langle a \rangle$ **(44%)**	**Pyramidal** $\langle c+a \rangle$ **(22%)**
0-0.05	1	3	0
0.05-0.10	0	5	0
0.10-0.15	1	5	0
0.15-0.20	0	8	0
0.20-0.25	3	7	1
0.25-0.30	3	9	2
0.30-0.35	4	8	4
0.35-0.40	7	10	6
0.40-0.45	13	10	9
0.45-0.50	28	12	16

pyramidal $\langle c+a \rangle$ $(i = 3)$ and j is the Schmid factor range $(1 \leq j \leq 10)$. The obtained results are presented in Tab. 4. If all the slip systems represented in Tab. 2 are actually

Table 3: Distribution of theoretical slip systems T_{ij} as function of their Schmid factor for 134 yield grains

Schmid factor	**Basal** $\langle a \rangle$	**Prismatic** $\langle a \rangle$	**Pyramidal** $\langle c+a \rangle$
0-0.05	43	75	114
0.05-0.10	39	65	108
0.10-0.15	55	57	102
0.15-0.20	39	42	88
0.20-0.25	29	31	72
0.25-0.30	45	35	73
0.30-0.35	33	33	66
0.35-0.40	45	24	68
0.40-0.45	30	24	67
0.45-0.50	44	16	46

activated in the experiment, the value of each pair R_{ij} in Tab. 4 would be 1. However, the activation of slip systems depends on their Schmid factor. Thus, slip systems with small Schmid factor is less likely to be activated than those with large Schmid factor (Tab. 4). By comparing the ratios R_{ij} of the same row in Tab. 4, it can be clearly observed that the critical resolved shear stress (CRSS) is different from a family to another. The representation of these ratios follows a cubic distribution (See Fig. 3), thus, using this table as a reference, the theoretical values presented in Tab. 3 can be formulated with cubic weighting function [6] as:

$$w_{ij} = T_{ij} \times ((j-1)/9)^3 \tag{2}$$

This function allowed to reduce the values of theoretical sliding having a small Schmid factor. In this step, the effects of crystallographic texture were eliminated. However,

Table 4: Distribution of the ratios R_{ij} between observed and theoretical slip systems

Schmid factor	**Basal** $\langle a \rangle$	**Prismatic**$\langle a \rangle$	**Pyramidal**$\langle c+a \rangle$
0-0.05	0.023	0.04	0
0.05-0.10	0	0.077	0
0.10-0.15	0.0181	0.087	0
0.15-0.20	0	0.1904	0
0.20-0.25	0.10	0.22	0.014
0.25-0.30	0.067	0.027	0.028
0.30-0.35	0.121	0.29	0.061
0.35-0.40	0.56	0.417	0.089
0.40-0.45	0.43	0.42	0.13
0.45-0.50	0.64	0.75	0.34

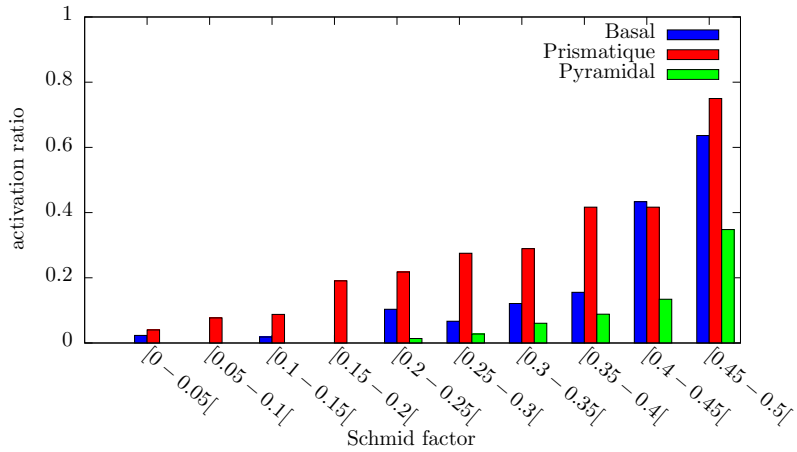


Figure 3: Evolution of the ratios R for each slip system type as function of Schmid factor range.

the CRSS of the different sliding types is not yet taken into consideration. The results obtained using Eq. 2 are presented in Tab. 5.

The probability density function of each pair of Tab. 5 is given as:

$$p_{ij} = \frac{w_{ij}}{\sum_{i=1}^{3} \sum_{j=1}^{10} w_{ij}} \tag{3}$$

Hence, the prediction of the number of slip systems which can be observed experimentally was possible. It can be performed by multiplying the obtained probability density function by the total number N of observed sliding O_{ij} presented in Tab. 2 as:

$$E_{ij} = p_{ij} \times N \tag{4}$$

The results were then reported for each pair (slip system-Schmid factor) in Tab. 6.

It was observed that the results of the expected slip systems (Tab. 6) were significantly different from those experimentally observed (Tab. 2). Noted that until this step, the

CRSSs are always assumed the same for all the slip systems types. The next step of this methodology consists to minimize the difference between the observed and expected values by identifying the CRSSs ratios. The expected number of slip systems E_{ij} can be

Table 5: Distribution of weighted theoretical slip systems w_{ij} for the 134 yielding grains

Schmid factor	**Basal** $\langle a \rangle$	**Prismatic** $\langle a \rangle$	**Pyramidal** $\langle c+a \rangle$
0-0.05	0	0	0
0.05-0.10	0.053	0.089	0.1481
0.10-0.15	0.603	0.625	1.119
0.15-0.20	1.445	1.556	3.259
0.20-0.25	2.546	2.721	6.320
0.25-0.30	7.716	6.001	12.517
0.30-0.35	9.778	9.778	19.555
0.35-0.40	21.173	11.292	31.994
0.40-0.45	21.069	16.855	47.059
0.45-0.50	44	16	46

thus modified by introducing the CRSS of each type i designated by τ_i^c as:

$$M_{ij} = \frac{a}{\tau_i^c} E_{ij} \tag{5}$$

Where a is a unknown parameter, it can be found if at least one of the $CRSS_i$ is determined. However, in the most of previous investigations, only the relative CRSSs were identified (see [6]). The optimal values of CRSS can be estimated by minimizing the

Table 6: Distribution of the expected slip systems E_{ij} as function of their Schmid factor

Schmid factor	**Basal**$\langle a \rangle$	**Prismatic**$\langle a \rangle$	**Pyramidal**$\langle c+a \rangle$
0-0.05	0	0	0
0.05-0.10	0.0274	0.0457	0.0759
0.10-0.15	0.309	0.320	0.573
0.15-0.20	0.740	0.797	1.671
0.20-0.25	1.305	1.395	3.241
0.25-0.30	3.956	3.077	6.418
0.30-0.35	5.013	5.013	10.027
0.35-0.40	10.857	5.790	16.406
0.40-0.45	10.804	8.643	24.129
0.45-0.50	22.562	8.204	23.588

cumulative error Er between the number of observed O_{ij} slip systems and the expected ones M_{ij}. This can be performed using the square difference equation as:

$$Er = \sqrt{d^2(O_{ij}, M_{ij})} = \sqrt{\sum_{i=1}^{3} \sum_{j=1}^{10} (O_{ij} - M_{ij})^2} \tag{6}$$

By replacing M_{ij} with $\frac{a}{\tau_i^c}E_{ij}$, Er can be rewritten:

$$Er = \sqrt{\sum_{i=1}^{3}\sum_{j=1}^{10}(O_{ij} - \frac{a}{\tau_i^c}E_{ij})^2} \tag{7}$$

The optimal τ_i^{*c} was therefore obtained by solving the first-order derivative equation as:

$$\frac{\partial Er}{\partial \tau_i^c} = 0 \rightarrow \tau_i^{*c} = a\frac{\sum_{j=1}^{10}(E_{ij})^2}{\sum_{j=1}^{10}O_{ij}E_{ij}} \tag{8}$$

The unknown parameter a vanishes by calculating the ratio between τ^{*c}. The relative CRSS are therefore given by:

$$\frac{\tau_1^{*c}}{\tau_2^{*c}} : \frac{\tau_2^{*c}}{\tau_2^{*c}} : \frac{\tau_3^{*c}}{\tau_2^{*c}} = 1.36 : 1 : 2.84 \tag{9}$$

for basal $\langle a\rangle$:prismatic $\langle a\rangle$:pyramidal $\langle c+a\rangle$ respectively. The obtained results were compared with some results found in the literature (Tab. 7).

Table 7: Estimated relative CRSS in comparison with those found in the literature for Ti-6Al-4V titanium alloy.

Basal $\langle a\rangle$	Prismatic $\langle a\rangle$	Pyramidal $\langle a\rangle$	Reference
1.36	1	2.84	the present study
1.05	1	1.68	[10]
1-1.5	1	3-5	[8]
0.93-1.3	1	1.1-1.6	[5]
1.43	1	4.23	[9]

In order to investigate the effects of grain size on the CRSS, tensile tests were performed until the beginning of plastic behavior (about 1 to 1.3% of total strain) for all T1-UFG, T1-FG and T1-SD microstructures presented in Tab. 1. A multi-scale numerical optimization of absolute CRSS was then carried out using the obtained CRSS ratios, the tensile curves, the crystallographic orientations of 500 grains, a local behavior model and scale transition rules available in `Z_optim` library as summarized in Fig. 4. Noted that the same procedure was repeated for each microstructure. The local behavior model of Méric-Cailletaud [11]was used. It gives a phenomenological description of each slip system behavior. In this model, the slip strain rate $\dot{\gamma}^s$ of system s is given as a form of power function of the resolved shear stress τ^s as:

$$\dot{\gamma}^s = \dot{v}^s sign(\tau^s - \chi^s) \tag{10}$$

With:

$$\dot{v}^s = \left\langle \frac{|\tau^s - \chi^s| - r^s}{K} \right\rangle^n \tag{11}$$

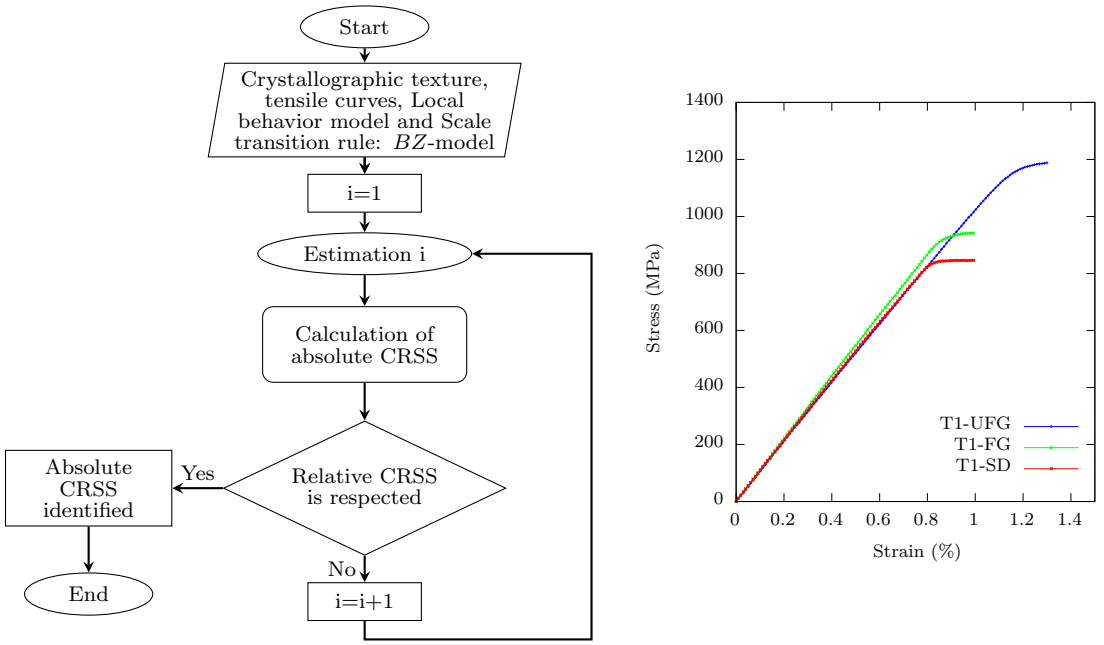


Figure 4: Methodology for optimizing the absolute CRSS: (a) the followed procedure uses a local behavior model of Méric-Cailletaud [11], Berveiller-Zaoui model [12] (BZ) for transition Scale and model parameters of Dick et al [10]. (b) The experimental tensile curves.

Where χ^s and r^s are the kinematic and the isotropic hardening variables of slip system s respectively, τ^s is the resolved shear stress of systems s , K and n characterize the material viscosity. The isotropic hardening r^s was considered constant and equal to the absolute Critical Resolved Shear Stress CRSS (τ_c^s).

$$r^s = \tau_c^s \tag{12}$$

Moreover, the hardening nonlinearity can be expressed by the nonlinear kinematic hardening of slip systems according to the Armstrong-Frederick equation: [13]:

$$\chi^s = C\alpha^s \tag{13}$$

With:

$$\dot{\alpha}^s = \dot{\gamma}^s - d\alpha^s\dot{\chi}^s \tag{14}$$

Where α^s is a state variable describing the evolution of kinematic hardening in slip system s. C and d are the material parameters. The kinematic hardening and the viscosity parameters determined by Dick et al. [10] were used. Berveiller-Zaoui model [12] (BZ) was chosen as a scale transition rule for the identification procedure. For this model, the localization of the stress tensor is given by Eq. (15):

$$\sigma^g = \Sigma + 2\mu\alpha(1-\beta) : (E^p - \varepsilon^{g,p}) \tag{15}$$

with:

$$\frac{1}{\alpha} = 1 + \frac{3}{2}\mu\frac{E^p_{eq}}{\Sigma_{eq}} \tag{16}$$

and

$$\beta = \frac{2(4-5\nu)}{15(1-\nu)} \tag{17}$$

where σ^g and Σ are respectively the stresses at mesoscopic (grain) and macroscopic (global) scales, $\varepsilon^{g,p}$ and E^p are respectively the local and global plastic strain, ν is the Poisson ratio, μ the shear modulus and ρ stands for a non linear accommodation parameter whose formulation is a function of the Von-Mises equivalent inelastic strain E^p_{eq} and stress Σ_{eq} at the macroscopic scale.

The comparison between the identification results of CRSS provided by the Meric-Cailletaud model using the Berveiller-Zaoui transition rule and the experimental tensile results is illustrated in Fig. 5.

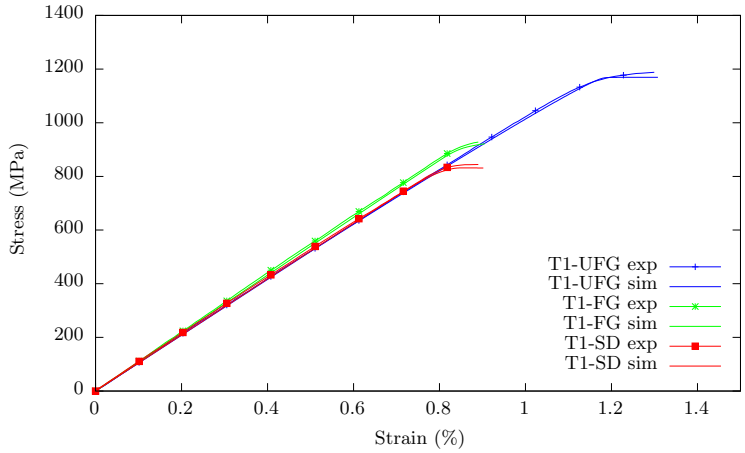


Figure 5: Comparison between experimental strain-stress curves and those provided using the identified CRSS and BZ transition scale rule for each Ti-6Al-4V microstructure

For each Ti-6Al-4V microstructure, the absolute CRSSs of slip systems types were reported in Tab. 8. they can be then formulated as a function of the inverse square root of the average grain size (Fig. 6) according to the Hall-Petch relationship [14, 15]:

$$\tau^c_i = K^{hp}_i \frac{1}{\sqrt{D}} + \tau^0_i \tag{18}$$

Where K^{hp}_i and τ^0_i are the Hall Petch slope and the friction lattice stress of slip systems type i respectively and D is the average grain size.

The local Hall-Petch slope was found to be 146, 114 and 225 $MPa.m^{-1/2}$ for basal $\langle a \rangle$, prismatic $\langle a \rangle$ and pyramidal $\langle c+a \rangle$ systems respectively. The increase of grain size leads to decrease the CRSS and therefore facilitates the accommodation of the plastic strain in coarse grains. The Hall-Petch slope of pyramidal $\langle c+a \rangle$ systems is very high compared

Table 8: Absolute Critical Resolved Shear Stress (CRSS).

Material	**Absolute CRSS (MPa)**		
	Basal	Prismatic	Pyramidal
T1-UFG	390	290	790
T1-FG	320	240	570
T1-SD	240	170	580
T1-SD	240	170	580

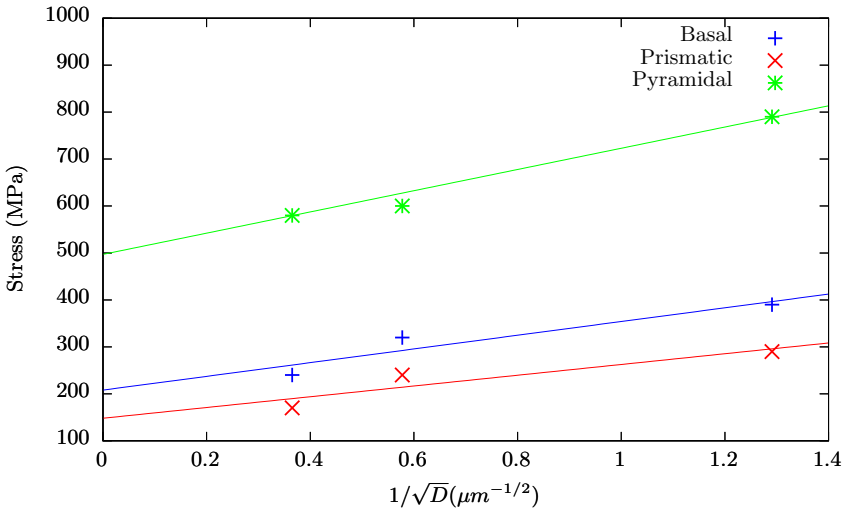


Figure 6: Effect of grain size on CRSS of slip systems types

with those of prismatic and basal systems which can lead to a significant decrease of pyramidal $\langle c+a \rangle$ CRSS in large grains.

3 CONCLUSIONS

A slip trace analysis followed by a statistical reasoning and a multi-scale numerical optimization were utilized in order to identify the critical resolved shear stress CRSS of basal $\langle a \rangle$, prismatic $\langle a \rangle$ and pyramidal $\langle c+a \rangle$ systems in three microstructures of Ti-6Al-4V alloy. A significant role of grain size was shown; by increasing the average grain size, the CRSS decreases . This effect was correctly modeled by the Hall-Petch relationship. Moreover, the dependence of CRSS on grain size varies from a type of sliding to another. Pyramidal $\langle c+a \rangle$ systems type shows the highest Hall-Petch slope, this leads to a significant decreasing of pyramidal CRSS in large grains which justifies its activation although its relative CRSS is more than 2.5 times of prismatic CRSS.

Acknowledgments

The authors wish to thank French Occitanie Region for the growth of research activities at the IMT-Mines Albi and Figeac IUT. The authors would also like to gratefully

acknowledge the NHK spring company-Japan (https://www.nhkspg.corjp/eng/) for its support by providing the material used in the contribution.

REFERENCES

[1] M. Philippe, E. Bouzy, and J. Fundenberger, "Textures and anisotropy of titanium alloys," *Materials Science Forum*, vol. 273-275, pp. 511–522, 1998.

[2] G. Gilles, W. Hammami, V. Libertiaux, O. Cazacu, J. Yoon, T. Kuwabara, A. Habraken, and L. Duchne, "Experimental characterization and elasto-plastic modeling of the quasi-static mechanical response of TA6V at room temperature," *Solids and Structures*, vol. 48, pp. 1277–1289, 2011.

[3] W. Tirry, F. Coghe, S. Bouvier, M. Gasperini, L. Rabet, and D. Schryvers, "A multiscale characterization of deformation twins in Ti-6Al-4V sheet material deformed by simple shear," *Materials Science and Engineering A*, vol. 527, pp. 4136–4145, 2010.

[4] J. Williams, R. Baggerly, and N. Paton, "Deformation behavior of HCP TiAl alloy single crystals," *Metallurgical and Materials Transactions A*, vol. 33, pp. 837–850, 2002.

[5] J. M. Perilla and J. Sevillano, "Two-dimensional sections of the yield locus of a Ti-6Al-4V alloy with a strong transverse_type crystallographic a-texture," *Materials Science and Engineering A*, vol. 201, pp. 103–110, 1995.

[6] H. Li, D. Mason, T. Bieler, C. Boelert, and M. Crimp, "Methodology for estimating the critical resolved shear stress ratios of a-phase Ti using EBSD-based trace analysis," *Acta Materialia*, vol. 61, pp. 7555–7567, 2013.

[7] D. Dunst and H. Mecking, "Analysis of experimental and theoretical rolling textures of two-phase titanium alloys," *Zeitschrift fuer Metallkunde*, vol. 87, pp. 498–507, 1996.

[8] J. Mayeur and D. McDowell, "A three-dimensional crystal plasticity model for duplex Ti6Al4V," *Plasticity*, vol. 23, pp. 1457–1485, 2007.

[9] S. Semiatin and T. Bieler, "Effect of texture and slip mode on the anisotropy of plastic flow and flow softening during hot working of Ti6Al4V," *Metallurgical and Materials Transactions A*, vol. 32, pp. 1787–1799, 2001.

[10] T. Dick and G. Cailletaud, "Fretting modelling with a crystal plasticity model of Ti6Al4V," *Computational Materials Science*, vol. 38, pp. 113–125, 2006.

[11] L. Méric, P. Poubanne, and G. Cailletaud, "Single crystal Modeling for Structural Calculations: Part 1model presentation," *Engineering Materials and Technology*, vol. 113, pp. 162–170, 1991.

[12] M. Berveiller and A. Zaoui, "An extension of the self-consistent scheme to plastically-flowing polycrystals," *Mechanics and Physics of Solids*, vol. 26, pp. 325–344, 1978.

[13] C. Frederick and P. Armstrong, "A mathematical representation of the multiaxial bauschinger effect," *Materials high temperature*, vol. 24, pp. 1–26, 2007.

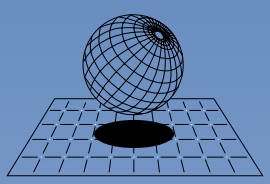
[14] E. Hall, "The deformation and ageing of mild steel: III discussion of results," *Proceedings of the Physical Society B*, vol. 64, pp. 747–753, 1951.

[15] N. Petch, "The cleavage strength of polycrystals," *the Iron and Steel Institute*, vol. 174, pp. 25–28, 1953.

AUTHORS INDEX

Akasaka, I. 48
Akiyama, M. 48
Amiri-Rad, A. 385
Antoulas, A. C. 145
Askew, J. 261
Atsushi, S. 402
Balzani, D. 170
Barandiarán, L. 435
Barriere, T. 369
Behrens, B. A. 211
Benmessaoud, F. 577
Bertoli, C. 519
Bessette, C. 553
Boher, C. 577
Brands, D. 223
Brezolin, A. 281
Brosius, A. 467, 499
Brunig, M. 489
Brünig, M. 81
Bumbieler, F. 544
Cao, X. 322
Carol, I. 411, 420, 435, 447, 456, 565
Chakir, R. 427
Cheikh, M. 577
Chekired, M. 553
Chugreev, A. 211
Cocks, A. C. F. 261
Commend, S. 529
Crusat, L. 420
Côté, J. 553
De Bellis, M. L. 235
de Francisco, M. 411
de Gregorio, D. 100
de Saxcé, G. 322
dos Santos, T. 281
DŽugan, J. 489
Eliáš, J. 305
Farahnak, P. 489
Felder, S. 249
Furushima, T. 38
Garcea, G. 100
Garolera, D. 420
Gens, A. 544
Gerke, S. 81, 489
Gosea, I. V. 145
Govaert, L. E. 385
Gries, T. 249
Grilli, N. 261
Guilleaume, C. 499
Haslinger, J. 133
Hennebert, J. 529
Hesseler, S. 249
Hikaru, S. 21
Hiromichi, M. 21
Holthusen, H. 249
Hora, P. 519
Hoyos Giraldo, J. D. 427
Hoyos Palacio, L. 334
Hrubesova, E. 112
Huang, W. 510
Iizuka, T. 31
Ijima, K. 314
Itoh, Y. 38
Jahns, H. 479
Jaqués, I. 447
Jinga, L. 553
Kajikawa, S. 48
Kawaguchi, H. 48
Keiichiro, K. 21
Kimura, H. 360
Kock, C. 211
Kuboki, T. 48
Kuonen, P. 529
Kuroda, K. 69
Küsters, N. 467
Lafarge, R. 467
Landkammer, P. 201
Leonetti, L. 100
Liaudat, J. 435, 456
Liguori, F. 100
Liu, W. 31
Lloberas-Valls, O. 157
Lu, C. 402
Lu, H. 510
Lukeš, V. 343
Lyamin, A. 121
López, C. M. 435, 456
Magisano, D. 100
Market, B. 322
Martemyanov, A. N. 536
Martínez, A. 456
Matsui, K. 181
Miyagawa, T. 38
Miyaki, H. 378

Mohammed, S. 369
Müller, D. 189
Nakamura, S. 181
Nguyen, A. D. 322
Nizam, Z. M. 314
Niño Navia, J. A. 427
Obiya, H. 314
Ohara, K. 59
Oliver, J. 157
Oueslati, A. 322
Pastukhov, L. V. 385
Petrov, Y. 395, 536
Pingaro, M. 235
Podlich, N. 121
Pohlkemper, F. 249
Pospisil, P. 112
Prat, P. 565
Pérez, A. 565
Qin, S. J. 510
Ramful, R. 360
Rapantova, N. 112
Raschi, M. 157
Reese, S. 249
Repin, S. 133
Rezai-Aria, F. 577
Rohan, E. 343
Rosa, P. 281
Rossi, R. 281
Rund, M. 489
Sakuma, A. 354, 360, 378
Sano, M. 59
Scheunemann, L. 223
Schröder, J. 223
Sekimoto, M. 59
Selma, B. 553
Selyutina, N. 395
Shimoda, K. 69
Shohei, K. 21
Shutov, A. V. 273
Simon, J. W. 249
Sloan, S. 121
Stahl, K. 189
Steinmann, P. 201
Stoffel, M. 322
Stoll, P. 519
Streichenberger , B. 427
Suzuki, S. 181
Suárez Guerrero, G. 334, 427
Sysala, S. 133
Takashi, K. 21
Tarleton, E. 261
Terashita, Y. 48
Tetsushi, O. 21
Thiele, K. 479
Tobie, T. 189
Tomiyama, M. 93
Tourchi, S. 544
Trovalusci, P. 235
Tulke, M. 499
Turjanicová, J. 343
Uebing, S. 223
Ueda, S. 354
Unglaub, J. 479
Urbanek, M. 489
Vallejo Morales, E. 334
van Dommelen, J. A. W. 385
Vaunat, J. 544
Vaz jr., M. 93
Velay, V. 577
Vidal, V. 577
Vu, M. N. 544
Vulliet, L. 529
Wattel, S. 529
Yamada, R. 38
Yamada, T. 181
Yamane, K. 69
Yasui, H. 38
Yoshihara, S. 38
Yoshizaki, N. 314
Yu, H. B. 510
Zahn, A. 170
Zhang, J. 378
Zhu, J. 31
Zistl, M. 81
Zuccaro, G. 100



CIMNE

International Center
for Numerical Methods in Engineering

www.cimne.com